Rauwendaal
Polymer Extrusion

Chris Rauwendaal

Polymer Extrusion

5th Edition

With contributions from
Paul J. Gramann, Bruce A. Davis, and Tim A. Osswald

HANSER

Hanser Publishers, Munich

Hanser Publications, Cincinnati

The Author:
Dr. Chris Rauwendaal
10556 Combie Road # 6677, Auburn, CA 95602-8908, USA

Distributed in North and South America by:
Hanser Publications
6915 Valley Avenue, Cincinnati, Ohio 45244-3029, USA
Fax: (513) 527-8801
Phone: (513) 527-8977
www.hanserpublications.com

Distributed in all other countries by
Carl Hanser Verlag
Postfach 86 04 20, 81631 München, Germany
Fax: +49 (89) 98 48 09
www.hanser-fachbuch.de

The use of general descriptive names, trademarks, etc., in this publication, even if the former are not especially identified, is not to be taken as a sign that such names, as understood by the Trade Marks and Merchandise Marks Act, may accordingly be used freely by anyone. While the advice and information in this book are believed to be true and accurate at the date of going to press, neither the author nor the editors nor the publisher can accept any legal responsibility for any errors or omissions that may be made. The publisher makes no warranty, express or implied, with respect to the material contained herein.

Library of Congress Cataloging-in-Publication Data
Rauwendaal, Chris.
Polymer extrusion / Chris Rauwendaal. -- 5th edition.
pages cm
ISBN 978-1-56990-516-6 (hardcover) -- ISBN 978-1-56990-539-5 (e-book) 1. Plastics--Extrusion. I. Title.
TP1175.E9R37 2013
668.4'13--dc23
2013037810

Bibliografische Information Der Deutschen Bibliothek
Die Deutsche Bibliothek verzeichnet diese Publikation in der Deutschen Nationalbibliografie; detaillierte bibliografische Daten sind im Internet über <http://dnb.d-nb.de> abrufbar.

ISBN 978-1-56990-516-6
E-Book ISBN 978-1-56990-539-5

All rights reserved. No part of this book may be reproduced or transmitted in any form or by any means, electronic or mechanical, including photocopying or by any information storage and retrieval system, without permission in writing from the publisher.

© Carl Hanser Verlag, Munich 2014
Production Management: Steffen Jörg
Coverconcept: Marc Müller-Bremer, www.rebranding.de, München
Coverdesign: Stephan Rönigk
Typsetted, printed and bound by Kösel, Krugzell
Printed in Germany

Preface to the Fifth Edition

It has been twelve years since the fourth edition of Polymer Extrusion was published and twenty six years since the book was first published. Extrusion technology continues to advance; as a result, a fifth edition is needed to keep the Polymer Extrusion book up to date and relevant.

New material has been added throughout the book. The general literature survey has been updated since several books on extrusion have been published since 2001. A new theory for predicting developing melt temperatures has been incorporated into Chapter 7. This theory allows accurate prediction of changes in melt temperature along the length of the extruder; complete analytical solutions are presented to the relevant equations. As a result, melt temperatures can be predicted without having to result to numerical techniques and computer simulation.

In Chapter 8, a new section on efficient extrusion of medical devices has been added. It covers good manufacturing practices in medical extrusion and automation. The effect of processing conditions and screw design on molecular degradation is covered in detail. Screws designs that minimize molecular degradation are discussed and explained.

In Chapter 11, the section on gels in extruded products has been expanded as this continues to be a problem experienced by many extrusion companies. There is also a new section on discolored specks in extruded products. In this section expressions are included that allow prediction of the incidence and frequency of specks or gels based on their frequency in the incoming raw material. Included is a discussion on new instruments that are now available to detect defects in pellets produced at the resin supplier with the ability to remove pellets with defects from the pellet stream.

Over the past five to ten years very high speed single screw extruders have been developed. These extruders are now commercially available and they are used by dozens of companies around the world. These machines run at speeds up to 1500 rpm; they achieve outputs that are about an order of magnitude above those of conventional extruders. This high speed single screw extruder technology is one of the most significant developments. Therefore, this topic has been added to the new edition in Chapter 2.

The author would like to thank Professor Jürgen Miethlinger and Michael Aigner from Johannes Kepler University in Linz, Austria for checking equations in Chapter 7 and finding a few mistakes; these have been corrected.

The author would also like to thank Cheryl Hamilton and Nadine Warkotsch at Carl Hanser Verlag for their encouragement and help in making the fifth edition a reality. The author is grateful for a long and fruitful relationship with Carl Hanser Verlag. Finally, I would like to extend a special thank you to my wife Sietske. She has supported and helped me in many ways for the past forty years. I am grateful for her love and support—I feel very fortunate to have a friend and spouse who makes life worth living.

Chris Rauwendaal
Auburn, California
October 2013

Contents

Preface to the Fifth Edition V

1 Introduction 1
1.1 Basic Process 1
1.2 Scope of the Book 2
1.3 General Literature Survey 3
1.4 History of Polymer Extrusion 6

Part I – Extrusion Machinery 11
2 Different Types of Extruders 13
2.1 The Single Screw Extruder 13
2.1.1 Basic Operation 15
2.1.2 Vented Extruders 16
2.1.3 Rubber Extruders 17
2.1.4 High-Speed Extrusion 22
2.1.4.1 Melt Temperature 22
2.1.4.2 Extruders without Gear Reducer 23
2.1.4.3 Energy Consumption 23
2.1.4.4 Change-over Resin Consumption 23
2.1.4.5 Change-over Time and Residence Time 24
2.2 The Multiscrew Extruder 24
2.2.1 The Twin Screw Extruder 24
2.2.2 The Multiscrew Extruder With More Than Two Screws 25
2.2.3 The Gear Pump Extruder 27
2.3 Disk Extruders 28
2.3.1 Viscous Drag Disk Extruders 28
2.3.1.1 Stepped Disk Extruder 28
2.3.1.2 Drum Extruder 30
2.3.1.3 Spiral Disk Extruder 31
2.3.1.4 Diskpack Extruder 31
2.3.2 The Elastic Melt Extruder 35
2.3.3 Overview of Disk Extruders 36
2.4 Ram Extruders 36
2.4.1 Single Ram Extruders 37
2.4.1.1 Solid State Extrusion 38
2.4.2 Multi Ram Extruder 41

2.4.3 Appendix 2.1 . . . 42
2.4.3.1 Pumping Efficiency in Diskpack Extruder . . . 42

3 Extruder Hardware . . . 49
3.1 Extruder Drive . . . 49
3.1.1 AC Motor Drive System . . . 49
3.1.1.1 Mechanical Adjustable Speed Drive . . . 50
3.1.1.2 Electric Friction Clutch Drive . . . 50
3.1.1.3 Adjustable Frequency Drive . . . 51
3.1.2 DC Motor Drive System . . . 53
3.1.2.1 Brushless DC Drives . . . 55
3.1.3 Hydraulic Drive System . . . 55
3.1.4 Comparison of Various Drive Systems . . . 58
3.1.5 Reducer . . . 59
3.1.6 Constant Torque Characteristics . . . 60
3.2 Thrust Bearing Assembly . . . 61
3.3 Barrel and Feed Throat . . . 64
3.4 Feed Hopper . . . 68
3.5 Extruder Screw . . . 70
3.6 Die Assembly . . . 72
3.6.1 Screens and Screen Changers . . . 72
3.7 Heating and Cooling Systems . . . 75
3.7.1 Electric Heating . . . 75
3.7.1.1 Resistance Heating . . . 75
3.7.1.2 Induction Heating . . . 76
3.7.2 Fluid Heating . . . 77
3.7.3 Extruder Cooling . . . 77
3.7.4 Screw Heating and Cooling . . . 80

4 Instrumentation and Control . . . 85
4.1 Instrumentation Requirements . . . 85
4.1.1 Most Important Parameters . . . 86
4.2 Pressure Measurement . . . 87
4.2.1 The Importance of Melt Pressure . . . 87
4.2.2 Different Types of Pressure Transducers . . . 88
4.2.3 Mechanical Considerations . . . 92
4.2.4 Specifications . . . 93
4.2.5 Comparisons of Different Transducers . . . 96
4.3 Temperature Measurement . . . 96
4.3.1 Methods of Temperature Measurement . . . 97
4.3.2 Barrel Temperature Measurement . . . 100
4.3.3 Stock Temperature Measurement . . . 102
4.3.3.1 Ultrasound Transmission Time . . . 105
4.3.3.2 Infrared Melt Temperature Measurement . . . 106
4.4 Other Measurements . . . 107
4.4.1 Power Measurement . . . 107

4.4.2 Rotational Speed . . . 109
4.4.3 Extrudate Thickness . . . 110
4.4.4 Extrudate Surface Conditions . . . 114
4.5 Temperature Control . . . 116
4.5.1 On-Off Control . . . 117
4.5.2 Proportional Control . . . 119
4.5.2.1 Proportional-Only Control . . . 119
4.5.2.2 Proportional and Integral Control . . . 123
4.5.2.3 Proportional and Integral and Derivative Control . . . 124
4.5.2.4 Dual Sensor Temperature Control . . . 125
4.5.3 Controllers . . . 126
4.5.3.1 Temperature Controllers . . . 126
4.5.3.2 Power Controllers . . . 126
4.5.3.3 Dual Output Controllers . . . 128
4.5.4 Time-Temperature Characteristics . . . 128
4.5.4.1 Thermal Characteristics of the System . . . 128
4.5.4.2 Modeling of Response in Linear Systems . . . 130
4.5.4.3 Temperature Characteristics with On-Off Control . . . 133
4.5.5 Tuning of the Controller Parameters . . . 135
4.5.5.1 Performance Criteria . . . 135
4.5.5.2 Effect of PID Parameters . . . 136
4.5.5.3 Tuning Procedure When Process Model Is Unknown . . . 137
4.5.5.4 Tuning Procedure When Process Model Is Known . . . 138
4.5.5.5 Pre-Tuned Temperature Controllers . . . 139
4.5.5.6 Self-Tuning Temperature Controllers . . . 140
4.6 Total Process Control . . . 140
4.6.1 True Total Extrusion Process Control . . . 141

Part II – Process Analysis . . . 147

5 Fundamental Principles . . . 149

5.1 Balance Equations . . . 149
5.1.1 The Mass Balance Equation . . . 149
5.1.2 The Momentum Balance Equation . . . 150
5.1.3 The Energy Balance Equation . . . 151
5.2 Basic Thermodynamics . . . 153
5.2.1 Rubber Elasticity . . . 157
5.2.2 Strain-Induced Crystallization . . . 159
5.3 Heat Transfer . . . 160
5.3.1 Conductive Heat Transfer . . . 160
5.3.2 Convective Heat Transfer . . . 161
5.3.3 Dimensionless Numbers . . . 161
5.3.3.1 Dimensional Analysis . . . 161
5.3.3.2 Important Dimensionless Numbers . . . 163
5.3.4 Viscous Heat Generation . . . 168
5.3.5 Radiative Heat Transport . . . 169
5.3.5.1 Dielectric Heating . . . 171
5.3.5.2 Microwave Heating . . . 173

5.4 Basics of Devolatilization 175
5.4.1 Devolatilization of Particulate Polymer 180
5.4.2 Devolatilization of Polymer Melts 181
Appendix 5.1 185
Example: Pipe Flow of Newtonian Fluid 185

6 Important Polymer Properties 191
6.1 Properties of Bulk Materials 191
6.1.1 Bulk Density 191
6.1.2 Coefficient of Friction 194
6.1.3 Particle Size and Shape 200
6.1.4 Other Properties 201
6.2 Melt Flow Properties 202
6.2.1 Basic Definitions 202
6.2.2 Power Law Fluid 208
6.2.3 Other Fluid Models 213
6.2.4 Effect of Temperature and Pressure 214
6.2.5 Viscoelastic Behavior 218
6.2.6 Measurement of Flow Properties 220
6.2.6.1 Capillary Rheometer 220
6.2.6.2 Melt Index Tester 223
6.2.6.3 Cone and Plate Rheometer 227
6.2.6.4 Slit Die Rheometer 228
6.2.6.5 Dynamic Analysis 230
6.3 Thermal Properties 233
6.3.1 Thermal Conductivity 234
6.3.2 Specific Volume and Morphology 236
6.3.3 Specific Heat and Heat of Fusion 239
6.3.4 Specific Enthalpy 241
6.3.5 Thermal Diffusivity 242
6.3.6 Melting Point 245
6.3.7 Induction Time 245
6.3.8 Thermal Characterization 247
6.3.8.1 DTA and DSC 247
6.3.8.2 TGA 247
6.3.8.3 TMA 248
6.3.8.4 Other Thermal Characterization Techniques 248
6.4 Polymer Property Summary 248

7 Functional Process Analysis 255
7.1 Basic Screw Geometry 255
7.2 Solids Conveying 258
7.2.1 Gravity Induced Solids Conveying 259
7.2.1.1 Pressure Distribution 262
7.2.1.2 Flow Rate 265
7.2.1.3 Design Criteria 266

7.2.2 Drag Induced Solids Conveying 268
7.2.2.1 Frictional Heat Generation 282
7.2.2.2 Grooved Barrel Sections 284
7.2.2.3 Adjustable Grooved Barrel Extruders 296
7.2.2.4 Starve Feeding Versus Flood Feeding 302
7.3 Plasticating 305
7.3.1 Theoretical Model of Contiguous Solids Melting 306
7.3.1.1 Non-Newtonian, Non-Isothermal Case 316
7.3.2 Other Melting Models 326
7.3.3 Power Consumption in the Melting Zone 330
7.3.4 Computer Simulation 332
7.3.5 Dispersed Solids Melting 333
7.4 Melt Conveying 340
7.4.1 Newtonian Fluids 343
7.4.1.1 Effect of Flight Flanks 348
7.4.1.2 Effect of Clearance 350
7.4.1.3 Power Consumption in Melt Conveying 353
7.4.2 Power Law Fluids 356
7.4.2.1 One-Dimensional Flow 356
7.4.2.2 Two-Dimensional Flow 361
7.4.3 Non-Isothermal Analysis 367
7.4.3.1 Newtonian Fluids with Negligible Viscous Dissipation 367
7.4.3.2 Non-Isothermal Analysis of Power Law Fluids 374
7.4.3.3 Developing Temperatures 387
7.4.3.4 Estimating Fully Developed Melt Temperatures 404
7.4.3.5 Assumption of Stationary Screw and Rotating Barrel 411
7.5 Die Forming 419
7.5.1 Velocity and Temperature Profiles 420
7.5.2 Extrudate Swell 429
7.5.3 Die Flow Instabilities 431
7.5.3.1 Shark Skin 431
7.5.3.2 Melt Fracture 432
7.5.3.3 Draw Resonance 434
7.6 Devolatilization 435
7.7 Mixing 441
7.7.1 Mixing in Screw Extruders 442
7.7.1.1 Distributive Mixing in Screw Extruders 447
7.7.2 Static Mixing Devices 457
7.7.2.1 Geometry of Static Mixers 460
7.7.2.2 Functional Performance Characteristics 464
7.7.2.3 Miscellaneous Considerations 468
7.7.3 Dispersive Mixing 469
7.7.3.1 Solid-Liquid Systems 469
7.7.3.2 Liquid-Liquid System 471
7.7.4 Backmixing 483
7.7.4.1 Cross-Sectional Mixing and Axial Mixing 483

7.7.4.2 Residence Time Distribution 485
7.7.4.3 RTD in Screw Extruders 487
7.7.4.4 Methods to Improve Backmixing 488
7.7.4.5 Conclusions for Backmixing 490
Appendix 7.1 491
Appendix 7.2 492
Appendix 7.3 493

8 Extruder Screw Design 509
8.1 Mechanical Considerations 510
8.1.1 Torsional Strength of the Screw Root 510
8.1.2 Strength of the Screw Flight 512
8.1.3 Lateral Deflection of the Screw 514
8.2 Optimizing for Output 519
8.2.1 Optimizing for Melt Conveying 519
8.2.2 Optimizing for Plasticating 530
8.2.2.1 Effect of Helix Angle 532
8.2.2.2 Effect of Multiple Flights 532
8.2.2.3 Effect of Flight Clearance 534
8.2.2.4 Effect of Compression Ratio 536
8.2.3 Optimizing for Solids Conveying 537
8.2.3.1 Effect of Channel Depth 537
8.2.3.2 Effect of Helix Angle 538
8.2.3.3 Effect of Number of Flights 539
8.2.3.4 Effect of Flight Clearance 539
8.2.3.5 Effect of Flight Geometry 539
8.3 Optimizing for Power Consumption 540
8.3.1 Optimum Helix Angle 541
8.3.2 Effect of Flight Clearance 543
8.3.3 Effect of Flight Width 544
8.4 Single-Flighted Extruder Screws 548
8.4.1 The Standard Extruder Screw 549
8.4.2 Modifications of the Standard Extruder Screw 550
8.5 Devolatilizing Extruder Screws 553
8.5.1 Functional Design Considerations 554
8.5.2 Various Vented Extruder Screw Designs 558
8.5.2.1 Conventional Vented Extruder Screw 558
8.5.2.2 Bypass Vented Extruder Screw 559
8.5.2.3 Rearward Devolatilization 560
8.5.2.4 Multi-Vent Devolatilization 561
8.5.2.5 Cascade Devolatilization 562
8.5.2.6 Venting through the Screw 563
8.5.2.7 Venting through a Flighted Barrel 564
8.5.3 Vent Port Configuration 565
8.6 Multi-Flighted Extruder Screws 568
8.6.1 The Conventional Multi-Flighted Extruder Screw 568

8.6.2 Barrier Flight Extruder Screws . . . 569
8.6.2.1 The Maillefer Screw . . . 572
8.6.2.2 The Barr Screw . . . 575
8.6.2.3 The Dray and Lawrence Screw . . . 578
8.6.2.4 The Kim Screw . . . 579
8.6.2.5 The Ingen Housz Screw . . . 580
8.6.2.6 The CRD Barrier Screw . . . 581
8.6.2.7 Summary of Barrier Screws . . . 582
8.7 Mixing Screws . . . 584
8.7.1 Dispersive Mixing Elements . . . 584
8.7.1.1 The CRD Mixer . . . 602
8.7.1.2 Mixers to Break Up the Solid Bed . . . 616
8.7.1.3 Summary of Dispersive Mixers . . . 618
8.7.2 Distributive Mixing Elements . . . 619
8.7.2.1 Ring or Sleeve Mixers . . . 621
8.7.2.2 Variable Depth Mixers . . . 622
8.7.2.3 Summary of Distributive Mixers . . . 623
8.8 Efficient Extrusion of Medical Devices . . . 624
8.8.1 Introduction . . . 624
8.8.2 Good Manufacturing Practices in Medical Extrusion . . . 625
8.8.3 Automation of the Medical Extrusion Process . . . 625
8.8.4 Minimizing Polymer Degradation . . . 626
8.8.5 Melt Temperatures Inside the Extruder . . . 626
8.8.6 Melt Temperatures and Screw Design . . . 627
8.8.7 Molecular Degradation and Screw Design . . . 630
8.8.8 Conclusions . . . 634
8.9 Scale-Up . . . 635
8.9.1 Common Scale-Up Factors . . . 635
8.9.2 Scale-Up for Heat Transfer . . . 638
8.9.3 Scale-Up for Mixing . . . 639
8.9.4 Comparison of Various Scale-Up Methods . . . 640
8.10 Rebuilding Worn Screws and Barrels . . . 642
8.10.1 Application of Hardfacing Materials . . . 644
8.10.1.1 Oxyacetylene Welding . . . 644
8.10.1.2 Tungsten Inert Gas Welding . . . 645
8.10.1.3 Plasma Transfer Arc Welding . . . 645
8.10.1.4 Metal Inert Gas Welding . . . 646
8.10.1.5 Laser Hardfacing . . . 646
8.10.2 Rebuilding of Extruder Barrels . . . 646

9 Die Design . . . 653
9.1 Basic Considerations . . . 654
9.1.1 Balancing the Die by Adjusting the Land Length . . . 655
9.1.2 Balancing by Channel Height . . . 659
9.1.3 Other Methods of Die Balancing . . . 662

9.2 Film and Sheet Dies 663
9.2.1 Flow Adjustment in Sheet and Film Dies 664
9.2.2 The Horseshoe Die 667
9.3 Pipe and Tubing Dies 668
9.3.1 Tooling Design for Tubing 671
9.3.1.1 Definitions of Various Draw Ratios 672
9.3.1.2 Land Length 673
9.3.1.3 Taper Angles 674
9.3.1.4 Special Features 676
9.4 Blown Film Dies 676
9.4.1 The Spiral Mandrel Geometry 679
9.4.2 Effect of Die Geometry on Flow Distribution 680
9.4.3 Summary of Spiral Mandrel Die Design Variables 684
9.5 Profile Extrusion Dies 684
9.6 Coextrusion 686
9.6.1 Interface Distortion 690
9.7 Calibrators 692

10 Twin Screw Extruders 697
10.1 Introduction 697
10.2 Twin versus Single Screw Extruder 699
10.3 Intermeshing Co-Rotating Extruders 701
10.3.1 Closely Intermeshing Extruders 701
10.3.2 Self-Wiping Extruders 704
10.3.2.1 Geometry of Self-Wiping Extruders 705
10.3.2.2 Conveying in Self-Wiping Extruders 713
10.4 Intermeshing Counter-Rotating Extruders 720
10.5 Non-Intermeshing Twin Screw Extruders 730
10.6 Coaxial Twin Screw Extruders 743
10.7 Devolatilization in Twin Screw Extruders 745
10.8 Commercial Twin Screw Extruders 749
10.8.1 Screw Design Issues for Co-Rotating Twin Screw Extruders 753
10.8.2 Scale-Up in Co-Rotating Twin Screw Extruders 756
10.9 Overview of Twin Screw Extruders 758

11 Troubleshooting Extruders 763
11.1 Requirements for Efficient Troubleshooting 763
11.1.1 Instrumentation 764
11.1.2 Understanding of the Extrusion Process 764
11.1.3 Collect and Analyze Historical Data (Timeline) 765
11.1.4 Team Building 766
11.1.5 Condition of the Equipment 766
11.1.6 Information on the Feedstock 767
11.2 Tools for Troubleshooting 768
11.2.1 Temperature Measurement Devices 768

11.2.2 Data Acquisition Systems (DAS) 769
11.2.2.1 Portable Data Collectors/Machine Analyzers 769
11.2.2.2 Fixed Station Data Acquisition Systems 770
11.2.3 Light Microscopy 772
11.2.4 Thermochromic Materials 773
11.2.5 Thermal Analysis 775
11.2.6 Miscellaneous Tools 775
11.3 Systematic Troubleshooting 776
11.3.1 Upsets versus Development Problems 776
11.3.2 Machine-Related Problems 776
11.3.2.1 Drive System 776
11.3.2.2 The Feed System 778
11.3.2.3 Different Feeding Systems 778
11.3.2.4 Heating and Cooling System 778
11.3.2.5 Wear Problems 780
11.3.2.6 Screw Binding 797
11.3.3 Polymer Degradation 803
11.3.3.1 Types of Degradation 803
11.3.3.2 Degradation in Extrusion 807
11.3.4 Extrusion Instabilities 820
11.3.4.1 Frequency of Instability 821
11.3.4.2 Functional Instabilities 828
11.3.4.3 Solving Extrusion Instabilities 833
11.3.5 Air Entrapment 834
11.3.6 Gels, Gel Content, and Gelation 836
11.3.6.1 Measuring Gels 839
11.3.6.2 Gels Created in the Extrusion Process 840
11.3.6.3 Removing Gels Produced in Polymerization 841
11.3.7 Die Flow Problems 843
11.3.7.1 Melt Fracture 843
11.3.7.2 Die Lip Build-Up (Die Drool) 845
11.3.7.3 V- or W-Patterns 846
11.3.7.4 Specks and Discoloration 846
11.3.7.5 Lines in Extruded Product 851
11.3.7.6 Optical Properties 853

12 Modeling and Simulation of the Extrusion Process 861
12.1 Introduction 861
12.2 Background 862
12.2.1 Analytical Techniques 862
12.2.2 Numerical Methods 864
12.2.2.1 Finite Difference Method 865
12.2.2.2 Finite Element Method 866
12.2.2.3 Boundary Element Method 867
12.2.3 Remeshing Techniques in Moving Boundary Problems 868
12.2.4 Rheology 870

12.3 Simulating 3-D Flows with 2-D Models 871
12.3.1 Simulating Flows in Internal Batch Mixers with 2-D Models 871
12.3.2 Simulating Flows in Extrusion with 2-D Models 877
12.3.3 Simulating Flows in Extrusion Dies with 2-D Models 881
12.4 Three-Dimensional Simulation 885
12.4.1 Simulating Flows in the Banbury Mixer with Three-Dimensional Models 885
12.4.2 Simulating Flows in Extrusion Dies with 3-Dimensional Models 887
12.4.3 Simulating Flows in Extrusion with 3-Dimensional Models 892
12.4.3.1 Regular Conveying Screw 892
12.4.3.2 Energy Transfer Mixer 893
12.4.3.3 Twin Screw Extruder 895
12.4.3.4 Rhomboidal Mixers and Fluted Mixers (Leroy/Maddock) 901
12.4.3.5 Turbo-Screw 906
12.4.3.6 CRD Mixer 908
12.4.4 Static Mixers 910
12.5 Conclusions 912

Conversion Constants 919
Length 919
Volume 919
Mass 920
Density 920
Force 920
Stress 921
Viscosity 921
Energy/Work 922
Power 922
Specific Energy 922
Thermal Conductivity 923
Temperature 923

Index 925

1 Introduction

1.1 Basic Process

The extruder is indisputably the most important piece of machinery in the polymer processing industry. To extrude means to push or to force out. Material is extruded when it is pushed through an opening. When toothpaste is squeezed out of a tube, it is extruded. The part of the machine containing the opening through which the material is forced is referred to as the extruder die. As material passes through the die, the material acquires the shape of the die opening. This shape generally changes to some extent as the material exits from the die. The extruded product is referred to as the extrudate.

Many different materials are formed through an extrusion process: metals, clays, ceramics, foodstuffs, etc. The food industry, in particular, makes frequent use of extruders to make noodles, sausages, snacks, cereal, and numerous other items. In this book, the materials that will be treated are confined to polymers or plastics.

Polymers can be divided into three main groups: thermoplastics, thermosets, and elastomers. Thermoplastic materials soften when they are heated and solidify when they are cooled. If the extrudate does not meet the specifications, the material can generally be reground and recycled. Thus, the basic chemical nature of a thermoplastic usually does not change significantly as a result of the extrusion process. Thermosets undergo a crosslinking reaction when the temperature is raised above a certain temperature. This crosslinking bonds the polymer molecules together to form a three-dimensional network. This network remains intact when the temperature is reduced again. Crosslinking causes an irreversible change in the material. Therefore, thermosetting materials cannot be recycled as can thermoplastic materials. Elastomers or rubbers are materials capable of very large deformations with the material behaving in a largely elastic manner. This means that when the deforming force is removed, the material completely, or almost completely, recovers. The emphasis of this book will be on thermoplastics; only a relatively small amount of attention will be paid to thermosets and elastomers.

Materials can be extruded in the molten state or in the solid state. Polymers are generally extruded in the molten state; however, some applications involve solid-state extrusion of polymers. If the polymer is fed to the extruder in the solid state and the material is melted as it is conveyed by the extruder screw from the feed port to the die, the process is called plasticating extrusion. In this case, the extruder performs an additional function, namely melting, besides the regular extrusion function. Sometimes the extruder is fed with molten polymer; this is called melt fed extrusion. In melt fed extrusion, the extruder acts purely as a pump, developing the pressure necessary to force the polymer melt through the die.

There are two basic types of extruders: continuous and discontinuous or batch type extruders. Continuous extruders are capable of developing a steady, continuous flow of material, whereas batch extruders operate in a cyclic fashion. Continuous extruders utilize a rotating member for transport of the material. Batch extruders generally have a reciprocating member to cause transport of the material.

1.2 Scope of the Book

This book will primarily deal with plasticating extrusion in a continuous fashion. Chapters 2, 3, and 4 deal with a description of extrusion machinery. Chapter 5 will briefly review the fundamental principles that will be used in the analysis of the extrusion process. Chapter 6 deals with the polymer properties important in the extrusion process. This is a very important chapter, because one cannot understand the extrusion process if one does not know the special characteristics of the material to be extruded. Understanding just the extrusion machinery is not enough. Rheological and thermal properties of a polymer determine, to a large extent, the characteristics of the extrusion process. The process engineer, therefore, should be a mechanical or chemical engineer on the one hand, and a rheologist on the other hand. Since most engineers have little or no formal training in polymer rheology, the subject is covered in Chapter 6, inasmuch as it is necessary for the analysis of the extrusion process.

Chapter 7 covers the actual analysis of the extrusion process. The process is analyzed in discrete functional zones with particular emphasis on developing a quantitative understanding of the mechanisms operational in each zone.

The theory developed in Chapter 7 is applied to the design of extruder screws in Chapter 8 and to the design of extruder dies in Chapter 9. Chapter 10 is devoted to twin screw extruders. Twin screw extruders have become an increasingly important branch of the extrusion industry. It is felt, therefore, that any book on extrusion cannot ignore this type of extruder. Troubleshooting extruders is covered in Chapter 11.

This is perhaps the most critical and most important function performed in industrial operation of extruders. Extrusion problems causing downtime or off-spec products can become very costly in a short period of time: losses can often exceed the purchase price of the entire machine in a few hours or a few days. Thus, it is very important that the process engineer can troubleshoot quickly and accurately. This requires a solid understanding of the operational principles of extruders and the basic mechanisms behind them. Therefore, the chapter on troubleshooting is a practical application of the functional process analysis developed in Chapter 7.

The final chapter of the book, Chapter 12 on modeling and computer simulation was added in the fourth edition. This chapter was written by Paul Gramann, Bruce Davis, and Tim Osswald; three workers who have made substantial contributions to the development of this branch of polymer processing. Computer aided engineering (CAE) is now an integral part of extrusion engineering and a current book on extrusion would not be complete without dealing with this important subject.

The book is therefore divided in four main parts. The first part deals with the hardware and/or mechanical aspects of extruders: this is covered in Chapters 2, 3, and 4. The second part deals with the process analysis: this is covered in Chapters 5, 6, and 7. The third part deals with practical applications of the extrusion theory: this is covered in Chapters 8, 9, 10, and 11. Part four is the chapter on modeling and computer simulation. Parts I, II, and IV can be studied independently; Part III, however, cannot be fully appreciated without studying Part II.

1.3 General Literature Survey

Considering the fact that there are already several books on extrusion of polymers, the question can be asked why the need for another book on extrusion. The three most comprehensive books written on extrusion as of the early 1980s were the books by Bernhardt [1], Schenkel [2], and Tadmor [5]. The book by Bernhardt is on polymer processing, but has a very good chapter on extrusion. It is well written and describes extrusion theory and its practical applications to screw and die design. Because of the age of the book, however, the extrusion theory is incomplete in that it does not cover plasticating—this theory was developed later by Tadmor [5]—and devolatilization theory.

The book by Schenkel [2] is a translation of the German text “Kunststoff Extruder-Technik” [3], which is an extension of the original book “Schneckenpressen fuer Kunststoffe” [4]. This book is very complete: dealing with flow properties of polymers, extrusion theory, and design of extrusion equipment. The emphasis of Schenkel’s book is on the mechanical or machinery aspects of extruders. As in Bernhardt’s

book, the book by Schenkel suffers from the fact that it was written a long time ago, in the early 1960s. Thus, the extrusion theory is incomplete and new trends in extrusion machinery are absent. The book by Tadmor [5] is probably the most complete theoretical treatise on extrusion. From a theoretical point of view, it is an outstanding book. It is almost completely devoted to a detailed engineering analysis of the extrusion process. Consequently, relatively little attention is paid to extrusion machinery and practical applications to screw and die design. In order to fully appreciate this book, the reader should possess a significant degree of mathematical dexterity. The book is ideally suited for those who want to delve into detailed mathematical analysis and computer simulation of the extrusion process. The book is less suited for those who need to design extruder screws and/or extruder dies, or those who need to solve practical extrusion problems.

Another book on extrusion is "Plastics Extrusion Technology" edited by Hensen et al. [44]. This is quite a comprehensive book dealing in detail with a number of extrusion processes, such as compounding, pipe extrusion, profile extrusion, etc. The book gives good information on the various extrusion operations with detailed information on downstream equipment. This book is an English version of the two-volume German original, "Kunststoff-Extrusionstechnik I und II" [45, 46]. Volume I, Grundlagen (Fundamentals), covers the fundamental aspects such as rheology, thermodynamics, fluid flow analysis, single- and twin-screw extruders, die design, heating and cooling, etc. Volume II, Extrusionsanlagen, covers various extrusion lines; this is the volume translated into English.

Another important addition to the extrusion literature is the book on twin screw extrusion by White [47]. This book has an excellent coverage of the historical development of various twin screw extruders. It also discusses in some detail recent experimental work and developments in twin screw theory. This book covers intermeshing and non-intermeshing extruders, both co- and counter-rotating extruders. Another extrusion process, which has been gaining interest and is being used more widely, is reactive extrusion. A good book on this subject was edited by Xanthos [48]; it covers applications, review, and engineering fundamentals of reactive extrusion.

Statistical process control in extrusion is covered by a book by Rauwendaal [49]; an updated version of this book also covering injection molding and pre-control was published in 2000 [56]. Mixing in extrusion processes is covered by a book edited by Rauwendaal [50]. It covers basic aspects of mixing and mixing in various extrusion machinery, such as single screw extruders, twin screw extruders, reciprocating screw extruders, internal mixers, and co-rotating disk processors. Another book on mixing is the book edited by Manas-Zloczower and Tadmor [51]. This book covers four major sections: mixing mechanisms and theory, modeling and flow visualization, material considerations, and mixing practices. The book on mixing in polymer processing [54] by Rauwendaal covers the basics of mixing and a comprehensive

description of mixing machinery. This book is written as a self-study guide with questions at the end of each chapter.

In order not to duplicate other texts on extrusion, this book will emphasize new trends and developments in extrusion machinery. The extrusion theory will be covered as completely as possible; however, the mathematical complexity will be kept to a minimum. This is done to enhance the ease of applying theory to practical cases and to make the book accessible to a larger number of people. A significant amount of attention will be paid to practical application of the extrusion theory to screw and die design and solving extrusion problems. After all, practical applications are most important to practicing polymer process engineers or chemists.

Various other books on extrusion have been written [6–22, 52]. These books generally cover only specific segments of extrusion technology: e. g., screw design, twin screw extrusion, etc., or provide only introductory material. Thus, it is felt that a comprehensive book on polymer extrusion with recent information on machinery, theory, and application does fulfill a need. There are several books on the more general subject of polymer processing [24–36], in addition to the book by Bernhardt [7] already mentioned. Many of these give a good review of the field of polymer processing, some emphasizing the general principles involved in process analysis [24–33] or machine design [34], while others concentrate more on a description of the process machinery and products [35, 36]. Since the field of polymer processing is tremendously large, books on the subject inevitably cover extrusion in less detail than possible in a book devoted exclusively to extrusion.

The book “Understanding Extrusion” [55] is a very much-simplified and abbreviated version of “Polymer Extrusion” without any equations in the main body of the text. Even though the mathematical level of Polymer Extrusion is at approximately the bachelors engineering level, the mathematics is too much for people who are not interested in the engineering details. Understanding Extrusion became an immediate best seller, indicating that a non-engineering level book on extrusion can attract a wide readership. This book is the basis of a computer based interactive training program on extrusion, ITX®.

The book “Troubleshooting the Extrusion Process—A Systematic Approach to Solving Plastic Extrusion Problems” [59] by del Pilar Noriega and Rauwendaal was the first book devoted exclusively to troubleshooting extrusion problems. A second edition of this book was published in 2010.

Chung’s book “Extrusion of Polymers” [57] covers some of the same material as Polymer Extrusion, however, it does not cover die design, troubleshooting, and modeling and computer simulation. As such, the book is limited in scope; it also suffers from the fact that most references are from before 1980. The book “Screw Extrusion: Technology and Science” [58] was edited by White and Potente. This book has a broad scope and multiple contributors; it covers fundamentals, single screw extru-

sion technology, reciprocating extruders, single screw extruder analysis and design, and multiscrew extrusion.

A recent book on extrusion is the book "Analyzing and Troubleshooting Single-Screw Extruders" [60] by Campbell and Spalding. The authors claim that this is the first book that focuses on the actual physics of the process-screw rotation physics. This claim is not entirely correct considering that the 4th edition of this book already examined this issue in detail, see Section 7.4.3.5.

1.4 History of Polymer Extrusion

The first machine for extrusion of thermoplastic materials was built around 1935 by Paul Troester in Germany [37]. Before this time, extruders were primarily used for extrusion of rubber. These earlier rubber extruders were steam-heated ram extruders and screw extruders; with the latter having very short length to diameter (L/D) ratios, about 3 to 5. After 1935, extruders evolved into electrically heated screw extruders with increased length. Around this time, the basic principle of twin screw extruders for thermoplastics was conceived in Italy by Roberto Colombo of LMP. He was working with Carlo Pasquetti on mixing cellulose acetate. Colombo developed an intermeshing co-rotating twin screw extruder. He obtained patents in many different countries and several companies acquired the rights to use these patents. Pasquetti followed a different concept and developed and patented the intermeshing counter-rotating twin screw extruder.

The first detailed analyses of the extrusion process were concerned with the melt conveying or pumping process. The earliest publication was an anonymous article [38], which is often erroneously credited to Rowell and Finlayson, who wrote an article of the same title in the same journal six years later [39]. Around 1950, scientific studies of the extrusion process started appearing with increased frequency. In the mid-fifties, the first quantitative study on solids conveying was published by Darnell and Mol [40]. An important conference in the development of extrusion theories was the 122nd ACS meeting in 1953. At this symposium, members of the Polychemicals Department of E. I. DuPont de Nemours & Co. presented the latest developments in extrusion theory [41]. These members, Carley, Strub, Mallouk, McKelvey, and Jepson were honored in 1983 by the SPE Extrusion Division for original development of extrusion theories. In the mid-sixties, the first quantitative study on melting was published by Tadmor [42], based on earlier qualitative studies by Maddock [43]. Thus, it was not until about 1965 that the entire extrusion process, from the feed hopper to the die, could be described quantitatively. The theoretical work since this time has concentrated, to a large extent, on generalizing and extending the

extrusion theory and the development of numerical techniques and computer methods to solve equations that can no longer be solved by analytical methods.

As a result, there has been a shift in the affiliation of the workers involved in scientific extrusion studies. While the early work was done mostly by investigators in the polymer industry, later workers have been academicians. This has created somewhat of a gap between extrusion theoreticians and practicing extrusion technologists. This is aggravated by the fact that some workers are so concerned about the scientific pureness of the work, which is commendable in itself, that it becomes increasingly unappealing to the industrial process engineer who wants to apply the work. One of the objectives of this book is to bridge this gap between theory and practice by demonstrating in detail how the theory can be applied and by analyzing the limitations of the theory.

Another interesting development in practical extrusion technology has been the concept of feed-controlled extrusion. In this type of extrusion, the performance is determined by the solids conveying zone of the extruder. By the use of grooves in the first portion (close to the feed port) of the extruder barrel, the solids conveying zone is capable of developing very high pressures and quite positive conveying characteristics (i. e., throughput independent of pressure). In this case, the diehead pressure does not need to be developed in the pumping or melt conveying zone; it is developed in the solids conveying zone. The feed zone overrides both the plasticating and the melt conveying (pumping) zone.

Thus, the extruder becomes solids conveying or feed controlled. This concept has now become an accepted standard in Western Europe, particularly in Germany. In the U. S., this concept has been met with a substantial amount of reluctance and skepticism. For the longest time, the few proponents of the feed-controlled extrusion were heavily outnumbered by the many opponents. As a consequence, only a small fraction of the extruders in the U. S. have been equipped with grooved barrel sections. However, there does seem to be a trend towards increasing acceptance of this concept. This is especially true in the blown film industry where the use of very high molecular weight polyethylene has led many processors to use grooved feed extruders.

One approach to making the grooved feed extruder more attractive is to make it adjustable. This can eliminate many of the disadvantages of current grooved feed extruders. The grooved feed section can be made adjustable by changing the depth of the grooves while the machine is operating. This makes the grooved feed extruder more versatile and allows a greater degree of control of the extrusion process. Adjustable grooved feed extruders are discussed in Chapter 7.

When a single screw extruder is used for demanding mixing and compounding operations it is often preferred that the extruder is starve fed rather than flood fed. Flood feeding often results in higher pressures inside the extruder and this can lead to an agglomeration of powdered fillers. When this occurs it may be difficult or

impossible to disperse the agglomerates formed in the extruder. With starve feeding the pressures inside the extruder are lower and can be controlled by adjusting the feed rate and/or the screw speed. As a result, there is less risk of agglomeration using starve feeding.

Around 2000, a new generation of mixing devices was developed to generate strong elongational flow to improve mixing, particularly dispersive mixing. It has long been known that elongational mixing is more effective than shear mixing. However, this knowledge was not translated into actual mixing devices until recently. These new mixing devices, such as the CRD mixer discussed in Chapter 7, use the same type of mixing mechanism active in high-speed co-rotating twin screw extruders. As a result, when these mixers are used in single screw extruders the mixing action can be comparable to that of twin screw compounders. In fact, these mixers are now successfully used in twin screw extruders as well.

The advent of effective new mixers for single screw extruders has improved the capabilities of conventional single screw extruders. An interesting application may be long single screw extruders (30 to 60D) with multiple downstream ports for compounding and direct extrusion. When such machines are starve fed they can be used in many applications now serviced by twin screw extruders. Because single screw extruders are considerably less expensive to purchase and to operate, this approach can offer substantial cost savings. This approach represents a significant departure from conventional extrusion technology; as a result, it may take some time before it is widely accepted in the extrusion industry. However, when a new technology makes technical and economic sense and it works, then sooner or later it will be adopted.

Very high speed single screw extruders have been commercially available since about 2005–2010. This is one of the most significant developments in single screw extrusion over the past several decades. These relatively small extruders (50–75 mm) that run at screw speeds as high as 1,000 to 1,500 rpm and achieve output rate about an order of magnitude above the rate of conventional extruders.

References

1. E.C. Bernhardt (Ed.), “Processing of Thermoplastic Materials,” Reinhold, NY (1959)
2. G. Schenkel, “Plastics Extrusion Technology and Theory,” Illiffe Books Ltd., London (1966), published in the USA by American Elsevier, NY (1966)
3. G. Schenkel, “Kunststoff Extruder-Technik,” Carl Hanser Verlag, Munich (1963)
4. G. Schenkel, “Schneckenpressen fuer Kunststoffe,” Carl Hanser Verlag, Munich (1959)
5. Z. Tadmor and I. Klein, “Engineering Principles of Plasticating Extrusion,” Van Nostrand Reinhold, NY (1970)
6. H.R. Simonds, A.J. Weith, and W. Schack, “Extrusion of Rubber, Plastics and Metals,” Reinhold, NY (1952)
7. E.G. Fisher, “Extrusion of Plastics,” Illiffe Books Ltd., London (1954)

8. R. Jacobi, “Grundlagen der Extrudertechnik,” Carl Hanser Verlag, Munich (1960)
9. W. Mink, “Grundzuege der Extrudertechnik,” Rudolf Zechner Verlag, Speyer am Rhein (1963)
10. A.L. Griff, “Plastics Extrusion Technology,” Reinhold, NY (1968)
11. R.T. Fenner, “Extruder Screw Design,” Illiffe Books, Ltd., London (1970)
12. N.M. Bikales (Ed.), “Extrusion and Other Plastics Operations,” Wiley, NY (1971)
13. P.N. Richardson, “Introduction to Extrusion,” Society of Plastics Engineers, Inc. (1974)
14. L.P.B.M. Janssen, “Twin Screw Extrusion,” Elsevier, Amsterdam (1978)
15. J.A. Brydson and D.G. Peacock, “Principles of Plastics Extrusion,” Applied Science Publishers Ltd., London (1973)
16. F.G. Martelli, “Twin Screw Extrusion, A Basic Understanding,” Van Nostrand Reinhold, NY (1983)
17. “Kunststoff-Verarbeitung im Gespraech, 2 Extrusion,” BASF, Ludwigshafen (1971)
18. “Der Extruder als Plastifiziereinheit,” VDI-Verlag, Duesseldorf (1977)
19. Levy, “Plastics Extrusion Technology Handbook,” Industrial Press Inc., NY (1981)
20. H. Potente, “Auslegen von Schneckenmaschinen-Baureihen, Modellgesetze und ihre Anwendung,” Carl Hanser Verlag, Munich (1981)
21. H. Herrmann, “Schneckenmaschinen in der Verfahrenstechnik,” Springer-Verlag, Berlin (1972)
22. W. Dalhoff, “Systematische Extruder-Konstruktion,” Krausskopf-Verlag, Mainz (1974)
23. E. Harms, “Kautschuk-Extruder, Aufbau und Einsatz aus verfahrenstechnischer Sicht,” Krausskopf-Verlag Mainz, Bd. 2, Buchreihe Kunststofftechnik (1974)
24. J.M. McKelvey, “Polymer Processing,” Wiley, NY (1962)
25. R.M. Ogorkiewicz, “Thermoplastics: Effects of Processing,” Illiffe Books Ltd., London (1969)
26. J.R.A. Pearson, “Mechanical Principles of Polymer Melt Processing,” Pergamon, Oxford (1966)
27. S. Middleman, “The Flow of High Polymers,” Interscience (1968)
28. R.V. Torner, “Grundprozesse der Verarbeitung von Polymeren,” VEB Deutscher Verlag fuer Grundstoffindustrie, Leipzig (1973)
29. S. Middleman, “Fundamentals of Polymer Processing,” McGraw-Hill, NY (1977)
30. H.L. Williams, “Polymer Engineering,” Elsevier, Amsterdam (1975)
31. J.L. Throne, “Plastics Process Engineering,” Marcel Dekker, Inc., NY (1979)
32. Z. Tadmor and C. Gogos, “Principles of Polymer Processing,” Wiley, NY (1979)
33. R.T. Fenner, “Principles of Polymer Processing,” MacMillan Press Ltd., London (1979)
34. N.S. Rao, “Designing Machines and Dies for Polymer Processing with Computer Programs,” Carl Hanser Verlag, Munich (1981)
35. J. Frados (Ed.), “Plastics Engineering Handbook,” Van Nostrand Reinhold, NY (1976)
36. S.S. Schwartz and S.H. Goodman, “Plastics Materials and Processes,” Van Nostrand Reinhold, NY (1982)

37. M. Kaufman, Plastics & Polymers, 37, 243 (1969)
38. N.N., Engineering, 114, 606 (1922)
39. H.S. Rowell and D. Finlayson, Engineering, 126, 249–250, 385–387, 678 (1928)
40. W.H. Darnell and A.J. Mol, SPE Journal, 12, 20 (1956)
41. J.F. Carley, R.A. Strub, R.S. Mallouk, J.M. McKelvey, and C.H. Jepson, 122nd Meeting of the American Chemical Society, Atlantic City, NJ (1953). The seven papers were published in Ind. Eng. Chem., 45, 970–992 (1953)
42. Z. Tadmor, Polym. Eng. Sci., 6, 3, 1 (1966)
43. B.H. Maddock, SPE Journal, 15, 383 (1959)
44. F. Hensen, W. Knappe, and H. Potente (Eds.), "Plastics Extrusion Technology," Carl Hanser Verlag, Munich (1988)
45. F. Hensen, W. Knappe, and H. Potente (Eds.), "Handbuch der Kunststoff-Extrusionstechnik, Band I Grundlagen," Carl Hanser Verlag, Munich (1989)
46. F. Hensen, W. Knappe, and H. Potente (Eds.), "Handbuch der Kunststoff-Extrusionstechnik, Band II Extrusionsanlagen," Carl Hanser Verlag, Munich (1989)
47. J.L. White, "Twin Screw Extrusion," Carl Hanser Verlag, Munich (1991)
48. M. Xanthos (Ed.) "Reactive Extrusion," Carl Hanser Verlag, Munich (1992)
49. C. Rauwendaal, "Statistical Process Control in Extrusion," Carl Hanser Verlag, Munich (1993)
50. C. Rauwendaal (Ed.) "Mixing in Polymer Processing," Marcel Dekker, NY (1991)
51. I. Manas-Zloczower and Z. Tadmor (Eds.), "Mixing and Compounding–Theory and Practice," Carl Hanser Verlag, Munich (1994)
52. M.J. Stevens, "Extruder Principles and Operation," Elsevier Applied Science Publishers, Essex, England (1985)
53. T.I. Butler and E.W. Veasey, "Film Extrusion Manual, Process, Materials, Properties," Tappi Press, Atlanta, GA (1992)
54. C. Rauwendaal, "Polymer Mixing, A Self-Study Guide," Carl Hanser Verlag, Munich (1998)
55. C. Rauwendaal, "Understanding Extrusion," Carl Hanser Verlag, Munich (1998)
56. C. Rauwendaal, "Statistical Process Control in Injection Molding and Extrusion," Carl Hanser Verlag, Munich (2000)
57. C.I. Chung, "Extrusion of Polymers, Theory and Practice," Carl Hanser Verlag, Munich (2000)
58. J.L. White and H. Potente (Eds.), "Screw Extrusion: Technology and Science," Carl Hanser Verlag, Munich (2001)
59. M. Noriega and C. Rauwendaal, "Troubleshooting the Extrusion Process," 1st edition, Hanser Verlag, Munich (2001)
60. G.A. Campbell and M.A. Spalding, "Analyzing and Troubleshooting Single-Screw Extruders," Hanser Verlag, Munich (2013)

PART I

Extrusion Machinery

2 Different Types of Extruders

Extruders in the polymer industry come in many different designs. The main distinction between the various extruders is their mode of operation: continuous or discontinuous. The latter type extruder delivers polymer in an intermittent fashion and, therefore, is ideally suited for batch type processes, such as injection molding and blow molding. As mentioned earlier, continuous extruders have a rotating member, whereas batch extruders have a reciprocating member. A classification of the various extruders is shown in Table 2.1.

2.1 The Single Screw Extruder

Screw extruders are divided into single screw and multi screw extruders. The single screw extruder is the most important type of extruder used in the polymer industry. Its key advantages are relatively low cost, straightforward design, ruggedness and reliability, and a favorable performance/cost ratio. A detailed description of the hardware components of a single screw extruder is given in Chapter 3.

The extruder screw of a conventional plasticating extruder has three geometrically different sections; see Fig. 2.1.

This geometry is also referred to as a "single stage." The single stage refers to the fact that the screw has only one compression section, even though the screw has three distinct geometrical sections! The first section (closest to the feed opening) generally has deep flights. The material in this section will be mostly in the solid state. This section is referred to as the feed section of the screw. The last section (closest to the die) usually has shallow flights. The material in this section will be mostly in the molten state. This screw section is referred to as the metering section or pump section. The third screw section connects the feed section and the metering section. This section is called the transition section or compression section. In most cases, the depth of the screw channel (or the height of the screw flight) reduces in a linear fashion, going from the feed section towards the metering section, thus causing a compression of the material in the screw channel. Later, it will be shown that this compression, in many cases, is essential to the proper functioning of the extruder.

The extruder is usually designated by the diameter of the extruder barrel. In the U.S., the standard extruder sizes are 3/4, 1, 1–1/2, 2, 2–1/2, 3–1/2, 4–1/2, 6, 8, 10, 12, 14, 16, 18, 20, and 24 inches.

Obviously, the very large machines are much less common than the smaller extruders. Some machines go up in size as large as 35 inches. These machines are used in specialty operations, such as melt removal directly from a polymerization reactor. In Europe, the standard extruder sizes are 20, 25, 30, 35, 40, 50, 60, 90, 120, 150, 200, 250, 300, 350, 400, 450, 500, and 600 millimeters. Most extruders range in size from 1 to 6 inches or from 25 to 150 mm. An additional designation often used is the length of the extruder, generally expressed as length to diameter (L/D) ratio. Typical L/D ratios range from 20 to 30, with 24 being very common. Extruders used for extraction of volatiles (vented extruders, see Section 2.1.2) can have an L/D ratio as high as 35 or 40 and sometimes even higher.

Table 2.1 Classification of Polymer Extruders

Screw extruders (continuous)	Single screw extruders	Melt fed
		Plasticating
		Single stage
		Multi stage
		Compounding
	Multi screw extruders	Twin screw extruders
		Gear pumps
		Planetary gear extruders
		Multi (>2) screw extruders
Disk or drum extruders (continuous)	Viscous drag extruders	Spiral disk extruder
		Drum extruder
		Diskpack extruder
		Stepped disk extruder
	Elastic melt extruders	Screwless extruder
		Screw or disk type melt extruder
Reciprocating extruders (discontinuous)	Ram extruders	Melt fed extruder
		Plasticating extruder
		Capillary rheometer
	Reciprocating single screw extruders	Plasticating unit in injection molding machines
		Compounding extruders such as the Kneader

2.1.1 Basic Operation

The basic operation of a single screw extruder is rather straightforward. Material enters from the feed hopper. Generally, the feed material flows by gravity from the feed hopper down into the extruder barrel. Some materials do not flow easily in dry form and special measures have to be taken to prevent hang-up (bridging) of the material in the feed hopper.

As material falls down into the extruder barrel, it is situated in the annular space between the extruder screw and barrel, and is further bounded by the passive and active flanks of the screw flight: the screw channel. The barrel is stationary and the screw is rotating. As a result, frictional forces will act on the material, both on the barrel as well as on the screw surface. These frictional forces are responsible for the forward transport of the material, at least as long as the material is in the solid state (below its melting point).

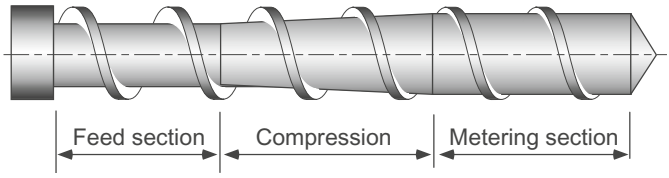


Figure 2.1 Geometry of conventional extruder screw

As the material moves forward, it will heat up as a result of frictional heat generation and because of heat conducted from the barrel heaters. When the temperature of the material exceeds the melting point, a melt film will form at the barrel surface. This is where the solids conveying zone ends and the plasticating zone starts. It should be noted that this point generally does not coincide with the start of the compression section. The boundaries of the functional zones will depend on polymer properties, machine geometry, and operating conditions. Thus, they can change as operating conditions change. However, the geometrical sections of the screw are determined by the design and will not change with operating conditions. As the material moves forward, the amount of solid material at each location will reduce as a result of melting. When all solid polymer has disappeared, the end of the plasticating zone has been reached and the melt conveying zone starts. In the melt-conveying zone, the polymer melt is simply pumped to the die.

As the polymer flows through the die, it adopts the shape of the flow channel of the die. Thus, as the polymer leaves the die, its shape will more or less correspond to the cross-sectional shape of the final portion of the die flow channel. Since the die exerts a resistance to flow, a pressure is required to force the material through the die. This is generally referred to as the diehead pressure. The diehead pressure is determined by the shape of the die (particularly the flow channel), the temperature

of the polymer melt, the flow rate through the die, and the rheological properties of the polymer melt. It is important to understand that the diehead pressure is caused by the die, and not by the extruder! The extruder simply has to generate sufficient pressure to force the material through the die. If the polymer, the throughput, the die, and the temperatures in the die are the same, then it does not make any difference whether the extruder is a gear pump, a single screw extruder, a twin screw extruder, etc.; the diehead pressure will be the same. Thus, the diehead pressure is caused by the die and by the flow process, taking place in the die flow channel. This is an important point to remember.

2.1.2 Vented Extruders

Vented extruders are significantly different from non-vented extruders in design and in functional capabilities. A vented extruder is equipped with one or more openings (vent ports) in the extruder barrel, through which volatiles can escape. Thus, the vented extruder can extract volatiles from the polymer in a continuous fashion. This devolatilization adds a functional capability not present in non-vented extruders. Instead of the extraction of volatiles, one can use the vent port to add certain components to the polymer, such as additives, fillers, reactive components, etc. This clearly adds to the versatility of vented extruders, with the additional benefit that the extruder can be operated as a conventional non-vented extruder by simply plugging the vent port and, possibly, changing the screw geometry.

A schematic picture of a vented extruder is shown in Fig. 2.2.

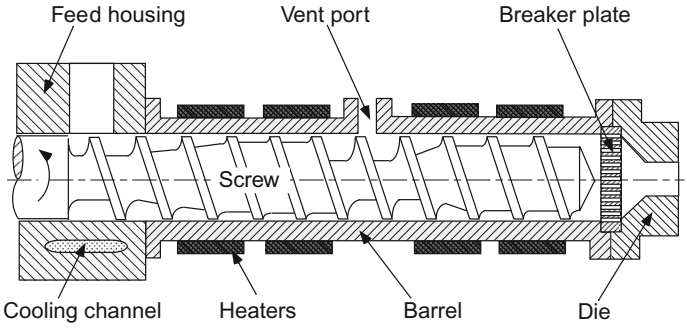


Figure 2.2 Schematic of vented extruder

The design of the extruder screw is very critical to the proper functioning of the vented extruder. One of the main problems that vented extruders are plagued with is vent flow. This is a situation where not only the volatiles are escaping through the vent port, but also some amount of polymer. Thus, the extruder screw has to be designed in such a way that there will be no positive pressure in the polymer under the vent port (extraction section). This has led to the development of the two-stage

extruder screw, especially designed for devolatilizing extrusion. Two-stage extruder screws have two compression sections separated by a decompression/extraction section. It is somewhat like two single-stage extruder screws coupled in series along one shaft. The details of the design of two-stage extruder screws will be covered in Chapter 8. Vented extruders are used for the removal of monomers and oligomers, reaction products, moisture, solvents, etc.

The devolatilization capability of single screw extruders of conventional design is limited compared to twin screw extruders. Twin screw extruders can handle solvent contents of 50% and higher, using a multiple-stage extraction system, and solvent content of up to 15% using singlestage extraction. Single screw vented extruders of conventional design usually cannot handle more than 5% volatiles; this would require multiple vent ports. With a single vent port, a single screw vented extruder of conventional design can generally reduce the level of volatiles only a fraction of one percent, depending, of course, on the polymer/solvent system.

Because of the limited devolatilization capacity of single screw extruders of conventional design, they are sometimes equipped with two or more vent ports. A drawback of such a design is that the length of the extruder can become a problem. Some of these extruders have a L/D ration of 40 to 50! This creates a problem in handling the screw, for instance when the screw is pulled, and increases the chance of mechanical problems in the extruder (deflection, buckling, etc.). If substantial amounts of volatiles need to be removed, a twin screw extruder may be more cost-effective than a single screw extruder. However, some vented single screw extruders of more modern design have substantially improved devolatilization capability and deserve equal consideration; see Section 8.5.2.

2.1.3 Rubber Extruders

Extruders for processing elastomers have been around longer than any other type of extruder. Industrial machines for rubber extrusion were built as early as the second half of the nineteenth century. Some of the early extruder manufacturers were John Royle in the U.S. and Francis Shaw in England. One of the major rubber extruder manufacturers in Germany was Paul Troester; in fact, it still is a producer of extruders. Despite the fact that rubber extruders have been around for more than a century, there is limited literature on the subject of rubber extrusion. Some of the handbooks on rubber [1–5] discuss rubber extrusion, but in most cases the information is very meager and of limited usefulness. Harms' book on rubber extruders [13] appears to be the only book devoted exclusively to rubber extrusion. The few publications on rubber extrusion stand in sharp contrast to the abundance of books and articles on plastic extrusion. Considering the commercial significance of rubber extrusion, this is a surprising situation.

The first rubber extruders were built for hot feed extrusion. These machines are fed with warm material from a mill or other mixing device. Around 1950, machines were developed for cold feed extrusion. The advantages of cold feed extruders are thought to be:

- Less capital equipment cost
- Better control of stock temperature
- Reduced labor cost
- Capable of handling a wider variety of compounds

However, there is no general agreement on this issue. As a result, hot feed rubber extruders are still in use today.

Cold feed rubber extruders, nowadays, do not differ too much from thermoplastic extruders. Some of the differences are:

- Reduced length
- Heating and cooling
- Feed section
- Screw design

There are several reasons for the reduced length. The viscosity of rubbers is generally very high compared to most thermoplastics; about an order of magnitude higher [5]. Consequently, there is a substantial amount of heat generated in the extrusion process. The reduced length keeps the temperature build-up within limits. The specific energy requirement for rubbers is generally low, partly because they are usually extruded at relatively low temperatures (from 20 to 120°C). This is another reason for the short extruder length. The length of the rubber extruder will depend on whether it is a cold or hot feed extruder. Hot feed rubber extruders are usually very short, about 5D (D = diameter). Cold feed extruders range from 15 to 20D. Vented cold feed extruders may be even longer than 20D.

Rubber extruders used to be heated quite frequently with steam because of the relatively low extrusion temperatures. Today, many rubber extruders are heated like thermoplastic extruders with electrical heater bands clamped around the barrel. Oil heating is also used on rubber extruders and the circulating oil system can be used to cool the rubber. Many rubber extruders use water cooling because it allows effective heat transfer.

The feed section of the rubber extruders has to be designed specifically to the feed stock characteristics of the material. The extruder may be fed with either strips, chunks, or pellets. If the extruder is fed from an internal mixer (e. g., Banbury, Shaw, etc.), a power-operated ram can be used to force the rubber compound into the extruder. The feed opening can be undercut to improve the intake capability of the extruder. This can be useful, because the rubber feed stock at times comes in relatively large particles of irregular shape. When the material is supplied in the form of

a strip, the feed opening is often equipped with a driven roll parallel to the screw to give a "roller feed". Material can also be supplied in powder form. It has been shown that satisfactory extrusion is possible if the powder is consolidated by "pill-making" techniques. Powdered rubber technology is discussed in detail in [6].

The rubber extrusion technology appears to be considerably behind the plastics extrusion technology. Kennaway, in one of the few articles on rubber extrusion [8], attributes this situation to two factors. The first is the frequent tendency of rubber process personnel to solve extrusion problems by changing the formulation of the compound. The second is the widespread notion that the extrusion behavior of rubbers is substantially different from plastics, because rubbers crosslink and plastics generally do not. This is a misconception, however, because the extrusion characteristics of rubber and plastics are actually not substantially different [9].

When the rubber is slippery, as in dewatering rubber extruders, the feed section of the barrel is grooved to prevent slipping along the barrel surface or the barrel I.D. may be fitted with pins. This significantly improves the conveying action of the extruder. The same technique has been applied to the thermoplastic extrusion, as discussed in Section 1.4 and Section 7.2.2.2.

The extruder screw for rubber often has constant depth and variable decreasing pitch (VDP); many rubber screws use a double-flighted design; see Fig. 2.3. Screws for thermoplastics usually have a decreasing depth and constant pitch; see Fig. 2.1.

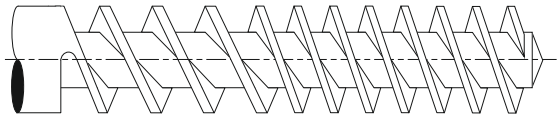


Figure 2.3
Typical screw geometry for rubber extrusion

Another difference with the rubber extruder screw is that the channel depth is usually considerably larger than with a plastic extruder screw. The larger depth is used to reduce the shearing of the rubber and the resulting viscous heat generation. There is a large variety of rubber extruder screws, as is the case with plastic extruder screws. Figure 2.4 shows the "Plastiscrew" manufactured by NRM.

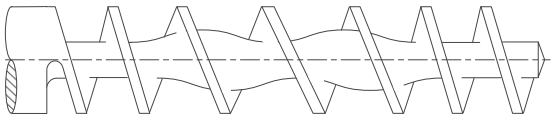


Figure 2.4
The NRM Plastiscrew

Figure 2.5 shows the Pirelli rubber extruder screw. This design uses a feed section of large diameter, reducing quickly to the much smaller diameter of the pumping section. The conical feed section uses a large clearance between screw flight and barrel wall. This causes a large amount of leakage over the flight and improves the batch-mixing capability of the extruder.

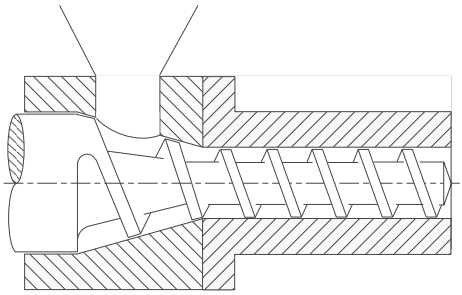


Figure 2.5
The Pirelli rubber extruder screw

Figure 2.6 shows the EVK screw by Werner & Pfleiderer [14]. This design features cross-channel barriers with preceding undercuts in the flights to provide a change in flow direction and increased shearing as the material flows over the barrier or the undercut in the flight. A rather unusual design is the Transfermix [10–13] extruder/mixer, which has been used for compounding rubber formulations. This machine features helical channels in both, the screw and barrel; see Fig. 2.7.

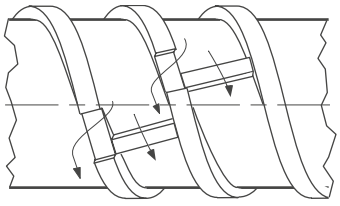


Figure 2.6
The EVK screw by Werner & Pfleiderer

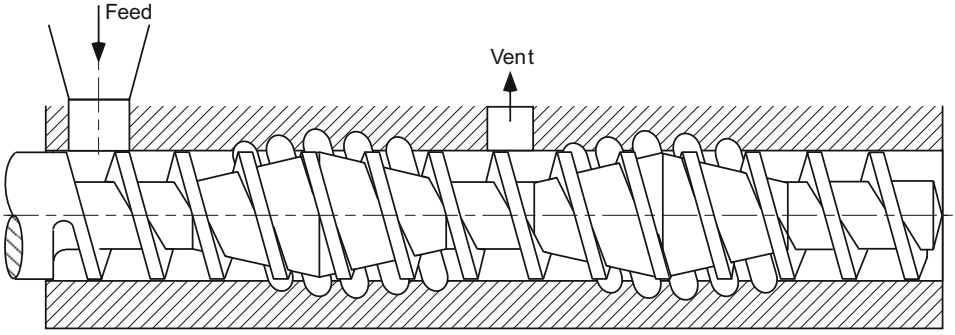


Figure 2.7 The Transfermix extruder

By a varying root diameter of the screw the material is forced in the flow channel of the barrel. A reduction of the depth of the barrel channel forces the material back into the screw channel. This frequent reorientation provides good mixing. However, the machine is difficult to manufacture and expensive to repair in case of damage.

Another rubber extruder is the QSM extruder [7, 15–20]. QSM stands for the German words “Quer Strom Misch,” meaning cross-flow mixing. This extruder has

adjustable pins in the extruder barrel that protrude all the way into the screw channel; see Fig. 2.8.

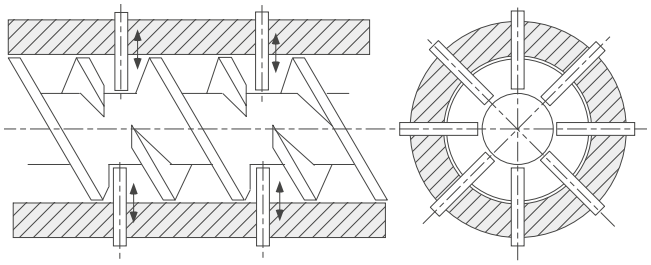


Figure 2.8 The QSM extruder (pin barrel extruder)

The screw flight has slots at the various pin locations. The advantages of this extruder in rubber applications are good mixing capability with a low stock temperature increase and low specific energy consumption. This extruder was developed by Harms in Germany and is manufactured and sold by Troester and other companies. Even though the QSM extruder has become popular in the rubber industry, its applications clearly extend beyond just rubber extrusion. In thermoplastic extrusion, its most obvious application would be in high viscosity, thermally less stable resins: PVC could possibly be a candidate, although dead spots may create problems with degradation. However, it can probably be applied wherever good mixing and good temperature control are required.

Another typical rubber extrusion piece of hardware is the roller die. A schematic representation is shown in Fig. 2.9.

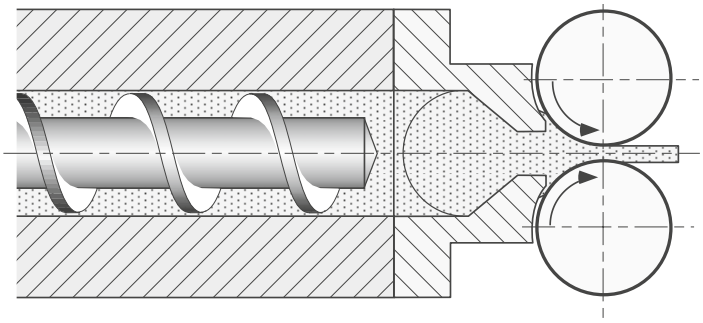


Figure 2.9 The roller die used in rubber extrusion

The roller die (B. F. Goodrich, 1933) is a combination of a standard sheet die and a calender. It allows high throughput by reducing the diehead pressure; it reduces air entrapment and provides good gauge control.

2.1.4 High-Speed Extrusion

One way to achieve high throughputs is to use high-speed extrusion. High-speed extrusion has been used in twin screw compounding for many years—since the 1960s. However, in single screw extrusion high speed extrusion has not been used on a significant scale until about 1995. Twin screw extruders (TSE) used in compounding typically run at screw speeds ranging from 200 to 500 rpm; in some cases screw speeds beyond 1000 rpm are possible. Single screw extruders (SSE) usually operate at screw speeds between 50 to 150 rpm.

Since approx. 1995, several extruder manufacturers have worked on developing high-speed single screw extruders (HS-SSE). Most of these developments have taken place at German extruder manufacturers such as Battenfeld, Reifenhäuser, Kuhne, and Esde. Currently, HS-SSEs are commercially available and have been in use for several years [108].

Battenfeld supplies a high speed 75-mm SSE that can run at screw speeds up to 1,500 rpm [109]. This machine can achieve throughputs up to 2,200 kg/hr. It uses a four-motor CMG torque drive with 390 kW made by K&A Knoedler.

2.1.4.1 Melt Temperature

One of the interesting characteristics of the HS-SSE is that the melt temperature remains more or less constant over a broad range of screw speed [108, 109], see Fig. 2.10.

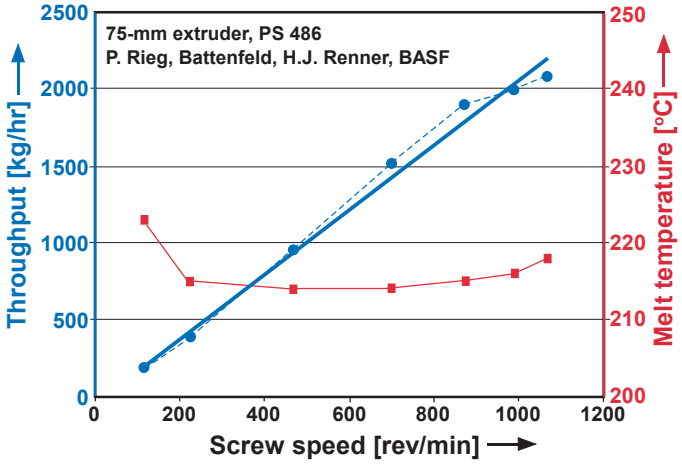


Figure 2.10
Throughput and melt temperature versus screw speed

This graph shows both the throughput in kg/hr and the melt temperature in °C. The temperature curve indicates that there is less than a 2°C change in melt temperature from 200 rpm up to about 1000 rpm. At screw speeds from 110 rpm to 225 rpm the melt temperature actually drops from about 223 to about 215°C.

In conventional extruders the melt temperature typically increases with screw speed. This often creates problems when we deal with high-viscosity polymers, particularly when they have limited thermal stability. In the example shown in Fig. 2.10 the melt temperature is essentially constant as screw speed increases from 200 to 1000 rpm. This is probably the result of two factors: the residence time of the polymer melt is reduced with increasing screw speed and the volume of the molten polymer likely reduces with increasing screw speed as the melting length becomes longer with increased screw speed.

2.1.4.2 Extruders without Gear Reducer

An important advantage of high-speed SSE is that a conventional gear reducer is no longer necessary. The gear reducer is one of the largest cost factors for a conventional extruder. As a result, extruders without a gear reducer are significantly less expensive compared to conventional extruders that achieve the same rate. A further advantage of the elimination of the gear reducer is a significant reduction in noise level. Contrary to what one would expect, HS-SSE actually run very quiet; the noise level is substantially lower than it is for conventional extruders with gear reducers.

2.1.4.3 Energy Consumption

Another benefit of high-speed SSE is the reduction in energy consumption. Rieg [108, 109] reports the following mechanical specific energy consumption.

The reduction in energy consumption listed in Table 2.2 is significant: between 35% and 45%. If the extruder runs PP at 2000 kg/hr, a reduction in SEC of 0.10 kWh/kg corresponds to a reduction in power consumption of 200 kW every hour. If the power cost is $0.10 per kWh (for consistency), the savings per hour will be $20 per hour, $480 per day, $3360 per week, and $168,000 per year at 50 weeks per year. Clearly, this can have a significant effect on the profitability of an extrusion operation.

Table 2.2 Specific Energy Consumption for Standard Extruder and High-Speed Extruder

Type of extruder	SEC with polystyrene [kWh/kg]	SEC with polypropylene [kWh/kg]
Standard extruder	0.19–0.21	0.27–0.29
High-speed extruder	0.10–0.12	0.17–0.19

2.1.4.4 Change-over Resin Consumption

Another important issue in efficient extrusion is the time and material used when a change in resin is made. With high-speed extruders the change-over time is quite short because the volume occupied by the plastic is small, while the throughput is very high.

Table 2.3 shows a comparison of the high-speed 75-mm extruder to a conventional 180-mm extruder running at the same throughput. The amount of material consumed in the change-over is 150 kg for the 75-mm extruder and 1300 kg for the 180-mm extruder. If we assume a resin cost of $1.00 per kg, the savings are $1,150.00 per change-over. If we have three change-overs per week the yearly savings in reduced resin usage comes to $172,500 per year. Clearly, this is not an insignificant amount.

Table 2.3 Comparison of Change-Over Time and Material Consumption

	75-mm extruder	180-mm extruder
Volume in the extruder [liter]	4	40
Material consumption for change-over [kg]	150	1300
Change-over time [min]	5	40

2.1.4.5 Change-over Time and Residence Time

Table 2.3 also shows that the change-over time for the 75-mm extruder is approx. 5 minutes, while it is approx. 40 minutes in the 180-mm extruder. Clearly, the reduced change-over time results from the fact that the volume occupied by the plastic is much smaller (4 liter) in the 75-mm extruder than in the 180-mm extruder (40 liter). If the change-over time can be reduced from 40 to 5 minutes, this means that 35 minutes are now available to run production, resulting in greater up-time of the extrusion line.

The small volume of the HS-SSE also results in short residence times. The mean residence time ranges from approx. 5 to 10 seconds. In conventional SSE the residence times are substantially longer; typically between 50 to 100 seconds. Since HS-SSE can run at relatively low melt temperatures, the chance of degradation is actually less in these extruders. There is ample evidence in actual high-speed extrusion operations that the plastic is less susceptible to degradation in these operations.

■ 2.2 The Multiscrew Extruder

2.2.1 The Twin Screw Extruder

A twin screw extruder is a machine with two Archimedean screws. Admittedly, this is a very general definition. However, as soon as the definition is made more specific, it is limited to a specific class of twin screw extruders. There is a tremendous variety of twin screw extruders, with vast differences in design, principle of opera-

tion, and field of application. It is, therefore, difficult to make general comments about twin screw extruders. The differences between the various twin screw extruders are much larger than the differences between single screw extruders. This is to be expected, since the twin screw construction substantially increases the number of design variables, such as direction of rotation, degree of intermeshing, etc. A classification of twin screw extruders is shown in Table 2.4. This classification is primarily based on the geometrical configuration of the twin screw extruder. Some twin screw extruders function in much the same fashion as single screw extruders. Other twin screw extruders operate quite differently from single screw extruders and are used in very different applications. The design of the various twin screw extruders with their operational and functional aspects will be covered in more detail in Chapter 10.

Table 2.4 Classification of Twin Screw Extruders

Intermeshing extruders	Co-rotating extruders	Low speed extruders for profile extrusion
		High speed extruders for compounding
	Counter-rotating extruders	Conical extruders for profile extrusion
		Parallel extruders for profile extrusion
		High speed extruders for compounding
Non-intermeshing extruders	Counter-rotating extruders	Equal screw length
		Unequal screw length
	Co-rotating extruders	Not used in practice
	Co-axial extruders	Inner melt transport forward
		Inner melt transport rearward
		Inner solids transport rearward
		Inner plasticating with rearward transport

2.2.2 The Multiscrew Extruder With More Than Two Screws

There are several types of extruders, which incorporate more than two screws. One relatively well-known example is the planetary roller extruder, see Fig. 2.11.

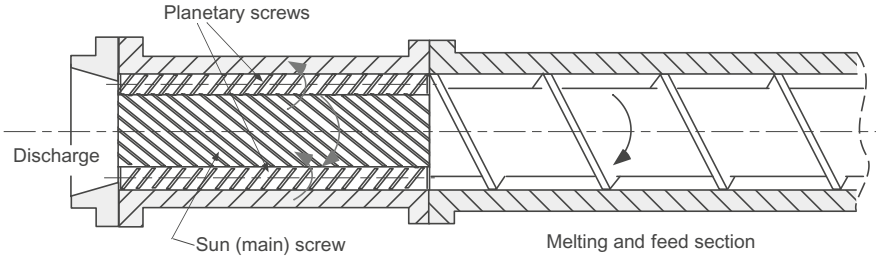


Figure 2.11 The planetary roller extruder

This extruder looks similar to a single screw extruder. The feed section is, in fact, the same as on a standard single screw extruder. However, the mixing section of the extruder looks considerably different. In the planetary roller section of the extruder, six or more planetary screws, evenly spaced, revolve around the circumference of the main screw. In the planetary screw section, the main screw is referred to as the sun screw. The planetary screws intermesh with the sun screw and the barrel. The planetary barrel section, therefore, must have helical grooves corresponding to the helical flights on the planetary screws. This planetary barrel section is generally a separate barrel section with a flange-type connection to the feed barrel section.

In the first part of the machine, before the planetary screws, the material moves forward as in a regular single screw extruder. As the material reaches the planetary section, being largely plasticated at this point, it is exposed to intensive mixing by the rolling action between the planetary screws, the sun screw, and the barrel. The helical design of the barrel, sun screw, and planetary screws result in a large surface area relative to the barrel length. The small clearance between the planetary screws and the mating surfaces, about ¼ mm, allows thin layers of compound to be exposed to large surface areas, resulting in effective devolatilization, heat exchange, and temperature control. Thus, heat-sensitive compounds can be processed with a minimum of degradation. For this reason, the planetary gear extruder is frequently used for extrusion/compounding of PVC formulations, both rigid and plasticized [21, 22]. Planetary roller sections are also used as add-ons to regular extruders to improve mixing performance [97, 98]. Another multiscrew extruder is the four-screw extruder, shown in Fig. 2.12.

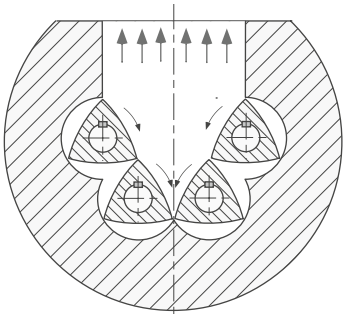


Figure 2.12
Four-screw extruder

This machine is used primarily for devolatilization of solvents from 40% to as low as 0.3% [23]. Flash devolatilization occurs in a flash dome attached to the barrel. The polymer solution is delivered under pressure and at temperatures above the boiling point of the solvent. The solution is then expanded through a nozzle into the flash dome. The foamy material resulting from the flash devolatilization is then transported away by the four screws. In many cases, downstream vent sections will be incorporated to further reduce the solvent level.

2.2.3 The Gear Pump Extruder

Gear pumps are used in some extrusion operations at the end of a plasticating extruder, either single screw or twin screw [99–106]. Strictly speaking, the gear pump is a closely intermeshing counterrotating twin screw extruder. However, since gear pumps are solely used to generate pressure, they are generally not referred to as an extruder although the gear pump is an extruder. One of the main advantages of the gear pump is its good pressure-generating capability and its ability to maintain a relatively constant outlet pressure even if the inlet pressure fluctuates considerably. Some fluctuation in the outlet pressure will result from the intermeshing of the gear teeth. This fluctuation can be reduced by a helical orientation of the gear teeth instead of an axial orientation.

Gear pumps are sometimes referred to as positive displacement devices. This is not completely correct because there must be mechanical clearances between the gears and the housing, which causes leakage. Therefore, the gear pump output is dependent on pressure, although the pressure sensitivity will generally be less than that of a single screw extruder. The actual pressure sensitivity will be determined by the design clearances, the polymer melt viscosity, and the rotational speed of the gears. A good method to obtain constant throughput is to maintain a constant pressure differential across the pump. This can be done by a relatively simple pressure feedback control on the extruder feeding into the gear pump [102]. The non-zero clearances in the gear pump will cause a transformation of mechanical energy into heat by viscous heat generation, see Section 5.3.4. Thus, the energy efficiency of actual gear pumps is considerably below 100%; the pumping efficiency generally ranges from 15 to 35%. The other 65 to 85% goes into mechanical losses and viscous heat generation. Mechanical losses usually range from about 20 to 40% and viscous heating from about 40 to 50%. As a result, the polymer melt going through the gear pump will experience a considerable temperature rise, typically 5 to 10°C. However, in some cases the temperature rise can be as much as 20 to 30°C. Since the gear pump has limited energy efficiency, the combination extruder-gear pump is not necessarily more energy-efficient than the extruder without the gear pump. Only if the extruder feeding into the gear pump is very inefficient in its pressure development will the addition of a gear pump allow a reduction in energy consumption. This could be the case with co-rotating twin screw extruders or single screw extruders with inefficient screw design.

The mixing capacity of gear pumps is very limited. This was clearly demonstrated by Kramer [106] by comparing melt temperature fluctuation before and after the gear pump, which showed no distinguishable improvement in melt temperature uniformity. Gear pumps are often added to extruders with unacceptable output fluctuations. In many cases, this constitutes treating the symptoms but not curing the actual problem. Most single screw extruders, if properly designed, can maintain

their output to within ± 1%. If the output fluctuation is considerably larger than 1%, there is probably something wrong with the machine; very often incorrect screw design. In these cases, solving the actual problem will generally be more efficient than adding a gear pump. For an efficient extruder-gear pump system, the extruder screw has to be modified to reduce the pressure-generating capacity of the screw.

Gear pumps can be used advantageously:

1. On extruders with poor pressure-generating capability (e.g., co-rotating twin screws, multi-stage vented extruders, etc.)
2. When output stability is required, better than 1%, i.e., in close tolerance extrusion (e.g., fiber spinning, cable extrusion, medical tubing, coextrusion, etc.)

Gear pumps can cause problems when:

1. The polymer contains abrasive components; because of the small clearances, the gear pump is very susceptible to wear.
2. When the polymer is susceptible to degradation; gear pumps are not self-cleaning and combined with the exposure to high temperatures this will result in degraded product.

2.3 Disk Extruders

There are a number of extruders, which do not utilize an Archimedean screw for transport of the material, but still fall in the class of continuous extruders. Sometimes these machines are referred to as screwless extruders. These machines employ some kind of disk or drum to extrude the material. One can classify the disk extruders according to their conveying mechanism (see Table 2.1). Most of the disk extruders are based on viscous drag transport. One special disk extruder utilizes the elasticity of polymer melts to convey the material and to develop the necessary diehead pressure.

Disk extruders have been around for a long time, at least since 1950. However, at this point in time the industrial significance of disk extruders is still relatively small compared to screw extruders.

2.3.1 Viscous Drag Disk Extruders

2.3.1.1 Stepped Disk Extruder

One of the first disk extruders was developed by Westover at Bell Telephone Laboratories: it is often referred to as a stepped disk extruder or slider pad extruder [24]. A schematic picture of the extruder is shown in Fig. 2.13.

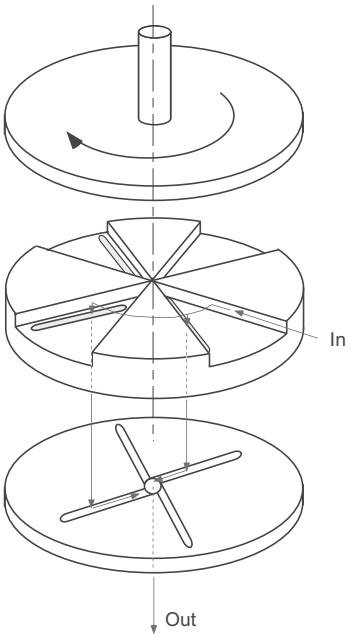


Figure 2.13
The stepped disk

The heart of the machine is the stepped disk positioned a small distance from a flat disk. When one of the disks is rotated with a polymer melt in the axial gap, a pressure build-up will occur at the transition of one gap size to another, smaller gap size; see Fig. 2.14.

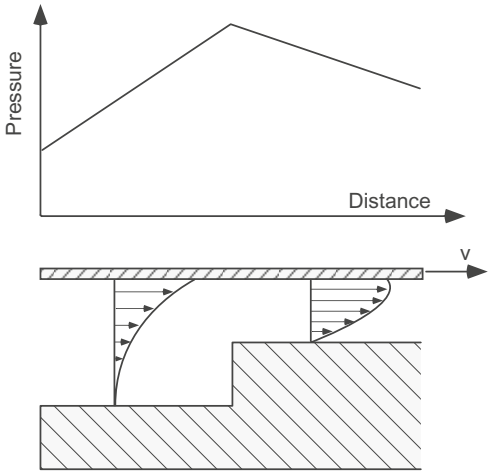


Figure 2.14
Pressure generation in the step region

If exit channels are incorporated into the stepped disk, the polymer can be extruded in a continuous fashion. The design of this extruder is based on Rayleigh's [25] analysis of hydrodynamic lubrication in various geometries. He concluded that the parallel stepped pad was capable of supporting the greatest load. The stepped disk

extruder has also been designed in a different configuration using a gradual change in gap size. This extruder has a wedge-shaped disk with a gradual increase in pressure with radial distance.

A practical disadvantage of the stepped disk extruder is the fact that the machine is difficult to clean because of the intricate design of the flow channels in the stepped disk.

2.3.1.2 Drum Extruder

Another rather old concept is the drum extruder. A schematic picture of a machine manufactured by Schmid & Kocher in Switzerland is shown in Fig. 2.15.

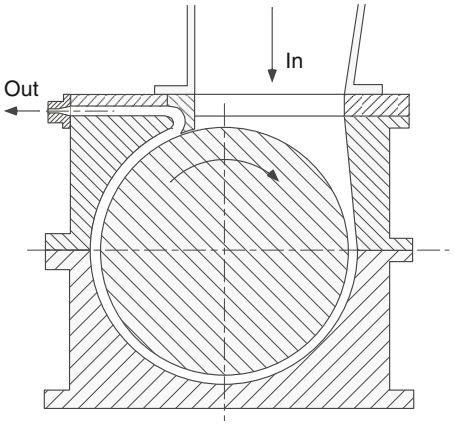


Figure 2.15
The drum extruder by Schmid & Kocher

Material is fed by a feed hopper into an annular space between rotor and barrel. By the rotational motion of the rotor, the material is carried along the circumference of the barrel. Just before the material reaches the feed hopper, it encounters a wiper bar. This wiper bar scrapes the polymer from the rotor and deflects the polymer flow into a channel that leads to the extruder die. Several patents [26, 27] were issued on this design; however, these patents have long since expired.

A very similar extruder (see Fig. 2.16) was developed by Askco Engineering and Cosden Oil & Chemical in a joint venture; later this became Permian Research. Two patents have been issued on this design [28, 29], even though the concept is very similar to the Schmid & Kocher design.

One special feature of this design is the capability to adjust the local gap by means of a choker bar, similar to the gap adjustment in a flat sheet die, see Section 9.2. The choker bar in this drum extruder is activated by adjustable hydraulic oil pressure. Drum extruders have not been able to be a serious competition to the single screw extruder over the last 50 years.

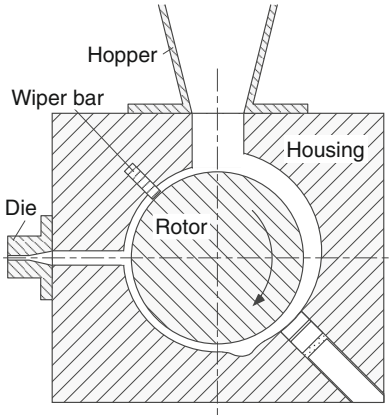


Figure 2.16
The drum extruder by Asko/Cosden

2.3.1.3 Spiral Disk Extruder

The spiral disk extruder is another type of disk extruder that has been known for many years. Several patented designs were described by Schenkel (Chapter 1, [3]). Similar to the stepped disk extruder, the development of the spiral disk extruder is closely connected to spiral groove bearings. It has long been known that spiral groove bearings are capable of supporting substantial loads. Ingen Housz [30] has analyzed the melt conveying in a spiral disk extruder with logarithmic grooves in the disk, based on Newtonian flow behavior of the polymer melt. In terms of melt conveying capability, the spiral disk extruder seems comparable to the screw extruder; however, the solids conveying capability is questionable.

2.3.1.4 Diskpack Extruder

Another development in disk extruders is the diskpack extruder. Tadmor originated the idea of the diskpack machine, which is covered under several patents [31–33]. The development of the machine was undertaken by the Farrel Machinery Group of Emgart Corporation in cooperation with Tadmor [34–39]. The basic concept of the machine is shown in Fig. 2.17.

Material drops in the axial gap between relatively thin disks mounted on a rotating shaft. The material will move with the disks almost a full turn, then it meets a channel block. The channel block closes off the space between the disks and deflects the polymer flow to either an outlet channel, or to a transfer channel in the barrel. The shape of the disks can be optimized for specific functions: solids conveying, melting, devolatilization, melt conveying, and mixing. A detailed functional analysis can be found in Tadmor's book on polymer processing (Chapter 1, [32]).

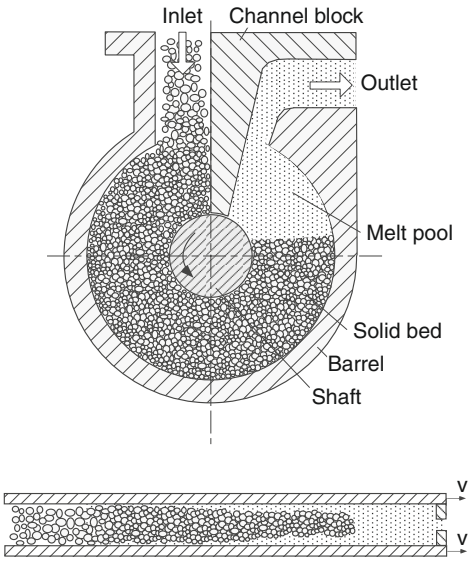


Figure 2.17
The diskpack extruder

It is claimed that this machine can perform all basic polymer-processing operations with efficiency equaling or surpassing existing machinery. Clearly, if the claim is true and can be delivered for a competitive price, the diskpack extruder will become an important machine in the extrusion industry. The first diskpack machines were delivered to the industry in 1982, still under a joint development type of agreement. Now, almost 20 years after the first diskpack machines were delivered, it is clear that the acceptance of these machines in the industry has been very limited. In fact, Farrel no longer actively markets the diskpack machine. In most of the publications, the diskpack machine is referred to as a polymer processor. This term is probably used to indicate that this machine can do more than just extruding, although the diskpack is, of course, an extruder.

The diskpack machine incorporates some of the features of the drum extruder and the single screw extruder. One can think of the diskpack as a single screw extruder using a screw with zero helix angle and very deep flights. Forward axial transport can only take place by transport channels in the barrel, with the material forced into those channels by a restrictor bar, as with the drum extruder. The use of restrictor bars (channel block) and transfer channels in the housing make it considerably more complex than the barrel of a single screw extruder.

One of the advantages of the diskpack is that mixing blocks and spreading dams can be incorporated into the machine as shown in Fig. 2.18(a).

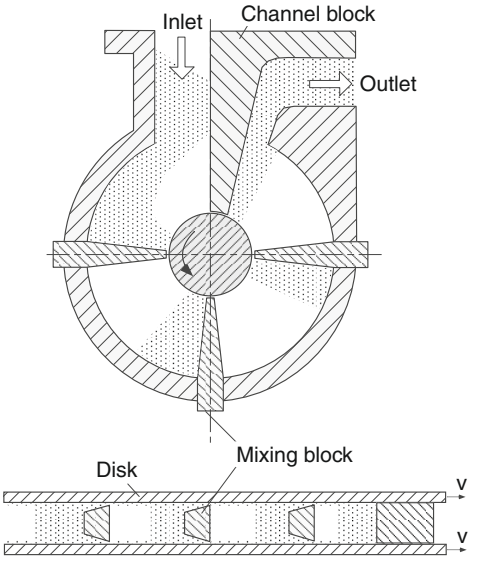


Figure 2.18(a)
Mixing blocks in the diskpack

Mixing blocks of various shapes can be positioned externally into the processing chamber. This is similar to the QSM extruder, only that in the QSM extruder the screw flight has to be interrupted to avoid contact. This is not necessary in the diskpack because the flights have zero helix angles; in other words, they run perpendicular to the rotor axis. By the number of blocks, the geometry of the block, and the clearance between block and disk, one can tailor the mixing capability to the particular application. The use of spreading dams allows the generation of a thin film with a large surface area; this results in effective devolatilization capability. The diskpack has inherently higher pressure-generating capability than the single screw extruder does. This is because the diskpack has two dragging surfaces, while the single screw extruder has only one, see Fig. 2.18(b).

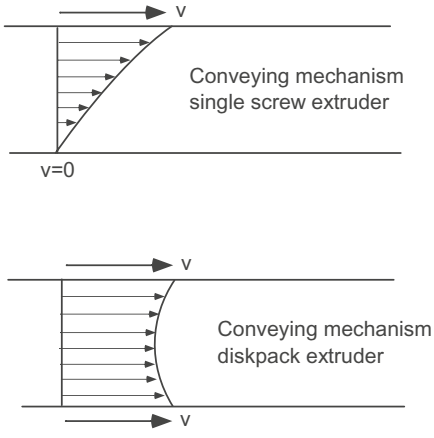


Figure 2.18(b)
Comparison of conveying mechanism in diskpack and single screw extruder

At the same net flow rate, equal viscosity, equal plate velocity, and optimum plate separation, the theoretical maximum pressure gradient of the diskpack is eight times higher than the single screw extruder [34]. Thus, high pressures can be generated over a short distance, which allows a more compact machine design. The energy efficiency of the pressure generation is also better than in the single screw extruder; the maximum pumping efficiency approaches 100%; see derivation in Appendix 2.1. For the single screw extruder, the maximum pumping efficiency is only 33% as discussed in Section 7.4.1.3. The energy efficiency of pressure generation is the ratio of the theoretical energy requirement (flow rate times pressure rise) to the actual energy requirement (wall velocity times shear stress integrated over wall surface). It should be noted that the two dragging plates' pumping mechanism exists only in tangential direction. The pumping in axial (forward) direction occurs only in the transfer channel in the housing. This forward pumping occurs by the one dragging plate mechanism as in the single screw extruder. The maximum efficiency for forward pumping, therefore, is only 33%. The overall pumping efficiency will be somewhere between 33 and 100% if the power consumption in the disk and channel block clearance is neglected.

Studies on melting in the diskpack were reported by Valsamis et al. [96]. It was found that two types of melting mechanism could take place in the diskpack: the drag melt removal (DMR) mechanism and the dissipative melt mixing (DMM) mechanism. The DMR melting mechanism is the predominant mechanism in single screw extruders; this is discussed in detail in Section 7.3. In the DMR melting mechanism, the solids and melt coexist as two largely continuous and separate phases. In the DMM melting mechanism, the solids are dispersed in the melt; there is no continuous solid bed. It was found that the DMM mechanism could be induced by promoting back leakage of the polymer melt past the channel block. This can be controlled by varying the clearance between the channel block and the disks. The advantage of the DMM melting mechanism is that the melting rate can be substantially higher than with the DMR mechanism, reportedly by as much as a factor of 3 [96].

Among all elementary polymer processing functions, the solids conveying in a diskpack extruder has not been discussed to any extent in the open technical literature. Considering that the solids conveying mechanism is a frictional drag mechanism (as in single screw extruders) and not a positive displacement type of transport (as in intermeshing counterrotating twin screw extruders, see Sections 10.2 and 10.4), it can be expected that the diskpack will have solids conveying limitations similar to those of single screw extruders, see Section 7.2.2. This means that powders, blends of powders and pellets, slippery materials, etc., are likely to encounter solids conveying problems in a diskpack extruder unless special measures are taken to enhance the solids conveying capability (e. g., crammer feeder, grooves in the disks, etc.).

Because of the more complex machine geometry, the cost per unit throughput of the diskpack is higher than for the conventional single screw extruder. Therefore, the diskpack does not compete directly with single screw extruders.

Applications for the diskpack are specialty polymer processing operations, such as polymerization, post-reactor processing (devolatilization), continuous compounding, etc. As such, the diskpack competes mostly with twin screw extruders. Presently, twin screw extruders are usually the first choice when it comes to specialty polymer processing operations.

2.3.2 The Elastic Melt Extruder

The elastic melt extruder was developed in the late 1950s by Maxwell and Scalora [40, 41]. The extruder makes use of the viscoelastic, in particular the elastic, properties of polymer melts. When a viscoelastic fluid is exposed to a shearing deformation, normal stresses will develop in the fluid that are not equal in all directions, as opposed to a purely viscous fluid. In the elastic melt extruder, the polymer is sheared between two plates, one stationary and one rotating; see Fig. 2.19.

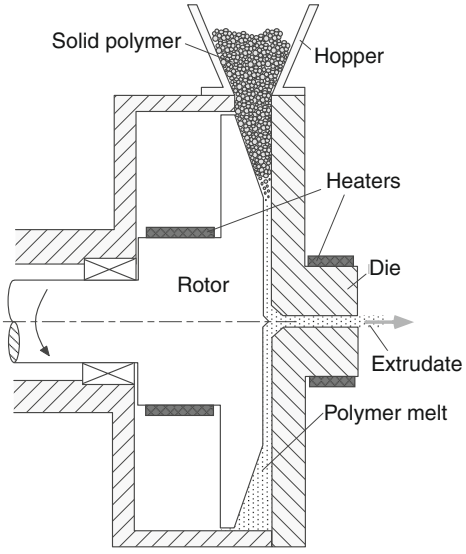


Figure 2.19
The elastic melt extruder

As the polymer is sheared, normal stresses will generate a centripetal pumping action. Thus, the polymer can be extruded through the central opening in the stationary plate in a continuous fashion. Because normal stresses generate the pumping action, this machine is sometimes referred to as a normal stress extruder.

This extruder is quite interesting from a rheological point of view, since it is probably the only extruder that utilizes the elasticity of the melt for its conveying. Thus,

several detailed experimental and theoretical studies have been devoted to the elastic melt extruder [42–47].

The detailed study by Fritz [44] concluded that transport by normal stresses only could be as much as two orders of magnitude lower than a corresponding system with forced feed. In addition, substantial temperature gradients developed in the polymer, causing substantial degradation in high molecular weight polyolefins. The scant market acceptance of the elastic melt extruder would tend to confirm Fritz's conclusions.

Several modifications have been proposed to improve the performance of the elastic melt extruder. Fritz [43] suggested incorporation of spiral grooves to improve the pressure generating capability, essentially combining the elastic melt extruder and the spiral disk extruder into one machine. In Russia [47], several modifications were made to the design of the elastic melt extruder. One of those combined a screw extruder with the elastic melt extruder to eliminate the feeding and plasticating problem. Despite all of these activities, the elastic melt extruder has not been able to acquire a position of importance in the extrusion industry.

2.3.3 Overview of Disk Extruders

Many attempts have been made in the past to come up with a continuous plasticating extruder of simple design that could perform better than the single screw extruder. It seems fair to say that, at this point in time no disk extruder has been able to meet this goal. The simple disk extruders do not perform nearly as well as the single screw extruder. The more complex disk extruder, such as the diskpack, can possibly outperform the single screw extruder. However, this is at the expense of design simplicity, thus increasing the cost of the machine. Disk extruders, therefore, have not been able to seriously challenge the position of the single screw extruder. This is not to say, however, that it is not possible for this to happen some time in the future. But, considering the long dominance of the single screw extruder, it is not probable that a new disk extruder will come along that can challenge the single screw extruder.

2.4 Ram Extruders

Ram or plunger extruders are simple in design, rugged, and discontinuous in their mode of operation. Ram extruders are essentially positive displacement devices and are able to generate very high pressures. Because of the intermittent operation of

ram extruders, they are ideally suited for cyclic processes, such as injection molding and blow molding. In fact, the early molding machines were almost exclusively equipped with ram extruders to supply the polymer melt to the mold. Certain limitations of the ram extruder have caused a switch to reciprocating screw extruders or combinations of the two. The two main limitations are:

1. Limited melting capacity
2. Poor temperature uniformity of the polymer melt

Presently, ram extruders are used in relatively small shot size molding machines and certain specialty operations where use is made of the positive displacement characteristics and the outstanding pressure generation capability. There are basically two types of ram extruders: single ram extruders and multi ram extruders.

2.4.1 Single Ram Extruders

The single ram extruder is used in small general purpose molding machines, but also in some special polymer processing operations. One such operation is the extrusion of intractable polymers, such as ultrahigh molecular weight polyethylene (UHMWPE) or polytetrafluoroethylene (PTFE). These polymers are not considered to be melt processable on conventional melt processing equipment. Teledynamik [48] has built a ram injection-molding machine under a license from Th. Engel who developed the prototype machine. This machine is used to mold UHMWPE under very high pressures. The machine uses a reciprocating plunger that densifies the cold incoming material with a pressure up to 300 MPa (about 44,000 psi). The frequency of the ram can be adjusted continuously with a maximum of 250 strokes/minute. The densified material is forced through heated channels into the heated cylinder where final melting takes place. The material is then injected into a mold by a telescoping injection ram. Pressures up to 100 MPa (about 14,500 psi) occur during the injection of the polymer into the mold.

Another application is the extrusion of PTFE, with again the primary ingredient for successful extrusion being very high pressures. Granular PTFE can be extruded at slow rates in a ram extruder [49–51]. The powder is compacted by the ram, forced into a die where the material is heated above the melting point and shaped into the desired form. PTFE is often processed as a PTFE paste [52, 53]. This is small particle size PTFE powder (about 0.2 mm) mixed with a processing aid such as naphta. PTFE paste can be extruded at room temperature or slightly above room temperature. After extrusion, the processing aid is removed by heating the extrudate above its volatilization temperature. The extruded PTFE paste product may be sintered if the application requires a more fully coalesced product.

2.4.1.1 Solid State Extrusion

An extrusion technique that has slowly been gaining popularity is solid-state extrusion. The polymer is forced through a die while it is below its melting point. This causes substantial deformation of the polymer in the die, but since the polymer is in the solid state, a very effective molecular orientation takes place. This orientation is much more effective than the one which occurs in conventional melt processing. As a result, extraordinary mechanical properties can be obtained.

Solid-state extrusion is a technique borrowed from the metal industry, where solid-state extrusion has been used commercially since the late 1940s. Bridgman [54] was one of the first to do a systematic study on the effect of pressure on the mechanical properties of metals. He also studied polymers and found that the glass transition temperature was raised by the application of pressure.

There are two methods of solid-state extrusion; one is direct solid-state extrusion, the other is hydrostatic extrusion. In direct solid-state extrusion, a pre-formed solid rod of material (a billet) is in direct contact with the plunger and the walls of the extrusion die, see Fig. 2.20. The material is extruded as the ram is pushed towards the die.

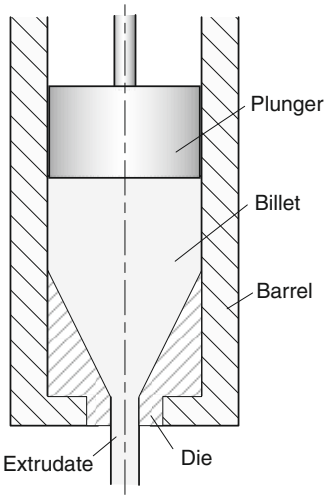


Figure 2.20
Direct solid state extrusion

In hydrostatic extrusion, the pressure required for extrusion is transmitted from the plunger to the billet through a lubricating liquid, usually castor oil. The billet must be shaped to fit the die to prevent loss of fluid. The hydrostatic fluid reduces the friction, thereby reducing the extrusion pressure, see Fig. 2.21.

In hydrostatic extrusion, the pressure-generating device for the fluid does not necessarily have to be in close proximity to the forming part of the machine. The fluid can be supplied to the extrusion device by high-pressure tubes.

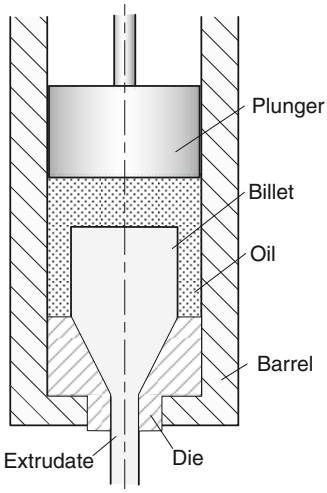


Figure 2.21
Hydrostatic solid state extrusion

Judging from publications in the open literature, most of the work on solid-state extrusion of polymers is done at universities and research institutes. It is possible, of course, that some companies are working on solid-state extrusion but are keeping the information proprietary. A major research effort in solid-state extrusion has been made at the University of Amherst, Massachusetts [50–64], University of Leeds, England [65–72], Fyushu University, Fukuoka, Japan [73–76], Research Institute for Polymers and Textiles, Yokohama, Japan [77–79], Battelle, Columbus, Ohio [80–83], and Rutgers University, New Brunswick, New Jersey [84–86]. As mentioned earlier, publications from other sources are considerably less plentiful [87–90]. Efforts have also been made to achieve the same high degree of orientation in a more or less conventional extrusion process by special die design and temperature control in the die region [91].

Table 2.5 shows a comparison of mechanical properties between steel, aluminum, solid state extruded HDPE, and HDPE extruded by conventional means.

Table 2.5 clearly indicates that the mechanical properties of solid-state extruded HDPE are much superior to the melt extruded HDPE. In fact, the tensile strength of solid-state extruded HDPE is about the same as carbon steel! There are some other interesting benefits associated with solidstate extrusion of polymers. There is essentially no die swell at high extrusion ratios (extrusion ratio is the ratio of the area in the cylinder to the area in the die). Thus, the dimensions of the extrudate closely conform to those of the die exit. The surface of the extrudate produced by hydrostatic extrusion has a lower coefficient of friction than that of the un-oriented polymer. Above a certain extrusion ratio (about ten), polyethylene and polypropylene become transparent. Further, solid-state extruded polymers maintain their tensile properties at elevated temperatures. Polyethylene maintains its modulus up to 120°C when it is extruded in the solid state at a high extrusion ratio. The thermal

conductivity in the extrusion direction is much higher than that of the un-oriented polymer, as much as 25 times higher. The melting point of the solid-state extruded polymer increases with the amount of orientation. The melting point of HDPE can be shifted to as high as 140°C.

Table 2.5 Comparison of Mechanical Properties

Material	Tensile modulus [MPa]	Tensile strength [MPa]	Elongation [%]	Density [g/cc]
Annealed SAE 1020	210,000	410	35	7.86
W-200 °F SAE 1020	210,000	720	6	7.86
Annealed 304 stainless steel	200,000	590	50	7.92
Aluminum 1100-0	70,000	90	45	2.71
HDPE solid state extruded	70,000	480	3	0.97
HDPE melt extruded	10,000	30	20–1000	0.96

A recent application of solid-state extrusion is the process developed by Synthetic Hardwood Technologies, Inc. [107]. This company has developed an expanded, oriented, wood-filled polypropylene (EOW-PP) that is about 300% stronger than regular PP. The process is based on technology developed at Aluminum Company of Canada Ltd. (Alcan) in the early 1990s to solidstate extrude PP. It involves ram extrusion/drawing of billets of PP just below the melting point with very high draw ratio and high haul-off tension (about 3 MPa) to freeze-in the high level of orientation. Alcan did not pursue the technology and Symplastics Ltd. licensed the patented process; this company started experimenting with adding small amounts of wood flour to the PP. However, Symplastics found the research and development too costly and sold the patents and lab extrusion equipment to Frank Maine who set up SHW to commercialize applications for the EOW-PP. The key to the SHW process is that it combines extrusion with drawing. As the polymer is oriented, the density drops about 50%, from about 1 g/cc to 0.5 g/cc. The die drawing also allowed substantial increases in line speed, from about 0.050 m/min to about 9 m/min. The properties achieved with EOW-PP are shown in Table 2.4 and compared to regular PP, wood, and oriented PP.

Solid-state extrusion has been practiced with coextrusion of different polymers [93]. Despite the large amount of research on solid-state extrusion and the outstanding mechanical properties that can be obtained, there does not seem to be much interest in the polymer industry. The main drawbacks, of course, are that solid-state extrusion is basically a discontinuous process, it cannot be done on conventional polymer processing equipment, and very high pressures are required to achieve solid-state extrusion. Also, one should keep in mind that very good mechanical properties can be obtained by taking a profile (fiber, film, tube, etc.) produced by conventional, con-

tinuous extrusion and exposing it to controlled deformation at a temperature below the melting point. This is a well-established technique in many extrusion operations (fiber spinning, film extrusion, etc.), and it can be done at a high rate. This method of producing extrudates with very good mechanical properties is likely to be more cost-effective than solid-state extrusion. It is possible that the die drawing process developed by SHW can make solid-state extrusion more attractive commercially by allowing large profiles to be processed at reasonable line speeds.

Table 2.6 Mechanical Properties of PP, Wood, OPP, and EOW-PP

	Flexural strength [MPa]	Flexural modulus [MPa]
Regular PP	50	1850
Wood	100	9000
Oriented PP	275	7600
EOW-PP	140	7600

2.4.2 Multi Ram Extruder

As mentioned before, the main disadvantage of ram extruders is their intermittent operation. Several attempts have been made to overcome this problem by designing multi-ram extruders that work together in such a way as to produce a continuous flow of material.

Westover [94] designed a continuous ram extruder that combined four plunger-cylinders. Two plunger-cylinders were used for plasticating and two for pumping. An intricate shuttle valve connecting all the plunger cylinders provides continuous extrusion.

Another attempt to develop a continuous ram extruder was made by Yi and Fenner [95]. They designed a twin ram extruder with the cylinders in a V-configuration, see Fig. 2.22.

The two rams discharge into a common barrel in which a plasticating shaft is rotating. Thus, solids conveying occurs in the two separate cylinders and plasticating and melt conveying occurs in the annular region between the barrel and plasticating shaft. The machine is able to extrude; however, the throughput uniformity is poor. The performance could probably have been improved if the plasticating shaft had been provided with a helical channel. But, of course, then the machine would have become a screw extruder with a ram-assisted feed. This only goes to demonstrate that it is far from easy to improve upon the simple screw extruder.

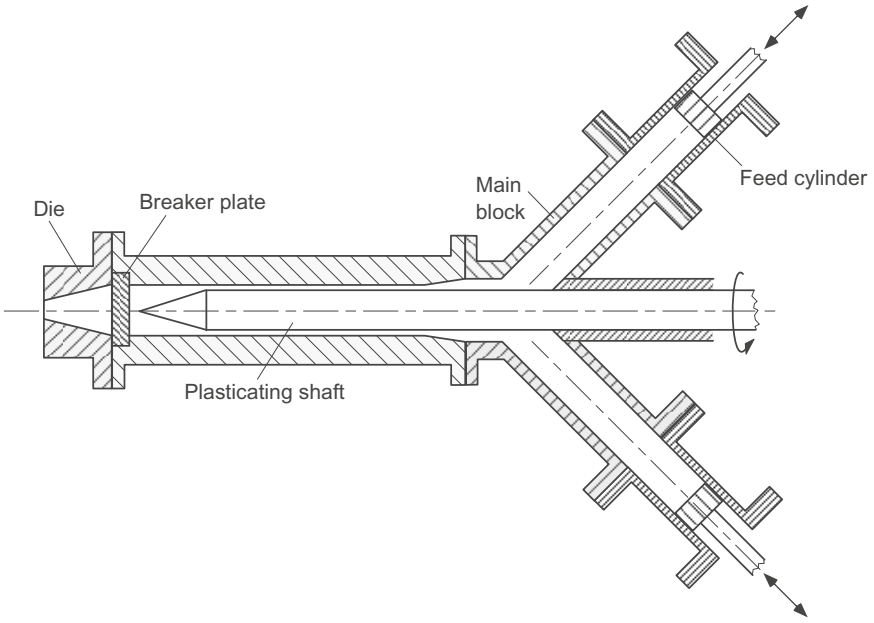


Figure 2.22 Twin ram extruder

2.4.3 Appendix 2.1

2.4.3.1 Pumping Efficiency in Diskpack Extruder

The velocity profile between the moving walls is a parabolic function when the fluid is a Newtonian fluid, see Section 6.2.1 and Fig. 2.23.

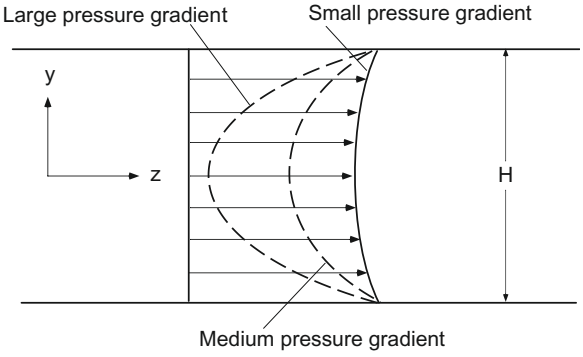


Figure 2.23
Velocity profiles between moving walls

The velocity profile for a Newtonian fluid is:

$$v(y) = v - \left(1 - \frac{4y^2}{H^2}\right)\frac{H^2 \Delta P}{8\mu \Delta L} \tag{1}$$

where v is the velocity of the plates, H the distance between the plates, and μ the viscosity of the fluid. The flow rate can be found by integrating v(y) over the width and depth of the channel; this yields:

$$\dot{V} = vWH - \frac{H^3 W \Delta P}{12 \mu \Delta L} \tag{2}$$

The first term on the right-hand side of the equalation is the drag flow term. The second term is the pressure flow term. The ratio of pressure flow to drag flow is termed the throttle ratio, r_d (see Section 7.4.1.3):

$$r_d = \frac{H^2 \Delta P}{12 v \mu \Delta L} \tag{3}$$

The flow rate can now be written as:

$$\dot{V} = vWH(1 - r_d) \tag{4}$$

The shear stress at the wall is obtained from:

$$\tau = \mu \frac{dv}{dy}\bigg|_{0.5H} = \frac{H \Delta P}{2 \Delta L} \tag{5}$$

The power consumption in the channel is:

$$Z_{ch} = 2\tau W \Delta L v = vHW\Delta P \tag{6}$$

The energy efficiency for pressure generation is:

$$\varepsilon = \frac{V \Delta P}{Z_{ch}} = 1 - r_d \tag{7}$$

Equation 7 is not valid for $r_d = 0$, because in this case both numerator and denominator become zero. From Eq. 7 it can be seen that when the machine is operated at low r_d values, the pumping efficiency can become close to 100%. This is considerably better than the single screw extruder where the optimum pumping efficiency is 33% at a throttle ratio value of 0.33 ($r_d = 1/3$).

References

1. J. LeBras, “Rubber, Fundamentals of its Science and Technology”, Chemical Publ. Co, NY (1957)
2. W.S. Penn, “Synthetic Rubber Technology, Volume I”, MacLaren & Sons, Ltd., London (1960)
3. W.J.S. Naunton, “The Applied Science of Rubber”, Edward Arnold Ltd., London (1961)

4. C.M. Blow, “Rubber Technology and Manufacture”, Butterworth & Co. Ltd., London (1971)
5. F.R. Eirich (Ed.), “Science and Technology of Rubber”, Academic Press, NY (1978)
6. C.W. Evans, “Powdered and Particulate Rubber Technology”, Applied Science Publ. Ltd., London (1978)
7. G. Targiel et al., 10. IKV-Kolloquium, Aachen March 12–14, 45 (1980)
8. A. Kennaway, Kautschuk und Gummi, Kunststoffe 17, 378–391 (1964)
9. G. Menges and J.P. Lehnen, Plastverarbeiter 20, 1, 31–39 (1969)
10. M. Parshall and A.J. Saulino, Rubber World, 2, 5, 78–83 (1967)
11. S.E. Perlberg, Rubber World, 2, 6, 71–76 (1967)
12. H.H. Gohlisch, Gummi, Asbest, Kunststoffe, 25, 9, 834–835 (1972)
13. E. Harms, “Kautschuk-Extruder, Aufbau und Einsatz aus verfahrenstechnischer Sicht”, Krausskopf-Verlag Mainz, Bd 2, Buchreihe Kunststofftechnik (1974)
14. G. Schwarz, Eur. Rubber Journal, Sept. 28–32 (1977)
15. G. Menges and E.G. Harms, Kautschuk und Gummi, Kunststoffe 25, 10, 469–475 (1972)
16. G. Menges and E.G. Harms, Kautschuk und Gummi, Kunststoffe 27, 5, 187–193 (1974)
17. E.G. Harms, Elastomerics, 109, 6, 33–39 (1977)
18. E.G. Harms, Eur. Rubber Journal, 6, 23 (1978)
19. E.G. Harms, Kunststoffe, 69, 1, 32–33 (1979)
20. E.G. Harms, Dissertation RWTH Aachen, Germany (1981).
21. S.H. Collins, Plastics Compounding, Nov./Dec., 29 (1982)
22. D. Anders, Kunststoffe, 69, 194–198 (1979)
23. D. Gras and K. Eise, SPE Tech. Papers (ANTEC), 21, 386 (1975)
24. R.F. Westover, SPE Journal, 18, 12, 1473 (1962).
25. Lord Raleigh, Philosophical Magazine, 35, 1–12 (1918)
26. German Patent: DRP 1,129,681
27. British Patent: BP 759,354
28. U.S. Patent: 3,880,564
29. U.S. Patent: 4,012,477
30. J.F. Ingen Housz, Plastverarbeiter, 10, 1 (1975)
31. U. S. Patent: 4,142,805
32. U.S. Patent: 4,194,841
33. U.S. Patent: 4,213,709
34. Z. Tadmor, P. Hold, and L. Valsamis, SPE Tech. Papers (ANTEC), 25, 193 (1979)
35. P. Hold, Z. Tadmor, and L. Valsamis, SPE Tech. Papers (ANTEC), 25, 205 (1979)
36. Z. Tadmor, P. Hold, and L. Valsamis, Plastics Engineering, Nov., 20–25 (1979)
37. Z. Tadmor, P. Hold, and L. Valsamis, Plastics Engineering, Dec., 30–38 (1979)

38. Z. Tadmor et al., The Diskpack Plastics Processor, Farrel Publication, Jan. (1982)
39. L. Valsamis, AIChE Meeting, Washington, D.C., Oct. (1983)
40. B. Maxwell and A. J. Scalora, Modern Plastics, 37, 107, Oct. (1959)
41. U.S. Patent: 3, 046,603
42. L.L. Blyler, Ph.D. thesis, Princeton University, NJ (1966)
43. H.G. Fritz, Kunststofftechnik, 6, 430 (1968)
44. H.G. Fritz, Ph.D. thesis, Stuttgart University, Germany (1971)
45. C.W. Macosko and J.M. Starita, SPE Journal 27, 30 (1971)
46. P.A. Good, A.J. Schwartz, and C.W. Macosko, AIChE Journal, 20, 1, 67 (1974)
47. V.L. Kocherov, Y.L. Lukach, E.A. Sporyagin, and G.V. Vinogradov, Polym. Eng. Sci., 13, 194 (1973)
48. J. Berzen and G. Braun, Kunststoffe, 69, 2, 62–66 (1979)
49. R.S. Porter et al., J. Polym. Sci., 17, 485–488 (1979)
50. C.A. Sperati, Modern Plastics Encyclopedia, McGraw-Hill, NY (1983)
51. S.S. Schwartz and S.H. Goodman, see Chapter 1, [36]
52. G.R. Snelling and J.F. Lontz, J. Appl. Polym. Sci., 3, 9, 257–265 (1960)
53. D.C.F. Couzens, Plastics and Rubber Processing, March, 45–48 (1976).
54. P.W. Bridgman, "Studies in Large Plastic Flow and Fracture", McGraw-Hill, NY (1952)
55. H.L.D. Push, "The Mechanical Behavior of Materials Under Pressure", Elsevier, Amsterdam (1970)
56. H.L.D. Push and A.H. Low, J. Inst. Metals, 93, 201 (1965/65)
57. F. Slack, Mach. Design, Oct 7, 61–64 (1982)
58. J.H. Southern and R.S. Porter, J. Appl. Polym. Sci., 14, 2305 (1970)
59. J.H. Southern and R.S. Porter, J. Macromol. Sci. Phys., 3–4, 541 (1970)
60. J.H. Southern, N.E. Weeks, and R.S. Porter, Macromol. Chem., 162, 19 (1972)
61. N.J. Capiati and R.S. Porter, J. Polym. Sci., Polym. Phys. Ed., 13, 1177 (1975)
62. R.S. Porter, J.H. Southern, and N.E. Weeks, Polym. Eng. Sci., 15, 213 (1975)
63. A.E. Zachariades, E.S. Sherman, and R.S. Porter, J. Polym. Sci. Polym. Lett. Ed., 17, 255 (1979)
64. A.E. Zachariades and R.S. Porter, J. Polym. Sci. Polym. Lett. Ed., 17, 277 (1979)
65. B. Parsons, D. Bretherton, and B.N. Cole, in: Advances in MTDR, 11th Int. Conf. Proc., S.A. Tobias and F. Koeningsberger (Eds.), Pergamon Press, London, Vol. B, 1049 (1971)
66. G. Capaccio and I.M. Ward, Polymer 15, 233 (1974)
67. A.G. Gibson, I.M. Ward, B.N. Cole, and B. Parsons, J. Mater. Sci., 9, 1193–1196 (1974)
68. A.G. Gibson and I.M. Ward, J. Appl. Polym. Sci. Polym. Phys. Ed., 16, 2015–2030 (1978)
69. P.S. Hope and B. Parsons, Polym. Eng. Sci., 20, 589–600 (1980)
70. P.S. Hope, I.M. Ward, and A.G. Gibson, J. Polym. Sci. Polym. Phys. Ed., 18, 1242–1256 (1980)

71. P.S. Hope, A.G. Gibson, B. Parsons, and I.M. Ward, Polym. Eng. Sci., 20, 54–55 (1980)
72. B. Parsons and I.M. Ward, Plast. Rubber Proc. Appl., 2, 3, 215–224 (1982)
73. K. Imada, T. Yamamoto, K. Shigematsu, and M. Takayanagi, J. Mater. Sci., 6, 537–546 (1971)
74. K. Nakamura, K. Imada, and M. Takayanagi, Int J. Polym. Mater., 2, 71 (1972)
75. K. Imada and M. Takayanagi, Int. J. Polym. Mater., 2, 89 (1973)
76. K. Nakamura, K. Imada, and M. Takayanagi, Int. J. Polym. Mater., 3, 23 (1974)
77. K. Nakayama and H. Kanetsuna, J. Mater. Sci., 10, 1105 (1975)
78. K. Nakayama and H. Kanetsuna, J. Mater. Sci., 12, 1477 (1977)
79. K. Nakayama and H. Kanetsuna, J. Appl. Polym. Sci., 23, 2543–2554 (1979)
80. D.M. Bigg, Polym. Eng. Sci., 16, 725 (1976)
81. D.M. Bigg, M.M. Epstein, R.J. Fiorentino, and E.G. Smith, Polym. Eng. Sci., 18, 908 (1978)
82. D.M. Bigg and M.M. Epstein, "Science and Technology of Polymer Processing", N.S. Suh and N. Sung (Eds.), 897, MIT Press (1979)
83. D.M. Bigg, M.M. Epstein, R.J. Fiorentino, and E.G. Smith, J. Appl. Polym. Sci., 26, 395–409 (1981)
84. K.D. Pae and D.R. Mears, J. Polym. Sci., B-6, 269 (1968)
85. K.D. Pae, D.R. Mears, and J.A. Sauer, J. Polym. Sci. Polym. Lett. Ed., 6, 773 (1968)
86. D.R. Mears, K.P. Pae, and J.A. Sauer, J. Appl. Phys., 40, 11, 4229–4237 (1969)
87. L.A. Davis and C.A. Pampillo, J. Appl., Phys., 42, 12, 4659–4666 (1971)
88. A. Buckley and H.A. Long, Polym. Eng. Sci., 9, 2, 115–120 (1969)
89. L.A. Davis, Polym. Eng. Sci., 14, 9, 641–645 (1974)
90. R.K. Okine and N.P. Suh, Polym. Eng. Sci., 22, 5, 269–279 (1982)
91. J.R. Collier, T.Y.T. Tam, J. Newcome, and N. Dinos, Polym. Eng. Sci, 16, 204–211 (1976)
92. J.H. Faupel and F.E. Fisher, "Engineering Design", Wiley, NY (1981)
93. A.E. Zachariades, R. Ball, and R.S. Porter, J. Mater. Sci., 13, 2671–2675 (1978)
94. R.R. Westover, Modern Plastics, March (1963)
95. B. Yi and R.T. Fenner, Plastics and Polymers, Dec., 224–228 (1975)
96. A. Mekkaoui and L.N. Valsamis, Polym. Eng. Sci., 24, 1260–1269 (1984)
97. H. Rust, Kunststoffe, 73, 342–346 (1983)
98. J. Huszman, Kunststoffe, 73, 3437–348 (1983)
99. J.M. McKelvey, U. Maire, and F. Haupt, Chem. Eng., Sept. 27, 94–102 (1976)
100. K. Schneider, Kunststoffe, 68, 201–206 (1978)
101. W.T. Rice, Plastic Technology, 87–91, Feb. (1980)
102. Harrel Corp., "Melt Pump Systems for Extruders", Product Description TDS-264 (1982)
103. J.M. McKelvey and W.T. Rice, Chem. Eng., 90, 2 89–94 (1983)
104. K. Kapfer, K. Eise, and H. Herrmann, SPE ANTEC, Chicago, 161–163 (1983)

105. C. L. Woodworth, SPE ANTEC, New Orleans, 122–126 (1984)

106. W. A. Kramer, SPE ANTEC, Washington, D. C., 23–29 (1985)

107. J. Schut, "Die Drawing Makes Plastic Steel," Plastics Technology, Online Article, March 5 (2001)

108. VDI Conference Extrusiontechnik 2006, "Der Einschnecken-Extruder von Morgen," VDI Verlag GmbH, Düsseldorf (2006)

109. P. Rieg, "Latest Developments in High-Speed Extrusion," Plastic Extrusion Asia Conference, Bangkok, Thailand, March 17–18, (2008); also presented at Advances in Extrusion Conference, New Orleans, December 9–10 (2008)

3 Extruder Hardware

In this chapter, the hardware components of a typical single screw extruder will be described. Each major component will be discussed with respect to its major function, the possible design alternatives, and how important the component is to the proper functioning of the extruder.

3.1 Extruder Drive

The extruder drive has to turn the extruder screw at the desired speed. It should be able to maintain a constant screw speed because fluctuations in screw speed will result in throughput fluctuations that, in turn, will cause fluctuations in the dimensions of the extrudate. Thus, constancy of speed is a very important requirement for an extruder drive. The drive also has to be able to supply the required amount of torque to the shank of the extruder screw. A third requirement for most extruder drives is the ability to vary the speed over a relatively wide range. In most cases, one would desire a screw speed that is continuously adjustable from almost zero to maximum screw speed. Over the years, various drive systems have been employed on extruders. The main drive systems are:

- AC motor drive systems
- DC motor drive systems
- Hydraulic drives

3.1.1 AC Motor Drive System

The two AC drive systems used on extruders are the adjustable transmission ratio drive and the adjustable frequency drive. The adjustable transmission ratio drive can be either a mechanical adjustable speed drive or an electric friction clutch drive.

3.1.1.1 Mechanical Adjustable Speed Drive

There are four basic types of mechanical adjustable speed (MAS) drives: belt, chain, wooden block, and traction type. The latter two are not used on extruders because they are limited to low input speeds and easily damaged by shock loads [1, 2].

Belt drives use adjustable sheaves. The axial distance between the sheaves can be varied: this changes the effective pitch at which the belt contacts the sheave. This, in turn, changes the transmission ratio. The speed is usually varied by a vernier screw mechanism, which is hand cranked or activated electrically. Belt drives are used up to 100 hp. The largest speed ratio is about 10:1, and a maximum speed is typically 4000 rpm. Belt drives have a reasonable efficiency, tolerate shock leads, and provide optimum smoothness in a mechanical drive. Disadvantages are heat generation, possibility of slippage, and relatively poor speed control. In addition, belt drives are subject to wear and, thus, are maintenance-intensive; belts generally have to be replaced every 2000 hours.

Chain drives come in two different designs. One design uses a chain where each link is composed of a number of laminated carriers through which a stack of hardened steel slats slide. The slats fit in the grooves of conical, movable sheaves. The other design uses a conventional sprocket chain, but uses extended pins to contact the sheaves. Chain drives are more durable than belts and can transmit higher torques. Additionally, their speed control is better than that of belt drives, about 1% of setting. Chain drives are more compact than belt drives and can operate at higher temperatures. On the negative side, chain drives are about twice as expensive as belt drives, they provide little shock load protection, they are suited only to relatively low speed operation, and their speed ratio is about half that of belt drives. The efficiency of both the chain and belt drive is about 90%.

Mechanical adjustable speed drives, nowadays, are rarely used in extruders because they are maintenance intensive, have limited speed control and speed ratio, and their power efficiency is not very good.

3.1.1.2 Electric Friction Clutch Drive

In the electric friction clutch drive, there is no direct mechanical connection between input and output shaft, eliminating mechanical friction and wear. Electrical forces are used to engage the input and output shaft. The three main types are hysteresis, eddy-current, and magnetic particle clutches. In the extrusion industry, the eddy-current drive has been widely applied in the past. The majority of the older extruders were equipped with eddy-current drives.

The popularity of this drive was, and still is to a large extent, due to the simplicity of the drive. In simple terms, the eddy-current drive consists of a fixed speed AC motor driving a steel drum; see Fig. 3.1.

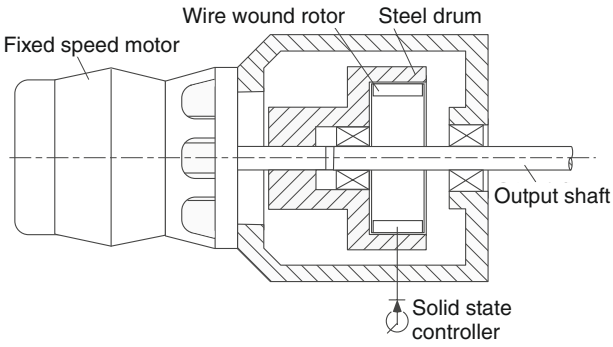


Figure 3.1
The eddy-current clutch

Inside this drum, a wire-wound rotor is positioned, with a small annular gap between rotor and drum. When a low-level current is applied to the rotor, it is dragged by the rotation of the drum at a somewhat lower rotational speed. When the voltage to the rotor is reduced, the slippage between the rotor and drum will increase. Thus, reduced voltage reduces the rotor speed, since the speed of the drum is constant. By controlling the voltage to the rotor, the rotor speed can be varied or it can be maintained at a steady speed under varying loads.

Typical operating characteristics for eddy-current drives are [3]:

- 30:1 speed range at constant torque
- Intermittent torque to 200% of rated torque
- Speed regulation: 0.5% of maximum speed
- Drift: 0.05% of maximum speed per °C
- Ability to deliver rated torque at stall conditions

The efficiency of the eddy-current drive is proportional to the difference between input and output speed. Thus, when an extruder is operated at low speeds for extended periods of time the eddy-current drive would not be a good candidate from an energy consumption point of view. It is possible to reduce this problem by using a two-speed AC motor to drive the eddy-current clutch [3, 4].

3.1.1.3 Adjustable Frequency Drive

Adjustable frequency drives use an AC squirrel cage induction motor connected to a solid-state power supply capable of providing an adjustable frequency to the AC motor. The AC squirrel cage induction motor has several advantages: low price, simplicity, ruggedness, no commutators and brushes, low maintenance, and compact construction. The cost of the adjustable frequency drive is mostly determined by the solid-state power supply. The power supply converts AC power to DC power. It then inverts the DC energy in order to provide the required frequency and voltage for the AC motor. Thus, full power is handled through two required sets of solid-state devices, unlike the single conversion used in the DC-thyristor system. Therefore, the

cost of an adjustable frequency drive used to be higher than a comparable DC drive, even though the DC motor itself is more expensive than the AC motor.

A common power supply is the six-step variable voltage inverter; see Fig. 3.2.

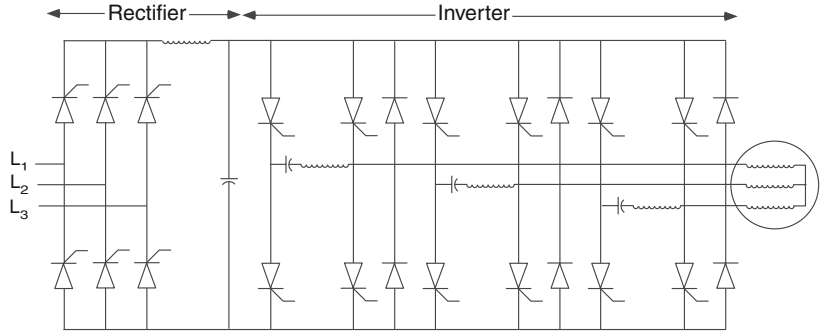


Figure 3.2 Six-step variable voltage inverter

Incoming three-phase AC power is rectified and smoothed to generate a variable voltage DC supply. This DC voltage is then switched among the three output phases to generate a step waveform that approximates a sinusoidal waveform. The switching is done by six SCRs (silicon-controlled rectifiers), which are sequentially fired at the proper frequency by a solid-state circuit.

The ratio of voltage to frequency must be held constant to maintain a constant torque capability as the motor speed is varied. Almost any speed/torque characteristic can be obtained by varying the voltage to frequency ratio. Because of limitations of the SCR cells, the maximum rating of adjustable frequency drives is presently around 300 hp. As better SCR cells are developed, this maximum rating is likely to increase.

The flux vector (FV) controlled variable frequency AC drives represent a relatively new technology made possible by developments in solid-state power switching devices and microprocessors. An FV drive is a variable frequency AC drive, able to control both the magnetizing current and torque producing current through vector calculations. FV drives achieve torque and speed control better than DC drives. They use a special AC motor, a “high efficiency” or “vector” duty motor, insulated sufficiently to handle the voltage spikes to which they are subjected by the “chopping” action of these drives. These motors are rugged, inexpensive, and low maintenance; therefore, they have low operating cost. Figure 3.3 shows a schematic of an FV drive.

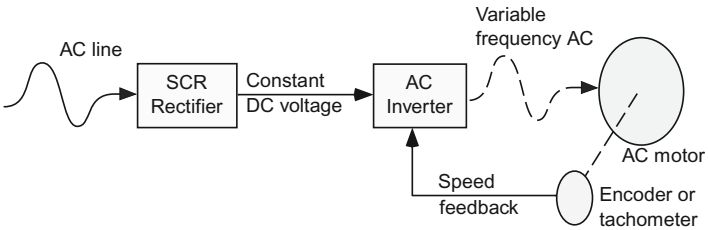


Figure 3.3 Schematic of flux vector drive

A speed regulation of 0.01% can be achieved with a 1000:1 speed range using an encoder and with constant torque characteristics. FV drives have a better power factor over the low speed range than DC drives because there is not the long delay in firing the SCRs to create a low DC voltage. FV drives provide constant torque up to the base speed, usually 1750 rpm. The 1750 base speed motors can operate in an extended speed range up to 3500 rpm. Low base speed vector duty motors with high horsepower have not become widely available at a competitive price. The cost of smaller FV drives is attractive; however, sizes over 100 hp tend to be more expensive than DC drives. Flux vector drives are available up to 400 hp. A further advantage of AC drives is that they do not require isolation transformers.

3.1.2 DC Motor Drive System

Some early DC extruder drives used fixed-speed AC motors to drive DC generators that produced the variable voltage for the DC motor. Nowadays, the DC motor drives usually operate from a solid-state power supply, since this power supply is generally more cost-effective than the motor generator set. The DC motor drive can be simpler and cheaper than the variable frequency drive, even when the higher cost of the DC motor is included. The smaller number of solid-state devices tends to give the DC drive a better reliability than the variable frequency drive. Brushes and commutator maintenance is the principal drawback to the use of DC motors. If the drive has to be explosion-proof, the additional expense associated with this option may be quite large for a DC drive, more so than with a variable frequency AC drive or a hydraulic drive. A schematic of the DC drive is shown in Fig. 3.4.

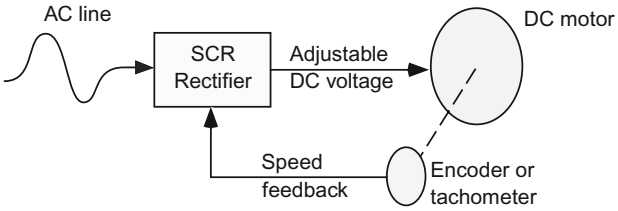


Figure 3.4
Schematic of DC drive

The DC drive can provide a speed range of up to 100:1. The DC motor can handle either a constant torque or constant load, and in some cases both (with field weakening). Any overload capacity presented to the motor must be provided in the sizing of the solid-state power supply. Generally, drives are provided with an overload capacity of 150% for one minute. The DC motor can be readily reversed by reversing the armature of the motor. For rapid stopping, resistors can be connected across the armature by a contactor, thereby providing dynamic braking at relatively low cost. DC motors respond quickly to changes in control signal due to their high ratio of torque to inertia.

The DC voltage from the solid-state power supply generally has a rather poor form factor. The magnitude of the form factor is dependent on the configuration of the rectifier circuitry. The poorer the form factor, the higher the ripple current in the DC motor. This increases motor heating and reduces the power efficiency. Several three-phase rectifier circuits are available for the AC line power into DC. Most drives over 5 hp use three-phase full wave circuitry. Figure 3.5 shows a three-phase half-controlled full wave rectifier.

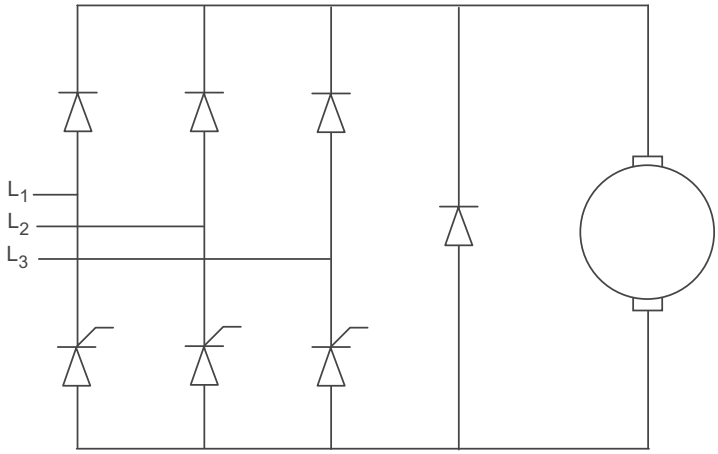


Figure 3.5 Three-phase half-controlled full wave rectifier

This circuit uses only three thyristors and four diodes. The drawback of this rectifier circuit is its high ripple current; the typical form factor is 1.05, with the ripple current frequency 180 Hz.

Another popular rectifier circuit is the full-controlled three-phase full wave rectifier. This circuit is more expensive because six thyristors are used. However, the form factor is much better, about 1.01, and the ripple current is 360 Hz. The higher frequency makes it easier to filter the ripple current. The half-controlled three-phase bridge rectifier circuit may require armature current smoothing reactors to reduce the ripple current. Another problem associated with the non-uniform DC input to the motor is the commutation. The motor must commutate under a relatively high degree of leakage reactance.

A potential safety hazard is the fact that with armature current feedback, the armature current is connected to the operator control and potentiometers may be operated at high potentials (500 V). This problem can be eliminated using isolation transformers or DC to DC chopper circuits.

3.1.2.1 Brushless DC Drives

Brushless DC drives have an advantage in that the motor does not contain brushes. As a result, the drive is less maintenance intensive. The motor contains permanent magnets; the size of the magnets determines the horsepower capability of the motor. The maximum power available today is around 600 hp. A schematic of the brushless DC drive is shown in Fig. 3.6.

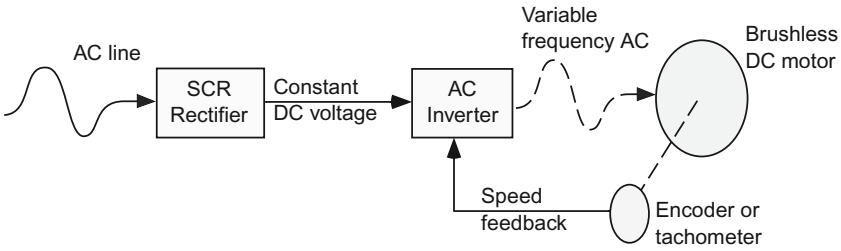


Figure 3.6 Schematic of brushless DC drive

Brushless DC drives have been used frequently with extruders. With the advent of flux vector AC drives, the brushless DC is used less; however, it still provides useful characteristics as shown in Table 3.2 in Section 3.1.4.

3.1.3 Hydraulic Drive System

A hydraulic drive generally consists of a constant speed AC motor driving a hydraulic pump, which, in turn, drives a hydraulic motor and, of course, the associated controls. The entire package is often referred to as a hydrostatic drive. Some of the advantages of a hydrostatic drive are stepless adjustment of speed, torque, and power; smooth and controllable acceleration; ability to be stalled without damage; and easy controllability.

Over the years, considerable improvements have been made to pumps and motors, resulting in improved stability, controllability, efficiency, reduced noise, and reduced cost. Hydrostatic drives are presently used in many demanding applications. At least three types of output performance are commonly available. Variable power, variable torque transmissions are based on a variable displacement pump supplying a variable displacement motor. These transmissions provide a combination of constant torque and constant power. These units are the most adjustable, most flexible, and most expensive. Constant torque, variable power transmissions are based on a variable displacement pump supplying fluid to a fixed displacement motor under constant load. Speed is controlled by varying pump delivery. This is generally considered the best general-purpose drive, with wide speed ranges, up to 40:1, and simple controls. Constant power, variable torque transmissions are based on a vari-

able displacement pump with a power limiter, driving a fixed displacement motor. The main strength of this transmission is its efficiency; however, the speed range is usually limited to 4:1.

Hydrostatic transmissions are available where the pump and motor are combined in a single rigid unit, usually referred to as close-coupled transmissions. This produces a very compact drive that can be encased in a sealed housing to protect it from its environment. By eliminating external plumbing, close coupling reduces noise, vibration, flow losses, and leakage.

Hydraulic drives can be controlled quite well. Advances in control sophistication have helped broaden the field in which hydrostatic drives are applied. Fast-acting pressure compensators reduce heat generation, eliminate the need for crossport relief valves, and simplify other control circuits. Load sensing controls increase operating efficiency by reducing unnecessary loads on the pump. Brake and bypass circuits eliminate the need for external actuation mechanical brakes. Power limiters eliminate prime-mover stalls by limiting the transmission output to a maximum value. And speed controls hold the output speed at a constant value, regardless of the prime mover speed.

The overall efficiency of hydrostatic drives can be quite good. For a well-designed system, the overall efficiency can be as high as 70% over a reasonably wide range. The use of accumulators and logic-type valves (cartridge) is beneficial to the efficiency of the drive, particularly when they are connected to programmable controls. Typical efficiency curves for a high torque, low speed hydraulic motor [6] are shown in Fig. 3.7.

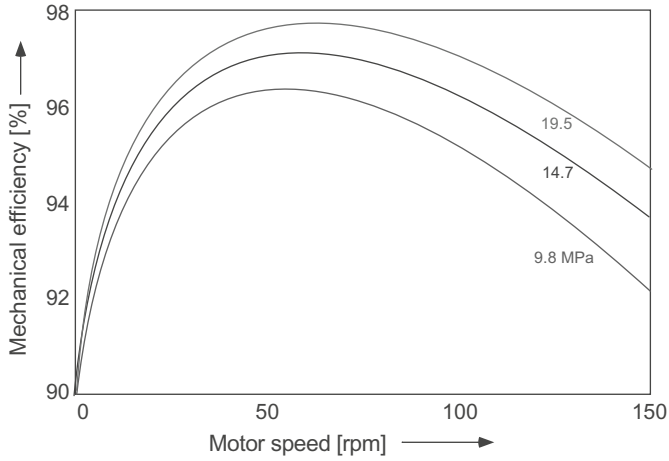


Figure 3.7 Efficiency curves for high torque, low speed hydraulic motor

It is seen that an excellent efficiency can be obtained in the range from zero to 150 rpm, which is the typical operating range for extruders. It can be further noticed that higher operating pressures increase the mechanical efficiency. The drawback of a higher working pressure is more strain on the seals, couplings, and other components; this can increase the cost of the drive.

One significant advantage of hydrostatic drives for extruders is the elimination of the need for a transmission between the hydraulic motor and extruder screw. Since low speed hydraulic motors are readily available, one can do away with the bulky, expensive gearbox found on most extruders. Therefore, when comparing the cost of a hydrostatic drive to a DC drive, one should include the cost of the gearbox in the cost of the DC drive. Another advantage is the fact that other components of the machine or auxiliary equipment can be operated hydraulically from the same hydraulic power supply. This is particularly advantageous for screen changers where the screen is changed by a hydraulic cylinder or in molding machines where the mold is opened and closed hydraulically. For these reasons, hydraulic drives have become almost standard for reciprocating extruders used in injection molding and blow molding.

It should be realized, however, that the operation of the reciprocating extruder as a plasticating unit of a molding machine is considerably different from a conventional rotating extruder. The screw rotation is stopped abruptly at the end of the plasticating cycle, then the screw is moved forward and remains in the forward position for some time. Then the screw starts rotating again and as material accumulates at the tip of the screw, the screw moves backward until enough material has accumulated. Then the cycle repeats itself. Thus, in this operation there is a frequent stop and go motion. The hydraulic drive is ideally suited for this type of operation. The operation of a conventional extruder is much more continuous, and therefore its drive requirements are different from a reciprocating extruder.

Despite the attractive features of hydrostatic drives, they are rarely used on regular (non-reciprocating) extruders. The reason for this situation is not obvious since the hydrostatic drive is in many respects competitive with, for instance, the SCR DC drive and in some respects better; e. g., there is no need for a gearbox. A possible reason is that the hydrostatic drive is still regarded with suspicion by many people. This is because early hydraulic drives were not very reliable and accurate. However, this situation has changed dramatically over the years, but the hydrostatic drive still seems to suffer from its early unfavorable reputation. Very few U. S. companies supply hydraulic drives for extruders: Feed Screws Division of New Castle Industries and Wilmington Plastics Machinery. It is claimed [5] that hydraulic drives are less expensive than DC drives on smaller extruders, up to about 90 mm.

3.1.4 Comparison of Various Drive Systems

Table 3.1 summarizes the functional requirements for drives used in extrusion machinery. This comparison is based on a paper by Kramer [32].

Table 3.1 Functional Requirement for Drives Used in Extrusion Machinery [32]

Machine	HP	Function	Torque	Speed control	Speed range	Regeneration or braking
Extruders	5–800	Melting	Constant	0.1%	100:1	No
Melt pumps	1–20	Pumping	Constant	0.01%	100:1	No
Pullers	0.25–15	Pulling	Constant	0.01%	20:1	Both
Winders	0.25–10	Winding	Variable	1%	20:1	Braking
Cutters	0.25–5	Cycling	Starting	0.01%	100:1	Braking

Table 3.2 compares the most important drive systems.

Table 3.2 Comparison of Different Drive Systems [32]

	DC with encoder	Brushless DC	AC servo	AC vector with encoder
Power range [HP]	0.25–2000	0.25–600	0.25–20	0.25–400
Starting torque	150%	150%	175%	150%
Speed regulation	1.0–0.01%	0.01%	0.01%	0.5–0.01%
Constant torque	20:1	1000:1	40:1	1000:1
Regenerative braking	Yes	No	No	Limited
Dynamic braking	Yes	Yes	Yes	Yes
Relative cost	Moderate	Moderate	High	Moderate
Operating cost	Moderate	Low	Low	Low
EMI and line noise	Good	Poor	Poor	Poor
Power factor	0.20–0.85	0.98	0.98	0.98

The power factor is also an important factor to consider. The power factor of the DC drive reduces slightly with load, but it drops drastically with speed. This becomes more severe as the horsepower increases. The power factor of the variable frequency AC drive is higher than the power factor of the DC drive and it is much less affected by speed. In fact, for small to medium horsepower variable frequency AC drives, the power factor is essentially independent of load and speed. The effect of the power factor on overall energy cost cannot be simply calculated by multiplying the line-to-shaft efficiency with the power factor.

The cost of electric power generally depends both on the actual power (KW) and the apparent power (KVA). The power factor is the ratio of actual power to apparent power. Most utilities incorporate a certain cost penalty if the power factor is consider-

ably below one for extended periods of time. The actual cost penalty will differ from one utility to another. Also, to determine the actual expenses for electric power for a certain production facility, an energy survey must be made of the entire facility. It is possible that the extruder drive has a small effect on the overall power factor. In that case, the power factor of the extruder drive is of little concern. If the overall power factor is strongly affected by the extruder drive(s), the power factor of the electric motor of the extruder drive may be a serious concern. In this case, an energy management system should be used to keep the overall power factor as high as possible.

With DC electric motors, power factor correction is sometimes used to improve the power factor of the drive [30]. This is done by incorporating capacitive components into the circuit. Capacitors produce leading reactive power whereas the phase-controlled rectifiers produce lagging reactive power. Thus, by adding appropriately sized capacitors, the power factor of the drive can be improved.

The line-to-shaft efficiency of DC motors is around 0.85 and about 0.80 for variable frequency AC motors. Considering that a typical two-stage gearbox has an efficiency of about 0.95, the overall efficiency for a DC drive is about 0.80 and about 0.75 for a variable frequency AC drive. The overall efficiency of a well-designed hydrostatic drive is around 0.70. Thus, the hydrostatic drive compares reasonably well with the AC and DC drives with regards to overall efficiency [31]. The drive efficiency of the DC motor drive and the adjustable frequency drive increases with rated speed, whereas the drive efficiency of the hydraulic drive is relatively independent of rated speed. The efficiency of the DC motor is better than other motors in the range of 20 to 100% rated speed; below 20% rated speed the hydraulic drive is more efficient.

The mechanical drive has a reasonable overall efficiency at full load and full speed. The advantage of this drive is that the efficiency does not change with speed. Thus, at low speeds this drive can actually be more efficient that the DC or AC drive. A drawback of the mechanical drive is the higher maintenance requirement.

Another consideration in choosing a drive is the speed drift. The eddy-current drive has a speed drift of about 0.4% per °C. The adjustable frequency AC drive has a speed drift of 0.05% or better. With a DC (SCR) drive using armature voltage control, the speed can vary 10% for the initial warm-up period of about 15 to 30 minutes. After the warm-up period, the drift will be about 1%. The speed drift can be reduced by using tachometer feedback and regulated field; this reduced the drift of the DC drive to about 0.25%.

3.1.5 Reducer

With AC or DC drives, a reducer is generally required to match the low speed of the screw to the high speed of the drive. The typical reduction ratio ranges from 15:1 to 20:1. The type of reducer most frequently used is the spur gear reducer, often in a

two-step configuration, i.e., two sets of intermeshing gears. A popular type of spur gear is the herringbone gear because the V-shaped tooth design practically eliminates axial loads on the gears. The efficiency of these gears is high, about 98% at full load and 96% at low load.

Some gearboxes are equipped with a quick-change gear provision, which allows one to change gear ratio rather quickly and easily. This feature can add significantly to the flexibility and versatility of the extruder. Of course, one has to make sure that the quick-change gear unit is designed in such a way that it does not significantly affect the transmission efficiency of the reducer.

Worm reduction gears have been used on rare occasions. Their advantage is low cost and compactness, but the efficiency is rather poor, between 90 and 75%. Some extruders do not have a direct connection between the drive and reducer but employ either a chain or a belt transmission. This type of setup allows a relatively simple change in overall reduction ratio by changing the sprocket or sheave diameter. An advantage of the belt drive is the fact that it provides protection against excessive torque. A distinct disadvantage is increased power consumption, as much as 5 to 10%. Another drawback is the fact that the chain or belt transmission is less reliable than the spur gear reducer and requires more maintenance.

3.1.6 Constant Torque Characteristics

Most extruders have a so-called “constant torque” characteristic. This means that the maximum torque obtainable from the drive, for all practical purposes, remains constant over the range of screw speed. The torque-speed characteristic can be used to determine the power-speed characteristic by using the well-known relationship between torque and power:

$$P = C\,T\,N \tag{3.1}$$

where T is torque, P power, N screw speed or motor speed, and C a constant ($C = 2\pi/60 \cong 0.1$ when N is expressed in revolutions per minute).

Thus, if torque is constant with speed, then it follows directly from Eq. 3.1 that the power is directly proportional to speed; see Fig. 3.8.

This means that the maximum power of the drive can only be utilized if the motor is running at full speed. Whenever the extruder output is power-limited, it is good practice to make sure the motor is running at full speed. If it is not, then a simple gear change can often alleviate the problem.

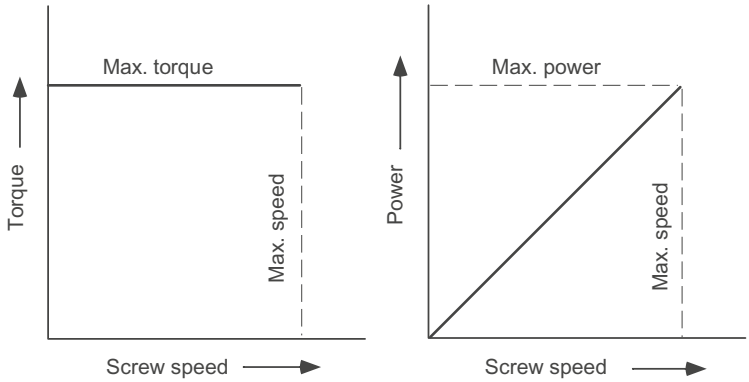


Figure 3.8 Torque and power versus screw speed

It is generally very expensive to solve a power limitation problem by installing a more powerful motor. The reason is that most gearboxes are matched in terms of power rating to the motor driving the gearbox. Thus, if the motor power is increased significantly, quite often the gearbox has to be replaced concurrently. This makes for a very expensive replacement. In fact, it could be more cost-effective to purchase an entirely new extruder. Mechanical power consumption is, to a very large extent, determined by the design of the extruder screw. There are many options to change the screw design, which will reduce the power consumption of the drive (see Chapter 8).

3.2 Thrust Bearing Assembly

The thrust bearing assembly is usually located at the point where the screw shank connects with the output shaft of the drive, which is generally the output shaft of the gearbox. Thrust bearing capability is required because the extruder generally develops substantial diehead pressure in the polymer melt. This diehead pressure is necessary to push the polymer melt through the die at the desired rate. However, since action = reaction, this pressure will also act on the extruder screw and force it towards the feed end of the extruder. Therefore, the thrust bearing capability has to be available to take up the axial forces acting on the screw. Clearly, the load on the thrust bearing is directly determined by the diehead pressure. The actual force on the screw is obtained by multiplying the diehead pressure with the cross-sectional area of the screw. Thus, when the size of the extruder increases, the load on the thrust bearing will increase at least as fast. A 150 mm (6 inch) extruder running with a diehead pressure of 35 MPa (about 5000 psi) will experience an axial thrust of about 620 kN (about 140,000 lbf). This illustrates that significant forces are act-

ing on the screw and proper design and dimensioning of the thrust bearing is critical to the trouble-free operation of the extruder.

Figure 3.9 shows a typical thrust bearing arrangement for a single screw extruder.

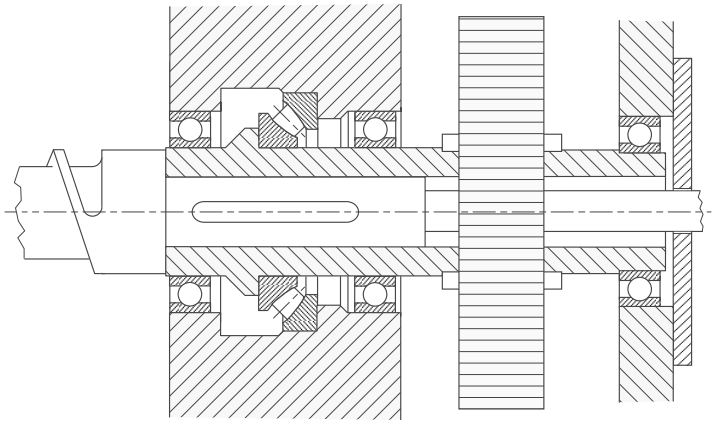


Figure 3.9 Thrust bearing assembly for single screw extruder

The screw shank is usually keyed or splined and fits into a driving sleeve in the bearing housing. Thrust bearings are designed to last a certain number of revolutions at a certain thrust load. Under normal operating conditions and reasonable diehead pressure (0–35 MPa), the thrust bearing will generally last as long as the life of the extruder. However, if the extruder operates with sharp fluctuations in diehead pressure and/or if the diehead pressure is unusually high (40–70 MPa), the life expectancy of the thrust bearing can reduce dramatically, particularly when the extruder screw runs at high speed.

The statistical rated life of a bearing is generally predicted using the following formula:

$$L_{10} = \left(\frac{C}{P}\right)^{K} \times 10^{6} \qquad [\text{rev}] \tag{3.2}$$

where L_{10} = rated life in revolutions

C = basic load rating

P = equivalent radial load

K = constant, 3 for ball bearings, and 10/3 for roller bearings

It is important to notice that increased load, i.e., increased diehead pressure, reduces the bearing life by a power of three or more! Also, the life L will be reached more quickly when the extruder runs at high speed. The predicted life, L_y, expressed in years, is obtained from the following expression:

$$L_y = \frac{1.9}{N}\left(\frac{C}{P}\right)^K \tag{3.3}$$

where L_y is predicted life in years and N the screw speed in revolutions per minute. This is based on 24 hours per day, 365 days per year operation. Thus, the expected lifetime of the thrust bearing is inversely proportional to the screw speed. Sharp fluctuations to the thrust load can further reduce the thrust bearing life. The effect of load fluctuation is usually assessed by means of load factors used in Eqs. 3.2 and 3.3. The handbook of the particular thrust bearing manufacturer or the extruder manufacturer should be consulted for the proper values of these load factors.

Extruder manufacturers often give the rated life of the thrust bearing as a B-10 life. This is expressed in hours at a particular diehead pressure, 35 MPa (5,000 psi), and screw speed, 100 rev/min. The B-10 life represents the life in hours at a constant speed that 90% of an apparently identical group of bearings will complete or exceed before the first evidence of fatigue develops; i. e., 10 out of 100 bearings will fail before rated life. The B-10 life at normal operating load should be at least 100,000 hours in order to get a useful life of more than 10 years out of the thrust bearing.

The predicted B-10 life at any diehead pressure and/or screw can be found by the following relationship:

$$B\text{-}10\,(P,N) = B\text{-}10_{Std} \times \frac{100}{N} \times \left(\frac{35}{P}\right)^K \tag{3.4}$$

where P is diehead pressure in MPa, N screw speed in rpm, constant K is 3 for ball bearings and 10/3 for roller bearings, and $B\text{-}10_{Std}$ is the B-10 life at P = 35 MPa and N = 100 rpm.

In single screw extruders, the design of the thrust bearing assembly is relatively easy since the diameter of the bearings can be increased without much of a problem in order to obtain the required load carrying capability. This situation is entirely different in twin screw extruders because of the close proximity of the two screws. This severe space limitation makes the proper design of the thrust bearing assembly in twin screw extruders considerably more difficult than in single screw extruders. Older twin screw extruders were often limited in diehead pressure capability exactly because of this thrust-bearing problem. A number of newer twin screw extruders have solved this problem sufficiently and can generally withstand almost the same diehead pressures as single screw extruders, although the rated life for the thrust bearings of a twin screw extruder is generally lower.

Figure 3.10 shows an example of a thrust bearing assembly of a counter-rotating twin screw extruder.

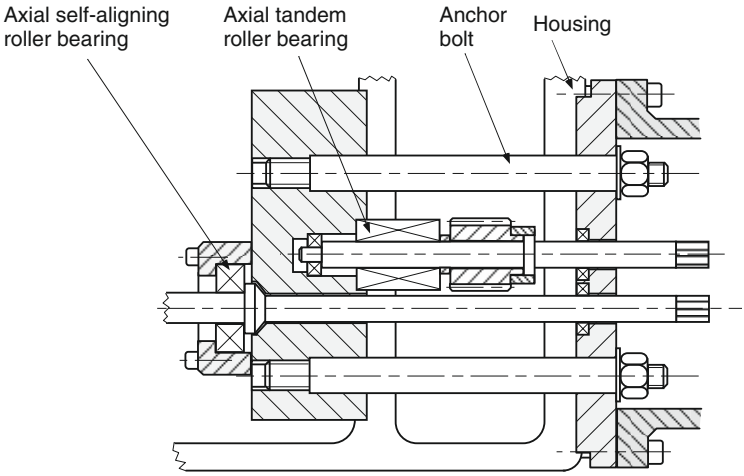


Figure 3.10 Thrust bearing assembly for counter-rotating twin screw extruder

The thrust bearing assembly consists of four or five roller bearings in tandem arrangement with a special pressure balancing system. Advantages and disadvantages of certain types of thrust bearings are listed in Table 3.3.

Fluid film thrust bearings have been applied to extruders on a few occasions. Their load carrying capability at low speed is generally poor and a loss of fluid film would have disastrous results. If a hydraulic drive is used to turn the screw, application of hydraulic thrust bearings may deserve some consideration. Reference 28 describes an extruder with hydraulic drive that incorporates a patented thrust bearing assembly with hydraulic axial screw adjustment. By measuring the pressure of the hydrostatic chamber of the thrust bearing, the pressure in the polymer melt at the end of the screw can be determined.

3.3 Barrel and Feed Throat

The extruder barrel is the cylinder that surrounds the extruder screw. The feed throat is the section of the extruder where material is introduced into the screw channel; it fits around the first few flights of the extruder screw. Some extruders do not have a separate feed throat unit; in these machines, the feed throat is an integral part of the extruder barrel. However, there are some drawbacks to this type of design. The feed throat casting is generally water-cooled. This is done to prevent an early temperature rise of the polymer. If the polymer temperature rises too high it may stick to the surface of the feed opening, causing a restriction to the flow into the extruder. Polymer sticking to the screw surface also causes a solids conveying prob-

lem, because the polymer particles adhering to the screw will not move forward and will restrict the forward movement of the other polymer particles.

Table 3.3 Comparison of Various Types of Thrust Bearings

Type	Advantages	Disadvantages
Ball thrust bearing	High speed capability	Low thrust capability
Angular contact ball thrust bearing	High speed capability, radial load capability	Lower thrust capability
Cylindrical roller thrust bearing	Higher capacity, minimum cost	Not true rolling contact, more heat generation
Spherical roller thrust bearing	Dynamic misalignment tolerability, almost true rolling contact, radial load capability	High cost/capacity ratio, difficult to lubricate
Tapered roller thrust bearing	True rolling contact, very high capacity, low flange loading	Difficult to lubricate, minimum sizes available, special alignment considerations
Tapered roller thrust bearing, V-flat	True rolling contact	Higher flange loading
Tapered roller thrust bearing, V-flat, aligning	Greater size flexibility, least cost per L-10 life, easy to lubricate, static misalignment tolerability	

At the point where the feed throat casting connects with the barrel, a thermal barrier should be incorporated to prevent heat from the barrel from escaping to the feed throat unit. In a barrel with an integral feed opening this is not possible. Therefore, heat losses will be greater and there is also the chance of overheating of the feed throat.

The geometry of the feed port should be such that the material can flow into the extruder with minimum restriction. Cross-sections of various feed port designs are shown in Fig. 3.11.

Figure 3.11(a) shows the usual feed port design. Figure 3.11(b) shows an undercut feed port as is often used on melt fed extruders. The danger with this design is the wedging section between screw and feed opening. If the melt is relatively stiff and/or highly elastic, significant lateral forces will act on the screw. These forces can be high enough to deflect the screw and force it against the barrel surface. This, of course, will lead to severe wear if the contact pressure is sufficiently high. This problem is more severe when this geometry is used for feeding solid polymer powder or pellets. This geometry, therefore, should only be used for feeding molten polymers. A better geometry would be the one shown in Fig. 3.11(c). It has an undercut to improve the intake capability, but the pronounced wedge is eliminated by a flat section oriented more or less in the radial direction.

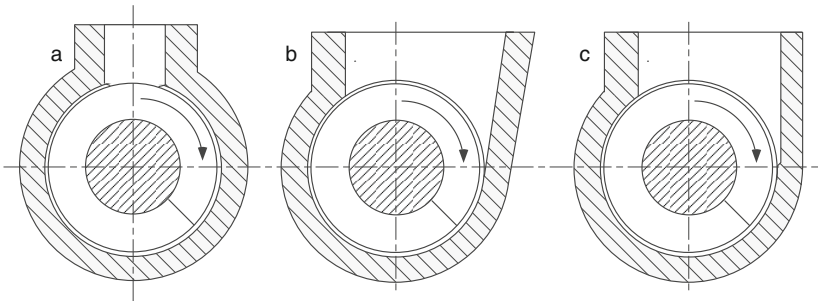


Figure 3.11 Different feed port geometries

The shape of the inlet opening is usually circular or square. The smoothest transition from feed hopper to feed throat will occur if the cross-sectional shape of the hopper is the same as the shape of the feed opening. Thus, a circular hopper should feed into a circular feed port. A study done by Miller [7] on various feed port openings did not reveal a noticeable advantage of increasing the length of the opening beyond one diameter. Michaeli et al. [33] found that the throughput can increase significantly when the axial length of the feed opening is increased beyond one diameter. A length of 1.5D to 2.5D can offer advantages in many cases.

Extruders equipped with grooved barrel sections often have a specially designed feed throat section to accommodate this grooved section. A schematic feed throat section is shown in Fig. 3.12, where the effective length of the grooves may range from three to five diameters.

The depth of the grooves varies with axial distance. The depth is maximum at the start of the grooved bushing and reduces to zero where the grooved section meets with the smooth extruder barrel.

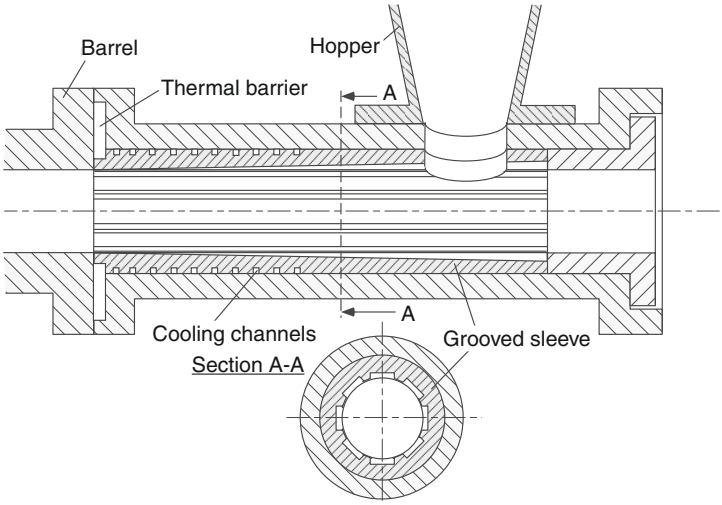


Figure 3.12 Grooved feed housing

Several important requirements in this feed section design are

- Very good cooling capability
- Good thermal barrier between feed section and barrel
- Large pressure capability

The requirement of good cooling is due to the large amount of frictional heat generated in the grooved barrel section. If the heat is not carried away quickly enough, the polymer will soften or even melt. This will severely diminish the effectiveness of the grooved barrel section. The requirement of a good thermal barrier between the grooved feed section and extruder barrel is to minimize the heat flow from the barrel to the feed section, so as to maximize the cooling capacity of the feed throat section. Very large pressures can be generated in the grooved feed section, from 100 to 300 MPa (about 15,000 to 45,000 psi). The feed section should be designed with the ability to withstand pressures of this magnitude otherwise spectacular modes of failure may occur.

The stresses between the polymer and the grooves can be very high. As a result, wear can be a significant problem, particularly when the polymer contains abrasive components. The splines in the grooved bushing, therefore, are generally made out of highly wear-resistant material (see Section 11.2.1).

The extruder barrel is simply a flanged cylinder. It has to withstand relatively high pressures, as high as 70 MPa (10,000 psi), and should possess good structural rigidity to minimize sagging or deflection. Many extruder barrels are made with a wear-resistant inner surface to increase the service life. The two most common techniques are nitriding and bimetallic alloying.

Nitriding can be done by ion-nitriding (by glow discharge or plasma) or by conventional nitriding techniques (gas nitriding or liquid bath nitriding). It is generally recognized that ion-nitriding yields superior results. In ion-nitriding, the barrel is first hardened and tempered to achieve the desired core properties. The barrel is then placed in a vacuum chamber and connected in a high voltage DC circuit with the barrel as the cathode and the vacuum chamber as the anode. The chamber is evacuated and nitrogen-bearing process gas is introduced. A potential difference of about 400 to 1000 volts is applied between vacuum chamber and barrel. This causes the nitrogen molecules to ionize, and the nitrogen ions collect on the barrel surface. The dissipation of the kinetic energy of the ions heats the barrel surface to the nitriding temperature. The nitrogen ions combine with the surface constituents to form the nitrides that impart hardness to the surface. The surface layer consists of a compound zone and a diffusion zone. The compound zone is usually about 5 to 8 microns thick (0.2–0.3 milli-in); it can be tailored to be either wear-resistant or corrosion-resistant. The total nitriding depth is about 0.4 mm (16 milli-in).

Bimetallic barrels are made by centrifugally casting a bimetallic alloy onto the inside of the barrel. The melting point of the bimetallic alloy is considerably lower

than the melting point of the barrel material. The barrel is charged with the alloy, capped, and heated while rotating slowly. When the proper temperature is reached, the barrel is rotated at a very high speed [27], forcing the molten alloy to form a uniform layer with a strong bond with the barrel. The last finishing step is honing to form a smooth surface. The depth of the bimetallic liner is usually about 1.5 to 2.0 mm (60 to 80 milli-in) with a uniform consistency throughout the depth of the liner.

Comparative wear tests [27] indicate that the wear performance of bimetallic barrel liners is better than nitrided barrel surfaces, with a predicted improvement in the barrel life of about four to eight times the life of a nitrided barrel. An additional drawback of the nitrided surface is that the hard compound zone is quite thin. Once the compound zone is worn away, wear will increase more rapidly because the diffusion zone is not as hard and wear-resistant. This becomes more severe as the diffusion zone wears away more deeply.

3.4 Feed Hopper

The feed hopper feeds the granular material to the extruder. In most cases, the material will flow by gravity, unaided, from the feed hopper into the extruder. Unfortunately, this is not possible with all materials. Some bulk materials have very poor flow characteristics and additional devices may be required to ensure steady flow into the extruder. Sometimes this can be a vibrating pad attached to the hopper to dislodge any bridges as soon as they form. In some cases, stirrers are used in the feed hopper to mix the material (and prevent segregation) and/or to wipe material from the hopper wall, if the bulk material tends to stick to the wall.

In order to achieve steady flow through the hopper there should be a gradual compression in the converging region and the hopper should have a circular cross section. Unfortunately, extruder manufacturers often make square feed hoppers with rapid compression in the converging region because such hoppers are easier to manufacture. Figure 3.13 shows both a good and poor hopper design.

Square feed hoppers with rapid compression usually work well with bulk materials with uniform pellet size. However, when there is a large variation in particle size and shape the square feed hopper is likely to cause conveying problems. This can happen for instance when regrind is added to the virgin material. For this reason it is better to use a circular hopper with gradual compression.

Crammer feeders are used for bulk materials that are very difficult to handle. Other materials, particularly those with low bulk density, tend to entrap air. If the air cannot escape through the feed hopper, it will be carried with the polymer and eventually appear at the die exit. In most cases, this will cause surface imperfections of the extrudate. In some cases, it causes small explosions when the air escapes from the die.

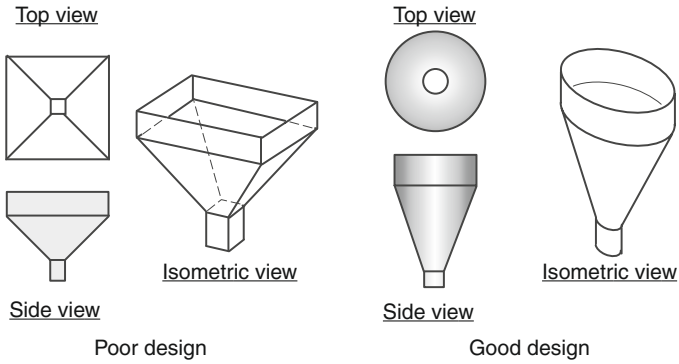


Figure 3.13 Poor and good feed hopper design

One method to overcome this air entrapment problem is to use a vacuum feed hopper. In principle, this is quite simple; however, in practice, a vacuum feed hopper is not a trivial matter. The first problem to occur is how to load the hopper without losing vacuum. This has led to the development of double hopper vacuum systems, in which material is loaded into a top hopper and the air is removed before the material is dumped in the main hopper (see Fig. 3.14).

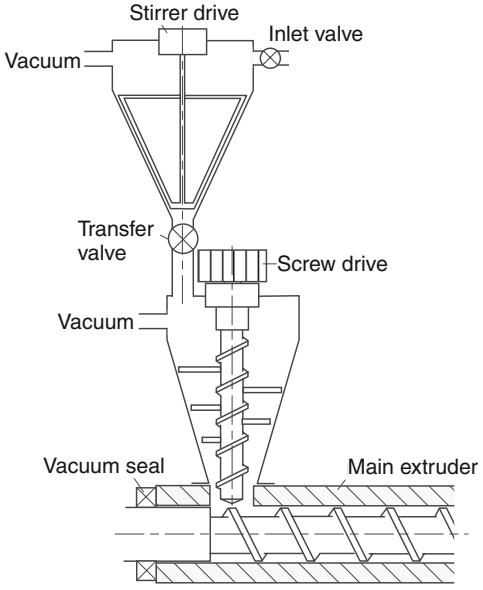


Figure 3.14
Double feed hopper vacuum system

A second critical point is the rear vacuum seal around the screw shank. This seal is exposed to sometimes-gritty materials. Leakage of air at this point can cause fluidization of material and adversely affect solids conveying in the extruder. Another method to avoid air entrapment is to use a two-stage extruder screw with a vent port in the barrel to extract air and any other volatiles that might be present in the polymer.

An important bulk material property with respect to the design of the hopper is the angle of internal friction (see Section 6.1). As a rule of thumb, the angle of the sidewall of the hopper to horizontal should be larger than the angle of internal friction. If the bulk material has a very large angle of internal friction, it will bridge in essentially any hopper. In this case, force-feeding may be the only way to solve this.

3.5 Extruder Screw

The extruder screw is the heart of the machine. Everything revolves around the extruder screw, literally and figuratively! The rotation of the screw causes forward transport, contributes to a large extent to the heating of the polymer, and causes homogenization of the material.

In simple terms, the screw is a cylindrical rod of varying diameter with a helical flight(s) wrapped around it. The outside diameter of the screw, from flight tip to flight tip, is constant on most extruders. The clearance between screw and barrel is usually small. Generally, the ratio of radial clearance to screw diameter is around 0.001, with a range of about 0.0005 to 0.0020.

The details of screw design will be discussed Chapter 8. In the U.S., a very common screw material is 4140 steel, which is a medium carbon, relatively low-cost material. A table of common screw materials used in polymer extrusion with their chemical composition is shown in Table 3.4. Table 3.6 shows some physical properties and cost comparison data. The selection of the proper screw base material and hardfacing material will be discussed in detail in Section 11.2.1.4.

Table 3.5 lists the European equivalents (or similar materials) to some of the materials listed in Table 3.4.

Table 3.4 Composition of Various Materials Used in Extruded Screws

	C	Si	Mn	F	S	Cr	Mo	Ni	V	Al	Cu	W	Co	Fe
Low carbon steel														
8620	0.21	0.30	0.80	0.035	0.035	0.50	0.20	0.55						97.37
Medium carbon steels														
4140	0.42	0.30	0.80	0.035	0.035	1.05	0.23							97.13
135	0.41		0.60	0.025	0.025	1.60	0.35			1.10				95.89
Stainless steels														
17-4	0.04	1.00	0.40			16.5		4.80			4.00			73.26
304	0.07	1.00	2.00	0.045	0.030	18.5		9.20						69.16
316	0.07	1.00	2.00	0.045	0.030	17.5	2.25	12.0						65.10

	C	Si	Mn	F	S	Cr	Mo	Ni	V	Al	Cu	W	Co	Fe
Tool steels														
H-13	0.40	1.00	0.35			5.35	1.35		1.00					90.55
D-2	1.50	0.25	0.30			12.0	0.80	0.60						84.55
D-7	2.35	0.40	0.40			12.5	0.95		4.00					79.40
Nickel based materials (highly corrosion resistant)														
276	0.02	0.05	1.00	0.030	0.030	15.5	16.0	55.5	0.35			4.00	2.50	5.00
Dni	3.00	1.00	0.50		0.010			94.9						0.60
Hardfacing materials														
St. 6	1.00	1.25				28.0						4.00	65.7	
St. 12	1.25					29.0						8.00	61.7	

Table 3.5 European Equivalents or Similar Materials

US designation	European designation
8620	21NiCrMo2
4140 Heat treated	42CrMo4
Nitralloy 135M	41CrAlMo7
304 Stainless steel	X5CrNi189
316 Stainless steel	X5CrNi189
H-13 Tool steel	X40CrMoV51
D-2 Tool steel	X155CrVMo121

Table 3.6 Properties of Various Screw Materials

	Ultimate tensile strength after HT [MPa]	Max. surface hardness after [RC] HT	Screw/ cost ratio	Used with hard-facing	Used with chrome
8620	900	60	1.5	No	Yes
4140 HT	2000	55–60	1.0	Yes	Yes
Nitralloy 135M	1400	60–74	1.2	Yes	Not advisable
17–4 PH	1400	65	2.0	Yes	No
304			1.5	Yes	No
316			1.5	Yes	No
H-13	1800	60–74	1.7	No	Yes
D-2	1650		1.7	No	Yes
D-7	1650		3.0	No	Yes
Hastelloy			3.0	Yes	No
Duranickel	1100		3.0	Yes	No

3.6 Die Assembly

In many extruders, a breaker plate is incorporated between the barrel and die assembly. The breaker plate is a thick metal disk with many, closely spaced parallel holes, parallel to the screw axis. There are two main reasons for using a breaker plate. One reason is to arrest the spiraling motion of the polymer melt and to force the polymer melt to flow in a straight-line fashion. Without a breaker plate, the spiraling motion could extend to the die exit and cause extrudate distortion. Another reason is to put screens in front of the breaker plate; the breaker plate then acts as a support for the screens. Screens are generally used for filtering contaminants out of the polymer. Sometimes screens are used for the sole purpose of raising the die-head pressure in order to improve the mixing efficiency of the extruder. This situation often indicates the use of an improper screw design. Another function of the breaker plate is improved heat transfer between the metal and the polymer melt. The reduced heat transfer distances in the breaker plate can improve the thermal homogeneity of the polymer melt.

If the exit opening of the extruder barrel does not match up with the entry opening of the die, an adaptor is used between barrel and die. Dies specifically designed for a certain extruder will usually not require an adaptor. However, since there is little standardization in extruder design and die design, the use of adaptors is quite common.

The die is one of the most critical parts of the extruder. It is here that the forming of the polymer takes place. The rest of the extruder basically has only one task: to deliver the polymer melt to the die at the required pressure and consistency. Thus, the die forming function is a very important part of the entire extrusion process.

Analysis of the flow in extrusion dies is very difficult because of the nature of the polymer melt. Die design, therefore, is largely still an empirical science. Flow behavior in the flow channels will be discussed in Section 7.5 and die design will be discussed in detail in Chapter 9.

3.6.1 Screens and Screen Changers

The screens before the breaker plate are generally incorporated to filter out contaminants. The coarsest screen (lowest mesh number) is usually placed against the breaker plate for support, with successively finer screens placed against it. A typical screen pack is one 100-mesh screen followed by one 60-mesh and one 30-mesh screen, with the 30-mesh placed against the breaker plate. Some extrusion operations use as many as twenty 325-mesh screens backed up by coarser screens, as reported by Flathers [10].

There are three important types of metallic filter medium: wire mesh, sintered powder, and random fiber. Wire mesh comes in a square weave or Dutch twill (woven in parallel diagonal lines). The different filter media do not perform equally with respect to their ability to hold contaminant, capture gels, etc. [11, 12]. A relative performance comparison is shown in Table 3.7.

Table 3.7 Performance Comparison of Different Filter Media

	Wire mesh, square weave	Wire mesh, Dutch twill	Sintered powder	Random metal fiber
Gel capture	Poor	Fair	Good	Very good
Contaminant capacity	Fair	Good	Fair	Very good
Permeability	Very good	Poor	Fair	Good

The commonly used square weave wire mesh has poor filtering performance; the only redeeming quality is good permeability. It is clear, therefore, that if filtering is very important, a different filter medium should be employed. Metal fibers stand out in ability to capture gels and hold contaminants. Gel problems are particularly severe in small gauge extrusion such as low denier fibers, thin films, etc. It is particularly for these applications that metal fiber filters have been applied. If the polymer is heavily contaminated, the screen will clog rather quickly. If the screens have to be replaced frequently, an automatic screen changer is often employed. In these devices, the pressure drop across the screens is monitored continuously. If the pressure drop exceeds a certain value, a hydraulic piston moves the breaker plate with screen pack out of the way, and at the same time a breaker plate with fresh screens is moved in position. These units are referred to as slide-plate screen changers; see Fig. 3.15.

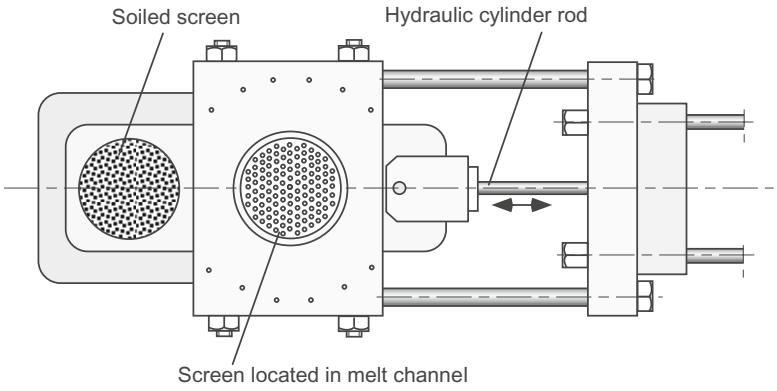


Figure 3.15 Slide-plate screen changer

With some screen changers, the screen change operation can be performed without having to shut down the extruder. The old screens can be removed and new screens put in place and the screen changer is ready for a new cycle. In operations where the polymer contains a high level of contaminants, screen changes may have to be made as often as every 5 to 10 minutes. Usually, however, the cycle time is measured in hours and not in minutes.

The breaker plate allows only a limited surface area to be used for filtering. If a substantial amount of filtering is required, downstream filtering units can be used. These devices use filter elements with large surface areas; a substantial amount of contaminants can be filtered out before the filter clogs up. Various companies manufacture these filtration systems. The filter elements come in various forms: plain cylinders, pleated cylinders, and leaf discs. Many of these devices can change over from one filter to another without disrupting the flow, in other words, without having to stop the extruder.

Another type of screen is the "autoscreen" system. This consists of a continuous steel gauze, which moves very slowly across the melt stream in a continuous fashion (see Fig. 3.16).

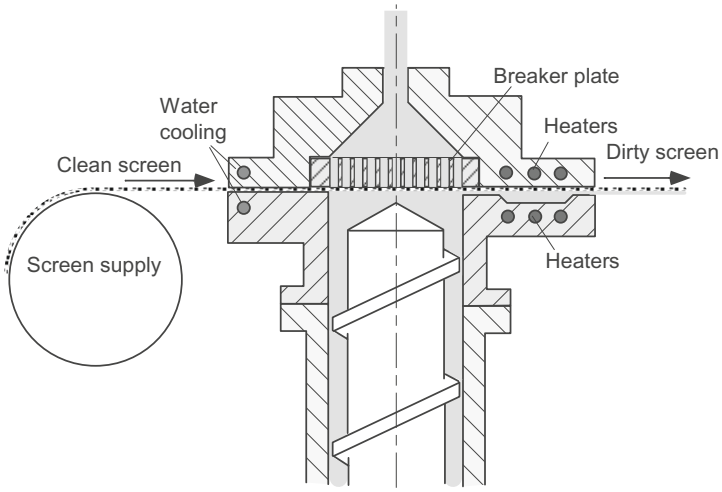


Figure 3.16 The autoscreen filter system

The movement occurs by the pressure drop over the screen; the higher the pressure drop, the more lateral force will be exerted on the screen. In other designs, the movement of the screen occurs by a motorized screen take-up. The seal is established by solidified or partially solidified polymer. The autoscreen allows a small amount of polymer to escape with the screen in a controlled fashion to carry the contaminants out and to provide a seal. Keeping a good seal requires close temperature control. Reduction of temperature can cause hang-up of the screen and increased temperatures can cause substantial leakage.

Several attempts have been made to model the flow through porous media and to predict the pressure drop as a function of flow rate and polymer flow properties. A number of interesting articles [13–26] are listed in the references.

3.7 Heating and Cooling Systems

Heating of the extruder is required for bringing the machine up to the proper temperature for start-up and for maintaining the desired temperature under normal operations. There are three methods of heating extruders: electric heating, fluid heating, and steam heating. Electric heating is the most common type of heating in extruders.

3.7.1 Electric Heating

Electric heating has significant advantages over fluid and steam heating. It can cover a much larger temperature range, and it is clean, easy to maintain, low cost, efficient, etc. For these reasons, electric heating has displaced fluid and steam heating in most applications. The electrical heaters are normally placed along the extruder barrel grouped in zones. Small extruders usually have two to four zones, while larger extruders have five to ten zones. In most cases, each zone is controlled independently so that a temperature profile can be maintained along the extruder. This can be a flat profile, increasing profile, decreasing profile, and combinations thereof, depending on the particular polymer and operation.

3.7.1.1 Resistance Heating

The most common barrel heaters are electric resistance heaters. This is based on the principle that if a current is passed through a conductor, a certain amount of heat is generated, depending on the resistance of the conductor and the current passed through it. The amount of heat generated is:

$$\dot{Q}_c = I^2R = VI = \frac{V^2}{R} \tag{3.5}$$

where I is the current, R the resistance, and V voltage. This equation is valid for direct (DC) as well as single-phase alternating current (AC), provided the current and voltage are expressed as root-mean-square (rms) values and the circuit is purely resistive (phase difference zero). With three-phase circuits, the heat generation is:

$$\dot{Q}_c = 3VI \tag{3.6}$$

Early band heaters used a resistance wire insulated with mica strips and encased in flexible sheet steel covers. These heaters are compact and low cost, but they are also fragile, not very reliable, and have limited power density. The maximum loading of these heaters is about 50 kW/m^2 (30 W/in^2) and maximum temperature about 500°C. Newer types of mica heaters reportedly can handle power densities up to 165 kW/m^2 (100 W/in^2). The efficiency of the heater and its life are largely determined by how good the contact is between the heater and the barrel over the entire contact area. Improper contact will cause local overheating, and this will result in reduced heater life or even premature burnout of the heater element. Special pastes are commercially available to improve the heat transfer between heater and barrel.

Ceramic band heaters generally last much longer than the mica-insulated heaters and they can withstand higher power densities, up to 160 kW/m^2 (100 W/in^2) or higher, and block temperatures up to 750°C. The disadvantages of heaters with ceramic insulation are that they are not flexible and tend to be bulky. However, some ceramic band heaters have a thin-line design with minimal space requirements. They usually come in halves that have to be bolted together around the extruder barrel.

Another type of heater is the "cast-in" heater. In this heater, the heating elements are cast in semicircular or flat aluminum blocks. The heat transfer in this heater is very good. This heater is reliable and gives good service life. Cast aluminum heaters have a maximum watt density of about 55 kW/m^2 (35 W/in^2) with a maximum operating temperature of about 400°C. Bronze castings can increase the power density to about 80 kW/m^2 (50 W/in^2) and a maximum operating temperature of about 550°C.

3.7.1.2 Induction Heating

In induction heating, an alternating electric current is passed through a primary coil that surrounds the extruder barrel. The alternating current causes an alternating magnetic field of the same frequency. This magnetic field induces an electromotive force in the barrel, causing eddy currents. The I^2R losses of the circulating current are responsible for the heating effect.

The depth of heating reduces with frequency. At normal frequencies of 50 or 60 Hz, the depth is approximately 25 mm. This is similar to the thickness of a typical extruder barrel. The advantage of this system, therefore, is the much reduced temperature gradients in the extruder barrel because the heat is generated quite evenly throughout the depth of the barrel as opposed to resistance-type barrel heaters.

Another advantage of inductive heating is reduced time lag in power input changes. Local overheating because of poor contact does not occur. Power consumption is low because of efficient heating and reduced heat losses, in spite of the fact that the power factor is lower than that of resistance heaters. It is possible to have a cooling

system directly on the barrel surface, allowing accurate temperature control with fast response. A major drawback of induction heating is its high cost.

3.7.2 Fluid Heating

Fluid heating allows even temperatures over the entire heat transfer area, avoiding local overheating. If the same heat transfer fluid is used for cooling, an even reduction in temperatures can be achieved. The maximum operating temperature of most fluids is relatively low, generally below 250°C. A few fluids can operate at high temperature; however, they often produce toxic vapors—this constitutes a considerable safety hazard. Fluid heating systems require considerable space, and installation and operating expenses are high. Another drawback with fluid heating is that if several zones need to be maintained at different temperatures, several independent fluid heating systems are required. This becomes rather expensive, bulky, and ineffective.

Steam heating is rarely used on extruders anymore, although most of the very early extruders were heated this way, particularly rubber extruders. Steam is a good heat transfer fluid because of its high specific heat. However, it is difficult to increase the temperature to sufficiently high temperatures (200°C and above) as required in polymer extrusion. This requires very high steam pressures; most extrusion plants nowadays are not equipped with proper steam generating facilities to do this. Additional problems are bulkiness, chance of leakage, corrosion, heat losses, etc.

3.7.3 Extruder Cooling

Extruder cooling in most extrusion operations is a necessary evil. In all cases, cooling should be minimized as much as possible; preferably, it should be eliminated altogether. The reason is that any amount of extruder cooling reduces the energy efficiency of the process, because cooling translates directly into lost energy. Heating of the extruder generally reduces the motor power consumption and thus contributes to the overall power requirement of the process. However, cooling does not contribute to the overall power requirement, and the energy extracted by cooling is wasted.

If an extrusion process requires a substantial amount of cooling, this is usually a strong indication of improper process design. This could mean improper screw design, excessive length-to-diameter ratio, or incorrect choice of extruder, e.g., single screw versus twin screw extruder.

The extrusion process is generally designed such that the majority of the total energy requirement is supplied by the extruder drive. The rotation of the screw

causes frictional and viscous heating of the polymer, which constitutes a transformation of mechanical energy from the drive into thermal energy to raise the temperature of the polymer. The mechanical energy generally contributes 70 to 80% of the total energy. This means that the barrel heaters contribute only 20 to 30%, discounting any losses.

If the majority of the energy is supplied by the screw, there is a reasonable chance that local internal heat generation in the polymer is higher than required to maintain the desired process temperature. Thus, some form of cooling is usually required. Many extruders use forced-air cooling by blowers mounted underneath the extruder barrel; see Fig. 3.17.

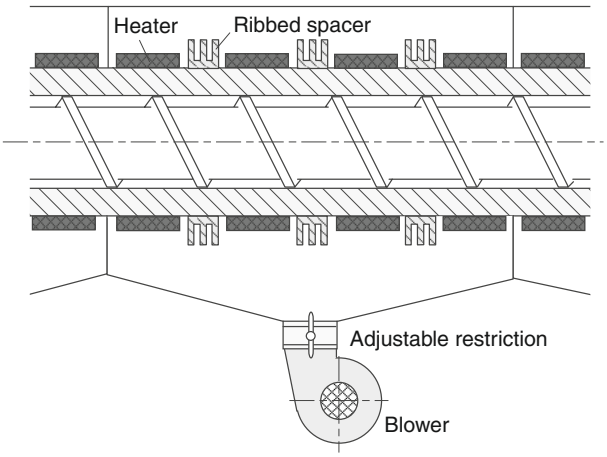


Figure 3.17
Extruder cooling by forced air

The external surface of the heaters or the spacers between the heaters is often made with cooling ribs to increase the heat transfer area and thus the cooling efficiency. Small extruders can often do without forced-air cooling because their barrel surface area is quite large compared to the channel volume, providing a relatively large amount of convective and radiative heat losses.

Some extruders operate without any forced cooling or heating. This is the so-called "autogenous" extrusion operation, not to be confused with adiabatic operation. An autogenous process is a process where the heat required is supplied entirely by the conversation of mechanical energy into thermal energy. However, heat losses can occur in an autogenous process. An adiabatic process is one where there is absolutely no exchange of heat with the surroundings. Clearly, an autogenous extrusion operation can never be truly adiabatic, rather only by approximation.

In practice, autogenous extrusion does not occur often because it requires a delicate balance between polymer properties, machine design, and operating conditions. A change in any of these factors will generally cause a departure from autogenous conditions. The closer one operates to autogenous conditions, the more likely it is

that cooling will be required. Given the large differences in thermal and rheological properties of various polymers, it is difficult to design an extruder that can operate in an autogenous fashion with several different polymers. Therefore, most extruders are designed to have a reasonable amount of energy input from external barrel heaters.

On the other hand, the energy input from the barrel heaters should not be too large. The problem with external heating is that this is associated with relatively large temperature gradients. In materials with low thermal conductivity, large temperature gradients are required to heat up the material by external heating at a reasonable rate. Since polymers have a low thermal conductivity, raising the polymer temperature by external heating is a slow process and involves large temperature gradients. Thus, locally high temperatures will occur at the metal/polymer interface. The combination of high temperatures and long heating times makes for a high chance of degradation. The heating by viscous heat generation is much more favorable in this respect, because the polymer is heated relatively uniformly throughout its mass. Thus, one would generally want the mechanical energy input to be more than 50% of the total energy requirement but less than about 90%.

Air cooling is a fairly gentle type of cooling, because the heat transfer rates are relatively small. This is not good if intensive cooling is required. On the other hand, there is an advantage in that when the air cooling is turned on, the change in temperature occurs gradually. With water cooling, a rapid and steep change in temperature will occur as soon as the water cooling is activated. From a control point of view, the latter situation can be more difficult to handle.

When substantial cooling is required, fluid cooling is used, with water being the most common heat transfer medium. It was mentioned in Section 3.3 that grooved barrel sections require intense cooling to be effective. In most cases, water is used to cool the grooved barrel section, just as it is used to cool the feed throat casting. One of the complications with water cooling is that evaporation can occur if the water temperature exceeds the boiling temperature. This is an effective way to extract heat, but it causes a sudden increase in cooling rate. From a control point of view, this constitutes a non-linear effect, and it is more difficult to properly control the extruder temperature if such sudden, non-linear effects occur. Thus, water cooling may place much higher demands on the temperature control system as compared to air cooling. The cooling efficiency of air can be increased by wetting the air; however, this requires cooling channels made out of corrosion-resistant material. This technique is used in a patented vapor cooling system [8, 9]. The latent heat of a vapor, which circulates around the extruder barrel, is extracted by a water cooling system that surrounds a condensing chamber located away from the barrel. A schematic of this vapor cooling system is shown in Fig. 3.18.

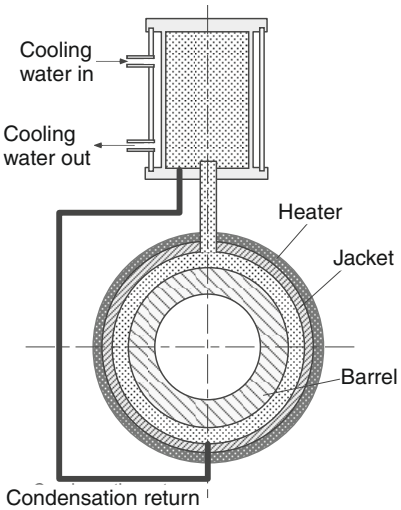


Figure 3.18
Extruder vapor cooling system

This type of vapor cooling is claimed to have a smooth operating characteristic and good temperature control.

Oil- or air-cooled extruders can use stepless cooling control, using proportional valves and positioning motors. These systems are relatively expensive, but they are reliable and require little maintenance. With water cooling, the cooling power is generally controlled by energizing a solenoid valve. For low temperatures (no flashing), usually a constant cycle rate is used with variable pulse width. The pulse width varies in proportion to the cooling power required. At high temperatures, where water is flashed to steam, more intensive cooling is possible. In these cases, a different cooling control can be used, known as a constant pulse width system. When cooling is required, the solenoid is energized by a pulse signal of predetermined length. The frequency of the pulse is varied in proportion to the cooling power required.

Finally, it should be remembered that cooling is a waste of energy and should be minimized as much as possible.

3.7.4 Screw Heating and Cooling

Thus far, the discussion has been focused on barrel heating and cooling. It is important to realize, though, that the barrel/polymer interface constitutes only about 50% of the total polymer/metal interface. Thus, with only barrel heating and/or cooling, only about 50% of the total surface area available for heat transfer is being utilized. The screw surface, therefore, constitutes a very important heat transfer surface. Many extruders do not use screw cooling or heating; they run with a so-called "neutral screw." If the external heating or cooling requirements are minor, then screw

heating or cooling is generally not necessary. However, if the external heating or cooling requirements are substantial, then screw heating or cooling can become very important, sometimes a necessity.

It is obvious that heating or cooling of the screw is slightly more difficult than barrel heating or cooling, because the screw is in motion. This means that one has to use rotary unions, slip rings, or other devices to transfer energy in or out of the extruder screw. These devices, however, have become rather standard in industry, and they are commonly available. Water cooling can be done even without the use of a rotary union. This involves running some copper tubing down into the bore of the extruder screw and connecting a water supply to the copper tube. The water will flow towards the end of the screw through the tube and will then flow back in the annular space between the tube and the bore of the screw. As the water reaches the shank end of the screw, it will simply drain away. This is a crude but effective type of screw cooling (see Fig. 3.19).

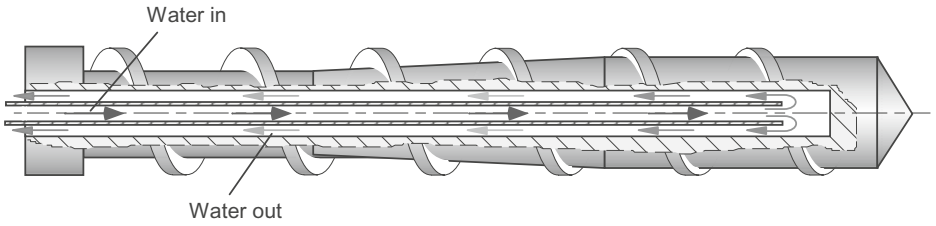


Figure 3.19 Simple screw cooling system

Screw cooling is generally arranged such that the fluid, water or oil, enters the screw via a rotary union, flowing into a pipe in the bore of the screw. The screw is cooled most at the discharge end of the pipe; further cooling occurs upstream as the fluid flows back to the rotary union. The point of maximum cooling can be adjusted by changing the location of the end of the pipe.

Sometimes the end of the pipe in the screw bore is made with an axially adjustable seal. This allows cooling of a selected section of the screw. Other adjustments that can be made are the flow rate and inlet temperature of the cooling medium. Thus, a considerable degree of flexibility in cooling conditions is possible. This is why screw cooling or heating adds significantly to the controllability of the process. In fact, some extrusion operations are simply impossible without the use of screw cooling. The two fluids most often used for cooling are water and oil.

In some cases, screw cooling is used to improve the pressure-generating capability of the screw. The screw is cooled all the way into the metering section. The colder screw surface freezes the polymer close to the screw or, at least, significantly increases the viscosity of the polymer melt close to the screw surface. This reduces the effective channel depth of the extruder screw and can result in improved pressure-generating capacity if the screw was cut too deep to begin with. Therefore, if

screw cooling is required to obtain sufficient pressure at the die, this is a strong indication that the design of the extruder screw is incorrect. Instead of cooling the screw, a better solution would be to modify the screw design, specifically to reduce the channel depth in the metering section. Determination of the optimum channel depth for pressure generation will be discussed in Chapter 8.

An interesting concept of screw cooling is the application of a heat pipe in the extruder screw. The heat pipe extends from the feed section to the metering section. In most cases, the temperature of the metering section will be considerably higher than the temperature of the feed section. This temperature difference will set up a heat flow in the heat pipe trying to diminish this temperature difference. Thus, the metering section will be cooled and the feed section will be heated. The advantage of this system is that it is self-contained, sealed, and heat losses from cooling are very small. A disadvantage is the fact that no external means of control is possible.

Screw heating is sometimes done with cartridge heaters located in the bore of the extruder screw. Power is supplied to the heater by slip rings on the shank of the screw. If the heater is axially adjustable, then the location of heating can be changed as desired. With this type of heating, one has to be careful to establish good contact between heater and screw. This almost requires installation of the heater in a pre-heated screw. If the heater is installed in a cold screw, good contact between heater and screw can be lost when the screw heats up. The requirement for tight contact between screw and heater would make it difficult to have an axially adjustable heater. In this case, one would have to use a heat transfer paste between screw and heater that allows good heat transfer but still a reasonable axial movement of the heater.

References

1. K. Rape, Power Transmission Design, 8, 36–38 (1982)
2. N.N., Modern Materials Handling, Oct. 6, 66–69 (1982)
3. L.J. McCullough, Tech. Papers IEEE Meeting, 755–757 (1978)
4. N.N., Generation Planbook, 144–147 (1982)
5. S. Collings, Plastics Machinery & Equipment, Sept. 26–29 (1982)
6. Machine Design, Fluid Power Reference Issue (1982)
7. R.L. Miller, SPE Journal, Nov., 1183–1188 (1964)
8. U.S. Patent 2,796,632
9. W.H. Willert, SPE Journal, 13, 6, 122–123 (1957)
10. N.T. Flathers, et al., Int. Plast. Eng., 1, 256 (1961)
11. H.M. Kennard, Plast. Eng., 30, 12, 59 (1974)
12. J.S. Singleton, paper presented at Filtration Society Conference, London, Sept. (1973)

13. W. C. Smith, Ph.D. thesis, University of Colorado (1974)
14. T. J. Sadowski and R. B. Bird, Trans. Soc. Rheol., 9, 2, 243 (1965)
15. R. J. Marshall and A. B. Metzner, Ind. Eng. Chem. Fund., 6, 393 (1967)
16. R. H. Christopher and S. Middleman, Ind. Eng. Chem. Fund., 4, 422 (1965).
17. D. F. James and D. R. McLaren, J. Fluid Mech., 70, 733 (1975)
18. R. E. Sheffield and A. B. Metzner, AIChE J., 22, 736 (1976)
19. G. Laufer, C. Gutfinger, and N. Abuaf, Ind. Eng. Chem. Fund., 15, 77 (1976)
20. E. H. Wissler, Ind. Eng. Chem. Fund., 10, 411 (1971)
21. Z. Kamblowski and M. D. Ziubinski, Rheol. Acta, 17, 176 (1978)
22. "Filtration of Polymer Melts," VDI Publication, Duesseldorf, Germany (1981)
23. J. A. Deiber and W. R. Schowalter, AIChE J., 27, 6, 912 (1981)
24. M. L. Booy, Polym. Eng. Sci., 22, 14, 895 (1982)
25. S. H. Collins, Plast. Compounding, March/April, 57–70 (1982)
26. D. S. Done and D. G. Baird, Techn. Papers 40th ANTEC, 454–457 (1982)
27. K. O'Brien, Plast. Technology, Feb., 73–74 (1982)
28. N. N., Int. Plast. Eng., 2, 92–95 (1962)
29. A. Bres, VDI-Nachrichten, 19, 42, 14 (1965)
30. R. G. Schieman, Reliance Electric Publication, D-7115, 1, 7 (1983)
31. C. J. Ceroke, Chemical Engineering, Nov. 12, 133–134 (1984)
32. W. A. Kramer, "Motors and Drives for Extrusion Applications," SPE ANTEC, 268–272 (1999)
33. C. Hiemenz, G. Ziegmann, B. Franzkoch, W. Hoffmanns, and W. Michaeli, "Verbesserung am Einschneckenextruder," in "Handbuch des 8. Kunststofftechnischen Kolloquiums," Aachen, p. 81–109 (1976)

4 Instrumentation and Control

4.1 Instrumentation Requirements

From a hardware point of view, extruder instrumentation is one of the most critical components of the entire machine. An important reason for this is that the internal workings of the extruder are totally obscured by the barrel and the die. In many cases, the only visual observation that can be made is of the extrudate leaving the die. When a problem is noticed in the extrudate, it is difficult to determine the source and location of the problem. Instrumentation makes it possible to determine what is happening inside the extruder. One can think of instrumentation as "the window to the process."

Good instrumentation enables a continuous monitoring of the "vital signs" of the extruder. These vital signs are pressure, temperature, power, and speed. These important process parameters need to be measured for process control, but they are also of vital importance in troubleshooting. Troubleshooting is only possible with good instrumentation. At the very minimum, one needs to know pressures, screw speed, and temperatures in order to properly diagnose an extrusion problem. A minimum set of instrumentation should include:

1. Diehead pressure before and after screen pack
2. Rotational speed of the screw
3. Temperature of polymer melt at the die
4. Temperatures along barrel and die
5. Cooling rate at each heat zone
6. Power consumption of each heat zone
7. Power consumption of the drive
8. Temperature of cooling water in feed housing
9. Flow rate of cooling water in feed housing

This is a minimum requirement. In many cases, additional measurements are required, e.g., in a vented extrusion operation the vacuum at the vent port should be monitored continuously. In some cases, one may want to measure polymer melt temperature at various locations in or outside the die to determine the melt temperature distribution—remember there is not just one melt temperature!

The parameters above relate just to the extruder. However, there are many more process parameters for the entire extrusion line and they, of course, depend on the line's specific components. Important parameters for any extrusion line are:

- Line speed
- Dimensions of the extruded product
- Cooling rate or cooling water temperature
- Line tension

Many other factors can influence the extrusion process, such as ambient temperature, relative humidity, air currents around the extruder, and plant voltage variations among others.

Incomplete instrumentation can severely hamper quick and accurate troubleshooting; in fact, it can turn troubleshooting from a logical step-by-step process into a guessing game. Without good instrumentation it can be days, weeks, or even months before a problem is located and solved. When an extrusion problem results in off-quality product or downtime, it is very important to find the cause of the problem quickly because such problems can be very costly. In some instances, a downtime of just one day is more expensive than an entire new extruder! In most cases, trying to save money on instrumentation is penny-wise and pound-foolish.

Good instrumentation allows problems to be detected early before becoming more severe and causing substantial damage to the extruder hardware or to the extrudate quality. It also allows process characterization for process development and optimization. It is further important for production control and record keeping, and it provides a means of interfacing the extruder to a computer.

4.1.1 Most Important Parameters

The most important process parameters are melt pressure and temperature. They are the best indicators of how well or how poorly an extruder functions. Process problems, in most cases, first become obvious from melt pressure and/or temperature readings. Just think what a doctor does when a patient comes into the office with a problem. Usually, the first check of the patient's condition is made by taking blood pressure and body temperature. These are two good indicators of the functioning of the human body. In the same fashion, melt pressure and temperature are good indicators of how the extruder is functioning.

4.2 Pressure Measurement

4.2.1 The Importance of Melt Pressure

Measurement of melt pressure is important for two reasons:

1. Process monitoring and control
2. Safety

The diehead pressure in the extruder determines the output from the extruder. It is the pressure necessary to overcome the resistance of the die. When the diehead pressure changes with time, the extruder output correspondingly changes and so do the dimensions of the extruded product; see Fig. 4.1. As a result, when we monitor how the pressure varies with time, we can see exactly how stable or unstable the extrusion process is.

It is best, therefore, to plot pressure with a chart recorder or better, to monitor the variation of pressure with a computer data acquisition system. A simple analog or digital display of pressure is much less useful.

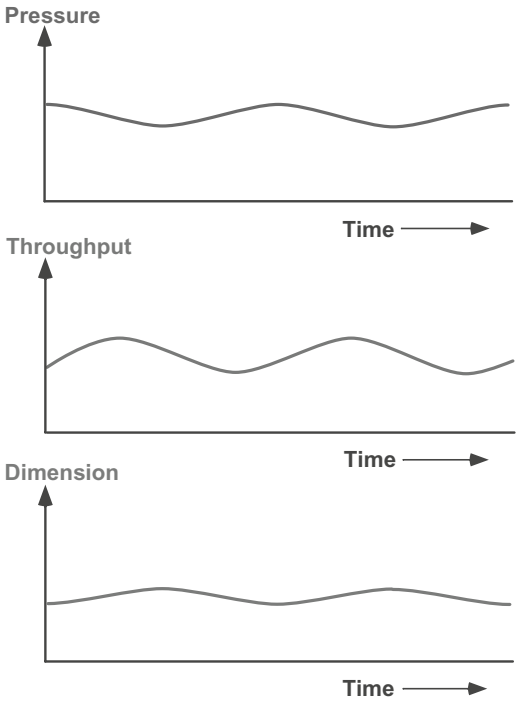


Figure 4.1
Pressure, throughput, and dimension as a function of time

It is also critically important to measure pressure in the extruder to prevent serious accidents that can happen when excessively high pressures are generated. *The very high pressures generated in the extruder can cause an explosion.* The barrel can crack

open under excessive pressure or the die may be blown from the extruder. Both situations are extremely dangerous and should be avoided. All extruders should have an over-pressure safety device, such as a rupture disk or a shear pin in the clamp holding the die against the extruder barrel. Even with such an over-pressure safety device, the extruder should have at least one melt pressure measurement, in order to overcome malfunctioning or disabled over-pressure devices. Pressure can build up very quickly without warning and cause a catastrophic explosion.

When monitoring pressure, it is a good idea to use an automatic shutoff when the pressure reaches a critical value. In pressure measurements, it is important to determine the absolute level of pressure, but it is equally important, if not more important, to determine changes in pressure with time. In most cases, pressure variation correlates closely with variation in the extruded product. Since high frequency (cycle time less than one second) pressure fluctuations are quite common in extrusion, a fast response measurement is important.

4.2.2 Different Types of Pressure Transducers

Pressure measurement on early extruders was done with grease-filled Bourdon gauges. The reliability of these gauges was not very good. At high temperatures, the grease tends to leak out; this causes inaccurate readings and product contamination. Polymer can hang up in the grease cavity; with time, it can form a hard plug, again causing inaccurate readings. The temperature dependence of the Bourdon gauge pressure measurement is also quite high. As a result, Bourdon gauges are hardly used anymore.

Nowadays there are a number of different pressure transducers. The most common ones in extrusion are the strain gauge transducer and the piezo-resistive transducer. In a strain gauge pressure transducer a strain gauge is bonded to a diaphragm. The melt pressure deforms the diaphragm and the strain gauge measures the deformation of the diaphragm; see Fig. 4.2. These units generally have good response and resolution. Since the strain gauge cannot be exposed to high temperatures, it is placed away from the heated polymer/barrel environment. Therefore, a mechanical or hydraulic coupling is used to transmit the deflection of the diaphragm to the strain gauge.

The strain gauge transducer can be either a capillary or a pushrod transducer. In these transducers, there are two diaphragms, one in contact with the plastic melt and the other some distance away from the hot plastic melt. The connection between the first and second diaphragm is hydraulic in the capillary type and a pushrod in the pushrod type; see Fig. 4.3. A strain gauge is attached to the second diaphragm to measure the deflection that can be related to the pressure at the first diaphragm.

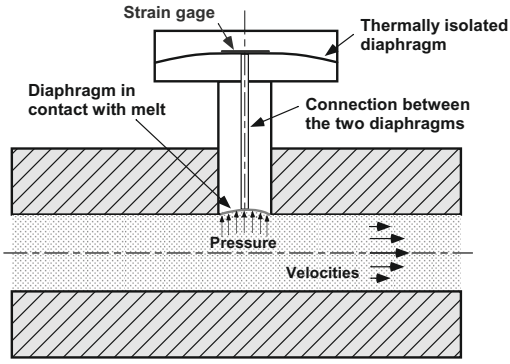


Figure 4.2
Principle of the strain gauge transsducer

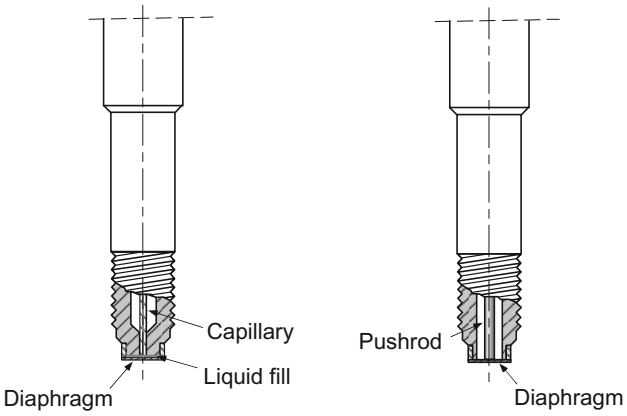


Figure 4.3
Capillary (left) and pushrod type (right) pressure transducer

Many capillary transducers are filled with mercury. Since the diaphragm of the transducer is quite thin, there is a danger of the diaphragm rupturing and leaking mercury into the plastic and into the workplace. Unfortunately, many transducers do not carry a label indicating that the transducer is filled with mercury, so adequate safety precautions are not always taken. It is important to make sure that mercury-filled transducers are not used in the extrusion of medical products and food packaging products. In these situations, other liquids can be used inside the transducer; the most common alternative to mercury is NaK (sodium-potassium).

Another type of transducer is the pneumatic pressure transducer. It has good robustness, but poor temperature sensitivity, poor dynamic response, and average measurement error. The capillary transducer has fair robustness, fair temperature sensitivity, and fair dynamic response. The total measurement error varies from 0.5 to 3% depending on the quality of the transducer. The pushrod is similar to the capillary transducer, except that it tends to have poor temperature sensitivity and poor total error. The piezo-resistive transducer has good robustness because of its relatively thick diaphragm, good temperature sensitivity, good dynamic response, and low measurement error. A comparison of different pressure transducers is shown in Table 4.1.

Table 4.1 Comparison of Various Pressure Transducers

Transducer type	Robustness	Temperature sensitivity	Dynamic response	Total error
Pneumatic	Good	Poor	Poor	About 1.5%
Capillary strain gauge*	Fair	Fair	Fair	0.5 to 3%
Pushrod strain gauge	Fair	Poor	Fair	About 3%
Piezoelectric	Good	Poor	Good	0.5–1.5%
Piezo-resistive	Good	Good	Good	0.2 to 0.5%
Optical	Good	Good	Good	About 0.5%

* Concern with mercury

Another transducer uses compressed air. The regulated air pressure is controlled such that there is a force balance between the measuring diaphragm and the balancing diaphragm. This is a purely pneumatic system. Pneumatic pressure transducers have good robustness but poor temperature sensitivity and dynamic response. There are also pressure transducers that use a measuring element with an unbonded wire strain gauge. The wires are part of a full bridge circuit. The measuring element is located directly behind the diaphragm, and the deflection of the diaphragm is transferred to the measuring element with a short rod. Temperature changes at the diaphragm affect all four arms of the bridge circuit and, therefore, have little effect on the measurement. Some pressure transducers are available with an internal thermocouple to provide temperature measurement capacity in addition to the pressure measurement capability.

Other pressure transducers use a piezoelectric element. A piezoelectric material has the ability to transform a very small mechanical deformation (input signal) into an electric output signal (voltage or current) without any external electric power supply. Quartz pressure transducers have been developed to measure large pressures in high temperature polymer melts. The absence of a membrane allows a very robust construction. This has led to widespread use in injection molding.

One of the main advantages of piezo pressure transducers is their outstanding dynamic response. The natural frequency of the piezo transducers is about 40 kHz. This allows accurate pressure measurements at a frequency up in the low kHz range. This is about three orders of magnitude better than the capillary type strain gauge pressure transducer. One of the main drawbacks of piezoelectric pressure transducers is that they cannot measure steady pressure accurately because the signal decays. Therefore, piezoelectric pressure transducers are limited to applications where the pressure changes over relatively short time frames (on the order of a few seconds or less). Another drawback of the piezoelectric transducer is that it cannot be exposed to high temperatures. The maximum use temperature is typically 120°C.

Some transducers use piezo-resistive semiconductors implanted into a small chip. The resistance of piezo-resistive materials changes with stress or strain. When the chip is bonded to a pressure-sensing diaphragm, the change in resistance can be measured with a Wheatstone bridge. The piezo-resistive element can provide a repeatable signal that is proportional to the pressure against the diaphragm. Figure 4.4 shows the sensing element of a piezo-resistive transducer.

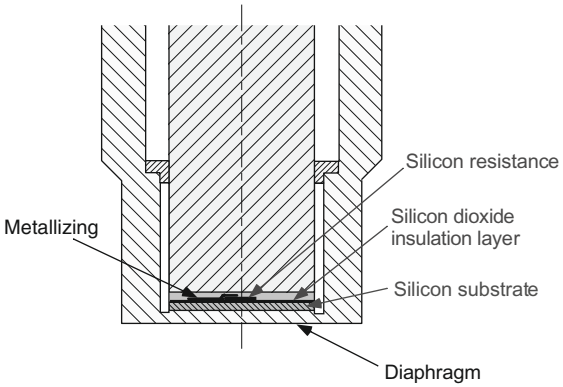


Figure 4.4
Sensing element of a piezo-resistive transducer

Piezo-resistive pressure transducers offer a number of advantages [82]. The transducer is quite robust because of the relatively thick diaphragm. There is no liquid fill inside the transducer; as a result, there is no concern about leakage of mercury. The natural frequency of piezo-resistive transducers is about three orders of magnitude better than strain gauge type transducers. As a result, the dynamic response of piezo-resistive transducers is very good compared to that of strain gauge transducers.

Optical pressure transducers can offer some important advantages. The German company FOS Messtechnik GmbH has developed several pressure transducers that use an optical method of measuring diaphragm deflection. This method allows very precise measurement of diaphragm movement; the maximum deformation of the diaphragm at normal pressure is only about 10 micron. This allows for a very rugged construction of the transducer; the diaphragm is about ten times thicker than that of conventional transducers. Also, the response time is quite short; the transducer can measure dynamic pressure up to 50 kHz. As a result, it can be applied in very fast control circuits.

The optical pressure sensor measures the deformation of the diaphragm with a quartz glass optical fiber. With an optical fiber a mirror on the backside of the diaphragm is illuminated and the reflected light intensity is measured with high resolution. The sensor can be used to temperatures as high as 600°C, in some cases even higher. Even though this type of transducer is not commonly used in the extrusion industry it offers some very important advantages over conventional pressure transducers.

4.2.3 Mechanical Considerations

Most diaphragms are made of stainless steel, 17-4 PH or Type 304. Type 17-4 stainless steel has a higher tensile strength and, under the same conditions, will be stressed at a lower percentage of yield, thus improving fatigue life. Another important design aspect is the connection between the diaphragm and the main body. This is generally done by welding using two welding configurations; see Fig. 4.5.

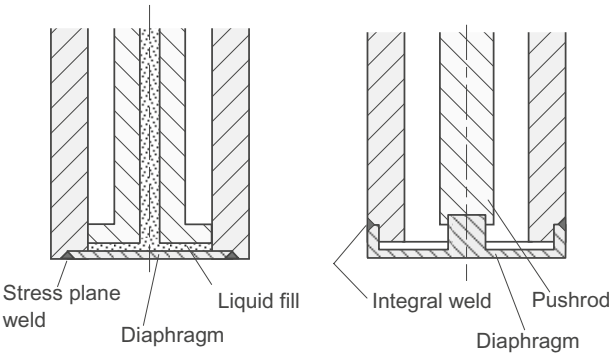


Figure 4.5
Weld configuration in capillary type (left) and pushrod type transducer

In the "stress plane" weld configuration, the area of the diaphragm under maximum stress coincides with the weld. This can create problems because the weld is different from the other parts of the diaphragm. The weld and the area right around it will be more susceptible to stress corrosion and brittleness problems. This is particularly true of Type 304 stainless steel because of embrittlement from carbide precipitation at the weld zone.

The integral weld places the weld zone in a non-stressed location. This configuration is typical of the force-rod design and can readily be recognized by the lack of weld bead at the circumference of the diaphragm. Some newer pressure transducers do not employ the welded diaphragm construction but use a non-welded, one-piece diaphragm and tip assembly.

If the pressure transducer is exposed to highly corrosive substances, the diaphragm can be made out of a highly corrosion-resistant material such as Hastelloy. This improvement in corrosion resistance is generally at the expense of non-linearity and hysteresis. These specifications can increase by as much as 0.5%. If the transducer is exposed to highly abrasive components, a very thin wear-resistant coating can be applied to the diaphragm. One manufacturer uses an electrolyzing process to deposit a thin coating on the diaphragm similar to hard chrome, but more wear-resistant.

The transducers with hydraulic coupling between the diaphragm and the strain gauge often use mercury; see Fig. 4.5 (left). The amount of mercury is very small. The channel between the diaphragm and strain gauge is a small capillary. This transducer, therefore, is sometimes referred to as a capillary-type transducer. Mer-

cury is used because of its low thermal expansion and high boiling point. The effect of temperature on the pressure measurement is rather small. The capillary-type transducer offers the advantage of a uniform liquid support behind the diaphragm. A potential hazard is rupture of the diaphragm. This will cause the release of mercury and will contaminate the extrudate and the production area.

Transducers with a mechanical coupling between diaphragm and strain gauge often use a force rod; see Fig. 4.5 (right). The force rod design offers the dependability of a direct mechanical link between the diaphragm and the strain gauge. The force rod construction does not result in a uniform loading of the diaphragm.

Piezoelectric pressure transducers can be designed in a very compact package. The required deflection to obtain a pressure reading can be very small because of the high sensitivity of the piezoelectric element. The deflection is generally measured in microns (μm); full pressure can be reached with a deflection of less than 10 μm [1, 2]. The temperature range is primarily determined by the insulation. Transducers with ceramic insulation can be exposed to temperatures as high as 350°C. The more common PTFE insulation allows temperatures up to 240°C. The linearity of these transducers is better than 1%. The sensitivity is in the range of a few pC/bar at pressures of up to 7500 bar (about 750 MPa or 110,000 psi).

4.2.4 Specifications

Specifications on pressure transducers from different manufacturers can vary significantly. It is important to understand how and to what extent certain specifications affect the accuracy of the measurement. Some of the more important specifications will be reviewed.

An ideal transducer would have an exactly linear relationship between pressure and output voltage. In reality, there will always be some deviation from the ideal linear relationship; this is referred to as non-linearity. A “best straight line” (BSL) is fitted to the non-linear curve. The deviation from BSL is quoted in the specifications and expressed as a percent of full scale (FS). The non-linear calibration curve is determined in the ascending direction, i. e., with the pressure going from zero to full rating.

The pressure measured in the ascending mode will be slightly different from the pressure measured in the descending mode; see Fig. 4.6.

This difference is termed hysteresis; it is expressed as a percent of full scale. The non-linearity and hysteresis errors can be reduced by using a 75 to 80% shunt resistor to calibrate the output indicator [3]. This procedure essentially reduces the non-linearity error at the 75%-reading to zero by impressing an additional voltage on the indicator that raises the non-linearity and hysteresis curves. The maximum deviation now occurs at full scale and maximum precision occurs at mid-range, where the transducer is most likely to be used in normal operating conditions.

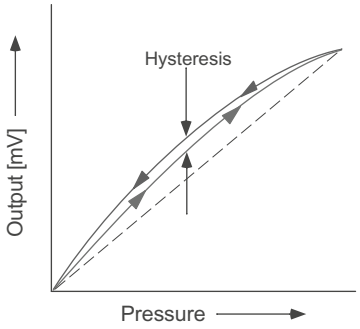


Figure 4.6
Hysteresis in a pressure transducer

Repeatability is a measure of the ability of a transducer to reproduce output readings when measuring pressure consecutively and in the same direction. It specifies the maximum deviation obtained by comparing output readings for the three ascending-descending full-scale loadings.

Temperature changes will cause variations in pressure reading. Thermal shift specifications indicate the maximum deviations expected due to temperature changes from room temperature to the specified limits of the operating range both for zero and for up-scale conditions. Deviations are expressed as a percent of full-scale rating for each degree of temperature above room temperature.

When a transducer is being selected, one should consider the accuracy of both the transducer itself and the readout equipment. The meter readout should be readable to an accuracy at least as good as the accuracy of the transducer.

In Germany, the VDMA (Verein Deutsche Maschinenbau Anstalten) has issued a publication (VDMA 24456) describing in detail the various aspects of pressure transducers. This publication also describes various test set-ups that can be used to test pressure transducers; both static and dynamic testing are discussed.

The dynamic behavior of pressure transducers is of particular interest in the analysis of extrusion instabilities. The procedure for dynamic testing described in VDMA 24456 was used to test various commercial pressure transducers. Puetz [4] published some dynamic test data for different pressure transducers (see Table 4.2).

Table 4.2 Dynamic Data of Various Pressure Transducers (Courtesy [4])

Company	Model	Range [bar]	Natural frequency [s^{-1}]	Damping [s^{-1}]	Limiting frequency [Hz]
Dr. Staiger		200	353	49	17
Dynisco	PT 422A	350	182	23	9
Dynisco	PT 420/12	350	628	69	30
Brosa		500	A.D.*	A.D.*	90
Rosemount	1401 A1	105	A.D.*	A.D.*	1

* A.D. is aperiodic damping

Dynamic testing of pressure transducers can be done by measuring the response to a pulse input. If the pulse occurs over a small period of time, the system will respond with a damped oscillation. A typical response is shown in Fig. 4.7.

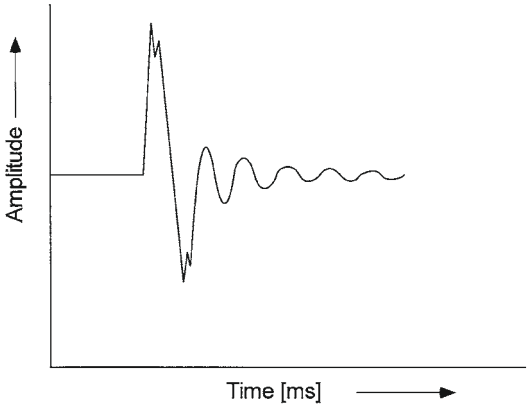


Figure 4.7
Typical pressure transducer pulse response

The response can be described by a function of the form:

$$f(t) = A\exp(-\delta t)\sin(\omega_d t + \varphi) \tag{4.1}$$

where: A = amplitude of oscillation

δ = damping constant

ω_d = natural frequency of the system

The characteristic values of the system can be determined from the pulse response. With these values, the amplitude-frequency (A-ω) and phase-frequency (α-ω) characteristics can be determined from the following relationships:

$$|F| = \frac{1}{\sqrt{(1 - T^2\omega^2)^2 + (2DT\omega)^2}} \tag{4.2}$$

$$\alpha = -\arctan\frac{2DT\omega}{1 - T^2\omega^2} \tag{4.3}$$

where D = degree of damping

T = period of oscillation of undamped system

Typical amplitude- and phase-frequency characteristics are shown in Fig. 4.8.

It can be seen from the amplitude-frequency curve of the transducer shown in Fig. 4.8 that an amplitude increase of 10% is reached at a frequency of about 80 rad/s (≈ 12.5 Hz). This means that pressure fluctuations with a frequency of 12.5 Hz will be measured with an error in amplitude of 10%; with a frequency of 30 Hz the error will be about 100%!

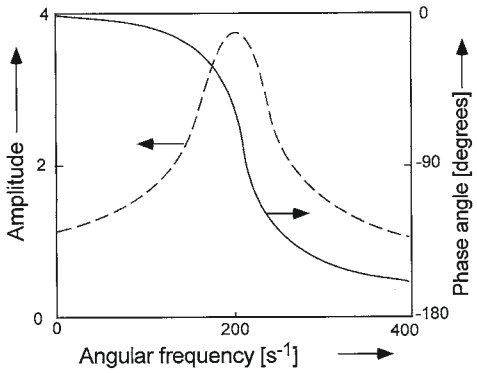


Figure 4.8
Typical amplitude- and phase-frequency curves

The limiting frequency shown in Table 4.2 represents the frequency at which the error in amplitude reaches 10%. It should be noted that the limiting frequencies listed in the table are considerably lower than the values sometimes claimed by pressure transducer manufacturers. Some transducer suppliers claim a flat frequency response up to 100 Hz; however, the data in Table 4.2 does not substantiate that number. As mentioned before, the dynamic response of piezo pressure transducers is far better (several orders of magnitude) than membrane-type pressure transducers.

4.2.5 Comparisons of Different Transducers

In general, electric transducers are more accurate than pneumatic transducers, while pneumatic transducers, in turn, are more accurate than mechanical transducers. Typical accuracy of electric transducers is ± 0.5 to 1.0%, pneumatic transducers about ± 1.5%, and mechanical transducers about ± 3% [4].

The reproducibility for electric systems is about ± 0.1 to ± 0.2%, for pneumatic systems about ± 0.5%, and about ± 1 to ± 2% for mechanical pressure transducers. The hysteresis with electric pneumatic transducers is about 0.1 to 0.2%, while it is as high as 4 to 5% with mechanical systems.

■ 4.3 Temperature Measurement

Temperature measurement occurs at various locations of the extruder: along the extruder barrel, in the polymer melt, and at the extrudate once it has emerged from the die. The choice of the type of temperature measurement will depend on what is being measured and where. First, the methods of temperature measurement will be reviewed.

4.3.1 Methods of Temperature Measurement

Temperature can be measured with resistive temperature sensors, thermocouple temperature sensors, and radiation pyrometers. There are two types of resistive temperature sensors: the conductive type and the semiconductor type. Both operate on the principle that the resistance of sensor material changes with temperature.

The conductive-type temperature sensor (RTD) uses a metal element to measure temperature. The resistance of most metals increases with temperature; thus, by measuring resistance, one can determine the temperature. Platinum is used where very precise measurements are required and where high temperatures are involved. Platinum is available in highly purified condition; it is mechanically and electrically stable and corrosion-resistant. Most of the RTD sensors have a wound wire configuration; although for some applications, metal-film elements are used.

The semiconductor type sensor utilizes the fact that the resistance of a semiconductor decreases with temperature. The most common type of semiconductor temperature sensor is the thermistor shown in Fig. 4.9.

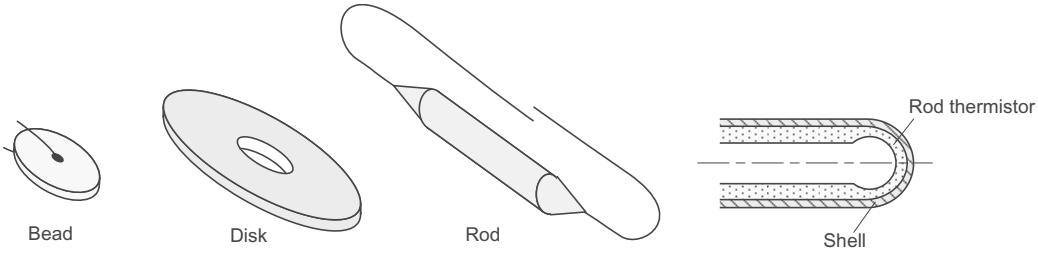


Figure 4.9 Thermistor

Because of their small size, thermistors can be used where other temperature sensors cannot be used. A typical resistance temperature (RT) curve is generally non-linear; this is one of the drawbacks of thermistors. However, techniques to deal with the thermistor non-linearity are now well established [14]; thus, the non-linearity is not a major problem. Other disadvantages are the low operating currents (< 100 μA) and the tendency to drift over time. An advantage is their quick response time.

Thermocouple (TC) temperature sensors are also known as thermoelectric transducers; a basic TC circuit is shown in Fig. 4.10.

A pair of wires of dissimilar metals are joined together at one end (hot junction or sensing junction) and terminated at the other end by terminals (the reference junction) maintained at constant temperature (reference temperature). When there is a temperature difference between sensing and reference junctions, a voltage is produced. This phenomenon is known as the thermoelectric effect. The amount of voltage produced depends on the temperature difference and the metals used.

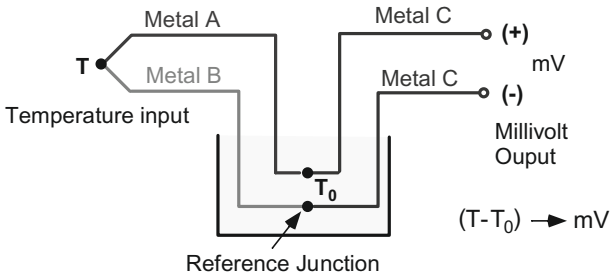


Figure 4.10
Basic thermocouple circuit

One of the most common TCs is the iron-constantan TC. Thermocouples come in various configurations, with exposed junction, grounded junction, ungrounded junction, surface patch, etc.; see Fig. 4.11.

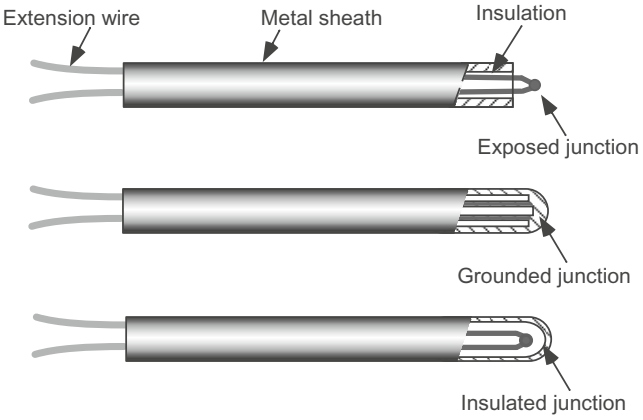


Figure 4.11
Various thermocouple configurations

Detailed information on thermocouples and their use in temperature measurements can be found in the book by Pollock [69], the ASTM publication on thermocouples [70], the NBS monograph on thermocouples [71], and the book by Baker and Ryder [72]. A comparison of various temperature sensors is shown in Table 4.3.

For temperature measurements on the emerging extrudate, contacting-type measurements are not suitable because of damage to the extrudate surface. For non-contacting temperature measurements, infrared (IR) detectors can be used. The intensity of the radiation depends on the wavelength and the temperature of a body. Non-contact IR thermometers can be used to determine the temperature of the plastic after it leaves the die. IR sensors can also be used to measure the melt temperature inside the extruder or die; see Section 4.3.3.2.

Table 4.3 Comparison of Various Temperature Sensors

	Thermocouple	RTD	Thermistor
Reproducibility	1–8°C	0.03–0.05°C	0.1–1°C
Stability	1–2 °C in 1 year	<0.1% in 5 years	0.1–3 °C in 1 year
Sensitivity	0.01–0.05 mV/°C	0.2–10 Ohm/°C	100–1000 Ohm/°C
Interchangeability	Good	Excellent	Poor
Temperature range	–250 to 2300°C	–250 to 1000°C	–100 to 280°C
Signal output	0–60 mV	1–6 V	1–3 V
Minimum size	25 µm diameter	3 mm diameter	0.4 mm diameter
Linearity	Excellent	Excellent	Poor
Response time	Good	Fair	Good
Point sensing	Excellent	Fair	Excellent
Area sensing	Poor	Excellent	Poor
Cost	Low	High	Low
Unique features	Greatest economy, wide range, common in extrusion	Greatest accuracy, very stable, less common in extrusion	Greater sensitivity, rarely used in extrusion

IR temperature measurement can give good temperature readings of the extrudate provided the following conditions are met:

1. The radiation from the extrudate must be wholly generated by the extrudate itself as a result of its temperature. Specifically, it must not contain significant levels of transmitted radiation from hot objects behind it and reflected radiation from hot objects in front of it.
2. The stream of radiation from the extrudate to the IR thermometer must be transmitted without absorption by the intervening atmosphere. This means that the IR thermometer must not operate in the spectral regions of atmospheric absorption bands.
3. The correct value for the emittance of the extrudate must be known and correctly introduced into the IR thermometer calibration.

Non-contact IR thermometers are used in a large number of extrusion operations: blown film, cast film, biaxially oriented film, sheet, extrusion coating, etc. In some IR thermometers, an entire surface can be scanned and isotherms can be determined. With additional instrumentation, quantitative information on the temperature distribution can be obtained [5]. Portable infrared thermometers can be used to spot check the process, maintain equipment, and do general plant maintenance; they are also very useful tools in troubleshooting.

Non-contact thermometers offer a number of benefits. The product is never touched or contaminated. Fast moving extruded products can be measured accurately and quickly. Temperature measurements can be made of a large area or a small spot. Many IR sensors have both analog and digital output; this allows temperature data

to be integrated into a closed-loop control system for remote temperature monitoring and analysis. An example of IR temperature sensing in extrusion coating is shown in Fig. 4.12.

In extrusion coating, a molten web from a film die is applied to paper, film, or foil as shown in Fig. 4.12. The distance between the die and the pressure and chill rolls is usually quite short; between 75 and 125 mm. The polymer melt temperature in this region has to be very hot for the melt to adhere to the substrate. A small IR sensor can easily measure the polymer melt temperature in this small space. The operator can monitor and adjust the die heater and the chill roll temperatures either manually or automatically.

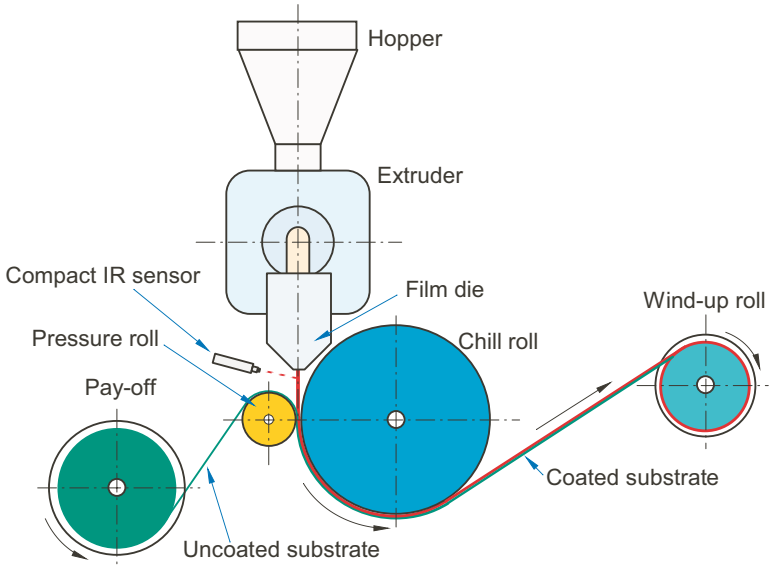


Figure 4.12 IR sensing in extrusion coating

4.3.2 Barrel Temperature Measurement

The barrel temperature needs to be measured to provide information on the axial barrel temperature profile and to provide a signal for the controllers of the barrel heaters and cooling devices. The temperature should be measured as close as possible to the inner barrel surface, since the polymer temperature is the primary concern. The worst possible location of the temperature sensor would be in the barrel heater itself. However, there are some commercial extruders where the temperature sensor is placed in the barrel heater to reduce the thermal lag of the system. The major drawback of this approach is that one controls the heater temperature and not the temperature of the polymer in the extruder barrel. Some extruders are equipped with a combination of deep-well and shallow-well temperature sensors to improve

the temperature control of the extruder [7, 8]. The advantages and disadvantages of deep-well and shallow-well temperature sensors in terms of temperature control are discussed in Section 4.5.2.4, as well as dual sensor temperature control.

In the measurement of barrel temperature, a temperature sensor is pressed into a well in the extruder barrel; the sensor is generally spring-loaded; see Fig. 4.13. Most temperature sensors are constructed with a metallic sheath to obtain sufficient mechanical strength. As a result, significant thermal conduction errors can occur.

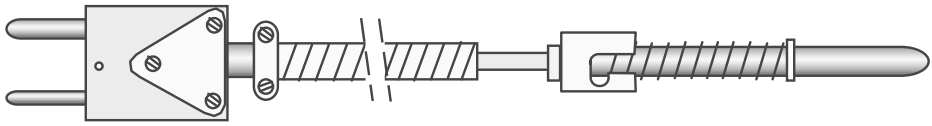


Figure 4.13 Spring-loaded temperature sensor

Figure 4.14 shows how the accuracy of the temperature measurement depends on the depth of the well and the type of temperature sensor [40].

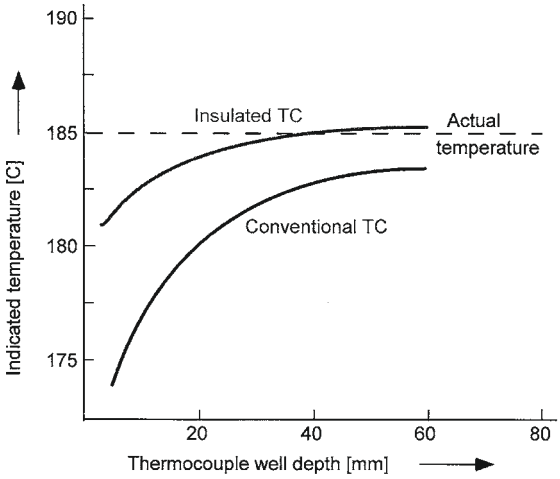


Figure 4.14
Dependence of temperature measurement on the depth of the well. The true barrel temperature is 185°C; the measurements were made in still air

This figure illustrates quite clearly that the depth of the well should be at least 30 mm to minimize the measurement errors. The characteristics of the temperature sensor itself have a strong effect on the accuracy of the measurement. If special precautions have been taken to minimize heat losses along the stem of the temperature sensor, the measurement error can be greatly reduced as compared to standard temperature sensors.

It is important to realize that barrel temperature measurement with a shallow well can be, and most likely will be, inaccurate. With a well depth of 10 mm, the measured temperature will probably be about 10°C below actual temperature. When air drafts occur around the extruder, the measured temperature can be as much as 25°C below the actual temperature. This is shown in Fig. 4.15.

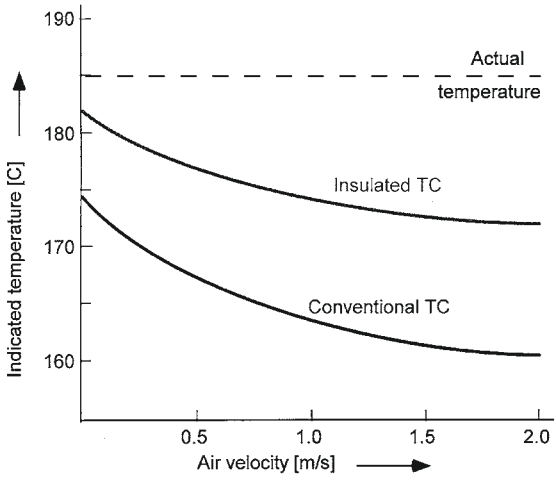


Figure 4.15
The effect of air current on the measured temperature

4.3.3 Stock Temperature Measurement

The measurement of the temperature of the polymer melt is of major importance. Unfortunately, several factors complicate the stock temperature measurement substantially. It is very important to be aware of these complications in order to properly appreciate the measured value.

Measurement of stock temperatures along the extruder barrel is difficult because of the rotation of the screw. To measure stock temperatures, the temperature sensor has to protrude into the polymer. The temperature sensors cannot be placed in the barrel because the protruding sensor would be damaged by the screw flight. One alternative is to place the temperature sensors in the screw channel. However, this is a rather complex operation [9–12]; it requires special thermocouple mountings and sliding contacts. Another alternative is to place the temperature sensors in the barrel and to machine slots in the screw flight at the location of the protruding sensor [13]. The disadvantage of this method is the substantial modification of the flow patterns in the extruder as a result of the slots in the screw flight. This, in turn, will change the actual temperature distribution in the polymer melt.

When considering the stock temperatures along the length of the extruder, it should be realized that the temperature, in most cases, varies much more strongly in the radial direction than in the axial direction. Radial temperature gradients will be particularly high in the plasticating region of the extruder. In this region, a thin melt film, with a melt film thickness in the order of 1 mm, separates the solid bed from the barrel. The temperature difference across this film is often in the range of 30 to 80°C. Thus, the radial temperature gradient will be of the order of 50,000°C per meter. This is about three orders of magnitude higher than the typical axial tem-

perature gradient in an extruder. Therefore, if one would try to measure stock temperature with a protruding temperature sensor, one would experience an extreme sensitivity to radial location of the sensor. The movement of the solid bed is another consideration. Any temperature sensor should avoid contact with the solid bed, since this would likely result in damage of the sensor.

The solids conveying and plasticating zone generally extend about two-thirds of the length of the extruder. This means that stock temperature measurements by immersion probes are really only possible in the last one-third of the extruder. The polymer temperature in the solids conveying and melting zone generally is maximum at or close to the barrel wall, as will be shown in Chapter 7. This means that measurement of barrel temperature is a good indication of the maximum stock temperature. Thus, barrel temperature measurement may be more meaningful, and certainly much easier, than stock temperature measurement with a protruding temperature sensor.

For these reasons, stock temperatures along the extruder are generally not measured on production extruders. Only a few, highly instrumented, development extruders are equipped with stock temperature measurement capability along the barrel. The situation is much simpler at the end of the barrel because there the screw flight is no longer present. The temperature sensor can protrude freely into the melt stream without danger of being damaged by the screw. However, even in this situation, there are several complicating factors involved in the temperature measurement.

Numerous detailed studies have been devoted to the measurement of temperature profiles in polymer melts flowing through channels. One of the most comprehensive studies on the theoretical and experimental aspects of temperature measurement of polymer melts was carried out by van Leeuwen [15–18]. Other studies on melt temperature measurement are listed in the following references [19–23]. When a polymer melt flows through a channel, a certain temperature profile will establish itself in the polymer melt. The temperature profile in a steady-state process after some time will become constant with respect to time; this is the so-called fully developed temperature profile.

The temperature at any point can be predicted from the equations of mass, momentum, and energy. When a temperature sensor, such as a thermocouple, is inserted into the polymer melt stream to measure the temperature of the melt, the steady-state flow is disturbed, and a new steady state will develop after a short time. Therefore, the measured temperature will be different from the true, undisturbed melt temperature. Thus, in order to determine the true melt temperature, certain corrections have to be made to the measured (disturbed) melt temperature. The factors that have to be taken into account are:

- Heat conduction along the probe
- Heat convection from the probe
- Energy dissipation at the probe due to shear heating

The design of the temperature sensor should be such that the above-mentioned errors are minimized. Various designs of temperature sensors for stock temperature measurement are shown in Fig. 4.16.

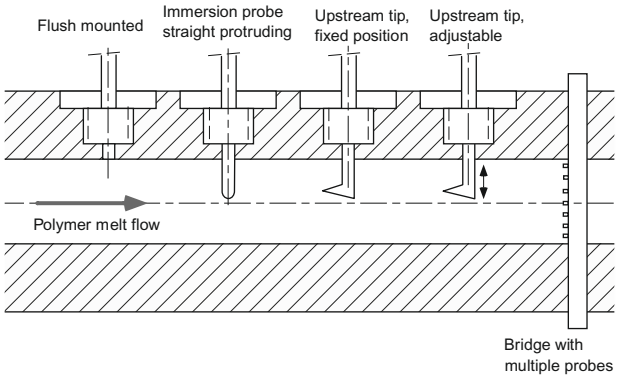


Figure 4.16
Various melt temperature sensor configurations

The flush-mounted temperature sensor does not disturb the flow in the channel. However, the sensor does not protrude into the melt stream. The measured temperature, therefore, will be more representative of the metal wall temperature than the polymer melt temperature. It should be remembered, though, that the temperature of the polymer melt at the wall will equal the metal temperature at the wall. The flush-mounted probe, therefore, will give a reasonably good indication of the temperature of the polymer melt at the interface. The problem with this design is that the maximum temperature of the polymer melt generally does not occur at the wall! Unlike the situation in the solids conveying and melting zone, the maximum temperature of the polymer melt in the melt conveying zone of the extruder (including adaptor and die) generally occurs some distance away from the wall. For this reason, a protruding sensor will yield information that is more meaningful.

The straight immersion sensor is simple and sturdy. It gives a reasonable indication of the stock temperature in the flow channel. This design, however, results in significant errors in the measured temperature because of shear heating and heat conduction along the probe. This is due to the perpendicular location of the probe with respect to the direction of flow. As an improved design, van Leeuwen [15] proposed the upstream probe. The sensor is oriented parallel to the flow, causing only a minimal disturbance to the flow at the point where the temperature is measured. The upstream probe is capable of measuring local temperatures. The parallel portion of the probe should be long and thin to reduce heat conduction errors and to be able to measure rapid changes in temperature. On the other hand, the mechanical strength of the probe should be sufficient to withstand the forces that a melt probe is normally exposed to. Damage can easily occur during start-up or shut-down. To avoid this problem, probes have been made with adjustable depth so that the probe is inserted into the polymer when steady conditions have been reached. At high flow

rates and high polymer melt viscosity, the forces that the polymer melt exerts on the immersion probe can be substantial. For these reasons, the parallel-to-flow portion of the probe is often made into a conical shape or a short, small diameter tube.

The depth adjustment capability has another use besides avoiding damage. It allows the measurement of the temperature profile across the depth of the flow channel using only one probe. Adjustable upstream temperature probes are currently commercially available, e.g., by Goettfert. However, their application in commercial extruders is still rather limited.

The bridge with multiple probes has the advantage of being able to monitor various temperatures at different locations at the same time. This allows a very careful monitoring of the thermal conditions in the polymer melt throughout the material. It is often possible to incorporate temperature probes in spider legs, torpedoes, etc., to obtain information on the polymer temperature away from the outside wall.

In Germany, the VDMA (Verein Deutsche Maschinenbau Anstalten) has issued a publication (VDMA 24485) to standardize evaluation and testing of temperature sensors. In this publication, a test setup is described that allows determination of the thermal conduction error as well as the transient response of the probe. From the transient response, one can determine the delay time, recovery time, and 90% time ($T_{0.9}$). Puetz [4] describes evaluation and comparison of five different temperature probes according to the procedure described in VDMA 24485. The upstream temperature probe proved to be much more accurate than the straight protruding temperature probe with a difference in measured temperature of about 10 to 15°C! Of the five probes, the only one able to determine temperature fluctuations occurring in less than one minute was the upstream probe with a small thin parallel section. The other temperature sensors could only measure temperature fluctuations occurring in more than one or two minutes. This means that conventional thermocouples are not suited to determine high frequency ($t < 1$ minute) extrusion instabilities.

4.3.3.1 Ultrasound Transmission Time

Research at the IKV in Aachen, Germany, has shown that the measurement of ultrasound transmission time (UTT) yields a useful quantity to characterize the thermodynamic condition of the polymer melt [68]. Advantages of the UTT measurement are:

- The transducer does not disturb the polymer melt flow.
- The UTT measurement is a result of linearly integrating measurement across the depth of the flow channel.
- The measurement is not affected by heat conduction errors or viscous heat dissipation.

Commercial applications of UTT measurement started in 1976; however, the method has not found widespread use. An important application in extrusion is the noncontacting temperature measurement of heat-sensitive materials. Protruding temperature sensors can easily cause degradation with such materials. The UTT measurement, pressure compensated, can be used for stock temperature control in a similar fashion as with the conventional melt temperature sensor (see Section 4.6).

The UTT measurement can be used in total extrusion line control. The use of UTT measurement reportedly has resulted in considerable technical improvements in product performance in several extrusion operations [68]. It should be noted, however, that the pressure compensation is rather involved and that the accuracy of the resulting temperature is only as good as the pressure measurement. In this respect, the melt temperature measurement by IR radiation is less complicated (see Section 4.3.1).

4.3.3.2 Infrared Melt Temperature Measurement

IR probes that can be mounted in an extruder barrel or die are commercially available [6]. These probes are used to measure a more or less average stock temperature over a certain depth of the polymer, about 1 to 5 mm for most unfilled polymers. The actual depth of the measurement is determined by the optical properties of the polymer melt, in particular the transmittance. The measurement is affected by variations in the consistency of the polymer melt. Thus, when fillers, additives, or other polymeric components are added, the temperature readings will be affected.

An important advantage of the IR stock temperature measurement is the rapid response time, which is about ten milliseconds. The response of conventional melt thermocouples is several orders of magnitude slower. This means that rapid temperature fluctuations can be made visible with IR allowing a more detailed study of the dynamic behavior of extruders and injection molding machines [83, 84].

The elements of an infrared melt temperature sensor are a sapphire window, an optical fiber, and a radiation sensor with associated signal-conditioning electronics as shown in Fig. 4.17. IR melt temperature probes are commercially available [85, 86] and fit in standard pressure transducer mounting holes. Because the sapphire window is flush with the barrel or die, the sensor does not protrude into the polymer melt. As a result, the sensor is less susceptible to damage, there is no chance of dead spots behind the sensor, and the melt velocities are not altered around the sensor. When melt velocities are changed, the melt temperatures will change as well. Therefore, the melt temperatures measured with an IR sensor are less affected by the actual measurement than with an immersion sensor.

The window material is usually sapphire, because it provides good abrasion resistance and can withstand high pressures. Obviously, there is a potential problem of build-up of material on the window, which could partially block the sensor window.

Calibration can be done using standard sources off-line or in-situ during static preheat using a thermocouple placed in close proximity to the IR probe. The temperature reading for the IR system will be influenced by the emissivity of the polymer melt and the stem heating effects.

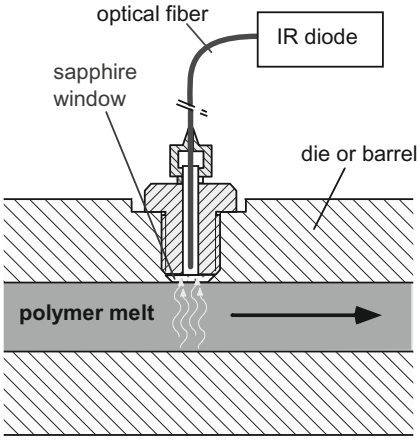


Figure 4.17
An infrared melt temperature sensor

4.4 Other Measurements

Pressure and temperature are two process parameters of major importance. There are, however, various other parameters, which cannot be ignored.

4.4.1 Power Measurement

The basic method to measure electrical power consumed by a load is to connect an ammeter in series with the load and a voltmeter across the load. In a DC circuit, the power is obtained by multiplying current with voltage. The same is true for an AC circuit where only a resistive load is concerned. In this case, the current and voltage are in phase. In an AC circuit, where the load has an inductive or capacitive component, the current and voltage are no longer in phase.

In an AC circuit with an inductive or capacitive component, there are two types of power. One is true or useful power, which is capable of doing useful work, e.g., turning the rotor of a motor. The other power is reactive power that cannot do useful work. Total power, which is known as apparent power, is the vectorial sum of true power and reactive power. The ratio between true power and apparent power is known as the power factor of the circuit.

The power factor, which is always less than 100%, is a function of the phase difference between the current and voltage in a circuit. The apparent power in a circuit can be measured by the basic volt and ammeter method. To distinguish apparent power from true power, apparent power is stated in units of volts-amperes. The true power, which is stated in units of watts, is measured by a wattmeter.

The power consumption of regular AC motors can be measured quite easily by using a readily available wattmeter. The power consumption of SCR-controlled DC motors and variable frequency AC motors is more difficult to measure because of the distorted wave form going into the motor. If a conventional wattmeter is used to measure power consumption of an SCR-controlled DC motor, substantial measurement error will be made, depending on the phase angle. On a DC motor, it is easier to measure the AC power going into the drive before the rectifier circuit. This measurement, of course, will include static losses in the drive and rectifier. Extruders with DC drive often have an armature current readout on the instrument panel. The approximate power consumption Z of the drive can be calculated from the armature current I_a by using the following relationship:

$$Z \approx 0.9 \frac{N_{act}}{N_{max}} I_a V_a \tag{4.4}$$

where N_{act} is the actual rpm, N_{max} the maximum rpm, I_a the armature current, and V_a the armature voltage. This relationship is accurate to approximately 5% and does not reflect the static losses in the drive.

A good method to measure the actual mechanical power consumed in the extrusion process is to measure the torque transmitted through the shank of the extruder screw. The actual power is obtained by multiplying the torque with the screw speed. In fact, this is an excellent method to determine the overall energy efficiency of the extruder drive system. This can be done by comparing the screw power to the total power consumption of the drive. Unfortunately, this type of data is not readily available. The torque can be measured with a torque transducer. Torque transducers generally measure the torsion of the shaft by means of a strain gauge on the shaft; the torque is directly proportional to the angular torsion of the shaft. Unfortunately, accurate torque transducers are quite expensive and, thus, can add significantly to the cost of an extruder.

The power consumption of the barrel and die heaters can be determined by measuring voltage and current to the heater. This works well in current proportioned temperature control. It does not work well with on-off control or time-proportioning temperature control. In the latter case, a wattmeter should be used with a power integrating function. In this case, the integrated power over a certain time period can be measured so that the average power consumption of the barrel heater can be established. Commercial extruders generally do not have sufficient instrumentation

to accurately determine the power consumption of the heaters; in many cases, it cannot be determined at all!

4.4.2 Rotational Speed

The magnetic pickup is a very common method for measuring rotational speed. The basic elements are a metallic-toothed wheel connected to the rotating shaft and a magnetic pickup or coil; see Fig. 4.18.

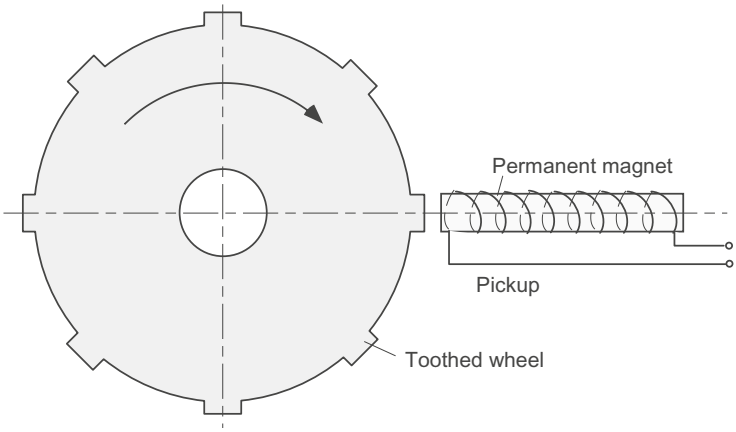


Figure 4.18 Magnetic pickup to measure rotational speed

The teeth of the wheel pass near the pickup coil. The pickup typically consists of a housing containing a small permanent magnet with a coil wound around it. A fixed magnetic field surrounds the pickup. When the teeth of the wheel pass through the field, a voltage pulse is induced in the coil. The frequency of the pulses depends on the number of teeth and the speed of rotation. Since the number of teeth is known, the pulse frequency can be related directly to the rotational speed. The pulses can be measured by a frequency counter or they can be converted to a DC voltage.

Another method for measuring rotational speed is the rotating disk and light sensor. Here, the basic elements are a perforated rotating disk connected to the rotating shaft, a light source, and a light sensor; see Fig. 4.19. A fixed light source is placed on one side of the disk in line with the holes. A light sensor is placed on the opposite side of the disk in line with the light source. When the perforated disk rotates, a pulsed output signal is produced. When the number of holes in the perforated disk is known, the pulse frequency can be converted to rotational speed, as with the magnetic pickup.

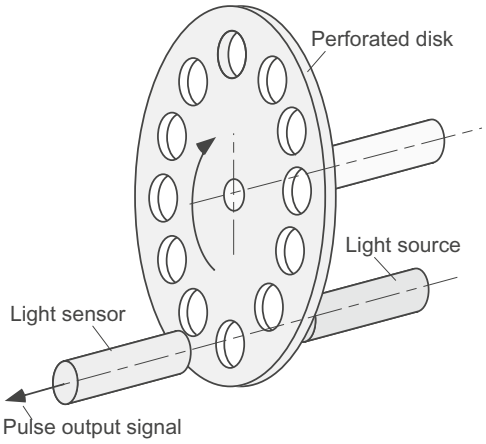


Figure 4.19
Optical speed measurement

Another simple method is to use an electrical tachometer. The small DC generator is coupled to the rotating shaft. The output voltage of the generator is fed to a voltmeter. The generator output voltage is directly proportional to the rotational speed of the shaft. Thus, the measured voltage can be directly converted into rpm.

4.4.3 Extrudate Thickness

A variety of methods are available to measure extrudate thickness. The methods can be broadly classified into contacting and non-contacting techniques. The contacting thickness measurement techniques are generally simple and inexpensive; however, the contact of the transducer with the extrudate can adversely affect the extrudate surface quality. In cases where the requirements for surface quality are very high, non-contacting thickness measurement is generally preferred.

In the contacting measurement techniques, the micrometer caliper is a common instrument. The micrometer, however, can only be used for pot measurements and this is done manually. A spring-loaded dial gauge can be moved over the extrudate if the thickness variations are small. Thus, the dial gauge can be used to monitor the variation of thickness with time, i. e., in the extrusion direction. If an accurate traversing mechanism is constructed, the dial gauge can also measure the thickness variation perpendicular to the extrusion direction. At the point of measurement, the opposite side of the extrudate has to be firmly supported to avoid measurement errors.

The micrometer and dial gauge are simple mechanical devices. In many cases, one would like to have a continuous record of the thickness measurement. The LVDT (linear variable differential transformer) provides an electrical signal that can be used to monitor the thickness on a recorder. The LVDT is a device in which the displacement of an iron core changes the inductive coupling between primary and secondary coils; see Fig. 4.20.

Movement of the core produces an AC output signal that reflects the amount and direction of movement. If an LVDT is used in thickness measurement, one has to check the effect of temperature on the accuracy because the extrudate is generally at an elevated temperature that may not be constant. The LVDT can be quite accurate; it can measure to an accuracy of about 1 μm.

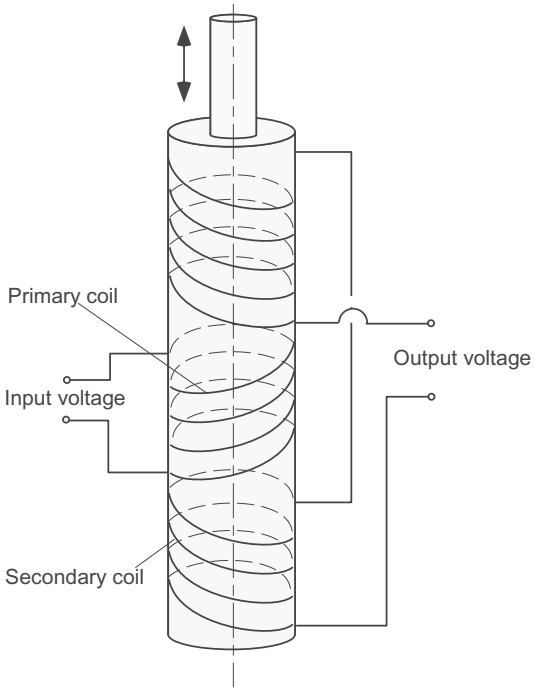


Figure 4.20
Linear variable differential transformer (LVDT)

Another more or less contacting thickness measurement technique is pneumatic gauging. The device consists of a nozzle fixed in position relative to a stop. Air at a constant supply pressure passes through a restriction and discharges through the nozzle; see Fig. 4.21.

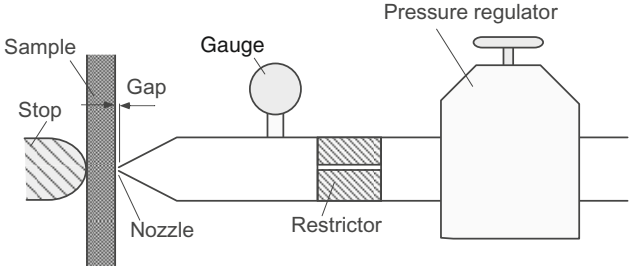


Figure 4.21
Pneumatic thickness gauge

The nozzle back pressure P depends on the gap between the measured surface and the nozzle opening. If the thickness increases, the gap decreases, restricting the discharge of air, thus increasing pressure P. The pressure gauge indicates deviation of the thickness from some normal value. With the proper design, this pressure is directly proportional to the deviation, limited, however, to a range of about 100 micron. The device is very sensitive, up to 0.0001 mm over a range of 0 to 2 mm. It is rugged and, with periodic calibration, quite accurate. The gauge is adaptable to automatic line control where the pressure signal is recorded or used to actuate an alarm when the thickness exceeds a certain threshold value.

Another contacting thickness measurement is the capacitance measurement. Metal plates are placed at either side of the polymer film. Thus, the material and plates form a capacitor, with the polymer acting as a dielectric. Since the capacitance depends on the thickness of the dielectric, the material thickness is determined by measuring the capacitance. The problem in applying this technique to extrusion is that it will be difficult to establish good contact between polymer and metal plates, particularly in continuous monitoring of thickness.

The thickness of a polymer extrudate can also be measured ultrasonically. In this type of measurement, the sensor uses mechanical vibrations of high frequencies, beyond the audio range, i.e. more than about 15,000 vibrations per second. The vibrations are produced by a transducer, which converts the electrical output of an oscillator to ultrasonic vibrations of corresponding frequencies.

There are two kinds of ultrasonic transducers: the magneto-strictive type and the piezoelectric type. The former consists of a metal rod placed in a coil driven by oscillator signals. The alternating magnetic field alternately elongates and compresses the rod. With one end of the rod fixed and the other end connected to a diaphragm, ultrasonic sound waves are produced.

The piezoelectric ultrasonic transducer is more common. When a voltage is applied to a piezoelectric material, it will compress or expand. If the voltage is alternating at ultrasonic frequency, the piezoelectric will compress and expand at the same frequency. The mechanical vibrations can be transferred to a diaphragm to produce ultrasonic sound waves.

For thickness measurement, the transducer is placed against the material. Ultrasonic vibrations pass through the material to the surface and are reflected back to the transducer. The time required for the vibrations to travel through the material depends on the thickness of the material. When resonance occurs, there is a sudden change in the load that the transducer offers the oscillator, producing a corresponding change in oscillator current. By determining the resonant frequency, the thickness of the material can be determined. Obviously, good contact is required between transducer and extrudate. This good contact is difficult to achieve in continuous thickness monitoring of a moving extrudate.

Ultrasonic measurements have also proven useful in the characterization of polymer melts (see Section 4.3.3.1). The ultrasonic transit time ("Laufzeit") is dependent on the elastic properties of the material, pressure, temperature, chemical composition, and structure. It has been found [37] that the ultrasonic transit time is a sensitive measure of the condition of the polymer melt, in particular melt homogeneity. In a process control system, the ultrasonic transit time can provide a more useful feedback control signal than a single melt temperature measurement.

Thus far, the discussion has dealt with contacting thickness measurements. In addition to the fact that there is contact between the sensor and the extrudate, there is another problem in that these methods cannot be applied to continuous thickness monitoring of annular profiles, i.e., tubes and pipes. In automated extrusion lines, non-contacting thickness measurement has become quite popular. Most of the non-contacting thickness measurement techniques are based on a radiation sensor picking up a signal from a radiation source.

Various types of radiation are used: α-rays, β-rays, γ-rays, X-rays, and infrared radiation. A continuous stream of radiation is emitted from a constant radiation source (X-ray tube or radioisotope), passes through the material whose thickness is being measured, and strikes the radiation sensor. As radiation passes through the extrudate, some of the radiation is absorbed and, as a result, the radiation reaching the sensor is less intense. The amount of absorption depends on the material's density and thickness. If the density is constant, the amount of radiation absorption is a direct measure of thickness.

The absorption of radiation is governed by the following relationship:

$$I(x) = I(o) \exp(-\mu x) \tag{4.5}$$

where I(x) is the intensity after transversing a distance x through a material with absorption coefficient μ; I(o) is the incident intensity. After proper calibration, very high accuracies can be achieved, down to 0.2 μm. Measurements can be made at high speeds. These factors have made the radiation type thickness measurement an almost standard tool on automated extrusion lines.

Nuclear radiation sensors cover a thickness range from 10 μm to about 3 mm. Some sensors come with air gap temperature sensors to compensate for changes in density of the air column as the temperature varies across the sheet. These sensors can be designed to automatically correct for dirt build-up and drift. A disadvantage of nuclear radiation is the potential health hazard. Very high standards have to be applied to the design of the measuring device to ensure that all radiation is contained within the instrument. With thick extrudate, relatively high radiation levels are required because of the exponential decay of radiation intensity with distance. Therefore, for relatively thick flat profiles, the LVDT type sensor may be more appropriate. Infrared sensors can be used for clear thin film in the thickness range of 2 to

200 μm. This sensor employs simultaneous valuation of the measurement and reference wavelength.

A problem with radiation sensors is that the measurement is affected by density or compositional variations in the material. This is because most of these sensors measure weight per unit area. Thus, when changes in density occur in the extrudate, the accuracy of the thickness measurement is directly affected. Some sensors have special compensation circuitry to eliminate the sensitivity to compositional changes. These sensors are referred to as "nondiscriminatory," meaning that additives, base resin, and variations in composition are measured equally [73]. Of course, the sensitivity to density variation can be used advantageously to detect flaws in the material, such as voids, contaminants, etc.

γ-rays and high-frequency X-rays have a relatively high penetrating capability and are almost exclusively used for thick parts, several millimeters up to as thick as 40 mm. However, they are also used for thicknesses down to about 100 μm. β-rays have less penetrating capability and are used for relatively thin parts, less than about 3 to 5 mm. Two isotopes are often used, Krypton-85 and Strontium-90. Krypton-85 is used in a measurement range of about 10 to 1000 g/m^2, with a corresponding thickness range of about 5 to 750 μm. Strontium-90 is employed in a measurement range of about 100 to 5000 g/m^2, with a corresponding thickness range of about 100 to 5000 μm [79]. A disadvantage of β-gauges is that they tend to drift and, thus, require frequent recalibration.

γ-ray thickness detectors often employ the "γ-backscattering" technique [80]. This type of measurement offers the advantage that the object is measured from one side, thus allowing simple installation and measurement of relatively complicated shapes. The isotope used is generally Americium-241, which has a half-life of about 450 years as opposed to about 10 years for the isotopes used in X-ray thickness detectors. Another advantage of this technique is that the gauge readings are relatively insensitive to changes in the composition of the material, allowing relatively simple electronics. Low-frequency X-rays (soft X-rays) are also used for thickness measurement of relatively thin products.

4.4.4 Extrudate Surface Conditions

In the extrusion of sheet and film, it is often very important that the surface conditions of the extrudate are maintained within a narrow range. Small irregularities, such as specks, have to be avoided in the more demanding applications, e. g., recording tapes, high-quality transparent sheet, etc. It is very difficult for the human inspector to accurately detect a small dirt sport of 1 mm diameter moving at a speed of 1 to 5 m/s, particularly if the web has a substantial width, more than 2 meters. For these demanding applications, automatic inspection systems are available.

An automatic inspection system uses various transducers that produce electrical signals representative of the surface condition of the web. These signals then have to be analyzed and interpreted. If a signal, or a number of signals, exceeds a preset detection threshold, an alarm is activated, and the area of concern can be further analyzed to determine what corrective action should be taken. Where visible flaws are to be detected, the transducers most commonly chosen are light-sensitive; they produce signals that are parametric measures of such physical phenomena as reflection, transmission, and the like.

Several commercial automatic inspection systems have been developed [24, 25] that utilize a laser scanning system. The web is scanned with a moving light beam from a laser flying spot scanner. The reflected or transmitted beam, which has been modified by the characteristics of the web, is picked up by a light-sensitive detector, a photomultiplier tube. This design allows a very high scan rate (more than 5000 scans per second) and permits 100% coverage of webs as wide as 4 m, moving at speeds of 1 m/s and higher.

The measurement of haze and luminous transmittance of transparent plastics is described in ASTM D1003 (American Society for Testing and Materials). The haze of a specimen is defined as the percentage of transmitted light, which, in passing through the specimen, deviates more than 2.5 degrees from the incident beam by forward scattering. Luminous transmittance is defined as the ratio of transmitted to incident light. The measurement of luminous reflectance, transmittance, and color is described in ASTM E308. The measurement of gloss is described in ASTM D523 and in DIN-Norm 67530 (Deutsche Industrie Norm is a German Industrial Standard).

The quantitative measurement of gloss of extruded sheet is described by Michaeli [26]. In this study, a goniophotometer was used to measure both the gloss height (maximum intensity of the reflected light beam) and the gloss sharpness expressed as the reciprocal width of the gloss distribution curve; the width is measured in degrees.

Quantitative characterization of the texture of extruded film was studied by Nadav and Tadmor [27, 28]. The samples were characterized by measuring light transmission through a film sample. The results were analyzed using the concepts of scale of segregation and intensity of segregation.

In the surface analysis of an extrudate, the irregularities in the size range of μm to mm (10^{-6} to 10^{-3} m) are of primary interest. These irregularities are responsible for the gloss, roughness, and color properties of the surface. Most methods of surface texture determination are based on reflection of light waves [29]. In transparent materials, non-uniformities in the composition of the material can cause significant changes in optical properties. These compositional variations cannot be assessed by the measurement of light reflection; however, by measuring light transmission the

effect of compositional variations can be determined accurately [30]. Compositional variations, such as voids or cracks, can be measured ultrasonically or by using microwaves or X-rays [31, 32]. The measurement with microwaves can be done in a continuous fashion; however, the imperfections have to be rather large (about 1 mm) to be detectable.

Color measurement requires the determination of the spectral distribution of the light reflected from the surface. In continuous color measurement, usually a limited number (e. g., three) of spectral regions are determined by measurement across a filter. Various commercial color-measuring instruments, colorimeters and spectrophotometers, are available today [33], including systems for monitoring continuous webs. These systems automatically provide data on color, opacity, and yellowing at one or several user-selected web locations.

Color measurement can also be tied in with the compound preparation step. The spectrophotometer thus provides a feedback control signal to adjust the level of colorants in order to obtain the desired color automatically [74, 75]. Some of the problems in assessing color and color difference were discussed by Osmer [34]. A good basic text on the principles and theory of color is the book by Billmeyer and Saltzman [76].

The orientation of the polymer molecules in the extrudate has a large effect on the physical properties. At the IKV in Aachen, Germany, a technique was developed to measure the anisotropy of an extrudate in a continuous fashion [35, 36]. The measurement is based on the compensation of the orientation birefringence; the phase difference from the transmission of the light wave through the polymer is reduced to zero by the use of a proper crystal. The birefringence value, thus obtained, has to be divided by the sample thickness to determine the optical phase difference. Therefore, the thickness has to be measured simultaneously. For practical purposes, the degree of anisotropy is often used. This is the actual birefringence divided by the maximum birefringence of the polymer. The degree of anisotropy, therefore, is no longer dependent on the sample thickness.

4.5 Temperature Control

The dynamic behavior of an extruder is significantly determined by the temperature control system on the extruder. It is, therefore, important to understand the basic characteristics of the various temperature control systems. Most control systems are closed-loop or feedback systems. The variable to be controlled is measured and this information is sent to a control unit. From the control unit a signal is sent to an actuator that adjusts the process such that the control variable is as close as possi-

ble to the desired value, the setpoint. Some systems are non-feedback or open-loop systems. These are used when the effect of the input signal on the process can be accurately predicted. This is generally not the case in extrusion and, as a result, feedback control systems are commonly used in extruders.

There are basically two ways to keep the level of a variable within certain limits: the on-off method and the modulating or continuous adjustment method. The on-off control is probably the simplest type of automatic control.

4.5.1 On-Off Control

In on-off control of temperature, the power to the extruder is full-on when the measured temperature is below the setpoint and completely off when the measured temperature is above the setpoint. This situation is shown in Fig. 4.22.

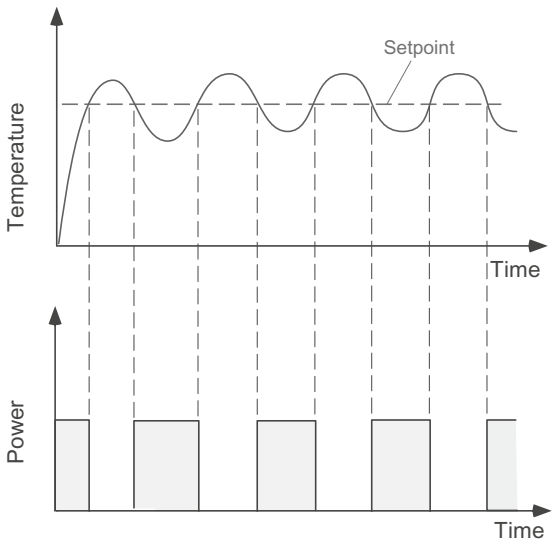


Figure 4.22
On-off temperature control

The temperature in most homes is controlled by thermostats using the on-off principle. On-off control is widely used in the industry to control temperature and other variables. In fact, some missile guidance systems use on-off control, indicating that accurate control in sophisticated systems can be achieved by on-off control. That is, of course, if the system characteristics lend themselves to such type of control.

One of the problems of applying on-off control to the heating and cooling of extruders is the significant thermal lag in these machines. There is an inherent delay between the time the controller calls for heat from the heater band, and the time when the heat actually reaches the sensor. The same holds true when the controller turns off. This thermal lag can be several minutes (about 5 minutes for a 90 mm

extruder); the larger the extruder, the longer the thermal lag will be. Putting the temperature sensor close to the heater (shallow well) reduces this thermal lag, but makes the sensed temperature less representative of the temperature of most importance—the temperature of the polymer inside the barrel.

The temperature resulting from this type of on-off control will be fluctuating around the setpoint. The frequency and amplitude of the temperature fluctuations will be determined by the thermal lag of the particular machine. A problem of on-off control is the possible effect of process disturbances and electrical noise interference, which can cause the output to cycle rapidly as the temperature crosses the setpoint. This condition can be detrimental to most final control elements such as contactors. To prevent this, an on-off differential or hysteresis is added to the controller function. This function requires that the temperature exceed the setpoint by a certain amount (half the differential) before the output will turn on again. Hysteresis will prevent the output from chattering if the peak-to-peak noise is less than the hysteresis. The amount of hysteresis determines the minimum temperature variation possible. However, process characteristics will add to this differential. Figure 4.23 shows a time-temperature diagram for an on-off controller with hysteresis.

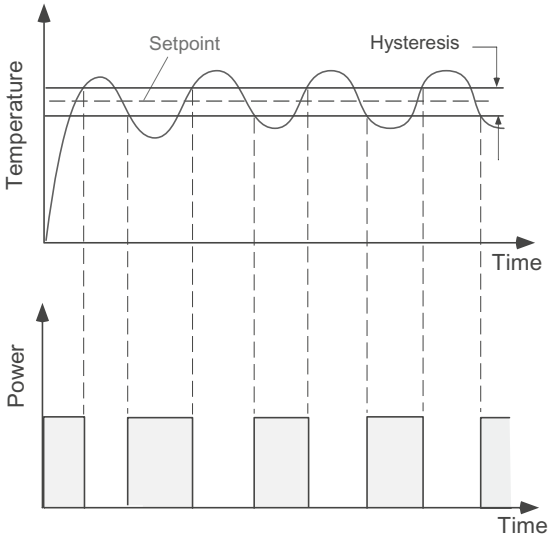


Figure 4.23
Time/power-temperature diagram for on-off control with hysteresis

A different representation of the hysteresis curve is shown in the transfer function of Fig. 4.24.

The transfer function describes the power-temperature relationship of a controller. When the temperature is ascending, the power is turned off when the temperature exceeds T_2; when the temperature is descending, the power is turned on when the temperature drops below T_1.

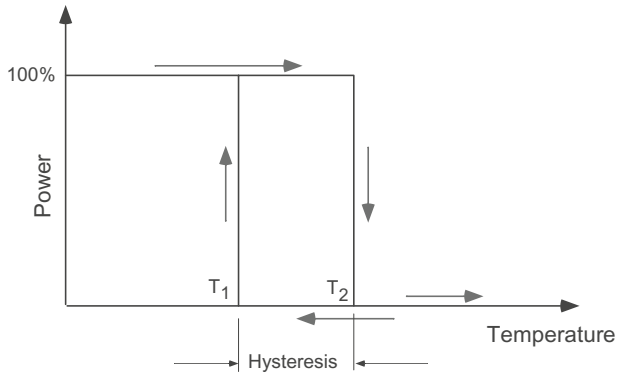


Figure 4.24
Transfer function of an on-off controller

4.5.2 Proportional Control

One of the drawbacks of on-off control is that there are only two power input levels possible: fully on and fully off. In essentially all practical cases, the power level required to maintain a certain temperature will be somewhere between 0 and 100% power. Therefore, application of on-off control will invariably lead to fluctuations of the actual temperature. To avoid this problem, a control system is needed that can adjust the power input level to the exact level required to maintain the temperature at the setpoint. Only then is it possible to maintain a steady temperature.

4.5.2.1 Proportional-Only Control

The proportional controller allows a continuous adjustment of the power input level (from 0 to 100%) depending on the actual temperature. The range of temperature over which the power is adjusted from 0 to 100% is called the proportional band. The proportional band is usually expressed as a percentage of instrument span and is often centered about the setpoint. Thus, in a controller with a 500°C span, a 5% proportional band would be 25 degrees about the setpoint. Sometimes, the setpoint is located at the upper temperature limit of the proportional band.

Figure 4.25 shows the transfer function for a reverse-acting controller.

It is called reverse-acting because the output decreases with increasing temperature. If the temperature is below the lower boundary of the proportional band, T_1, the power to the heaters is on 100%. Above the upper boundary of the proportional band, T_2, the power to the heaters is completely off. Within the proportional band, the power varies proportionally with temperature, from 100% power at T_1 to 0% power at T_2.

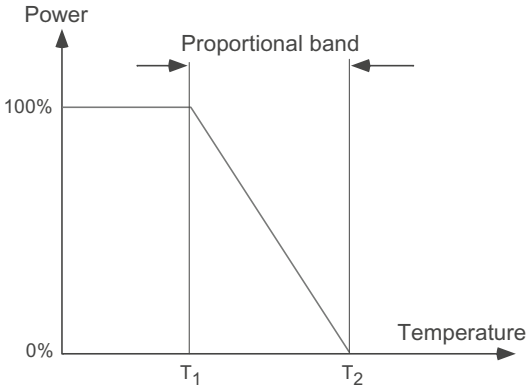


Figure 4.25
Transfer function for a reverse-acting proportional controller

The proportional band in most controllers is adjustable to obtain stable control under different process conditions. A narrower proportional band would result in a steeper transfer function or power-temperature relationship. In the extreme case when the width of the proportional band is reduced to zero, the proportional controller would act simply as an on-off controller. In that case, all the advantages of the proportional control would be lost.

The proportional band is often expressed as percent of span in the plastics industry, but it is also expressed as controller gain in other industries. The proportional band width in percent span and controller gain are related inversely:

$$\text{Gain} = \frac{100\%}{\text{Proportional band in percent span}} \tag{4.6}$$

Thus, reducing the width of the proportional band will increase the gain. A proportional band of 5% corresponds to a gain of 20, a proportional band of 4% corresponds to a gain of 25, etc.

A block diagram of a proportional control system is shown in Fig. 4.26.

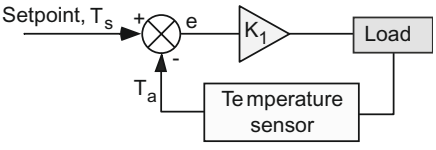


Figure 4.26
Block diagram of a proportional control system

The control system contains a comparator, which compares the actual temperature, T_a (measured by the temperature sensor), with the desired or setpoint temperature, T_s, to provide an error or deviation signal, e. The signal is positive when the process is below setpoint, zero when the process is at setpoint, and negative when the process is above setpoint. The proportional term, K_1, gives an output proportional to the error:

$$\text{Output} = K_1 e \tag{4.7}$$

When the setpoint is centered in the proportional band, the power is 50% when the error signal is zero, i. e., the process is at setpoint.

In a real process, it is rare that the power input required to maintain setpoint temperature is exactly 50% of full power. Therefore, the temperature will increase or decrease, adjusting the power level until an equilibrium condition exists. The temperature difference between the stabilized temperature and the setpoint is called offset or droop. The amount of offset can be reduced by narrowing the proportional band. However, the proportional band can be narrowed only so far before instability occurs. An illustration of a process coming up to temperature with an offset is shown in Fig. 4.27.

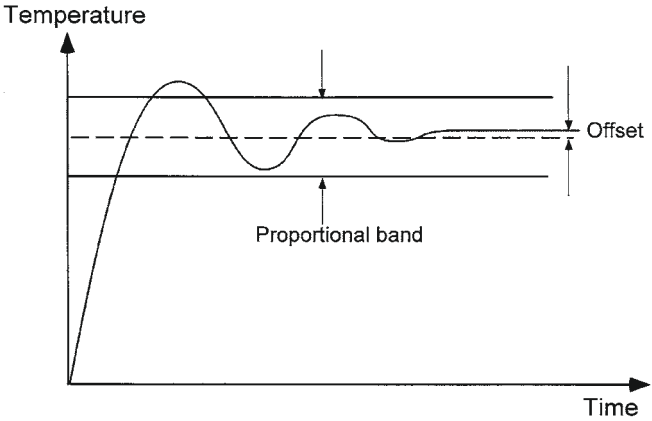


Figure 4.27
Process coming up to temperature with an offset

To understand the mechanism by which offset occurs with a proportional controller, one should look at the controller transfer curve and the process transfer curve at the same time, as in Fig. 4.28.

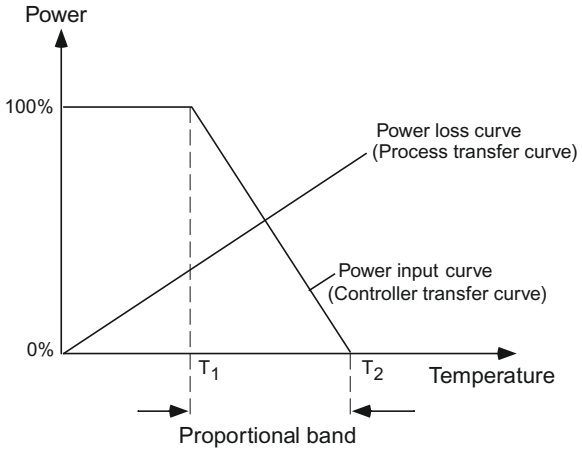


Figure 4.28
Controller transfer curve and process transfer curve

The process transfer curve indicates the power-temperature characteristic of the actual system, i.e., the extruder and its surroundings. This curve indicates how much power is required to maintain a certain temperature level on the machine. The higher the temperature level that needs to be maintained, the more power will be required. For most machines, the relationship between temperature and power requirement will be approximately linear. The power requirement is determined by the heat losses in the system by conduction, convection, and radiation. By improving the thermal insulation of the extruder, the heat losses can be reduced. This will directly affect the process transfer curve; adding insulation will reduce the power requirements at a certain temperature, resulting in a reduced slope of the process transfer curve. Obviously, this will also improve the energy efficiency of the entire process.

Figure 4.28 shows the controller transfer curve (power input curve) superimposed on the process transfer curve (power loss curve). The point where the two curves intersect is the temperature where the input power to the heaters is in equilibrium with the power losses. If the point of intersection occurs above the setpoint, there will be a positive droop; if it occurs below the setpoint, the droop will be negative. From Fig. 4.28 it is now clear how the offset can be eliminated without changing the width of the proportional band. This is done by shifting the entire proportional band to a higher or lower temperature. Figure 4.29 illustrates the effect of resetting the proportional band.

This resetting can be done manually or automatically. With manual reset, a potentiometer is used to electrically shift the proportional band. The amount of shifting has to be done in small increments until the controller power output matches the process power demand as setpoint temperature.

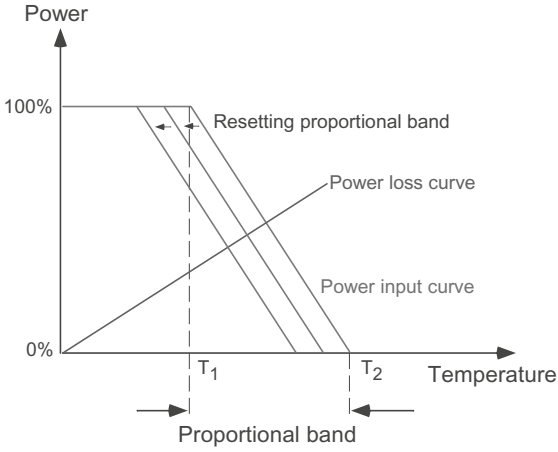


Figure 4.29
Effect of resetting the proportional band

4.5.2.2 Proportional and Integral Control

Automatic reset is done by using an electronic integrator to perform the reset function. The deviation or error is integrated with respect to time, and the result is added to the deviation signal to move the proportional band. The block diagram of proportional control with automatic reset is shown in Fig. 4.30.

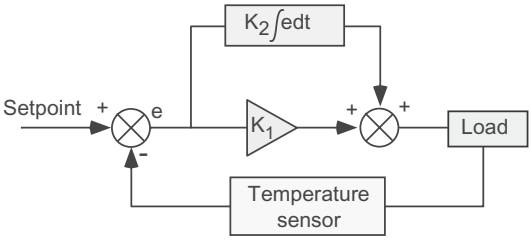


Figure 4.30
Block diagram for PI control system

The output now becomes:

$$\text{Output} = K_1 e + K_2 \int edt \tag{4.8}$$

The K_1 term operates exactly as in a simple proportional controller. The integration term K_2 has to be made long enough so that it will be negligible at the frequencies when the control loop has 180 degrees phase shift. These are the critical frequencies for loop stability. If this is done, the K_2 term will not have an effect on the stability of the loop, but it will accomplish its task, i. e., eliminate the offset.

The integrator keeps adjusting the level of the proportional band until the deviation is zero. When this condition is achieved, the input to the integrator becomes zero and its output stops changing. At this point, the correct amount of reset is held by the integrator. If the process heat requirements should change, a deviation would again occur, which the integrator would integrate, and corrective action would be applied. This corrective action has to be applied rather slowly to avoid oscillations. The automatic reset term can be thought of as a slow gain, as opposed to the proportional term, which can be considered a fast gain.

One problem that can occur in a proportional controller with automatic reset is "reset windup." This occurs when the integrator has acted on the error signal when the temperature is outside the proportional band. The resulting large "woundup" output of the integrator causes the proportional band to move so far that the setpoint is outside the band. The temperature must pass the setpoint before the controller output will change. As the temperature crosses the setpoint, the deviation signal changes sign and the integrator output starts to decrease or unwind. The result can be a large temperature overshoot. This can be prevented by stopping the integrator from acting if the temperature is outside the proportional band. This function is referred to as reset windup inhibit or reset inhibit.

One characteristic of all proportional plus integral (PI) controllers is that the temperature often overshoots the setpoint on start-up. This occurs because the automatic reset begins acting when the temperature reaches the lower boundary of the proportional band. As the temperature reaches the setpoint, the reset action has already moved the proportional band higher, causing excess heat output. As the temperature exceeds the setpoint, the sign of the deviation signal reverses and the integrator brings the proportional band back to the position required to eliminate the offset. This situation is illustrated in Fig. 4.31.

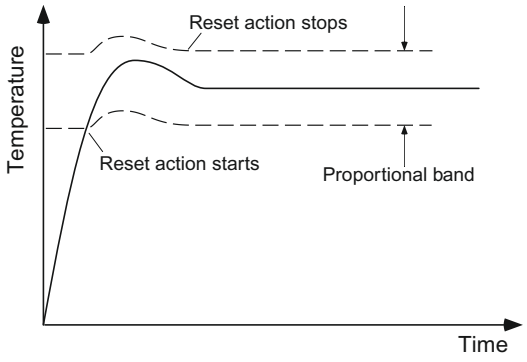


Figure 4.31
Temperature during start-up with PI control

4.5.2.3 Proportional and Integral and Derivative Control

One drawback of the automatic reset is its relatively slow response. The response time can be reduced by addition of a second corrective term, which acts on the rate of change in temperature. A block diagram of a proportional plus integral plus derivative (PID) control system is shown in Fig. 4.32.

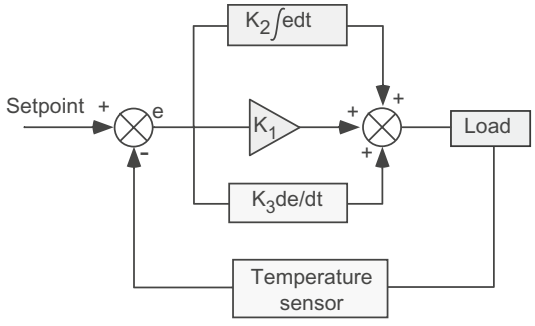


Figure 4.32
Block diagram of PID control system

The second corrective term yields a signal proportional to the rate of change in the error signal. This rate of change is the derivative of the measured temperature with respect to time, thus the term derivative control. The output of the PID control is:

$$\text{Output} = K_1 e + K_2 \int e\,dt + K_3 \frac{de}{dt} \tag{4.9}$$

The derivative control comes into action when a transient occurs. This action is immediate; it does not wait until the error builds up, but it responds directly to the rate of change of the error. Corrective action will be taken in the shortest possible time, and the magnitude of the temperature deviation, caused by an upset, will be greatly reduced.

Derivative control helps to prevent overshooting or undershooting the setpoint. It is an anticipatory function that adjusts the controller output, in advance, to anticipated needs. This reduces the time lag it takes for the controller to respond to a change in the process. Derivative control is more important on machines with a long thermal lag. Therefore, derivative control is important for large extruders. Small extruders, with their inherently shorter thermal lag, may not benefit much from a derivative type of temperature control.

A drawback of the rate control is the fact that it has a destabilizing influence on the control loop. Therefore, it has to be sized carefully to maintain adequate stability in the control loop. In spite of this, the derivative control can generally yield an improvement in response time by a factor of two to four.

4.5.2.4 Dual Sensor Temperature Control

A few commercial temperature control systems are based on dual input from two temperature sensors. One temperature sensor is located in a deep well and measures temperature close to the polymer. The other temperature sensor is located in a shallow well and measures temperature close to the heater/cooler. The dual sensor temperature control can combine the advantages of deep-well-only control and shallow-well-only control, but can largely eliminate the drawbacks of these types of control.

The deep-well-only control is well established and reliable; however, its main drawback is slow response to changes in external conditions, such as changes in ambient temperature, heater line voltage variations, changes in cooling water temperature, etc. On the other hand, the response to changes in internal conditions is quite rapid. Examples are changes in screw speed, viscosity, changes in the polymer, temperature changes in the polymer, etc. The shallow-well-only control has the advantage of being able to respond quickly to changes in external conditions but slowly to changes in internal conditions.

One dual sensor control system uses a weighted average of the signals from the two sensors. By doing this, the advantages of both deep-well and shallow-well can be enjoyed to some extent; however, the same is true about the disadvantages. Another system uses two different temperature control loops. The first one uses only the deep-well sensor and controls the power to the heater. The second loop uses only the shallow-well sensor. This is a cascade loop. It does not control the heaters directly, but acts on the first loop in such a manner as to keep the temperature at the deep

well at the setpoint. Both of these dual sensor temperature control systems have been patented [38, 39].

4.5.3 Controllers

4.5.3.1 Temperature Controllers

There are two types of temperature controllers: analog and digital. An analog controller contains a number of discrete components—resistors, capacitors, integrated circuits, operational amplifiers—and performs its control algorithm through these components. In a digital controller, a microprocessor replaces the discrete components of the analog unit with integrated circuit chip logic. It takes analog input, converts it into a digital signal, and then performs its control algorithm through a stored computer program, which the microprocessor executes.

Microprocessor-based controllers offer great flexibility in that controller function can be changed readily by simply changing a few steps in the program. Thus, the controller function can be modified by changing the software without having to make any modifications to the hardware.

The temperature controller is not capable of handling the high currents required to power the heater bands. For this reason, a power controller is linked between the temperature controller and the heater band. The temperature controller dictates to the power controller how much power to supply to the heaters.

4.5.3.2 Power Controllers

A relatively inexpensive, time-proportioning power controller is the mercury contactor. With this switch, there is no zero-crossing detection, so there will be some noise in the circuit when the contactor is turned on and off.

This problem can be avoided by using a zero-crossover-fired power controller. This is a time-proportioning system controlled by the temperature controller. Being zero-voltage fired, this controller's circuit is free of RF noise. In other words, the switching occurs when no voltage is on the line.

A disadvantage of the contactors is their limited life span; they are usually replaced after one million operations. In a typical operation, contactors are operated once every 20 seconds. This gives a reasonable compromise between temperature ripple and load life. Operation every 20 seconds means 4320 operations per day, or one million operations in about 230 days. One will have to replace the contactor every 230 days. If there are eight controllers per machine, the machine will be down about once a month on the average.

A newer type of power controller is the true proportional power controller—also known as current proportioning controller or phase-angle-fired proportional con-

troller. The term “true proportional” means that the power to the heater is adjusted on a continuous basis. This provides a smooth, stepless output of power. This is particularly useful for extruder dies where rapid and smooth response is very important. True power proportioning is less wearing on the heater bands because it eliminates the on-off cycling.

True proportional control is obtained with solid-state switching of loads through SCRs, triacs, and similar solid-state devices. This allows a reduction of cycle time to the millisecond level. If the cycle time is reduced to one-half the power line period (8.3 ms for 60 Hz), then the proportioning action is referred to as stepless control or phase-fired control. A 50% phase-fired output is shown in Fig. 4.33.

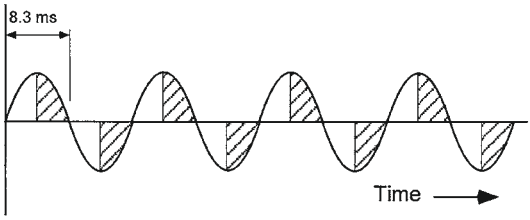


Figure 4.33
A 50% phase-fired output

It is clear that SCR power controllers can also be used for time proportioning power control by increasing the cycle time. However, this type of use does not utilize the inherent advantages of the SCR power controller.

In a true proportional controller, the SCR switches extremely fast—in the order of half a microsecond. This rapid switching causes radio frequency interference (RFI) to be generated on the power lines. This can cause interference with nearby computer and communications equipment. A further problem is that the power drawn from the power lines has a severely distorted wave shape. This can result in extra charges from the power company.

These problems can be avoided by the use of RFI-free or zero-crossing SCR circuitry. A characteristic very much like time proportioning is used, but the power is always turned on and off at the instant when the power line voltage is zero, as shown in Fig. 4.34.

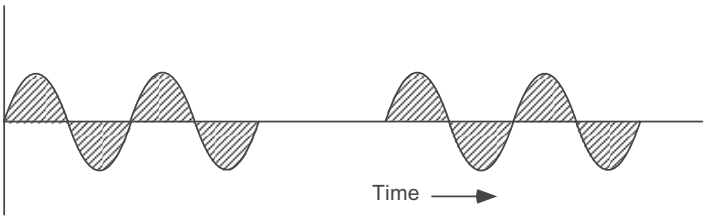


Figure 4.34 RFI-free power proportioning

Another type of power controller is the solid-state relay power controller. This controller is reliable and inexpensive. It is zero-crossover fired, thus it does not generate RFI. However, to use the controller at its rated current level, it must be provided with a good heat sink.

4.5.3.3 Dual Output Controllers

Controlling the temperature of an extruder may require adding heat to the machine by the barrel heaters or taking heat out of the machine by cooling. Since a substantial amount of heat is generated internally in the extrusion process, cooling is often required to maintain the desired process temperature. For this reason, it is important to utilize dual output temperature controllers. These are controllers that control both the heating as well as the cooling process.

Thus, if proportional temperature control is used in heating, then proportional temperature control should also be used in cooling. This would seem to be an obvious requirement. However, a large number of commercial extruders come standard with PID heating control and on/off cooling control. The fact that such extruders are built and the fact that customers buy such extruders illustrates that concern about precise temperature control is not very widespread. Such extruders would only be appropriate if the process is designed such that extruder cooling is not used in normal operations—a situation that is unlikely to occur in actual practice. Dual output controllers, nowadays, are only slightly more expensive than single output controllers. Thus, cost is only a minor consideration.

4.5.4 Time-Temperature Characteristics

Thus far, the discussion has focused on the various types of temperature controllers. However, the real issue is how the actual temperature of the extruder will change as a result of the action of the temperature controller. In order to determine this, one has to consider the thermal characteristics of the actual system, in this case the extruder.

4.5.4.1 Thermal Characteristics of the System

The thermal characteristics of the system determine how the output signal (temperature) varies with changes in input (heat). One of the simplest and most common methods to determine the system characteristics is to measure response of temperature to a step change in heating power; see Fig. 4.35.

This temperature/time curve is often referred to as the process reaction curve or simply the response curve.

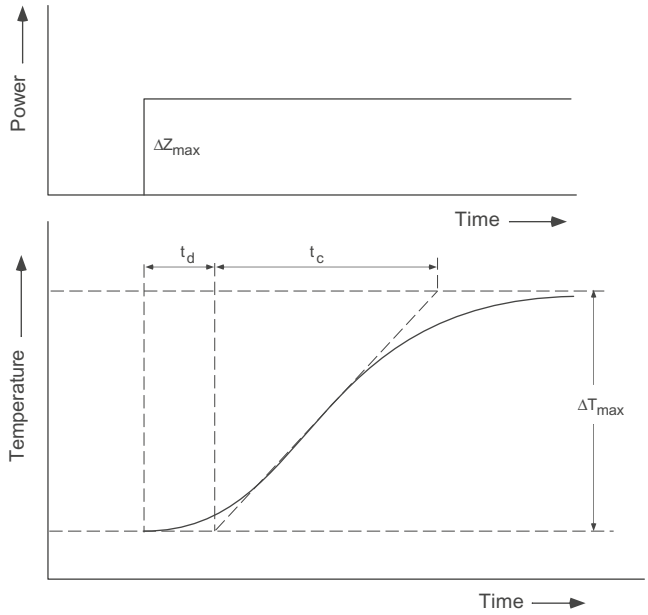


Figure 4.35 Temperature response to step change in heater power

From the response curve, several parameters can be established that are important in understanding the behavior of the system. The dead time (t_d) is the time to the intersection of the maximum temperature gradient. The constant K_s indicates the ratio of maximum temperature rise to the step change in power. ($K_S = \Delta T_{max}/\Delta Z_{max}$) The time constant ($t_c$) is the maximum change in temperature divided by the maximum temperature gradient.

The dead time in extruders can range from about 1 to 5 minutes. This constitutes one of the main problems in temperature control, because this means that the effect of a change in power input level is not felt until after at least 1 minute. This thermal lag time is influenced by the depth of the temperature sensor, the thermal conductivity of the barrel, and the design of the barrel heaters. A typical time constant in an extruder can range from 30 to 120 minutes. This value depends on the heating capacity and the specific heat and mass of the extruder barrel.

Although these parameters do not fully describe the system, they can be used to make approximate predictions of the degree of difficulty in temperature control [41].

$t_d/t_c \leq 0.1$ easy control

$0.1 < t_d/t_c < 0.3$ reasonable control

$t_d/t_c \geq 0.3$ difficult control

4.5.4.2 Modeling of Response in Linear Systems

In a linear control system, the relationship between input y and output x can be described by a differential equation:

$$A_n \frac{d^n x}{dt^n} + A_{n-1} \frac{d^{n-1} x}{dt^{n-1}} + \ldots + A_1 \frac{dx}{dt} + A_0 x = y \tag{4.10}$$

The order of the differential equation determines the order of the control system. Thus, a first order control system is described by:

$$A_1 \frac{dx}{dt} + A_0 x = y \tag{4.11}$$

After a long time ($t \rightarrow \infty$), the following relationship is valid:

$$A_0 x = y \tag{4.12}$$

Thus, a change in input will produce a proportional change in the output. If $t_c = A_1/A_0$ and $K_s = 1/A_0$, Eq. 4.11 can be written as:

$$t_c \frac{dx}{dt} + x = K_s y \tag{4.13}$$

The solution to this differential equation, when the input variable is given a step change of 1, is the well-known exponential relationship of a first order control system.

$$x = K_s \left[1 - \exp\left(-t/t_c\right)\right] \tag{4.14}$$

where t_c is the system time constant and K_s the system gain. Various step response functions are shown in Fig. 4.36. Figure 4.36(a) shows a first order system, Fig. 4.36(b) a higher order system, and Fig. 4.36(c) a first order system with lag time.

In reality, most systems do not behave in a truly linear fashion, but the assumption of linearity can usually be justified over a small region near the operating point (linearization).

If a mathematical description of the system characteristics is not possible, the system parameters have to be determined experimentally. If the step response function is of a higher order than one (see Fig. 4.36[b]), the response can be approximated by a first order response function with lag time.

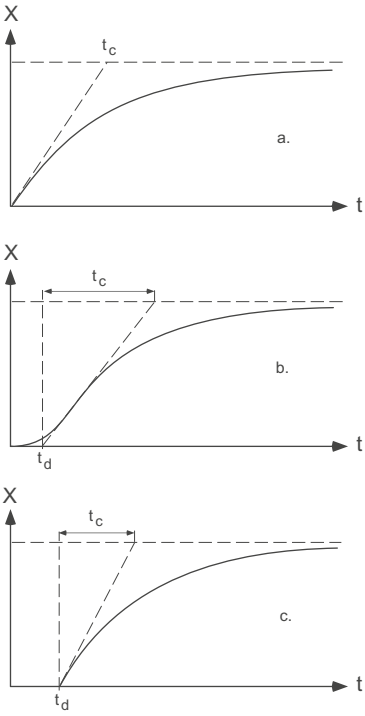


Figure 4.36(a–c)
Various step response functions

If the following control is now considered (see Fig. 4.37):

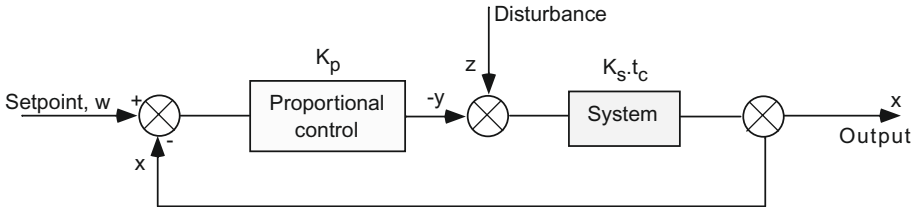


Figure 4.37 First order control system

The response function of the system can be described by:

$$t_c \frac{dx}{dt} + x = K_s (z - y) \tag{4.15}$$

For the controller:

$$y = K_p (x - w) \tag{4.16}$$

If Eqs. 4.15 and 4.16 are combined, the equation for the closed-loop control system is obtained:

$$\frac{t_c}{1+K_sK_p}\frac{dx}{dt} + x = \frac{K_s}{1+K_sK_p}(z+K_pw) \tag{4.17}$$

When the effect of a disturbance (step change) at a constant setpoint is considered (z = 1 and w = 0):

$$\frac{t_c}{1+K_sK_p}\frac{dx}{dt} + x = \frac{K_s}{1+K_sK_p} \tag{4.18}$$

After a very long time ($t \to \infty$), the output will attain the following value:

$$x\ (t \to \infty) = \frac{K_s}{1+K_sK_p} \tag{4.19}$$

The time constant of the closed-loop system is:

$$t^* = \frac{t_c}{1+K_sK_p} \tag{4.20}$$

Thus, one can conclude that the remaining deviation x ($t \to \infty$) reduces with the increased proportionality constant K_p of the controller. The time constant also reduces with increased K_p.

A step change in setpoint (w = 1 and z = 0) is described by:

$$\frac{t_c}{1+K_sK_p}\frac{dx}{dt} + x = \frac{K_sK_p}{1+K_sK_p} \tag{4.21}$$

After a very long time ($t \to \infty$), the output will attain the following value:

$$x\ (t \to \infty) = \frac{K_sK_p}{1+K_sK_p} \tag{4.22}$$

Thus, the change in output increases with the proportionality constant K_p of the controller and the system gain K_s. In this example, it was assumed that there was no dead time in the system. If a dead time is present, then output fluctuations will occur upon changes in input. In this case, the control loop can become unstable, depending on the actual dead time and the proportionality constant of the controller. The effect of changes in setpoint or a disturbance is more difficult to analyze in higher order systems. The controller parameters have to be selected such that the control loop is stable in all cases.

4.5.4.3 Temperature Characteristics with On-Off Control

The approximate time/temperature characteristics of a simple on-off controller are relatively easy to visualize. If a dual output on-off control is considered, then a typical temperature/time curve can be shown as in Fig. 4.38.

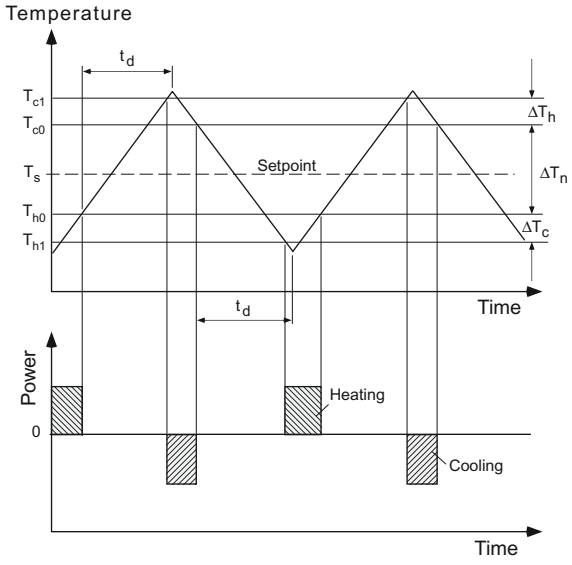


Figure 4.38
Typical temperature/time curve for a dual output on-off control

If the system heats up from ambient temperature, the heating power will be turned off when the temperature reaches:

$$T_{ho} = T_s - \frac{1}{2}\Delta T_n \tag{4.23}$$

where T_s is the symmetrically located setpoint and ΔT_n is the neutral temperature zone in which no heating or cooling takes place, also referred to as a dead band. If there is a dead time t_d in the system, the temperature will continue to rise for this length of time. When the temperature reaches t_{c1}, cooling is turned on. However, if the dead time t_d is long enough, the actual temperature can continue to rise.

$$T_{c1} = T_s + \frac{1}{2}\Delta T_n + \Delta T_h \tag{4.24}$$

where ΔT_h is the hysteresis loop width.

When the dead time has elapsed, the temperature will start to drop. The cooling will be turned off when the temperature drops below T_{co}.

$$T_{co} = T_s + \frac{1}{2}\Delta T_n \tag{4.25}$$

The temperature will continue to drop for a time period of t_d. When the temperature drops below t_{h1}, the heating is turned on again. After another time period of t_d, the temperature will start to increase again. This temperature cycle will repeat itself if the thermal conditions of the process remain the same. The maximum temperature T_{max} is:

$$T_{max} = T_{ho} + t_d v_h \tag{4.26}$$

where v_h is the rate of temperature rise upon heating.

The minimum temperature T_{min} is:

$$T_{min} = T_{co} - t_d v_c \tag{4.27}$$

where v_c is the rate of temperature drop upon cooling.

The maximum temperature swing ΔT_{max} is:

$$\Delta T_{max} = T_{ho} - T_{co} + t_d (v_h + v_c) = \Delta T_n + t_d (v_h + v_c) \tag{4.28}$$

If a typical value of the neutral zone is 10°C, a typical value of the dead time 2 minutes, and the rate of temperature change 6°C/min, then the maximum temperature swing becomes 35°C! This assumes that the rate of temperature change in heating is the same as in cooling ($v_h = v_c$). These values are typical of a dual output on-off controller on an extruder. Because of the resulting large fluctuations in temperature, on-off control is not very desirable if accurate temperature control is required.

If the neutral zone is wide enough, the temperature may not reach the point at which the cooling is turned on. Cooling can be avoided if:

$$v_h t_d < \Delta T_n + \Delta T_h \tag{4.29}$$

This situation is portrayed in Fig. 4.39.

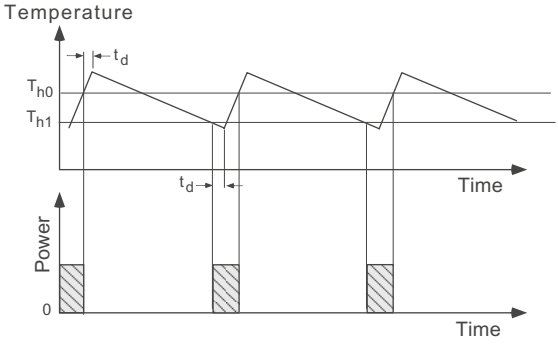


Figure 4.39 Temperature/time curve without cooling

In this case, the maximum temperature swing is:

$$\Delta T_{max} = \Delta T_h + t_d \left(v_h + v_c^{\,1} \right) \tag{4.30}$$

The rate of temperature change upon cooling $v_c^{\,1}$ is much slower in this case because it is passive cooling. In other words, the barrel cooling has not been activated; the temperature drops simply as a result of heat losses in the system. If ΔT_h = 1°C, t_d = 2 min, v_h = 6°C/min, and $v_c^{\,1}$ = 2°C/min, the maximum temperature swing is ΔT_{max} = 17°C. Thus, the amplitude of the temperature fluctuation is cut in half as compared to the first case. However, even a temperature fluctuation of 17°C would still be considered unacceptable in most extrusion operations.

4.5.5 Tuning of the Controller Parameters

4.5.5.1 Performance Criteria

The proper selection, design, or tuning of controllers requires controller criteria that are most appropriate for the particular application. Some response criteria include overshoot, decay ratio, rise time, response time, frequency of oscillation, phase and gain margin error integrals, etc. [42–48]. Three common error integrals are integral of square error (ISE), integral of absolute error (IAE), and integral time and absolute error (ITAE). Some of these criteria are illustrated in Fig. 4.40 showing the response of a control system to a step change in input.

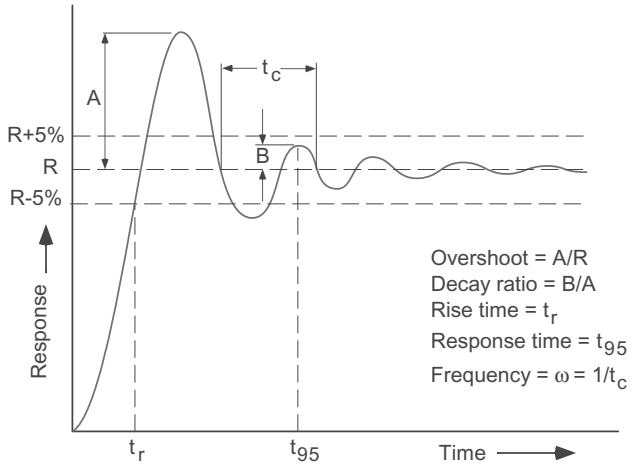


Figure 4.40 Performance criteria from a response curve

4.5.5.2 Effect of PID Parameters

Tuning of a PID controller should ideally lead to values of the P, I, and D terms of the controller that result in the most favorable actual control performance. The P-term is described by the proportional gain K_p or the proportional bandwidth X_p. The effect of changing the proportional band is shown in Fig. 4.41.

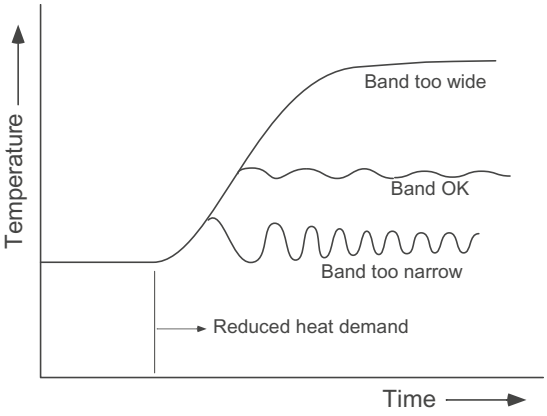


Figure 4.41
Effect of bandwidth setting X_p

A narrow proportional band can result in strong oscillations, while a wide proportional band will result in a large offset, in the absence of reset function. The I-term provides the reset function and is described by the integration time constant t_i or reset time constant. The effect of different values of the reset time constant is shown in Fig. 4.42.

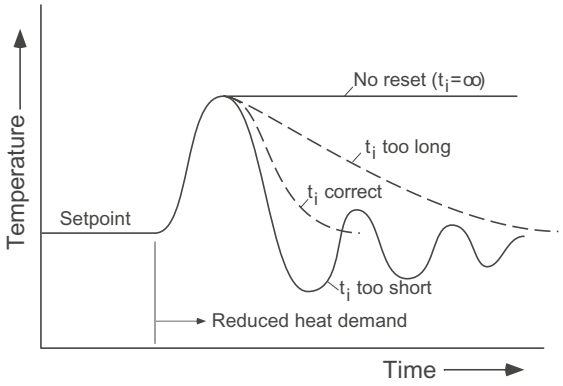


Figure 4.42
Effect of reset time constant, t_i

When the reset time constant is too long, the process will come back to the setpoint very slowly. On the other hand, when the reset time constant is too short, oscillations will occur. The reset time constant is generally considered optimum when the temperature returns to setpoint as rapidly as possible without overshoot.

The derivative term is characterized by the derivative time constant t_d or rate time constant. The effect of different rate time constants is shown in Fig. 4.43.

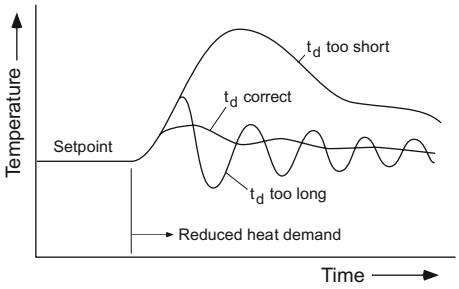


Figure 4.43
Effect of derivative time constant, t_d

When the rate time constant is too long, the temperature changes too rapidly, resulting in overshoot and oscillations.

When the rate time constant is too short, the temperature will return to setpoint too slowly. The correct rate time constant will return the temperature to setpoint with a minimum of oscillations.

4.5.5.3 Tuning Procedure When Process Model Is Unknown

The tuning technique that is applied will depend on whether or not the process model is known. When the process model is not known, the most widely used tuning techniques incorporate the ultimate-period method, the reaction-curve method, and various search methods.

The ultimate-period method, also called Ziegler-Nichols method [42], starts by obtaining dynamic response data. These data are obtained by tuning out the integral and derivative actions of the controller and using only the proportional control mode. The proportional gain is gradually increased until the closed-loop system is forced to cycle continuously at the point of instability. The proportional gain at the point of continuous cycling (ultimate gain) and the period of oscillation (ultimate period) identify the frequency response of the open-loop system at one point. Recommended controller settings are shown in Table 4.4.

Table 4.4 Recommended Controller Settings Based on Ultimate Gain K_u and Ultimate Period t_u

Control	Criterion	Gain	Reset time	Rate time
P	1/4 decay	$0.5K_u$	–	–
PI	1/4 decay	$0.45K_u$	$0.833t_u$	–
PID	1/4 decay	$0.6K_u$	$0.5t_u$	$0.125t_u$
PID	Some overshoot	$0.33K_u$	$0.5t_u$	$0.33t_u$
PID	No overshoot	$0.2K_u$	$0.33t_u$	$0.5t_u$

The reaction-curve method is based on the open-loop response of the process to a step input. This response curve can be used to derive the dynamic characteristics of the process. If the process can be described by a first-order lag and dead time, the controller setting can be calculated.

The controller is placed on manual control and a step change ΔS is applied. With a recorder, note the size of the step change and time of application. The reaction curve should be approximately as shown in Fig. 4.44.

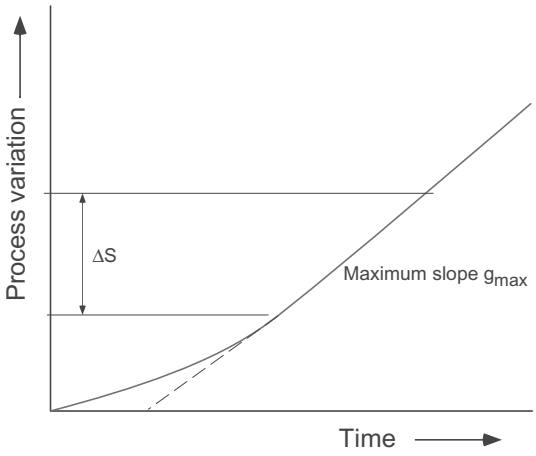


Figure 4.44
Typical reaction curve

Determine the rate of change per unit step change in the manipulated variable, $g_1 = g_{max}/\Delta S$. The recommended controller parameter settings, based on the quarter-decay performance criterion, are shown in Table 4.5.

Table 4.5 Recommended Controller Settings Based on Reaction Curve Process Test

Control	Gain	Reset time	Rate time
P	$1/g_1t_1$	–	–
PI	$0.9/g_1t_1$	$3t_1$	–
PID	$1.2/g_1t_1$ to $2/g_1t_1$	$2.5t_1$ to $2t_1$	$0.5t_1$ to $0.3t_1$

The two previous tuning techniques require a reasonably detailed control-loop analysis. In practice, many controllers are tuned by trial-and-error methods based on process experience. Both the Ziegler-Nichols method and the reaction-curve method are based on the assumption that the disturbances enter the process at one particular point. These methods, therefore, do not always give satisfactory results. In these cases, the final adjustments must be made by trial-and-error search methods.

4.5.5.4 Tuning Procedure When Process Model Is Known

Various techniques are available for the experimental determination of process model. Astron [77] and Eykhoff [78] have given a survey of different identification techniques. The most common technique is to apply a step or impulse perturbation and to evaluate the transfer function from the resulting transient response. A more sophisticated technique is the stochastic identification technique. In this technique,

input variations of a known random form are applied. The similar statistical properties in input and output variables are then correlated, eventually yielding the process transfer function. The transfer function is the ratio of the Laplace transform of the responding variable (output) to the Laplace transform of the disturbing variable (input).

The experimental determination of the process model requires good instrumentation with sufficient dynamic response. Once the transfer function is known, the tuning can be based on Bode plots, Nyquist diagrams, or analytical methods. Bode plots and Nyquist diagrams represent the transient performance characteristics based on the open-loop frequency-response function. The logarithmic or Bode plot shows how the phase angle and the magnitude of the direct-transfer function depend on the frequency. In the polar or Nyquist diagram, the magnitude and phase angle of the direct-transfer function are plotted as a vector with the frequency as a parameter. The normal design criterion for control systems using the frequency-response approach is the specification of the gain margin and the phase margin of the open-loop system. Common criteria are 30 degrees for phase margin and 1.7 to 3 for the gain margin. The tuning or design of the controller is accomplished by adding the controller frequency-response characteristics to the system characteristics to achieve the desired phase and gain margins for the combined system.

Analytical techniques generally involve two areas. The first is the direct solution of the system differential equations in the Aime domain, usually by state variables. The second area is optimization of a specific performance criterion. The criteria for optimization by analytical techniques usually involve minimum response time or an integral time-cost function.

4.5.5.5 Pre-Tuned Temperature Controllers

Several controller manufacturers supply temperature controllers where the parameters are factory-tuned and non-adjustable. The parameter settings are based on long-term experience with temperature controllers in extrusion applications. This is possible because the thermal characteristics of most extruders are rather similar. Advantages of this approach are easier installation and less chance of controller tampering by unqualified personnel.

Controllers with non-adjustable parameters are not well suited to extrusion operations where changes in temperature are very rapid (water cooling, blown film, etc.) or very slow combined with long dead times, as may occur in very large machines. Typical controller settings for pre-tuned controllers are shown in Table 4.6.

In Table 4.6, X_p is the proportional band, t_i the reset (integrating) time constant, and t_d the rate (derivative) time constant.

Table 4.6 Typical Parameters for Pre-Tuned Controllers

Control	Non-adjustable	Adjustable
PD	X_p = 5% t_d = 0.5 min.	X_p = 0–10%
PID	X_p = 8% t_i = 8 min. t_d = 0.5 min.	X_p = 0–10%

4.5.5.6 Self-Tuning Temperature Controllers

Self-tuning temperature controllers are also available in extrusion [49]. They have become commercially available since around 1982. These controllers are microprocessor-based; they are programmed to detect certain process conditions and adjust the controller parameters when necessary. These adjustments are made internally by the controller itself without the help of an operator.

The terminology used to describe these controllers is rather confusing. They are referred to as adaptive-tuning controllers, self-tuning controllers, and automatic-tuning controllers, but these terms mean different things to different suppliers. Clearly, the ability of the controller to re-tune its parameter settings will be only as good as the software. Some controllers tune their parameter settings during start-up, but do not re-tune when operating conditions have been reached. Other controllers tune their parameter settings during start-up, but continue to re-tune—if deemed necessary by the internal software—once operating conditions have been reached. Again, other controllers require a predetermined process disturbance other than start-up, to tune the controller parameters; they may or may not re-tune when operating conditions have been reached.

To properly evaluate the goodness of the self-tuning controller, one would have to know the details of the internal controller software. However, suppliers of self-tuning controllers are not likely to give out such information because the software is the main factor that sets one controller apart from another. Thus, the details of the software will likely be treated as proprietary information. Therefore, the best method to evaluate a self-tuning controller is to install the controller on an extrusion line and closely monitor the actual performance.

■ 4.6 Total Process Control

There is a definite trend in extrusion towards total process control. In a total extrusion control system, temperature measurement and control are tied in with pressure control, thickness gauging, motor load and speed, and possibly other process func-

tions. Between the extremes of simple discrete temperature control and total process control, there are many intermediate levels of controls. Melt temperature control systems have been used for quite some time already. In this type of control, the settings of the first two or three zones closest to the point of melt temperature measurement are continuously adjusted to maintain a constant melt temperature. The temperature settings of the zones are changed automatically by a cascade-type control system. Only low frequency changes in melt temperature can be controlled in this fashion because the response of the barrel temperature zones to changes in setpoint is quite slow.

Melt pressure control systems are also quite common in extrusion. The screw speed is varied continuously in order to maintain a constant pressure. Newer commercial systems incorporate in one microprocessor-based unit combined control of melt temperature, melt pressure, extrudate thickness and/or width, and possibly other process variables. Other control systems are geared towards total plant control. In addition to the regular extrusion control, such a control system can handle upstream raw-material handling, metering of regrind and/or additives, auxiliary extruders in a coextrusion system, drive and temperature control on a gear pump, biaxial orientation in a tenter frame, in-line coating of the extruded web, tension control, corona treating stations, slitting, rewinding, etc.

4.6.1 True Total Extrusion Process Control

Concentrating on the control of the extrusion process, it is clear from the literature [54–68] that true total extrusion process control is quite complicated and has not been fully achieved in practice. Under true total process control, the process is considered a multivariable system and the interaction between the variables is known and fully taken into account in the control scheme. One can therefore assume that many commercial microprocessor-based controllers that control melt temperature, pressure, and extrudate dimensions are most likely built with more or less independent control loops, each controlling only one variable. These controllers more or less consolidate multiple discrete controllers into one convenient package without major changes to the individual control characteristics. This may reduce cost but does not necessarily improve overall control performance.

The first requirement in the development of a true extrusion process control is a dynamic process model. The goodness of the process control will depend very strongly on the accuracy of the process model. However, obtaining a good dynamic process model is quite complicated in practice. The dynamic process model can, in principle, be derived from extrusion theory, and various attempts in that direction have indeed been made [50–54]. As will be discussed in Chapter 7, extrusion theory to date has not been developed to a point that the entire process can be predicted

with a sufficient degree of accuracy. Also, the theoretical prediction of extruder performance requires a substantial amount of computation. Thus, following the phenomenological approach, to derive a dynamic process model from extrusion theory is likely to be quite complex, relatively inaccurate, and requires much computation. However, it is possible that a simplified theoretical model in combination with experimental data could yield an accurate dynamic process model.

Most work on the development of dynamic process models has been empirical; this work is usually referred to as process identification. As mentioned earlier, two classes of empirical identification techniques are available: one uses deterministic (step, pulse, etc.) functions, the other stochastic (random) identification functions. With either technique, the process is perturbed and the resulting variations of the response are measured. The relationship between the perturbing variable and the response is expressed as a transfer function. This function is the process model. Empirical identification of process models by the deterministic method has been reported by various workers [55–58]. A drawback of this method is the difficulty in obtaining a measurable response while restricting the process to a linear response (small perturbation). If the perturbation is large, the process response will be nonlinear and the representations of the process with a linear process model will be inaccurate.

Stochastic identification techniques, in principle, provide a more reliable method of determining the process transfer function. Most workers have used the Box and Jenkins [59] time-series analysis techniques to develop dynamic models. An introduction to these methods is given by Davies [60]. In stochastic identification, a low amplitude sequence (usually a pseudorandom binary sequence, PRBS) is used to perturb the setting of the manipulated variable. The sequence generally has an implementation period smaller than the process response time. By evaluating the auto- and cross-correlations of the input series and the corresponding output data, a quantitative model can be constructed. The parameters of the model can be determined by using a least squares analysis on the input and output sequences. Because this identification technique can handle many more parameters than simple first-order plus dead-time models, the process and its related noise can be modeled more accurately.

Identification of the noise and its probable causes usually leads to the most effective method of removing these disturbances.

The time series method also contains the means for determining the goodness of the model fit by examining the cross- and auto-correlations between the residual and the input sequence. From Box and Jenkins's models, a minimum variance control strategy can be determined, resulting in a minimum deviation of the controlled variable. Tuning procedures can also be accurately determined from the model. The structure and initial parameters for self-tuning regulators can be determined from the minimum variance controller.

A drawback of the stochastic identification technique is its complexity and the substantial computational requirements. Only a limited number of investigators have applied this technique to the extrusion process. Parnaby et al. [61–63] did the first work on stochastic identification of extrusion process models. A hierarchical automatic optimal control scheme was developed and evaluated on a laboratory extrusion line [63]. The only operator input required was the desired output rate and die inlet melt temperature. A variable die restriction was used to adjust diehead pressure and throughput. Considerable improvements in control were obtained, particularly in the control of diehead pressure. Other applications of stochastic identification to extrusion have been made by Patterson et al. [64, 65], Costin [66, 67], and at the IKV in Aachen [81].

References

1. H. Recker et al., Plastverarbeiter, 28, 1, 1–8 (1977)
2. J.D. Lenk, "Handbook of Controls and Instrumentation," Prentice-Hall Inc. (1980)
3. D.B. Hoffman and N. Sarasohn, Plastics Design and Process, July, 20–23 (1972)
4. H. Puetz in "Messen und Regeln beim Extrudieren," VDI-Verlag GmbH, Duesseldorf (1982)
5. K.H. School in "Der Extruder als Plastifiziereinheit," VDI-Verlag GmbH, Duesseldorf (1977)
6. A. Galskoy and K.K. Wang, Plastics Engineering, Nov., 42–45 (1978)
7. H.E. Harris, Plastic Technology, Feb., 22–29 (1982)
8. S.H. Walton, The Wire Association International (1977)
9. H. Janeschitz-Kriegl, Proc 7th Int'l Congress on Rheology, Brown Univ., Providence, RI (1963)
10. H. Janeschitz-Kriegl and J. Schijf, Plastics & Polymers, 37, Dec., 523–527 (1969)
11. D.I. Marshall, I. Klein, and R.H. Uhl, Soc. Plastics Engrs. J., 20, 329 (1964)
12. L.P.B.M. Janssen, G.H. Noomen, and J.M. Smith, Plastics & Polymers, 43, Aug., 135–140 (1975)
13. N. Wheeler, Techn. Papers ANTEC, Pittsburgh, PA, Jan. (1962)
14. H.L. Trietly, EDN, 28, 2, 93–96 (1983)
15. J. van Leeuwen, M. Goren, A.A. Grimbergen, and J.C. Molijn, Plastica, 17, 6, 269–277 (1969)
16. J. van Leeuwen, M. Goren, A.A. Grimbergen, and J.C. Molijn, Plastica, 17, 7, 319–326 (1969)
17. J. van Leeuwen, M. Goren, A.A. Grimbergen, and J.C. Molijn, Plastica, 17, 8, 371–386 (1969)
18. J. van Leeuwen, Polym. Eng. Sci., 7, 98–109 (1967)
19. W. Schlaeffer, J. Schijf, and H. Janeschitz-Kriegl, Plastics & Polymers, 39, June, 193–199 (1971)

20. M. Hulatt and W.L. Wilkinson, Plastics and Rubber Processing, March, 15–18 (1977)
21. H.J. Kim and E.A. Collins, Polym. Eng. Sci., 11, 83 (1971)
22. E.A. Collins and F.E. Filisko, AICHE J., 16, 399 (1970)
23. H.T. Kim and J.P. Darby, SPE J., 26, 31–36 (1970)
24. F. T. Farrace, "Standardization of an Automatic Inspection System," Nondestructive Testing Standards—A Review, ASTM STP 624, Harold Berger (Ed.), American Society for Testing and Materials, 231–245 (1977)
25. H. Droscha, Kunststoffe, 72, 5, 257–259 (1982)
26. W. Michaeli, "Zur Analyse der Flachfolien und Tafelextrusions-Prozesse," Ph. D. Thesis IKV, TH Aachen (1975)
27. N. Nadav, M.Sc. Thesis, Technion, Israel Institute of Technology
28. N. Nadav and Z. Tadmor, Chem. Eng. Sci., 28, 2115–2126 (1973)
29. H. Recker et al., Plastverarbeiter 28, 1, 1–8 (1977) and 28, 3 137–142 (1977)
30. F.L. Binsberger, J. Polym. Sci. 11, 10, 1915–1929 (1967)
31. H. Hermann, Kunststoffe, 61, 11, 839–842 (1971)
32. G. Wittig, Material Pruefung, 16, 10, 327 (1974)
33. N.N., Plastics Technology, 28, 11, 18 (1982)
34. D. Osmer, Plastics Compounding, Jan/Feb., 14–24 (1983)
35. H. Hensel, "Die Orientierungsdoppelbrechung," Ph.D. thesis IKV, TM Aachen (1975)
36. G. Menges, et al., Plastverarbeiter, 24, 2, 73–77 (1973)
37. P. Fischer, Plastverarbeiter, 29, 5, 231–243 (1978)
38. U.S. Patent 3,866,669
39. U.S. Patent 4,272,466
40. H. Goermar and H. Puetz, Kunststoffe, 69, 9, 588–590 (1979)
41. H. Recker, "Messen und Regeln beim Extrudieren," VDI-Verlag GmbH, Duesseldorf, (1982), p. 46
42. J.G. Ziegler and N.B. Nichols, Trans. ASME, 64, 11, 759 (1942)
43. K.L. Chien, J.A. Hrones, and S.B. Resweck, Trans. ASME, 74, 175 (1952)
44. E. Pester and E. Kollman, Elektrische Ausruestung, 3–8 and 45–52 (1960)
45. J.A. Miller, A.M. Lopez, C.L. Smith and P.W. Murrill, Control Engineering, 14, 12, 72 (1967)
46. P.D. Roberts, Measurement and Control, 9, 227, June (1976)
47. C.L. Smith, Instruments & Control Systems, 43–46, Sept. (1976)
48. R.F. Bayless, Plastics Engineering, 24, 3, 59–72, March (1978)
49. R. Chostner, Plastics Technology, 68–70, Feb. (1983)
50. R.B. Kirby, SPE Journal, 18, 1273 (1962)
51. W.L. Krueger, SPE Journal, 18, 1282 (1962)
52. D.H. Reber, R.E. Lynn Jr., and E.J. Freech, Polym. Eng. Sci., 13, 346 (1973)

53. Z. Tadmor, S.D. Lipshitz, and R. Lavie, Polym. Eng. Sci., 14, 112 (1974)
54. N. Brauner, R. Lavie, and Z. Tadmor, Int. IFAC Conference on Instrumentation and Automation in the Paper, Rubber, and Plastics Ind., 3rd Proc., Brussels, 6, 353 (1978)
55. N.R. Schott, Ph.D. Dissertation, Univ. of Arizona (1971)
56. W. Fontaine, Ph.D. Dissertation, Ohio State Univ. (1975)
57. S. Dormeier, SPE ANTEC Tech. Papers, 25, 216 (1979)
58. D. Fingerle, J. Elastomers Plast., 10, 293 (1978)
59. G.E.P. Box and G.M. Jenkins, "Time Series Analysis Forecasting and Control," Revised Edition, Holden-Day, San Francisco, CA (1976)
60. W.D.T. Davies, "System Identification for Self-Adaptive Control," Wiley-Interscience, NY (1970)
61. J. Parnaby, A.K. Kochhar, and B. Woods, Polym. Eng. Sci., 15, 594 (1975)
62. A.K. Kochhar and J. Parnaby, Automatica, 13, 177 (1977)
63. A.K. Kochhar and J. Parnaby, Int. Mech. Eng. (Lond.), Proc., 192, 299 (1978)
64. G.A. Hassan and J. Parnaby, Polym. Eng. Sci., 21, 276 (1981)
65. I. Patterson, P. Brandin, and J. Parin, SPE ANTEC Tech. Papers, 25, 166 (1979)
66. M.H. Costin, M.Sc. Thesis, McMaster University, Hamilton, Canada (1981)
67. M.H. Costin, P.A. Taylor, and J.D. Wright, Polymer Eng. Sci., 22, 393 (1982)
68. H.G. Wiegand, "Prozessautomatisierung beim Extrudieren und Spritzgiessen von Kunststoffen," Carl Hanser Verlag (1979)
69. D.D. Pollock, "The Theory and Properties of Thermocouple Elements," ASTM publication STP 492
70. "Manual on the Use of Thermocouples in Temperature Measurements," ASTM publications STP 470 B
71. "Thermocouple Reference Tables," NBS Monograph 125.
72. H.D. Baker, E.A. Ryder, and N.H. Baker, "Temperature Measurement in Engineering," Vol. I and II, Omega Press
73. E.L. Sarber, Plastics Technology, 50–55, June (1983)
74. N.N., Plastics Compounding, 21–32, March/April (1980)
75. E. Galli, Plastics Compounding, 18–26, March/April (1983)
76. F.W. Billmeyer and M. Saltzman, "Principles of Color Technology," John Wiley & Sons (1966)
77. K.J. Astrom, "An Introduction to Stochastic Control Theory," Academic Press, NY (1970)
78. P. Eykhoff, "System Identification," Wiley-Interscience (1974)
79. H. Marchand, Plast. Techn., Feb., 67–70 (1984)
80. A. Kirkland, Plast. Techn., Feb., 97–99 (1981)
81. 12. Kunststofftechnisches Kolloquium, IKV Aachen, Germany 176–185 (1984)
82. W. Michaeli, U. Langkamp, B. Schäfer, and J. Kraack, Kunststoffe, 85, 1912–1914 (1995)

83. W. Obendrauf, C. Kukla, and G. R. Langecker, Kunststoffe, 83, 971–974 (1993)
84. T. Nietsch, P. Cassagneu, and A. Michel, International Polymer Processing, XII, 4, 307–315 (1997)
85. J. Coughlin, Modern Plastics, April, 101–105 (1992)
86. X. Shen, R. Malloy, and J. Pacini, SPE ANTEC Technical Papers, 918–926 (1992)

PART II

Process Analysis

5 Fundamental Principles

Before going into a detailed process analysis of extrusion, it may be useful to review the basic principles that will be applied in analysis. One can think of the basic principles as the tools used in the process analysis. This chapter is meant to be a review, not an exhaustive dissertation on the subject. For more in-depth and detailed information, the reader is referred to general texts, such as the one by Bird et al. [1] and others [2–4].

5.1 Balance Equations

In extrusion, as well as in many other processes, one deals with the transport of mass, momentum, and energy. Balance equations are used to describe the transport of these quantities. They are universal physical laws that apply to all media (solids and fluids). Matter is considered as a continuum. Thus, the volume over which the balance equation is formulated must be large enough to avoid discontinuities.

5.1.1 The Mass Balance Equation

The mass balance equation, also referred to as the equation of continuity, is simply a formulation of the principles of the conservation of mass. The principle states that the rate of mass accumulation in a control volume equals the mass flow rate into the control volume minus the mass flow rate out of the control volume. In Cartesian coordinates (x, y, z), the mass balance equation for a pure fluid can be written as:

$$\frac{\partial \rho}{\partial t} + \frac{\partial}{\partial x}(\rho v_x) + \frac{\partial}{\partial y}(\rho v_y) + \frac{\partial}{\partial z}(\rho v_z) = 0 \tag{5.1}$$

If a steady-state process is analyzed, the first term of Eq. 5.1 (the time derivation of density) will equal zero; the same is true for Eq. 5.2. The mass balance equation expressed in cylindrical coordinates (r, θ, z) is:

$$\frac{\partial \rho}{\partial t}+\frac{1}{r}\frac{\partial}{\partial r}(\rho r v_r)+\frac{1}{r}\frac{\partial}{\partial \theta}(\rho v_\theta)+\frac{\partial}{\partial z}(\rho v_z)=0 \tag{5.2}$$

If the fluid is considered incompressible, the density terms (ρ) disappear in Eqs. 5.1 and 5.2. In one-dimensional steady state flow problems (velocity components in only one direction), the mass balance equation is automatically satisfied and does not enter into the calculations. In two-dimensional flow problems (no velocity component in the third coordinate direction), the mass balance is satisfied by the introduction of a stream function [1].

5.1.2 The Momentum Balance Equation

The momentum of a body is the product of its mass and velocity. Since velocity is a vector, momentum is also a vector. The momentum balance equation describes the conservation of momentum; it is also referred to as the equation of motion.

Momentum can be transported by convection and conduction. Convection of momentum is due to the bulk flow of the fluid across the surface; associated with it is a momentum flux. Conduction of momentum is due to intermolecular forces on each side of the surface. The momentum flux associated with conductive momentum transport is the stress tensor. The general momentum balance equation is also referred to as Cauchy's equation. The Navier-Stokes equations are a special case of the general equation of motion for which the density and viscosity are constant. The well-known Euler equation is again a special case of the general equation of motion; it applies to flow systems in which the viscous effects are negligible.

In polymer flow systems, the inertia and body forces are generally negligible. For these systems, the momentum balance equation in Cartesian coordinates can be written as:

$$\frac{\partial P}{\partial x}=\frac{\partial \tau_{xx}}{\partial x}+\frac{\partial \tau_{xy}}{\partial y}+\frac{\partial \tau_{xz}}{\partial z} \tag{5.3a}$$

$$\frac{\partial P}{\partial y}=\frac{\partial \tau_{yx}}{\partial x}+\frac{\partial \tau_{yy}}{\partial y}+\frac{\partial \tau_{yz}}{\partial z} \tag{5.3b}$$

$$\frac{\partial P}{\partial z}=\frac{\partial \tau_{zx}}{\partial x}+\frac{\partial \tau_{zy}}{\partial y}+\frac{\partial \tau_{zz}}{\partial z} \tag{5.3c}$$

or in cylindrical coordinates:

$$\frac{\partial P}{\partial r} = \frac{1}{r}\frac{\partial}{\partial r}(r\tau_{rr}) + \frac{1}{r}\frac{\partial \tau_{r\theta}}{\partial \theta} - \frac{\tau_{\theta\theta}}{r} + \frac{\partial \tau_{rz}}{\partial z} \tag{5.4a}$$

$$\frac{1}{r}\frac{\partial P}{\partial \theta} = \frac{1}{r^2}\frac{\partial}{\partial r}(r^2\tau_{r\theta}) + \frac{1}{r}\frac{\partial \tau_{\theta\theta}}{\partial \theta} + \frac{\partial \tau_{\theta z}}{\partial z} \tag{5.4b}$$

$$\frac{\partial P}{\partial z} = \frac{1}{r}\frac{\partial}{\partial r}(r\tau_{rz}) + \frac{1}{r}\frac{\partial \tau_{\theta z}}{\partial \theta} + \frac{\partial \tau_{zz}}{\partial z} \tag{5.4c}$$

The analysis of many flow problems can be simplified by considering only one component of the equation of motion, the one in the direction of flow. Further simplifying assumptions are often necessary in order to solve the problem. In the analysis of isothermal processes, only two balance equations are needed, the mass and momentum balance. In order to solve the problem, additional information is required. This is information on how the fluid deforms under application of various stresses. This information is described by the constitutive equation of the fluid; see also Section 6.2 on melt flow properties.

An example of the use of momentum balance in pipe flow of a Newtonian fluid is given in Appendix 5.1.

5.1.3 The Energy Balance Equation

The energy balance equation states that the rate of increase in specific internal (thermal) energy in a control volume equals the rate of energy addition by conduction plus the rate of energy dissipation. The principle of energy conservation is also described by the first law of thermodynamics; see Section 5.2. If a constant density is assumed, the energy equation can be written as:

$$\dot{E}_{acc} + \dot{E}_{conv} = \dot{E}_{cond} + \dot{E}_{diss} \tag{5.5}$$

where

$$\dot{E}_{acc} = \rho C_v \frac{\partial T}{\partial t} \tag{5.5a}$$

$$\dot{E}_{conv} = \rho C_v \left(v_x \frac{\partial T}{\partial x} + v_y \frac{\partial T}{\partial y} + v_z \frac{\partial T}{\partial z} \right) \tag{5.5b}$$

$$\dot{E}_{cond} = \frac{\partial}{\partial x}\left(k\frac{\partial T}{\partial x}\right) + \frac{\partial}{\partial y}\left(k\frac{\partial T}{\partial y}\right) + \frac{\partial}{\partial z}\left(k\frac{\partial T}{\partial z}\right) \tag{5.5c}$$

$$\dot{E}_{diss} = \tau_{xx}\frac{\partial v_x}{\partial x} + \tau_{yy}\frac{\partial v_y}{\partial y} + \tau_{zz}\frac{\partial v_z}{\partial z} + \tau_{xy}\left(\frac{\partial v_x}{\partial y} + \frac{\partial v_y}{\partial x}\right) + \tau_{xz}\left(\frac{\partial v_x}{\partial z} + \frac{\partial v_z}{\partial x}\right) + \tau_{yz}\left(\frac{\partial v_y}{\partial z} + \frac{\partial v_z}{\partial y}\right) \tag{5.5d}$$

$\dot{E}_{acc}$ is the accumulation term, $\dot{E}_{conv}$ the convection term, $\dot{E}_{cond}$ the conduction term, and $\dot{E}_{diss}$ the dissipation term. Equation 5.5(c) is an expression of Fourier's law of heat transfer; see also Section 5.3.1. In cylindrical coordinates, only the convection, conduction, and dissipation terms change:

$$\dot{E}_{conv} = \rho C_v\left(v_r\frac{\partial T}{\partial r} + \frac{v_\theta}{r}\frac{\partial T}{\partial \theta} + v_z\frac{\partial T}{\partial z}\right) \tag{5.6a}$$

$$\dot{E}_{cond} = \frac{1}{r}\frac{\partial}{\partial r}\left(kr\frac{\partial T}{\partial r}\right) + \frac{1}{r}\frac{\partial}{\partial \theta}\left(k\frac{1}{r}\frac{\partial T}{\partial \theta}\right) + \frac{\partial}{\partial z}\left(k\frac{\partial T}{\partial z}\right) \tag{5.6b}$$

$$\dot{E}_{diss} = \tau_{rr}\frac{\partial v_r}{\partial r} + \tau_{\theta\theta}\frac{1}{r}\left(\frac{\partial v_\theta}{\partial \theta} + v_r\right) + \tau_{zz}\frac{\partial v_z}{\partial z} + \tau_{r\theta}\left(r\frac{\partial}{\partial r}\frac{v_\theta}{r} + \frac{1}{r}\frac{\partial v_r}{\partial \theta}\right) + \tau_{rz}\left(\frac{\partial v_z}{\partial r} + \frac{\partial v_r}{\partial z}\right) + \tau_{\theta z}\left(\frac{1}{r}\frac{\partial v_z}{\partial \theta} + \frac{\partial v_\theta}{\partial z}\right) \tag{5.6c}$$

The energy equation has to be used to analyze non-isothermal processes. In these situations, there are generally four unknown variables: velocity, stress, pressure, and temperature. In order to solve such a non-isothermal problem, one more equation is needed in addition to the three balance equations. The missing relationship is the constitutive equation of the fluid; this relationship basically describes the relationship between stress and deformation. In polymer extrusion, the material undergoes large changes in temperatures as it is transported along the extruder. Consequently, the energy equation is used extensively in the analysis of the extrusion process.

5.2 Basic Thermodynamics

Thermodynamics is concerned with energy, the exchange and transportation of energy in a system. The first law of thermodynamics is a statement of the principle of conservation of energy. For a closed (constant mass) system, the first law of thermodynamics is expressed by:

$$\Delta E = Q - W \tag{5.7}$$

where ΔE is the total energy change of the system, Q is heat added to the system, and W is work done by the system. The total energy change ΔE can be split up into several terms, each representing the change in energy of a particular form:

$$\Delta E = \Delta E_k + \Delta E_p + \Delta U \tag{5.8}$$

where ΔE_k is the change in kinetic energy, ΔE_p is the change in gravitational potential energy, and ΔU is the change in internal energy. By definition, the kinetic energy is:

$$E_k = \frac{mv^2}{2} \tag{5.9}$$

where m is mass and v is velocity.

The gravitational potential energy is:

$$E_p = mza_g \tag{5.10}$$

where z is the elevation above a reference level and a_g the local acceleration of gravity. These energy functions are common to both mechanics and thermodynamics.

The internal energy function U, however, is peculiar to thermodynamics. It represents the kinetic and potential energies of the molecules, atoms, and subatomic particles that make up the system on a microscopic scale. There is no known way to determine absolute values of U. Fortunately, only changes of ΔU are needed and these can be derived experimentally. When the state of the system is fixed, the internal energy U is fixed. If Eq. 5.8 is used in Eq. 5.7, the first law of thermodynamics can be written as:

$$\Delta E_k + \Delta E_p + \Delta U = Q - W \tag{5.11}$$

If the sum of the kinetic and potential energies of the system does not change, this equation becomes

$$\Delta U = Q - W \tag{5.12}$$

or in differential form:

$$dU = \delta Q - \delta W \tag{5.13}$$

If, in addition, the process is adiabatic (Q = 0), Eq. 5.12 becomes

$$\Delta U = - W \tag{5.14}$$

Note that in Eq. 5.13 the differential signs on Q and W are written δ, whereas the differential sign of U is d. There is a fundamental difference between a property like U and the quantities Q and W. A property like U always has a value dependent only on the state. A process that changes the state of a system changes U. Thus, dU represents an infinitesimal change in U, and integration gives a difference between two values of the property:

$$\int_{U_1}^{U_2} dU = U_2 - U_1 = \Delta U \tag{5.14a}$$

On the other hand, Q and W are not properties of the system and depend on the path of the process. Thus δ is used to denote an infinitesimal quantity. Integration gives a finite quantity and not a difference between the two values:

$$\int \delta Q = Q \quad \text{and} \quad \int \delta W = W \tag{5.14b}$$

Thus, integration of Eq. 5.13 yields Eq. 5.12.

Special thermodynamic functions are defined as a matter of convenience. The simplest such function is the enthalpy H, explicitly defined for any system by the mathematical expression:

$$H = U + PV \tag{5.15}$$

where P is pressure and V is volume.

The enthalpy has units of energy and is a system property like U, P, and V. Whenever a differential change occurs in a system, its properties change by:

$$dH = dU + d(PV) \tag{5.16}$$

The amount of heat in a closed PVT system that must be added to accomplish a given change of state depends on how the process is carried out. Only for a reversible process where the path is fully specified is it possible to relate the heat to a property of the system. On this basis, the specific heat at a constant volume can be defined:

$$C_v = \left(\frac{\delta Q}{dT}\right)_v \tag{5.17}$$

It represents the amount of heat required to increase the temperature by dT when the system is held at a constant volume. C_v is a property of the system; this follows from Eq. 5.12. For a constant volume, reversible process $dU = \delta Q$, because no work can be done without volume changes. Thus, the specific heat at a constant volume can be related to the internal energy by:

$$C_v = \left(\frac{\partial U}{\partial T}\right)_v \tag{5.18}$$

Thus, for a constant volume process

$$dU = \delta Q = C_v dT \tag{5.19}$$

Equation 5.19 is a useful relationship. If specific heat and temperature changes are known, then the amount of heat required to accomplish this change in temperature can be determined. If the amount of heat and the specific heat are known, then the resulting change in temperature can be calculated. This relationship is indispensable in the analysis of the extrusion process. For instance, if the amount of viscous heat generation in a certain amount of polymer is known, then the resulting adiabatic temperature rise can be determined if the specific heat of the polymer is known.

The specific heat at constant pressure is defined as:

$$C_p = \left(\frac{\delta Q}{dT}\right)_P \tag{5.20}$$

It represents the amount of heat required to increase the temperature by dT when the system is heated in a reversible process at a constant pressure. Using Eqs. 5.13 and 5.16 it can be shown that:

$$C_p = \left(\frac{\partial H}{\partial T}\right)_P \tag{5.21}$$

Thus, C_p is also a property of the system. Further

$$dH = \delta Q = C_p dT \tag{5.22}$$

In polymer melts, the material is generally considered to be incompressible; in this case $C_v = C_p$. The actual relationship between C_v and C_p is given by Eq. 6.94.

Entropy is an intrinsic property of a system. For a reversible process, changes in entropy are given by:

$$dS = \frac{\delta Q}{T} \tag{5.23}$$

The second law of thermodynamics states that the entropy change of any system and its surroundings, considered together, is positive and approaches zero for any process, which approaches reversibility. The mathematical expression of the second law is simply:

$$\int_1^2 \frac{\delta Q}{T} \leq S_2 - S_1 \tag{5.24}$$

The left term is the entropy transfer, $\delta Q/T$; it forms a direct link with the heat transfer (δQ) if the temperature at the system boundary is T. Entropy transfer as a concept makes the distinction between heat transfer and work transfer as parallel forms of energy transfer. Only the transfer of energy as heat is accompanied by entropy transfer. The work transfer interaction is not accompanied by entropy transfer. The term on the right of the inequality sign is the entropy change; it is a thermodynamic property. The inequality sign in Eq. 5.24 expresses the essence of the second law of thermodynamics. The change from state 1 to state 2 can occur over various paths. The difference between possible paths is described by the strength of the inequality sign. The entropy generation expresses this difference quantitatively:

$$S_{gen} = S_2 - S_1 - \int_1^2 \frac{\delta Q}{T} \geq 0 \tag{5.25}$$

Thus, a thermodynamic process is accompanied by entropy generation. When $S_{gen} > 0$, the process is considered irreversible; when $S_{gen} = 0$, the process is considered reversible. It should be noted that the entropy generation S_{gen} is, of course, path dependent and, therefore, not a thermodynamic property as opposed to the entropy change S_2–S_1. In fluid flow the volumetric rate of entropy generation is:

$$\dot{S}_{gen} = \frac{1}{T}\left[\frac{\partial}{\partial x}\left(k\frac{\partial T}{\partial x}\right) + \frac{\partial}{\partial y}\left(k\frac{\partial T}{\partial y}\right) + \frac{\partial}{\partial z}\left(k\frac{\partial T}{\partial z}\right)\right] + \tag{5.26}$$

$$+ \frac{1}{T}\left[\tau_{xx}\frac{\partial v_x}{\partial x} + \tau_{yy}\frac{\partial v_y}{\partial y} + \tau_{zz}\frac{\partial v_z}{\partial z}\right] +$$

$$+ \frac{1}{T}\left[\tau_{xy}\left(\frac{\partial v_x}{\partial y} + \frac{\partial v_y}{\partial x}\right) + \tau_{xz}\left(\frac{\partial v_x}{\partial z} + \frac{\partial v_z}{\partial x}\right) + \tau_{yz}\left(\frac{\partial v_y}{\partial z} + \frac{\partial v_z}{\partial y}\right)\right]$$

The first bracketed (square) term is the conductive energy flux, which is the same as used in the energy Eq. 5.5(c). The other bracketed terms represent the dissipative energy flux, as used also in the energy Eq. 5.5(d). Thus, the volumetric rate of entropy generation can be written as:

$$\dot{S}_{gen} = \frac{1}{T}\left(\dot{E}_{cond} + \dot{E}_{diss}\right) \tag{5.27}$$

5.2.1 Rubber Elasticity

The theory of rubber elasticity is largely based on thermodynamic considerations. It will be briefly discussed as an example of how thermodynamics can be applied in polymer science. For more detailed information the reader is referred to the various textbooks [10–13]. It is assumed that there is a three-dimensional network of chains, that the chain units are flexible and that individual chain segments rotate freely, that no volume change occurs upon deformation, and that the process is reversible (i. e., true elastic behavior). Another usual assumption is that the internal energy U of the system does not change with deformation. For this system the first law of thermodynamics can be written as:

$$dU = TdS - \delta W \tag{5.28}$$

If the equilibrium tensile force is F and the displacement dl then the work done by the system is:

$$\delta W = PdV - Fdl \tag{5.29}$$

The change in U with respect to l at a constant temperature and volume is:

$$\left(\frac{\partial U}{\partial l}\right)_{T,V} = T\left(\frac{\partial S}{\partial l}\right)_{T,V} + F \tag{5.30}$$

Thus, the equilibrium tensile force F is determined by the change in internal energy with deformation and the change in entropy with deformation. An ideal rubber is defined as a material for which the change in internal energy with deformation equals zero. Thus, the only contribution to the force F is from the entropy term:

$$F = -T\left(\frac{\partial S}{\partial l}\right)_{T,V} \tag{5.31}$$

When a rubber is deformed, its entropy S changes. The long chains tend to adopt a most probable configuration; this is a highly coiled configuration. When the material is stretched, the chains uncoil, resulting in a less probable chain configuration. When the force is removed, the system wants to return to the more probable coiled-

up state. Thus, the entropy of the system increases. The basic problem in the theory of rubber elasticity is a statistical mechanical problem of determining the change in entropy in going from an undeformed state to a deformed state. The extension ratio α is defined as:

$$\alpha = \frac{l}{l_o} = \frac{l_o + \Delta l}{l_o} = 1 + \varepsilon \tag{5.32}$$

where l_o is the original length, Δl the increase in length, and ε the elongational strain.

If a cube of unit length dimension is considered, the force will equal the stress σ. Equation 5.31 can now be written as:

$$\sigma = -T\left(\frac{\partial S}{\partial \alpha}\right)_{T,V} \tag{5.33}$$

The most probable state of a system is the state that has the greatest number of ways, Y, of being realized. The entropy S is related to this number of complexions Y by the Boltzmann relation:

$$S = C_B \ln Y \tag{5.34}$$

where C_B is the Boltzmann constant (1.38E–23 J/°K).

The change in entropy upon extension can be expressed as:

$$\Delta S = -\frac{1}{2} N C_B \left(\alpha^2 + \frac{2}{\alpha} - 3\right) \tag{5.35}$$

where N is the number of freely orienting chain segments. Substituting this expression into Eq. 5.33 yields the stress-extension ratio relationship:

$$\sigma = N C_B T \left(\alpha - \frac{1}{\alpha^2}\right) \tag{5.36}$$

The number of chains per unit volume can be related to the density ρ and the average molecular weight between crosslinks M_c:

$$N = \frac{\rho N_A}{M_c} \tag{5.37}$$

where N_A is Avogadro's number (6.025E23 mol^{-1}).

Considering that $N_A C_B$ is the gas constant R (8.314 J/mol °K), Eq. 5.36 can be written as:

$$\sigma = \frac{\rho RT}{M_c}\left(\alpha - \frac{1}{\alpha^2}\right) \tag{5.38}$$

The elastic modulus can be determined by:

$$E = \frac{d\sigma}{d\varepsilon} = \frac{d\sigma}{d\alpha} = \frac{\rho RT}{M_c}(1 + 2\alpha^{-3}) = \frac{\rho RT}{M_c}\left[1 + 2(1+\varepsilon)^{-3}\right] \tag{5.39}$$

For small extensional strains the elastic modulus becomes:

$$E = \frac{3\rho RT}{M_c} \tag{5.40}$$

For a linear and isotropic material the shear modulus G is related to the extensional modulus by:

$$G = \frac{2}{2(1+\nu)} \tag{5.41}$$

where ν is Poisson's ratio; $\nu = ½$ for ideal rubbers.

Thus, the shear modulus can be obtained from:

$$G = \frac{\rho RT}{M_c} \tag{5.42}$$

5.2.2 Strain-Induced Crystallization

It has been observed that the crystallization behavior of polymers is modified when the material is strained. This behavior has been found in rubbers and in thermoplastics [14]. In thermoplastics, the effect of strain on crystallization behavior has been studied quite extensively in solutions, in melt, and in solid state. For instance, it has been found that flowing polymer melts can crystallize at temperatures that are substantially above the crystallization temperature of the same material in a quiescent state. This strain-induced crystallization is generally explained in terms of thermodynamic processes. During a phase change, the Gibbs free energy is:

$$\Delta G = \Delta H - T\Delta S \tag{5.43}$$

where S is the conformational entropy.

For an equilibrium process $\Delta G = 0$. This would be the case for crystallization or melting at the melting point. The melting point T_m, therefore, is:

$$T_m = \frac{\Delta H}{\Delta S} \tag{5.44}$$

When the polymer is being deformed, the molecules are oriented to some extent and this reduces the conformational entropy. If the material is considered to be entropy-elastic, the energy expended in the deformation of the polymer will reduce the entropy but not affect the internal energy. This point was discussed in some detail by Astarita [15]. Thus, if the enthalpy is unaffected by orientation and the entropy reduced, the melting point will increase with increasing orientation. This melting point elevation will increase the degree of super-cooling, the driving force of crystallization. The anisotropy of the oriented polymer favors crystallization in the direction of orientation and discourages it orthogonally. This explains the change in crystal growth mechanism from the three-dimensional (spherulitic) to the unidimensional (fibrillar) growth.

5.3 Heat Transfer

Heat transfer takes place by three mechanisms: conduction, convection, and radiation. In conductive heat transfer, the heat flows from regions of high temperature to regions of low temperature. The transfer takes place due to motion at the molecular level. Matter must be present in order for conduction to occur. The material itself does not need to be in motion for conduction to take place; in fact, many times the conducting medium will be stationary. In a solid material, the only mode of heat transfer is conduction [16]. In convection, heat transfer is due to the bulk motion of the fluid. Convective heat transfer only occurs in fluids. In radiation, heat or radiant energy is transferred in the form of electromagnetic waves.

5.3.1 Conductive Heat Transfer

The most important relationship in conductive heat transfer is Fourier's law; for conduction in the x direction:

$$\dot{Q}_x = -k_x A_x \frac{\partial T}{\partial x} \tag{5.45}$$

where $\dot{Q}_x$ is the heat flow (rate of conduction), k_x the thermal conductivity, A_x the area normal to heat flow, and T temperature.

For conduction in the y and z directions, Fourier's law is simply:

$$\dot{Q}_y = -k_y A_y \frac{\partial T}{\partial y} \tag{5.46}$$

and

$$\dot{Q}_z = -k_z A_z \frac{\partial T}{\partial z} \tag{5.47}$$

Fourier's law states that the heat will flow from high to low temperatures. The heat flow is proportional to the thermal conductivity, the temperature gradient, and the cross-sectional area normal to heat flow. Thus, in order to calculate the heat flow, one has to know the thermal conductivity of the material and the temperature distribution within the material. The temperature distribution has to be determined by solving the energy equation (Eq. 5.5) as discussed in Section 5.1.3.

5.3.2 Convective Heat Transfer

Convective heat transfer is considerably more difficult to analyze than conductive heat transfer in a stationary material. This is simply due to the fact that more terms have to be carried in the energy equation (Eq. 5.5) that has to be solved in order to find the temperature distribution. Many practical problems encountered in polymer processing are described by equations that do not allow simple analytical solutions. In many cases, therefore, one has to use numerical techniques to obtain solutions to the problem.

5.3.3 Dimensionless Numbers

It is quite common in process engineering to describe certain phenomena by relating dimensionless combinations of physical variables. These combinations are referred to as dimensionless groups or dimensionless numbers. This approach offers a number of advantages. One is assured that the equations are dimensionally homogeneous. By using dimensionless numbers, the number of variables describing the problem can be reduced. One can predict the effect of a change in a certain variable even if the problem cannot be completely solved. If the dimensionless numbers describing the problem remain the same, then the solution to the problem will remain unchanged, even if individual variables are varied. The latter characteristic is very useful in scale-up problems; see also Section 8.8.

5.3.3.1 Dimensional Analysis

Dimensionless numbers can be derived by making the appropriate balance equations dimensionless when the problem can be fully described. (See the example on heat transfer in Newtonian fluid between two plates later in this section.) Dimensionless numbers can also be derived from dimensional analysis; this approach is

used if the problem cannot be completely described mathematically. An example of dimensional analysis is the determination of the force F that a sphere of diameter D encounters in a fluid with viscosity η when the relative velocity between sphere and fluid is v. From physical arguments, it can be deduced that F has to be a function of diameter, velocity, fluid density, and viscosity:

$$F = F(D, v, \rho, \eta) \tag{5.48}$$

Even though the actual form of the equation is not known, the equation has to be dimensionally homogeneous. This is also true if the force is written in the following form:

$$F = CD^a v^b \rho^c \eta^d \tag{5.49}$$

The dimensions of the these variables can be expressed in length L, time t, and mass M; thus, F(L t^{-2} M), D(L), v(Lt^{-1}), ρ(L^{-3} M), and η($L^{-1}t^{-1}$ M). The requirement for dimensional homogeneity yields:

$$L = L^a L^b L^{-3c} L^{-d} \tag{5.50a}$$

$$t^{-2} = t^0 t^{-b} t^0 t^{-d} \tag{5.50b}$$

$$M = M^0 M^0 M^c M^d \tag{5.50c}$$

From the three Eqs. 5.50(a) to 5.50(c), three of the unknowns (a, b, c, and d) can be expressed as a function of the fourth. If a, b, and c are expressed as a function of d, this yields:

$$a = 2 - d \tag{5.51a}$$

$$b = 2 - d \tag{5.51b}$$

$$c = 1 - d \tag{5.51c}$$

With this relationship, Eq. 5.49 can be rewritten as:

$$\frac{F}{\rho v^2 D^2} = C\left(\frac{\eta}{\rho v D}\right)^d \tag{5.52}$$

The original number of variables has now been reduced from 5 to 2 dimensionless numbers. The dimensionless number on the right-hand side of Eq. 5.52 is the well-known Reynolds number:

$$N_{Re} = \frac{\rho v D}{\eta} \tag{5.53}$$

The Reynolds number represents the ratio of inertia forces (ρvD) to viscous forces (η). In the flow of a fluid through a flow channel, turbulent flow will occur when the Reynolds number is above the critical Reynolds number, which is about 2100. Below the critical Reynolds number, laminar flow takes place; this is also referred to as streamline flow or viscous flow. In polymer processing, the polymer melt viscosity is generally very high. As a result, the Reynolds number in polymer processing is very small, typically 10^{-3}. Therefore, in polymer processing, the process melt flow is always laminar. The low Reynolds number generally allows one to neglect the effect of inertia and body force, as was done in the formulation of the momentum balance equation, Eq. 5.3.

5.3.3.2 Important Dimensionless Numbers

Several important dimensionless numbers in combined heat and momentum transfer in fluids can be derived by considering the simple flow of a Newtonian fluid between two flat plates, one stationary and one moving at velocity, v; see Fig. 5.1.

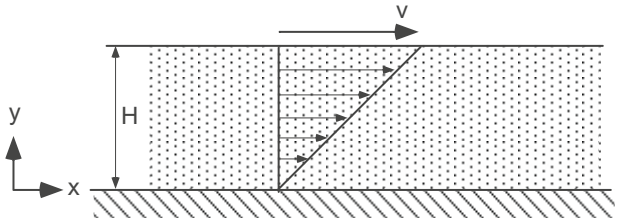


Figure 5.1
Drag flow between two flat parallel plates

If it is assumed that only conduction and viscous dissipation play a role of importance, the energy balance can be written as:

$$k\frac{\partial^2 T}{\partial y^2}+\tau_{xy}\frac{\partial v_x}{\partial y}=0 \tag{5.54}$$

When the fluid is Newtonian, the shear stress can be written as (see Section 6.2.1):

$$\tau_{xy}=\mu\frac{\partial v_x}{\partial y} \tag{5.55}$$

Thus, Eq. 5.54 becomes:

$$k\frac{\partial^2 T}{\partial y^2}+\mu\left(\frac{\partial v_x}{\partial y}\right)^2=0 \tag{5.56}$$

If the pressure gradient in flow direction is assumed to be zero, i.e. only drag flow, the velocity gradient becomes:

$$\frac{\partial v_x}{\partial y} = \frac{v}{H} \tag{5.57}$$

Thus, Eq. 5.56 becomes

$$\frac{\partial^2 T}{\partial y^2} = -\frac{\mu v^2}{H^2} \tag{5.58}$$

By integrating twice, the temperature profile is obtained:

$$T(y) = -\frac{\mu v^2}{2kH^2} y^2 + C_1 y + C_2 \tag{5.59}$$

If the temperature at the stationary wall is T_0, $T(y = 0) = T_0$ and T_1 at the moving wall, $T(y = H) = T_1$, the integration constants can be calculated:

$$C_2 = T_0 \tag{5.60a}$$

$$C_1 = \frac{T_1 - T_0}{H} + \frac{\mu v^2}{2kH} \tag{5.60b}$$

The temperature profile can now be written as:

$$T = -\frac{\mu v^2}{2kH^2} y^2 + \left(\frac{T_1 - T_0}{H} + \frac{\mu v^2}{2kH} \right) y + T_0 \tag{5.61}$$

This is essentially the same equation as Eq. 7.92 describing the temperature profile in the melt film in the melting region of an extruder. The equation can now be written in the following dimensionless form:

$$\frac{T - T_0}{T_1 - T_0} = \frac{y}{H} + \frac{\mu v^2}{2k(T_1 - T_0)} \left(1 - \frac{y}{H} \right) \frac{y}{H} \tag{5.62}$$

If the dimensionless temperature is T^0 and dimensionless distance y^0, then Eq. 5.62 can be written as:

$$T^0 = y^0 + \frac{1}{2} N_{Br} \left(1 - y^0 \right) y^0 \tag{5.63}$$

The Brinkman number N_{Br} is a measure of the importance of viscous heat generation relative to the heat conduction resulting from the imposed temperature difference ΔT ($= T_1 - T_0$):

$$N_{Br} = \frac{\mu v^2}{k\Delta T} \tag{5.64}$$

If the Brinkman number is larger than 2, there is a maximum temperature at a position intermediate between the two walls; see Fig. 5.2.

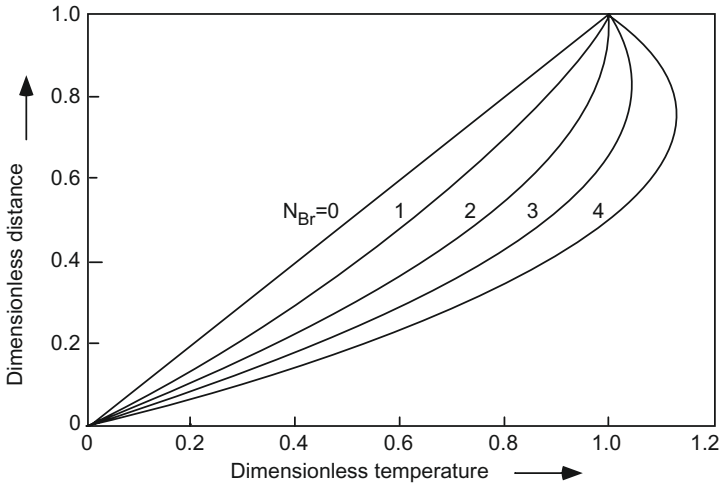


Figure 5.2 Temperature profiles at various Brinkman numbers

In the previous problem, only conduction and dissipation were considered to play a role. If the analysis is now extended to include the effect of convection, the energy equation becomes:

$$\rho C v_x \frac{\partial T}{\partial x} = k \frac{\partial^2 T}{\partial y^2} + \tau_{xy} \frac{\partial v_x}{\partial y} \tag{5.65}$$

This equation can be made dimensionless by introducing the following dimensionless variables:

$$T^0 = \frac{T}{\Delta T} \tag{5.66a}$$

$$y^0 = \frac{y}{H} \tag{5.66b}$$

$$x^0 = \frac{x}{L} \tag{5.66c}$$

$$v_x^0 = \frac{v_x}{v} \tag{5.66d}$$

This results in the following expression:

$$\frac{\rho C v H^2}{kL} v_x^0 \frac{\partial T^0}{\partial x^0} = \frac{\partial^2 T^0}{\partial (y^0)^2} + \frac{\mu v^2}{k\Delta T}\left(\frac{\partial v_x^0}{\partial y^0}\right)^2 \tag{5.67}$$

The first dimensionless group is the Graetz number:

$$N_{Gz} = \frac{\rho C v H^2}{kL} = \frac{v H^2}{\alpha L} \tag{5.68}$$

where α is the thermal diffusivity; see Section 6.3.5. Equation 5.67 can now be written as:

$$N_{Gz}\, v_x^0 \frac{\partial T^0}{\partial x^0} = \frac{\partial^2 T^0}{\partial (y^0)^2} + N_{Br}\left(\frac{\partial v_x^0}{\partial y^0}\right)^2 \tag{5.69}$$

Because this equation does not have a simple analytical solution it is generally solved by some numerical technique. However, regardless of the actual solution, as long as the Graetz and Brinkman numbers are constant, the solution to the problem will remain unchanged.

The Graetz number can be considered to be a ratio of two time values, one being the time required to reach thermal equilibrium through conduction in the direction normal to the flow direction (dimension H), the other time being the average residence time in the flow channel of length L. Thus, the Graetz number is a measure of the importance of conduction normal to the flow, relative to the thermal convection in the direction of flow. If the Graetz number is large, the conduction normal to the flow is large relative to the convection in flow direction. This situation often occurs in extruders in the flow through the screw channel and die flow channels.

A dimensionless number closely related to the Graetz number is the Peclet number:

$$N_{Pe} = \frac{vH}{\alpha} = N_{GZ}\frac{L}{H} \tag{5.70}$$

The Peclet number provides a measure of the importance of thermal convection relative to thermal conduction. The Peclet number in polymer processing is often quite large, typically of the order of 10^3 to 10^5. This indicates that convective heat transport is often quite important in polymer melt flow.

Another important dimensionless number is the Nusselt number:

$$N_{Nu} = \frac{hL}{k} \tag{5.71}$$

where h is the interfacial heat transfer coefficient.

The Nusselt number is basically a dimensionless temperature gradient averaged over the heat transfer surface. The Nusselt number represents the ratio of the heat transfer resistance estimated from the characteristic dimension of the object (L/k) to the real heat transfer resistance (1/h). In many convective heat transfer problems, the Nusselt number is expressed as a function of other dimensionless numbers, e. g., the Reynolds number and the Prandtl number.

The Prandtl number is:

$$N_{Pr} = \frac{C_p \eta}{k} = \frac{\eta}{\alpha \rho} \tag{5.72}$$

The Prandtl number is simply the ratio of kinematic viscosity (η/ρ) to thermal diffusivity (α). Physically, the Prandtl number represents the ratio of the hydrodynamic boundary layer to the thermal boundary layer in the heat transfer between fluids and a stationary wall. In simple fluid flow, it represents the ratio of the rate of impulse transport to the rate of heat transport. It is determined by the material properties; for high viscosity polymer melts, the number is of the order of 10^6 to 10^{10}.

The Nahme number or Griffith number is:

$$N_{Na} = \frac{\alpha_T v^2 \eta}{k} \tag{5.73}$$

where α_T is the temperature coefficient of viscosity η as defined in Eq. 6.40.

The Nahme number can be considered to be the ratio of viscous dissipation to thermal conduction in the direction perpendicular to flow. Large values of the Nahme number (>1) indicate that the temperature non-uniformities created by the viscous dissipation have a substantial effect on the resulting velocity profile. Thus, if the Nahme number is large, a non-isothermal flow analysis has to be made in order to maintain sufficient accuracy. If the Nahme number is small, an isothermal analysis can yield relatively accurate results. The Nahme number is also referred to as the Griffith number.

The Biot number is:

$$N_{Bi} = \frac{H}{T_m - T_w} \left(\frac{\partial T}{\partial x} \right)_w \tag{5.74}$$

The Biot number is a dimensionless heat transfer number. When the Biot number is zero, there is no exchange of heat; i. e., adiabatic conditions exist. When the Biot number is infinitely large, the wall temperature T_w equals the melt temperature T_m; this corresponds to isothermal conditions. Normal values for the Biot number in extrusion dies range from 1 to 100, depending strongly on the presence and amount of insulation.

The Fourier number is:

$$N_{Fo} = \frac{\alpha t}{H^2} \tag{5.75}$$

The Fourier number is a convenient number in the analysis of transient heat transfer problems, i.e., where the temperature changes with time. The Fourier number can be considered to be a ratio of two time values: one is the actual time value, the other is the time necessary to reach thermal equilibrium in the sample by conduction. If the Fourier number is large (>1), the sample will reach thermal equilibrium within the considered time frame. If the Fourier number is small (<0.1), only the skin of the sample will have changed in temperature, while the bulk of the material will be largely unaffected. In many cases, the temperature distribution is about 90% uniform when the Fourier number equals unity.

The thermal diffusivity of most polymers is about 10^{-7} m^2/s. If a polymer slab 1 mm thick is heated from two sides (H = 0.0005 m), after approximately 2.5 s the temperature in the slab will be quite uniform. If the slab is 10 mm thick, the uniform temperature conditions will not be approached until after 250 s or 4.17 min. This explains, at least partly, why it is difficult to obtain uniform melt temperatures in an extruder where the screw has very deep channels. In fact, if the channels are too deep, it is unlikely that the melting process can be completed in the extruder. A typical average residence time in a single screw extruder is about 1 to 3 min.

5.3.4 Viscous Heat Generation

Viscous heat generation is the dissipation of mechanical energy in a viscous fluid. The last term in the energy Eq. 5.5(d) shows the viscous dissipation in the most general case. In the simpler case of unidirectional shear, the viscous heat generation per unit volume is:

$$\dot{E}_d = \tau\dot{\gamma} \tag{5.76}$$

If the flow properties of the fluid can be described by a power law equation (see Section 6.2.2), the viscous heat generation per unit volume is:

$$\dot{E}_d = m\dot{\gamma}^{n+1} \tag{5.77}$$

where m is the consistency index and n the power law index. The power law index is unity for a Newtonian fluid and between one and zero for a pseudo-plastic fluid such as polymer melts. From Eq. 5.77 it can be seen that the viscous heat generation increases more than proportionally with the shear rate. This has important implications in the extrusion process; this will be discussed in Chapter 7.

Viscous heat generation occurs throughout a fluid. The local rate of heat generation depends on the local shear rate. If the shear rate is constant throughout the entire volume of a fluid, the viscous heat generation will be uniform throughout the fluid. This is the case in pure drag flow (Couette flow), i.e., flow without the presence of pressure differences in the flow direction; see Section 6.2.1. If the shear rate is not uniform throughout the volume, the viscous heat generation will not be uniform either. This is the case in pure pressure flow (Poiseuille flow) through a pipe. In this flow situation, the shear rate in the center is zero and maximum at the wall. Consequently, the viscous heat generation in the center is zero and maximum at the wall just as with the shear rate. Since viscous heat generation occurs throughout a fluid, it is an effective way of heating a polymer melt because it will result in a relatively uniform temperature increase if the shear rate is approximately constant throughout the fluid.

5.3.5 Radiative Heat Transport

Heat radiation consists of electromagnetic waves with a wavelength (λ) range of 0.5 to 10 microns. All bodies emit electromagnetic waves as a result of the thermal agitation of their molecules. The rate at which a body emits radiant energy depends mostly on its temperature. Between two surfaces, an exchange of radiation can take place if the intermediate space is transparent to the radiation spectrum. If the temperatures of the two surfaces are different, the sum of the two opposite heat flows generally will not be equal to zero.

The rate of emission of radiant energy is given by the Stefan-Boltzmann law:

$$\dot{Q} = eC_{SB}AT^4 \tag{5.78}$$

where e is the emissivity, C_{SB} the Stefan-Boltzmann constant, A the area of the object, and T the absolute temperature (°K). For a perfectly "black" body, the emissivity equals unity. The precise value of the Stefan-Boltzmann constant C_{SB} can be derived from other physical constants by the relationship:

$$C_{SB} = \frac{2\pi^5 C_B^4}{15 v_1^{\,2} C_{Pl}^{\,3}} = 5.6697\text{E-}8 \left[\frac{W}{m^2 {}^\circ K^4}\right] \tag{5.79}$$

where C_B is the Boltzmann constant (1.38054E–23 J/°K), v_1 the speed of light (2.997925E8 m/s), and C_{Pl} the Planck constant of action (6.6256E–34 Js).

For a "black" body, the spectral distribution of energy flux is given by Planck's law of radiation. The wavelength at which this intensity is maximumal is inversely proportional to the absolute temperature. This is Wien's law; it can be formulated as:

$$\lambda_{max} T = 2.898\text{E-}3 \ [m°K] \tag{5.80}$$

At room temperature λ_{max} = 10 μm (infrared) and at 6000 °K λ_{max} = 0.5 μm (green). The fact that the color of a body depends on its temperature is used in optical temperature measurements. This is often referred to as infrared temperature measurement even though some measurements may occur outside the infrared region of the spectrum. The infrared region ranges from a wavelength of 0.7 μm to about 400 μm.

A perfectly black body emits the maximum amount of radiation based on its temperature; its emissivity is unity. According to Kirchhoff's law, its absorptivity will also be unity. In reality, surfaces have emissivities and absorptivities for infrared radiation that are less than unity. The actual value will depend on the material, the surface roughness, the temperature, and the wavelength of the radiation.

Absorptivity values are usually given as average values. For most non-metallic surfaces, this value is larger than 0.8. Clean polished metal surfaces have absorptivities ranging between 0.05 and 0.20.

The radiative heat transfer between two surfaces is primarily determined by their emissivities, absorptivities, and temperatures. For each surface, the amount of radiation leaving the surface is the sum of the emitted radiation ($eC_{SB}T^4 = eq_b$) plus the reflected radiation $(1 - a)q_i$:

$$Q = eq_b + (1 - a)\,q_i \tag{5.81}$$

where a is the absorptivity and q the heat flux; q_b is the black body radiation and q_i is the incident radiation.

Also, the net energy flux leaving the surface equals its own emission minus the fraction of the incident radiation that is absorbed by the wall:

$$q_n = eq_b - aq_i \tag{5.82}$$

If the wall is at the same temperature as its surroundings, the net energy flux will be zero and $q_b = q_i = C_B T^4$. In this case, the emissivity has to equal the absorptivity (e = a); this is known as Kirchhoff's law. From Eq. 5.81, it can be deduced that the energy flux through any plane in a space equals $q_b = C_{SB}T^4$.

In order to calculate the incident radiation q_{ik} reaching wall k, one has to know the fractions f_{jk}, indicating what part of the total radiation of wall j reaches wall k. The geometrical factors, called view factors, are calculated by integration. In doing this, one has to take into account the fact that the radiation intensity depends on the angle with which the radiation hits the surface. In the simple case of two large parallel surfaces (1 and 2), both fractions are equal to unity: $f_{12} = f_{21} = 1$. Consider the case where one body (body 1 with area A_1 and temperature T_1) is totally enclosed by another body (body 2 with area A_2 and temperature T_2). The incident radiation on wall 1 (A_1q_{i1}) equals f_{21} multiplied with the total radiation of wall 2 ($f_{21}A_2q_2$). Thus, the radiation heat flux reaching body 1 (q_{i1}) equals the total radiation heat flux leaving body 2 (q_2). Therefore:

$$q_{n1} = q_1 - q_{i1} = q_1 - q_2 \tag{5.83a}$$

and

$$q_{n1} = q_{b1} - \frac{1-a_1}{a_1} q_{n1} - q_{b2} + \frac{1-a_2}{a_2} q_{n2} \tag{5.83b}$$

The next radiation transport from body 1 ($q_{n1}A_1$) and from body 2 ($q_{n2}A_2$) are related by:

$$q_{n1}A_1 + q_{n2}A_2 = 0 \tag{5.84}$$

This is valid because the energy lost by body 1 is gained by body 2. The net radiation flux leaving body 1 can be expressed as:

$$q_{n1} = C_{SB}(T_1^4 - T_2^4)\left(\frac{a_1 a_2 A_2}{a_1 A_1 + a_2 A_2 - a_1 a_2 A_1}\right) \tag{5.85}$$

The heat transfer coefficient for radiation h_s can now be expressed as:

$$h_s = C_{SB}\left(\frac{T_1^4 - T_2^4}{T_1 - T_2}\right)\left(\frac{a_1 a_2 A_2}{a_1 A_1 + a_2 A_2 - a_1 a_2 A_1}\right) \tag{5.86}$$

At room temperature and relatively small temperature differences, the value of h_s will be above 5 W/m²°C. This value is large enough that it cannot be neglected relative to free convection. Obviously, at higher temperatures the contribution of the radiative heat transport increases substantially.

Since radiative heating at elevated temperatures (above 300°C) generally occurs in the infrared region, it is often referred to as infrared (IR) heating. The applications of IR heating in polymer processing are numerous: thermoforming, film extrusion, orientation, embossing, coating, laminating, ink drying, and fusing. It is also used in curing filament-wound structures and in the manufacture of slit polypropylene yarns out of polypropylene film. Paint drying and baking is the largest single use for infrared heating. In polymer processing, thermoforming is probably the largest outlet for infrared heating. A good series of papers on infrared heating of plastics was written by Kraybill [19–21].

5.3.5.1 Dielectric Heating

Dielectric heating occurs when a dielectric material is placed in an electric field that alternates at high frequency. A dielectric material is an electric insulator and it has a low conductivity (high resistivity). Materials with a resistivity higher than 10^9 ohm-cm are generally considered to be dielectric; most polymers fall into this cate-

gory. Dielectric energy, also referred to as radio-frequency energy, occupies the frequency spectrum of about 10 to 100 megahertz.

In dielectric heating, heat is generated throughout the mass of material. In plastics, this can be a very beneficial feature, considering the low thermal conductivity of plastics. Since heat will be transferred away most quickly at the walls, dielectric heating often results in a temperature profile where the highest temperature occurs in the center and the lowest temperature at the wall. This is opposite to conductive heating where the highest temperature will occur at the wall. Also, because heat is generated throughout the material, temperature gradients are likely to be small in dielectric heating as compared to conductive heating. Dielectric heating is uniform throughout a mass of material because all of the polar molecules are oriented by an electric field. The oscillations of the molecules resulting from the alternating field produce heat through molecular friction. The rate at which electrical energy can be dissipated in a dielectric material per unit volume $\dot{Q}$ is proportional to the frequency of the electric field f and to the square of the electric field strength E.

$$\dot{Q} = 2\pi E^2 f \varepsilon_o \varepsilon \tan\delta \tag{5.87}$$

where ε_o is absolute permittivity of free space (8.854E–12 farad/m), ε relative permittivity or dielectric constant of the material, and $\tan\delta$ the loss tangent or dissipation factor. From Eq. 5.87, it is clear that fast heating can be accomplished most easily by increasing the field strength; the heating rate increases with the field strength square! The maximum field strength that can be applied is determined by the dielectric strength of the material to be heated. If the field strength is too high, dielectric breakdown will occur. This will result in sparking and can cause severe damage to the material. If the heating rate at the maximum allowable field strength is too slow, further increases can be obtained by increasing the frequency. Most polymers have a dielectric strength that ranges between 100 and 200 kV/cm, a dielectric constant that ranges between 2 and 4, and a dissipation factor that ranges between 0.01 and 0.0001.

Dissipation factor, power factor, loss angle, etc. are important terms in dielectric heating. They are defined as follows:

loss angle = $\delta = 90 = \varphi$

phase angle = φ

power factor = $\cos\varphi = \sin\delta$

dissipation factor = $\cot\varphi = \tan\delta$ (also loss tangent)

loss factor = $\varepsilon\tan\delta = \varepsilon\cot\varphi$

For most polymers, the loss angle is quite small, thus $\sin\delta \approx \tan\delta$; in other words the power factor and dissipation factor are almost equal.

When components of a material have different loss factors, selective heating will occur. The loss factor of most materials increases with moisture content. Regions with high moisture content will heat faster than others; thus, more water will be removed from high moisture regions. This will result in a uniform moisture distribution in the material. Non-polar polymers such as polyethylene will not heat well at all in a high frequency field. The relative response to dielectric heating can be made to respond better by adding additives to the polymer. An example of this is the radio frequency heating of ultrahigh molecular weight polyethylene (UHMWPE), containing small amounts of Frequon [18].

Table 5.1 Relative Response of Various Polymers to Dielectric Heating

Polymer	Loss factor	Response
ABS	0.025	Fair
Acetal	0.025	Fair
Cellulose acetate	0.15	Fair
Epoxy resins	0.12	Fair
Polyamide	0.16	Fair
Polycarbonate	0.03	Fair
Polyester	0.05	Fair
Polyethylene	0.0008	None
Polyimide	0.013	Poor
Polymethyl-methacrylate	0.09	Fair
Polypropylene	0.001	None
Polystyrene	0.001	None
Polytetrafluoroethylene	0.0004	None
Polyvinylchloride	0.4	Good
Rubber, compounded	0.13	Fair
Silicones	0.009	None
Urea-formaldehyde	0.2	Good
Water	0.4	Good

Dielectric or radio frequency heating is used in various parts of the polymer processing industry. Some examples are preheating for molding, curing of thermosetting resins, heat-sealing of film, drying of coatings on web substrates, flow molding, etc.

5.3.5.2 Microwave Heating

Microwave heating is a close cousin of dielectric heating; the main difference being the higher frequencies of microwaves, ranging from about 1000 to 100,000 MHz. This is about two to three orders of magnitude higher than the frequency spectrum

of dielectric energy. By definition, the wavelength of microwave energy must lie in the range of the spectrum between 1 m and 1 mm. This corresponds to a frequency range of 300 MHz (3E8 Hz) to 300 GHz (3E11 Hz). The frequencies that can be used in the U.S. are controlled by the Federal Communications Commission. For industrial applications, the two most important microwave frequencies are 915 MHz and 2450 MHz. The lower frequency is generally used for high-powered systems (over 200 kW) where the power factor of the material is reasonably high. The higher frequency is used for low-power systems (less than 100 kW) where the material has a relatively low power factor. Consumer microwave ovens operate at 2450 MHz.

When a dielectric material is placed in a microwave field, the dipolar molecules will tend to align their dipole moment along the field intensity vector. When the field intensity vector varies sinusoidally with time, the direction of the vector will reverse every half cycle. This will cause a realignment of the polar molecules. The internal friction that has to be overcome involves a loss of energy from the electromagnetic wave. This results in the conversion of a portion of the electromagnetic energy into thermal energy. In this case, the heat generation is proportional to the number of reversals of the electric field vector, i.e., the frequency. The amount of displacement that occurs during each reversal is determined by the electric field strength. Thus, the heat generation is also a function of the electric field strength, just as with RF heating.

The rate of heating by microwave energy is described by the same equation used for radio frequency heating, Eq. 5.87. Thus, the amount of heating depends on the field strength, frequency, and loss factor. The latter factor is a material property; the first two factors are dependent on the details of the hardware.

The heat is generated throughout the material; however, the power level reduces with depth of penetration. The depth at which the power is reduced to one-half is given by:

$$H_{0.5} = \frac{0.11\,\lambda_0}{\varepsilon \tan\delta} \tag{5.88}$$

where λ_0 is the wavelength in free space, ε the permittivity or dielectric constant of the material, and δ the loss angle. Considering that wavelength is the speed of light divided by the frequency, Eq. 5.88 can also be written as:

$$H_{0.5} = \frac{3.3E7}{f\,\varepsilon \tan\delta} \tag{5.89}$$

From these expressions, one can see that the depth of penetration reduces with increasing frequency and with increasing loss factor.

If heat losses due to conduction, convection, radiation, or change of state are neglected, the rate of increase in temperature $\dot{T}$ from the absorption of microwave energy can be determined from the following equation:

$$\dot{T} = \frac{\dot{Q}}{C_p \rho} \tag{5.90}$$

where $\dot{Q}$ is the rate of energy dissipation per unit volume from Eq. 5.87, C_p is the specific heat, and ρ the material density.

The penetrating action of microwave energy enables rapid and uniform heating of large cross-sections. With conventional heating methods (hot air, steam, infrared, fluidized bed, etc.), the rate of heating is limited by the poor thermal conductivity of polymers. This is not the case in microwave heating; very short heating chambers can be used.

Applications of microwave heating are drying, continuous curing of polymers (rubbers, filled polyethylenes, etc.), preheating for compression or transfer molding, bonding, etc.

5.4 Basics of Devolatilization

In devolatilization, one or more volatile components are extracted from the polymer. The polymer can be either in the solid state or in the molten state. Two processes occur in the devolatilization process. First, the volatile components diffuse to the polymer-vapor interface; then the volatile components evaporate at the interface and are carried away. Thus, the first part of the process is a diffusional mass transport and the second part a convective mass transport. If the diffusional mass flow rate is less than the convective mass flow rate, the process is diffusion-controlled. In polymer-volatile systems, the diffusion constants are generally very low, and, therefore, in many polymer devolatilization processes the process is diffusion-controlled.

The important relationship in diffusional mass transport is Fick's law. It states that in a one-dimensional diffusion, the positive mass flux of component A is related to a negative concentration gradient. It can be written as:

$$J_A = -D'_{AB} \frac{dC_A}{dy} \tag{5.91}$$

where J_A is the diffusional mass flow rate, C_A the local concentration of component A, and D'_{AB} the binary diffusivity.

Fick's law is valid for constant densities and for relatively low concentrations of component A in component B. The term binary mixture is used to describe a two-component mixture. A binary diffusivity is the diffusion constant of one component of a binary mixture. The diffusional mass transport is driven by a concentration

gradient, as described by Fick's law. This is very similar to Fourier's law, which relates heat transport to a temperature gradient; see Eq. 5.45. It is also very similar to Newton's law, which relates momentum transport to a velocity gradient; see Eq. 6.16. Because of the similarities in diffusional mass transport, heat transport, and momentum transport, many problems in diffusion are described with equations of the same form as used in heat transfer problems or momentum transfer problems. Also, several of the dimensionless numbers that are used in heat transfer problems (see Section 5.3.3) are also used in diffusional mass transfer problems.

For a binary system of constant density, where a low concentration component A is diffusing through the other component, the equation of continuity for component A can be written as:

$$\frac{\partial C_A}{\partial T} + v_x \frac{\partial C_A}{\partial x} + v_y \frac{\partial C_A}{\partial y} + v_z \frac{\partial C_A}{\partial z} = D'_{AB}\left[\frac{\partial^2 C_A}{\partial x^2} + \frac{\partial^2 C_A}{\partial y^2} + \frac{\partial^2 C_A}{\partial z^2}\right] \tag{5.92}$$

This equation of continuity, which incorporates Fick's law, is used to describe diffusional transport problems. In most analyses of diffusion processes, it is assumed that the concentration at the liquid-vapor or solid-vapor interface is the equilibrium concentration between the vapor phase and the liquid or solid phase. When a liquid phase of a mixture is in equilibrium with a vapor phase of that mixture, the partial pressure of one component depends on the temperature, pressure, and entire composition of the mixture. Partial pressure $\overline{P}_A$ of component A is defined as:

$$\overline{P}_A = P x_A \tag{5.93}$$

where x_A is the mole fraction of component A in the gas mixture and P is the total pressure on the mixture.

The partial pressure for ideal gases is described by Dalton's law:

$$\overline{P}_A = \frac{x_A R_o T n}{V} \tag{5.94}$$

where R_o is the gas constant, T is the absolute temperature, n is the number of weight moles of gas, and V is the volume.

For a binary mixture, the composition is completely specified by x'_A, which is the mole fraction of component A in the liquid in equilibrium. In this case, the partial pressure of component A will be a function of pressure, temperature, and x'_A. If the properties of the liquid are pressure-independent, and if the gases behave as ideal gases, then the partial pressure of component A at constant temperature can be written as a function of only x'_A. If the liquid phase consists of only one component, the partial pressure of A equals the vapor pressure of pure A. The partial pressure of component A, P_{-A}, is described as a function of x' by Henry's law. It states that P_A is directly proportional to x'_A at low concentrations of component A:

$$\overline{P}_A = H_A x'_A \tag{5.95}$$

where H_A is the Henry's law constant.

The Henry's law constant depends on the temperature, the volatility, and the pressure. It is not valid for substances such as electrolytes, which dissociate in solution. For ideal solutions, Henry's law is valid over the entire range of concentrations (0–100%), and the Henry's law constant equals the vapor pressure of that component.

Polymer-solvent mixtures are highly non-ideal. Because of the very long polymer molecules, the polymer exerts an influence far in excess of its molar concentration. This behavior is often described by the Flory-Huggins relations [22, 23]:

$$\ln\frac{\overline{P}}{P_o} = \ln(1-V_p) + \left(1-\frac{1}{DP}\right)V_p + \chi V_p^{\,2} \tag{5.96}$$

where P is the effective partial pressure of the volatile component, P_o is the vapor pressure of the pure volatile component, DP is the degree of polymerization, V_p is the volume fraction of the polymer, and χ is an interaction parameter.

For polymer-solvent systems where the solvent is chemically similar, the interaction parameter generally falls within the range of 0.3 to 0.5. If the volatile component is fully miscible, a first approximation of the interaction parameter is χ = 0.4. If the volatile component is not fully miscible, the interaction parameter χ = 0.5.

For polymers with a high degree of polymerization and relatively small concentrations of the volatile component A, the Flory-Huggins relationship can be simplified to:

$$\ln\frac{\overline{P}}{P_o} = \ln V_A + 1 + \chi \tag{5.97}$$

where V_A is the volume fraction of the volatile component A. According to Eq. 5.97, the ratio of partial pressure to vapor pressure is directly proportional to V_A and depends exponentially on the interaction parameter χ. The $\overline{P}/P_o$ ratio as a function of V_A at various values of the interaction parameter is shown in Fig. 5.3.

Figure 5.3 is based on Eq. 5.96 with a degree of polymerization DP = 1000.

It can be seen that when the concentration of the volatile component is below 5%, the relationship between $\overline{P}$ and V_A is essentially linear. In this range, Henry's law can be applied with reasonable accuracy and Eq. 5.97 can be used. At concentrations above 5% considerable deviations from Henry's law (linear behavior) occur and the Flory-Huggins (F-H) relationship, or a similar relationship, should be used. In many cases, it has been observed that the interaction parameter χ of the F-H relationship is concentration dependent to the extent that this concentration dependence cannot be neglected. This indicates that the basic assumptions underlying the F-H relationship are not fulfilled.

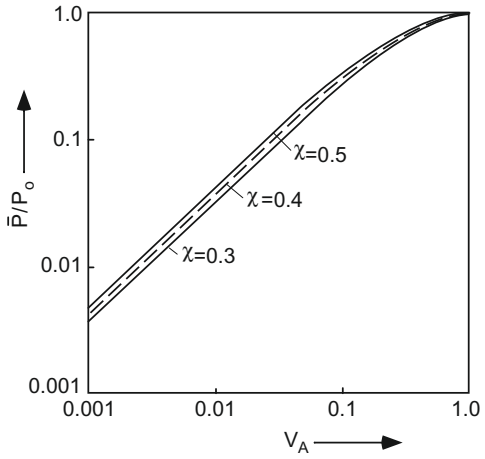


Figure 5.3
$\bar{P}/P_0$ ratio versus V_A for three values of the interaction parameter

An improved theory for vapor-liquid equilibrium of mixtures based on free-volume considerations was proposed by Prigogine [24, 25]. This theory has been further developed by various workers, e.g., Flory [26]. Bonner and Prausnitz [27] discuss the new theory in detail and describe its application with a number of examples.

The viscosity of a polymer melt generally reduces with increased amounts of volatile component. Figure 5.4 shows the viscosity of polystyrene as a function of the solvent concentration. In this example the solvent is ethylbenzene [28].

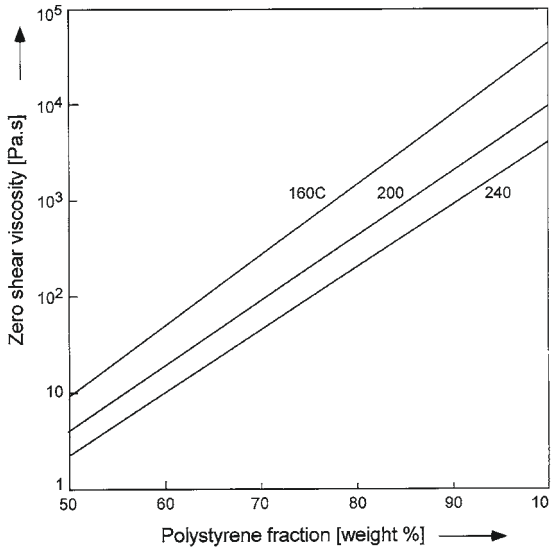


Figure 5.4
Viscosity of polystyrene as a function of solvent concentration

It can be seen that in this example the viscosity reduces exponentially with the solvent concentration. A 10% change in solvent concentration causes approximately a 5× change in viscosity. Thus, if the initial solvent concentration is 20% and the final

concentration almost zero, the viscosity increase as a result of devolatilization will be about 25 ×! This indicates that when substantial amounts of volatiles are removed from a polymer melt, very large increases in viscosity can occur as a result of the devolatilization.

The flow of concentrated polymer solutions and polymer melts is essentially always laminar as a result of the high viscosity. Heat transfer in such flow systems is quite poor because the heat transfer occurs primarily by conduction and the thermal conductivity in most cases is very low; see also Section 6.3.1.

The diffusion in concentrated polymer solutions is much slower than in low viscosity (low molecular weight) liquids. The diffusion coefficients for concentrated polymer solutions range from about 10^{-8} m^2/s to 10^{-12} m^2/s. For low viscosity liquids, the diffusion coefficients generally range from about 10^{-6} m^2/s to 10^{-7} m^2/s. The difference is several orders of magnitude! The diffusion rate is highly temperature-dependent. At higher temperatures, the vibration of segments of the polymer molecules becomes more pronounced and the density of the polymer reduces. As a result, diffusion of a volatile component will occur at a higher rate. The rate of diffusion will generally also depend on the actual concentration of the volatile component. The presence of a low molecular weight component increases the mobility of the polymer molecules. Thus, the rate of diffusion will tend to be higher at large concentrations of the volatile component. Figure 5.5 shows the diffusion coefficient as a function of the solvent concentration at various temperatures for a system of PMA and methylacetate [29].

This figure clearly shows the temperature and concentration dependence of the diffusion coefficient.

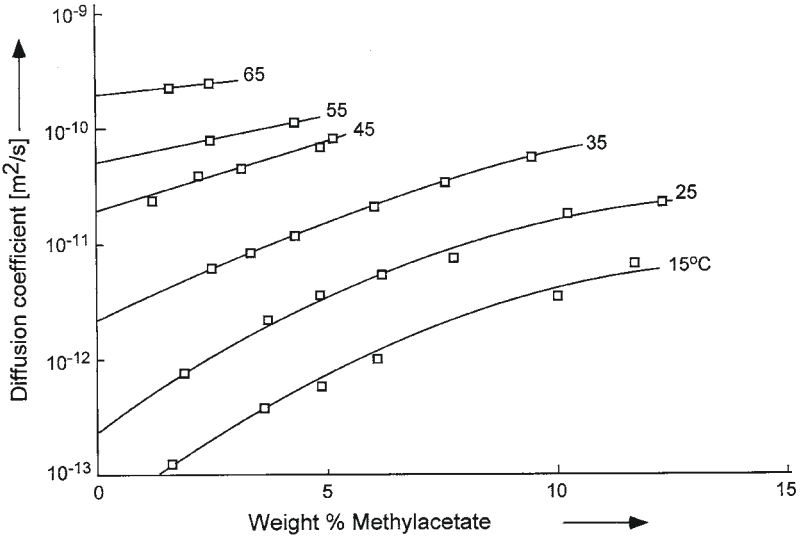


Figure 5.5 Diffusion coefficient as a function of solvent concentration

5.4.1 Devolatilization of Particulate Polymer

Theoretical description of devolatilization of particulate polymer can generally be achieved with a relatively high degree of accuracy. In most cases, the process will be diffusion controlled. The diffusion coefficients in solid polymers are very low, ranging from about 10^{-12} m²/s to 10^{-14} m²/s. The temperature in the polymeric particle can usually be taken as constant since the thermal diffusivity ($\alpha \approx 10^{-7}$ m²/s) is many orders of magnitude higher than the diffusion coefficient.

In the case of spherical particles with low concentrations of volatile components for which the concentration dependence of the diffusion coefficient can be neglected, the diffusion equation in spherical coordinates can be written as:

$$\frac{\partial C}{\partial t} = \frac{2D'}{r}\frac{\partial C}{\partial r} + D'\frac{\partial^2 C}{\partial r^2} \tag{5.98}$$

where C is the concentration of the volatile component and D′ the diffusion coefficient.

If C_e is the equilibrium concentration at the interface and C_o the initial concentration, then the solution to Eq. 5.98 can be written in terms of the average concentration $\overline{C}$ as a function of time [30]:

$$\frac{\overline{C} - C_e}{C_o - C_e} = \frac{6}{\pi^2}\sum_{i=1}^{\infty}\frac{1}{i^2}\exp\left(-\frac{\pi^2 i^2 D't}{R^2}\right) \tag{5.99}$$

where R is the radius of the spherical particle.

The equilibrium concentration C_e is usually very small relative to the initial concentration C_o, therefore, the C_e term is often neglected. In this case:

$$\frac{\overline{C} - C_e}{C_o - C_e} \cong \frac{\overline{C}}{C_o} \tag{5.99a}$$

If the temperature cannot be assumed constant, then the equations have to be solved numerically. The same is true if the diffusion coefficient is dependent on the concentration.

In many cases, however, one can reasonably assume a linear dependence on the diffusion coefficient on concentration:

$$D' = D'_o\left(1 + \alpha_c C\right) \tag{5.100}$$

where α_c is the coefficient describing the concentration dependence of the diffusion coefficient.

Figure 5.6 shows the dimensionless concentration $\overline{C}/C_o$ as a function of dimensionless time $D'_o t/R^2$ at various values of the parameter $\alpha_c C_o/D'$ as determined by Meier [31].

The top curve, for which this parameter is zero, represents the case for which the diffusion coefficient is independent of concentration and is described by Eq. 5.99.

The dimensionless $D'_o t/R^2$ can be considered a Fourier number for diffusion.

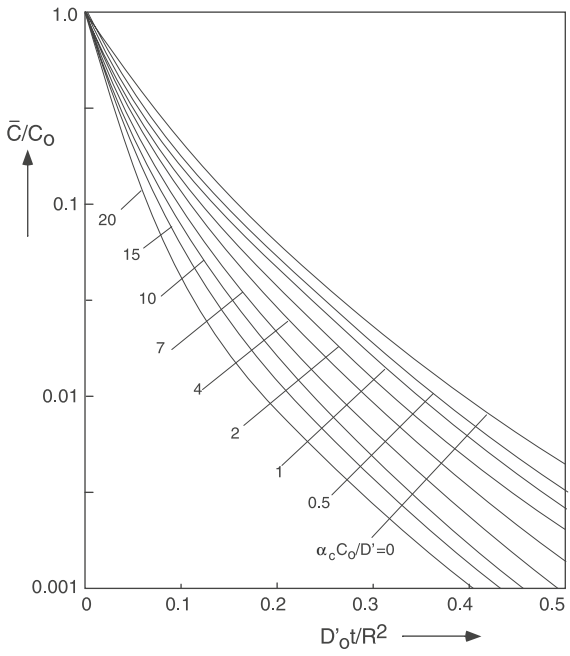


Figure 5.6
Dimensionless concentration versus dimensionless time

5.4.2 Devolatilization of Polymer Melts

In the devolatilization of polymer solutions and polymer melts, the diffusion of the volatile component is in many cases the rate-controlling part of the process. It is generally assumed that the concentration at the interface is at the equilibrium concentration corresponding to the partial pressure of the volatile component in the vapor. A concentration gradient will form in the melt film, and the diffusion rate will be determined by the slope of the concentration gradient. If the volatile concentration is large, the viscosity of the liquid will be relatively low and the mass transport of the volatile component will often occur by bubble transport. This is frequently referred to as foam devolatilization. This causes a rather rapid reduction in volatile concentration and results in a rapid increase in viscosity of the liquid. The increasing viscosity inhibits the formation of bubbles, and as the volatile concentration becomes low, the mass transport will be governed solely by molecular diffusion. The

devolatilization process of polymer melts is usually analyzed as a diffusion-controlled process. Relatively little work has been done to study and analyze foam devolatilization [32, 35–37]. Devolatilization in single screw extruders generally occurs at relatively low levels of volatiles; therefore, foam devolatilization is usually not considered to play a role of importance in devolatilizing extrusion. However, research at Farrel Corp. indicates that foam devolatilization occurs quite readily and may determine the devolatilization process to a large extent [38, 39].

A technique that is often employed in devolatilization of polymer solutions is flash devolatilization [34]. In this technique, the polymer solution is delivered to a flash point under high pressure and at temperatures above the boiling point of the volatile component. The solution is then expanded through a nozzle; large amounts of volatiles can thus be extracted rather quickly. The foamy liquid that results from this operation is often exposed to another devolatilization step to remove residual amounts of volatiles. This second step is generally a conventional melt film devolatilization, where the material in the film is continuously renewed to obtain an effective extraction of the volatiles.

Stripping agents such as water are often added to the polymer to enhance the devolatilization process. The improvement is obtained by bubble formation, which substantially improves the devolatilization process.

Consider a liquid polymer film with surface area A and depth H moving in direction x in plug flow with a volumetric flow rate $\dot{V}_f$. The film is losing a volatile solute by evaporation in the y direction at a rate of $\dot{E}$. If the mass transport in the y direction occurs by molecular diffusion only, and if both dispersion in the x direction and changes in $\dot{V}_f$ due to loss of volatile are neglected, an expression for $\dot{E}$ can be developed. The exposure time of the film λ_f is defined as:

$$\lambda_f = \frac{HA}{\dot{V}_f} \tag{5.101}$$

The characteristic time for diffusion is defined as:

$$\lambda_D = \frac{H^2}{D'} \tag{5.102}$$

where D′ is the molecular diffusivity of the volatile solute in the liquid polymer.

It can be shown [30] that if $\lambda_f/\lambda_D \leq 0.1$, the film can be considered of infinite depth. In this case, the layer in which the concentration is varying is much thinner than the total thickness of the melt film H. The stage efficiency X for this situation can be expressed as:

$$X = \left(\frac{4\lambda_f}{\pi\lambda_D}\right)^{1/2} \tag{5.103}$$

The stage efficiency is the actual rate of evaporation divided by the maximum possible rate of evaporation:

$$X = \frac{\dot{E}}{\dot{V}_f (C_o - C_e)} \tag{5.104}$$

where C_o is the initial volatile concentration and C_e the concentration of the volatile component in the liquid phase, which is in equilibrium with the vapor phase.

If $\lambda_f/\lambda_D > 0.1$, the melt film cannot be considered infinite. The stage efficiency in this case can be described by:

$$X = 1 - \frac{8}{\pi^2} \exp\left(- \frac{\pi^2 \lambda_f}{4\lambda_D} \right) \tag{5.105}$$

If the film can be considered infinite, the concentration profile can be described by:

$$\frac{\partial C}{\partial t} = D' \frac{\partial^2 C}{\partial y^2} \tag{5.106}$$

With boundary conditions $C(0) = C_e$ and $C(\infty) = C_o$, the actual concentration profile as a function of time becomes:

$$\frac{C - C_e}{C_o - C_e} = \mathrm{erf}\left(\frac{y}{\sqrt{4D't}} \right) \tag{5.107}$$

The same problem in conductive heat transport will be discussed in Section 6.3.5. The error function erf(x) is defined by Eq. 6.99. Figure 5.7 shows the concentration profile at various values of the parameter $\sqrt{D't}$.

The penetration depth is about 0.1 mm when $\sqrt{D't} = 25 \cdot 10^{-6}$ [m]. If the diffusion coefficient is assumed to be $D' \approx 10^{-8}$ m^2/s, then the corresponding time is 0.0625 s. If the diffusion coefficient is assumed to be $D' = 10^{-6}$ m^2/s, then the corresponding time is $6.25 \cdot 10^{-4}$ s. Since these are typical values of the diffusion coefficient, the assumption of infinite melt film thickness may not be valid in the analysis of devolatilization in extrusion equipment. A typical exposure time of the melt film in an extruder is of the order of one second; a typical melt film thickness is 0.1 mm ($\approx$ 0.004 in).

The rate of diffusion J at the interface per unit area and per unit time is determined by:

$$J = \frac{-1}{t} \int_o^t D' \left(\frac{\partial C}{\partial y} \right)_{y=0} dt = 2(C_o - C_e) \left(\frac{D'}{\pi t} \right)^{1/2} \tag{5.108}$$

Thus, the diffusional transport reduces with $1/\sqrt{t}$. The initial diffusional mass transport will be the highest; thereafter, it will reduce with time according to Eq. 5.108. Thus, in order to maintain high devolatilization efficiency, it is very important that the surface through which the volatile is escaping is frequently renewed. This can be achieved by feeding the film into a mixer.

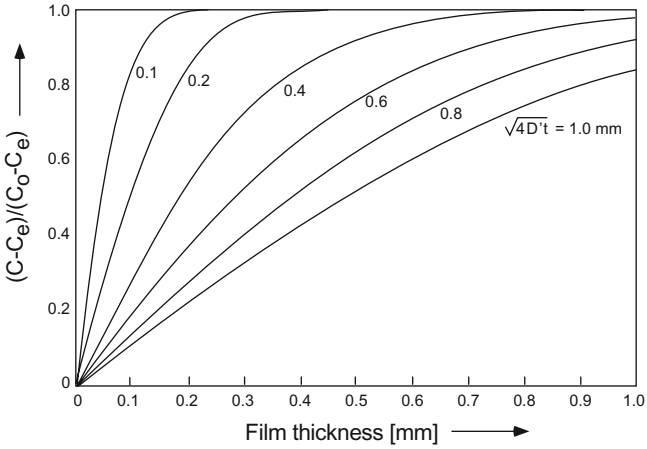


Figure 5.7
Concentration profile versus depth at various values of $(D't)^{0.5}$

The material leaving the mixer will have a homogeneous composition with the same average volatile level as the film entering the mixer. The material leaving the mixer can be spread into a new film with more volatiles diffusing out and evaporating. The process can be repeated many times. It can be demonstrated [33], assuming ideal mixing, that for each n-th stage:

$$\frac{C_n - C_e}{C_0 - C_e} = (1 - X)^n \tag{5.109}$$

The improved devolatilization efficiency with surface renewal can be assessed by comparing the residual concentration C_n after n ideal surface renewals with exposure time between film renewal λ_f to the residual concentration $C(n\lambda_f)$ with the same total exposure time but without surface renewal by:

$$\frac{C_n - C_e}{C(n\lambda_f) - C_e} = \frac{[1 - X(\lambda_f)]^n}{1 - X(n\lambda_f)} \tag{5.110}$$

Figure 5.8 shows the ratio $C_n/C(n\lambda_f)$ for various values of λ_f/λ_D, assuming that the value of C_e is very small and negligible.

It is clear from Fig. 5.8 that surface renewal can yield a considerably lower residual concentration compared to the case without surface renewal. The improvement in devolatilization efficiency becomes more pronounced when the ratio λ_f/λ_D becomes

larger. When the ration $\lambda_f/\lambda_D > 0.1$, a single curve represents the $C_n/C(n\lambda_f)$ versus n relationship. In this case, Eq. 5.110 can be written as:

$$\frac{C_n - C_e}{C(n\lambda_f) - C_e} = \left(\frac{8}{\pi^2}\right)^{n-1} \tag{5.111}$$

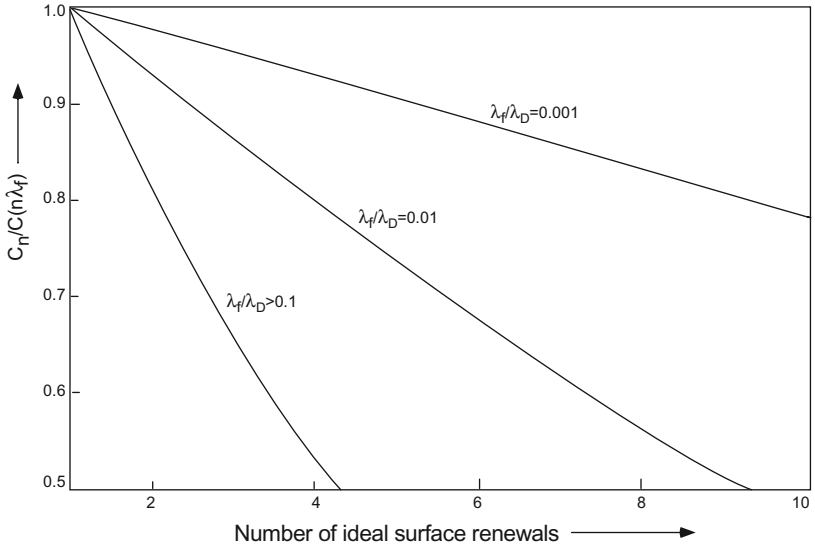


Figure 5.8 Ratio of $C_n/C(n\lambda_f)$ for various values of λ_f/λ_D

When the ratio λ_f/λ_D is very small (< 0.001), the benefits of surface renewal are relatively minor. In actual polymer processing equipment, the surface renewal process will generally not be ideal, because only a fraction of the bulk material will be spread out into a thin film. Therefore, the actual devolatilization efficiency would be expected to be less than predicted by Eqs. 5.109 through 5.111.

Appendix 5.1

Example: Pipe Flow of Newtonian Fluid

In pipe flow, the fluid moves as a result of a pressure gradient along the pipe; see Fig. 5.9.

The velocity at the wall is zero and maximum at the center. The velocity gradient (shear rate) is zero in the center and maximum at the wall. The momentum balance for this case can be determined by taking a force balance on a small fluid element as shown in Fig. 5.9; this gives:

$$dp\left[\pi(r+dr)^2 - \pi r^2\right] = d\tau\, 2\pi(r+dr)dz \tag{1}$$

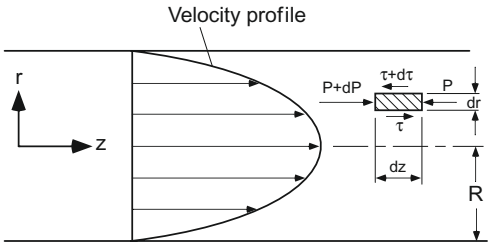


Figure 5.9
Flow through a circular pipe

This results in:

$$\frac{d\tau}{dr} = \frac{1}{2}\frac{dP}{dz} \tag{2}$$

This same result can be obtained directly from momentum balance Eq. 5.4(c) by eliminating the stress derivatives in the tangential (θ) and axial direction (z); this yields:

$$\frac{dP}{dz} = \frac{1}{r}\,\frac{d(r\tau)}{dr} \tag{3}$$

Verify that Eqs. 2 and 3 are the same when $\tau/r = d\tau/dr$, which is true in this case. For a Newtonian fluid, the shear stress can be related to the velocity gradient by:

$$\tau = \mu\frac{dv}{dr} \tag{4}$$

where μ is the Newtonian viscosity; see also Section 6.2. Inserting Eq. 4 into Eq. 2 or 3 gives:

$$\frac{d^2v}{dr^2} = \frac{g_z}{2\mu} \tag{5}$$

where g_z is the axial pressure gradient $\left(g_z = \frac{dP}{dz}\right)$.

By integrating once, the velocity gradient is obtained:

$$\frac{dv}{dr} = \frac{g_z r}{2\mu} + C_1 \tag{6}$$

Since the velocity gradient is zero at the center (r = 0), the integration constant C_1 has to be zero. The velocity profile is obtained by integrating Eq. 6:

$$v = \frac{g_z r^2}{4\mu} + C_2 \tag{7}$$

The integration constant C_2 can be determined from the condition that the velocity at the wall is zero, i.e., v(R) = 0. This yields:

$$C_2 = -\frac{g_z R^2}{4\mu} \tag{8}$$

Thus, the velocity profile becomes:

$$v = \frac{g_z}{4\mu}(r^2 - R^2) \tag{9}$$

The velocity at the center (r = 0) is maximum and is given by:

$$v_{max} = -\frac{g_z R^2}{4\mu} \tag{10}$$

The velocity is positive when the pressure gradient is negative. The velocity profile can now be expressed as:

$$v = v_{max}\left(1 - \frac{r^2}{R^2}\right) \tag{11}$$

The volumetric flow rate can now be determined by integrating the velocity over the cross-sectional area of the pipe:

$$\dot{V} = \int_0^R v 2\pi r dr \tag{12}$$

With Eq. 9, the flow rate can be determined to be:

$$\dot{V} = -\frac{\pi g_z R^4}{8\mu} \tag{13}$$

This is the well-known Poiseuille equation, first published in 1840 [40]. The flow rate is directly proportional to the pressure gradient and inversely proportional to the fluid viscosity. The flow rate depends strongly on the radius; it increases with the radius to the fourth power.

References

1. R.B. Bird, W.E. Stewart, and E.N. Lightfoot, "Transport Phenomena," Wiley, NY (1960)
2. J.R. Welty, C.E. Wicks and R.E. Wilson, "Fundamentals of Momentum, Heat and Mass Transport," Wiley, NY (1969)
3. C. Truesdell and R.A. Toupin, "The Classical Field Theories," in Handbuch der Physik, Vol. III, Springer, Berlin (1960)
4. W.J. Beek and K.M. Muttzall, "Transport Phenomena," Wiley, NY (1975)
5. L.E. Sisson and D.R. Pitts, "Elements of Transport Phenomena," McGraw-Hill, NY (1972)
6. W.C. Reynold and H.C. Perkins, "Engineering Thermodynamics," 2nd Edition, McGraw-Hill, NY (1977)
7. G.J. Van Wylen and R.E. Sonntag, "Fundamentals of Classical Thermodynamics," 2nd Edition, Wiley, NY (1973)
8. R.W. Haywood, "Equilibrium Thermodynamics," Wiley, NY (1980)
9. A. Bejan, "Entropy Generation through Heat and Fluid Flow," Wiley, NY (1982)
10. P.J. Flory, "Principles of Polymer Chemistry," Cornell University Press, Ithaca, NY (1953)
11. L.R.G. Treloar, "The Physics of Rubber Elasticity," 2nd Edition, Oxford Univ. Press, Oxford (1958)
12. F. Bueche, "Physical Properties of High Polymers," Wiley–Interscience, NY (1962)
13. A.V. Tobolsky, "Properties and Structure of Polymers," Wiley, NY (1960)
14. R.L. Miller (Ed.) "Flow-Induced Crystallization in Polymer Systems," Gordon and Breach Science Publishers, NY (1979)
15. G. Astarita, Polym. Eng. Sci., 14, 730–733 (1974)
16. H.S. Carslaw and J.C. Jaeger, "Conduction of Heat in Solids," 2nd Edition, Oxford Univ. Press, Oxford (1959)
17. R. Siegel and J.R. Howell, "Thermal Radiation Heat Transfer," 2nd Edition, McGraw-Hill (1981)
18. B. Miller, Plastics World, March, 99–104 (1981)
19. R.R. Kraybill, SPE ANTEC, Vol. 27, 590–592 (1981)
20. R.R. Kraybill and W.J. Hennessee, SPE ANTEC, Vol. 28, 826–829 (1982)
21. R.R. Kraybill, SPE ANTEC, Vol. 29, 466–468 (1983)
22. P.J. Flory, J. Chem. Phys., 10, 51 (1942)
23. M.L. Huggins, Ann. NY Acad. Sci., 43, 9 (1942)
24. I. Prigogine, N. Trappeniers and V. Mathot, Disc. Farad. Soc., 15, 93 (1953); J. Chem. Phys., 21, 559 (1953)
25. I. Prigogine, "The Molecular Theory of Solutions," North Holland, Amsterdam (1957)
26. P.J. Flory, J. Am. Chem. Soc., 87, 1833 (1965)

27. D.C. Bonner and J.M. Prausnitz, AIChE J., 19, 943 (1973)
28. E. Schumacher, M.Sc. Thesis, Univ. of Stuttgart, Germany (1966)
29. H. Fujita, A. Kishimoto and K. Matsumoto, Trans. Faraday Soc., 56, 424 (1960)
30. I. Crank, "The Mathematics of Diffusion," 2nd Edition, Clarendon Press, Oxford (1975)
31. E. Neier, Chemie Ing. Techn., 42, 20 (1970)
32. R.E. Newman and R.H.M. Simon, 73rd Annual AIChE Meeting, Chicago (1980)
33. J.A. Biesenberger, Polym. Eng. Sci., 20, 1015–1022 (1980)
34. M.H. Pahl in "Entgasen von Kunststoffen," VDI-Verlag GmbH, Duesseldorf (1980)
35. K.G. Powell and C.D. Denson, Paper No. 41a presented at the Annual Meeting of the AIChE in Washington, DC (1983)
36. H.J. Yoo and C.D. Han, Paper No. 41b presented at the Annual Meeting of the AIChE in Washington, DC (1983)
37. M. Amon and C.D. Denson, Polym. Eng. Sci., 24, 1026–1034 (1984)
38. M.A. Rizzi, P. Hold, M.R. Kearney, and A.D. Siegel, Paper No. 41e presented at the Annual Meeting of the AIChE in Washington, DC (1983)
39. P.S. Mehta, L.N. Valsamis, and Z. Tadmor, Polym. Process Eng., 2, 103–128 (1984)
40. J.L. Poiseuille, Compte Rendus, 11, 961 and 1041 (1840); 12, 112 (1841)

6 Important Polymer Properties

To understand the extrusion process, it is not enough just to know the hardware aspects of the machine. To fully understand the entire process, one also has to know and appreciate the properties of the material being extruded. The characteristics of the polymer determine, to a large extent, the proper design of the machine and the behavior of the process. There are two main classes of properties important in the extrusion process: the rheological properties and the thermal properties. The rheological properties describe how the material deforms when a certain stress is applied. The rheological properties of the bulk material are of importance in the feed hopper region of the extruder. The rheological properties of the polymer melt are important in the plasticating zone, the melt conveying zone, and the die forming region. Thermal properties allow prediction of temperature changes in the polymer and how the polymer reacts to these temperature changes.

6.1 Properties of Bulk Materials

Some of the most important properties of the bulk material are the bulk density, the coefficient of friction, and particle size and shape. From these properties, the transport behavior of the bulk material can be described with reasonable accuracy. These properties will be discussed in more detail in the following section.

6.1.1 Bulk Density

The bulk density is the density of the polymeric particles, including the voids between the particles. It is determined by filling a container of certain volume (1 liter or more) with the bulk material without applying pressure or tapping. The content is then weighed and the bulk density is obtained by dividing the material weight by the volume. In order to get reproducible results, the dimensions of the container should be several orders of magnitude larger than the particular dimen-

sion.* Low bulk density materials (ρ_b < 0.2 g/cc) tend to cause solids conveying problems, either in the feed hopper or in the feed section of the extruder. Materials with irregularly shaped particles tend to have a low bulk density; examples are fiber scrap or film scrap (flakes). When the bulk density is low, the mass flow rate will be low as well. Thus, the solids conveying rate may be insufficient to supply the downstream zones (plasticating and melt conveying) with enough material. Special devices and special extruders have been designed to deal with these low bulk density materials. A crammer feeder, as shown in Fig. 6.1, is a device used to improve the solids transport from the feed hopper into the extruder barrel.

Special extruders have been designed with the diameter of the feed section larger than the transition and metering section. Two possible configurations, both found commercially, are shown in Fig. 6.2.

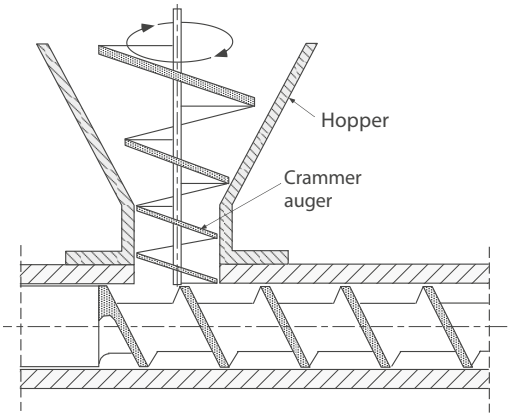


Figure 6.1
Example of crammer feeder

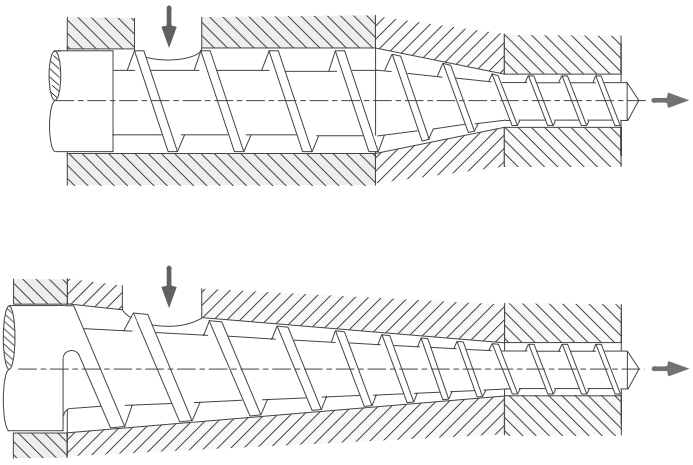


Figure 6.2
Two examples of extruders designed to handle low bulk density feed

* ASTM D1895 describes standard test methods for apparent density (bulk density), bulk factor (ratio bulk density to actual density), and pourability of plastic materials.

Since scrap or regrind is more difficult to handle, it is often blended with the virgin material to reduce the handling problems.

The bulk density at atmospheric pressure is useful but limited information. It is very important to know how the bulk density changes with pressure, because the compressibility of the bulk material determines, to a large extent, the solids conveying behavior. Compaction occurs by a rearrangement of the particles and an actual deformation of the particles. The difference between the loosely packed (untapped) bulk density and the packed or tapped bulk density is sometimes referred to as compressibility. This is actually the compression due to rearrangement of the particles. Thus, it would be better to refer to this property as rearrangement compressibility. When the rearrangement compressibility is large, this indicates that the material is prone to packing in storage. This can result in discharge problems. The difference between free-flowing and non-free-flowing is said to occur at a rearrangement compressibility of approximately 20% [1]. Other workers [2] put the boundary between free-flowing and non-free-flowing at an angle of repose of about 45°, with the non-free-flowing material having an angle repose of more than 45° and the free-flowing materials an angle of repose less than 45°. The angle of repose is the included angle formed between the side of a cone-shaped pile of material and the horizontal plane; see Fig. 6.3.

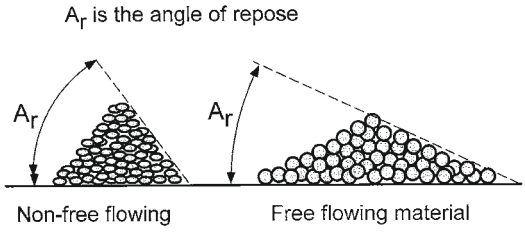


Figure 6.3
Angle of repose

The above-mentioned boundaries between free-flowing and non-free-flowing are only approximate indicators. They are used because of their simplicity and ease of measurement. However, neither rearrangement compressibility nor the angle of repose are true measures of the flowability of particulate materials. Free-flowing materials are also referred to as non-cohesive materials and non-free-flowing materials as cohesive materials. The shear stress at incipient internal shear deformation in non-cohesive materials can be uniquely related to the normal stress. Consequently, the coefficient of cohesion (see Eq. 6.6) is zero for non-cohesive particulate materials.

When the rearrangement compressibility is about 40%, the material will have a very strong tendency to pack in the feed hopper, and the chance of discharge problems will be very high. The tendency towards packing can be assessed in a qualitative fashion by the hand squeeze test. Material is squeezed in the hand, and the condition of the material is observed after squeezing. If the material has formed a hard

clump that cannot be easily broken up, this indicates a moderately compressible material. If the material does not clump at all but flows after squeezing, this indicates a low compressibility and a relatively free-flowing material.

Many investigators have studied the compression characteristics of bulk materials [3–14]; a number of these studies have dealt with polymeric bulk materials. The compaction process is quite complicated for a number of reasons. The distribution of stresses in the material during compaction is rather complex and depends very much on the geometry and surface conditions of the compression apparatus and the detailed characteristics of the bulk material. The effect of pressure on bulk density is often described by an empirical relationship:

$$\zeta = \zeta_0 \exp(-\chi P) \tag{6.1}$$

where ζ is the porosity, ζ_0 the porosity at zero pressure, P the pressure, and χ the compressibility coefficient.

It should be realized that Eq. 6.1 is an approximate relationship. The actual compaction behavior will depend strongly on the details of the compaction apparatus and the compacting procedures and conditions.

6.1.2 Coefficient of Friction

The coefficient of friction of the bulk material is another very important property. One can distinguish both internal and external coefficient of friction. The internal coefficient of friction is a measure of the resistance present when one layer of particles slides over another layer of particles of the same material. The external coefficient of friction is a measure of the resistance present at an interface between the polymeric particles and a wall of a different material of construction. The coefficient of friction is simply the ratio of the shear stress at the interface to the normal stress at the interface. Friction itself is the tangential resistance offered to the sliding of one solid over another.

In discussing the coefficient of friction, one has to specify whether it is a static or dynamic coefficient of friction. The static coefficient of friction, f*, is determined by

$$f^* = \frac{\tau_{ij}^*}{\tau_{ii}} \tag{6.2}$$

where τ_{ij}^* is the maximum shear stress just before sliding occurs and τ_{ii} is the corresponding normal stress.

The dynamic coefficient of friction f is determined by

$$f = \frac{\tau_{ij}}{\tau_{ii}} \tag{6.3}$$

where τ_{ij} is the actual shear stress during sliding motion and τ_{ii} is the corresponding normal stress.

A common way to determine the static coefficient (external) is the measurement of the angle of slide. The object is put on a surface and the angle of the surface with the horizontal plane is increased until the object just begins to slide. The angle that corresponds to the onset of sliding is the slide angle and the coefficient of static friction equals the tangent of the angle of slide. Thus,

$$f^* = \tan\beta_s \tag{6.4}$$

where f^* is the external coefficient of static friction and β_s the angle of slide.

Bowden and Tabor [23] attributed friction to two factors, one factor being the adhesion that occurs at the regions of real contact. The actual area of contact is several orders (about four) of magnitude smaller than the apparent contact area. If sliding is to take place, the local regions of adhesion have to be sheared. The second factor is the plowing, grooving, or cracking of one surface by the asperities of the other. In static friction, the only factor of importance is the adhesion at the contact sites. In dynamic friction, the plowing factor starts to play a role whereas the adhesion factor reduces in significance.

Measurement of the external coefficient of friction of particulate polymers is very difficult because of the very large number of variables that influence the coefficient of friction. Many investigators have made elaborate measurements on the external coefficient of friction [24–32]. The result of this work is that many variables have been identified that affect the frictional behavior; however, most measurement techniques do not yield accurate and reproducible results that can be used in the analysis of the extrusion process. The most elaborate measurements and the most meaningful results have probably been obtained at the DKI in Darmstadt, Germany [95]. It is possible to obtain reproducible results by very careful experimental techniques and special surface preparation of the metal wall. However, the frictional coefficients determined in this fashion are hardly representative of the frictional process conditions occurring in an extruder.

Some of the variables that affect the coefficient of friction are temperature, sliding speed, contact pressure, metal surface conditions, particle size of polymer, degree of compaction, time, relative humidity, polymer hardness, etc.

The coefficient of friction is very sensitive to the condition of the metal surface. The coefficient of friction of a polymer against an entirely clean metal surface is very low initially, as low as 0.05 or less. However, after the polymer has been sliding on the surface for some time, the coefficient of friction will increase substantially and may stabilize at a value about an order of magnitude higher than the initial value. This behavior was described in detail by Schneider [24, 25] for a variety of polymers. This effect is attributed to the transfer of polymer to the metal surface. Instead of

pure polymer-metal friction, the actual situation is a polymer-metal/polymer friction. It has also been found that the measured coefficient of friction is changed if the metal surface is accidentally touched by hand. The finger greases actually change the metal surface conditions and the resulting coefficient of friction. The unavailability of accurate and appropriate data on coefficient of friction is one of the main stumbling blocks in being able to accurately predict extruder performance. Predictions of the solids conveying rate and pressure development from theory are very sensitive to the actual values of the coefficient of friction; e. g. see Fig. 7.16. Thus, for accurate prediction, the coefficient of friction should be known to at least a one percent accuracy; however, this is usually not feasible.

A comprehensive survey of the work on polymer friction was put together by Bartenev and Lavrentev [32]. An exhaustive study on frictional properties was undertaken at the DKI (Deutsches Kunststoff-Institut) in Darmstadt, Germany, sponsored by the VDMA (Verband Deutscher Maschinen- und Anlagenbau). The data was compiled in a book [95] that contains frictional properties of 27 different polymers, with the coefficient of friction given as a function of temperature, sliding velocity, and normal pressure. The measurements were made on the universal disk-Tribometer (see Section 11.2.1.2, Fig. 11.9), using conditions that closely resemble the friction process in a screw extruder. This publication is probably the most complete compilation of frictional properties determined under controlled and meaningful conditions with good reproducibility (better than 10%).

A typical plot of external coefficient of friction versus temperature at various pressures is shown in Fig. 6.4(a).

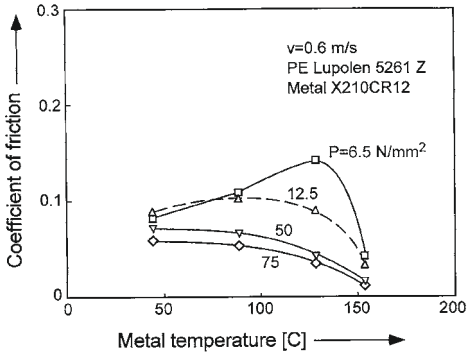


Figure 6.4(a)
Coefficient of friction versus temperature

The material is polyethylene (Lupolen 5261 Z) and the sliding velocity is 0.60 m/s. At low pressures, the coefficient of friction increases with temperature, reaches a peak at the melting point, and then starts to drop rapidly. At high pressures, the coefficient of friction drops monotonically with temperature.

If the transport of particulate polymer occurs by plug flow, then the only frictional coefficient of importance is the external coefficient of friction. This condition is usu-

ally assumed in the solids conveying zone of an extruder with a smooth barrel surface. However, if there is any internal deformation occurring within the particulate material, the internal coefficient of friction will also start to play a role of importance. This is the case when one analyzes the flow of material through a feed hopper or in the solids conveying zone of an extruder when the barrel surface is grooved at the feed section or when the channel is not fully filled so that no pressure increase and no compacting can take place.

The flowability of a particulate material is determined by its shear properties. When internal shear deformation is just about to occur, the local shear stress is called the shear strength. The shear strength is a function of the normal stress; this functional relationship is referred to as the yield locus (YL). For a free-flowing material, the yield locus under fully mobilized friction conditions is

$$\tau = f_i^* \sigma = \tan\beta_i \sigma \tag{6.5}$$

where f_i^* is the internal static coefficient of friction, β_i the angle of internal friction ($\beta_i = \arctan f_i^*$), τ the shear strength, and σ the normal stress.

The shear strength of non-free-flowing (cohesive) materials is not a unique function of the normal stress. The shear strength of these materials increases with pressure. The YL is a function of consolidation pressure and consolidation time. Thus, the shear strength has to be described by a series of yield loci, each curve representing a certain consolidation pressure and time. These curves can often be described by:

$$\tau = (\sigma + \sigma_a)\tan\beta_i = \tau_c + \sigma \tan\beta_i \tag{6.6}$$

where σ_a is an apparent tensile strength, which is obtained by extrapolating the yield locus to zero shear stress; see Fig. 6.4(b).

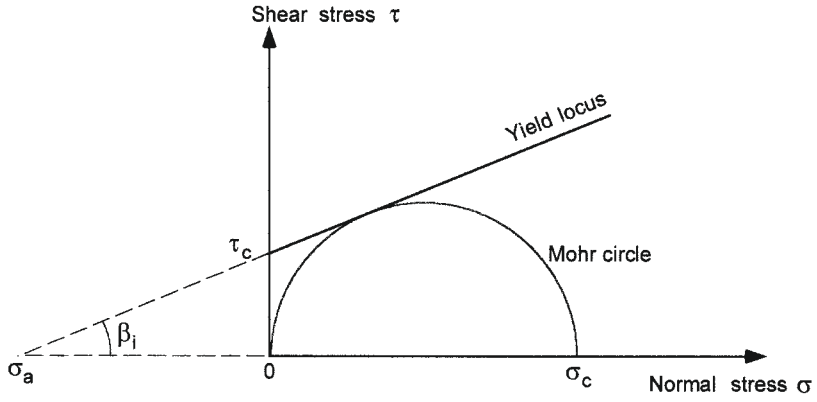


Figure 6.4(b) Unconfined yield strength of a cohesive material

The actual tensile strength is usually less than the apparent tensile strength. The value of the shear stress at zero normal stress is often referred to as the coefficient of cohesion $\tau_c = \sigma_a \tan\beta_i$. This coefficient is a measure of the magnitude of the cohesive forces in the particulate material that must be overcome for internal shearing to occur.

In a state of incipient failure, the yield locus is tangent to the Mohr circle. The Mohr circle graphically represents the equilibrium stress condition at a particular point at any orientation for a system in a condition of static equilibrium in a two-dimensional stress field. The equilibrium static conditions can also be applied to sufficiently slow steady flows. The maximum principal stress σ_c in Fig. 6.4(b) is called the unconfined yield strength. This is the maximum normal stress, under incipient failure conditions, at a point where the other principal stress becomes zero. Such a situation occurs on the exposed surface of an arch or dome in a feed hopper at the moment of failure; see Fig. 7.5(b). In the analysis of bridging in feed hoppers, the unconfined yield strength becomes a very important parameter. The magnitude of the unconfined yield strength is determined by the YL and depends, therefore, on the consolidation pressure and time.

The principal stresses in cohesive materials can be related by:

$$\sigma_{max} = \frac{1+\sin\beta_i}{1-\sin\beta_i}\sigma_{min} + \sigma_C \tag{6.7}$$

where σ_{max} is the maximum normal stress and σ_{min} the minimum normal stress.

For a cohesive particulate material, each YL curve ends at a point where the normal stress equals the consolidation pressure. Mohr circles can now be drawn that are tangent to the end point of the various yield loci. The envelope of these circles is called the effective yield locus (EYL). This is generally a straight line passing through the origin; see Fig. 6.5.

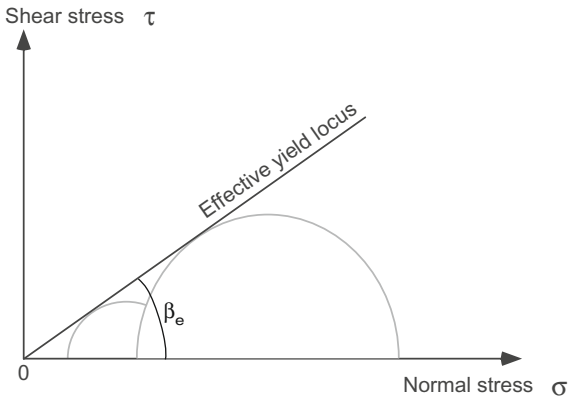


Figure 6.5
Effective yield locus

The angle between the EYL and the normal stress axis is called the effective angle of friction, β_e. The EYL describes the shear stress-normal stress characteristics of a particulate material that is consolidated and being sheared under the same stress conditions. This applies directly to a steady flow situation because, in this case, shearing takes place throughout the particulate material. The Mohr circle describing the stress condition at any point must be tangent to the EYL. When the stress field is such that the Mohr circle describing the stress field is below the EYL, no shearing flow will occur. The effective yield locus for a non-cohesive material will coincide with the yield locus. Thus, the effective angle of friction will equal the internal angle of friction ($\beta_e = \beta_i$ for a non-cohesive material).

A shearing cell was developed by Jenike [42] to measure shear properties of particulate solids; see Fig. 6.6.

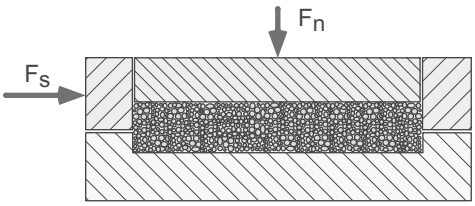


Figure 6.6
The shearing cell developed by Jenike [42]

In addition to the determination of the various YL curves and the EYL, the shearing cell can also be used to measure the YL curve between the particulate solids and the confining wall. This is referred to as the wall yield locus (WYL), and it generally lies considerably below the YL. If the WYL is a straight line, it can be described by:

$$\tau_w = \tau_{wa} + \sigma_w \tan\beta_w = \tau_{wa} + f_w^* \sigma_w \tag{6.8}$$

where β_w is the wall angle of friction, f_w^* the static coefficient of friction at the wall ($f_w^* = \tan\beta_w$), τ_w the shear stress at the wall, and τ_{wa} the adhesive shear stress at the wall.

Rautenbach and Goldacker [43, 44] described an apparatus developed to measure the internal frictional properties of particulate solids under steady shear. They found that after exceeding the shear strength, the deformation occurred in one or more discrete shear planes. The thickness of these planes was in the order of only a few particle diameters. Thus, they did not observe the development of a continuous velocity gradient throughout the material. These observations were made with non-cohesive polymeric powders. Based on these observations, a dynamic internal coefficient of friction f_i was defined, representing the ratio of steady shear stress to steady normal stress. It was found that the dynamic internal coefficient of friction was independent of velocity and pressure, slightly dependent on temperature and particle size, and strongly dependent on particle shape. In all cases, the dynamic internal coefficient of friction was much higher (about five times) than the dynamic

external coefficient of friction. The dynamic angle of internal friction (φ_i = arctan f_i) was found to relate reasonably well with the angle of repose β_r according to the expression:

$$\varphi_i \cong 0.75\beta_r \tag{6.9}$$

This expression is empirical and should only be used to estimate the approximate value of φ_i.

6.1.3 Particle Size and Shape

The range of polymeric particles used in extrusion is quite wide, from about 1 micron to about 10 mm. Figure 6.7 shows the nomenclature generally used to describe particulate solids of a certain particle size range.

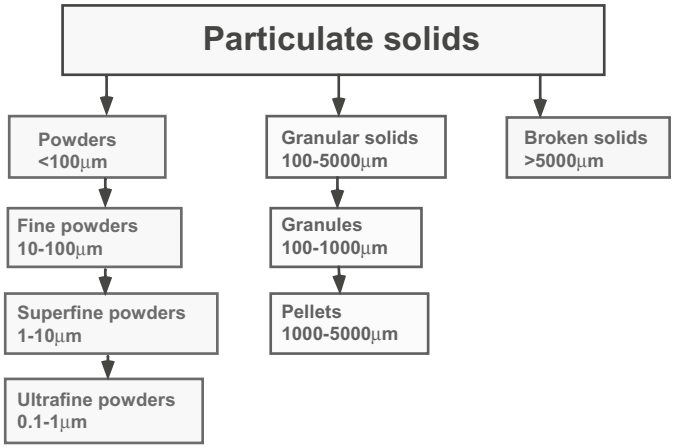


Figure 6.7 Nomenclature in particulate materials

Particle size can be determined by a variety of techniques, microscopic measurement being one of the most common techniques. If the particles have a considerable particle size distribution, one would like to measure this distribution. In this case, microscopic measurement becomes very time consuming, unless it is tied in to an automatic or semi-automatic image analyzer that can generate the distribution curve. Sieving is a simple and popular technique; however, particles should be larger than about 50 micron. Values obtained by sieving of non-spherical particles must be modified to conform with those obtained by methods that yield data on equivalent spherical diameter (esd). The esd is the diameter of a sphere having the same volume as the non-spherical particle. Sedimentation methods are used for particles less than 50 micron. Light transmission or scattering is another method used for particle size measurement.

Other important parameters in particle analysis are surface area, pore size, and volume. The basic method for measuring surface area involves determining the quantity of an inert gas, usually nitrogen, required to form a layer one molecule thick on the surface of a sample at cryogenic temperature. Many techniques are used for pore size measurement: impregnation with molten metal, particle beam transmission, water absorption, freezing point depression, microscopy, mercury intrusion, and gas condensation and evaporation. The last three techniques are most often utilized.

The particle shape can generally be established by simple visual observation or by using a microscope. The transport characteristics of particulate solids are quite sensitive to the particle shape. Both the internal and external coefficient of friction can change substantially with variations in particle shape even if the major particle dimensions remain unchanged. Small differences in the pelletizing process can cause major problems in a downstream extrusion process. Variations in the ratio of regrind to virgin polymer can cause variations in the extrusion process.

The ease of solids transport is often determined by the particle size. Pellets are generally free-flowing and do not have a strong tendency to entrap air. From a solids conveying point of view, pelletized materials are the easiest to work with. Granules are often free-flowing, sometimes semi-free-flowing; they are more likely to entrap air. Semi-free-flowing granules may require special feeding devices (such as a vibrating pad on the hopper) to ensure steady flow. Powders tend to be cohesive and also tend to entrap air. Therefore, in most cases, special precautions have to be taken to successfully extrude powder material. The degree of difficulty in extrusion of powders generally increases with reducing particle size. Broken solids usually consist of fiber or film scrap. The particles are generally of irregular shape and the bulk density is often very low. This type of particulate solid is also problematic from a solids conveying point of view, because the particles tend to interlock and resist vibration. Static build-up can also be a problem in these materials; this can be solved by the use of a static eliminator.

6.1.4 Other Properties

A variety of other properties can affect the conveying characteristics of the bulk material. Hygroscopic materials tend to absorb moisture; this may cause agglomeration and reduce the flowability of the material. Additives that act as external lubricants can change the frictional characteristics and adversely affect the solids transport in the extruder.

6.2 Melt Flow Properties

Knowledge of the flow properties of the polymer melt is very important in the analysis of the extrusion process. The first traces of melt generally appear only a few diameters from the feed opening of the extruder. The metering end of the extruder is, in many cases, completely filled with polymer melt. The polymer melt flow properties determine to a large extent the characteristics of the extrusion process. Knowledge of the melt flow properties allows accurate optimization of the screw design and the process operating conditions. If the melt flow properties are not known, the selection of the extruder screw and the determination of the process operating conditions becomes a trial and error process at best.

6.2.1 Basic Definitions

Before going into detail on the flow behavior of polymer melts, it may be useful to describe and define some of the basic terminology used in fluid flow.

Drag Flow: Flow caused by the relative motion of one or more boundaries with respect to the other boundaries that contain the fluid.

This is also referred to as Couette flow, although Couette flow is only a specific type of drag flow. Drag flow is important in extrusion. The two major boundaries that contain the polymer in the extruder are the barrel surface and the screw surface. Since the screw is rotating in a stationary barrel, one boundary is moving relative to the other; this causes drag flow to occur.

Pressure Flow: Flow caused by the presence of pressure gradients in the fluid; in other words, local differences in the pressure.

One of the most common examples of pressure flow (pressure-driven flow) is the flow of water that occurs when one opens a water faucet. This flow occurs because the pressure upstream is higher than the pressure at the faucet. There is no relative motion of the fluid boundaries (wall of the water pipe); thus, this is pure pressure flow. In most extruder dies, the flow through is a pure pressure-driven flow. The polymer melt flows through the die as a result of the fact that the pressure at the die inlet is higher than the pressure at the outlet. The flow rate is determined by the pressure at the die inlet, often referred to as diehead pressure. In some extruder dies, the polymer coats a part that moves through the die, e. g., a wire coating die. In such a die, the flow is not a pure pressure flow but a combination of drag flow (as a result of the moving wire) and pressure flow (as a result of the diehead pressure).

Shear: Occurrence of velocity differences in a direction normal to flow.

A fluid is sheared when velocity differences in normal direction occur in the fluid, as shown in Fig. 6.8.

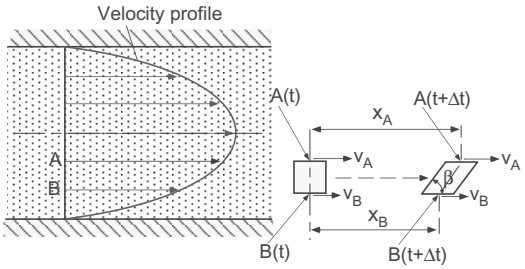


Figure 6.8
Shearing of a fluid in flow through a pipe

Elongation: Occurrence of velocity differences in the direction of flow.

Elongational deformation of a fluid occurs when the velocity changes in the direction of flow, as shown in Fig. 6.9.

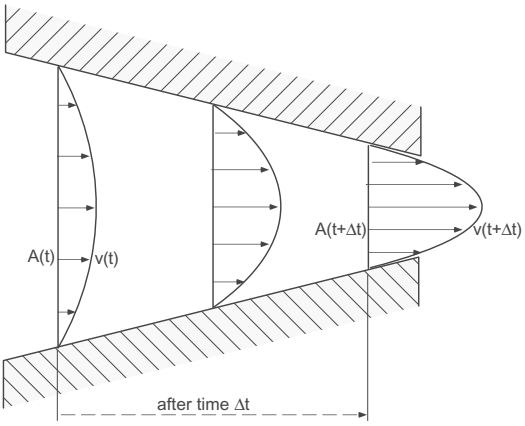


Figure 6.9
Elongational flow in a converging flow channel

Plug Flow: A flow situation where all fluid elements move at the same velocity, i. e., flow without shear.

Plug flow generally does not happen in polymer melts, except in the case of wall slip (PVC). However, it does occur with granular polymeric solids. The solids conveying theory of single screw extruders is based on the assumption of plug flow of the solid polymer.

Shear Rate ($\dot{\gamma}$): The difference in velocity per unit normal distance (normal to the direction of flow).

The rate of shearing or shear rate is one of the most important parameters in polymer melt processing. If the process is to be described quantitatively, the shear rate in the fluid at any location needs to be known. The shear rate is generally written with the Greek letter gamma, $\dot{\gamma}$, with the dot above the gamma indicating a time derivate $\left(\dot{\gamma} = \frac{d\gamma}{dt}\right)$. In terms of Fig. 6.8, the shear rate between points A and B can be approximated as:

$$\dot{\gamma}_{AB} \cong \frac{v_A - v_B}{AB} \tag{6.10}$$

Equation 6.10 is only valid for very small values of the normal distance AB. More accurately, the shear rate is:

$$\dot{\gamma}_{AB} = \lim \frac{v_A - v_B}{AB}\Bigg|_{AB \to 0} = \frac{dv(y)}{dy} \tag{6.11}$$

From Eq. 6.11, it can be seen that the local shear rate equals the local gradient of the velocity profile. Thus, if the velocity profile is known, the shear rate at any location can be determined.

Shear Strain (γ): Displacement (in the direction of flow) per unit normal distance over a certain time period.

The shear strain is generally written with the Greek letter gamma (γ), this time without the dot! The relationship between shear rate ($\dot{\gamma}$) and shear strain (γ) is:

$$\dot{\gamma} = \frac{d\gamma}{dt} \quad \text{and} \quad \gamma = \int \dot{\gamma} dt \tag{6.12}$$

In terms of Fig. 6.8, the shear strain can be written as:

$$\gamma_{AB} \cong \frac{x_A - x_B}{AB} = \frac{\Delta x}{\Delta y}\Bigg|_{AB} = \cot\beta \tag{6.13}$$

The units of shear rate are s^{-1} and the shear strain is a dimensionless number.

Shear Stress (τ): The stress required to achieve a shearing type of deformation.

When a fluid is sheared, a certain force will be required to bring about that deformation. This force divided by the area over which it works is the shear stress. The shear stress is generally written with the Greek letter tau (τ). In a simple example, shown in Fig. 6.10, the shear stress is:

$$\tau = \frac{F}{A} \tag{6.14}$$

and the shear rate is:

$$\dot{\gamma} = \frac{v}{\Delta y} \tag{6.15}$$

Shear Viscosity (η_s): The resistance to shear flow. Quantitatively, the shear viscosity is determined from the ratio of shear stress and shear rate.

$$\eta_s = \frac{\tau}{\dot{\gamma}} \tag{6.16a}$$

The shear viscosity is generally written with the Greek letter eta (η); the units of viscosity are stress x time. The viscosity is usually expressed in Poise (= dyne-s/cm²) or Pa·s (= 10 Poise). In order to determine the shear viscosity of a fluid, one has to determine the shear rate in a certain shear deformation and the corresponding shear stress. Special instruments are available to determine the viscosity of polymer melts; these are referred to as rheometers.

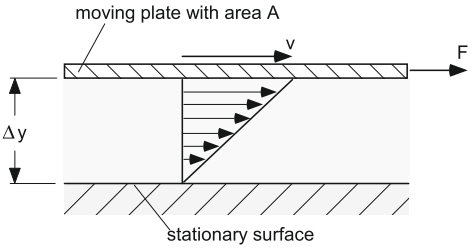


Figure 6.10
Simple shear deformation

Elongational Viscosity (η_e): The resistance to elongational flow. Quantitatively, the elongational viscosity is determined from the ratio of elongational stress and elongation rate.

$$\eta_e = \frac{\sigma}{\varepsilon} \tag{6.16b}$$

The elongational viscosity is substantially higher than the shear viscosity. It is at least three times higher than the shear viscosity but in many cases much higher.

Newtonian Fluid: A fluid whose viscosity is *in*dependent of the shear rate.

Most low viscosity liquids and gases behave as a Newtonian fluid. In a plot of shear stress versus shear rate, a Newtonian fluid will exhibit a linear relationship; see Fig. 6.11, curve b. Therefore, Newtonian fluids are also referred to as linear fluids.

A plot of shear stress versus shear rate is generally referred to as a "flow curve."

Non-Newtonian Fluid: A fluid whose viscosity is *de*pendent on the shear rate.

High viscosity polymer melts behave as non-Newtonian fluids, with the viscosity reducing with increase shear rate.

Another type of non-Newtonian fluid is a dilatant fluid. The viscosity of a dilatant fluid increases with increasing shear rate; see Fig. 6.11, curve a.

The reduction of viscosity with increasing shear rate is called pseudo-plastic behavior; see Fig. 6.11, curve c. The shear stress-shear rate relationship of non-Newtonian fluids is non-linear. Therefore, non-Newtonian fluids are also referred to as non-linear fluids.

The concepts of shear rate, shear stress, and viscosity are extremely important in developing a thorough understanding of the extrusion process (and other polymer processing operations). Therefore, a few examples will be given to illustrate how shear rate and shear stress can be determined in simple geometries.

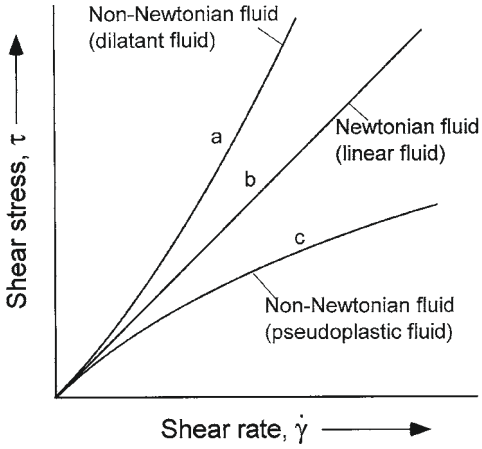


Figure 6.11
Flow curves of a dilatant fluid, a Newtonian fluid, and a pseudo-plastic fluid

Example: Co-axial Cylinders; see Fig. 6.12.

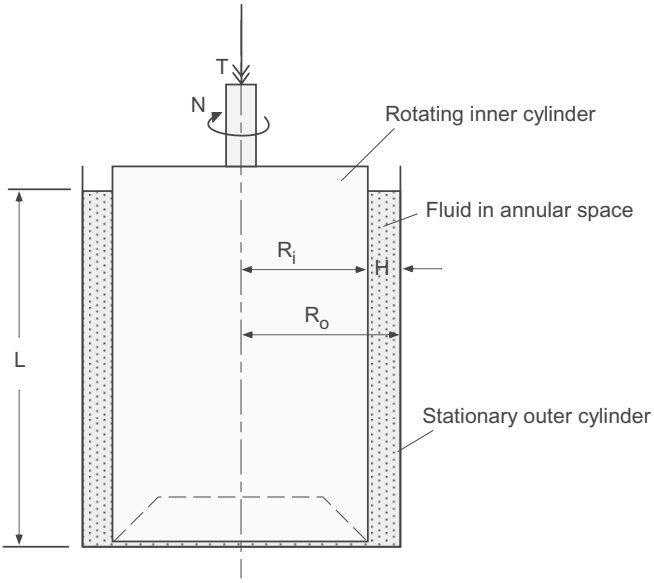


Figure 6.12
Co-axial cylinders:
outer cylinder stationary,
inner cylinder rotating

The fluid is contained in the annular space, with one boundary formed by the inner cylinder and the other boundary formed by the outer cylinder. Since the inner boundary is moving with respect to the outer boundary, a drag flow will be set up in the fluid and the fluid will be sheared. The shear rate in the fluid will be the difference in velocity divided over the normal distance. Thus,

$$\dot{\gamma} \cong \frac{v_o - v_i}{R_o - R_i} = \frac{2\pi R_i N}{H} \tag{6.17}$$

This expression is reasonably accurate as long as the radial clearance (H) is small relative to the radius. The shear rate equals the circumferential velocity of the inner cylinder (velocity of the outer cylinder is zero, $v_o = 0$) divided by the radial clearance. Thus, if the geometry and rotational speed are known, the shear rate can be directly determined from that information. The shear rate will be high when the diameter of the inner cylinder is large, when the rotational speed is high, or when the radial clearance is small.

The shear stress acting on the fluid is obtained from the torque T that is necessary to rotate the inner cylinder. The total shear force F acting on the inner cylinder is the shear stress τ multiplied with the area of the inner cylinder ($2\pi R_i L$):

$$F = \frac{T}{R_i} = 2\pi R_i L \tau \tag{6.18}$$

Thus, the shear stress is:

$$\tau = \frac{T}{2\pi R_i^2 L} \tag{6.19}$$

Measurement of the torque, therefore, allows the determination of the shear stress. The shear viscosity can now be determined as well:

$$\eta = \frac{\tau}{\dot{\gamma}} = \frac{TH}{4\pi^2 R_i^3 LN} \tag{6.20}$$

The co-axial cylinder geometry can thus be used to determine the viscosity of a fluid. In practice, this geometry is mostly used to determine flow properties of low viscosity liquids.

Example: Screw Extruder; see Fig. 6.13.

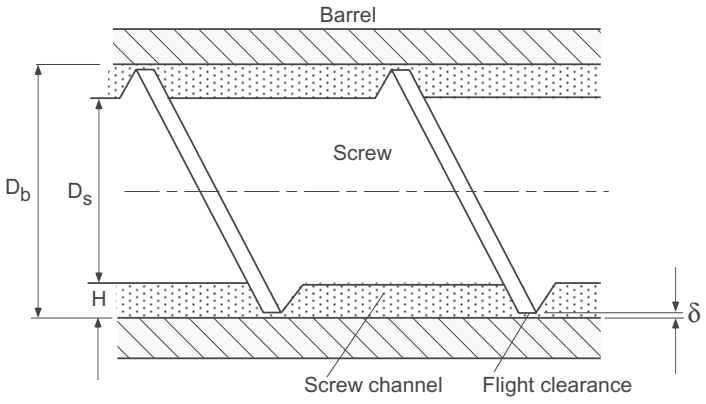


Figure 6.13
The screw extruder

The geometry of a screw extruder is quite similar to the c-oaxial cylinder set-up. The difference is the presence of the helical flight wrapped around the core of the screw. It is often assumed that the screw root and barrel surfaces can be approximated by flat plates – this is called the flat plate approximation. With this approximation the shear rate in the screw channel is:

$$\dot{\gamma}_{ch} \cong \frac{\pi(D-2H)N}{H} = \pi N\left(\frac{D}{H}-2\right) \tag{6.21a}$$

where D is the O.D. of the screw, H the channel depth, and N the rotational speed of the screw in rev/s.

In most analyses of flow in screw extruders using the flat plate system (FPS) it is assumed that the barrel rotates relative to a stationary screw. This actually yields more accurate results than moving the screw relative to a stationary barrel; this will be discussed in more detail in Section 7.4.3.4. When the barrel moves relative to a stationary screw the shear rate becomes:

$$\dot{\gamma}_{ch} \cong \frac{\pi DN}{H} \tag{6.21b}$$

The approximately equal sign (≅) is used because Eqs. 6.21(a) and 6.21(b) are based on the FPS and neglect the effect of curvature. For a more accurate analysis one has to use cylindrical or helical coordinates; this will be discussed in Section 7.4. Equation 6.21 is essentially the same expression as found for the co-axial cylinder problem, Eq. 6.17. The polymer melt between the screw flight and the barrel is exposed to a different shear rate:

$$\dot{\gamma}_{cl} \cong \frac{\pi DN}{\delta} \tag{6.22}$$

The channel depth H is, in most cases, much larger than the radial flight clearance δ. Therefore, the shear rate in the clearance will be much higher than the shear rate in the screw channel. A typical value of D/H is 20 and a typical value of D/δ is 1000. Thus, the shear rate in the flight clearance will be approximately 50 times higher than the shear rate in the screw channel. This has important implications for the operation of the extruder, as will be discussed in more detail in the next two chapters.

6.2.2 Power Law Fluid

In the previous section, it was discussed that polymer melts are pseudo-plastic fluids. The fact that the polymer melt viscosity reduces with shear rate is of great importance in the extrusion process. It is, therefore, important to know the extent of

change that will occur in a particular polymer. The general shape of the viscosity-shear rate curve for a pseudo-plastic polymer melt will look as shown in Fig. 6.14.

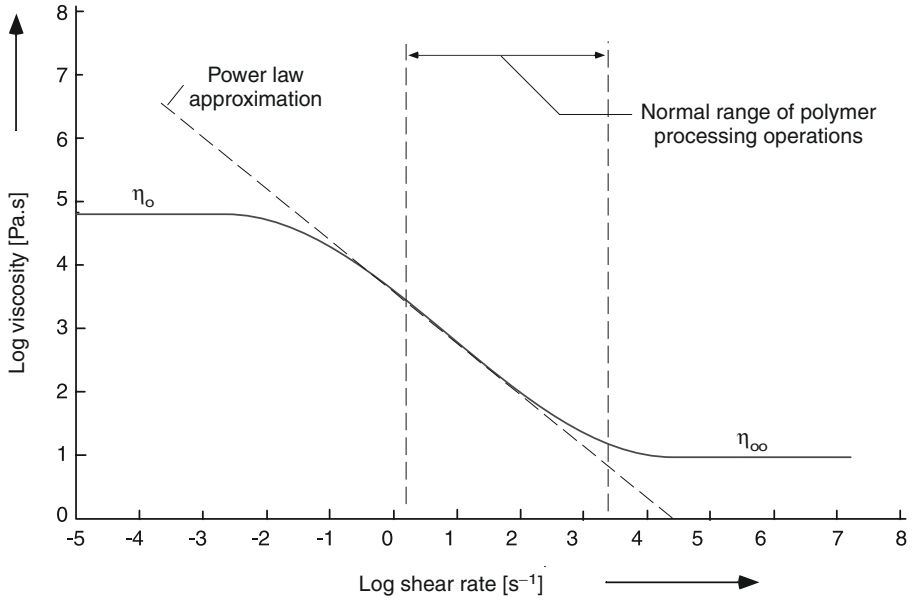


Figure 6.14 General pseudo-plastic behavior

The viscosity at very low shear rates is essentially independent of shear rate. Thus, the fluid behaves as a Newtonian fluid at low shear rates. The low shear rate plateau value η_0 is often referred to as the low shear limiting Newtonian viscosity. The high shear rate plateau value η_∞ is often referred to as the high shear limiting Newtonian viscosity. This value is difficult to determine experimentally because the effects of pressure and temperature become very pronounced at these high shear rates (over 10^6 s^{-1}).

The range of shear rates encountered in most polymer processing operations is approximately 1 to 10,000 s^{-1}. It can be seen in Fig. 6.14 that within this range the viscosity-shear rate curve can be reasonably approximated with a straight-line relationship. This is true for most polymers. It should also be noted that Fig. 6.14 uses a double logarithmic scale. The log-log scale is convenient because the viscosity changes about 4 to 5 orders of magnitude over more than 10 orders of magnitude change in shear rate. A straight-line relationship on a log-log plot indicates that the variables can be related by a power law equation. This is generally written as:

$$\eta = m\,\dot{\gamma}^{n-1} \quad \text{or} \quad \tau = m\,\dot{\gamma}^{n} \tag{6.23}$$

where m is the consistency index and n the power law index. This law is often referred to as the power law of Ostwald and de Waele [15, 16]. The power law index

indicates how rapidly the viscosity reduces with shear rate. For pseudo-plastic fluids, the power law index ranges from 1 to 0. When the power law index is unity, the fluid is Newtonian and the consistency index becomes the Newtonian viscosity. The power law index indicates the degree of non-Newtonian behavior. If the power law index ranges from 0.8 to 1.0, the fluid is almost Newtonian. If the power law index is less than 0.5, the fluid is strongly non-Newtonian. It turns out that most large volume commodity polymers fall into this latter category, e. g., polyethylene, polyvinylchloride, polystyrene, styrene acrylonitrile, acrylonitrile butadiene styrene, etc. Examples of polymers with a relatively high power law index are polycarbonate, polyamide, polyethylene terephthalate, polysulfone, and polyphenylene sulphide. The approximate power law index for a number of polymers is shown in Table 6.1 at the end of this chapter.

Equation 6.23 can be used if the shear rate is positive throughout the flow channel being considered. If the shear rate changes sign at some point in the flow channel, a more general power law equation should be used:

$$\tau = m \left| \dot{\gamma} \right|^{n-1} \dot{\gamma} \tag{6.24a}$$

Another form of the power law equation that is used quite often is:

$$\dot{\gamma} = \varphi \left| \tau \right|^{s-1} \tau \tag{6.24b}$$

where φ is the specific fluidity and s the pseudo-plasticity index. The pseudo-plasticity index s is the reciprocal of the power law index n = 1/s. The specific fluidity φ is related to the consistency index by:

$$\varphi = m^{-1/n} = m^{-s} \tag{6.24c}$$

Power law equations (Eqs. 6.23–6.24) can be used to describe simple viscometric flow, i. e., flow with velocity components in only one direction. For more complicated flow situations, a more general power law expression should be used. In order to do this, the rate of deformation tensor Δ_{ij} has to be introduced. The components of Δ_{ij} in Cartesian coordinates are:

$$\Delta_{xx} = 2\frac{\partial v_x}{\partial x} \qquad \Delta_{xy} = \Delta_{yx} = \frac{\partial v_x}{\partial y} + \frac{\partial v_y}{\partial x} \tag{6.25a}$$

$$\Delta_{yy} = 2\frac{\partial v_y}{\partial y} \qquad \Delta_{xz} = \Delta_{zx} = \frac{\partial v_x}{\partial z} + \frac{\partial v_z}{\partial x} \tag{6.25b}$$

$$\Delta_{zz} = 2\frac{\partial v_z}{\partial z} \qquad \Delta_{yz} = \Delta_{zy} = \frac{\partial v_y}{\partial z} + \frac{\partial v_z}{\partial y} \tag{6.25c}$$

The components of Δ_{ij} in cylindrical coordinates are:

$$\Delta_{rr} = 2\frac{\partial v_z}{\partial r} \qquad \Delta_{r\theta} = \Delta_{\theta r} = r\frac{\partial}{\partial r}\left(\frac{v_\theta}{r}\right) + \frac{1}{r}\frac{\partial v_r}{\partial \theta} \tag{6.25d}$$

$$\Delta_{\theta\theta} = 2\left(\frac{1}{r}\frac{\partial v_\theta}{\partial \theta} + \frac{v_r}{r}\right) \qquad \Delta_{\theta z} = \Delta_{z\theta} = \frac{\partial v_\theta}{\partial z} + \frac{1}{r}\frac{\partial v_z}{\partial \theta} \tag{6.25e}$$

$$\Delta_{zz} = 2\frac{\partial v_z}{\partial z} \qquad \Delta_{zr} = \Delta_{rz} = \frac{\partial v_z}{\partial r} + \frac{\partial v_r}{\partial z} \tag{6.25f}$$

Because the viscosity is a scalar, it can be a function only of the scalar invariants of the rate of deformation tensor. There are three combinations of the components of the rate of deformation tensor (Δ_{ij}), which are scalar invariants. They define any state of deformation rate independently of the coordinate system. They are referred to as the principal invariants of the rate of deformation tensor:

$$I_1 = \Delta_{ii} \tag{6.26a}$$

$$I_2 = \Delta_{ij}\,\Delta_{ij} \tag{6.26b}$$

$$I_3 = \det \Delta \tag{6.26c}$$

where "det" means the determinant of the enclosed matrix.

Equation 6.26 uses the summation convention on repeated subscripts.

In Cartesian coordinates:

$$I_1 = \Delta_{xx} + \Delta_{yy} + \Delta_{zz} \tag{6.27a}$$

$$I_2 = \Delta_{xx}^2 + \Delta_{yy}^2 + \Delta_{zz}^2 + 2\Delta_{xy}^2 + 2\Delta_{xz}^2 + 2\Delta_{yz}^2 \tag{6.27b}$$

$$I_3 = \begin{vmatrix} \Delta_{xx} & \Delta_{xy} & \Delta_{xz} \\ \Delta_{yx} & \Delta_{yy} & \Delta_{yz} \\ \Delta_{zx} & \Delta_{zy} & \Delta_{zz} \end{vmatrix} \tag{6.27c}$$

If a fluid can be considered incompressible, the first principal invariant of the rate of deformation tensor will be zero, $I_1 = 0$. The third principal invariant vanishes in many simple flow situations, like axial flow in pipe, tangential flow between concentric cylinders, etc. In more general terms, the third invariant is zero in rectilinear flow and in two-dimensional flow.

The power law expression can now be written in general terms:

$$\tau_{ij} = \left(m\left|\sqrt{0.5I_2}\right|^{n-1}\right)\Delta_{ij} \tag{6.28}$$

In Cartesian coordinates, $0.5I_2$ is obtained by using Eqs. 6.27(b) and 6.25.

$$0.5I_2 = 2\left(\frac{\partial v_x}{\partial x}\right)^2 + 2\left(\frac{\partial v_y}{\partial y}\right)^2 + 2\left(\frac{\partial v_z}{\partial z}\right)^2 + \left(\frac{\partial v_y}{\partial x} + \frac{\partial v_x}{\partial y}\right)^2 + \left(\frac{\partial v_z}{\partial y} + \frac{\partial v_y}{\partial z}\right)^2 + \left(\frac{\partial v_x}{\partial z} + \frac{\partial v_z}{\partial x}\right)^2 \tag{6.29}$$

Similarly, in cylindrical coordinates:

$$0.5I_2 = 2\left(\frac{\partial v_r}{\partial r}\right)^2 + 2\left(\frac{1}{r}\frac{\partial v_\theta}{\partial \theta} + \frac{v_r}{r}\right)^2 + 2\left(\frac{\partial v_z}{\partial z}\right)^2 + \left[r\frac{\partial}{\partial r}\left(\frac{v_\theta}{r}\right) + \frac{1}{r}\frac{\partial v_r}{\partial \theta}\right]^2 + \left(\frac{1}{r}\frac{\partial v_z}{\partial \theta} + \frac{\partial v_\theta}{\partial z}\right)^2 + \left(\frac{\partial v_r}{\partial z} + \frac{\partial v_z}{\partial r}\right)^2 \tag{6.30}$$

With these more general expressions (Eqs. 6.28–6.30), more complicated flow situations can be described, i. e., flow with velocity components in two or three directions. It should be remembered that the power law description is an approximation; it is not accurate over the entire range of shear rate. However, in most practical polymer processing problems, the use of the power law equation yields sufficiently accurate results. The major advantage of the power law equation is its simplicity, despite the appearance of Eqs. 6.28–6.30. The relationship between stress and rate of deformation can be described with only two fluid properties, the consistency index m and power law index n. A drawback of the power law is that it does not allow construction of a time constant from the constants m and n. This is a problem in the analysis of transient flow phenomena where a characteristic time constant is necessary to describe the flow situation.

The truncated power law of Spriggs [17] allows a more accurate description. It is written as:

$$\eta = \eta_0 \qquad \text{for} \quad \dot{\gamma} \le \dot{\gamma}_0 \tag{6.31a}$$

$$\eta = \eta_0 \left(\frac{\dot{\gamma}}{\dot{\gamma}_0}\right)^{n-1} \qquad \text{for} \quad \dot{\gamma} > \dot{\gamma}_0 \tag{6.31b}$$

In this model, there are three constants: a zero shear rate viscosity η_0, a characteristic time $1/\dot{\gamma}_0$, and a dimensionless power law index n. This model contains the horizontal asymptote for small $\dot{\gamma}$ and the power law for large $\dot{\gamma}$.

6.2.3 Other Fluid Models

The sinh law was proposed by Ehring [18] and can be written as:

$$\eta = t_0 \tau_0 \left(\frac{\operatorname{arcsinh} t_0 \dot{\gamma}}{t_0 \dot{\gamma}} \right) \tag{6.32}$$

where τ_0 is a characteristic stress and t_0 a characteristic time. Other workers have modified the Ehring model to improve its flexibility and accuracy in describing stress-deformation rate relationships:

$$\eta = t_0 \tau_0 \left(\frac{\operatorname{arcsinh} t_0 \dot{\gamma}}{t_0 \dot{\gamma}} \right)^{A_1} + A_2 \tag{6.33}$$

A polynomial relationship was proposed by Rabinowitsch and Weissenberg; it can be written as [20a]:

$$\dot{\gamma} = \alpha_1 \tau + \alpha_3 \tau^3 \tag{6.34}$$

where α_1 and α_3 are rheological constants depending on the nature of the fluid.

The Carreau model [19] has the useful properties of the truncated power law model but avoids the discontinuity in the first derivative; it can be written as:

$$\frac{\eta - \eta_\infty}{\eta_0 - \eta_\infty} = \left[1 + (\lambda \dot{\gamma})^2 \right]^{\frac{n-1}{2}} \tag{6.35}$$

where η_0 is the zero shear rate viscosity, η_∞ is the infinite shear rate viscosity, λ is a time constant, and n is the dimensionless power law index. The Ellis model [20b] describes the viscosity as a function of shear stress:

$$\frac{\eta_0}{\eta} = 1 + \left(\frac{\tau}{\tau_{1/2}} \right)^{\alpha - 1} \tag{6.36}$$

where η_0 is the zero shear rate viscosity, $\tau_{1/2}$ the value of the shear stress at which $\eta = \eta_{0/2}$, and $\alpha - 1$ is the slope of $(\eta_0/\eta) - 1$ versus $\tau/\tau_{1/2}$ on log-log paper. The Ellis model is relatively easy to use and many analytical results have been obtained with this model; a recent example is the analysis of flow in screw extruders by Steller [99]. Actually, the Ellis model is a more general form of the Rabinowitsch equation. The latter is a special case of the Ellis model when the constant $\alpha = 3$.

Another model in which the viscosity is described as a function of shear stress is the Bingham model [20]. This model is used for fluids with a yield stress τ_0. Below this yield stress, the viscosity is infinite (no motion); above the yield stress, the viscosity is finite (motion occurs). The Bingham Fluid model is written as:

$$\eta = \infty \qquad \text{for} \quad \tau \leq \tau_0 \tag{6.37a}$$

$$\eta = \mu_0 + \frac{\tau_0}{\dot{\gamma}} \quad \text{for} \quad \tau > \tau_0 \tag{6.37b}$$

This model is primarily used for slurries and pastes. The parameters τ_0 and μ_0 can be related empirically to the volume fraction of solids φ, the particle diameter D_p, and the viscosity of the suspending fluid μ_s:

$$\tau_0 = 312.5 \frac{\varphi^3}{D_p^2} \tag{6.38}$$

$$\mu_0 = \mu_s \exp\left[\varphi\left(\frac{5}{2} + \frac{14}{\sqrt{D_p}}\right)\right] \tag{6.39}$$

where D_p is measured in μm and τ_0 in Pascal.

Many other fluid models have been proposed. For a more detailed discussion, the reader is referred to the literature [17, 20–22, 54, 94].

6.2.4 Effect of Temperature and Pressure

The effect of shear rate on viscosity has been discussed in some detail in the previous sections. However, there are some other variables that also affect the viscosity. Two important variables that influence the viscosity are temperature and pressure. The effect of these variables is generally not as strong as the effect of shear rate; however, in many cases, the effect of temperature and/or pressure on viscosity cannot be neglected.

When the viscosity is plotted against shear rate at several temperatures, the curve generally lowers with increasing temperature; see Fig. 6.15.

This is a result of the increased mobility of the polymer molecules. For the time being, it is assumed that no irreversible changes occur as a result of degradation. However, whenever experiments or processes are conducted at elevated temperatures, the possible effects of degradation have to be taken into account. There will be more on degradation in Section 11.3.

It is convenient to plot viscosity as a function of shear stress to evaluate the effect of temperature. This is shown in Fig. 6.16 where the same data shown in Fig. 6.15 is plotted in terms of viscosity and shear stress.

For many polymers, the shape of the viscosity-shear stress curve does not change appreciably with temperature. With many polymers, the curves can be shifted along lines of constant shear stress to produce a master curve. By comparing Fig. 6.15 to

Fig. 6.16, it is clear that a shift along lines of constant shear rate would not produce a good fit. Figure 6.15 shows a line of constant shear stress; it makes an angle of 45° with both axes. The curves should be shifted in the direction of this constant shear stress line to produce a good master curve. Figure 6.16 also shows lines of constant shear rate. It can be seen in Fig. 6.16 that the effect of temperature is greater at lower temperature; this is true for many polymers. It should be mentioned that most polymers do not have as strong a temperature dependence as the polymer shown in Figs. 6.15 and 6.16.

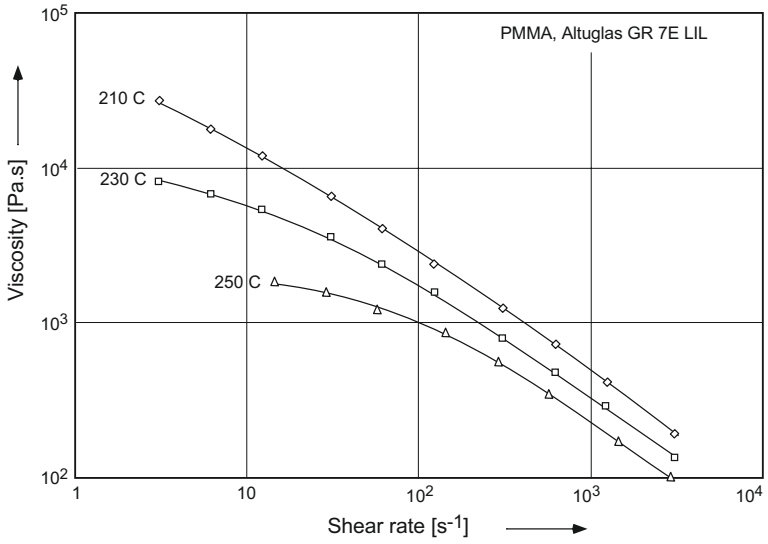


Figure 6.15 Viscosity versus shear rate at various temperatures

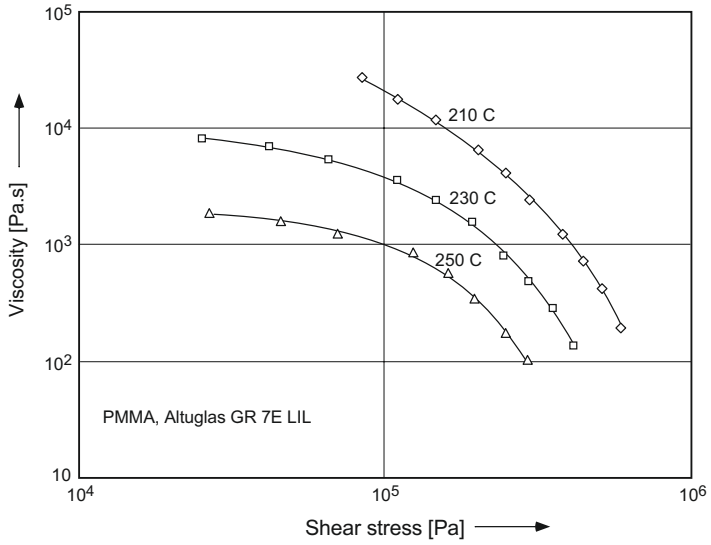


Figure 6.16 Viscosity versus shear stress at various temperatures

The shift factor a_T is a function of the temperature. For polyolefins, the relationship can be written as:

$$a_T = \exp\left[\frac{E}{R}\left(\frac{1}{T}-\frac{1}{T_r}\right)\right] \tag{6.40}$$

where E is the activation energy, R the universal gas constant, and T_r the reference temperature in degrees Kelvin. Equation 6.40 is known as Andrade's Law [98]. It is applicable to semi-crystalline and amorphous polymers above T_g + 100°C.

For amorphous polymers, the Williams-Landel-Ferry (WLF) equation is often used:

$$a_T = \exp\left[\frac{-C_1(T-T_r)}{C_2+(T-T_r)}\right] \tag{6.41}$$

where C_1 and C_2 are material constants.

If the reference temperature T_r is taken about 43 °K above the glass transition point T_g, the constants C_1 and C_2 are essentially the same for a large number of amorphous polymers (C_1 = 8.86 and C_2 = 101.6). This results in the following equation:

$$a_T = \exp\left[\frac{-8.86(T-T_g-43)}{101.6+(T-T_g-43)}\right] \tag{6.41b}$$

The glass transition temperature of a number of polymers is shown in Table 6.2. Equation 6.41(b) gives a reasonable description of the temperature dependence of the viscosity in the range of T_g to T_g + 100°C.

A popular empirical form of the temperature dependence of viscosity is:

$$a_T = \exp[\alpha_T(T_r - T)] \tag{6.42}$$

where α_T is a temperature coefficient that can be considered constant as long as the temperature range considered is relatively small.

The power law equation including the temperature effect can then be written as:

$$\tau = m_r a_T \dot{\gamma}^n \tag{6.43a}$$

or

$$\eta = m_r a_T \dot{\gamma}^{n-1} \tag{6.43b}$$

The temperature sensitivity of the viscosity varies widely for different polymers. As a general rule, amorphous polymers have a high temperature sensitivity, while semi-crystalline polymers have a relatively low temperature sensitivity. Polyvinylchloride (PVC) and polymethyl methacrylate (PMMA) are two polymers with a very

high temperature sensitivity of the viscosity. Polyethylene and polypropylene both have quite low temperature sensitivity.

The relative change in viscosity per degree of temperature can be determined from:

$$\frac{\partial \eta(T)}{\eta(T_r)\partial T} = \frac{\partial a_T}{\partial T} \tag{6.44}$$

If the expression for a_T is used for amorphous polymers (Eq. 6.41), one obtains:

$$\frac{\partial \eta(T)}{\eta(T_r)\partial T} = \frac{-C_1C_2}{[C_2 + (T - T_r)]^2} \exp\left[\frac{-C_1(T - T_r)}{C_2 + (T - T_r)}\right] \tag{6.45}$$

This relationship is shown in Fig. 6.17 where the relative viscosity change is plotted against $T-T_g$ for $C_1 = 8.86$, $C_2 = 101.6$, and $T_r = T_g + 43$.

It can be seen that the temperature sensitivity drops dramatically (several decades) when $T-T_g$ increases. The closer a polymer is to its glass transition temperature, the larger the temperature sensitivity of the viscosity. This explains why polymers whose normal process temperatures are close to their glass transition temperature exhibit a high temperature sensitivity in processing. Examples are polystyrene, polyvinylchloride, and polymethyl methacrylate. In general, polymers that are processed considerably above their glass transition temperature (more than 150°C above T_g) show a relatively small temperature sensitivity. Examples are polyethylene, polypropylene, and polyamide.

The effect of pressure on viscosity is relatively insignificant in most polymer processing operations, where pressures generally do not exceed 35 MPa (5000 psi). It has been found, however, that the effect of pressure on viscosity becomes quite significant at pressures substantially above 35 MPa. In fact, in careful rheological measurements, the effect of pressure on both viscosity and density has to be considered even at pressures around 35 MPa.

Special rheometers have been constructed to measure the effect of pressure on viscosity. Various workers have presented data on the pressure dependence on viscosity [33–40]. The viscosity as a function of pressure is generally written as:

$$\eta(P) = \eta(P_r)\exp[\alpha_p(P - P_r)] \tag{6.46}$$

The values of the pressure sensitivity term α_p vary considerably from one polymer to another. For polystyrene, increases in viscosity at fixed shear stress and about 150°C have been reported [34, 36, 40] of 200 to 1000 times over a pressure rise of 100 MPa (15,000 psi). For polyethylene at the same temperature and pressure conditions, the viscosity increased only 4 to 5 fold. At a temperature of 200°C and a pressure rise of 100 MPa (15,000 psi), the increase in viscosity of polystyrene was reported to be about 30 to 50 fold, about 10 to 20 times lower than at 150°C!

Data on the pressure sensitivity of the viscosity is quite scarce. It has been found empirically [41] that the relative change in viscosity with pressure divided by the relative change in viscosity with temperature is approximately constant for many polymers:

$$\frac{\frac{1}{\eta}\left(\frac{\partial \eta}{\partial P}\right)}{\frac{1}{\eta}\left(\frac{\partial \eta}{\partial T}\right)} \cong -5E-7\left[^{\circ}C/Pa\right] \tag{6.47}$$

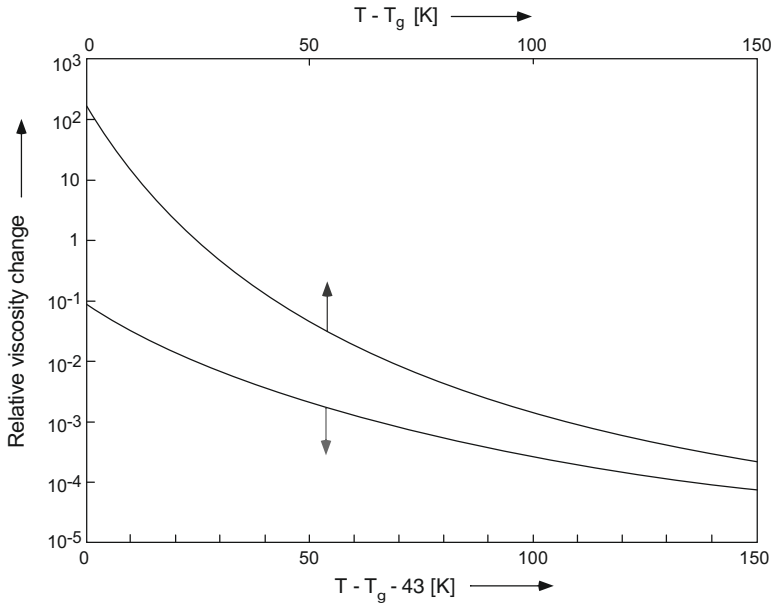


Figure 6.17 Relative change in viscosity versus $T-T_g$

The numerator can be determined from Eqs. 6.40 through 6.45. Thus, Eq. 6.47 provides a convenient, though approximate, method to determine the pressure sensitivity of the viscosity of a polymer. From Eq. 6.47, it is clear that a polymer with a high temperature sensitivity of the viscosity will also have a high pressure sensitivity of the viscosity. This explains the large differences in pressure sensitivity of the viscosity between polystyrene and polyethylene, as mentioned earlier.

6.2.5 Viscoelastic Behavior

Thus far, the polymer melt has been considered as a purely viscous fluid. In a purely viscous fluid, the energy expended in deformation of the fluid is immediately dissipated and is non-recoverable. The other extreme is the purely elastic material where

the energy expended in deformation of the fluid is not dissipated at all; the deformation is completely reversible and the energy completely recoverable.

Polymers are partly viscous and partly elastic. In the molten state, polymers are primarily viscous but will be elastic to some extent. This behavior is generally referred to as viscoelastic behavior. This characteristic is responsible for the swelling of the extrudate as it emerges from an extruder die. The swelling is caused by elastic recovery of strain imparted to the polymer in and before the die. The swelling is not instantaneous, but takes a finite time to fully develop. This indicates that the rearrangement of the polymer structure takes a certain amount of time; this can range from a fraction of a second to several minutes or even hours, depending on the polymer and the temperature. The polymer properties, therefore, are a function of time and depend on the deformation history of the polymer. The deformation history is often referred to as the shear history; however, it is not only shearing deformation that affects the polymer properties but elongational deformation as well.

In fluids with time-dependent behavior, the effects of time can be either reversible or irreversible. If the time effects are reversible, the fluids are either thixotropic or rheopectic. Thixotropy is the continuous decrease of apparent viscosity with time under shear and the subsequent recovery of viscosity when the flow is discontinued. Rheopexy is the continuous increase of apparent viscosity with time under shear; it is also described by the term anti-thixotropy. A good review on thixotropy was given by Mewis [45]. Polymer melts do exhibit some thixotropic effects; however, thixotropy can also occur in inelastic fluids. The time scale of thixotropy is not necessarily associated with the time scale for viscoelastic relaxation.

For a proper description of the flow of a polymer melt, the viscoelastic properties have to be taken into account, including the dependence on deformation history. Some experimental and theoretical work on time-dependent effects is covered in the following references [46–53]; many other publications have been devoted to this subject. Unfortunately, the viscoelastic models that include memory effects (i. e., the dependence on deformation history) are quite complex and difficult to apply. Also, there does not seem to be any model that is widely accepted as being able to describe polymer melt flow accurately over a wide range of flow geometries and conditions. Practicing process engineers probably will find these models difficult to apply to actual extrusion problems. As a result, the workers in this field generally are specialists in rheology.

In the quantitative analysis of most extrusion problems, the polymer melt generally is considered to be a viscous, time-independent fluid. This assumption is, of course, a simplification, but it usually allows one to find a relatively straightforward solution to the problem. This assumption will be used throughout the rest of this book, unless indicated otherwise. In the analysis of any flow problem, however, it should be remembered that elastic effects may play a role. Also, some flow phenomena, such as extrudate swell, clearly cannot be analyzed unless the elastic behavior of

the polymer melt is taken into account. For more information on the rheology of viscoelastic fluids, the reader is referred to the literature [17, 20–22, 54–64, 100, 101]. Six of these references [58–63] do not go into great mathematical complexities and are relatively easy to understand for people not specialized in rheology.

6.2.6 Measurement of Flow Properties

Whenever a process engineer uses flow property data, he should know on what instrument and how these data were determined in order to properly assess the validity of the data. Instruments to determine flow properties are generally referred to as rheometers. The rheometers that will be briefly described in the next few sections are the capillary rheometer, the melt indexer, the cone and plate rheometer, the slit die rheometer, and dynamic mechanical rheometers. For a more detailed description of these and other rheometers, the reader is referred to the literature [64–66]. A brief but good survey of commercial rheometers was presented by Dealy [92].

6.2.6.1 Capillary Rheometer

A capillary rheometer is basically a ram extruder with a capillary die at the end; see Fig. 6.18.

As the piston moves down, it forces the molten polymer through the capillary. The shear stress in the capillary at the wall (τ_{cw}) can be related to the pressure drop along the capillary (ΔP_c) by the following equation:

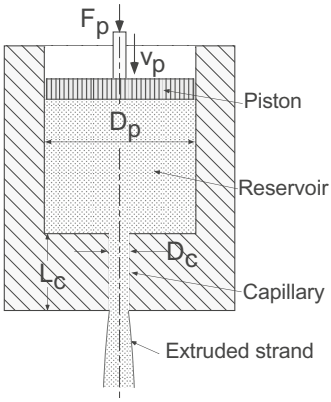


Figure 6.18
Schematic of capillary rheometer

$$\tau_{cw} = \frac{\Delta P_c D_c}{4 L_c} \tag{6.48}$$

If the piston diameter is much larger than the capillary diameter ($D_p > D_c$) and if entrance effects are neglected, then:

$$\Delta P_C \cong \frac{4F_p}{\pi D_p^2} \tag{6.49}$$

By inserting Eq. 6.49 into Eq. 6.48, the wall shear stress in the capillary can be related to the force on the piston. Thus, by measuring the force on the piston, the wall shear stress in the capillary can be determined. To avoid problems with entrance effects, it is good practice to do measurements with a long capillary (high L/D, 20 to 40). It is even better to do measurements with two capillaries of the same diameter but different length, one having a length of almost zero. The actual pressure drop along the capillary of length L_c is now:

$$\Delta P_c = \frac{4}{\pi D_p^2}\left[F_p(L_C) - F_p(L_C = 0)\right] \tag{6.50}$$

The apparent shear rate at the capillary wall can be determined from the flow rate $\dot{V}$ through the capillary. This can be determined from Eqs. 6 and 13 in Appendix 5.1.

$$\dot{\gamma}_{aw} = \frac{32\dot{V}}{\pi D_c^3} \tag{6.51}$$

The flow rate is determined by the area and the velocity of the piston:

$$\dot{V} = v_p \frac{\pi}{4} D_p^2 \tag{6.52}$$

The apparent shear rate at the capillary wall can now be expressed as a function of the piston velocity:

$$\dot{\gamma}_{aw} = \frac{8D_p^2 v_p}{D_c^3} \tag{6.53}$$

Thus, by measuring the piston velocity one can determine the apparent shear rate at the capillary wall. At this point, the apparent viscosity can be determined by dividing the shear stress by the apparent shear rate:

$$\eta_a = \frac{\tau_{cw}}{\dot{\gamma}_{aw}} \cong \frac{F_p D_c^3}{2\pi D_p^4 v_p} \tag{6.54}$$

The terms apparent shear rate and apparent viscosity are used because Eq. 6.51 is valid only for Newtonian fluids. Therefore, if the fluid is non-Newtonian, the actual value of the shear rate at the capillary wall will be different. If the fluid behaves as a power law fluid with power law index n, the actual shear rate at the capillary wall is:

$$\dot{\gamma}_w = \frac{3n+1}{4n}\dot{\gamma}_{aw} = \frac{(3n+1)8\dot{V}}{n\pi D_c^3} \tag{6.55}$$

Thus, for a power law fluid, the actual viscosity is related to the apparent viscosity by:

$$\eta = \frac{4n}{3n+1}\eta_a \tag{6.56}$$

If the capillary rheometer is used to compare different polymers, it is not necessary to go through the various correction procedures. However, if one wants to know the absolute values of the viscosity, it is important to apply the various correction factors. The most important corrections are the correction of the shear rate for non-Newtonian fluid behavior (often referred to as Rabinowitsch correction) and the correction of the shear stress for entrance effects (often referred to as Bagley correction). These are the most common corrections applied to capillary rheometers. Other corrections that are sometimes considered are corrections for viscous heating, corrections for the effect of pressure on viscosity, corrections for compressibility, correction for time effects, etc. If many corrections are applied to the data, the whole measurement and data analysis procedure can become very complex and time consuming.

Figure 6.19 shows how the relative flow rate ($\dot{V}/\dot{V}_o$) through a capillary depends on the relative pressure drop along the capillary die (P/P_o) for three different values of the power law index: n = 1, n = 1/2, and n = 1/3.

In all cases, the flow rate increases as the die pressure increases. However, there is a very large difference in behavior between fluids of different power law index. For a Newtonian fluid (n = 1), a 10-fold increase in pressure results in a 10-fold increase in flow rate. For a power law fluid with n = 1/2, a 10-fold increase in pressure results in a 100-fold increase in flow rate. For a power law fluid with n = 1/3, a 10-fold increase in pressure results in a 1000-fold increase in flow rate! Essentially, the same results are valid for any extrusion die. It is clear, therefore, that the power law index of a polymer melt, to a large extent, will determine its extrusion behavior.

It is very important to know the power law index of a material. This is why the viscosity has to be determined over a wide range of shear rates. The shear rate range should be representative of the shear rates encountered in polymer processing equipment, which is usually 0 to 10,000 s^{-1}.

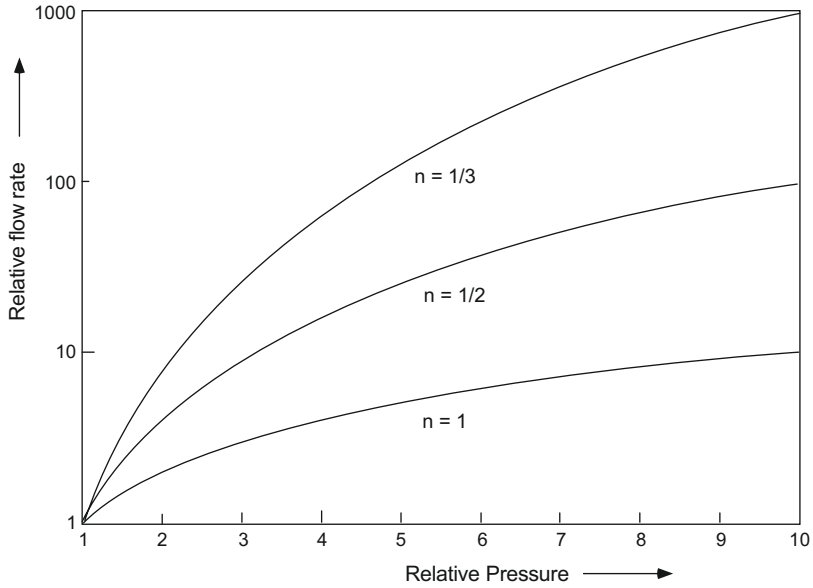


Figure 6.19 Relative flow rate versus relative pressure drop

Advantages of the capillary rheometer are:

1. Ability to measure very high shear rates ($\cong 10^6\ s^{-1}$).
2. Ability to measure extrudate swell characteristics.
3. Ability to measure melt fracture characteristics.
4. Relatively easy to use.

Disadvantages of the capillary rheometer are:

1. The polymer is not exposed to a uniform shear rate.
2. Various corrections have to be applied to the data.
3. It does not yield an accurate description of viscoelastic behavior.
4. It is unreliable at high shear rates (temperature effects).

6.2.6.2 Melt Index Tester

The melt index tester is essentially a simple capillary rheometer. The piston is pushed down by a weight; see Fig. 6.20(a) [99].

The melt index is the number of grams of polymer extruded in a time period of 10 minutes. Details of the geometry and test procedures are described in ASTM D1238.

The melt index tester is used in many companies to quickly test the polymer melt. Unfortunately, many times MI data is the only information available on the polymer melt flow properties.

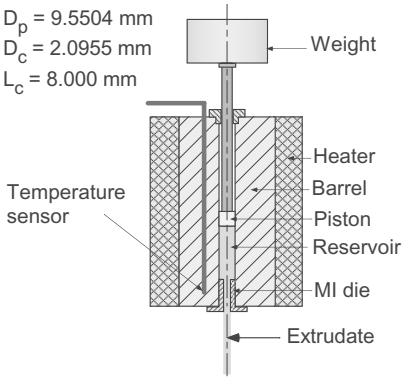


Figure 6.20(a)
The melt index tester

From the dimensions of the MI apparatus, the weight on the plunger, and the MI value, one can determine the approximate shear stress, shear rate, and viscosity. By using Eqs. 6.48 and 6.49, the shear stress at the capillary wall can be determined from:

$$\tau_w \cong \frac{F_p D_c}{\pi L_c D_p^2} = 8.97\, F_p \qquad [\text{Pa}] \tag{6.57}$$

where F_p is the weight on the plunger in grams. The flow rate through the capillary can be expressed as:

$$\dot{V} = \frac{MI}{600\rho} \qquad [\text{g/s}] \tag{6.58}$$

where MI is expressed in grams per 10 minutes and the density ρ in g/cm^3. The apparent shear rate can now be determined by using Eq. 6.51:

$$\dot{\gamma}_{aw} = 1.845\frac{MI}{\rho} \qquad [\text{s}^{-1}] \tag{6.59a}$$

The apparent shear rate is thus directly proportional to the MI value and inversely proportional to the polymer melt density. The apparent viscosity can now be determined from:

$$\eta_a \cong \frac{4.86\rho F_p}{MI} \qquad [\text{Pa - s}] \tag{6.59b}$$

From Eq. 6.59(b) it can be seen that the polymer melt viscosity is inversely proportional to the MI value; see Fig. 6.20(b).

The melt index can be measured at a number of different conditions as far as load and temperature are concerned. A number of standardized conditions are listed in Table 6.1.

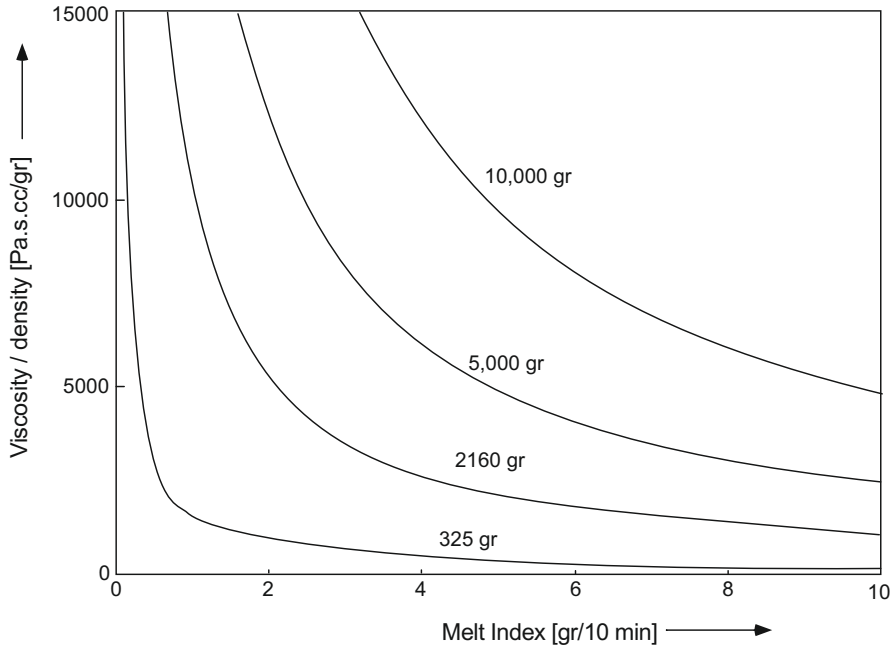


Figure 6.20(b) Viscosity/density ratio versus MI at various plunger weights

Table 6.1 Standardized Conditions for Melt Index Testing

T Condition	Temperature [°C]	Load* [g]
A	125	325
B	125	2160
C	150	2160
D	190	325
E	190	2160
F	190	21600
G	200	5000
H	230	1200
I	230	3800
J	265	12500
K	275	325

T Condition	Temperature [°C]	Load [g]
L	230	2160
M	190	1050
N	190	10000
O	300	1200
P	190	5000
Q	235	1000
R	235	2160
S	235	5000
T	250	2160
U	310	12500

* This includes the piston weight of 325 g.

A high MI value corresponds to a low polymer melt viscosity, and a low MI value corresponds to a high polymer melt viscosity. The term “fractional melt index material” refers to a polymer with a melt index less than one. These are materials with high melt viscosities, and they generally have higher power consumption and die-head pressure in extrusion as compared to polymers with higher melt index values.

As an example, consider a polymer with MI = 0.2 g/10 min and density $\rho = 1.0$ g/cm^3; the MI is determined under condition E (F_p = 2160 g). The approximate viscosity of this material is 52,488 Pa·s at a shear rate of about 0.37 s^{-1}. If the MI = 20 g/10 min with everything else the same, the viscosity would be about 525 Pa·s at a shear rate of about 37 s^{-1}. It should be noted that these figures are very approximate and should be regarded as estimates rather than firm numbers. Considering that the standard MI capillary is quite short (about 4 L/D), the entrance effect will be considerable. Therefore, the error in the expression for the wall shear stress (Eq. 6.57) can be considerable. Consequently, the error in the expression for the apparent viscosity (Eq. 6.59(b)) can also be considerable.

A large drawback of the MI test is that it yields single-point data. Thus, it does not give any idea about the degree of non-Newtonian behavior of the material. This drawback can be negated by running the melt indexer with several different weights on the plunger; however, this is not done very often. Another drawback is the relatively poor reproducibility of the melt indexer; under the best circumstances it is about 15% (plus or minus).

When the melt index is measured with two different weights on the plunger, the two values are sometimes referred to as the high and low load melt index. When the high load melt index is measured with a 10 kg weight and the low load melt index with 2.16 kg, the ratio of melt index values is often reported as the I10/I2 ratio–the two decimal points of the 2.16 are generally omitted. This value allows a determination of the degree of shear thinning of the polymer. When the I10/I2 ratio is about 4.6, the fluid is Newtonian; when I10/I2 is between 10 and 20, the fluid is weakly shear thinning. When the I10/I2 ratio is greater than 50, the fluid is strongly shear thinning.

An advantage of the melt indexer is its low costs and ease of operation. It should be noted that the melt indexer generally operates at low shear rates (see Eq. 6.59(a)) that are not representative of shear rates usually encountered in the extrusion process. Thus, the MI value is not a good indicator of the extrusion processing behavior of a polymer.

Advantages of the melt indexer are:

1. The instrument is simple and inexpensive.
2. It is easy to operate.
3. It is widely available.

Disadvantages of the melt indexer are:

1. It yields only single-point data.
2. It has limited accuracy and reproducibility.
3. It is not a good indicator of processability.
4. It is not an accurate description of viscoelastic behavior.

There are two melt index methods (ASTM D1238, ISO 1133). In method A only the temperature is controlled and the operator times the MI and weighs the extruded strand. Method A yields a melt flow rate (MFR) expressed in g/10 min. In method B a sensor measures the position of the piston, and the volume of extruded plastic is determined automatically. Method B yields a melt volumetric rate or MVR; this is expressed in cm^3/10 min. The MFR is related by the MVR by the following expression:

$$MFR = \rho MVR \tag{6.60}$$

where ρ is the melt density in g/cm^3.

6.2.6.3 Cone and Plate Rheometer

In a cone and plate rheometer, the polymer melt is situated between a flat and a conical plate. In most rheometers, the cone is rotating and the plate is stationary; however, this is not absolutely necessary. The basic geometry is shown in Fig. 6.21.

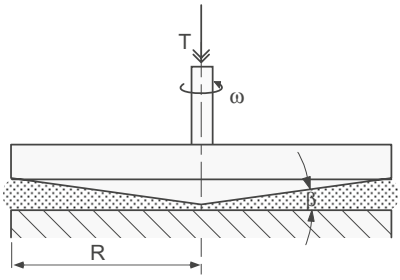


Figure 6.21
Cone and plate rheometer

If the cone rotates with an angular velocity ω and the cone angle β is very small, the shear rate in the fluid is given by [57]:

$$\dot{\gamma} = \frac{\omega}{\beta} \tag{6.61}$$

Because of the conical geometry, the shear rate is uniform throughout the fluid. The torque necessary to rotate the cone is related to the shear stress by:

$$T = \frac{2}{3}\pi R^3 \tau \tag{6.62}$$

The viscosity can now be determined from:

$$\eta = \frac{\tau}{\dot{\gamma}} = \frac{3T\beta}{2\pi R^3 \omega} \tag{6.63}$$

Thus, the viscosity can be directly determined from measurement of torque and rotational speed. If the fluid between the cone and plate is viscoelastic, the plates will be pushed apart when the fluid is sheared. The force with which the plates are pushed apart F is related to the first normal stress difference N_1 in the fluid:

$$F = \frac{\pi R^2}{2} N_1 \tag{6.64}$$

The first normal stress difference is an accurate indicator of the viscoelastic behavior of a fluid. Thus, with the cone and plate rheometer, one can accurately determine some viscoelastic characteristics of a fluid.

The cone and plate rheometer is susceptible to irregularities at the liquid-air interface and to secondary flows. As a result, the shear rate in steady shear measurements has to be quite low to avoid the above-mentioned problems. In general, the shear rate should not exceed 1 s^{-1}; data above this rate should be regarded with caution.

Advantages of the cone and plate rheometer:

1. Its ease of operation.
2. It has uniform shear rate distribution.
3. It also measures first normal stress difference.
4. Its uniform temperature distribution.

Disadvantages of the cone and plate rheometer:

1. It is limited to low shear rates (< 1 s^{-1}).
2. These instruments tend to be expensive.

The disadvantage of the low shear rate limitation can be negated by applying an oscillatory rotary motion to the moving plate. Thus, one can measure complex viscosity as a function of frequency; see also Section 6.2.6.5 on dynamic analysis. In this fashion, frequency levels up to about 500 radians/s are possible; this corresponds to shear rates of about 500 s^{-1}.

6.2.6.4 Slit Die Rheometer

A slit die rheometer is an extruder die with a rectangular flow channel with provisions to measure pressures at various axial locations. The slit die is either directly connected to an extruder or to a gear pump, which, in turn, is connected to an extruder. A typical slit die geometry is shown in Fig. 6.22.

By measuring the flow rate $\dot{V}$ through the flow channel, the apparent shear rate at the wall can be determined:

$$\dot{\gamma}_{aw} = \frac{6\dot{V}}{H^2 W} \tag{6.65}$$

where H is the slit height and W the slit width (W>>H).

For a power law fluid with power law index n, the actual shear rate at the wall is:

$$\dot{\gamma}_w = \frac{2n+1}{3n}\dot{\gamma}_{aw} \tag{6.66}$$

The shear stress at the wall can be determined from the gradient of the measured pressure profile (dP/dz):

$$\tau_w = -\frac{dP}{dz}\frac{H}{2} \tag{6.67}$$

The apparent viscosity can be determined from:

$$\eta_a = \frac{\tau_w}{\dot{\gamma}_{aw}} = \frac{H^3 W}{12\dot{V}}\frac{dP}{dz} \tag{6.68}$$

For a power law fluid, the actual viscosity is:

$$\eta = \frac{3n}{2n+1}\eta_a = \frac{nH^3 W}{4(2n+1)\dot{V}}\frac{dP}{dz} \tag{6.69}$$

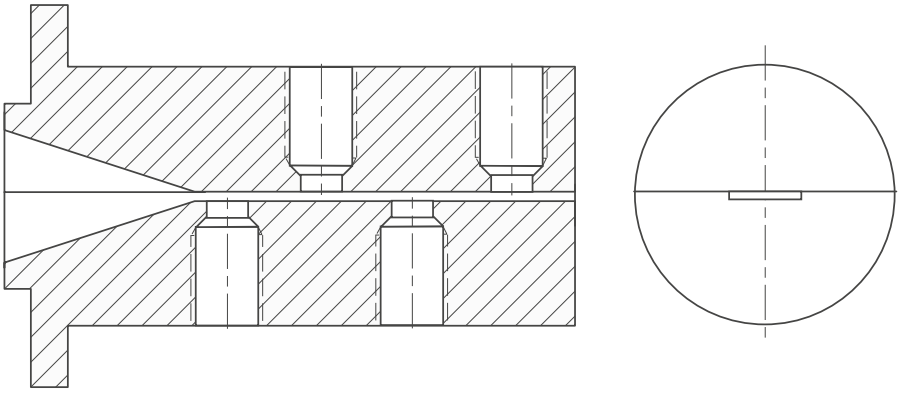


Figure 6.22 Slit die viscometer

These equations are valid provided the ratio of width to height is large; in most cases W/H > 10. If the pressure gradient is constant, the pressure can be extrapolated to the exit of the die. Several workers have found positive exit pressure by using this procedure [54]. This exit pressure can be related to the first normal stress difference provided the velocity profile remains fully developed right up to the die exit:

$$N_1(\dot{\gamma}_w) = P_{exit} + \tau_w\left(\frac{dP_{exit}}{d\tau_w}\right) \tag{6.70}$$

However, the theoretical justification of this relationship seems to be questionable, as discussed by Boger and Denn [67]. From a practical view, it is very difficult to extrapolate from pressure readings that range from several MPa up to about 30 or 40 MPa down to exit pressures that range from less than 0.1 MPa to about 0.2 MPa. This is particularly true if only two pressure transducers are situated in the fully developed region, as appears to have been the case in several experimental results reported in the literature [68–70]. Another problem is the assumption of a constant pressure gradient. It has been shown [71] that the effects of temperature and pressure will generally cause a significant non-linearity. This raises serious doubts about the validity of a linear extrapolation of the pressure profile.

An interesting aspect of the slit die rheometer is the fact that the polymer has a significant temperature and shear history by the time it reaches the slit die. This can affect the rheological properties, as reported by the author [71]. On the other hand, if viscosity data is to be used for die design purposes, the slit die viscometer is most likely to produce pertinent viscosity data.

Advantages of the slit die rheometer:

1. It operates in a useful shear rate range.
2. It yields accurate shear viscosity versus shear rate data.
3. It yields data representative of behavior during actual extrusion.

Disadvantages of the slit die rheometer:

1. Commercial rheometers tend to be expensive.
2. Proper and frequent calibration of pressure transducers is important to ensure accurate results.
3. It is difficult to determine data that can be related to the viscoelastic behavior of the polymer.

6.2.6.5 Dynamic Analysis

Several rheometers do not subject the polymer to a steady rate of deformation but to an oscillatory deformation, usually sinusoidal simple shear. If the angular frequency is ω, and the shear strain amplitude γ_0, the shear strain γ can be written as a function of time:

$$\gamma(t) = \gamma_0 \sin(\omega t) \tag{6.71}$$

The shear rate is determined by differentiating the shear strain with respect to time. The shear rate is:

$$\dot{\gamma}(t) = \gamma_0 \omega \cos(\omega t) = \dot{\gamma}_0 \cos(\omega t) \tag{6.72}$$

Dynamic analysis is generally used to study the linear viscoelastic properties of polymers. The region of linear viscoelastic behavior is where a material function, such as shear modulus or shear viscosity, is independent of the amplitude of the strain or strain rate. Polymers follow linear viscoelastic behavior when the strain or strain rate is sufficiently small. Thus, if the strain amplitude is sufficiently small, the shear stress can be written as:

$$\tau(t) = \tau_0 \sin(\omega t + \delta) \tag{6.73}$$

where τ_0 is the amplitude of the shear stress and δ the phase angle between stress and strain. The phase angle is often referred to as loss angle. For a purely elastic material, there is no phase shift between stress and strain, thus δ is zero. For a purely viscous material, there will be a maximum phase shift between stress and strain, or δ is 90°.

Equation 6.73 can be rewritten by introducing an in-phase modulus G' (real) and a 90° out-of-phase modulus G'' (imaginary):

$$\tau(t) = \gamma_0 [G' \sin(\omega t) + G'' \cos(\omega t)] \tag{6.74}$$

The storage modulus G' represents the elastic contribution associated with energy storage; it is a function of the stress and strain amplitude and the phase angle:

$$G' = \frac{\tau_0}{\gamma_0} \cos\delta \tag{6.75}$$

Similarly, the loss modulus G'' represents the viscous contribution associated with energy dissipation; it is:

$$G'' = \frac{\tau_0}{\gamma_0} \sin\delta \tag{6.76}$$

Both G' and G'' are components of the complex modulus G*. The magnitude of the complex modulus, as shown in Fig. 6.23, is:

$$|G^*| = \sqrt{(G')^2 + (G'')^2} \tag{6.77}$$

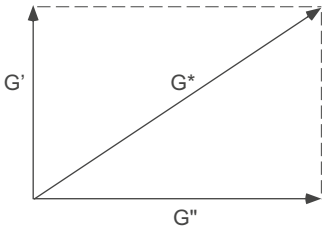


Figure 6.23
Complex modulus G*

A complex notation is frequently used to describe the relationship between stress and strain. If stress and strain are written as:

$$\gamma = \gamma_0 \exp(i\omega t) \tag{6.78a}$$

$$\tau = \tau_0 \exp[i(\omega t + \delta)] \tag{6.78b}$$

then the complex modulus can be written as:

$$G^* = \frac{\tau}{\gamma} = \frac{\tau_0}{\gamma_0}(\cos\delta + i\sin\delta) = G' + iG'' \tag{6.79}$$

Equation 6.73 can be rewritten in yet a different form by introducing an in-phase viscosity η' and out-of-phase viscosity η''. The real part η', the dynamic viscosity, represents the viscous contribution associated with energy dissipation. The imaginary part η'' represents the elastic contribution associated with energy storage. The shear stress can be written as a function of η' and η'' as follows:

$$\tau(t) = \dot{\gamma}_0[\eta'\cos(\omega t) + \eta''\sin(\omega t)] \tag{6.80}$$

The dynamic viscosity is related to the loss modulus by:

$$\eta' = \frac{G''}{\omega} = \frac{\tau_0}{\dot{\gamma}_0}\sin\delta \tag{6.81}$$

The imaginary part of the viscosity is related to the storage modulus by:

$$\eta'' = \frac{G'}{\omega} = \frac{\tau_0}{\dot{\gamma}_0}\cos\delta \tag{6.82}$$

Both η' and η'' are components of the complex viscosity η^*. The magnitude of the complex viscosity is:

$$|\eta^*| = \sqrt{(\eta')^2 + (\eta'')^2} \tag{6.83}$$

In complex notation, the complex viscosity can be expressed as a function of η' and η'':

$$\eta^* = \frac{\tau}{\dot{\gamma}} = \frac{\tau_0}{\dot{\gamma}_0}(\sin\delta - i\cos\delta) = \eta' - i\eta'' \tag{6.84}$$

The tangent of the phase angle is often used in characterization of viscoelastic material. The "tan δ" can be determined from:

$$\tan\delta = \frac{G''}{G'} = \frac{\eta'}{\eta''} \tag{6.85}$$

The attractiveness of dynamic analysis is that an accurate determination of the viscoelastic behavior can be made. A common geometry for dynamic measurements is the cone and plate rheometer. In dynamic analysis, the viscosity components can be measured up to an angular frequency of about 500 radians/s. Cox and Merz [72] found empirically that the steady shear viscosity corresponds to the complex viscosity if the shear rate in s^{-1} is plotted on the same scale as the angular frequency in radians/s. This can be stated as:

$$\left| \eta^*(\omega) \right| = \eta(\dot{\gamma}) \Big|_{\dot{\gamma}=\omega} \tag{6.86}$$

This empirical rule seems to hold up quite well for most polymers. Using this rule, it is possible to determine viscosity data up to 500 s^{-1} with a cone and plate rheometer by applying an oscillatory motion to the cone. This would be impossible if a steady rotational motion was applied to the cone. In steady shear measurements on a cone and plate rheometer, the maximum shear rate that can be measured is around 1 s^{-1}, which is much too low for applications to extrusion problems. The same is true for measurements in the parallel plate test geometry. Thus, the dynamic measurement extends the shear rate measurement range considerably, while still being able to take advantage of the cone and plate geometry.

Dynamic mechanical analysis is not limited to just shear deformation; it is also used with elongational deformation. Further, dynamic mechanical analysis is employed in the characterization of solids as well as liquids. In 1982, a new standard was established, ASTM D4065, to standardize procedures for testing all types of materials.

■ 6.3 Thermal Properties

By the nature of the plasticating extrusion process, thermal properties are very important. In the early portion of the extruder, solid polymer particles are heated to the melting point. In the midportion of the extruder, the molten polymer is raised in temperature to a level considerably above the melting point while the remaining solid particles continue to heat up and melt. In the last portion of the extruder, the molten polymer has to reach a thermally homogeneous state. When the extrudate leaves the extruder die, it has to be cooled down, usually to room temperature. Through this whole process, the polymer experiences a complicated thermal history. The thermal properties of the polymer are crucial to being able to describe and analyze the entire extrusion process.

6.3.1 Thermal Conductivity

The thermal conductivity of a material is essentially a proportionality constant between the conductive heat flux and the temperature gradient driving the heat flux. The thermal conductivity of polymers is quite low, about two to three orders of magnitude lower than most metals. From a processing point of view, the low thermal conductivity creates some real problems. It very much limits the rate at which polymers can be heated and plasticated. In cooling, the low thermal conductivity can cause non-uniform cooling and shrinking. This can result in frozen-in stresses, deformation of the extrudate, delamination, shrink voids, etc.

The thermal conductivity of amorphous polymers is relatively insensitive to temperature. Below the T_g, the thermal conductivity increases slightly with temperature; above the T_g, it reduces slowly with temperature. The thermal conductivity above the T_g as a function of temperature can be approximated by [41]:

$$k(T) = \frac{6T_g - T}{5T_g} k(T_g) \tag{6.87}$$

where the temperature is expressed in °K.

In most extrusion problems, however, the thermal conductivity of an amorphous polymer can be assumed to be independent of temperature.

The thermal conductivity of semi-crystalline polymers is generally higher than amorphous polymers. Below the crystalline melting point, the thermal conductivity reduces with temperature; above the melting point, it remains relatively constant. The thermal conductivity increases with density and, thus, with the level of crystallinity. The thermal conductivity at constant temperature as a function of density can generally be written as:

$$k(\rho) = k_r + C_\rho(\rho - \rho_r) \tag{6.88}$$

The change in thermal conductivity with temperature is relatively linear at temperatures above 0°C. The thermal conductivity as a function of temperature can be described with:

$$k(T) = k_o - C_T T \tag{6.89}$$

where T is in °C and $k_0 = k\ (T = D)$.

The temperature coefficient of the thermal conductivity C_T for a particular polymer seems to be relatively independent of the actual density. Thus, the combined density and temperature dependence can be described by:

$$k(\rho, T) = [k_r + C_\rho(\rho - \rho_r)]_{T_o} - C_T T \tag{6.90}$$

For polyethylene, the thermal conductivity as a function of density and temperature can be described by:

$$k(\rho, T) \cong 0.17 + 5(\rho - 0.90) - 0.001T \quad [J/ms°C] \tag{6.91}$$

where T is in °C and ρ in g/cm³.

Equations 6.89 through 6.91 become less accurate as the temperature approaches the melting point because non-linearities become significant. Therefore, these expressions should be used as approximations. Above the melting point, the thermal conductivity of polyethylene is about 0.25 J/ms °C.

The thermal conductivity is dependent on the orientation of the polymer. If the polymer is highly oriented, substantial differences in thermal conductivity can occur in the direction of orientation and perpendicular to it. The difference can be as high as almost 100% in PMMA as shown by Eiermann and Hellwege [73]. Hansen and Bernier [74] found differences in thermal conductivity as much as 20-fold in HDPE.

Compacted polymer particles have a lower thermal conductivity because of the presence of voids between the particles. Based on experimental data, Yagi and Kunii [75] proposed a model for the thermal conductivity of the bed. For fine particles and low temperatures, the thermal conductivity of the bed can be written as:

$$k_b = \frac{k_g \rho_b / \rho_p}{F + k_g / k_p} \tag{6.92}$$

where k_g is the thermal conductivity of the gas occupying the voids, k_p the thermal conductivity of the polymer particles, ρ_b the bulk density, ρ_p the density of the polymer particles, and F a function of the density ratio, ρ_b/ρ_p (a power law relationship). Langecker [96, 97] performed extensive measurements of the thermal conductivity of isotropically compressed polymeric powders. He found an essentially linear relationship between the thermal conductivity and the bulk density. In the range of ρ_b/ρ_p from 0.5 to 1.0, the data on polyethylene can be approximated by:

$$k_b = \frac{1}{3} k_p (5\rho_b/\rho_p - 2) \tag{6.93}$$

The dependence of thermal conductivity and diffusivity of polyethylene on temperature, density, and molecular parameters was investigated by Kamal, Tan, and Kashani [93]. Their publication contains a good review of prior experimental work on thermal conductivity.

6.3.2 Specific Volume and Morphology

The polymer density ρ is a function of pressure, temperature, and cooling rate. Specific volume $\hat{V}$ is the reciprocal of density, $\hat{V} = 1/\rho$. The general P, $\hat{V}$, T diagram of an amorphous polymer is shown in Fig. 6.24.

If the material is cooled very slowly, the specific volume will reach a lower value than at a relatively high cooling rate. In simple terms, at a low cooling rate the polymer molecules, because of their thermal motion, have more opportunity to position themselves closer together. This reduces the free volume of the polymer, i. e., the volume fraction not occupied by polymer molecules. Below the glass transition temperature, the thermal motion of the polymer molecules is drastically reduced and the free volume remains approximately constant. Therefore, the change in specific volume with temperature is much larger above T_g than below T_g. The reduction in specific volume below T_g is primarily due to the reduced thermal motion of the polymer molecules.

Increasing the molecular weight increases the glass transition temperature as shown in the Fox and Flory equation:

$$T_g = T_{g\infty} - \frac{K}{\overline{M}_n} \tag{6.94}$$

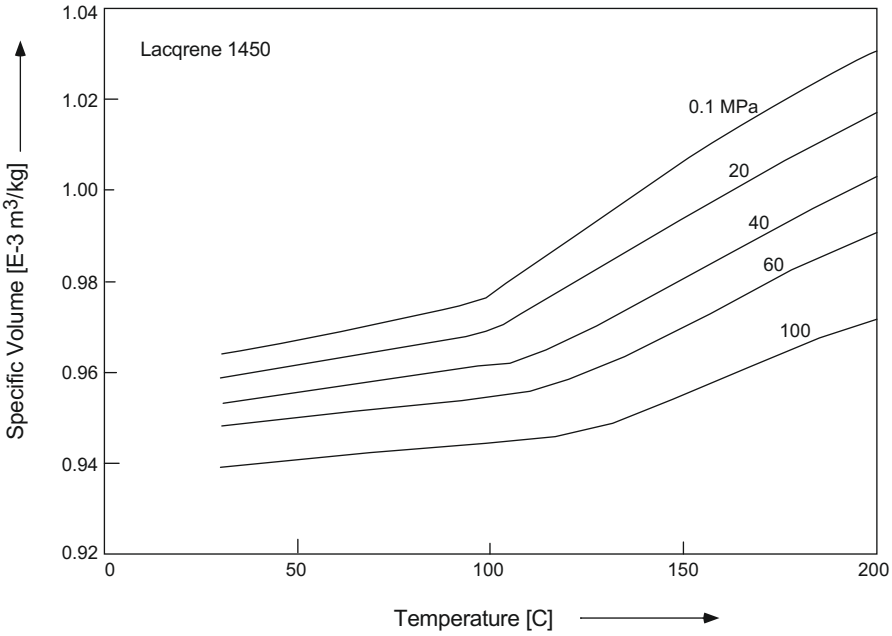


Figure 6.24 P, $\hat{V}$, T diagram of an amorphous polymer

where $T_{g\infty}$ is the glass transition temperature for infinite molecular weight and constant K is a parameter of the polymer.

When the $\hat{V}$, T curve is determined at a higher pressure, the specific volume will reduce. The reduction above T_g will be more significant than below T_g because of the larger free volume above T_g. Another interesting phenomenon is the shift of the T_g to a higher temperature when the pressure is increased. In the normal range of processing pressures (P < 100 MPa), the pressure dependence of T_g can generally be neglected.

When the cooling rate is fast, the material goes through the transition region at a higher temperature and has a larger specific volume at temperatures below this region. This is because the polymer molecules have not had sufficient time to position themselves in a preferred configuration. As the polymer relaxes, it will reduce in specific volume until it eventually reaches the specific volume corresponding to a low cooling rate.

A general P, $\hat{V}$, T diagram of a semi-crystalline polymer is shown in Fig. 6.25.

The behavior in the liquid state is essentially the same as amorphous polymers. In the transition region, an abrupt change in slope occurs as crystallization begins to take place. This is the crystallization temperature T_c. If the material is cooled very rapidly, the crystallization rate can be depressed, depending on the crystallization kinetics. In fact, in some materials with sufficiently slow crystallization kinetics, the crystallization can be almost completely suppressed by rapid cooling. A well-known example is polyethylene terephthalate (PET). If PET is rapidly quenched, it is almost completely amorphous with a density of about 1.33 g/–cm^3. If it is cooled slowly, it will crystallize with a resulting higher density of about 1.40 g/–cm^3.

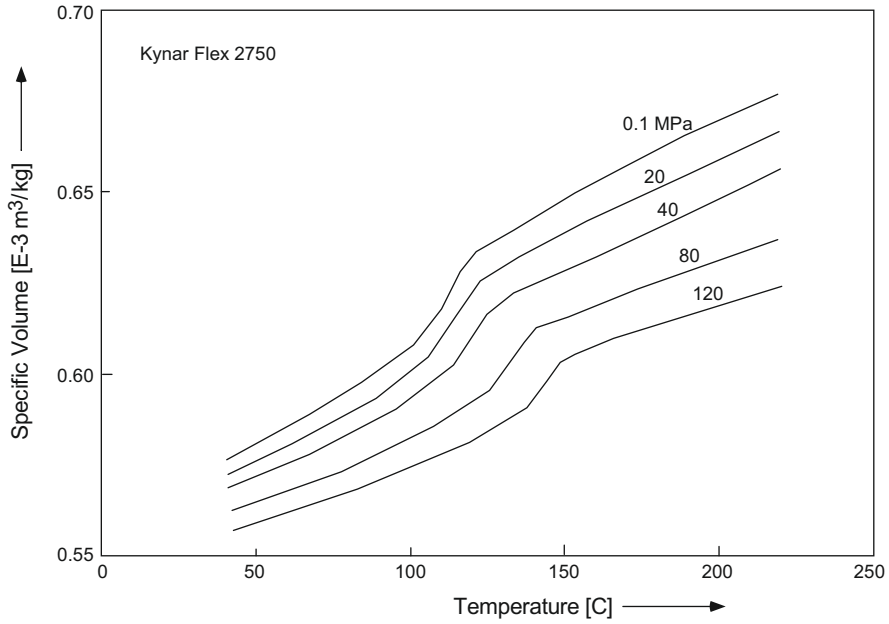


Figure 6.25 P, $\hat{V}$, T diagram of a semi-crystalline polymer

The percent crystallinity of polymers with rapid crystallization kinetics is not much affected by the cooling rate; however, the crystallite morphology may be strongly affected. These differences in morphology can cause significant changes in physical properties. As the extrudate is cooled, the skin will cool most rapidly and the interior region of the extrudate will cool more slowly. This will cause corresponding changes in polymer morphology. Annealing can also modify the polymer morphology, particularly the crystalline regions. Annealing is the process of exposing the polymer to an elevated temperature for a certain period of time. This is sometimes done as a post-extrusion operation to control the polymer morphology and physical properties. In polymers with a high level of crystallinity, annealing causes thickening of the lamellae and an increase of the melting point. The relationship between crystallite size and melting point is given by Hoffman and Lauritzen's equation [81]:

$$T_m = T_m^0 \left(1 - \frac{2\sigma_e}{\Delta H_f L} \right) \tag{6.95}$$

where σ_e is the surface free energy, $T_m{}^0$ the equilibrium melting temperature, ΔH_f the heat of fusion, and L the lamella thickness.

The application of stress can further cause significant changes in the polymer morphology; see also Section 5.2.2. In flow-induced crystallization of dilute polymer solutions, a shish-kebab crystal morphology develops. In melt-crystallized polymers, a spherulitic crystal morphology develops, made up of folded chain lamellae. Deformation of the polymer below the melting point can cause very effective orientation of the polymer molecules. This can result in a high degree of anisotropy in the material with very good mechanical properties in the orientation direction. Examples are solid-state extrusion and fiber drawing; many other examples are available.

The change in specific volume below T_c is primarily due to the increasing degree of crystallinity. Therefore, the volume change in semi-crystalline polymers is considerably larger than those experienced with amorphous polymers. When the semi-crystalline polymer is cooled from the melt at elevated pressure, the T_c shifts to a higher temperature. This phenomenon can be described by the Clausius-Clapeyron equation, which relates the equilibrium melting point at any pressure to the melting point at atmospheric pressure:

$$T_m(P) = T_m(P_{atm}) \exp\left[\frac{(\hat{V}_a - \hat{V}_c)(P-1)}{\Delta H_f} \right] \tag{6.96}$$

where $\hat{V}_a$ and $\hat{V}_c$ are the amorphous and crystalline specific volumes, P is the hydrostatic pressure in atmospheres, and ΔH_f is the heat of fusion of the polymer at atmospheric pressure. The melting point elevation can be significant in polymer melts, i. e., for polyethylene about 7 °C per 20 MPa (≅ 3000 psi). A polymer melt under high pres-

sure is thus under a higher degree of supercooling. This will affect the crystallization behavior of the material, an effect most noticeable in processes where high pressure commonly occurs, such as injection molding. As mentioned earlier and also in Section 5.2.2, this effect can be further magnified if the polymer melt is under stress. The melting point elevation with pressure explains the large compressibility values for polymer melts found by some investigators [76]. Actually, the sudden increase of compressibility at elevated pressures indicates the onset of crystallization.

The P, $\hat{V}$, T diagram of HDPE is shown in Fig. 6.26.

Various workers have developed empirical relationships between P, $\hat{V}$, and T. Among those are the equations of Spencer and Gilmore [77], Breuer and Rehage [78], Kamal and Levan [79], and Simha and Olabisi [80].

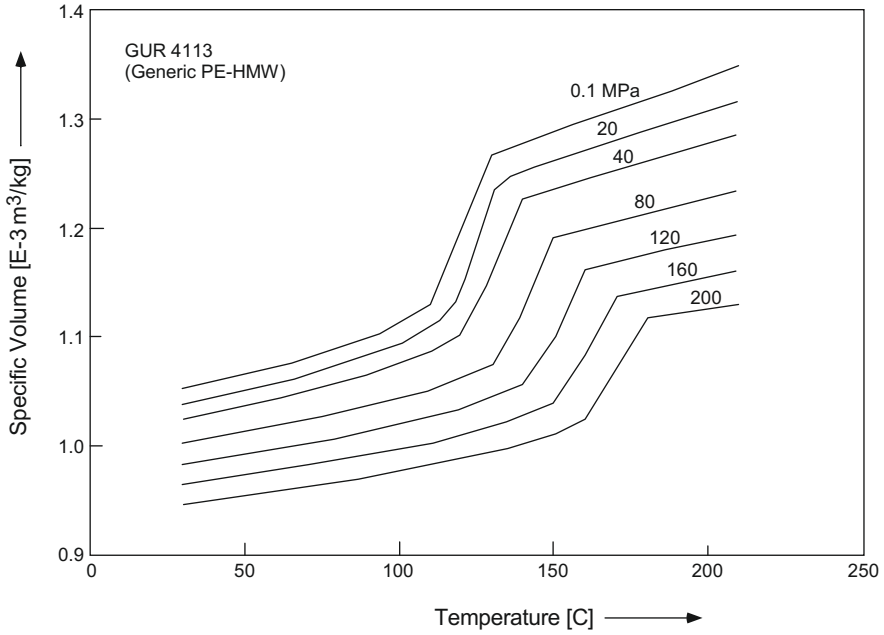


Figure 6.26 P, $\hat{V}$, T diagram of high density polyethylene (HDPE)

6.3.3 Specific Heat and Heat of Fusion

The specific heat is the amount of energy required to raise a unit mass of a material one degree in temperature. In S.I. units, specific heat is expressed in J/kg °K. It can be measured either at constant pressure C_p or at constant volume C_v. The two values are related by:

$$C_p = C_v + T\hat{V}\frac{\alpha_v^2}{\kappa} \tag{6.97a}$$

where the expansion coefficient α_v is:

$$\alpha_v = \frac{1}{\hat{V}}\left(\frac{\partial \hat{V}}{\partial T}\right)_P \tag{6.97b}$$

and the compressibility:

$$\kappa = -\frac{1}{\hat{V}}\left(\frac{\partial \hat{V}}{\partial P}\right)_T \tag{6.97c}$$

The specific heat at constant pressure is larger than the specific heat at constant volume because additional energy is required to bring about the volume change against external pressure P.

The specific heat of amorphous polymers increases with temperature in approximately a linear fashion below and about T_g. A step-like change occurs around the glass transition temperature as shown in Fig. 6.27(a). With semi-crystalline polymers, the step change at T_g is much less pronounced; however, a very distinct maximum occurs at the crystalline melting point. At the melting point, the specific heat is theoretically infinite for a material with a perfectly uniform crystalline structure, as shown in Fig. 6.27(b). Since this is not the case in semi-crystalline polymers, these materials exhibit a melting peak of certain width as show in Fig. 6.27(c). The narrower the peak, the more uniform the crystallite morphology.

The specific heat above the melting point increases slowly with temperature. The area under the melting peak of the C_p, T curve equals the heat of fusion ΔH_f multiplied with the crystalline weight fraction. Both the heat of fusion and the percent crystallinity are dependent on the thermomechanical history of the polymer, as discussed in the previous section.

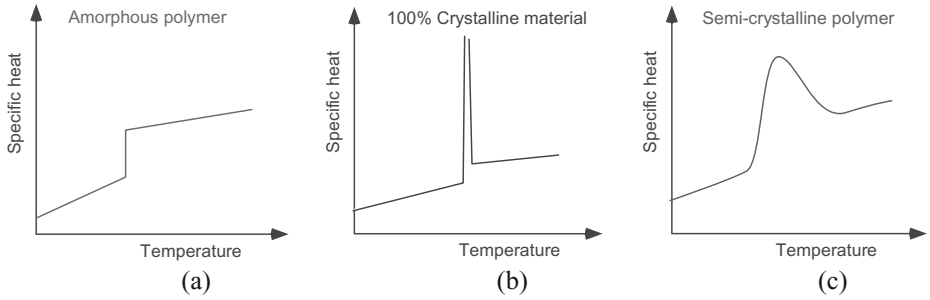


Figure 6.27 Specific heat as a function of temperature

6.3.4 Specific Enthalpy

A very useful thermal property in polymer processing is the specific enthalpy. It is defined by:

$$\hat{H} = \int_{T_1}^{T_2} C_p(T)\,dT \tag{6.98}$$

If T_1 is taken as ambient temperature and T_2 as the process temperature, the specific enthalpy indicates how much energy is required to accomplish this temperature rise. This can be considered to be the theoretical minimum specific energy requirement in the extrusion process.

Figure 6.28 shows $\hat{H}$, T curves for several amorphous and semi-crystalline polymers.

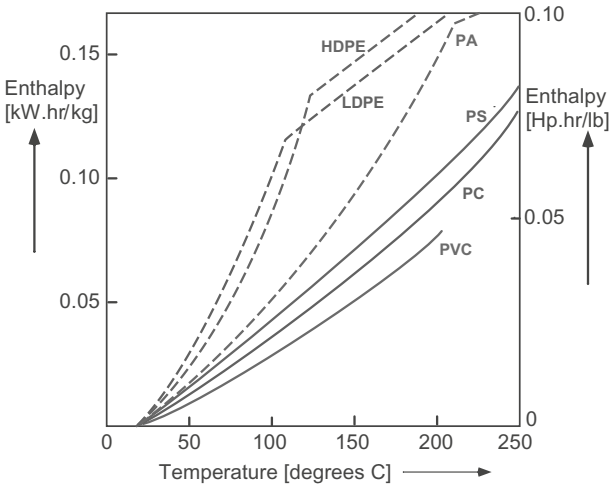


Figure 6.28
Enthalpy-temperature curves for several polymers

The first observation is that amorphous polymers have a continuous rise in $\hat{H}$ while semi-crystalline polymers exhibit an abrupt change in slope at the melting point. The second observation is that amorphous polymers generally have much lower $\hat{H}$ values than semi-crystalline polymers over the same ΔT. If one compares PVC to LDPE from T_1 = 20°C to T_2 = 150°C, the $\hat{H}$ (PVC) ≅ 0.05 kWhr/kg (0.03 hphr/lb), while $\hat{H}$ (LDPE) ≅ 0.13 kWhr/kg (0.08 hphr/lb). Thus, if the throughput of the extrusion process is 100 kg/hr and the process temperature 150°C, the theoretical power requirement is 5 kW for PVC and 13 kW for LDPE.

Thus, based on the thermal properties of the polymers, there is a very significant difference in power requirement between PVC and LDPE, about a 3:1 ratio! A standard 24 L/D extruder that runs fine with LDPE is likely to have too high a power consumption for PVC. This will result in high stock temperatures and increased chance of degradation, particularly in the case of PVC, and especially with rigid

PVC. The thermal properties of PVC dictate an extrusion process with low specific energy consumption and short residence times to minimize high melt temperatures and high temperature exposure time. This is the main reason that closely intermeshing twin screw extruders have become so popular for RPVC. These machines have low specific energy consumption, short residence times, narrow residence times distribution, and good control over stock temperatures. Long single screw extruders are generally not well suited for RPVC extrusion. As a result, a higher level of stabilizers has to be added to the polymer to enable it to survive the extrusion process without too much degradation. This increases the compound cost and may be more expensive in the long run than processing the material on a more suitable machine.

6.3.5 Thermal Diffusivity

The thermal diffusivity is a property derived from thermal conductivity, specific heat, and density. The relationship is:

$$\alpha = \frac{k}{\rho C_p} \tag{6.99}$$

The thermal diffusivity is a very useful quantity in transient heat transfer problems, as discussed in Section 5.3.1.

The thermal diffusivity can be calculated from the values k, ρ, and C_p; however, in most cases it is measured directly. In fact, the thermal diffusivity can be measured more easily and accurately than the thermal conductivity. If a thick slab of material, initially at T_0, is suddenly exposed to an elevated temperature T_1 at one wall and maintained at this temperature, the temperature distribution can be described by:

$$\frac{\partial T}{\partial t} = \alpha \frac{\partial^2 T}{\partial y^2} \tag{6.100}$$

if it is assumed that α is independent of temperature.

Equation 6.100 is a shortened version of the general energy balance equation (Eq. 5.5) valid for simple unidirectional conduction. This is a standard handbook problem; the solution is (see [1] of Chapter 5):

$$\frac{T(y,t) - T_0}{T_1 - T_0} = 1 - \mathrm{erf}\left(\frac{y}{\sqrt{4\alpha t}}\right) \tag{6.101}$$

In Eq. 6.101 erf (x) stands for error function; this is defined as:

$$\mathrm{erf}\,(x) = \frac{2}{\sqrt{\pi}} \int_0^x \exp(-t^2)\,dt \tag{6.102}$$

This integral cannot be solved easily; however, tabular or graphical representations of the error function are available in various handbooks, e. g. [82]. Figure 6.29 shows the function 1–erf (x), the complementary error function.

Equation 6.101 describes conductive heating of a semi-infinite slab. It is valid as long as thermal penetration thickness δ_t is less than the slab thickness. Essentially all temperature change (99%) takes place within the thermal penetration thickness, which is given by:

$$\delta_t = 4\sqrt{\alpha t} \tag{6.103}$$

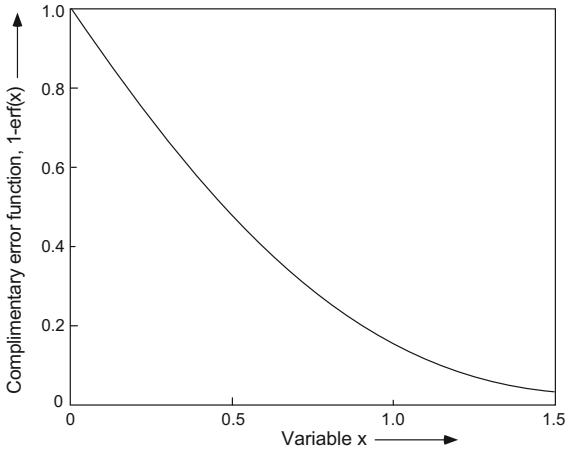


Figure 6.29
Complementary error function

The time, temperature profiles in a slab with double-sided heating are given by Eq. 7.99.

With Eqs. 6.101 and 6.102, the temperature as a function of time and distance is completely described. Thus, by doing simple temperature measurements on a slab of material with one wall suddenly exposed to a higher temperature, the thermal diffusivity can be determined in a relatively straightforward fashion.

This example illustrates how the thermal diffusivity can be measured and how it is used to describe heat conduction problems. For amorphous polymers and polymer melts, diffusivity is approximately linear with the velocity of sound v_s; the proportionality constant is about 6E–13 [41]:

$$\alpha = Cv_s \tag{6.104}$$

The sound velocity is related to the molar sound velocity function F_R or Rao function, the molar volume per structural unit V_m, and the Poisson ratio *v*. It can be written as:

$$v_s = \left(\frac{F_R}{V_m}\right)^3 \left[\frac{3(1-\upsilon)}{1+\upsilon}\right]^{1/2} \tag{6.105}$$

The Poisson ratio for liquids is 1/2 and for isotropic solids 1/3. The Poisson ratio for polymers below T_g is approximately 1/3 and above T_g about 1/2. The ratio of the Rao function and the molar volume is approximately constant for many amorphous polymers [41]; the ratio is about 55. Thus, the thermal diffusivity can be approximated with:

$$\alpha = \left[\frac{3(1-\upsilon)}{1+\upsilon}\right]^{1/2} 10^{-7} \tag{6.106}$$

with α expressed in m^2/s.

The ratio F_R/V_m is related to the compressibility κ and density ρ by:

$$\rho\kappa = \left[\frac{F_R}{V_m}\right]^{-6} \tag{6.107}$$

With Eq. 6.107, one can write the expression for the sound velocity as follows:

$$\alpha = \left[\frac{3(1-\upsilon)}{1+\upsilon}\right]^{1/2} 10^{-7} \tag{6.108}$$

The thermal diffusivity of most polymers is around 10^{-7} m^2/s. In the analysis of most extrusion problems, the thermal diffusivity is considered to be constant. In reality, however, the thermal diffusivity depends on pressure, temperature, and orientation. The anisotropy of the thermal diffusivity of uniaxially stretched polyethylene was studied by Kilian and Pietralla [83]. They found large differences between the thermal diffusivity in the orientation direction and perpendicular to the orientation direction, as high as 20:1. The pressure dependence of the thermal conductivity, thermal diffusivity, and specific heat of some polymers was studied by Andersson and Sundqvist [84]. They found that the thermal conductivity and thermal diffusivity increase with pressure. At very high pressures (≅ 4000 MPa), the thermal conductivity and thermal diffusivity about double. However, at pressures within the range of normal polymer processing, pressures less than 100 MPa (≅ 15,000 psi), the changes are less than 5%. At 30 MPa (≅ 5000 psi), the expected change in thermal conductivity and thermal diffusivity is about 1 to 2%; this will be negligible in most cases. The specific heat reduces with increasing pressure; however, in the polymer processing range, the changes are quite small – less than 0.5% at 100 MPa (≅ 15,000 psi).

6.3.6 Melting Point

The melting point is the temperature at which the crystallites melt. Since the crystallites are not perfectly uniform, there is really not one single melting point but a melt temperature range. The melting point is often taken as the temperature at the peak of the DSC curve; see Section 6.3.8.

The melting point is dependent on the pressure and crystallite morphology as discussed in Section 6.3.3. It can be measured quite easily and accurately. The melting point dictates, to some extent, the process temperatures necessary in extrusion. As a general rule, the process temperatures are about 50°C above the melting point. If the process temperature is too close to the melting point, the polymer melt viscosity will be too high, resulting in excessive power consumption. If the process temperature is too far above the melting point, the polymer may degrade.

For homopolymers, the melting temperature depends on the molecular weight of the polymer:

$$\frac{1}{T_m} - \frac{1}{T_{m_\infty}} = \frac{2RM_0}{\Delta HM_n} \tag{6.109}$$

where $T_{m\infty}$ is the melting temperature for an infinite length polymer molecule and M_0 is the molecular weight of the monomer.

6.3.7 Induction Time

The induction time of a polymer is a very useful quantity in process design, process optimization, and troubleshooting. It represents the amount of time elapsed at a certain temperature and in a certain atmosphere before the effects of degradation become measurable. Essentially, the induction time indicates how long a polymer can be exposed to a certain temperature before it starts to degrade.

In extrusion, one would like to make sure that the longest residence time in the machine at a certain process temperature is less than the induction time at the same temperature. Thus, if one knows the residence times to be expected in the extrusion process and if one knows how the induction time varies with temperature, the process temperature at which degradation will be avoided can be accurately determined. This is a very useful tool in process engineering, particularly if one deals with a polymer of limited thermal stability.

If degradation occurs during the extrusion process, there are two approaches that one can take to the problem. One is to modify the process so as to reduce the chance of degradation. The other approach is to modify the polymer to improve its thermal stability. The changes to the process should result in lower stock temperatures, and/

or reduced exposure time to elevated temperatures, and possibly exclusion of degradation-promoting substances (e.g., oxygen, certain additives, certain metal components of the tooling or substrate, etc.). If the changes to the process cannot alleviate the degradation problem, one has to consider the polymer itself. The thermal stability (induction time) of most polymers can be improved by adding stabilizers to the polymer, such as antioxidants. If process changes cannot solve the problem of degradation, the thermal stability of the polymer should be improved by adding stabilizers to it. Of course, one may opt to select a different polymer altogether.

In some cases, the thermal stability of a polymer or a compound is so poor that it cannot be extruded without degradation under any conditions. This can be conclusively determined if induction time data are available. The process engineer can then go back to the polymer chemist and explain exactly what changes should be made to the polymer. This procedure eliminates the question of whether the problem is caused by the polymer or by the process. Thus, induction time data can act as a bridge between the process engineer and polymer chemist and allow them to communicate and cooperate in a useful fashion.

It is clear that the induction time is a strong function of temperature. For many polymers, a plot of induction time against reciprocal absolute temperature will form approximately a straight line on semi-log paper, as shown in Fig. 6.30.

This indicates that the induction time reduces exponentially with temperature. Curve A in Fig. 6.29 is an HDPE as received from the manufacturer and curve B is an ethylene acrylic acid (EAA) as received from the manufacturer. The HDPE can be processed at 200°C without noticeable degradation; however, EAA shows clear signs of degradation at that temperature. It should be processed at about 160°C to avoid degradation.

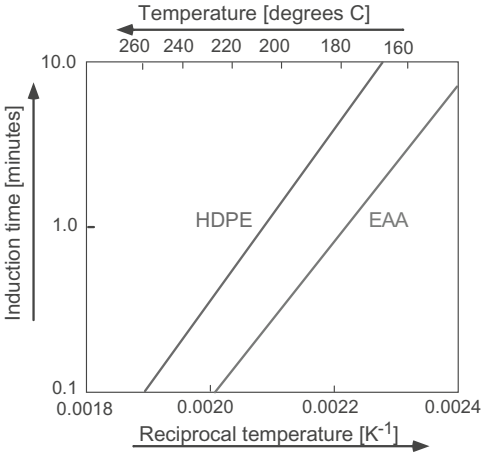


Figure 6.30
Induction time versus temperature

The relationship between induction time t_{ind} and temperature T can generally be expressed as an Arrhenius equation:

$$t_{ind} = A \exp\left(\frac{E}{RT}\right) \tag{6.110}$$

where A is a time constant, E the activation energy, and R the universal gas constant.

The induction time can be conveniently determined on a TGA, but other instruments can be used as well, for instance a DSC. Thermal characterization will be discussed in the next section.

6.3.8 Thermal Characterization

In thermal characterization, a controlled amount of heat is applied to a sample and its effect measured and recorded. In isothermal operations, the effect is recorded as a function of time at constant temperature. In a programmed temperature operation, the temperature is changed in a predetermined fashion, e.g., at a certain rate, and the effect is recorded as a function of temperature. General texts on thermal characterization include Wendlandt [85], Daniels [86], and Turi [87].

6.3.8.1 DTA and DSC

Differential thermal analysis (DTA) and differential scanning calorimetry (DSC) are similar techniques. They measure change in the heat capacity of a sample. These techniques can be used to determine various transition temperatures (T_m, T_g, T_α, T_β, etc.), specific heat, heat of fusion, percent crystallinity, onset of degradation temperature, induction time, reaction rate, crystallization rate, etc. A DSC instrument operates by compensating electrically for a change in sample heat. The power for heating is controlled in such a way that the temperature of the sample and the reference is the same. The vertical axis of a DSC temperature scan shows the heat flow in cal/s.

A DTA instrument operates by measuring the change in sample temperature with respect to an inert reference. Newer DTA instruments with externally mounted thermocouple and reproducible heat path have a precision comparable to the DSC. Older DTA instruments with the thermocouple placed in the sample were less accurate and reproducible.

6.3.8.2 TGA

A thermogravimetric analyzer measures the change in weight of a sample due to volatilization, reaction, or absorption from the gas phase. With polymers, the TGA is used to measure the amount and loss of moisture or diluent, and rates and tempera-

tures of reactions. It is a convenient instrument to determine the polymer induction time, as discussed in Section 6.3.7. Sample size is usually less than one gram, thus the amount of polymer required for characterization is minimal.

6.3.8.3 TMA

In thermomechanical analysis (TMA), the change in mechanical properties is measured as a function of temperature and/or time. A probe in contact with the sample moves as the sample undergoes dimensional changes. The movement of the probe is measured with an LVDT. The sample deformations that can be measured are compression, penetration, extension, and flexure or bending.

6.3.8.4 Other Thermal Characterization Techniques

While TMA refers to a measurement of a static mechanical property, there are also techniques that employ dynamic measurement. In the torsional braid analysis (TBA), a sample is subjected to free torsional oscillation. The natural frequency and the decay of oscillations are measured. This provides information about the viscoelastic behavior of materials. However, these measurements are elaborate and time consuming. In dynamic mechanical analysis (DMA), a sample is exposed to forced oscillations. A large number of useful properties can be measured by this technique; see also Section 6.2.6.5.

In thermal optical analysis (TOA), the conversion of plane-polarized light to elliptically polarized light is measured in semi-crystalline polymers. The intensity of the depolarized light transmitted through a sample is a function of the level of crystallinity. Melting and recrystallization phenomena can be analyzed; the technique does not appear to be sensitive to glass transitions [88]. The TOA technique is also referred to as thermal depolarization analysis (TDA) and depolarized light intensity method (DLI).

■ 6.4 Polymer Property Summary

In Table 6.2 a number of rheological and thermal properties have been tabulated for several important generic polymers. These data have been gathered from numerous sources, including the author's own measurements. The data should be used as estimates only, because measurement techniques may differ and because considerable differences in properties can occur in one particular polymer as a result of variations in molecular weight distribution, additives, thermomechanical history, etc. Actual measurement of polymer properties should always be preferred above published data. However, actual measurement is not always possible, in which case the table may provide useful information.

Finally, some useful references should be mentioned containing data on polymer properties. Nielson's book [89] on polymer properties is an exhaustive survey of a large number of physical properties. The book by van Krevelen [41] is an excellent book on polymer properties and their relationship to chemical structure. The VDMA series on properties for polymer processing [90, 91, 95] contains a large amount of data on thermal properties [90], melt flow properties [91], and frictional properties [95]. Other useful data can be found in the yearly issues of the International Plastics Selector Books, the yearly Modern Plastics Encyclopedia, the Plastics Technology Manufacturing Handbook and Buyers' Guide, etc.

Nowadays, a substantial amount of information is available on the internet, and polymer properties are no exception. Many resin suppliers have data available on their website, and there are a number of electronic polymer databases available. One of the most useful databases is CAMPUS, acronym for Computer Aided Material Preselection by Uniform Standards. CAMPUS has become the most successful and widely used materials database for plastics. More than 25 international resin suppliers provide technical data on their products; more than 100,000 copies have been distributed in Europe alone.

Table 6.2 Useful Properties of a Number of Generic Polymers

Polymer	k [J/ms°C]	C_p [J/g°C]	ρ [g/cm³]	T_g [°C]	T_{mp} [°C]	n [–]	dη/ηdT [°C⁻¹]
PS	0.12	1.20	1.06	101	–	0.30	0.08
PVC	0.21	1.10	1.40	80	–	0.30	0.20
PMMA	0.20	1.45	1.18	105	–	0.25	0.20
SAN	0.12	1.40	1.08	115	–	0.30	0.20
ABS	0.25	1.40	1.02	115	–	0.25	0.20
PC	0.19	1.40	1.20	150	–	0.70	0.05
LDPE	0.24	2.30	0.92	–120/–90	120	0.35	0.03
LLDPE	0.24	2.30	0.92	–120/–90	125	0.60	0.02
HDPE	0.25	2.25	0.95	–120/–90	130	0.50	0.02
PP	0.15	2.10	0.91	–10	175	0.35	0.02
PA-6	0.25	2.15	1.13	50	225	0.70	0.02
PA-6.6	0.24	2.15	1.14	55	265	0.75	0.03
PET	0.29	1.55	1.35	70	275	0.60	0.03
PBT	0.21	1.25	1.35	45	250	0.60	0.03
PVDF	0.16	1.38	1.76	–40	170	0.38	0.03
FEP	0.20	1.18	2.15	70	275	0.60	0.04

k is the thermal conductivity
C_P is the specific heat at constant pressure
ρ is the density
T_g is the glass transition temperature
T_{mp} is the crystalline melting point
n is the power law index
dη/ηdT is the relative change in viscosity with temperature

The data in the CAMPUS database has been obtained with uniform, standardized test methods as descriribed in ISO 10350, ISO 11403-1, and ISO 11403-2. CAMPUS is distributed free of charge to customers directly from the resin manufacturers. In fact, CAMPUS data from a number of resin suppliers can be downloaded from their websites at no cost. CAMPUS is available in five languages: English, German, French, Spanish, and Italian [102]. Some of the data in this chapter are actually from this database.

M-Base Engineering + Software GmbH in Aachen, Germany (www.m-base.de) makes available a program, MCBase, that allows the user to search, compare, and perform queries of all CAMPUS data that the user has loaded into the databank. MCBase has several features not available in CAMPUS such as WLF and power-law curve fitting of viscosity data, substitute grade search, exclude function, and enhanced text search options.

References

1. R. C. Wahl, Plastics World, 64–67, Nov. (1978)
2. J. R. Mitchell, Chem. Eng. (U. K.), 177–183, Feb. (1977)
3. D. Train and C. J. Lewis, 3rd Congress European Federation of Chemical Engineers, London, June 20–29 (1962)
4. A. W. Jenike, P. J. Elsey, and R. H. Woolley, Proc. Am. Soc. Test Mater., 60, 1168 (1960)
5. R. S. Spencer, G. D. Gilmore, and R. M. Wiley, J. Appl. Phys., 21, 527–531 (1950)
6. D. Train, Trans. Inst. Chem. Eng. 35, 262–265 (1957)
7. W. M. Long, Powder Metall., No. 6, 73–86 (1980)
8. K. Schneider, Chem. Eng. Techn., 41, 142 (1969)
9. E. Goldacker, Ph. D. thesis, IKV, Aachen, Germany (1971)
10. K. Umeya and R. Hara, Polym. Eng. Sci., 18, 366–371 (1978)
11. K. Umeya and R. Hara, Polym. Eng. Sci., 20, 778–782 (1980)
12. N. M. Smith and J. Parnaby, Polym. Eng. Sci., 20, 830–833 (1980)
13. K. Kawakita and K. H. Luedde, Powder Techn., 4, 61 (1970)
14. R. J. Crawford, Polym. Eng. Sci., 22, 33–306 (1982)
15. W. Ostwald, Kolloid-2, 36, 99–117 (1925)
16. A. de Waele, Oil and Color Chem. Assoc. J., 6, 33–88 (1923)
17. R. B. Bird, R. C. Armstrong, and O. Hassager, “Dynamics of Polymeric Liquids,” Vol. I, p. 209, Wiley, NY (1977)
18. H. Eyring, Ind. Eng. Chem., 50, 1036–1040 (1958)
19. P. J. Carreau, Ph. D. thesis, Univ. of Wisconsin, Madison (1968)
20. M. Reiner, “Deformation Strain and Flow,” a) p. 258, b) p. 246, Interscience Publishers, NY (1960)

21. J. M. McKelvey, "Polymer Processing," Wiley, NY (1962)
22. A. H. P. Skelland, "Non-Newtonian Flow and Heat Transfer," Wiley, NY (1967)
23. F. P. Bowden and D. Tabor, "Friction and Lubrication of Solids," Oxford Univ. Press, London (1950)
24. K. Schneider, Ph. D. thesis, IKV, Aachen, Germany (1968)
25. K. Schneider, Kunststoffe, 59, 97–102 (1969)
26. C. I. Chung, W. J. Hennessee, and M. H. Tusim, Polym. Eng. Sci., 17, 9–20 (1977)
27. J. Huxtable, F. N. Cogswell, and J. D. Wriggles, Plast. Rubber Proc. Appl., 1, 87–93 (1981)
28. H. Chang and R. A. Daane, SPE 32nd ANTEC, San Francisco, p. 335, May (1974)
29. R. B. Gregory, SPE J., 25, 55–59 (1969)
30. G. M. Gale, SPE 39th ANTEC, Boston, p. 669, May (1981)
31. J. A. D. Emmanuel and L. R. Schmidt, SPE 39th ANTEC, Boston, p. 672, May (1981)
32. G. M. Bartenev and V. V. Lavrentev, "Friction and Wear of Polymers," Elsevier, NY (1981)
33. B. Maxwell and A. Jung, Modern Plastics, 35, 3, 174–180 (1957)
34. R. F. Westover, SPE Trans. 1, 14–20 (1962)
35. V. Semjonov, Rheologica Acta, 2, 138–142 (1962); 4, 133–137 (1965); 6, 154–170 (1967)
36. R. C. Penwell, R. S. Porter, and S. Middleman, J. Polym. Sci. A2, 9, 4, 731–745 (1971).
37. P. H. Goldblatt and R. S. Porter, J. Appl. Polym. Sci., 20, 1199–1208 (1976)
38. I. J. Duvdevani and I. Klein, SPE J., Dec., 41–45 (1967)
39. S. T. Choi, J. Polym. Sci. A2, 6, 2043–2049 (1968)
40. F. N. Cogswell, Plastics and Polymers, 41, 30–43 (1973)
41. D. W. van Krevelen, "Properties of Polymers, Correlations with Chemical Structure," Elsevier, NY (1972)
42. A. W. Jenike, "Gravity Flow of Bulk Solids," Bulletin No. 108 of the Utah Engineering Experimental Station, Univ. of Utah, Salt Lake City (1961)
43. R. Rautenbach and E. Goldacker, Kunststoffe, 61, 104–107 (1971)
44. E. Goldacker and R. Rautenbach, Chemie Ing. Techn. 44, 405–410 (1972)
45. J. Mewis, J. Non-Newtonian Fluid Mech., 6, 1–20 (1979)
46. J. M. Dealy and W. K. W. Tsang, J. Appl. Polym. Sci., 26, 1149–1158 (1981)
47. T. Y. Liu, D. S. Soong, and M. C. Williams, Polym. Eng. Sci., 21, 675–687 (1981)
48. J. L. White and W. Minoshima, Polym. Eng. Sci., 21, 1113–1121 (1981)
49. C. M. Vrentas and W. W. Graessley, J. Non-Newtonian Fluid Mech., 9, 339–355 (1981).
50. G. De Cleyn and J. Mewis, J. Non-Newtonian Fluid Mech., 9, 91–105 (1981)
51. J. Mewis and G. De Cleyn, AIChE J., 28, 900–907 (1982)
52. J. Mewis and M. M. Denn, J. Non-Newtonian Fluid Mech., 12, 69–83 (1983)
53. D. Acierno, F. P. LaMantia, G. Marrucci, and G. Titomanlio, J. Non-Newtonian Fluid Mech., 1, 125–146 (1976)

54. C.D. Han, "Rheology in Polymer Processing," Academic Press, NY (1976)
55. J.D. Ferry, "Viscoelastic Properties of Polymers," 3rd edition, Wiley, NY (1980)
56. J.J. Aklonis, W.J. MacKnight, and M. Shen, "Introduction to Polymer Viscoelasticity," Wiley-Interscience, NY (1972)
57. K. Walters, "Rheometry," Wiley, NY (1975)
58. R.S. Lenk, "Polymer Rheology," Applied Science Publ. LTD, London (1978)
59. J.A. Brydson, "Flow Properties of Polymer Melts," 2nd edition, George Godwin Limited, London (1981)
60. F.N. Cogswell, "Polymer Melt Rheology," George Godwin Limited, London (1981)
61. "Praktische Rheologie der Kunststoffe," VDI-Verlag GmbH, Duesseldorf (1978)
62. O. Plajer, "Praktische Rheologie fuer Kunststoffschmelzen," Zechner & Huethig Verlag GmbH, Speyer, Germany (1970)
63. L.E. Nielsen, "Polymer Rheology," Marcel Dekker, NY (1977)
64. "Rheometry: Industrial Applications," K. Walters (Ed.), Research Studies Press, Chichester, England (1980)
65. J.R. Van Wazer, J.W. Lyons, K.Y. Kim, and R.E. Colwell, "Viscosity and Flow Measurement, A Laboratory Handbook of Rheology," Interscience Publishers, NY (1963)
66. J.M. Dealy, "Rheometers for Molten Plastics," Van Nostrand Reinhold Co., NY (1982)
67. D.V. Boger and M.M. Denn, J. Non-Newtonian Fluid Mech., 6, 163–185 (1980)
68. R.D. Pike, D.E. Baird, and M.D. Read, SPE 41st ANTEC, Chicago, 312–315 (1983)
69. C.D. Han, J. Appl. Polym. Sci., 15, 2567–2577 (1971)
70. J.L.S. Wales, J.L. den Otter, and H. Janeschitz-Kriegl, Rheol. Acta, 4, 146–152 (1965)
71. C. Rauwendaal and F. Fernandez, SPE 42nd ANTEC, 282–287, New Orleans (1984)
72. W.P. Cox and E.H. Merz, J. Polym. Sci., 28, 619–622 (1958)
73. K. Eiermann and K.H. Hellwege, J. Polym. Sci., 57, 99 (1962)
74. D. Hansen and G.A. Bernier, Polym. Eng. Sci., 12, 204 (1972)
75. S. Yagi and D. Kunii, AIChE J., 3, 373 (1957)
76. B. Maxwell et al., SPE Trans., 4, 165 (1964)
77. R.S. Spencer and G.D. Gilmore, J. Appl. Phys., 20, 502 (1949), 21, 523 (1950)
78. H. Breuer and G. Rehage, Kolloid Z.Z. Polym., 216, 166 (1967)
79. M.R. Kamal and N.T. Levan, Polym. Eng. Sci., 13, 131 (1973)
80. O. Olabisi and R. Simha, Macromolecules, 8, 206 (1975); 211 (1975)
81. W. Thompson, Phil. Mag., 42, 448 (1971)
82. H.B. Dwight, "Tables of Integrals and Other Mathematical Data," 3rd edition, p. 275 MacMillan, NY (1957)
83. H.G. Kilian and M. Pietralla, Polymer, 19, 664–672 (1978)
84. P. Andersson and B. Sundqvist, J. Polym. Sci., 13, 243–251 (1975)
85. W.W. Wendlandt, "Thermal Methods of Analysis," Wiley, NY (1979)

86. T. Daniels, “Thermal Analysis,” Anchor Press, London (1973)
87. E.A. Turi (Ed.), “Thermal Characterization of Polymeric Materials,” Academic Press, NY (1981)
88. G.W. Miller and R.S. Porter, “Analytical Calorimetry,” Vol. 2, p. 407 Plenum Press, NY (1970),
89. L.E. Nielson, “Mechanical Properties of Polymers and Composites,” Vol. 1 and 2, Marcel Dekker, NY (1974)
90. “Kenndaten fuer die Verarbeitung Thermoplastischer Kunststoffe, Teil I, Thermodynamik,” Carl Hanser, Munich (1979)
91. “Kenndaten fuer die Verarbeitung Thermoplastischer Kunststoffe, Teil II, Rheologie,” Carl Hanser, Munich (1982)
92. J.M. Dealy, Plast. Eng., March, 57–61 (1983)
93. M.R. Kamal, V. Tan, and F. Kashani, Adv. Polym. Tech., 3, 89–98 (1983)
94. C.J.S. Petrie, “Elongational Flows,” Pitman (1979)
95. “Kenndaten fuer die Verarbeitung Thermoplastischer Kunststoffe, Teil III, Tribologie,” Carl Hanser, Munich (1983)
96. G.R. Langecker and R. Rautenbach, Powder Techn., 15, 39–42 (1976)
97. G.R. Langecker, Dissertation, IKV, Aachen, Germany (1977)
98. H. Schott, J. Appl. Polym. Sci., 6, 529 (1962)
99. R. Steller and J. Iwko, “Generalized Flow of Ellis Fluid in the Screw Channel,” International Polymer Processing, Mar. (2001) pp. 241–248
100. R.I. Tanner, “Engineering Rheology,” Oxford University Press, New York (1985)
101. G.V. Gordon and M.T. Shaw, “Computer Programs for Rheologists,” Carl Hanser Verlag, Munich (1994)
102. H. Breuer, et al., “CAMPUS Set for its Global Breakthrough,” Kunststoffe, 84, 8, 1003–1012 (1994)

7 Functional Process Analysis

Chapters 5 and 6 on fundamental principles and important polymer properties are meant to be a preparation for the material covered in this chapter. In this chapter, the central part of this book, the six main functions of an extruder will be described and analyzed. The main functions are solids conveying, plasticating or melting, melt conveying or pumping, devolatilization, mixing, and die forming. The material in this chapter is key to developing a thorough understanding of the extrusion process and indispensable in taking an engineering approach to screw design, die design, and troubleshooting.

Each function will be discussed separately. The mechanism behind each function will be described in detail. The emphases will be on developing a thorough understanding and quantitative description of the entire extrusion process from a functional point of view. In later chapters, this knowledge will be applied to practical aspects, such as screw design, die design, troubleshooting, etc. It should be realized that in dividing the extruder into functional zones, these zones are not discrete but, to some extent, overlapping. Their boundaries can shift when polymer properties or operating conditions change. For instance, in the melt conveying zone, there will be a certain amount of mixing taking place as well; thus, the mixing zone will overlap the melt conveying zone. On the other hand, the geometrical sections of the screw are fixed; they are discrete and non-overlapping. The geometrical sections of a standard screw are the feed, compression, and metering sections.

7.1 Basic Screw Geometry

The analysis of the functional zones of the extruder requires knowledge of the basic relationships describing the geometry of an extruder screw. The geometry of the flight along the screw surface can be constructed by unrolling the flight onto a flat plane. On a flat surface, the flight along the screw surface will form a right triangle as shown on the right-hand triangle in Fig. 7.1. The base of the triangle is one-half of the flight pitch if the height of the triangle is half the circumference at the screw surface. The flight lead or pitch S is the axial distance between two points on the

flight separated by a full turn of the flight. The flight pitch is the same as the flight lead for a single-flighted screw. However, for a multi-flighted screw the pitch is the lead divided by the number of flights. The top angle of the triangle is the helix angle of the screw surface φ_s. If points along the screw surface are connected to corresponding points along the altitude of the triangle, one constructs the helical geometry of the flight along the surface of the root of the screw.

The same procedure can be used to construct the helical geometry of the flight along the O.D. of the screw as shown in the left-hand side of Fig. 7.1.

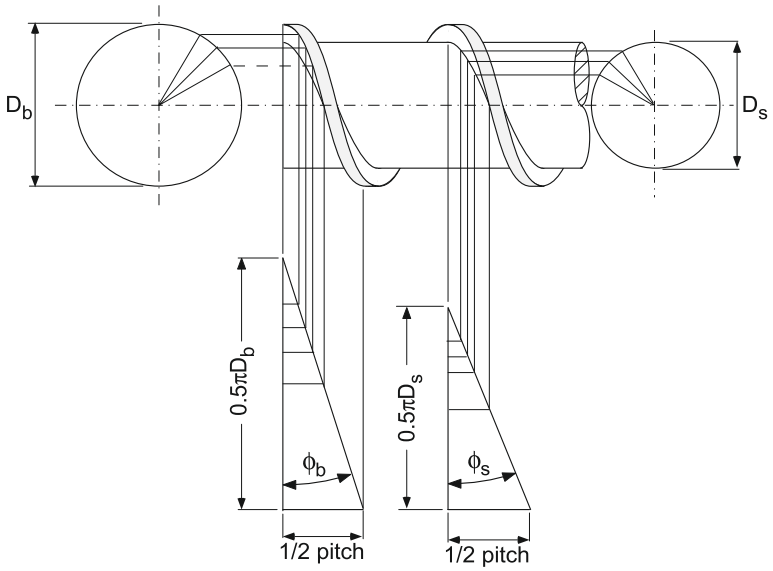


Figure 7.1 Construction of a basic screw geometry

It should be noted that the helix angle at the O.D. of the screw φ_b is different from the helix angle at the root of the screw φ_s. The screw geometry is usually represented by straight flights, as shown in Fig. 7.2.

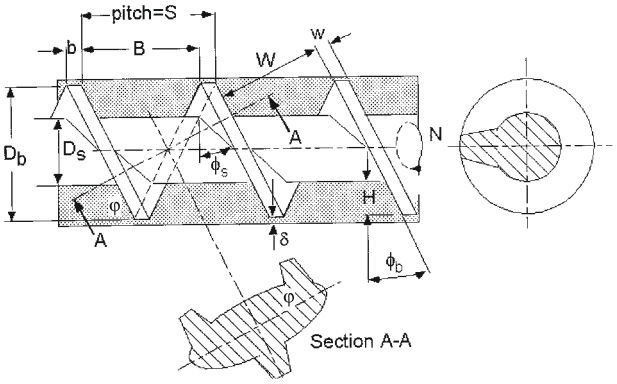


Figure 7.2
Screw with flights drawn straight

However, in reality the flights are S-shaped, as seen in Fig. 7.1. If a cross-section is made perpendicular to the flights, it can be seen that the screw channel is not a true rectangle. The bottom and top surface of the screw channel are curved and the flight flanks diverge. Thus, the channel width is larger at the screw O.D. than at the root of the screw.

Important geometrical relationships will be given next. The pitch of the screw equals the sum of the axial channel width and the axial flight width.

$$S = (B + b) \tag{7.1}$$

The lead L is the pitch times the number (p) of parallel flights.

$$L = p(B + b) \tag{7.2}$$

The helix angle at the barrel surface φ_b is determined by the ratio of the pitch and the circumference at the barrel surface.

$$\varphi_b = \arctan\left(\frac{S}{\pi D_b}\right) \tag{7.3}$$

Similarly, the helix angle φ_m at the middle of the channel is:

$$\varphi_m = \arctan\left(\frac{S}{\pi D_m}\right) \tag{7.4}$$

The helix angle φ_s at the root of the screw is:

$$\varphi_s = \arctan\left(\frac{S}{\pi D_s}\right) \tag{7.5}$$

The perpendicular channel width at the barrel surface is:

$$W_b = B\cos\varphi_b \tag{7.6}$$

The perpendicular channel width at the middle of the channel is:

$$W_m = B\cos\varphi_m \tag{7.7}$$

The perpendicular channel width at the root of the screw is:

$$W_s = B\cos\varphi_s \tag{7.8}$$

The channel width at the barrel surface is related to the pitch and the helix angle at the barrel surface as follows:

$$W_b + w = S\cos\varphi_b \tag{7.9}$$

The channel width in the middle of the channel can be expressed as:

$$W_m = \pi D_m \sin\varphi_m - w \tag{7.10a}$$

Subscript m refers to the dimensions at the midpoint of the channel, and the diameter at the midpoint of the channel equals the barrel diameter minus the flight height ($D_m = D_b - H$).

Equation 7.10(a) is valid only for single-flighted screws (p = 1).

If the screw has p parallel flights, then:

$$W_m = \frac{\pi D_m \sin\varphi_m}{p} - w \tag{7.10b}$$

The channel dimensions used without subscripts are related to the O.D. of the screw.

7.2 Solids Conveying

The solids conveying zone extends from the feed hopper down several diameters into the extruder barrel. The first traces of molten polymer generally do not appear until about three or four diameters into the barrel, measured from the feed port. Since the conveying process in the feed hopper is considerably different from the conveying process in the screw channel, the solids conveying zone will be divided into the gravity induced solids conveying zone (feed hopper) and the drag induced solids conveying zone (extruder screw).

Some feed hoppers are equipped with crammer feeders; see Fig. 7.3.

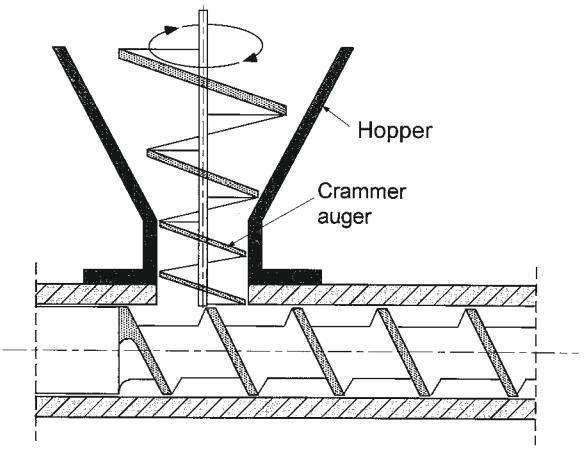


Figure 7.3
Crammer feeder

This is a feed hopper with a rotating screw in the discharge region. The screw is incorporated to augment the solids conveying rate by the action of the rotating screw. In such a feed hopper, gravity induced solids conveying and drag induced solids conveying occur simultaneously at the same location. In this case, the two types of solids conveying cannot be separated but must be analyzed together.

7.2.1 Gravity Induced Solids Conveying

Most feed hoppers have a cylindrical top section and a truncated conical section at the bottom; see Fig. 7.4.

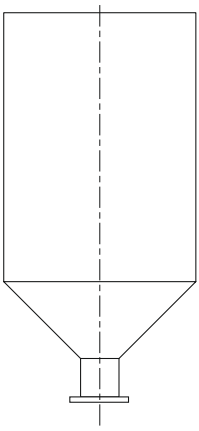


Figure 7.4
Typical feed hopper

The driving force for solids conveying is gravity. Based on the bulk properties and the hopper geometry, one would like to be able to calculate the stress distribution in the hopper, the velocity profiles in the hopper, and finally the discharge rate. Unfortunately, the analysis of flow of granular materials in hoppers is rather complicated as a result of the complex flow behavior of granular material, as discussed in Section 6.1. In most cases, the results of the analysis are approximate and apply only to a limited number of cases. Even the relatively simple problem of a non-cohesive bulk material flowing through a hopper has not been completely solved. Not surprisingly, the situation is worse for the more realistic problem of a cohesive particulate material flowing through a hopper.

Theoretical and experimental work on the transport of bulk material started in earnest around 1960. A collection of experimental and theoretical work was presented at a joint ASME-CSME Conference on Mechanics Applied to the Transport of Bulk Materials [1] and the U.S.-Japan seminars on Continuum Mechanical and Statistical Approaches in the Mechanics of Granular Materials [2]. Books on particulate solids have been written by Orr [3] and Brown and Richards [4]. Review articles have been published by Richards [5], Wieghardt [6], and Savage [7]. Some of the pioneering work on flow of bulk solids was done by Jenike [8, 9].

In the flow of bulk materials through a hopper, one generally distinguishes between two types of flow. In mass flow or hopper flow, the entire volume of particulate solids moves down toward the exit; there are no stagnating regions. The other type of flow is funnel flow. In funnel flow, the bulk material flows out through a flow channel, the wall of the flow channel being formed by stationary particles of the bulk material. In funnel flow, therefore, there is at least one stagnating region; see Fig. 7.5.

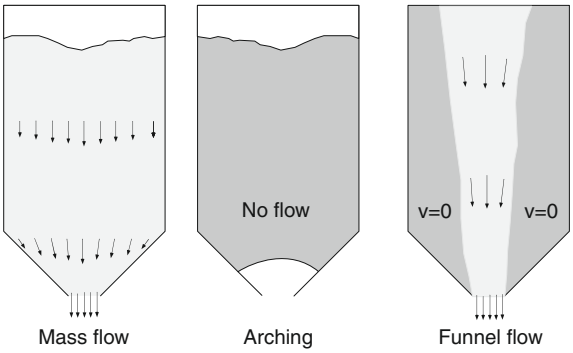


Figure 7.5
Various types of flow that can occur in feed hoppers

A common flow problem in hopper flow is arching or bridging. The particles form a natural bridge able to support the material above it. As mentioned in Section 6.1, highly compressible materials have a strong tendency towards bridging. With such materials, the hopper is often equipped with a vibrating pad to dislodge any bridges that might form by a continuous mechanical vibration of the hopper. It is possible to derive criteria to avoid arching; these can be used in the design of feed hoppers and will be discussed later. Piping is a disturbance that occurs in funnel flow. An annular ring of stationary bulk material is formed. The material in this stagnating region is able to support the material above it and the exposed surface of the internal, empty channel.

Both in arching and in piping, the material is consolidated to the extent that it can support the material above it and form an exposed surface. Thus, both these flow problems are typical of cohesive (non-free-flowing) particulate solids. This is particularly true for materials with a high, unconfined yield strength σ_c; see Section 6.1.2 and Fig. 6.4(b).

In the analysis of flow of granular material, two types of flow can be distinguished. The first is slow frictional flow where the particles remain in continuous contact with each other; the internal forces result from Coulomb friction between contacting particles. The second type of flow is much more rapid; the particles are not in constant contact with their neighbors. The energy associated with the velocity fluctuations is comparable to that of the mean motion. In this type of flow, the internal forces arise because of the transfer of momentum during collisions between particles. The constitutive relations for this rapid flow are rate-dependent. This type of flow, therefore, is referred to as viscous flow (sometimes just rapid flow). Steady,

viscous flows are generally described by elliptic partial differential equations [10–13].

In gravity flow through feed hoppers, it can be assumed that the flow is sufficiently slow that the particles are in constant contact and that momentum transfer by collisions between particles is negligible. The flow through a feed hopper can thus be considered to be frictional flow. Various workers [14–21] have made experimental studies of the flow patterns in feed hoppers. In some studies, dyed particles were used, e.g., [17]; in others, X-ray techniques were employed to determine the flow patterns in the hopper [15, 16]. In other studies [18, 19, 21], a stereoscopic technique was used. This involves taking photographs of the flow field at short time intervals. Sequential photographs are analyzed using a stereocomparator; this results in a three-dimensional model of the displacement field from which the velocity field can be determined. This technique is limited to two-dimensional flows, but does not require tracers and enables determination of the entire flow field.

The flow of bulk material in a feed hopper is generally quite different in the various sections of the hopper; see Fig. 7.6.

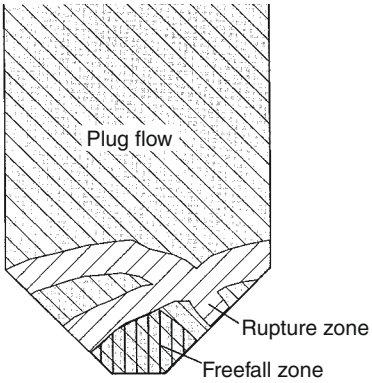


Figure 7.6
Various flow regimes in a feed hopper

The flow in the cylindrical hopper section tends to be plug flow. The plug flow zone is bound by a rupture zone at the bottom of the plug flow zone. The rupture zone is situated approximately at the cylinder-cone transition. This zone is characterized by intense relative deformation of the granular material. Below the rupture zone, further down in the conical section, there may be local regions of plug flow. These local plug flow regions are generally bound by the hopper wall and the rupture zone. Finally, in the bottom part of the conical section the particles flow out freely; this is referred to as the free-flow zone.

Unfortunately, at this point in time, the understanding of the mechanics of flow of bulk solids is not well enough developed that this flow behavior can be predicted theoretically. The main area of uncertainty is the proper constitutive equation for bulk materials relating stress and strain rates. Because the theory is not well developed, only a few aspects of gravity flow in hoppers will be discussed further. These

are pressure distribution in feed hoppers, criteria to avoid flow disturbances, and flow rate predictions. It should be remembered that the following relationships have limited applicability and accuracy in terms of their predictive ability.

7.2.1.1 Pressure Distribution

In the cylindrical portion of a hopper the pressure distribution can be derived if the following assumptions are made:

1. The vertical compressive stress is constant over any horizontal plane.
2. The ratio of horizontal and vertical stresses is constant and independent of depth.
3. The bulk density is constant.
4. The wall friction is fully mobilized, meaning that the particulate material is in incipient slip conditions at the wall.

A force balance over a differential element (see Fig. 7.7) gives:

$$\rho_b \, g \, \pi R^2 + \pi R^2 dP = (\tau_{wa} + f_w^* kP) \, 2\pi R \, dh \tag{7.11}$$

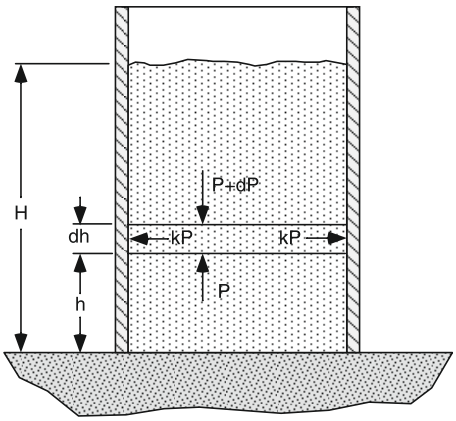


Figure 7.7
Illustration of force balance

where ρ_b is bulk density, g the gravitational acceleration, f_w^* the coefficient of friction at the wall, and k the ratio of compressive stress in the horizontal direction to compressive stress in the vertical direction. The shear stress at the wall is determined by Eq. 6.8. An expression for the ratio k can be found if it is assumed that the maximum principal stress is in the vertical direction. The ratio k can be determined from Eq. 6.7.

$$k = \frac{1 - \sin\beta_e}{1 + \sin\beta_e} \tag{7.12}$$

where β_e is the effective angle of internal friction.

Equation 7.12 applies if the particulate solids are in a condition of steady flow; it also applies to cohesionless materials in a condition of incipient flow. Integration of Eq. 7.11 yields the pressure distribution:

$$P = \frac{\rho_b g R - 2\tau_{wa}}{2f_w^* k} + \frac{1}{2f_w^* k} \exp\left(\frac{2f_w^* kh}{R} + \text{constant}\right) \tag{7.13}$$

If the pressure at h = H is taken as zero and if the adhesive wall shear stress is zero, Eq. 7.13 reduces to the well-known Janssen Equation derived in 1895 [22]:

$$P = \frac{\rho_b g R}{2f_w^* k}\left[1 - \exp\frac{2f_w^* k(h - H)}{R}\right] \tag{7.14}$$

If the value of H is sufficiently large, the pressure becomes independent of vertical distance; this limiting pressure value is:

$$P_{max} = \frac{\rho_b g R}{2f_w^* k} \tag{7.15}$$

The maximum pressure is directly proportional to the bulk density and cylinder radius and inversely proportional to the coefficient of friction at the wall and the ratio k.

Walker [23] made a more rigorous analysis of the pressure distribution in vertical bins. He assumed a plastic equilibrium in the particulate solids with the Mohr circles representing the stress condition at a certain level touching the effective yield locus. Walker derived the following expression for the pressure profile in a vertical cylinder:

$$P = \frac{\rho_b g R}{2BD^*}\left[1 - \exp\frac{2BD^*(h - H)}{R}\right] \tag{7.16}$$

where D* is defined as a distribution factor relating the average vertical stress with the vertical stress near the wall. In principle, this distribution function D* can be evaluated by solving the entire stress field, as discussed by Walters and Nedderman [24]. However, as a first approximation, the distribution factor can be assumed to be unity. The ratio of shear stress to normal stress at the wall, B, is given by:

$$B = \frac{\sin\beta_e \sin 2\beta^*}{1 - \sin\beta_e \cos 2\beta^*} \tag{7.17}$$

where β^* is the angle between the major principal plane and the cylinder wall.

The angle β^* is related to the effective angle of friction β_e and the wall angle of friction β_w = arctan f_w^* by:

$$2\beta^* = \beta_w + \arcsin\frac{\sin\beta_w}{\sin\beta_e} \tag{7.18}$$

where the arcsin value is to be larger than 90°.

Walker also derived equations for the stress distribution in a conical hopper section. These equations have clear practical importance because most feed hoppers are designed with conical sections. The pressure distribution for mass flow conditions is given by:

$$P = \left(\frac{h}{h_o}\right)^c P_o + \frac{\rho_b\, g\, h}{c-1}\left[1-\left(\frac{h}{h_o}\right)^{c-1}\right] \qquad \text{for } c \neq 1 \tag{7.19}$$

and

$$P = \frac{h}{h_o} P_o + \rho_b g\, h \ln\left(\frac{h_o}{h}\right) \qquad \text{for } c = 1 \tag{7.20}$$

where h_o is the height where the vertical pressure is P_o. This height can be taken as the height of the conical hopper section, as shown in Fig. 7.8.

The coefficient c for conical hoppers is:

$$c = \frac{2B'D^*}{\tan\alpha} \tag{7.21}$$

where α is the hopper half-apex angle; see Fig. 7.8.

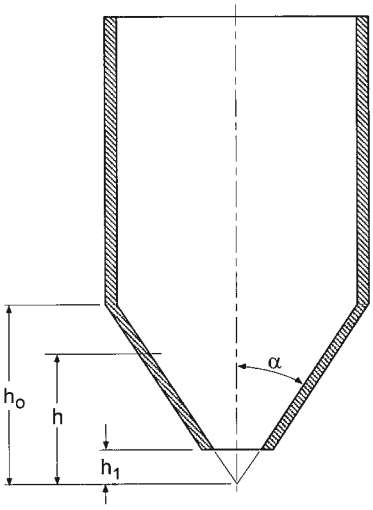


Figure 7.8
Conical hopper configuration

The coefficient c for wedge-shaped hoppers is:

$$c = \frac{B'D^*}{\tan\alpha} \tag{7.22}$$

The stress ratio B′ is given by:

$$B' = \frac{\sin\beta_e \sin(2\alpha + 2\beta^*)}{1 - \sin\beta_e \cos(2\alpha + 2\beta^*)} \tag{7.23}$$

In the convergent hopper section, angle β^* is given by:

$$2\beta^* = \beta_w + \arcsin\frac{\sin\beta_w}{\sin\beta_e} \tag{7.24}$$

where the arcsin value is to be less than 90°!

If the initial pressure in the conical section is zero, the maximum pressures will occur somewhere along the conical section. In most cases, however, a cylindrical hopper section is placed on top of the conical hopper section. In these situations, the initial pressure distribution in the conical section will be determined by the final pressure distribution in the cylindrical section. If the stress distributions do not match, rupture zones may form in the transition region as observed by Lee et al. [15]. Instabilities of stress conditions at the transition region have been discussed by Bransby and Blair-Fish [25].

7.2.1.2 Flow Rate

The flow rate of granular materials is independent of the head if the head is sufficiently large. This experimental result was known as early as 1852, when Hagen presented an equation for the flow rate through a circular opening [26]:

$$\dot{M} = J_a \frac{\pi}{4} \rho_b \left[g (D_a - f_c d_p)^5 \right]^{0.5} \tag{7.25}$$

where J_a is a parameter called the non-dimensional axisymmetric flow rate, D_a is the diameter of the aperture, d_p is the particle diameter, and f_c is a correction factor of the order one. This result can be obtained from a dimensional analysis; see Section 5.3.3. For a two-dimensional slot of length L and width W, the flow rate is:

$$\dot{M} = JL\rho_b \left[g (W - f_c d_p)^3 \right]^{0.5} \tag{7.26}$$

where J is the non-dimensional flow rate for slot outlets.

The flow rate seems to be determined, to a large extent, by what happens in the vicinity of the discharge opening. This concept forms the basis of most of the early analyses of flow rate. Brown [27] derived the following expression for the non-dimensional flow rate for a slot outlet in case of mass flow:

$$J = \frac{\int_0^{\alpha} (\cos\alpha')^{1/2} \, d\alpha'}{(2 \sin^3\alpha)^{1/2}} \tag{7.27}$$

Johanson [28] developed the following expression for steady flow of non-cohesive bulk materials:

$$J = (2\ \tan\alpha)^{-1/2} \tag{7.28}$$

This result is obtained by assuming the flow in the hopper to be one-dimensional and further assuming that at the orifice the convective acceleration in the upper converging flow is equal to the gravitational acceleration g, appropriate for the freely falling particles below the orifice level.

Savage [29] derived flow rate equations for a frictional Coulomb material by assuming radial body forces and neglecting wall friction:

$$J = \left[\frac{1+k}{2(1-2k)\sin\alpha}\right]^{1/2} \tag{7.29}$$

where k is given by Eq. 7.12.

Equation 7.29 generally overestimates the flow rate by about 40 to 100%, as determined by comparison to experimental results. Savage [30] extended his analysis to include the effect of wall friction by solving the equations of motion by the method of integral relations. The flow rates were lower than predicted with Eq. 7.29, but still higher than experimental values. Savage and Sayed [31] improved the earlier analysis [30] and derived an expression for the flow rate in a two-dimensional wedge-shaped hopper:

$$J^2 = \frac{(2B-4A-C)(G\alpha^2+3E)}{2g\sin\alpha\,(A+B+C)(H\alpha^2+3F)} \tag{7.30}$$

where the constants are given in Appendix 7.1.

The closed-form solution of the flow rate was derived by using a mean normal stress averaged for the width of the hopper. A more accurate analysis considered the detailed variations of the stresses throughout the hopper. Predictions based on Eq. 7.30 agreed well with the numerical results from the more accurate analysis; the differences were generally less than one percent. An interesting theoretical prediction is the increase in flow rate when the wall friction is increased at large hopper half-angles. This result is not intuitively obvious but has been experimentally observed [32–34].

7.2.1.3 Design Criteria

Jenike [8, 9] and his coworkers did extensive work on gravity flow of bulk solids, both experimental and theoretical. He developed design methods and criteria for hoppers and bins with steady mass flow without disturbances. In determining various flow criteria, Jenike used a function termed “flow factor”. This flow factor is the ratio of the consolidating pressure σ_1 to the stress acting on an exposed surface $\overline{\sigma}_1$:

$$ff = \frac{\sigma_1}{\overline{\sigma}_1} \tag{7.31}$$

The stress acting on an exposed surface is also the only non-zero principal stress, because the exposed surface is assumed self-supporting and traction-free (i.e., no shear stresses acting on the surface). The flow factor is determined by the geometry of the hopper and the properties of the bulk material. Another function used by Jenike is the "flow function". This flow function is the ratio of the consolidating pressure σ_1 to the unconfined yield strength σ_c, as defined in Section 6.1.2:

$$FF = \frac{\sigma_1}{\sigma_c} \tag{7.32}$$

The flow function is a material property; it gives an indication of the flowability of a bulk material:

	FF >	10	free flowing material
10 >	FF >	4	easy flowing material
4 >	FF >	1.6	cohesive material
	FF <	1.6	very cohesive, non-flowing material

As a general rule, solids that do not contain particles smaller than approximately 0.2 mm are free flowing; thus, most granular solids are free flowing and most powders are to some extent cohesive.

The exposed surface, whether it is an arch or a pipe, is stable when the unconfined yield strength σ_c is higher than the stress acting on the exposed surface $\overline{\sigma}_1$ and unstable when σ_c is less than σ_1. The condition for no arching or piping, therefore, is:

$$\sigma_c < \overline{\sigma}_1 \quad \text{or} \quad FF > ff \tag{7.33}$$

In order to obtain quantitative results, the flow factor has to be determined; this requires knowledge of the stress field in the hopper. Closed-form expressions for ff are not available, except for the simplest case of flow through a straight cylinder. Results from numerical analysis are given by Jenike [8, 9] in graphical form for plane symmetry and axial symmetry.

If steady flow is desired, the hopper geometry should be designed such that mass flow will take place; no stagnating regions should occur. In this case, the solids flow along the walls of the hopper. The wall, therefore, must be sufficiently steep and the flow channel must not have any sharp corners, abrupt transitions, or discontinuities in frictional properties at the wall. As a rule, the hopper half-angle a should not exceed α_{max}, with α_{max} determined from:

$$\alpha_{max} = 55° - \frac{1}{2}\beta_e \tag{7.34}$$

where β_e is the effective angle of internal friction.

The minimum outlet dimension to avoid doming was formulated by Jenike [8] as:

$$D \geq c\frac{\sigma_c}{\rho_b} \tag{7.35}$$

where c = 2 for circular outlets and c = 1.8 for square outlets. The critical yield stress σ_c is determined from the point of intersection of the appropriate flow function and flow factor. Walker [35] and Eckhoff [36] published experiments showing that the Jenike method considerably overdesigns the critical outlet dimensions, as much as a hundred percent or more. Engstad [37] has formulated a relationship for the critical outlet dimension that is claimed to be more accurate and results in less overdesign. The critical outlet dimension, according to Engstad's analysis, is given by:

$$D = \frac{(2-2\sin\beta_i)}{\sin\beta_i}\frac{\sigma_{co}}{\rho Y_b} \tag{7.36}$$

where the various terms of Eq. 7.36 are given in Appendix 7.2.

From an analysis of the flow field in a hopper, criteria can be formulated for preventing arching and funneling. These criteria place restrictions either on the dimensions of the outlet or the slope of the walls. Another approach is to modify the hopper geometry into a nonlinear, curved shape in order to obtain optimum flow conditions. Lee [38] designed a hyperbolic hopper by making certain assumptions about the rate of change of the horizontal cross-section with respect to axial distance. Richmond [39] suggested that in an optimum hopper, the material would be on the verge of arching at any point. By using a one-dimensional analysis, this condition could be achieved, resulting in an exponential profile. Gardner [40] proposed a solution based on having a single surface at any level in the hopper on the verge of arching. Richmond and Morrison [41] used a modified procedure based on arching being imminent only along the axis of the hopper. For this case, positive pressures exist at all other points in the hopper. This approach leads to smoothly curved funnel-shaped hoppers. However, the optimum shape will have to be modified if the converging hopper section is connected to a cylindrical hopper section. A practical drawback of this approach is that such a carefully tailored curved hopper geometry is difficult to manufacture and could become quite expensive.

7.2.2 Drag Induced Solids Conveying

Once the particulate solids have reached the feed port of the extruder, the material will flow down until it is situated in the screw channel. At this point, the gravity induced flow mechanism will essentially cease. In most extruders, the screw and barrel are placed in a horizontal direction and the role of gravity becomes a very minor one. In fact, in most analyses of solids conveying in single screw extruders,

the effect of gravity is assumed to be negligible. The material in the screw channel will move forward as a result of the relative motion between boundaries of the solids, i.e., the screw surface and the barrel surface. The flow rate of the solids is determined by the forces acting on the solids. These forces are largely determined by the frictional forces acting on the solids at the boundaries.

It has been found experimentally that, in most cases, polymeric particulate solids compact readily in the early portion of the screw channel. As a result, the solids form into a solid bed and the solids move down the screw channel in plug flow; thus, at any cross-section of the solid bed all elements move at the same velocity. In other words, there is no internal deformation taking place inside the solid bed. This compaction of the particulate solids into a solid bed can occur only if there is a sufficient amount of pressure generation in the screw channel.

If there is not enough pressure generation in the screw channel, the particulate solids will not form a solid bed. In this case, plug flow will not occur; there will be internal deformation in the solid material. As a result, the solids conveying process will be less steady compared to plug flow. The type of non-plug flow that occurs when the channel is only partially filled with polymer particles has been referred to as "Archimedean transport" [42]. Archimedean transport will occur if the intake rate of the extruder is less than the plug flow solids conveying rate. In metered starve fed extrusion, the Archimedean transport is created intentionally. In some cases, Archimedean transport occurs accidentally if the flow rate through the feed hopper is too low or if the feed port geometry of the extruder is too small. Archimedean solids transport is also likely to occur if the pressure at the end of the solids conveying zone is low. An example would be a screw type solids conveying device (a screw feed) where the discharge pressure at the end of the solids conveying zone is zero. Archimedean transport is essentially always associated with a partially filled screw channel; see Fig. 7.9.

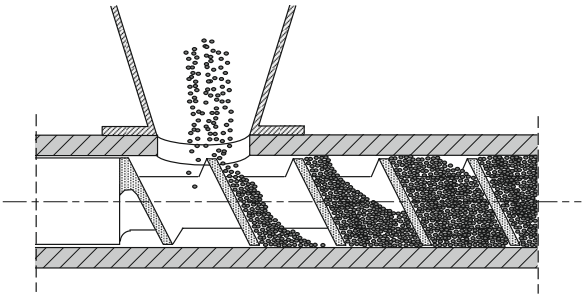


Figure 7.9
Archimedean transport in the first few turns of the screw

Pressure generation cannot take place if the screw channel is not fully filled and consequently compaction and plug flow cannot occur.

It has been observed [44] that even under normal extrusion conditions, Archimedean transport can occur for a short length. Observations of the filling action in the

feed port have shown that the flow of material from the hopper to the screw channel is such that little pressure is likely to be transmitted. During some parts of the filling cycle, empty spaces in the screw channel have been observed. This indicates that virtually no pressure exists for some time periods. Thus, Archimedean transport can occur over a short distance in the feed port region.

The solids transport resulting from the relative motion of the boundaries of the solid material is referred to as drag induced solids conveying. For optimum solids conveying, the particulate solids should compact easily and move in plug flow. It is important to note that properties of the bulk material that are advantageous in the gravity flow in the feed hopper can be detrimental in the drag induced solids conveying in the screw channel. An example is the flow function, defined by Eq. 7.22. For optimal gravity flow in the feed hopper, one would like to have a bulk material with a large value of the flow function. However, such a material will not form a strong solid bed because the yield strength will be low relative to the compacting pressure. Thus, such a material may well be problematic in the drag induced solids conveying zone because of internal deformation of the solid bed.

The first comprehensive analysis of solids transport in single screw extruders was made by Darnell and Mol in 1956 [43]. Later, numerous workers extended the work of Darnell and Mol; however, the basic analysis has remained relatively unchanged. In order to come to a quantitative description of the drag induced solids conveying process, the following assumptions were made by Darnell and Mol:

1. The particulate solids behave like a continuum.
2. The solid bed is in contact with the entire channel wall, i. e., the barrel surface, the root of the screw, the flank of the active flight, and the flank of the passive flight.
3. The channel depth is constant.
4. The flight clearance can be neglected.
5. The solid bed moves in plug flow.
6. The pressure is a function of down-channel distance only.
7. The coefficient of friction is independent of pressure.
8. Gravitational forces are neglected.
9. Centrifugal forces are neglected.
10. Density changes in the plug are neglected.

The first five assumptions are made in most analyses of solids conveying. The last five assumptions have been relaxed by various workers. The general approach to solids conveying analysis is to consider an element of the solid bed in the screw channel and determine all forces that are acting on this solid bed element. The most important forces are the frictional forces at the boundaries and the forces resulting from pressure gradients in the solid bed.

Figure 7.10 shows the various forces acting on the solid bed element; the screw is considered stationary and the barrel rotating.

F_r is the friction force between the solid bed and the root of the screw:

$$F_r = PWdz\,f_s \tag{7.37}$$

where f_s is the dynamic coefficient of friction on the screw surface.

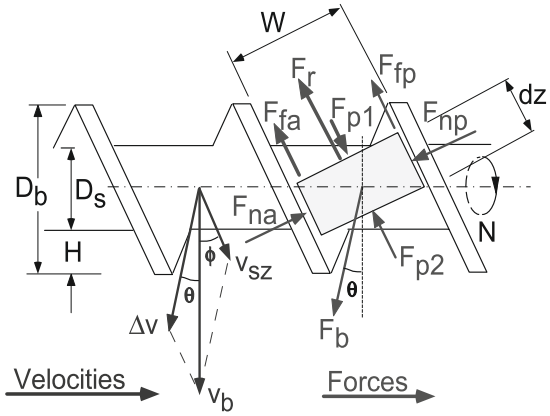


Figure 7.10
Forces acting on a solid plug element and corresponding velocity diagram

F_{na} is the normal force on the solid bed on the active flight flank:

$$F_{na} = PHdz + F^* \tag{7.38}$$

where F^* is an extra normal force, which is unknown.

F_{np} is the normal force on the solid bed on the passive flight flank:

$$F_{np} = PHdz \tag{7.39}$$

F_{fa} is the frictional force between the solid bed and the active flight flank:

$$F_{fa} = F_{na} f_s \tag{7.40}$$

F_{fp} is the frictional force between the solid bed and the passive flight flank:

$$F_{fp} = PHdz\,f_s \tag{7.41}$$

F_{p1} is the force against the face of the solid plug element resulting from the local pressure P:

$$F_{p1} = WHP \tag{7.42}$$

F_{P2} is the force against the face of the solid plug element resulting from the local pressure P^{p2}+ dP:

$$F_{p2} = WH(P + dP) \tag{7.43}$$

Obviously, if the pressure gradient in the down-channel direction is zero, then $F_{p1} = F_{p2}$. The final force F_b is the frictional force between the solid bed and the barrel surface:

$$F_b = PWdz\, f_b \tag{7.44}$$

where f_b is the dynamic coefficient of friction on the barrel surface.

The force F_b makes an angle θ with the plane perpendicular to the screw axis; see Fig. 7.10. The direction of force F_b is determined by the direction of the vectorial velocity difference between the barrel and the solid bed:

$$\Delta\vec{v} = \vec{v}_b - \vec{v}_{sz} \tag{7.45}$$

where $\vec{v}_b$ is the barrel velocity and $\vec{v}_{sz}$ the solid bed velocity vector. From the velocity diagram in Fig. 7.10, the direction of $\Delta\vec{v}$ and F_b becomes clear. The angle θ is the solids conveying angle. If the solids conveying angle can be determined, then the solid bed velocity can be calculated directly from it:

$$v_{sz} = v_b\left[\cos\varphi - \frac{\sin\varphi}{\tan(\theta+\varphi)}\right] \tag{7.46a}$$

Equation 7.46(a) can be rewritten as follows:

$$v_{sz} = v_b\frac{\sin\theta}{\sin(\theta+\varphi)} \tag{7.46b}$$

The vectorial velocity difference Δv between the barrel velocity v_b and the solid bed velocity v_{sz} is:

$$\Delta v = (v_b^2 + v_{sz}^2 - 2|v_b||v_{sz}|\cos\varphi)^{1/2} \tag{7.47}$$

Δv as a function of v_b, θ, and φ is given in Eq. 7.61.

Once the solid bed velocity is known, the solids conveying rate is simply determined from:

$$\dot{M}_s = \rho HpWv_{sz} = \rho HWpv_b\frac{\sin\theta}{\sin(\theta+\varphi)} \tag{7.48}$$

where ρ is the solid bed density and p the number of parallel flights.

At this point, there are two unknowns: the extra force F* and the solids conveying angle θ. The solution procedure followed by Darnell and Mol was to break up all forces into their axial and tangential components. The sum of all forces in the axial direction is taken to be zero, assuming that acceleration is negligible. The tangential force components are used in a torque balance with the net torque also assumed to be zero. The extra force F* is then eliminated from the two balance equations and an expression for the solids conveying angle results. Darnell and Mol also included the

dependence of the helix angle and flight width on radial distance. The same procedure has been followed by many other workers, e.g., Tadmor and Broyer [45, 46].

Considering that in most extruder screws the screw diameter is much larger than the channel depth (D/H >> 1, usually about 5), the change in channel width and helix angle over the depth of the channel will be rather small. If it is assumed that the channel curvature can be neglected, the screw channel can be unrolled onto a flat plane. The error that is made in this process may be acceptable considering the limited accuracy and reproducibility of most data on the coefficient of friction, as discussed in Section 6.1.2. Two simplifications result from this assumption. The first one is that now the channel width and helix angle are constant over the depth of the channel. The second simplification is that the extra force F* can be determined directly from a force balance in the cross-channel direction:

$$F^* = F_b \sin(\theta + \varphi) \tag{7.49}$$

An expression for the solids conveying angle θ is obtained from a force balance in the down-channel direction:

$$PWdz\, f_b\left[\cos(\theta+\varphi) - f_s \sin(\theta+\varphi)\right] = WHdP + Pdz\, f_s (W + 2H) \tag{7.50}$$

Equation 7.50 can be integrated to give the pressure as a function of down-channel distance. If the pressure at z = 0 is taken as $P(z = 0) = P_o$, the solution is:

$$\ln\frac{P}{P_o} = \left\{\frac{f_b}{H}\left[\cos(\theta+\varphi) - f_s\sin(\theta+\varphi)\right] - f_s\left(\frac{W+2H}{WH}\right)\right\} z \tag{7.51}$$

Equation 7.51 indicates that at a certain solids conveying angle the pressure will increase exponentially with down-channel distance. This means that very high pressures can be generated in the solids conveying zone, at least theoretically. Equation 7.51 can be worked out further to yield a closed-form expression for the solids conveying angle:

$$\theta = \arcsin\left[\frac{(1+f_s^2-k^2)^{1/2} - f_s k}{1+f_s^2}\right] - \varphi \tag{7.52}$$

where:

$$k = \frac{H}{f_b z}\ln\frac{P}{P_o} + \frac{f_s}{f_b}\left(1 + \frac{2H}{W}\right) \tag{7.52a}$$

If curvature is taken into account the expression for the solids conveying angle can be written as:

$$\theta = \arcsin\left[\frac{(1+K^2-M^2)^{1/2} - KM}{1+K^2}\right] \tag{7.53}$$

where:

$$K = \frac{D_m(\sin\varphi_m + f_s\cos\varphi_m)}{D_b(\cos\varphi_m - f_s\sin\varphi_m)} \tag{7.53a}$$

and:

$$M = M_1 + M_2 + M_3 \tag{7.53b}$$

$$M_1 = \frac{2Hf_s}{W_b f_b}\sin\varphi_b\left(K + \frac{D_m}{D_b}\operatorname{cotan}\varphi_m\right) \tag{7.53c}$$

$$M_2 = \frac{W_s f_s}{W_b f_b}\sin\varphi_b\left(K + \frac{D_s}{D_b}\operatorname{cotan}\varphi_s\right) \tag{7.53d}$$

$$M_3 = \frac{W_m H}{W_b z_b f_b}\sin\varphi_m\left(K + \frac{D_m}{D_b}\operatorname{cotan}\varphi_m\right)\ln\frac{P_1}{P_o} \tag{7.53e}$$

Equation 7.52 is considerably more compact than Eq. 7.53. Figure 7.11 compares the two solutions for a 75-mm (3-inch) extruder with a square pitch at various values of the channel depth.

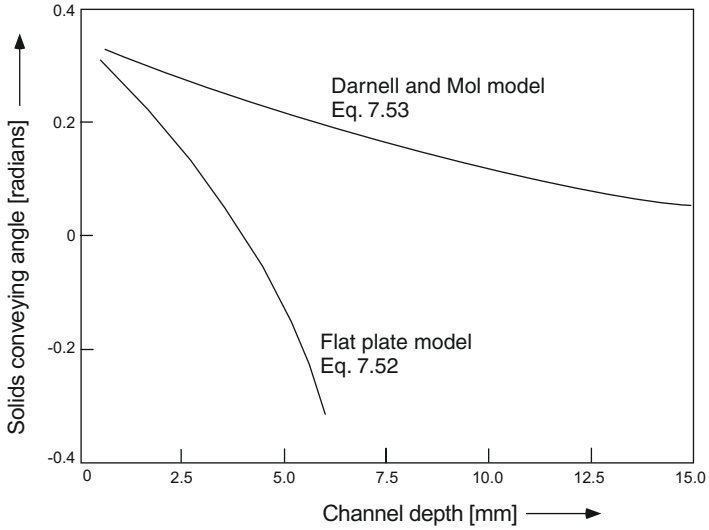


Figure 7.11 Solids conveying angle vs. channel depth calculated with Eqs. 7.52 and 7.53

The results from the two equations are very close for small values (H < 0.01 D) of the channel depth. However, for larger values of the channel depth (H > 0.05 D) the results are quite different. Considering that in most extruder screws H > 0.05 D, Eq. 7.52 will not yield accurate results for typical values of the channel depth in the feed section.

Figure 7.11 shows that the solids conveying angle reduces with the channel depth of the screw. An increase in channel depth increases the surface area of the screw while the barrel surface area stays the same. This means that the retarding force increases while the driving force for conveying does not change. As a result, the solids conveying angle reduces with increasing channel depth.

From Eqs. 7.52 and 7.53 the solids conveying angle, and thus the solids conveying rate, can be calculated if the pressure gradient is known. This process can also be reversed. If the actual solids conveying rate is known, the pressure gradient can be calculated using Eq. 7.51. However, the solids conveying angle in Eq. 7.51 must be expressed as a function of the solid bed velocity. The pressure profile derived from Eq. 7.52 (flat plate model) can be written as:

$$P(z) = P_0 \exp\left[\left(f_b \frac{1 - a f_s}{(a^2+1)^{1/2}} - f_s \frac{W + 2H}{W}\right)\frac{z}{H}\right] \tag{7.54a}$$

where: $a = \tan(\theta + \varphi) = \dfrac{v_b \sin\varphi}{v_b \cos\varphi - v_{sz}}$

The pressure profile derived from Eq. 7.53 (Darnell and Mol) can be written as:

$$P(z) = P_0 \exp\left[\frac{\cos\theta - K\sin\theta - M_1 - M_2}{M_3}\right] \tag{7.54b}$$

From Eq. 7.54 it can be seen that the exponential term will increase with f_b and decrease with f_s. Thus, the pressure rise will be most rapid when f_b is large and f_s is small. The exponential term is inversely proportional to the channel depth H; thus, the pressure will rise more slowly when the channel depth is increased.

The transport of the solids down the screw channel can be compared to a nut located on a long threaded rotating shaft. If the nut can freely rotate with the shaft, it will not move in the axial direction. However, if the nut is kept from rotating with the shaft, it will move in the axial direction. In the extruder, the frictional force on the barrel wall will keep the solid bed from freely rotating with the screw. The frictional force on the barrel, therefore, constitutes the driving force of the solid bed. The frictional force on the screw surface constitutes a retarding force on the solid bed. If the frictional force on the barrel is zero, no forward transport will occur. If the frictional force on the screw is zero, maximum forward transport will occur. From the velocity diagram of this extreme case, Fig. 7.10, it can be seen that the maximum solids conveying angle in this case is:

$$\theta_{max} = \frac{\pi}{2} \tag{7.55}$$

The maximum solid bed velocity in this case is:

$$v_{sz-max} = \frac{v_b}{\cos\varphi} \tag{7.55a}$$

And thus the maximum solids conveying rate is:

$$\dot{M}_{s-max} = \frac{\rho W H v_b}{\cos\varphi} \cong \rho \pi^2 D^2 H N \tan\varphi \tag{7.55b}$$

The approximately equal sign is used because the flight width is neglected in the right-hand expression. For optimum solids conveying, the frictional force on the barrel should be maximum and the frictional force on the screw should be minimum. This is clear from simple qualitative arguments without any elaborate analysis or equations. One would like, therefore, to have a low coefficient of friction on the screw and a high coefficient of friction on the barrel. In many instances, the screw is chrome-plated or nickel-plated and highly polished to minimize the friction on the surface. Special platings are available where the surface is impregnated with a fluoropolymer to give a low coefficient of friction; see also Section 11.2.1.4. On the other hand, the surface of the barrel should be rough to increase the frictional force on the barrel. Many extruders have grooves machined into the internal barrel surface in the solids conveying zone to improve the solids conveying performance. This will be discussed in more detail in Section 7.2.2.2.

With the equations developed so far, the solids conveying performance can be analyzed as a function of screw geometry and polymer properties. The effect of channel depth on solids conveying rate is shown in Fig. 7.12; the results are from the flat plate model.

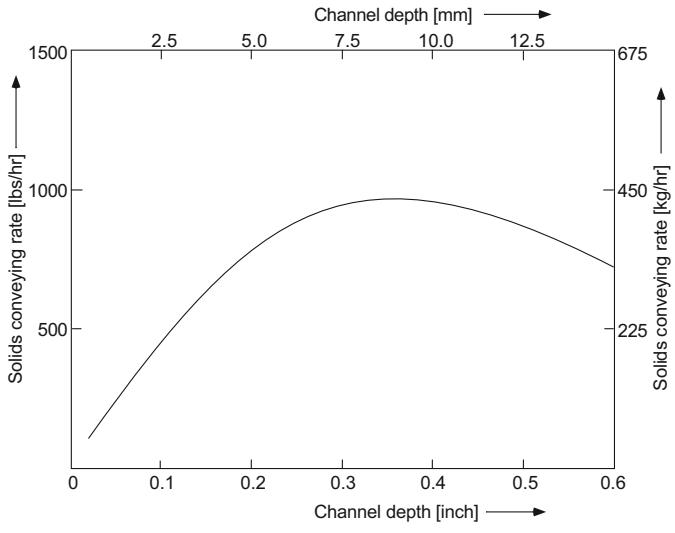


Figure 7.12 Solids conveying rate versus channel depth for 75-mm extruder

The curve shown is for a 75-mm extruder running at 100 rpm, assuming $f_s = 0.2$, $f_b = 0.3$, and the pressure ratio is 25:1. At low values of the channel depth, the solids conveying rate increases with channel depth. However, if the channel depth is further increased, the solids conveying rate reaches a maximum and then reduces with further increase in the channel depth. The result can be explained by considering the forces acting on the solid bed. If the channel depth is increased, the frictional force on the screw will increase, while the frictional force on the barrel will remain unchanged. Thus, the retarding force increases while the driving force stays the same. This has to result in a reduction of the solids conveying angle. The reduction of the solids conveying angle causes a reduction in the solids conveying rate. However, the increase in channel depth increases the cross-sectional area of the screw channel and this causes an increase in the solids conveying rate. This explains why the solids conveying rate increases at first and then decreases. The solids conveying angle as a function of channel depth is shown in Fig. 7.11. It is clear that the solids conveying angle drops monotonically with channel depth.

It should be noted, that the effect of the channel depth on the solids conveying rate as determined from a flat plate analysis is different when the curvature of the channel is taken into account. In reality, when the channel depth increases, the area of the flight flanks will increase but the area of the root of the screw will decrease; this decrease is not taken into account in the flat plate model. The contact area A_b between the differential element of the solid bed and the barrel is:

$$A_b = (\pi D \sin\varphi_b - w)\Delta z_b \tag{7.56}$$

In the flat plate model, the contact area between the solid bed and the screw is:

$$A_s = \left[\pi(D - 2H)\sin\varphi_b - w + 2H\right]\Delta z_b \tag{7.57a}$$

while in the curved plate model the contact area is:

$$A_s = \left[\pi(D - 2H)\sin\varphi_s - w + H(\Delta z_b / \Delta z_s + 1)\right]\Delta z_b \tag{7.57b}$$

Both the helix angle φ_s and the down-channel incremental distance Δz_s are different in the curved plate model. The flat plate model considerably overestimates the contact area between the solid bed and the screw. Therefore, when the curvature is taken into account, the solids conveying rate will increase in a monotonic fashion with the channel depth as long as the pressure rise is sufficiently small. This demonstrates that the assumptions underlying a model have to be critically evaluated each time the model is used to analyze the influence of a certain parameter.

Equations 7.57(a) and (b) assume a zero radius of curvature between the flight flank and the screw root. If the radius R_c is taken into account, the screw contact area is reduced by $R_c(4 - \pi)$. From this point of view one would like to use a large radius; i.e., $R_c = H$. The resulting flight geometry is shown in Fig. 7.13 and also in

Fig. 8.4(a) of Section 8.2.3. In this case, the screw contact area in the flat plate model becomes:

$$A_s = [\pi(D-2H)\sin\varphi_b - w - H(\pi-2)]\,\Delta z_b \tag{7.57c}$$

Considering that the ratio of channel depth to channel width is usually about 1/10, using a radius of curvature equal to the channel depth can reduce the contact area between solid bed and screw by about 6 to 7%, while the contact area between solid bed and barrel remains unchanged. Another advantage of the large flight radius is that the flight width at the screw O.D. can be reduced so that the channel cross-sectional area can be at least as large as with a small flight radius. If the flight width at the screw O.D. is maintained at the same value, a flight curvature of R_c = H will reduce the channel cross-sectional area by $2H^2(\pi/4-1)$. With a usual ratio of channel width to channel depth, this will result in a reduction in cross-sectional area of about 4%. Thus, the beneficial effect of a large flight radius (reduced screw contact area) is larger than the adverse effect (reduced cross-sectional area of the screw channel). An additional benefit of the large flight radius is the reduced chance of solid bed deformation; see Section 8.2.3.

The effect of flight radius on extruder performance was studied by Spalding et al. [238]. They found that the solids conveying rate with large radius was improved at high levels of pressure development and reduced at low levels of pressure. The authors postulate that the improvement in solids conveying rate at high pressures is due to a change in forwarding forces when a large radius is employed. When the pushing radius is small the extra force F* is parallel to the barrel surface as shown in the left-hand side of Fig. 7.13. However, with a large pushing radius the extra force F* points to the barrel at an angle α and this causes the normal force at the barrel to be increased by F* sinα as shown in the right-hand side of Fig. 7.13. This will increase the driving force in the conveying process.

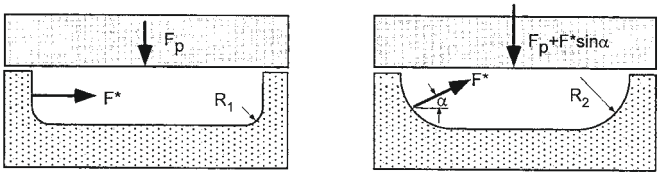


Figure 7.13 Schematic of forces with small (left) and large (right) flight flank radius

Spalding et al. recommend using a flight flank radius in the feed section of about 1/4 of the channel depth. However, the basis for this recommendation is not entirely clear because the radii tested were all larger (0.54 H and 1.71 H) than 1/4 of the channel depth (0.25 H). This recommendation may be appropriate for smooth bore extruders where the pressure development in solids conveying is modest. This recommendation most likely is not appropriate for grooved feed extruders because the pressure development in these extruders is usually substantial.

Another method to reduce the screw contact area is to use flat slanted flight flanks, i. e., a trapezoidal flight geometry; see also Fig. 8.4(b). If the flight flank angle is 45°, the screw contact area in the flat plate model becomes:

$$A_s = [\pi(D - 2H)\sin\varphi_b - w + H(2\sqrt{2} - 2)]\,\Delta z_b \tag{7.57d}$$

When the channel width is about ten times the channel depth, the screw contact area will be reduced by about 10%. However, the cross-sectional area of the screw channel will be reduced by the same percentage. Thus, the net effect will be less beneficial than the curved flight geometry.

A multi-flighted screw geometry can adversely effect the solids conveying performance for two reasons. An additional flight will reduce the open cross-sectional area of the screw channel, causing a reduction in solids conveying rate at a constant solid bed velocity. An additional flight will also change the wetted surface area of the screw. When the channel depth is small the wetted screw surface will reduce with additional flights. However, with large values of the channel depth the wetted screw surface will increase with multiple flights. The combined effect can cause a substantial reduction in solids conveying rate. This is shown in Fig. 7.14 for a 75-mm extruder screw under the same conditions as described in Fig. 7.11.

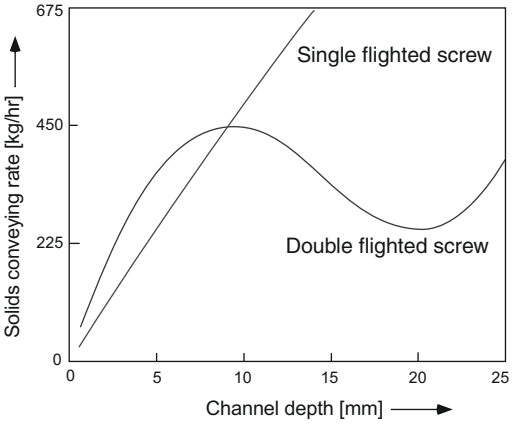


Figure 7.14
Solids conveying rate versus channel depth for 75-mm screw showing both a single- and a double-flighted geometry; results based on model with curvature

When the channel depth is small the double-flighted screw actually has a higher solids conveying rate than the single-flighted screw. At larger values of the channel depth the single-flighted screw has a higher rate than the double-flighted screw. This effect tends to be more severe on smaller extruders as shown in Fig. 7.15. At very small values of the channel depth (H < 0.5 mm) the solids conveying rate of the double-flighted screw is again greater than for the single-flighted screw. When the channel depth increases beyond 1 mm, the rate for the double-flighted screw drops rapidly and becomes zero when the depth H = 1.6 mm. Considering that the feed depth for any screw will have to be at least the size of a typical polymer pellet (3–4 mm), it is obvious that for a small diameter screw a double-flighted geometry in the feed section can result in very low output or even no output at all.

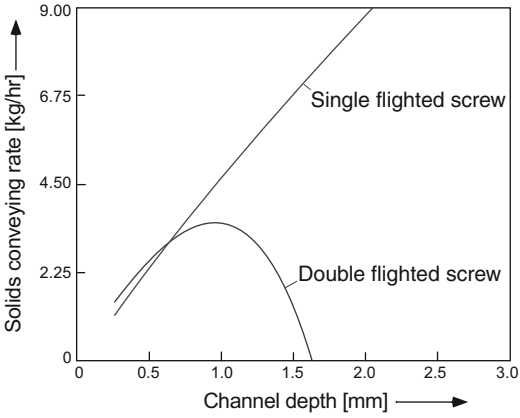


Figure 7.15
Solids conveying rate versus channel depth for single- and double-flighted screw with 25-mm diameter; results based on model with curvature

At larger values of the channel depth the difference between a single- or double-flighted screw geometry can mean the difference between output or no output at all. This has been experimentally observed by the author in unpublished studies on solids conveying in single screw extruders. A short 4 L/D 19-mm extruder, used just for solids conveying, was outfitted with a single-flighted screw and yielded reasonable output with open discharge and with moderate discharge pressures. The same extruder with a double-flighted screw and all other dimensions unchanged did not yield any output at all, even with open discharge.

Clearly, this adverse effect of multiple flights on solids conveying performance will be less severe as the screw diameter increases. Nevertheless, the adverse effect is there and it should be taken into account. It can also be seen in Fig. 7.15 that the optimum channel depth becomes smaller as the geometry is changed from a single-flighted to a double-flighted screw geometry. The effect of the number of flights will reduce as the coefficient of friction on the barrel becomes larger relative to the friction on the screw. In extruders with grooved barrel sections, therefore, one would expect a much smaller adverse effect due to multiple flights as compared to an extruder with a standard smooth barrel.

The predicted solids conveying rate is very sensitive to the values of the coefficient of friction; changes in coefficient of friction of 20% can cause changes in rate of 100 to 1000% as shown in Fig. 7.16. At high values of the barrel friction the rate does not change much with the coefficient of friction. However, at low values of the barrel friction the rate changes substantially with coefficient of friction.

This has several important implications. If accurate predictions are required for application of the theory to an actual extrusion problem, very accurate data on the coefficient of friction will be required. However, measurement of accurate and meaningful data on coefficient of friction is very difficult, as discussed in Section 6.1.2. The reproducibility of measured data on the coefficient of friction generally ranges from 10 to 50%. This means that the solids conveying rate predicted from these data

cannot be very accurate in a quantitative sense. The predicted results should be analyzed in a qualitative sense. In that respect, the solids conveying theory is very useful in analyzing extrusion problems and in screw design. Thus, the theory should be used to uncover the important trends.

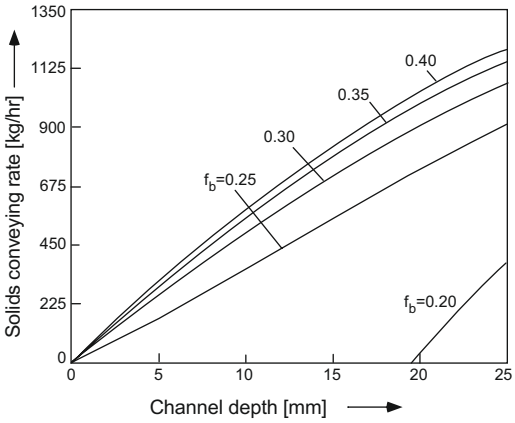


Figure 7.16
Solids conveying rate versus channel depth for 75-mm screw for several values of the coefficient of friction against the barrel; the coefficient of friction against the screw is 0.2

If the actual solids conveying performance is as sensitive to the coefficient of friction as the theory indicates, small changes in the actual coefficient of friction can have a substantial effect on the entire extrusion process. This is particularly true for low values of the coefficient of friction against the barrel. The high sensitivity to the coefficient of friction will tend to result in unstable extruder performance. At high values of the barrel coefficient of friction the extruder performance will be less affected by changes in friction and the extruder will be more stable under these conditions. This explains why grooved feed extruders tend to be more stable than smooth bore extruders.

An external means of altering the coefficient of friction is the temperature setting. By changing the barrel temperature, the coefficient of friction on the barrel will change, and by changing the screw temperature the coefficient of friction on the screw will change. Thus, small changes in the temperature in the feed section can have a large effect on the overall extruder performance. This behavior has been observed by several workers. Kessler, Bonner, Squires, and Wolf [47] reported a rather convincing case concerning the extrusion of nylon on a 82.55-mm (3.25-inch) diameter extruder. A 28°C (50°F) increase in the rear barrel temperature reduced the diehead pressure fluctuation from about 2.8 MPa (400 psi) down to about 0.4 MPa (60 psi).

Ideally, the barrel temperature should be set to the temperature at which f_b is maximum, and the screw temperature to the temperature at which f_s is minimum. If the coefficient of friction is known as a function of temperature, then the optimum barrel and screw temperature can be determined directly from the friction data. Unfortunately, in most practical situations, data on the coefficient of friction as a

function of temperature are not known. Thus, in most cases, the optimum barrel and screw temperatures have to be determined by trial and error. The effect of the rear barrel temperature on extruder performance is generally larger than any other temperature zone. In practice, therefore, considerable attention should be paid to the proper fine-tuning of the rear barrel temperature zones.

7.2.2.1 Frictional Heat Generation

If one would want to determine optimum temperature settings from data on the coefficient of friction at various temperatures, there is an additional complication that should be taken into account. This complication is the frictional heat generation that occurs in the solids conveying zone. As a result of this frictional heat generation, the temperature at the interface between solid bed and barrel may be substantially higher than the barrel temperature setting indicates.

In any sliding motion where a frictional force is operational, there will be frictional heat generation between the two bodies. The skeptic can experimentally verify this fact by climbing up a rope for a reasonable distance and then sliding down while keeping the hands tightly clamped around the rope. In a very short distance, the effects of frictional heat generation between the rope and the hands will become noticeable. Most likely, the experimenter will develop a healthy respect for what frictional heat generation is capable of doing. The rate of frictional heat generation equals the product of the frictional force F_f and the relative velocity Δv:

$$\dot{Q} = F_f \Delta v = f\, F_n \Delta v \tag{7.58}$$

where F_n is the normal force and f the coefficient of friction.

On the screw surface, the relative velocity between the solid bed and screw is simply the solid bed velocity. Thus, the frictional heat generation on the screw is:

$$\dot{Q}_s = P f_s (W + 2H) v_{sz} dz + F^* v_{sz} \tag{7.59}$$

where $F^* = P f_b W \sin(\theta + \varphi) dz$.

Written in different form:

$$\dot{Q}_s = P v_{sz} dz \left[f_s (W + 2H) + f_b W \sin(\theta + \varphi) \right] \tag{7.60}$$

On the barrel surface, the relative velocity between solid bed and barrel can be written as:

$$\Delta v = v_b \frac{\sin\varphi}{\sin(\theta + \varphi)} \tag{7.61}$$

The frictional heat generation on the barrel surface is:

$$\dot{Q}_b = P\, f_b W v_b \frac{\sin\varphi}{\sin(\theta + \varphi)} dz \tag{7.62}$$

In most cases, the solid bed velocity v_{sz} will be small compared to the relative velocity between solid bed and barrel Δv. Therefore, the frictional heat generation will generally be higher on the barrel surface than on the screw surface. The frictional heat generation of the barrel surface is dissipated into two fluxes, one conducting the heat into the solid bed and the other conducting the heat into the extruder barrel. The actual temperature profile of the solid bed will depend strongly on the heat flux in the barrel. If the barrel is intensely cooled, the majority of the frictional heat generation will conduct away through the barrel.

This tends to slow down the temperature development at the interface and extends the length of the solids conveying zone. When the temperature at the interface reaches the melting point, the solids conveying zone will terminate because polymer melt will form at the interface and the solid-to-solid frictional mechanism will cease to operate.

It should be noted in Eqs. 7.59 through 7.62 that the frictional heat generation is directly proportional to the local pressure. Earlier it was determined that the local pressure increases exponentially with down-channel distance; see Eqs. 7.51 and 7.54. Therefore, the frictional heat generation will increase exponentially with down-channel distance. As a result, the temperature at the interface will closely follow the local pressure. This is shown qualitatively in Fig. 7.17.

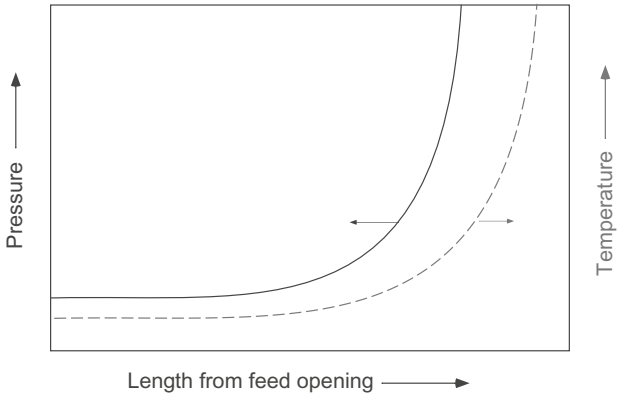


Figure 7.17
Pressure and temperature profile along the length of the extruder

When the local pressure becomes sufficiently high, the temperature at the interface will reach the melting point. This can happen even if the barrel is not heated. In this case heat required for melting is supplied only by the frictional heating. This occurs in auto-thermal extrusion operations; these are operations without active barrel heating or cooling.

When a melt film forms at the barrel surface the exponential rise in pressure will terminate because the solid-to-solid frictional mechanism breaks down. In fact, this pressure/temperature relationship constitutes a built-in safety mechanism against the development of very high pressures. The temperature rise resulting from the

pressure rise limits the maximum pressure that can develop in the solids conveying zone. Thus, the extruder self-regulates the maximum pressure that develops in the solids conveying zone. By intensely cooling the barrel, the maximum pressure can be increased considerably because the onset of melting will be delayed. Obviously, the maximum pressure that can develop will also depend on the actual coefficients of friction and the screw geometry.

Because of the inherent non-isothermal nature of the solids conveying process, accurate prediction of the actual solids conveying process becomes quite difficult. Not because the mathematics are so complicated—they are relatively straightforward—but because the coefficient of friction should be known as a function of temperature and pressure. This information is generally not available. Unless this information is available, a complete non-isothermal solids conveying analysis would not be very useful. Detailed calculations of non-isothermal solids conveying were performed by Tadmor and Broyer [46]. Their numerical calculations of pressure and temperature profiles showed that the temperature rise very closely follows the pressure rise.

7.2.2.2 Grooved Barrel Sections

In Section 7.2.2, it was discussed how solids conveying can be improved by increasing the roughness of the internal barrel surface. This conclusion can be reached without detailed theoretical analysis; it is obvious from simple qualitative arguments. The desirability of a large coefficient of friction at the barrel was recognized as early as 1941 by Decker [48] as a result of a very simplified analysis. One of the simplest methods of ensuring a high coefficient of friction on the barrel is to machine grooves into the barrel surface.

In the late 1960s, several theoretical and experimental studies were made on the effect of grooved barrel sections on solids conveying performance and overall extruder performance; see for example references 49 through 51. This work was mostly done in Germany. It was soon realized that substantial improvements could be made to the extruder performance by using grooved barrel sections. The main benefits of the grooved barrel section were found to be:

1. Substantially improved output
2. Substantially improved extrusion stability
3. Lower pressure sensitivity of the output

Since these benefits appeal to most extrusion processors, grooved barrel sections have become quite popular. Also, the use of grooved barrel sections allows processors to extrude materials that cannot be processed on conventional extruders, e. g., very high molecular weight polyethylenes and powders. A grooved feed housing is shown in Fig. 7.18.

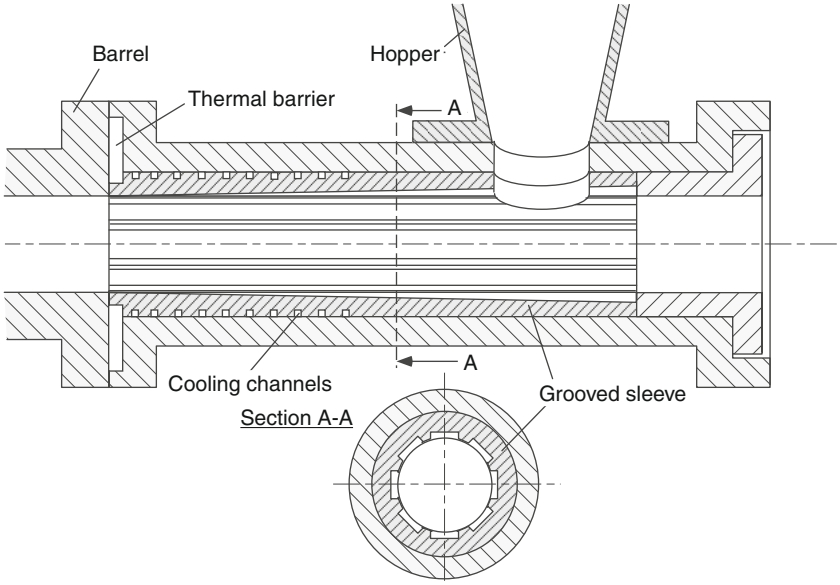


Figure 7.18 A grooved barrel section

In a typical grooved feed extruder the groove length from the feed port is about 3 to 5 D. The groove depth generally reduces in a linear fashion, reaching zero depth at the end of the grooved section. Cooling channels are located relatively close to the internal barrel surface. This is important because the cooling capacity of the grooved barrel section has to be high. The high cooling capacity is necessary to avoid too high a temperature rise at the internal barrel surface. Melting should be avoided if the effectiveness of the grooved barrel section is to be maintained. From the discussions in the previous section it is clear that with a grooved barrel section there will be a very large frictional heat generation at the barrel surface. Thus, good cooling is crucial to the proper operation of a grooved barrel section. For the same reason, a thermal barrier is generally designed between the grooved barrel section and the smooth barrel section.

In applying the grooved barrel concept to existing extruders, a word of caution is in order. The high effective coefficient of friction at the barrel surface results in a rapid rise in pressure; this is obvious from Eq. 7.54. However, when the solids conveying section is intensely cooled, the built-in safety mechanism against high pressures can break down. In fact, these grooved barrel sections are designed to ensure that the safety mechanism breaks down because melting has to be avoided in the grooved barrel section. As a result, extremely high pressures can develop in the grooved barrel section. Pressures of 100 to 300 MPa (15,000 to 45,000 psi) are not uncommon. Therefore, these extruders have to be specially designed to withstand these high pressures. Otherwise, mechanical failure of the barrel will occur. Thus, if a grooved barrel section is used in an existing extruder, it is prudent to keep the length of the

grooved section reasonably short (1 to 2 D) in order to avoid excessive pressures. Obviously, this will limit the benefits that one can derive from a grooved barrel section.

Another practical consideration is the wear of the grooves. Since the active edge of the groove is exposed to very high stresses, considerable wear can occur, particularly if the polymer contains abrasive components. Therefore, the grooved barrel section is generally made out of a strong wear-resistant material in order to maintain optimum performance over a long period of time.

The benefits of a grooved barrel section can be analyzed from the theory of drag induced solids conveying developed in Section 7.2.2. Figure 7.19 shows how the solids conveying rate varies with the coefficient of friction on the barrel f_b, for a situation where the pressure gradient is zero.

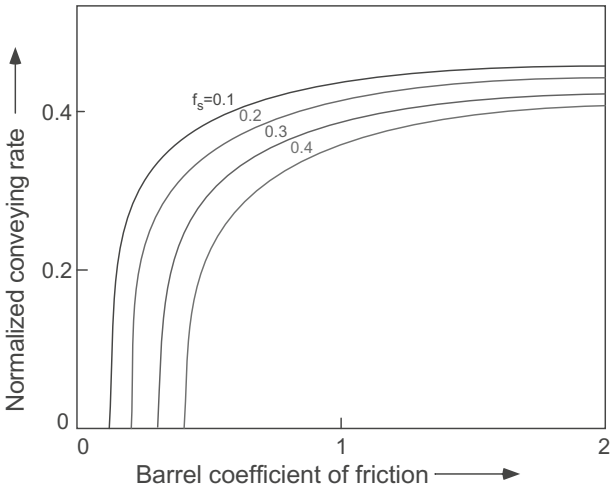


Figure 7.19
Solids conveying rate versus barrel coefficient of friction

The figure shows curves of constant coefficient of friction on the screw f_s. Four typical values are shown: $f_s = 0.1$, $f_s = 0.2$, $f_s = 0.3$, and $f_s = 0.4$. It can be seen that the curve rises steeply when f_b is small, but later reaches a plateau at high f_b values. Two major problems are evident when barrel coefficient of friction is close to the screw coefficient of friction. One is that the solids conveying rate is considerably below the theoretical maximum value. The second, more important, problem is that small changes in f_b will result in very large changes in the solids conveying rate when $f_b \cong f_s$. This will lead directly to surging of the extruder. Since small variations in the friction on the barrel are bound to occur by the nature of the process, there is a high possibility of extrusion instabilities when f_b is approximately equal to f_s. Thus, this constitutes an unstable operating point.

When the coefficient of friction at the barrel is increased to a value about two or three times the coefficient of friction at the screw, the solids conveying rate increases substantially. At the same time, the slope of the curve is reduced. When $f_b >> f_s$,

small variations in the barrel friction will result only in small changes in the solids conveying rate. Thus, the process will be inherently much more stable when f_b is much larger than f_s. This explains how grooved barrel sections can substantially improve extrusion stability.

Figure 7.20 shows how the solids conveying rate varies with the pressure gradient along the solids conveying zone.

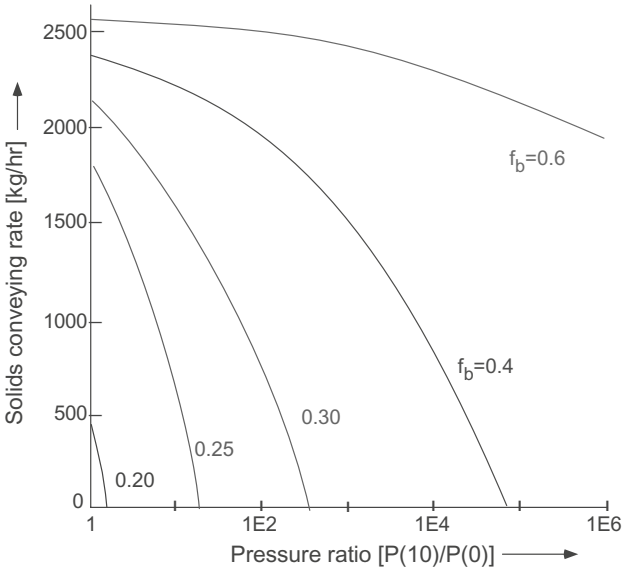


Figure 7.20
Solids conveying rate versus pressure ratio

When $f_b = f_s$, the solids conveying rate at a zero pressure gradient is quite small and the rate drops off quickly as the pressure gradient increases. At a relatively small pressure gradient, the rate becomes zero. As f_b is increased at constant f_s, the rate at zero pressure gradient increases and the fall-off with pressure gradient becomes less severe. At relatively high values of f_b, the fall-off with pressure gradient becomes very small; in fact, the output becomes essentially independent of back-pressure. This indicates a high degree of positive displacement behavior, which is quite unusual in conventional extruders. However, many workers, e.g., [52, 53], have experimentally verified the fact that the output is essentially independent of back-pressure when an extruder is equipped with a grooved barrel section. Thus, the three main benefits of grooved barrel sections, high output, good stability, and pressure-independent output, can be predicted directly from theory.

Besides the high pressures and the wear problems, there are a few other disadvantages of grooved barrel sections. The main disadvantage is probably the fact that a substantial amount of energy is lost through the intensive cooling of the grooved barrel section. Nowadays, with the increasing cost of and concern about energy, this energy loss is more of a factor than it was in the past. Detailed measurements of energy consumption in various sections of the grooved barrel extruder were made

by Menges and Hegele [54]. They found that as much as 30 to 40% of the mechanical energy is lost through the cooling water; about 60% of the mechanical energy is dissipated in the solids conveying zone. In the worst case, the specific energy loss through the cooling water is about 150 KJ/kg = 0.042 kWhr/kg (0.07 Hphr/lb). By improving the thermal barrier between the grooved barrel section and smooth barrel section, the specific energy loss can be reduced to about 100 KJ/kg = 0.028 kWhr/kg (0.046 Hphr/lb). However, considering that the specific enthalpy (see Section 6.3.4) of the polymer is generally around 0.06 kWhr/kg (0.10 Hphr/lb), the losses in the grooved barrel section are quite substantial. In a later publication, Menges [55] reports a total mechanical energy loss through the cooling water of about 14%. The mechanical energy is the energy supplied by the screw, which is transformed into heat by frictional and viscous heat generation. Helmy [229] reported lower specific energy consumption with grooved barrel extrusion with HMWPE and MMWPE than with smooth barrel extrusion. He also found lower melt temperatures with grooved barrel extrusion. However, with normal polyethylene, Helmy found the specific energy consumption of the grooved barrel extruder to be about 10 to 25% higher than the smooth barrel extruder.

Energy losses in the grooved barrel section can be reduced by reducing the amount of cooling. This can be achieved by a closed-loop temperature control of the grooved barrel section, as discussed by Menges, Feistkorn, and Fischback [237]. They found that the energy efficiency in the grooved feed section could be increased from 45 to 80% by increasing the cooling water temperature from 5 to 70°C.

Another related drawback of the grooved barrel extruder is its higher torque requirement. On a modification of an existing extruder, this generally requires a gear change; in some cases, a new high torque drive may be necessary. However, this should not be a problem on a new extruder designed for operation with a grooved barrel section.

Another disadvantage of the grooved barrel section is that material can accumulate in the grooves; this can cause problems with a product changeover. Also, the screw geometry has to be adapted to the presence of a grooved barrel section. Screw design rules that work for conventional extruders do not work for extruders with grooved barrel sections. In extruders with grooved barrel sections, the extruder screws generally have a much lower compression ratio (if at all), a shallower feed section, and a deeper metering section. The melting and mixing capability must also be greater because complete melting and thermal homogeneity are more difficult to achieve; higher output at the same screw speed means shorter residence time, thus, less time for completion of melting and for mixing (lower shear strain).

Despite the disadvantages, extruders with grooved barrel sections have found widespread acceptance in Europe. In many cases, the grooved barrel section has become a standard instead of an option. Somewhat surprisingly, the acceptance of grooved barrel sections in the U.S. has been quite slow. One reason may be that U.S. extruder

manufacturers have not promoted the grooved barrel concept vigorously. As of 2001, the number of grooved barrel extruders in the U.S. is still relatively small.

Most grooved barrel sections used in the past had axial grooves running parallel to the axis of the screw. A relatively recent development is the barrel section with helical grooves. One of the first publications on the subject was an article by Langecker et al. [56]. They claimed a higher conveying efficiency as compared to axial grooves and a 20% reduction in energy consumption; this corresponded to a 45% reduction in energy loss through cooling of the grooved barrel section. Langecker et al. also found that screws with a very small compression ratio were most suitable for use with helically grooved barrel sections; in some cases, compression ratios of unity or slightly less than unity (actually a decompression screw) gave optimal performance. Langecker filed for a patent [57] on the helical groove idea as far back as 1972. Another patent on barrel sections with helical grooves was issued to Maillefer [58] in 1979.

Grünschloß [59] presented an analysis of a barrel section with helical grooves, attempting to explain the advantages of the helical grooves over axial grooves. Grünschloß examines a situation where the grooves in the barrel are quite wide and deep, similar to the channel in the screw. Thus, transport occurs in the barrel channel as well as in the screw channel. He also assumes no shearing between the bulk in the screw channel and in the barrel channel.

The effect of the helical grooves can be explained by considering the velocity diagram, shown earlier in Fig. 7.10. Figure 7.21(left) shows a typical velocity diagram with a smooth barrel. The frictional heat generation is direction-determined by the relative velocity between the barrel and the solid bed Δv and the coefficient of friction between the barrel and the solid bed f_b. Figure 7.21(right) shows a velocity diagram with axial grooves in the barrel.

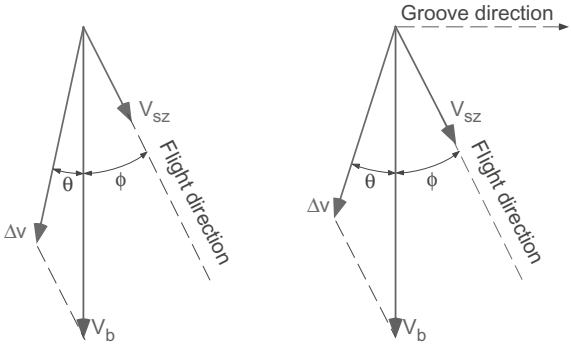


Figure 7.21
Velocity diagram with smooth barrel (left) and axially grooved barrel (right)

With the grooves in the axial direction, there will be no movement of the material in the barrel grooves. The frictional heat generation in this situation will be determined again by Δv and the effective coefficient of friction on the barrel surface f_{eb}. With axial grooves, the relative velocity difference between the barrel and solid bed will be somewhat smaller than with a smooth barrel. However, the effective coeffi-

cient of friction on the barrel surface f_{eb} will be much higher as a result of the grooves. The net effect is that the frictional heat generation will be much higher than with a smooth barrel.

The effective coefficient of friction will be partially determined by the contact of the solid bed in the screw channel and the barrel flight tip surface, and partially by the contact of the solid bed in the screw channel and the solid bed in the barrel grooves. Friction at the barrel flight tip surface is similar to friction at a smooth barrel wall. However, friction at the solid bed in the barrel grooves will be of an entirely different nature. To a certain extent the internal friction of the polymer will determine the friction, but the friction will be augmented by the action of the active edge of the barrel grooves. If the groove is relatively wide compared to the barrel flight width, one can assume that an effective coefficient of friction is roughly determined by the internal coefficient of friction of the polymer. Since the internal coefficient of friction is generally two to three times higher than the external coefficient of friction, it can be assumed that the effective coefficient of friction with axial grooves is about two to three times as high as compared to a smooth barrel. This explains the high frictional heat generation in axially grooved barrels.

The frictional heat generation can be reduced by reducing the effective coefficient of friction or by reducing the velocity difference between the solid bed in the screw channel and the barrel. Reducing the effective coefficient of friction will adversely affect the solids conveying rate and pressure generating capability. However, the velocity difference can be reduced by using helical grooves. This is explained by the velocity diagrams in Fig. 7.22.

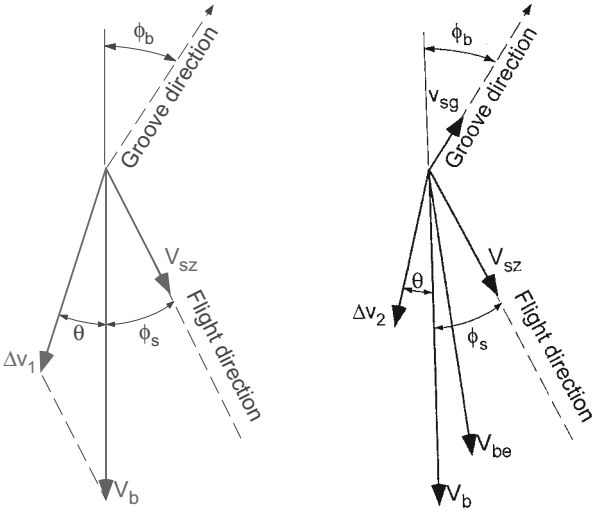


Figure 7.22
Velocity diagram with helical barrel grooves without (left) and with (right) transport in the barrel groove

The velocity diagram in the case of no material movement in the barrel grooves is shown in the left-hand side of Fig. 7.22. If the material in the barrel grooves is stationary with respect to the barrel, the effective barrel velocity equals the actual bar-

rel velocity. The effective velocity difference Δv_1 in the case of no material movement in the barrel grooves is:

$$\Delta\vec{v}_1 = \vec{v}_b - \vec{v}_{sz} \tag{7.63}$$

However, the situation will change significantly if there is movement of the material in the barrel grooves. The right-hand side of Fig. 7.22 shows the situation where the velocity of the material in the barrel grooves is v_{sg}. In this case, the effective barrel velocity becomes v_{be}; this is determined from vectorial addition of the barrel velocity v_b and the solid bed velocity in the barrel grooves v_{sg}:

$$\vec{v}_{be} = \vec{v}_b + \vec{v}_{sg} \tag{7.64}$$

The magnitude of v_{be} is determined by the following relationship:

$$v_{be} = (v_b^2 + v_{sg}^2 - 2\left| v_b \right\| v_{sg} \left| \cos\varphi_b \right)^{1/2} \tag{7.65}$$

where φ_b is the barrel groove helix angle.

The relative velocity between the solid bed in the screw channel and the material in the barrel grooves Δv_2 is determined from the vectorial differences between v_{be} and v_{sz}:

$$\Delta\vec{v} = \vec{v}_{be} - \vec{v}_{sz} = \vec{v}_b + \vec{v}_{sg} - \vec{v}_{sz} \tag{7.66}$$

From Fig. 7.22 it is clear that the effective relative velocity can be reduced substantially if there is movement of the material in the barrel grooves. The magnitude of the effective velocity difference Δv_2 is:

$$\begin{aligned}\Delta v_2^2 = {} & v_b^2 + v_{sz}^2 + v_{sg}^2 + 2v_b(v_{sg}\cos\varphi_b - v_{sz}\cos\varphi_s) + \\ & 2v_{sz}v_{sg}(\sin\varphi_s\sin\varphi_b - \cos\varphi_s\cos\varphi_b)\end{aligned} \tag{7.67}$$

where φ_s is the helix angle of the screw and φ_b the helix angle of the barrel.

It can be easily seen from Fig. 7.22 that the effective velocity difference Δv_2 is minimized when:

$$v_{sg}\sin\varphi_b = v_{sz}\sin\varphi_s \tag{7.68}$$

This is the case when the helix angle on the barrel φ_b equals the solids conveying angle of the solid bed in the screw channel θ_s. Thus, the effective velocity difference and the frictional heat generation is minimized when:

$$\varphi_b = \theta_s \tag{7.69}$$

If this condition can be achieved, the conveying efficiency of the solid bed in the screw channel will be high because of a large frictional force acting on it at the barrel surface. At the same time, however, the velocity difference between the solid bed

in the screw channel and the material in the barrel groove is minimized, resulting in a substantially reduced frictional heat development in the grooved section. This approach to the conveying mechanism in grooved barrel sections demonstrates that the claimed advantages of helical grooves can be confirmed by an engineering analysis. Therefore, it does seem to make sense to use helical grooves instead of axial grooves. Helical grooves have the potential to eliminate one of the main drawbacks of axial grooves, that is, the substantial loss of energy as a result of the very high frictional heat generation and the need for intensive cooling, causing loss of energy through cooling of the grooved barrel section.

In the actual extrusion process, the solids conveying angle θ_s will not be absolutely constant along the length of the screw. In the initial portion of the channel, a substantial amount of compacting will often take place, resulting in corresponding reductions in the solid bed velocity, and, thus, in the solids conveying angle θ_s; see Eq. 7.48. The theoretically optimum barrel helix angle θ_b, therefore, will vary along the axial length of the grooved barrel section. This would be quite difficult to machine, however, and could make the grooved section relatively expensive. From a practical point of view, it would seem reasonable to make the barrel helix angle equal to the solids conveying angle based on a fully compacted solid bed. With a fully compacted solid bed, the pressure and frictional heat generation are very high and, thus, more of a concern.

In order to obtain an expression for the optimum helix angle of the barrel groove(s), the forces acting on the solid bed in the screw channel and on the solid bed in the barrel groove can be analyzed in similar fashion as done for the smooth barrel. Figure 7.23 shows the forces acting on the solid bed in the screw channel and the corresponding velocity diagram.

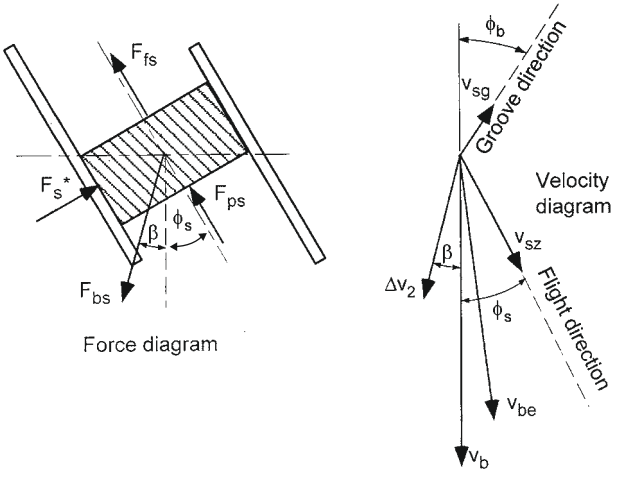


Figure 7.23
Force and velocity diagram of a solid bed in the screw channel

The frictional force acting on the barrel surface F_{bs} makes an angle β with the tangential direction. This angle is determined by the direction of the velocity vector Δv_2. If it is assumed that the frictional force F_{bs} is determined by the internal friction of the bulk material, then the force can be expressed as:

$$F_{bs} = P\, f_i\, W_s\, dz_s \tag{7.70}$$

The extra force F^*_s can be determined from a force balance in the cross-channel direction:

$$F_s^{\bullet} = F_{bs}\sin(\varphi_s + \beta) = P\, f_i\, W_s \sin(\varphi_s + \beta) dz_s \tag{7.71}$$

The frictional force on the screw F_{fs} can be determined from:

$$F_{fs} = P\, f_s\, (W_s + 2H_s) dz_s \tag{7.72}$$

The net pressure force acting on the solid bed element is:

$$F_{ps} = \frac{dP}{dz_s} W_s H_s dz_s \tag{7.73}$$

The relationship between angle β and the pressure gradient in the screw down-channel direction is obtained by a force balance in the screw down-channel direction:

$$F_{bs}\cos(\varphi_s + \beta) - F_s^* f_s = F_{fs} + F_{ps} \tag{7.74}$$

This yields the following equation:

$$P\, f_i \left[\cos(\varphi_s + \beta) - f_s \sin(\varphi_s + \beta)\right] = P\, f_s \left(1 + \frac{2H_s}{W_s}\right) + \frac{dP}{dz_s} H_s \tag{7.75}$$

Figure 7.24 shows the forces acting on the solid bed in the barrel groove and the corresponding velocity diagram.

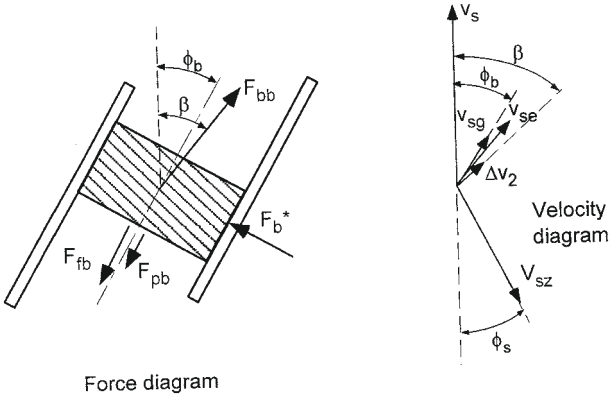


Figure 7.24
Force and velocity diagram of solid bed element in a barrel groove

In using the velocity diagram, it should be kept in mind that the barrel is now taken as being stationary and the screw moving at a tangential velocity $v_s = -v_b$. The solid bed is moving at velocity v_{sg}. The velocity of the solid bed in the screw channel with respect to the stationary barrel is v_{se}; this is determined by the vectorial addition of v_s and v_{sz}:

$$\vec{v}_{se} = \vec{v}_s + \vec{v}_{sz} \tag{7.75a}$$

The frictional force acting on the screw surface F_{bb} makes the same angle β with the tangential direction. The angle, in this case, is determined by the vectorial difference of v_{se} and v_{sg}:

$$\Delta\vec{v}_2 = \vec{v}_{se} - \vec{v}_{sg} = \vec{v}_s + \vec{v}_{sz} - \vec{v}_{sg} \tag{7.76}$$

The frictional force F_{bb} is determined from:

$$F_{bb} = P\, f_i W_b\, dz_b \tag{7.77}$$

The extra force F_b^* is determined from a force balance in the cross-groove direction:

$$F_b^* = F_{bb}\sin(\beta - \varphi_b) \tag{7.78}$$

The frictional force on the barrel surface is:

$$F_{fb} = P\, f_b (W_b + 2H_b) dz_b \tag{7.79}$$

The force resulting from the pressure gradient is:

$$F_{pb} = \frac{dP}{dz_b} W_b H_b dz_b \tag{7.80}$$

As before, the relationship between angle β and the pressure gradient in the barrel down-groove direction is obtained by a force balance on the solid bed element in the down-groove direction:

$$P\, f_i\left[\cos(\beta - \varphi_b) - f_b\sin(\beta - \varphi_b)\right] = P\, f_b\left(1 + \frac{2H_b}{W_b}\right) + \frac{dP}{dz_b} H_b \tag{7.81}$$

The optimum barrel helix angle φ_b^* is the one for which the velocity difference Δv_2 is minimized; this occurs when $\varphi_b = \theta_s$ and $\beta = 0$. At this point, the pressure gradient in the down-channel direction can be expressed in known quantities:

$$\frac{dP}{dz_s} = \frac{P\, f_i}{H}(\cos\varphi_s - f_s\sin\varphi_s) - \frac{P\, f_s}{H_s}\left(1 + \frac{2H_s}{W_s}\right) \tag{7.82}$$

This pressure gradient can now be inserted into Eq. 7.81 to yield an expression for the optimum barrel helix angle. It should be remembered that the relationship between the down-channel coordinate z_s and the down-groove coordinate z_b is:

$$z_b \sin\varphi_b = z_s \sin\varphi_s \tag{7.83}$$

The expression for the optimum barrel helix angle now takes the following form:

$$\cos\varphi_b^* = A_1 \sin\varphi_b^* + A_2 \tag{7.84}$$

where:

$$A_1 = \frac{H_b}{H_s \sin\varphi_s}\left(\cos\varphi_s - f_s - \frac{f_s}{f_i} - \frac{2H_s f_s}{f_i W_s}\right) - f_b \tag{7.84a}$$

and

$$A_2 = \frac{f_b}{f_i}\left(1 + \frac{2H_b}{W_b}\right) \tag{7.84b}$$

The solution to Eq. 7.84 can be expressed in the now familiar form:

$$\varphi_b^* = \arcsin\left[\frac{(1 + A_1^2 - A_2^2)^{1/2} - A_1 A_2}{1 + A_1^2}\right] \tag{7.85}$$

Equation 7.85 allows the calculation of the optimum barrel helix angle if the screw geometry is known and if the various coefficients of friction, internal and external, are known as well. The solution for the optimum helix angle is not completely analytical because A_2 contains a term W_b that is dependent on the barrel helix angle. This can be solved by initially guessing a value of W_b, then calculating φ_b^* according to Eq. 7.85. The W_b can be calculated with:

$$W_b = \frac{\pi D \sin\varphi_b^*}{p_b} - w_{bg} \tag{7.85a}$$

where w_{bg} is the perpendicular barrel flight width and p_b the number of parallel grooves in the barrel. The calculated value of W_b can then be used to calculated φ_b^* again. This process can be repeated until the initial value of W_b and the calculated value of W_b are within a certain tolerance. Convergence is very rapid and accurate values of φ_b^* are generally obtained in two or three iterations.

Figure 7.25 shows φ_b^* as a function of the screw helix angle when $f_b = f_s = 0.2$, $f_i = 0.6$, and $H_s = 15.24$ mm (0.6 in). The optimum barrel helix angle increases with the screw helix angle and with reducing barrel groove depth. The optimum barrel angle is relatively insensitive to the internal coefficient of friction as shown in Fig. 7.26.

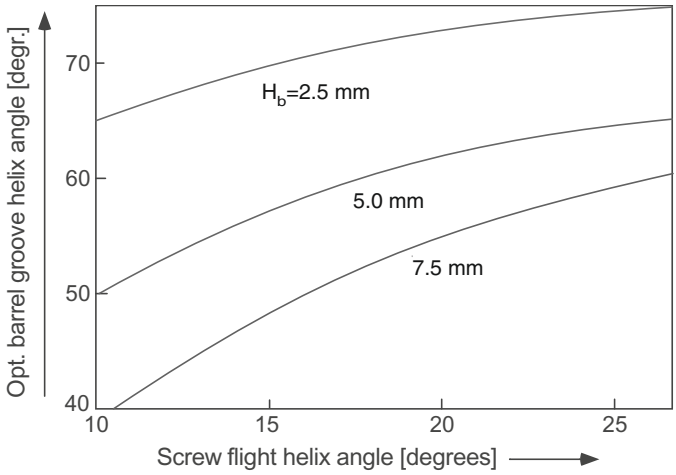


Figure 7.25 Optimum barrel groove helix angle versus the screw flight helix angle at various values of the barrel groove depth

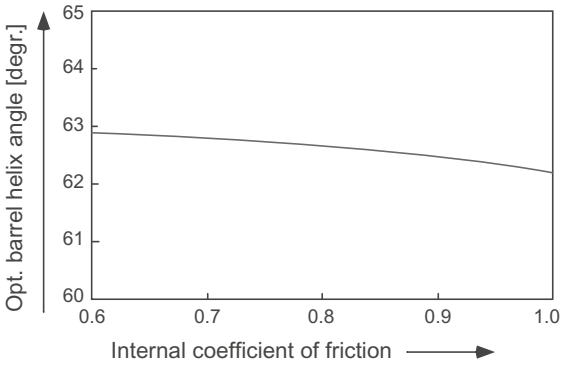


Figure 7.26
Optimum barrel groove helix angle versus the internal coefficient of friction

7.2.2.3 Adjustable Grooved Barrel Extruders

Grooved feed extruders offer considerable advantages over conventional extruders, such as higher throughput, better stability, and the ability to process very high molecular weight polymers. There are some important disadvantages as well, for instance, higher motor load, wear is more likely, high pressures in the grooved region, and the screw design has to be adapted.

The disadvantages of the grooved feed extruder disappear when the grooved feed extruder is made with a mechanism that allows adjustment of the groove depth. Recent developments in grooved feed extruders incorporate an adjustment mechanism that allows the depth of the grooves to be changed during actual operation from zero to full depth. These developments will be described and some operational data from actual extrusion experiments will be presented.

7.2.2.3.1 Problems with Grooved Feed Extruders

The use of a conventional compression screw in a grooved feed extruder often results in poor extruder performance and rapid wear of the equipment. This happens when the solids conveying efficiency is too high for the melting and melt conveying zones of the extruder to keep up. It is advantageous to have a means of controlling the solids conveying efficiency of the extruder, so that it can be adjusted to achieve the most efficient and consistent operation of the extruder. One common method of adjusting the solids conveying efficiency is to change the temperature of the barrel in the feed section of the extruder. The drawback of a temperature adjustment is that it generally only has a weak effect on the solids conveying efficiency. It is also possible to change the temperature of the screw in the feed section of the extruder. However, this suffers from the same problem as barrel temperature adjustment and, further, screw temperature control is more complicated than barrel temperature control.

7.2.2.3.2 Eliminating Drawbacks with Grooved Feed Extruders

A more effective method of controlling the solids conveying efficiency is by adjusting the groove geometry. The solids conveying efficiency is determined by the number of grooves, the length of the grooves, the orientation of the grooves, and the depth of the grooves. A continuous adjustment of the number of grooves is not possible. Adjustment of the length or the orientation of the grooves is possible, but likely to be mechanically complex. The typical axial length of the grooves is three to five barrel diameters. Thus, the adjustment length would have to be in the same range; this is a rather long length. The most convenient method of controlling the solids conveying efficiency would appear to be to adjust the depth of the grooves. The groove depth usually varies from about 2 to 3 mm to zero. Therefore, the adjustment has to be only about 2 to 3 mm.

7.2.2.3.3 The Adjustable Grooved Feed Extruder

The adjustable grooved feed extruder developed at Rauwendaal Extrusion Engineering [246] uses a grooved feed section in which the depth of the grooves can be continuously adjusted while the extruder is in operation. Parallel developments have taken place in Poland at the Technical University of Lublin [244, 245]. Earlier concepts have been developed [247], however, due to the complexity of the adjustment mechanism, these have not been applied on a wide scale.

There are two basic methods by which the groove depth can be adjusted:

1. By moving an insert (key) in the barrel groove in radial direction.
2. By moving a tapered key along a barrel groove with reducing depth in axial direction.

A prototype of the first mechanism has been constructed; experimental results will be discussed later in this section.

7.2.2.3.4 Groove Depth Adjustment by Radial Movement of Keys

Figure 7.27 depicts an example of a mechanism where the keys are moved radially, showing the axial and perpendicular cross-section of a feed housing (4) with three axial grooves. The groove depth is adjustable by means of electromechanical actuators directly connected to keys. The keys can move radially, allowing a simple and direct adjustment of the groove depth. Only one actuator is necessary for each groove. Other adjustment mechanisms are possible as well.

The depth of each groove is individually adjustable with electromechanical actuators (1) located at the outside of the feed housing. The actuator stem (2) is connected to the back end of the key, allowing a radial movement of the key in the housing. The key is located in a slot (7) in the feed housing. Both the key and the key slot have a shoulder to ensure that the minimum groove depth can be no less than zero. In other words, the key cannot move beyond the internal diameter of the feed housing. Figure 7.27 shows the position of the keys with zero groove depth.

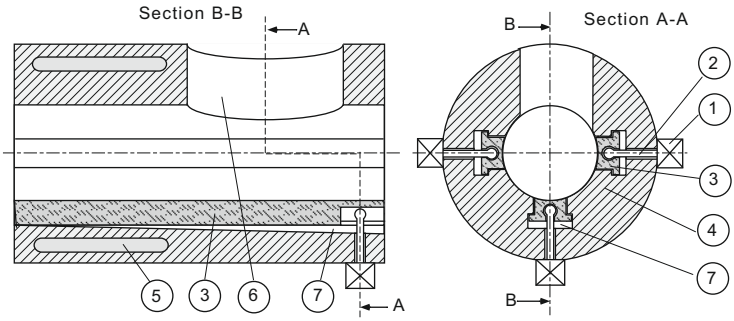


Figure 7.27 Feed housing with adjustable groove depth, zero groove depth position

The keys are made to pivot at the end of the grooves, so that the downstream end of the grooves always tapers to a zero depth. This avoids hang-up of material at the end of the grooves. Another advantage of this arrangement is that only one actuator is required for each groove, thus minimizing the cost of the adjustment mechanism. The position of the keys in the position with maximum groove depth is shown in Fig. 7.28. In this position the keys have been pulled into the key slots as far as possible.

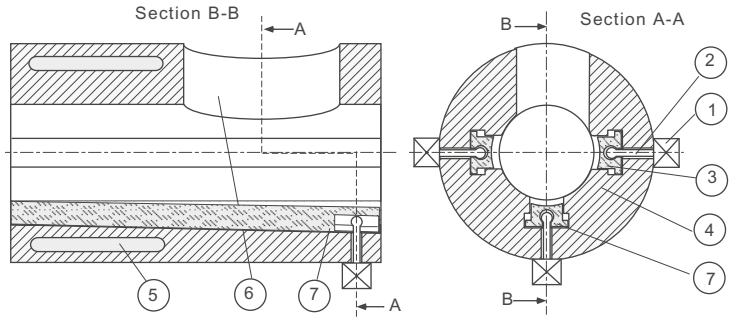


Figure 7.28 Feed housing with adjustable groove depth, maximum groove depth position

The feed housing can have a standard feed opening (6). The feed opening in Fig. 7.27 is offset to improve the feeding capability. The feed housing also has cooling channels to keep the temperatures low enough to avoid melting of the plastic particles in the grooved feed housing. Cooling channels are easy to incorporate since the groove depth adjustment mechanism takes up little space.

7.2.2.3.5 Groove Depth Adjustment by Axial Movement of Tapered Keys

One of the drawbacks of the pivoting key mechanisms is that there is a chance of material getting between the key and the keyway. When this happens, the key cannot move radially outward and mechanical problems may occur. One way of circumventing this problem is to make the keys and keyways tapered, and adjust the groove depth by sliding the keys along the base of the keyways. This is illustrated schematically in Fig. 7.29.

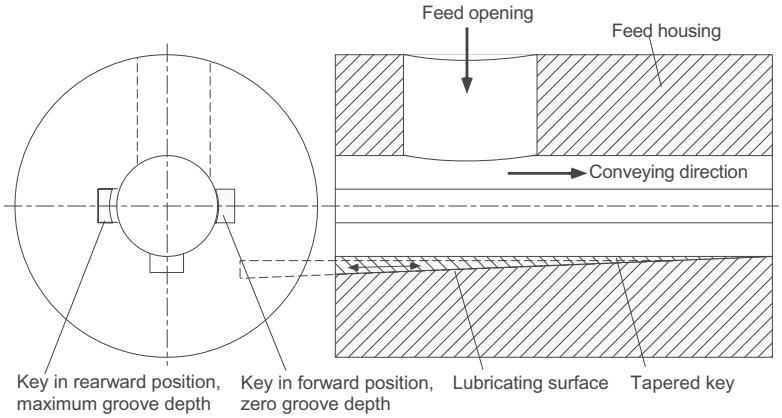


Figure 7.29 Groove depth adjustment by sliding key axially

The keys can be moved individually or together. One possible method of moving the keys is to use a rack-and-pinion mechanism. The advantage of the sliding key mechanism is that there is very little chance that material will get between the keys and the keyways. Another advantage is that the sliding key mechanism has few parts and is easy to manufacture.

The bottom of the key can be a self-lubricating material to ensure good sliding action. The key cross-section (at least part of it) should be made such that the keys will stay in place, even if they are in a vertical position. Some possible groove geometries that can accomplish this are shown in Fig. 7.30.

There are several advantages of the adjustable groove depth:

- The efficiency of the feed throat can be adjusted to the conveying characteristics of the material as well as the conveying behavior of the screw.
- Since the groove depth can be adjusted to zero depth, the feed throat can be easily cleaned out upon material change-over; in other words, no material can get trapped in the grooves.

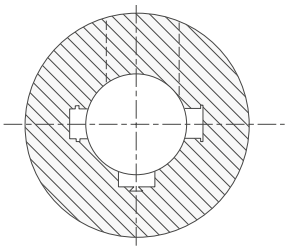


Figure 7.30
Various groove geometries to secure key

- The depth of the grooves can be adjusted while the machine is running, allowing optimization of the groove depth under actual operating conditions.
- With electronic actuators the groove depth can be adjusted quickly, automatically, and precisely; the groove depth can be automatically optimized to produce the smallest pressure variation at the discharge end of the extruder or to achieve other process objectives.
- The adjustable depth of the grooves allows a grooved feed to be easily used on vented extruders. The groove depth can be adjusted to make sure that vent flow does not occur.
- Being able to adjust the depth of the grooves in a feed housing will greatly expand and improve process adjustment capability of screw extruders.

Current screw extruders are quite limited in the ability to control the process. The primary control parameters are screw speed and machine temperatures (barrel, die, and screw). Screw speed is directly linked to output; as a result, rapid and substantial changes in screw speed will result in output changes. This limits the use of screw speed as a process control variable to optimize the process under semi-steady-state conditions. Machine temperatures can only be changed slowly; thus, they cannot be used to make fast adjustments to the process. Also, temperatures usually do not have a strong effect on the conveying characteristics of the extruder. As a result, machine temperature changes have only limited effect on the extruder conveying performance. With the ability to influence the conveying characteristics rapidly and strongly, groove depth adjustment is likely the most powerful method to optimize extruder performance. It will allow a single screw extruder to run a wider range of plastics by adjusting the conveying characteristics of the machine to the characteristics of the plastic. Similarly, a single extruder can use a wider range of extruder screws and still perform well.

7.2.2.3.6 Experimental Results

An experimental adjustable grooved feed extruder was developed and manufactured with a diameter of 25 mm and a length-to-diameter ratio of 18:1. The feed housing was equipped with two grooves containing pivoting keys, allowing a continuous adjustment of the groove depth during operation of the extruder. The angle over which the keys can be moved ranges from 0 to 0°54′ (0.0157 radians or 0.90

degrees). The screw speed ranged from 177 to 279 rpm. No heat was applied to the barrel from the barrel heaters; in fact, the barrel heaters were switched off after start-up of the extruder. The material processed was an MDPE.

Figure 7.31 shows how the throughput varies with the angle of inclination at four different screw speeds (177, 211, 248, and 279 rpm). In all cases, the throughput increases with the angle of inclination; the increase in throughput is greater at higher screw speeds (about 12%).

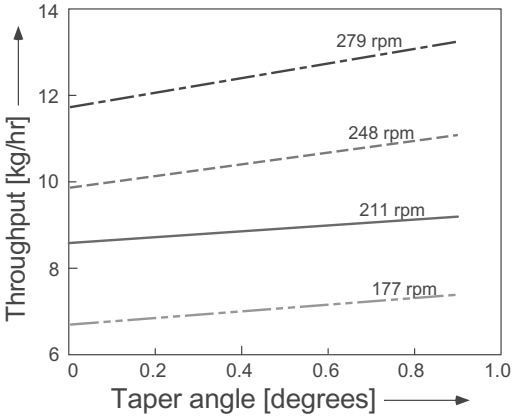


Figure 7.31
Throughput versus taper angle

Figure 7.32 shows the specific energy consumption, SEC, at again four screw speeds. The SEC increases with the angle of inclination. This is to be expected since the effective coefficient of friction at the barrel increases with the groove depth. Figure 7.33 shows barrel, die, and melt temperatures plotted against the angle on inclination. All temperatures increase with the groove depth. The results show that the extrusion process can be strongly influenced by adjustment of the groove depth.

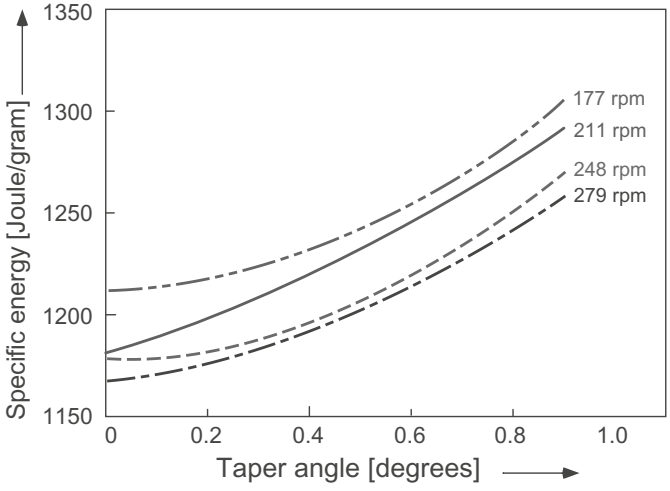


Figure 7.32
Specific energy consumption versus taper angle

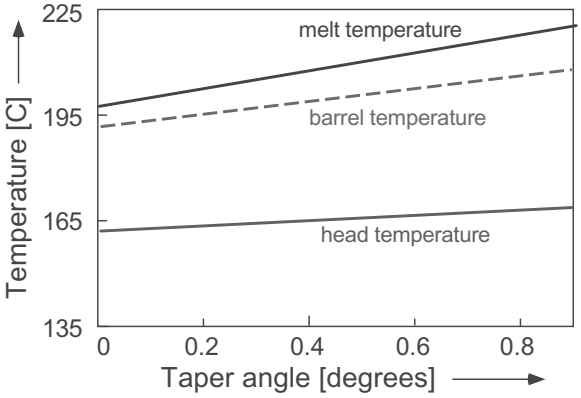


Figure 7.33
Temperatures versus the groove taper angle

7.2.2.3.7 Outlook for Adjustable Grooved Feed Extruders

The adjustable grooved feed extruder offers the advantages of a conventional grooved feed extruder while largely eliminating its disadvantages. The advantages of a grooved feed extruder are higher output, better process stability, and the ability to process very high molecular weight polymers, such as VHMWPE. Additional advantages are that the conveying efficiency of the grooved feed section can be matched to the characteristics of the polymer and the screw, the feed housing can be easily cleaned out upon material change-over, and adjusting the groove depth during operation allows process optimization under actual operating conditions. Further, optimization of the groove depth can be done automatically by feedback of the head pressure fluctuations (and/or other process parameters) to the groove depth adjustment. Additionally, the adjustable grooved feed extruder can be used on vented extruders or extruders with downstream feed port without fear of vent flow.

The main advantage of the adjustable grooved feed extruder is that it offers an increased level of control and versatility that has never before been possible. As a result, the extruder can process a wider range of materials and can operate with a greater number of different screw geometries and still maintain good process stability and product quality. The adjustable grooved feed extruder may increase acceptance of grooved feed extruders in the United States.

7.2.2.4 Starve Feeding Versus Flood Feeding

Most single screw extruders are flood fed; this means that the bottom section of the feed hopper is completely filled with material and the screw will take in as much material as it can handle. When an extruder is flood fed the output is determined primarily by the screw speed. Flood feeding is illustrated in Fig. 7.34.

With flood feeding, high pressures are generated in the solids conveying and plasticating zones of the extruder. These high pressures tend to agglomerate ingredients that later need to be dispersed and distributed [247–249]. As a result, flood feeding can be detrimental to the mixing capability of the extruder.

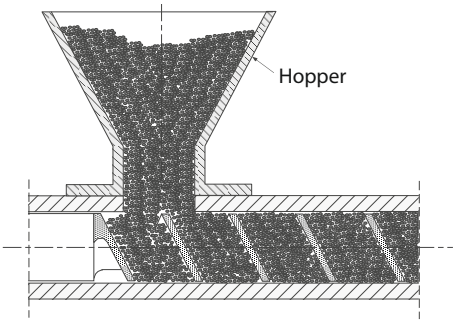


Figure 7.34
Flood feeding

In starve feeding the material is metered into the extruder with a feeder. As a result, there is no accumulation of material at the feed opening and the throughput is determined by the feeder and not by the screw speed. The first several turns of the screw are partially filled with material without any pressure development in this part of the extruder. The screw channel does not become completely filled until some distance from the feed opening; at this point the pressure will start building up in the extruder. In effect, starve feeding reduces the effective length of the extruder. Starve feeding is illustrated in Fig. 7.35.

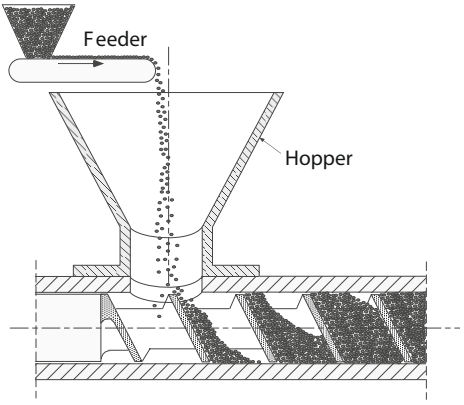


Figure 7.35
Starve feeding

One of the benefits of starve feeding is that the pressures along the extruder are lower than in flood feeding. Therefore, there is less chance of agglomeration, resulting in improved mixing action in the extruder. Recently, a number of workers have analyzed the effect of starve feeding on the mixing capability of extruders and injection molding machines [250–253]. Without exception these investigators found major improvements in mixing quality in starve feeding compared to flood feeding. Starve feeding has been the standard mode of operation for twin screw extruders used in compounding. However, the benefits of starve feeding are not limited to twin screw extruders. Mixing in single screw extruders can be improved significantly by using starve feeding. With starve feeding single screw extruders can be used for more demanding mixing jobs, in some cases competing with twin screw extruders.

In starve feeding the screw speed can be varied at constant throughput. Also, the throughput can be varied at constant screw speed. As a result, there is a greater degree of control of the extrusion process. This is beneficial as long as the extruder is long enough to achieve complete melting and mixing of the polymer. Without sufficient machine length, starve feeding will not result in acceptable performance. In most cases the length of the extruder should be 30 D or longer to use starve feeding successfully. With grooved feed extruders the feed intensity can be controlled by the degree of starvation. The effect of a grooved feed section will depend on the length over which the grooved section is completely filled. Since this can be controlled by the degree of starvation (actual feed rate divided by flood feed rate) starve feeding in a sense allows control of the effective length of a grooved feed section. As such, this is an alternative to the adjustable grooved feed extruder discussed in Section 7.2.2.3.

Another benefit of starve feeding has to do with melting. In single screw extruders the solid bed is usually compacted into a dense, continuous solid bed that extends over a considerable length of the extruder. This solid bed forms a helical ribbon that reduces in size as melting progresses along the extruder. At the point where the solid ribbon disappears the melting process is completed and the melt conveying process starts. This type of melting is referred to as contiguous solids melting (CSM)—it is typical of single screw extruders. A typical melting length in CSM is from 10 to 15 D.

In an intermeshing twin screw extruder (TSE) it is not possible for the solids to form a continuous solid bed because there are no continuous channels along the screws. As a result, the melting in an intermeshing TSE is different from the CSM type melting. In the melting zone of TSEs the solid particles generally maintain their individuality as melting progresses. The individual solid particles are suspended in a melt matrix and the particle size reduces as melting progresses. This type of melting is referred to as dispersed solids melting (DSM). The melting length in DSM is often quite short, about 2 to 3 D, about five times shorter than the melting length in CSM.

The high melting efficiency of DSM makes twin screw extruders very versatile machines because it makes more machine length available for other tasks, such as mixing, degassing, chemical reactions, etc. Clearly, if DSM can be achieved on single screw extruders it will greatly increase the utility of single screw extruders. It seems safe to say that one of the important ingredients for achieving DSM on single screw extruders is starve feeding. To achieve DSM high pressures in solids conveying have to be avoided; this can be readily accomplished with starve feeding. Obviously, other ingredients will be required as well, such as good screw design with effective mixing elements—these issues will be discussed in Chapter 8.

7.3 Plasticating

The second functional zone in the extruder is the plasticating zone or melting zone. The melting zone starts as soon as melt appears, usually after 3 to 5 diameters from the feed opening. Since most of the frictional heat generation in the solids conveying zone generally occurs at the barrel-solid bed interface, the first traces of melt usually appear at the barrel surface. It should be noted that the start of melting does not necessarily occur where the measured barrel temperature profile exceeds the melting point. The temperature at the barrel-solid bed interface can be quite different from the measured barrel temperature. In fact, melting can often be initiated without any external heating simply by the action of the frictional heat generation.

As melting proceeds, the initial melt film at the barrel surface will grow in thickness. This is particularly true in the very early stages of melting because the thin melt film is subjected to a high rate of shearing, causing a rapid temperature rise in the material and a high melting rate. Once the thickness of the melt film exceeds the radial flight clearance, the melt will flow into the screw channel, displacing the contiguous solid bed. In most cases, the solid bed will be pushed against the passive flight flank and the melt will start to accumulate in a melt pool between the solid bed and the active flight flank.

Maddock [60] was the first to accurately describe the melting behavior in single screw extruders. His observations were based on screw extraction experiments, where the screw is stopped with material still in the extruder and the machine is rapidly cooled. The screw is then pushed out of the extruder barrel, generally with a hydraulic piston. The material in the screw channel can then be analyzed at various axial locations along the screw. Maddock's description was accurate but only qualitative; he did not attempt to model the melting process to allow a quantitative description of the melting process. This type of melting is described as the contiguous solids melting (CSM) model.

Several years later, Tadmor and coworkers did extensive experimental work on melting in single screw extruders [61]. In addition to the experimental work, Tadmor performed a theoretical analysis of the plasticating process and developed the now classic Tadmor melting model [62]. This was a major contribution to the extrusion theory, particularly since melting was the one major extruder function for which a theoretical model had not been developed. Theoretical models for solids conveying and melt conveying or pumping had already been developed in the 1950s or earlier. However, the melting theory was not developed until the mid-1960s.

As discussed, the melting in twin screw extruders occurs by dispersed solids melting. A theoretical model of dispersed solids melting will be presented in Section 7.3.5.

7.3.1 Theoretical Model of Contiguous Solids Melting

An idealized cross-section of the screw channel in the melting zone is shown in Fig. 7.36. It is assumed that the screw is stationary; thus, in a cross-section perpendicular to the screw flights, the barrel moves towards the active flight at velocity v_{bx}, which is the cross-channel component of the barrel velocity v_b. As a result of this motion, the thin melt film between the solid bed and the barrel is sheared at a high rate. This will cause substantial viscous heat generation in the melt film; see also Section 5.3.4. Since the melt film is quite thin, the effect of pressure gradients on the velocity profile in the melt film will be quite small. Therefore, the flow in the melt film will be essentially drag flow, and the shear rate and viscous heat generation will be relatively uniform along the depth of the melt film.

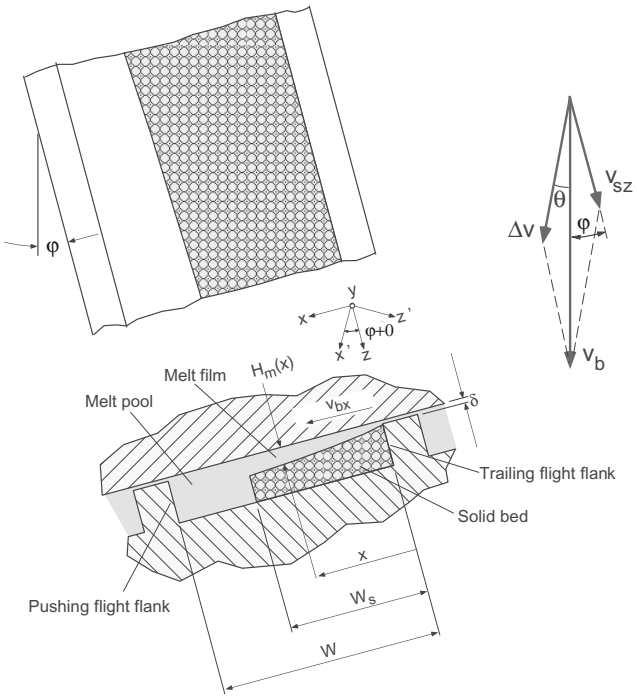


Figure 7.36
The Tadmor melting model

The melt flows from the melt film towards the active flight flank. Only a small fraction of the material can flow through the clearance. As a result, the majority of the melt will flow into the melt pool. A circulating flow will be set up in the melt pool as a result of the barrel velocity. Since most of the viscous heat generation occurs in the upper melt film, it is generally assumed that all melting takes place at the upper solid bed-melt film interface. As melting proceeds, the cross-sectional area of the solid bed will reduce and the cross-sectional area of the melt pool will tend to increase. The melt pool, therefore, will exert considerable pressure on the solid bed. This reduces the width of the solid bed, while the melt film between the solid bed

and the barrel remains relatively constant. In order for this mechanism to work, the solid bed has to be continuously deformable. The width of the solid bed reduces as more material melts away from the barrel side of the solid bed. Thus, the material in the solid bed close to the solid-melt interface moves towards the interface as melting proceeds. This occurs at a velocity v_{sy}, the solid bed melting velocity. This velocity determines the melting rate of the solid bed.

There are basically two sources of energy utilized for melting in the extruder. The first and generally the most important one is the mechanical energy supplied by the screw, which is transformed into heat by a process of viscous heat generation. The second source of energy is the heat supplied by the external barrel heaters and possibly by screw heaters. In most extruders, the majority of the energy will be supplied by the screw, about 80 to 90% or more. There is a very good reason for this. Energy supplied by the screw will be dissipated primarily in the melt film. The resulting viscous heat generation will be relatively uniform throughout the material. Thus, the temperature rise in the polymer melt will be relatively uniform and the heat transfer distances will be small.

The heat supplied by the barrel heaters has to be conducted through the entire thickness of the barrel and through the entire thickness of the melt film before it can reach the solid bed. Problems with this energy transport are considerable heat losses by conduction, convection, and radiation. Another, probably more severe, problem is the low thermal conductivity of the polymer. The heat has to be transferred across the entire melt film thickness. Therefore, the conductive heat flux will be small, particularly when the melt film thickness is large. Increasing the barrel temperature can accelerate the heating process; however, this temperature is limited by the possibility of degradation of the polymer.

If melting only occurs by heating from the barrel heaters without viscous heat generation, the rate of melting is unacceptably slow. This is precisely why ram extruders have such a poor plasticating capability; there is little or no viscous heat generation in these types of extruders; see Section 2.4. This also explains why reciprocating single screw extruders have become so popular on injection molding machines, even though they are more complex than ram extruders. Thus, it should be clear that the key to the plasticating ability of screw extruders is the viscous heat generation in the polymer melt.

In order to be able to predict the melting rate, the amount of heat flowing towards the solid-melt interface has to be known. This can be determined if the temperature profiles in the melt film and in the solid bed are known. The temperature profile in the melt film can be determined from the velocity profile in the melt film. In order to derive an expression for the temperature profile in the melt film, the following assumptions are made:

1. The process is a steady-state process.
2. The polymer melt density and thermal conductivity are constant.

3. Convective heat transfer is neglected.
4. Conductive heat transfer occurs only in a direction normal to interface.

With these assumptions, the general energy equation (Eq. 5.5) can be simplified to:

$$k_m \frac{d^2T}{dy^2} + \tau_{x'y} \frac{\partial v_{x'}}{\partial y} = 0 \tag{7.86}$$

The shear stress can be determined from the equation of motion. In order to derive an expression for the shear stress, additional assumptions are made:

1. The polymer melt flow is laminar.
2. Inertia and body forces are negligible.
3. There is no slip at the walls.
4. There are no pressure gradients in the melt film.
5. The temperature dependence of the viscosity can be neglected.

With these assumptions, the general equation of motion (Eq. 5.3) can be simplified to:

$$\frac{d\tau_{x'y}}{dy} = 0 \tag{7.87}$$

The direction of coordinate x′ is determined by the vectorial velocity difference between the barrel and the solid bed; see Fig. 7.36. The magnitude of this velocity difference Δv, the relative velocity, is given by Eq. 7.47, and the angle θ with the tangential direction is:

$$\theta = \arctan\left(\frac{v_b \sin\varphi}{v_b \cos\varphi - v_{sz}}\right) - \varphi \tag{7.88}$$

This angle θ is essentially the same angle as the solids conveying angle discussed in Section 7.2.2. If the polymer melt behaves as a Newtonian fluid, Eq. 7.87 becomes:

$$\frac{d^2 v_{x'}}{dy^2} = 0 \tag{7.89}$$

By integrating twice and taking the boundary conditions $v_{x'}(0) = 0$ and $v_{x'}(H_m) = \Delta v$, the following linear velocity profile is obtained:

$$v_{x'} = \frac{y}{H_m} \Delta v \tag{7.90}$$

Equation 7.86 now becomes:

$$k_m \frac{d^2 T}{dy^2} + \mu \left(\frac{\Delta v}{H_m}\right)^2 = 0 \tag{7.91}$$

The boundary conditions are $T(0) = T_m$ and $T(H_m) = T_b$. By integrating twice, a quadratic temperature profile is obtained:

$$T(y) = \left(\frac{-\mu \Delta v^2}{2k_m H_m{}^2} \right) y^2 + \left(\frac{2k_m \Delta T_b + \mu \Delta v^2}{2k_m H_m} \right) y + T_m \tag{7.92}$$

where $\Delta T_b = T_b - T_m$.

From Eq. 7.92, the heat flow into the interface $\dot{Q}$ can now be determined. By using Fourier's law, Eq. 5.45, the heat flow per unit area (heat flux) becomes:

$$-\dot{q}_m = \frac{-\dot{Q}_{in}}{A} = k_m \frac{dT(0)}{dy} = \frac{2k_m \Delta T_b + \mu \Delta v^2}{2H_m} \tag{7.93}$$

The temperature profile in the solid bed can be determined from the energy equation (Eq. 5.5) applied to a moving solid slab:

$$\rho_s C_s v_{sy} \frac{dT}{dy} = k_s \frac{d^2 T}{dy^2} \tag{7.94}$$

If the temperature at the interface is taken at the melting point, $T(0) = T_m$, and the temperature far away from the interface is taken as a reference temperature $T(-\infty) = T_r$, then the temperature profile in the solid bed becomes:

$$T(y) = \Delta T_r \exp\left(\frac{y v_{sy}}{\alpha_s} \right) + T_r \tag{7.95}$$

where $\Delta T_r = T_m - T_r$.

The reference temperature T_r is typically the temperature at which the solid polymer particles are introduced into the extruder. In Eq. 7.95, it is assumed that the bulk of the solid bed is at T_r and that only a relative thin skin is heating up. The validity of this assumption depends primarily on the total thickness of the solid bed and the residence time of the solid bed in the extruder. The validity of the assumption can be tested by analyzing the Fourier number as discussed in Section 5.3.3. If the thickness of the solid bed is about 10 mm and the residence time less than one or two minutes, the assumption is probably valid. However, if the solid bed thickness is in the range of 3 to 4 mm at the same residence times, the assumption is clearly not valid. Thus, the assumption should not be used when the thickness of the solid bed is less than about 5 mm (0.2 in) because, in reality, the solid bed is heated from all sides. This means that Eq. 7.95 should not be used for small diameter extruders with shallow channels and should not be used towards the end of melting if the solid bed thickness has reduced to less than 5 mm.

The actual temperature profile in the solid bed will change with axial location. The developing temperature profile can be described with Eq. 6.98 for one-sided heating,

as discussed in Section 6.3.5. The temperature profile in the center for two-sided heating is shown in Fig. 7.37. The vertical axis shows the dimensionless temperature and the horizontal axis shows the Fourier number, as discussed in Section 5.3.3. Figure 7.37 is a graphical representation of the equation describing the developing temperature profile in a finite slab heated from both sides when y = 0 ([16] of Chapter 5).

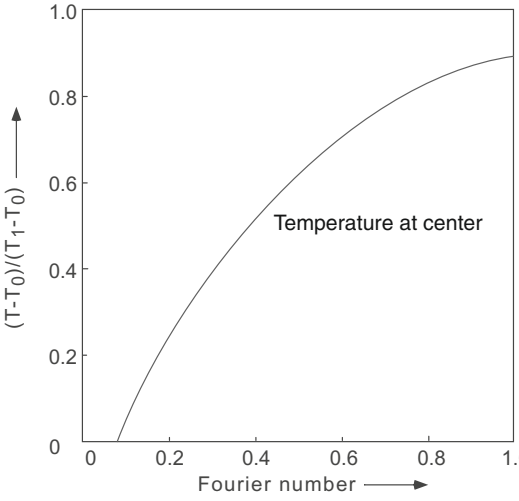


Figure 7.37
Temperature profile in a solid bed with two-sided heating

$$\frac{T_1 - T}{T_1 - T_0} = 2\sum_{n=0}^{\infty} \frac{(-1)^n}{(n+0.5)\pi} \exp\left[-\left(n+\frac{1}{2}\right)^2 \pi^2 \alpha t/b^2\right] \cos\frac{\pi\, y(2n+1)}{2b} \tag{7.96}$$

where b is half the slab thickness.

Within an accuracy of about 10 to 20%, the following approximation can be made for the temperature profile at the center of the slab:

$$\frac{T_1 - T}{T_1 - T_0} \cong \frac{\alpha\, t}{b^2} \tag{7.97}$$

This approximation can be used to obtain a corrected reference temperature T_r^*, where T_r^* increases with axial distance along the screw:

$$T_r^* = T_r + \left(\frac{4\alpha_s z}{v_{sz} H_s^2}\right) \Delta T_r \tag{7.98}$$

where the term in parentheses represents the Fourier number of the solid bed.

This corrected reference temperature T_r^* can be used in Eq. 7.95 instead of T_r.

The effect of this correction will be an accelerated melting towards the end of the melting zone. The heat flux from the interface into the solid bed q_{out} is again determined from Fourier's law:

$$-\dot{q}_{out} = -\frac{\dot{Q}_{out}}{A} = k_s \frac{dT(0)}{dy} = \rho_s C_s v_{sy} \Delta T_r \tag{7.99}$$

A more correct determination of the heat flux into the solid bed could be made by using Eq. 7.96 and differentiating the temperature with respect to the normal distance y.

An additional complication is that the solid bed is assumed to be freely deformable. This means that the heat transfer situation is no longer determinate. Equations 7.97 through 7.99 can only be used if the rate of deformation of the solid bed is small relative to the rate of heat conduction into the solid bed. A typical solid bed melt velocity (v_{sy}) is 0.2 mm/s. The thermal penetration thickness ($4\sqrt{\alpha t}$, see Eq. 6.99[a]) is about 1.3 mm in one second when the thermal diffusivity (α) is 10^{-7} m^2/s. Thus, the rate of heat conduction into the solid bed is about one order of magnitude higher than the rate of deformation of the solid bed. Thus, the rate of deformation of the solid bed, in most cases, is relatively small compared to the rate of heat conduction into the solid bed.

The temperature profiles in the melt film and solid bed are shown in Fig. 7.38.

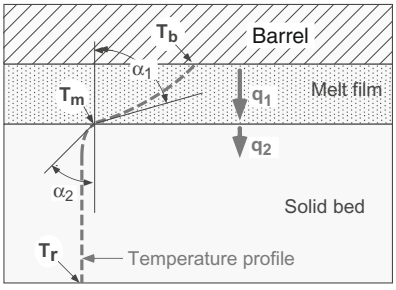


Figure 7.38
Temperature profiles and heat fluxes in CSM type melting

From a heat balance of the interface, the melting rate can be determined. The heat used to melt the polymer at the interface is determined by the heat flux into the interface minus the heat flux out of the interface:

$$v_{sy}\rho_s \Delta H_f = \frac{2k_m \Delta T_b + \mu \Delta v^2}{2H_m} - \rho_s C_s v_{sy} \Delta T_r \tag{7.100}$$

The melting velocity v_{sy} now becomes:

$$v_{sy} = \frac{2k_m \Delta T_b + \mu \Delta v^2}{2\rho_s H_m \Delta H} \tag{7.101}$$

where $\Delta H = \Delta H_f + C_s \Delta T_r$.

The factor ΔH can be considered the heat sink; it is the enthalpy difference between T_m and T_r. As melting occurs along the direction of relative motion of the solid bed, more molten polymer will accumulate in the melt film. Along a length of dx′, the increase in mass flow as a result of melting is:

$$\Delta \dot{M}_l' = \rho_s v_{sy} dx' \tag{7.102}$$

The prime with the mass flow indicates mass flow per unit length. The prime with the x-coordinate indicates the direction determined by the vectorial difference between the barrel and solid bed; see Fig. 7.36. This increase in mass flow will require an increase in melt film thickness. The corresponding increase in drag flow rate is:

$$\Delta \dot{M}_l' = \frac{1}{2} \rho_m \Delta v \, dH_m \tag{7.103}$$

It can be assumed that the changes in melt film thickness occur only in direction x′ of solid bed relative motion. In that case, by using Eqs. 7.101 through 7.103, a differential equation describing the melt film thickness can be formulated:

$$H_m dH_m = \left(\frac{2k_m \Delta T_b + \mu \Delta v^2}{\rho_m \Delta v \Delta H} \right) dx' \tag{7.104}$$

If the melt film thickness at x′ = 0 is taken as the local radial clearance δ between flight and barrel, then the melt film thickness can be expressed as:

$$H_m(x') = \left[\frac{(4k_m \Delta T_b + 2\mu \Delta v^2)}{\rho_m \Delta v \Delta H} x' + \delta^2 \right]^{1/2} \tag{7.105}$$

The amount of polymer melting over the entire solid bed width can be found by:

$$\frac{d\dot{M}p}{dz'} = \int_0^{W_s'} \rho_s v_{sy} dx' = \int_{H_m(O)}^{H_m(W_s')} \frac{1}{2} \rho_m \Delta v \, dH_m \tag{7.106}$$

where W_s' is the solid bed width in direction x′.

This represents the melting rate per unit length in direction z′ (see Fig. 7.36); it can be written as:

$$\frac{d\dot{M}p}{dz'} = \frac{1}{2} \rho_m \Delta v \, H_m \Big|_{H_m(0)}^{H_m(W_s')} \tag{7.107}$$

If the clearance is considered to be negligible, $H_m(0) = 0$, the melting rate is:

$$\frac{d\dot{M}_p}{dz'} = \sqrt{\frac{(2k_m \Delta T_b + \mu \Delta v^2)}{2\Delta H} \rho_m \Delta v W_s'^{1/2}} = \Omega \sqrt{W_s'} \tag{7.108}$$

Equation 7.108 expresses the melting per unit length in direction z′. The direction x′ is determined by the relative velocity Δv. The relationship between x′ and the cross-channel coordinate x is: $x = x'\sin(\theta + \varphi)$. The relationship between z′ and the down-channel coordinate z is: $z' = z\sin(\theta + \varphi)$. Thus, the melting rate per unit down-channel distance is:

$$\frac{d\dot{M}_p}{dz} = \Omega\sqrt{W_s'}\sin(\theta + \varphi) \tag{7.109a}$$

The relationship between z′ and axial coordinate l is $l = z'\cos\theta$. Thus, the melting rate per unit axial length is:

$$\frac{d\dot{M}_p}{dl} = \frac{\Omega\sqrt{W_s'}}{\cos\theta} \tag{7.109b}$$

The relationship between the solid bed width W_s' in x′-direction and W_s in cross-channel direction is $W_s = W_s'\sin(\theta + \varphi)$. With this relationship, the melting rate per unit down-channel length can be written as:

$$\frac{d\dot{M}_p}{dz} = \Omega_1\sqrt{W_s} \tag{7.109c}$$

where:

$$\Omega_1 = \left[\frac{(2k_m\Delta T_b + \mu\Delta v^2)\rho_m v_b \sin\varphi}{2\Delta H}\right]^{1/2} \tag{7.109d}$$

This result will become obvious when it is realized that $\Delta v\sin(\theta + \varphi) = v_b\sin\varphi$; see Eq. 7.61.

From Eq. 7.107, it can be seen that the effect of a non-zero radial flight clearance is to reduce the local melting rate. This means that screw or barrel wear in the plasticating zone will reduce the melting performance of the extruder; see also Section 8.2.2.3. From Eqs. 7.108 and 7.109, the contribution from heat conduction $2k_m\Delta T_b$ and the contribution from the viscous heat generation $\mu\Delta v^2$ can be clearly distinguished. As mentioned earlier, the viscous heat generation term is generally larger than the heat conduction term.

These equations can also explain why sometimes an increase in barrel temperature does not result in improved melting performance. When the barrel temperature T_b is increased, the heat conduction term increases; however, the viscous heat generation term will decrease because the viscosity in the melt film will decrease with increasing temperature of the melt film. If the reduction in the viscous heat generation is larger than the increase in heat conduction, the net result will be a reduced melting rate as shown in Fig. 7.39.

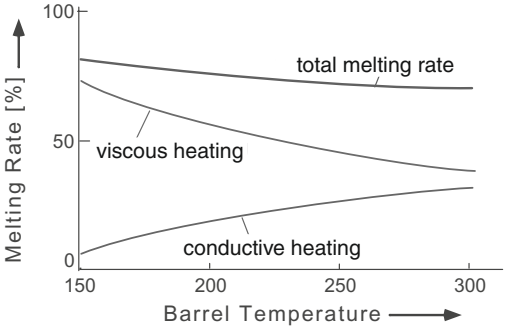


Figure 7.39
Effect of barrel temperature on melting rate when the viscosity is highly temperature sensitive

This can occur in polymers whose melt viscosity is very sensitive to temperature, such as PMMA, PVA, PVC, etc. For temperature dependence of melt viscosity, see Section 6.2.4 and Table 6.1.

When the melt viscosity is not very sensitive to temperature the reduction in viscous heating with barrel temperature will be small. As a result, the melting rate will likely increase with barrel temperature as shown in Fig. 7.40.

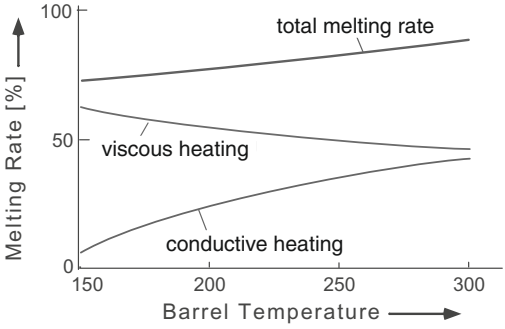


Figure 7.40
Effect of barrel temperature on melting rate when the viscosity is not highly temperature sensitive

Another interesting observation is that the local melting rate is directly determined by the width of the solid bed. Obviously, the maximum solid bed width is the channel width. The solid bed width in the very early part of melting can be assumed to be equal to the channel width. As melting proceeds, the solid bed width will generally reduce and, consequently, the local melting rate will reduce with it. In most cases, the highest melting rate is achieved at the start of melting; the melting rate then reduces monotically with axial distance as the solid bed width reduces. This is an important consideration in screw design. For good melting performance, one would like to maintain a relatively wide solid bed over a substantial length in order to maintain the highest possible melting rate. This point will be discussed in more detail in Chapter 8 on screw design.

It should be noted that Eqs. 7.102 through 7.109 are slightly different from the equations developed by Tadmor [62]; see also reference 5 of Chapter 1. The reason is that Tadmor assumed a constant melt film thickness. However, it is clear that the melt film

thickness has to increase with cross-channel distance to accommodate the increased amount of melt. Both Shapiro [63] and Vermeulen [64, 65] have analyzed this point in detail and demonstrated that in a consistent model the melt film thickness must vary with cross-channel distance. If the melt film thickness is assumed to be constant, very high cross-channel pressure gradients must occur to allow additional material in the melt film. These pressure gradients are of such high magnitude as to be unrealistic. If the thickness of the melt film is assumed constant across the width of the solid bed, the predicted melting rate will be lower by a factor of $\sqrt{2}$ compared to the case where the melt film thickness varies across the width of the solid bed.

The one unknown left at this point is the width of the solid bed. A relationship for the change in solid bed width with down-channel distance can be obtained from a mass balance of the solid bed in the down-channel direction. This can be written as:

$$d\dot{M}_p = -\rho_s v_{sz} d(H_s W_s) \tag{7.110}$$

In the melting zone, the channel is generally tapered; thus, the channel depth varies linearly with down-channel distance:

$$H = H_f - A_z z \tag{7.111}$$

where H_f is the channel depth of the feed section and A_z the degree of taper in the down-channel direction.

From Eqs. 7.109 and 7.110, a differential equation is obtained describing the change in solid bed:

$$-\frac{\Omega_1 \sqrt{W_s}}{\rho_s v_{sz}} = H_s \frac{dW_s}{dz} + W_s \frac{dH_s}{dz} \tag{7.112}$$

The thickness of the solid bed H_s is primarily determined by the channel depth. Thus, it can be assumed that the change in H_s with distance equals the change in channel depth with distance:

$$\frac{dH_s}{dz} = \frac{dH}{dz} = -A_z \tag{7.113}$$

This is an important point because this means that without melting, the compression in the channel would cause an increase in solid bed width. In this case:

$$dW_s = \frac{A_z}{H_s} dz \tag{7.113a}$$

In the absence of melting the solid bed width will increase directly proportional to distance. Thus, there are two mechanisms affecting the width of the solid bed. Melting will cause a reduction of the solid bed width, but at the same time, channel taper will cause an increase in solid bed width. The reduction in W_s from melting should

always exceed the increase in W_s from compression. If the compression is too rapid, with large A_z, the melting cannot reduce the solid bed width fast enough. As a result, the solid bed width will increase and plug the channel as it reaches the width of the screw channel. This puts an upper bound on the maximum compression ratio that can be applied in the plasticating section of an extruder screw; see more on this in Section 8.2.2.

From Eqs. 7.112 and 7.113, the following differential equation for the solid bed width is obtained if it is assumed that $H \cong H_s$:

$$-\frac{\Omega_1}{\rho_s v_{sz}}\sqrt{W_s} = H\frac{dW_s}{dz} - W_s A_z \tag{7.114}$$

The solution for this equation is:

$$W_s = W_1\left[\frac{\Omega_1}{A_z v_{sz}\rho_s\sqrt{W_1}} - \left(\frac{\Omega_1}{A_z v_{sz}\rho_s\sqrt{W_1}} - 1\right)\left(\frac{H_f}{H_f - A_z z}\right)^{1/2}\right]^2 \tag{7.115}$$

where W_1 is the solid bed width at $z = 0$.

The total length for melting can be obtained by setting $W_s = 0$:

$$Z_T = \frac{H_f v_{sz}\rho_s\sqrt{W_1}}{\Omega_1}\left(2 - \frac{A_z v_{sz}\rho_s\sqrt{W_1}}{\Omega_1}\right) \tag{7.116}$$

From Eq. 7.115, it can be seen that an extreme condition is reached when the term $\Omega_1/(A_z v_{sz}\rho_s\sqrt{W_1})$ becomes unity. In this case, the solid bed width becomes independent of down-channel distance, and the shortest possible melting length is obtained $Z_T = H_f/A_z$. However, this condition cannot be achieved in practice because there is no room for the polymer melt. Thus, in practical extrusion operations, the term $\Omega_1/(A_z v_{sz}\rho_s\sqrt{W_1})$ has to be larger than unity to ensure a continuous reduction in solid bed width with distance and to avoid plugging.

7.3.1.1 Non-Newtonian, Non-Isothermal Case

A more realistic prediction of the melting performance can be obtained if the polymer melt is considered non-Newtonian and non-isothermal. However, this extension of the analysis results in coupled energy and momentum equations. Such problems generally do not allow analytical solutions. One approach to this problem, as suggested by Tadmor [61], is to assume a certain temperature profile and solve the equations. If a quadratic temperature profile is assumed, the solution becomes quite elaborate containing many error functions. Evaluation of the solutions requires substantial numerical analysis and number crunching; for details, the reader is referred to reference 5 of Chapter 1. If a linear temperature profile is assumed in the melt film, the solution becomes more manageable. The constitutive equation is:

$$\tau_{x'y} = m_r a_T \left(\frac{dv_{x'}}{dy} \right)^n \tag{7.117}$$

where $a_T = \exp[\alpha_T(T_m - T)]$; see also Eq. 6.40.

The equation of motion (Eq. 5.3) becomes:

$$\frac{d\tau_{x'y}}{dy} = 0 \tag{7.118}$$

This equation can be integrated to give:

$$\tau_{x'y} = K_1 \tag{7.119}$$

where K_1 is an integration constant.

The assumed temperature profile can be written as:

$$T(y) = \Delta T_b \frac{y}{H_m} + T_m \tag{7.120}$$

When this expression is substituted in Eq. 7.117, the velocity gradient will become dependent on normal distance y. Equation 7.117 becomes:

$$\frac{dv_{x'}}{dy} = \left(\frac{K_1}{m_r} \right)^s \exp\left(\frac{K_2}{H_m} y \right) \tag{7.121}$$

where $K_2 = s\alpha_T \Delta T_b$ and s is the reciprocal power law index s = 1/n.

With boundary conditions $v_x'(0) = 0$ and $v_x'(H_m) = \Delta v$, the solution becomes:

$$v_{x'}(y) = \Delta v \left[\frac{1 - \exp(K_2 y / H_m)}{1 - \exp K_2} \right] \tag{7.122}$$

The shear rate distribution is determined by taking the first derivative of $v_{x'}(y)$ with respect to y:

$$\frac{dv_{x'}}{dy} = -\frac{\Delta v K_2 \exp(K_2 y / H_m)}{H_m (1 - \exp\ K_2)} \tag{7.123}$$

The velocity gradient as a function of y can now be inserted into the energy equation, Eq. 7.86. By taking boundary conditions $T(0) = T_m$ and $T(H_m) = T_b$, the solution becomes:

$$T(y) = T_m + \frac{\Delta T_b y}{H_m} + \frac{B_2 H_m^2}{K_2^2} \left[\exp\left(\frac{K_2 y}{H_m} \right) - 1 - (\exp K_2 - 1) \frac{y}{H_m} \right] \tag{7.124a}$$

where:

$$B_2 = -\frac{m_r}{k_m} \left[\frac{\Delta v K_2}{H_m (\exp K_2 - 1)} \right]^{n+1} \tag{7.124b}$$

For a temperature-independent fluid ($\alpha_T = 0$), the factor K_2 becomes zero. When K_2 approaches zero:

$$B_2 \rightarrow -\frac{m_r}{k_m}\left(\frac{\Delta v}{H_m}\right)^{n+1} \tag{7.124c}$$

and

$$\left[\exp\left(\frac{K_2 y}{H_m}\right) - 1 - (\exp K_2 - 1)\frac{y}{H_m}\right] \rightarrow \frac{1}{2}K_2^2\left(\frac{y^2}{H_m^2} - \frac{y}{H_m}\right) \tag{7.124d}$$

Thus, for a temperature-independent power law fluid, the temperature profile is:

$$T(y) = T_m + \frac{\Delta T_b}{H_m}y + \frac{m_r H_m^2}{2k_m}\left(\frac{\Delta v}{H_m}\right)^{n+1}\left(\frac{y}{H_m} - \frac{y^2}{H_m^2}\right) \tag{7.124e}$$

For a temperature-independent Newtonian fluid (n = 1), the temperature profile becomes:

$$T(y) = T_m + \frac{\Delta T_b}{H_m}y + \frac{\mu \Delta v^2}{2k_m}\left(\frac{y}{H_m} - \frac{y^2}{H_m^2}\right) \tag{7.124f}$$

Equation 7.124(f) corresponds, of course, to Eq. 7.92 derived earlier and also to Eq. 5.62. From Eq. 7.124(a), the heat flux from the melt film into the solid melt interface can be calculated. The first derivative of T(y) with respect to y is:

$$\frac{dT}{dy} = \frac{\Delta T_b}{H_m} + \frac{B_2 H_m}{K_2^2}\left(K_2 \exp\frac{K_2 y}{H_m} - \exp K_2 + 1\right) \tag{7.125}$$

The heat flux from the melt film into the interface is:

$$-\dot{q}_m = k_m \frac{dT(0)}{dy} = \frac{k_m \Delta T_b}{H_m} + \frac{k_m B_2 H_m}{K_2^2}(K_2 - \exp K_2 + 1) \tag{7.126}$$

The heat balance for the interface now becomes:

$$v_{sy}\rho_s \Delta H_f = \frac{k_m \Delta T_b + B_3}{H_m} - \rho_s C_s v_{sy} \Delta T_r \tag{7.127}$$

where:

$$B_3 = \frac{k_m B_2 H_m^2}{K_2^2}(K_2 - \exp K_2 + 1) \tag{7.128}$$

Equation 7.127 corresponds to Eq. 7.100, describing the Newtonian, temperature-independent fluid. From Eq. 7.127, the solid bed melting velocity can be obtained:

$$v_{sy} = \frac{k_m \Delta T_b + H_m B_3}{\rho_s H_m \Delta H} \tag{7.129}$$

Following the same procedure that was used to derive Eq. 7.105, the melt film thickness can be expressed as:

$$H_m(x') = \left[\frac{(4k_m \Delta T_b + 4B_3)x'}{\rho_m \Delta v \Delta H} + \delta^2 \right]^{1/2} \tag{7.130}$$

For a temperature-independent power law fluid, factor B_3 becomes:

$$B_3 = \frac{m_r H_m^2}{2} \left(\frac{\Delta v}{H_m} \right)^{n+1} \tag{7.128a}$$

and the melt film thickness becomes:

$$H_m(x') = \left[\frac{4k_m \Delta T_b + 2m_r H_m^2 (\Delta v / H_m)^{n+1}}{\rho_m \Delta v \, \Delta H} x' + \delta^2 \right]^{1/2} \tag{7.130a}$$

Equation 7.130(a) becomes equal to Eq. 7.105 when the power law index n is set to unity.

The melting rate per unit-down channel length is still described by Eq. 7.107. If the clearance between flight and barrel is assumed zero, the melting rate is:

$$\frac{d\dot{M}p}{dz'} = \left[\frac{k_m \Delta T_b + B_3}{\Delta H} \rho_m \Delta v W_s' \right]^{1/2} = \Omega * \sqrt{W_s'} \tag{7.131}$$

By the same transformations as used before, the melting rate per unit length in z′ direction can be rewritten as the melting rate per unit down-channel length z:

$$\frac{d\dot{M}p}{dz} = \Omega_2 \sqrt{W_s'} \sin(\theta + \varphi) = \Omega_1^* \sqrt{W_s} \tag{7.132}$$

where:

$$\Omega_1^* = \left[\frac{(k_m \Delta T_b + B_3) \rho_m v_b \sin\varphi}{\Delta H} \right]^{1/2} \tag{7.132a}$$

This value Ω_1^* can be used in the equations describing the solid bed width profile along the melting zone.

7.3.1.1.1 Melting of Temperature-Dependent Power Law Fluid

Rauwendaal [270] published a melting theory for temperature-dependent fluids and presented an exact analytical solution of power law fluids. This represents an important extension of the previous theories in that it allows accurate assessment of the effect of the temperature dependence of the melt viscosity. The following assumptions are made:

1. The process is steady state
2. Polymer melt density and thermal conductivity are constant

3. Convective heat transfer is negligible
4. Conductive heat transfer only in normal direction
5. Polymer melt flow is laminar
6. Inertia and body forces are negligible
7. No slip at the walls
8. No pressure gradient in the melt film
9. The temperature profile in the melt film is fully developed

The equation of motion takes the same form as Eq. 7.118. The constitutive equation of the polymer melt is expressed as:

$$\tau_{x'y} = m\left|\frac{dv_{x'}}{dy}\right|^{n-1}\frac{dv_{x'}}{dy} \tag{7.133}$$

where:

$$m = m_0 \exp[\alpha(T_0 - T)]$$

When the dimensionless temperature is defined as $\theta = \alpha(T - T_0)/n$ and dimensionless normal coordinate $\zeta = y/H_m$ the energy equation can be written as:

$$\frac{d^2\theta}{d\zeta^2} + C_1 \exp\theta = 0 \tag{7.134}$$

where:

$$C_1 = \frac{\alpha H_m^2 \tau_0^{1+s}}{n k m_0^s} \tag{7.135}$$

and:

$$\tau_0 = \left|\frac{1}{v}\int_0^{H_m} m^{-s} dy\right|^{-n} \tag{7.136}$$

When the maximum in the temperature profile in the melt film occurs at $\zeta^* > 0$ the temperature profile can be determined to be [271]:

$$\theta(\zeta) = \ln\left[A\,\mathrm{sech}^2(y_1\,\zeta + y_2)\right] \tag{7.137}$$

where

$$C = \sqrt{2C_1} \tag{7.138}$$

$$y_1 = \frac{C\sqrt{A}}{2} \tag{7.139}$$

$$y_2 = \frac{\theta_m}{2} - \ln\left(\sqrt{A} + \sqrt{A - \exp\theta_m}\right) \tag{7.140}$$

Temperature θ_m is the dimensionless melt temperature. The value of A determines the maximum temperature $\theta^* = \ln A$; it can be determined from:

$$\left[\frac{sN_{Na}}{4}\right]^s = 2A(-y_2 - y_3)\left[\frac{1}{1+e^{2y_2}} - \frac{1}{1+e^{-2y_3}}\right]^{s+1} \tag{7.141}$$

where:

$$y_3 = \frac{\theta_m}{2} - \ln\left(\sqrt{A} + \sqrt{A - \exp\theta_b}\right) \tag{7.142}$$

and the Nahme number:

$$N_{Na} = \frac{\alpha\, m_0\, v^{n+1}}{k\, H_m^{n-1}} \tag{7.143}$$

The analytical solution, Eq. 7.137, has been compared to finite element solutions with very good agreement between analytical and numerical results [271]. From Eq. 7.137 the heat flux from the melt film into the interface can be determined. Using Fourier's law the heat flux becomes:

$$-q_{in} = \frac{n\, k_m}{\alpha\, H_m}\frac{d(0)}{d\zeta} = \frac{2n\, k_m}{\alpha\, H_m}\,(-y_2 - y_3)\sqrt{1 - \frac{1}{A}\exp\theta_m} \tag{7.144}$$

The heat flux from the interface into the solid bed q_{out} is determined from the temperature profile in the solid bed. This is given by Eq. 7.99. The melting rate can be determined from a heat balance at the interface. This can be written as:

$$v_{sy}\,\rho_s \Delta H_f = \frac{2nk_m}{\alpha H_m}(-y_2 - y_3)\sqrt{1 - \frac{1}{A}\exp\theta_m} - \rho_s C_s v_{sy}\,\Delta T_r \tag{7.145}$$

where ΔH_f is the latent heat of fusion. The melt velocity becomes:

$$v_{sy} = \frac{\Phi_1}{\rho_s H_m} \tag{7.146}$$

where:

$$\Phi_1 = \frac{2n\, k_m(-y_2 - y_3)}{\alpha\, \Delta H}\sqrt{1 - \frac{1}{A}\exp\theta_m} \tag{7.147}$$

and:

$$\Delta H = \Delta H_f + C_s\,\Delta T_r \tag{7.148}$$

Factor ΔH is the enthalpy difference between T_m and T_r. The melt film thickness H_m can be determined from a mass balance in direction x'. This leads to the following expression:

$$H_m(x') = \sqrt{\frac{4\Phi_1}{\rho_m \Delta H} + \delta^2} \tag{7.149}$$

In the derivation of Eq. 7.149 it is assumed that the dependence of A on x′ can be neglected. The melting rate per unit length in direction z′ can be determined by integrating the melting velocity over the width of the solid bed as shown in Eq. 7.106. The integral can be evaluated using Eqs. 7.103 and 7.146, and results in:

$$\frac{d\dot{M}_p}{dz'} = \rho_m \Delta v \left[\sqrt{\frac{\Phi_1 W_s'}{\rho_m \Delta v} + \frac{\delta^2}{4}} - \frac{\delta}{2} \right] \tag{7.150}$$

The melting rate per unit length in down-channel direction z can be determined by considering that $z' = z \sin(\theta + \varphi)$ and $\Delta v \sin(\theta + \varphi) = v_b \sin\varphi$. Thus, the melting rate per unit length z becomes:

$$\frac{d\dot{M}_z}{dz} = \sqrt{\rho_m v_{bx} \Phi_1 W_s + 0.25 \rho_m^2 v_{bx}^2 \delta^2} - 0.5 \rho_m v_{bx} \delta \tag{7.151}$$

The solid bed width can be determined from a mass balance of the solid bed in the down-channel direction as expressed by Eq. 7.110. This leads to the following differential equation:

$$-\left(aW_s + b^2\right)^{0.5} + b = c_1 (H_1 - A_z z) \frac{dW_s}{dz} - c_2 W_s \tag{7.152}$$

where:

$a = \rho_m v_{bx} \Phi_1$

$b = 0.5\, \rho_m v_{bx} \delta$

$c_1 = \rho_s V_{sz}$

$c_2 = \rho_s V_{sz} A_z$

The solution to Eq. 7.152 can be written as:

$$\frac{H_1}{H_1 - A_z z} = c_3 \left(-c_2 W_s + \sqrt{aW_s + b^2} - b \right) \left(\frac{a/c_2 - \sqrt{aW_s + b^2} - b}{b - \sqrt{aW_s + b^2}} \right)^{\frac{a}{a - 2bc_2}} \tag{7.153}$$

where:

$$c_3 = \frac{1}{-c_2 W_1 + \sqrt{aW_1 + b^2} - b} \left(\frac{b - \sqrt{aW_1 + b^2}}{a/c_2 - \sqrt{aW_1 + b^2} - b} \right)^{\frac{a}{a - 2bc_2}}$$

It is assumed that at z = 0 the width of the solid bed is W_1 and the depth of the solid bed H_1. The problem is simpler when the flight clearance is taken as zero. In this case, the width of the solid bed can be described by:

$$\frac{H_1}{H_1 - A_z z} = \left[\frac{\sqrt{a} - c_2 \sqrt{W_s}}{\sqrt{a} - c_2 \sqrt{W_1}} \right]^2 \tag{7.154}$$

With Eq. 7.154 the solid bed profile can be written as:

$$W_s(z) = \left[\frac{\sqrt{a}}{c_2} - \left(\frac{\sqrt{a}}{c_2} - \sqrt{W_1}\right)\left(\frac{H_1}{H_1 - A_z z}\right)^{0.5}\right]^2 \tag{7.155}$$

The length required to complete melting z_0 can be determined by setting the solid bed width equal to zero. This results in the following expression for the melting length:

$$z_0 = \frac{H_1}{A_z}\left(1 - \frac{c_2}{ac_3}\right) \tag{7.156}$$

When the flight clearance is taken as zero the melting length becomes:

$$z_0 = \frac{H_1}{A_z}\left[1 - \left(1 - c_2\sqrt{\frac{W_1}{a}}\right)^2\right] \tag{7.157}$$

The shortest melting length occurs when $\sqrt{a} = c_2\sqrt{W_1}$. In this case, the melting length becomes $z_0 = H_1/A_z$. From Eq. 7.155 it can be seen that in this situation the solid bed width becomes independent of down-channel distance z. In other words, the solid bed width remains constant. Clearly, this minimum length cannot be achieved in practice because there will be no room for the polymer melt to accumulate.

With these equations the melting process of a temperature-dependent power law fluid can be completely described. From Eq. 7.151 it can be seen that the melting rate decreases with increasing flight clearance. Figure 7.41 shows how the melting rate is affected by the flight clearance.

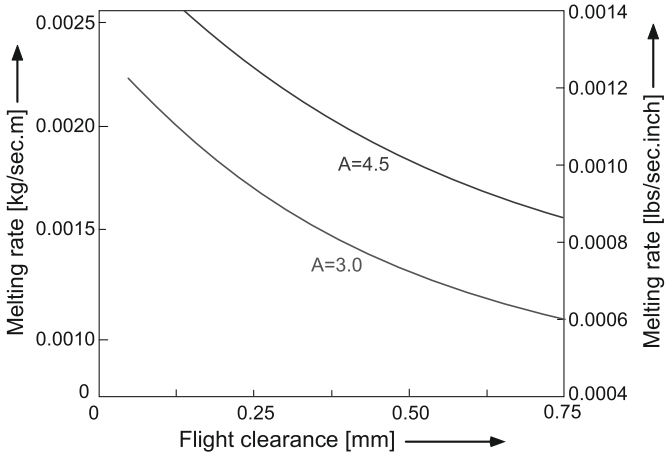


Figure 7.41
Melting rate versus flight clearance

These results are for a 63-mm extruder running a 0.2 melt index HDPE at a screw speed of 60 rpm. It is clear that increased flight clearance significantly reduces melting performance. It is important, therefore, to keep the flight clearance small in the melting zone of the extruder.

The effect of barrel temperature on melting performance can be predicted in a quantitative way. Figure 7.42 shows how the melting rate changes with barrel temperature for two values of the Nahme number as expressed by Eq. 7.143. Low Nahme numbers indicate little viscous dissipation, while high Nahme numbers correspond to high levels of viscous dissipation.

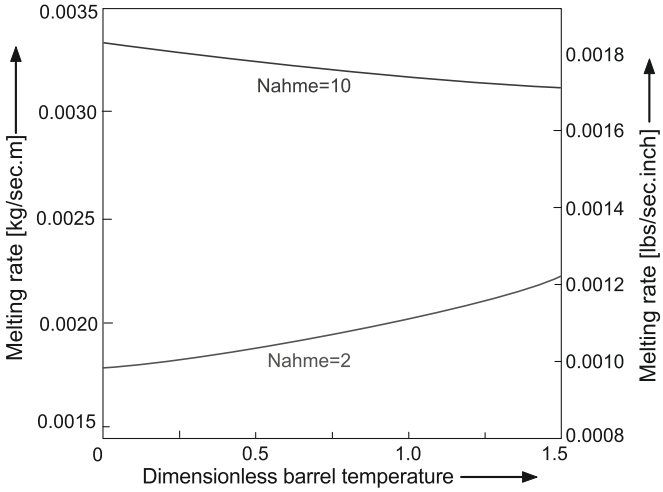


Figure 7.42
Melting rate versus barrel temperature (θ_m = 0 and n = 0.5)

At low Nahme numbers the melting rate increases with barrel temperature. However, at high values of the Nahme number the melting rate reduces with increasing barrel temperature. There is a critical Nahme number above which increasing barrel temperature results in reduced melting rate. At a power law index of n = 0.5 the critical Nahme number is about 4.5. The critical Nahme number increases with the power law index as shown in Fig. 7.43.

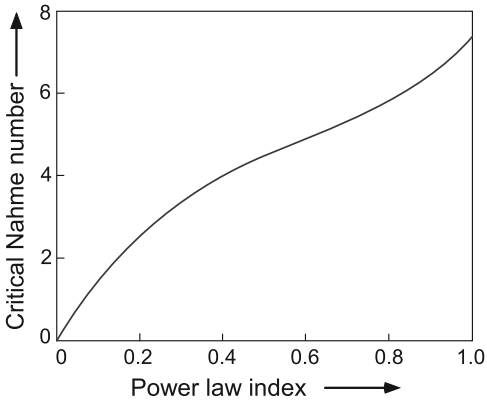


Figure 7.43
Critical Nahme number versus power law index

The temperature coefficient of the melt viscosity has a strong effect on the temperature profile in the melt film and, thus, on the melting rate. The melting rate reduces when the temperature coefficient increases. This is shown in Fig. 7.44.

It is clear from Fig. 7.44 that predictions of melting performance based on an analysis of a temperature-independent fluid will significantly overestimate the melting performance. As a result, such predictions should be treated with caution.

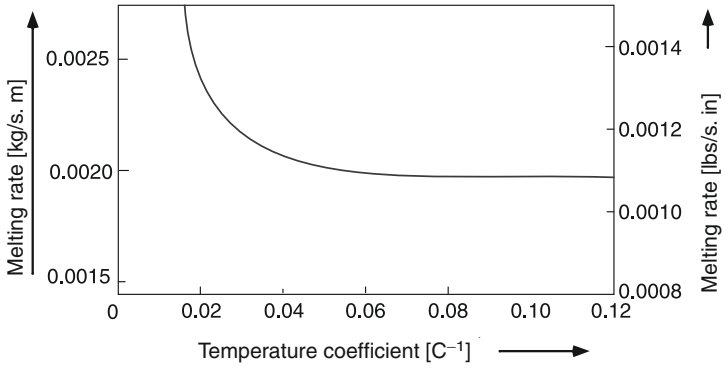


Figure 7.44 Melting rate versus the temperature coefficient

In screw design it is important to make sure that the compression in the transition section of the screw is gentle enough to avoid plugging. This is a situation where the melting cannot keep up with the channel compression, resulting in an increase of the width of the solid bed. When this happens the solid bed will get stuck in the channel and severe instabilities can occur. From Eq. 7.155 it can be determined that plugging can be avoided when the following inequality is satisfied:

$$\Phi_1 > \frac{\rho_s^2 v_{sz}^2 A_z^2 W_1}{\rho_m v_{bx}} \tag{7.158}$$

If the length of the transition section is L_c, plugging can be avoided when:

$$L_c > \frac{\rho_s v_{sz} H_1 (X_c - 1)\sqrt{W_1}\sin\varphi}{X_c \sqrt{\rho_m v_{bx} \Phi_1}} \tag{7.159}$$

where X_c is the compression ratio of the screw.

From Eq. 7.159 it can be seen that the length of the transition section has to increase with the channel depth of the feed section H_1, with the compression ratio X_c, with the throughput $\rho_s v_{sz} H_1 W_1$, and with the helix angle φ. The maximum possible compression ratio is directly determined by L_c. A short transition section requires a low compression ratio to avoid plugging.

7.3.2 Other Melting Models

After Tadmor's first publication on melting, many others started to study melting in single screw extruders. As a result, many publications appeared in the technical literature in the 1970s and beyond. This section will review the various melting models proposed and analyze their advantages and disadvantages.

Many workers have repeated the screw extraction experiments as done by Maddock and later by Tadmor and coworkers; the majority of the workers confirmed the basic Tadmor melting model. Two exceptions are the finds of Klenk [66–68] and Dekker [69]. Klenk observed the melting of PVC and noticed the melt pool located against the passive flight flank. This melting behavior was also observed by Gale [81] and Mennig [82] in PVC extrusion. Klenk attributed the unusual melting behavior to the slippage of the PVC melt along the wall. It should be mentioned that other workers have found the normal melting model with PVC [61, 70]. Yet other workers [71] have found the melt pool location shifting from the passive flight to the active flight with increasing screw speed in PVC extrusion. Cox, et al. [80] observed the unusual melting behavior with the melt pool at the passive flight in extrusion of LDPE powder as well as the normal melting behavior. The unusual behavior occurred particularly at low screw speeds, with shallow channels, and with high barrel temperatures. Thus, the Tadmor melting model may not be valid in all cases.

Dekker [69] made observations of the melting behavior of polypropylene. He did not detect a clear melt pool at any side of the channel, but the solid bed was more or less suspended in a melt film. Lindt [72, 73] developed a mathematical model describing this melting behavior, which is shown in Fig. 7.45.

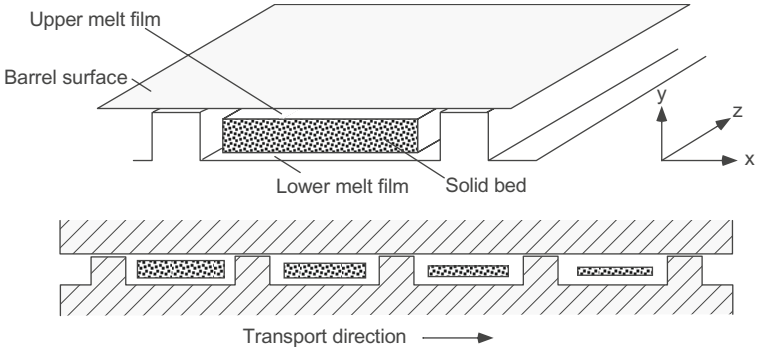


Figure 7.45 The Dekker/Lindt melting model

Some of the important assumptions in this model are:

1. The solid bed does not deform.
2. The solid bed is completely surrounded by a melt film and melting occurs at the entire circumference of the solid bed.
3. The melt film is constant in the cross-channel direction.

Assumption 3 causes some difficulties because a constant melt film thickness requires the presence of excessively large pressure gradients to accommodate the increased amount of polymer melt. This conflicts directly with Assumption 1. A detailed analysis of the Lindt melting model was made by Gieskes [74] and Meijer [75]. It appears that the Lindt melting model is unlikely to occur in the early stages of melting, but it may possibly occur in the later stages of melting.

A melting model in which the solid bed is considered to be subjected to a limited amount of deformation was proposed by Edmondson and Fenner [76–79]. However, their analysis contains certain inconsistencies as pointed out by Meijer [75]. Donovan [83, 84] extended the Tadmor analysis by removing the assumption of constant solid bed velocity and by incorporating the gradual heating of the solid bed along the melting zone. As mentioned earlier, Shapiro [63] and Vermeulen [64, 65] included the increasing melt film thickness with cross-channel distance. Shapiro, Pearson, and coworkers have developed one of the most elaborate extensions of the Tadmor analysis [63, 85–87]. Their model is a five-zone model as shown in Fig. 7.46.

The assumptions are more realistic and broader than most other analyses of melting. This can improve the accuracy of the model, but, unfortunately, it also increases the complexity of the computations quite substantially.

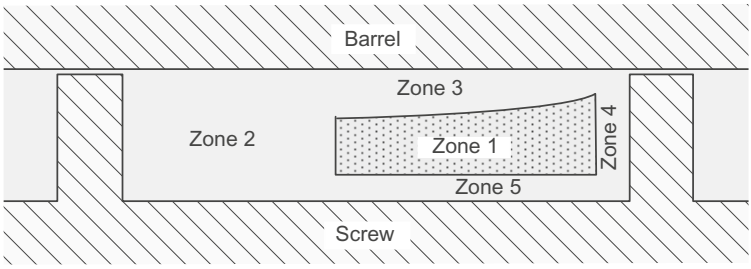


Figure 7.46 Illustration of the five-zone melting model

Hinrichs and Lilleleht [88] included the effect of flight clearance and used a helical coordinate system to account for the channel curvature. Sundstrom and Young [89] examined the effect of convective heat transfer and found that it can play an important role in the melting process, resulting in a melting rate about 20% higher than the predictions based on conductive heat transfer only. Sundstrom and Lo [89a] studied melting of amorphous polymers. They assumed the polymer-melt interface to be at the glass transition temperature and used a modified WLF equation to determine the shift factor for the temperature dependence of the viscosity. Chung [90, 91] analyzed the effect of finite solid bed thickness, varying solid bed density, and varying solid bed velocity. Later Chung developed a screw simulator to study melting behavior of polymers. A substantial amount of experimental and theoretical work [94–97] on melting was done using the screw simulator.

An interesting approach to the analysis of melting in single screw extruders was taken by Viriyayuthakorn and Kassahun [234]. They developed a new plasticating extrusion analysis program based on a finite element method capable of simulating three-dimensional flow with phase change. This program contains a number of new features that had not been incorporated in earlier work (prior to 1984) on melting in single screw extruders. The solid-melt phase change in this program was handled differently from prior work on melting. The conventional approach is to determine the location of the interface and use an energy balance of the interface to calculate the melting rate, as exemplified by Eq. 7.100. This method can introduce errors if the location of the interface is not accurately known and if the material does not have a sharp melting point, as is the case for most polymers. The technique used by Viriyayuthakorn and Kassahun is to absorb the latent heat of fusion term in the specific heat capacity and formulate the problem as though there is no phase change. Thus, a functional dependence of the specific heat capacity on temperature is used. This eliminates the need to first assume a certain melting model. The melting model is actually predicted from the calculations, something earlier workers have not been able to do.

Results from computer simulations for a HDPE polymer show that the Maddock/Tadmor melting mechanism occurs in the early stages of melting. At the beginning of the compression section, the solid bed tends to become totally encapsulated, while towards the end of the melting, the solid bed breaks apart into several pieces. At the time of publication of the paper by Viriyayuthakorn and Kassahun, no direct comparison was available between theoretical predictions and experimental results. Therefore, no statement can be made about the accuracy of the predictions. However, regardless of the accuracy of the predictions, this model provides new capabilities that no doubt will prove very useful in future work on the analysis of plasticating extrusion.

A drawback of the program is the need for very large computational capability. The simulations were performed on a Cray-1 computer, a computer not readily available to most process engineers. Even on this extremely powerful computer, one simulation took as long as several hours. However, considering the dramatic improvement in the number-crunching capability of new computers, the limitations in computational capabilities of computers in 2013 are less of a concern than they were in 1984 when Viriyayuthakorn and Kassahun presented their paper.

Chung and coworkers have developed simple analytical expressions to predict the melting behavior of polymers [95]. They developed analytical expressions valid for non-Newtonian fluids with temperature-dependent viscosity, following an approach very similar to Pearson's [87].

The melting rate per unit area is:

$$\frac{d\dot{M}_p}{dA} = \dot{M}_p^0 \rho_m \Delta v \tag{7.160}$$

where M^0_p is the dimensionless melting efficiency; it represents the melting capacity per unit melting area per unit sliding distance. Various functional forms of $\dot{M}^0_p$ are given in [95]. A simple expression that yields accurate results is:

$$\dot{M}^0_p = \left(\frac{k_m \, \Delta T_b \, F_1(K_2)}{\rho_m \, \Delta H \, \Delta v \, W'_s} \right)^{1/2} \tag{7.161}$$

where K_2 is defined in Eq. 7.121 and $F_1(K_2)$ is:

$$F_1(K_2) = \frac{2(K_2 + 1 - \exp K_2)}{K_2(1 - \exp K_2)} \tag{7.162}$$

By curve fitting, the function $F_1(K_2)$ can be approximated by:

$$F_1(K_2) \cong \frac{20}{19 + (1 + K_2)^2} \tag{7.163}$$

If the melt viscosity is temperature independent, $K_2 = 0$ and $F_1(K_2) = 1$. By inserting Eq. 7.161 in Eq. 7.160, the melting rate per unit melt area becomes:

$$\frac{d\dot{M}_p}{dA} = \left(\frac{\rho_m \, k_m \, \Delta v \, \Delta T_b \, F_1(K_2)}{\Delta H \, W'_s} \right)^{1/2} \tag{7.164}$$

The melting rate per unit length normal to the sliding direction is obtained by multiplying Eq. 7.164 with W_s':

$$\frac{d\dot{M}_p}{dz'} = \left(\frac{\rho_m \, k_m \, \Delta v \, \Delta T_b \, F_1(K_2)}{\Delta H} \right)^{1/2} \sqrt{W'_s} \tag{7.165}$$

Equation 7.165 is comparable to Eq. 7.131; both equations are closed-form analytical solutions. However, Eq. 7.165 is more compact and easier to use. A word of caution is in order. Equation 7.165 has been experimentally verified with the screw simulator. The results of the screw simulator may not fully apply to actual melting in a single screw extruder. For instance, the screw simulator uses a molded solid polymer sample of one cubic inch. The solid bed in the extruder consists of compressed, partially sintered, polymeric particles. It is clear that an actual solid bed, as occurs in the melting zone of an extruder, may have different characteristics in terms of heat transfer properties and deformation behavior, as compared to a molded solid block of the same material.

Equation 7.165 can be written in terms of melting rate per unit down-channel by making the same coordinate transformation as discussed earlier in Eq. 7.109:

$$\frac{d\dot{M}_p}{dz} = \left(\frac{\rho_m \, k_m v_b \sin\varphi \, \Delta T_b \, F_1(K_2)}{\Delta H} \right)^{1/2} \sqrt{W_s} \tag{7.166}$$

7.3.3 Power Consumption in the Melting Zone

The mechanical power consumption in the melting zone can be determined by breaking down the power consumption in three parts: the power consumed in the melt film dZ_{mf}, the power consumed in the melt pool dZ_{mp}, and the power consumed in the clearance between flight and barrel dZ_{cl}. The power consumed in shearing the melt film is described by:

$$dZ_{mf} = v_b dz' \int_0^{W_s'} (\tau_{yz'} \sin\theta + \tau_{yz'} \cos\theta) dx' \tag{7.167}$$

where $\tau_{yx'}$ is the shear stress in the direction x' of the relative velocity Δv between the solid bed and the barrel; see also Fig. 7.23(a). If the material can be described as a power law fluid, the shear stresses can be written as:

$$\tau_{yx'} = m \left(\frac{dv_{x'}}{dy} \right)^n \tag{7.168}$$

and:

$$\tau_{yz'} = m \left(\frac{dv_{z'}}{dy} \right)^n \tag{7.169}$$

It is assumed that the flow in the melt film is a drag flow, i. e., pressure gradients are neglected in this case:

$$\tau_{yx'} = m \left(\frac{\Delta v}{H_m} \right)^n \tag{7.170}$$

and:

$$\tau_{yz'} = 0 \tag{7.171}$$

The melt film thickness can be written according to Eq. 7.130:

$$H_m(x') = (K_4 x' + \delta^2)^{1/2} \tag{7.172}$$

where:

$$K_4 = \frac{4k_m \Delta T_b + 4B_3}{\rho_m \Delta v \Delta H} \tag{7.173}$$

Factor B_3 is given by Eq. 7.128. The power consumption in the melt film can now be expressed as:

$$dZ_{mf} = m v_b dz' \Delta v^n \cos\theta \int_0^{W_s'} \frac{dx'}{(K_4 x' + \delta^2)^{n/2}} \tag{7.174}$$

By using Eq. 7.172, the integral can be rewritten as:

$$dZ_{mf} = mv_b\, dz'\, \Delta v^n \cos\theta \int_{\delta}^{H_{ms}} \frac{2H_m^{1-n}}{K_4} dH_m \tag{7.175}$$

where $H_{ms} = H_m(W_s')$, which is the maximum melt film thickness. The solution to Eq. 7.175 can be written as:

$$dZ_{mf} = mv_b\, dz'\, \Delta v^n \cos\theta \frac{2}{K_4(2-n)} \left(H_{ms}^{2-n} - \delta^{2-n}\right) \tag{7.176}$$

With $z' = z \sin(\theta + \varphi)$, the power consumption in the melt film can be written as:

$$dZ_{mf} = mv_b dz \sin(\theta+\varphi)\cos\theta \frac{2\Delta v^n}{K_4(2-n)} \left(H_{ms}^{2-n} - \delta^{2-n}\right) \tag{7.177}$$

From Eqs. 7.176 and 7.177, it can be seen clearly that the power consumption in the melt film reduces with increasing clearance.

The power consumption in the melt pool will be relatively small compared to the other two terms. Because of the relatively complicated flow pattern in the melt pool, the derivation of the power consumption for a power law fluid will be rather involved. To simplify matters considerably, the power consumption in the melt pool can be approximated with the power consumption in a screw channel of width $W_m = W - W_s$ with a Newtonian fluid:

$$dZ_{mp} = (1 + 3r_d + 4\tan^2\varphi) \frac{p\mu W_m v_{bz}^2 dz}{H} \tag{7.178}$$

The derivation of this expression will be discussed in Section 7.4.1.3 on melt conveying.

The power consumption in the clearance can be easily determined if it is assumed that the velocity profile in the clearance is dominated by drag flow. In that case, the power consumption in the clearance can be written as:

$$dZ_{cl} = \frac{p\, v_b^{1+n}\, m\, w\, dz}{\delta^n} \tag{7.179}$$

The total mechanical power consumption in the melting zone now becomes:

$$dZ = dZ_{mf} + dZ_{mp} + dZ_{cl} \tag{7.180}$$

7.3.4 Computer Simulation

One of the general problems of the melting theories is that the most realistic models are also the most complex. However, if the complexity goes beyond the level of the equations developed earlier, analytical solutions become very difficult to obtain, if not impossible. In this case, one has to use numerical techniques and computer simulation to find solutions to the equations. The main question is whether the more complex analysis will result in improved predictive ability. Relaxing certain assumptions may result in an improvement in accuracy that is relatively insignificant compared to the inherent uncertainties in most melting models. These are, among others, the actual location of the solid bed and melt pool, the shear strength and tensile strength of the solid bed as a function of time, temperature, and pressure, the actual melt film temperature, the actual temperature at the screw surface, the contribution of melting at the sides of the solid bed and at the screw surface, etc. The actual temperature in the melt film is most likely not fully developed, and convective heat transport should be considered in determining the actual temperature profile.

Therefore, one has to strike a balance between the degree of sophistication of the analysis and the practical usefulness of the analysis. This balance will depend on the particular interests of the individual. For industrial applications the degree of sophistication of the analysis of melting, as described in Section 7.3.1, is probably sufficient to analyze most practical extrusion problems. However, in some instances one may want to go into much more detail on certain aspects of the melting process.

Analyses that require numerical techniques to arrive at solutions tend to be quite time consuming and require skilled personnel to develop the computer programs and to interpret the results of the computer simulations. Many people in the extrusion industry do not have the time or inclination to work through elaborate and complex analyses of melting. In this case, the preferred action is to use a less complicated analysis that yields analytical results. In most cases, actual predictions of melting performance can be made with a relatively simple programmable calculator.

Another approach is to use a computer program developed elsewhere to analyze the problem. Nowadays many commercial packages are available to simulate the plasticating extrusion process. In most cases this offers the most expedient approach to advanced analysis of melting. The danger is that if a person using such program is not intimately familiar with the theory behind the program, the assumptions, and the validity of the assumptions, it is possible that improper conclusions will be drawn from the predicted results.

When using commercial simulation packages it is important that the theory behind it is clearly described with assumptions and simplifications. If this is not the case and the user does not really know what type of analysis they are actually using, the value of the results will be questionable. Early extruder simulation packages had

some serious deficiencies. In some cases suppliers of simulation software programs made claims that simply were not correct. As a result, computer simulation in extrusion had a less than perfect reputation. It has taken many years for computer simulation in extrusion to regain respectability. Modeling and computer simulation will be covered in detail in Chapter 12.

7.3.5 Dispersed Solids Melting

As mentioned earlier, the CSM type melting is the one that has been most often observed in single screw extruders. However, in some experimental studies it was found that the solid particles are not contiguous but dispersed in a melt matrix [256–258] as illustrated in Fig. 7.47.

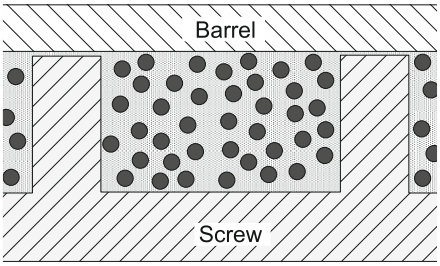


Figure 7.47
Dispersed solids melting (DSM)

In fact, in several extruders, dispersed solids melting (DS) is more likely to occur than contiguous solids melting. This is particularly true of extruders that do not feature a continuous, uninterrupted channel for material flow. Examples are twin screw extruders and pin barrel extruders.

CSM is more likely to occur in single screw extruders where the material is conveyed along a continuous screw channel. However, even in a single screw, DSM can occur. In fact, certain screw geometries have been developed with the specific purpose to initiate the dispersed solids melting process. Examples are the double wave screw [254] and the HP screw [255]. It has been found experimentally that the DSM process can produce more efficient melting than the CSM process. Despite the recognized importance of DSM in extrusion, very few theoretical analyses have been devoted to this type of melting. Yucheng and Hanxiong [255] performed a theoretical analysis of DSM using a six-block model. The non-isothermal, non-Newtonian model requires numerical techniques to obtain solutions. Unfortunately, no details were presented on the theoretical description of the model. Some of the important conclusions by Yucheng and Hanxiong are:

1. DSM can reduce power consumed by the screw by as much as 30%
2. The temperature is more uniform and lower
3. DSM can shorten the total melting length

Rauwendaal [259] presented the first theoretical model of DSM that allows analytical description of the melting process. In the following, this theory will be described in detail. Predictions from the DSM theory will be compared to the CSM theory.

7.3.5.1.1.1 Dispersed Solids Melting Theory

In the DSM model it will be assumed that the solid particles are uniform, spherical, and dispersed in a melt matrix. This means a minimum volume of polymer melt has to be available to fill the space between the solid particles. For the closest packing of regular spheres the minimum polymer melt volume fraction is about 40%. For more random packing configurations it will be closer to 50%. This means that the DSM theory can only be applied after about half the solid material has already melted.

It is further assumed that the melting of solid particles is uniform, i. e., not dependent on the location of the particle in the channel. The heat available for melting will be determined by the net heat conducted into the channel (through barrel and screw) and the viscous heat generation in the polymer melt. The viscous heat generation is determined by using the dissipation model for filled polymers developed by Geisbüsch [260]. The system is considered a two-phase polymer system with the shearing taking place in the polymer melt matrix. The viscosity of such a two-phase system as determined by theological measurements yields "integral" values of the viscosity, η_i, as a function of an "integral" shear rate, $\dot{\gamma}_i$. The viscous heat generation is determined by the product of shear stress and shear rate. In a two-phase system the viscous dissipation has to be corrected by a factor F_d. This factor, according to Limper [261], is given by:

$$F_d = (1-\Phi)K \tag{7.181}$$

where Φ is the solids volume fraction.

The correction factor K according to Neumann [262] can be written as:

$$K = \left[1 - \frac{6\Phi}{\pi} + \frac{1}{2}\left(\frac{4\Phi}{\pi}\right)^{\frac{3}{2}}\right]^{-1} \tag{7.182}$$

The expression for F_d can thus be written as:

$$F_d = \frac{1-\Phi}{1-a\Phi+b\Phi^{1.5}} \tag{7.183}$$

where $a = 6/\pi$ and $b = 0.5(4/\pi)^{1.5}$.

Function $F_d(M)$ is graphically represented in Fig. 7.48.

The viscous heat generation per unit volume for a power law fluid can be written as:

$$q_v = F_d\, m_i\, \dot{\gamma}_i^{n+1} \tag{7.184}$$

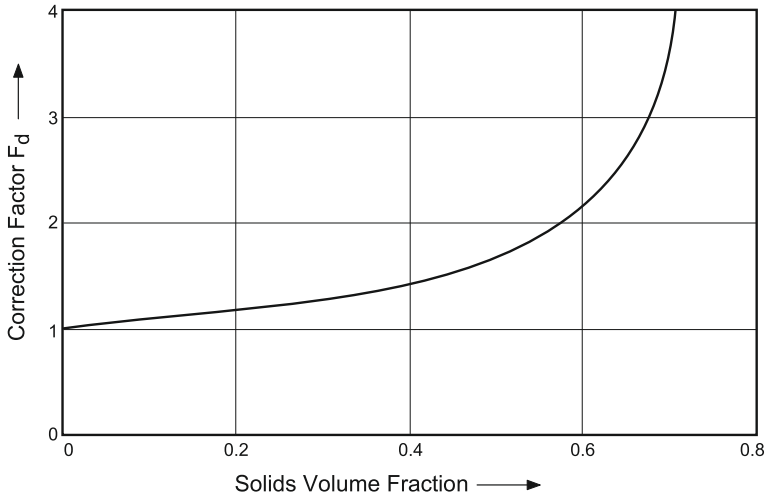


Figure 7.48 Correction factor F_d versus the solids volume fraction

At this point the integral viscosity has to be expressed as a function of the volume fraction solid. A number of relationships have been proposed to describe the increase in viscosity with volume fraction solid. Good reviews are incorporated in the two-volume book on polymer blends by Paul and Newman [263]; some other references are 264 through 267. A useful expression is the Maron-Pierce relationship, which for a power law fluid results in the following expression for the consistency index:

$$m_i(\Phi) = m_0\left(\frac{\Phi_{max}}{\Phi_{max} - \Phi}\right)^2 \tag{7.185}$$

In this expression m_0 is the consistency index of the unfilled polymer melt and Φ_{max} the solids volume fraction at close packing. A typical value of Φ_{max} is about 0.6 for spherical particles. Non-spherical particles usually have lower maximum solid fraction. Figure 7.49 shows the consistency index ratio $m_i(\Phi)/m_0$ as a function of the solids volume fraction as expressed in Eq. 7.185.

The heat required to raise the temperature of the solids to the melting point and to melt the solids comes from the viscous dissipation and the net heat conducted into the polymer from the barrel and the screw. It is assumed that there is a gradual and uniform reduction in the solid particles, thus reducing the solids volume fraction Φ. The change in the solids fraction over an increment of time can be related to the heat added to the polymer in the same time increment. Thus, the energy balance can be written as:

$$\rho_s \, \Delta\hat{E}_p \, d\Phi = (q_v + q_c)dt \tag{7.186}$$

where $\Delta\hat{E}_p$ is the enthalpy difference between the initial solids temperature and the melting point.

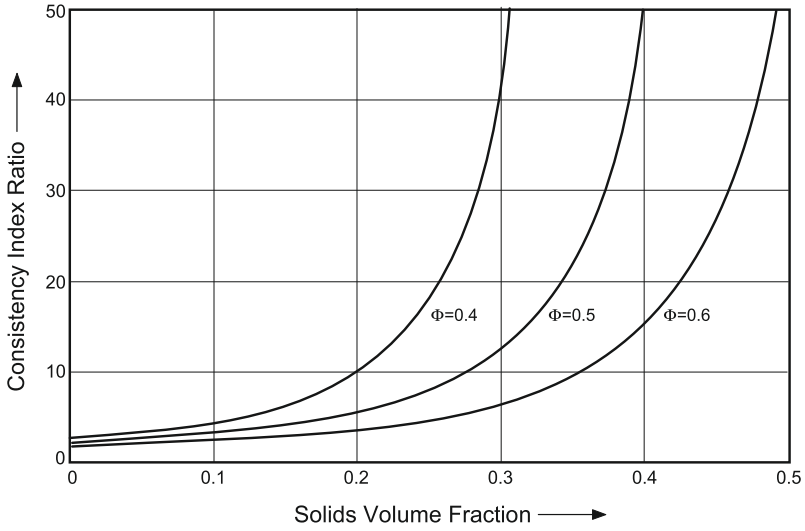


Figure 7.49 Consistency index ratio versus solids volume fraction

The net heat flux per unit depth of the channel conducted into the screw channel is obtained from:

$$q_c = \frac{k_r}{H}\frac{dT_r}{dy}\bigg|_{y_r} - \frac{k_b}{H}\frac{dT_b}{dy}\bigg|_{y_b} \tag{7.187}$$

where the subscript r refers to the screw and b to the barrel.

At this point we will assume that the conductive heating term is negligible compared to the viscous heating term ($q_c << q_v$). This is a reasonable assumption for high viscosity polymers, particularly when the extruder is operated at high screw speed. With both F_d and m functions of the solids fraction, the melting time t_p is determined by integrating the Φ-terms in Eq. 7.186 from Φ_1 to 0 and the time part of the equation from 0 to t_p. Thus, we obtain the following equation:

$$\int_{\Phi_1}^{0} \frac{d\Phi}{F_d(\Phi)\, m(\Phi)} = \int_{0}^{t_p} \frac{\dot{\gamma}^{n+1} dt}{\rho_s \Delta\hat{E}_p} \tag{7.188}$$

where Φ_1 is the solids volume fraction at the beginning of the dispersed solids melting process.

The left-hand integral of Eq. 7.188 is a function of the initial solids volume fraction; we will write it as $I(\Phi_1)$. Solution of the integral yields a closed-form, but lengthy expression:

$$I(\Phi_1)=\left(1-\frac{1}{c}\right)^2(a-1)\ln(1-\Phi_1)+\left(a+\frac{2-2a}{c}+\frac{a-1}{c^2}\right)\Phi_1+\left(\frac{a-1}{2c^2}-\frac{a}{c}\right)\Phi_1^2+\frac{a}{3c^2}\Phi_1^3+$$
$$+b\left(1-\frac{1}{c}\right)^2\left[\ln\left(\frac{1+\Phi_1^{0.5}}{1-\Phi_1^{0.5}}\right)-2\Phi_1^{0.5}-\frac{2}{3}\Phi_1^{1.5}\right]+\frac{b(2c-1)\Phi^{2.5}}{2.5c^2}-\frac{b\Phi_1^{3.5}}{3.5c^2} \qquad (7.189)$$

where $c = \Phi_{max}$.

Figure 7.50 shows how $I(\Phi_1)$ depends on Φ_1.

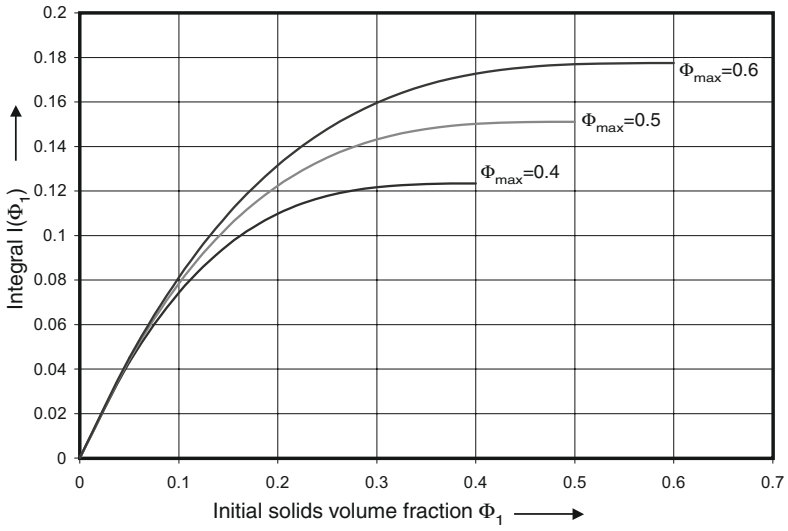


Figure 7.50 Integral $I(\Omega_1)$ versus solids volume fraction

If the integral shear rate can be taken as the ratio of the barrel velocity and the channel depth, the melting time can be expressed as:

$$t_p=\frac{I(\Phi_1)\,H^{n+1}\,\rho_s\,\Delta\hat{E}_p}{m_0\,v_b^{n+1}} \qquad (7.190)$$

where it is assumed that the channel depth is constant.

The melting time values for DSM from Eq. 7.190 can be compared to the melting time for CSM. The melting time in the CSM model to go from a solids fraction of Φ_1 to zero can be expressed as [259]:

$$t_p=\frac{(\Phi_1\,W_1)^{n/(n+1)}}{\Omega_2\,v_{sz}}=\frac{2(n+1)\,\rho_s H}{n\Delta v}\left[\frac{\Delta\hat{E}_p}{m(n+1)}\left(\frac{\Phi_1 W_1}{\rho_m v_{bx}}\right)^n\right]^{\frac{1}{n+1}} \qquad (7.191)$$

where:

$$\Omega_2=\frac{n\Omega_1}{(n+1)\rho_s v_{sz} H_1}$$

The axial melting length can be determined by relating the melting time to the average velocity of the polymer. This leads to the following expression for the axial melting length:

$$l_p = \frac{I(\Phi_1)\,\dot{V}\,H^n\,\rho_s\,\Delta\hat{E}_p}{m_0\,\pi\,D\,v_b^{n+1}} \tag{7.192}$$

With Eq. 7.192 the melting length in DSM can be compared to the melting length in CSM, which can be written as [259]:

$$l_p = \frac{\sin\varphi(\Phi_1\,W_1)^{n/(n+1)}}{\Omega_2} = \frac{2(n+1)\,\rho_s\,H\,v_{sz}\,\sin\varphi}{n\Delta v}\left[\frac{\Delta\hat{E}_p}{m(n+1)}\left(\frac{\Phi_1 W_1}{\rho_m v_{bx}}\right)^n\right]^{\frac{1}{n+1}} \tag{7.193}$$

7.3.5.1.1.2 Comparison of CSM to DSM Model

At this point we can compare predictions from the CSM model to the DSM model. First, the effect of power law index on melting time is shown in Fig. 7.51. The data are for a 50 mm extruder running at 60 rpm with an output of 1.0E-5 m^3/s. The material data is typical for LDPE, melt density 780 kg/m^3, solid density 920 kg/m^3, $\Delta\hat{E}_p$ is 3.0E5 N·m/kg, and the consistency index is m = 20,000 Pa·s^n. The melting times are compared based on an initial solids fraction of 0.5. For all the values of the power law index the DSM time is significantly shorter than the CSM time; the difference becomes larger with smaller values of the power law index.

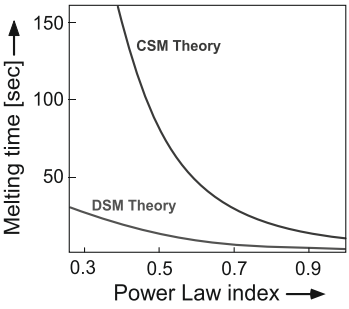


Figure 7.51
Melting time versus power law index for DSM and CSM

The effect of the consistency index on the melting time is shown in Fig. 7.52; the power law index is 0.5. In this case, again, the DSM time is considerably shorter than the CSM time. The effect of screw speed on melting time is shown in Fig. 7.53. The melting time reduces rapidly with screw speed. Doubling the screw speed reduces the melting time by a factor of almost three. Again, the DSM time is much shorter than the CSM time. Thus, over a wide range of values for the screw speed, power law index, and consistency index, the predicted melting efficiency with the DSM model is consistently better than with the CSM model.

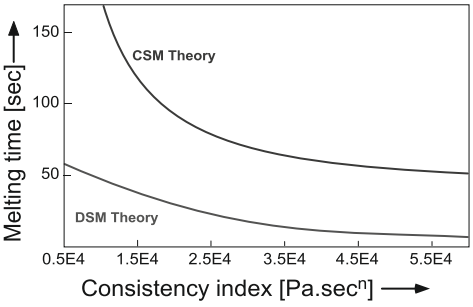


Figure 7.52
Melting time versus consistency index for DSM and CSM

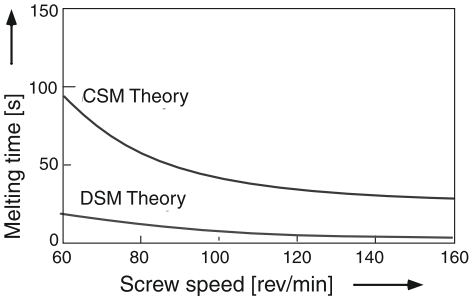


Figure 7.53
Melting time versus screw speed for DSM and CSM

7.3.5.1.1.3 DSM versus CSM Type Melting

This theoretical model for dispersed solids melting allows analytical solutions for a temperature-independent power law fluid. The model presented is based on the assumption that the conductive heating term is negligible, the channel depth constant, and the pellet size is uniform at a particular cross-section of the channel. Obviously, for analysis of more realistic cases the assumptions will have to be relaxed. When comparing the melting efficiency of the DSM model to the CSM model, dispersed solids melting is considerably more efficient than contiguous solids melting. This is true over a wide range of values of the consistency index, power law index, and screw speed.

These results suggest that solid bed breakup is not necessarily bad for the melting efficiency. However, the solid bed breakup would have to be complete, i. e., to the level of the individual pellets making up the solid bed. For single screw extruders it can be advantageous to modify the screw channel geometry in the plasticating zone to intentionally induce solid bed breakup. This approach has already been taken in some instances [254, 255]. A new dispersive mixing device developed by Rauwendaal [268, 269] has been successfully used to disperse unmelted polymer fragments (see Section 8.7.1.2).

In single screw extrusion there is a commonly held belief that solid bed breakup should be avoided if at all possible. Most barrier extruder screws are based on this premise. They are designed to minimize the chance of solid bed breakup. The type

of solid bed breakup that can be detrimental to extruder performance is partial solid bed breakup. In this case the solid bed breaks up in large chunks, much larger than the size of the individual pellet. It is this partial solid bed breakup that barrier screws attempt to avoid. However, DSM type melting can substantially improve melting in a single screw extruder. If a consistent DSM can be achieved in single screw extruders it will enable a quantum jump improvement in the performance of these machines.

More work is necessary on dispersed solids melting, both theoretical and experimental. Certainly the possibility to enhance melting efficiency by inducing solid bed breakup in single screw extruders is potentially very attractive. The challenge will be to initiate complete solid bed breakup without creating partial solid bed breakup in single screw extruders. The melting process is often the rate-determining part of the extrusion process. As a result, improved melting will allow corresponding improvements in throughput.

There are probably a number of factors that will have to be combined to generate DSM in single screw extruders. The pressure build-up in the solids will have to be controlled and kept to a relatively low level to avoid making the solid bed difficult to break up. As discussed in Section 7.2.2.4, starve feeding is an effective method of controlling the pressure build-up in the solids. As a result, starve feeding is probably a necessary ingredient to generate DSM in single screw extruders. It is probably very difficult to generate DSM in a flood fed grooved feed extruder because of the high pressure generated in the solids conveying zone.

The second ingredient is a screw geometry that can break down agglomerated solids. This will require special screw geometries. At this point in time, only little information is available on screw geometries that can achieve efficient dispersion of unmelted polymer (see Section 8.7.1.2). A third ingredient is a sufficient length of the machine to allow for partially filled regions along the extruder. Most likely DSM type single screw extruders will have to be at least 30 D long, and perhaps longer than that.

7.4 Melt Conveying

The melt conveying zone of the extruder starts at the point where the melting process is just completed. The melt conveying zone is also referred to as a pumping zone because, in most cases, the polymer melt has to be transported towards the die against a considerable head pressure. The melt conveying in an extruder was the subject of engineering studies as early as 1922 [98]. The early work on melt conveying in extruders dealt with Newtonian fluids with temperature-independent vis-

cosity. This is a very convenient case to analyze because it is simple and yields clean, straightforward analytical solutions. The reason is that the cross-channel flow can be analyzed independent of the down-channel flow for a Newtonian fluid with temperature-independent viscosity. Also, the pressure flow can be analyzed separate from the drag flow and the results can be superimposed.

These simplifications cannot be made when the fluid is non-Newtonian or when the viscosity is temperature dependent. Most analyses on melt conveying can be categorized by the six most important assumptions made about the process:

1. Shear stress-shear rate relationship
   a) Linear (Newtonian)
   b) Non-linear (non-Newtonian)
2. Flow situation
   a) One-dimensional (down-channel only)
   b) Two-dimensional (down- and cross-channel)
   c) Three-dimensional (down-, cross-channel, and radial)
3. Effect of the flight flanks
   a) Negligible (infinite channel width)
   b) Not negligible (finite channel width)
4. Temperature effects
   a) Melt viscosity temperature independent
   b) Melt viscosity temperature dependent
5. Flight clearance
   a) Negligible (zero flight clearance)
   b) Not negligible (finite flight clearance)
6. Channel curvature
   a) Negligible (flat place approximation)
   b) Not negligible (cylindrical or helical analysis)

The infinite channel width assumption applies to shallow channels, channels with a width-to-depth ratio higher than 10 ($W/H > 10$). If the depth of the channel is large relative to the width of the channel, the effect of the flight flanks on the down-channel velocity profile has to be taken into account. Several reviews of the work on melt conveying in extruders have been written [101–106].

In addition to the six main assumptions of the analysis of melt conveying, there are a few more that are sometimes considered, such as elastic effects, the influence of an oblique channel end, etc. After the Newtonian analysis had been mostly worked out, non-Newtonian fluids were analyzed in the early 1960s. This adds significantly to the complexity of the analysis, and generally the equations cannot be solved ana-

lytically, but have to be solved by numerical techniques. The simplest non-Newtonian case that can be considered is the one-dimensional, isothermal flow of the power law fluid in a channel of infinite width. This problem has been studied by various investigators [107–113], but a closed-form solution was not obtained until 1983 [114]. An exact analytical solution to even this simple problem has not been found to this date.

Relaxing other assumptions, i.e., temperature-dependent viscosity, two- or three-dimensional flow, finite channel width, etc., substantially increases the degree of difficulty. Such analyses have been the subject of several Ph.D. studies [102, 115–121]. The level of complexity can be increased almost at will by further relaxing the assumptions. However, this work can reach such a high level of complexity and sophistication that the usefulness to practicing polymer processing engineers becomes questionable. One should always try to balance the increased generality of the predictions against the time and effort spent on solving increasingly more complex problems. Somewhere, one can reach a point of diminishing return.

To the practicing process engineer, the most important question should be whether the more general analysis will be applicable; e.g., are all the boundary conditions well known, and will it result in more accurate predictions. For instance, it probably does not make much sense to use a sophisticated non-isothermal melt conveying analysis to predict the melt temperature at the end of the screw if the actual screw temperature in the process is unknown. These practical considerations do not necessarily apply to the academic. On the other hand, it would make sense to perform a non-isothermal analysis to predict the effect of barrel temperature fluctuations on melt temperature or conveying rate. Besides the complications already discussed, there is the additional complication that the polymer melt is not a pure, inelastic power law fluid and significant time-dependent effects can occur (e.g., [122–128]).

The next section will start with an analysis of melt conveying of isothermal fluids. This will be followed by a non-isothermal analysis of melt conveying of cases that allow exact analytical solutions. More general analyses of the effect of temperature on flow will be discussed in more detail in Chapter 12 on modeling and computer simulation. In the next section, melt conveying of Newtonian fluids and non-Newtonian fluids will be analyzed. The non-Newtonian fluids will be described with the power law equation (Eq. 6.23). The effect of the flight flank will be discussed and the difference between one- and two-dimensional analysis will be demonstrated with particular emphasis on the implications for actual extruder performance.

7.4.1 Newtonian Fluids

A very simple analysis of melt conveying can be made if the following assumptions are made:

1. The fluid is Newtonian
2. The flow is steady
3. The viscosity is temperature-independent
4. There is no slip at the wall
5. Body and inertia forces are negligible
6. The channel width can be considered infinite
7. The channel curvature is negligible (flat plate model)

The geometry is now simplified to Fig. 7.54.

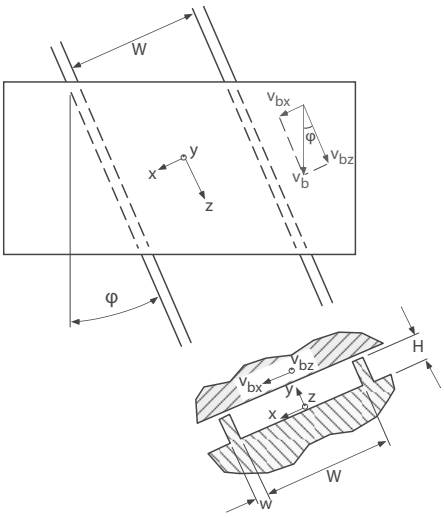


Figure 7.54
Flat plate model for melt conveying

A flat plate is moving at velocity v_b over a flat rectangular channel with angle φ between v_b and the flights of the channel.

The equation of motion in the down-channel direction for this problem can be written as:

$$\frac{\partial P}{\partial z} = g_z = \frac{\partial \tau_{yz}}{\partial y} \tag{7.194}$$

The pressure is a function of down-channel coordinate z only. Therefore, Eq. 7.194 can be integrated to give the shear stress profile in the radial direction (y):

$$\tau_{yz} = \tau_o + g_z y \tag{7.195}$$

where τ_o is the shear stress at the screw surface, as yet unknown.

For a Newtonian fluid, Eq. 7.195 can be written as:

$$\mu \frac{dv_z}{dy} = \tau_o + g_z y \tag{7.196}$$

By integration of Eq. 7.196, the down-channel velocity as a function of normal distance y is obtained. By using boundary conditions $v_z(0) = 0$ and $v_z(H) = v_{bz}$, the following expression is obtained:

$$v_z(y) = \left(\frac{v_{bz}}{H} - \frac{g_z H}{2\mu} \right) y + \frac{g_z}{2\mu} y^2 \tag{7.197}$$

The flow rate in the down-channel direction is obtained by integrating the down-channel velocity over the cross-sectional area of the screw channel:

$$\dot{V} = \int_o^H p\, W\, v_z dy = \frac{1}{2} p\, W\, H\, v_{bz} - \frac{pW H^3 g_z}{12\mu} \tag{7.198}$$

where p is the number of parallel flights and W the perpendicular channel width.

This represents the volumetric throughput of the melt conveying zone. The first term after the equal sign in Eq. 7.198 is the drag flow term. It represents the flow rate in pure drag flow, i. e., without a pressure gradient in the down-channel direction:

$$\dot{V}_d = \frac{1}{2} p\, W\, H\, v_{bz} \tag{7.199}$$

The second term of Eq. 7.198 is the pressure flow term. It represents the flow rate in pure pressure flow, i. e., without relative motion between the screw and barrel (zero screw speed):

$$\dot{V}_p = \frac{pW H^3 g_z}{12\mu} \tag{7.200}$$

Note that the pressure flow reduces the output when the pressure gradient is positive, which is often the case in actual extrusion operations.

Equation 7.198 is useful because the output of the extruder can be determined from this equation. The effect of changes in screw geometry becomes quite obvious from Eq. 7.198. Particularly, the effect of channel depth is interesting. The drag flow rate is directly proportional to the channel depth, but the pressure flow rate increases with the channel depth cubed. Thus, the pressure flow increases much faster with channel depth than drag flow. For this reason, the channel depth in the metering section is usually made quite shallow. The optimum channel depth that will give the highest output at a given screw speed and pressure gradient can be determined directly from Eq. 7.198; see also Section 8.2.1.

The optimum channel depth can be determined by setting:

$$\frac{\partial \dot{V}}{\partial H} = 0 \tag{7.201}$$

This results in the following optimum channel depth H*:

$$H^* = \left(\frac{2\mu v_{bz}}{g_z} \right)^{1/2} \tag{7.202}$$

The optimum helix angle can be determined from:

$$\frac{\partial \dot{V}}{\partial \varphi} = 0 \tag{7.203}$$

This results in the following optimum helix angle φ*:

$$\tan 2\varphi^* = \frac{6\mu v_b}{g_a H^2} \tag{7.204}$$

where g_a is the axial pressure gradient ($g_a = g_z/\sin\varphi$). At the optimum channel depth the output becomes:

$$\dot{V}(H^*) = \frac{1}{3} W H v_{bz} = \frac{2}{3} \dot{V}_d \tag{7.205}$$

At the optimum channel depth H*, the optimum helix angle becomes:

$$\varphi^* = 30° \tag{7.206}$$

When the channel depth and helix angle are both at their optimum value, the output becomes:

$$\dot{V}(H^*, \varphi^*) = \frac{B H v_b}{4} \cong 1.4 H N D^2 \tag{7.207}$$

where B is the axial channel width and N is the screw speed ($B \cong \pi D \tan\varphi$ and $v_b = \pi DN$).

Another interesting observation is that the volumetric drag flow rate is independent of any fluid property for Newtonian fluids. Thus, the drag flow rate for water will be the same as oil, molten nylon, etc. The drag flow rate is directly proportional to screw speed because $v_{bz} = \pi DN\cos\varphi$, where N is the screw speed.

Many extruder screws are designed such that the drag flow is considerably larger than the pressure flow. In these cases, the approximate output of the extruder is determined from Eq. 7.199. If the mass flow rate is required, the volumetric flow rate is simply multiplied with the polymer melt density. The reason that many

screws are designed to have a relatively small pressure flow is that the extrusion operation tends to become less sensitive to diehead pressure fluctuations. If the pressure flow is only 10% of the total throughput, a 50% change in diehead pressure will cause only a 5% change in output. On the other hand, if the pressure flow is 50% of the total throughput, a 50% change in diehead pressure will cause a 25% change in output.

There are two ways to achieve a relatively low-pressure sensitivity. One way is to reduce the depth of the channel in the metering section of the screw. The other way is to reduce the pressure gradient in the melt conveying zone by building up pressure in earlier zones, the plasticating and/or the solids conveying zone. The most common way to achieve the latter situation is by employing a grooved barrel section, as discussed in Section 7.2.2.2. Down-channel velocity profiles for various values of the pressure flow (pressure gradient) are shown in Fig. 7.55.

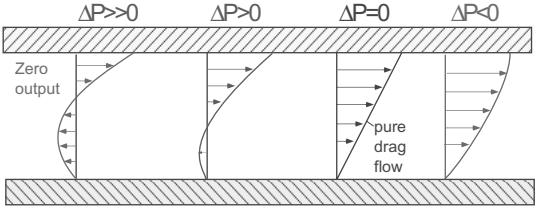


Figure 7.55
Down-channel velocity profiles

When the pressure change is zero ($\Delta P = 0$), the velocity profile is linear; this represents pure drag flow. When the pressure change is negative ($\Delta P < 0$), the velocities between the screw and barrel will be increased relative to the drag flow velocities. When the pressure change is positive ($\Delta P > 0$) the melt conveying zone is generating pressure and the velocities will be reduced relative to the drag flow velocities. When the pressure drop is very large ($\Delta P >> 0$) the output becomes zero. In this case, the forward drag flow rate equals the rearward pressure flow rate.

By the same procedure employed to derive the down-channel velocity, the cross-channel velocity can be determined:

$$v_x(y) = \left(\frac{v_{bx}}{H} - \frac{g_x H}{2\mu}\right) y + \frac{g_x}{2\mu} y^2 \tag{7.208}$$

In this case, g_x can be determined from the condition that there is no net flow in the cross-channel direction:

$$\int_0^H v_x \, dy = 0 \tag{7.209}$$

The cross-channel pressure gradient is:

$$g_x = \frac{6\mu v_{bx}}{H^2} \tag{7.210}$$

The resulting cross-channel velocity profile is:

$$v_x = -\frac{2v_{bx}}{H}y + \frac{3v_{bx}}{H^2}y^2 \tag{7.211}$$

The cross-channel velocity profile is shown in Fig. 7.56.

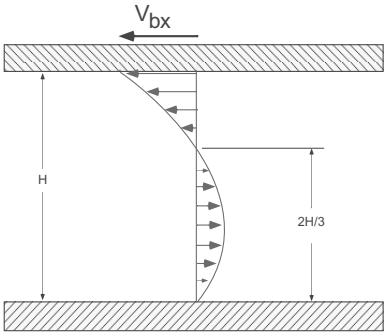


Figure 7.56
Cross-channel velocity profile

It can be seen that the cross channel velocity at y = 2H/3 is zero. Thus, the material in the top one-third of the channel moves towards the active flight flank and the material in the bottom two-thirds of the channel moves towards the passive flight flank. It is clear that in reality the situation becomes more complex at the flight flanks because normal velocity components must exist to achieve the circulatory flow patterns in the cross-channel direction. However, these normal velocity components will be neglected in this analysis. Normal velocity components were analyzed by Perwadtshuk and Jankow [129] and several other workers. The actual motion of the fluid is the combined effect of the cross- and down-channel velocity profiles. This is shown in Fig. 7.57.

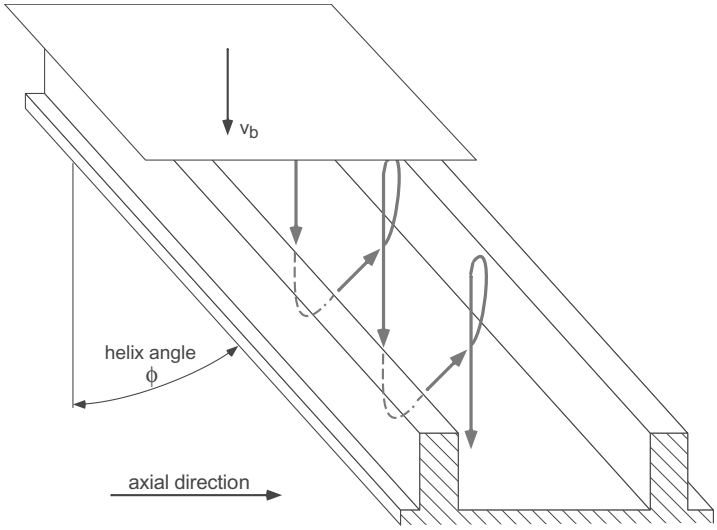


Figure 7.57 Fluid motion in melt conveying zone

A fluid element follows a spiraling path along the length of the screw channel. Close to the barrel surface it flows in the direction of the barrel. When it gets close to the pushing flight flank the element will move down toward the lower portion of the screw channel where it will cross the channel. When the element gets close to the trailing flight flank it moves up along the flight flank until it gets close to the barrel and then the cycle starts again. As more pressure is developed, the spirals are closer together as shown in Fig. 7.58 where the path of a fluid element is shown viewed from the top of the unrolled channel.

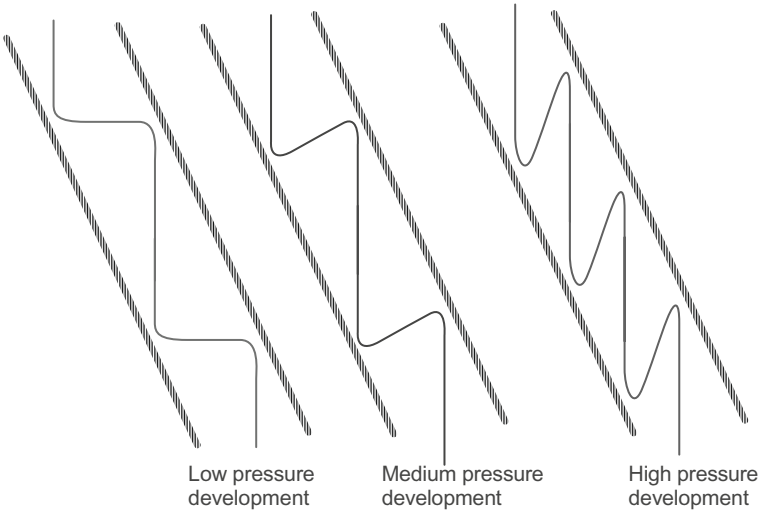


Figure 7.58 Fluid motion at various levels of pressure development

As the melt conveying zone develops more pressure the spirals are pushed more closely together. In the extreme case of closed discharge (zero output) there is no axial component to the flow. In this case fluid elements move tangentially close to the barrel surface and in the opposite direction close to the screw surface; the screw flights act as a plough, so there is mixing but no forward flow.

7.4.1.1 Effect of Flight Flanks

If the channel width cannot be considered infinite, the equation of motion in the down-channel direction becomes:

$$\frac{\partial P}{\partial z} = g_z = \frac{\partial \tau_{yz}}{\partial y} + \frac{\partial \tau_{xz}}{\partial x} \tag{7.212}$$

Equation 7.212 is an expanded form of Eq. 7.194.

Considering the fluid Newtonian allows Eq. 7.212 to be written as:

$$\frac{\partial P}{\partial z} = \mu \left(\frac{\partial^2 v_z}{\partial y^2} + \frac{\partial^2 v_z}{\partial x^2} \right) \tag{7.213}$$

The solution to this equation is more difficult than the solution to Eq. 7.194. The case of pure pressure flow was first solved by Boussinesq [130] in 1868. The solution to the combined drag and pressure flow was first published in 1922 [98]; the authorship of this publication remains a question. Since the 1922 publication, numerous workers have presented solutions to this problem. Meskat [131] reviewed various solutions and demonstrated that they were equivalent. The velocity profile resulting from the drag flow can be written as:

$$v_{zd}(x,y) = \frac{4v_{bz}}{\pi} \sum_{1,3,5\ldots}^{\infty} \frac{\sinh(i\pi y/W)}{i\sinh(i\pi H/W)} \sin(i\pi x/W) \tag{7.214}$$

The velocity profile resulting from the pressure flow can be written as:

$$v_{zp}(x,y) = \frac{g_z}{\mu}\left[\frac{y^2}{2} - \frac{Hy}{2} + \frac{4H^2}{\pi^3} \sum_{1,3,5\ldots}^{\infty} \frac{\cosh[i\pi W/H(x/W - 1/2)]}{1^3\cosh(i\pi W/2H)} \sin(i\pi y/H)\right] \tag{7.215}$$

The combined velocity is simply:

$$v_z(x,y) = v_{zd} + v_{zp} \tag{7.216}$$

The volumetric output can be conveniently expressed in the following form:

$$\dot{V} = \frac{1}{2} pW\,H\,v_{bz}F_d - \frac{pW\,H^3 g_z}{12\,\mu} F_p \tag{7.217}$$

where the shape factor for drag flow F_d is:

$$F_d = \frac{16W}{\pi^3 H} \sum_{1,3,5\ldots}^{\infty} \frac{1}{i^3} \tanh\left(\frac{i\pi\,H}{2W}\right) \tag{7.218}$$

and the shape factor for pressure flow F_p is:

$$F_p = 1 - \frac{192H}{\pi^5 W} \sum_{1,3,5\ldots}^{\infty} \frac{1}{i^5} \tanh\left(\frac{i\pi W}{2H}\right) \tag{7.219}$$

In the range of most extruder screws ($H/W < 0.6$), the shape factors F_d and F_p can be quite accurately approximated with the following expressions:

$$F_d = 1 - 0.571\frac{H}{W} \tag{7.220}$$

and:

$$F_p = 1 - 0.625\frac{H}{W} \tag{7.221}$$

Equations 7.220 and 7.221 are considerably easier to evaluate than the exact expressions, Eqs. 7.218 and 7.219. With the approximate expressions for the shape factor, the volumetric output can be expressed as:

$$\dot{V} = \frac{1}{2} p\,(W - 0.571H) H\, v_{bz} - \frac{(W - 0.625H)\, p\, H^3 g_z}{12\,\mu} \tag{7.222}$$

In most extruder screws, the ratio of channel depth to channel width H/W will range from 0.10 to 0.03, with the latter value being more common than the former. This means that the correction as a result of the shape factors is usually less than 2% and essentially always less than 5%.

7.4.1.2 Effect of Clearance

Another source of error that can become quite important is the leakage flow through the clearance between the flight and the barrel. A normal design clearance (radial) is 0.001 D, where D is the diameter of the screw. When the clearance is normal, the flow through the clearance will be quite small. However, if the screw and/or barrel is subject to wear, the actual clearance can increase substantially beyond the normal design clearance. This can cause a considerable reduction in output and it is important to know how to evaluate the effect of clearance flow.

The clearance reduces the drag flow rate. The drag flow rate is reduced by a factor δ/H. The corrected drag flow becomes:

$$\dot{V}_d = \frac{1}{2} W(H - \delta)\, v_{bz} \tag{7.223}$$

where δ is the radial clearance.

The proper derivation of the pressure induced leakage flow is rather involved. For details of the derivation, the reader is referred to the publications of Mohr and Mallouk [228], Tadmor [103], or Rauwendaal [271]. The total volumetric output including the effect of leakage can be written as:

$$\dot{V} = \frac{p\, W(H - \delta)\, v_{bz}}{2} - \frac{p\, W\, H^3 g_z}{12\,\mu}(1 + f_L) \tag{7.224}$$

The correction factor for pressure induced leakage through the flight clearance can be written as:

$$f_L = \frac{\mu\, w\, \delta^3}{\mu_{cl} W H^3} + \frac{(W + w)\,\mu\,\delta^3}{\mu W \delta^3 + \mu_{cl} w H^3}\left[\frac{6\,\mu\, v_{bz}(H - \delta)}{H^3 g_z} + \frac{W + w}{W \tan^2\varphi}\right] \tag{7.225}$$

where:

$$W = \frac{\pi D \sin\varphi}{p} - w \tag{7.225a}$$

and:

$$v_{bz} = \pi D N \cos\varphi \tag{7.225b}$$

The viscosity in the clearance μ_{cl} is differentiated from the viscosity in the channel μ because, in reality, the viscosity in the clearance will be substantially different from the viscosity in the channel as a result of differences in local temperature and shear rate. When the flight clearance is close to the normal design clearance, the value of f_L will be very close to zero and can be neglected unless extreme accuracy is required. However, when the radial clearance is considerably larger than the normal design clearance, for instance, as a result of wear, the actual value of f_L should be used in the expression for the total volumetric output, Eq. 7.224.

It is interesting to note that even when the down-channel pressure gradient g_z is zero, there is a pressure induced leakage flow. This results from the drag induced cross channel pressure gradient.

A significantly simpler expression for the pressure induced leakage flow is obtained by taking the following approach. The pressure induced leakage flow through the flight clearance can be approximated by considering the flight clearance as a rectangular slit of width $\pi D\cos\varphi$, height δ, and depth w, with a pressure differential across the flight of ΔP_f. By using the equations in Table 7.1, Section 7.5.1, the leakage flow can be written as:

$$\dot{V}_l = \frac{\pi D \cos\varphi\, \delta^3}{12\,\mu_{cl}} \frac{\Delta P_f}{w} + \frac{p\, w\, \delta^3}{12\,\mu_{cl}} g_z \tag{7.226}$$

The pressure differential across the flight results from both the down-channel pressure gradient g_z and the cross-channel gradient g_x. The latter is a drag induced pressure gradient; thus, it is present even in pure drag flow. When the actual leakage flow is very small, the cross-channel pressure gradient is given by Eq. 7.210. The pressure differential across the flight can now be written as:

$$\Delta P_f = g_z \frac{\pi D \cos\varphi}{p} + g_x W \tag{7.227}$$

where W is the cross-channel width.

The effect of down-channel and cross-channel pressure gradient of the pressure differential across the flight is illustrated in Fig. 7.59.

The leakage flow can now be written as:

$$\dot{V}_l = \frac{\pi D\, \delta^3 \cos\varphi}{12\,\mu_{cl} w} \left(\frac{\pi D\, g_z \cos\varphi}{p} + \frac{6\mu\mu_{bx} W}{H^2} \right) + \frac{p\, w\, \delta^3}{12\,\mu_{cl}} g_z \tag{7.228}$$

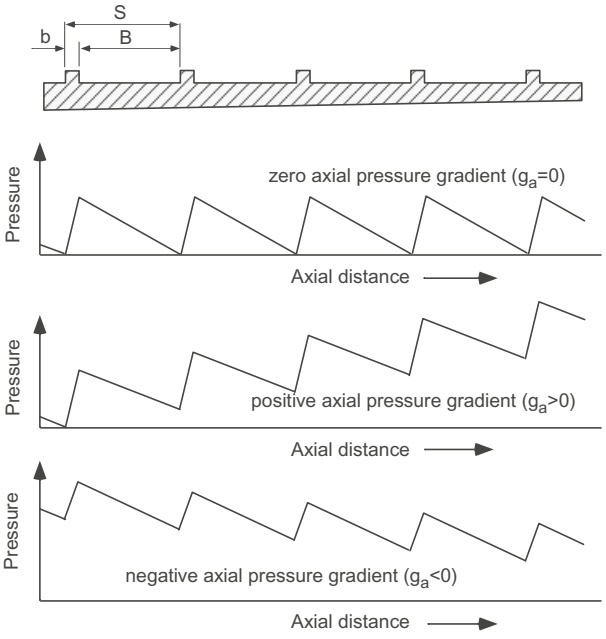


Figure 7.59
Axial pressure profiles at various pressure gradients

The difference between Eqs. 7.228 and 7.224 is less than 5% at normal values of the clearance and about 10% at clearance values of about four times the normal value.

Equation 7.228 can be made more accurate by using an improved equation for the cross-channel pressure gradient. Leakage through the flight clearance will reduce the cross-channel pressure gradient to a value lower than the one given by Eq. 7.210. In Section 10.5, a more accurate expression for the drag induced pressure gradient is derived, taking into account the leakage flow over the flight clearance; see Eqs. 10.108 through 10.112. If the viscosity in the clearance μ_{cl} is differentiated from the viscosity in the channel μ, the same approach leads to the following drag induced cross-channel pressure gradient:

$$g_x = \frac{6\,\mu\,\mu_{cl}\,(H-\delta)\,w\,v_{bx}}{\mu_{cl}\,w\,H^3 + \mu\,W\,\delta^3} \tag{7.229}$$

Thus, the more accurate expression of the leakage flow can be written as:

$$\dot{V}_1 = \frac{\pi\,D\,\delta^3 \cos\varphi}{12\,\mu_{cl}\,w}\left(\frac{\pi\,D\,g_z\,\cos\varphi}{p} + \frac{6\,\mu\,\mu_{cl}\,(H-\delta)w\,W\,v_{bx}}{\mu_{cl}\,w\,H^3 + \mu\,W\,\delta^3}\right) + \frac{p\,w\,\delta^3}{12\,\mu_{cl}}\,g_z \tag{7.230}$$

For normal values of the flight clearance, however, Eq. 7.228 will generally give sufficiently accurate results.

The drag induced pressure differential across the flight plays an important role and cannot be neglected. The value of the leakage flow at normal clearance values

(δ = 0.001 D) is about 0.01% of the drag flow rate; at four times the normal clearance, the leakage flow is about 1% of the drag flow rate. Thus, the leakage flow becomes significant only when the clearance is larger than about four times its normal value.

The total volumetric output, including the effect of leakage, Eq. 7.228, can be written:

$$\dot{V} = \frac{p\,W(H-\delta)v_{bz}}{2} - \frac{p\,W\,H^3 g_z}{12\,\mu} - \frac{\pi\,D\,\delta^3\cos\varphi}{12\,\mu_{cl}\,w}\left(\frac{\pi\,D\,g_z\cos\varphi}{p} + \frac{6\,\mu\,v_{bx}\,W}{H^2}\right) - \frac{p\,w\,\delta^3}{12\,\mu_{cl}}g_z \qquad (7.231)$$

7.4.1.3 Power Consumption in Melt Conveying

The power consumption in the melt conveying zone is an important parameter to consider in screw design and in the analysis of actual extrusion operations. The power consumed for pumping in the channel is:

$$dZ_{ch} = p\,v_{bz}dz\int_0^W \tau_{yz}(H)dx + p\,v_{bx}dz\int_0^W \tau_{yx}(H)dx \qquad (7.232)$$

where the shear stresses are related to the barrel surface.

If the material is Newtonian:

$$\tau_{yx}(H) = \mu\frac{dv_x}{dy}\bigg|_H \qquad (7.233)$$

and:

$$\tau_{yz}(H) = \mu\frac{dv_z}{dy}\bigg|_H \qquad (7.234)$$

The shear stresses can be evaluated from Eqs. 7.223 and 7.224 and the equations for down-channel velocity profile, Eq. 7.197 or 7.216, and the-cross channel velocity profile, Eq. 7.211. The power consumption in the screw channel can be written as:

$$dZ_{ch} = (1 + 3r_d + 4\tan^2\varphi)\frac{p\,\mu\,W\,v_{bz}^2 dz}{H} \qquad (7.235)$$

where r_d is ratio of pressure flow to drag flow:

$$r_d = \frac{H^2 g_z}{6\,\mu\,v_{bz}} \qquad (7.236)$$

Equation 7.236 is valid if the clearance is negligible. The ratio of pressure flow to drag flow is often referred to as the throttle ratio (Drossel quotient in German). It enables a compact expression for the combined drag and pressure flow:

$$\dot{V} = \frac{p\,W\,H\,v\,b\,z}{2}(1 - r_d) \qquad (7.237)$$

The specific energy consumption in the channel can be determined by dividing the power consumption by the throughput:

$$\hat{Z}_{ch} = \frac{dZ_{ch}}{\dot{V}} = \frac{2\,\mu\, v_{bz}\, dz}{H^2} \frac{1 + 3r_d + 4\tan^2\varphi}{1 - r_d} \tag{7.238}$$

The pumping efficiency is the ratio of the theoretical energy requirement to develop pressure ΔP (= $\dot{V}\Delta P$) divided by the actual energy requirement (= dZ_{ch}). Thus, the pumping efficiency in the channel can be written as:

$$\varepsilon_{ch} = \frac{\dot{V}\Delta P}{dZ_{ch}} = \frac{3r_d - 3r_d^2}{1 + 3r_d + 4\tan^2\varphi} \tag{7.239}$$

The optimum pumping efficiency can be determined by setting the first derivative of the pumping efficiency with respect to the throttle ratio equal to zero:

$$\frac{d\varepsilon_{ch}}{dr_d} = 0 \tag{7.240}$$

This yields the following expression for the optimum throttle ratio r_d^*:

$$r_d^* = -\frac{1 + 4\tan^2\varphi}{3} \pm \frac{2(1 + 5\tan^2\varphi + 4\tan^4\varphi)}{3}^{1/2} \tag{7.241}$$

By inserting the optimum throttle ratio from Eq. 7.241 into Eq. 7.239 for the pumping efficiency, one can determine the optimum pumping efficiency in the channel. When the helix angle is zero, the optimum throttle ratio is 1/3 or –1 and the optimum pumping efficiency is also 1/3. A throttle ratio of –1 represents a large negative pressure gradient; this is not a situation that is likely to occur in practice. When the helix angle increases, the optimum throttle ratio increases, but the optimum pumping efficiency decreases. This is shown in Fig. 7.60.

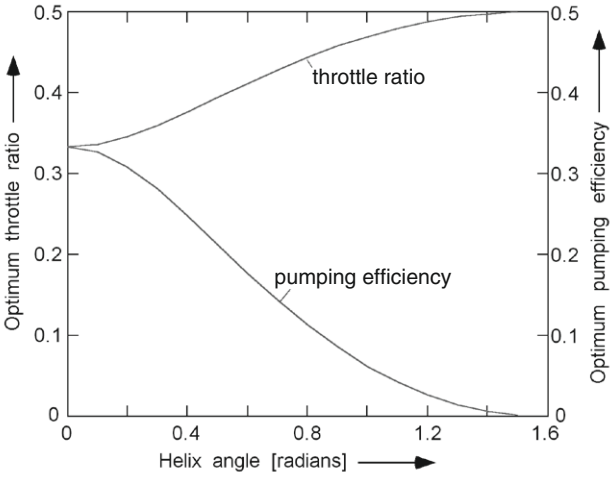


Figure 7.60
Optimum throttle ratio and pumping efficiency versus helix angle

Thus, the highest pumping efficiency of the channel that can possibly be obtained is only 33.33%. The other 66.67% of the energy is dissipated in the fluid as heat. In practice, the actual pumping efficiency will be around 10% or less. The screw pump, therefore, is rather inefficient in developing pressure. Other types of pumps, such as a gear pump, can be more efficient in generating pressure. However, in many extrusion operations, the energy dissipated in the fluid is not wasted but effectively used to bring the polymer melt to the required melt temperature. Heating the polymer melt by viscous heat generation is more effective than heating by external barrel heaters.

The power consumption in the clearance can be determined quite easily if it is assumed that the velocity profile in the clearance is dominated by drag flow. The power consumption in the clearance can then be written as:

$$dZ_{cl} = \frac{p\, v_b^2\, \mu_{cl}\, w\, dz}{\delta} \tag{7.242}$$

where w is the perpendicular flight width ($w = b\cos\varphi$).

The power consumption in the clearance is directly proportional to the number of parallel flights, the local viscosity, and the flight width, and is inversely proportional to the radial clearance. It will be shown later that a substantial portion (in some cases 50% or more) of the total power consumption is consumed in the clearance. Therefore, the geometry of the flight clearance becomes an important geometrical variable when it comes to minimizing power consumption.

The power consumption necessary to build up pressure in the polymer is determined by multiplying the volumetric flow rate with the pressure rise:

$$dZ_p = \dot{V} g_z dz \tag{7.243}$$

The total pumping efficiency can now be determined from:

$$\varepsilon = \frac{dZ_p}{dZ_{ch} + dZ_{cl}} \tag{7.244}$$

The total pumping efficiency will usually be about 10% or less. The amount of power that is dissipated in the fluid as heat is:

$$dZ_{diss} = dZ_{ch} + dZ_{cl} - dZ_p \tag{7.245}$$

This power should be used to calculate the temperature increase in the polymer melt. Since the pumping efficiency is usually less than 10%, the amount of power dissipated in the screw channel will generally be more than 90% of the total power input.

7.4.2 Power Law Fluids

In this section, the effect of the pseudo-plastic behavior of the polymer melt on the conveying characteristics will be analyzed by describing the polymer melt as a power law fluid. As before, the flow is considered to be steady, fully developed, and isothermal, and leakage flow is neglected. The effect of the flight flanks on the down-channel velocity profile will be neglected. At first, the analysis will be one-dimensional, considering only the down-channel velocity. Thus, the effect of cross-channel flow will initially be neglected. Later, the analysis will be extended to a two-dimensional case, considering both the down-channel and cross-channel velocity.

7.4.2.1 One-Dimensional Flow

For the one-dimensional analysis, the equation of motion is described by Eqs. 7.194 and 7.195. The constitutive relationship, the power law equation, is written as:

$$\tau_{yz} = m\left|\frac{dv_z}{dy}\right|^{n-1}\frac{dv_z}{dy} \tag{7.246}$$

Equation 7.246 combined with Eq. 7.195 describes the basic problem. It is convenient to write the resulting equation in dimensionless form. For this purpose, the following dimensionless quantities are defined: the dimensionless depth $\xi = y/H$, the dimensionless down-channel velocity $v^0{}_z = v_z/v_{bz}$, and a reduced pressure gradient Γ_R. The reduced pressure gradient is defined as:

$$\Gamma_R = \left(\frac{Hg_z}{m}\right)^s \frac{H}{v_{bz}} \tag{7.247}$$

where s is the reciprocal power law index (s = 1/n).

Equation 7.246 can be integrated to give:

$$\left|\frac{dv_z^0}{d\xi}\right|^{n-1}\frac{dv_z^0}{d\xi} = \Gamma_R^n(\xi - \lambda) \tag{7.248}$$

Variable λ in Eq. 7.248 represents the location where the shear rate is zero, which is also the location of the extremum in the velocity profile. This value needs to be known to eliminate the absolute value in Eq. 7.248. For the time being, only positive pressure gradients g_z will be considered. If the extremum occurs in the screw channel, then $0 \le \lambda \le 1$. When $\xi \ge \lambda$, Eq. 7.248 can be written as:

$$\frac{dv_z^0}{d\xi} = \Gamma_R(\xi - \lambda)^s \tag{7.249}$$

By integration and by using the appropriate boundary condition $v_z^0(1) = 1$, the following expression is obtained:

$$v_z^0 = 1 - \frac{\Gamma_R}{s+1}[(1-\lambda)^{s+1} - (\xi-\lambda)^{s+1}] \tag{7.250}$$

Similarly, for $\xi \leq \lambda$, the expression becomes:

$$v_z^0 = \frac{\Gamma_R}{s+1}[(\lambda-\xi)^{s+1} - \lambda^{s+1}] \tag{7.251}$$

At $\xi = \lambda$, the two velocities from Eqs. 7.250 and 7.251 should be the same. From this equality, the following equation for λ results:

$$\lambda^{s+1} - (1-\lambda)^{s+1} + \frac{s+1}{\Gamma_R} = 0 \tag{7.252}$$

From this equation, the value of λ can be determined. The condition for the existence of an extremum within the actual flow region is $\Gamma_R \geq s + 1$. The maximum velocity can be written as:

$$v_z^0 - \max = \frac{\Gamma_R}{s+1} \tag{7.253}$$

The extremum falls outside of the actual flow regime when $\Gamma_R < s + 1$. By using the same procedure, the equation for λ when $\Gamma_R < s + 1$ becomes:

$$(-\lambda)^{s+1} - (1-\lambda)^{s+1} + \frac{s+1}{\Gamma_R} = 0 \tag{7.254}$$

Both the dimensionless velocity $v^0{}_z$ and the dimensionless flow rate $\dot{V}^0$ can be written into single expressions:

$$v_z^0 = \frac{|\xi-\lambda|^{s+1} - |\lambda|^{s+1}}{|1-\lambda|^{s+1} - |\lambda|^{s+1}} \tag{7.255}$$

and:

$$\dot{V}^0 = \frac{2}{s+2}(1 - \lambda - \Gamma_R|\lambda|^{s+1}) \tag{7.256}$$

The dimensionless flow rate is the actual flow rate divided by the drag flow rate, thus:

$$\dot{V}^0 = \frac{2\dot{V}}{W\,H\,v_{bz}} \tag{7.257}$$

Later in Section 8.2.1, it will be shown that if the channel depth is optimized to give the highest output, the corresponding value of $\lambda = 0$. Thus, the corresponding optimum dimensionless flow rate is:

$$\dot{V}^{0}_{opt} = \frac{2}{s+2} = \frac{2n}{1+2n} \tag{7.258}$$

And thus the optimum actual flow rate is:

$$\dot{V}_{opt} = \frac{n}{1+2n} W H v_{bz} \tag{7.259}$$

For a Newtonian fluid (n = 1), Eq. 7.259 becomes equal to Eq. 7.205.

The velocity profiles at $\lambda = 0.1$ and various values of the power law index n are shown in Fig. 7.61.

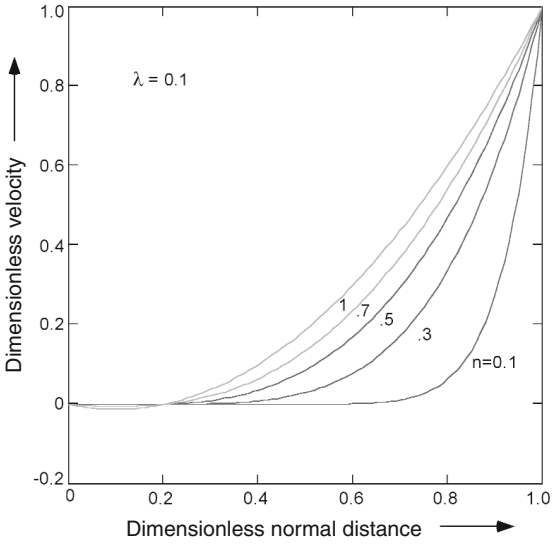


Figure 7.61
Dimensionless velocity versus dimensionless normal distance

It is clear from Fig. 7.61 that the velocities reduce and the velocity profiles start to approach plug flow as the power law index becomes smaller. As a result, the throughput reduces with reducing power law index.

In order to determine the velocity profile and the flow rate, the value of λ has to be known. This involves solving Eq. 7.252 or Eq. 7.254. This is normally done by using a numerical technique, e.g., Newton-Raphson. Exact analytical solutions are only possible for the special case when s is a positive integer. However, by rewriting the equations and by performing a series expansion, a closed-form solution can be obtained. If a new variable x is introduced in Eq. 7.252 with $x = \lambda - 0.5$, then the equation can be rewritten as:

$$(0.5+x)^{s+1} - (0.5-x)^{s+1} + \frac{s+1}{\Gamma_R} = 0 \tag{7.260}$$

By performing a series expansion of the first two terms of Eq. 7.260 and neglecting the x terms of order four and higher, the following equation is obtained:

$$\frac{1}{3}s(s-1)2^{2-s}x^3 + 2^{1-s}x + \frac{1}{\Gamma_R} = 0 \tag{7.261}$$

This is a standard third order (cubic) equation that can be readily solved. There is only one root that is real; the solution for λ when $\Gamma_R \geq s + 1$ is:

$$\lambda = \frac{1}{2} + (q_1 + q_2)^{1/3} + (q_1 - q_2)^{1/3} \tag{7.262}$$

where:

$$q_1 = -3\frac{2^{s-3}}{s(s-1)\Gamma_R} \tag{7.263}$$

and:

$$q_2 = \left[q_1^2 + (2s^2 - 2s)^{-1/2}\right]^{1/3} \tag{7.264}$$

This solution will be accurate when x is close to zero, which will generally be the case. In the region for which Eq. 7.260 applies, the values of λ will range between 0 and 0.5, thus x will range between –0.5 and 0.

Equation 7.254 can be rewritten by introducing a new variable $x = \lambda + 1$. After series expansion and neglecting x terms of order three and higher, a quadratic equation is obtained. The solution for λ when $\Gamma_R < s + 1$ is:

$$\lambda = \frac{-C_2 \pm (C_2^2 - 4C_1C_3)^{1/2}}{2C_1} - 1 \tag{7.265}$$

where:

$$C_1 = \frac{1}{2}s(s+1)(1-2^{s-1}) \tag{7.266}$$

$$C_2 = (s+1)(2^s - 1) \tag{7.267}$$

$$C_3 = 1 - 2^{s+1} + \frac{s+1}{\Gamma_R} \tag{7.268}$$

Again, this solution will be accurate when x is close to zero. In the region where Eq. 7.254 applies, the value of λ will range from 0 (where $\Gamma_R = s + 1$) to $-\infty$ when the pressure gradient is zero. Therefore, Eq. 7.265 cannot give accurate results at very small pressure gradients. However, at larger pressure gradients, Eq. 7.265 will give accurate results. The limited accuracy of the solution at small pressure gradients does not have much practical significance. In the analysis of real extruders, one is

primarily concerned about the effect of large pressure gradients, not about the effect of small pressure gradients. The flow rate at small pressure gradients will be nearly equal to the drag flow rate. The predictions of the analytical solutions can now be plotted in the often-used dimensionless form.

This is shown in Fig. 7.62, where the dimensionless output is plotted as a function of the dimensionless pressure gradient g_z^0, where:

$$g_z^0 = \frac{g_z H}{6m}\left(\frac{H}{v_{bz}}\right)^n = \frac{\Gamma_R^n}{6} \tag{7.269}$$

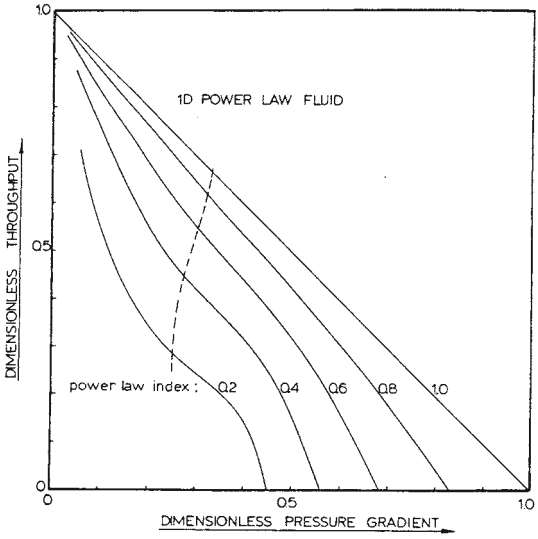


Figure 7.62
Dimensionless throughput versus dimensionless pressure gradient from closed-form solution

For a Newtonian fluid (n = 1), the familiar linear output-pressure relationship is found. However, when the power law index is less than unity, substantial deviations from Newtonian characteristics occur. The deviations increase as the material becomes more pseudo-plastic (more strongly non-Newtonian). The result is that for a pseudo-plastic fluid, the pressure generating capability is drastically reduced compared to a Newtonian fluid. Or, at the same pressure gradient, the output is drastically reduced. For a fluid with a power law index less than 0.8, the use of the equations for Newtonian fluids will result in large errors!

Comparisons of Fig. 7.62 to similar figures determined by other workers from numerical techniques, e.g., [132] or [106], reveal essentially indistinguishable results. This is a first indication that the analytical solutions for λ are quite accurate. Up to this point, only positive pressure gradients have been considered. From Eq. 7.256, it can be demonstrated rather easily that the output values for negative pressure gradients can be obtained from the following relationship:

$$\dot{V}^0(-g_z^0) = 2 - \dot{V}^0(+g_z^0) \tag{7.270}$$

The dashed line in Fig. 7.62 shows at what point along each curve λ becomes zero. When λ is zero, the extremum in the velocity profile occurs right at the screw surface. The dimensionless throughput in this case is:

$$\dot{V}^0 = \frac{2}{2+s} = \frac{2n}{1+2n} \tag{7.271}$$

This is the same value as the optimum dimensionless flow rate described by Eq. 7.258. It is interesting to note that this throughput is determined only by the power law index. The data above the dashed line have been determined with Eq. 7.265. In this case, $\Gamma_R < s + 1$ and no extremum occurs in the velocity profile. The data below the dashed line have been determined with Eq. 7.262. In this case, $\Gamma_R \geq s + 1$ and an extremum does occur in the velocity profile.

7.4.2.2 Two-Dimensional Flow

In this section, the previous analysis will be extended to include the effect of cross-channel flow. The cross-channel flow does not directly affect the conveying rate, but it does affect the total shear rate to which the polymer is exposed. Therefore, the viscosity will be affected and thus the actual flow rate is affected as well. If the helix angle reduces to zero, there will be no cross-channel flow, and the results of the two-dimensional analysis will be identical to the one-dimensional analysis. This limiting case has been studied by Tadmor [133] and Dyer [134]. More general two-dimensional analyses can be found in references 132 through 145. Steller [297] developed an analytical solution for 2-D flow of a power law fluid and later [298] for an Ellis fluid. The solution, however, requires numerical analysis to evaluate the solution. Rauwendaal [271] studied the 2-D flow problem in screw extruders including the effect of leakage flow; the effect of leakage flow increases significantly when the polymer melt becomes more shear thinning.

The difference between the one-dimensional and the two-dimensional analysis will increase with increasing helix angle and reducing power law index. From a practical point of view, the use of a two-dimensional analysis becomes important when large helix angles and strongly non-Newtonian fluids are analyzed. The equation of motion in the down-channel direction is the same as used before; see Eq. 7.194. A similar expression has to be used for the cross-channel direction. The shear stress profiles can be written as:

$$\tau_{yz} = \tau_{zo} + g_z y \tag{7.272}$$

$$\tau_{yx} = \tau_{xo} + g_x y \tag{7.273}$$

The magnitude of the total shear stress is obtained from:

$$\tau = (\tau_{yx}^{\ 2} + \tau_{yz}^{\ 2})^{1/2} \tag{7.274}$$

The power law equation for the two-dimensional flow can be written as:

$$\tau = m\left[\left(\frac{dv_x}{dy}\right)^2 + \left(\frac{dv_2}{dy}\right)^2\right]^{\frac{n-1}{2}}\left(\frac{dv}{dy}\right) \tag{7.274a}$$

The direction of shear stress τ and velocity v is determined by τ_{yz} and τ_{yx}. At this point, there are three unknowns: the cross-channel pressure gradient g_x, the cross-channel shear stress at the screw surface τ_{xo}, and the down-channel shear stress at the screw surface τ_{zo}. At the time of writing, no analytical solutions to this problem are known. In fact, an analytical solution does not seem possible. Therefore, some numerical scheme has to be used in order to determine the unknowns. Because this problem is of considerable importance to the proper analysis of melt conveying, it will be discussed in some detail.

Some initial values of g_x, τ_{xo}, and τ_{zo} can be selected, for instance, by calculating the values for the Newtonian case. From those initial values, the corresponding velocity profiles and the flow rates in the cross-channel direction can be determined. The velocity profile in the x and z directions can be determined from:

$$\frac{dv_x}{dy} = \frac{\tau_{yx}}{m^s}\left(\tau_{yx}{}^2 + \tau_{yz}{}^2\right)^{\frac{1-n}{2n}} \tag{7.275}$$

and:

$$\frac{dv_z}{dy} = \frac{\tau_{yz}}{m^s}\left(\tau_{yx}{}^2 + \tau_{yz}{}^2\right)^{\frac{1-n}{2n}} \tag{7.276}$$

The net flow rate in the cross-channel direction should be zero if it is assumed the leakage over the flight is negligible. The cross-channel flow rate is:

$$\dot{V}_x = \int_0^H v_x dy = 0 \tag{7.277}$$

The accuracy of the initial guesses of g_x, τ_{xo}, and τ_{zo} can be evaluated by calculating $v_x(H)$, $v_z(H)$ and $\dot{V}_x$. This can be done by using a standard numerical technique to integrate Eqs. 7.275, and 7.276, e. g., Simpson's rule. The calculated values are then compared to the actual values: v_{bx}, v_{bz}, and 0 respectively. Unless the initial values are perfect, there will be residuals:

$$\Delta v_x = \int_0^H \frac{dv_x}{dy} dy - v_{bx} \tag{7.278}$$

$$\Delta v_z = \int_0^H \frac{dv_z}{dy} dy - v_{bz} \tag{7.279}$$

$$\Delta \dot{V}_x = \int_0^H v_x dy - 0 \tag{7.280}$$

New values of g_x, τ_{xo}, and τ_{zo} can be obtained by using a Newton-Raphson scheme. The residuals can be expressed as:

$$\Delta v_x = \frac{\partial v_x}{\partial g_x}\Delta g_x + \frac{\partial v_x}{\partial \tau_{xo}}\Delta \tau_{xo} + \frac{\partial v_x}{\partial \tau_{zo}}\Delta \tau_{zo} \tag{7.281}$$

$$\Delta v_z = \frac{\partial v_z}{\partial g_x}\Delta g_x + \frac{\partial v_z}{\partial \tau_{xo}}\Delta \tau_{xo} + \frac{\partial v_z}{\partial \tau_{zo}}\Delta \tau_{zo} \tag{7.282}$$

$$\Delta \dot{V}_x = \frac{\partial \dot{V}_x}{\partial g_x}\Delta g_x + \frac{\partial \dot{V}_x}{\partial \tau_{xo}}\Delta \tau_{xo} + \frac{\partial \dot{V}_x}{\partial \tau_{zo}}\Delta \tau_{zo} \tag{7.283}$$

The partial derivatives can be determined by selecting a second set of data for g_x, τ_{xo}, and τ_{zo} with values very close to the first values. When this is done, Δg_x, $\Delta \tau_{xo}$, and $\Delta \tau_{zo}$ can be calculated by solving the three linear equations, which is a straightforward operation. The new values of g_x, τ_{xo}, and τ_{zo} can now be determined from:

$$g_x - \text{new} = g_x - \text{old} + \Delta g_x \tag{7.284}$$

$$\tau_{xo} - \text{new} = \tau_{xo} - \text{old} + \Delta \tau_{xo} \tag{7.285}$$

$$\tau_{zo} - \text{new} = \tau_{zo} - \text{old} + \Delta \tau_{zo} \tag{7.286}$$

The iteration is repeated until the relative difference between the new and old value is less than a certain value, depending on the accuracy required. The throughput is determined from:

$$\dot{V}_z = \int_0^H v_z dy \tag{7.287}$$

A short Fortran program to perform this numerical procedure is given in Appendix 7.3. The program converges rapidly; the solution is usually obtained in five iterations. Figure 7.63 shows the dimensionless throughput-pressure gradient relationship from the two-dimensional analysis for a helix angle of zero degrees.

As mentioned before, these results should be the same as the results from the one-dimensional analysis as shown in Fig. 7.62. By comparing the two figures, it is clear that the results are virtually identical. This confirms the accuracy of the analytical solution for the one-dimensional flow of a power law fluid. The difference is generally less than 1%, except at small values of the dimensionless pressure gradient $g_z^0 < 0.1$. The loss of accuracy at low pressure gradients was predicted earlier and should not pose a serious problem in the analysis of real extrusion problems.

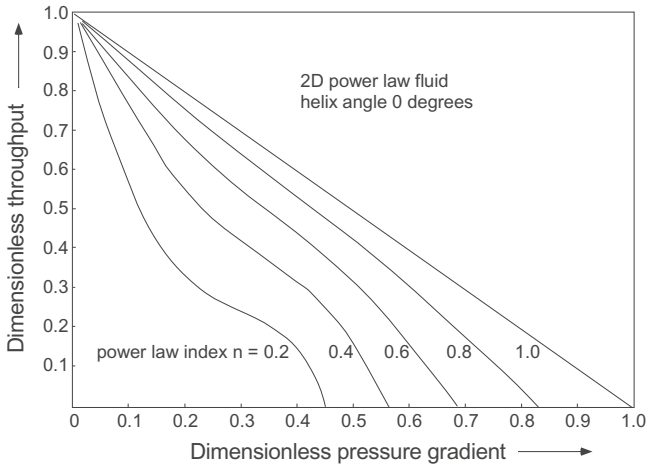


Figure 7.63 Dimensionless throughput versus dimensionless pressure gradient from 2-D analysis for helix angle equals zero

Figure 7.64 shows the dimensionless throughput versus pressure gradient for a helix angle of 17.66° (square pitch screw).

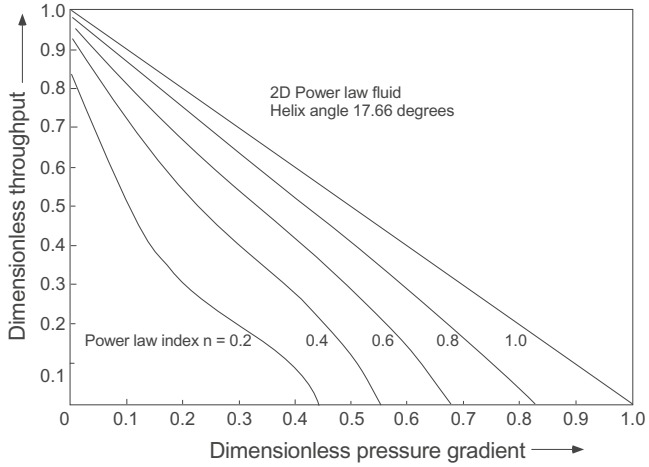


Figure 7.64 Dimensionless throughput versus dimensionless pressure gradient from 2-D analysis for helix angle equals 17.66°

The dimensionless throughput at 17.66° helix angle is considerably lower than a zero helix angle. The difference is about 10% at small pressure gradients and about 40% at large pressure gradients when the power law index is less than one-half. At larger values of the power law index, the difference is generally less than 10%. This means that application of the equations for the one-dimensional case will lead to substantial errors for standard helix angles when the power law index is less than one-half! When the power law index is larger than one-half, these equations will be reasonably accurate.

It should be noted that a reduction in the dimensionless throughput does not necessarily mean that the actual throughput reduces as well. Obviously, when the helix angle is zero, the actual throughput will be zero. The dimensionless throughput is determined from:

$$\dot{V}^0 = \frac{2}{H v_{bz}} \int_0^H v_z \, dy \tag{7.288}$$

The actual volumetric throughput is related to the dimensionless throughput by:

$$\dot{V} = \frac{1}{2} H \, W \, v_{bz} \, \dot{V}^0 \cong \frac{1}{2} \pi^2 \, D^2 \, N \, H \sin\varphi \cos\varphi \, \dot{V}^0 \tag{7.289}$$

The second equality of Eq. 7.289 is correct if the flight width is negligible. Figure 7.65 shows the dimensionless throughput versus pressure gradient for five helix angles when the power law index is one-half.

The dimensionless throughput reduces with increasing helix angle over the entire pressure gradient range. This demonstrates again that the equation for the one-dimensional case should not be used for large helix angles and/or small values of the power law exponent.

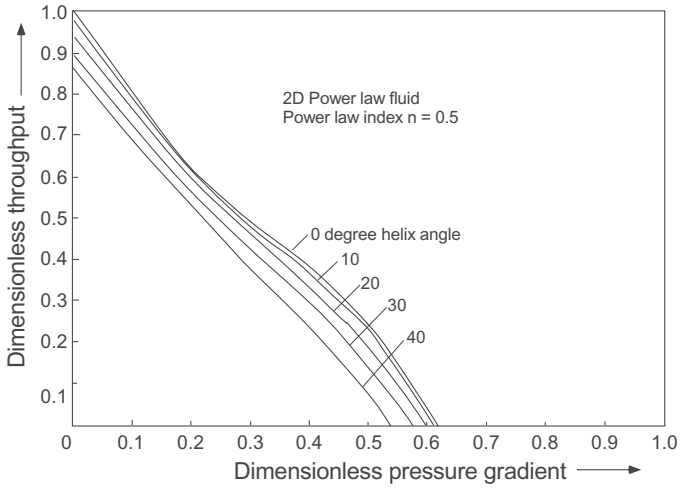


Figure 7.65 Dimensionless throughput versus dimensionless pressure gradient for several helix angles

From Figs. 7.62 through 7.65, it becomes clear that the Newtonian output-pressure gradient relationship is unacceptably inaccurate when the power law index of the polymer melt is less than 0.8. The one-dimensional power law (1-DPL) output-pressure gradient relationship is accurate only for small helix angles. Thus, for accurate results, a two-dimensional power law (2-DPL) analysis should be used. However, the 2-DPL analysis does not yield analytical solutions; numerical techniques have to be

used to obtain results. One way to avoid complex calculations is to use the Newtonian output-pressure gradient relationship with correction factors for non-Newtonian behavior of the polymer melt. Figure 7.66 shows the dimensionless output versus pressure gradient for an expression of $\dot{V}^0$ that incorporates such correction factors.

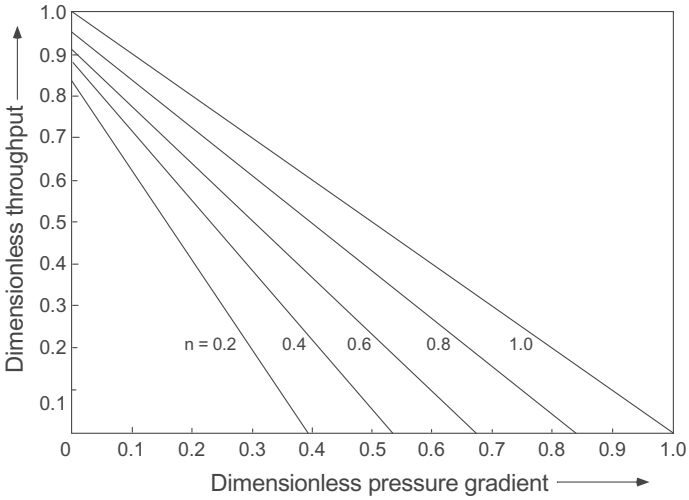


Figure 7.66 Dimensionless throughput versus dimensionless pressure gradient using linear approximation

The correction factors apply to helix angles in the range of 15 to 25° and are determined to minimize the difference with 2-DPL analysis. The dimensionless output is written as:

$$\dot{V}^0 = \frac{8+2n}{10} - \frac{3}{1+2n} g_z^0 \tag{7.290}$$

By using Eq. 7.269 for g_z^0 and Eq. 7.257 for $\dot{V}^0$, the Newtonian output-pressure gradient relationship with the correction factors for non-Newtonian behavior can be written as:

$$\dot{V} = \left(\frac{4+n}{10}\right) p\, W\, H\, v_{bz} - \left(\frac{1}{1+2n}\right) \frac{p\, W\, H^3 g_z}{4\mu} \tag{7.291}$$

where μ is calculated at the Couette shear rate in the channel ($\dot{\gamma} = v_{bz}/H$); thus

$$\mu = m\left(\frac{v_{bz}}{H}\right)^{n-1} \tag{7.292}$$

With this equation, the difference with results from a 2-DPL analysis will generally be less than 10% when the power law index lies in the range of 0.3 to 1.0. Essentially all polymers fall in this range of power law indici. Thus, Eq. 7.291 should provide a

useful relationship between output and pressure gradient for use in the analysis of practical extrusion problems. Of course, Eq. 7.291 is 100% accurate when the power law index equals unity, i. e., for a Newtonian fluid. The correction factors in Eqs. 7.290 and 7.291 have been determined for helix angles normally used in the extrusion industry, with the helix angle usually ranging from about 15 to 25°. If helix angles considerably below or above this range are used, then other correction factors will be more appropriate.

Another method to avoid complex calculations is to use an effective viscosity to be used in the Newtonian equation in order to predict output for a non-Newtonian fluid. This method was proposed by Booy [132]. A drawback of this method is that it only corrects the pressure flow term. As a result, the method does not work at small pressure gradients. The effective viscosity ratio has to be obtained from a graph. The ratio can be approximated by taking the effective viscosity ratio equal to the power law index. However, the latter approximation will be considerably less accurate than Eq. 7.291.

Potente [235] also proposed approximate equations to predict the output as a function of pressure gradient for power law fluids. However, Potente's equations are only valid in a limited range of the dimensionless output $\dot{V}^0$, for $0.6 \leq \dot{V}^0 \leq 1$. Thus, for a power law fluid with index n = 0.3, the equations are valid only when the dimensionless pressure gradient g_z^0 is less than about 0.1. In practical extrusion problems, one is generally more concerned about the effect of large pressure gradients than about the effect of small pressure gradients. Therefore, the equations developed by Potente have limited usefulness.

7.4.3 Non-Isothermal Analysis

We will now address the effect of temperature on melt conveying. First, we will analyze fully developed temperature profiles. These conditions exist when the temperatures no longer change in the flow direction; the region before is called the region of developing temperatures. We will address Newtonian fluids first and then analyze power law fluids.

7.4.3.1 Newtonian Fluids with Negligible Viscous Dissipation

For a Newtonian fluid (n = 1) the momentum balance equation can be written as:

$$\frac{d}{d\xi}\left[e^{b\Theta}\frac{d\Phi}{d\xi}\right] = 6r \tag{7.293}$$

The dimensionless velocity Φ is defined as:

$$\Phi = \frac{v_z(y)}{v} \tag{7.294}$$

The dimensionless temperature is defined as:

$$\Theta = \frac{T - T_s}{T_b - T_s} \tag{7.295}$$

The dimensionless normal distance is defined as:

$$\xi = \frac{y}{H} \tag{7.296}$$

The throttle ratio r is given by Eq. 7.236 and the factor b is given by:

$$b = \alpha(T_s - T_b) \tag{7.297}$$

where α is the temperature coefficient of the viscosity.

The moving surface, the barrel, is at temperature T_b and the stationary surface, the screw, is at temperature T_s. The momentum balance equation can be integrated to yield the velocity gradient:

$$\frac{d\Phi}{d\xi} = 6re^{-b\Theta}(\xi - \xi_0) \tag{7.298}$$

The integration constant ξ_0 corresponds to the normal coordinate where the shear stress is zero and the velocity profile has an extremum. If it is assumed that the viscosity is determined by a linear temperature profile the velocity gradient can be written as:

$$\frac{d\Phi}{d\xi} = 6re^{-b\xi}(\xi - \xi_0) \tag{7.299}$$

The velocity profile can be obtained by integrating the velocity gradient; this results in the following expression:

$$\Phi(\xi) = 6re^{-b\xi}\left(-\frac{\xi}{b} - \frac{1}{b^2} + \frac{\xi_0}{b}\right) + \Phi_0 \tag{7.300}$$

The integration constants can be evaluated from the boundary conditions $\Phi(0) = 0$ and $\Phi(1) = 1$. This leads to the expression for ξ_0:

$$\xi_0 = \frac{-b}{6r(1 - e^{-b})} + \frac{1 - be^{-b} - e^{-b}}{b(1 - e^{-b})} \tag{7.301}$$

Integration constant Φ_0 becomes:

$$\Phi_0 = 6r\left(\frac{1}{b^2} - \frac{\xi_0}{b}\right) \tag{7.302}$$

Figure 7.67 shows the velocity profiles for b = 1.0 and several values of the throttle ratio r.

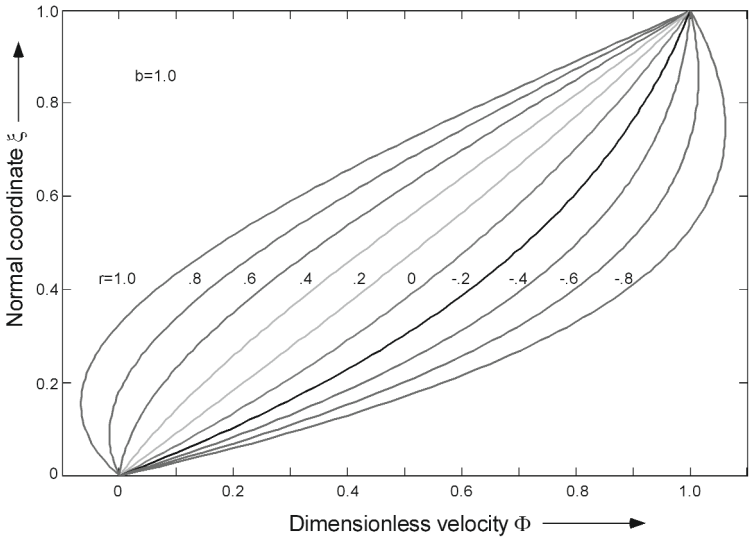


Figure 7.67 Dimensionless velocity versus normal distance at b = 1

The velocity profile for pure drag flow (r = 0) is curved such that the velocities are increased from the linear profile that occurs in isothermal flow. The lines at various r-values are closely grouped together. Therefore, changes in pressure gradient will have a relatively small effect on the velocity profile and, thus, on the flow rate.

The velocity profiles at b = –1 are shown in Fig. 7.68.

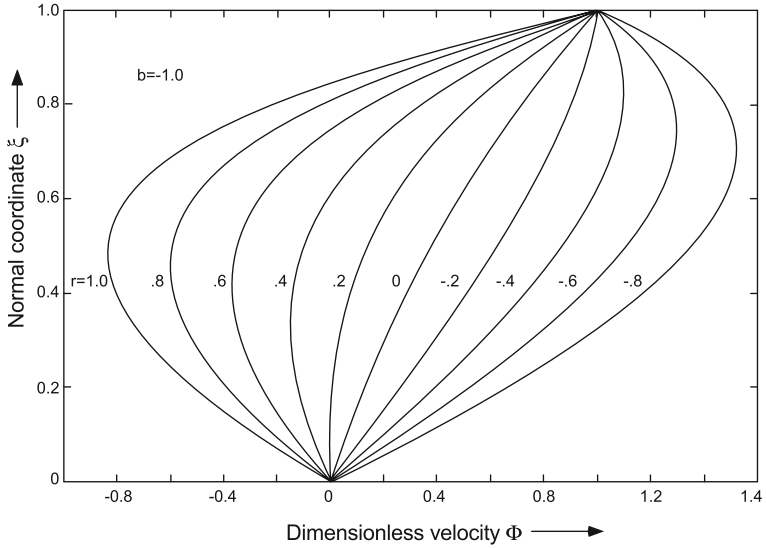


Figure 7.68 Dimensionless velocity versus normal distance at b = –1

In this case the velocity profile at r = 0 is curved such that the velocities are decreased from the linear profile. Also, the lines at various r-values are spaced further apart. As a result, changes in pressure gradient will have a relatively large effect on the velocity profile and flow rate. This indicates less stable extrusion operation at negative values of b, in other words, when the barrel temperature is higher than the screw temperature.

The effect of the value of b on the velocity profile is shown in Fig. 7.69.

Figure 7.69 compares the velocities at b-values of –1, 0, and 1 at a throttle ratio of r = 0. It is clear that the temperature effect is significant even in pure drag flow (r = 0). The effect is greater for higher values of the throttle ratio. This is shown in Fig. 7.70.

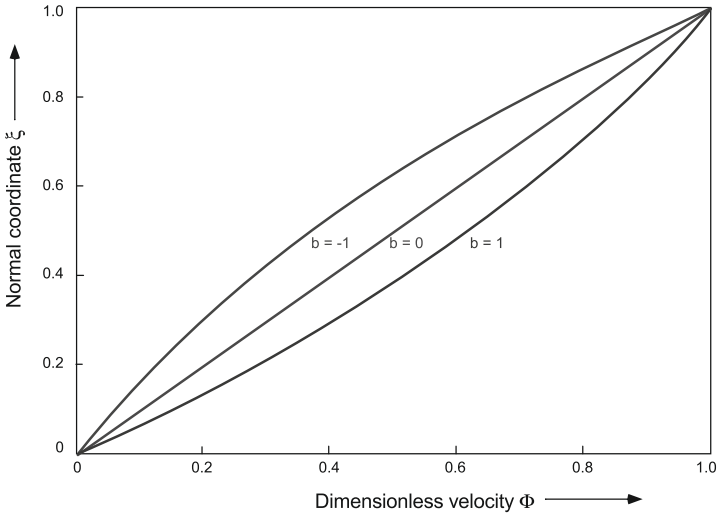


Figure 7.69 Dimensionless velocity versus normal distance for three b values at r = 0

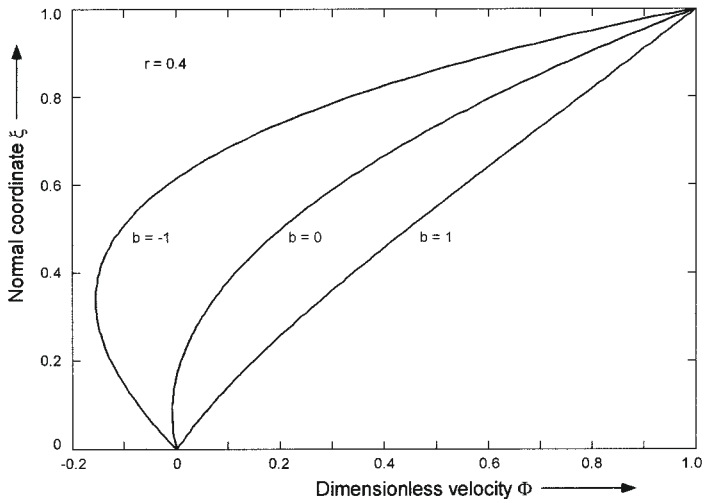


Figure 7.70 Dimensionless velocity versus normal distance for three b values at r = 0.4

The volumetric flow rate can be determined by integrating $\Phi(\xi)$ from $\xi = 0$ to $\xi = 1$. This leads to the following expression for the dimensionless flow rate:

$$\Psi = 6r\left[\left(e^{-b}-1\right)\left(\frac{1}{b^2}+\frac{2}{b^3}-\frac{\xi_0}{b^2}\right)+\frac{2}{b^2}-\frac{\xi_0}{b}\right] \tag{7.303}$$

Figure 7.71 shows how the dimensionless flow rate changes with factor b.

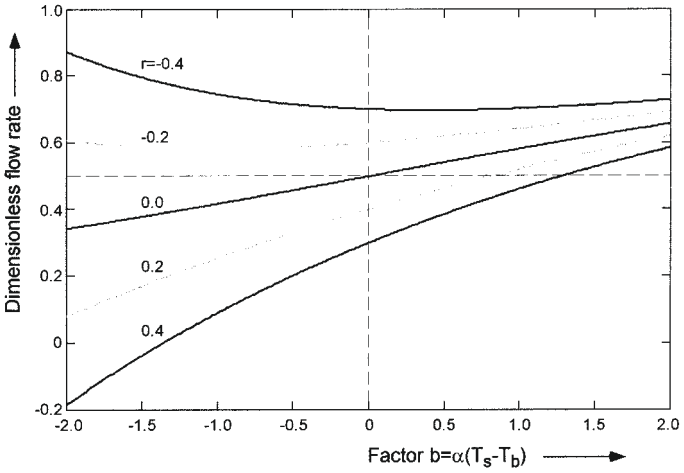


Figure 7.71 Dimensionless flow rate versus b for several values of the throttle ratio (r)

The flow rate increases with b for positive values of the throttle ratio. For r = –0.2 and r = –0.4 the curves are fairly flat and the effect of temperature is slight. At positive values of the throttle ratio the effect of temperature is significant and increases with the throttle ratio. For positive r-values the flow rate increases with b. This means increasing the screw temperature at constant barrel temperature will increase the flow rate. This points to a positive effect of internal screw heating. At constant screw temperature, reducing the barrel temperature will increase the flow rate.

At very high values of factor b the dimensionless flow rate will approach the value of unity. This value corresponds to plug flow. Obviously, this condition will not be reached in real operations.

When the viscosity is temperature independent (b = 0) the flow rate is:

$$\Psi(b = 0) = 0.5\ (1 - r) \tag{7.304}$$

The relative flow rate can be defined at the ratio of $\Psi(b)/\Psi(b = 0)$. Figure 7.72 shows how the relative flow rate varies with b for several values of the throttle ratio.

In Fig. 7.72 all the curves intersect at b = 0 where the relative flow rate equals unity. The curve for r = –0.2 is rather flat. For larger values of r the slope increases and, thus, the effect of temperature. As a result, temperature related extrusion instabili-

ties are more likely to occur at large positive pressure gradients. For positive pressure gradients the temperature sensitivity of the flow rate reduces with b. As a result, increasing the screw temperature relative to the barrel temperature (or reducing the barrel temperature relative to the screw temperature) will not only increase the flow rate but it will also improve extrusion stability.

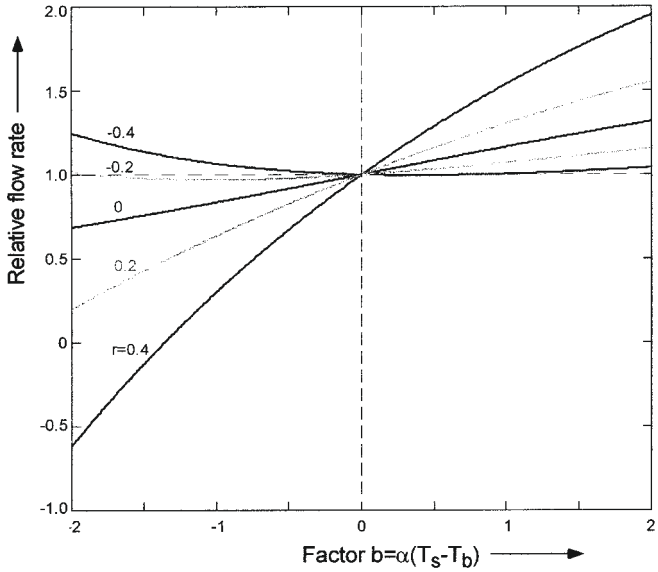


Figure 7.72 Relative flow rate versus b for several values of the throttle ratio r

An approximate solution for the temperature profile can be obtained by inserting Eq. 7.298 for the velocity gradient into the energy equation. This leads to the following expression for the second derivative of the temperature:

$$\Theta'' = A_1 e^{-b\xi}(\xi - \xi_0)^2 \tag{7.305}$$

where A_1 is given by:

$$A_1 = -36r^2 N_{Br} \tag{7.306}$$

The Brinkman number N_{Br} is defined as:

$$N_{Br} = \frac{m(T_s)v^2}{k(T_b - T_s)} \tag{7.307}$$

The temperature profile can be obtained by integrating twice.

$$\Theta(\xi) = A_1 e^{-b\xi}\left[\frac{\xi^2}{b^2} + \left(\frac{4}{b^3} - \frac{2\xi_0}{b^2}\right)\xi + \frac{\xi_0^2}{b^2} + \frac{6}{b^4} - \frac{4\xi_0}{b^3}\right] + A_2\xi + A_3 \tag{7.308}$$

Integration constants A_2 and A_3 can be evaluated from the thermal boundary conditions. The most general thermal boundary conditions are obtained by prescribing the local heat flux with the Biot modulus. The thermal boundary condition at the screw surface can thus be written as:

$$\Theta'(0) = -N_s\Theta(0) \tag{7.309}$$

Similarly, the thermal boundary condition at the barrel surface becomes:

$$\Theta'(1) = N_b[\Theta(1) - 1] \tag{7.310}$$

Integration constant A_3 becomes:

$$A_3 = \frac{-B_3 + B_1 + N_s B_2 + N_b B_4 - N_s N_b B_2 - N_b B_1 - N_b}{-N_b + N_s N_b - N_s} \tag{7.311}$$

and:

$$A_2 = -B_1 - N_s B_2 - N_s A_3 \tag{7.312}$$

where:

$$B_1 = \frac{A_1(2b\xi_0 - 2 - b^2\xi_0^2)}{b^3} \tag{7.313}$$

$$B_2 = \frac{A_1(-4b\xi_0 + 6 + b^2\xi_0^2)}{b^4} \tag{7.314}$$

$$B_3 = \frac{A_1 e^{-b}(-b^2 + 2b^2\xi_0 - 2b + 2b\xi_0 - 2 - b^2\xi_0^2)}{b^3} \tag{7.315}$$

$$B_4 = \frac{A_1 e^{-b}(b^2 + 4b - 2b^2\xi_0 - 4b\xi_0 + 6 + b^2\xi_0^2)}{b^4} \tag{7.316}$$

When the screw surface is isothermal the integration constants become $A_2 = -B_1$ and $A_3 = -B_2$. When the screw is adiabatic and the barrel isothermal the integration constants become $A_2 = -B_1$ and $A_3 = B_1 - B_4 + 1$.

Figure 7.73 shows the dimensionless temperature versus normal distance for several values of the throttle ratio.

The condition $N_s = 0$ corresponds to adiabatic conditions at the screw surface. As a result, the temperature gradient at the screw surface ($\xi = 0$) is zero. The condition $N_b = 1000$ corresponds to almost isothermal conditions at the barrel surface ($\xi = 1$). As a result, the temperature at $\xi = 1$ equals unity for all curves. The screw temperature increases when the throttle ratio reduces as a result of higher shear rates at the screw surface.

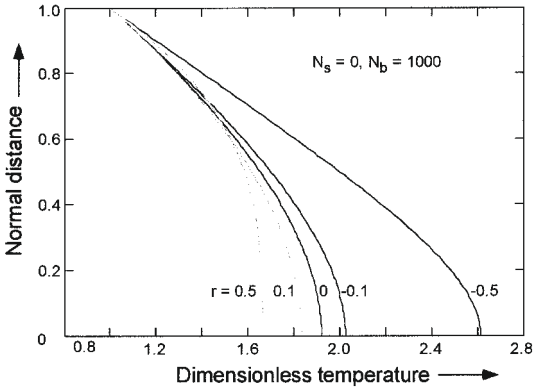


Figure 7.73
Dimensionless temperature versus normal distance with b = 1 and for several values of the throttle ratio (N_s = 0 and N_b = 1000)

The solution for the velocity profile and flow rate is correct as long as the viscous dissipation can be neglected. The solution for the temperature profile is approximate because of the assumption of a linear temperature profile for viscosity determination. If the calculated temperature profile deviates sharply from the linear profile the error in the temperature profile can be significant. This issue will be addressed in the following section.

7.4.3.2 Non-Isothermal Analysis of Power Law Fluids

We will first analyze temperature profiles in pure drag flow of power law fluids with negligible dissipation. This will be followed by an analysis of power law fluids with the effects of dissipation included.

7.4.3.2.1 Power Law Fluid with Negligible Dissipation

The energy equation for pure drag flow can be written as:

$$\frac{d^2\Theta}{d\xi^2} = 0 \tag{7.317}$$

The corresponding velocity profile can be written as:

$$\Phi(\xi) = \frac{1 - e^{-bs\xi}}{1 - e^{-bs}} \tag{7.318}$$

The velocity profile at several values of b is shown in Fig. 7.74. When b > 0 (screw temperature higher than barrel temperature), the velocities increase; when b < 0, the velocities decrease.

The dimensionless flow rate is obtained by integrating $\Phi(\xi)$ from $\xi = 0$ to $\xi = 1$. This leads to:

$$\Psi = \frac{2n - 2b - 2ne^{-bs}}{b(e^{-bs} - 1)} \tag{7.319}$$

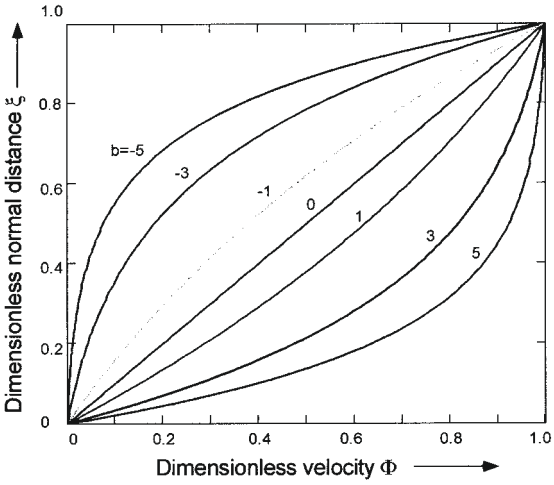


Figure 7.74 Dimensionless velocity versus dimensionless normal distance

Figure 7.75 shows how the relative flow rate changes with b at several values of the power law index.

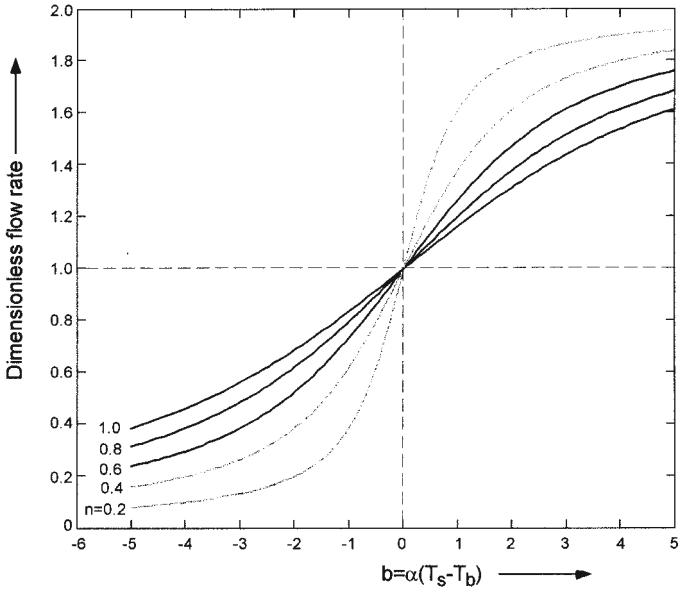


Figure 7.75 Dimensionless flow rate versus term $b = \alpha(T_s - T_b)$

The flow rate increases when b increases. The temperature sensitivity increases when the power law index becomes smaller. This indicates that strongly shear thinning fluids will be more sensitive to temperature fluctuations than weakly shear thinning fluids. Based on the results with Newtonian fluids it can be expected that the sensitivity to temperature fluctuations will get worse with large positive values of the pressure gradient.

7.4.3.2.2 Pure Drag Flow of Power Law Fluid with Dissipation Included

The power law fluid problem in pure drag flow was solved by Gavis and Laurence [302] without the assumption of negligible viscous dissipation. Their analysis was based on parallel plates of equal temperature. Rauwendaal [271] extended this analysis to parallel plates maintained at different temperatures; this analysis will be presented next. The momentum equation for pure drag flow can be integrated to express the shear stress as follows:

$$\tau_{zy} = m\left|\frac{dv_z}{dy}\right|^{n-1}\frac{dv_z}{dy} = \tau_0 \tag{7.320}$$

This expression can be integrated to express the velocity as a function of m. With boundary conditions $v_z(0) = 0$ and $v_z(H) = v$ we obtain:

$$v_z = \tau_0^s \int_0^y m^{-s} dy \tag{7.321}$$

where:

$$\tau_0 = v^n \left(\int_0^H m^{-s} dy \right)^{-n} \tag{7.322}$$

The energy equation for a power law fluid with a fully developed temperature profile can be written as:

$$k\frac{d^2T}{dy^2} + m\left|\frac{dv_z}{dy}\right|^{n-1}\left(\frac{dv_z}{dy}\right)^2 = 0 \tag{7.323}$$

where:

$$m = m_0 e^{\alpha(T_0 - T)} \tag{7.324}$$

The energy equation can now be written as:

$$\frac{d^2T}{dy^2} + \frac{\tau_0^{1+s}}{km_0^s} e^{\alpha s(T-T_0)} = 0 \tag{7.325}$$

With the dimensionless temperature $\Theta_1 = \alpha s(T-T_0)$ and the dimensionless normal coordinate $\xi = y/H$ the energy equation becomes:

$$\Theta_1'' + C_1 e^{\Theta_1} = 0 \tag{7.326}$$

where:

$$C_1 = \frac{\alpha H^2 \tau_0^{1+s}}{nkm_0^s} \tag{7.327}$$

This type of second-order ordinary differential equation can be solved by multiplying the equation by Θ_1'. By integrating each term we obtain:

$$\frac{1}{2}\left(\frac{d\Theta_1}{d\xi}\right)^2 + \int C_1 e^{\Theta_1} d\Theta_1 = \text{constant} \tag{7.328}$$

The first derivative of temperature Θ_1 can thus be written as:

$$\frac{d\Theta_1}{d\xi} = \pm\left[A_0 - 2\int C_1 e^{\Theta_1} d\Theta_1\right]^{0.5} \tag{7.329}$$

This can be rewritten by evaluating the integral:

$$\frac{d\Theta_1}{d\xi} = \pm C\left[A - e^{\Theta_1}\right]^{0.5} \tag{7.330}$$

where:

$$C = \sqrt{2C_1} \tag{7.331}$$

The $\Theta_1(\xi)$ curve has a maximum at $\xi^*(\Theta_1 = \ln A)$. When $T_b > T_s$, the first derivative Θ_1' will be positive when $\xi < \xi^*$ and the plus sign will be used in Eq. 7.330. When $\xi > \xi^*$, the first derivative will be negative and the minus sign must be used in this interval. When $\xi^* > 1$, the solution with the plus sign will be valid over the entire depth of the channel. When $T_s > T_b$, the signs in Eq. 7.330 will be opposite from those used when $T_b > T_s$. When isothermal boundary conditions are used, $\Theta_1(0) = \alpha s(T_s - T_0)$ and $\Theta(1) = \alpha s(T_b - T_0)$. When $T_b > T_s$, Eq. 7.330 can be integrated to give:

$$C\xi = \int_{\Theta_{1s}}^{\ln A} \frac{d\Theta}{\left(A - e^{\Theta}\right)^{0.5}} - \int_{\ln A}^{\Theta_1} \frac{d\Theta}{\left(A - e^{\Theta}\right)^{0.5}} \tag{7.332}$$

Equation 7.332 can also be used when $T_b < T_s$, as long as $\xi^* > 0$. The integrals in Eq. 7.332 can be evaluated by considering that:

$$\int_{x_1}^{x_2} \frac{d\Theta_1}{\left(A - e^{\Theta_1}\right)^{0.5}} = \left[-\frac{2}{\sqrt{A}} \ln\left(\frac{\sqrt{A} + \sqrt{A - e^{\Theta_1}}}{\sqrt{e^{\Theta_1}}}\right)\right]_{x_1}^{x_2} \tag{7.333}$$

By working out the integrals the temperature Θ_1 can be expressed as a function of ξ. After some rearrangement the following expression is obtained:

$$\Theta_1(\xi) = \ln\left[A\left(\frac{Y}{2} + \frac{1}{2Y}\right)^{-2}\right] \tag{7.334}$$

where:

$$Y = \frac{\exp(0.5\Theta_{1s} + 0.5C\sqrt{A}\xi)}{\sqrt{A} + \sqrt{A - \exp\Theta_{1s}}} \tag{7.335}$$

By further rearrangement Eq. 7.334 can be cast in the same form as used by Gavis and Laurence. The temperature thus becomes:

$$\Theta_1(\xi) = \ln\left[A\operatorname{sech}^2(y_1\xi + y_2)\right] \tag{7.336}$$

where:

$$y_1 = 0.5C\sqrt{A} \tag{7.337}$$

and:

$$y_2 = 0.5\Theta_{1s} - \ln\left(\sqrt{A} + \sqrt{A - e^{\Theta_{1s}}}\right) \tag{7.338}$$

The value of integration constant A is evaluated by using thermal boundary condition $\Theta_1(1) = \alpha s(T_b - T_0) = \Theta_{1b}$. Thus, constant A is obtained by solving the following equation:

$$(\sqrt{A} + \sqrt{A - \exp\Theta_{1s}})(\sqrt{A} + \sqrt{A - \exp\Theta_{1b}}) = \exp(\bar{\Theta} + 0.5C\sqrt{A}) \tag{7.339}$$

where:

$$\bar{\Theta} = 0.5\Theta_{1s} + 0.5\Theta_{1b} \tag{7.340}$$

When the wall temperatures are equal such that $\Theta_{1s} = \Theta_{1b} = 0$, Eq. 7.339 reduces to:

$$A = \cosh^2\left(0.25C\sqrt{A}\right) \tag{7.341}$$

In this case y_2 becomes $y_2 = -0.5y_1$ and Eq. 7.336 can be written as:

$$\Theta_1(\xi) = \ln\left[A\operatorname{sech}^2(y_1\xi - 0.5y_1)\right] \tag{7.342}$$

Equations 7.341 and 7.342 are identical to those derived by Gavis and Laurence; they can be considered as describing a special case of the more general problem whose solution is described by Eqs. 7.336 and 7.339.

In order to determine the actual temperature profile from Eq. 7.336, Eq. 7.339 has to be solved first to obtain the value of constant A. Figure 7.76 graphically shows A as a function of C at three values of $\Delta\Theta_1$, where $\Delta\Theta_1$ is the difference in temperature between the moving wall Θ_{1b} and the stationary wall Θ_{1s}.

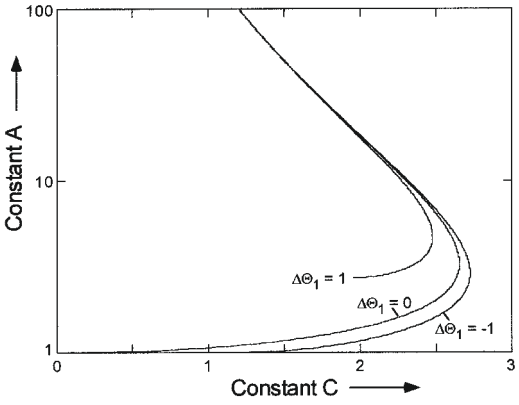


Figure 7.76
Constant C versus constant A for various values of $\Delta\Theta_1$

Below C_{max} there are two values of A for each value of C. The value of C_{max} reduces as $\Delta\Theta_1$ increases. There are no solutions to the problem for $C > C_{max}$. Since C has to be equal to or smaller than C_{max} there is a maximum shear stress that can be determined from the expression for C_1 (Eq. 7.327). The maximum shear stress can be written as:

$$(\tau_0)_{max} = \left[\frac{n\,k\,m_0^s C_{max}^2}{2\alpha H^2}\right]^{\frac{1}{1+s}} \tag{7.343}$$

The maximum shear stress reduces as $\Delta\Theta_1$ increases because the value of C_{max} reduces as shown in Fig. 7.76. It appears that for each value of C below C_{max} there are two solutions for the temperature and velocity profile. However, there is an additional relationship that fixes the actual value of integration constant A. In order to determine this relationship the velocity profile has to be determined first.

7.4.3.2.2.1 Velocity Profile and Flow Rate

The velocity profile can be determined from Eqs. 7.321 and 7.322; it can be written in dimensionless form as follows:

$$\Phi(\xi) = \frac{\int_0^{\xi} e^{\Theta_1} d\xi}{\int_0^1 e^{\Theta_1} d\xi} \tag{7.344}$$

where the dimensionless velocity $\Phi(\xi) = v_z(\xi)/v$.

The flow rate $\dot{V}$ per unit width can be determined from:

$$\dot{V} = vH\int_0^1 \Phi(\xi) d\xi \tag{7.345}$$

Using Eq. 7.334 or 7.336 for the temperature profile the velocity profile can be written as:

$$\Phi(\xi) = \frac{\Phi_1}{e^{-2y_2} + e^{2y_1\xi}} + \Phi_2 \tag{7.346}$$

where:

$$\Phi_1 = \frac{\left(1 + e^{-2y_2}\right)\left(e^{-2y_2} + e^{2y_1}\right)}{1 - e^{2y_1}} \tag{7.347}$$

and:

$$\Phi_2 = \frac{e^{-2y_2} + e^{2y_1}}{e^{2y_1} - 1} \tag{7.348}$$

Using the expression for the velocity profile the flow rate can be determined by integration. This leads to the following expression:

$$\frac{\dot{V}}{vH} = \Phi_2 + \frac{\Phi_1 e^{2y_2}}{2y_1} \ln\left[\frac{e^{2y_1}(1 + e^{-2y_2})}{e^{2y_1} + e^{-2y_2}}\right] \tag{7.349}$$

Up to this point the actual plate velocity has not entered into the picture. By using the plate velocity v the actual value of constant A can be determined. From Eq. 7.321 the integral can be written as:

$$\int_0^1 e^{\Theta_1} d\xi = \left(\frac{m_0}{\tau_0}\right)^s \frac{v}{H} \tag{7.350}$$

Thus the numerator in Eq. 7.344 has to obey the same equality. This leads to the following expression:

$$\frac{m_0^s v}{\tau_0^s H} = \frac{4\sqrt{A}}{C}\left[\frac{1}{1 + e^{2y_2}} - \frac{1}{1 + e^{C\sqrt{A} + 2y_2}}\right] \tag{7.351}$$

By using Eqs. 7.327 and 7.331 the shear stress τ_0 can be expressed as:

$$\tau_0 = \left(\frac{n k m_0^s C^2}{2\alpha H^2}\right)^{\frac{1}{1+s}} \tag{7.352}$$

By rearranging Eq. 7.339 constant C can be expressed as a function of A:

$$C = \frac{-2y_2 - 2y_3}{\sqrt{A}} \tag{7.353}$$

where:

$$y_2 = 0.5\Theta_{1s} - \ln\left(\sqrt{A} + \sqrt{A - e^{\Theta_{1s}}}\right) \tag{7.354}$$

and:

$$y_3 = 0.5\Theta_{1b} - \ln\left(\sqrt{A} + \sqrt{A - e^{\Theta_{1b}}}\right) \tag{7.355}$$

By expressing both C and τ_0 as a function of A and inserting these expressions in Eq. 7.351, an equation for A is obtained that yields a unique solution of A in terms of known variables, i. e., n, k, m_0, α, H, v, Θ_{1s}, and Θ_{1b}. Thus, the equation for A becomes:

$$\left(\frac{N_{Na}}{4n}\right)^s = 2A(-y_2 - y_3)^{s-1}\left[\frac{1}{1+e^{2y_2}} - \frac{1}{1+e^{-2y_3}}\right]^{s+1} \tag{7.356}$$

where N_{Na} is the Nahme number. For a temperature dependent power law fluid this can be expressed as:

$$N_{Na} = \frac{\alpha\, m_0\, v^{n+1}}{kH^{n-1}} \tag{7.357}$$

Equation 7.356 shows that the value of constant A depends on the Nahme number N_{Na}, the power law index n, and wall temperatures Θ_{1s} and Θ_{1b}.

There does not appear to be a general, explicit solution for constant A. Thus, in most cases a numerical scheme has to be used to determine the value of A. A simple solution can be found for the special case of a Newtonian fluid with equal wall temperatures. In this case, A depends only on the Nahme number with the following linear relationship:

$$A = \frac{N_{Na}}{8} + 1 \tag{7.358}$$

The value of constant A is determined from Eq. 7.356 and, thus, a unique solution for the temperature profile, velocity profile, and flow rate is obtained. Figure 7.77 shows the right-hand term of Eq. 7.356 as a function of A at a power law index of n = 0.5 and $\Theta_{1s} = 0$.

Three curves are shown for different values of the dimensionless barrel temperature: $\Theta_{1b} = 0$, $\Theta_{1b} = -1$, and $\Theta_{1b} = +1$. Curves as shown in Fig. 7.77 can be used to find a graphical solution to Eq. 7.356. We will take the following example:

v = 0.2 m/s
H = 0.005 m
α = 0.02 C^{-1}
n = 0.5 (s = 2)
m_0 = 10^4 $N \cdot s^n/m^2$
k = 0.24 N/s·C

The left-hand term of Eq. 7.356 is 6.94; the corresponding value of constant A = 2.9 when $\Theta_{1s} = \Theta_{1b} = 0$. The corresponding maximum temperature $\Theta_1^* = \ln A = 1.07$ and the actual maximum temperature $T^* - T_0 = n\Theta_1^*/\alpha = 26.64°C$. Since $\Theta_{1s} = \Theta_{1b} = 0$ the wall temperatures are $T_s = T_b = T_0$. Thus, the maximum temperature in this case is about 26.6°C above the wall temperatures. Clearly, in this case there is a significant amount of viscous heat generation.

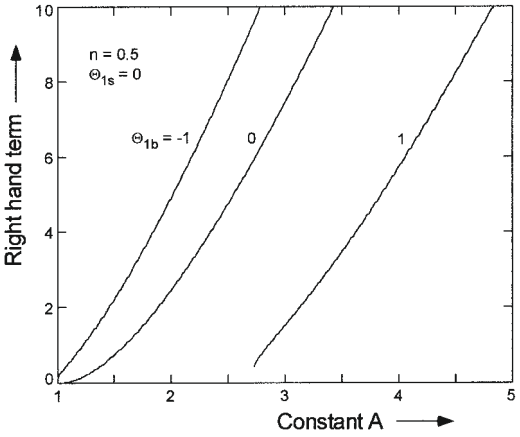


Figure 7.77
Right-hand term of equation Eq. 7.356

When $\Theta_{1s} = 0$ and $\Theta_{1b} = 1$ the value of A = 4.24 as shown in Fig. 7.77. The maximum temperature is $\Theta_1^* = 1.44$ and $T^* - T_0 = 29.83°C$. Thus, a significant increase in the temperature of the moving wall (25°C higher) causes only a small increase in the maximum temperature (about 3°C).

At this point the temperature and corresponding velocity profiles can be determined. Figure 7.78 shows the temperature profile at three values of A for the case of equal plate temperatures.

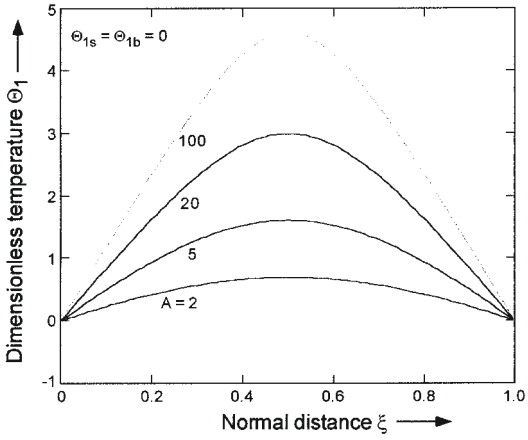


Figure 7.78
Temperature profiles when $\Theta_{1s} = \Theta_{1b} = 0$ at several values of A

The temperature profile is symmetric around the $\xi = 0.5$ axis. The maximum temperature increases with larger values of A. The corresponding velocity profiles are shown in Fig. 7.79.

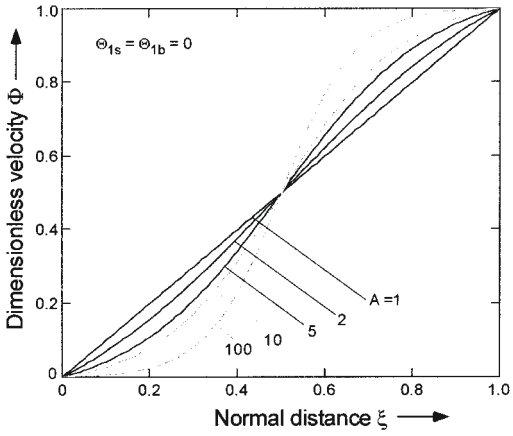


Figure 7.79
Velocity profiles when $\Theta_{1s} = \Theta_{1b} = 0$ at several values of A

In the lower half of the channel ($\xi < 0.5$) the velocities decrease with increasing A, while in the upper half of the channel the velocities increase with A. Since the velocity curves are anti-symmetric the total flow rate does not change with varying A.

When the wall temperatures are different the effect of temperature changes significantly. Figure 7.80 shows the temperature profile at three values of A when $\Theta_{1s} = 0$ and $\Theta_{1b} = 1$.

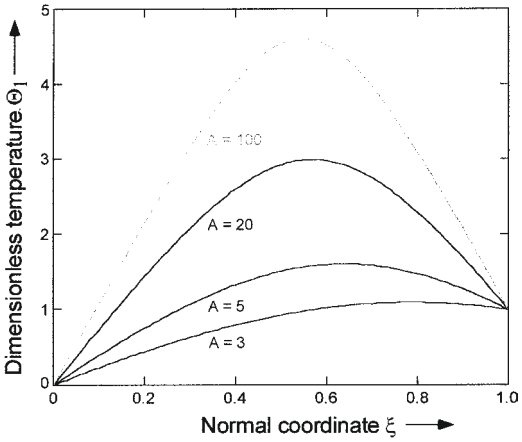


Figure 7.80
Temperature profiles when $\Theta_{1s} = 0$ and $\Theta_{1b} = 1$ at several values of A

The temperature profiles are now no longer symmetric. The maximum temperature still increases with larger values of A. The corresponding velocity profiles are shown in Fig. 7.81.

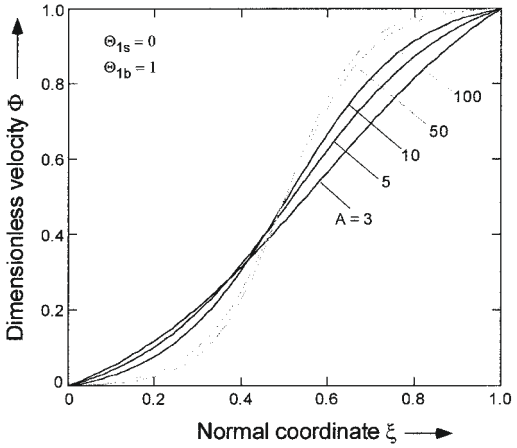


Figure 7.81
Velocity profiles when $\Theta_{1s} = 0$ and $\Theta_{1b} = 1$ at several values of A

The velocities in the lower half of the channel are still reduced with increasing A. However, there is no corresponding increase in the velocities in the upper half of the channel. At low values of A the velocities are decreased throughout the channel, while at higher values of A the velocities in the upper portion are increased relative to the linear velocity profile. As a result, the flow rate is reduced when the barrel temperature is higher than the screw temperature.

Temperature profiles for the case where the screw temperature is higher than the barrel temperature are shown in Fig. 7.82.

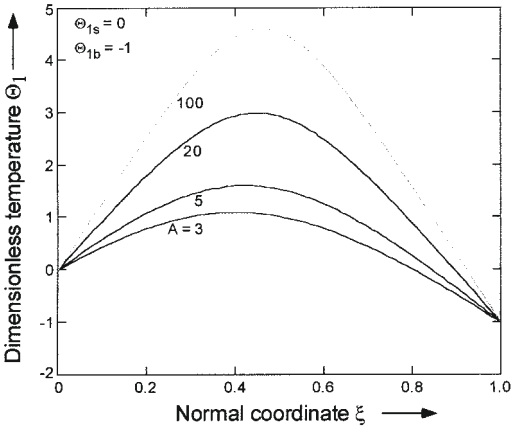


Figure 7.82
Temperature profiles for several values of A when $\Theta_{1s} = 0$ and $\Theta_{1b} = -1$

The corresponding velocity profiles are shown in Fig. 7.83.

When the screw temperature is higher than the barrel temperature the velocities are increased relative to the case with equal wall temperatures. As a result the flow rate increases as the screw temperature is increased relative to the barrel temperature. The effect of applied temperature difference on flow rate is shown in Fig. 7.84.

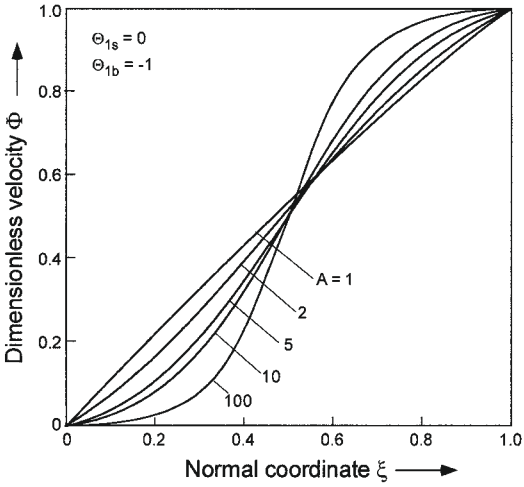


Figure 7.83
Velocity profiles for adiabatic screw at various A values when $\Theta_{1s} = 0$ and $\Theta_{1b} = -1$

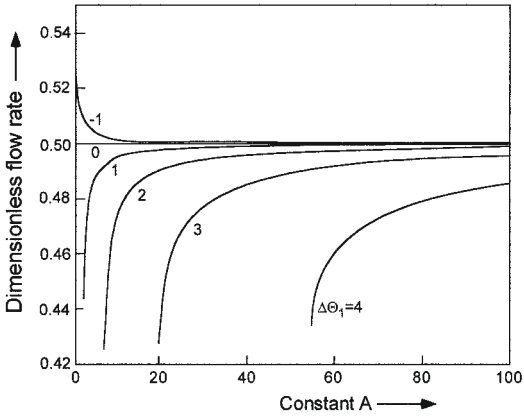


Figure 7.84
Flow rate versus constant A at various values of $\Delta\Theta_1$

The flow rate reduces as $\Delta\Theta_1$ increases, but it increases with the value of A. It is clear from Fig. 7.84 that the temperature difference $\Delta\Theta_1$ can have a significant effect on the flow rate.

The equations presented up to this point are valid when $T_b > T_s$. However, the equations are also valid when $T_b < T_s$ as long as the location of the extremum of the temperature Θ_1^* occurs at $\xi^* > 0$. From Eq. 7.336 it can be determined that the extremum occurs at:

$$\xi^* = \frac{y_2}{y_2 + y_3} \tag{7.359}$$

The extremum occurs at the screw surface when $y_2 = 0$. In this case:

$$A = e^{\Theta_{1s}} \tag{7.360}$$

Thus, the equations presented are valid for cases where $\xi^* \geq 0$ even when $T_b < T_s$. When $\xi^* < 0$, Eq. 7.332 changes to:

$$C\xi = -\int_{\Theta_{1s}}^{\Theta_1} \frac{d\Theta}{\sqrt{A - e^{\Theta}}} \tag{7.361}$$

All subsequent equations remain the same except the equation for y_2. When $\xi^* < 0$ the value of y_2 can be determined from:

$$y_2 = \ln\left(\sqrt{A} + \sqrt{A - e^{\Theta_{1s}}}\right) - 0.5\Theta_{1s} \tag{7.362}$$

7.4.3.2.2.2 Adiabatic Screw and Isothermal Barrel

We will now consider thermal boundary conditions with an adiabatic screw and isothermal barrel. In this case, the thermal boundary condition at the screw surface can be written as:

$$\left.\frac{d\Theta_1}{d\xi}\right|_{\xi=0} = 0 \tag{7.363}$$

When this condition is inserted into Eq. 7.330 we obtain Eq. 7.360. The actual temperature at the screw surface $\Theta_{1s} = \ln A$. Equation 7.332 now becomes:

$$C\xi = -\int_{\ln A}^{\Theta_1} \frac{d\Theta}{\sqrt{A - e^{\Theta}}} \tag{7.364}$$

The temperature profile can now be written as:

$$\Theta = \ln\left[A\,\mathrm{sech}^2(y_1\xi)\right] \tag{7.365}$$

In this case the previously developed expressions for the velocity profile and the flow rate can be used by setting $y_2 = 0$. Temperature profiles for an adiabatic screw and isothermal barrel at various values of A are shown in Fig. 7.85.

The maximum temperature occurs at the screw surface. The maximum temperature increases with A. The corresponding velocity profiles are shown in Fig. 7.86.

The shape of the velocity profiles with one adiabatic wall is considerably different from the shape with two isothermal walls. In the latter case the velocity profile has a typical s-shape while in the former case there is monotonic reduction in the slope of the curves when $A > 1$. The velocities with an adiabatic screw are higher than with an isothermal screw. As a result, the flow rate is increased considerably compared to the isothermal drag flow rate. When $A = 1$ the flow rate equals 0.5; the flow rate increases with the value of A. When A becomes very large, the flow rate approaches unity and the velocity profile approaches plug flow.

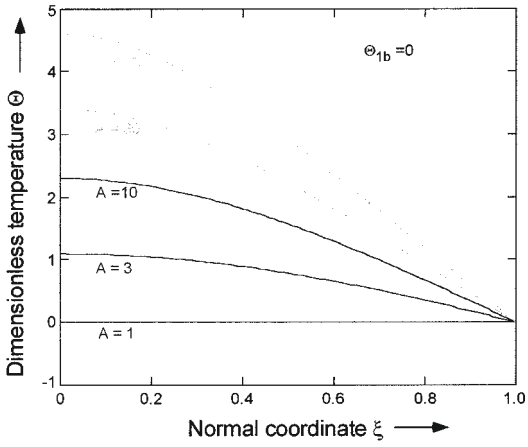


Figure 7.85
Temperature profiles with adiabatic screw for various values of A

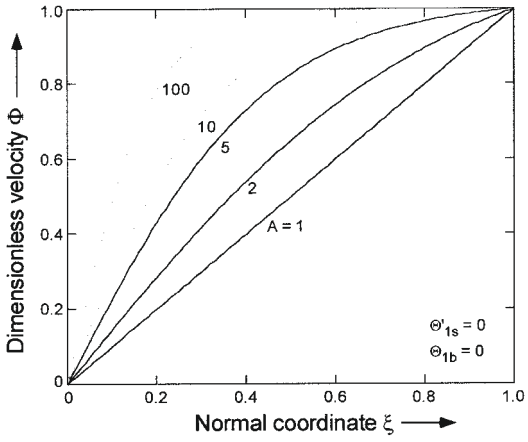


Figure 7.86
Velocity profiles for several values of A

7.4.3.3 Developing Temperatures

In the previous section we analyzed the fully developed temperatures in drag flow with corresponding velocity profiles and flow rates. Non-uniform temperatures can clearly have a significant effect on velocities and flow rates. However, before using expressions for the fully developed temperatures we should investigate whether the temperatures are indeed fully developed. This can be determined from an analysis of developing temperatures in drag flow. This problem was investigated in detail by Rauwendaal [303]; some of the important elements of this analysis will be presented; for details, the reader is referred to the original reference.

The velocity profile for drag flow of a power law fluid between two flat plates can be expressed as:

$$\Phi(\xi) = \frac{\left|\xi - \xi_0\right|^{1+s} - \left|\xi_0\right|^{1+s}}{\left|1 - \xi_0\right|^{1+s} - \left|\xi_0\right|^{1+s}} \tag{7.366}$$

The volumetric flow rate per unit width can be written as:

$$\dot{V} = \frac{vH}{2+s}\left[1-\xi_0 - \frac{(1+s)\left|\xi_0\right|^{1+s}}{\left|1-\xi_0\right|^{1+s} - \left|\xi_0\right|^{1+s}}\right] \tag{7.367}$$

where ξ_0 is the location where the shear stress equals zero and the velocity reaches a extremum; s is the reciprocal power law index, s = 1/n.

The value of ξ_0 is determined by solving:

$$\left|\xi_0\right|^{1+s} - \left|1-\xi_0\right|^{1+s} + \frac{g_*^s}{g_z\left|g_z\right|^{s-1}} = 0 \tag{7.368}$$

where g_z is the pressure gradient, $g_z = dP/dz$, and:

$$g* = \frac{mv^n}{H^{n+1}}(1+s)^n \tag{7.369}$$

The solution to Eq. 7.368 can be found graphically by plotting ξ_0 versus g_*/g_z at various values of the power law index. This is shown in Fig. 7.87.

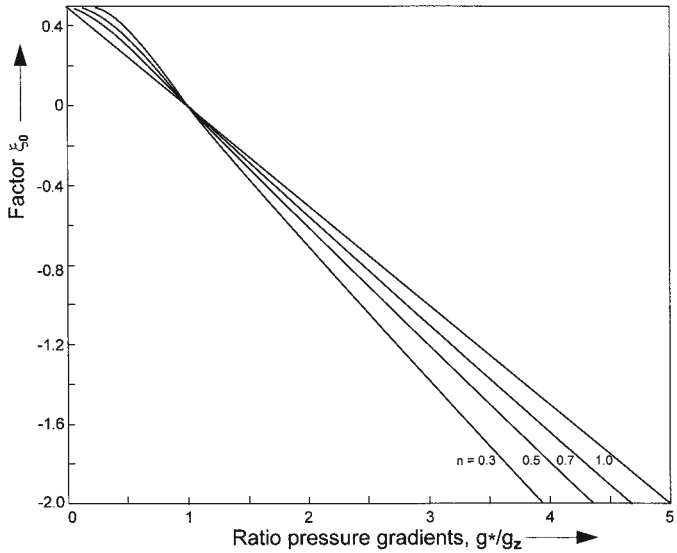


Figure 7.87 Graph of ξ_0 versus g_*/g_z at various values of the power law index

The energy equation can be written in dimensionless form by using dimensionless normal coordinate $\xi = y/H$ and down-channel coordinate $\xi = z/H$; this yields:

$$\Phi N_{Pe}\frac{d\theta}{d\xi} = \frac{\partial^2\theta}{\partial\xi^2} + N_{Br}\left(\frac{d\Phi}{d\xi}\right)^{n+1} \tag{7.370}$$

The Peclet number is given by:

$$N_{Pe} = \frac{vH}{\alpha_d} \tag{7.371}$$

where α_d is the thermal diffusivity of the fluid.

The Brinkman number is given by:

$$N_{Br} = \frac{mv^{n+1}}{k(T_b - T_s)H^{n-1}} \tag{7.372}$$

The fully developed temperature profile can be determined by solving the energy Eq. 7.370 without the first term. Using the general thermal boundary conditions expressed by Eq. 7.309 and 7.310 the fully developed temperature can be written as:

$$\theta_\infty = C_0\left(\left|\xi - \xi_0\right|^{s+3} - \left|\xi_0\right|^{s+3}\right) + C_1\xi + C_2 \tag{7.373}$$

where:

$$C_0 = \frac{-N_{Br}}{(s+2)(s+3)}\left[\frac{1+s}{\left|1-\xi_0\right|^{1+s} - \left|\xi_0\right|^{1+s}}\right]^{n+1} \tag{7.374}$$

$$C_1 = \frac{C_0 N_b N_s\left(\left|1-\xi_0\right|^{s+3} - \left|\xi_0\right|^{s+3}\right) + C_0 N_s(s+3)\left|1-\xi_0\right|^{s+2} - N_b C_0(s+3)\left|\xi_0\right|^{s+2} - N_b N_s}{N_b - N_s N_b - N_s} \tag{7.375}$$

$$C_2 = -\frac{C_0}{N_s}(s+3)\left|\xi_0\right|^{s+2} - \frac{C_1}{N_s} \tag{7.376}$$

The developing temperature profile can be expressed analytically [303]; however, the expressions are rather involved and not easily evaluated. Therefore, the solution will not be presented here. The issue that is of most practical importance is the thermal development length (ζ_{TD}). This is defined as the distance in flow direction over which the difference between the original temperature and the fully developed temperature reduces to one percent of its initial value. The thermal development length depends largely on the Peclet number and the thermal boundary conditions. When the heat flux at the boundaries is greater than zero the thermal development length $\xi_{TD} = 0.2N_{Pe}$; these conditions are the most likely to occur in practice. When isothermal conditions exist at the walls the thermal development length can increase to $\xi_{TD} = 0.24N_{Pe}$.

The thermal development length will depend on the plate velocity, plate separation, and the thermal diffusivity since these variables determine the Peclet number; see Eq. 7.371. Typical values of the Peclet number range from 10^3 to 10^6 due to the low value of the thermal diffusivity. This means that the flow length will often be

insufficient to reach fully developed thermal conditions, particularly when the plate separation is large. This issue will be addressed in more detail in Chapter 12. In practice this means that with large extruders (diameter greater than 100 mm) fully developed thermal conditions are not likely to be reached in the extruder.

When adiabatic conditions occur at the walls (zero heat flux), the thermal development length becomes infinite because the temperatures will continue to rise indefinitely. However, the ultimate shape of the temperature profile (θ_u) for this case can be determined. For pure drag flow (zero pressure gradient) θ_u becomes:

$$\theta_u = N_{Br}\left(\frac{\xi^3}{3} - \frac{\xi^2}{2}\right) \tag{7.377}$$

This temperature profile is shown in Fig. 7.88 at several values of the Brinkman number.

The temperature gradient at the wall is zero. The difference between the wall temperatures increases with the Brinkman number. When the Brinkman number is zero all temperatures are the same because there will be no dissipation. In this case, the thermal development length is zero as well. For non-zero values of the Brinkman number the thermal development length is infinite.

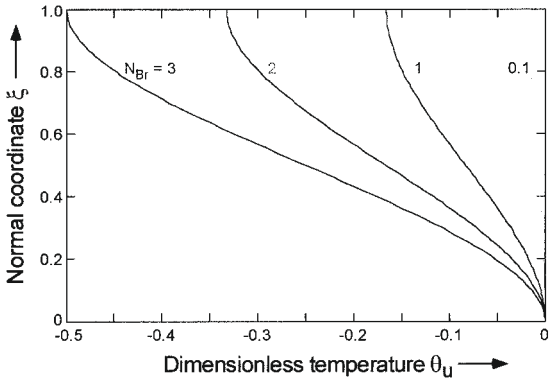


Figure 7.88
Ultimate shape of the temperature profile with adiabatic walls

7.4.3.3.1 Temperature Development in Screw Extruders

Viscous dissipation and the resulting increase in melt temperature are important in most polymer extrusion operations. Existing theories do not allow a simple prediction of temperature development without resorting to numerical techniques. This section describes the development of an analytical theoretical model that allows the calculation of developing melt temperatures in a single screw extruder. The model is based on simplified flow in screw extruders. Initially, we consider only flow in the screw channel and assume the leakage flow through the flight clearance is negligible. The dissipation in the flight clearance is added later.

The polymer melt is considered a power law fluid with a temperature dependent consistency index. We take into account viscous dissipation and heat transfer through the barrel; these are the main factors affecting the melt temperatures. As a result, the analytical results are useful in developing an understanding of the role of the different variables that affect the melt temperature development in the polymer extrusion process. The role of the power dissipated in the flight clearance is briefly discussed and a simple method to include this effect in the temperature calculations is presented. The effect of the flight clearance is significant for polymers that are not strongly shear-thinning and for multi-flighted screws.

7.4.3.3.2 Power Consumption

The viscous dissipation of a power law fluid is determined from the consistency index (m), the shear rate ($\dot{\gamma}$), and the power law index (n). If we neglect the power consumed in the flight clearance the viscous dissipation can be written as:

$$q_s = m\dot{\gamma}^{n+1} = m\left(\frac{\pi DN}{H}\right)^{n+1} \tag{7.378}$$

We will use as an example an extruder screw with an outside diameter (D) of 60 mm, a channel depth (H) of 4 mm, a length (L) of 10 D, and running at a rotational speed (N) of 100 rpm or 1.67 rev/sec. The polymer is a medium viscosity, low density polyethylene with the following properties: the consistency index of the polymer is m = 25,120 Pa·s^n and the power law index n = 0.3 [-]. With these data, the power dissipation becomes q_s = 7,324,273 W/m^3 (7324.3 kW/m^3). This is the specific power consumption per unit volume. The volume between the barrel and the screw can be approximated with:

$$V = \pi DHL \tag{7.379}$$

This means that the actual power consumption can be determined from:

$$Z = \frac{mL(\pi D)^{n+2}N^{n+1}}{H^n} \tag{7.380}$$

With a volume of V = 0.0004524 m^3, the power consumption becomes Z = 3313.5 and W = 3.313 kW. This power consumption will result in an increase in melt temperature, which will be discussed next.

7.4.3.3.3 Temperature Increase

In order to determine the corresponding increase in melt temperature, we need to know the specific heat and the melt density of the polymer. We will take the specific heat C_p = 2300 J/kg°C and the melt density ρ = 750 kg/m^3. The adiabatic temperature rise (no heat transfer at the walls) can be determined as follows:

$$\Delta T_a = \frac{Z}{\rho C_p \dot{V}} = \frac{Z}{C_p \dot{M}} \tag{7.381}$$

where $\dot{V}$ is the volumetric flow rate in axial direction and $\dot{M}$ the mass flow rate. If we have a mass flow rate of 92.7 kg/hr (0.02574 kg/s), then the adiabatic temperature rise is ΔT_a = 55.97°C. This mass flow rate is typical for a 60-mm extruder running at a screw speed of 100 rpm. As a result, we can expect a considerable increase in melt temperature by viscous dissipation over a length of 10 D. Equation 7.381 assumes that the shear rate is determined only by the tangential velocity differences in the extruder screw and that the axial velocity gradients are negligible for the determination of the melt temperature rise. These are generally reasonable assumptions for screw extruders.

The flow rate for screw extruders can be predicted from the following equation:

$$\dot{V} = 0.5(1 - r_t) W H v_{bz} = 0.5(1 - r_t)(\pi D)^2 H N \sin\varphi \cos\varphi \tag{7.382}$$

where r_t is the throttle ratio (pressure flow divided by drag flow) and φ is the flight helix angle.

With Eq. 7.382 we can express the adiabatic temperature rise as follows:

$$\Delta T_a = \frac{2mL}{\rho C_p H (1 - r_t) \sin\varphi \cos\varphi} \left(\frac{\pi D N}{H}\right)^n \tag{7.383}$$

From this equation, the various parameters that influence the temperature rise by viscous dissipation can be clearly distinguished. The temperature rise increases with consistency index (m), the length (L), the screw diameter (D), the screw speed (N), and the power law index (n). The temperature rise reduces with melt density (ρ), the specific heat (C_p), the channel depth (H), the throttle ratio (r_t), and the helix angle (φ).

7.4.3.3.4 Effect of Temperature Dependent Viscosity

The actual rise in melt temperature will generally be less than the values predicted by Eqs. 7.381 and 7.383. One of the reasons for this is that the melt viscosity reduces with increasing temperature. The temperature dependence of the viscosity for a power law fluid can be written as follows:

$$\eta(T) = m_r \exp[a(T_r - T)] \dot{\gamma}^{n-1} \tag{7.384}$$

This means that the consistency index is made to be temperature dependent using an exponential dependence of temperature with a temperature coefficient of a. The consistency index m_r is the value at reference temperature T_r.

7.4.3.3.5 Adiabatic Case [Dissipation without Conductive Heat Transfer]

We can determine the temperature rise over an infinitesimally small axial distance dx. This leads to the following differential equation:

$$\frac{dT}{dx} = B_1 \exp\left[a(T_r - T)\right] \tag{7.385}$$

Constant B_1 can be written as:

$$B_1 = \frac{m_r (\pi D)^{n+2} N^{n+1}}{H^n C_p \dot{M}} \tag{7.386}$$

This differential equation can be solved with the boundary condition $T(x = 0) = T_0$. The temperature as a function of axial distance x can now be written as:

$$T(x) = \frac{1}{a} \ln\left(e^{aT_0} + aB_1 x e^{aT_r}\right) \tag{7.387}$$

If we make the initial temperature T_0 = 190°C equal to the reference temperature and take the temperature coefficient to be a = 0.02°C−1, then the temperature after 10 D becomes T(x = 0.6) = 227.56°C. This means that the adiabatic temperature rise with a temperature dependent viscosity is 37.56°C compared to 55.97°C for a temperature independent viscosity. Therefore, this indicates that temperature dependence of the viscosity results in a significantly lower temperature rise.

Figure 7.89 shows how the melt temperature changes over distance for several values of the temperature coefficient (a). For very low values of "a," the melt temperature increases linearly with distance. This corresponds to the temperature profile for a temperature independent fluid.

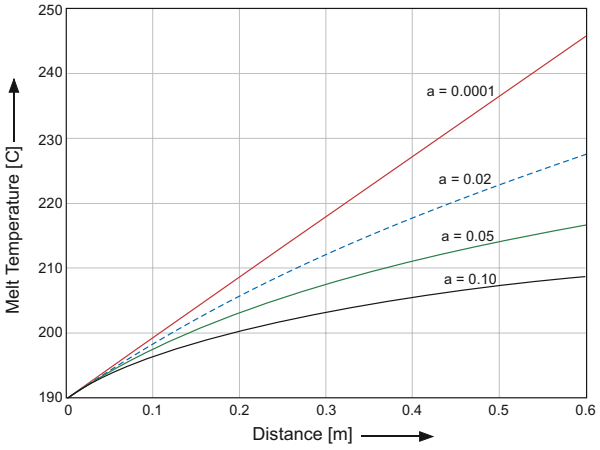


Figure 7.89 Melt temperature vs. distance for several values of temperature coefficient "a"

When the temperature coefficient increases, the melt temperatures reduce. Most semi-crystalline polymers have a temperature coefficient of about 0.02; amorphous polymers generally have a temperature coefficient of about 0.05. Figure 7.89 shows that an increase in the temperature coefficient from 0.02 to 0.05 reduces the temperatures significantly, about 10°C after a length of 10 D.

7.4.3.3.6 Effect of Screw Speed and Throttle Ratio

Figure 7.90 shows how the temperature development is affected by screw speed assuming adiabatic conditions.

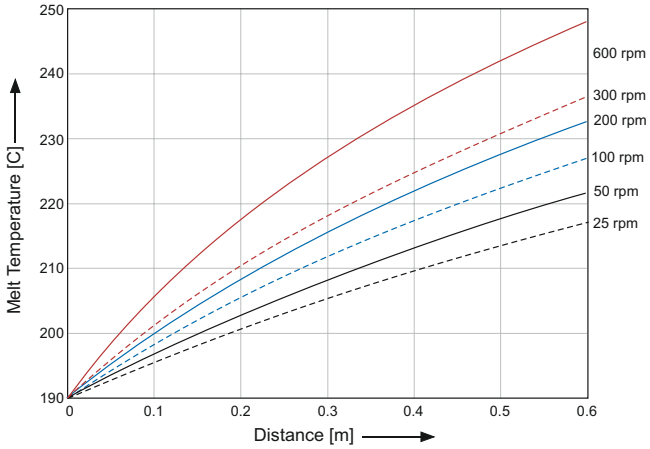


Figure 7.90 Temperature vs. distance for several values of the screw speed

The effect of increasing screw speed diminishes at higher screw speeds. Increasing the screw speed from 25 to 50 rpm increases the final temperature by about 5°C, while an increase from 100 to 200 rpm increases the final temperature about 4°C.

Figure 7.91 shows how the temperature development is affected by the value of the throttle ratio, again assuming adiabatic conditions. The values of the throttle ratio range from –0.5 to +0.5. The last number in the parentheses behind T represents the throttle ratio. For instance, T(x, 0.02, 1.67, –0.5) means temperature (T) as a function of axial distance (x) at a temperature coefficient a = 0.02, a screw speed of N = 1.67 rev/sec, and a throttle ratio of r_t = –0.5. The lowest value of throttle ratio (–0.5) results in the lowest increase in melt temperature. Negative values of the throttle ratio correspond to a negative axial pressure gradient, and a mass flow rate that is higher than the drag flow rate. Higher mass flow rates result in shorter residence times and, thus, also in lower melt temperatures. When the polymer melt is exposed to a certain shear rate for a shorter time the resulting increase in melt temperature is reduced.

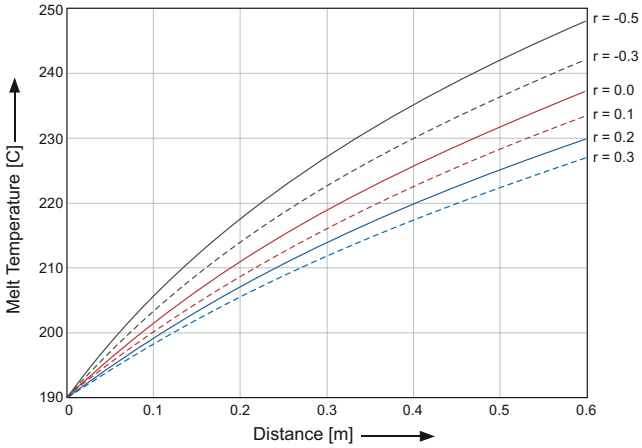


Figure 7.91 Temperature vs. distance for several values of the throttle ratio

When the throttle ratio is zero, the mass flow rate equals the drag flow rate; in this case the axial pressure gradient is zero. When the throttle ratio is positive, the axial pressure gradient is positive and the mass flow rate is less than the drag flow rate. This results in longer residence times and higher melt temperatures.

Figure 7.92 shows how the adiabatic temperature development is affected by the value of the throttle ratio and the screw speed. The top curve is actually two curves almost completely overlapping. One curve corresponds to a screw speed of 1.67 rev/sec (100 rpm) and a throttle ratio of 0.4, while the other curve corresponds to a screw speed of 9.3 rev/sec (558 rpm) and a throttle ratio of 0. The bottom curve is also two curves that are almost completely overlapping. One curve corresponds to a screw speed of 1.67 rev/sec (100 rpm) and a throttle ratio of –0.5, and the other curve corresponds to a screw speed of 0.42 rev/sec (25 rpm) and a throttle ratio of 0.

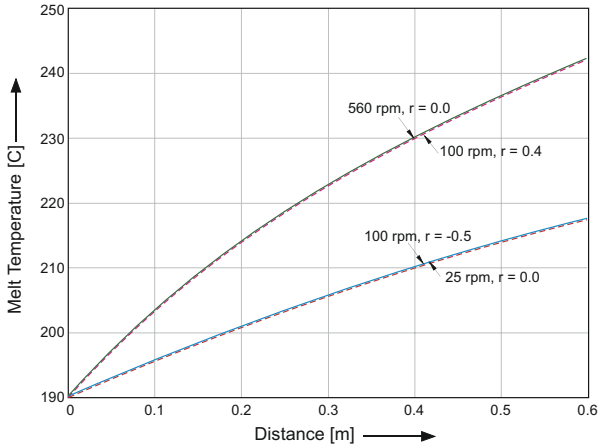


Figure 7.92 Temperature vs. distance for different values of screw speed and throttle ratio

These two sets of curves indicate that an increase in screw speed can be offset by a reduction in the throttle ratio. The throttle ratio is determined by the inlet and outlet pressure of the melt conveying zone. It is clear, therefore, that reducing barrel pressure will reduce polymer melt temperature. This can be achieved by using a less restrictive screen pack, a less restrictive extrusion die, higher die temperatures, or by using a melt pump to generate most of the diehead pressure.

7.4.3.3.7 Conductive Heat Transfer without Dissipation

We can also determine the temperature development for the case of zero viscous dissipation and non-zero conductive heat transfer. If the heat flux is determined by the temperature difference between the melt temperature, T, and the barrel coolant temperature, T_c, at distance h away from the barrel I.D., the heat flux can be written as

$$q_c = k_b \frac{T - T_c}{h} \tag{7.388}$$

where k_b is the thermal conductivity of the barrel.

The temperature gradient resulting from heat conduction can be expressed as follows:

$$\frac{dT}{dx} = -\frac{k\left(T - T_c\right)\pi D}{hC_p\dot{M}} = -A_2(T - T_c) \tag{7.389}$$

With boundary condition $T(x = 0) = T_0$ the change in melt temperature resulting from conductive heat transfer can be written:

$$\Delta T_c(x) = (T_0 - T_c)(e^{-A_2 x} - 1) \tag{7.390}$$

Equation 7.390 is useful for cases where the conductive heat transfer is important and the viscous heat generation negligible. In most realistic polymer extrusion operations, both the viscous dissipation and the heat conduction are important. The combined effect of these factors will be discussed next.

7.4.3.3.8 Temperature Development with Dissipation and Conduction

Equation 7.387 applies only to temperature development with viscous dissipation under adiabatic conditions, that is, without heat transfer through the barrel or the screw. In reality, however, there will be conductive heat transfer through the barrel. If the heat transfer through the barrel is constant, the temperature gradient is determined by both viscous dissipation and conduction. In this case, the temperature gradient can be expressed as:

$$\frac{dT}{dx} = B_1 e^{a(T_r - T)} - B_2 \tag{7.391}$$

Constant B_1 is given by Eq. 7.386; constant B_2 is given by:

$$B_2 = \frac{q_c \pi D}{C_p \dot{M}} \tag{7.392}$$

The units of B_1 and B_2 are [°C/m]; these are units of temperature gradient. Constant B_1 represents the contribution of viscous heating, and constant B_2 represents the contribution of conductive heat transfer. Variable q_c is the heat flux through the barrel wall. Subject to boundary condition $T(x = 0) = T_0$ the differential equation can be solved. The solution can be written as:

$$T(x) = \frac{1}{a} \ln \left[\left(e^{aT_0} - \frac{B_1}{B_2} e^{aT_r} \right) e^{-aB_2 x} + \frac{B_1}{B_2} e^{aT_r} \right] \tag{7.393}$$

For very small values of B_2, the results of Eq. 7.393 become the same as the results of Eq. 7.387. As such, Eq. 7.393 is a more general description of the developing temperature than Eq. 7.387.

Equation 7.393 allows determination of the thermal development length, x_{fd}. This is the axial distance necessary for the temperature to reach fully developed conditions, i. e., the temperature no longer changes with distance. Since the temperature gradient generally does not reach a zero value until x reaches infinity, it is more practical to define a thermal development length based on the distance at which the temperature gradient falls below a certain value B_0. We can set the value of this limiting temperature gradient at $B_0 = 10$[°C/m]. The fully developed temperature can be determined from Eq. 7.390 as follows:

$$B_0 = B_1 e^{a(T_r - T)} - B_2 \tag{7.394}$$

This leads to the following equation for the fully developed temperature:

$$T_{fd} = T_r - \frac{1}{a} \ln \frac{B_0 + B_2}{B_1} \tag{7.395}$$

When we insert this value of the temperature into Eq. 7.393, we can determine the thermal development length; this can be written as:

$$x_{fd} = -\frac{1}{aB_2} \ln \left[\left(\frac{B_0 B_1}{B_0 + B_2} \right) \left(\frac{e^{aT_r}}{B_1 e^{aT_r} - B_2 e^{aT_0}} \right) \right] \tag{7.396}$$

Equations for the fully developed temperature were developed by Rauwendaal [326]. However, Eq. 7.395 yields more accurate results because it takes into account the temperature dependence of the viscosity as well as the shear thinning behavior of the polymer melt.

7.4.3.3.9 Temperature Profiles with Dissipation and Conduction

With Eqs. 7.391 through 7.396, we can evaluate the combined effect of conduction and viscous dissipation on the temperature development. Figure 7.93 shows the temperature profiles for different screw speeds (0.42, 0.83, 1.67, 3.34, 5.00, and 10.00 rev/sec) with a heat flux of –10,000 W/m^2. The results of Fig. 7.93 can be compared to those of Fig. 7.91, which does not include the effect of conduction.

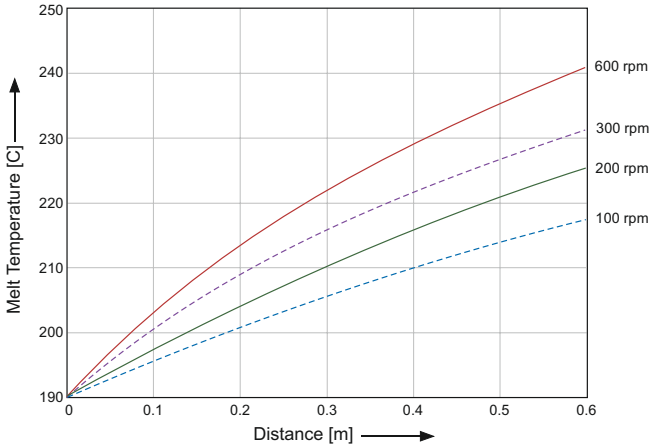


Figure 7.93 Temperature profiles at different screw speeds with heat flux of –10,000 W/m^2

Comparison of Figs. 7.91 and 7.93 shows that the melt temperatures reduce when conduction is taken into account and the heat flux is negative (i. e., the melt is cooled). The reduction in melt temperature is small for high screw speed. However, the reduction in temperature becomes significant at lower screw speed. At 100 rpm with a heat flux of –10,000 W/m^2, the melt temperature drops about 14°C to about 214°C.

Figure 7.94 shows the temperature profiles at three different screw speeds with and without conduction; the heat flux is –10,000 W/m^2. At a screw speed of 10 rev/sec (600 rpm), the temperature drops about 2°C after a distance of 10 D. At a screw speed of 3.34 rev/sec (200 rpm), the melt temperature drops about 6.5°C; at 0.83 rev/sec (50 rpm) the melt temperature drops about 27°C. Clearly, at low screw speeds, the melt temperature can be affected significantly by conduction through the barrel. The reason for the large effect of barrel cooling at low screw speed is because the residence time of the polymer increases with reducing screw speed. As a result, more time is available to remove heat from the polymer melt at low screw speed.

The thermal development length is plotted against screw speed in Fig. 7.95 at several values of the temperature coefficient. The heat flux at the barrel is set at –10,000 W/m^2 and the value of B_0 is set at 10°C/m. This figure clearly shows that the thermal development length reduces with increasing values of the temperature coefficient. This is to be expected because increasing values of the temperature coefficient reduce the amount of viscous dissipation when the temperature goes up.

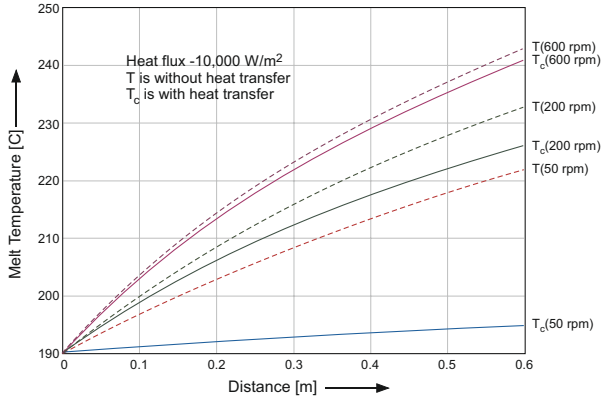


Figure 7.94 Temperature profiles at different screw speeds, with and without heat transfer. T is the temperature without heat transfer and T_c is the temperature with heat transfer

For the case shown in Fig. 7.95 the thermal development length becomes longer than the typical metering section of an extruder when the screw speed is greater than about 1 rev/sec (60 rpm). This means that at high screw speeds it cannot be expected that the melt temperatures become fully developed within the length of the extruder.

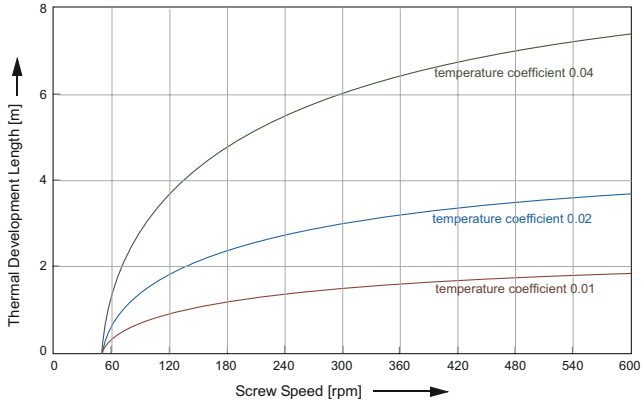


Figure 7.95 Thermal development length vs. screw speed

Figure 7.95 shows that the thermal development length becomes zero at a screw speed of about 0.7 rev/sec. It is evident from Eq. 7.396 that the thermal development length is zero when $B_1 = (B_2 + B_0)\exp[a(T_0 - T_r)]$. From this relationship, we can determine the screw speed at which the thermal development length becomes zero.

$$N_0 = \left[\frac{\dot{M} C_p H^n}{m_r (\pi D)^{n+2}} \left(B_0 + \frac{q_c \pi D}{C_p \dot{M}} \right) e^{a(T_0 - T_r)} \right]^{\frac{1}{n+1}} \tag{7.397}$$

When B_0 is taken as zero, Eq. 7.397 represents the screw speed at which the viscous dissipation equals the heat transfer. At this critical screw speed, the melt temperature does not change at all along the length of the extruder screw. This critical value of the screw speed is not dependent on the mass flow rate and specific heat; it can be written as follows:

$$N_{crit} = \left[\frac{q_c H^n e^{a(T_0 - T_r)}}{m_r (\pi D)^{n+1}} \right]^{\frac{1}{n+1}} \tag{7.398}$$

Thus, the critical screw speed depends on the heat flux, channel depth, temperature coefficient, initial melt temperature, reference temperature, consistency index, screw diameter, and power law index. The critical screw speed increases with the heat flux and channel depth, and reduces with the power law index, consistency index, and screw diameter. The effect of the power law index is shown in Fig. 7.96.

Even relatively small increases in the power law index, e. g., from 0.3 to 0.5, can reduce the critical screw speed significantly. This indicates that small increases in the power law index can cause significant increases in viscous heating and melt temperature. This is known in practice when we consider the extrusion characteristics of LLDPE relative to LDPE [325]. The power law index of LLDPE is considerably higher than that of LDPE. As a result, LLDPE tends to have more power consumption, higher melt temperatures, higher diehead pressures, and is more susceptible to melt fracture.

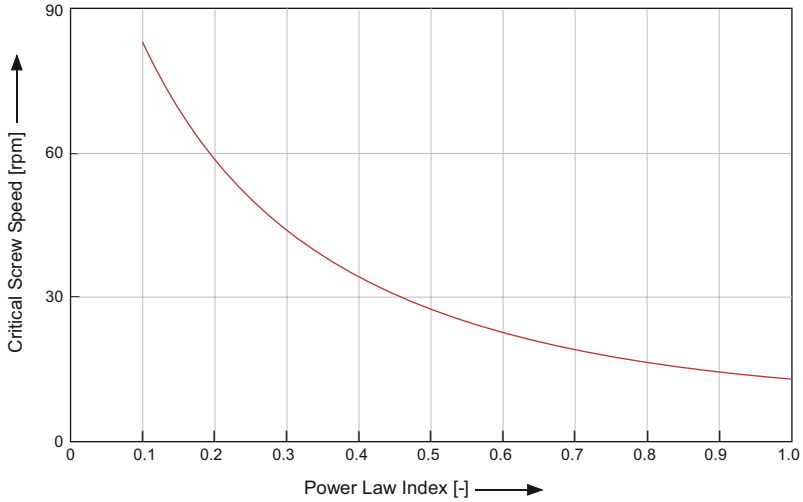


Figure 7.96 Critical screw speed vs. power law index for heat flux of 10,000 W/m^2

Equation 7.398 can be rewritten to determine the critical heat flux that is necessary to carry away the heat generated by viscous dissipation. This critical heat flux can be written as follows:

$$q_{c-crit} = \frac{m_r (\pi DN)^{n+1}}{H^n e^{a(T_0 - T_r)}} \tag{7.399}$$

This equation indicates that the amount of cooling necessary to maintain constant melt temperature increases with the consistency index, screw diameter, screw speed, and power law index. The critical heat flux reduces with increasing channel depth and temperature coefficient. Equation 7.399 provides a practical tool to determine the cooling capacity required to remove the amount of heat generated by viscous dissipation.

7.4.3.3.10 Comparison to Numerical Calculations

To compare the results of the analytical solutions to numerical calculations, several simulations were performed with a 60-mm square pitch extruder screw using the Compuplast Flow 2000 simulation software. Figure 7.97 shows the increase in melt temperature over the length of a 10 D long screw with an O.D. of 60 mm and a channel depth of 4 mm. The polymer melt flow properties are the same as used in the earlier example. The temperature field is shown as a color contour plot.

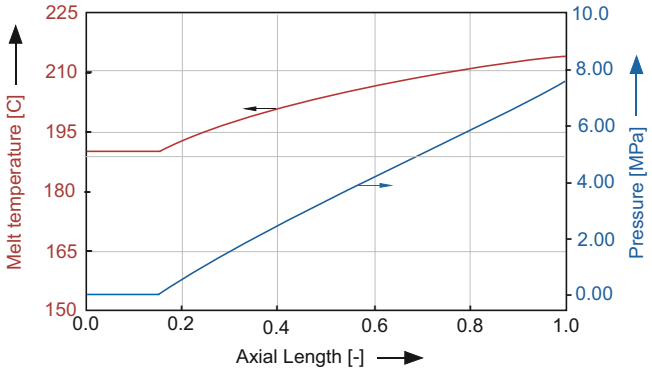


Figure 7.97 Melt temperature field for 60-mm extruder at 100 rpm

Figure 7.97 shows that the increase in melt temperature is about 24°C. The adiabatic temperature rise (Eq. 7.387) is about 37°C. The difference between these two values is largely due to the fact that the numerical predictions include heat transfer to the barrel. The heat flux (q_c) calculated in the numerical simulation is about $q_c = -10{,}000$ W/m^2. Considering that the total heat transfer area (πDL) is 0.113 m^2 the total heat loss is about 1130 W. We can relate this heat loss with a reduction in melt temperature by conductive heat transfer.

$$\Delta T_c = \frac{q_c \pi DL}{C_p \dot{M}} \tag{7.400}$$

The reduction in melt temperature from this heat loss is about 19°C. This explains to a large extent the difference in predicted melt temperatures seen when comparing the analytical solution to the numerical solution.

The temperature rise with dissipation and heat conduction (Eq. 7.393) is about 23°C with a heat flux of –10,000 W/m^2; see Fig. 7.93 with screw speed of 1.67 rev/sec (100 rpm). These results compare favorably to the numerical results; thus, the analytical solutions correspond closely to the numerical calculations.

Figure 7.98 shows the numerical predictions of melt temperature and pressure along the length of the extruder as a simple line graph. This graph can be compared to Fig. 7.93; it shows that the predicted temperature profiles exhibit a pattern similar to that shown in Fig. 7.98. This indicates that the analytical equations appear to yield reasonable results.

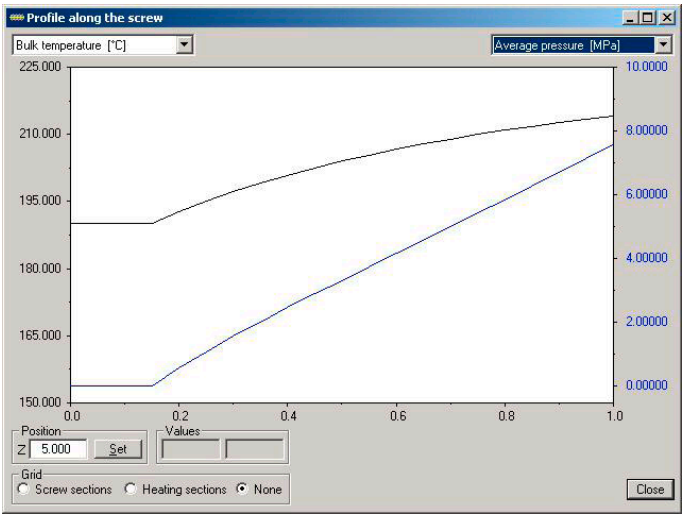


Figure 7.98 Melt temperature and pressure profiles along the length of the extruder

The heat flux may not be constant along the length of the extruder. In this case, the temperature profiles in different sections of the extruder may have to be determined separately to take into account different heat fluxes in different parts of the extruder. The same is true if the screw geometry changes along the length of the melt conveying part of the screw.

7.4.3.3.11 Discussion

The equations derived in this section allow a realistic calculation of developing melt temperatures along an extruder screw. Many authors have studied developing melt temperatures [327–329]; however, closed-form analytical solutions as presented in this section have not been published before. Most realistic calculations of developing melt temperatures in screw extruders require numerical analysis. For instance,

Derezinski solved the problem numerically with the barrel temperature as the boundary condition and a power law viscosity [337]. Later the analysis was extended to include a Carreau-Yasuda viscosity model [338].

Heat transfer through extruder barrels has been discussed by a number of authors as well [330–334]. The equations developed here allow determination of axial temperature profiles if the heat transfer rate through the barrel is known. With good instrumentation on an extruder, it is possible to determine the amount of heat removed through the barrel.

It should be noted that the melt temperatures calculated in this section represent the bulk average temperature at a certain axial location along the extruder screw. At a certain cross-section, the melt temperatures will vary in both radial and circumferential directions. In order to predict both the axial and the cross-sectional temperature profiles, a 3-D analysis has to be performed [335]. Such analyses invariably require numerical techniques to solve the pertinent equations.

The analysis as developed to this point assumes that the effect of flight clearance is negligible. This assumption is not unreasonable for the prediction of melt temperature as long as the flight clearance is small so that the flight provides an efficient wiping action [336]. However, this assumption is less reasonable for the prediction of power consumption (Eq. 7.380) because a significant amount of power can be dissipated in the flight clearance. This is particularly true for polymers with relatively high values of the power law index, i. e., weakly shear thinning materials.

Equation 7.380 can be expanded to take into account the power dissipated in the flight clearance. This leads to the following equation:

$$Z = Z_c + Z_f \tag{7.401}$$

where the power consumed in the channel is as follows:

$$Z_c = \frac{mL_c(\pi D)^{n+2}N^{n+1}}{H^n} \tag{7.402}$$

and the power consumed in the flight clearance is given by:

$$Z_f = \frac{mL_f(\pi D)^{n+2}N^{n+1}}{\delta^n} \tag{7.403}$$

where δ is the radial flight clearance, L_c the axial channel length, and L_f the axial flight length.

Equations 7.401 through 7.403 allow a more realistic calculation of the power consumption. The melt temperature rise in the flight clearance is generally small because the heat is effectively conducted away due to the fact that the clearance

melt film thickness is very small compared to the channel depth [336]. With Eqs. 7.401 through 7.403, the total power consumption can be written as follows:

$$Z = m(\pi D)^{n+2} N^{n+1} \frac{L_c}{H^n}\left(1 + \frac{L_f}{L_c}\frac{H^n}{\delta^n}\right) \tag{7.404}$$

Usually the axial flight length is about one-tenth of the channel length ($L_f = 0.1\ L_c$) and the flight clearance is about 2% of the channel depth ($\delta = 0.02\ H$). With these numbers, the power consumed in the flight clearance is about 30% of the power consumed in the channel when n = 0.3, about 70% when n = 0.5, and about 150% when n = 0.7. Clearly, for values of the power law index over 0.3, the power consumption in the clearance cannot be neglected in most cases. For multi-flighted screws, the power consumed in the flight clearance is even more significant and certainly not negligible.

The bracketed term on the right-hand side of Eq. 7.404 can be used to as a correction term in Eqs. 7.381 through 7.400 to incorporate the effect of the power dissipated in the flight clearance. Obviously, for polymers with a relatively large value of the power law index, the correction can be significant.

7.4.3.3.11.1 Conclusions

This section describes the derivation of analytical equations of developing melt temperatures in screw extruders. The analytical equations for temperature as a function of axial distance are useful in predicting axial melt temperature profiles. The advantage of analytical equations is that the factors influencing temperature development can be easily identified and their effect determined in a quantitative fashion. Both the temperature and shear rate dependence of the viscosity strongly affect the developing temperatures in the extruder.

The analytical predictions compare well to numerical predictions. This indicates that the analytical equations can be useful in the analysis of melt temperature development in single screw extruders. The results indicate that the melt temperatures can become fully developed if the heat flux through the barrel is substantial and if the screw speed is not too high. When the screw speed is high and the consistency index large it is not likely that the melt temperatures will be fully developed at the discharge end; this is particularly true for large diameter extruders.

7.4.3.4 Estimating Fully Developed Melt Temperatures

It is very useful to be able to predict melt temperature in extrusion, particularly in the extrusion of temperature sensitive polymers. Examples are extrusion of crosslinkable polymers, foamed polymers, and polymers that are susceptible to degradation. Unfortunately, the proper calculation of melt temperature is rather involved and requires the use of numerical techniques, the most popular being finite element analysis.

In this section we will describe a method to predict the fully developed melt temperature in screw extruders based on simple analytical expressions. The method is easy to use and leads to quantitative results with a minimum of time expenditure.

7.4.3.4.1 Melt Temperature Calculation

The fully developed melt temperature is reached when the viscous heat generation is balanced by the heat flux away from the polymer melt. The viscous dissipation in the extruder will cause an increase in melt temperature resulting in reduced viscosity, which will result in a reduction in viscous dissipation. The melt temperature will reach a steady state value when the viscous dissipation has reduced to the point that it equals the heat flux from the polymer melt.

The viscous dissipation is determined by the product of shear stress and shear rate. The average shear rate in the screw channel can be approximated by the Couette shear rate:

$$\dot{\gamma} = \frac{\pi D N}{H} \tag{7.405}$$

where D is the barrel diameter, N the screw rotational speed, and H the depth of the screw channel.

If the melt viscosity is described with a power law equation, the viscous dissipation can be written as:

$$q_v = m\,\dot{\gamma}^{1+n} = m\left(\frac{\pi D N}{H}\right)^{1+n} \tag{7.406}$$

where m is the consistency index and n the power law index of the polymer melt.

The consistency index is a function of melt temperature. The temperature dependence of the consistency index can be written as:

$$m(T) = m_0 \exp\left[\alpha_T (T_0 - T)\right] \tag{7.407}$$

where T is the temperature, T_0 the reference temperature, m_0 the consistency index at temperature T_0, and α_T the temperature coefficient of the viscosity. The viscous dissipation can thus be written as:

$$q_v = m_0 \exp\left[\alpha_T (T_0 - T)\right]\left(\frac{\pi D N}{H}\right)^{1+n} \tag{7.408}$$

The viscous dissipation is a specific power consumption, i. e., power per unit volume. In S. I. units it is expressed in Watts per cubic meter [W/m^3]. The heat flux away from the polymer melt is determined by the heat flux from the melt to the barrel and screw. If the screw is neutral the heat flux to the screw is usually small and can be assumed to be negligible. If screw cooling is used, this assumption will not be correct. The heat flux (heat flow per unit cross-sectional area) for cooling the polymer melt is determined by Fourier's law of conductive heat transport:

$$q_c = -k_b \frac{\partial T}{\partial r} \tag{7.409}$$

Where k_b is the thermal conductivity of the barrel, $\partial T/\partial r_b$ is the temperature gradient in the barrel at the polymer/metal interface. If q_c occurs over unit length, then q_c represents the power per unit volume. Thus, if q_c is divided by the thickness, t, over which the heat conduction occurs, it attains the units of specific power, just as q_v.

In many cases, the temperature at the inside and outside barrel surfaces will not be known. In those situations we have to find another method to determine the heat flux through the barrel. This issue was studied Radovich [277] who compared the cooling capability of air- and water-cooled extruder barrels.

The melt temperature will rise initially and then level off as the viscous dissipation reduces with increasing melt temperature. When a steady state is achieved, the melt temperature no longer changes along the length of the extruder. This is called the fully developed melt temperature or equilibrium melt temperature. This temperature T_e can be determined from a simple energy balance equating the viscous dissipation to the conductive heat loss:

$$m_0 \exp\left[\alpha_T (T_0 - T_e)\right]\left(\frac{\pi D N}{H}\right)^{1+n} = k_b \frac{T_{bo} - T_{bi}}{t_b^2} \tag{7.410}$$

where T_{bi} is the inside barrel temperature, T_{bo} the outside barrel temperature, and t_b the thickness of the barrel.

This equation leads to the following expression for the fully developed melt temperature:

$$T_e = T_0 - \frac{1}{\alpha_T} \ln\left(\frac{q_c}{q_{v0}}\right) \tag{7.411}$$

where q_c is given by Eq. 409 and q_{v0} is the viscous dissipation in the polymer melt at the reference temperature T_0; it can be written as:

$$q_{v0} = m_0 \dot{\gamma}^{1+n} \tag{7.412}$$

We now have a quantitative, analytical expression from which the fully developed temperature can be calculated. If we define the equilibrium melt temperature rise ΔT_e as the difference between the reference temperature and the fully developed temperature, $\Delta T_e = T_e - T_0$, we can write:

$$\Delta T_e = -\frac{1}{\alpha_T} \ln\left(\frac{q_c}{q_{v0}}\right) \tag{7.413}$$

When $q_c > q_{v0}$ the equilibrium melt temperature rise will be negative; when $q_c < q_{v0}$ the equilibrium melt temperature rise will be positive. Equation 7.413 provides a simple and convenient expression from which the effect of the various factors influencing the melt temperature becomes clear. These effects can be easily quantified as discussed next.

7.4.3.4.2 Influence of Important Parameters

There are several factors that affect the melt temperature. They can be categorized in three main categories:

- *Material properties:* barrel thermal conductivity, melt consistency index, power law index, and temperature coefficient of the melt viscosity
- *Operational parameters:* screw speed and barrel temperature difference
- *Machine design parameters:* barrel diameter, barrel thickness, and channel depth

The effect of the various parameters is shown qualitatively in the following table.

Table 7.1 The Effect of Various Parameters on Equilibrium Melt Temperature Rise

	$k_b\uparrow$	$m\uparrow$	$n\uparrow$	$\alpha_T\uparrow$	$N\uparrow$	$T_b\uparrow$	$D\uparrow$	$t_b\uparrow$	$H\uparrow$
ΔT_e	↓	↑	↑	↓	↑	↓	↑	↑	↓

As shown in Table 7.1, an increase in the thermal conductivity of the barrel material reduces the melt temperature. Considering that the thermal conductivity of various metals varies substantially, it makes sense to consider using a highly conductive barrel material if low melt temperatures are required. The thermal conductivity of various metals is shown in Table 7.2. Corrosion-resistant metals tend to have a low conductivity, while copper-containing alloys have a conductivity about three to five times higher than carbon steel.

An increase in the consistency index will increase melt temperatures because the viscous dissipation will increase; see Eqs. 7.406 and 7.408. The numeric value of the consistency index is the same as the viscosity at shear rate one ($\dot{\gamma} = 1$) for a power law fluid. The consistency index, therefore, is closely related to the melt index (MI). A low melt index indicates a high value of the consistency index. Clearly, it will be much more difficult to control melt temperature for a low MI material than for a

high MI material. Figure 7.99 shows a graph of the equilibrium melt temperature rise versus consistency index for two values of the cooling flux (q_c = 10,000 W/m^3 and q_c = 100,000 W/m^3) and the coefficient of viscosity α_T = 0.02 [K^{-1}].

Table 7.2 Thermal Conductivity of Various Metals

	Thermal conductivity	
Material	**[W/m°K]**	**[BTU ft/ft²hr°F]**
Hastelloy C276	11.25	6.5
Inconel 718	11.42	6.6
Inconel 625	9.86	5.7
Monel 400	21.80	12.6
Monel 500	17.47	10.1
4140 steel	42.56	24.6
4340 steel	42.21	24.4
17–4 stainless	17.82	10.3
316 stainless	16.09	9.3
304 stainless	16.29	9.4
AlZnMgCu	160	92.5
CuBe-2	115	66.5
CuCoBe	210	122.4
Z 434	105	60.7

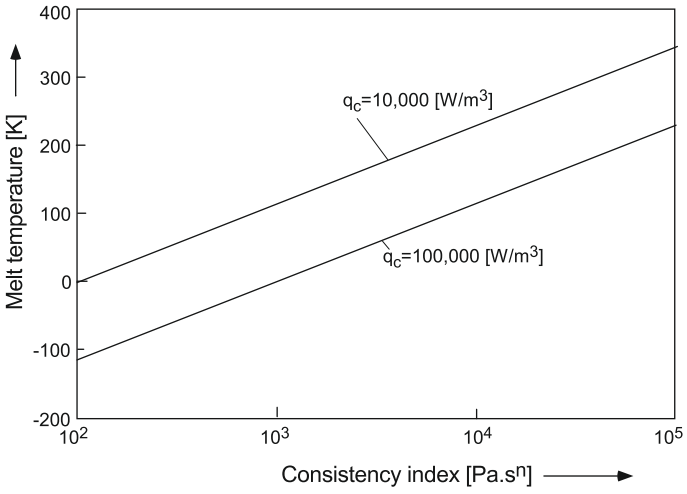


Figure 7.99 Equilibrium melt temperature rise versus consistency index

The straight-line relationship using a semi-log scale indicates that the melt temperature increases exponentially with the consistency index. An increase in the cooling flux by a factor of ten reduces the melt temperature rise by about 115°K for all values of the consistency index.

The power law index is a measure of the degree of shear thinning. Lower values of the power law index result in lower viscosity values at high shear rates. In other words, as the power law index becomes smaller, the polymer becomes more shear thinning. This will have a strong effect on the melt temperature rise, particularly at high shear rates, as shown in Fig. 7.100.

Figure 7.100 shows that an increase in power law index from 0.3 to 0.6 will increase the melt temperature about 35°K at a shear rate of 10 s^{-1} and about 70°K at a shear rate of 100 s^{-1}. This indicates that the power law index has a powerful effect on melt temperature (excuse the pun!). Figure 7.100 explains why LDPE tends to run at lower melt temperatures than LLDPE or metallocenes. LDPE has a power law index of about 0.3, while LLDPE and metallocenes have a power law index of about 0.6.

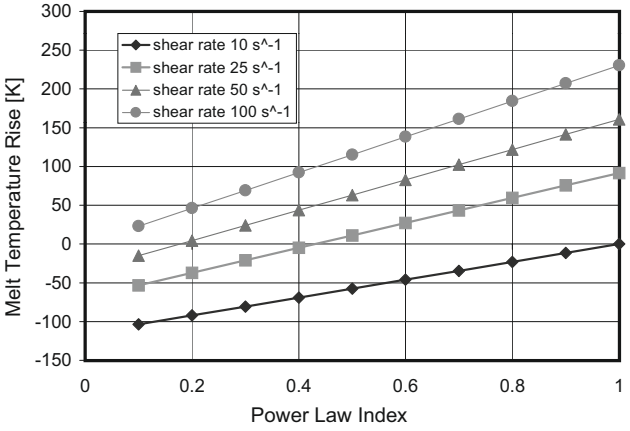


Figure 7.100
Equilibrium melt temperature rise versus power law index

The effect of the temperature coefficient of the melt viscosity is quite clear from Eq. 7.413. When the temperature coefficient of the viscosity (α_T) increases, the melt temperature rise will reduce. Amorphous polymers generally have a much greater temperature coefficient than semi-crystalline polymers; the difference is about a factor of ten. This means that the melt temperature rise in semi-crystalline polymers will be about ten times greater than in amorphous polymers.

An increase in screw speed will raise the viscous dissipation and thus the melt temperature. Since shear rate is directly proportional to screw speed (see Eq. 7.405), the effect of screw speed can be seen from Fig. 7.100. However, it is more obvious by re-plotting the data with the shear rate along the horizontal axis; see Fig. 7.101.

Increasing screw speed will increase shear rate correspondingly. Figure 7.101 shows that the melt temperature increases rapidly at low screw speed and more slowly at higher screw speed. As discussed earlier, higher values of the power law index result in higher melt temperatures.

Increasing the barrel diameter will increase the shear rate—other factors being constant. This will increase viscous dissipation and melt temperatures as discussed earlier. Another problem with larger barrel diameters is that the heat transfer surface area increases with the diameter squared, while the channel volume increases with the diameter cubed. As a result, the heat transfer becomes less effective with larger diameter extruders. It is well known in the extrusion industry that the ability to influence melt temperature by changes in barrel temperature is very limited for large extruders.

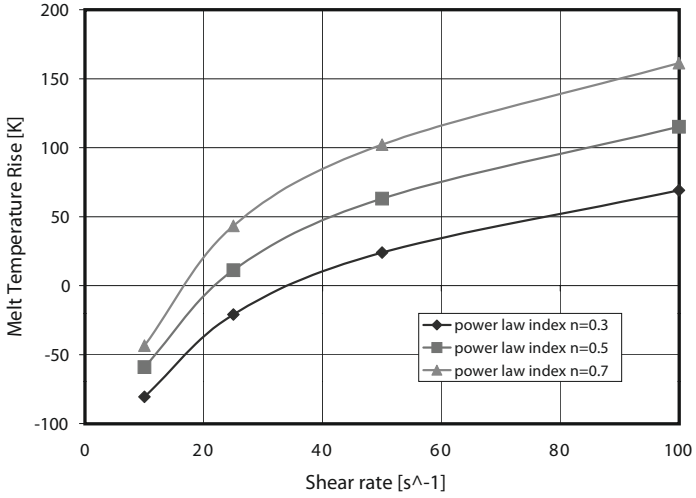


Figure 7.101 Equilibrium melt temperature rise versus shear rate

Increasing the barrel thickness will reduce the heat flux through the barrel assuming that the inner and outer barrel temperatures are the same. As a result, a thicker barrel will result in higher melt temperatures.

Finally, increasing the channel depth will reduce the shear rate and viscous heating as discussed earlier; this will result in lower melt temperatures. In fact, the channel depth is one of the most critical screw design parameters to control melt temperature. Deep-flighted screws are used when the viscous dissipation and melt temperatures have to be minimized. That is why screws used to extrude rubbers generally have deep channels. The same is true for cooling extruders in tandem extrusion lines for foamed polymers.

7.4.3.4.3 Discussion

This analysis provides a simple and fast method to estimate the fully developed melt temperature in screw extruders. The effect of material properties, processing conditions, and machine design parameters can be determined quantitatively. As a result, the analysis can be used to predict how melt temperature will change when another

plastic is extruded and how the screw design or processing conditions should be changed to change melt temperature.

It should be noted that there are several simplifying assumptions in the analysis. We have assumed that the melt temperatures are uniform across the depth of the channel. In reality this is not the case; in fact, large melt temperature changes can occur across the depth of the channel. We can assume that the melt temperature calculated with this analysis corresponds to a bulk average melt temperature. We have also assumed that the fully developed melt temperature is reached before the end of the extruder. This is a reasonable assumption for small diameter extruders; however, this may not be a good assumption for large diameter extruders as discussed in the previous section.

It was also assumed that the viscous dissipation in the flight clearance does not affect the melt temperature in the screw channel. This would appear to be a questionable assumption. However, finite element analysis has shown that the actual melt temperature rise in the clearance region is relatively small [278]. The reason for this is that the heat transfer in the flight clearance is very effective because the clearance is generally quite thin.

Lastly, it was assumed that the details of the screw geometry do not affect the heat transfer to the barrel; this is not completely true. The number of flights, the flight clearance, the flight helix angle, and the flight width all affect the heat transfer from the polymer melt to the barrel. If we want to study the effect of these parameters in detail we have to use a more complicated, numerical analysis.

7.4.3.5 Assumption of Stationary Screw and Rotating Barrel

The theory developed up to this point is based on a model where the screw is stationary and the barrel rotates around the screw. It is assumed that the flow that results is the same as when the barrel is stationary and the screw rotates in the opposite direction. This assumption was considered valid for over fifty years until several workers challenged this assumption, first in the early 1990s [272–276], and then more recently [323]. Because of the importance of this issue we will critically analyze this assumption to determine to what extent the assumption is correct. Flow will be analyzed using the parallel plate assumption with either the barrel or the screw considered moving. Flow will also be analyzed without the parallel plate assumption, using a cylindrical coordinate system, again considering both cases. This analysis is based on a study by Osswald et al. [281].

7.4.3.5.1 Parallel Plate Analysis with Moving Screw

The parallel plate analysis with moving barrel and Newtonian fluid was already discussed in Section 7.4.1. If we take the barrel stationary and the screw moving at velocity $v_{st} = \pi D_s N$, the velocity profile can be determined from Eq. 7.196 using the

following boundary conditions: $v_t(y = 0) = v_{st}$ and $v_t(y = H) = 0$. This results in the following velocity profile in the tangential direction:

$$v_t(y) = \frac{g_t(y^2 - yH)}{2\mu} - v_{st}\frac{y}{H} + v_{st} \tag{7.414}$$

The maximum tangential pressure gradient occurs when there is no net output from the extruder. The maximum pressure gradient can be determined from:

$$\int_0^H v_t(y)dy = v_{st}H - \dot{V}_{tl} \tag{7.415}$$

If it is assumed, again, that the leakage flow is negligible ($\dot{V}_{tl} = 0$), the pressure gradient can be determined to be:

$$g_{tmax} = -\frac{6\mu v_{st}}{H^2} \tag{7.416}$$

With this, the tangential velocity profile at closed discharge can be written as:

$$v_t(y) = \frac{-3v_{st}}{H^2}y^2 + \frac{2v_{st}}{H}y + v_{st} \tag{7.417}$$

The corresponding velocity profile with moving barrel is:

$$v_t(y) = \frac{-3v_{bt}}{H^2}y^2 + \frac{2v_{bt}}{H}y \tag{7.418}$$

The tangential shear rate can be obtained by taking the first derivative of v_t with respect to normal distance; this results in the following expression:

$$\dot{\gamma}_t = \frac{-6v_{st}}{H^2}y + \frac{2v_{st}}{H} \tag{7.419}$$

The corresponding expression with moving barrel is:

$$\dot{\gamma}_t = \frac{-6v_{bt}}{H^2}y + \frac{2v_{bt}}{H} \tag{7.420}$$

It is clear that Eq. 7.419 is quite close to Eq. 7.420; the difference is in the tangential velocity term. Equation 7.393 uses v_{bt}, while Eq. 7.419 uses v_{st}. The difference between these two velocities is determined by the screw diameter D and the channel depth H. In most plastic extruders, the channel depth is about 0.05 D; this will result in a difference between v_{bt} and v_{st} of about 10%. Thus, there is a difference in the tangential velocities and shear rates when we take the screw moving rather than the barrel moving in the flat plate model. However, when the channel depth is small relative to the screw diameter, the difference is not substantial.

7.4.3.5.2 Flow Analysis Using Cylindrical Coordinates

To determine the velocities in the cylindrical coordinate system (CCS), the momentum equation has to be expressed in cylindrical coordinates. Again, the flow is assumed to be in steady state; inertia, centrifugal, and gravitational forces are assumed negligible and the fluid viscosity constant. For the angular component this can be written as:

$$\frac{\partial}{\partial r}\left[\frac{\partial(rv_\theta)}{r\partial r}\right]=\frac{g_\theta}{\mu r} \tag{7.421}$$

If we assume that the angular pressure gradient g_θ is constant and that the angular velocity depends only on normal distance r, the velocity can be obtained by double integration:

$$v_\theta(r)=\frac{g_\theta}{\mu}\left(\frac{r}{2}\ln r-\frac{r}{4}\right)+\frac{1}{2}c_1 r+\frac{c_2}{r} \tag{7.422}$$

Constants c_1 and c_2 have to be determined from the boundary conditions. The cylindrical system is shown in Fig. 7.102.

7.4.3.5.3 Cylindrical System with Rotating Barrel

When the barrel rotates and the screw is stationary, the boundary conditions are $v_\theta(R_s) = 0$ and $v_\theta(R_b) = -\Omega R_b$, where Ω is the angular velocity ($\Omega = 2\pi N$); see Fig. 7.102. From these conditions we can determine c_1 and c_2:

$$c_1=\frac{-4\pi N R_b^2}{R_b^2-R_s^2}+\frac{g_\theta}{\mu}\left[\frac{1}{2}-\frac{R_b^2\ln R_b-R_s^2\ln R_s}{R_b^2-R_s^2}\right] \tag{7.423}$$

$$c_2=\frac{2\pi N R_b^2 R_s^2}{R_b^2-R_s^2}+\frac{g_\theta R_b^2 R_s^2(\ln R_b-\ln R_s)}{2\mu(R_b^2-R_s^2)} \tag{7.424}$$

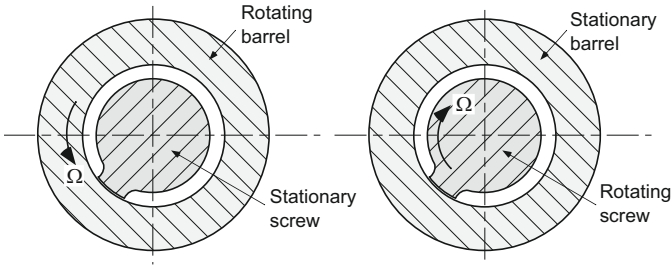


Figure 7.102
The cylindrical system in two kinematic conditions

When $g_\theta = 0$, Eq. 7.421 describes the drag flow between concentric cylinders with the outer cylinder rotating around the stationary inner cylinder. The angular pressure gradient at closed discharge is determined from a mass balance. In this case

the tangential flow rate equals the tangential leakage flow, both per unit axial length:

$$\dot{V}_t = \int_{R_s}^{R_b} v_\theta dr = -\dot{V}_{tl} \tag{7.425}$$

If the leakage flow is considered negligible, the angular pressure gradient at closed discharge can be determined from Eq. 7.425 using Eqs. 7.422 through 7.424:

$$g_{\theta max} = \frac{8\pi\mu N(1-\beta^2+2\beta^2 \ln)}{4\beta^2 \ln^2 \beta-(1-\beta^2)^2} \tag{7.426}$$

where β is the ratio of the radii: $\beta = R_s/R_b$.

When β approaches unity, g_θ/R_b approaches the tangential pressure gradient in the flat plate case. The angular shear rate is determined from the first derivative of the angular velocity; this leads to:

$$\dot{\gamma}_\theta = \frac{g_\theta(2 \ln r+1)}{4\mu} + \frac{c_1}{2} + c_2 \ln r \tag{7.427}$$

7.4.3.5.4 Cylindrical System with Rotating Screw

When the screw rotates and the barrel is stationary, the boundary conditions are $v_\theta(R_s) = \Omega R_{sN}$ and $v_\theta(R_b) = 0$, where Ω is the angular velocity ($\Omega = 2\pi N$). From these conditions we can determine c'_1 and c'_2:

$$c'_1 = \frac{-4\pi N R_s^2}{R_b^2 - R_s^2} + \frac{g_\theta}{\mu}\left[\frac{1}{2} - \frac{R_b^2 \ln R_b - R_s^2 \ln R_s}{R_b^2 - R_s^2}\right] \tag{7.428}$$

$$c'_2 = \frac{2\pi N R_b^2 R_s^2}{R_b^2 - R_s^2} + \frac{g_\theta R_b^2 R_s^2 (\ln R_b - \ln R_s)}{2\mu(R_b^2 - R_s^2)} \tag{7.429}$$

When $g_\theta = 0$ these equations describe the drag flow between concentric cylinders with the inner cylinder rotating inside the stationary outer cylinder.

The maximum angular pressure gradient is determined from a mass balance. The tangential flow rate has to equal the tangential flow with the screw minus the tangential leakage flow, both per unit axial length:

$$\dot{V}_t = \int_{R_s}^{R_b} v_\theta dr = \pi N(R_b^2 - R_s^2) - \dot{V}_{tl} \tag{7.430}$$

If the leakage flow is considered negligible, the maximum angular pressure gradient can be determined to be exactly the same expression as for the moving barrel case, i. e. Eq. 7.416. At this point the angular velocities for the barrel rotating, $v_{b\theta}(r)$,

can be compared to the angular velocities for the screw rotating, $v_{s\theta}(r)$. The velocity profiles are the same if the following condition is fulfilled:

$$v_{s\theta}(r) - 2\pi Nr = v_{b\theta}(r) \tag{7.431}$$

This condition states that the velocities with the barrel turning should be the same as the velocities with the screw turning relative to a cylindrical coordinate system rotating with the screw at $2\pi N$ radians/second. In fact, the left-hand side of Eq. 7.431 describes the velocities seen by an observer rotating with the screw. It turns out that this condition is fulfilled exactly for all values of the angular pressure gradient. Some investigators have neglected to make the correction expressed in Eq. 7.431 and incorrectly concluded that the velocities in the two kinematic conditions were different.

Figure 7.103 shows the velocities as a function of radial distance.

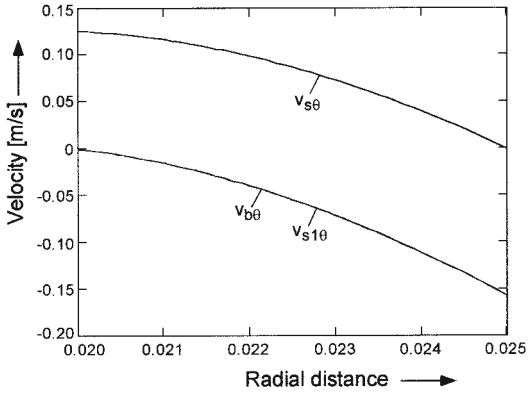


Figure 7.103 Velocities $v_{s\theta}$ and $v_{b\theta}$ versus radial distance

The top curve shows the velocities with rotating screw and the bottom curve shows the velocities with rotating barrel; the angular pressure gradient for both curves is –1E5 [Pa/rad]. When the top curve is shifted according to the transformation in Eq. 7.431, the corrected velocities fall exactly on the bottom curve. Even though only one curve is visible, there are actually two curves in the graph: the two curves overlay exactly.

7.4.3.5.5 Flow Rate

The flow rate can be determined by integrating the velocity profile (Eq. 7.422) from R_s to R_b. This results in the following expression per unit axial width:

$$\dot{V} = \pi N R_b^2 \left[1 - \frac{2R_s^2 \ln(R_b/R_s)}{R_b^2 - R_s^2}\right] - \frac{g_\theta}{4\mu}\left[\frac{R_b^2}{2} - \frac{R_s^2}{2} - \frac{2R_b^2 R_s^2 \ln^2(R_b/R_s)}{R_b^2 - R_s^2}\right] \tag{7.432}$$

Equation 7.432, which is for the moving barrel case, is exactly the same as for the moving screw case. This expression can be compared to the corresponding flow rate expression for the parallel plate system. For the flat plate system with moving barrel this can be written as:

$$\dot{V} = \pi N R_b (R_b - R_s) - \frac{g_\theta (R_b - R_s)^3}{6\mu (R_b + R_s)} \tag{7.433}$$

For the flat plate system with moving screw this can be written as:

$$\dot{V} = \pi N R_s (R_b - R_s) - \frac{g_\theta (R_b - R_s)^3}{6\mu (R_b + R_s)} \tag{7.434}$$

The three expressions are compared graphically in Fig. 7.104 where the flow rate per unit width is plotted against the pressure gradient. The screw root radius is 0.090 m, the barrel radius 0.100 m, the viscosity 500 Pa·s, and the screw speed 60 rpm.

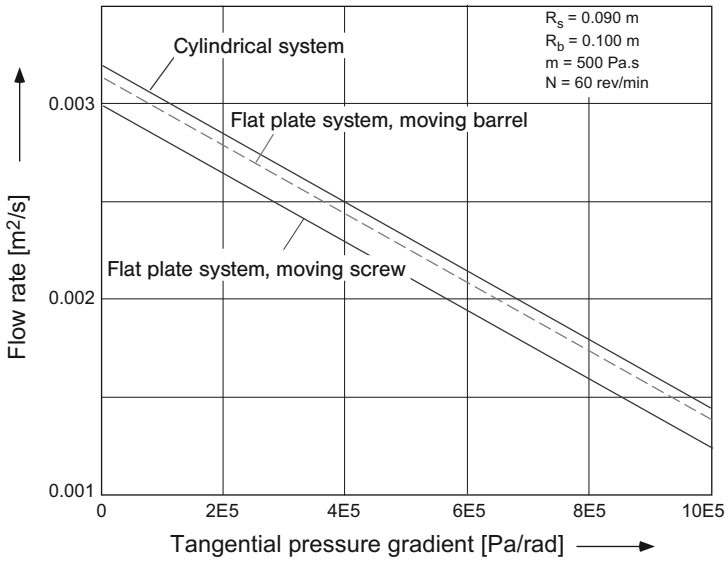


Figure 7.104 Flow rate versus tangential pressure gradient for cylindrical and flat plate system; flow rate is per unit axial width

The flow rate for the cylindrical system is slightly higher than for the flat plate system with the moving barrel. The difference is quite small, less than 2% when the channel depth is 10% of the barrel radius (5% of barrel diameter). This value is a typical metering depth for extruder screws. However, the difference between the cylindrical system and the flat plate with moving screw is much larger, between 10 and 15%. This indicates that the flat plate analysis with moving screw results in large errors.

The difference between the cylindrical and flat plate system will increase when the H/D ratio increases. This is shown in Fig. 7.105 where the flow rate is plotted against the screw root radius.

Figure 7.105 illustrates that the difference between the cylindrical and flat plate system increases when the screw root radius reduces. When the root radius is 80% of the barrel radius, the flow rate in the flat plate system with moving barrel is about 4% lower than the cylindrical system. However, the flow rate in the flat plate system with moving screw is about 30% lower. The flat plate system with moving screw results in significant errors and should not be used in serious analysis of screw extruders.

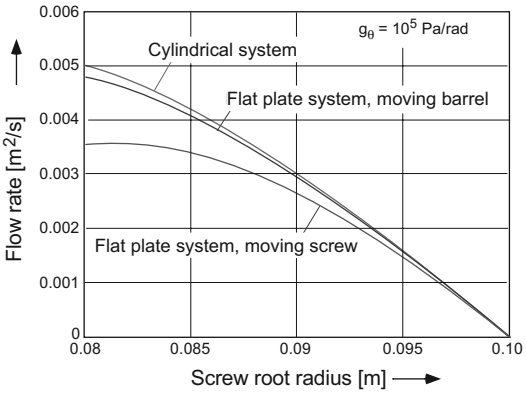


Figure 7.105
Flow rate versus screw root radius for cylindrical and flat plate system

The flow rate expressions can be expressed in terms of cross-channel (x) and down-channel coordinates by considering that the tangential pressure gradient g_t can be expressed as:

$$g_t = g_x \sin\varphi + g_z \cos\varphi \tag{7.435}$$

7.4.3.5.6 Discussion on Kinematic Conditions

In the flat plate system the velocities and shear rates for the case where the barrel moves relative to a stationary screw are different from the case where the screw moves relative to the stationary barrel. The difference is determined by the screw root diameter D_s and the barrel diameter D_b. In most single screw extruders where the root diameter is close to the barrel diameter, the difference between the two analyses is relatively small, about 10%. However, when the root diameter is considerably smaller than the barrel diameter the flat plat analysis with moving screw results in serious errors. The reason for the differences in the flat plate system is the fact that it cannot account for the curvature of the channel.

In the cylindrical system there is no difference in velocities between the rotating barrel and rotating screw cases; the velocities are exactly the same. When the velo-

cities are the same the shear rates and flow rates are the same as well. The results of 3-D boundary element analysis using the geometry of an actual extruder screw confirm that there is no difference between the two kinematic conditions [281]; the same results were obtained with 3-D finite element analysis. Further, careful extrusion experiments with a 150-mm extruder confirmed that there is no difference between rotating the barrel and rotating the screw [281]. The experimental 150-mm extruder was capable of rotating either the screw or the barrel. The barrel was constructed of a cast acrylic tube and the screw machined from an aluminum cylinder. The screw was filled with a 10,000 centistokes silicone fluid and back-pressure was controlled with a valve. Tracer dyes were injected in the screw channel. The screw was rotated one revolution, causing a distortion of the tracer material. The barrel was then rotated one revolution in the same direction; this brought the tracer material back to the original position and shape. This process was repeated several times with negligible change in the shape of the tracer.

Several other workers have confirmed the validity of the moving barrel assumption. A thorough study was conducted by Pape et al. [279, 280] using finite element analysis comparing the moving screw to the moving barrel case. The results of this analysis indicate that velocities with the moving barrel are the same as with the moving screw. Pape et al. also investigated non-isothermal flow conditions.

With these results there is strong evidence that rotating the barrel results in the same flow as opposite rotation of the screw, as long as one is dealing with highly viscous fluids (creeping flow). With the preponderance of evidence supporting the moving barrel assumption one would expect that this issue would have been put to rest once and for all. However, a recent study by Sikora and Sasimowski [276] using a helical coordinate system (HCS) claims a difference between the two kinematic conditions. Considering that the CCS is a special case of the HCS it would appear that it is not possible for the HCS analysis to show a difference between the two kinematic conditions while the CCS shows no difference. At the time of this writing, the source of this discrepancy has not yet been determined.

The deformation of the fluid depends on the magnitude of the strain rate tensor, which, in turn, depends on its second invariant. The invariants of the strain rate tensor are independent of their frame of reference. As a result, the deformation is the same if the screw rotates (fixed coordinate system) or if the barrel rotates (rotating coordinate system). The only difference between the two kinematic conditions arises from centrifugal and Coriolis forces. Spalding et al. [282] demonstrated with a 3-D finite element analysis of a single screw extruder that for polymer melts the centrifugal and Coriolis force effects are negligible. This means that with a helical coordinate system the flow with a rotating barrel should be the same as with a rotating screw. The only reason that the flat plate system indicates a difference between the two kinematic conditions is that it does not account for the curvature of the channel.

7.5 Die Forming

In this functional zone, the shaping of the polymer takes place. In many respects, the die forming zone is the most important functional zone because the actual shape of the final product develops in this zone. The die forming zone is essentially always a pressure consuming zone. The pressure built up in the preceding functional zones is used in the die forming zone. The diehead pressure is the pressure required to force the polymer melt through the die. The diehead pressure is not determined by the extruder but by the extruder die. The variables that affect the diehead pressure are:

1. The geometry of the flow channel in the die
2. The flow properties of the polymer melt
3. The temperature distribution in the polymer melt
4. The flow rate through the die

When these variables remain the same, the diehead pressure will be the same whether a single screw extruder or a twin screw extruder is used. The main function of the extruder is to supply a homogeneous polymer melt to the die at the required rate and diehead pressure. The rate and diehead pressure should be steady and the polymer melt should be homogeneous in terms of temperature and consistency. Die design and analysis of flow in dies are two of the most complicated elements of polymer process engineering. One of the reasons is that in a proper analysis of the die forming process, the polymer melt can no longer be assumed to be purely viscous because some important die flow phenomena such as extrudate swell (often erroneously referred to as die swell) cannot be explained with this simplifying assumption. Therefore, the polymer melt has to be analyzed as a viscoelastic fluid, and this complicates the analysis of the die forming process considerably.

Even if the polymer melt is assumed to be purely viscous, the analysis will generally be quite complicated because many dies have flow channels of complex shape. As a result, accurate analysis of flow in extrusion dies generally requires three-dimensional flow analysis. This presents quite a challenge for simple Newtonian fluids. Three-dimensional flow analysis of viscoelastic non-Newtonian fluids is beyond the capabilities of most (if not all) die designers. Not surprisingly, die designers often take an empirical approach to die design.

There are only two basic flow channel geometries that are rather easy to analyze: the circular flow channel and the slit flow channel (rectangular cross section with $W >> H$). Most other geometries are quite difficult to analyze.

7.5.1 Velocity and Temperature Profiles

Velocity profiles and temperature profiles in extruder dies are intimately related because of the high polymer melt viscosity and because the melt viscosity is temperature dependent. It is important to understand and appreciate this interrelationship in order to understand the die forming process and the variables that influence this process. The relationship between velocity and temperature profiles can be illustrated by considering the down-channel velocity profile in a circular die. Typical velocity profiles are shown in Fig. 7.106 for several values of the power law index.

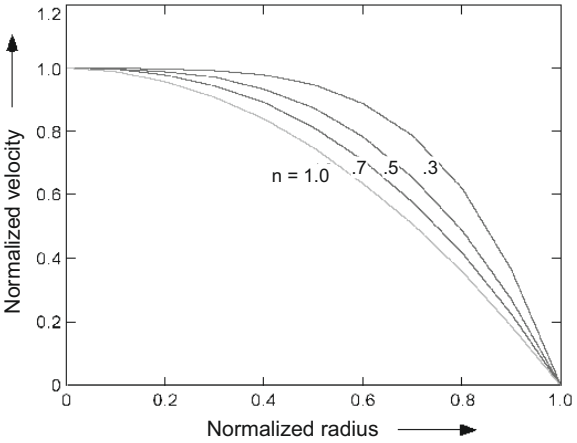


Figure 7.106
Velocity versus radius for power law fluid at various values of the power law index n

The more or less parabolic velocity profile is observed that is typical of pressure driving flow (pipe flow). The velocity curve for the Newtonian fluid (n = 1) is an exact parabola. The curves for the non-Newtonian fluid are not purely parabolic (quadratic); they have a flattened center region and a larger gradient at the wall. From the velocity profile, one can obtain the shear rate profile by determining the local gradients of the velocity profile. This is described in Fig. 7.107 for both the Newtonian and non-Newtonian fluid. For all curves the shear rate in the center of the flow channel is zero and the highest shear rate occurs at the wall. The wall shear rate for the non-Newtonian fluid, however, is considerably higher than for the Newtonian fluid.

As a result of the velocity gradients, there will be heat generation in the fluid from the viscous dissipation of energy. In rectilinear flow, the rate of energy dissipation per unit volume is given by:

$$\dot{E}_d = \tau_{yz} \frac{dv_z}{dy} \tag{7.436}$$

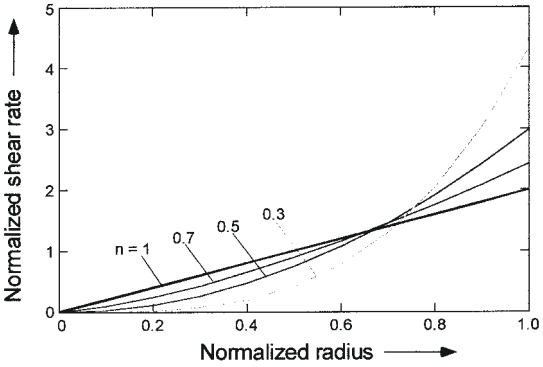


Figure 7.107
Shear rate versus radial distance for several values of the power law index

This is a simplified version of the general expression for energy dissipation, Eq. 5.5d. If the fluid can be described by the power law equation, then Eq. 7.436 becomes:

$$\dot{E}_d = m\left|\frac{dv_z}{dy}\right|^{n+1} = m\,\dot{\gamma}^{n+1} \tag{7.437}$$

Thus, the local viscous dissipation is determined by the local shear rate raised to the power n + 1. Since the highest shear rate occurs at the wall, it is clear that the highest viscous dissipation will also occur at the wall. As a result of the non-uniform shear rate distribution in the flow channel, there will be a non-uniform viscous heat generation in the flow channel. The largest amount of viscous heat generation occurs at the wall. As a result of the viscous heat generation, the temperature of the polymer melt will increase. But since the viscous heat generation is non-uniform across the flow channel, the temperature rise of the polymer melt will also be non-uniform across the flow channel.

Because the die wall material usually has a thermal conductivity much higher than polymer melts, adiabatic conditions are not likely to be achieved. On the other hand, it is also not likely that the wall temperature will remain constant. In this case, the heat flux through the wall would be such as to maintain a perfectly constant temperature along the wall. This is referred to as an isothermal wall boundary condition. Because of the high thermal conductivity of the wall, the isothermal boundary condition is more likely to occur than the adiabatic boundary condition. Adiabatic conditions can be approached if the die is very well insulated. In most actual cases, the true thermal boundary condition will be somewhere between isothermal and adiabatic, depending on the design of the die and external conditions around the die. A typical temperature profile resulting from the velocity profiles shown in Fig. 7.106 is shown in Fig. 7.108.

Initially, the maximum temperature will occur close to the wall; later, this maximum will shift towards the center. A quantitative method of evaluating temperature profiles will be discussed next.

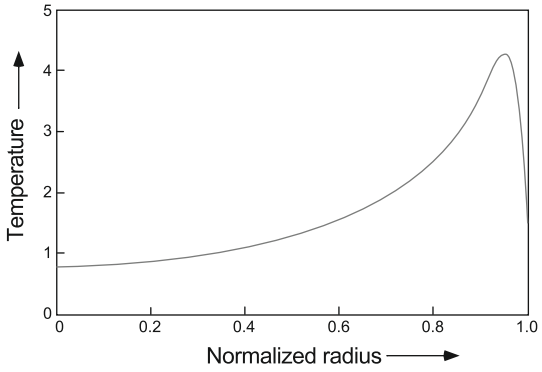
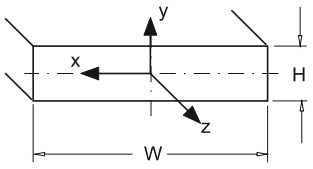


Figure 7.108
Temperature versus radial distance

Important relationships for shear stress, shear rate, velocity, and flow rate for the pressure flow of power law fluids in a slit flow channel are given in Fig. 7.109. Figure 7.110 shows the same relationships for a circular flow channel. These relationships are valid for fluids with temperature independent viscosity.



$$\tau_{yz} = g_z y \;;\; \tau_w = \frac{1}{2} g_z H$$

$$-\dot{\gamma}_{yz} = \left(\frac{g_z}{m} y\right)^s \;;\; \dot{\gamma}_w = \frac{2(s+2)\dot{V}}{WH^2}$$

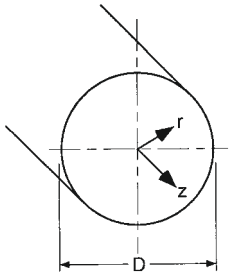
$$v_z = v_{max}\left[1 - \left(\frac{2y}{H}\right)^{s+1}\right]$$

$$v_{max} = \frac{H}{2(s+1)}\left(\frac{Hg_z}{2m}\right)^s$$

$$\bar{v}_z = \left(\frac{s+1}{s+2}\right) v_{max}$$

$$\dot{V} = \frac{WH^2}{2(s+2)}\left(\frac{Hg_z}{2m}\right)^s$$

Figure 7.109 Pressure flow of a power law fluid through a slit



$$\tau_{rz} = \frac{g_z}{2} r \;;\; \tau_w = \frac{1}{4} g_z D$$

$$-\dot{\gamma}_{rz} = \left(\frac{g_z}{2m} r\right)^s \;;\; \dot{\gamma}_w = \frac{8(s+3)\dot{V}}{\pi D^3}$$

$$v_z = v_{max}\left[1 - \left(\frac{2r}{D}\right)^{s+1}\right]$$

$$v_{max} = \frac{D}{2(s+1)}\left(\frac{Dg_z}{4m}\right)^s$$

$$\bar{v}_z = \left(\frac{s+1}{s+3}\right) v_{max}$$

$$\dot{V} = \frac{\pi D^3}{8(s+3)}\left(\frac{Dg_z}{4m}\right)^s$$

Figure 7.110 Pressure flow of a power law fluid through a circular channel

Dinh and Armstrong [146] have developed general analytical solutions for the local temperature change due to viscous dissipation for non-Newtonian fluids. Their results apply to fluids with flow properties that are insensitive to temperature. The dimensionless normal distance is defined as $y^0 = 2y/H$ for a slit or $y^0 = 2y/D$ for a circular flow channel. The dimensionless velocity is defined as $v^0_z = v_z/v_{max}$; it can be expressed in terms of dimensionless normal distance as follows:

$$v^0 = 1 - (y^0)^{s+1} \tag{7.438}$$

Since the analysis deals with rectilinear flow, the subscript of the velocity will be deleted.

The dimensionless viscosity is defined as:

$$\eta_r = \frac{\eta}{\eta_o} = \left|\frac{dv^0}{dy^0}\right|^{n-1} \tag{7.439}$$

where:

$$\eta_o = m\left(\frac{v_{max}}{H}\right)^{n-1} \tag{7.439a}$$

The energy equation expressed in terms of dimensionless quantities can be written as:

$$v^0 \frac{\partial\theta}{\partial z^0} = \frac{\partial^2\theta}{\partial(y^0)^2} + \eta_r\left(\frac{dv^0}{dy^0}\right)^2 \tag{7.440}$$

where:

$$\theta = \frac{k(T - T_o)}{\eta_o v^2_{max}} \tag{7.440a}$$

$$z^0 = \frac{kz}{\rho C_p v_{max} H^2} \tag{7.440b}$$

The following boundary conditions will be considered:

$$\text{at } z^0 = 0,\ \theta = 0 \tag{7.440c}$$

$$\text{at } y^0 = 0,\ \frac{\partial\theta}{\partial y^0} = 0 \tag{7.440d}$$

$$\text{at } y^0 = 1,\ \frac{\partial\theta}{dy^0} = -N\theta \tag{7.440e}$$

where N is the Biot number as defined in Eq. 5.74. When N is zero, there is no exchange of heat; adiabatic conditions prevail. When N is infinitely large, the wall temperature equals the temperature of the polymer melt; this corresponds to isothermal conditions. Normal values for the Biot number in extruder dies range from 1 to 100. As long as the Biot number is non-zero, there will be a fully developed temperature profile. However, when the Biot number is zero, the temperature in the fluid will continue to rise without limit.

The fully developed temperature profile θ_1 is the solution to the following differential equation:

$$\frac{d^2\theta_1}{d(y^0)^2} = -\eta_r\left(\frac{dv^0}{dy^0}\right)^2 \tag{7.441}$$

with the following boundary condition:

$$\frac{d\theta_1(0)}{dy^0} = 0 \text{ and } \frac{d\theta_1(1)}{dy^0} = -N\theta_1(1) \tag{7.441a}$$

The solution to this equation is:

$$\theta_1(y^0) = \left(\frac{n+1}{n}\right)^{n+1}\left[\frac{1}{N} + \frac{n^2}{(2n+1)(3n+1)} - \frac{(y^0)^{3+s}n^2}{(2n+1)(3n+1)}\right] \tag{7.442}$$

where s is the reciprocal power law index (s = 1/n).

Equation 7.442 is a very useful relationship for determining fully developed temperature profiles in pipe flow law fluids. The maximum fully developed temperature always occurs at the center of the flow channel as can be seen from Eq. 7.442 as well as from Fig. 7.111, which illustrates the fully developed temperature profile under isothermal wall conditions and at various values of the power law index.

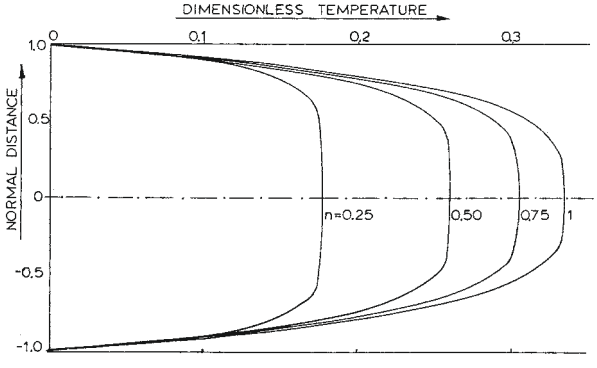


Figure 7.111
Fully developed temperature profiles, isothermal wall conditions

As the fluid becomes more pseudo-plastic, the fully developed temperature profile becomes more flattened in the center. The temperature remains almost constant in a center region, which extends for about half the channel height. The larger temperature gradients occur in a relatively thin region at the walls.

The temperature profile as a function of normal distance and down-channel distance is postulated to be of the form:

$$\theta(y^0, z^0) = \theta_1 - \sum_i c_i x_i(y^0) \exp(-a_i z^0) \tag{7.443}$$

For the details of the determination of eigenfunctions x_i and eigenvalues a_i, the reader is referred to the paper by Dinh and Armstrong [146]. The eigenvalues are given by:

$$a_j = \left[\frac{\left(j - \frac{1}{4}\right)\pi - \alpha}{\int_0^1 \sqrt{v^0}\, dy^0} \right]^2 \tag{7.444}$$

where j = 1, 2, 3,... and α is given by:

$$\alpha = \arctan \frac{-3\left[3^{1/3}\Gamma\left(\frac{2}{3}\right) + (\dot{\gamma}_w a)^{-1/3} N\Gamma\left(\frac{1}{3}\right)\right]}{\left[3^{5/6}\Gamma\left(\frac{2}{3}\right) - 3^{1/2}(\dot{\gamma}_w a)^{-1/3} N\Gamma\left(\frac{1}{3}\right)\right]} \tag{7.445}$$

where $\pi/3 \le \alpha \le 2\pi/3$, $\dot{\gamma}_w$ is the dimensionless shear rate at the wall, and $\Gamma(p)$ is the gamma function. The gamma function is defined as:

$$\Gamma(p) = \int_0^\infty x^{p-1} \exp(-p) dx \tag{7.446}$$

where:

$\Gamma(p+1) = p\Gamma(p)$ if $p > 0$

$\Gamma(p+1) = p!$ if p is a positive integer

$\Gamma(1) = 1$

$\Gamma\left(\frac{1}{2}\right) = \pi^{1/2}$

In evaluating the eigenvalues using Eq. 7.444, a convenient relationship involving the gamma function is:

$$\int_0^1 x^{c_1-1}(1-x)^{c_2-1}dx = \int_0^\infty \frac{x^{c_1-1}}{(1+x)^{c_1+c_2}}dx = \frac{\Gamma(c_1)\Gamma(c_2)}{\Gamma(c_1+c_2)} \tag{7.447}$$

The eigenfunctions x_j are given by:

$$x_j \cong (v^0)^{-1/4}\left(\sqrt{a_j}\int_{y^0}^1 \sqrt{v^0}dy^0\right)^{1/2} F \tag{7.448}$$

where:

$$F = \left[3^{1/3}\Gamma\left(\frac{2}{3}\right)J_{-1/3}\left(\sqrt{a_j}\int_{y^0}^1 \sqrt{v^0}dy^0\right) + (\dot{\gamma}_w a)^{-1/3}N\Gamma\left(\frac{1}{3}\right)J_{1/3}\left(\sqrt{a_j}\int_{y^0}^1 \sqrt{v^0}dy^0\right)\right] \tag{7.449}$$

where J_v is the Bessel function of the first kind of order v.

The Bessel function J_v is given by:

$$J_v(x) = \left(\frac{1}{2}x\right)^v \sum_{i=0}^{\infty} \frac{(-0.25\,\chi^2)^i}{i!\Gamma(i+v+1)} \tag{7.450}$$

The expansion coefficients c_i in Eq. 7.443 for the slit problem are given by:

$$c_i = \frac{\int_0^1 \theta_1 v^0 x_i dy^0}{\int_0^1 v^0 x_i^2 dy^0} \tag{7.451}$$

If the fluid is a power law fluid and the wall condition is isothermal, the eigenvalues become:

$$a_j = \left[2\sqrt{\pi}\frac{\Gamma\left(\frac{3}{2}+\frac{1}{1+s}\right)}{\Gamma\left(1+\frac{1}{1+s}\right)}\left(j-\frac{7}{12}\right)\right]^2 \tag{7.452}$$

The dimensionless temperature as a function of dimensionless normal distance for Newtonian fluid is shown in Fig. 7.112.

With isothermal conditions the fully developed temperature profile is reached when $z^0 > 5$. With adiabatic conditions the temperature profile continues to increase along the length of the channel.

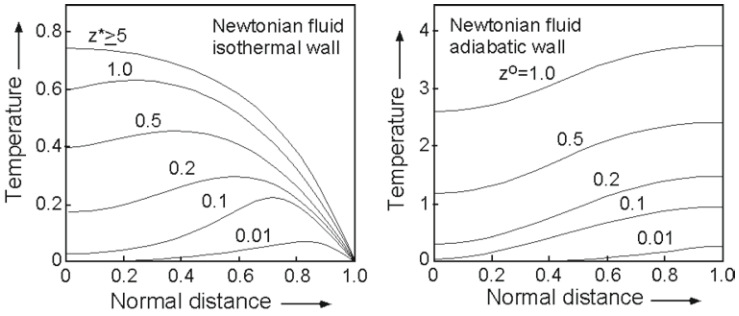


Figure 7.112 Dimensionless temperature versus normal distance for Newtonian fluid with isothermal conditions (left) and adiabatic conditions (right)

Figure 7.113 shows the temperature profiles for a power law fluid with power law index n = 0.5.

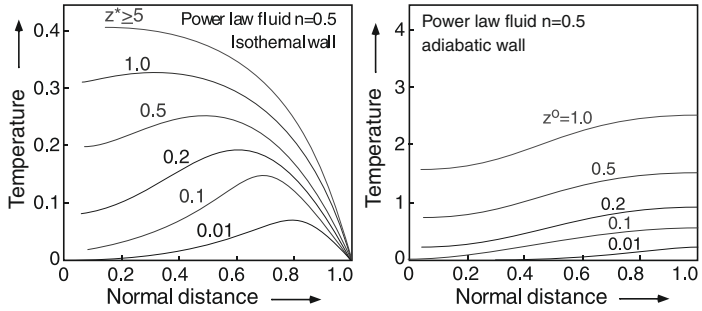


Figure 7.113 Dimensionless temperature versus normal distance for power law fluid with power law index n = 0.5 with isothermal conditions (left) and adiabatic conditions (right)

The dimensionless temperature and down-channel distance in Figs. 7.112 and 7.113 are related to the average fluid velocity. In comparing Fig. 7.112 to 7.113, it is seen that increased pseudo-plasticity reduces the temperature build-up in the polymer melt at equal volumetric flow rates. It is also quite apparent that the temperature build-up under adiabatic conditions is substantially higher than under isothermal conditions.

The fully developed temperature profile, Eq. 7.442, is rather easy to calculate. However, the developing temperature profile, Eqs. 7.443–7.452, involves some rather lengthy and complex calculations. Although the solutions to the developing temperature profiles are analytical, obtaining actual results still requires computations that go beyond the capabilities of most pocket calculators. In many practical cases, one would like to know to what extent the actual temperature profile approaches the fully developed temperature profile. This can be determined by using a dimensionless axial distance Z_{Gz}, defined as:

$$Z_{Gz} = \frac{Z}{LN_{Gz}} \tag{7.453}$$

where L is the length of the channel and N_{Gz} the Graetz number as defined in Eq. 5.68. If $Z_{Gz} \geq 1$, the temperature profile will be essentially fully developed in most practical heat transfer situations as analyzed, for instance, by Winter [147]. For a slit flow channel, the axial length Z_1 at which the temperature profile will be fully developed can now be expressed as:

$$Z_1 = \frac{\dot{V}H}{\alpha W} = \frac{H^2\bar{v}}{\alpha} \tag{7.454}$$

If we use some typical numbers H = 0.003 [m], $\dot{V}$ = 0.1 [m/s], and α = 1E–7 [m^2/s] then the length Z_1 = 9 [m]. Considering that most dies are no longer than about 0.5 m it is clear that the temperatures in dies generally will not get close to fully developed conditions. In most practical extrusion operations, the length of the die land is much too short to reach a fully developed temperature profile. Thus, in order to determine the actual stock temperatures, one must evaluate the developing temperature profile.

The total amount of power dissipated in the flow channel of a die is simply determined by the product of flow rate and pressure drop along the flow channel. Thus:

$$Z_d = \dot{V}\Delta P \tag{7.455}$$

If it is assumed that all this power is used to raise the temperature of the polymer melt, i.e., adiabatic conditions, then the volume average rise in melt temperature can be determined from:

$$\Delta\bar{T} = \frac{\Delta P}{\rho C_p} \tag{7.456}$$

Thus, the volume average adiabatic temperature rise is directly proportional to the pressure drop. If the pressure drop is 30 MPa (= 4350 psi), a typical volume average temperature rise is about 10°C. In most cases, however, the actual volume average temperature rise will be less because heat transfer will take place at the die wall. In other words, adiabatic conditions will not occur in actual extrusion operation. It is important to realize, though, that local temperatures can be considerably higher than the volume average temperature. The highest shear rates occur at the wall, and consequently the highest viscous heat generation occurs at the wall. Therefore, the polymer close to the wall will heat up much faster than the polymer in the center region of the channel. Thus, it is quite possible that a local temperature rise close to the wall can be considerably higher than the volume average temperature rise.

In extrusion, one is always concerned about temperature uniformity. One of the important requirements of the extruder is to deliver to the die a polymer melt of uniform consistency and temperature. However, it should be realized that, even if the polymer melt entering the die is uniform in temperature, non-uniformities in

temperature will develop in the die as a result of the non-uniform velocity gradients. This is inherent to die flow. The temperature build-up and non-uniformities can be reduced by reducing the shear rate. This can be achieved by lowering the flow rate through the die or by opening up the die flow channel. Another possibility is to use coextrusion with the outer layer being thin and of low viscosity. One can also use an external lubricant in the polymer to reduce a die flow problem; however, this may introduce other problems as well (e.g., solids conveying problems, loss of mechanical properties, etc.).

7.5.2 Extrudate Swell

A well-known and typical phenomenon in polymer melt extrusion is the swelling of the extrudate as it leaves the die. This is sometimes referred to as die swell; however, it is not the die but the polymer that swells. The elasticity of the polymer melt is largely responsible for the swelling of the extrudate upon leaving the die. This is primarily due to the elastic recovery of the deformation that the polymer was exposed to in the die. The elastic recovery is time-dependent. A die with a short land length will have a large amount of swelling, while a long land length will reduce the amount of swelling. The polymer has what is often called a "fading memory." A deformation can be recovered to a large extent shortly after the occurrence of the deformation; however, after longer times the recoverable deformation reduces. Thus, a certain amount of relaxation occurs in the die depending on the geometry of the flow channel.

It should be noted that extrudate swelling is not unique to viscoelastic fluids. It can also occur in an inelastic or purely viscous fluid; this has been demonstrated experimentally and theoretically. Obviously, in an inelastic fluid, the mechanism of extrudate swell is not an elastic recovery of prior deformation. The swelling is caused by a significant rearrangement of the velocity profile as the polymer leaves the die; this is shown in Fig. 7.114.

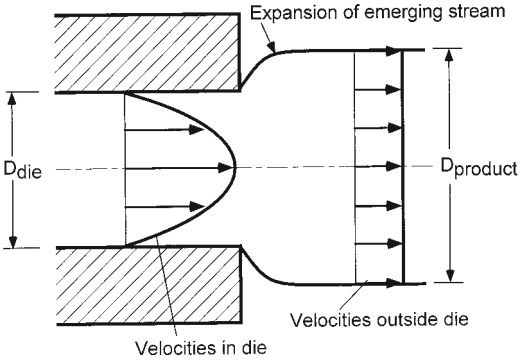


Figure 7.114
Change in velocity profiles in the die exit region

The velocity profile changes from an approximately parabolic velocity profile in the die to a straight velocity profile (plug flow) a short distance away from the die. In a Newtonian fluid, this causes a small amount of extrudate swelling (about 10%) at low Reynolds numbers ($N_{re} < 16$). Viscoelastic fluids exhibit about the same amount of swelling at low shear rates, but much larger amounts of swelling can occur at high shear rates (over 200%!).

One of the main problems with extrudate swell is that it is generally not uniformly distributed over the extrudate. This means that some areas of the extrudate swell more than others. If the geometry of the exit flow channel of the die is made to match the geometry of the required product, the uneven swelling will cause a distortion of the extrudate and the required product geometry cannot be obtained. Drawdown cannot cure this problem! Therefore, the geometry of the exit flow channel must generally be different from the required product geometry. This can be understood by analyzing the velocity profiles in the flow channel. Figure 7.115 shows the velocity profile in a flow channel with a square cross-section; the figure shows the upper right quadrant with the solid lines indicating points of equal velocity.

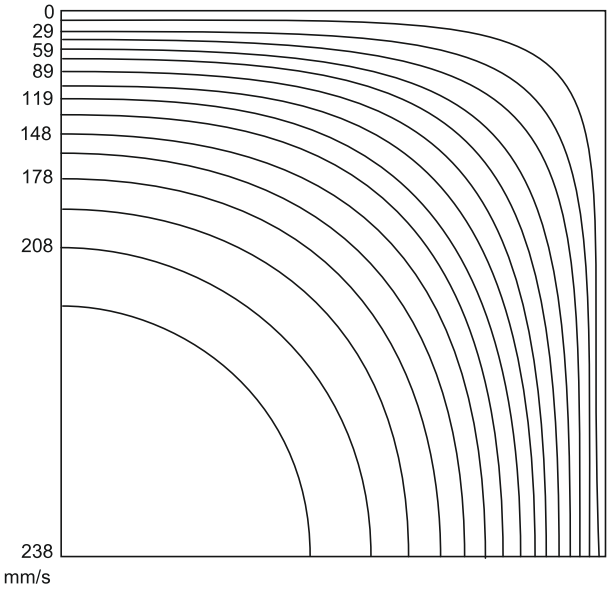


Figure 7.115
Velocity profile in square channel

It can be seen that the shear rates at the wall vary significantly. The wall shear rate in the corner is relatively low, while the highest shear rate occurs at the middle of the wall. Therefore, the elastic recovery in the middle will be larger than the elastic recovery at the corners. This results in "bulged" extrudate. It is not possible to obtain a perfectly square extrudate with a perfectly square flow channel. To eliminate this problem one has to modify the shape of the flow channel to compensate for the uneven swelling of the extrudate. A good die designer must anticipate the

amount of uneven swelling and design the flow channel accordingly. This is a difficult task, and the determination of the flow channel geometry is often done by a "trial and error" process.

Accurate mathematical prediction of the die swell profile is quite difficult and, therefore, determination of the proper flow channel geometry to minimize uneven swelling by engineering calculations is generally not practical. The non-uniform extrudate swell and the correction of the flow channel geometry are illustrated in Fig. 7.116.

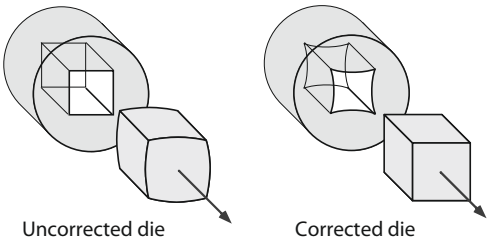


Figure 7.116
Uneven swelling of extrudate and possible correction

The amount of swelling is very much dependent on the nature of the material. Some polymers exhibit considerable swell (100 to 300%), e. g., polyethylenes; other polymers exhibit lower swell, e. g., polyvinylchloride. When PVC is extruded at relatively low temperatures (165 to 175°C), the swell ranges from 10 to 20% only. This is one of the reasons that PVC is such a popular material in profile extrusion; it conforms quite well to the geometry of the die flow channel and has good melt strength.

7.5.3 Die Flow Instabilities

In extrusion, certain die flow instabilities can occur that may seriously affect the entire extrusion process and render the extruded product unacceptable. Two very important die flow instabilities are shark skin and melt fracture.

7.5.3.1 Shark Skin

Shark skin manifests itself as a regular ridged surface distortion, with the ridges running perpendicular to the extrusion direction. A less severe form of shark skin is the occurrence of matness of the surface, where the glossy surface cannot be maintained. Shark skin is generally thought to be formed in the die land or at the exit. It is dependent primarily on the temperature and the linear extrusion speed. Factors such as shear rates, die dimensions, approach angle, surface roughness, L/D ratio, and material of construction seem to have little or no effect on shark skin.

The mechanism of shark skin is postulated to be caused by the rapid acceleration of the surface layers of the extrudate when the polymer leaves the die; this is illus-

trated in Fig. 7.117. If the stretching rate is too high, the surface layer of the polymer can actually fail and form the characteristic ridges of the shark skin surface [148]. High-viscosity polymers with narrow molecular weight distribution (MWD) seem to be most susceptible to shark skin instability [149, 150].

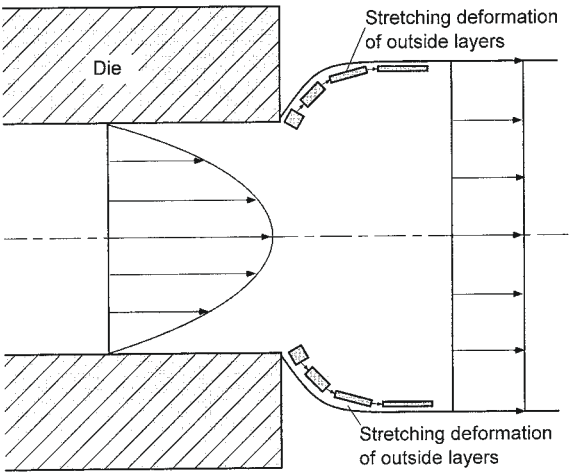


Figure 7.117 Change in velocity profile in the die exit region

The shark skin problem can generally be reduced by reducing the extrusion velocity and increasing the die temperature, particularly at the land section. There is some evidence that running at very low temperatures can also reduce the problem [151]. Selection of a polymer with a broad MWD will also be beneficial in reducing shark skin. Using an external lubricant can also reduce the problem. This can be done by using an additive to the polymer or by coextruding a thin, low-viscosity outer layer.

7.5.3.2 Melt Fracture

Melt fracture is a severe distortion of the extrudate, which can take many different forms: spiraling, bambooing, regular ripple, random fracture, etc.; see Fig. 7.118.

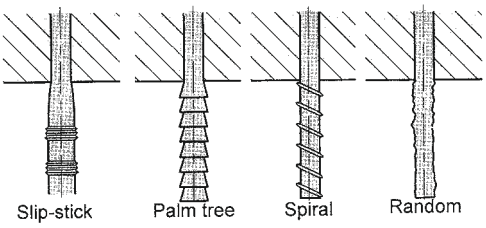


Figure 7.118 Various forms of melt fracture

It is not a surface defect like shark skin, but is associated with the entire body of the molten extrudate. However, many workers do not distinguish between shark skin and melt fracture, but lump all these flow instabilities together under the term melt fracture. There is a large amount of literature on the subject of melt fracture (e.g., [152–164]). Despite the large number of studies on melt fracture, there is no clear

agreement as to the exact cause and mechanism of melt fracture. It is quite possible that the mechanism is not the same for different polymers and/or different flow channel geometries [169]. Linear polymers tend to develop an instability of the shear flow in the die land, while branched polymers tend to develop instabilities in the converging region of the die flow channel.

However, there is relatively uniform agreement that melt fracture is triggered when a critical wall shear stress is exceeded in the die. This critical stress is in the order of 0.1 to 0.4 MPa (15 to 60 psi). A number of mechanisms have been proposed to explain melt fracture. Some of the more popular ones are:

1. Critical elastic deformation in the entry zone
2. Critical elastic strain
3. Slip-stick flow in the die

The effect of the entry zone has been demonstrated by many workers. In general, the smaller the entry angle, the higher the deformation rate at which instability occurs. Gleissle [230] has proposed a critical elastic strain as measured by recoverable strain. Based on measurements with 11 fluids, he proposed the existence of a critical value of the ratio of first normal stress difference to the shear stress, the average value being 4.63 for 11 widely different fluids with a standard deviation of about 5%. Much larger differences were found in the critical shear stress, the average being 3.7E5 Pa with a standard deviation of about 55%. In 1961, Benbow, Charley, and Lamb [232, 233] introduced the slip-stick mechanism to explain flow instability and extrudate distortion. Above a certain critical stress, the polymer melt is believed to experience intermittent slipping due to lack of adhesion between the melt and the die wall in order to relieve excessive deformation energy absorbed as a result of flow through a die. A large number of workers have observed slippage by various techniques.

More recent work by Utracki and Gendron on pressure oscillations in extrusion of polyethylenes [231] led them to conclude that the pressure oscillation does not seem to be related to elasticity or slip. They conclude that the parameter responsible for pressure oscillations is the critical strain (Hencky) value ε_c of the melt. For LLDPE, $\varepsilon_c < 3$, for HDPE, $\varepsilon_c < 2$, while for LDPE, $\varepsilon_c > 3.5$. The instability seems to be based on the inability of the polymer melt to sustain levels of strain larger than the critical strain.

Streamlining the flow channel geometry has been found to reduce the tendency for melt fracture in branched polymers. Increased temperatures, particularly at the wall of the die land, enable higher extrusion rates before melt fracture appears. The critical wall shear stress appears to be relatively independent of the die length, radius, and temperature. The critical stress seems to vary inversely with molecular weight, but seems to be independent of MWD. Certain polymers exhibit a super-extrusion region, above the melt fracture range, where the extrudate is not distorted

[165]. This process is particularly advantageous with polymers that melt fracture at relatively low rates, such as FEP. In superextrusion, the polymer melt is believed to slip relatively uniformly along the die wall. The occurrence of slip in extruder dies has been studied by a number of investigators, e.g., [166, 168]. However, it is still not clear whether the slip is actual loss of contact of polymer melt and metal wall or whether it is failure of a thin polymeric layer very close to the metal surface.

The melt fracture problem can be reduced by streamlining the die, increasing the temperature at the die land, running at lower rates, reducing the MW or the polymer melt viscosity, increasing the cross-sectional area of the exit flow channel, or by using an external lubricant. In some instances, the melt fracture problem can be solved by going to superextrusion; this process is used particularly often in the wire coating industry where high line speeds are quite important for economic production.

7.5.3.3 Draw Resonance

Draw resonance occurs in processes where the extrudate is exposed to a free surface stretching flow, such as blown film extrusion, fiber spinning, and blow molding. It manifests itself in a regular cyclic variation of the dimensions of the extrudate. An extensive review [169] and an analysis [170] of draw resonance were done by Petrie and Denn. Draw resonance occurs above a certain critical draw ratio while the polymer is still in the molten state when it is taken up and rapidly quenched after take-up.

Draw resonance will occur when the resistance to extensional deformation decreases as the stress level increases. The total amount of mass between die and take-up may vary with time because the take-up velocity is constant but not necessarily the extrudate dimensions. If the extrudate dimensions reduce just before the take-up, the extrudate dimensions above it have to increase. As the larger extrudate section is taken up, a thin extrudate section can form above it; this can go on and on. Thus, a cyclic variation of the extrudate dimensions can occur. Draw resonance does not occur when the extrudate is solidified at the point of take-up because the extrudate dimensions at the take-up are then fixed [171, 172]. Isothermal draw resonance is found to be independent of the flow rate. The critical draw ratio for almost-Newtonian fluids such as nylon, polyester, polysiloxane, etc., is approximately 20. The critical draw ratio for strongly non-Newtonian fluids such as polyethylene, polypropylene, polystyrene, etc., can be as low as 3 [173]. The amplitude of the dimensional variation increases with draw ratio and drawdown length.

Various workers have performed theoretical studies of the draw resonance problem by linear stability analysis. Pearson and Shah [174, 175] studied inelastic fluids and predicted a critical draw ratio of 20.2 for Newtonian fluids. Fisher and Denn [176] confirmed the critical draw ratio for Newtonian fluids. Using a linearized stability

analysis for fluids that follow a White-Metzner equation, they found that the critical draw ratio depends on the power law index n and a viscoelastic dimensionless number. The dimensionless number is a function of the die take-up distance, the tensile modulus, and the velocity at the die. Through their analysis, Fisher and Denn were able to determine stable and unstable operating regions. In some instances, draw resonance instability can be eliminated by increasing the draw ratio, although under most operating conditions draw resonance is eliminated by reducing the draw ratio.

White and Ide [177–180] demonstrated experimentally and theoretically that polymers whose elongational viscosity increases with time or strain do not exhibit draw resonance, but undergo cohesive failure at high draw ratios. A polymer that behaves in such a fashion is LDPE. Polymers whose elongational viscosity decreases with time or strain do exhibit draw resonance at low draw ratios and fail in a ductile fashion at high draw ratios. Examples of polymers that behave in such a fashion are HDPE and PP. Lenk [181] proposed a unified concept of melt flow instability. His main conclusions are that all flow instabilities originate at the die entrance and that melt fracture and draw resonance are not distinct and separate flow phenomena; both are caused by elastic effects that have their origin at the die entrance. Lenk's analysis, however, is purely qualitative and does not offer much help in the engineering design of extrusion equipment or in determining how to optimize process conditions to minimize instabilities.

■ 7.6 Devolatilization

Devolatilization is a function that is not performed on all extruders, as opposed to the other functions, such as solids conveying, melting, melt conveying, and mixing. Therefore, devolatilizing extruders are relatively specialized. However, as polymer processing operations become more sophisticated, it is becoming less unusual for the extruder to be used for continuous devolatilization. There have been relatively few engineering analyses of the devolatilization process in extruders. The first major effort seems to have been the work by Latinen [182]. Other analytical studies of devolatilization in extruders have been made by Coughlin and Canevari [183], Roberts [184], Biesenberger [185, 186], and Denson [236]. The physical model of devolatilization in a single screw extruder is shown in Fig. 7.119.

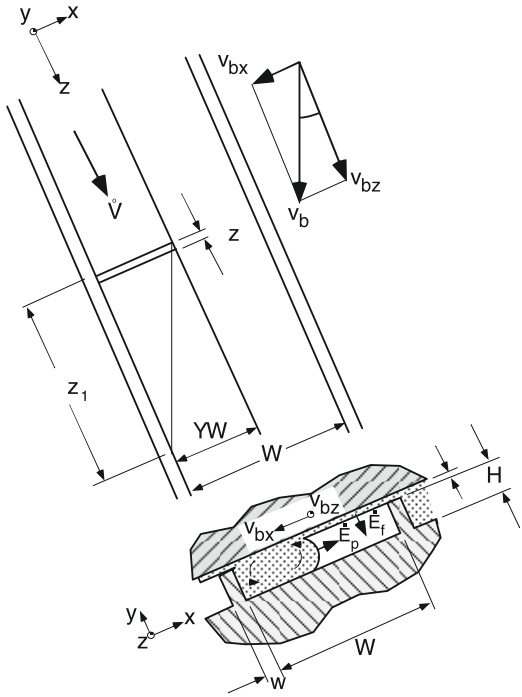


Figure 7.119
Model for devolatilization in screw extruders

The exposure time λ_f of the wiped film as it travels with the barrel surface from the flight clearance to the melt pool is:

$$\lambda_f = \frac{1-Y}{N} \tag{7.457}$$

where N is the screw speed and Y the fraction of the channel width occupied by the melt pool. If the channel is partially filled, then $Y < 1$ and Y represents the degree of fill in the extraction section.

The total volumetric flow rate of the wiped film is:

$$\dot{V}_f = v_b\, h_m L_b \tag{7.458}$$

where h_m is the melt film thickness and L_b is the total axial length of the devolatilizing zone.

The feedback ratio n_f is:

$$n_f = \dot{V}_f / \dot{V} \tag{7.459}$$

where $\dot{V}$ is the total volumetric flow rate through the extruder.

The feedback ratio is the part of the material that splits off of the main material flow to form a film through which volatiles are escaping. The feedback ratio n_f can be interpreted as the extent of the surface renewal of the melt film. As the melt film

enters the melt pool, again a certain amount of back mixing will take place, depending on the width of the melt pool and the helix angle. The melt pool will also lose volatiles because of the exposed surface. The exposure time of the exposed surface of the melt pool is limited because of the circulatory motion in the melt pool. Roberts [184] approximated the exposure time of the melt pool by:

$$\lambda_p = \frac{H}{v_{bx}} \tag{7.460}$$

where H is the channel depth and v_{bx} the cross-channel component of the barrel velocity.

The local bulk evaporation rate $\dot{E}_p(z)$ can be expressed as:

$$\dot{E}_p(z) = 2\left(\frac{D'}{\pi\lambda_p}\right)^{1/2} H\,\Delta z\left[C(z) - C_e\right] \tag{7.461}$$

where D′ is the diffusion coefficient, C(z) the local bulk average concentration of the melt pool, and C_e the equilibrium concentration at the vapor-liquid interface. For a derivation of Eq. 7.461, see Section 5.4.2.

The local film evaporation $\dot{E}_f(z)$ can be expressed as:

$$\dot{E}_f(z) = v_{bx}\,H_f\Delta z\left[C(z) - C'(z)\right] \tag{7.462}$$

where C′(z) is the concentration of the film reentering the melt pool at point z, having left the melt pool a distance Δz_1 downstream; see Fig. 7.119. The formulation of the model can be completed by taking a steady-state material balance on the volatile component over a differential element of volume of a thickness Δz. The balance simply states that the reduction in convective transport of the volatile component equals the film evaporation plus the bulk evaporation:

$$\dot{V}\left[C(z) - C(z+\Delta z_1)\right] = \dot{E}_p(z) + \dot{E}_f(z) \tag{7.463}$$

Now the value $C(z + \Delta z_1)$ has to be determined to obtain C′(z). Concentration $C(z + \Delta z_1)$ is the initial concentration of the melt film. This melt film reenters the melt pool at location z with concentration C′(z). As suggested by Roberts [184], a Taylor's series expansion about z can be used:

$$C(z+\Delta z_1) = C(z) + \frac{dC(z)}{dz}\Delta z_1 + \frac{d^2C(z)}{dz^2}\frac{\Delta z_1^2}{2} + \ldots \tag{7.464}$$

Terms of order three and higher will be assumed to be negligible. The concentration C′(z) at which the polymer reenters the melt pool is the initial concentration $C(z + \Delta z_1)$ of the film as it leaves the melt pool minus the amount of volatiles lost through

evaporation in the film during film exposure time λ_f. If X_f is the stage efficiency of the diffusing film, the concentrations $C'(z)$ and $C(z + \Delta z_1)$ can be related by:

$$\frac{C'(z)-C_e}{C(z+\Delta z_1)-C_e}=1-X_f \tag{7.465}$$

By using Eqs. 7.464 and 7.465, the mass balance equation can be rewritten as:

$$v_{bx}\,H_f(1-X_f)\frac{\Delta z_1^2}{2}\frac{d^2C}{dz^2}+\left[v_{bx}H_f(1-X_f)\Delta z_1-\dot{V}\right]\frac{dC}{dz} \tag{7.466}$$
$$-\left[X_f\,v_{bx}H_f+k_pH\right]\,(C-C_e)=0$$

where:

$$k_p=\left(\frac{4D'}{\pi\lambda_p}\right)^{1/2} \tag{7.466a}$$

Equation 7.439 can be written in dimensionless form:

$$\frac{1}{N_{Pe}}\frac{d^2\hat{C}}{d\hat{z}^2}-\frac{d\hat{C}}{d\hat{z}}-E_x\hat{C}=0 \tag{7.467}$$

where:

$$\hat{z}=\frac{z}{L} \tag{7.467a}$$

$$\Delta\hat{z}_1=\frac{\Delta z_1}{L} \tag{7.467b}$$

$$N_{Pe}=\left(\frac{2}{\Delta\hat{z}_1}\right)\left(\frac{1}{n_f(1-X_f)\Delta\hat{z}}-1\right) \tag{7.467c}$$

$$E_x=\frac{n_fX_f+k_pH\,L/\dot{V}}{1-n_f(1-X_f)\Delta\hat{z}_1} \tag{7.467d}$$

$$n_f=\frac{v_{bx}H_fL}{\dot{V}} \tag{7.467e}$$

$$\hat{C}=\frac{C-C_e}{C_o-C_e} \tag{7.467f}$$

The Peclet number NP_e represents the effect of longitudinal backmixing. Backmixing can be neglected when the Peclet number is very large ($N_{Pe} >> 1$). In the extreme case of pure plug flow, the Peclet number $N_{Pe} = \infty$; when $N_{Pe} = 0$, the entire flow channel acts as an ideal mixer.

The extraction number E_x is a measure of the overall devolatilization efficiency. The backmixing term disappears when the melt film thickness is zero. This is to be expected because the backmixing is caused by the transport in the melt film. If the film thickness is zero, there can be no transport in the melt film and consequently no backmixing. If the film stage efficiency $X_f = 1$, the backmixing term will disappear as well. This is also easy to understand because in this case the concentration $C'(z)$ at which the melt film reenters the melt pool is known and will equal C_e. Thus, the Taylor's series expansion is no longer necessary and the first-order differential equation can be determined directly from the mass balance, Eq. 7.463.

The magnitude of the backmixing effect will be directly determined by the distance Δz_1. This distance is directly related to the degree of fill Y, and the channel width W, and the helix angle φ:

$$\Delta z_1 = \frac{Y\,W}{\tan\varphi} \tag{7.468}$$

The channel width W, however, is also a function of the helix angle. If the screw is single flighted and if the flight width is negligible, distance Δz_1 can be written as:

$$\Delta z_1 = Y\,\pi\,D\cos\varphi \tag{7.469}$$

From Eq. 7.469, it can be seen that for a certain size extruder the backmixing effect will increase with the degree of fill in the extraction section. Thus, the channel depth in the extraction section should be significantly larger than the channel depth of the preceding screw section, the metering section. The backmixing effect will also increase when the helix angle becomes smaller. Thus, one would like to have a relatively small helix angle in the extraction section to increase the backmixing effect.

If the backmixing effect can be neglected ($N_{Pe} >> 1$), Eq. 7.467 becomes simply:

$$\frac{d\hat{C}}{d\hat{z}} = -E_x\hat{C} \tag{7.470}$$

The concentration thus becomes an exponential function of distance. If $\hat{C}(0) = 1$, the concentration profile becomes:

$$\hat{C} = \exp(-E_x\hat{z}) \tag{7.471}$$

where:

$$E_x = n_f X_f + k_p HL/\dot{V} \tag{7.471a}$$

The devolatilization efficiency of the machine X_T is a function of the individual stage efficiency X and the extent of surface renewal. In continuous equipment, such as screw extruders, the extent of surface renewal is described by the factor n_f (Eq. 7.459 or 7.467e); in batch devolatilizers, the extent of surface renewal is described by n, the discrete number of surface renewals. The film stage efficiency X_f is a function of the surface-to-volume ratio and the exposure time λ_f. It can generally be written as a single function of the ratio λ_f/λ_D. Thus, the overall efficiency X_T can be described as a function of the surface renewal factor n_f and the ratio λ_f λ_D:

$$X_T = X_T(n_f, \lambda_f/\lambda_D) \tag{7.472}$$

where λ_D is the characteristic time for diffusion in the film ($\lambda_D = h_m^2/D'$).

The effectiveness of the devolatilization operation is strongly dependent on the actual length of the devolatilization zone L_B. In actual extrusion the length L_B can be considerably longer than the length of the extraction section of the screw L_e. Thus, the length L_B can extend into the pump section of the extruder. This is determined by the filled length of the pump section L_{pf}.

If the length of the pump section is L_p, the actual devolatilization length L_B can be determined from:

$$L_B = L_e + L_p - L_{pf} \tag{7.473}$$

where L_e is the length of the extraction section, L_p the length of the pump section, and L_{pf} the filled length of the pump section. The latter can be calculated from melt conveying theory if the following parameters are known:

1. The geometry of the pump section
2. The throughput
3. The flow properties of the polymer
4. The diehead pressure

From the melt conveying theory of Newtonian fluids, the length L_{pf} can be determined from:

$$L_{pf} = \frac{p\,W\,H^3\,P\sin\varphi}{6\,\mu\,pW\,H\,v_{bz} - 12\,\mu\dot{V}} \tag{7.474}$$

where P is the diehead pressure.

This equation does not take into account the leakage flow or the effect of the flight flanks. The diehead pressure P is related to the total volumetric flow rate $\dot{V}$ by the die constant K:

$$P = K\,\dot{V} \tag{7.475}$$

In most two-stage devolatilizing extruder screws, the throughput $\dot{V}$ is determined by the metering section as a result of its shallow channel depth H_m. If the throughput is determined by the drag flow rate of the metering section and if the helix angle and the number of parallel flights is constant, the expression for L_{pf} can be simplified to:

$$L_{pf} = \frac{pW\,H^3 H_m K \sin\varphi}{12\,\mu\,(H - H_m)} \tag{7.476}$$

Thus, in order to keep L_{pf} short and L_B long, the depth of the metering section H_m should be small compared to the depth of the pump section H. Also the restriction of the die K should be made as small as possible.

7.7 Mixing

Mixing can be broadly defined as a process to reduce the non-uniformity of a composition. The basic mechanism of mixing is to induce physical relative motion of the ingredients. The types of motion that can occur are molecular diffusion, turbulent motion, and convective motion. The first two types of motion are essentially limited to gases and low-viscosity liquids. Convective motion is the predominant motion in high-viscosity liquids, such as polymer melts. As discussed in Section 5.3.3, polymer melts are not capable of turbulent motion as a result of their high viscosity; motion in polymer melts is always by laminar flow.

Convective mixing by laminar flow is referred to as laminar mixing. This is the type of mixing that occurs in polymer melt extrusion. The mixing action generally occurs by shear flow and elongational flow. If the components to be mixed are compatible fluids and do not exhibit a yield point, the mixing is distributive. This is sometimes referred to as extensive mixing. The process of distributive mixing can be described by the extent of deformation or strain to which the fluid elements are exposed. The actual stresses involved in this process are irrelevant in the description of the distributive mixing.

If the mixture contains a component that exhibits a yield stress, then the actual stresses involved in the process become very important. If the component exhibiting a yield point is a solid, this type of mixing is referred to as dispersive mixing, sometimes as intensive mixing. In dispersive mixing, a solid component needs to be broken down, but the breakdown only occurs after a certain minimum stress (yield stress) has been exceeded. If the component exhibiting a yield point is a liquid, the mixing process is referred to as homogenization. An example of dispersive mixing is the manufacture of a color concentrate where the breakdown of the pigment agglo-

merates below a certain critical size is of critical importance. An example of distributive mixing is the manufacture of a polymer blend, where none of the components exhibit a yield point.

Distributive mixing and dispersive mixing are not physically separated. In dispersive mixing, there will always be distributive mixing. However, the reverse is not always true. In distributive mixing, there can be dispersive mixing only if there is a solid component with a yield stress and if the stresses acting on this component exceed the yield stress.

A very important aspect of the study of mixing is the characterization of the mixture. A complete characterization requires the specification of the size, shape, orientation, and spatial location of every discrete element of the minor component. This, of course, is generally impossible. Various theories and techniques have been devised to describe and measure the goodness of mixing [187–200]. Some of the characterization techniques are quite sophisticated and can be time consuming. Quantitative characterization is very important to workers doing research on mixing. However, such techniques are not always practical in actual polymer processing operations. Visual observation, although qualitative, is often sufficiently accurate to determine whether a product is acceptable or not. Therefore, the various characterization theories and techniques will not be discussed here. For more information on this subject, the reader is referred to the literature [187–200, 301]. In this section, the primary emphasis will be on the description of the mixing process in a screw extruder.

7.7.1 Mixing in Screw Extruders

Mixing is an essential function of the screw extruder. It occurs in all screw extruders as opposed to devolatilization, which is done only on specialized machines. The mixing zone in the extruder extends from the start of the plasticating zone to the end of the die, assuming that significant mixing only takes place when the polymer is in the molten state. The fact that mixing starts at the beginning of the melting zone presents a practical and an analytical problem. It means that at the end of the melting zone there will be a considerable non-uniformity in the mixing history of the polymer.

A polymer element that melts early will be exposed to a significant mixing history by the time it reaches the end of the melting zone. On the other hand, a polymer element that melts at the very end of the melting zone will have hardly any mixing history at the end of the melting zone.

Similar problems occur in the melt conveying zone. A polymer element at about 2/3 of the height of the channel will have no cross-channel velocity component and as a result will have a short residence time in the melt conveying section and little mixing

history. A polymer element at about 1/3 of the channel will have considerable cross-channel velocity and relatively low down-channel velocity. As a result, this element will have a long residence time in the melt conveying zone and a large mixing history. This can be verified by analyzing the velocity profiles in the metering section as discussed in Section 7.4. It is clear, therefore, that the mixing action is not uniformly applied to all elements of the polymer melt. As a result of the inherent transport process in a screw extruder there will be considerable non-uniformities in the intensity of the mixing action and the duration of the mixing action. This is also true for the extruder die. Fluid elements in the center of the flow channel are exposed to a very low shear rate, and their residence is short because the velocities are highest in the center. Fluid elements at the wall are exposed to high shear rates, and their residence time is long because of the low velocities at the wall. Thus, even if a perfectly mixed fluid enters a die, non-uniformities can be expected as the fluid leaves the die.

The mixing process in extruders is generally analyzed by determining the velocity profiles occurring in the screw channel. From the velocity profiles, the deformation at various locations in the fluid can be determined. In most analyses, the fluid is considered Newtonian, the components have the same flow properties (i.e., a rheologically homogeneous fluid mixture), and the flow through the flight clearance is neglected. Another common assumption is a two-dimensional flow pattern in the screw channel; only flow in down-channel and cross-channel directions are considered.

When two viscous liquids are mixed, the interfacial area increases and the striation thickness decreases. Spencer and Wiley [201] have proposed to use the interfacial area as a quantitative measure of the goodness of mixing. Mohr et al. [189] used the striation thickness to describe the mixing process. If a surface element with arbitrary orientation is located in a simple shear flow field, the surface area A after a total shear strain of γ can be demonstrated to be [201]:

$$A = A_o\sqrt{1-2\cos\alpha_x\cos\alpha_y\gamma+\cos^2\alpha_x\gamma^2} \tag{7.477}$$

where A_o is the original surface area, α_x the angle of the vector normal to A_o with the x axis, and α_y the angle of the vector normal to A_o with the y axis.

Angles α_x, α_y, and α_z determine the initial orientation of the surface element under consideration. The three angles are related by:

$$\cos^2\alpha_x+\cos^2\alpha_y+\cos^2\alpha_z=1 \tag{7.478}$$

If the total shear strain is very large ($\gamma >>1$), then Eq. 7.477 becomes:

$$A = A_o\left|\cos\alpha_x\right|\gamma \tag{7.479}$$

Equation 7.479 indicates that the increase in interfacial area is directly proportional to the total shear strain and $\cos\alpha_x$. Thus, the total shear strain is an important variable in the description of the mixing process in a shear flow field. The initial orientation α_x is also very important. If the initial surface is oriented parallel to the flow field ($\alpha_x = 90°$), then the increase in interfacial area is zero. However, if the initial surface orientation is perpendicular to the flow field ($\alpha_x = 0$), then the increase in interfacial area is maximum. At low strains, it can be seen from Eq. 7.477 that the interfacial area can increase or decrease with strain, depending on the initial orientation.

If the interfaces are initially randomly oriented, the mean change in interfacial area becomes [202]:

$$A = \frac{1}{2} A_o \gamma \tag{7.480}$$

Equation 7.480 is valid when the total strain is very large ($\gamma >> 1$). The striation thickness is defined as the total volume divided by half the total interfacial surface:

$$s = \frac{V}{A/2} \tag{7.481}$$

If the minor component is initially introduced as randomly oriented cubes of height H and with a volume fraction φ, the striation thickness can be expressed as:

$$s = \frac{2H}{3\varphi\gamma} \tag{7.482}$$

Thus, the striation thickness is directly proportional to the initial domain size of the minor component and inversely proportional to the volume fraction and total shear strain. This indicates that a small striation thickness is achieved more easily when the initial domain size of the minor component is small and the volume fraction large.

The striation thickness is a commonly used measure of mixing. In simple shear the striation thickness reduces with the shear strain as follows:

$$\frac{s}{s_0} = \frac{1}{\sqrt{1+\gamma^2}} \tag{7.483}$$

The relationship between the striation thickness and the total shear strain is shown in Fig. 7.120. The initial orientation of the striation is perpendicular to the flow field ($\alpha_x = 0$); this is the optimum orientation.

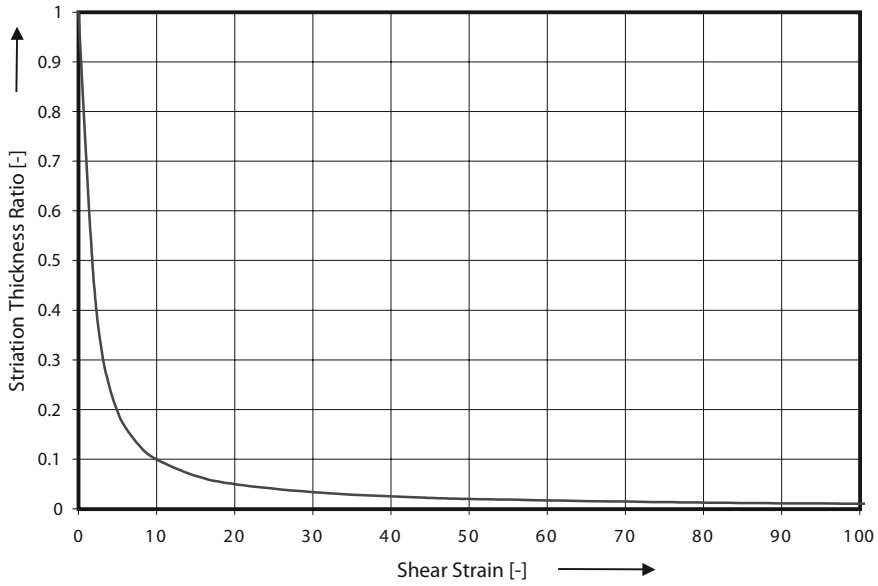


Figure 7.120 Striation thickness ratio versus total shear strain

It is interesting to note that the striation thickness reduces rapidly in the first 5 to 10 units of shear strain. After 10 units of shear, the striation thickness has reduced to about 10% of its original value. However, after about 10 to 20 units of shear strain, the striation thickness reduces only very slowly. There is very efficient mixing in the first 10 to 20 units of shear strain and inefficient mixing beyond 20 units of shear strain.

The reason that the mixing efficiency reduces with shear strain is that the orientation of the striation changes with shear strain. The striation becomes more and more oriented in the direction of flow as the shear strain increases. As a result, mixing for a long time does not make much sense because most of the mixing is achieved within the first 20 units of shear strain. However, the distributive mixing efficiency can be improved dramatically by reorienting the striations during the mixing process.

If the simple shear field is disrupted by a short mixing section that produces a randomly oriented minor component, the interfacial area at the outlet of the mixing section is:

$$A_1 = \frac{1}{2} A_o \gamma_1 \tag{7.484}$$

where γ_1 is the total shear strain the fluid is exposed to before the mixing section. It is assumed that the shear strain in the mixing section itself is insignificant. If the simple shear field is restored after the mixing section, then the total interfacial area after another exposure to shear strain γ_1 becomes:

$$A_2 = 0.5A_1\,\gamma_1 = A_o(0.5\,\gamma_1)^2 \tag{7.485}$$

Similarly, after n mixing sections and n shear strain exposures of the same magnitude γ_1, the total interfacial area will be:

$$A_n = A_o(0.5\gamma_1)^n \tag{7.486}$$

From Eq. 7.486, it can be seen that the generation of interfacial area can be increased substantially by inclusion of mixing sections that randomize the minor component. The improvement can be evaluated by comparing n mixing sections and $n\gamma_1$ strain exposures to simple shear mixing without mixing sections but the same total strain exposure. The ratio of the interfacial area is:

$$\frac{A_n(\gamma_1)}{A_1(n\,\gamma_1)} = \frac{(0.5\,\gamma_1)^{n-1}}{n} \tag{7.487}$$

The striation thickness versus shear strain with various reorientation events is shown in Fig. 7.121.

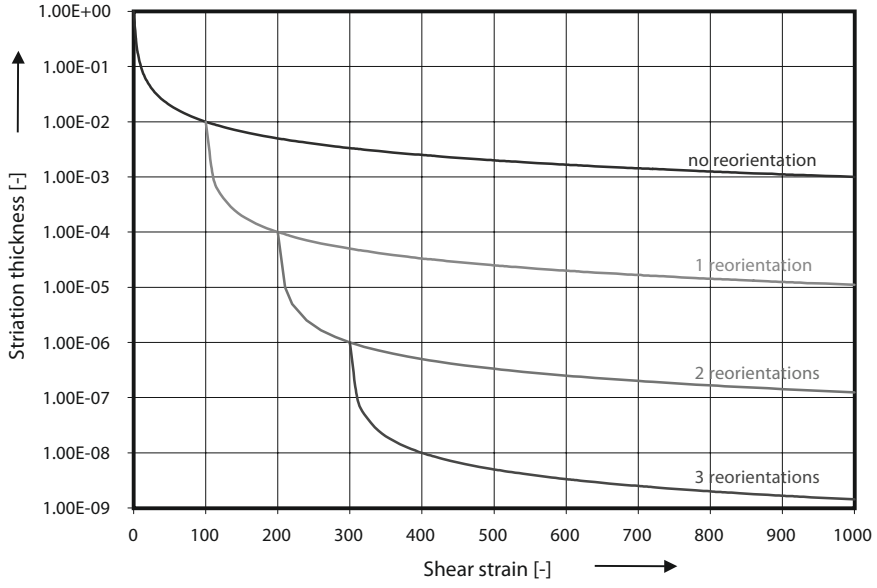


Figure 7.121 Striation thickness versus shear strain with various reorientation events

In Fig. 7.121 reorientation occurs after 100 units of shear strain. Without reorientation the striation thickness reduces to about 10^{-3} after 1000 units of shear strain. With one reorientation the striation thickness reduces to about 10^{-5}, with two reorientations to about 10^{-7}, etc. Clearly, reorientation can achieve improvements in distributive mixing by orders of magnitude. It is a powerful tool in mixing operations.

It is obvious that randomizing mixing sections greatly improves the generation of interfacial area and thus the mixing performance. Erwin and Ng [205] constructed an experimental mixing apparatus by which the results of Eqs. 7.486 and 7.487 and Fig. 7.121 have been experimentally verified. However, the mixing apparatus does not lend itself to practical mixing operations.

If the mixing section is capable of orienting the minor component in the most favorable direction, i.e., perpendicular to the velocity, the total interfacial area after n mixing sections and n shear strain exposures of magnitude γ_1 will be:

$$A_n = A_0(C\gamma_1)^n \tag{7.488}$$

where C = 1/2 if the initial orientation is random and C = 1 if the initial orientation is most favorable.

Equations 7.486 and 7.487 demonstrate, at least qualitatively, that incorporation of mixing devices can substantially improve laminar mixing performance. In a dynamic mixing device, such as an extruder, it may be difficult to design a mixing section that will orient the minor component in the most favorable orientation. However, random orientation may be more feasible. In a static mixing device, it is easier to control the orientation of the minor component, and effective laminar mixing can occur in such mixing devices; see Section 7.7.2.

7.7.1.1 Distributive Mixing in Screw Extruders

The shear rate in the polymer melt is found by taking the first derivative of the velocity. The velocity profiles for Newtonian fluids were derived in Section 7.4.1. From Eq. 7.197 we can determine the down-channel shear rate:

$$\dot{\gamma}_{yz} = \frac{dv_z}{dy} = \frac{\pi D N \cos\varphi}{H}\left(1 - 3r_d + 6r_d\frac{y}{H}\right) \tag{7.489}$$

The down-channel shear rates are shown in Fig. 7.122.

When the pressure gradient is positive the shear rates increase toward the barrel surface, when the pressure gradient is zero the shear rate is constant, and when the pressure gradient is negative the shear rates reduce toward the barrel surface.

The cross-channel shear rate is determined the same way:

$$\dot{\gamma}_{yx} = 2\frac{\pi D N \sin\varphi}{H}\left(-1 + 3\frac{y}{H}\right) \tag{7.490}$$

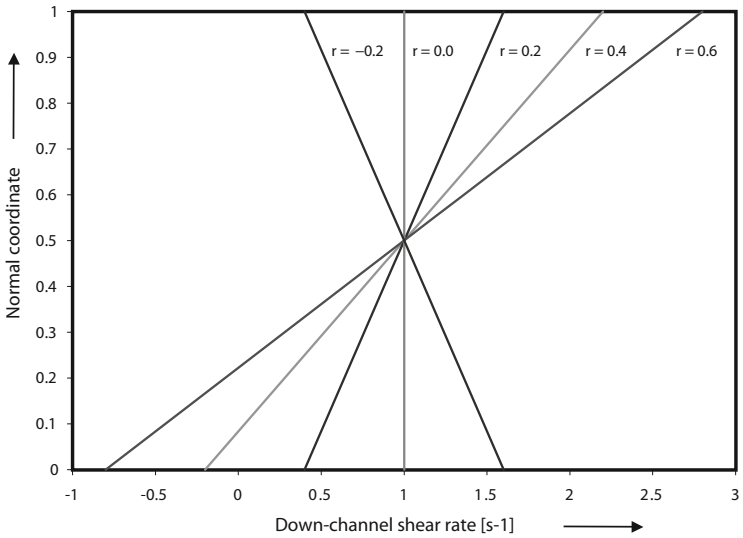


Figure 7.122 Down-channel shear rates for several values of the throttle ratio

The cross-channel shear rate profile is shown in Fig. 7.123.

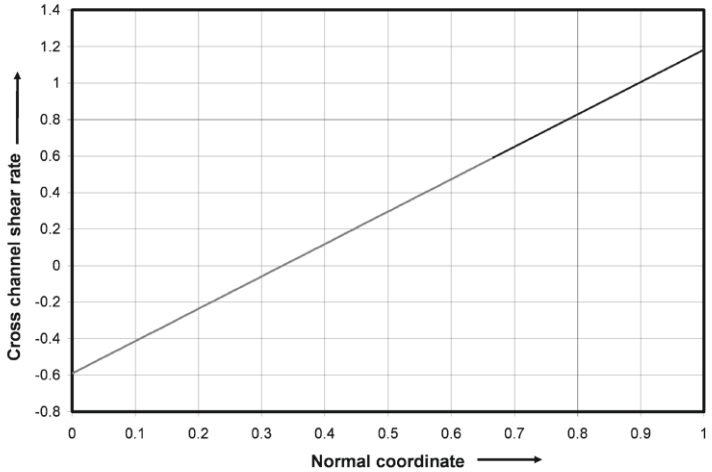


Figure 7.123 Cross-channel shear rate versus normal distance

In the bottom of the channel the fluid is exposed to negative shear rates, and in the top of the channel the fluid is exposed to positive shear rates. This has important consequences for the mixing that occurs in screw extruders. At the top of the channel the fluid elements travel in the direction of the barrel, while at the bottom of the channel the fluid elements travel across the channel. The position of a fluid element in the upper portion of the channel (y) corresponds to a complementary position in the lower portion of the channel (y_c) as shown in Fig. 7.124.

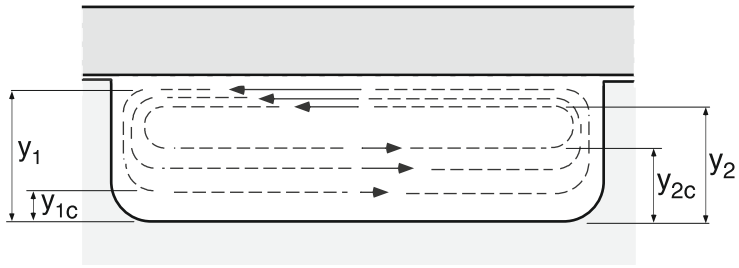


Figure 7.124 Position y and complementary position y_c in screw channel

The time that a fluid element spends in the upper portion of the channel (t_u) is determined by the width of the channel and the cross-channel velocity:

$$t_u(y) = \frac{W}{|v_x(y)|} \tag{7.491}$$

A similar expression is used to determine the time spent in the lower portion of the channel. The total residence time over axial length L of the extruder screw is determined from Eq. 7.492.

$$t(y) = \left[\frac{2L}{3v_b \sin(2\varphi)(1-r_d)}\right] \frac{3yH - H^2 + 3H(H^2 + 2yH - 3y^2)^{0.5}}{yH - y^2 + y(H^2 + 2yH - 3y^2)^{0.5}} \tag{7.492}$$

The residence time as a function of the normal distance is shown in Fig. 7.125.

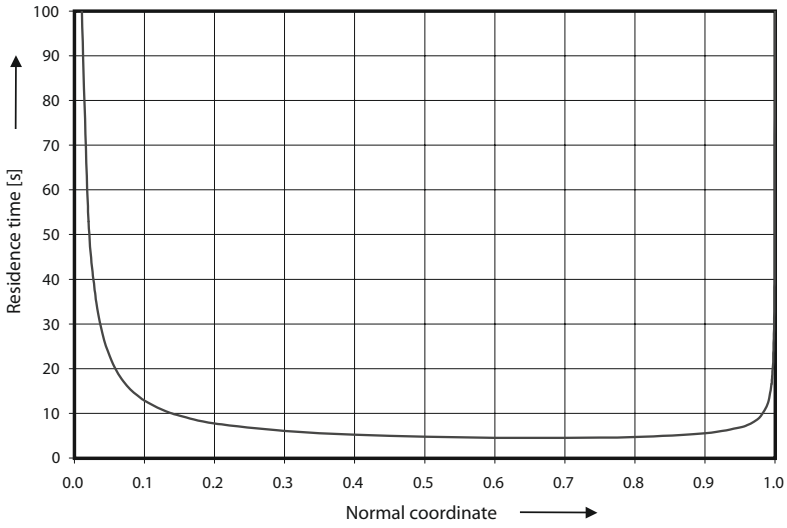


Figure 7.125 Residence time versus normal distance (dimensionless)

It is clear from Fig. 7.125 that the residence time in the center region of the channel has the lowest residence time; the minimum occurs at y = 2H/3. There is a rather broad region (from about 10 to 90% of the depth of the channel) where the residence time is quite low. The residence time increases towards the screw and barrel surface and reaches infinity at y/H = 0 (screw root) and y/H = 1 (barrel). The long residence time layer on the screw surface is substantially thicker than at the barrel surface. This indicates that problems due to long residence time, such as degradation, are more likely to occur at the screw surface than at the barrel surface.

The time fraction spent in the upper portion of the channel is determined from:

$$f_u(y) = \frac{t_u(y)}{t_u(y) + t_l(y_c)} \tag{7.493}$$

This fraction is shown in Fig. 7.126.

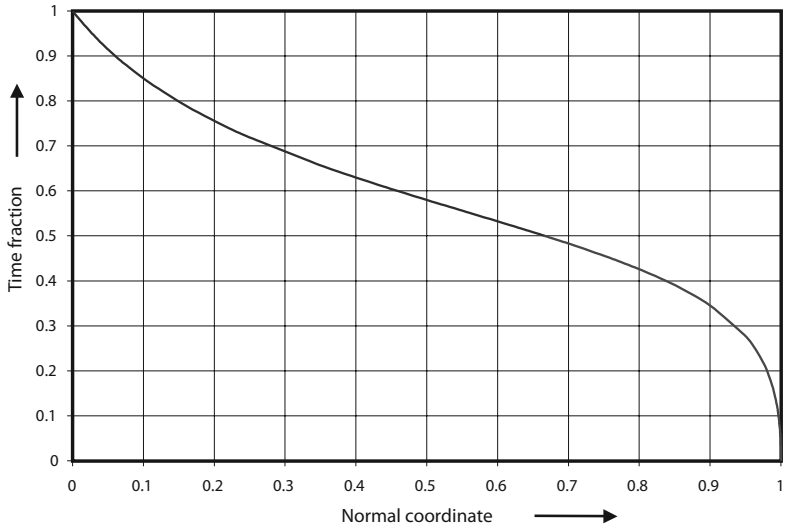


Figure 7.126 The fraction of time in the lower and upper portion of the channel versus normal distance

The lowest value $f_u = 0$ occurs at y/H = 1; the highest value $f_u = 0.5$ occurs at y = 2/3. This indicates that the fluid elements spend much more time in the lower portion of the channel than in the upper portion. It is worthwhile to analyze the cross-channel flow in more detail. We can distinguish two types of re-circulation, one in the outer region and one in the inner region of the channel. The outer region A is bounded by $0.91H \le y \le H$ (region A_u) and $0 \le y_c \le H/3$ (region A_l). The inner region is bounded by $y \le 0.91$ and $y_c \ge H/3$; see Fig. 7.127.

Interestingly, the shearing in the lower region A is in the negative direction, while the shearing in the upper region A is in the positive direction. This means that the mixing that occurs in the lower portion of the channel is counteracted by the mixing

in the opposite direction in the upper portion of the channel. In fact, there is a demixing action going on as a result of the exposure to positive and negative shear rates! This is illustrated by the shear deformation of a rectangular element in Fig. 7.127.

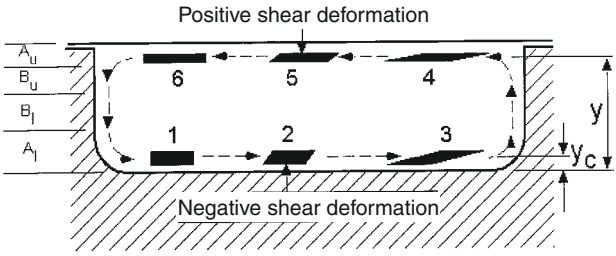


Figure 7.127 Cross-channel flow and resulting shear deformation

The situation is quite different in region B. Here the shearing in the lower part of region B is in the same direction as in the upper part. As a result, the mixing in the upper portion of region B enhances the mixing in the lower portion of region B. Therefore, there are no demixing effects occurring in region B, the inner re-circulating region, only in region A, the outer re-circulating region.

The total cross-channel shear strain can be determined by adding the shear strain in the upper portion of the channel to that in the lower portion of the channel. The total cross-channel shear strain can thus be written as:

$$\gamma_x = \dot{\gamma}_x(y)\, f_u\, t(y) + \dot{\gamma}_x(y_c)(1 - f_u)\, t(y_c) \tag{7.494}$$

Figure 7.128 shows the cross-channel shear strain as a function of normal distance for one value of the throttle ratio $r_d = 0.1$, assuming that $\pi DN/H = 1$.

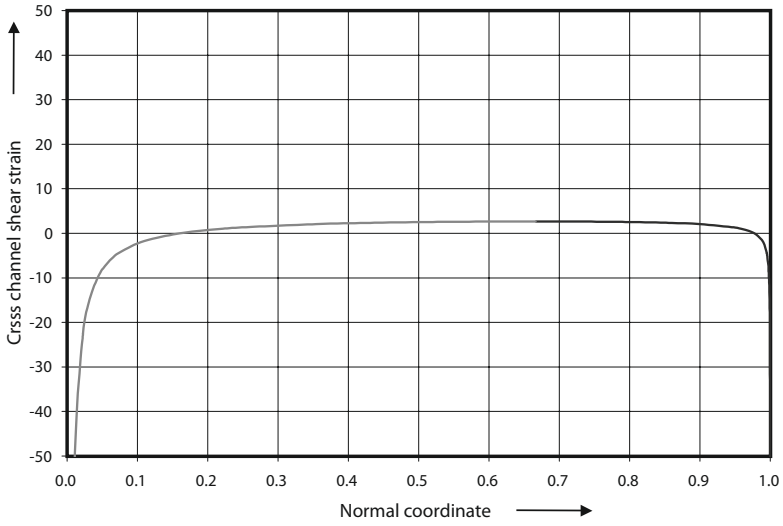


Figure 7.128 The cross-channel shear strain versus normal distance (dimensionless)

The shear strain reaches $-\infty$ at the screw and barrel surface. The shear strain becomes zero at y = 0.98H and y_c = 0.16H; this corresponds to the streamline where the shear strain in region A_u is canceled exactly by the opposite shear in region A_l. The cross-channel shear strain reaches a maximum at y = (2/3)H; this is where the cross-channel velocity becomes zero. The value of the maximum shear increases with increasing throttle ratio r_d, because the residence time increases when the throttle ratio increases.

Similar to the total cross-channel shear strain, the total down-channel shear strain can be written as:

$$\gamma_z = \dot{\gamma}_z(y)\, f_u\, t(y) + \dot{\gamma}_z(y_c)\,(1 - f_u)\, t(y_c) \tag{7.495}$$

Figure 7.129 shows the down-channel shear strain as a function of the normal distance at several values of the throttle ratio r_d.

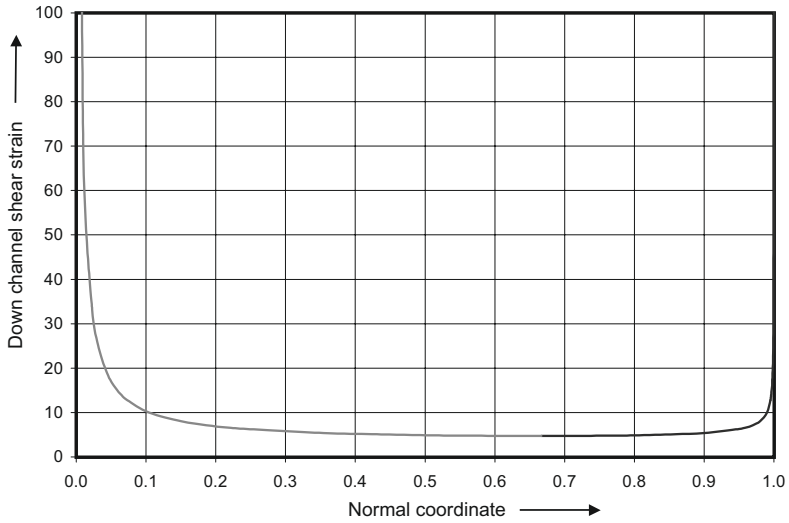


Figure 7.129 Down-channel shear strain versus normal distance for r_d = 0.1

When r_d = 0, the down-channel shear strain curve has exactly the same form as the residence time curve; this is due to the fact that the down-channel shear rate is constant when r_d = 0. When r_d = 1/3, the down-channel shear strain becomes independent of the normal coordinate y. When r_d > 1/3 the down-channel shear strain becomes negative close to the screw and barrel surface. This is due to the fact that the shear rates at the screw surface become negative when r_d > 1/3.

The magnitude of the total shear strain is obtained by vectorial addition of the cross- and down-channel shear strains. This leads to the following expression of the total shear strain:

$$\gamma = \sqrt{\left(\gamma_x^2 + \gamma_z^2\right)} \tag{7.496}$$

With this expression the distributive mixing process in the melt conveying zone of a single screw extruder can be evaluated quantitatively. The total shear versus normal distance for several values of the throttle ratio is shown in Fig. 7.130.

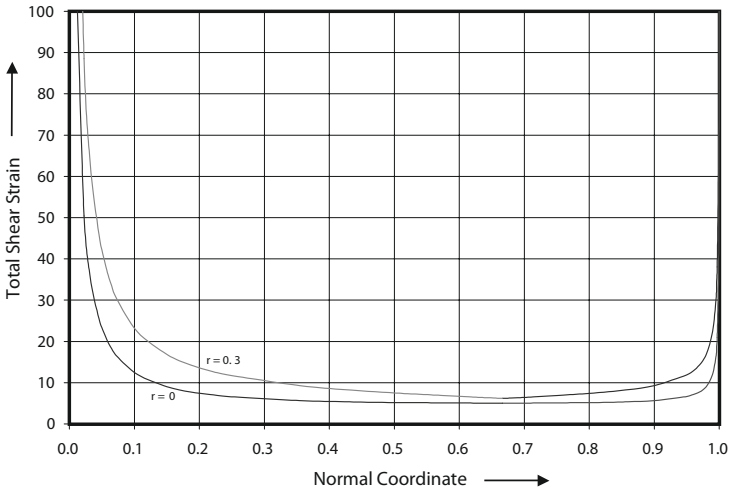


Figure 7.130 Total shear strain versus normal distance (dimensionless) at two r_d values

The total strain depends strongly on both the normal distance and on the throttle ratio. Fluid elements close to the wall experience a high level of shear strain and, thus, will be well mixed. Elements further away from the wall experience a lower level of strain and will not be mixed as well as elements close to the wall.

The shear strain in the center region increases with the throttle ratio. When the throttle ratio is one-third or greater, the shear strain reaches a minimum close to the wall; this corresponds to the location where the down-channel shear strain approaches zero. Mixing is improved by increasing the throttle ratio; this can be done by increasing the restriction at the end of the screw, for instance, by increasing the number of screens of the screen pack. Such an increase in mixing, however, is at the expense of output. Since reduced output will increase residence time and polymer melt temperatures, there will be an increased chance of degradation. Therefore, increasing the restriction of the screen pack is often not the most efficient way of improving mixing.

The shear strains in both x and z directions can be used to calculate the striation thickness:

$$s = \frac{s_0}{\Phi_v \left[1 + \sqrt{1+\gamma_z^2} + \sqrt{1+\gamma_x^2}\right]} \tag{7.497}$$

where Φ_v is the volume fraction of the minor component and s_0 the initial striation thickness.

Since γ_x and γ_z depend on the normal distance, the striation thickness will depend on the normal distance as well. Thus, the non-uniform cross- and down-channel shear strain will result in non-uniform mixing in the screw channel. Unfortunately, poor mixing ability is typical of single screw extruders with straight conveying screws, i.e., without mixing sections. The best method to really improve mixing in single screw extruders is to incorporate mixing sections. This topic will be discussed in Chapter 8. Another reason that mixing sections can be important is the substantial non-uniformities in melt temperature that can occur in screw extruders. If a melt with non-uniform melt temperatures is discharged into an extrusion die, a number of problems can occur that affect the quality of the extruded product. Melt temperature distributions will be discussed in Chapter 12.

The energy requirement to achieve a certain amount of increase in interfacial area was studied by Erwin [204]. In uniaxial extension flow, the energy per unit volume is related to the surface area increase as shown in Eq. 7.498.

$$E_{ue} = \frac{12\eta}{t}\left(\ln\frac{5A}{4A_o}\right)^2 \tag{7.498}$$

where η is the viscosity of the fluid and t the duration of the extensional deformation.

In biaxial extensional flow, the energy per unit volume is:

$$E_{be} = \frac{3\eta}{t}\left(\ln\frac{5A}{4A_o}\right)^2 \tag{7.499}$$

In plane strain elongation (two-dimensional elongation), the energy per unit volume is:

$$E_{ps} = \frac{4\eta}{t}\left(\ln\frac{2A}{A_o}\right)^2 \tag{7.500}$$

In simple shear, the energy per unit volume is:

$$E_{ss} = \frac{4\eta}{t}\left(\frac{A}{A_o}\right)^2 \tag{7.501}$$

Figure 7.131 shows the normalized energy per unit volume versus the ratio of interfacial areas for uniaxial extension and simple shear flow.

For the same increase in interfacial area, extensional flow is substantially more energy efficient than shear flow. When the area ratio becomes larger than 100, the energy requirement in simple shear is several orders of magnitude higher than extensional flow. This is an important advantage of extensional flow, particularly for dispersive mixing. Lower energy consumption results in less viscous dissipation

and lower melt temperatures. With lower melt temperatures greater stresses can be generated in the polymer melt, thus improving dispersive mixing. Dispersive mixing will be discussed in Section 7.7.3.

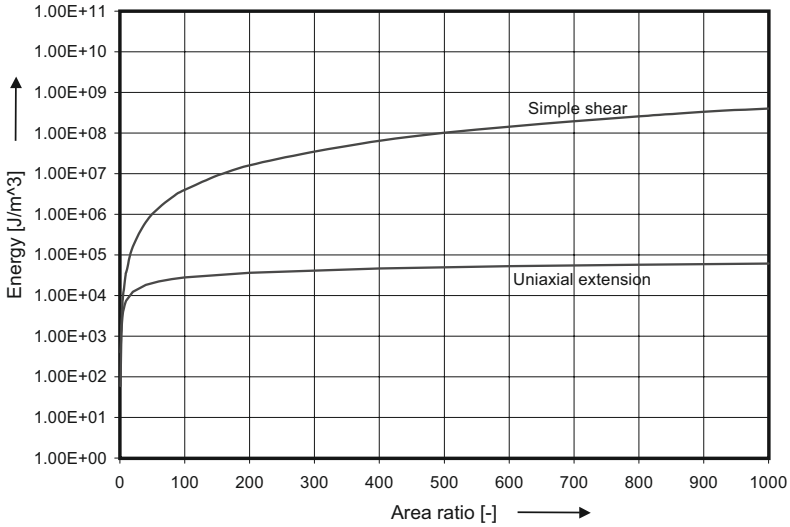


Figure 7.131 Energy consumption versus area ratio for shear and elongational flow

In continuous mixers, different fluid elements will invariably experience different amounts of strain, as discussed earlier for the screw extruder. Tadmor and Lidor [206] proposed the use of strain distribution functions (SDF), similar to residence time distribution functions (RTD). The SDF for a continuous mixer $f(\gamma)d\gamma$ is defined as the fraction of exiting flow rate that experienced a strain between γ and $d\gamma$. It is also the probability of an entering fluid element to exit with that strain. The cumulative SDF, $F(\gamma)$, is defined by the following expression:

$$F(\gamma) = \int_{\gamma_0}^{\gamma} f(\gamma)d\gamma \tag{7.502}$$

where γ_0 is the minimum strain.

$F(\gamma)$ represents the fraction of exiting flow rate with strain less than or equal to γ. The mean strain of the exiting stream is:

$$\bar{\gamma} = \int_{\gamma_0}^{\infty} \gamma\, f(\gamma)d\gamma \tag{7.503}$$

Tadmor and Pinto [207] used the weighted average total strain (WATS) to describe mixing performance in the non-homogeneous flow field of a single screw extruder. This is defined as:

$$\mathrm{WATS} = \int_{0}^{\infty} \gamma(t)\, f(t)dt \tag{7.504}$$

where f(t) is the RTD function and γ(t) the strain undergone by a fluid element at time t. The WATS does not produce an experimentally measurable quantity describing mixing, as discussed by Ottino and Chella [208] in an extensive review of laminar mixing of polymeric liquids. Another limitation is that the initial orientation of the minor component is not considered, and changes in orientation are not taken into account. Ottino [209, 210] developed a description of laminar mixing using the mathematical structure of continuum mechanics. This description allows evaluation of the role of initial orientation and the definition of mixing efficiency. This approach was applied to mixing in single screw extruders [211]. The mixing achieved was expressed in terms of mixing cup average area stretch "η". This factor was found to depend on down-channel distance, channel width-to-height ratio, helix angle, throttle ratio, and the initial orientation. The effect of helix angle and throttle ratio (ratio of pressure flow to drag flow) is shown in Fig. 7.132.

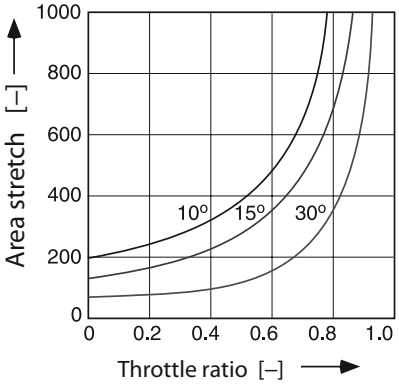


Figure 7.132 Area stretch versus throttle ratio

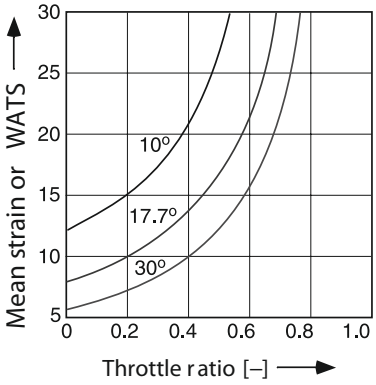


Figure 7.133 Mean strain versus throttle ratio

The mixing in single screw extruders was also studied by Tadmor and Klein [103] who used the mean strain to evaluate the mixing performance of the extruder; their result is shown in Fig. 7.133.

By comparing Fig. 7.132 to Fig. 7.133, it is clear that Tadmor's results correspond reasonably well with Ottino's results. The mixing performance improves as the throttle ratio increases. This is to be expected since the output per revolution will decrease, thus the mean residence time will increase with the throttle ratio, while the local shear rates will remain approximately the same. The mixing performance reduces as the helix angle increases from 10 to 30°. As the helix angle increases, the output per revolution increases as well, resulting in a reduced residence time. The residence time seems to play an overriding role because the cross-channel mixing improves with increasing helix angle, but the overall mixing performance reduces. Thus, the reduction in mean residence time overrides the effect of improved cross-channel mixing as the helix angle increases from 10 to 30°. Equation 7.206 (see also

Chapter 8) shows that 30° happens to be the optimum helix angle for Newtonian fluids with respect to output. This means that at a helix angle of 30°, the shortest residence time is achieved, provided the depth of the channel is optimum as well.

Analyses of laminar mixing in screw extruders generally deal with highly simplified problems. The leakage flow through the flight is usually neglected, as well as the normal velocity components close to the flight flanks. Just these two simplifications constitute a severe limitation on the validity and applicability of results of any mixing analysis. The normal velocity components achieve a reorientation of the minor component. When the normal velocity components are neglected, the reorientation of the interfacial area cannot be properly accounted for. This is a particularly severe problem in the analysis of multi-flighted mixing sections, such as the Dulmage mixing section; see Section 8.7.2.

The laminar mixing action can only be analyzed if the exact flow patterns are known. This can be done reasonably well for simple rectangular flow channels in an extruder screw. However, when mixing sections are incorporated into the extruder screw, the flow patterns generally become quite complex. In one respect, this is desirable because complex velocity profiles tend to improve the mixing effectiveness. However, on the other hand, the mathematical description of the velocity profiles can become very involved. This is particularly true when the minor fluid component has flow properties that are different from the major fluid components, i.e., when the fluid mixture is rheologically non-homogeneous.

As a result, quantitative analysis of mixing sections in extruders can be complicated. Therefore, development of mixing devices has been mostly empirical up to about the end of the last millennium. With the advent of more powerful numerical techniques it is now possible to do a complete three-dimensional flow analysis of mixing devices with complex geometry. The boundary element method has proven to be particularly useful in the analysis of complex mixers. Mixing devices will be discussed in detail in Chapter 8 and numerical techniques and computer simulation in Chapter 12.

7.7.2 Static Mixing Devices

Mixing in extruders occurs not only along the extruder screw but also from the end of the screw to the exit of the die. The flow through the die and possible adapter is a pressure-driven flow where the flow velocities in the center of the channel are high and zero at the wall, see Fig. 7.134.

This velocity profile results in a non-uniform shear rate profile with high shear rates at the wall and zero shear rate at the center of the channel; see Fig. 7.134. For a power law fluid in a circular channel the axial velocity profile can be written as [16]; see Fig. 7.110:

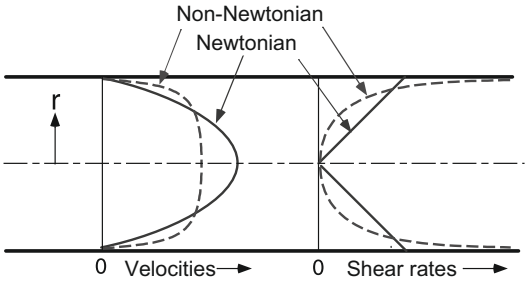


Figure 7.134
Velocity and shear rate profiles in pressure flow through a straight channel

$$v(r) = \frac{s+3}{s+1}\,\bar{v}\left[1-\left(\frac{2r}{D}\right)^{s+1}\right] \tag{7.505}$$

The shear rate profile is determined by taking the first derivative of the velocity with respect to normal distance r. Thus, the shear rate becomes:

$$\dot{\gamma}(r) = \frac{2(s+3)\,\bar{v}}{D}\left(\frac{2r}{D}\right)^{s} \tag{7.506}$$

The residence time of a fluid element over length L as a function of radial distance is simply:

$$t(r) = \frac{L}{v(r)} \tag{7.507}$$

The shear strain exposure is the shear rate multiplied with the shear exposure time. Thus, the shear strain as a function of radial distance becomes:

$$\gamma(r) = \dot{\gamma}(r)\,t(r) = \frac{2(s+1)\,L/D}{(D/2r)^{s} - 2r/D} \tag{7.508}$$

From the expression above it is clear that the shear strain distribution in the channel is very non-uniform. The shear strain in the center is zero, while it approaches infinity at the wall, as shown in Fig. 7.135.

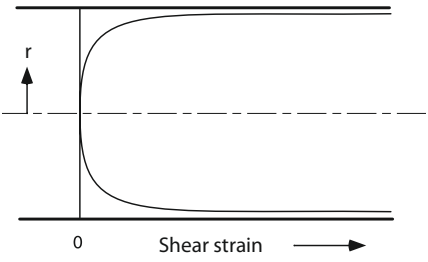


Figure 7.135
Shear strain distribution in pressure flow through a straight channel

The equations above are based on the assumption that the flow is laminar, which will generally be the case for polymer melts due to their high viscosity. If, however, turbulent flow takes place, then even in a simple circular channel efficient mixing can occur. When two fluids of equal density are introduced side by side into an empty pipe with diameter D, then the degree of mixing after length L can be expressed as [260]:

$$\left(\frac{s}{\sigma_0}\right)^2 = 10^{-mL/D} \tag{7.509}$$

where s is the sample standard derivation, σ_0 the initial standard derivation, and m is a coefficient that depends on the Reynolds number.

According to Hiby [289] the mixing quality in most practical mixing operations is sufficient when the coefficient of variation is less than one-hundredth. The coefficient of variation, COV, is the sample standard deviation divided by the average concentration. Thus, the Hiby requirement can be written as:

$$\frac{s}{\overline{C}} \leq 0.01 \tag{7.510}$$

where s is the sample standard deviation and $\overline{C}$ the average concentration.

Other sources consider the mixing sufficient when the coefficient of variation is less than 0.05 [261]. At a Reynolds number of 8000 the value of m = 0.046 and the pipe length will have to be about 90 D before sufficient mixing is achieved. Various methods can be used to shorten this length as discussed, e. g., by Hartung and Hiby [290] and Fleischmann [291].

In regular laminar flow through a straight pipe without mixing elements, the length of the pipe will have to be about 90 D before sufficient mixing is achieved. Clearly, this is much too long for practical applications in plastics extrusion. The mixing action in laminar pressure flow can be substantially improved by incorporating static mixing devices in the channel. These devices split and reorient the flow and, thus, impart improved distributive mixing to the fluid. Because these mixers have no moving parts, they are often referred to as motionless mixers. Some of the advantages of static mixing devices are:

- Can be used for fluids with a wide range of viscosities
- Continuous mixing device
- Small space requirement
- No moving parts, little or no wear, no noise
- Temperature insensitive
- Low operational cost

7.7.2.1 Geometry of Static Mixers

Static mixing devices usually consist of a combination of identical elements, stacked in series with each element turned ninety degrees relative to the next element. The first static mixer, the Multiflux mixer, was described by Sluijters [243]. This mixer developed at AKZO Corporation of the Netherlands splits the flow in rectangular converging and diverging channels; see Fig. 7.136.

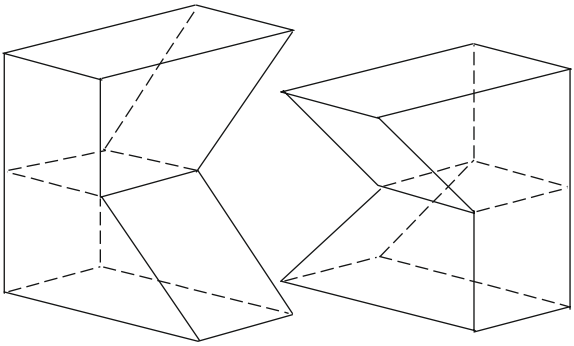


Figure 7.136
Channel geometry in the Multiflux mixer

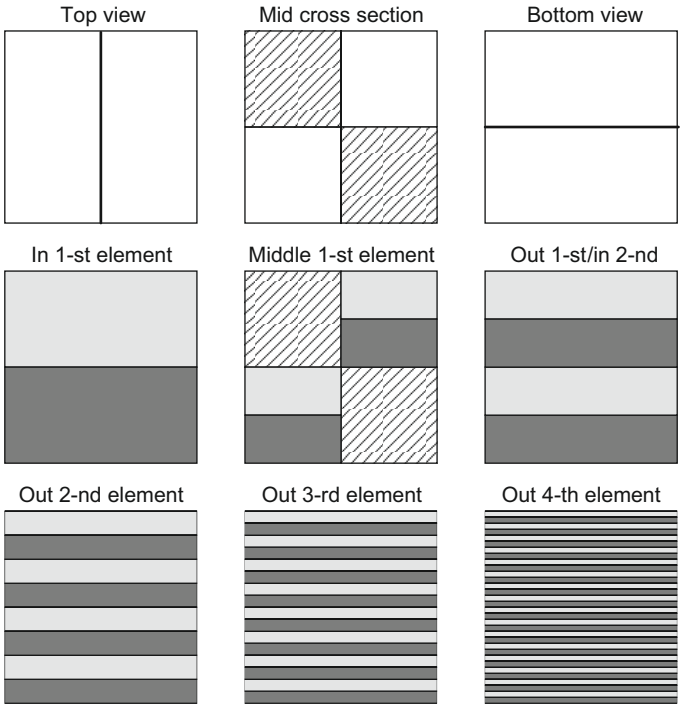


Figure 7.137
The Multiflux static mixer

Each element of the Multiflux mixer has two channels, as shown in Fig. 7.136. The channels start with a rectangular cross-section and then taper to a square cross-section in the middle of the element. From the square cross-section the channel

opens up again to a rectangular cross-section; however, the exit rectangle is perpendicular to the inlet rectangle. The resulting mixing action is shown in Fig. 7.137. A recent numerical study on the flow and layer distribution in the Multiflux mixer was published by van der Hoeven et al. [283].

The ISG mixer has four circular channels in each element, with material from the outside being led to the inside and vice versa; see Fig. 7.138. The flow through this mixer is not very streamlined and the individual channels are quite small, making this mixer unattractive for high-viscosity or thermally sensitive materials.

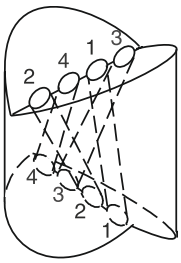


Figure 7.138
The ISG static mixer

The SMV mixer developed by the Swiss company Sulzer is made up of stacked corrugated plates with adjacent plates having opposite orientation. The length of one element is about one diameter; usually several elements are placed in series with one element turned 90° relative to the element next to it. Because of the splitting and reorientation within one element, the mixing action is quite efficient. The mixer geometry and mixing action is shown in Fig. 7.139. This mixer is primarily used for low-viscosity fluids.

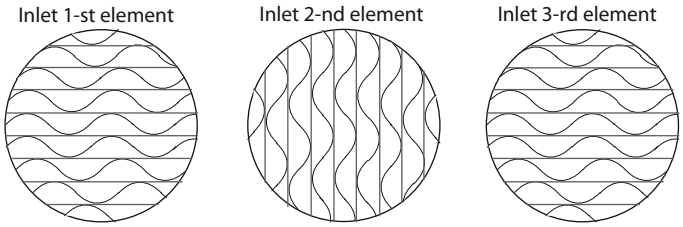


Figure 7.139
The SMV static mixer

The SMX mixer is manufactured and sold by Sulzer under license from Bayer. In fact, this mixer used to be called the BMK mixer, which stands for Bayer Kontinuierlich Mischer (German for Bayer Continuous Mixer). It consists of crossed bars forming an approximately 45° angle with the axis of the pipe; see Fig. 7.140.

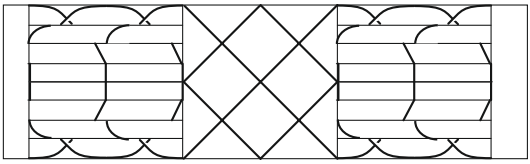


Figure 7.140
The SMX static mixer

This mixer is also described in Chapter 12, where Fig. 12.53 shows a picture of the mixer geometry, and Fig. 12.54 shows simulated particle tracking through the mixer, while Fig. 12.55 shows the predicted pressure profile. The bars split the flow into layers, which are distributed over the cross-section of the pipe. The degree of mixing increases exponentially with the number of mixing elements. Adjacent elements are turned 90° relative to one another. The mixing action of the SMX element is based on the flow around a tilted bar. When the bar is perpendicular to the flow, the flow splits and recombines behind the bar; see Fig. 7.141 left. However, when the bar is positioned at an angle to the flow, the flow splits but does not recombine behind the bar as a result of secondary flows changing the flow pattern; see Fig. 7.141 right.

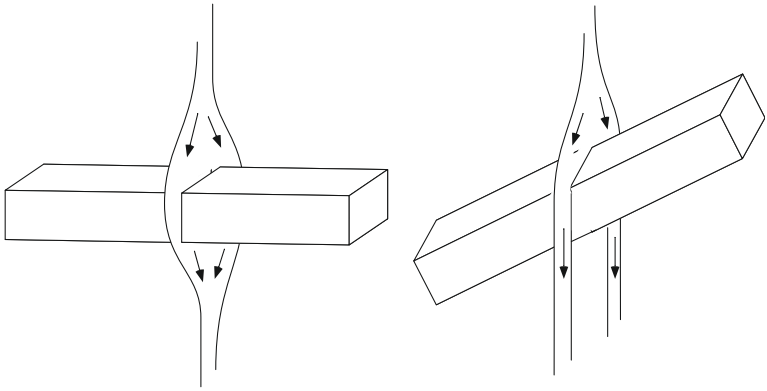


Figure 7.141 Flow splitting with straight and oblique bars

A relatively simple static mixer [245] is the twisted tape mixer developed by Kenics. The geometry of this mixer is shown in Fig. 7.142. The Kenics mixer is made up of plates that are twisted over 180°, and in some cases over 90°. The next plate is oriented at a 90° angle relative to the preceding plate. As a result, the material gets split and reoriented as it flows through the various elements of the mixer. Studies on this static mixer have been published by C. D. Han et al. [215] and others. The advantage of the Kenics mixer is its simple design and ease of cleaning.

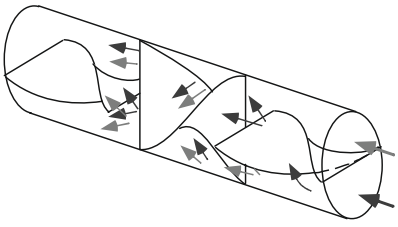


Figure 7.142
The Kenics static mixer

A static mixer that incorporates the twisted tape concept in a different configuration is the Equalizer from Komax Systems. Each element contains six circular channels with a twisted tape in each channel; see Fig. 7.143. The tape in each element is

twisted such that a centered additive input will be converted to a pattern with radial spokes. The second mixing element turns the melt stream inside out. This process repeats itself when a number of elements are placed in series.

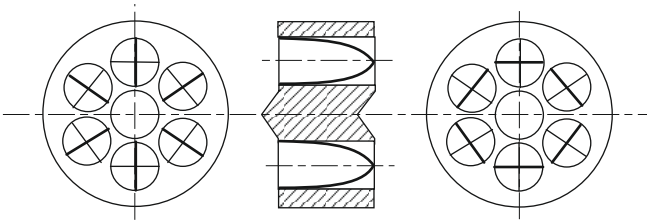


Figure 7.143
The Equalizer from Komax Systems

Another mixer that incorporates the twisted tape feature is the Hi-mixer from the Japanese company Toray. The elements consist of a cylinder with two circular channels and a cone-shaped entrance and exit. Within the circular channels is the twisted tape, twisted over 180°; see Fig. 7.144.

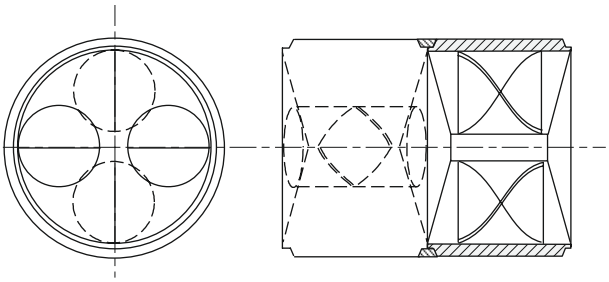


Figure 7.144
The Hi-mixer from Toray

Passing through the mixer, the fluid is split in two smaller flows, split again by the twisted tape and reoriented. The velocity then drops as the fluid enters the chamber between two elements, and the process repeats itself in the next element that is turned 90° relative to the first element.

Yet another variation of the twisted tape mixer is the bent and split tape mixer. An example is the Komax mixer shown in Fig. 7.145. It consists of slat steel plates of which the ends are split and bent about 45° in the opposite direction.

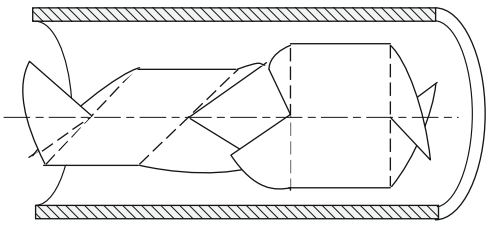


Figure 7.145
The Komax mixer

A relatively recent development in static mixers is the Dispersive/Distributive Static Mixer (DDSM) [308]. This mixer is specifically designed to generate strong elongational flow for improved dispersive mixing. The DDSM is an extension of the CRD

mixing technology [299] described in Section 8.7.1. The mixer is also described in Chapter 12, where Fig. 12.56 shows the geometry of the DDSM, while Fig. 12.57 shows calculated streamlines of particles flowing through the mixer. Figure 12.58 shows the flow number of the particles flowing through the mixer. The DDSM technology has also been applied to breaker plates. The mixing capability of an extruder can be improved with minimum disruption to the process by using a breaker plate that is also a static mixing device.

7.7.2.2 Functional Performance Characteristics

There are many more static mixing devices used in the polymer processing industry; in fact, the number is so large that it is not possible to list them all. Two characteristics are of critical importance in application of any static mixing device in actual extrusion operations. The first one, obviously, is the mixing capacity. The second one is the resistance that the static mixer offers to flow, i. e., the pressure drop along the static mixer.

7.7.2.2.1 Mixing

The mixing capacity is clearly related to the number of striations and the striation thickness. Several expressions have been proposed for various static mixers that relate the number of striations to the number of mixing elements, e. g., see [260, 263]. The mixing in static mixers can generally be described as ordered plug convective mixing. The striation thickness decreases from one mixing element to the next. The reduction in striation thickness can be expressed by:

$$s = \frac{s_0}{k^n} \tag{7.511}$$

where n is the number of elements of the static mixer and k is a factor that is determined by the geometry of the mixer. For the Kenics mixer k = 2, the Komax mixer k = 2, the ISG mixer k = 4, the SMX mixer k = 4, and the SMV mixer k = 8.

In experimental studies, however, the striation concept is not often used. This has to do with the difficulty in accurately determining the number of striations beyond the level of coarse mixing. Another measure of mixing is the coefficient of variation (COV), discussed earlier. The COV has been used in several experimental studies to compare the goodness of mixing in various static mixers.

The COV is dependent on flow rate and sample size. Therefore, one has to be careful in comparing data from different sources. Allocca [218] compared several static mixers in terms of their COV/length characteristics. For all mixers the COV reduces exponentially with length. However, the rate at which the COV reduces varies considerably. Most twisted tape type mixers require a substantial length to accomplish good mixing, while other mixers accomplish the same task in a much shorter distance. If a value of COV = 0.05 represents good mixing, then the minimum length

required for the most efficient static mixer is L = 10 D; see Table 7.3. For the less efficient static mixers the minimum length may have to be L = 30 D or more. Clearly, with such long length one should be concerned about pressure drop, residence time, and chance of degradation.

7.7.2.2.2 Pressure Drop

The other important performance characteristic is the pressure drop. A comparison of various static mixers was reported by Allocca [218]; this is shown in Table 7.3. The experimental set-up that was used to quantify the mixing capability of the various static mixers is shown in Fig. 7.146.

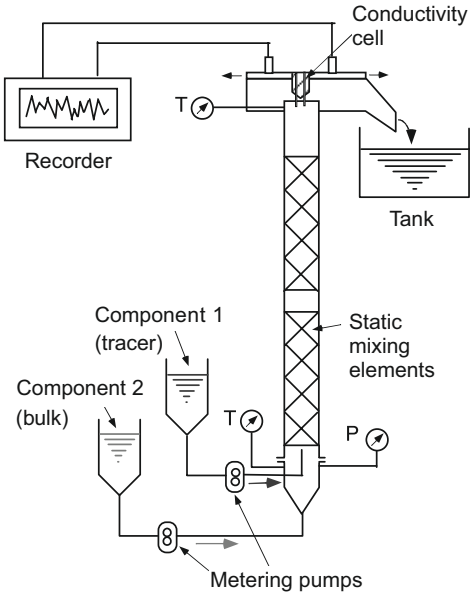


Figure 7.146
Test set-up for static mixing elements

The comparison is based on the length required to obtain a COV of 0.05 or less. From this table it becomes clear that good mixing performance is not directly linked to pressure drop. Some relatively inefficient static mixers have low pressure drop, while others have a high pressure drop.

The pressure drop in a static mixer with laminar flow can be determined from:

$$\Delta P = \frac{4}{\pi} N_{SM} \frac{\eta \dot{V} L}{D^4} \tag{7.512}$$

where N_{SM} is a constant depending on the mixer geometry (see Table 7.3), η is the viscosity, $\dot{V}$ the volumetric flow rate, L the length, and D the diameter. For an empty pipe the value of N_{SM} = 32; the lowest value that is achieved for static mixers is about 200, while the highest is about 10,000.

Table 7.3 Comparison of Various Commercial Static Mixers [218]

MIXER	*L/D	N_{SM}	Vol_{rel}	$Hold\text{-}up_{rel}$	D_{rel}	L_{rel}	ΔP_{rel}
Koch SMX	9	1237	1.0	1.0	1.0	1.0	1.0
Koch SMXL	26	245	1.8	1.8	0.8	2.4	0.6
Koch SMV	18	1430	4.6	4.5	1.3	2.7	2.3
Kenics	29	220	1.9	1.8	0.8	2.7	0.6
Etoflo HV	32	190	2.0	2.0	0.8	2.7	0.6
Komax	38	620	8.9	8.2	1.3	5.4	2.1
Lightnin	100	290	29.0	27.0	1.4	15.3	2.6
PMR	320	500	511.0	460.0	2.4	86.0	14.5
Toray	13	1150	1.9	0.9	1.1	1.6	1.35
N-Form	29	544	4.5	3.8	1.1	3.6	1.4
Ross ISG	10	9600	9.6	3.4	2.1	2.3	8.6

*The L /D ratio refers to the ratio required to achieve COV < 0.05

7.7.2.2.3 Residence Time Distribution

Another performance characteristic of interest is the residence time distribution, RTD, of the mixer. The residence time is a strong function of the distance from the wall. The residence time is short for fluid elements in the center of the channel, but long for elements close to the wall. Data on RTD for various static mixers was presented by Pahl and Muschelknautz [309]; see Fig. 7.147.

The data is shown in normalized form with normalized concentration on the vertical axis and normalized residence time on the horizontal axis. It is clear that the RTD for the static mixers shown in Fig. 7.147 is considerably narrower than the RTD in an empty pipe. In terms of RTD, there are no major differences between the various static mixing devices.

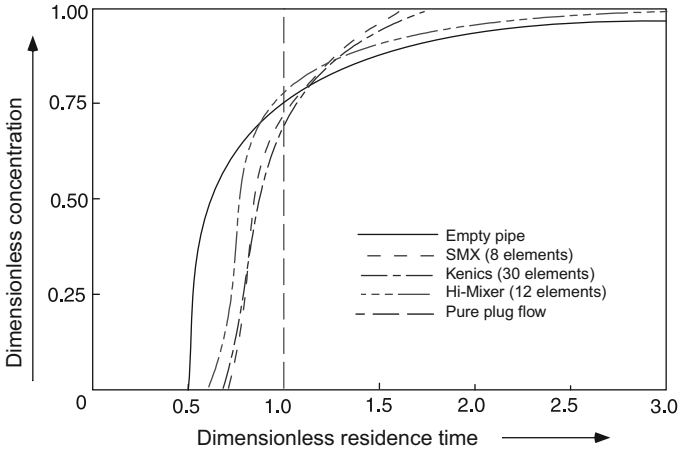


Figure 7.147 RTD data for different static mixers

7.7.2.2.4 Thermal Homogenization

In many applications of static mixers the ability to reduce melt temperature nonuniformities is important. Various studies have been made on the thermal homogenization in static mixers. Nauman [310] introduced the concept of thermal time distribution to characterize the degree of thermal homogeneity. Some models may predict a higher level of thermal homogenization than experimentally observed. This was the case in studies by Cliff and Wilkinson [311] where a traversing thermocouple was used to measure radial temperature distribution at the outlet of a 20 mm diameter Kenics mixer with nine elements. It was found that significant temperature variations remained at the outlet when two viscoelastic fluids differing only in temperature were introduced at the inlet. Tracer studies showed that a viscoelastic fluid streamline can be deflected rather than divided by the leading edge of an element. Such behavior, obviously, can reduce the mixing action in a static mixing device.

Craig [312] reports on an investigation of the performance of a large diameter static mixer used as a continuous reactor for styrene polymerization. It was shown the mixer behaved adiabatically. This was confirmed by computer simulation using models that had been verified experimentally. Better results were obtained with a static mixer that carries a heat transfer fluid supplied via manifold connections from external headers. A comparison of different static mixers with respect to thermal homogenization, pressure drop, and mixing efficiency was published by Mueller [313].

7.7.2.2.5 Mixing Materials with Different Viscosities

The discussion so far has focused on compatible materials of similar viscosity, i. e., simple mixing. In many cases, however, it is necessary to admix low-viscosity additives into a polymer melt. This can involve very high viscosity ratios, as much as ten million to one, and is very difficult for most static mixers. As the viscosity ratio increases, the length of the mixer required also increases. If the length of the mixer is insufficient, the low-viscosity component can separate in the form of splash-out. The splash-out limit, beyond which no further splash-out can be detected, is shown in Fig. 7.148 for SMX type mixing elements for several polymer/additive mixtures.

Another difficult mixing job is the mixing of high-viscosity fluid in a low-viscosity matrix. Drop rupture occurs when the drop extension exceeds a critical value. The extension of the drop is determined by the ratio of shear forces to surface forces. Therefore, sufficiently high forces have to be present in the mixer long enough to achieve dispersive mixing. A combination of shear and extensional flow is more effective in reducing drop size than only shear flow. Since some static mixers have elongational flow components, some degree of mixing is possible when high-viscosity components need to be mixed in a lower viscosity matrix and the viscosity ratio is not too large. For large viscosity ratios, clearly, dynamic mixing devices will be much more efficient.

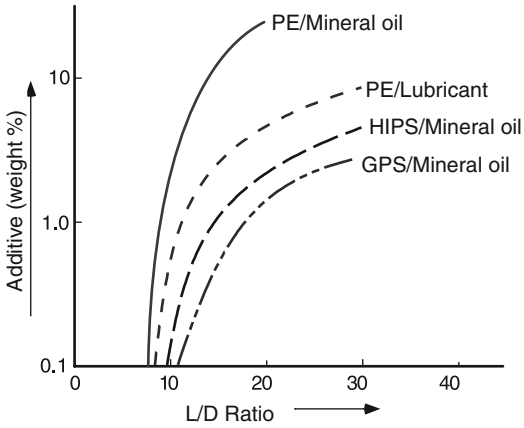


Figure 7.148
Splash-out limit for SMX mixer for several polymer-additive mixtures

7.7.2.3 Miscellaneous Considerations

In the discussion on residence time distribution it was mentioned that the RTD of a static mixer tends to be narrower than the RTD of a narrow pipe. However, in addition to the RTD the actual residence times are important as well. Static mixers always add extra volume between the extruder and the die. Therefore, when a static mixer is used, the mean residence time will always increase when the entire extrusion system is considered, i.e., extruder, static mixer, and die. If the static mixer section is long, which it should be to give good mixing, then the increase in mean residence time can be considerable. This should be a concern in thermally less stable polymers.

The fact that static mixers have no moving parts means that they have no pressure generating capability. Therefore, static mixing devices always consume pressure and, thus, require the extruder to generate more pressure. This results in reduced extruder efficiency and higher stock temperatures in the extruder. The lack of pressure generating capability and the additional residence time in static mixers are problems that are not present in screw mixing sections. These points should be carefully considered when a decision is made to use a dynamic or static mixing device.

Other considerations that should play a role in the selection of a static mixing device is the mechanical strength, streamlining, operator friendliness, and price. Clearly, the static mixer should be strong enough to withstand the forces acting on it during use, assembly, and disassembly. Some static mixers have been known to collapse under the pressure of the polymer melt. A streamlined design is necessary to avoid dead spots and to reduce the chance of degradation. Operator friendliness refers to ease of assembly, installation, removal, disassembly, and ability to clean. An operator-friendly design will enhance the change of success in actual production operations. Finally, price is a consideration that cannot be avoided. The comparison in price should not only be between various static mixers but also between a dynamic

and a static mixing device. A mixing section on the extruder screw may well be less expensive and achieve better mixing than a static mixer, provided, of course, that an efficient screw mixing section is selected.

7.7.3 Dispersive Mixing

The discussion so far has primarily been concerned with distributive laminar mixing. However, in actual extrusion operations the requirement for good dispersive mixing is often more critical than the distributive mixing. This is particularly true in extrusion of compounds with pigments or in small gauge extrusion (e. g., low denier fiber spinning, thin film extrusion, etc.). In dispersive mixing, the actual stresses acting on the agglomerates determine whether or not the agglomerate will break down. The breakdown stress will depend on the size, shape, and nature of the agglomerate. The stresses acting on the agglomerate will depend on the flow field and the rheological properties of the fluid.

7.7.3.1 Solid-Liquid Systems

One of the first engineering analyses of dispersive mixing was made by Bolen and Colwell [220]. They assumed that the agglomerates break when the internal stresses, induced by viscous drag on the particles, exceed a certain threshold value. Bird et al. [221] analyzed the forces acting on a single agglomerate in the form of a rigid dumbbell, consisting of two spheres of radii r_1 and r_2. The centers of the spheres are separated by a distance L, and the dumbbell is located in a homogeneous flow field of an incompressible Newtonian fluid. As a result of the viscous drag acting on the spheres, a force will develop in the connector. The force depends on the drag on each sphere and on the orientation of the dumbbell. Tadmor [222] adopted Bird's approach and extended the analysis to spheres of different radius and to include the effect of Brownian motion.

In a steady simple shear flow, the maximum connector force develops when the dumbbell is oriented at a 45° angle to the direction of shear; this force is:

$$F_{max} = 3\pi\ \mu_s\ \dot{\gamma}\ L \frac{r_1\ r_2}{r_1 + r_2} \tag{7.513}$$

where μ_s is the shear viscosity of the fluid, $\dot{\gamma}$ the shear rate, L the length of the dumbbell, and r_1 and r_2 the radii of the dumbbell.

When the spheres are in contact with each other, Eq. 7.513 reduces to:

$$F_{max} = 3\pi\ \eta_s\ \dot{\gamma}\ r_1\ r_2 = 3\pi\ \tau_s\ r_1\ r_2 \tag{7.514}$$

From Eqs. 7.513 and 7.514, it can be seen that the force in the connector is directly proportional to the shear stress and to the product of the radii. Thus, in the same

flow field, the force in the connector (breakdown force) reduces as the sizes of the spheres reduce. If the breakdown force of the agglomerate remains about constant, the breakdown will proceed until a certain minimum agglomerate size is reached. Further breakdown will not occur because the flow field will be unable to generate sufficient breakdown force in the agglomerate. For a steady elongational flow, the maximum force in the connector is obtained when the dumbbell is aligned in the direction of flow. When the spheres are in contact with each other, the maximum force is:

$$F_{max} = 6\pi \eta_e \dot{\varepsilon} r_1 r_2 = 6\pi \tau_e r_1 r_2 \tag{7.515}$$

where η_e is the elongational viscosity, τ_e the elongational stress, and $\dot{\varepsilon}$ is the rate of elongation.

Equations 7.514 and 7.515 assume that the spheres do not affect the flow field and that dumbbell interaction can be neglected. By comparing Eqs. 7.514 and 7.515, it can be seen that the breakdown force in elongational flow is twice as large as in simple shear at the same rate of deformation and viscosity. However, the elongational viscosity of polymer melts is greater than the shear viscosity. The elongational viscosity at low strain rates is at least three times higher than the shear viscosity, while at higher strain rates the elongational viscosity can be more than three times higher. As a result, the hydrodynamic forces generated in elongational flow are higher than in shear flow and, as a result, dispersive mixing is more efficient.

In most commercial mixers used for dispersive mixing, the actual flow patterns in the mixer will be a combination of shear flow and elongational flow. The flow patterns are often complex and require advanced numerical techniques to allow accurate analysis of flow. Only recently has it become possible to perform a full 3-D analysis of complex mixing devices. This allows a complete engineering approach to the design of mixing devices [299]; see also Chapter 12. In the past, mixing devices were developed based largely on experience, empirical knowledge, and intuition with very little, if any, engineering analysis.

From Eqs. 7.514 and 7.515 it can be seen that the breakdown force is directly proportional to the viscosity of the matrix. This has some important practical implications. Dispersive mixing should be done at as low a temperature as possible to increase the viscosity and thus the breakdown force. If both a dispersive and a distributive mixing element are required in a single screw extruder, the dispersive element should be placed upstream of the distributive element. This placement is more likely to result in a relatively low stock temperature at the inlet of the dispersive mixing element, while the stock temperature at the inlet of the distributive mixing element will be relatively high as a result of the viscous heat generation in the dispersive mixing element. The low stock temperature in the dispersive mixing element will enhance dispersive mixing, while the high stock temperature in the distributive mixing element will improve the energy efficiency of the distributive mixing step.

The need for high viscosity in dispersive mixing explains why it is often easier to produce a masterbatch of a high filler loading and let it down later, than to produce a compound with relatively low filler loading. The viscosity of the masterbatch will be much higher and, therefore, the dispersive mixing action will be much more effective. Masterbatching is a very common technique in the mixing and compounding industry. It should be remembered that in many instances, agglomerate breakdown can be achieved more effectively in high speed solid-solid mixing than in liquid-solid mixing [225–227]. The forces that can be transmitted in solid-solid mixing are generally much higher than in liquid-solid mixing, and agglomerate breakdown will occur faster and to a larger extent, resulting in very finely dispersed particles.

Dispersive mixing in single screw extruders was studied in detail by Martin [223, 224]. An interesting finding of this study was that dispersive mixing is determined not only by the shear stress acting on an agglomerate, but also by the exposure time. It was found that in dispersive mixing of carbon blacks, a certain minimum shear stress exposure time was necessary to accomplish breakdown; this minimum exposure time was about 0.2 s. Below this minimum exposure time, no breakdown occurred no matter how high the shear stress. This finding runs counter to common belief that dispersive mixing is only determined by the actual level of stress acting on the agglomerate. However, the minimum stress exposure time is a very important consideration in the design of dispersive mixing equipment, such as a dispersive mixing section on an extruder screw. It was also found that the mixing performance of an extruder is very much dependent on the length of the plasticating zone, which depends on the operating conditions. Incorporation of mixing sections can substantially improve an extruder's mixing performance and enable deepening of the metering section as compared to screws without mixing sections.

7.7.3.2 Liquid-Liquid System

In the previous section we discussed dispersive mixing in solid-liquid systems. Another important type of dispersive mixing is in liquid-liquid systems. This occurs when we mix incompatible or partially incompatible polymer melts. The production of polymer blends is very important in the polymer industry; as a result, liquid-liquid dispersive mixing has received significant attention over the last two or more decades.

In the deformation of droplets in immiscible systems the interfacial stress will affect the deformation once the drop size falls below a critical value. The deformation is determined by the ratio of viscous stress to interfacial stress; this ratio is called the Weber or Capillary number. This number can be expressed as:

$$\mathrm{Ca} = \frac{\tau}{\Gamma/R} = \frac{\eta\dot{\gamma}}{\Gamma/R} \tag{7.516}$$

where τ is the viscous stress, Γ the interfacial tension, η the matrix viscosity, $\dot{\gamma}$ the shear rate, Γ/R the interfacial stress, and R the radius. When the Capillary number

is large, larger than the critical Capillary number, the viscous stress will dominate the interfacial stress and drops will undergo affine stretching. The critical Capillary number is usually around unity ($Ca_{crit} \approx 1$). When the Capillary number is small ($Ca \leq Ca_{crit}$) the interfacial stresses dominate the viscous stresses, which results in stable drop sizes.

Taylor [64] found that in simple shear flow, a dispersed drop with viscosity ratio p = 1 breaks up when the Ca > 0.5. Breakup seems to occur when the shear stress and the interfacial stress are of the same order of magnitude. The critical Capillary number depends on the type of flow and on the viscosity ratio. In the mixing process two regimes can typically be distinguished:

A) a viscous stress-dominated regime ($Ca >> Ca_{crit}$)

B) an interfacial stress-dominated regime ($Ca \approx Ca_{crit}$)

In the early stages of mixing, regime A tends to prevail. Typical values for the parameters of the Capillary number are:

viscosity	η = 100 Pa·s
shear rate	$\dot{\gamma}$ = 100 s^{-1}
interfacial tension	Γ = 0.01 N/m
radius	R = 0.001 m

The resulting Capillary number Ca = 1000, which is much larger than the critical Capillary number, and the drops are stretched into fine threads. In the later stages of mixing, regime B will prevail. Assume that the drop size has reduced to R = 1E–6 m, then the Capillary number becomes Ca = 1. Thus, with a small enough drop size, the Capillary number will approach the critical Capillary number ($Ca \approx Ca_{crit}$).

7.7.3.2.1 Breakup under Quiescent Conditions

When droplets are suspended in a viscous matrix that is exposed to a shearing and/or elongational flow, the drop will be stretched into long filaments. This stretching does not go on indefinitely; at some point the thread becomes thin enough for interfacial tension to start playing a role. In other words, the surfaces become active. According to the example above, interfacial tension starts to become important when the thread radius is around 1 micron.

The interfacial tension will want to reduce the interface between the two phases, minimizing the surface-to-volume ratio. The smallest surface-to-volume ratio is achieved in a sphere, S/V = 3/R. Thus, an extended liquid thread will tend to break up due to the interfacial tension. The breakup is initiated by small disturbances at the interface, so-called Rayleigh disturbances. These disturbances grow due to the interfacial tension and eventually breakup can occur. The progress of the breakup process is illustrated in Fig. 7.149.

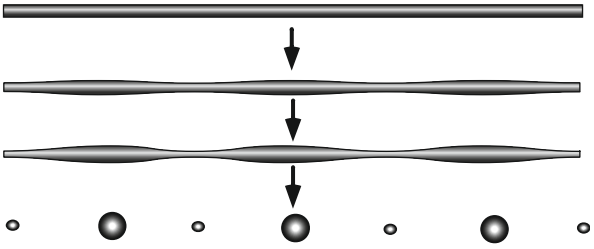


Figure 7.149
Schematic representation of the breakup process, top to bottom

The first theoretical analysis of the breakup of a Newtonian thread in a quiescent Newtonian matrix was performed over a century ago by Rayleigh [284]. The disturbances that initiate the breakup process are often referred to as Rayleigh disturbances. Rayleigh analyzed only the effect of surface tension, neglecting the viscosities of the two phases. This work was extended by Tomotika [285] by including the effect of viscosity. The analysis considers a sinusoidal liquid cylinder; the radius as a function of axial distance z is:

$$R(z) = \overline{R} + \alpha \sin(2\pi z / \lambda) \tag{7.517}$$

where λ is the wavelength and α the disturbance amplitude.

The average radius can be expressed as:

$$\overline{R} = \sqrt{R_0^2 - \frac{\alpha^2}{2}} \tag{7.518}$$

The disturbance amplitude grows exponentially in time:

$$\alpha = \alpha_0 \exp(q\, t) \tag{7.519}$$

The growth rate q is given by:

$$q = \frac{\Gamma\, \Omega(\lambda, p)}{2\eta\, R_0} \tag{7.520}$$

where α_0 is the original disturbance amplitude, p the viscosity ratio, and R_0 the initial thread radius. It can be determined that when the wavelength is greater than the thread circumference, the interfacial area decreases when α increases. Thus, the liquid thread is unstable to distortions with wavelengths greater than the thread circumference. Initially, disturbances of all wavelengths may be present. There is, however, only one disturbance that grows the fastest and will cause breakup. The wavelength of the fastest growing disturbance is the dominant wavelength (λ_m); it depends only on the viscosity ratio; see Fig. 7.150.

Breakup will occur when the distortion amplitude equals the average thread radius; this occurs when $\alpha = 0.8R_0$. The time necessary to reach this distortion is:

$$t_b = \frac{1}{q} \ln \frac{0.8\,R_0}{\alpha_0} \tag{7.521}$$

Kuhn [69] proposed an estimate of the initial amplitude α_0 based on the temperature fluctuations due to Brownian motion. The resulting expression shows that the time to break increases with the matrix viscosity and thread radius and reduces with interfacial tension. The radius of the newly formed droplets R_d can be determined from the conservation of mass:

$$R_d = \sqrt[3]{0.75\,\lambda_m R_0^2} \tag{7.522}$$

When the viscosity ratio p = 1, the dominant wavelength is $\lambda_m = 11.22\ R_0$; see Fig. 7.150. The newly formed droplet according to Eq. 7.522 will be $R_d = 2.034 R_0$, about twice the radius of the original thread. The new drop radius will be a function only of the viscosity ratio; the relationship is shown in Fig. 7.151.

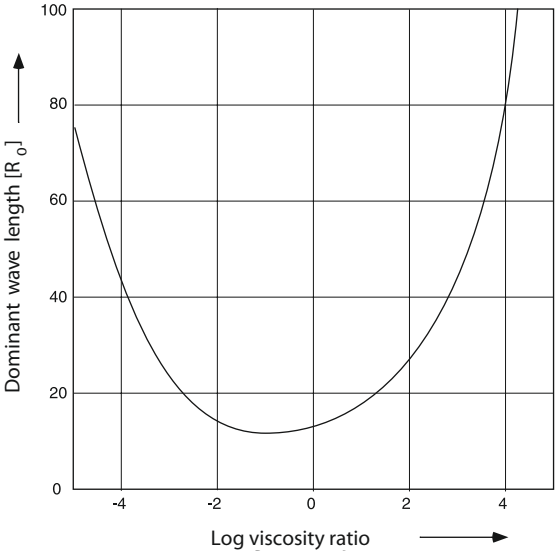


Figure 7.150
The dominant wavelength versus the viscosity ratio

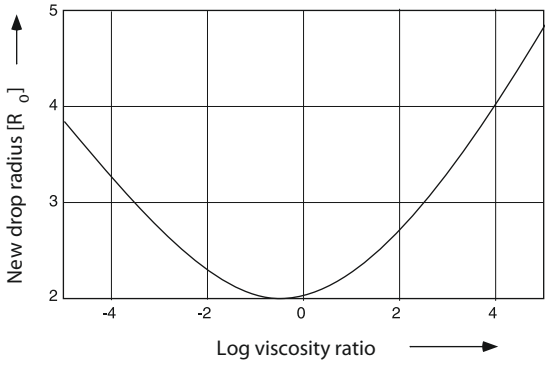


Figure 7.151
The new drop radius versus the viscosity ratio

For viscosity ratios typically encountered (1E–3 < p < 1E+2), the radius will be about 2 to 2.5 times the original thread radius. In some cases, small drops form together with larger drops; see Fig. 7.149. These satellite drops form in the last stage of the breakup process due to the rapid growth of Rayleigh disturbances on the fine filaments in the necked-down regions. Tjahjadi et al. [314] numerically investigated the formation of satellite droplets. They found unique radius distributions of satellite and sub-satellite droplets for several viscosity ratios. As the viscosity ratio increases, the number of satellite droplets decreases and their radius increases.

7.7.3.2.2 Breakup in Flow

The previous discussion focused on the breakup of liquid thread suspended in a quiescent Newtonian fluid. In real mixing operations quiescent conditions will usually not occur, except perhaps for short periods of time. The more important issue, therefore, is how the breakup occurs when the system is subjected to flow. Good reviews on the breakup of liquid threads are available from Acrivos [304], Rallison [305], and Stone [306]. Probably the most extensive experimental study on drop breakup was performed by Grace [286]; data was obtained over an enormous range of viscosity ratios: 10^{-6} to 10^{+3}! Grace determined the critical Weber (Capillary) number for breakup both in simple shear and in 2-D elongation; the results are represented in Fig. 7.152.

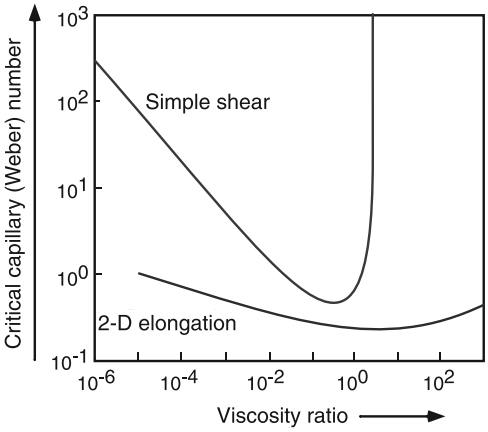


Figure 7.152
Critical Capillary (Weber) number versus the viscosity ratio, after Grace [286]

The interesting feature of the data from Grace is that the critical Capillary number for shear flow goes to infinity when the viscosity ratio reaches a value of four. This means that it is not possible to break up drops in shear flow when the viscosity of the drop is more than four times higher than the matrix. Such a problem does not exist in elongational flow. Also, the critical Capillary number in elongational flow is lower than in shear flow, particularly at viscosity ratios much below or above unity. Clearly, elongational flow is more efficient in breaking liquid threads into droplets than shear flow. An empirical expression for the critical Capillary number in shear flow was proposed by De Bruijn [287]:

$$\log Ca_{crit} = -0.506 - 0.0994 \log Ca + 0.124(\log Ca)^2 - \frac{0.115}{\log Ca - 0.611} \tag{7.523}$$

Janssen [294] studied the breakup of a viscous thread in stretching flow, both theoretically and experimentally. In a quiescent matrix one disturbance wavelength is dominant; in an extending matrix the waves are continuously stretched. Different disturbance wavelengths are dominant at different times. As a result, the breakup is postponed in elongational flow compared to quiescent conditions.

Janssen found that when the stretching rate is increased, the liquid thread is thinned further before breakup; this leads to smaller drops. A higher viscosity of either the matrix or the drops retards interfacial motions and postpones breakup, leading to smaller drops. At a constant matrix viscosity and low stretching rate, a higher liquid thread viscosity will lead to smaller drops. The results of the theoretical analysis were presented in graphical form; no simple explicit expression was found. The dimensionless drop radius resulting from breakup of a Newtonian liquid thread extending at a uniform rate is shown in Fig. 7.153.

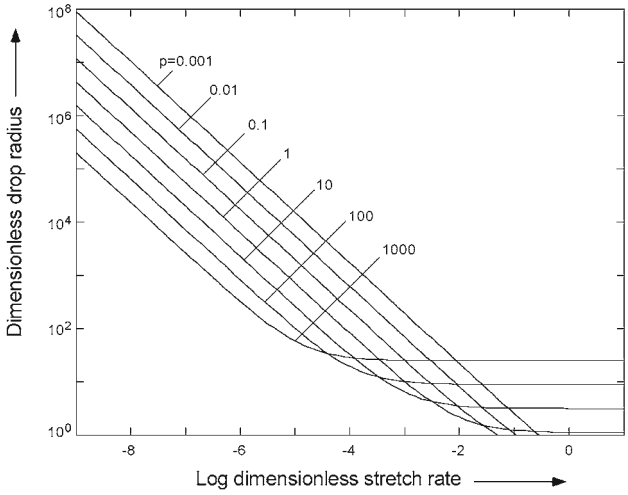


Figure 7.153
Dimensionless drop radius versus dimensionless stretch rate

The dimensionless drop radius r* is the actual drop radius divided by the initial amplitude α_0. The dimensionless stretching rate e is the actual stretching rate e multiplied with the matrix viscosity and the initial amplitude and divided by the interfacial tension; thus $e^* = \eta_m e \alpha_0 / \Gamma$. The curves in Fig. 7.153 can be fit quite well with an expression of the form:

$$r^* = 0.0131 p^{-0.442} (e^*)^{-0.946} + 1.12 p^{0.452} \tag{7.524}$$

At low values of the dimensionless stretching rate the drop radius reduces in a power law fashion (i.e., straight line on log-log scale); this portion of the curve is described by the first right-hand side term. At higher values of the dimensionless

stretching rate the drop radius reaches an asymptotic plateau; this portion of the curve is described by the second right-hand term. At this point, the drop radius becomes independent of the stretching rate and depends only on the viscosity ratio. Figure 7.153 indicates that the drop radius reduces as the viscosity ratio increases, at least for low values of the dimensionless stretch rate.

Rumscheidt and Mason [288] distinguish four classes of deformation and breakup in simple shear flow depending on the viscosity ration p. When $p > 1$, the deformed drop has rounded ends, while for smaller p values the ends become pointed. When $p < 0.1$, very small droplets break off and form the sharply pointed ends—this is called *tipstreaming*. This is caused by gradients in interfacial tension due to convection of surfactants along the drop surface. The interfacial tension is lowered at the tip, causing very small droplets to break off.

An important parameter in the breakup process is the time required for deformation and breakup. This was measured by Grace [286] under quasi-equilibrium conditions. His results are represented in Fig. 7.154.

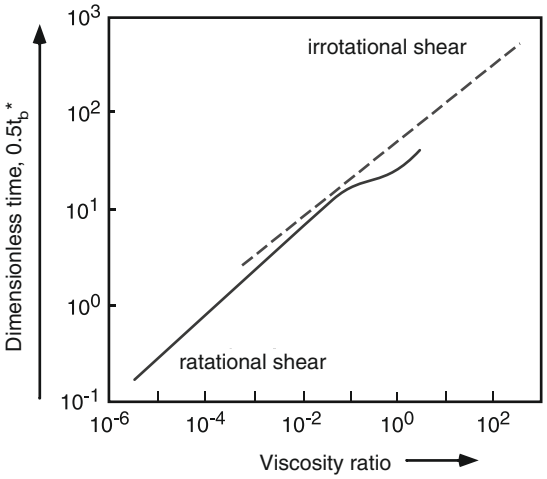


Figure 7.154
Dimensionless time for drop breakup versus viscosity ratio

Clearly, the dimensionless breakup time is strongly dependent on the viscosity ratio. The dimensionless breakup time is given by:

$$t_b^* = \frac{t\,\Gamma}{\eta_m R_0} \tag{7.525}$$

Grace [286] found that the breakup time decreases upon exceeding the critical Weber number. Similar experiments by Elemans [307] did not show a decrease in breakup time upon exceeding the critical Weber number. The breakup time for viscosity ratios between 0.1 and 1 was found to be around 50 to 100, i. e., $t_b^* = 50–100$. Experimental work in an opposed-jet device [66] found that with flow occurring a droplet will stretch, while during the no-flow condition, breakup occurs via necking. This is illustrated in Fig. 7.155.

The transient experiment shown in Fig. 7.155 mimics conditions occurring in an extruder. In an extruder, drops are exposed to high rates of deformation as they approach the flight tip, while, after passing through the flight clearance, the rate of deformation is relatively low. A drop is stretched in an elongational flow and after the flow stops, the drop breaks by a necking-in mechanism.

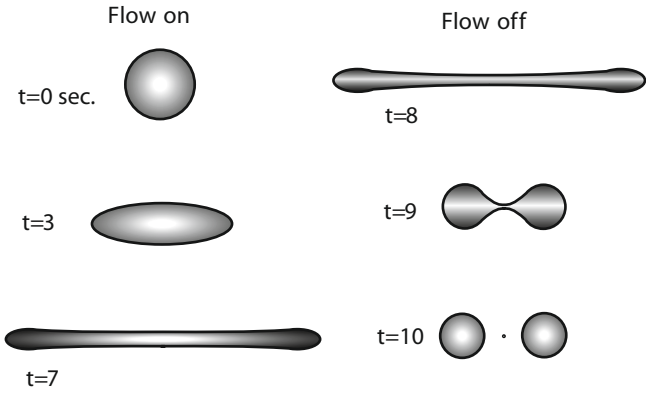


Figure 7.155 Deformation and breakup of drop in opposed-jet device

Once the flow has stopped, the interfacial tension drives two competing processes. One is the relaxation back to the original sphere; the other is the development of capillary waves. Capillary waves are like Rayleigh disturbances on a liquid thread. The relaxation of the drop is caused by the pressure difference over the interface of the drop:

$$\Delta P = \Gamma\left(\frac{1}{R_1}+\frac{1}{R_2}\right) \tag{7.526}$$

where R_1 and R_2 are the principal radii of curvature. At the ends of the threads where the radius is small ($R_1 = R_2 = R$), the pressure difference is large ($\Delta P = 2\Gamma/R$). In the middle of the thread the radius approaches infinity ($R_1 \rightarrow \infty$) and $\Delta P = \Gamma/R$. As a result, this pressure difference flow takes place from the end of the extended drop towards the center. When a disturbance is present at the interface, a pressure difference will develop between the center of the disturbance and the bulb-shaped ends. This pressure difference is also described by Eq. 7.526. If the time scale for the growth of the disturbance is less than the time scale for relaxation, the drop will break as shown in Fig. 7.155. Otherwise, relaxation will occur without breakup.

7.7.3.2.3 Coalescence

The work discussed thus far dealt with deformation and breakup of isolated drops. In real mixing operations the dispersed phase has a large enough volume fraction that interaction between the drops cannot be neglected. Elmendorp [78] found in

experiments that coalescence becomes important in the mixing of immiscible systems even at volume fractions of the dispersed phase as low as a few percent. As the volume fraction increases phase inversion will take place. The critical volume fraction for phase inversion depends strongly on the viscosity ratio.

Theoretical work on coalescence has been done by a number of workers, e.g., Chesters [292], Elmendorp [293], and Janssen [294]. Important parameters in the coalescence are the volume fraction of the dispersed phase and the flow field, because these determine the frequency of collisions, the contact force, and the interaction time. When drops approach each other, the matrix material between the drops has to be removed for coalescence to take place. When the film of matrix material is below a critical value, instabilities rupture the film and the drops coalesce.

7.7.3.2.4 Collision of Drops

The collision frequency of a drop as a function of the shear rate $\dot{\gamma}$ and the volume fraction of the dispersed phase φ can be written as:

$$C = \frac{8}{\pi}\dot{\gamma}\varphi \tag{7.527}$$

It is interesting to note that the collision frequency is independent of the drop radius. On the average a drop collides every time t:

$$t = \frac{1}{C} = \frac{\pi}{8\dot{\gamma}\varphi} \tag{7.528}$$

In other words, a drop collides on the average after a total shear strain of $\gamma = \pi/8\varphi$.

7.7.3.2.5 Film Drainage

Initially, the drops approach according to the velocity gradient of the external flow field. The drainage rate $-dh/dt$ is of the order $\dot{\gamma}R$. At a certain separation h_0 the hydrodynamic interaction becomes significant and the collision starts. The driving force for film drainage is the contact force F that acts during the interaction time t_{int}. The drainage rate decreases and the thickness asymptotically decays to zero. When a critical film thickness h_{crit} is reached, instabilities grow at the interface and film rupture occurs; the drops coalesce.

The separation distance h_0 can be determined from:

$$h_0 = R\left(\frac{3}{16}\right)^{1/4} p^{1/2} Ca^{3/4} \tag{7.529}$$

The contact force is the Stokes drag force:

$$F = 6\pi\eta_m\dot{\gamma}R^2 \tag{7.530}$$

The critical film thickness can be calculated from:

$$h_{crit} = \left[\frac{A\,R}{8\pi\,\Gamma}\right]^{1/3} \tag{7.531}$$

where A is the Hamaker constant, R the drop radius, and Γ the interfacial tension.

The critical film thickness for rupture is of the order of 50 Å. If the interaction time of the drops is too short to reach the critical film thickness, the drops will not coalesce. The drainage of the film is the rate-determining step in coalescence of deformable drops in polymer blends. Various models have been proposed to describe the film drainage. One model assumes fully mobile interfaces, another model assumes immobile interfaces, and a third model assumes partially mobile interfaces. The mobility of the interfaces is strongly dependent on the presence of impurities, such as surfactants. Surfactants reduce the mobility of the interfaces due to interfacial tension gradients [315].

Elmendorp showed [78] that the model based on fully mobile interfaces underpredicts the experimental coalescence time, while the model based on immobile interfaces over-predicts the coalescence time. A model based on partially mobile interfaces was proposed by Chester [316]; the coalescence time in this model is:

$$t_c = \frac{\pi\eta_d F^{0.5}}{2(2\pi\,\Gamma/R)^{1.5}}\left(\frac{1}{h_c} - \frac{1}{h_0}\right) \tag{7.532}$$

where h_c is the critical film thickness for rupture, η_d the viscosity of the dispersed phase, and F the contact force. Chester's model is valid for cases where the viscosity ratio is close to unity. When the viscosity ratio is large ($p \gg 1$) the model for immobile interfaces is appropriate. When the viscosity ratio is very small ($p \ll 1$) the model for fully mobile interfaces should be used.

In polymer blends compatibilizers can reduce the mobility of the interface. Compatibilizers often result in a finer morphology; this is due to three factors:

1. Delay of breakup due to lower surface tension, yielding thinner threads and smaller droplets.
2. Increase in the Weber number enabling the flow to break into smaller droplets before the critical Weber number is reached.
3. Reduced coalescence.

The influence of the contact force F is not intuitively obvious; one would expect a higher contact force to lead to faster coalescence. According to the models with immobile and partially mobile interfaces, the coalescence time increases with the contact force. This is due to the fact that the flattened area between the two deformable colliding drops increases with F, requiring more film material to be drained over a longer distance.

The effect of the contact force has important implications for real mixing operations. It can be expected that coalescence is not likely to occur in regions of high deformation rates, due to the high contact forces. However, in these regions deformation of drops leading to breakup will likely take place. Coalescence will take place preferentially in regions of low deformation rates and low contact force, while drop deformation will be minimal and breakup will occur under semi-quiescent conditions. The probability of coalescence P_c in simple shear with the Chester model can be expressed as:

$$P_c = \exp\left[\frac{-c\,R\,p\,Ca}{h_c}\right] \tag{7.533}$$

where c is a constant of order unity. According to this equation, coalescence is enhanced by small drop radius R, low viscosity ratio p, and low Capillary number Ca. A low Capillary number occurs at low matrix viscosity, low shear rate, or high interfacial tension.

7.7.3.2.6 Models for Dispersive Mixing of Immiscible Liquids

Janssen [294] developed a model for dispersive mixing using a two-zone model similar to the model used by Manas-Zloczower for dispersive mixing of a polymer melt with an agglomerated filler [317]. The model uses a strong zone (high deformation rate) where affine stretching and thread breakup occurs and a weak zone (low deformation rate) where coalescence and also thread breakup take place. The residence time in the strong zone is short, while the residence time in the weak zone is relatively long. The Janssen model is shown schematically in Fig. 7.156.

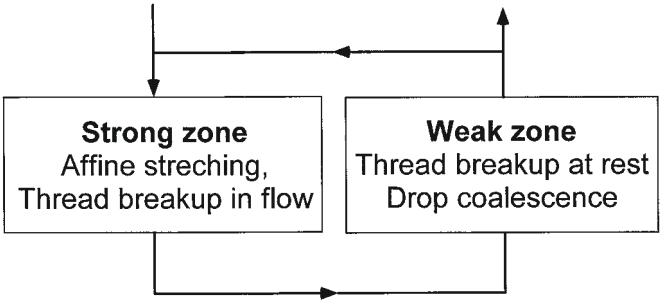


Figure 7.156 Schematic representation of the Janssen model

Some of the results of the Janssen model are quite interesting. It was found that a high viscosity of the dispersed phase promotes a finer dispersion due to the delay of thread breakup and coalescence. In general, lower viscosities of either phase result in coarser morphology. Highly viscous systems cannot be dispersed finer than 0.1 micron since coalescence starts to dominate as the drop size reduces much below 1 micron.

The commercial blend Noryl GTE is a practical example of immiscible fluids where a large viscosity ratio leads to a fine morphology. In Noryl GTE a high-viscosity PPE (polyphenylene ether) is dispersed in a much lower viscosity polyamide, viscosity ratio $p \approx 20$. Simply looking at the critical Weber number for drop breakup (see Fig. 7.152) suggests that a fine dispersion cannot be obtained in shear flow since $p >> 1$. By using the two-zone model, however, it is predicted that this blend can be dispersed to a length scale of 0.1 micron. This confirms commercial reality: Noryl GTE blends processed on twin screw extruders do indeed achieve fine dispersions with a length scale of around 0.1 micron.

A series of articles was published by Utracki et al. [318–322] on the modeling of mixing of immiscible fluids in a twin screw extruder. The fourth paper in the series [321] incorporates several refinements of the earlier model, one of the most important refinements being the incorporation of the effect of coalescence. The model considers two breakup mechanisms, both based on the micro-rheology. One breakup mechanism is the drop fibrillation and disintegration into fine droplets when the Weber number is greater than four times the critical Weber number. The second mechanism is drop splitting that occurs when the Weber number is below four times the critical Weber number.

Utracki et al. [321] found that there is a large difference between computed and experimental values if coalescence effects are not taken into account. By incorporating coalescence into the model, good agreement was obtained between predicted and experimentally determined drop diameters. It was further found that the morphology evolution of the PE/PS blend is not very sensitive to output rate or screw speed. The morphology development is, however, strongly dependent on the screw configuration.

7.7.3.2.7 Summary of Liquid-Liquid Dispersive Mixing

In the early stages of the mixing process the length scale of the minor component is such that the Capillary (Weber) number is much larger than the critical Capillary number. In this situation, the mixing is distributive with passive interfaces; interfacial tension is negligible. The deformation of the drops is affine and occurs as in miscible liquids. Only the total strain is important in describing the mixing process at this point.

The affine deformation of the drops causes the drops to extend into long thin threads, which is referred to as fibrillation. This process continues until the local radii become so small that the Weber (Capillary) number starts to approach the critical Weber number. At this point the threads become unstable and disintegrate as a result of interfacial tension-driven processes; the interfaces are now active. The most important mechanisms are the growth of Rayleigh disturbances in the mid-part of the thread, end-pinching, retraction, and necking in the case of relatively short dumbbell-shaped threads.

In dispersive mixing the morphology is determined both by the strain rate and the time duration of the strain rate; these are not interchangeable as they are in distributive mixing. Therefore, the time scales of the competing processes in the mixing process are quite important. For instance, if the interaction time between two drops is too short, coalescence will not take place. These time scales are determined by the viscosities, the elastic properties, and the interfacial properties.

The morphology at the end of mixing is the result of the balance between breakup and coalescence processes. This morphology can change in the operations following the mixing process. The flow through a pelletizing die can further modify the morphology, as can cooling in a water bath. Further processing, such as molding or extrusion, can, and most likely will, cause additional changes in the morphology.

The theories developed thus far do a reasonable job predicting the behavior of Newtonian fluids. Further work needs to be done on viscoelastic fluids. Work by Milliken and Leal [300], De Bruijn [287], and Janssen [294] showed that the change in the critical Weber number is not too significant when viscoelasticity is introduced to the dispersed phase. The effect of viscoelasticity will be dependent on the time scale of the processes involved; in rapid deformation occurring in very short times, viscoelasticity will have a substantial effect.

7.7.4 Backmixing

Mixing is a critical function in most extrusion operations. One of the most difficult mixing tasks is backmixing. An extrusion operation where good backmixing is very important is when a low percentage color concentrate, CC, is added to a virgin polymer. In this case, the initial distance between the CC pellets may be 100 mm or greater. If the final striation thickness needs to be reduced to the micron level, the reduction of the striation thickness needs to be at least five orders of magnitude—this is quite a tough task!

This section will analyze how the velocity profiles, axial mixing, and residence time distribution are related. It will be shown why simple conveying screws have poor axial mixing capability. New mixer geometries that are specifically designed to improve backmixing will be discussed.

7.7.4.1 Cross-Sectional Mixing and Axial Mixing

Most analyses of mixing focus on cross-sectional mixing, e.g., [301]. The cross-sectional mixing is determined mostly by the Couette shear rate between the rotating screw and stationary barrel. Typical values of the Couette shear rate in single screw extruders range from 50 to 100 s^{-1}. With a typical residence time in the melt conveying zone of about 20 s, the resulting total shear strain ranges from about 1000 to 2000 units. This means that the striation thickness in cross-sectional mixing is

reduced by about three orders of magnitude. In many cases, this is not enough to achieve a level of mixing that appears uniform by visual inspections.

Axial mixing or backmixing occurs by pressure flow. For pressure flow of a power law fluid between parallel plates, the dimensionless velocity $\varphi = v/v_{max}$ can be written as a function of the dimensionless normal coordinate $\xi = 2y/H$ as follows:

$$\varphi(\xi) = 1 - \xi^{\frac{n+1}{n}} \tag{7.534}$$

Figure 7.157 shows the velocity distribution for several values of the power law index.

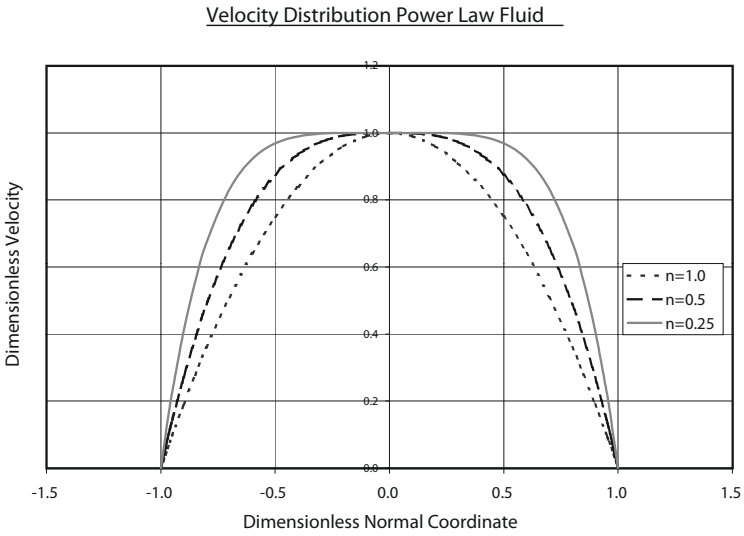


Figure 7.157 Velocity profiles for various power law index values

The velocity profile for a Newtonian fluid (n = 1.0) is a parabola. The shear rate in the center of the channel is zero. As a result, no mixing will take place there. The center region flattens as the power law index reduces. In other words, the velocity profile becomes closer to a plug flow profile as the power law index approaches zero. This means that the low shear rate region expands as the fluid becomes more shear thinning. Thus, the region with poor mixing becomes larger when the power law index reduces.

From this simple analysis it becomes clear that the situation for backmixing is substantially more difficult than for cross-sectional mixing. For shear thinning fluids there is a considerable region in the center of the channel where little or no axial mixing takes place.

7.7.4.2 Residence Time Distribution

The RTD can be determined from the velocity profiles in the channel. The axial flow in a screw extruder is a pressure flow because there are no axial velocity components of the screw or barrel. As a first approximation, the axial pressure flow can be considered a flow between parallel plates. The velocity profile for pressure flow of a power law fluid between parallel plates is (see Fig. 7.109):

$$\dot{V} = \frac{nWH^2}{2(1+2n)}\left(\frac{H\Delta P}{2mL}\right)^{\frac{1}{n}} \tag{7.535}$$

where W is the width of the channel, H the height of the channel, ΔP the pressure drop over axial length L, n the power law index, and m the consistency index of the fluid.

The velocity profile can be written as:

$$v(y) = \frac{nH}{2(1+n)}\left(\frac{H\Delta P}{2mL}\right)^{\frac{1}{n}}\left[1-\left(\frac{2y}{H}\right)^{1+\frac{1}{n}}\right] \tag{7.536}$$

where normal coordinate y ranges from –H/2 to +H/2.

The velocity profile can be written as:

$$v(y) = v_{max}\left[1-\left(\frac{2y}{H}\right)^{1+\frac{1}{n}}\right] \tag{7.537}$$

The external RTD function f(t)dt can be determined from:

$$f(t)dt = \frac{d\dot{V}}{\dot{V}} = \frac{2(2n+1)}{(n+1)H}\left[1-\left(\frac{2y}{H}\right)^{1+\frac{1}{n}}\right]dy \tag{7.538}$$

Coordinate y can be expressed as a function of time by the following substitution:

$$t = \frac{L}{v(y)} \tag{7.539}$$

With this substitution, the external RTD function can be written as:

$$f(t)dt = \frac{n(2n+1)}{(n+1)^2}\left(1-\frac{t_0}{t}\right)^{\frac{-1}{n+1}}\frac{t_0^2}{t^3}dt \tag{7.540}$$

The minimum residence time t_0 can be determined from:

$$t_0 = \frac{L}{v_{max}} \tag{7.541}$$

The cumulative RTD function F(t) can be found by integrating the external RTD function; it can be expressed as:

$$F(t) = \left(1 - \frac{t_0}{t}\right)^{\frac{n}{n+1}} \left(1 + \frac{n}{n+1}\frac{t_0}{t}\right) \tag{7.542}$$

For a Newtonian fluid the RTD function becomes:

$$F(t) = \left(1 - \frac{t_0}{t}\right)^{\frac{1}{2}} \left(1 + \frac{t_0}{2t}\right) \tag{7.543}$$

If we express the RTD as a function of the dimensionless residence time θ, where θ is the actual residence time divided by the mean residence time, we get:

$$F(\theta) = \left(1 - \frac{n+1}{(2n+1)\theta}\right)^{\frac{n}{n+1}} \left(1 + \frac{n}{(2n+1)\theta}\right) \tag{7.544}$$

The expression above for a power law fluid has not been published before. With this expression the RTD can plotted at several values of the power law index n; see Fig. 7.158.

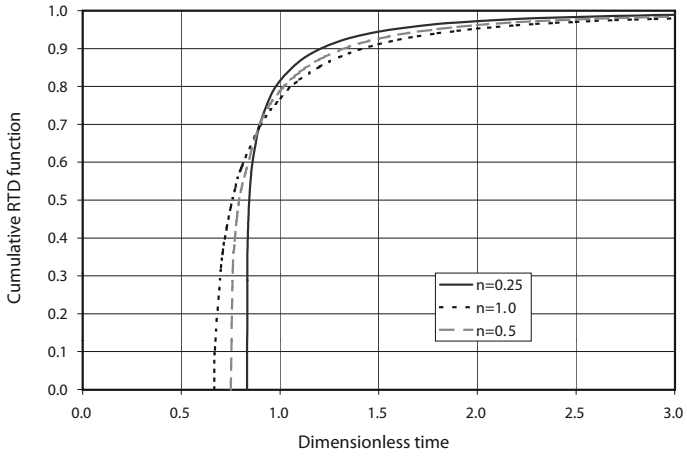


Figure 7.158 Residence time distribution curves for several power law index values

It is clear from Fig. 7.158 that the RTD becomes narrower as the value of the power law index reduces. This means that backmixing reduces as the fluid becomes more shear thinning (lower power law index). Figure 7.158 confirms what we have already

seen in the velocity profiles of Fig. 7.157. As the fluid becomes more shear thinning, the velocity profile becomes closer to plug flow and, consequently, the RTD becomes narrower and backmixing more problematic.

7.7.4.3 RTD in Screw Extruders

Pinto and Tadmor [295] developed expressions for the RTD in single screw extruders. The cumulative RTD function can be written as:

$$F(t) = F(\xi) = 0.5\left(3\xi^2 - 1 + (\xi - 1)\sqrt{1 + 2\xi - 3\xi^2}\right) \tag{7.545}$$

The dimensionless time θ (time divided by mean residence time) can be expressed as a function of the dimensionless normal coordinate ξ:

$$\theta = \frac{3\xi - 1 + 3\sqrt{1 + 2\xi - 3\xi^2}}{6\xi(1 - \xi + \sqrt{1 + 2\xi - 3\xi^2})} \tag{7.546}$$

The two expressions above were derived for a Newtonian fluid using the flat plate approximation considering both down- and cross-channel velocity components. Figure 7.159 shows the RTD for a single screw extruder as well as for pressure flow of a Newtonian fluid between flat plates.

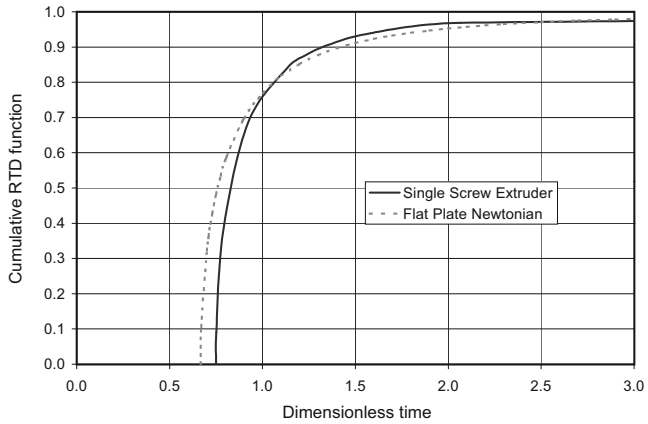


Figure 7.159 RTD of single screw extruder and flat plate

The single screw RTD is narrower than the flat plate RTD because of the re-circulation of the fluid in the screw channel. Fluid spends more time in the lower portion of the channel ξ = 0 to 2/3 than in the upper portion of the channel ξ = 2/3 to 1.

In order to properly determine the RTD of an extruder we have to consider not only down- and cross-channel velocity components but also normal velocity components that occur at the flight flanks. This will require a numerical analysis: either FDA, FEA, or BEA. Even though the depth of the channel is usually quite small compared to the channel width, the residence time at the flight flanks is substantial because

the normal velocities are quite small. Joo and Kwon [296] pointed out limitations of the Pinto analysis. As one would expect, the Pinto model under-predicts the residence times relative to a full three-dimensional analysis, particularly with large values of the axial pressure gradient.

The Pinto RTD for a single screw extruder is narrower than the RTD for pressure flow between a flat plate for a Newtonian fluid. The effect of shear thinning is to further narrow the RTD as discussed earlier. These two effects explain why backmixing is such a critical issue in screw extruders.

7.7.4.4 Methods to Improve Backmixing

A major concern in backmixing is the fluid in the center region of the screw channel where the axial shear strain is zero or close to zero. In a simple conveying screw the fluid in the inner recirculation region will stay within this region until it reaches the end of the screw. When this happens, the material flowing into the die will be poorly mixed.

Mixing pins and slots in the screw flights will improve axial mixing because they achieve a short-term splitting and reorientation of the fluid. The effect of mixing pins on backmixing is illustrated in Fig. 7.160.

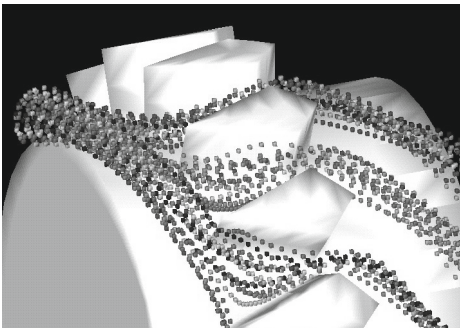


Figure 7.160
Particle tracking results in a mixing section with elongational mixing pins

These results were obtained using a three-dimensional BEM flow analysis. It is clear that one row of mixing pins has limited effect on axial mixing. Backmixing can be improved by varying the spacing between the pins, thus intentionally creating streams of different axial velocities.

The challenge in improving axial mixing is to efficiently transfer fluid from the inner re-circulation region to the outer region and vice versa. A simple but effective method of doing this is the inside-out mixer shown in Fig. 7.161.

The flight in this mixer is offset so that the material in the center region is cut by the offset flight and then pushed to the screw and barrel surfaces by the normal pressure gradients that occur at the flight flank. Results of particle tracking using BEM are shown in Fig. 7.162.

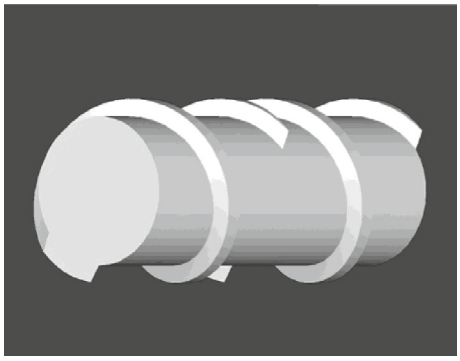


Figure 7.161
Solid model of inside-out mixer

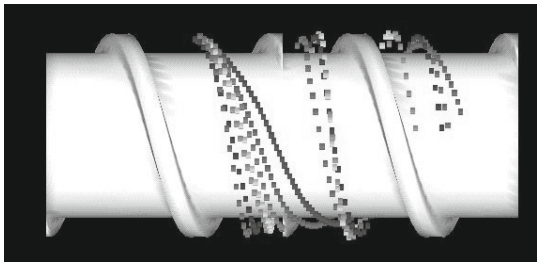


Figure 7.162
Particle tracking in the inside-out mixer

The redistribution of the material is shown in Fig. 7.163.

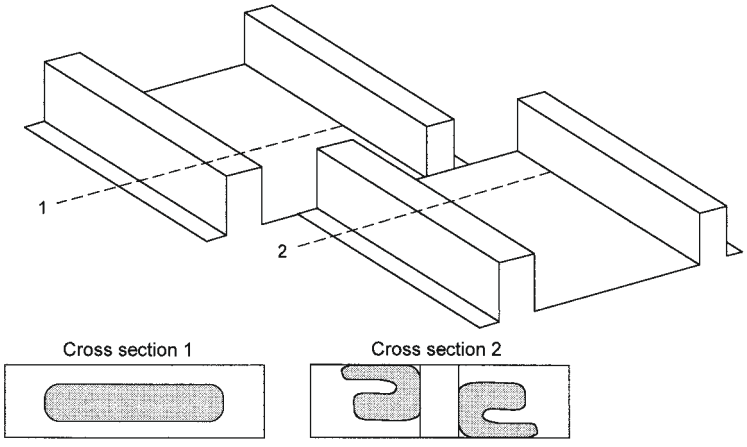


Figure 7.163 Redistribution in the inside-out mixer

This shows how the fluid from the center region is cut by the offset flight and pushed to the screw surface at the pushing side of the flight and to the barrel surface at the trailing side of the flight. It is clear that a considerable axial distance is necessary to bring about the redistribution of the material.

7.7.4.5 Conclusions for Backmixing

Backmixing is one of the most difficult mixing tasks in screw extruders. This is due to the fact that the axial strain rates in the extrusion process are very low, particularly in the center region of the channel. The axial velocity profile is close to plug flow, particularly for strongly shear thinning fluids. Backmixing problems are especially severe when adding a small percentage concentrate to the extruder. When both the polymer and concentrate are in pellet form, the initial striation thickness can be of the order of 100 mm. If a final striation thickness of 1 micron is required, the axial mixing has to achieve a reduction of striation thickness of at least five orders of magnitude.

Considering that the axial shear rate in melt conveying is close to zero in the center region of the channel, it is clear that axial mixing will be insufficient unless efficient mixing devices are used. The most efficient way to improve axial mixing is to redistribute material from the center of the channel to the outer region of the channel and vice versa. One mixer that aims to achieve such redistribution is the inside-out mixer. Another mixer that was designed specifically to improve axial mixing is the CRD7 mixer; see Fig. 7.164.

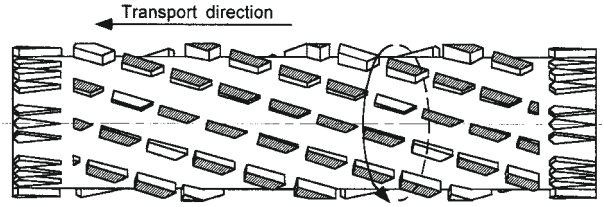


Figure 7.164
The CRD7 mixer

Another method of reducing mixing problems with color concentrates is to reduce the initial striation thickness. This can be done by reducing both the natural and color pellet size. Granules are better than pellets and powder is better than granules from a mixing point of view. Smaller particle sizes may lead to other problems though, such as conveying problems and air entrapment. Adding the colorant in liquid form can also reduce the initial striation thickness. This is a main reason liquid colorants are used. However, they can create problems by forming a lubricating layer on the barrel surface and reducing the conveying efficiency of the extruder.

Appendix 7.1

Constants of Equation 7.30

$$\alpha_{11} = 1 + \frac{\sin\beta_e \sin 2\psi_w}{2\psi_w - \pi} \tag{1}$$

$$\alpha_{12} = \frac{\alpha^2 \sin\beta_e}{2\psi_w - \pi}\left\{\frac{2\cos 2\psi_w}{2\psi_w - \pi} + \sin 2\psi_w\left[1 - \frac{2}{(2\psi_w - \pi)^2}\right]\right\} + \frac{\alpha^2}{3} \tag{2}$$

$$\alpha_{13} = \sin\beta_e \sin 2\psi_w\left[\frac{2}{2\psi_w - \pi} + \frac{1}{\alpha}\right] \tag{3}$$

$$\alpha_{14} = \alpha\sin\beta_e \sin 2\psi_w + \frac{2\alpha^2 \sin\beta_e}{2\psi_w - \pi}\left\{\frac{2\cos 2\psi_w}{2\psi_w - \pi} + 2\sin 2\psi_w\left[1 - \frac{2}{(2\psi_w - \pi)^2}\right]\right\} \tag{4}$$

$$\alpha_{21} = \frac{-\sin\beta_e}{2\psi_w - \pi}(1 + \cos 2\psi_w) \tag{5}$$

$$\alpha_{22} = \frac{\alpha^2 \sin\beta_e}{2\psi_w - \pi}\left[\frac{2\sin 2\psi_w}{2\psi_w - \pi} + \frac{2(1 + \cos 2\psi_w)}{(2\psi_w - \pi)^2} - \cos 2\psi_w\right] \tag{6}$$

$$\alpha_{23} = -\sin\beta_e(1 + \cos 2\psi_w)\left[\frac{2}{2\psi_w - \pi} + \frac{1}{\alpha}\right] \tag{7}$$

$$\alpha_{24} = \alpha(1 - \sin\beta_e \cos 2\psi_w) + \frac{2\alpha^2 \sin\beta_e}{2\psi_w - \pi}\left[\frac{2\sin 2\psi_w}{2\psi_w - \pi} + \frac{2(1 + \cos 2\psi_w)}{(2\psi_w - \pi)^2} - \cos 2\psi_w\right] \tag{8}$$

$$\beta_{11} = \frac{-\rho g \sin\alpha}{\alpha} \tag{9}$$

$$\beta_{12} = \rho c_m \lambda \tag{10}$$

$$\beta_{21} = \frac{-\rho g(\cos\alpha - 1)}{\alpha} \tag{11}$$

$$A = \alpha_{11}\alpha_{22} - \alpha_{21}\alpha_{12} \tag{12}$$

$$B = \alpha_{11}\alpha_{24} + \alpha_{13}\alpha_{22} - \alpha_{21}\alpha_{14} - \alpha_{23}\alpha_{12} \tag{13}$$

$$C = \alpha_{13}\alpha_{24} - \alpha_{23}\alpha_{14} \tag{14}$$

$$E = \beta_{11}(\alpha_{22} + \alpha_{24}) - \beta_{21}(\alpha_{12} + \alpha_{24}) \tag{15}$$

$$F = \rho(\alpha_{24} - 2\alpha_{22}) \tag{16}$$

$$G = \beta_{21}(\alpha_{11} + \alpha_{13}) - \beta_{11}(\alpha_{21} + \alpha_{23}) \tag{17}$$

$$H = -\rho(\alpha_{23} - 2\alpha_{21}) \tag{18}$$

where β_e is the effective angle of internal friction and Ψ is the angle between the major principal stress and the radial r-axis. Further:

$$\psi_w = \frac{\pi}{2} + \frac{1}{2}\left(\arcsin\frac{\sin\beta_w}{\sin\beta_e} + \beta_w\right) \tag{19}$$

$$c_m = \frac{1}{\alpha\overline{V}}\int_o^\alpha v^2 d\alpha \quad (c_m = 1 \text{ for uniform velocity profile}) \tag{20}$$

$$\lambda = r\overline{V} = \frac{r}{\alpha}\int_o^\alpha v d\alpha \tag{21}$$

where v is the radial velocity component.

Appendix 7.2

Constants of the Engstad Equation 7.36

σ_{co} is the constant part of the failure function; the unconfined yield strength is written as:

$$\sigma_c = k\sigma_1 + \sigma_{co} \tag{1}$$

The term Y_b is determined from:

$$Y_b = \frac{(\beta_w + \alpha)\sin\alpha}{\sin^2(\beta_w + \alpha)} + \frac{\sin\beta_w}{\sin(\beta_w + \alpha)} - \frac{kY}{2(X-1)}\frac{\sin\alpha + \sin(2\beta_w + \alpha)}{\sin\alpha}(1 + \sin\beta_e) \tag{2}$$

For a passive stress state:

$$X = \frac{\sin\beta_e}{1 - \sin\beta_e}\left[\frac{\sin\alpha + \sin(2\beta_p + \alpha)}{\sin\alpha}\right] \tag{3}$$

$$Y = \frac{(\beta_p + \alpha)\sin\alpha + \sin\beta_p \sin(\beta_p + \alpha)}{(1 - \sin\beta_e)\sin^2(\beta_p + \alpha)} \tag{4}$$

$$\beta_p = \frac{1}{2}\left(\beta_w + \arcsin\frac{\sin\beta_w}{\sin\beta_e}\right) \quad \text{with } 0 < \arcsin \text{ value} < \frac{\pi}{2} \tag{5}$$

For an active state:

$$X = \frac{\sin\beta_e}{1+\sin\beta_e}\left[\frac{\sin(2\beta_a+\alpha)-\sin\alpha}{\sin\alpha}\right] \tag{6}$$

$$Y = \frac{\left(\alpha+\beta_a-\frac{\pi}{2}\right)\sin\alpha+\cos\beta_a\cos(\alpha+\beta_a)}{(1+\sin\beta_e)\cos^2(\alpha+\beta_a)} \tag{7}$$

$$\beta_a = \frac{1}{2}\left(\beta_w+\arcsin\frac{\sin\beta_w}{\sin\beta_e}\right) \quad \text{with } \frac{\pi}{2} < \text{arcsin value} < \pi \tag{8}$$

Appendix 7.3

This is a Fortran program to analyze two-dimensional flow of a power law fluid.

```
    PROGRAM EXP
    REAL H
    DIMENSION C(200), Z(201), TX(201), TY(201, T(201), S(201), SX(201)
    DIMENSION SY(201), VX(201), VY(201), DX(201), DY(201), A(4, 4), B(3)
    DIMENSION GRA (3), DOX(3), SOY(3), SOQ(3)
    READ (6, 20) M, NPRVEL
20  FORMAT (2I10)
    READ (6, 30) REV, RK, D
    READ (6,30) HMIN, DELH, HMAX
    READ (6,30) GMIN, DELG, GMAX
    READ (6,30) RNMIN, DELRN, RNMAX
    READ (6, 30) PHIMIN, DELPHI, PHIMAX
    READ (6,30) PGMIN, DELPG, PGMAX
    WRITE (7, 29) M, NPRVEL
29  FORMAT (SI10)
30  FORMAT (3F10.4)
    WRITE (7, 31) REV
31  FORMAT (' SCREW SPEED IN RPM IS', F10.2)
    WRITE (7,32) HMIN
32  FORMAT (' CHANNEL DEPTH IN CM IS', F10.4)
    WRITE (7,320) DELH
320 FORMAT (' INCREMENTAL DEPTH IN CM IS', F10.4)
    WRITE (7,321) HMAX
321 FORMAT (' MAXIMUM DEPTH IN CM IS', F10.4)
    WRITE (7, 33) D
33  FORMAT (' SCREW DIAMETER IN CM IS', F10.4)
    WRITE (7, 34) RK
34  FORMAT (' POWER LAW CONST. IN POISE IS', F14.4)
    WRITE (7, 36) GMIN
36  FORMAT (' INITIAL RED. PRESS. GRADIENT IS', F10.6)
    WRITE (7, 37) DELG
37  FORMAT (' INCREMENTAL PRESS. GRADIENT IS', F10.6)
    WRITE (7.38) GMAX
38  FORMAT (' FINAL PRESSURE GRADIENT IS ', F10.6)
    WRITE (7, 39) RNMIN
```

```
39  FORMAT (' INITIAL POWER LAW INDEX IS ', F10.6)
    WRITE (7.41) DELRN
40  FORMAT (' INCREMENTAL POWER LAW INDEX IS ', F10.6)
    WRITE (7, 41) RNMAX
41  FORMAT (' FINAL POWER LAW INDEX IS ', F10.6)
    WRITE (7, 42) PHIMIN
42  FORMAT (' INITIAL HELIX ANGLE IN DEGR. IS ', F10.4)
    WRITE (7, 43) DELPHI
43  FORMAT (' INCREMENTAL HELIX ANGLE IS ', F10.4)
    WRITE (7, 44) PHIMAX
44  FORMAT (' FINAL HELIX ANGLE IN DEGREES IS ', F10.4)
    WRITE (7, 440) PGMIN
440 FORMAT (' INITIAL AXIAL PRESS. GRADIENT IN PSI/INCH ', F10.4)
    WRITE (7, 441) DELPG
441 FORMAT (' INCREMENTAL AXIAL PRESS. GRADIENT IS ', F10.4)
    WRITE (7,444)
444 FORMAT (' ', ' REDTHRUPUT PRESS-GRAD HELIXANGLE AC-THRUPUT
    DIM', X 'THRUPUT DOWNCHA-TX CROSSCH-TY CONSTANTCY')
    H=HMIN
    G-GMIN
    RN=RNMIN
    PG=PGMIN
    TXO=10000.0
    TYO=10000.0
    CY=10000.0
    REV-REV/60.0
    PHIMIN=PHIMIN*17.4533/1000.0
    DELPHI=DELPHI*17.4533/1000.0
    PHIMAX=PHIMAX*17.4533/1000.0 PHI=PHIMIN
45  UO=3.14159*D*REV*COS (PHI)
    VO=UO*TAN (PHI)
    IF (PG .EQ. 0) GO TO 48
    CX=27145.67*SIN (PHI) *PG
C   ABOVE LINE USED WITH CONSTANT AXIAL PRESSURE GRADIENT
    GO TO 49
48  CX=6.0*RK*G/H*(UO/H)**RN
49  NR=0
50  DO 70 I=1, ((4*M)+1)
    Z(I)=(FLOAT (I-1))*H/(4.*(FLOAT (M)))
    TX (I)=TXO+(CX*Z (I))
    TY (I)=TYO+(CY*Z (I))
    T (I)=((TX (I)**2)+(TY Ii)**2))**.5
    S (I)=(T (I)/RK)**(1./RN)
    SX (I)=S (I)*TX (I)/T (I)
    SY (I)=S (I)*TY (I)/T (I)
70  CONTINUE
    VX (1)=0.0
    VY (1)=0.0
    DO 80 I=2, M+1
    K=((FLOAT (I-2))*4)
    DO 90 J=1, 5
    L=K+J
    DX (J)=SX (L)
    DY (J)=SY (L)
90  CONTINUE
    CALL SIMP (4, DX, UMX)
    CALL SIMP (4, DY, UMY)
    VX (I)=VX (I-1)+(UMX*H/(4.*(FLOAT (M))))
    VY (I)=VY (I-1)+(UMY*H/(4.*(FLOAT (M))))
```

```
80  CONTINUE
    CALL SIMP (M VX, XOX)
    CALL SIMP (M, VY, YOY)
    QX=XOX*H/(FLOAT (M))
    QY=YOY*H/(FLOAT (M))
250 DIVX=VX (M+1)-UO
    DIVY=VY (M+1)-VO
    DIVQ=QY
    IF (NR-1) 180, 185, 185
180 STVX=DIVX
    STVY=DIVY
    STVQ=DIVQ
C   WRITE (7, 251) TXO, TYO, CY, STVX, STVY, STVQ
251 FORMAT (6E12.3)
183 IF ((AMAX1 (STVX, STVY, STVQ))-1E-5) 500, 500, 187
187 LAL=1
    NR=NR+1
    GRA (1)=0.01*TXO
    TXO=TXO+GRA (1)
    GO TO 50
184 SOX (LAL)=DIVX-STVX
    SOY (LAL)=DIVY-STVY
    SOQ (LAL)=DIVQ-STVQ
    IF (LAL-2) 200, 210, 220
200 LAL=2
201 TXO=TXO-GRA (1)
202 GRA (2)=0.01*TYO
    TYO=TYO+GRA (2)
    GO TO 50
210 LAL=3
    TYO=TYO-GRA (2)
    GRA (3)=0.01*CY
    CY=CY+GRA (3)
    GO TO 50
220 LAL=1
    CY=CY-GRA (3)
    DO 270 MP=1, 3
    A (1, MP)=SOX (MP)/GRA (MP)
    A (2, MP)=SOY (MP)/GRA (MP)
    A (3, MP)=SOQ (MP)/GRA (MP)
270 CONTINUE
    B (1)=STVX
    B (2)=STVY
    B (3)=STVQ
    OK=A (2, 1)/A (1,1)
    A (2, 2)=A (2,2)-(A(1, 2)*OK)
    A (2, 3)=A (2, 3)-(A(1, 3)*OK)
    B (2)=B (2)-(B(1)*OK)
    OK=A (3, 1)/A (1, 1)
    A (3, 2)=A (3, 2)-(A (1, 2)*OK)
    A (3, 3)=A (3, 3)-(A (1, 3)*OK)
    B (3)=B (3)-(B(1)*OK)
    OK=A (3, 2)/A (2, 2)
    A (3, 3)=A (3, 3)-(A (2, 3)*OK)
    B (3)=B (3)-(B(2)*OK)
    DLCY=B (3)/A (E, E)
    DLTY=(B (2)-(A (2, 3)*DLCY))/A (2, 2)
    DLTX=B (1)-(A (1, 3)*DLCY)
    DLTX=(DLTX-(A (1, 2)*DLTY))/A (1, 1)
```

```
    TXO=TXO+DLTX
    TYO=TYO+DLTY
    CY=CY+DLCY
    NR=0
    GOTO 50
500 QRED=QX*2.0/(H*UO)
    QREDA=QRED*SIN (2.0*PHI)
    QA=QX*3.14159*D*SIN (PHI)
    GA=CX*H/(6.0*RK)*(H/UO)**RN
    PHIDGR=PHI*1000.0/17.4533
    WRITE (7, 501) QREDA, GA, PHIDGR, QA, QRED, TXO, TYO, CY
501 FORMAT (8E11.4)
    IF (QX .LT. 0) GO TO 560
    CONTINUE
    IF (NPRVEL .NE. 1) GO TO 556
    WRITE (7, 10000)
1000 FORMAT ('1')
554 WRITE (7, 555) (Z((4*I)+1), VX (I), VY (I), I=1, M)
555 FORMAT (3E15.4)
556 IF (G .GE. GMAX) GO TO 560
    G=G+DELG
    GO TO 45
557 IF (PG .GE. PGMAX) GO TO 600
558 PG=PG+DELPG
    PHI=PHIMIN
    H=HMIN
    WRITE (7, 559) PG
559 FORMAT (' NEW AXIAL PRESSURE GRADIENT IS ', F10.4)
    GO TO 45
560 IF (RN .GE. RNMAX) GO TO 570
    RN=RN+DELRN
    G=GMIN
    WRITE (7, 565) RN
565 FORMAT (' NEW POWER LAW EXPONENT IS ', F6.3)
    TXO=10000.0
    TYO=10000.0
    CY=10000.0
    GO TO 45
570 IF (PHI .GE. PHIMAX) GO TO 580
    PHI=PHI+DELPHI
    G=GMIN
    TXO=10000.0
    TYO=10000.0
    CY=10000.0
    GO TO 45
580 IF (H .GE. HMAX) GO TO 558
    H=H+DELH
    PHI=PHIMIN
    WRITE (7, 585) H
585 FORMAT (' NEW CHANNEL DEPTH IS ', F10.4)
    TXO=10000.0
    TYO=10000.0
    GO TO 45
600 STOP
    END
    SUBROUTINE SIMP (I, C, S)
    DIMENSION C (200)
    S=0.
    DO 55 L=1, (I-1), 2
    S=S+(2.*C(L))+4.*C(L+1))
```

```
55  CONTINUE
    S=((S+(C(I+1)))-C(1))/3.
    RETURN
    END
    40
SCREW SPEED IN RPM IS 100.00
CHANNEL DEPTH IN CM IS 0.2500
INCREMENTAL DEPTH IN CM IS 0.0200
MAXIMUM DEPTH IN CM IS 0.2500
SCREW DIAMETER IN CM IS 6.3500
POWER LAW CONST. IN POISE IS 10000.0000
INITIAL RED. PRESS. GRADIENT IS 0.300000
INCREMENTAL PRESS. GRADIENT IS 0.050000
FINAL PRESSURE GRADIENT IS 0.300000
INITIAL POWER LAW INDEX IS 1.000000
INCREMENTAL POWER LAW INDEX IS 0.200000
FINAL POWER LAW INDEX IS 1.000000
INITIAL HELIX ANGLE IN DEGR. IS 10.0000
INCREMENTAL HELIX ANGLE IS 2.5000
FINAL HELIX ANGLE IN DEGREES IS 50.0000
INITIAL AXIAL PRESS. GRADIENT IN PSI/INCH 3000.0000
INCREMENTAL AXIAL PRESS. GRADIENT IS 2000.0000
MAXIMUM AXIAL PRESS. GRADIENT INPSI/INCH 15000.0000
```

References

1. S.C. Cowin (Ed.) “Mechanics Applied to the Transport of Bulk Materials,” ASME, New York (1979)
2. S.C. Cowin and M. Satake (Eds.) “Continuum Mechanical and Statistical Approaches in the Mechanics of Granular Material,” Proceedings U.S.-Japan Seminar, Sendai, Japan, Gakumutsu Bunken Fukyu-Kai (1978)
3. C. Orr, Jr., “Particulate Technology,” Macmillan, New York (1966)
4. R.L. Brown and J.C. Richards, “Principles of Powder Mechanics,” Pergamon Press, Oxford (1966)
5. J.E. Richards (Ed.) “The Storage and Recovery of Particulate Solids,” Inst. Chem. Eng., Working Party Rep. (1966)
6. K. Wieghardt, Ann. Rev. Fluid Mech., 7, 89–114 (1975)
7. S.B. Savage, J. Fluid Mech., 92, 53–96 (1979)
8. A.W. Jenike, “Gravity Flow of Bulk Solids,” Bulletin No. 108 of the Utah Engineering Experimental Station, Univ. of Utah, Salt Lake City (1961)
9. A.W. Jenike, “Storage and Flow of Solids,” Bulletin No. 123 of the Utah Engineering Experimental Station, Univ. of Utah, Salt Lake City (1964)
10. M. Shahinpoor and J.S.S. Siah, J. Non-Newtonian Fluid Mech., 9, 147–156 (1981)
11. M. Shahinpoor, J. Non-Newtonian Fluid Mech., 12, 31–38 (1983)
12. K.I. Kanatani, Int. J. Eng. Sci., 17, 419–432 (1979)
13. J.T. Jenkins and S.C. Cowin, in [1], p. 79–89
14. R.L. Brown and P.G. Hawksley, Fuel, 26, 171 (1947)

15. J. Lee, S.C. Cowin, and J.S. Templeton, Trans. Soc. Rheol., 18, 247–269 (1974)
16. P.M. Blair-Fish and P.L. Bransby, Trans. A.S.M.E., J. Eng. Ind., 95, 17–26 (1973)
17. G.C. Gardner, Chem. Eng. Sci., 21, 261–273 (1966)
18. M. Levinson, B. Shmutter, and W.L. Resnick, Powder Technol., 16, 29–43 (1977)
19. L. Bates and D. Kershan, Chem. Eng. Progress, 71, 66–68 (1975)
20. L.M. Connelly, in [1], pp. 35–59
21. R. Butterfield, R.M. Harkness, and K.Z. Andrews, Geotechnique, 8, 308 (1970)
22. H.A. Janssen, Zeitschrift VDI, 1045 (1895)
23. D.M. Walker, Chem. Eng. Sci., 21, 975–997 (1966)
24. J.K. Walters and P.M. Nedderman, Chem. Eng. Sci., 28, 1907–1908 (1973)
25. P.L. Bransby and P.M. Blair-Fish, Chem. Eng. Sci., 29, 1061–1074 (1974)
26. G. Hagen, Berliner Monatsberichte Akad. d. Wiss, 35–42 (1852)
27. R.L. Brown, Nature, 191, 458–461 (1961)
28. J.R. Johanson, Trans. S.M.E., 232, 69–80 (1965)
29. S.B. Savage, Br. J. Appl. Phys., 16, 1885–1888 (1965)
30. S.B. Savage, Ph.D. thesis, McGill Univ., Montreal (1967)
31. S.B. Savage and M. Sayed, in [1], pp. 1–24
32. J.M. Rausch, Ph.D. thesis, Princeton Univ. (1948)
33. J. Bosley, C. Schofield, and C.A. Shook, Trans. Inst. Chem. Eng., 47, T147–T153 (1968)
34. W.N. Sullivan, Ph.D. thesis, California Institute of Technology, Pasadena (1972)
35. D.M. Walker, Powder Technol., 1, 228 (1967)
36. R.K. Eckhoff and P.G. Leversen, Powder Technol., 10, 51 (1974)
37. G. Engstad, Chem. Eng. Sci., 30, 1273–1283 (1975)
38. Y. Lee, Combustion, 32, 20–27 (1960)
39. O. Richmond, Mech. Eng., 85, 46–49 (1963)
40. G.C. Gardner, Chem. Eng. Sci., 18, 35–39 (1963)
41. O. Richmond and H.L. Morrison, in [1], pp. 103–111
42. J.F. Ingen Housz in "Fortschritte beim Extrudieren," Carl Hanser Verlag, Munich (1976)
43. W.H. Darnell and E.A.J. Mol, SPE J., 12, 20 (1956)
44. J.G.A. Lovegrove, Ph.D. thesis, London Univ. (1972)
45. E. Broyer and Z. Tadmor, Polym. Eng. Sci., 12, 12–24 (1972)
46. Z. Tadmor and E. Broyer, Polym. Eng. Sci., 12, 378–386 (1972)
47. H.B. Kessler, R.M. Bonner, P.H. Squires, and C.F.W. Wolf, SPE J., 16, 267 (1960)
48. H. Decker, "Die Spritzmaschine," P. Troester, Hanover, W. Germany (1941)
49. A. Schneiders, Plastverarbeiter, 19, 797–799 (1968)
50. G. Menges, W. Predoehl, R. Hegele, R. Kosel, and W. Elbe, Plastverarbeiter, 20, 79–88 and 188–190 (1969)

51. G. Fuchs, Plastverarbeiter, 19, 765–771 (1968) and 20, 237–244 (1969)
52. W.L. Krueger, SPE ANTEC, Boston, 676–678 (1981)
53. R. Rautenbach and E. Goldacker, Kunststoffe, 61, 104–107 (1971)
54. G. Menges and R. Hegele, Plastverarbeiter, 23, 332–338 (1975)
55. B. Franzkoch and G. Menges, SPE ANTEC, Washington, DC, 512–515 (1978)
56. E. Langecker, G.R. Langecker, and W. Fillman, Plastverarbeiter, 28, 531–535 (1977)
57. E. Langecker, German patent application DDS 22 05426, filed February 2, 1972
58. C. Maillefer, U.S. Patent 4,154,535 (also CH 612375, FR 2,385,517, DE 2,813,585, and SE 7,80,3477)
59. E. Gruenschlosz, SPE ANTEC, New Orleans, 160–165 (1979)
60. B.H. Maddock, SPE ANTEC, New York, 383 (1959)
61. Z. Tadmor, I. Duvdevani, and I. Klein, Polym. Eng. Sci., 7, 198 (1967)
62. Z. Tadmor, Polym. Eng. Sci., 6, 185 (1966)
63. J. Shapiro, Ph.D. thesis, Cambridge Univ., England (1971)
64. J.R. Vermeulen, P.M. Gerson, and W.J. Beek, Chem. Eng. Sci., 26, 1445–1455 (1971)
65. J.R. Vermeulen, P.G. Scargo, and W.J. Beek, Chem. Eng. Sci., 26, 1457–1465 (1971)
66. G. Menges and P. Klenk, Kunststoffe, 57, 590 (1967)
67. P. Klenk, Rheol. Acta., 7, 75–78 (1968)
68. P. Klenk, Plastverarbeiter, 21, 537 (1968)
69. J. Dekker, Kunststoffe, 66, 130 (1976)
70. T.E. Fahey, M.Sc. thesis, Case Western Reserve Univ., September (1981)
71. F.R. Kulas and N.P. Thorshaug, J. Appl. Polym. Sci., 23, 1781–1794 (1979)
72. J.T. Lindt, Polym. Eng. Sci., 16, 284–291 (1976)
73. J.T. Lindt, Polym. Eng. Sci., 21, 1162–1166 (1981)
74. K.A. Gieskes, Internal Report, Twente Univ. of Technology, Mech. Eng. Dept., the Netherlands (1979)
75. H.E.H. Meijer, Ph.D. thesis, Twente Univ. of Technology, the Netherlands (1980)
76. J.R. Edmondson, Ph.D. thesis, Univ. of London (1972)
77. I.R. Edmondson and R.T. Fenner, Polymer, 16, 49 (1975)
78. R.T. Fenner, Polymer, 18, 617 (1977)
79. A.P.D. Cox and R.T. Fenner, Polym. Eng. Sci., 20, 562–571 (1980)
80. A.P.D. Cox, J.G. Williams, and D.P. Isherwood, Polym. Eng. Sci., 21, 86–92 (1981)
81. G.M. Gale, Plast. Polym., 6, 183 (1970)
82. G. Mennig, Kunststoffe, 71, 359–362 (1981)
83. R.C. Donovan, Polym. Eng. Sci., 11, 247–257 (1971)
84. R.C. Donovan, Polym. Eng. Sci., 11, 485–491 (1971)
85. J. Shapiro, A.L. Halmos, and J.R.A. Pearson, Polymer, 17, 905–918 (1976)

86. A.L. Halmos, J.R.A. Pearson, and R. Trottnow, Polymer, 19, 1199–1216 (1978)
87. J.R.A. Pearson, Int. J. Heat Mass Transfer, 19, 405–511 (1976)
88. D.R. Hinrichs and L.U. Lilleleht, Polym. Eng. Sci., 18, 422–426 (1978)
89. D.W. Sundstrom and C.C. Young, Polym. Eng. Sci., 12, 59–63 (1972)
89a. D.W. Sundstrom and J.R. Lo, Polym. Eng. Sci., 18, 422–426 (1978)
90. C.I. Chung, Mod. Plast., 45, 178 (1968) and 45, 110 (1968)
91. C.I. Chung, SPE J., 26, 32 (1970)
92. C.I. Chung, Polym. Eng. Sci., 11, 93–98 (1971)
93. C.I. Chung, R.J. Nichols, and G.A. Kruder, Polym. Eng. Sci., 14, 29 (1974)
94. E.M. Mount and C.I. Chung, Polym. Eng. Sci., 18, 711–720 (1978)
95. E.M. Mount, J.G. Watson, and C.I. Chung, Polym. Eng. Sci., 22, 729–737 (1982)
96. D.E. McClelland and C.I. Chung, Polym. Eng. Sci., 23, 100–104 (1983)
97. K.H. Chung and C.I. Chung, Polym. Eng. Sci., 23, 191–196 (1983)
98. N. N., Engineering, 114, 606 (1922) This publications is often attributed to H.S. Rowell and D. Finlayson; however, this is disputed by Holmes [99]. Rowell and Finlayson did publish on the subject later in 1928 [100].
99. D.B. Holmes, Ph.D. thesis, Delft University of Technology, the Netherlands (1967)
100. H.S. Rowell and D. Finlayson, Engineering, 126, 249 (1928)
101. H.A.A. Helmy, Ph.D. thesis, Univ. of Bradford, England (1975)
102. R.T. Fenner, "Extruder Screw Design," Illiffe, London (1970)
103. Z. Tadmor and I. Klein, "Engineering Principles of Plasticating Extrusion," van Nostrand Reinhold Comp., New York (1970)
104. J. Nebrensky, J.F.T. Pittman, and J.M. Smith, Polym. Eng. Sci., 13, 209 (1973)
105. R.T. Fenner, Polymer, 18, 617 (1977)
106. Z. Tadmor and C.E. Gogos, "Principles of Polymer Processing," John Wiley & Sons, New York (1979)
107. Y. Mori and T.K. Matsumoto, Rheol. Acta, 1, 240 (1958)
108. R.E. Colwell and K.R. Nicholls, Ind. Eng. Chem., 51, 841 (1959)
109. W.E. Ball and R.E. Colwell, 43rd Nat'l. Mtg. AIChE, Tulsa, OK, Sept. (1960)
110. D.J. Weeks and W.J. Allen, J. Mech. Eng. Sci., 4, 380 (1962)
111. B.S. Clyde and W.A. Holmes-Walker, Int. Plast. Eng. 2, 338 (1962)
112. F.W. Kroesser and S. Middleman, Polym. Eng. Sci., 5, 231 (1965)
113. R.W. Flumerfelt, M.W. Pierick, S.L. Cooper, and R.B. Bird, Ind. Eng. Chem., 8, 354 (1969)
114. C.J. Rauwendaal, SPE ANTEC, Chicago, 186–199 (1983)
115. H.J. Zamodits, Ph.D. thesis, Univ. of Cambridge, England (1964)
116. B. Yates, Ph.D. thesis, Univ. of Cambridge, England (1968)
117. B. Martin, Ph.D. thesis, London Univ., England (1972)

118. K. Palit, Ph.D. thesis, London Univ., England (1972)
119. N.R. Neelakantan, Ph.D. thesis, Univ. of Wales, England (1974)
120. K.P. Choo, Ph.D. thesis, Univ. of Wales, England (1977)
121. H. Kuehnle, Kunststoffe, 5, 267 (1982)
122. D.E. Hanson, Polym. Eng. Sci., 9, 405 (1967)
123. Z.K. Walczak, J. Appl. Polym. Sci., 17, 153 (1973)
124. M. Rokuda, J. Appl. Polym. Sci., 23, 463 (1979)
125. J.M. Dealy and W.K.W. Tsang, J. Appl. Polym. Sci., 26, 1149 (1981)
126. T.Y. Liu, D.S. Soong, and M.C. Williams, Polym. Eng. Sci., 21, 675 (1981)
127. J.W. White and W. Minoshima, Polym. Eng. Sci., 21, 1113 (1981)
128. B. Maxwell and A. Breckwoldt, J. Rheol., 25, 55 (1981)
129. W.P. Perwadtschuk and V.I. Jankow, Plaste und Kautschuk, 28, 36–44 (1981)
130. J. Boussinesg, J. Mathematique Pures et Appliquees, series 2, 13, 377–424 (1968)
131. W. Meskat, Kunststoffe, 45, 87 (1955)
132. M.L. Booy, Polym. Eng. Sci., 21, 93 (1981)
133. Z. Tadmor, Polym. Eng. Sci., 6, 203 (1966)
134. D.F. Dyer, AIChE J., 15, 823 (1969)
135. R.M. Griffith, Ind. Eng. Chem., 1, 180 (1962)
136. K. Hayashida, Rheol. Acta, 2, 261 (1962)
137. H. Kruger, Kunststoffe, 10, 711 (1963)
138. D.R. Rea and W.R. Schowalter, Trans. Soc. Rheol., 11, 125 (1967)
139. H.J. Zamodits and J.R.A. Pearson, Trans. Soc. Rheol., 13, 357 (1969)
140. K. Palit and R.T. Fenner, AIChE J., 18, 628 (1972)
141. H.H. Winter, Rheol. Acta., 1, 1 (1978)
142. M.L. Hami and J.F.T. Pittman, Polym. Eng. Sci., 20, 339 (1980)
143. K.P. Choo, N.R. Neelakantan, and J.F.T. Pittman, Polym. Eng. Sci., 20, 349 (1980)
144. K.P. Choo, M.L. Hami, and J.F.T. Pittman, Polym. Eng. Sci., 21, 100 (1981)
145. J. Nebrensky, J.F.T. Pittman, and J.M. Smith, Polym. Eng. Sci., 13, 209 (1973)
146. S.M. Dinh and R.C. Armstrong, AIChE J., 28, 294–301 (1982)
147. H.H. Winter, Polym. Eng. Sci., 15, 84–89 (1975)
148. F.N. Cogswell, J. Non-Newtonian Fluid Mech., 2, 373–47 (1977)
149. M.T. Dennison, Trans. J. Plast. Inst., 35, 803–808 (1967)
150. J.J. Benbow and E.R. Howells, Trans. J. Plast. Inst., 30, 240–254 (1960)
151. British Patent 32559/72.
152. J.P. Tordella, in "Rheology," Vol. 4, F.R. Eirich (Ed.), Academic Press, New York (1969) Chapter 3
153. J.L. White, Appl. Polym. Symp., No. 20, 155 (1973)

154. J.M. Lupton and J.W. Regester, Polym. Eng. Sci., 5, 235 (1965)
155. L.L. Blyler and A.C. Hart, Polym. Eng. Sci., 10, 193 (1970)
156. S.M. Barnett, Polym. Eng. Sci., 7, 168 (1967)
157. E. Boudreaux and J.A. Cuculo, J. Macromol. Sci.–Rev. Macromol. Chem., C16, 39–77 (1977–1978)
158. C.D. Han and R.R. Lamonte, Polym. Eng. Sci., 11, 385 (1971)
159. J.L. den Otter, Rheol. Acta, 10, 200–207 (1971)
160. T.W. Huseby, Trans. Soc. Rheol., 10, 181–190 (1966)
161. A.P. Metzger and C.W. Hamilton, SPE Trans., 4, 107–112 (1964)
162. G.V. Vinogradov et al., Polym. Eng. Sci., 12, 323–334 (1972)
163. J.J. Benbow and P. Lamb, SPE Trans., 3, 7–17 (1963)
164. W. Phillippoff and F.H. Gaskins, Trans. Soc. Rheol., I, 263–284 (1958)
165. U.S. Patent 2,991,508 by R.T. Fields and C.F.W. Wolf to E.I. Du Pont de Nemours and Company, issued July 11, 1961
166. A.M. Kraynik and W.R. Schowalter, J. Rheol., 25, 95–114 (1981)
167. R.F. Westover, Polym. Eng. Sci., 6, 83 (1966)
168. R.A. Worth, J. Parnaby, and H.A.A. Helmy, Polym. Eng. Sci., 17, 257 (1977)
169. C.J.S. Petrie and M.M. Denn, AIChE J., 22, 109–236 (1976)
170. C.J.S. Petrie and M.M. Denn, AIChE J., 22, 236–246 (1976)
171. J.C. Miller, SPE Trans., 3, 134 (1963)
172. S. Kase, J. Appl. Polym. Sci., 18, 3279 (1974)
173. G.F. Cruz-Saenz, G.J. Donnelly, and C.B. Weinberger, AIChE J., 22, 441 (1976)
174. J.R.A. Pearson and Y.T. Shah, Trans. Soc. Rheol., 16, 519 (1972)
175. J.R.A. Pearson and Y.T. Shah, Ind. Eng. Chem. Fundam., 13, 134 (1979)
176. R.J. Fischer and M.M. Denn, Chem. Eng. Sci., 30, 1129 (1975)
177. Y. Ide and J.L. White, J. Appl. Polym. Sci., 20, 2511–2531 (1976)
178. Y. Ide and J.L. White, J. Non-Newtonian Fluid Mech., 2, 281–298 (1977)
179. Y. Ide and J.L. White, J. Appl. Polym. Sci., 22, 1061–1079 (1978)
180. J.L. White and Y. Ide, J. Appl. Polym. Sci., 22, 3058–3074 (1978)
181. R.S. Lenk, J. Appl. Polym. Sci., 22, 1781–1785 (1970)
182. G.A. Latinen, ACS Adv. in Chem. Series, 34, 235 (1962)
183. R.W. Coughlin and G.P. Canevari, AIChE J., 15, 560 (1969)
184. G.W. Roberts, AIChE J., 16, 878 (1970)
185. J.A. Biesenberger, Polym. Eng. Sci., 20, 1015 (1980)
186. J.A. Biesenberger and G. Kessides, Polym. Eng. Sci., 22, 832 (1982)
187. J.T. Bergen, G.W. Carrier, and J.A. Krumbansh, SPE ANTEC, Detroit (1958)
188. P.V. Danckwerts, Appl Sci. Res., Sec. A3, 279–296 (1952)

189. W.D. Mohr, R.L. Saxton, and C.H. Jepson, Ind. Eng. Chem., 49, 1855 (1957)
190. N. Nadav and Z. Tadmor, Chem. Eng. Sci., 28, 2115 (1973)
191. W.M. Hess, V.E. Chirico, and P.C. Vegvari, Elastomerics, Jan., 24–35 (1980)
192. D.H. Sebastian and J.A. Biesenberger, SPE ANTEC, Chicago, 121–123 (1983)
193. H.J. Suchanek, SPE ANTEC, Chicago, 117–120 (1983)
194. T. Dobroth, G. Druhak, and L. Erwin, SPE ANTEC, Chicago, 124–126 (1983)
195. G. Krassowski and G. Mennig, Kunststoffe, 73, 127–131 (1983)
196. Z. Tadmor and C. Gogos, "Principles of Polymer Processing," Wiley, New York (1979) Chapter 7
197. R.J. Cembrole, Rubber Chem. Technol., 56, 233–243 (1983)
198. K.K. Mohanty, J.M. Ottino, and H.T. Davis, Chem. Eng. Sci., 37, 905 (1982)
199. J.W. Hiby, Int. Chem. Eng., 21, 197 (1981)
200. C.L. Tucker, Chem. Eng. Sci., 36, 1829 (1982)
201. R.S. Spencer and R.M. Wiley, J. Colloid Sci., 6, 133 (1951)
202. L. Erwin, Polym. Eng. Sci., 18, 572–576 (1978)
203. L. Erwin, Polym. Eng. Sci., 18, 738–740 (1978)
204. L. Erwin, Polym. Eng. Sci., 18, 1044–1047 (1978)
205. K.Y. Ng and L. Erwin, Polym. Eng. Sci., 21, 212–217 (1981)
206. Z. Tadmor and G. Lidor, Polym. Eng. Sci., 16, 450–461 (1976)
207. G. Pinto and Z. Tadmor, Polym. Eng. Sci., 10, 279–288 (1970)
208. J.M. Ottino and R. Chella, Polym. Eng. Sci., 23, 357–379 (1983)
209. J.M. Ottino, Ph.D. thesis, Univ. of Minnesota, Minneapolis, MN (1979)
210. J.M. Ottino, W.E. Ranz, and C.W. Macosko, AIChE J., 27, 565–577 (1981)
211. R. Chella and J.M. Ottino, Ind. Eng. Chem. Fundam., 24, 170–180 (1985)
212. S.M. Skoblar, Plast. Technol., Oct., 37–43 (1974)
213. G. Smoluk, Plastics World, May, 40–43 (1978)
214. N.R. Schott, B. Weinstein, and D. LaBombard, Chem. Eng. Prog., 71, 54–58 (1975)
215. C.D. Han and Y.W. Kim, J. Appl. Polym. Sci., 19, 2831–2843 (1975)
216. E.B. Nauman, AIChE J., 25, 246–258 (1979)
217. P.T. Allocca, paper presented at the 73rd Annual AIChE Meeting, Chicago, Nov. (1980)
218. P.T. Allocca, Fiber Producer, April, 12–19 (1982)
219. J.M. Ottino, AIChE J., 29, 159–161 (1983)
220. W.R. Bolen and R.E. Colwell, SPE J., 14, 24–28 (1958)
221. R.B. Bird, H.R. Warner, Jr., and D.C. Evans, "Kinetic Theory and Rheology of Dumbbell Suspension with Brownian Motion," Fortschritte Hochpolymerenforschung, Springer Verlag, 8, 1–90 (1971)
222. Z. Tadmor, Ind. Eng. Chem. Fundam., 15, 346–348 (1976)

223. G. Martin, Industrie-Anzeiger, 93, 2651–2656 (1971)
224. G. Martin, Ph.D. thesis, Univ. of Stuttgart, Germany (1972)
225. B. Miller, Plastics World, Jan., 58–64 (1982)
226. T.B. Reeve and W.L. Dills, J. Color Appearance, 1, 25–29 (1971)
227. N. N., Plast. Compd., Jan./Feb., 20–32 (1981)
228. W.D. Mohr and R.S. Mallouk, Ind. Eng. Chem., 51, 765 (1959)
229. H.A.A. Helmy, SPE ANTEC, Chicago, 146–150 (1983)
230. W. Gleiszle, Rheol. Acta, 21, 484 (1982)
231. L.A. Utracki and R. Gendron, J. Rheol., 5, 28, 601–623 (1984)
232. J.J. Benbow, R.V. Charley, and P. Lamb, Nature, 192, 223 (1961)
233. J.J. Benbow and P. Lamb, SPE Trans., Jan., 7–17 (1963)
234. M. Viriyayuthakorn and B. Kassahun, SPE ANTEC, New Orleans, 81–84 (1984)
235. H. Potente, Rheol. Acta, 22, 387–395 (1983)
236. C.D. Denson, Adv. Chem. Eng., 12, 61–104 (1983)
237. G. Menges, W. Feistkorn, and G. Fischbach, Kunststoffe, 74, 695–699 (1984)
238. M.A. Spalding, J. Dooley, and K.S. Hyun, "The Effect of Flight Radii Size on the Performance of Single-Screw Extruders," SPE ANTEC, 190–194 (1999)
239. A. Kraemer, "Erfahrungen beim Einsatz von Extrudern mit genuteter Einzugzone," Kunststoffe, 78, 21–26 (1988) [1]
240. M. del Pilar Noriega E. et al., "Incremento de Productividad en la Extrusion con Zonas de Alimentacion Ranurada," Technologia del Plastico, April, 29–35 (1997) [2]
241. B. Davis et al., "Grooved Feed Single Screw Extruders—Improving Productivity and Reducing Viscous Heating Effects," Polym. Eng. Sci., 38, no. 7, 1199 (1998) [3]
242. D. Boes et al., "30 Jahre Nutenextruder," Kunststoffe, 80, 659–664 (1990) [4]
243. R. Sikora, J. Sikora, and J. Diakun, "Wytlasczarka do Tworzyw Wielkoczasteczkowych," Zgloszenie Patentowe w UP RP nr. P 303397
244. R. Sikora and J. Sikora, "Wytlasczarka Autotermiczna," Zgloszenie Patentowe w UP RP nr. P 304302
245. H. Peiffer and H. Eberhardt, U.S. Patent 4,678,339 (1987)
246. C.J. Rauwendaal, U.S. Patent 5,909,958, "Screw Extruder with Adjustable Groove Depth" (1999)
247. G.M. Gale, 49th SPE ANTEC, 95 (1991)
248. G.M. Gale, Adv. Polym. Technol., 16, no. 4, 251 (1997)
249. M.H. Mack, Plast. Eng., 47, no. 12, 39 (1991)
250. M.R. Thompson, G. Donoian, and J.C. Christiano, 57th SPE ANTEC, 145 (1999)
251. P. Elemans and J.M. van Wunnik, "The Effect of Feeding Mode on the Dispersive Mixing Efficiency in Single-Screw Extrusion," 58th SPE ANTEC, 265–267 (2000)
252. P. Elemans, "Enhancing Dry-Color Efficiency in Starve-Fed Injection Molding," 58th SPE ANTEC, 2582–2586 (2000)

253. K. Luker, paper presented at the Continuous Compounding Conference, Beachwood, Ohio, Nov. 14–15 (2000)
254. G.A. Kruder and W.N. Calland, SPE ANTEC, 74–85 (1990)
255. P. Yucheng and H. Hanxiong, Sixth Polym. Proc. Soc. Meeting, Paper 04–19 (1990)
256. F. Zhu and L. Chen, Polym. Eng. Sci., 31, 1113–1116 (1991)
257. R.J. Nichols and F. Kheradi, Mod. Plast., 61, 70 (1984)
258. S. Jakopin and P. Franz, AIChE Diamond Jubilee Meeting Technical Papers, Washington D.C. (1983)
259. C.J. Rauwendaal, "Comparison of Two Melting Models," Adv. Polym. Technol., 15, no. 2, 135–144 (1996)
260. P. Geisbüsch, Thesis, RWTH, Aachen, Germany (1980)
261. A. Limper, Thesis, RWTH, Aachen, Germany (1985)
262. W. Neumann, Report from the IKV, Aachen, Germany (1984)
263. D.R. Paul and S. Newman (Eds.), "Polymer Blends," Academic Press (1978)
264. T Kitano, T. Kataoka, and T. Shirota, Rheol. Acta, 20 (1981)
265. A.V. Shenoy and D.R. Saini, Polym. Compos., 7 (1986)
266. M. Takahashi, S. Suzuki, H. Nitanada, and E. Aria, J. Am. Ceram. Soc., 71 (1988)
267. J. Laven and H.N. Stein, J. Rheol., 35, 1523–1549 (1991)
268. C.J. Rauwendaal, U.S. Patent 5,932,159 (1999)
269. C.J. Rauwendaal, U.S. Patent 6,136,246 (2000)
270. C. Rauwendaal, "Melting Theory for Temperature-Dependent Fluids, Exact Analytical Solution for Power Law Fluids," Adv. Polym. Technol., 11, 19–25 (1992)
271. C.J. Rauwendaal, Doctoral Thesis, Twente University, Enschede, The Netherlands (1988)
272. M.S. Tamura, J.M. Henderson, R.L. Powell, and C.F. Shoemaker, J. Food Process Eng., 16, 93–126 (1993)
273. G.A. Campbell et al., SPE ANTEC, Boston, 201 (1995)
274. G.A. Campbell et al., Polym. Eng. Sci., 32, no. 23, 1765 (1992)
275. G.A. Campbell et al., International Polymer Processing, VII, no. 4, 240 (1992)
276. R. Sikora and E. Sasimowski, "Polymer Flow Velocity in the Helical Channel on Dependence of a Coordinate System," Int. Polym. Process., 15, no. I 3, 221–232 (2000)
277. J.L. Radovich, "An Experimental Comparison of Heat Removal in Water or Air Cooled Aluminum Barrel Coolers," TAPPI Polymers, Laminations & Coatings Conference, 103–107 (1995)
278. C.J. Rauwendaal and J. Anderson, "Finite Element Analysis of Flow in Extruders," 52nd SPE ANTEC, 298–305, San Francisco, CA (1994)
279. J. Pape, H. Potente, and C. Obermann, "Influence of Model Simplifications on the Accuracy of Simulation Results in Single Screw Extruders," 15th Annual Meeting of the Polymer Processing Society, Den Bosch, the Netherlands (1999)

280. J. Pape, Diplomarbeit, Universität-GH Paderborn, KTP–Institut für Kunststofftechnik, Paderborn, Germany (1999)

281. C.J. Rauwendaal, T.A. Osswald, G. Tellez, and P.J. Gramann, "Flow Analysis in Screw Extruders–Effect of Kinematic Conditions," Int. Polym. Process., XIII, no. 4, 327–333 (1998)

282. M.A. Spalding, J. Dooley, K. Hyun, and S. Strand, SPE ANTEC Technical Papers, 39, 1533 (1993)

283. J.C. van der Hoeven, R. Wimberger-Friedl, and H.E.H. Meijer, "Homogeneity of Multilayers Produced with a Static Mixer," Polym. Eng. Sci., 41, no. 1, 32–42 (2001)

284. J.W.S. Raleigh, Philos. Mag., 34, 145 (1892)

285. S. Tomotika, Proc. Roy. Soc., Ser. A, 150, 322 (1935)

286. H.P. Grace, Chem. Eng. Commun., 14, 225 (1982)

287. R A. De Bruijn, Ph.D. thesis, Eindhoven University, the Netherlands (1989)

288. F.D. Rumscheidt and S.G. Mason, J. Colloid Sci., 16, 238 (1961)

289. J.W. Hiby, Verfahrenstechnik, 4, p. 538–543 (1970)

290. K. Hartung and J.W. Hiby, Chem. Eng. Technol., 44, 1051–1056 (1972)

291. F.P. Fleischman, Chem. Anlagen-Verfahren, Jan., 39–43 (1972)

292. A.K. Chesters, Trans. Ind. Chem. Eng. A, 69, 259 (1991)

293. J.J. Elmendorp, Ph.D. thesis, Delft University, the Netherlands (1986)

294. J. Janssen, Ph.D. thesis, Eindhoven University, the Netherlands (1993)

295. G. Pinto and Z. Tadmor, Polym. Eng. Sci., 10, 279 (1970)

296. J.W. Joo and T. H. Kwon, Polym. Eng. Sci., 33, 15, 959 (1999)

297. R.T. Steller, "Theoretical Model for Flow of Polymer Melts in the Screw Channel," Polym. Eng. Sci., 30, no. 7, 400–407 (1990)

298. R.T. Steller, "Generalized Flow of Ellis Fluid in the Screw Channel," Polym. Eng. Sci. Nov. (2001)

299. C.J. Rauwendaal, T. Osswald, P. Gramann, and B. Davis, "Design of Dispersive Mixing Sections," Int. Polym. Process., XIV, no. 1, 1–7 (1999)

300. W.J. Milliken and L.G. Leal, J. Non-Newtonian Fluid Mech., 42, 231 (1992)

301. C.J. Rauwendaal, "Polymer Mixing, A Self-Study Guide," Carl Hanser Verlag, Munich (1998)

302. J. Gavis and R.L. Laurence, Ind. Eng. Chem. Fundam., 7, 232–239, 525–527 (1968)

303. C. Rauwendaal and J.F. Ingen Housz, J. Reinf. Plast. Compos., 9, 583–601, Nov. (1990)

304. A. Acrivos, 4th Ann. N.Y. Acad. Sci., 404, 1 (1983)

305. J.M. Rallison, Ann. Rev. Fluid Mech., 16, 45 (1984)

306. H.A. Stone, Ann. Rev. Fluid Mech., 26 (1994)

307. P.H.M. Elemans, Ph.D. thesis, Eindhoven University, the Netherlands (1989)

308. P. Gramann, C. Rauwendaal, B. Davis, and T. Osswald, "A New Dispersive and Distributive Mixer for the Compounding of Highly Viscous Materials," 57th SPE ANTEC, 162–166 (1999)

309. M. H. Pahl and E. Muschelknautz, Chem. Eng. Tech., 51, 347–364 (1979)

310. E. B. Mauman, AIChE J., 25, 246–258 (1979)

311. M. J. Cliff and W. L. Wilkinson, Second European Conference on Mixing, Cambridge, UK, 15 (1977)

312. T. D. Craig, Polym. Eng. Sci., 27, 1386–1389 (1987)

313. W. Mueller, Verfahrenstechnik, 15, 105–111 (1981)

314. M. Tjahadi, H. A. Stone, and J. M. Ottino, J. Fluid Mech., 243, 297 (1992)

315. A. Tadros, B. Vincent, in: P. Becher (Ed.) Encyclopedia of Emulsion Technology I (1983); II (1985); III (1987), Marcel Dekker, New York

316. A. K. Chesters, Trans. Ind. Chem. Eng., 69, 259 (1991)

317. I. Manas-Zloczower, A. Nir, and Z. Tadmor, Rubber Chem. Technol., 55, 1250 (1982)

318. L. A. Utracki and Z. H. Shi, Polym. Eng. Sci., 32, 1824 (1992)

319. Z. H. Shi and L. A. Utracki, Polym. Eng. Sci., 32, 1834 (1992)

320. L. A. Utracki et al., Polym. Eng. Sci., 32, 1842 (1992)

321. L. A. Utracki et al., Polym. Eng. Sci., 35, 115–127 (1995)

322. L. A. Utracki et al., Polym. Networks Blends, 3, 167 (1993)

323. G. A. Campbell and M. A. Spalding, "Analyzing and Troubleshooting Single-Screw Extruders," Hanser Verlag, Munich (2013)

324. C. Rauwendaal, "Polymer Extrusion," 4th ed., Carl Hanser Verlag, Munich (2001)

325. C. Rauwendaal, "Analysis of Extrusion Characteristics of LLPDE," Conference Proceedings, 41st SPE ANTEC, Chicago, IL, 151–154 (1983)

326. C. Rauwendaal, "Estimating Fully Developed Melt Temperature in Extrusion," Conference Proceedings, 58th SPE ANTEC, Orlando, FL, 307–311 (2000)

327. I. Sbarski, E. Kosior, and S. Bhattacharya, "Temperature Rise in the Extrusion of Highly Viscous Composite Materials," Int. Polym. Process., XII, no. 4, 341 (1997)

328. H. Ockendon and J. R. Ockendon, "Variable Viscosity Flows in Heated and Cooled Channels," J. Fluid Mech., 83, 177–190 (1977)

329. T. H. Sun, "Variable Viscosity Flow in Heated and Cooled Channel with Internal Viscous Dissipation," Adv. Polym. Technol., 8, no. 1, 1–4 (1988)

330. W. M. Davis, "Heat Transfer in Extruder Reactors," Chem. Eng. Progress, Nov., 35–42 (1988); also Section 7 in "Reactive Extrusion, Principles and Practice," M. Xanthos (Ed.), Carl Hanser Verlag, Munich (1992)

331. W. A. Kramer, "Extruder Barrel Cooling," Conference Papers, 45th SPE ANTEC (1987)

332. C.D Han, "Analysis of the Performance of a Cooling Extruder in Thermoplastic Foam Extrusion," Conference Proceedings, 45th SPE ANTEC (1987)

333. J. L. Radovich, "An Experimental Comparison of Heat Removal in Water or Air Cooled Aluminum Barrel Coolers," TAPPI Polymers, Laminations & Coatings Conference, 103–107 (1995)

334. E. Steward and B. Kramer, "Air versus Water Cooled Single Screw Extruders," Technical Papers, Conference Proceedings, 61st SPE ANTEC (2003)

335. J. Anderson and C. Rauwendaal, “Finite Element Analysis of Flow in Extruders,” Conference Proceedings, 52nd SPE ANTEC, 298–305 (1994)

336. C. Rauwendaal, “Leakage Flow in Screw Extruders,” Doctoral Thesis, Twente University of Technology, Department of Mechanical Engineering-Polymer Processing, the Netherlands (1988)

337. S. Derezinski, “Dimensionless Curves for Extruder Melt Temperature and Flow,” Conference Proceedings, 45th ANTEC, Soc. Plast. Eng., May 1987, 98–102 (1987)

338. S. Derezinski, “Heat Transfer Coefficients in Extruder Melt Sections,” Conference Proceedings, 54th ANTEC, Soc. Plast. Eng., May, 417–421 (1996)

8 Extruder Screw Design

The single most important mechanical element of a screw extruder is the screw. The proper design of the geometry of the extruder screw is of crucial importance to the proper functioning of the extruder. If material transport instabilities occur as a result of improper screw geometry, even the most sophisticated computerized control system cannot solve the problem. Screw design is often still considered to be more of an art than a science. As a result, misconceptions about certain aspects of screw design still abound today. Since the theory of single screw extrusion is now well-developed (see Chapter 7), the design of screws for single screw extruders can be based on solid engineering principles. Thus, screw design for single screw extruders should no longer be an art, but a science based firmly on the principles of polymer processing engineering.

Unfortunately, people involved in screw design are not always up-to-date on extrusion theory. As a result, many extruder screws in use today perform considerably below maximum possible performance, solely because of improper screw design. An example is the still-common use of the square pitch extruder screw. This is a screw with constant pitch with the pitch being equal to the diameter of the screw; this pitch corresponds to a helix angle of 17.66°. It can be demonstrated quite easily that the square pitch is far from optimum with respect to melting and melt conveying for a number of polymers. This fact has been known since the early 1950s, yet most extruder screws in use today still use the constant square pitch design.

A factor that may have contributed to the state of affairs in screw design is that there has not been a comprehensive text dealing with screw design. The objective of this chapter is to demonstrate how extrusion theory can be used to properly design extruder screws. Hopefully, this will provide a solid foundation, based on engineering principles, from which better and more effective screw designs can be developed in the future. The principles of screw design are not only important in designing new extruder screws, but also in the analysis of processing problems of an existing extrusion line. It is important to be able to recognize whether a problem is related to poor screw design or to another part of the process. Thus, knowledge of the basic principles of screw design is important to essentially every person involved with extruders.

8.1 Mechanical Considerations

Regardless of the details of the screw geometry, it is important that the screw has sufficient mechanical strength to withstand the stresses imposed by the conveying process in the extruder.

8.1.1 Torsional Strength of the Screw Root

An important requirement for the extruder screw is the ability to transmit the torque required to turn the screw. The most critical area of the screw in this respect is the feed section. In the feed section, the cross-sectional area of the root of the screw is generally the smallest and, thus, the torsional strength the lowest. Also, in the feed section, the entire torque has to be transmitted, while further downstream only a fraction of the total torque has to be transmitted. The torque that is transmitted can be determined from the power to the screw, Z_{screw}, and the screw rpm, N.

$$T = C\frac{Z_{screw}}{N} \tag{8.1}$$

where Z_{screw} is the power to the screw, N the rotational speed of the screw, and C a conversion constant.

If Z is expressed in horsepower and N in rev/min., the constant C must equal 7120.9 to give a torque expressed in Newton-meter. If Z is expressed in kilowatt, constant C equals 9549.3. This formula is based on the relationship between torque, angular frequency ω, and power:

$$Z = T\,\omega = \frac{2\pi\,T\,N}{60} \tag{8.2}$$

where ω is expressed in radians/s and N in rpm.

From Eq. 8.1, it can be seen that the transmitted torque is directly proportional to the horsepower and inversely proportional to the screw speed. The power to the screw is related to the motor power by:

$$Z_{screw} = Z_{motor}\ \ \varepsilon_{motor}\ \ \varepsilon_{transmission} \tag{8.3}$$

where ε_{motor} is the efficiency of the motor and $\varepsilon_{transmission}$ the efficiency of the transmission.

The total efficiency is generally around 0.75. Thus, the power to the screw will be about 75% of the motor power. The stresses in the screw shaft as a result of the torque on the screw are shown in Fig. 8.1.

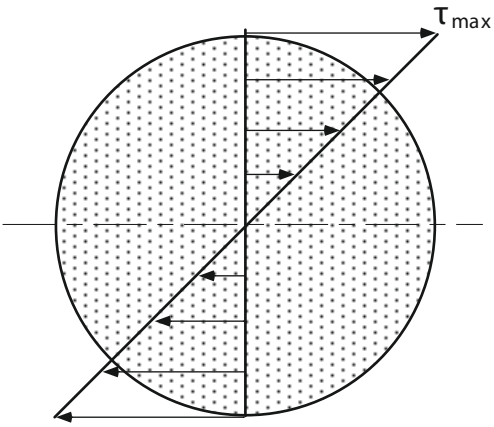


Figure 8.1
Stresses in the screw shaft

The shear stress in the shaft resulting from torque T can be expressed as:

$$\tau = \frac{2Tr}{\pi R^4} = \frac{Tr}{J} \tag{8.4}$$

where J is the polar moment of inertia.

The maximum stress occurs at the circumference (r = R), and the maximum stress is:

$$\tau_{max} = \frac{2T}{\pi R^3} = \frac{TR}{J} \tag{8.5}$$

In order to avoid failure in the screw shaft, the maximum stress should be less than the allowable stress τ_a of the metal of the screw. The allowable stress of metal ranges from about 50 to 100 MPa. Thus, in order to have sufficient torsional strength, the following inequality should hold:

$$R > \left(\frac{2T}{\pi \tau_a}\right)^{1/3} \tag{8.6}$$

From Eq. 8.6, the maximum channel depth in the feed section can be calculated:

$$H_{max} = \frac{1}{2}D - \left(\frac{2T}{\pi \tau_a}\right)^{1/3} \tag{8.7}$$

where D is the O. D. of the extruder screw.

Consider, as an example, a 150-mm extruder, running at 80 rpm and consuming 200 hp at the screw. The torque to the screw, according to Eq. 8.1, is T = 17810 N · m. If τ_a = 100 MPa, then the maximum channel depth in the feed section becomes:

$$H_{max} = 0.0750 - 0.0484 = 0.0266\,[m] = 26.6\,[mm] \tag{8.8}$$

It should also be realized that Eqs. 8.6 and 8.7 are valid for solid screws only. If the screw is cored for cooling or heating, the torsional strength of the screw shaft will be reduced. In this case, the polar moment of inertia of the screw shaft becomes:

$$J = \frac{\pi (R_s^4 - R_c^4)}{2} \tag{8.9}$$

where R_s is the radius of the root screw and R_c is the radius of the core channel in the screw.

8.1.2 Strength of the Screw Flight

The primary loading of the screw flights occurs by the pressure differential ΔP between the leading and trailing side of the flight. In addition, there will be loading from the shear stress acting on the tip of the flight as a result of the leakage flow through the clearance. This situation is shown in Fig. 8.2.

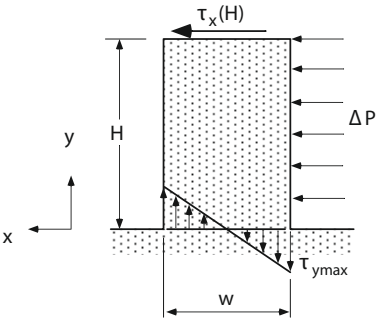


Figure 8.2
Stresses acting on a screw flight

As a result of the stresses acting on the screw flight, there will be a distribution of normal stresses in the flight that reaches a maximum value at the screw surface. The torque resulting from this normal stress distribution counteracts the torque resulting from τ_x and ΔP. If the maximum normal stress at the wall is τ_{ymax}, then a torque balance per unit flight length yields:

$$\frac{1}{6} w^2 \tau_{ymax} = \frac{1}{2} H^2 \Delta P + H w \tau_x(H) \tag{8.10}$$

Thus, the maximum normal stress is:

$$\tau_{ymax} = \frac{3H^2 \Delta P}{w^2} + \frac{6H \tau_x(H)}{w} \tag{8.11}$$

The cross flight shear stress τ_x acting in the screw flight also reaches a maximum at the screw surface. The maximum shear stress τ_{max} is obtained from a simple force balance in the x-direction:

$$w\,\tau_{xmax} = w\,\tau_x(H) + H\,\Delta P \tag{8.12}$$

Thus, the maximum shear stress is:

$$\tau_{xmax} = \tau_x(H) + \frac{H}{w}\Delta P \tag{8.13}$$

For the combined shear and normal stress, the following criterion can be used:

$$\tau_{comb} = (\tau_{ymax}^{\ 2} + 3\tau_{xmax}^{\ 2})^{1/2} < \tau_a \tag{8.14}$$

From Eqs. 8.11 through 8.14, the ratio of flight height to flight width can be determined such that $\tau_{comb} < \tau_a$. If the shear stress τ_x (H) at the tip of the flight can be neglected, the ratio of the flight height to flight width should be:

$$\frac{H}{w} < \left[\frac{1}{3}\left(\frac{1}{4} + \frac{\tau_a^2}{\Delta P^2}\right)^{1/2} - \frac{1}{6}\right]^{1/2} \tag{8.15}$$

This relationship is shown in Fig. 8.3.

The ratio of flight height to flight width can be thought of as a slenderness ratio. In general, the ratio of the allowable stress to pressure difference, $\tau_a/\Delta P$, will be larger than 25. Thus, a slenderness ratio of 2 (a common value used in screw design) will yield more than adequate strength if the shear stress at the flight tip is negligible. In some instances, the shear stress at the flight tip cannot be neglected. For instance, a situation where considerable lateral forces are acting on the screw is when there is metal-to-metal contact between screw flight and barrel. In such a case, very large shear stresses can act on the flight tip and these stresses must then be taken into account. However, this is a rather abnormal situation and should be avoided if at all possible.

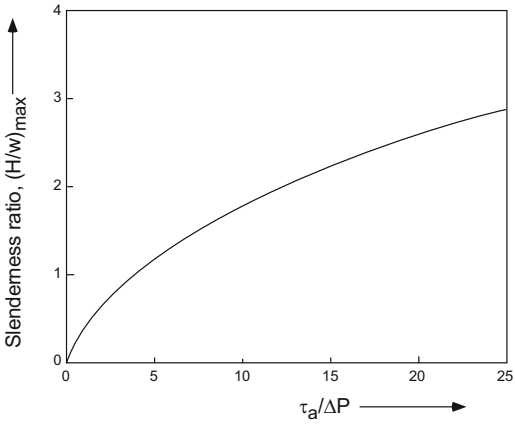


Figure 8.3
Slenderness ratio versus $\tau_a/\Delta P$

It should be noted that the stress concentration in the base of the flight can be reduced significantly if the flight width is varied with flight height; see Fig. 8.4.

An additional advantage of the flight geometries shown in Fig. 8.4 is that the flight width at the tip can be reduced considerably compared to the standard flight geometry without increasing the stresses in the base of the flight. It will be shown later that there are substantial functional benefits that can be derived from the flight geometries as shown in Fig. 8.4; see also Section 7.2.2.

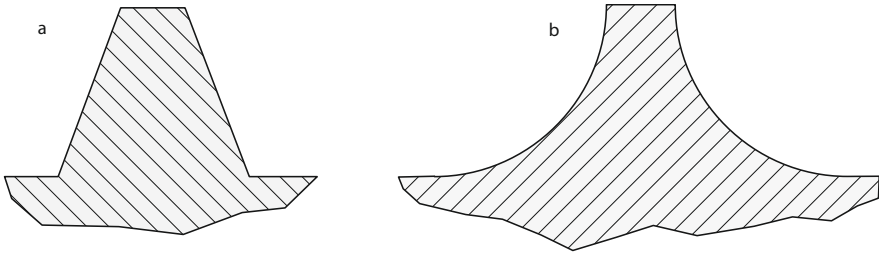


Figure 8.4 Flights with varying flight width

8.1.3 Lateral Deflection of the Screw

There are various causes that will tend to deflect the screw. The most obvious cause is the force of gravity acting on the screw. If the drive support of the screw is considered rigid and the supporting function of the polymer and barrel is neglected, then the sagging of the screw by its own weight can be represented by Fig. 8.5.

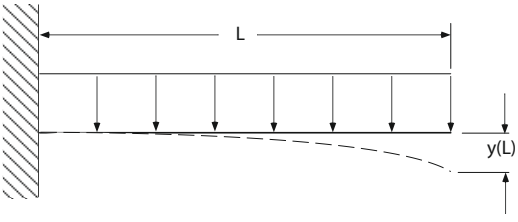


Figure 8.5
Screw as a cantilever

The amount of sag at the end of the screw is:

$$Y(L) = \frac{qL^4}{8EI} \tag{8.16}$$

where q is the force per unit length from the weight of the screw, E is the screw elastic modulus, and I is the moment of inertia. If the presence of the screw channel is neglected, then Eq. 8.16 can be written as:

$$Y(L) = \frac{2a_g \rho L^4}{E D^2} \tag{8.17}$$

where a_g is the gravitational acceleration and ρ the density of the screw material.

Consider a 150-mm extruder screw with a density of 7850 kg/m^3 and an elastic modulus of 210 GPa (= 210E9 Pa); the sag for this example is:

$$Y(L) = 3.256E-5\ L^4 \tag{8.18}$$

The unrestrained sag as a function of screw length is shown in Fig. 8.6.

It is clear that the unrestrained sag starts to exceed the standard radial clearance (≅ 0.2 mm) when the L/D ratio exceeds 10. At normal L/D ratios of 20 to 30, the unrestrained sag is about one to two orders of magnitude larger than the standard radial clearance. From these simple considerations, it is obvious that the polymer between the screw and barrel must play a considerable support function to prevent contact between screw and barrel. The supporting force necessary to counteract the sagging by the weight of the screw has to increase very strongly when the L/D is increased.

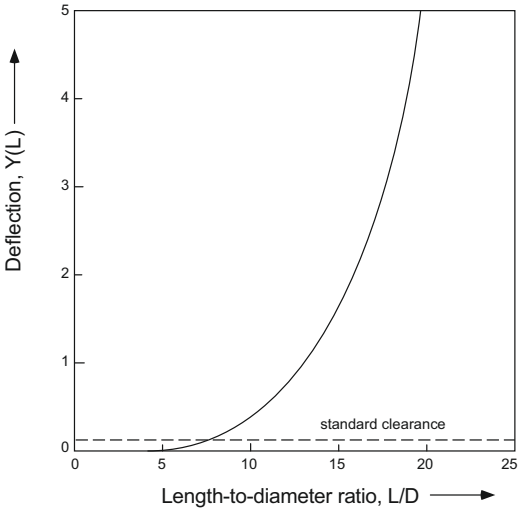


Figure 8.6
Unrestrained sag versus screw length

Another mechanism that can cause lateral movement of the screw is buckling. The collapse force required to cause buckling of a uniform cantilever is:

$$F = \frac{\pi^2 EI}{4L^2} \tag{8.19}$$

Thus, the head pressure necessary to cause buckling is: $\frac{\pi D^4}{64}$

$$P = \frac{\pi^2 ED^2}{64L^2} \tag{8.20}$$

because the moment of inertia I = $\frac{\pi D^4}{64}$.

The critical head pressure for buckling as a function of the L/D ratio is shown in Fig. 8.7.

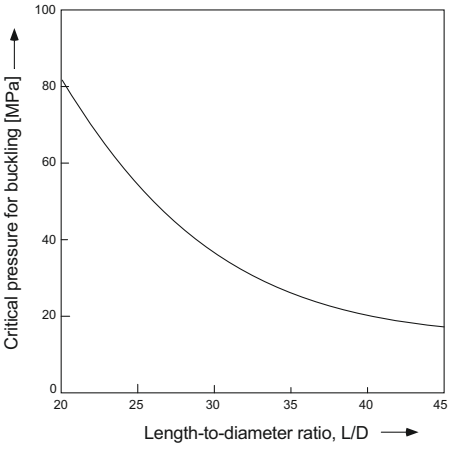


Figure 8.7
Critical head pressure versus L/D ratio

The elastic modulus is taken as 210 GPa. Considering that normal head pressures range from 20 to 60 MPa, it is clear that the occurrence of buckling is a distinct possibility when the L/D is greater than 20. The equations above do not take into account the weakening of the screw as a result of the screw channel. Fenner and Williams [1] analyzed the effect of channel depth and compression ratio. They found that the critical head pressure for buckling reduces when the channel depth is taken into account. At a ratio of H/D = 0.05 and a compression ratio C = 3, their predicted critical head pressure values are less than half of those predicted by Eq. 8.20 and shown in Fig. 8.7. This simply indicates that buckling is more likely to occur when the L/D is greater than 20. Thus, the polymer will have to support the screw in the center region of the extruder to prevent screw-to-barrel contact as a result of buckling. However, the lateral force resulting from buckling F_b is of the order:

$$F_b \cong 4F\,\delta / L \cong \pi D^2\, P\,\delta / L \tag{8.21}$$

where F is the force acting on the end of the screw.

Since the ratio δ/L is about 0.00005, the lateral force resulting from buckling will be quite small.

Another possible deflection mechanism is the occurrence of whirling. Whirling occurs when a shaft reaches a critical speed and becomes dynamically unstable with large lateral amplitudes. This phenomenon is due to the resonance frequency when the rotational speed corresponds to the natural frequencies of lateral vibration of the shaft. For uniform beams vibrating in flexure, the natural frequencies can be expressed as:

$$f_w = C_n \left(\frac{a_g EI}{w_1 L^4} \right)^{1/2} \tag{8.22}$$

where a_g is the gravitational acceleration and w_1 is the weight per unit length.

The value C_n for a beam with one end clamped and one end free is $C_n = 0.560$. For a circular beam, the critical rotational speed becomes ($N = 2\pi f$):

$$N_w = 0.88 \frac{D}{L^2} \left(\frac{E}{\rho} \right)^{1/2} \tag{8.23}$$

When E = 210 GPa and $\rho = 7850$ kg/m^3, the critical rotational speed can be written as:

$$N_w = \frac{4549.5}{D(L/D)^2} \tag{8.24}$$

For a 150-mm extruder with L = 30 D, the critical whirling speed $N_w = 33.7$ rev/s = 2022 rpm. It is clear from these numbers that whirling is not likely to occur in normal extrusion operations. Fenner and Williams [1] also calculated the critical rotational speed for whirling in extruders; however, they used an incorrect equation for the whirling speed. Instead of using weight per unit length, they used mass per unit length in Eq. 8.22. As a result, their values of the whirling speed are lower by a factor of $\sqrt{a_g}$.

Another possible cause of lateral deflection of the screw is non-uniform pressure distribution around the circumference of the screw. Figure 8.8 shows a possible pressure distribution that will result in a considerable lateral force on the screw.

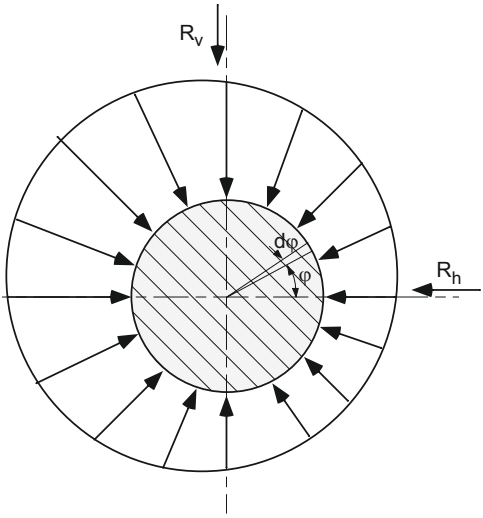


Figure 8.8
Circumferential pressure distribution that can cause screw deflection

The horizontal reaction component can be determined from:

$$R_h = \int_0^{2\pi} P(\varphi) \cos\varphi R d\varphi \tag{8.25}$$

The vertical reaction component can be determined from:

$$R_v = \int_0^{2\pi} P(\varphi) \sin\varphi R d\varphi \tag{8.26}$$

If the pressure is on the average ΔP larger on the left side than on the right side, the horizontal reaction force over length L is:

$$R_h = \Delta P\, D\, L \tag{8.27}$$

If D = L = 150 mm and ΔP = 1 MPa (≅ 145 psi), the reaction force will be 22.5 kN (≅ 5000 lbf.) In reality, the situation is more complicated because the pressure varies both in down-channel and cross-channel directions. However, from this simple example, it is clear that even a small pressure differential of only 1 MPa can cause a significant lateral reaction force on the screw. The reaction force is of such magnitude that it can easily deflect the screw into the barrel and cause substantial wear. This type of pressure-induced deflection is most likely to occur when the pressure reaches a sharp maximum or minimum somewhere along the screw. It is also more likely to occur with large helix angles (greater than 20°) as compared to small helix angles (smaller than 20°), and with single-flighted screws as compared to double-flighted screws.

A likely location for sharp pressure peaks is the end of the compression section. Many experimental studies have found that the pressure profile along the length of the extruder reaches a maximum close to the end of the compression section of the screw [77]. If the compression ratio is high, there is a chance of plugging of the solid bed. This can cause local pressure peaks that can deflect the screw into the barrel. It is interesting to note that generally the most severe wear does indeed occur towards the end of the compression section. This indicates that quite often the compression ratio is too high for the materials being processed, causing sharp pressure peaks towards the end of the compression section.

If one considers all the possible causes of lateral screw deflection, gravity, buckling, whirling, and pressure-induced deflection, it seems that pressure-induced deflection is the most likely cause of lateral deflection. The wear caused by pressure-induced deflection is most likely located towards the end of the compression section. This type of wear can be quite dramatic. The author experienced a case where a 150-mm extruder was wearing at a rate of about 1 mm (0.040 inch) in about 24 hours. The cause turned out to be the installation of a relatively long grooved barrel section without a corresponding change in screw design. A reduction of

the length of the grooved barrel section solved the problem; a change in screw design (lower compression ratio) probably would have solved the problem as well. However, this example illustrates that pressure-induced screw deflection can cause severe wear problems. Unfortunately, this type of problem is not easy to diagnose because the exact pressure profile along the length of the extruder is generally not known. Another complicating factor is that this type of wear may take several weeks or even months to become significant. This can make it difficult to relate the wear to the event that triggered it because there can be a considerable time lag or induction time.

8.2 Optimizing for Output

Generally, the objective of a screw design is to deliver the largest amount of output at acceptable melt quality. Unfortunately, high output and mixing quality are, to some extent, conflicting requirements. As output goes up, residence time goes down and with it the time available to mixing the polymer melt. As a result, the mixing quality goes down when the output increases. However, the mixing quality can generally be restored by incorporating mixing sections, either a mixing section along the screw or a static mixing section.

It is also important to realize that all functional zones of the extruder are interdependent. It makes little sense to drastically increase the pumping capacity if the melting rate is the real bottleneck in the process. Thus, before designing a new extruder screw to replace an existing screw, one should determine what part of the extruder is limiting the rate. This process will be covered in Chapter 11 on troubleshooting extruders.

8.2.1 Optimizing for Melt Conveying

The melt conveying theory discussed in Section 7.4 can be used to determine the optimum screw geometry for melt conveying. This optimum geometry will not normally be used in the metering section of the extruder screw. The optimum channel depth for output can be determined from:

$$\frac{\partial \dot{V}}{\partial H} = 0 \tag{8.28}$$

The volumetric melt conveying rate for a Newtonian fluid, neglecting the effect of the flight flanks, is given by Eq. 7.198. Considering that the channel width $W = (\pi D \sin\varphi/p) - w$, down-channel barrel velocity $v_{bz} = \pi D N \cos\varphi$, and down-channel pres-

sure gradient $g_z = g_a \sin\varphi$, where g_a is the axial pressure gradient, Eq. 7.198 can be written as:

$$\dot{V} = 0.5\pi DNH(\pi D \sin\varphi\cos\varphi - pw\cos\varphi) - \frac{H^3 P}{12\eta L}(\pi D\sin^2\varphi - pw\sin\varphi) \tag{8.29}$$

where L is the axial distance over which pressure P is built up; thus, the axial pressure gradient $g_a = P/L$.

The polymer melt viscosity η will depend on the local shear rate in the screw channel. If it is assumed that the representative shear rate in the channel is the Couette shear rate and that the polymer melt behaves as a power law fluid, which melt viscosity can be represented by:

$$\eta = m\left(\frac{\pi D N}{H}\right)^{n-1} \tag{8.30}$$

where m is the consistency index and n the power law index; see Eq. 6.23.

The optimum channel depth for output rate H_r^* can now be determined from Eqs. 8.28 through 8.30.

$$H_r^* = \left[\frac{6(\pi D N)^n m L}{(n+2) P \tan\varphi}\right]^{\frac{1}{n+1}} \tag{8.31}$$

The optimum depth depends on the diameter, screw speed, power law index, consistency index, pressure gradient, and helix angle. The optimum helix angle for output can be determined from:

$$\frac{\partial \dot{V}}{\partial \varphi} = 0 \tag{8.32}$$

By using the same equations for the melt conveying rate, the optimum helix angle for output rate φ_r^* has to be determined from the following equations:

$$\frac{\pi D\cos^2\varphi_r^* - \pi D\sin^2\varphi_r^* + pw\sin\varphi_r^*}{2\pi D\sin\varphi_r^*\cos\varphi_r^* - pw\cos\varphi_r^*} = \frac{P H^{n+1}}{6mL(\pi DN)^n} \tag{8.33}$$

Equation 8.33 cannot be easily solved in the form it is in. However, the equation can be simplified considerably if it is assumed that w = 0 and by defining a dimensionless down-channel pressure gradient g_z^0. Equation 8.33 can now be written as:

$$\frac{\cos^2\varphi_r^* - \sin^2\varphi_r^*}{2\cos\varphi_r^*} = g_z^0(\cos\varphi_r^*)^n \tag{8.34}$$

where:

$$g_z^0 = \frac{P\,H^{n+1}\sin\varphi}{6mL(\pi DN\cos\varphi)^n} \tag{8.35}$$

The optimum helix angle now has to be determined from:

$$2\cos^2\varphi_r^* - 2g_z^0(\cos\varphi_r^*)^{n+1} = 1 \tag{8.36}$$

For the Newtonian case (n = 1), the solution becomes:

$$\cos\varphi_r^* = \left(\frac{1}{2-2g_z^0}\right)^{1/2} \tag{8.37}$$

For the extreme non-Newtonian case (n = 0), the solution is:

$$2\cos^2\varphi_r^* - 2g_z^0(\cos\varphi_r^*)^{n+1} = 1 \tag{8.38}$$

Figure 8.9 shows the optimum helix angle as a function of the dimensionless down-channel pressure gradient for n = 1 and n = 0.

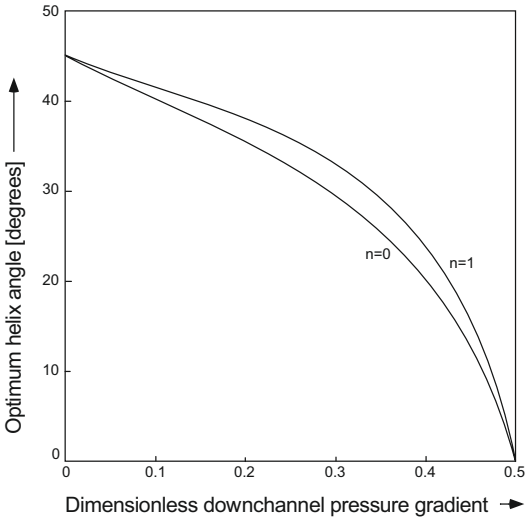


Figure 8.9
Optimum helix angle versus dimensionless down-channel pressure gradient

It can be seen that the two curves are relatively close; thus, the effect of the pseudoplastic behavior is not very pronounced.

It may be more interesting to optimize the channel depth and helix angle simultaneously. This can be done by inserting Eq. 8.31 into Eq. 8.33. After some calculations, the optimum helix angle can be determined to be:

$$\sin\varphi_r^* = \left(\frac{n}{2n+2}\right)^{1/2} + \hat{w}\left(\frac{n+2}{4n}\right) \tag{8.39}$$

where $\hat{w}$ is a reduced flight width:

$$\hat{w} = \frac{p\,w}{\pi\,D} \tag{8.39a}$$

where p is the number of flights, w the perpendicular flight width, and D the screw O.D.

The details of the derivation can be found in an article on screw design of two-stage extruder screws [2]. The optimum helix angle is only a function of the power law index and the reduced flight width. Figure 8.10 shows the optimum helix angle as a function of the power law index at various values of the reduced flight width.

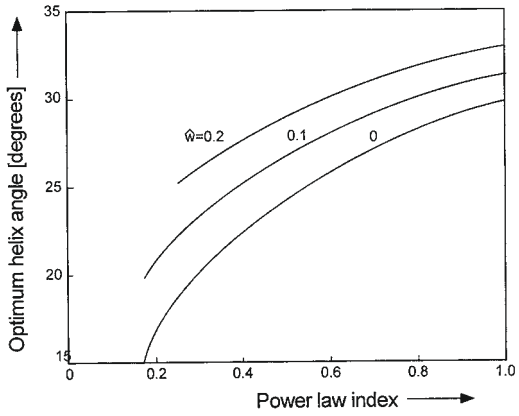


Figure 8.10
Optimum helix angle versus power law index in simultaneous optimization

The simplicity of Eq. 8.39 makes it a useful and convenient expression for optimizing the geometry of the melt conveying zone of an extruder. For polymer melts with a power law index in the range of 0.3 to 0.4 and typical values of the flight width, the optimum helix angle is about 22 to 24°.

The corresponding optimum channel depth can be found by inserting Eq. 8.39 into Eq. 8.31. The optimum channel depth resulting from simultaneous optimization is simply:

$$H_r^* = \left[\frac{6m\,v_b^n}{(n+2)g_a \tan\varphi_r^*}\right]^{\frac{1}{n+1}} \tag{8.40}$$

Unfortunately, the optimum channel depth is dependent on many more variables than the optimum helix angle. The latter depends only on the power law index and reduced flight width. In addition to these variables, the optimum channel depth also depends on the screw speed, screw diameter, consistency index, and pressure gradient. This means that it is not possible to design a universally optimum screw geometry. Thus, one has to determine the most likely operating parameters that the screw is likely to encounter and design for those parameters.

It should be noted that fundamentally it is not entirely correct to take an expression derived for a Newtonian fluid and insert a power law viscosity form into it. However, if this simplification is not made, the analysis becomes much more complex and analytical solutions much more difficult to obtain, if not impossible. Results of the analytical solutions have been compared to results of numerical computations for a two-dimensional flow of a power law fluid. In most cases, the results are within 10 to 20% [2]. It should be noted that the results are exact when the power law index is unity, i. e., for Newtonian fluids. However, if the optimum depth and helix angle for a pseudo-plastic fluid are calculated using expressions valid for Newtonian fluids only, very large errors can result, particularly when the power law index is about one-half or less. It is therefore very important to take the pseudo-plastic behavior into account, because the large majority of polymers are strongly non-Newtonian.

Instead of optimizing the screw geometry for output, it may be desirable to optimize for pressure-generating capability.

The optimum depth H_p^* and helix angle φ_p^* for pressure generation is found by setting:

$$\frac{\partial P}{\partial H} = \frac{\partial P}{\partial \varphi} = 0 \tag{8.41}$$

An expression for pressure P can be found by rewriting Eq. 8.29. The optimum channel depth is:

$$H_p^* = \frac{(n+2)}{(n+1)} \frac{2\dot{V}}{\pi^2 D^2 N \cos\varphi(\sin\varphi - \hat{w})} \tag{8.42}$$

The optimum helix angle has to be determined from:

$$\frac{\cos\varphi_p^*(2\sin\varphi_p^* - \hat{w})}{(\sin\varphi_p^* - \hat{w})^2} = \frac{\pi^2 D^2 N H}{2\dot{V}} \tag{8.43}$$

When the depth and helix angle are optimized simultaneously, Eq. 8.42 is inserted into Eq. 8.43. The resulting optimum helix angle for simultaneous optimization of the pressure-generating capacity is:

$$\sin\varphi_p^* = \left(\frac{n}{2n+2}\right)^{1/2} + \hat{w}\left(\frac{n+2}{4n}\right) \tag{8.44}$$

Comparing this result to the optimum helix angle for output φ_r^*, Eq. 8.39, it is clear that the two expressions are exactly the same, thus:

$$\varphi_p^* = \varphi_r^* = \varphi^* \tag{8.45}$$

The optimum channel depth for simultaneous optimization for pressure generation is found by inserting Eq. 8.39 into Eq. 8.37. The resulting expression can be shown to be identical to Eq. 8.35, thus:

$$H_p^* = H_r^* = H^* \tag{8.46}$$

Therefore, simultaneous optimization of depth and helix angle for output yields the same results as simultaneous optimization for pressure-generating capability.

It should be noted that the expressions for optimum channel depth are only valid when the pressure gradient is positive. When the pressure gradient is negative, the pressure flow will be in the forward direction and the output increases with channel depth without reaching a maximum value. In this situation, the depth of the metering section will be determined by the requirements for complete melting and good mixing.

The optimum channel depth and helix angle can also be determined from the melt conveying theory of power law fluids when the flow is considered to be one-dimensional; see also Section 7.4.2. By combining Eqs. 7.256 and 7.257, the output can be written as:

$$\dot{V} = \frac{W H v_{bz}}{s+2}\left(1-\lambda-\Gamma_R|\lambda|^{s+1}\right) \tag{8.47}$$

where:

$$\Gamma_R = \frac{(g_a \sin\varphi)^s H^{1+s}}{m^s v_b \cos\varphi} \tag{8.47a}$$

The optimum channel depth can again be determined by taking the partial derivative of output $\dot{V}$ and setting the result equal to zero. The resulting expression is:

$$1-\lambda-(s+2)\Gamma_R|\lambda|^{s+1} - H\frac{\partial\lambda}{\partial H}\left[1+\Gamma_R(s+1)|\lambda|^s\right] = 0 \tag{8.48}$$

For large positive pressure gradients, Eq. 7.252 should be used to evaluate the first derivative of λ with respect to channel depth H. This results in the following expression:

$$\frac{\partial\lambda}{\partial H} = \frac{(s+1)}{H\Gamma_R}\frac{1}{\left[\lambda^s+(1-\lambda)^s\right]} = \frac{1}{H}\frac{(1-\lambda)^{s+1}-\lambda^{s+1}}{\lambda^s+(1-\lambda)^s} \tag{8.49}$$

Inserting Eq. 8.49 into Eq. 8.48 yields an expression with only λ and s:

$$1-\lambda+\frac{(s+1)(s+2)|\lambda|^{s+1}}{\lambda^{s+1}-(1-\lambda)^{s+1}} + \frac{\lambda^{s+1}-(1-\lambda)^{s+1}-(s+1)^2|\lambda|^2}{\lambda^s+(1-\lambda)^s} \tag{8.49a}$$

A complete solution of Eq. 8.49(a) may be rather involved; however, it can be seen quite easily that $\lambda = 0$ is a solution of Eq. 8.49(a). Thus, the channel depth is optimized when $\lambda = 0$, i.e., when the velocity gradient becomes zero at the screw surface. The optimum helix angle is obtained by taking the first derivative of output $\dot{V}$ and setting the result equal to zero. This results in the following expression:

$$2\cos 2\varphi^*(1-\lambda-\Gamma_R|\lambda|^{s+1})+\sin 2\varphi^*\left[-\frac{\partial\lambda}{\partial\varphi}-\frac{\partial\Gamma_R}{\partial\varphi}|\lambda|^{s+1}-\Gamma_R(s+1)|\lambda|^s\frac{\partial\lambda}{\partial\varphi}\right]=0 \quad (8.49b)$$

For simultaneous optimization of channel depth and helix angle, $\lambda = 0$ and Eq. 8.49(b) becomes:

$$\frac{\partial\lambda}{\partial\varphi}=2\cot an 2\varphi^* \quad (8.49c)$$

When $\lambda = 0$, the first derivative of λ with respect to helix angle φ, determined from Eq. 7.252, becomes:

$$\frac{\partial\lambda}{\partial\varphi}=\frac{1}{(s+1)^2}\frac{\partial\Gamma_R}{\partial\varphi}=\frac{s+\tan^2\varphi}{(s+1)\tan\varphi} \quad (8.49d)$$

Inserting Eq. 8.49(d) into Eq. 8.49(c) yields the solution of the optimum helix angle:

$$\tan\varphi^*=\left(\frac{1}{s+2}\right)^{1/2}=\left(\frac{n}{1+2n}\right)^{1/2} \quad (8.49e)$$

To compare this result with the result from the modified Newtonian analysis, Eq. 8.44, the optimum helix angle can be written as:

$$\sin\varphi^*=\left(\frac{n}{1+3n}\right)^{1/2} \quad (8.50)$$

Equation 8.50 obviously is different from Eq. 8.44 when the flight width is neglected ($\hat{w} = 0$).

Figure 8.11 compares the results of simultaneous optimization from the modified Newtonian analysis and the one-dimensional power law analysis.

It is clear that the one-dimensional power law analysis yields higher values of the optimum helix angle than the modified Newtonian analysis, except when the power law index is unity.

Figure 8.12(a) compares the results of simultaneous optimization from the modified Newtonian analysis and the two-dimensional power law analysis, obtained by numerical computations [2].

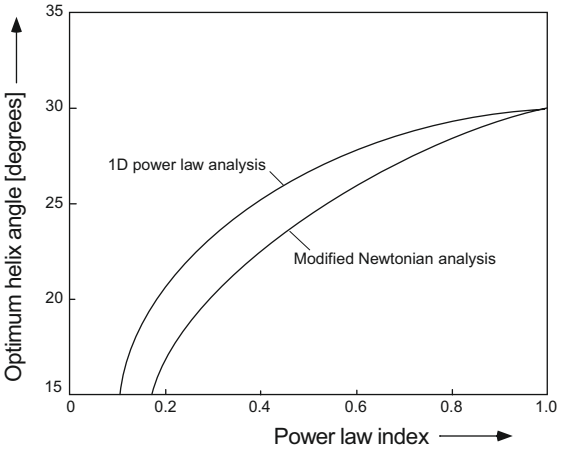


Figure 8.11
Optimum helix angle versus power law index, resulting from modified Newtonian analysis and one-dimensional power law analysis

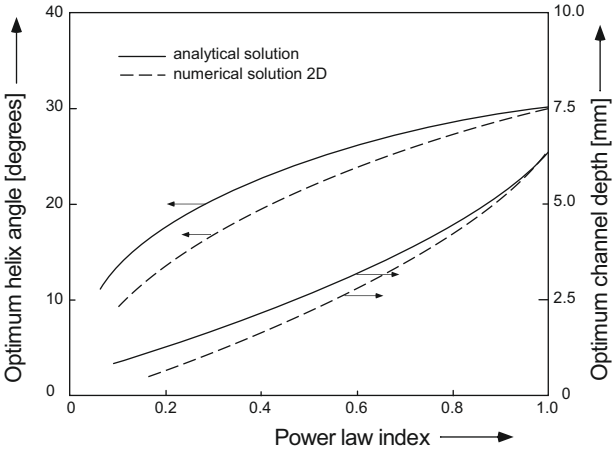


Figure 8.12(a)
Optimum helix angle versus power law index, resulting from modified Newtonian analysis and two-dimensional power law analysis

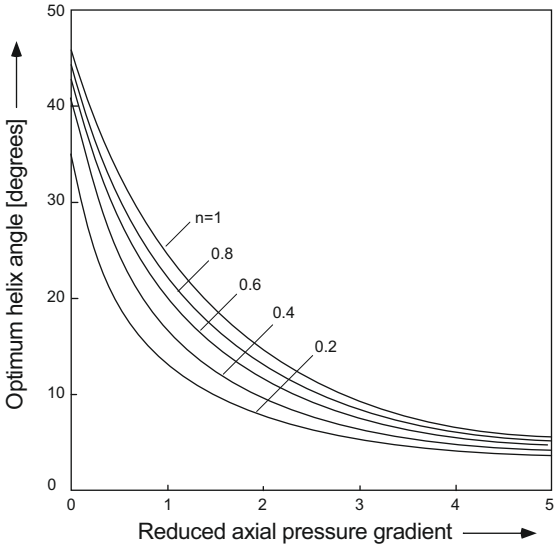


Figure 8.12(b)
Optimum helix angle versus reduced axial pressure gradient, resulting from two-dimensional power law analysis (numerical)

It can be seen that the values of the optimum helix angle from the modified Newtonian analysis are about 10 to 20% above those from the two-dimensional power law analysis. This indicates that the results from the modified Newtonian analysis, Eq. 8.44, may be more appropriate than the results from the one-dimensional power law analysis. The use of one-dimensional power law analysis leads to errors when the helix angle is substantially above zero, as discussed in Section 7.4.2. Therefore, one would like to use a two-dimensional power law analysis. However, there are no analytical solutions for this case. From numerical computations, it is possible to develop a plot of optimum helix angle as a function of a dimensionless axial pressure gradient g^0_a, where g^0_a is:

$$g^0_a = \frac{HP}{6mL}\left(\frac{H}{v_{bz}}\right)^n \tag{8.51}$$

The plot of the optimum helix angle versus dimensionless axial pressure gradient is shown in Fig. 8.12(b).

It should be noted that the optimum helix angle in Fig. 8.12(b) is not the result of simultaneous optimization of channel depth and helix angle, but optimization of the helix angle only. Figure 8.13 shows the optimum helix angle versus dimensionless down-channel pressure gradient as again determined from a two-dimensional analysis of a power law fluid.

Figure 8.13 can be compared directly to the results of the modified Newtonian analysis shown in Fig. 8.9. It is quite clear that the modified Newtonian analysis underestimates the effect of the non-Newtonian behavior.

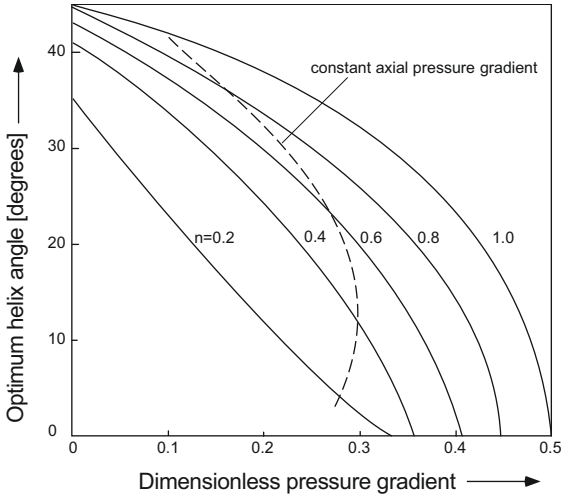


Figure 8.13
Optimum helix angle versus dimensionless down-channel pressure gradient, resulting from two-dimensional power law analysis (numerical)

Another approach to optimization of the screw geometry for melt conveying can be made by using the Newtonian flow rate equation with correction factors for pseudoplastic behavior; see Eq. 7.291. If the flight width is neglected this equation can be written as:

$$\dot{V} = \left(\frac{4+n}{10}\right)\pi^2 D^2 H\, N \sin\varphi\cos\varphi - \left(\frac{1}{1+2n}\right)\frac{\pi D\, H^3 g_a \sin^2\varphi}{4\mu} \tag{8.52}$$

The optimum helix angle can be determined by taking the first derivative of output $\dot{V}$ with respect to the helix angle and setting the result equal to zero. This results in the following expression for the optimum helix angle φ^*:

$$\frac{\cos^2\varphi^* - \sin^2\varphi^*}{\cos\varphi^*} = \frac{30}{(1+2n)(4+n)} g_z^0 \cos\varphi^* \tag{8.53}$$

The solution is:

$$\cos\varphi^* = \left[2 - \frac{30 g_z^0}{(1+2n)(4+n)}\right]^{-1/2} \tag{8.53a}$$

where the dimensionless down-channel pressure gradient is given by:

$$g_z^0 = \frac{g_z H^2}{6\mu v_{bz}} \tag{8.53b}$$

Figure 8.14(a) shows the optimum helix angle as determined from Eq. 8.53(a) as a function of the dimensionless pressure gradient at various values of the power law index.

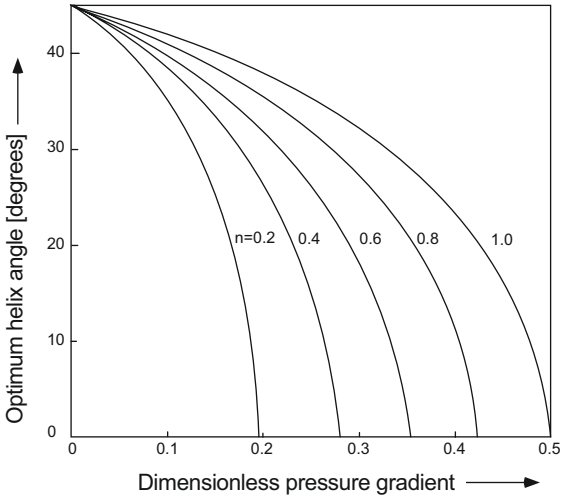


Figure 8.14(a)
Optimum helix angle versus dimensionless down-channel pressure gradient, derived from output of Eq. 8.52 (analytical results)

It can be seen that the optimum helix angle is strongly dependent on the power law index. Comparison with results from the two-dimensional power law analysis, shown in Fig. 8.13, indicates a reasonable agreement when the power law index is larger than one-half (n > 0.5), but relatively large differences when the power law index is smaller than one-half (n < 0.5).

If the optimum helix angle is expressed as a function of the axial pressure gradient, the optimum helix angle becomes:

$$\tan 2\varphi^* = \frac{2(1+2n)(4+n)\mu v_b}{5 g_a H^2} \tag{8.54}$$

If the reduced axial pressure gradient g_a^0 is defined as:

$$g_a^0 = \frac{H^2 g_a}{6\mu v_{b2}} \tag{8.54a}$$

then the optimum helix angle can be expressed as:

$$\varphi^* = 0.5 \arctan\left[\frac{(1+2n)(4+n)}{15 g_a^0}\right] \tag{8.54b}$$

Similarly, the optimum channel depth can be determined to be:

$$H^* = \left[\frac{(4+n)(1+2n)2m(v_b \cos\varphi)^n}{15 g_a \sin\varphi}\right]^{\frac{1}{1+n}} \tag{8.54c}$$

A very simple expression for the optimum helix angle was obtained by Rauwendaal [82]. The optimum helix angle in degrees can be expressed as:

$$\varphi^* = 13.5 + 16.5n \tag{8.54d}$$

The optimum helix angle as a function of reduced axial pressure gradient according to Eq. 8.54(b) is shown in Fig. 8.14(b).

Figure 8.14(b) can be compared directly to Fig. 8.12(b) showing results from a two-dimensional power law analysis. The agreement between the two sets of results is quite reasonable.

Summarizing, it can be concluded that for simultaneous optimization of the channel depth and helix angle, the modified Newtonian analysis yields reasonably accurate results when compared to the two-dimensional power law analysis. The important equations are Eq. 8.39 for the optimum helix angle and Eq. 8.40 for the optimum channel depth. The results of simultaneous optimization from a one-dimensional power law analysis are less accurate than the modified Newtonian analysis.

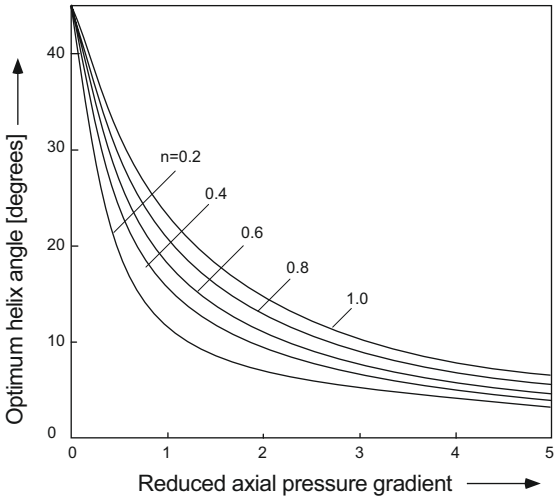


Figure 8.14(b)
Optimum helix angle versus reduced axial pressure gradient

For optimization of just the helix angle or the channel depth, the results from the Newtonian flow rate equation with correction factors for pseudo-plastic behavior, Eq. 8.54, are more accurate than the results from the modified Newtonian analysis, Eq. 8.36. It should again be noted that simultaneous optimization only makes sense for relatively large positive pressure gradients. When the pressure gradient is negative, the output increases monotonically with channel depth. In this case, there is no optimum channel depth.

8.2.2 Optimizing for Plasticating

The geometry for optimum melting performance can be determined from the equations developed in Section 7.3. A convenient relationship to use is the total axial melting length. It is convenient because the effect of varying the helix angle can be evaluated directly, whereas the total down-channel melting length has to be converted to axial melting length for a one-to-one comparison. The total axial melting length can be determined from Eq. 7.116:

$$L_T = \frac{H_f v_{sz} \rho_s \sqrt{W_1} \sin\varphi}{\Omega_1} \left(2 - \frac{A_1 v_{sz} \rho_s \sqrt{W_1} \sin\varphi}{\Omega_1} \right) \tag{8.55}$$

The initial solid bed width W_1 is:

$$W_1 = \frac{\pi D \sin\varphi}{P} - w \tag{8.56}$$

The solid bed velocity can be expressed as:

$$v_{sz} = \frac{\dot{M}}{\rho_s H_f (\pi D \sin\varphi - pw)} \tag{8.57}$$

The term Ω_1 is given by Eq. 7.109(d); it can be written as:

$$\Omega_1 = \left[\frac{[2k_m \Delta T_b + \mu(v_b^2 + v_{sz}^2 - 2v_b v_{sz}\cos\varphi)]\rho_m v_b \sin\varphi}{2\Delta H} \right]^{1/2} \tag{8.58}$$

The term A_1 in Eq. 8.55 is the compression in axial direction. A_1 is related to the compression in down-channel direction A_z by:

$$A_z = A_1 \sin\varphi \tag{8.59}$$

With these equations, the effect of various geometrical variables can be determined. Figure 8.15 shows the total axial melting length as a function of the helix angle at various values of the flight width.

The results shown in Fig. 8.15 are predictions for a 50-mm extruder running at a screw speed of 100 rpm with an output of 100 kg/hr.; the barrel temperature is set 50°C above the melting point of the polymer. The channel depth in the feed section is 5 mm, the axial compression A_1 = 0.008, and the number of flights p = 1. The following polymer properties were used:

Melt density	ρ	= 7800 kg/m^3
Thermal conductivity	k_m	= 0.25 J/ms °K
Melt viscosity	μ	= 1500 Ns/m^2
Enthalpy change	ΔH	= 4.5E5 J/kg

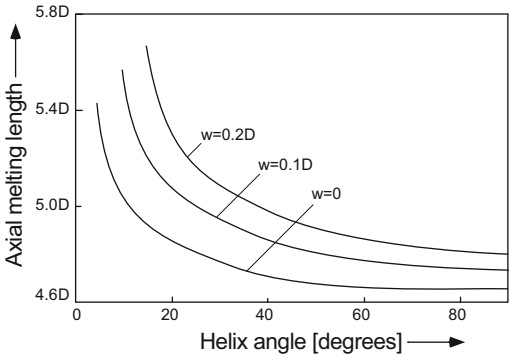


Figure 8.15
Axial melting length versus helix angle

These properties are typical of polyethylene; see Table 6.1.

8.2.2.1 Effect of Helix Angle

From Fig. 8.15, it can be seen that the melting length reduces strongly with helix angle at relatively small angles. At larger helix angles, the melting length reduces weakly with helix angle. Very little improvement is obtained by increasing the helix angle beyond 30°. The melting length increases as the flight width increases, particularly at small helix angles. It is clear from Fig. 8.15 that there is no optimum helix angle for which the axial melting length reaches a minimum. The shortest melting length is obtained at a helix angle of 90°; however, the melting length at 90° is only about 3% less than the melting length at 30° and about 8% less than the melting length at 17.66° (square pitch). Considering that a helix angle of 90° does not produce any forward drag transport, it makes little sense to apply such an extreme helix angle for the sake of melting.

8.2.2.2 Effect of Multiple Flights

From Eqs. 8.55 through 8.58, the effect of the number of parallel flights can be evaluated directly. Figure 8.16 shows the axial melting length versus helix angle for a single-flighted, double-flighted, and triple-flighted screw design.

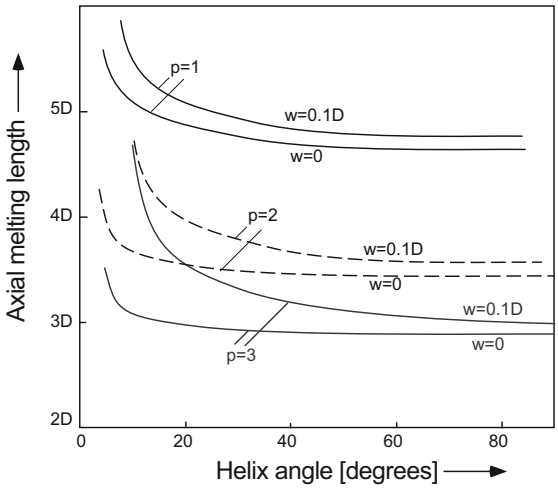


Figure 8.16
Axial melting length versus helix angle for 1, 2, and 3 parallel flights

The predictions are for the same example used earlier in this section. It is clear from Fig. 8.16 that the melting length can be reduced substantially when the number of flights is increased, provided the helix angle is sufficiently large. It can be easily shown that the melting length with p parallel flights L(p) is related to the melting length with one flight L(1) by:

$$L(p) = \frac{L(1)}{\sqrt{p}} \tag{8.60}$$

Eq. 8.60 is valid for zero compression screws ($A_1 = 0$) when the flight width w is negligible; however, it is reasonably accurate even if $A_1 \neq 0$. Figure 8.16 shows curves with flight width w = 0 and w = 0.1 D for each number of flights. This is shown to demonstrate that the effect of flight width becomes more pronounced as the number of flights is increased. Substantial errors can be made if the flight width is neglected in a multi-flighted screw geometry. Figure 8.16 also shows that the effect of the helix angle on melting length becomes stronger when the number of flights is increased. With three parallel flights, the melting length at 90° is about 20% less than at 17.66° (square pitch), while in the single-flighted design the difference is only about 8%.

The beneficial effect of multiple flights can be explained by the reduced average melt film; see Fig. 8.17.

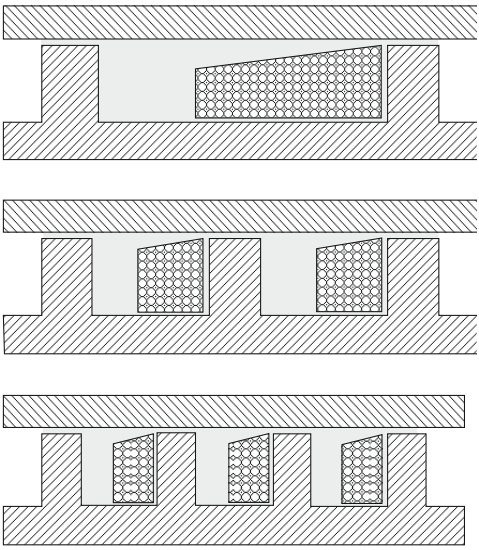


Figure 8.17
Melting in multi-flighted screw geometry

As the number of flights is increased, the width of the individual solid beds becomes smaller. As a result, the average melt film thickness reduces, because the melt film thickness increases with the solid bed width. The thinner melt film will improve heat conduction through the melt film and increase the viscous heat generation in the melt film, causing improved melting performance.

For optimum melting performance, the most favorable geometry is a multi-flighted design with relatively narrow flights and relatively large helix angle, around 25 to 30°. This combination of screw geometry variables is important because a multi-flighted geometry with a small helix angle may actually reduce the melting performance.

The effect of the helix angle, flight width, and number of flights can also be analyzed in terms of the volumetric efficiency of the extruder screw. This is defined simply as

the channel volume divided by the total volume of channel and flight. The volumetric efficiency ε_v can be expressed as:

$$\varepsilon_v = 1 - \frac{p\,w}{\pi\,D\sin\varphi} \tag{8.61}$$

Figure 8.18 shows the volumetric efficiency as a function of the helix angle at various numbers of flights.

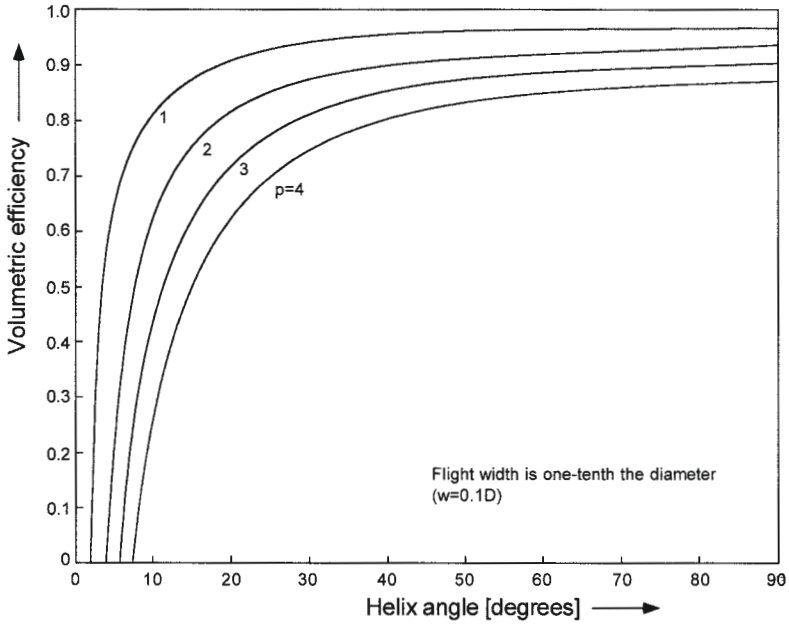


Figure 8.18 Volumetric efficiency versus helix angle for various numbers of flights

The volumetric efficiency rises sharply at small helix angles and more slowly at large helix angles. The highest ε_v is obtained when the helix angle is 90°. When the number of parallel flights is increased at a small helix angle, the volumetric efficiency drops considerably. When φ = 17.66° (square pitch), the volumetric efficiency is about 85% at p = 1, but it drops to about 50% at p = 4. When φ = 30°, the volumetric efficiency is about 95% at p = 1 and drops to about 75% at p = 4. Thus, the adverse effect of multiple flights on volumetric efficiency is much less severe at large helix angles than it is at small helix angles.

8.2.2.3 Effect of Flight Clearance

The melting rate for a non-zero clearance can be determined from Eq. 7.107; it can be written as:

$$\frac{d\dot{M}p}{dz'} = \frac{1}{2}\rho_m \Delta v\, H_m (W_s') - \frac{1}{2}\rho_m \Delta v\, \delta \tag{8.62}$$

Equation 8.62 expresses the melting rate per unit length z′, where z′ is the direction of the relative velocity between the solid bed and barrel. The melting rate per unit down-channel distance z can be written as:

$$\frac{d\dot{M}p}{dz} = \left[\Omega_1^2\, W_s + \left(\frac{1}{2}\rho_m \delta\, v_b \sin\varphi\right)^2\right]^{1/2} - \frac{1}{2}\rho_m \delta\, v_b\, \sin\varphi \tag{8.63}$$

From Eq. 8.63, it is clear that the melting rate reduces with increasing clearance. Figure 8.19(a) shows the melting rate as a function of radial clearance for the example used earlier, when $\varphi = 17.66°$ and $W_s = ½\ D$.

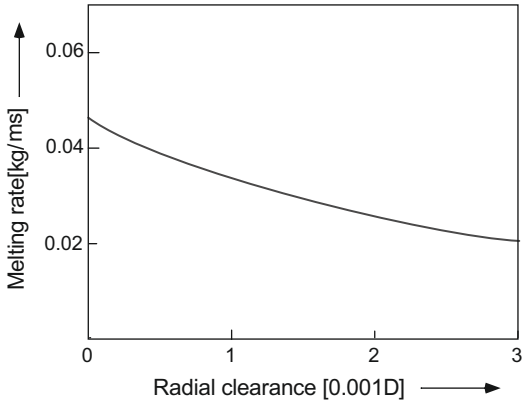


Figure 8.19(a)
Melting rate versus radial clearance

The melting rate drops monotonically with increasing radial clearance. Considering that the standard clearance is 0.001 D; a doubling of the standard clearance causes a reduction in melting rate of about 25%. A tripling of the standard clearance causes a reduction in melting rate of about 35%. It is clear that wear in the plasticating zone of the extruder has a detrimental effect on the melting performance. It is important, therefore, to make sure that the radial clearance in this region is within reasonable limits. Unfortunately, screw and barrel wear often occur in the plasticating zone of the extruder, as discussed in Section 8.1.3. This type of wear will adversely affect the melting performance and thus reduce overall extruder performance. Symptoms of this can be temperature non-uniformities and throughput and pressure fluctuations. If these problems occur, it is good practice to check for screw and barrel wear. If the clearance is more than two or three times the standard clearance, the screw and/or barrel should be replaced.

Wear in the compression section of the screw is often caused by large compression ratios. This will be discussed next.

8.2.2.4 Effect of Compression Ratio

The compression of the channel depth tends to widen the solid bed, as discussed in Section 7.3. Melting tends to reduce the width of the solid bed. If compression is too rapid, the melting may be insufficient and the solid bed can grow in width. This will generally cause plugging of the channel by the solid bed and should be avoided if at all possible. Plugging will cause output fluctuations, but it may also cause wear in the compression section of the screw, as discussed in Section 8.1.3. It was discussed in Section 7.3 that plugging can be avoided if:

$$\frac{\Omega_1}{A_z v_{sz} \rho_s \sqrt{W_1}} > 1 \tag{8.64}$$

The compression ratio X_c is the channel depth in the feed section divided by the channel depth in the metering section. The axial length of the compression section is L_c. Thus, in order to avoid plugging, the length of the compression section should obey the following inequality:

$$L_c > \frac{v_{sz} \rho_s \sqrt{W_1} H_f (X_c - 1) \sin\varphi}{\Omega_1 X_c} \tag{8.65}$$

From Eq. 8.65, the minimum allowable length of the compression section can be determined if the compression ratio is known. Figure 8.19(b) shows the minimum L_c versus the compression ratio for the example used earlier.

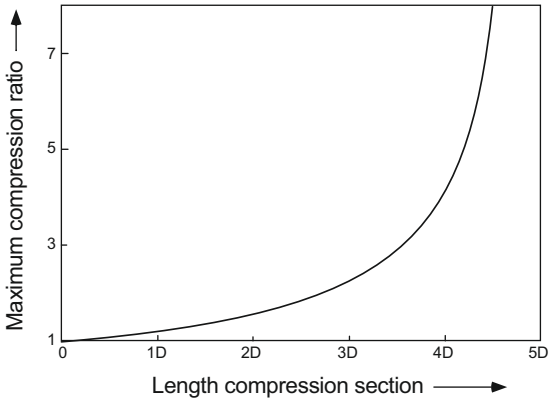


Figure 8.19(b)
Minimum length of compression section versus compression ratio

If a large compression ratio is used, the length of the compression section must be quite long to avoid plugging.

The most dangerous combination in design of the compression section is a large compression ratio and a short compression section length. This will lead very easily to plugging. Rapid compression screws should be avoided for this very reason. One of the myths in screw design is that certain polymers, e.g., nylon, require a very

rapid compression screw in order to extrude properly. Many screws have been designed with a compression length of less than one diameter. Such a screw can only work if the majority of the melting occurs before the compression section. However, this defeats the purpose of having a compression section in the first place. Rapid compression screws do not make much sense from a functional point of view because they are susceptible to surging and wear. It is important to realize that in general polymers do not require a very rapid compression screw in order to extrude properly. The benefits of very rapid compression screws are imaginary and based on a serious misconception. Obviously, a very rapid compression is quite possible in the second stage of a two-stage extruder screw, because essentially all the melting should take place in the first stage; see Section 8.5.2.

8.2.3 Optimizing for Solids Conveying

Optimization of the solids conveying process is very important because solids conveying is the basis of the entire plasticating extrusion process. If instabilities occur in the solids conveying zone, these instabilities will transmit to the downstream zones and cause fluctuations in output and pressure. It was already discussed in Section 7.2.2.2 that grooved barrel sections provide a powerful tool to improve solids conveying rate and stability. There are, however, some important considerations with respect to screw design to optimize the solids conveying process.

8.2.3.1 Effect of Channel Depth

It was discussed in Section 7.2.2 that there appears to be an optimum channel depth for which the solids conveying rate reaches a maximum. At low values of the pressure increase over the solids conveying section, this optimum channel depth is indeed apparent because this optimum channel depth does not occur when the channel curvature is taken into account. At higher values of the pressure increase, however, there is an actual optimum channel depth even when the channel curvature is taken into account. This is shown in Fig. 8.20 for a 114-mm (4.5-in) extruder running at 60 rpm; the coefficient of friction is 0.5 on the barrel and 0.3 on the screw. When the pressure gradient increases, the optimum channel depth decreases.

The optimum channel depth can be obtained by taking the first derivative of the solids conveying rate $\dot{M}_s$ with respect to the channel depth H and setting the result equal to zero:

$$\frac{\partial \dot{M}_s}{\partial H} = 0 \tag{8.66}$$

Equation 8.66 does not have a simple closed form solution. The optimum channel depth can be evaluated by using a numerical or graphical method. The optimum

channel depth will increase with the coefficient of friction on the barrel. It will decrease with the coefficient of friction on the screw, the number of flights, and the pressure gradient. Unfortunately, the actual coefficients of friction are generally not known with a great degree of precision; thus, accurate prediction of the optimum channel depth is usually not possible. The channel depth in the feed section of screws used in smooth bore extruders is often about 0.15 to 0.20D. In grooved feed extruders the feed section depth is often about 0.1D.

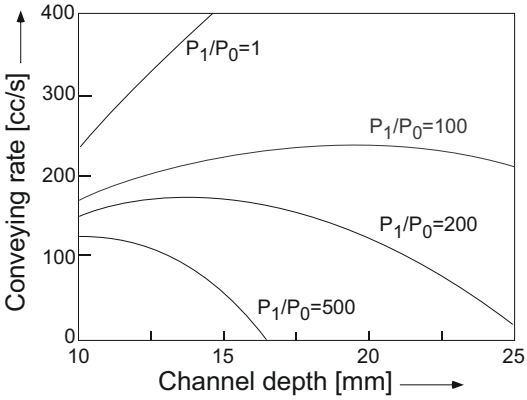


Figure 8.20
Solids conveying rate versus channel depth

8.2.3.2 Effect of Helix Angle

The helix angle in the feed section will also have an optimum value for which the solids conveying rate reaches a maximum. This is obvious if one realizes that a zero-degree helix angle results in zero rate and a 90° helix angle also results in zero rate. Thus, somewhere between zero and 90°, the solids conveying rate will reach a maximum. The optimum helix angle can be determined from:

$$\frac{\partial\theta}{\partial\varphi}+\frac{\tan\theta}{\tan\varphi}=\frac{\tan\theta}{\tan(\theta+\varphi)}\left(1+\frac{\partial\theta}{\partial\varphi}\right) \tag{8.67}$$

where:

$$\frac{\partial\theta}{\partial\varphi}=\frac{1}{\cos(\theta+\varphi)}\frac{\partial}{\partial\varphi}\left[\frac{(1+f_s^2-k^2)^{1/2}-f_s k}{1+f_s^2}\right]-1 \tag{8.68}$$

Equation 8.68 does not have a convenient analytical solution. Thus, the optimum helix angle can be determined by using a numerical or graphical method. Again, the coefficients of friction need to be known to determine the optimum helix angle. Therefore, accurate prediction of the optimum helix angle is usually not possible. In most extruder screws, the helix angle in the feed section ranges from 15 to 25°, with the most common angle being 17.66°.

8.2.3.3 Effect of Number of Flights

The effect of the number of parallel flights in the feed section has already been discussed in Section 7.2.2. Increasing the number of parallel flights reduces the open cross-sectional area of the channel (see Fig. 8.18) and increases the area of contact between the solid bed and screw. Both of these factors have a negative impact on the solids conveying performance, particularly when the helix angle is relatively small. The volumetric efficiency shown in Fig. 8.18 is the open cross-sectional area relative to the total area between the root of the screw and the barrel.

8.2.3.4 Effect of Flight Clearance

If the solid polymeric particles are compacted into a solid bed, there will be practically no leak flow through the flight clearance. In many cases, the flight clearance is smaller than the particle size of the polymer. Thus, even if the polymer particles are not fully compacted, the actual radial clearance will generally not be too critical for solids conveying performance.

8.2.3.5 Effect of Flight Geometry

Dekker [3] studied the effect of various flight geometries on solids conveying performance. He proposed that many extrusion instabilities might be due to internal deformation of the solid bed. Internal deformation is more likely to occur when the internal coefficient of friction of the polymer particles is low. Spherical particles tend to have a lower internal coefficient of friction than non-spherical (e.g. cylindrical) particles and are, therefore, more susceptible to internal solid bed deformation. This may explain the often observed difference in extrusion behavior between strand pelletized and die-face pelletized material.

Dekker [3] compared a trapezoidal flight geometry to a standard rectangular flight geometry. He found that the trapezoidal geometry resulted in higher throughput and more stable extrusion performance, particularly at a high screw speed. The trapezoidal flight geometry is also better from a stress distribution point of view as discussed in Section 8.1.2; see Fig. 8.4(a). It can be expected that the curved flight geometry shown in Fig. 8.4(b) results in similar benefits in terms of solids conveying as the trapezoidal flight geometry shown in Fig. 8.4(a); see also Section 7.2.2. Another important benefit of these flight geometries is that the contact area between the solid bed and the screw is reduced. This should have an additional positive effect on solids conveying performance.

Spalding et al. [64] studied the effect on the flight flank radius on solids conveying performance. They found that a larger flight flank radius could improve solids conveying when the level of pressure development in the solids conveying zone is high. Spalding et al. recommend using a flight flank radius of about 1/4 the channel depth of the feed section. However, the basis of this recommendation is not clear from the

data presented in the paper. A flight flank radius of 0.25H is quite small relative to the depth of the channel. A flight flank radius of 0.5 to 1.0H will generally result in better performance than a radius of 0.25H because it provides a gentler transition from the root of the screw to the flight flank. Also, it will create a greater extra normal force at the barrel surface, thus increasing the driving force acting on the solid bed.

8.3 Optimizing for Power Consumption

In some cases, optimizing for power consumption may be more important than optimizing the output. This is the case if the power consumption is excessive, causing high stock temperatures and increasing the chance of degradation. Some polymers have inherent properties that result in high power consumption. A typical example is linear low density polyethylene, LLDPE, and the newer metallocene polyethylenes. The cause of high power consumption is generally high polymer melt viscosity. The problem can be particularly severe if the viscosity remains high at high shear rates, i.e., if the polymer is not very shear thinning (large power law index). The most difficult polymers with respect to power consumption are low melt index polymers (fractional M.I.) with relatively large power law indici. Such polymers require special attention to the screw design in order to minimize the power consumption.

The screw geometry that will result in the least amount of power consumption can be determined from the expressions of power consumption developed in Chapter 7. In this section, attention will be focused on the melt-conveying zone. However, other functional zones can be analyzed by the same procedure. Equations for power consumption in melt conveying are given in Section 7.4.1.3. When optimizing for power consumption, one should be concerned about the power consumption at a certain level of throughput. Minimizing power consumption without considering the throughput does not make much sense. The power consumption is optimum when the ratio of power consumption to throughput reaches a minimum. This ratio is the specific energy consumption, SEC. It is the mechanical energy expended per mass of material and is usually expressed in kWhr/kg or hphr/lb. A high level of SEC translates into a large amount of energy expended per mass of polymer; this will result in large temperature increases in the polymer and possibly degradation. Thus, the optimum screw geometry for power consumption is that geometry for which the ratio of power consumption to output reaches a minimum.

8.3.1 Optimum Helix Angle

The optimum helix angle φ* for power consumption can be determined by setting:

$$\frac{\partial Z}{\partial \varphi}\dot{V} = \frac{\partial \dot{V}}{\partial \varphi}Z \tag{8.69}$$

To evaluate the first derivative of power consumption Z with respect to helix angle φ, the power consumption has to be written as an explicit function of the helix angle. Using the equation in Section 7.4.1.3 the following expressions can be derived:

$$Z = a_1 + a_2\sin^2\varphi + a_3\sin\varphi\cos\varphi + \frac{a_4}{\sin\varphi} \tag{8.70}$$

where:

$$a_1 = \frac{p\mu\pi D v_b^2 dl}{H} \tag{8.71a}$$

$$a_2 = \frac{3p\mu\pi D v_b^2 dl}{H} \tag{8.71b}$$

$$a_3 = \frac{p\pi D v_b H g_a dl}{2} \tag{8.71c}$$

$$a_4 = \frac{p\mu_{cl} w v_b^2 dl}{8} \tag{8.71d}$$

To evaluate the first derivative of output $\dot{V}$ with respect to the helix angle φ, the output has to be written as an explicit function of the helix angle. The output can be written as:

$$\dot{V} = b_1\sin\varphi\cos\varphi + b_2\sin^2\varphi \tag{8.72}$$

where:

$$b_1 = \frac{1}{2}\,p\pi D v_b (H-\delta) - \frac{(\pi D)^2 + (p\,b)^2}{12\,\mu_{cl} b\,p} g_a\,\delta^3 \tag{8.73a}$$

$$b_2 = -\frac{p\pi D H^3 g_a}{12\,\mu} - \frac{\pi^2 D^2 \delta^3\,\mu\,v_b}{2\,H^2\,\mu_{cl}\,b} \tag{8.73b}$$

The optimum helix angle now has to be found from the following equation:

$$\left(a_2\sin 2\varphi + a_3\cos 2\varphi - a_4\frac{\cos\varphi}{\sin^2\varphi}\right)\left(\frac{1}{2}b_1\sin 2\varphi + b_2\sin^2\varphi\right) = \left(b_1\cos 2\varphi + b_2\sin 2\varphi\right)\left(a_1 + a_2\sin^2\varphi + a_3\sin\varphi\cos\varphi + \frac{a_4}{\sin\varphi}\right) \tag{8.74}$$

This equation does not have an obvious simple, analytical solution. One can find the solution either graphically or by using a numerical technique, such as the Newton-Raphson method. Figure 8.21 shows the optimum helix angle as a function of channel depth for a 50-mm extruder, running at 100 rpm.

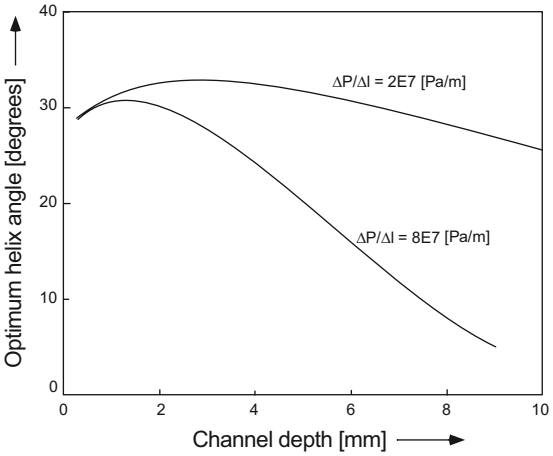


Figure 8.21
Optimum helix angle versus channel depth

The flight width is 0.1 D, the radial clearance 0.001 D, and the number of flights is one. The power law index of the polymer melt is 0.5, the consistency index m = 1E4 Pa·s^n, and the melt density 0.8 g/cm^3. It can be seen from Fig. 8.21 that the optimum is relatively insensitive to the changes in the channel depth when the pressure gradient is moderate. However, at relatively high pressure gradients, the optimum helix angle depends strongly on the channel depth; at large channel depth values, the optimum helix angle becomes quite small.

Figure 8.22 shows the actual specific energy consumption, SEC, at the optimum helix angle as a function of channel depth.

The SEC at a small channel depth is quite high, but reduces with increasing channel depth. When the pressure gradient is high, the SEC reaches a minimum and starts to increase when the channel depth is further increased. Figure 8.22 thus illustrates a graphical method to determine the optimum channel depth for power consumption when both the channel depth and the helix angle are optimized simultaneously. It can further be seen in Fig. 8.22 that the higher pressure gradient causes a substantially higher specific energy consumption. In the normal channel depth range, H = 0.01 D–0.05 D, so the difference in SEC is about 50%. This will improve the mixing efficiency of the metering section, but it will also cause more viscous heat generation in the melt and may overheat the polymer.

The optimum channel depth H* can be calculated from:

$$\frac{\partial Z}{\partial H}\dot{V} = \frac{\partial \dot{V}}{\partial H} Z \tag{8.75}$$

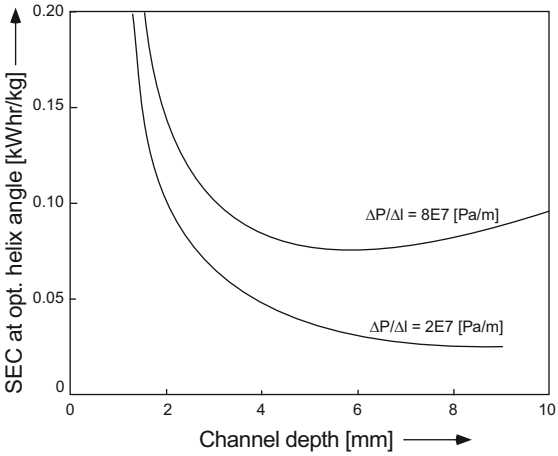


Figure 8.22
SEC at optimum helix angle versus channel depth

This results in another lengthy expression similar to Eq. 8.74. This expression is difficult to solve analytically and is generally solved numerically or graphically, as shown in Fig. 8.22.

8.3.2 Effect of Flight Clearance

The effect of the radial clearance on the optimum helix angle is shown in Fig. 8.23 for two values of the pressure gradient.

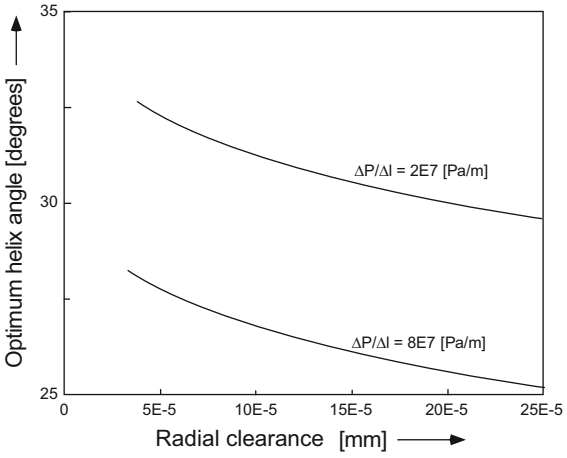


Figure 8.23
Optimum helix angle versus radial clearance

It can be seen that the radial clearance has relatively little effect on the optimum helix angle. The corresponding SEC as a function of clearance is shown in Fig. 8.24.

It can be seen that there is an optimum value of the clearance δ^* for which the SEC reaches a minimum value. For the large pressure gradient, the optimum clearance $\delta^* \cong$ 20E-5 m and for the small pressure gradient, $\delta^* >$ 30E-5 m. Thus, the standard

radial clearance is not necessarily the best clearance in the metering section of the extruder. However, as discussed in Section 8.2.2, the radial clearance in the plasticating zone should be as small as possible to enhance the melting capacity. This indicates that a varying clearance along the length of the extruder may not be a bad idea. This can be achieved by varying the barrel inside diameter and/or the screw outside diameter. Unfortunately, wear usually occurs right at a location where it should not happen: in the compression section. If wear would occur in the metering section, it could actually have a beneficial effect.

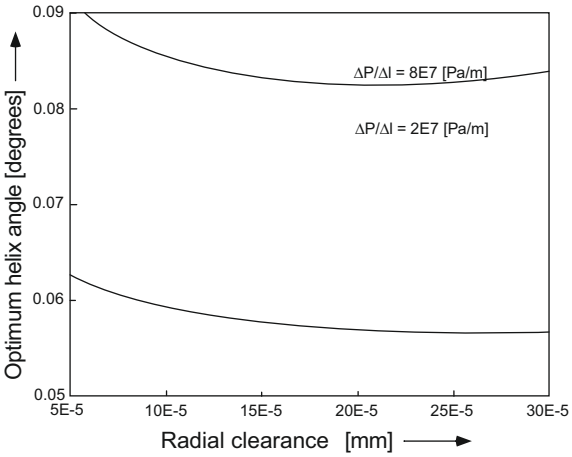


Figure 8.24
SEC at optimum helix angle versus radial clearance

The optimum radial clearance can be determined from:

$$\frac{\partial Z}{\partial \delta}\dot{V} = \frac{\partial \dot{V}}{\partial \delta}Z \tag{8.76}$$

Again, the resulting equation cannot be easily solved analytically. Thus, the optimum clearance can be found by solving Eq. 8.76 numerically or graphically.

8.3.3 Effect of Flight Width

If the various contributions to power consumption are carefully examined, it can be seen that a substantial portion is consumed in the clearance between the flight tip and the barrel; see, for instance, Eq. 8.71(d). The power consumption in the clearance is inversely proportional to the radial clearance and directly proportional to the total flight width pw. However, the viscosity in the clearance will generally be lower than the viscosity in the channel since the polymer melt is pseudo-plastic. Figure 8.25 shows how the ratio of power consumption in the clearance Z_{cl} to the total power consumption Z_t depends on the ratio of flight width w to channel width plus flight width W + w for a polymer with a power law index n = 0.5.

Figure 8.25 shows that the relative contribution of the power consumption in the clearance increases strongly when the flight width increases. A typical ratio of w/(W + w) is about 0.1; in the example shown in Fig. 8.25 this corresponds to a power consumption in the clearance of about 40% of the total power consumption! The power consumed in the clearance does not serve any useful purpose. It does not aid in transporting the polymer forward, but causes a viscous heating of the polymer. Therefore, one would like to make the flight width as narrow as possible to reduce the power consumption in the clearance. The power consumption in the clearance will be more pronounced when the material is more Newtonian in flow behavior, i.e., less shear-thinning. This is shown in Fig. 8.26, where Z_{cl}/Z_t is plotted against the power law index of the polymer melt. The viscosity in the clearance is determined from:

$$\mu_{cl} = m\left(\frac{v_b}{\delta}\right)^{n-1} \tag{8.77}$$

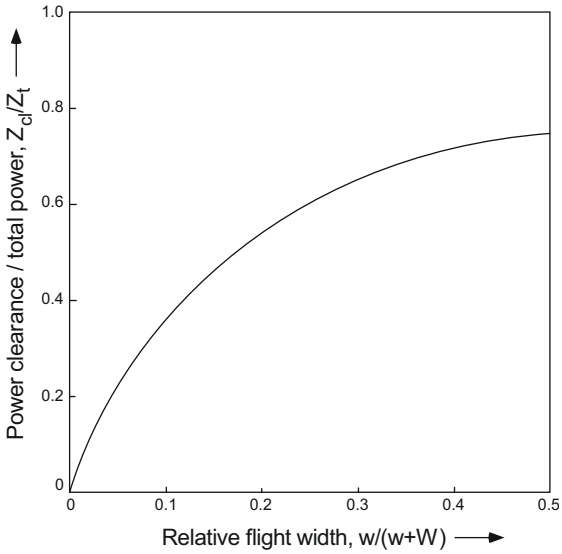


Figure 8.25
Z_{cl}/Z_{total} versus w/(W+w)

The viscosity in the channel is determined from:

$$\mu = m\left(\frac{v_b}{H}\right)^{n-1} \tag{8.78}$$

The results shown in Figs. 8.25 and 8.26 are for a standard radial clearance of 0.001 D.

The contribution of the power consumption in the clearance rises dramatically when the power law index increases. When the fluid is Newtonian, around 80% of the total power is consumed in the clearance! Thus, problems with excessive power consump-

tion are more likely to occur when the material of a certain melt index is less shear thinning. This is the main reason behind the extrusion problems encountered with materials such as linear low-density polyethylene, LLDPE [4, 5], and metallocenes.

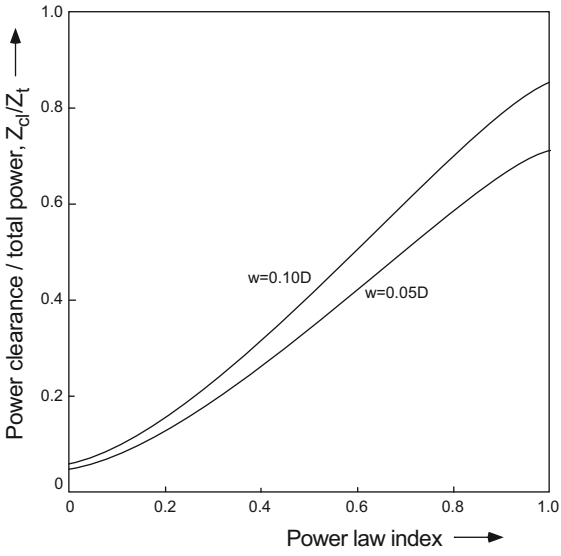


Figure 8.26
Z_{cl}/Z_{total} versus the power law index

The most logical way to reduce power consumption in the metering section is to reduce the ratio w/(W + w). This can be achieved in two ways. One is to increase the channel width W by increasing the helix angle, as discussed in Section 8.3.1. The other approach is to reduce the flight width itself. The combination of increasing the helix angle and decreasing the flight width is obviously most effective. This allows a reduction of the w/(W + w) ratio from a typical value of 0.1 down to around 0.03. The minimum flight width is not determined by functional considerations but by mechanical considerations. Functionally, one would like the flight width to be almost infinitely thin. However, there must obviously be sufficient mechanical strength in the flight to withstand the forces acting on it. These mechanical considerations are discussed in detail in Section 8.1.2. The flight width in the metering section w_m can be considerably narrower than the flight width in the feed section w_f because the flight height or channel depth is much smaller in the metering section. In order to keep the mechanical stresses in the flight approximately the same, the following rule can be used to determine the flight width in the metering section.

$$w_m = w_f \left(\frac{H_m}{H_f} \right)^{1/2} \tag{8.79}$$

Considering that the flight width in the feed section is generally about 0.1 D, Eq. 8.79 can be written as:

$$w_m = \frac{w_f}{\sqrt{X_c}} = \frac{D}{10\sqrt{X_c}} \tag{8.80}$$

where X_c is the channel depth ratio H_f/H_m.

Based on these considerations, a new screw design was recently developed to reduce power consumption in materials like LLDPE; the screw is often referred to as the LL-screw [4, 5].

Figure 8.27 shows a standard screw geometry and the LL-screw geometry. Both screws have a 38 mm (1.5 in) diameter and a 24 L/D ratio.

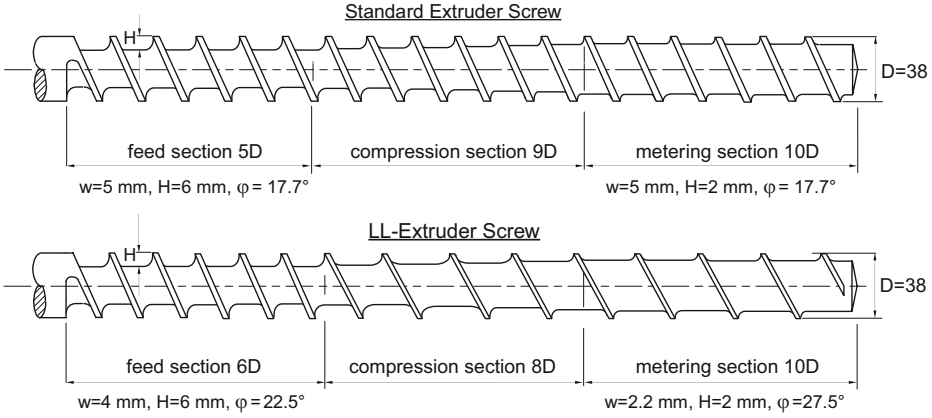


Figure 8.27 The LL-extruder screw versus a standard extruder screw

Essentially, the two screws differ in the helix angle and the flight width. Thus, the differences in performance between the two screws can be attributed solely to these two geometrical factors. Figure 8.28 shows the predicted output versus hp curves for the two screws shown in Fig. 8.27.

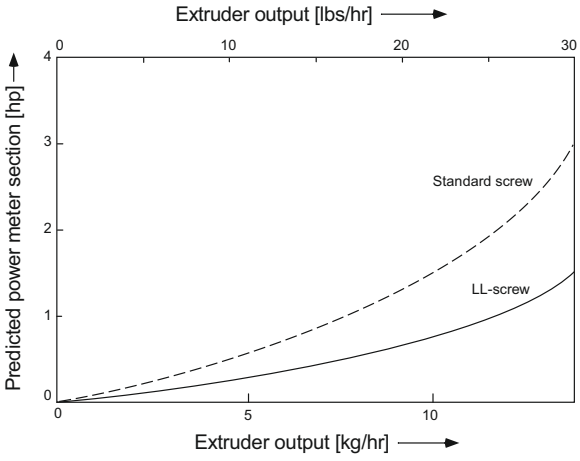


Figure 8.28
Predicted output versus power consumption

Figure 8.29 shows the actual output versus hp curves for the same two screws.

It is clear that the optimized geometry of the LL-screw results in considerably lower power consumption compared to the standard geometry. The drop in power consumption is around 35 to 40%! It is also interesting to note that the predicted power consumption, Fig. 8.28, agrees quite well with the actual power consumption, Fig. 8.29. The difference in the ordinates is caused by the fact that Fig. 8.28 is predicted power for the metering section only, while Fig. 8.29 is actual total power consumption. A patent was issued on the LL-screw [65]; Migrandy Corporation obtained a license to supply extruder screws using this technology.

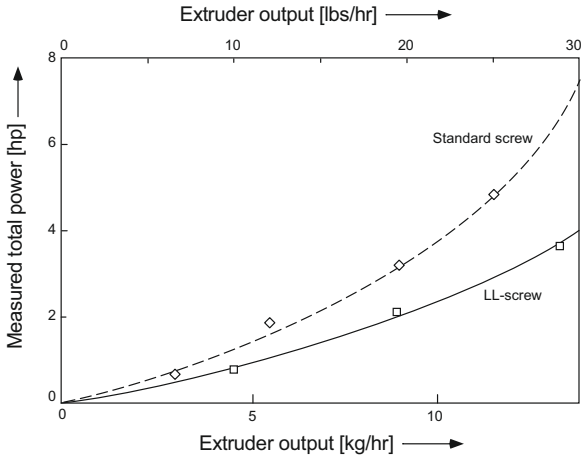


Figure 8.29
Actual output versus power consumption

It should be noted that the benefits of a reduced flight width and increased helix angle are valid for the plasticating zone as well. The power consumption in the plasticating zone of the extruder is also reduced when the flight width is reduced. In Section 8.2.2, it was discussed that increasing the helix angle improves melting performance. Thus, the combination of increased helix angle and reduced flight width should have a beneficial effect not only on the melt conveying zone, but also on the melting zone of the extruder.

8.4 Single-Flighted Extruder Screws

In the previous sections of this chapter, screw design was analyzed by functional performance. By using the extrusion theory developed in Chapter 7, it was shown how the screw design can be determined quantitatively for optimum performance. In this section, screw design will be approached from another angle. Screw designs in use today will be described and their advantages and disadvantages will be discussed and analyzed.

8.4.1 The Standard Extruder Screw

In many discussions on extrusion, reference is made to a so-called standard or conventional extruder screw. In order to define this term more quantitatively, the general characteristics of the standard extruder will be listed; see also Fig. 8.30:

- Total length 20–30 D
- Length of feed section 4–8 D
- Length of metering section 6–10 D
- Number of parallel flights 1
- Flight pitch 1 D (helix angle 17.66°)
- Flight width 0.1 D
- Channel depth in feed section 0.15–0.20 D
- Channel depth ratio 2–4

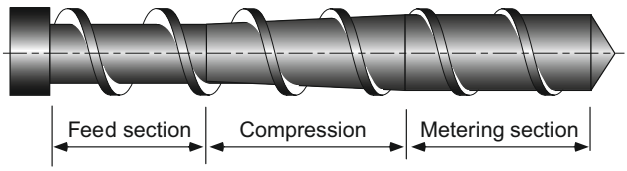


Figure 8.30
The standard extruder screw

These dimensions are approximate, but it is interesting that the majority of the extruder screws in use today have the general characteristics listed above. For profile extrusion of PA, PC, and PBTB, Brinkschroeder and Johannaber [46] recommend a channel depth in the feed section of $H_f \cong 0.11\ (D + 25)$ and a channel depth in the metering section of $H_m \cong 0.04\ (D + 25)$, where channel depth H and diameter D are expressed in mm. Based on these guidelines, the geometry of a standard extruder screw can be determined easily.

Based on the design methodology developed in Sections 8.2 and 8.3, it should be clear that the standard screw design is by no means an optimum screw design. It has developed over the last several decades mostly in an empirical fashion and works reasonably well with many polymers. However, significant improvements in performance can be made by functional optimization using extrusion theory. In this light, it is somewhat surprising that the standard extruder screw is still so popular today. It probably indicates a lack of awareness of the implications of extrusion theory on screw design and the improvements that can be realized from functional optimization of the screw geometry. Another interesting note is that several manufacturers of extruder screws claim to use sophisticated computer programs to optimize the screw geometry, but often still end up with a standard square pitch screw. It can be shown from an elementary analysis that the square pitch geometry is not optimum for melting or melt conveying. Thus, if the result of the screw optimization by computer is a square pitch geometry, this indicates that either the computer program is incorrect or the person using the program is not using it correctly.

8.4.2 Modifications of the Standard Extruder Screw

There are a large number of modifications of the standard extruder screw in use today. It will not be possible to mention all of them, but an effort will be made to discuss the more significant ones. Figure 8.31 shows the standard screw with an additional flight in the feed section.



Figure 8.31 Standard screw with additional flight in the feed section

The additional flight is intended to smooth out the pressure fluctuation caused by the flight interrupting the in-flow of material from the feed hopper every revolution of the screw. An additional benefit of the double-flighted geometry is that the forces acting on the screw are balanced; thus, screw deflection is less likely to occur. On the negative side, the additional flight reduces the open cross-sectional channel area and increases the contact area between solid bed and screw. Thus, pressure surges may be reduced, but the actual solids conveying rate will be reduced as well. As a result, a double-flighted feed section in smooth bore extruders often results in reduced performance.

Figure 8.32(a) shows a variable pitch extruder screw.



Figure 8.32(a) Variable pitch extruder screw with increasing pitch

The varying pitch allows the use of the locally optimum helix angle, i. e., optimum helix angle for solids conveying in the feed section and optimum helix angle for melt conveying in the metering section of the screw. This design is covered by a U. S. patent [6] and is described in a 1980 ANTEC paper [7]. Figure 8.32(b) shows a variable pitch extruder screw as often used for rubber extrusion; see also Section 2.1.4.



Figure 8.32(b)
Variable pitch extruder screw with reducing pitch

In this design, the pitch decreases with axial distance as opposed to the screw shown in Fig. 8.32(a). The reducing pitch causes a lateral compression of the material in the screw channel; as a result, the normal compression from the reducing channel depth can be reduced or eliminated altogether. In fact, many of these variable reducing pitch screws maintain the same channel depth along the entire length of the screw.

It should be noted that the variable reducing pitch screw is not a high-performance screw. It is designed primarily to exert minimal shear to the polymer; the L/D ratio is generally quite short, about 10. This screw has been used extensively for rubber extrusion. A smaller than square pitch flight geometry can be beneficial for highly shear thinning polymers. When the power law index is less than 0.2 a smaller than square pitch flight geometry will actually improve melt conveying; see Eq. 8.54(d).

A major supplier of LLDPE used to recommend a variable reducing pitch (VRP) screw for extrusion with LLDPE [61]. Considering the approach developed in Section 8.3, this screw design would seem inappropriate for LLDPE. As discussed in Section 8.3, power consumption can be reduced by increasing the helix angle and flight clearance and by reducing the flight width. The VRP screw recommended for LLDPE does not reduce the flight width and reduces the helix angle. This combination of screw design parameters results in increased power consumption instead of reduced power consumption.

The reason, however, that this VRP screw works is that the clearance between flights and barrel is substantially larger than the normal design clearance—about double! This design feature is not much emphasized, however it is the key to the performance of the VRP screw for LLDPE because the power consumption in the flight clearance plays such an overriding role in LLDPE extrusion. Based on the arguments developed in Section 8.3, it is clear that a variable increasing pitch (VIP) screw with a larger flight clearance will be significantly better than the VRP screw. A disadvantage of the larger clearance is reduced melting capacity and reduced heat exchange between the polymer melt and barrel. As a result, the VRP screw with increased flight clearance may not be suitable for extrusion of polymers other than LLDPE.

Figure 8.33 shows an extruder screw without a metering section; the so-called zero-meter screw [8].

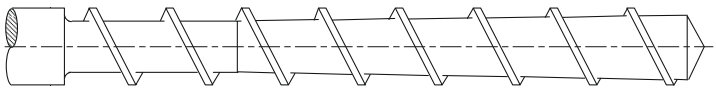


Figure 8.33 Zero-meter extruder screw

This screw is more appropriate for a plasticating unit of an injection molding machine. The zero-meter screw is used to reduce the temperature build-up in the material by deepening the depth of the channel in the melt conveying zone of the extruder. The obvious drawback is that the pressure generating capability of the screw will be adversely affected, but this is not a major concern in injection molding applications. In other applications, however, the approach outlined in Section 8.3 is recommended. An extension of the zero-meter screw is the zero-feed zero-meter screw shown in Fig. 8.34.

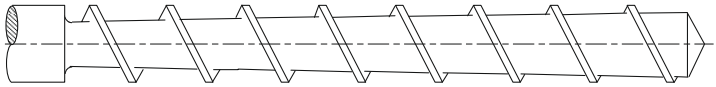


Figure 8.34 Zero-feed zero-meter extruder screw

This screw essentially consists of only a compression section. This allows a very gradual compression of the material. The screw has been in commercial use for many years and has been successfully used with many polymers, in particular nylon.

The exact opposite of the zero-feed zero-meter screw is the very rapid compression screw, shown in Fig. 8.35.

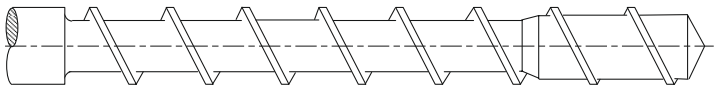


Figure 8.35 Rapid compression screw

The length of the compression section is generally less than 1 D in these screws. Unfortunately, this screw is often referred to as a nylon screw. This is unfortunate because it implies that nylon should be extruded on a rapid compression screw. However, this is a major misconception in screw design and the success of the zero-feed zero-meter screw with nylon should make that quite clear. Nylon has a relatively narrow melting range and turns into a relatively low viscosity melt quite readily. However, this does not mean that the compression should be very rapid. The maximum compression can be determined from Eq. 8.64. The relative width of the melting range of the polymer is totally immaterial to the determination of the maximum compression of the extruder screw. The low melt viscosity of nylon will reduce the melting rate, and it indicates that a gradual compression screw will be much more appropriate for nylon than a rapid compression screw. This was conclusively demonstrated as early as 1963 by Bonner [9], who found that the gradual compression screw reduced air entrapment, reduced pressure and output fluctuations, and improved extruder quality.

The zero-meter screw is used to reduce the viscous heat generation (power consumption) in the melt conveying zone of the extruder by having a relatively deep channel in this portion of the screw, with the depth reducing linearly with distance. Another similar approach is the decompression screw shown in Fig. 8.36.

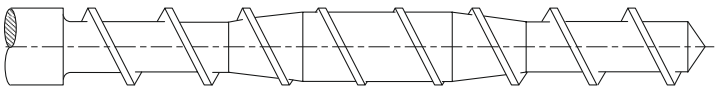


Figure 8.36 Decompression screw

The final portion of the screw has a deep channel section following a decompression section. The channel depth is constant over the last screw section. Again, the deeper channel in the final screw section will reduce the pressure generating capability of the screw. A more effective power reduction can be obtained by not only changing the channel depth, but the channel depth, helix angle, flight width, and radial clearance in an optimum fashion as discussed in Section 8.3.

■ 8.5 Devolatilizing Extruder Screws

Devolatilizing extruder screws are used to extract volatiles from the polymer in a continuous fashion. Such extruders have one or more vent ports along the length of the extruder through which volatiles escape. Some of the applications of vented extruders are:

- Removal of monomers and oligomers in the production of polymers (e.g., PS, HDPE, PP).
- Removal of reaction products of condensation polymerization (e.g., water, methanol) and oligomers from nylon and polyesters.
- Removal of air with filled polymers, particularly with glass fiber reinforced polymers.
- Removal of residual carrier fluid in emulsion and suspension polymerization (e.g., PS, PVC).
- Removal of water from hygroscopic polymers (e.g., ABS, PMMA, PA, PC, SAN, CA, PU, PPO, polysulfone); all polymer particles can have surface moisture left from underwater pelletizing or surface condensation from storage at varying temperatures and relative humidity.
- Removal of solvent and unreacted monomers in solution polymerization (e.g., HDPE).
- Removal of volatile components in compounding of polymers with additives and other ingredients.

Removal of water from hygroscopic polymers is a common use of vented extruders. Most polymers require less than 0.2% moisture in order to properly extrude. In some polymers, this percentage is considerably lower, e.g., PMMA < 0.1%, ABS < 0.1%, CA < 0.05%, PBTB < 0.05%, and PC < 0.02%. Many polymers have an equilibrium moisture content at room temperature and 50% R.H. (relative humidity) that is considerably higher than the maximum allowable percentage moisture content for extrusion. Some values of the equilibrium moisture content of hygroscopic polymers [10] are: ABS 1.5%; PMMA 0.8%; PBTP 0.2%; PC 0.2%; and PA 3%. Such poly-

mers require significant drying or extrusion devolatilization to manufacture good products. In many cases, extrusion devolatilization is preferred over drying.

Conventional two-stage extruders can generally reduce the level of volatiles only a fraction of one percent. For example, for PP/xylene with an initial solvent concentration of 0.3 to 1.0%, the amount of solvent removed by single vent extrusion is about 50%.

8.5.1 Functional Design Considerations

Figure 8.37 shows a typical two-stage devolatilizing extruder screw.

The screw consists of at least five distinct geometrical sections. The first three sections, feed, compression, and metering, are the same as on a conventional screw. After the metering section there is a rapid decompression followed by the extraction section, which, in turn, is followed by a rapid compression and a pump section. Two important functional requirements for good devolatilization are zero pressure in the polymer under the vent port and completely molten polymer under the vent port.

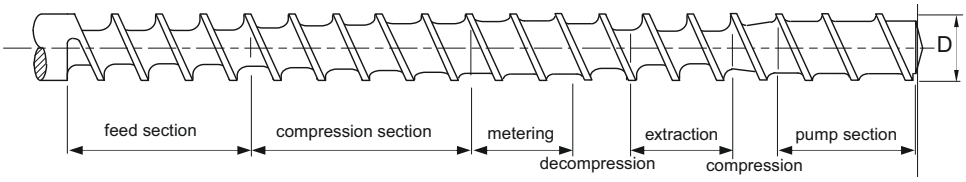


Figure 8.37 Typical two-stage devolatizing extruder screw

The requirement for zero pressure is made to avoid vent flow, i.e., polymer melt escaping through the vent port. The complete fluxing requirement has several reasons. If the polymer is not completely molten in the metering section, there may not be a good seal between the vent port and the feed opening. This will limit the amount of vacuum that can be applied at the vent port. A good vacuum is generally quite important in order to obtain effective devolatilization. Another reason for the complete melting requirement has to do with diffusion coefficients. The devolatilization process in extruders is often controlled by diffusion [2]: see also Section 7.6.

Diffusion coefficients are very much temperature dependent. When the polymer is below the melting point, diffusion generally occurs at an extremely low rate. The polymer, therefore, should be above the melting point to increase the rate of diffusion and with it the devolatilization efficiency. Even when the polymer is in the molten state, the diffusion coefficients can often be increased substantially by increasing the temperature of the polymer melt [11]. Further, when the polymer is in the molten state, surface renewal is possible. This greatly enhances the devolatilization process. The extent of surface renewal is a strong function of the screw

design; a multi-flighted, large pitch extraction section will be beneficial to the devolatilization efficiency. Thus, for the highest devolatilization effectiveness, the polymer should be completely molten and at relatively high temperature when it reaches the extrusion section. The complete melting requirement can be worked out by the procedure developed in Section 8.2.2.

The requirement for zero pressure can be fulfilled by ensuring that the channel in the extraction section is only partially filled with polymer. There is no chance of pressure build-up, at least in the down-channel direction, when the screw channel is not fully filled. In order to achieve this partial fill, the depth of the extraction section has to be considerably larger than the depth of the metering section, usually at least three times larger, and the transport capacity of the pump section must be larger than the transport capacity of the metering section. In other words, one has to make sure that the polymer can be transported away from the vent port at a rate at least as high as the rate with which it can be supplied to the vent section. If the transport capacity of the pump section is insufficient, the polymer melt will back up in the pump section and eventually escape through the vent port.

If the flight pitch is constant and the polymer melt viscosity can be described by Eq. 8.78, the maximum diehead pressure for effective devolatilization can be written as [2]:

$$P_{max} = \frac{6 v_b^n \, m \, L}{\tan\varphi} \left(\frac{H_p - H_m}{H_p^{n+2}} \right) \tag{8.81}$$

This equation was derived by assuming a zero pressure gradient in the metering section and by using the Newtonian throughput-pressure relationship, Eq. 7.198. The optimum channel depth in the pump section H_p^* can be obtained by setting:

$$\frac{\partial P_{max}}{\partial H_p} = 0 \tag{8.82}$$

This results in the following expression for the optimum channel depth in the pump section:

$$H_p^* = \frac{(n+2) H_m}{n+1} \tag{8.83}$$

The ratio of depth in the pump section to depth in the metering section is often referred to as pump ratio X_p. The optimum pump ratio H_p^* according to Eq. 8.83 is only a function of the power law index; this is shown in Fig. 8.38.

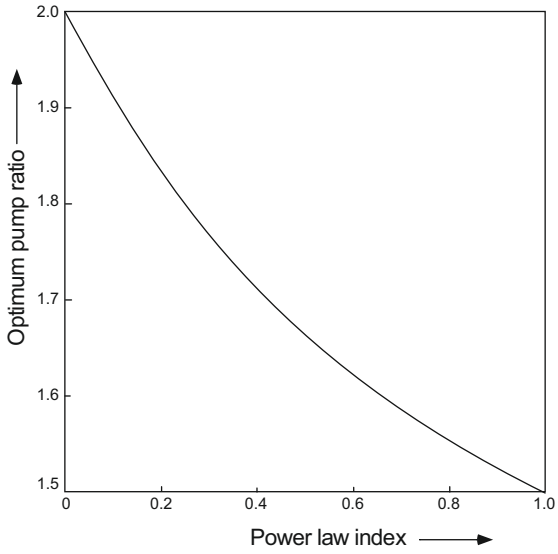


Figure 8.38
Optimum pump ratio versus power law index

The pump ratio should increase when the power law index decreases. The practical lower limit is 1.5 and should be used for polymers with almost Newtonian flow characteristics. The upper limit of the pump ratio is 2.0 and should be used for polymers with very strong pseudo-plastic flow behavior.

Strictly speaking, one cannot insert a power law melt viscosity in the Newtonian throughput-pressure relationship, as discussed earlier in Section 8.2.1. Thus, Eqs. 8.81 and 8.83 are not 100% accurate. However, they are much more accurate than predictions based on pure Newtonian behavior, because the latter can cause substantial errors; see, for instance, Figs. 7.62 through 7.66. The dimensionless maximum pressure is shown as a function of the pump ratio X_p in Fig. 8.39.

The dimensionless maximum pressure is the actual maximum pressure divided by the peak maximum pressure for the Newtonian case ($X_p = 1.5$). The dimensionless maximum pressure can be expressed as:

$$P^0_{max} = \frac{P_{max}}{P^*_{max}(n=1)} = \frac{27(X_p - 1)}{4X_p^{n+2}} \left(\frac{v_b}{H_m} \right)^{n-1} \tag{8.84}$$

Figure 8.39 shows clearly that the peak maximum pressure is highest for the Newtonian fluid and reduces steadily when the power law index reduces. This indicates that the pressure generating capacity reduces as the fluid becomes more shear thinning. At the same time, the optimum pump ratio increases with reducing power law index. From Eq. 8.84, it can be seen that the dimensionless maximum pressure also depends on the average shear rate in the screw channel. Figure 8.40 shows how the dimensionless maximum pressure varies with the pump ratio at several values of the average shear rate.

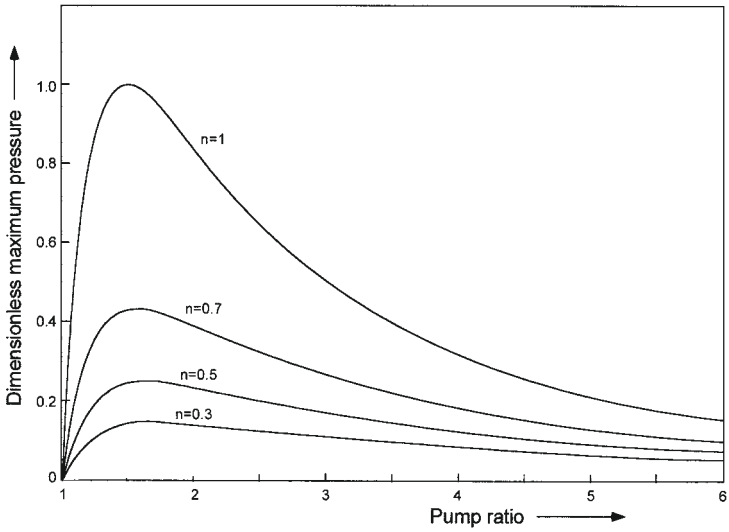


Figure 8.39 Dimensionless maximum pressure versus pump ratio

It is evident from Fig. 8.40 that increases in shear rate have a strong effect on the pressure generating capability. This can be seen clearly from the following relationship:

$$\frac{P^0_{max}(\dot{\gamma}_1)}{P^0_{max}(\dot{\gamma}_2)} = \left(\frac{\dot{\gamma}_1}{\dot{\gamma}_2}\right)^{n-1} = \left(\frac{N_1}{N_2}\right)^{n-1} \tag{8.85}$$

where N is the screw speed.

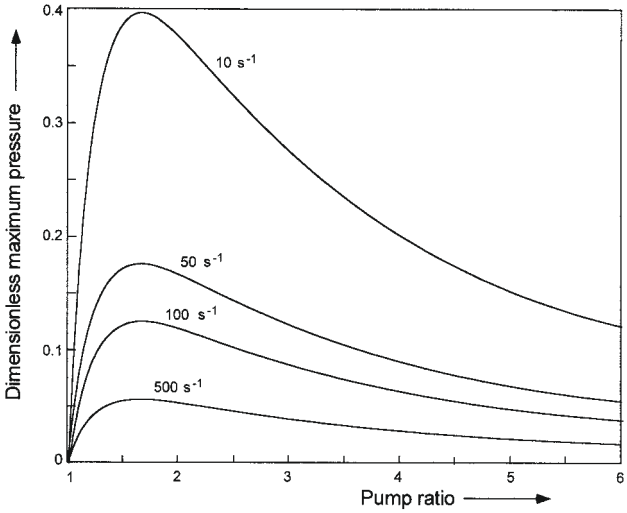


Figure 8.40
Dimensionless pressure versus pump ratio for n = 0.5 and various shear rates

In practical terms, this has important implications. It means that when the screw speed is increased, the pressure generating capability increases less than proportional to the screw speed.

Thus, if the output increases approximately proportional to the screw speed, at some point the diehead pressure can exceed P_{max}, causing vent flow. This will happen more readily when the material is more shear thinning, i.e., when the power law index is closer to zero.

8.5.2 Various Vented Extruder Screw Designs

There are many different designs of devolatilizing single screw extruders with widely differing devolatilization capacity. Some of the more common ones will be described and discussed next.

8.5.2.1 Conventional Vented Extruder Screw

The conventional vented extruder screw is shown in Fig. 8.37. In many cases, mixing sections are incorporated into the metering section of the screw to improve the homogeneity of the melt entering the extraction section. The volatiles travel with the polymer up to the vent port. This type of venting is referred to as forward devolatilization. The length of the extraction zone is usually 2 to 5 D. The channel depth in the extraction section is large, particularly if the polymer foams in the extraction section. The channel depth in the extraction section can be as large as 0.4 D on large diameter extruders, 0.3 D on smaller extruders. In order to achieve frequent surface renewal, the extraction section is often designed with multiple flights; see Fig. 8.41(a).

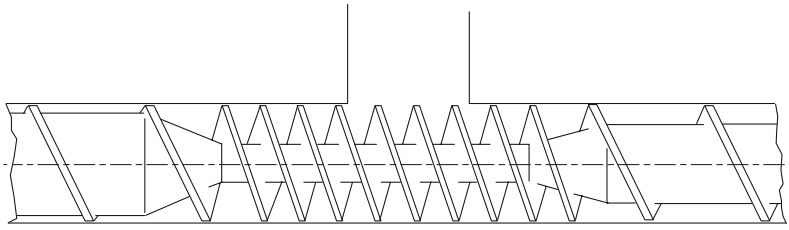


Figure 8.41(a) Extraction section with multiple flights

For the same reason, the helix angle is often increased from the conventional 17.66° (square pitch) to as high as 40° [12].

As discussed in Section 8.5.1, the optimum pump ratio ranges from 1.5 to 2.0. In practice, the pump ratio is often selected in the range from 1.2 to 1.4. However, these lower pump ratios make the extruder more susceptible to vent flow. Sometimes vent flow is avoided by starve feeding the extruder. However, if starve feeding

is necessary to avoid vent flow, it indicates a deficiency in the screw design and it might be better to modify the screw or design a new one. Carley [13] recommends the use of rear valving to adjust the flow rate of the material entering the extraction section. This is shown schematically in Fig. 8.41(b).

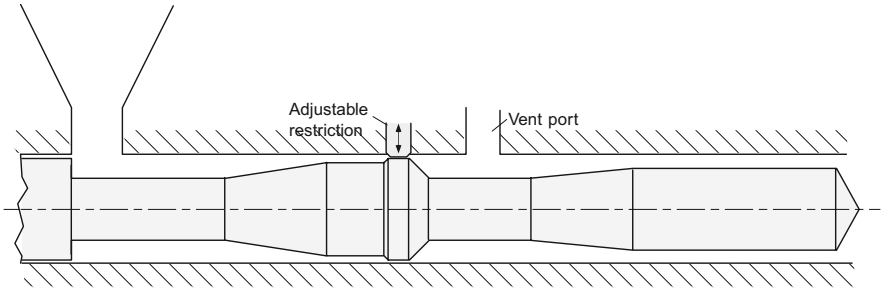


Figure 8.41(b) Rear valving

Another approach was taken by Heidrich [56], who developed a vented extruder with axial adjustment capability of the screw. This allows variation of a conical gap at the end of the metering section; an example of this feature is shown in Fig. 8.45. In vented extruders without external adjustment capability of the first stage resistance, it is generally a good idea to incorporate a pressure consuming mixing element. This improves melt homogeneity and reduces the pressure of the melt entering the extraction section.

8.5.2.2 Bypass Vented Extruder Screw

Another method to control the flow rate into the extraction section is to use a bypass system. This system was proposed by Willert of Egan Machinery Company [14]. Maddock and Matzuk [15] discussed the principles of the bypass vented extruder and described actual experiments with different screw geometries. The bypass vented extruder is shown schematically in Fig. 8.42.

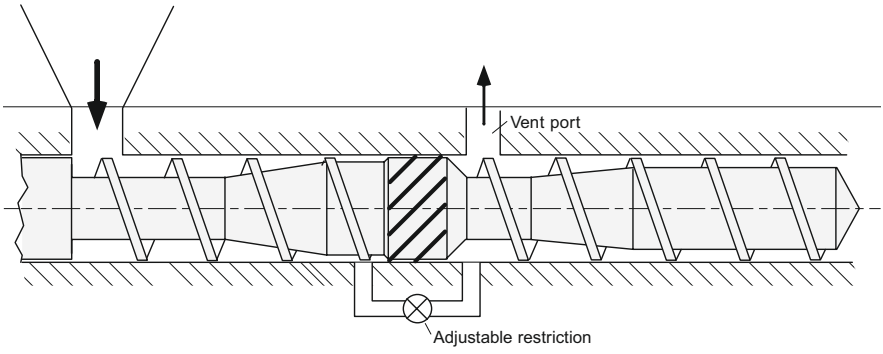


Figure 8.42 Bypass vented extruder system by Egan

The polymer melt is forced from the metering section into a bypass flow channel by incorporating a multi-flighted screw section with reversed pitch and shallow channels between the metering section and the extraction section. The bypass channel has one or more adjustable restrictions to control the rate of flow into the extraction section. The polymer flows from the bypass channel into the beginning of the extraction section. Maddock and Matzuk concluded that bypass venting allows a wider range of operation, is less susceptible to instabilities, and is less operator-sensitive.

A different bypass venting system was described by Anders [16]; it is shown in Fig. 8.43.

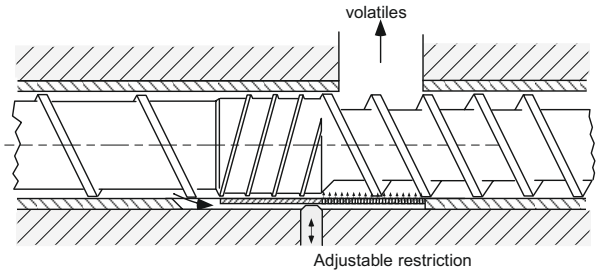


Figure 8.43
Bypass vented extruder system by Berstorff

The melt flows from the metering section into a bypass channel, which runs essentially parallel to the screw. The melt is forced into the bypass channel by a shallow multi-flighted screw section of reversed pitch located just downstream of the bypass channel inlet. The bypass channel extends about 2 D into the extraction section. The polymer melt flows into the extraction section through a large number of holes. This increases the surface area generation and improves the devolatilization efficiency. The bypass channel has adjustable restrictions to control the flow of material to the extraction section. The devolatilization capability is further enhanced by using a multi-flighted, large pitch design in the extraction section. The bypass system described by Anders is used in multi-stage vented extrusion.

8.5.2.3 Rearward Devolatilization

Rearward devolatilization is used on melt fed extruders. In rearward devolatilization, the volatiles are extracted upstream of the feed opening of the extruder. This is shown schematically in Fig. 8.44.

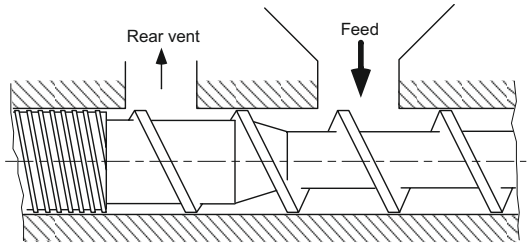


Figure 8.44
Rearward devolatilization

This machine is used in melt fed extrusion. The vent port is generally located at least 1 D from the feed opening to avoid polymer melt getting to the vent port. To improve the devolatilization capability, the melt is often forced into the extruder through numerous small holes; examples of this feature are shown in Figs. 8.45 and 8.48.

In order to avoid plugging of the vent port, a feedback control mechanism can be incorporated that controls the degree of fill of the extruder. This can be done by measuring the pressure at the beginning of the metering section and by using this reading to adjust the screw speed or feed rate to maintain the same pressure and thus the same degree of fill.

8.5.2.4 Multi-Vent Devolatilization

Multi-vent devolatilization is used when large amounts of volatiles need to be removed from the polymer. In a well-designed system, as much as 15% of volatiles can be removed in one extrusion operation. Figure 8.45 shows a schematic of a multi-stage system used for devolatilization of molten polystyrene.

This system incorporates rearward venting, stranding of the melt at the inlet to increase surface area, variable gap before the section vent port by axial screw adjustment, water injection, and bypass venting at the final vent port. Such a system can reduce the monomer level from 15% down to as low as 0.1% in one operation. Such devolatilization performance is quite comparable to that of twin screw devolatilization systems.

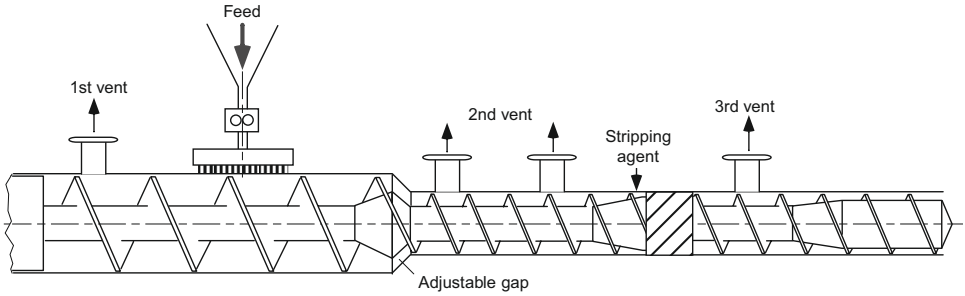


Figure 8.45 Efficient multi-stage degassing system

At high levels of volatiles, the initial devolatilization will be quite rapid because the process will occur primarily by a foam devolatilization; see Section 5.4.2. When the volatile level reduces, the devolatilization will occur by molecular diffusion, reducing the rate of devolatilization considerably. In this situation, the devolatilization can be greatly improved by injecting a stripping agent into the polymer. The stripping agent is generally introduced in or right before a mixing section. This causes foaming of the polymer at the extraction section, resulting in much improved devolatilization. A common stripping agent is water; also used are low boiling organics or

nitrogen. In some cases, the volatile and the stripping agent can form an azeotropic mixture, which boils at a lower temperature than either of the components. An example is styrene monomers and water [17].

A more conventional three-stage extruder screw is shown in Fig. 8.46.

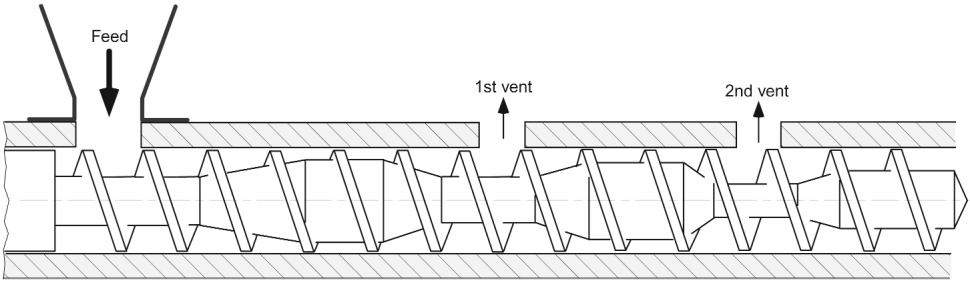


Figure 8.46 Conventional three-stage extruder screw

This system has two vent ports and is used in applications where a single vent port cannot remove a sufficient amount of volatiles. It is used, for instance, in ABS extrusion as described by Brozenick and Kruder [18] and with acrylic, polycarbonate, polypropylene, etc., as described by Nichols, Kruder, and Ridenour [19]. This system can remove moisture levels as high as 5 to 7%.

8.5.2.5 Cascade Devolatilization

In many polymer devolatilization systems, two extruders are arranged in a cascade arrangement. The first extruder is primarily used for solids conveying, plasticating, and mixing. The section extruder is primarily used for melt conveying, i. e., for pumping. The first extruder is often a multi-screw extruder; the second extruder is generally a single screw extruder. Figure 8.47 shows a planetary gear extruder feeding a single screw extruder.

The venting takes place between the first and second extruder. The system shown in Fig. 8.47 is often used for devolatilization of PVC. The devolatilization effectiveness can be improved by stranding the polymer melt as it enters the second extruder. This is shown in Fig. 8.48.

The distance of the strand die to the second extruder is made reasonably long to improve devolatilization. The distance is limited by the fact that the strands cannot cool below the point where the intake of the second extruder is affected.

The major advantage of the cascade devolatilizing system is that the control of the output of the first stage to the pressure generating capability of the second stage is much better than in a single extruder devolatilization system. Obviously, the cost will be higher, and the decision for one system or the other must be based on the importance of improved flexibility and controllability.

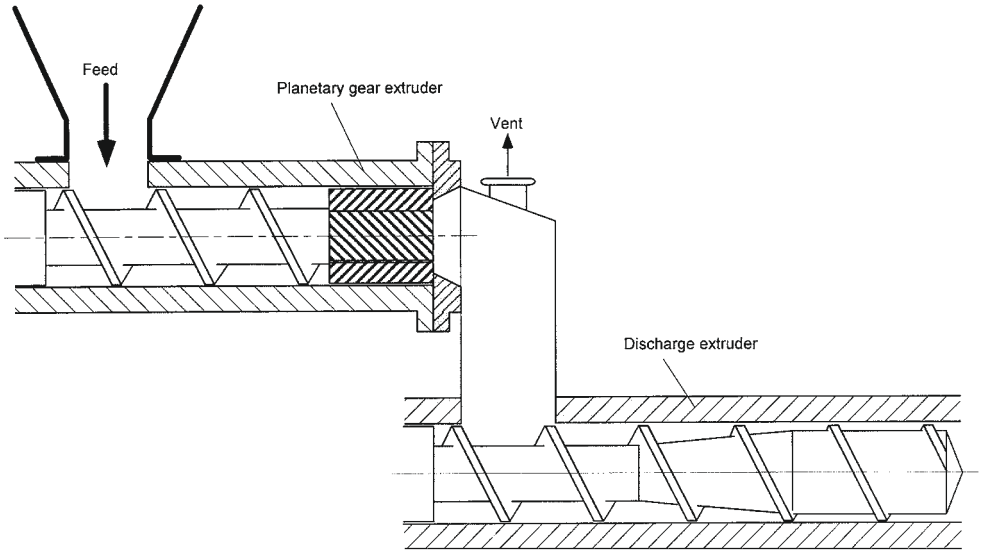


Figure 8.47 Cascade devolatilization with a planetary gear extruder feeding a single screw extruder

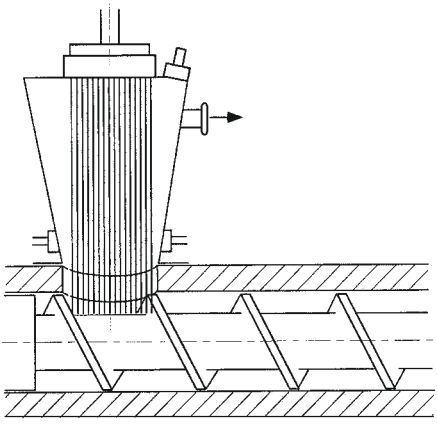


Figure 8.48
Stranding for improved degassing

8.5.2.6 Venting through the Screw

An interesting development in devolatilizing extrusion was described by Bernhardt in 1956 [20]. In this extruder, the volatiles are removed through the screw instead of through a vent port in the barrel. The screw has a hollow core connecting with a lateral hole in the extraction section of the screw; see Fig. 8.49(a).

The volatiles are withdrawn through a rotary union at the rear of the screw. This venting was tested in practice on acrylic and was found to perform reliably for extensive periods of time. This process is also used for processing PET powder with conventional two-stage screws. This concept has also been applied to barrier screws.

Eastman Kodak Company received a patent (U.S. Patent 6,164,810) on a barrier screw with a vent hole located within about two diameters from the end of the feed section, between a main flight and a barrier flight. The vent hole is located such that there is little chance of polymer plugging the vent hole. The volatiles are vented out to the back of the screw through an axial bore. This screw design can be used to process PET powder into film.

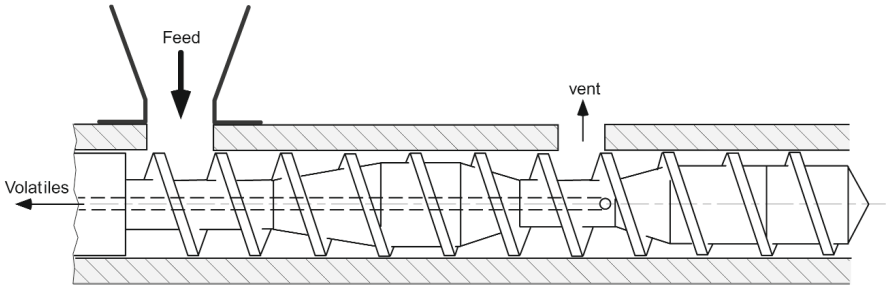


Figure 8.49(a) Venting through the screw

In the past barrier screws were used only with PET pellets because pellets are not susceptible to air entrapment. Powders, however, are susceptible to air entrapment and do not process well on conventional barrier screws. The internally vented barrier screw developed by Eastman achieves higher throughputs of PET powder. This screw design can also be used for other hygroscopic resins like ABS.

An obvious advantage of this approach is that venting can be done on an extruder not equipped with a vent port in the barrel. An equally obvious disadvantage is that plugging of the vent channel in the screw may cause a complete shut-down. The plug may be removed by a blast of high-pressure air into the core of the screw. However, if this does not work, the screw has to be pulled and cleaned. Plugging of the vent channel in the screw, however, may not be as much of a problem as one might think. It should be remembered that the polymer has to adhere to the barrel in order to move forward; however, it does not have to adhere to the screw. Thus, a vent port in the barrel is much more likely to accumulate molten polymer than a vent port in the screw, particularly if the vent port is located close to the trailing flight flank. This type of venting, however, does not seem to have found widespread acceptance.

8.5.2.7 Venting through a Flighted Barrel

Kearney and Hold [62] proposed a new devolatilizer with helical flights in the barrel and a smooth screw section (rotor); see Fig. 8.49(b). This device is called a rotating drum devolatilizer (RDD).

The barrel has multiple helical flights as shown in Fig. 8.49(b). Each turn of the helical channels has an oblong opening following the helical path of the channel. The volatiles are removed through these openings, which are located in the same angular

position. The vent openings of channels operating at the same vacuum level are covered by a single manifold. Upstream of the vent opening is a replaceable melt barrier, which is used to provide a hydraulic seal between the various stages. The material moves through the RDD by virtue of the contact between the polymer melt and the rotor. Therefore, there is little tendency of the material to accumulate in the vent port. This situation is similar to the conditions existing in venting through the screw described in Section 8.5.2.6. The multiple flights in the housing provide for good mixing and surface renewal, resulting in effective devolatilization. The rotating drum devolatilizer can, in principle, be mounted on the end of an existing extruder. However, full exploitation of its potential benefits will probably require incorporation into new machinery, specially designed to take advantage of the benefits of the RDD.

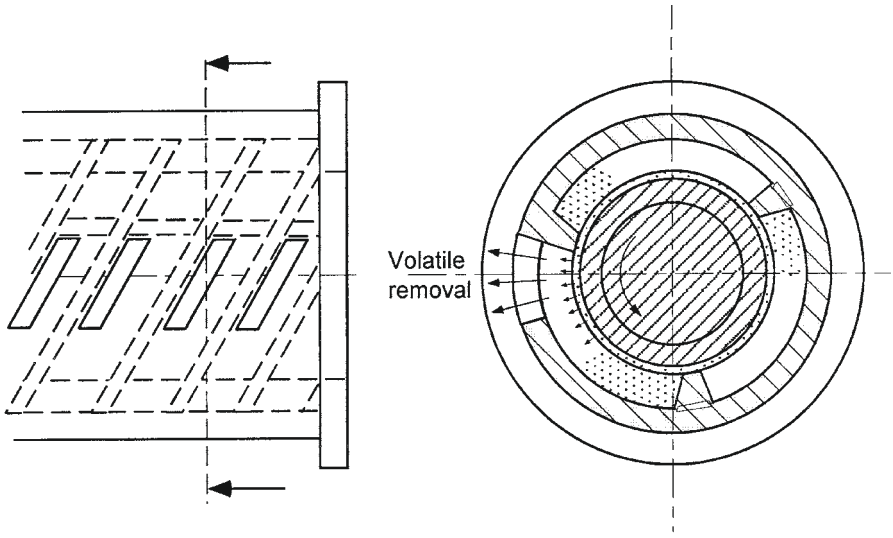


Figure 8.49(b) Rotating drum devolatilizer

8.5.3 Vent Port Configuration

As discussed in Section 8.5.2.6, the polymer has to adhere to the barrel in order to be conveyed forward. This means that a vent port in the barrel is likely to pick up molten polymer. It is almost inevitable, simply by the nature of the conveying process in a screw extruder. For this reason, most vented single screw extruders tend to have a gradual accumulation of polymer in the vent port, requiring periodic cleaning of the vent port in order to maintain devolatilization efficiency. In order to minimize accumulation of polymer in the vent port, it is important that the shape of the vent port be such that there is a minimal chance of material hanging up. For this reason, the leading edge of the vent port is often undercut, with the undercut making a small angle with the O.D. of the screw. This is shown in Fig. 8.50(a).

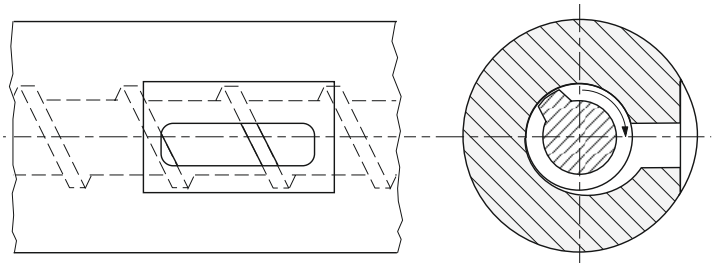


Figure 8.50(a) Vent port geometry to avoid vent flow with undercut to minimize vent port build-up

In addition to the undercut, the vent port is often offset from the vertical, again to minimize the chance of polymer scraping off at the leading edge of the vent port. The length of the vent port is usually 0.5 to 1.5 D and the width about 0.25 to 0.75 D.

Another vent port geometry is shown in Fig. 8.50(b).

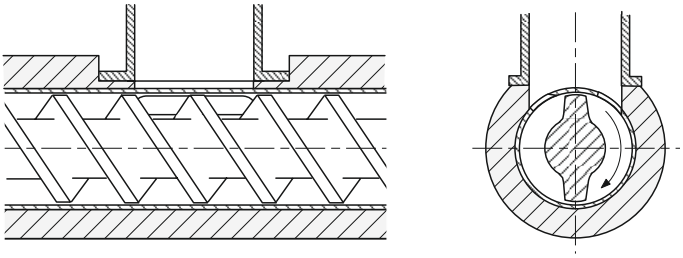


Figure 8.50(b) Vent port geometry to avoid vent flow (b) with dual openings in the barrel liner

Again, this geometry minimizes the chance of polymer melt being scraped off at the leading edge of the vent port.

Another interesting vent port design is shown in Fig. 8.50(c).

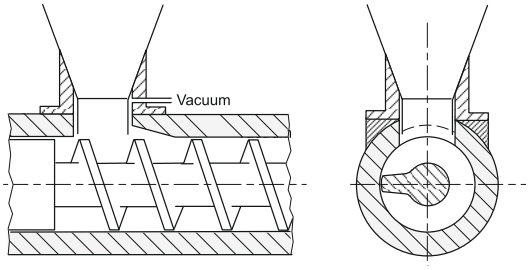


Figure 8.50(c)
Combined feed and vent port

In this design, the feed port is combined with the vent port. The volatiles are removed through the annular space between the feed pipe and the feed port housing. The system is used in conjunction with a vacuum feed hopper as described by

Franzkoch [21]. Such a system allows devolatilization to occur in the feed hopper section of the extruder. This type of devolatilization is successfully used with powders, particularly when the material in the hopper can be heated. The vacuum feed hopper system and some of the problems associated with it are discussed in Section 3.4. Hopper devolatilization of pellets is generally unsuccessful because the larger particle size reduces the surface area and thus the devolatilization effectiveness, as discussed in Section 5.4.1.

A very simple vent port that minimizes the chance of build-up in the vent opening is shown in Fig. 8.51(a).

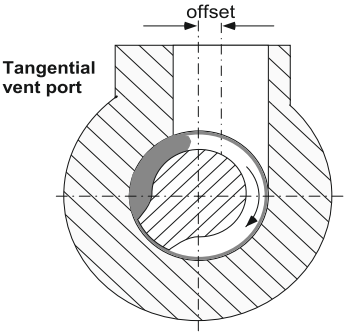


Figure 8.51(a)
Tangential vent port geometry

The tangential vent port is easy to manufacture and eliminates the need to place a deflector plug in the vent port. It can be beneficial to move the vent port from a vertical position to a horizontal position or even a position where the opening is in the downward direction. This can be useful when condensate forms inside the vent opening because the condensate will flow away from the screw rather than into it. This is shown in Fig. 8.51(b).

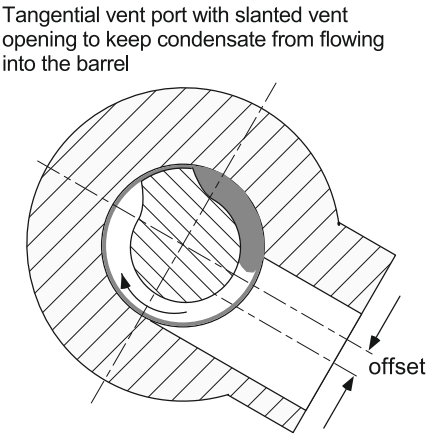


Figure 8.51(b)
Vent port with a downward orientation

8.6 Multi-Flighted Extruder Screws

There are a large number of screw geometries using multiple flights. The additional flights can be the same as the main flight; this geometry will be referred to as the conventional multi-flighted screw. In other designs, the additional flight(s) is different in geometry and function from the main flight; this geometry will be referred to as the barrier flight screw geometry.

8.6.1 The Conventional Multi-Flighted Extruder Screw

The conventional multi-flighted extruder screw has a number of advantages and disadvantages. The basic geometry is shown in Fig. 8.52.

The multi-flighted screw geometry adversely affects the solids conveying and melt conveying rate, as discussed in Chapter 7 and Sections 8.2.1 and 8.2.3. On the other hand, however, the multi-flighted screw geometry can significantly improve melting performance, as discussed in Section 8.2.2, provided the helix angle is sufficiently large. The multi-flighted screw geometry adversely affects power consumption, as discussed in Section 8.3, particularly when the polymer melt is low in melt index and is relatively Newtonian in its flow behavior.

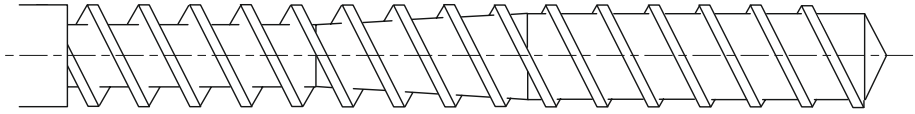


Figure 8.52 Conventional multi-flighted extruder screw

An advantage of the double-flighted screw geometry is the symmetry of the screw flights. This can reduce the tendency of screw deflection by abrupt changes in pressure along the screw channel; this point was discussed in Section 8.1.3. Another possible advantage of a double-flighted screw geometry in the feed section is a more regular intake of material, as discussed in Section 8.4.2. Design considerations of double-flighted extruder screws were discussed by Maddock [22] based on computer simulations. He predicts higher melting rate and reduced power consumption. The latter prediction seems incorrect and must have resulted from improper consideration of the power consumption in the flight clearance. However, the prediction of improved melting is correct and this seems to be the main benefit of a multi-flighted screw geometry. Since solids conveying and melt conveying rates are adversely affected by a multi-flighted geometry, it makes sense to incorporate multiple flights only along a particular section of the screw. This should be the screw section where melting will occur. Two possible screw designs are shown in Fig. 8.53.

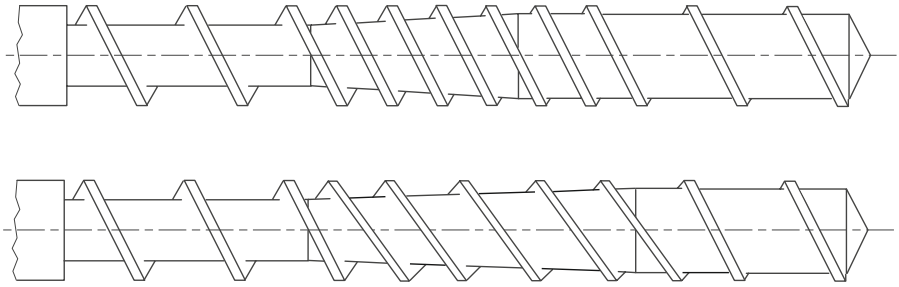


Figure 8.53 Multiple-flighted extruder screws for improved melting

8.6.2 Barrier Flight Extruder Screws

Barrier flight extruder screws have been around since the early 1960s. Presently, barrier screws enjoy widespread popularity in the U.S. Every major U.S. extruder manufacturer offers at least one type of barrier flight extruder screw. There are various types of barrier screws and there is little agreement as to which type is better than the other. Even the advantages and disadvantages of barrier screws compared to regular single-flighted screws are not widely known or agreed upon. In this section, a functional analysis will be made of barrier screws based on extrusion theory. From this analysis, the advantages and disadvantages of barrier screws will become clear, also indicating the preferred geometrical configuration for certain applications.

The inventor of the barrier flight extruder screw is Maillefer, a pioneer in the field of extrusion. He first applied for a patent in Switzerland on December 31, 1959 [23], and later applied for patents in various other countries. Patents were granted, among other countries, in Germany [24] and in England [25]. Maillefer filed a patent application in the U.S. on December 20, 1960. However, Maillefer did not obtain a patent in the U.S. because of a particular provision in U.S. patent law. Geyer from Uniroyal filed a patent application for a barrier screw on April 5, 1961, several months after Maillefer's filing date [26].

Geyer's patent application describes a barrier flight extruder screw almost identical to the one invented by Maillefer. As a result, an interference procedure developed which resulted in the granting of Geyer's patent and the rejection of Maillefer's claim to the patent. This may seem rather surprising because Maillefer filed his patent application several months before Geyer did. The explanation is that Maillefer, by U.S. patent law, was treated as a foreign national, while Geyer was treated as a U.S. national. If Uniroyal could demonstrate that Geyer conceived of this invention before Maillefer filed his application, which Uniroyal managed to do in court, Uniroyal would be legally entitled to the patent. Maillefer, being considered a foreign national, could not use the priority date based on the conception of the idea.

This bit of history explains why seven years elapsed between the filing of Geyer's patent and the date of issue (April 2, 1968). It is an interesting situation because such an interference does not arise very often. It is also interesting because Uniroyal has enforced its patent quite rigorously; various lawsuits have been filed as a result of alleged infringement of the Geyer patent. Uniroyal issued licenses to several companies, among others to the old Sterling Extruder Corporation, who used to sell the screw under the name Sterlex High Performance Screw.

The principle of all barrier screws is very much the same. At the beginning of the barrier section a barrier flight is introduced into the screw channel. The clearance between the barrier flight and the barrel is generally larger than the clearance between the main flight and the barrel. The barrier clearance is large enough so that polymer melt can flow over the barrier, but it is too small for solid polymer particles to flow over the barrier. As a result, the solid bed will be located at the active side of the barrier flight and the polymer melt mostly at the passive side of the barrier flight. Thus, the barrier flight causes a phase separation, confining the solid bed to one side of the barrier flight while allowing the polymer melt to the other side. This is illustrated in Fig. 8.54.

Thus, the barrier screw has a solids channel and a melt channel. In the down-channel direction, the solids channel reduces in cross-sectional area, while the melt channel correspondingly increases in cross-sectional area. At the end of the barrier section, the solids channel reduces to zero, while the melt channel starts to occupy the full channel again.

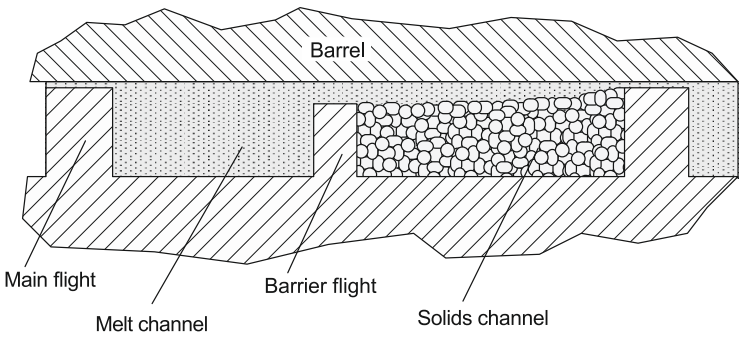


Figure 8.54 Phase separation in a barrier screw

This geometry ensures complete melting of the solids because the solids cannot travel beyond the barrier section unless they are able to cross the barrier clearance. This is only possible if the particle has reduced to a size that will allow rapid melting after any possible crossing of the barrier. Another benefit of the barrier design is that all the polymer has to flow through the barrier clearance where it is briefly subjected to relatively high levels of shear. This causes a certain amount of mixing, similar to the mixing in a fluted mixing element; see Section 8.7.1.

By the nature of the barrier geometry, the solid bed is confined to a channel that is considerably narrower than the total channel width. This has a possible benefit that the solid bed is less likely to break up, although this has not been conclusively demonstrated. On the other hand, it limits the space available to the solid bed. Thus, the screw design will have to be tailored more carefully to the melting profile of the solid bed. The solid bed is more likely to plug the solids channel. Melting must begin considerably before the start of the barrier section in order to allow the introduction of the barrier flight. If this were not the case, plugging would occur immediately.

In order to obtain maximum melting efficiency, the solids channel should be filled from flank to flank with solid polymer with only a thin melt film between the solid bed and the barrel. Obviously, this also represents a situation that can easily develop into plugging because the melting has to match the reducing cross-section of the solids channel. In practice, therefore, there is likely to be more polymer melt in the solids channel than just in the melt film. The assumption of the solid bed occupying the full width of the solids channel can be used to determine the maximum possible melting rate. It should be realized, however, that this rate is not likely to be realized in practice. The comparable melting performance of a regular compression screw can be obtained by using the ideal compression A_1^*:

$$A_1^* = \frac{\Omega_1}{v_{sz}\,\rho_s\sqrt{W_1}\,\sin\varphi} \tag{8.86}$$

This results in the following ideal axial melting length for a standard compression screw; see Eqs. 7.116 and 8.55:

$$L_T^* = \frac{H_f v_{sz}\,\rho_s\sqrt{W_1}\sin\varphi}{\Omega_1} \tag{8.87a}$$

or as down-channel melting length:

$$Z_T^* = \frac{H_f v_{sz}\,\rho_s\sqrt{W_1}}{\Omega_1} = \frac{H_f}{\psi} \tag{8.87b}$$

where ψ is given by Eq. 8.91(a).

The following analysis of the melting performance of various barrier screws is based on the analysis developed by Meijer and Ingen Housz [27]. This analysis provides a clear and logical approach to the determination of the melting capacity as a function of the barrier section geometry.

8.6.2.1 The Maillefer Screw

The Maillefer extruder screw is shown in Fig. 8.55.

The main feature of this barrier screw is that the helix angle of the barrier flight is larger than the helix angle of the main flight. As a result, there is a continuous reduction in the width of the solids channel and a corresponding increase in the width of the melt channel. This geometry allows a smooth and gradual change of the solids channel as well as the melt channel. A drawback of this geometry is that the solids channel reduces in width. This causes a corresponding reduction in melting rate, since this is directly determined by the width of the solid bed.



Figure 8.55
The Maillefer screw

The melting performance of the Maillefer screw geometry can be analyzed by a down-channel mass balance:

$$\frac{d\dot{M}_s}{dz} = \frac{d\dot{M}_p}{dz} \tag{8.88}$$

where:

$$\dot{M}_s = \rho_s v_{sz} W_s H_s \tag{8.88a}$$

The right-hand term, the melting rate per unit down-channel distance, is given by Eq. 7.109(c). In the analysis of the melting performance, a complication arises in that the solid bed velocity cannot be assumed constant. This can be appreciated by comparing the solid bed width profile of a standard screw with constant channel depth to the channel width profile of the solids channel in a Maillefer screw. The width of the solid bed W_s in a standard zero-compression screw as a function of down-channel distance z can be written as:

$$\frac{W_s}{W_1} = \left(1 - \frac{z}{Z_T}\right)^2 \tag{8.89}$$

where W_1 is the channel width and Z_T the total melting length. This expression is derived based on the assumption that the solid bed velocity v_{sz} is constant along the melting zone. This relationship is shown in Fig. 8.56.

At the beginning of melting, the width of the solid bed reduces quite rapidly. As melting proceeds, the solid bed width continues to decline but the rate of change reduces with distance. At the final stage of melting, the rate of reduction of solid bed width approaches zero. This varying rate of change in the width of the solid bed is due to the fact that the melting rate reduces as the width of the solid bed reduces.

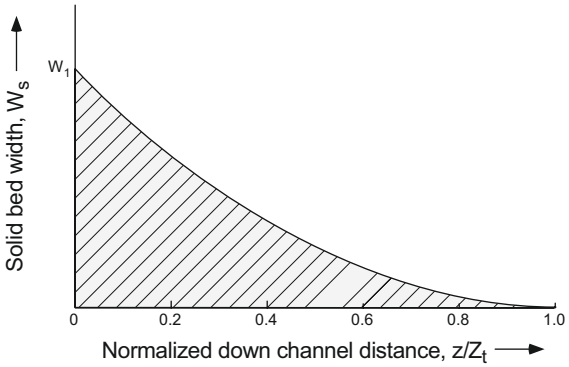


Figure 8.56
Solid bed width profile with constant solid bed velocity

The width of the solids channel of the Maillefer screw can be written as:

$$W_{1s} = W_1 - z\tan\Delta\varphi = W_1\left(1 - \frac{z}{Z_T}\right) \tag{8.90}$$

where $\Delta\varphi$ is the difference in helix angle between the main flight and barrier flight and Z_T is the total length of the barrier section in the down-channel direction.

The relationship becomes clear from examination of a picture of the unwrapped geometry of the Maillefer barrier section; this is shown in Fig. 8.57.

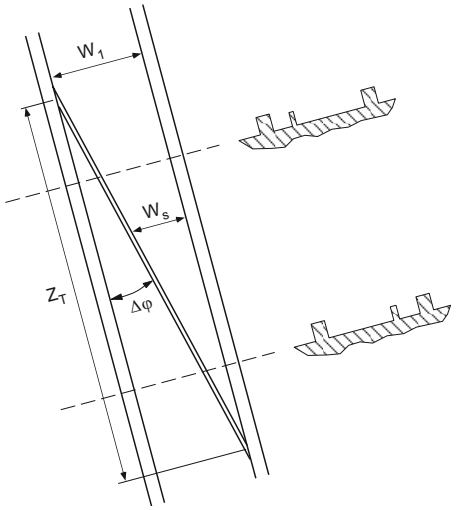


Figure 8.57
Unwrapped Maillefer barrier geometry

By comparing the channel width profile, Fig. 8.57, to the solid bed width profile in a standard screw with constant solid bed velocity, Fig. 8.56, it is clear that the two profiles are considerably different. If the solid bed is to occupy the full width of the channel W_{1s} in the Maillefer screw, the velocity of the solid bed will have to change along the barrier section. This may require substantial deformations in the solid bed, but it will be assumed that the solid bed is capable of undergoing the required

deformations. In reality, the solid bed may not occupy the full width of the channel. However, this is not important at this point since the objective of this exercise is to determine the highest possible melting rate with the Maillefer screw geometry.

If it is assumed that the solid bed width equals the channel width W_{1s}, Eq. 8.88 can be written as:

$$\frac{dv_{sz}}{dz}\left(1-\frac{z}{Z_T}\right)-\frac{v_{sz}}{Z_T}=-\frac{v_{sz}\psi}{H}\left(1-\frac{z}{Z_T}\right)^{1/2} \tag{8.91}$$

where:

$$\psi=\frac{\Omega_1}{\rho_s v_{sz} W_1^{1/2}} \tag{8.91a}$$

This equation cannot be solved without making some simplifying assumptions. Meijer and Ingen Housz [27] solved this problem by initially taking the term $v_{sz}\psi$ constant and evaluating this term by its value at the beginning of melting, i.e., $v_{sz}\psi = v_{szo}\psi_o$. This results in the following expression:

$$\frac{v_{sz}}{v_{szo}}\left(1-\frac{z}{Z_T}\right)=1-\frac{2\psi_o Z_T}{3H}\left[1-\left(1-\frac{z}{Z_T}\right)^{3/2}\right] \tag{8.92}$$

When $z = Z_T$, the left-hand term becomes zero; for the right-hand term to be zero as well, the melting length has to be:

$$Z_T=-\frac{3H}{2\psi_o}=\frac{3}{2}Z_T^* \tag{8.93}$$

where Z_T^* is the shortest possible melt length in the down-channel direction for a standard compression screw; see Eq. 8.87(b).

By substituting Eq. 8.93 into Eq. 8.92, an expression is obtained for the solid bed velocity as a function of down-channel distance z:

$$\frac{v_{sz}}{v_{szo}}=\left(1-\frac{z}{Z_T}\right)^{1/2} \tag{8.94}$$

Equation 8.94 can now be inserted into Eq. 8.91 to obtain a more accurate solution of Eq. 8.91. This can be done by writing Ω_1 as a function of v_{sz}, following Meijer and Ingen Housz [27]:

$$\Omega_1=\Omega_0\left[1+E\left(1-\frac{v_{sz}}{v_{szo}}\right)\right] \tag{8.95}$$

where E is the coefficient relating Ω_1 to v_{sz}.

By ignoring higher order terms of E, the solution becomes:

$$Z - \text{Maillefer} = \frac{3}{2}\left(1 - \frac{E}{4}\right)\frac{H}{\psi} \tag{8.96}$$

This represents the shortest possible melting length with a Maillefer-type barrier screw. A reasonable maximum value of E = 0.4; this results in the following melting length:

$$Z - \text{Maillefer} \cong \frac{4}{3} Z_T^* \tag{8.97}$$

Thus, the best melting length in a Maillefer screw is about 30% longer than an ideal compression screw. For comparison, it is interesting to note that a non-ideal compression screw with a channel depth ratio of 4:1 has a total melting length of $Z_T = 3/2Z_T^*$, as can be determined from Eq. 7.116. From a theoretical analysis of the melting performance of a Maillefer screw, it can be concluded that the best melting length is about 30% longer than an ideal compression screw and about 10% shorter than a standard compression screw with a compression ratio of four. Considering that the maximum melting performance of the Maillefer screw is only about 15% better than a standard compression (4:1) screw, it can be concluded that the Maillefer screw does not offer a significant benefit over a standard compression screw in terms of melting performance, particularly since the actual melting performance of the Maillefer screw will be less than the maximum melting performance.

The advantage of the Maillefer screw is primarily the physical separation of the melt pool and the solid bed. As a result, there is less chance of formation of a melt film between the solid bed and the screw and, therefore, there is less chance of solid bed breakup. Thus, the melting process can occur in a more stable fashion but not necessarily at a higher rate.

8.6.2.2 The Barr Screw

The Barr screw is shown in Fig. 8.58.

The initial part of the barrier section is the same as the Maillefer screw. However, when the melt channel is sufficiently wide, the barrier flight starts to run parallel to the main flight.

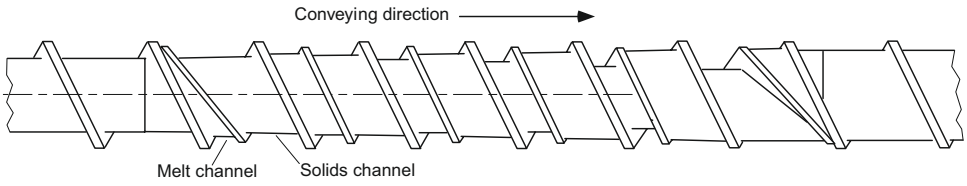


Figure 8.58 The Barr screw

The cross-sectional area of the solids channel is then reduced by reducing the channel depth while at the same time the channel depth of the melt channel is increasing. The advantage of this geometry is that the solids channel width is not continuously reducing, as in the Maillefer geometry, but remains constant at a relatively large value. This increases the solid-melt interfacial area and improves the melting performance. It has a few drawbacks as well, however. Since the melt channel is narrow and quite deep in the latter part of the barrier section, the melt conveying efficiency of the melt channel will be less than in the Maillefer screw. Also, at the end of the barrier section the melt channel changes from a narrow, deep channel to a wide, shallow channel over a short length. This rapid change in channel geometry will not be conducive to stable flow conditions. These relatively abrupt changes in channel geometry do not occur in the Maillefer screw.

The Barr screw was developed by Barr and Chung when they worked at the old Hartig Plastics Machinery Division of Midland-Ross Corporation. Barr applied for a patent in August 1971, the patent was issued in October 1972 [28]. Hartig used to sell barrier screws covered by this patent under the names "MC3" and MC4" screw. Later when Barr and Chung left Hartig, Chung applied for a patent on a modified Barr screw. The application was filed in July 1975 and the patent issued in January 1977 [29]. The modification consists primarily of a difference in the transition from the final melt channel geometry to the metering section. Screws covered by this later patent are sold by Robert Barr, Inc. under the names Barr II, Barr III, and Barr ET screw. In 1982, Uniroyal brought suit against Robert Barr, Inc. for patent infringement. The suit was settled for an undisclosed amount of money.

A very similar barrier screw is described by Willert in a patent application dated August 26, 1981 [30]. The difference in the barrier screw is that the main flight becomes a barrier flight at the beginning of the barrier section, while at the same time the main flight branches off at an angle and then starts to run parallel to the barrier flight. The barrier screw design is shown in Fig. 8.59.

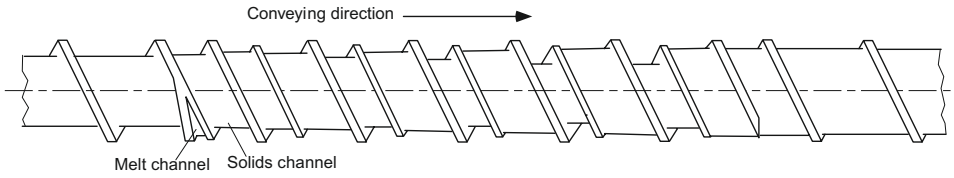


Figure 8.59 The Lacher/Hsu/Willert barrier screw

Interestingly enough, Willert's description is essentially identical to the patent of Hsu [32]. This patent was filed in January 1973 and issued January 1975. Screws covered by Hsu's patent used to be sold under the name "Maxmelt Screw" by the Plastics Machinery Division of Hoover Universal. Coincidentally, Hsu used to work at Hartig at the time when the basic concepts of the Barr screw were being devel-

oped. Another patent on a barrier screw was obtained by Lacher [57] from NRM Corporation in 1966. This geometry is also very similar to the one described by Hsu [32] and Willert [30]. Both Maillefer and NRM became licensees of Uniroyal.

The melting performance of the Barr screw can be analyzed by the same procedure followed for the Maillefer screw. The initial portion of the barrier section can be analyzed just as a Maillefer screw. If z_{T1} is the length of the initial Maillefer portion of the barrier section, the solid bed velocity at $z = Z_{T1}$ is approximately:

$$v_{sz} = v_{szo}\left(1 - \frac{Z_{T1}}{Z_T}\right)^{1/2} \tag{8.98}$$

The melting length of the Maillefer portion is:

$$Z_{T1} = \frac{3\,H\,Z_{T1}}{2\psi\,Z_T} \tag{8.99}$$

In the parallel portion of the barrier section, the width of the solids channel is constant. The highest melting performance will be reached if the width of the solid bed fills the entire width of the solids channel. If the solid bed velocity is assumed constant, the total melting length can be found by using the equations derived from the standard extruder screw; see Eq. 7.116. The total melting length for the parallel barrier portion is simply:

$$Z_{T2} = \frac{H}{\psi}\left(1 - \frac{Z_{T1}}{Z_T}\right) \tag{8.100}$$

The total melting of the barrier section is the sum of Eqs. 8.99 and 8.100. This results in the following expression for the melting length of the Barr screw:

$$Z - \text{Barr} = \frac{H}{\psi}\left(1 + \frac{1}{2}\frac{Z_{T1}}{Z_T}\right) \tag{8.101}$$

In Eq. 8.101, the effect of the varying solid bed velocity on Ω_1 has been neglected. Since the solid bed varies only in the initial portion of the barrier section, this will not affect the accuracy very much as long as the initial Maillefer section is relatively short relative to the total length of the barrier section.

In comparison to the melting length Z_T^* of the ideal compression screw, the melting length of the Barr screw is:

$$Z - \text{Barr} = \left(1 + \frac{Z_{T1}}{2Z_T}\right)Z_T^* \tag{8.102}$$

A typical ratio of Z_{T1}/Z_T is about 0.2. Thus, the shortest possible melting length of the Barr screw is about 10% longer than the Z_T^* of the ideal compression screw and about 25% shorter than the melting length of the standard compression (4:1) screw. The Barr screw is slightly more efficient than the Maillefer screw in terms of melting performance, about 15%. Thus, the Barr screw is marginally better than the Maillefer screw in melting performance. However, the Maillefer screw is better in terms of melt conveying performance in the barrier section.

8.6.2.3 The Dray and Lawrence Screw

The Dray and Lawrence screw is shown in Fig. 8.60.

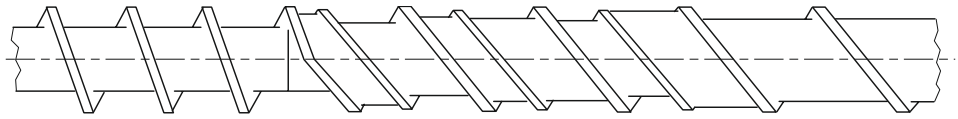


Figure 8.60 The Dray and Lawrence screw

The screw geometry is very similar to the Barr screw with the one major difference being an abrupt change in helix angle in the main flight at the point where the barrier flight is introduced. This allows the width of the solids channel to stay just as wide as the full channel width of the feed section. Obviously, this is done in an attempt to maintain the solids channel as wide as possible. However, this also causes an abrupt change in the direction of the solid bed velocity, and this can lead to instabilities.

If the effect of the change in helix angle on Ω_1 is neglected, the melting length can be shown to be [27]:

$$Z - DL = \frac{H}{\psi}\left(\frac{\sin\varphi_f}{\sin\varphi_b}\right)^{1/2} = \left(\frac{\sin\varphi_f}{\sin\varphi_b}\right)^{1/2} Z_T^* \tag{8.103}$$

where φ_f is the helix angle in the feed section and φ_b the helix angle in the barrier section.

In this case, however, the down-channel melting length does not provide a good basis for comparison because the helix angle is different along the screw. The total axial melting length can be expressed as:

$$L - DL = \left(\frac{\sin\varphi_b}{\sin\varphi_f}\right)^{1/2} L_T^* \tag{8.104}$$

If typical values are used for φ_b and φ_f, the melting length of the Dray and Lawrence screw will about 10 to 20% longer than the ideal compression screw. The melting performance of the Dray and Lawrence screw is thus about the same as the Barr screw and slightly better than the Maillefer screw. A patent on this barrier screw

was applied for by Dray of Feed Screw, Inc. and Lawrence of Owens-Illinois, Inc. [31]. The patent was filed in May 1970 and was issued in March 1972. The screw based on this patent was sold by Feed Screw, Inc. under the name "Efficient Screw." At the end of the barrier section, the melt channel has to make a transition to the melt channel of the metering section. Since the solids channel is quite wide, this transition tends to be quite abrupt, even more so than with the Barr screw. Thus, the Dray and Lawrence screw has two abrupt changes in screw channel geometry, one at the beginning and one at the end of the barrier section. This will tend to make the screw more susceptible to surging types of instabilities than the Maillefer screw, which has much more gradual transitions in the screw channel geometry.

8.6.2.4 The Kim Screw

The Kim screw is basically an improvement of the Dray and Lawrence screw. A picture of the Kim screw is shown in Fig. 8.61.

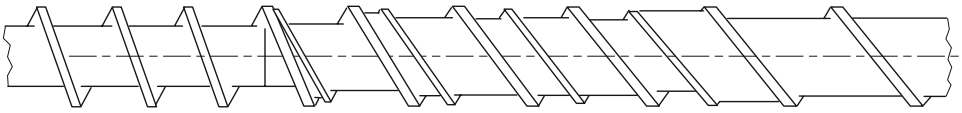


Figure 8.61 The Kim variable pitch barrier screw (VPB)

In the Kim screw, the helix angle of the main flight and the barrier flight is changed gradually to obtain a smooth transition from feed section to barrier section. In the Kim screw, the width of the solids channel remains constant as with the Dray and Lawrence screw. A patent was filed in August 1972 and issued February 1975 [33]. The patent was reissued in August 1975 [34] with the number of claims reduced from six to two. The assignee is B.F. Goodrich Company. The screw was licensed to Davis-Standard Division of Crompton & Knowles Corporation and sold under the name "VPB" screw, which stands for variable pitch barrier screw. The VPB screw is covered both by the early Uniroyal patent [26] and the B.F. Goodrich patent [34].

Again, the melting performance can be analyzed by the procedure used for the Maillefer screw. Because of the continuously varying helix angle, the analysis is rather involved. Ingen Housz and Meijer [27] found for the total melting length of the Kim screw:

$$L - Kim = \frac{3\hat{W}_s(1+0.5\hat{W}_s)}{2[(1+\hat{W}_s)^{3/2}-1]} L_T^* \tag{8.105}$$

where $\hat{W}_s$ is the ratio of the final melt channel width W_{1m} to the initial solids channel width W_{1s}:

$$\hat{W}_s = \frac{W_{1m}}{W_{1s}} \tag{8.105a}$$

The value of $\hat{W}_s$ in the Kim screw is one, which results in the following value of the melting length:

$$L - Kim \cong \frac{5}{4} L_T^* \tag{8.106}$$

This means that the melting performance of the Kim screw is slightly lower than the Dray and Lawrence screw and the Barr screw. It has an advantage over the Dray and Lawrence screw in that the transition from feed to barrier section occurs more smoothly. However, at the end of the barrier section the same difficulty arises as with the Dray and Lawrence screw.

8.6.2.5 The Ingen Housz Screw

The Ingen Housz screw combines a barrier geometry with multi-flighted geometry to obtain significant improvements in melting. A picture of the barrier section geometry is shown in Fig. 8.62.

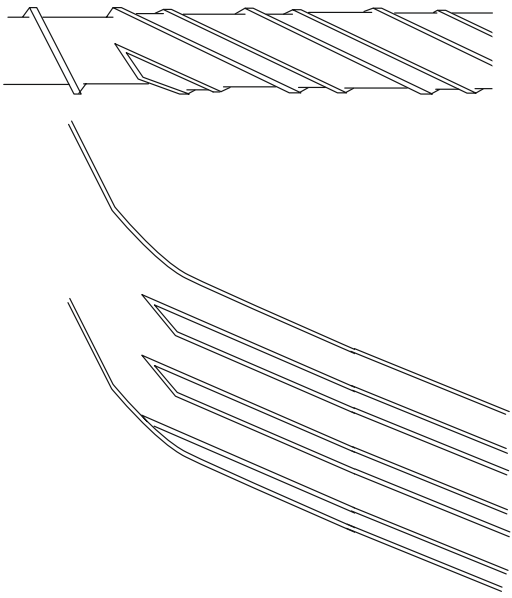


Figure 8.62
The Ingen Housz screw

The barrier section geometry is shown with the screw channel unrolled onto a flat plane. The solid bed is divided into several parallel solid channels. The melt is collected in several parallel melt channels. It is possible to achieve this multi-flighted geometry by a significant increase in the helix angle. The total melting length can be expressed as [27]:

$$L - IH = \left(\frac{1 + \hat{W}_s}{p} \right)^{1/2} L_T^* \tag{8.107}$$

With $\hat{W}_s = 0.25$ and p = 3 the total melting length becomes:

$$L - IH \cong 0.65 L_T^* \tag{8.108}$$

This means that with this barrier screw geometry it is possible to obtain a minimum melting length that is shorter than the ideal compression screw. In fact, the multi-flighted barrier screw geometry is the only one that yields significant benefits in terms of melting performance compared to the standard compression screw. A U.S. patent on the Ingen Housz screw was issued August 19, 1980 [35].

The Ingen Housz barrier screw has a few drawbacks that may or may not be significant. At the start of the barrier section, the solid bed is sliced into several narrower solid beds. This requires easy deformability of the solid bed. If there is considerable resistance against this deformation in the solid bed, it could lead to instabilities. The melt conveying in the barrier section occurs in deep, narrow channels with a large helix angle. As a consequence, the melt conveying capacity will be poor. This essentially requires the use of a grooved barrel section in the feed section of the extruder to ensure a negative pressure gradient along the barrier section to reach sufficient melt conveying rate. Finally, the transition from the barrier section to the metering section will be difficult if the metering section is of conventional geometry. However, if a grooved barrel section is used, the metering section can be deleted altogether since pressure build-up in the melt conveying zone is no longer necessary.

Results of extensive experimental tests with the Ingen Housz screw are described by Ingen Housz and Meijer [36]. Tests were run on a 60-mm extruder with LDPE, HDPE, and PP. The high melting capacity of the screw could only be utilized if sufficient solids conveying capacity was made available by the use of a grooved barrel section. Outputs as high as 200 kg/hr at 100 rpm were achieved while the total length of the screw was only 16 D. The output was found to be sensitive to the particle size of the polymer. High outputs were achieved with larger particles, while the output with smaller particle size polymer was considerably lower, sometimes as much as 50%. This demonstrates that the output can never be higher than the solids conveying rate in the feed section. Even with the grooved barrel section, the solids conveying rate for some polymers was insufficient to supply the melting section with enough material to utilize the full melting capacity.

8.6.2.6 The CRD Barrier Screw

The CRD (Chris Rauwendaal Dispersive mixing) barrier screw was developed to enhance the dispersive mixing action when the polymer melt is forced over the barrier flight. The unique feature of the CRD barrier screw is that the barrier flight is designed to generate elongational flow as the plastic melt passes over the barrier flight. This can be done by making the pushing flight flank of the barrier flight curved or slanted. This creates a wedge-shaped region between the barrier flight

and the barrel in which the plastic melt accelerates as it passes over the barrier flight. The acceleration creates the elongational deformation in the plastic melt.

Figure 8.63 shows a conventional barrier flight geometry (left) next to a CRD barrier flight geometry on the right. The benefit of the CRD barrier flight geometry is improved dispersive mixing and reduced energy dissipation, which results in lower melt temperatures.

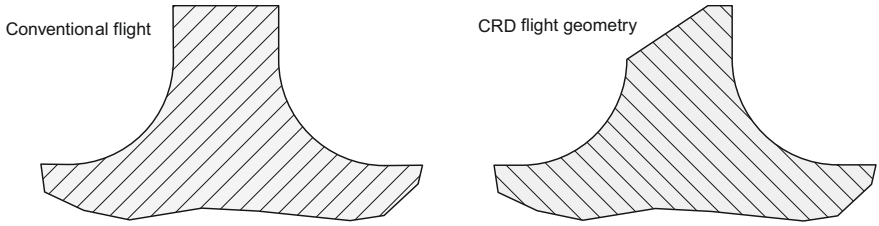


Figure 8.63 Standard barrier flight (left) vs. CRD barrier flight (right)

A drawback of most barrier screws is that their distributive mixing capability is rather poor. As a result, the CRD barrier screw will generally be equipped with a CRD mixing section downstream of the barrier section to improve both dispersive and distributive mixing. CRD mixing sections will be discussed in Section 8.7.1.1. A photograph of a CRD5 mixing section is shown in Fig. 8.64.



Figure 8.64 CRD5 mixing section

8.6.2.7 Summary of Barrier Screws

The characteristics of the various barrier screws are summarized in Table 8.1. The Maillefer screw has many desirable characteristics despite the fact that its melting performance is not quite as good as the other barrier screws. The Ingen Housz screw clearly has the best melting performance; however, this is at the expense of geometrical simplicity.

From a functional analysis, a double-flighted Maillefer (DFM) screw would seem to be a good compromise between considerations concerning geometry and output. With a double-flighted geometry, the melting performance can be improved about 30% in the best case. This would make the DFM screw more efficient in melting capacity than the Barr screw, the Dray and Lawrence screw, and the Kim screw. In order to minimize the adverse effect of the additional flight, the helix angle of the

main flight should be relatively large. However, the helix angle should not be too large in order to maintain good melt conveying capability. A helix angle of about 25° would seem like a reasonable compromise. Figure 8.65 shows a possible configuration of the DFM screw.

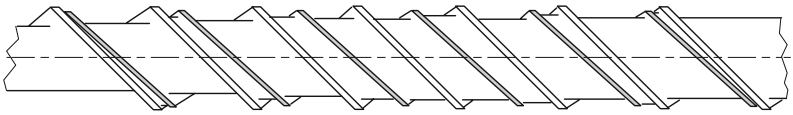


Figure 8.65 Double-flighted barrier screw

Extruder manufacturer Davis-Standard introduced a similar double-flighted barrier screw at the 2000 National Plastics Exhibition in Chicago, Illinois. The characteristics of the DFM screw are included in Table 8.1.

A double-flighted compression screw (4:1 ratio) has a melting capacity only slightly less than the DFM screw (see Table 8.1) and better than the Barr screw, the Dray and Lawrence screw, and the Kim screw. The double-flighted compression screw will be easier to manufacture than any barrier screw. The advantage of barrier screws, that they keep unmelted material from reaching the metering section, can also be obtained by incorporating a fluted mixing section at the beginning of the metering section.

Table 8.1 Characteristics of Various Barrier Extruder Screws

	Transition from feed-barrier	Transition barrier-meter	Minimum melting length L_T*	Melt conveying capacity	Ease of manufacture
Maillefer	Smooth	Smooth	1.3L	Good	Good
Barr	Smooth	Abrupt	1.1L	Fair	Fair
DL	Abrupt	Abrupt	1.1L	Fair	Fair
Kim	Smooth	Abrupt	1.2L	Fair	Difficult
Ingen Housz	Abrupt	Abrupt	0.65L	Poor	Difficult
DFM	Smooth	Smooth	0.9L	Good	Good
Compression (4:1) single-flighted	Smooth	Smooth	1.5L	Good	Excellent
Compression (4:1) double-flighted	Smooth	Smooth	1.1L	Good	Excellent

L_T* minimum melting length in regular compression screw

Table 8.2 summarizes advantages and disadvantages of barrier screws.

Barrier screws became popular because they generally replaced simple conveying screws and were able to improve performance. However, when comparing barrier screws to well-designed non-barrier screws with mixing sections, the barrier screw generally does not perform as well and is more expensive. In a barrier screw, there

is less space available for the solid bed; as a result, they are inherently more susceptible to plugging of the solid bed, which leads to surging. One situation where a barrier screw can offer an advantage is in deep-flighted large diameter screws. In such screws, melting will not be efficient, and a barrier geometry can force the solid bed close to the barrel to improve melting compared to the performance of a non-barrier type screw.

Table 8.2 Summary of Barrier Screw Characteristics

Advantages of barrier screw	Disadvantages of barrier screws
More stable operation than simple conveying screw	Not better than well designed non-barrier screws with good mixing sections
Some dispersive mixing as melt flows over the barrier flight	More expensive than non-barrier screws, particularly with OEMs*
Little chance of unmelted material traveling beyond the barrier section	Inherently more susceptible to plugging because less space for solid bed
Widely available in the polymer extrusion industry	Barrier screws have to be carefully tailored to melting characteristics of the polymer; as a result, barrier screws are not good general-purpose screws

*OEM is Original Equipment Manufacturer

■ 8.7 Mixing Screws

The mixing capacity of standard extruder screws is limited as discussed in Section 7.7. As a result, many modifications have been made to the standard extruder screw, in an effort to improve the mixing capacity. The number of mixing elements that have been used on extruder screws is very large. Therefore, it is not possible to discuss all mixing screws used in the industry. This discussion will be limited to the more common and important types of mixing elements. Before selecting a mixing element, it is important to determine whether distributive or dispersive mixing is required; see Section 7.7. Therefore, the mixing sections will be divided into distributive and dispersive mixing sections to indicate their preferred application.

8.7.1 Dispersive Mixing Elements

Dispersive mixing elements are used when agglomerates or droplets, such as gels, need to be broken down. This is particularly important in small or thin gauge extrusion, e. g., fiber spinning, thin film extrusion. The most common dispersive mixing section is the fluted or splined mixing section. In this mixing section, one or more barrier flights are placed along the screw such that the material has to flow over the barrier flight(s). In the barrier clearance the material is subjected to a high shear

rate; the corresponding shear stress should be large enough to break down the particles in the polymer melt. A well-known fluted mixing section is the Union Carbide (UC) mixing section invented by LeRoy [37]; see Fig. 8.66(a).

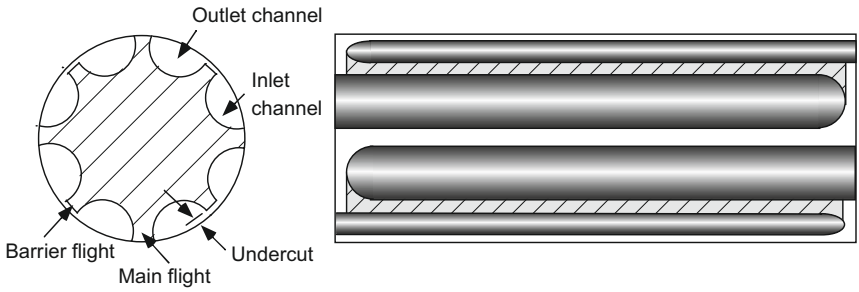


Figure 8.66(a) The LeRoy mixing section (also called Maddock or UC mixing section)

Maddock from Union Carbide published results of experiments with this mixing section [38]; since then the mixing section is often referred to as the Maddock mixing section.

The UC mixing section has longitudinal splines, i.e., a barrier flight helix angle of 90°. All material has to flow over the barrier flight because the inlet channel is closed at the end of the mixing section. Thus, all of the material is forced over the barrier flight, yielding a uniform dispersive mixing action. A drawback of this mixing section is that it is pressure consuming, i.e., it reduces the output of the extruder. Also, the longitudinal geometry with constant channel depth results in stagnating regions. Thus, the design will be less suitable with materials of limited thermal stability.

A recent version of the LeRoy/Maddock mixer is the BT mixer developed by Luker [102, 103]; see Fig. 8.66(b). In this fluted mixer, the inlet channels are open at the beginning as well as at the end of the mixer. The purpose of this arrangement is to allow material leaving the exit channels to flow back into the inlet channels. Potentially, this allows the material to experience more than one exposure to the high stress regions of the mixer. The drawback of this arrangement is that it is possible for the material to flow through the inlet channel without flowing over the barrier flight.

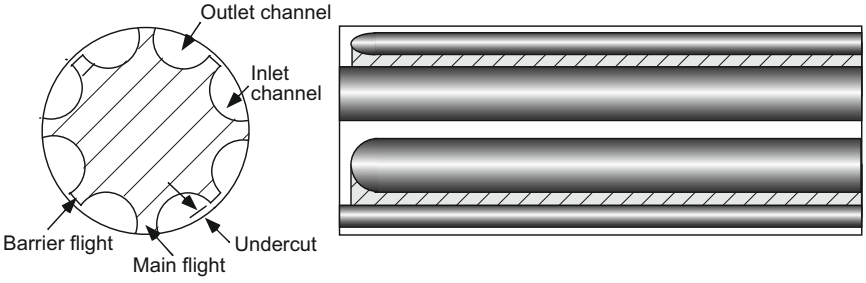


Figure 8.66(b) The BT mixer

The open inlet channel eliminates the advantage of regular fluted mixers where all of the incoming material is forced over a barrier flight. It is claimed that the BT mixer generates elongational flow; however, it is not clear how this elongational flow is generated. The best way to determine if elongational flow occurs in a mixer is to perform a full 3-D flow analysis. Full 3-D analysis of the conventional LeRoy mixer indicates that elongational flow does indeed occur in the mixer; see Section 12.4.3.4. However, the elongational flow occurs in a region with low strain rate (and thus low stresses). Unfortunately, elongational flow at low strain rate is ineffective for dispersive mixing because high stresses are required to rupture the agglomerates or droplets. There has been no report of a full 3-D flow analysis of the BT mixer and no quantitative assessment of the elongational flow in the mixer.

A more effective way to generate multiple high stress exposures is to use a fluted mixer with one or more intermediate flutes between each inlet and outlet flute. The intermediate flutes are normally closed at both ends so that all incoming material is forced over the barrier flight of the flute. An example is the CRD fluted mixer shown in Fig. 8.92, which has four intermediate flutes between each inlet and outlet flute. As a result, all material passing through the mixer is exposed to four high stress exposures as shown by the arrows in Fig. 8.92. The helical orientation of the flutes reduces the pressure drop and improves dispersive mixing. Further, the barrier flight has a wedge-shaped pushing flight flank to generate strong elongational flow for effective dispersive mixing. Different mixing flight geometries are shown in Fig. 8.82; another version of the CRD fluted mixer is shown in Fig. 8.66(c). The CRD mixer is covered by two U.S. patents [79, 80] and several international patents.

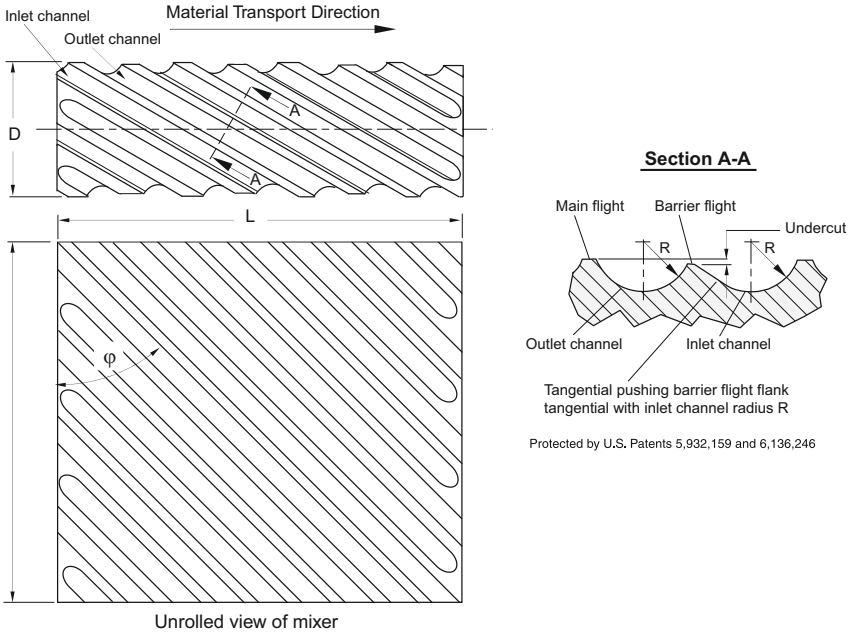


Figure 8.66(c) The CRD fluted mixer

Another fluted mixing section is the Egan mixing section invented by Gregory and Street [47]; see Fig. 8.67.

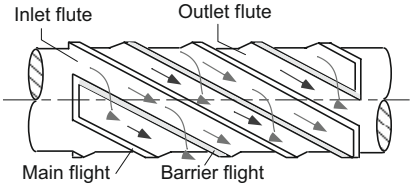


Figure 8.67
The Egan fluted mixing section

In this mixing section, the splines run in a helical direction, i.e., the barrier flight helix angle is less than 90°. The advantage of the helical splines is the fact that this enables forward drag transport in the inlet and outlet channel. As a result, the fluted mixing section with helical flutes will consume less pressure than the fluted mixing section with longitudinal flutes; see Fig. 8.75. Thus, the helically fluted mixing will reduce the extruder output to a lesser extent. In fact, if the mixing section is properly designed it can even generate pressure, causing an improvement in extruder output. Another feature of the Egan mixing section is a gradual reduction of the depth of the inlet channel, leading to zero depth at the end of the mixing section. This channel depth profile is reversed in the outlet channel. The channel depth taper reduces the chance of hang-up of material, and thus reduces the chance of degradation.

A similar mixing device was later patented by Gregory [48]. The difference between this mixing device and the Egan mixing section is a constant depth in inlet and outlet channel and a concave channel geometry. Another similar mixing section was patented by Dray [49]; see Fig. 8.68.

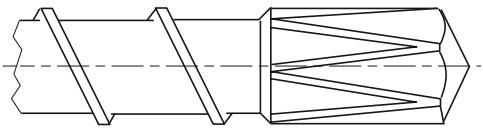


Figure 8.68
The Dray fluted mixing section

The main difference in this mixing section is that the outlet channel is open at the start of the mixing section. Thus, not all material is forced over the barrier clearance. Therefore, this mixing device will not result in a uniform shear history of the material. An extreme form of a fluted mixing section is the annular blister ring; see Fig. 8.69.

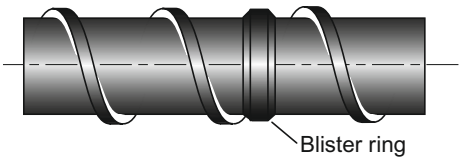


Figure 8.69
Blister ring mixing section

The annular blister ring is simply a smooth cylindrical screw section with a small radial clearance. All the material has to pass through this clearance to exit from the extruder. Since no positive drag transport takes place over the barrier clearance, the

pressure drop over the blister ring will be high compared to other fluted mixing sections. A blister ring with a small barrier clearance will generally cause a significant reduction in output. The pressure drop over the blister ring can be written by using the expressions in Table 7.1:

$$\Delta P = \frac{2\,m\,\Delta L}{\delta}\left[\frac{2\dot{V}\,(s+2)}{\pi\,D\,\delta^2}\right]^n \tag{8.109}$$

This expression is for a power law fluid and is valid if the effect of the screw rotation on the melt viscosity can be neglected. In reality, however, the effective viscosity in the clearance will be reduced as a result of the rotation of the screw. The shear stress is composed of a shear stress in the tangential direction and a shear stress in the axial direction. The tangential shear stress can be determined by evaluating the stress at the center of the channel where the axial shear stress is zero. This yields the following expression for the shear stress in the tangential direction:

$$\tau_t = m\left(\frac{\pi\,D\,N}{\delta}\right)^n \tag{8.110}$$

The tangential shear stress is constant over the depth of the channel. The axial shear stress can be related to the axial pressure gradient by a simple force balance; this yields:

$$\tau_a = y\frac{\Delta P}{\Delta L} \tag{8.111}$$

The total shear stress is obtained by vectorial addition of the axial and tangential shear stress:

$$\tau = \left[m^2\left(\frac{\pi\,D\,N}{\delta}\right)^{2n} + \left(y\frac{\Delta P}{\Delta L}\right)^2\right]^{1/2} \tag{8.112}$$

The axial velocity gradient can be determined from:

$$\frac{dv}{dy} = \left(\frac{\tau}{m}\right)^s \frac{\tau_a}{\tau} = \frac{1}{m^s}\tau_a\tau^{s-1} \tag{8.113}$$

The axial velocity is obtained by integration of the axial velocity gradient:

$$v = \int\left(\frac{dv}{dy}\right)dy + C \tag{8.114}$$

And the volumetric flow rate is obtained by integration of the axial velocity:

$$\dot{V} = \int_0^{\delta/2} 2\pi\,D\,v\,dy \tag{8.115}$$

Closed form solutions of Eqs. 8.114 and 8.115 are only possible for a few specific values of the power law index n, namely those for which (1–n)/2n is an integer. Worth [50] derived a solution for a power law index value n = 1/3. This is a useful case because many of the high-volume commodity polymers have a power law index close to 1/3; see also Table 6.1. When n = 1/3, the throughput as a function of pressure can be written as:

$$\dot{V} = \frac{\pi D \Delta P}{m^3 \Delta L}\left[\frac{\delta^3 \tau_t^2}{12} + \frac{\delta^5}{80}\left(\frac{\Delta P}{\Delta L}\right)^2\right] \tag{8.116}$$

The pressure drop now has to be found by solving a cubic equation. This solution can be written as:

$$\Delta P = (q + r)^{1/3} + (q - r)^{1/3} \tag{8.117}$$

where:

$$q = \frac{40 m^3 \Delta L^3 \dot{V}}{\pi D \delta^5} \tag{8.118a}$$

$$p = \frac{-20 \tau_t^2 \Delta L^2}{9\delta^2} \tag{8.118b}$$

$$r = (q^2 - p^3)^{1/2} \tag{8.118c}$$

A comparison of the pressure drop predicted with Eq. 8.118 to the ΔP predicted with Eq. 8.109 is shown in Fig. 8.70.

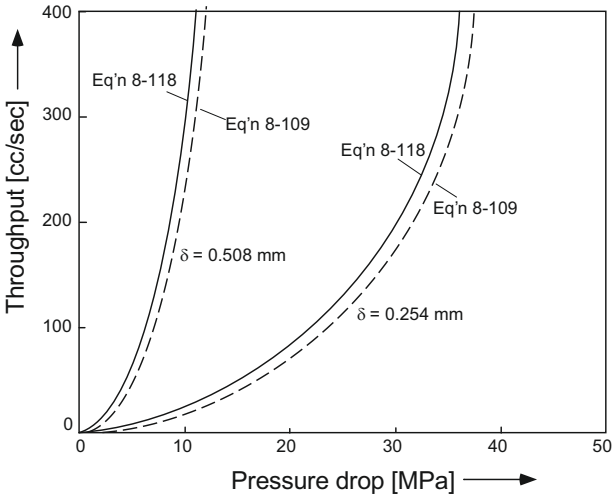


Figure 8.70
Pressure drop over blister ring

The prediction is for a 114-mm (4.5 in) extruder running at 100 rpm with a blister length of 12.7 mm (0.5 in) and a flow rate of 131 cm^3/s (8 in^3/s). The reduction of the pressure drop as a result of the screw rotation is about 15%. This indicates that the simple Eq. 8.109 gives a reasonably accurate prediction of the pressure drop.

The pressure drop in a fluted mixing section can be calculated for a Newtonian fluid. The first theoretical analysis was performed by Tadmor and Klein [51]. Their final equation for the pressure drop contains five dimensionless numbers, which makes determination of the effect of certain design variables rather indirect. A non-isothermal and non-Newtonian analysis was performed by Lindt et al. [52]. This analysis requires numerical techniques to solve the equations. Therefore, this analysis can only be used if one develops the computer software to perform the calculations. A simpler analysis was made by the author [53], leading to closed form analytical solutions from which the effect of the most important design variables can be easily evaluated.

To determine the pressure drop as a function of flow rate, one pair of inlet and outlet channels will be examined in detail; see Fig. 8.71.

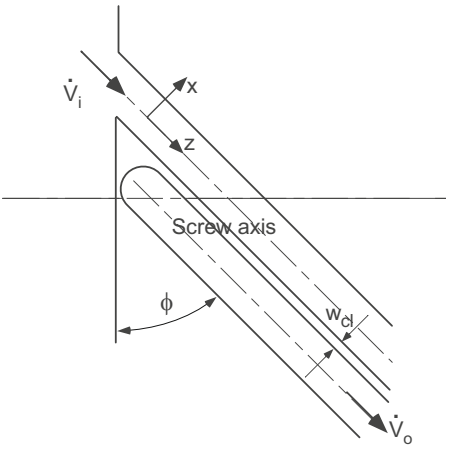


Figure 8.71
Inlet and outlet of a fluted mixer

The volumetric flow rate at the entrance to the inlet channel is $\dot{V}_i(o)$, where the subscript i refers to the inlet channel. $\dot{V}_i(o)$ is the total volumetric output of the extruder divided by the number of inlet channels. The flow rate through the inlet channel decreases in the down-channel direction as a result of leakage over the barrier flight. At the same time there is a corresponding increase in the flow rate through the outlet channel. If the fluid is considered Newtonian and isothermal, the flow rate in the inlet channel as a function of down-channel distance z can be written as:

$$\dot{V}_i(z) = \frac{1}{2} F_d W H (1 - 2\delta/H) v_b \cos\varphi - \frac{1}{12\mu} F_p W H^3 \frac{dP_i}{dz} \tag{8.119}$$

where δ is the radial clearance of the barrier flight.

Equation 8.119 is a simplified form of the equations presented in Section 7.4.1.2. The radial clearance of the non-barrier flight is taken to be zero. The initial pressure gradient G_1 in the inlet channel can be obtained from:

$$G_1 = \frac{dP_i(o)}{dz} = \frac{6\mu F_d (1-2\delta/H)^2 v_b \cos\varphi}{F_p H^2} - \frac{12\mu \dot{V}_i(o)}{F_p W H^3} \tag{8.120}$$

The flow rate in the exit or outlet channel $\dot{V}_e(z)$ can be written as:

$$\dot{V}_e(z) = \frac{1}{2} F_d W H v_b \cos\varphi - \frac{1}{12\mu} F_p W H^3 \frac{dP_e}{dz} \tag{8.121}$$

The subscript e refers to the exit channel. Considering that the flow rate at the exit of the outlet channel $\dot{V}_e(z_m)$ equals the flow rate at the entry to the inlet channel $\dot{V}_i(o)$, the pressure gradient at the exit of the outer channel G_2 can be written as:

$$G_2 = \frac{6\mu F_d v_b \cos\varphi}{F_p H^2} - \frac{12\mu \dot{V}_i(o)}{F_p W H^3} \tag{8.122}$$

The leakage flow from the inlet channel to the outlet channel $\dot{V}_1$ is a combination of drag flow and pressure flow. The leakage flow per unit down-channel distance $\dot{V}_1'$ can be written as:

$$\dot{V}_1' = \frac{1}{2} v_b \delta \sin\varphi + \frac{\delta^3}{12\mu_{c1} w_{c1}} (P_i - P_e) \tag{8.123}$$

where w_{c1} is the perpendicular barrier flight width and μ_{c1} the polymer melt viscosity in the clearance.

From a mass balance, it follows that the local flow rate in the exit channel equals the total flow rate minus the local flow rate in the inlet channel:

$$\dot{V}_e(z) = \dot{V}_i(o) - \dot{V}_i(z) \tag{8.124}$$

This equation leads to the following relationship between the two pressure gradients:

$$\frac{dP_i(z)}{dz} + \frac{dP_e(z)}{dz} = \frac{12\mu}{F_p W H^3} \left[F_d W H (1-\delta/H) v_b \cos\varphi - \dot{V}_i(o) \right] \tag{8.125}$$

Equation 8.125 is valid when the local channel width W and channel depth H of the inlet channel are the same as those of the outlet channel. If the dimensions of both channels do not change with down-channel distance, the sum of the pressure gradients will be constant along the length of the mixing section. In this case, Eq. 8.125 can be written as:

$$\frac{dP_i(z)}{dz} + \frac{dP_e(z)}{dz} = -A_1 \tag{8.126}$$

Thus, the pressure in the exit channel can be related to the pressure in the inlet channel by:

$$P_e = -A_1 z + A_2 - P_i \tag{8.127}$$

where:

$$A_1 = \frac{12\,\mu}{F_p W H^3}\left[\dot{V}_i(o) - F_d W H (1-\delta/H)\, v_b \cos\varphi\right] \tag{8.127a}$$

Another important relationship can be obtained by considering that the local change in flow rate of the inlet channel over an incremental increase in down-channel distance equals the local leakage flow:

$$\frac{d\dot{V}_i}{dz} = -\dot{V}_l' \tag{8.128}$$

If the channel dimensions do not change in the down-channel direction, Eq. 8.128 can be written as:

$$\frac{F_p W H^3}{12\,\mu}\frac{d^2 P_i}{dz^2} = \frac{1}{2} v_b\, \delta \sin\varphi + \frac{\delta^3}{12\,\mu_{cl}\, w_{cl}}(P_i - P_e) \tag{8.129}$$

With Eq. 8.127, the differential equation can be written as:

$$\frac{d^2 P_i}{dz^2} - B_1 P_i = \frac{1}{2} A_1 B_1 z + \frac{6\,\mu v_b\, \delta \sin\varphi}{F_p W H^3} - \frac{1}{2} A_2 B_1 \tag{8.130}$$

where:

$$B_1 = \frac{2\,\mu\,\delta^3}{F_p W H^3\, \mu_{cl}\, w_{cl}} \tag{8.130a}$$

Equation 8.130 is a non-homogeneous equation of the second order. The solution to the homogeneous equation is:

$$P_i^* = C_1 \exp(-B_2 z) + C_2 \exp(B_2 z) \tag{8.131}$$

where:

$$B_2 = \sqrt{B_1} \tag{8.131a}$$

An obvious particular solution is:

$$P_i^{**} = -\frac{1}{2} A_1 z - \frac{3\mu_{cl}\, w_{cl}\, v_b \sin\varphi}{\delta^2} + \frac{1}{2} A_2 \tag{8.132}$$

The general solution is the sum of the solution to the homogeneous equation plus the particular solution. Thus, the pressure profile in the inlet channel can be described by:

$$P_i = C_1 \exp(-B_2 z) + C_2 \exp(B_2 z) - \frac{1}{2} A_1 z - \frac{3\mu_{cl}\, w_{cl}\, v_b \sin\varphi}{\delta^2} + \frac{A_2}{2} \tag{8.133}$$

With Eq. 8.127, the pressure profile in the outlet channel can be written as:

$$P_e = C_1 \exp(-B_2 z) - C_2 \exp(B_2 z) - \frac{1}{2} A_1 z + \frac{3\mu_{cl}\, w_{cl}\, v_b \sin\varphi}{\delta^2} + \frac{A_2}{2} \tag{8.134}$$

Two boundary conditions are necessary to evaluate constants C_1 and C_2. The following boundary conditions can be used:

$$\frac{dP_i(o)}{dz} \cong \frac{dP_e(z_m)}{dz} \cong \frac{6\mu F_d (1-\delta/H)\, v_b \cos\varphi}{F_p H^2} - \frac{12\mu \dot{V}_i(o)}{F_p W H^3} \tag{8.135}$$

This results in the following expressions for C_1 and C_2:

$$C_1 = \frac{-6\mu \dot{V}_i(o)}{F_p W B_2 H^3 [\exp(-B_2 z_m) - 1]} \tag{8.136}$$

$$C_2 = \frac{-6\mu \dot{V}_i(o)}{F_p W B_2 H^3 [1 - \exp(B_2 z_m)]} \tag{8.137}$$

Figure 8.72 shows the pressure profile in the inlet channel and outlet channel for a 114-mm (4.5-in) extruder running at 100 rpm with a throughput of 164 cm³/s (10 in³/s).

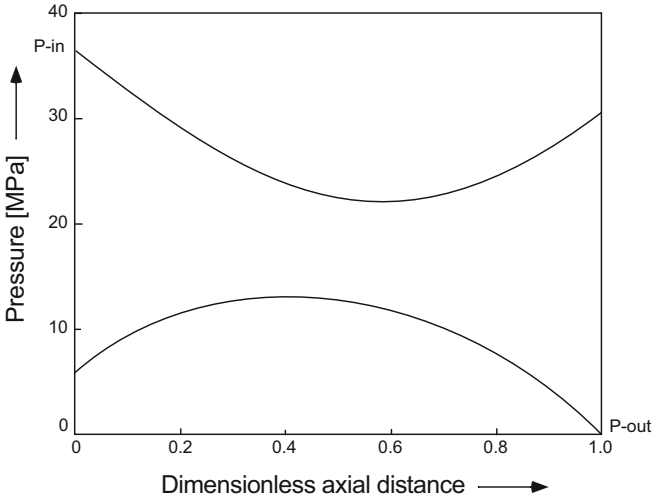


Figure 8.72
Pressure profiles in inlet and outlet channels

The length of the mixing section is 2 D, the barrier clearance is 0.5 mm (0.020 in), the helix angle is 45°, and the number of inlet channels is 3. The local viscosity is evaluated with the power law equation by using the Couette shear rate; the consistency index is 13,800 Pa · s^n (2 psi·s^n) and the power law index is 0.5. The pressure in the inlet channel reduces initially but later starts to increase again. This indicates some degree of pressure generating capability of the inlet channel. In the outlet channel, the pressure rises initially and drops in the later portion of the channel. Thus, both the inlet channel and outlet channel have some pressure generating capability. This is primarily achieved by the helical orientation of the flutes.

The importance of the helix angle is shown in Fig. 8.73.

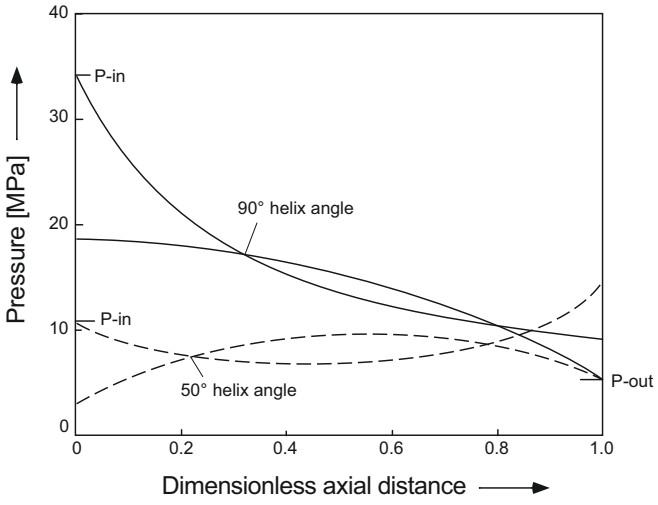


Figure 8.73
Pressure profiles with two helix angles

Two sets of pressure profiles are shown, one for a mixing section with a 90° helix angle and one for a mixing section with a 50° helix angle. In this case, the barrier clearance is 0.635 mm (0.025 in) and the throughput is 131 cm^3/s (8 in^3/s). The profiles are determined such that the final pressure has the same value (5 MPa = 725 psi). It is evident that the helix angle has a strong effect on the pressure profiles and the total pressure drop. There is a significant pressure generation in the inlet channel and outlet channel of the helical mixing section, resulting in a relatively small total pressure drop. On the other hand, there is no pressure generating capacity in the axially oriented mixing section as evidenced by the monotonic drop in pressure in both the inlet and outlet channel. This results in a rather large total pressure drop, about three times as high as the helically oriented mixing section!

The total pressure drop over the mixing section ΔP_m is simply:

$$\Delta P_m = P_i(o) - P_e(z_m) \tag{8.138}$$

With Eqs. 8.133 through 8.137, this results in the following expression for the pressure drop over the mixing section:

$$\Delta P_m = \frac{2T[1+\exp(B_2 z_m)]}{1-\exp(B_2 z_m)} - \frac{6\mu_{cl}\, w_{cl}\, v_b \sin\varphi}{\delta^2} + \frac{A_1\, z_m}{2} \tag{8.139}$$

where:

$$T = \frac{-6\mu \dot{V}_i(o)}{F_p W H^3 B_2} \tag{8.139a}$$

When $B_2 z_m$ ranges between 0 and 1, the following approximation can be made:

$$\frac{1+\exp(B_2 z_m)}{1-\exp(B_2 z_m)} \cong \frac{-2}{B_2\, z_m} \tag{8.140}$$

The total pressure drop can now be written as the sum of two terms:

$$\Delta P_m \cong \Delta P_{cl} + \Delta P_{ch} \tag{8.141}$$

The pressure drop in the clearance ΔP_{cl} is given by the first two terms on the right-hand side of Eq. 8.139. The pressure drop inlet and outlet channel ΔP_{ch} is the last term of Eq. 8.139.

The first term ΔP_{cl} is the pressure drop caused by the clearance. When $B_2 z_m$ is less than unity, Eq. 8.140 can be used to express ΔP_{cl} as:

$$\Delta P_{cl} = \frac{12\mu_{cl}\, w_{cl}}{z_m\, \delta^3}\left[\dot{V}_i(o) - \frac{\delta L_m v_b}{2}\right] \tag{8.142a}$$

When $B_2 z_m$ is larger than unity, ΔP_{cl} can be expressed as:

$$\Delta P_{cl} = \frac{12\mu_{cl}\, w_{cl}}{z_m\, \delta^3}\left[\left(\frac{3}{4} + 0.3\ B_2\, z_m\right)\dot{V}_i(o) - \frac{\delta L_m v_b}{2}\right] \tag{8.142b}$$

The second term ΔP_{ch} is the pressure drop in the inlet and outlet channel; this can be written as:

$$\Delta P_{ch} = \frac{6\mu z_m}{F_p W H^3}\left[\dot{V}_i(o) - F_d W (H-\delta) v_b \cos\varphi\right] \tag{8.143}$$

The first term ΔP_{cl} is inversely proportional to the cube of the barrier clearance. Thus, when the barrier clearance is small, the pressure drop over the clearance will increase very rapidly and will be the major component of the total pressure drop. The pressure drop over the clearance ΔP_{cl} can be made zero by making sure that the

drag flow rate over the barrier clearance equals the flow rate at the entrance to the inlet channel. Thus, the mixing section should be designed such that:

$$\frac{1}{2}\delta L_m v_b \geq \dot{V}_i(o) \tag{8.144}$$

If the flow rate through the mixing section is assumed to be about two-thirds of the drag flow rate of the preceding screw section and the axial length is about two diameters ($L_m \cong D$), then Eq. 8.144 can be simplified to the following form:

$$\delta \geq C\frac{D}{p} \tag{8.145}$$

D is the screw diameter, p is the number of inlet channels, and the constant C in many cases is about 0.01. When the pressure drop over the clearance is zero, the total pressure drop becomes simply:

$$\Delta P_m = \Delta P_{ch} = \frac{6\mu z_m}{F_p W H^3}\left[\dot{V}_i(o) - F_d W (H-\delta) v_b \cos\varphi\right] \tag{8.146}$$

The pressure drop over the channel reaches its maximum value when the helix angle is 90°. Thus, this corresponds to the most unfavorable geometry because it will result in the largest drop in output. If the channel depth and helix angle are optimized simultaneously, the pressure drop in the channel will reach a minimum when the helix angle is 52.24° [63]. The corresponding optimum channel depth is $H^* = 0.314\dot{V}/(F_p D^2 N)$.

The various factors that influence the pressure drop over the mixing section can now be easily analyzed. The pressure drop increases proportionally with the flow rate through the mixing section, as shown in Fig. 8.74.

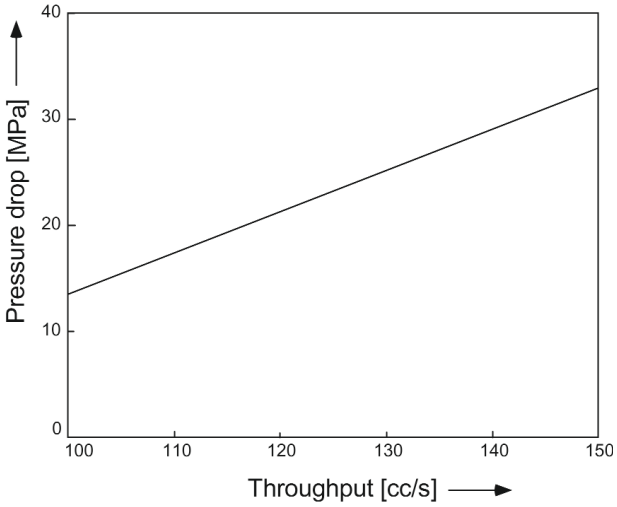


Figure 8.74
Pressure drop versus flow rate

Therefore, the design of the mixing section has to be matched to the preceding screw section in order to avoid excessive pressure drop. The effect of the helix angle is shown in Fig. 8.75.

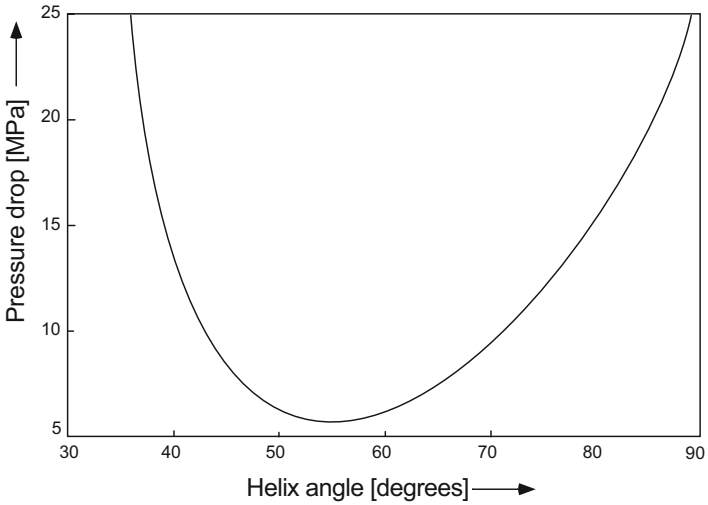


Figure 8.75 Pressure drop versus helix angle

As discussed earlier, the helix angle has a strong effect on the pressure drop. The minimum pressure drop occurs at a helix angle between 50 and 60°. Below a helix angle of 50° and above 60° the pressure drop increases quite rapidly. Thus, the proper value of the helix angle is around 50 to 60°. The optimum helix angle for shear thinning fluids is less than 50°.

The effect of the barrier flight width is shown in Fig. 8.76.

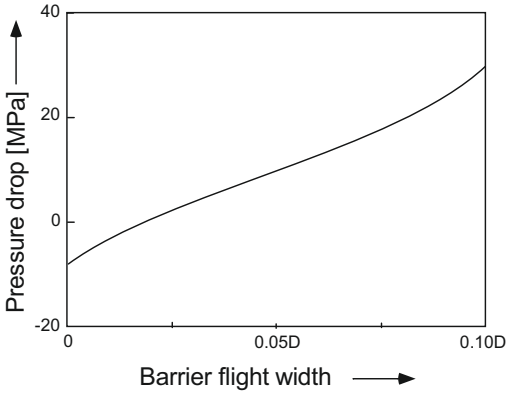


Figure 8.76
Pressure drop versus barrier flight width

The pressure drop increases in an approximately proportional fashion with the barrier flight width. This is true if the pressure drop over the clearance is positive ($\Delta P_{cl} > 0$). When the pressure drop over the clearance is made zero ($\Delta P_{cl} = 0$), the width of

the barrier flight no longer affects the total pressure drop (see Eq. 8.146). In all cases, however, the width of the barrier flight will strongly influence the power consumption and the viscous heat generation in the material.

The effect of the barrier clearance is shown in Fig. 8.77.

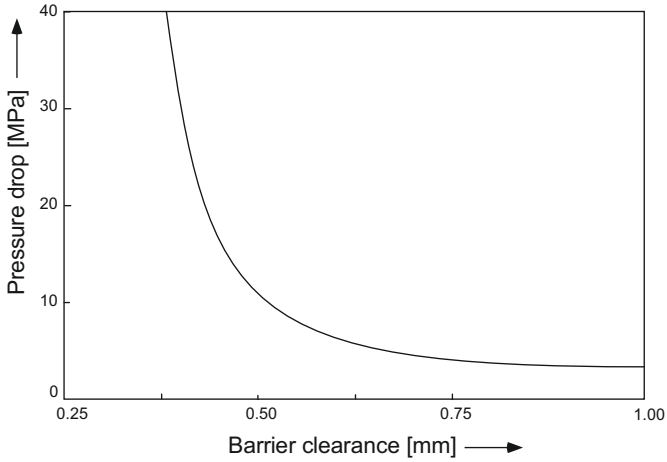


Figure 8.77 Pressure drop versus barrier flight clearance

When the clearance is less than about 1/2 mm (0.020 in), the pressure drop increases quite dramatically. When the clearance is larger than about 3/4 mm (0.030 in), the effect of the clearance becomes quite small. In fact, when the clearance is larger than 1 mm (0.040 in), the pressure drop starts to increase because of the reduced drag flow in the inlet channel. It should be noted, however, that changes in the barrier flight width and barrier clearance directly affect the dispersive mixing capability of the mixing section.

Dispersion of agglomerates or gels requires the application of a certain minimum stress to break down the particles. The minimum stress level depends on the nature of the particle as discussed by Martin [54] and Tadmor et al. [55]. For carbon black, the critical stress level as determined by Martin [54] was found to be around 60 kPa (9 psi). In addition to a minimum stress, there is also a minimum high stress exposure time as discussed by Martin [54]. When the duration of high stress is below a minimum exposure time, no dispersion will occur even at very high stress levels. For carbon black, Martin [54] found the minimum exposure time to be about 0.2 s. This means that the width of the barrier flight should be large enough so that the residence time of the polymer in the clearance exceeds the minimum exposure time t_{min}. Therefore, the width of the barrier clearance should be:

$$w_{cl} > \frac{\pi D N \sin\varphi}{120} t_{min} \tag{8.147}$$

where N is expressed in revolutions per minute.

If the critical stress level is τ_{min}, the barrier clearance should be:

$$\delta < \frac{\pi D N}{60}\left(\frac{m}{\tau_{min}}\right)^{\frac{1}{n}} \tag{8.148}$$

Thus, the barrier flight width w_{cl} and the barrier clearance δ have to be designed for both pressure drop and dispersive mixing capacity.

The effect of the degree of non-Newtonian behavior is shown in Fig. 8.78.

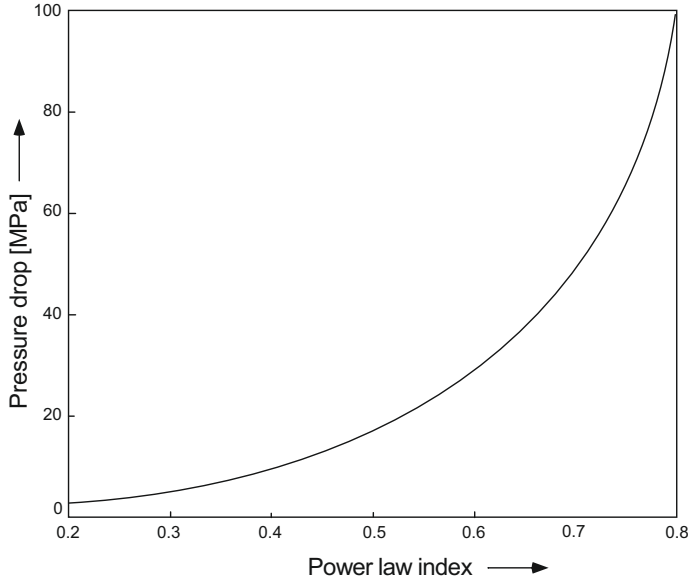


Figure 8.78 Pressure drop versus power law index

The effect of the pseudo-plasticity is determined by evaluating the local viscosity with the power law equation:

$$\mu = m\,\dot{\gamma}^{n-1} \tag{8.149}$$

where m is the consistency index, $\dot{\gamma}$ the local shear rate, and n the power law index (see also Eq. 6.23). If the local shear rate is approximated by the Couette shear rate, the viscosity in the clearance becomes:

$$\mu_{cl} = m\left(\frac{\pi D N}{\delta}\right)^{n-1} \tag{8.150}$$

Similarly, the viscosity in the channel:

$$\mu = m\left(\frac{\pi D N}{H}\right)^{n-1} \tag{8.151}$$

As the power law index increases, the pressure drop increases quite substantially. Therefore, materials with relatively Newtonian flow characteristics can be expected to cause higher pressure drops than strongly non-Newtonian materials. For example, a material like LLDPE will give a much higher pressure drop than regular LDPE of the same melt index because of the larger power law index of LLDPE [4, 5].

The effect of the axial length of the mixing section is shown in Fig. 8.79(a).

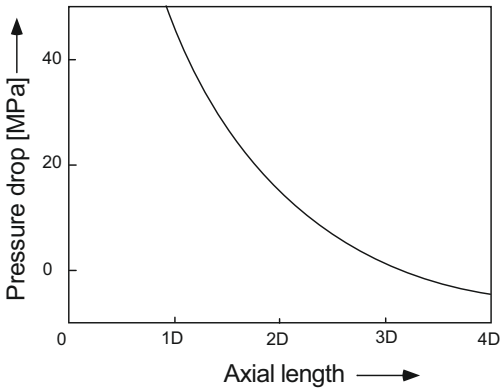


Figure 8.79(a)
Pressure drop versus axial length

The pressure drop reduces substantially when the axial length is increased. Axial lengths of less than 2 D generally create excessive pressure drops.

Finally, the effect of the number of inlet channels is shown in Fig. 8.79(b).

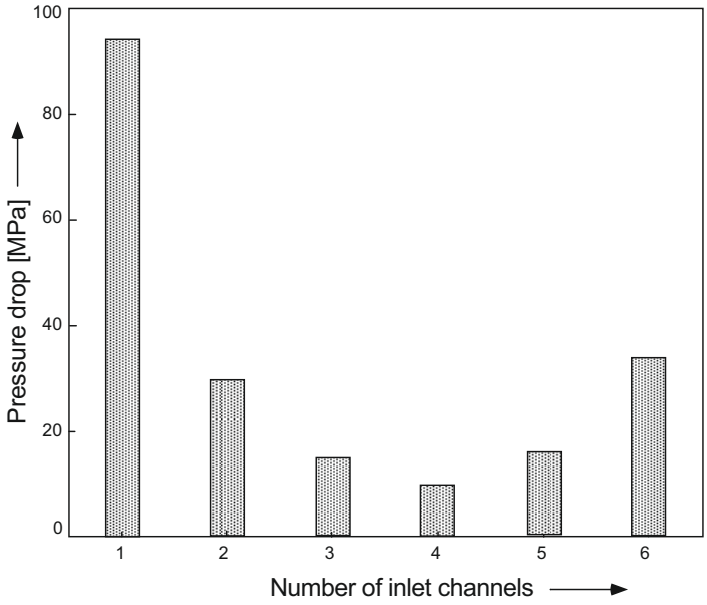


Figure 8.79(b) Pressure drop versus the number of inlet channels

The pressure drop initially reduces with the number of inlet channels but later increases. Thus, there is an optimum number of inlet channels that results in the lowest pressure drop across the mixing section. The optimum number of inlet channels is generally about three or four.

The most important design features for a fluted mixing section can be summarized as follows. The helix angle should be about 50 to 60°, the clearance should not be smaller than about 1/2 mm (0.020 in), and the axial length should not be less than 2 D.

Further, the number of inlet channels should be three or four. The chance of hold-up of material can be reduced by tapering the channel depth. The chance of hold-up can be further reduced by tapering the channel width. This leads to the geometry shown in Fig. 8.80.

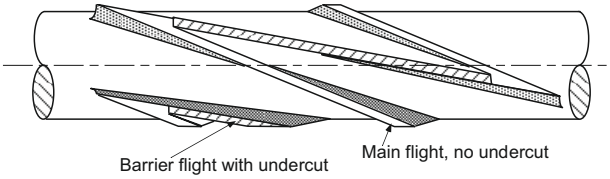


Figure 8.80
Z-shaped fluted mixing section

This geometry has the additional advantage that the pressure drop at the inlet to the mixing section is substantially reduced. This entrance pressure drop has not been taken into account in the analysis. However, it is obvious that the entrance pressure drop in conventional fluted mixing sections can be substantial because the material is forced from the wide screw channel into a number of narrow inlet channels.

Obviously, all barrier-type extruder screws (see Section 8.6.2) impart some degree of dispersive mixing to the polymer because all the polymer has to flow over the barrier flight to leave the extruder. Thus, every polymer element is exposed to a brief but relatively intensive shearing in the barrier clearance. Simulation of fluted mixers is discussed in Section 12.4.3.4; see also Fig. 12.43 and Fig. 12.44.

Dispersive mixing also occurs in the double wave mixing screw; see Fig. 8.81.

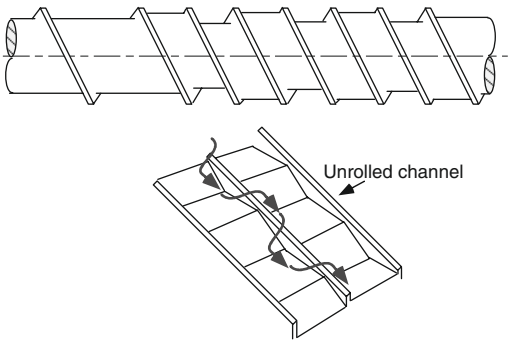


Figure 8.81
The double wave screw

This screw was developed by Kruder of HPM [39] and is basically an extension of the single channel wave screw [40]. Polymer is forced over the center barrier flight by a cyclic variation of the channel depth. When one channel is increasing in depth, the other is reducing. When the first channel reaches its maximum depth, the other channel reaches its minimum depth. Then the first channel starts to reduce in depth and the other channel starts to increase in depth. This process is repeated many times. This screw design improves mixing performance, but the screw is relatively expensive to manufacture.

8.7.1.1 The CRD Mixer

As discussed in Section 7.7.3, dispersive mixing in shear flow is substantially less efficient than in elongational flow. Important requirements for dispersive mixing elements were formulated by Rauwendaal [66]; they are:

1. The mixing section should have a high stress region, HSR, where the material is subjected to high, preferably elongational, stresses to break down agglomerates and droplets.
2. The HSR should be designed such that the exposure to high shear stresses occurs only for a short time to avoid excessive power consumption and melt temperature rise.
3. All fluid elements should experience the same high stress level multiple times to achieve uniform and efficient mixing.

If we analyze current dispersive mixers based on these requirements, we find that most current dispersive mixers only meet these requirements partially.

The most commonly used dispersive mixer in single screw extruders is the LeRoy mixer, popularized by Maddock. There are several versions of the fluted mixing section [66] commercially available, with the helical LeRoy being a popular mixing section because of its low pressure drop and good streamlining. Like the LeRoy mixer, most current dispersive mixers rely on shear stresses to achieve breakdown of the agglomerates. However, because elongational flow has open streamlines and generates higher stresses, it is more effective in breaking down agglomerates and droplets [67]. Therefore, elongational stresses are preferred in a dispersive mixer. A new dispersive mixer based on the generation of elongational flow was developed at the NRC in Montreal, Canada [68]. This extensional flow mixer (EFM) is placed at the discharge end of an extruder, and the flow through the mixer is pressure driven because the EFM is a static mixer.

In most current (shear flow) dispersive mixers, the material passes through the HSR only once, thus severely limiting the level of dispersion that can be achieved. To achieve a fine level of dispersion it is generally necessary for the agglomerates or droplets to be broken down several times. Therefore, a single pass through a high stress region is not sufficient in most cases and multiple passes through a high

stress region are critical. If the agglomerate is of the order of 1000 μm and needs to be reduced to the 1 μm level, it will take about 10 rupture events if we assume that each rupture event reduces the agglomerate size by 50%. It should be noted that drop breakup does not always reduce the drop size by 50%. The most efficient mechanism for dispersing liquids is to deform droplets into extended threads at high capillary number and let them disintegrate into smaller droplets. The droplets that form can be much smaller than the initial droplet size—formation of over 10,000 droplets from a single drop has been reported.

If each pass through a high stress region produces one rupture, then it becomes clear that a dispersive mixer that exposes the polymer melt to only one high stress exposure is not likely to achieve a fine level of dispersion. This is an important reason why current dispersive mixers in single screw extruders generally do not work well. The lack of strong elongational flow and multiple passes through the HSRs explain why current dispersive mixers for single screw extruders have limited dispersive mixing capability.

With the requirements formulated above, new geometries have been developed that substantially improve dispersive mixing; these mixers are protected by U.S. and international patents [79, 80]. These mixers, called CRD mixers, can be incorporated along the extruder screw. As stated earlier, the key to the enhanced mixing efficiency is the generation of elongational flow in the high stress regions and achieving multiple passes of all fluid elements through the HSRs.

Elongational flow is not easily achieved in screw extruders. It is generated most efficiently by modifying the leading flight flanks of a mixing section such that the space between the flank and the barrel becomes wedge shaped. Such geometries create lobal mixing and are used in twin screw extruders [69]. This can be done by either slanting the leading flight flank or by using a curved flight flank geometry as shown in Fig. 8.82.

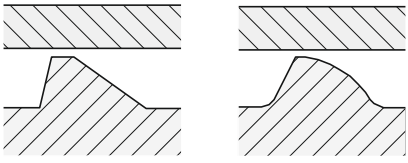


Figure 8.82
Flight geometries to create elongational flow (the arrows indicate the movement of the screw flight relative to the barrel)

Multiple passes through the HSRs can be achieved by using a multi-flighted geometry combined with a generous flight clearance. A possible geometry is shown in Fig. 8.83.

In order to achieve multiple passes through the HSRs, they should be designed such that significant flow takes place through them. This issue was studied by Tadmor and Manas-Zloczower [70]. Substantial flow through the HSR can be achieved by

increasing the flight clearance. However, this is only part of the story because without randomization of the polymer melt, increasing the flight clearance will only result in mixing of the outer re-circulating region [66]. Another problem with a large flight clearance is that it leaves a thick stagnant layer of polymer melt on the barrel surface. Using at least one wiping flight in addition to the mixing flights can circumvent this problem. One version of the CRD mixer is shown in Fig. 8.83.

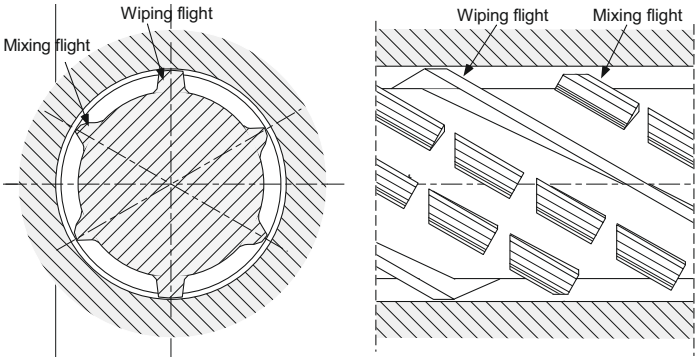


Figure 8.83 Six-flighted CRD mixer with two continuous wiping flights and four slotted mixing flights

Instead of incorporating separate wiping and conveying flights, it is possible to use one or more flights that incorporate wiping and mixing segments along their length. A possible geometry is shown in Fig. 8.84. Complete barrel wiping can be achieved by making sure that at least one wiping flight segment is present at every axial position along the mixer.

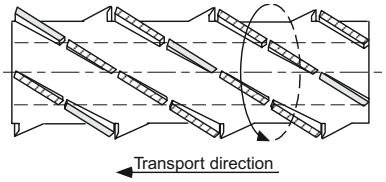


Figure 8.84
Four-flighted CRD mixer with wiping flight segments followed by three mixing flight segments

By intentionally incorporating distributive mixing in the dispersive mixer, randomization of the fluid elements can be achieved. This gives each fluid element equal chance to experience the dispersive lobal mixing action. Without this, only fluid elements in the outer re-circulating region (shell) would participate in the dispersive mixing process [66, 71]. Slotted flight geometries have proven to be quite effective for distributive mixing [72]. The helix angle of the mixing flights can be positive, negative, and even zero. It is possible to use elements with 90° helix angle and stagger the elements to achieve forward or rearward conveying, similar to kneading blocks in co-rotating twin screw extruders. The difference is that the dispersion disks can be designed to achieve maximum dispersion without the geometric con-

straints associated with self-wiping action [66]. An example of a collection of staggered dispersion disks is shown in Fig. 8.85.

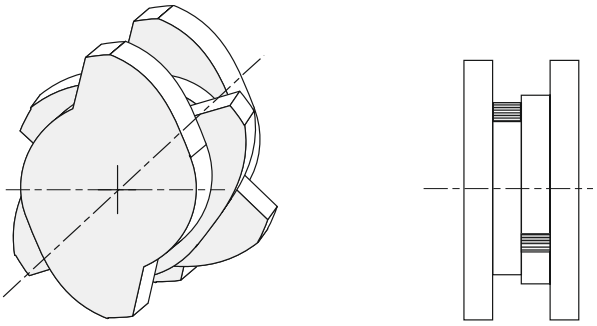


Figure 8.85
Staggered dispersion disks

The mixer should be designed such that all fluid elements are exposed to a minimum number of passes through the high stress region. This requires a high enough flow rate through the high stress regions and efficient distributive mixing. Determination of the appropriate clearance of the mixing flights is discussed in the next section.

8.7.1.1.1 Determining Flight Clearance with Passage Distribution Function

According to Tadmor and Manas-Zloczower [70] the passage distribution function can be written as:

$$G_k = \frac{\lambda^k e^{-\lambda}}{k!} \tag{8.152}$$

where k is the number of passes through the clearance, and the dimensionless time $\lambda = t_r/\bar{t}$ is the ratio of the residence time t_r and the mean residence time $\bar{t}$ of the control volume. The residence time for a Newtonian fluid can be approximated as follows:

$$t_r = \frac{2z}{v_{bz}(1-r)} \tag{8.153}$$

where z is the helical length of the screw section considered, v_{bz} the down-channel barrel velocity, and r the throttle ratio (pressure flow rate divided by drag flow rate). The mean residence time is the ratio of the control volume WHΔz to the volumetric leakage flow rate over the flight; it can be determined from:

$$\bar{t} = \frac{2W\,H}{\delta\, v_{bx}\left(1+\frac{W}{w_f}\frac{\delta^2}{H^2}\right)} \tag{8.154}$$

where W is the channel width, H the channel depth, δ the radial flight clearance, v_{bx} the cross-channel barrel velocity, and w_f the flight width. The dimensionless time can be written as:

$$\lambda = \frac{L\,\delta\left(1+\frac{W}{w_f}\frac{\delta^2}{H^2}\right)}{W\,H\,(1-r)\cos\varphi} \tag{8.155}$$

where L is the axial length corresponding to down-channel distance z. The fraction of the fluid experiencing zero passes through the clearance is:

$$G_0 = e^{-\lambda} \tag{8.156}$$

The G_0 fraction is a very important characteristic of an open design type mixer. It should be low to ensure that most of the fluid experiences at least one or more passes through the clearance. In single screw extruders with a simple conveying screw the λ value is typically about 0.1. This corresponds to a G_0 fraction of around 0.9. In this case, most of the fluid passes through the extruder without ever passing through the clearance. The passage distribution function for this case is shown in Fig. 8.86(a).

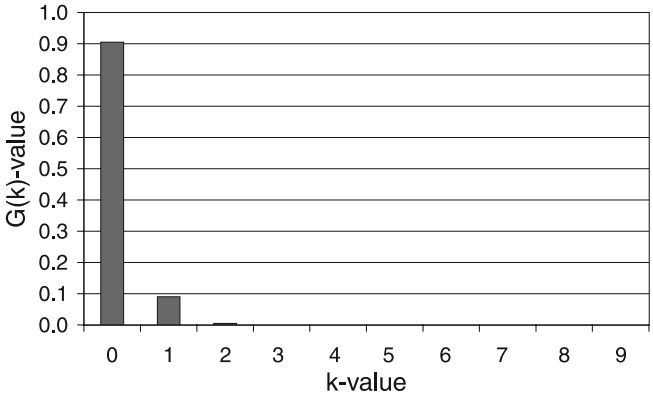


Figure 8.86(a)
The passage distribution function for λ = 0.1

We can use the expressions above to determine the minimum λ value that will yield a G_0 less than 0.01, meaning that less than 1% of the fluid will not pass through the clearance at all. This is achieved when the dimensionless time $\lambda > 4.6$. For certain values of L, H, W, r, φ, and w_f we can then determine how large the flight clearance δ has to be to make $\lambda > 4.6$ or $G_0 < 0.01$. The passage distribution function for $\lambda = 4.6$ is shown in Fig. 8.86(b).

The distribution at $\lambda = 4.6$ is quite different from that at $\lambda = 0.1$. With $\lambda = 4.6$, the G_0 fraction is quite low and most of the fluid experiences four passes through the HSR. The value G_4 is about 0.19; this means that about 19% of the fluid passes through the HSR four times.

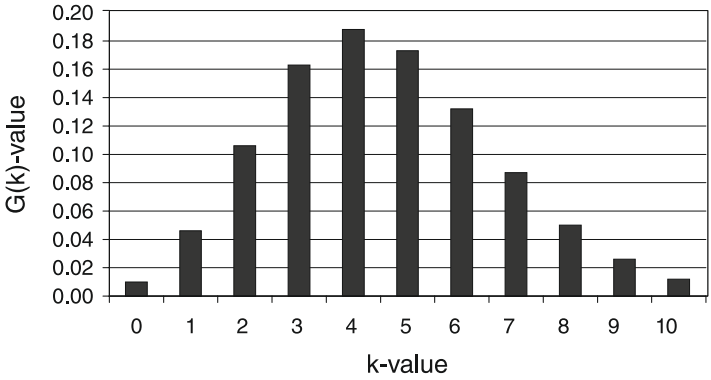


Figure 8.86(b) The passage distribution function for $\lambda = 4.6$

When L = 3W, r = 0, and $\varphi = 17.67°$, the ratio of δ/H has to be about 0.8 to achieve a $G_0 < 0.01$. Clearly, with such a high ratio of δ/H it will be almost impossible to create large stresses in the clearance and to accomplish effective dispersive mixing. From Eq. 8.155 it is clear what geometric variables we have to change to achieve a low G_0 fraction at a small clearance. We can do this by:

1. increasing L, the length of the mixing section
2. increasing φ, the helix angle
3. reducing w_f, the width of the flight
4. increasing the number of flights. Increasing the number of flights reduces the channel width, W.

If we increase the helix angle from 17.67° to 60° with the other values being the same, the δ/H ratio has to be about 0.35 or greater for the G_0 fraction to be less than 0.01. This value is still rather large, but substantially better than 0.8. The δ/H ratio can be further reduced by increasing the length of the mixing section, reducing the flight width, or by increasing the helix angle even more. The point is that this procedure allows a first order determination of the design variables. Further refinement of the initial values can be obtained from computer simulation.

8.7.1.1.2 Determining Flight Clearance with Respect to Stress Level

Another important requirement for dispersive mixing is that the stresses generated in the HSR are high enough to achieve rupture of the agglomerate or droplet. The highest shear stresses occur in the region where the mixing flight has the smallest flight clearance. The shear rate at this point can be expressed as:

$$\dot{\gamma} = \frac{\pi D N}{\delta} \tag{8.157}$$

If the shear viscosity of the polymer melt is η_s, the maximum shear stress can be written as:

$$\tau_{max} = \frac{\pi \eta_s D N}{\delta} \tag{8.158}$$

If the critical shear stress required for rupture is τ_{crit}, the maximum flight clearance that can achieve dispersion can be expressed as:

$$\delta_{max} = \frac{\pi \eta_s D N}{\tau_{crit}} \tag{8.159}$$

If the viscosity is η_s = 500 Pa·s, the screw diameter D = 120 mm, the screw speed N = 1.5 rev/s, and the critical shear stress τ_{crit} = 140,000 Pa, then the maximum clearance of the mixing flight is δ_{max} = 2 mm.

8.7.1.1.3 Determining the Proper Flight Flank Geometry

As explained earlier, for efficient dispersion it is more important to achieve elongational stresses than shear stresses. Elongational stresses are generated in the wedge-shaped region between the pushing flight flank and the barrel. The elongation rate in the wedge can be obtained by using a procedure suggested by Cogswell [73]. The average stretch rate close to the entrance of the flight clearance can thus be written as:

$$\dot{\varepsilon} \approx \frac{(1 + r_d)\, \pi D N \delta \tan \alpha}{H^2} \tag{8.160}$$

where α is the wedge angle between the pushing flight flank and the barrel surface, and r_d is the throttle ratio (pressure flow rate divided by drag flow rate).

The elongational stress can thus be expressed as:

$$\sigma \approx \frac{(1 + r_d)\, \pi\ N \delta \eta_e \tan \alpha}{H^2} \tag{8.161}$$

where η_e is the elongational viscosity.

If the critical elongational stress required for rupture is σ_{crit}, the following inequality must be satisfied for dispersion to occur:

$$\frac{(1 + r_d)\, \pi\ N \delta \eta_e \tan \alpha}{H^2} \geq \sigma_{crit} \tag{8.162}$$

From this expression the critical parameters for the flight flank geometry can be determined. Unfortunately, the expressions above are valid only for small values of the wedge angle α. As a result, these expressions have limited usefulness. If we

assume that the drag flow in the channel is forced through the flight clearance, the average stretch rate can be approximated by:

$$\dot{\varepsilon} \approx \frac{\pi D N \tan\alpha}{2\delta} \tag{8.163}$$

With this expression, we can determine a maximum flight clearance for dispersive mixing based on the requirement that the elongational stress must be greater than the critical elongational stress. This leads to the following expression:

$$\delta_{max} = \frac{\pi D N \eta_e \tan\alpha}{2\sigma_{crit}} \tag{8.164}$$

If the diameter D = 120 mm, the screw speed N = 1.5 rev/s, the elongational viscosity η_e = 1,500 Pa·s, α = 30°, and the critical elongational stress σ_{crit} = 100,000 Pa, then the maximum flight clearance is δ_{max} = 2.45 mm. The expressions above can be used for a first order approximation of the critical geometrical parameters of the mixer. For accurate determination, numerical techniques are necessary to capture the complexity of actual flow.

8.7.1.1.4 Slot Geometry

The slots in the mixing section can be used to achieve efficient distributive mixing, similar to mixing in a Saxton mixing section; see Section 8.7.2. The slot geometry used in most distributive mixers is a straight slot. For dispersive mixing, however, it is better to use a tapered slot because this will create additional elongational flow as material passes through the slot. The geometry of the slot can be made such that the flight maintains full wiping capability. The geometry of the slotted flight is shown in Fig. 8.87.

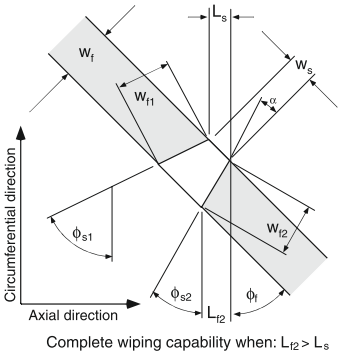


Figure 8.87
Flight geometry with tapered slot

The flight maintains complete wiping capability when the axial component of the pushing slot flank, L_{f2}, is greater than the axial slot width, L_s. This is the case when:

$$\sin^2\phi_f \cot\phi_{s2} + \sin\phi_f \cos\phi_f \leq \frac{w_f}{w_s} \tag{8.165}$$

When the flight helix angle $\varphi_f = 45°$, the inequality simplifies to:

$$\cot\varphi_{s2} + 1 \leq 2w_f / w_s \tag{8.166}$$

Figure 8.88 shows the smallest values of the slot flank angle for which the inequality above is satisfied.

As Fig. 8.88 indicates, the slot flank angle must be increased as the ratio of flight width to slot width decreases. When the slot width is twice the flight width, the slot flank angle has to be 90° to maintain full wiping. As a result, this will be the smallest value of the width ratio that will be practical. The preferred range of the flight to slot width ratio is from 1:1 to 3:1.

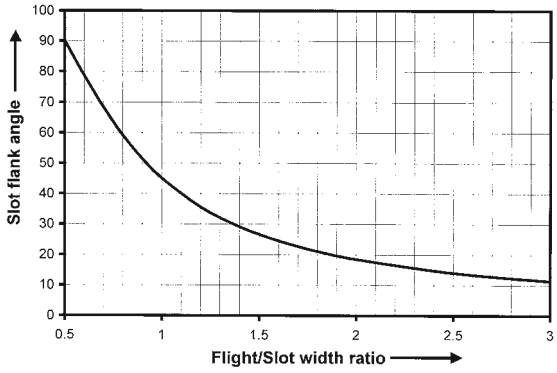


Figure 8.88
Minimum slot flank angle for flight helix angle of 45°

8.7.1.1.5 Computer Simulation

The analytical approach to mixer design has some severe limitations because of the difficulties in analyzing flow in a complicated mixer geometry. A better approach to analyze complicated mixers is to use mathematical modeling and computer simulation. One simulation tool that lends itself well to the analysis of complicated mixer geometries is the boundary element method (BEM). This method allows a determination of the optimum value of the flight clearance, flight flank geometry, and spacing of the slots to achieve the proper combination of dispersive and distributive mixing action. Recently, a three-dimensional BEM package was developed at the University of Wisconsin in Madison [74] and commercialized by The Madison Group [75].

To help determine the flight flank geometry and clearance, a two-dimensional BEM analysis was initially performed. To evaluate the strength of the elongational flow versus the shear flow, the flow number [76] was analyzed. The flow number is the ratio of the magnitude of the rate of deformation tensor $\dot{\gamma}$ to the sum of $\dot{\gamma} + \omega$, where ω is the magnitude of the vorticity tensor.

$$\chi = \frac{\dot{\gamma}}{\dot{\gamma} + \omega} \tag{8.167}$$

When χ = 1.0 the flow is pure elongational flow, χ = 0.5 simple shear flow, and χ = 0.0 pure rotational flow. A high value of the flow number is desired for effective mixing. Greater hydrodynamic forces are generated in elongational flow as discussed in Section 7.7.3. Also, elongational flow can disperse high viscosity droplets such as gels while shear flow is incapable of dispersing gels.

Using the BEM simulation, the flow number and forces at any point in the mixer can be computed. Moreover, particles can be tracked through the mixer to determine streamlines and detect possible stagnant regions. Figure 8.89(a) shows the calculated streamlines in the mixing section.

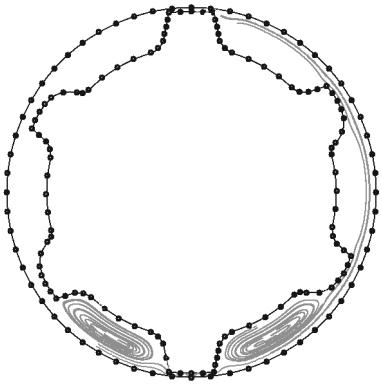


Figure 8.89(a)
Predicted streamlines in CRD mixer shown in Fig. 8.83

Here, at every time step, the strain rates and flow numbers are calculated. Figure 8.89(b) shows the flow number of a particle as it flows through the system.

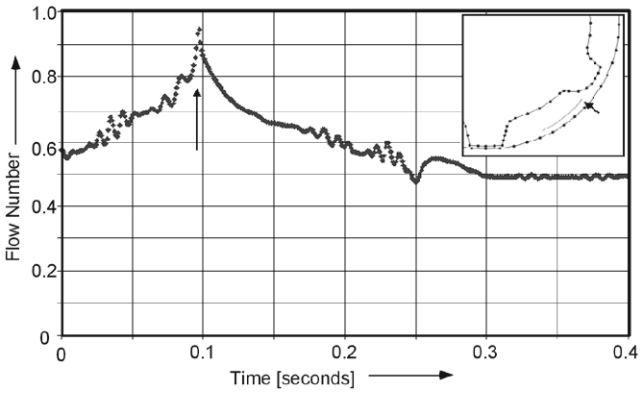


Figure 8.89(b)
Flow number versus time for a point traveling through the nip region of the mixer shown in Fig. 8.82

Flow numbers are achieved as high as 0.95, indicating that strong elongational flow can be generated in the new mixers. Similarly, Fig. 8.90 shows the magnitude of the rate of deformation tensor of the particle as it flows through the system.

As the particle approaches the flight, it “feels” an increase in the elongational flow. While passing over the top of the flight, the elongational flow switches to shear flow,

but at the same time the magnitude of the rate of deformation tensor increases. This effect will increase the mixing capability of the system.

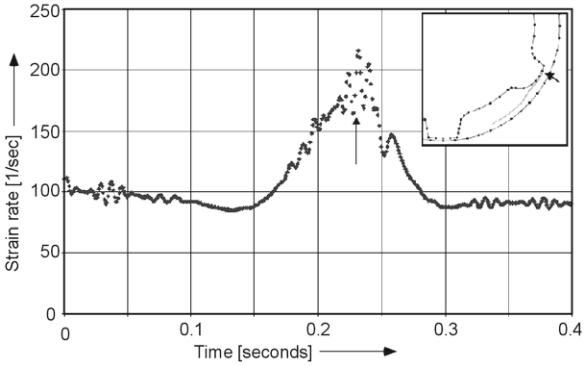


Figure 8.90
Strain rate versus time for points traveling through the nip

One of the goals of this mixing section is to provide improved distributive mixing as well as dispersive mixing. Introducing grooves in the modified flight will increase the distributive mixing and at the same time allow the re-circulation areas shown in Fig. 8.89(a) to be broken up. To calculate the splitting of the material (distributive mixing effect) as it flows through the mixer, a three-dimensional BEM analysis was performed. Figure 8.91 shows how a grouping of particles flows through a region of the mixer.

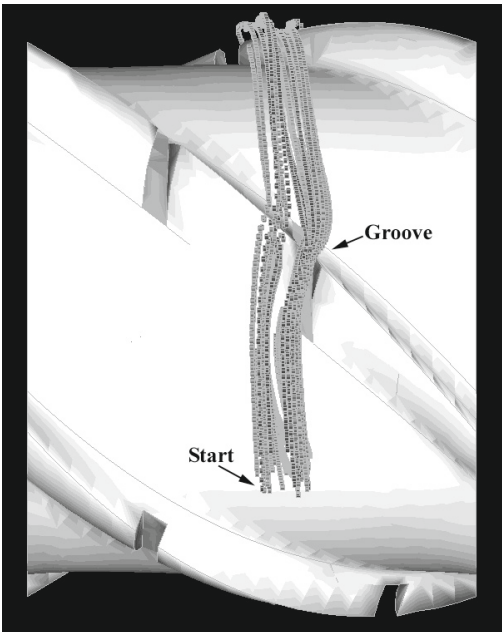


Figure 8.91
Tracking of multiple points in 3-D simulation

As expected, some particles flow over the modified flight while others flow through the groove. Again, this effect will increase the distributive and dispersive mixing capability of the mixer. Simulation of the CRD mixer is discussed further in Section 12.4.3.6 (see Figs. 12.48 to 12.50).

One of the findings of the BEM simulations was that the number of passes through the mixing clearance reduces as the pressure gradient along the mixer reduces. This effect was also observed in mixing experiments when tests were performed at low discharge pressure. In extrusion experiments [77], it was found that the mixing quality reduces when the discharge pressure is low, less than 5 MPa. Obviously, this problem is inherent in any open mixer design. It can be avoided by adopting a closed mixer design, such as the fluted mixer. Figure 8.92(a) shows the geometry of a CRD fluted mixer that achieves four passes through the mixing clearance.

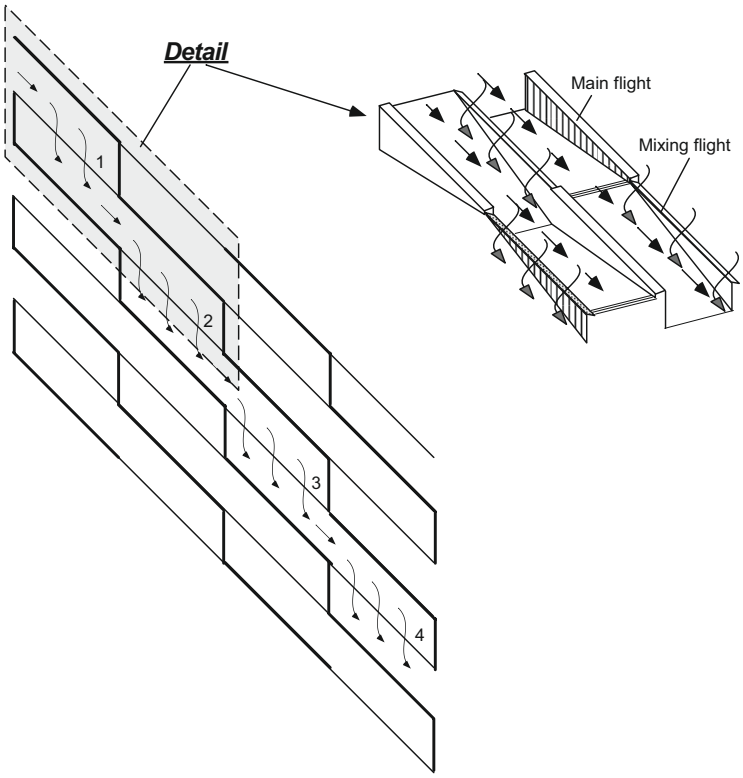


Figure 8.92(a) A fluted CRD mixer

The advantage of this geometry is that all fluid elements are exposed to four passages of the mixing clearance regardless of the discharge pressure. The disadvantage is that the distributive mixing capability is reduced relative to the open mixer and extruder output will tend to be lower.

Another method of making sure that all fluid elements are exposed to the elongational mixing action is to use rings of elongational mixing pins (EMP). The pins have the shape of an elongated polygon as shown in Fig. 8.92(b). The rings take up very little space and provide many splitting and reorientation events in addition to the elongational mixing action. The axial EMP shown in Fig. 8.92(b) obviously has no forward pumping capability. This can be a benefit in some applications such as grooved feed extruders.

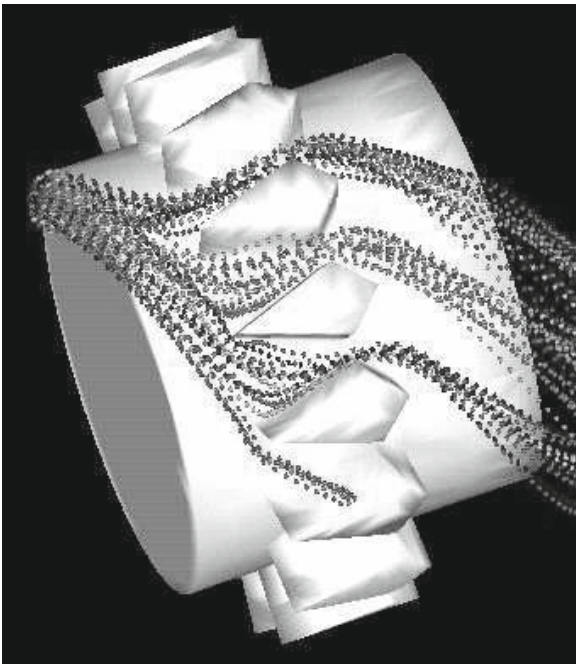


Figure 8.92(b)
A CRD-EMP mixer

8.7.1.1.6 Applications of the CRD Mixer

The CRD mixer has been commercially available since late 1998; as of early 2013 there are over 2000 CRD mixing screws in operation. The first CRD screw was used in a foamed profile extrusion operation, resulting in improved product quality and process stability. This company now has 50 extrusion lines running with CRD mixing screws. Foamed plastic extrusion is one of the most critical operations with regard to mixing and melt temperature control. Since the CRD mixer can improve mixing without increasing viscous dissipation it is well suited for foamed polymer extrusion.

The second application of the CRD mixer was in the production of color concentrates (CC) on a single screw compounding extruder. The machine was a two-stage extruder and two CRD mixers were used at the end of the first and second stages. The CC quality was improved to the point that dispersing agents could be eliminated from the compounds run on this extruder. CRD mixers are used in single screw extrud-

ers, twin screw extruders, injection molding machines, and blow molding machines. Other applications of the CRD are post-consumer reclaim with filler, medical applications, heat shrinkable tubing, blown film extrusion, profile extrusion, fiber spinning, sheet extrusion, and reactive extrusion.

CRD mixers are used in molding operations. Injection molding screws have been equipped with regular CRD mixers, and a new non-return valve (NRV) has been developed that incorporates CRD mixing elements within the NRV [81]. This CRD-NRV is a slide ring NRV with three EMP rings along the length of the valve as shown in Fig. 8.93.

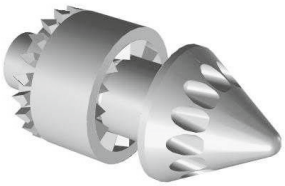


Figure 8.93
CRD non-return valve for injection molding

The first EMP ring is placed at the start of the NRV. The second EMP ring is machined into the internal diameter of the ring. The last EMP ring is machined into the conical tip of the NRV in the form of conical holes. The CRD-NRV fits within the same space as a regular NRV and thus allows simple installation.

There are now several twin screw extruders that use CRD mixing elements to enhance the distributive and dispersive mixing action. This is not surprising for non-intermeshing twin screw extruders, but it is for intermeshing twin screw extruders because it is generally believed that conventional kneading disks provide good dispersive mixing.

8.7.1.1.7 Conclusions

The CRD mixer technology allows single screw extruders to achieve dispersive mixing as good as that of intermeshing twin screw extruders; this was confirmed by mixing experiments [77]. This finding contradicts traditional thinking about mixing in single screw extruders [78]. The new mixer technology allows single screw extruders to be used in applications where thus far only twin screw extruders could be considered. Thus, the use of single screw extruders can be broadened significantly. The CRD mixers can be incorporated into existing or new extruder screws, making implementation simple and inexpensive. Mixers that are mounted downstream of extruders are more difficult to install and more expensive.

The new mixers can improve mixing not only in single screw extruders, but also in non-intermeshing twin screw extruders. Current tangential extruder have limited dispersive mixing capability. Using the new mixer technology can improve the dispersive mixing capability of these extruders. Some aspects of the mixing technology can even be applied to intermeshing twin screw extruders to improve dispersive

mixing. In fact, currently several intermeshing twin screw extruders are using CRD type mixing elements. Also, internal mixers can benefit from this new mixer technology; this applies to both batch and continuous internal mixers. In internal mixers the empirical sigma type mixing rotor can be replaced with a more efficient CRD type rotor designed from sound engineering principles.

The boundary element method is a useful tool in the development and design of mixing sections with complex geometry. BEM provides a tool that allows a quantitative approach to the design of mixing devices. The BEM results of the new mixers indicate that strong elongational flow can indeed be generated by the wedge-shaped geometry of the mixing flights. Also, multiple passes through the HSRs can be achieved, provided that the mixing flight clearance is properly dimensioned.

Multi-flighted CRD mixers expose all the material to multiple high stress events to achieve a fine dispersion. Conventional mixers, like the Maddock, expose the material to only one high stress event, thus limiting the mixing efficiency. The CRD mixer is designed with elongational mixing action and forward pumping capability, allowing effective mixing without increasing power consumption or melt temperatures. As a result, the CRD mixer can be made quite long with typical lengths of 6 D. Some of the important benefits of the elongational mixing action are lower melt temperatures, less melt temperature fluctuation, reduced die lip buildup, and the ability to disperse gels—shear based mixers cannot disperse gels.

8.7.1.2 Mixers to Break Up the Solid Bed

In extrusion visualization experiments it is frequently observed that large chunks break off from the solid bed and travel far down the length of the screw [89]. There are two basic methods to deal with this problem. One is to use some type of a barrier device to keep the large clusters of pellets from traveling to the end of the screw. This can be done with a barrier screw or with a fluted mixing section. The drawback of this method is that there is the risk of choking the polymer flow when too much unmelted material accumulates at the end of the barrier section. Another method is to break up the large clusters into much smaller clusters or even pellets. The advantage of this approach is that it actually improves melting as discussed in Section 7.3.1.2.

The CRD mixer described above is normally designed to break up agglomerates into much smaller aggregates or even individual particles; the final size is typically at the micron or submicron level. However, the same principle can be applied to break up large clusters of unmelted polymer particles into smaller clusters or individual particles (usually pellets) at the millimeter level. A number of variations of the CRD mixer have been developed with the specific objective to break up clusters of unmelted particles—these mixers are called the Cluster Buster™ or CB mixer [89]. An example of the CB mixer is shown in Fig. 8.94.

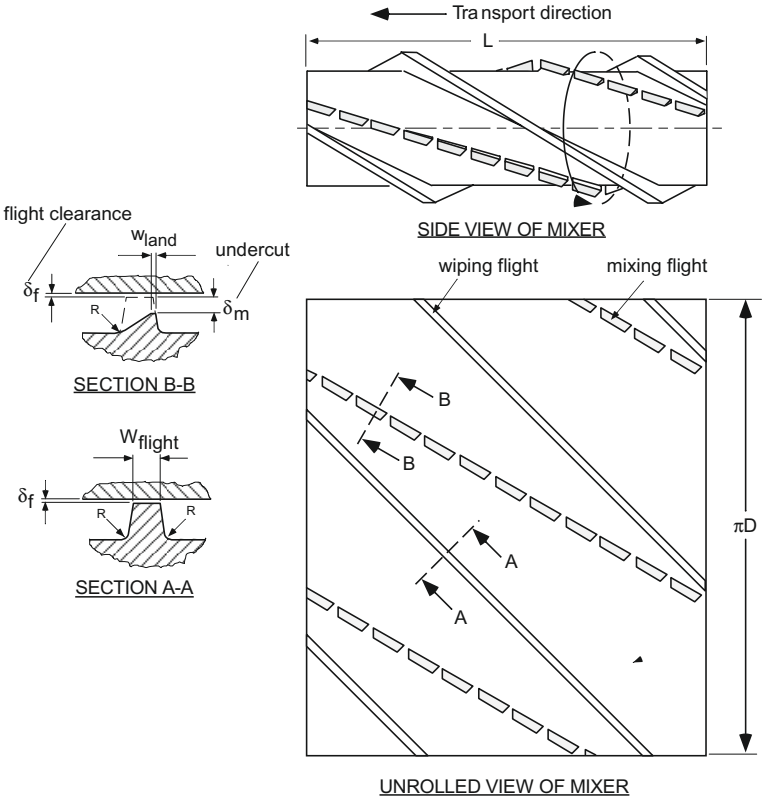


Figure 8.94 The Cluster Buster mixer

Experiments with the CB mixer have shown significant improvement in extrudate quality and process stability, allowing higher throughput rates to be achieved. The CB mixer makes it possible to generate a dispersed solids melting (DSM) mechanism toward the end of the melting zone in single screw extruders. Since DSM melting is significantly more effective than the conventional contiguous solids melting, the CB mixer accelerates melting and improves the melt quality produced by the screw.

Other mixing screws have been developed in the past to disrupt the solid bed and mix unmelted with melted material. The double wave screw shown in Fig. 8.80 breaks up the solid bed and mixes the material by forcing a cross-channel flow by the cyclic variation in channel depth. The principle of the double wave screw was used by Barr in his energy transfer (ET) screw [90]. The ET section is basically a double wave section with occasional undercuts in both flights to force a cross-channel mixing between the two channels. Modeling of the ET mixer is discussed in Section 12.4.3.2; see also Figs. 12.23 to 12.25.

8.7.1.3 Summary of Dispersive Mixers

Table 8.3 lists important attributes of dispersive mixers. The most important issues for the dispersive mixing capability are the type of flow and the number of passes through the high stress regions.

Table 8.3 Comparison of Dispersive Mixers for Single Screw Extruders

Mixer	Pressure drop	Dead spots	Barrel wiped	Cost of mixer	Number of passes	Distributive mixing	Type of flow
Blister	High	Some	No	Low	1	Poor	Shear
Egan	Fair	No	Yes	Fair	1	Fair	Shear
LeRoy/Maddock	Fair	Yes	Yes	Fair		Fair	Shear
Fluted CRD	Low	No	Yes	Fair	>1	Fair	Elongation
Zorro	Low	No	Yes	Fair	1	Fair	Shear
Double wave	Low	No	Yes	Med.	>1	Fair	Shear
Energy transfer	Low	No	Yes	Med.	>1	Fair	Shear
Helical LeRoy	Low	No	Yes	Fair	1	Fair	Shear
Planetary gear	Fair	No	Yes	High	>1	Excellent	Shear
CRD mixer	Low	No	Yes	Fair	>1	Good	Elongation
CB mixer	Low	No	Yes	Fair	>1	Good	Elongation

The blister ring has few attractive attributes. One advantage of the blister ring is that it takes up little space. The differences between the fluted mixers (Egan, LeRoy, fluted CRD, Zorro, and helical LeRoy) are relatively small with the exception that the fluted CRD can generate elongational flow. Both the planetary gear mixer and the CRD achieve multiple passes through the high stress regions with effective flow splitting and, as a result, have good dispersive and distributive mixing capability. The planetary gear mixer, however, is quite expensive. The double wave screw and the energy transfer screw are designed to mix unmelted and melted material by forcing cross-channel flow in a double-flighted section with varying channel depth. This geometry is difficult to manufacture; as a result, the cost of these mixers is relatively high.

The CRD and CB mixers are the only dynamic mixers specifically designed to create strong elongational flow. This allows more effective dispersive mixing with lower viscous dissipation. Elongational mixers are the only mixers that have the capability of dispersing gels. The CB mixer is specifically designed to break up clusters of unmelted particles to generate dispersed solids melting. This accelerates the melting process and improves melt quality. Since the CRD and CB mixers achieve flow splitting and reorientation they also have effective distributive mixing capability.

8.7.2 Distributive Mixing Elements

Distributive mixing is needed where different polymers are blended together with the viscosities reasonably close together. Distributive mixing is easier to achieve than dispersive mixing. Essentially any disruption of the velocity profiles in the screw channel will cause distributive mixing. A common distributive mixing element is the pin mixing section; see Fig. 8.95.

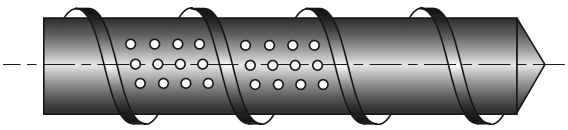


Figure 8.95
The pin mixing section

The pins cause disturbances in the velocity profile and thus cause mixing. Many different patterns have been used to place the pins; however, there is little agreement as to what pattern is most effective.

Another well-known mixing element is the Dulmage mixing section shown in Fig. 8.96.

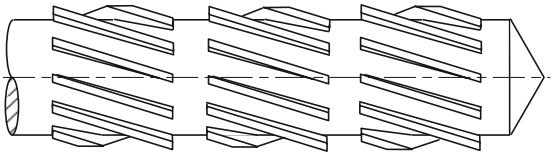


Figure 8.96
The Dulmage mixing section

The Dulmage mixer is a multi-flighted mixer with circumferential grooves machined into the flights to create a number of slots in the flights. The polymer is divided into many narrow channels combined, divided again, etc. This design was patented almost 30 years ago with Dow Chemical as the assignee [41]. The drawback of the circumferential grooves is that the barrel is not completely wiped by the screw. This can create problems with stagnation and reduced heat transfer between the polymer melt and the barrel. A relatively similar mixing section is the Saxton mixing section, shown in Fig. 8.97.

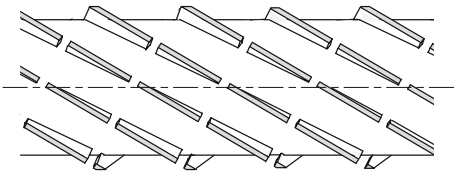


Figure 8.97
The Saxton mixing section

The difference between the Saxton and the Dulmage mixers is that the slots in the Saxton mixer are machined in the helical rather than the circumferential direction. The advantage of this geometry over the Dulmage is that the Saxton mixer completely wipes the barrel surface. Therefore, there is less chance of stagnation and

better heat transfer between the polymer melt and the barrel. This design was patented in 1961 with the assignee being E.I. DuPont de Nemours and Company [42]. Pineapple-shaped mixing sections are also used for distributive mixing; see Fig. 8.98.

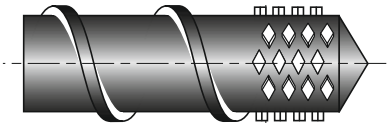


Figure 8.98 The pineapple mixing section

The pineapple mixer is basically a form of a Saxton type mixer with enough slots machined into the flights that the flight segments become diamond shaped. Mixing in pineapple mixers was studied in detail by Rios et al. [99, 100] both experimentally and through numerical simulation of flow using the boundary element method. This study is discussed in detail in Section 12.4.3.4; see also Figs. 12.37 to 12.42.

A simple screw geometry with slots machined into the flights is shown in Fig. 8.99.

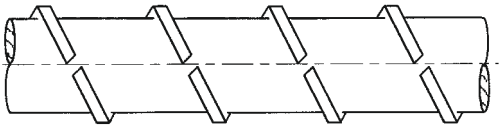


Figure 8.99
The slotted extruder screw

A Swedish company, Axon, has patented such a design in many European countries [43]. Many other slotted mixing sections have been developed over the years.

A new concept in mixing screws was developed by J. Fogarty [98]. This screw, the Turbo-Screw™, has rectangular openings (windows) machined into the screw flights to enhance mixing and heat transfer. This patented [101] screw geometry requires considerable flight height; therefore, this design can be applied to extrusion operations where deep flighted screws are necessary. One example of such an operation is foamed plastic extrusion where deep flighted screws are used in the secondary extruder to cool down the polymer melt. The Turbo-Screw has been used extensively in foamed plastic operations and has allowed significant increases in throughput as a result of its improved mixing and heat transfer capability. The Turbo-Screw is discussed in more detail in Section 12.4.3.5; see also Figs. 12.45 to 12.47.

Another distributive mixing section is the cavity transfer mixing (CTM) section shown in Fig. 8.100.

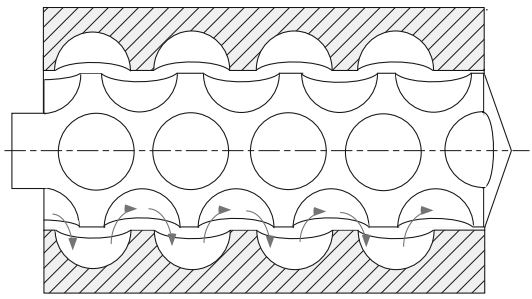


Figure 8.100
The cavity transfer mixer

This mixing section was developed by Gale at RAPRA. It was licensed in the U.S. by David-Standard. It is interesting to note that the cross-cavity mixer concept was described in a patent as early as 1961 [45]. The CTM mixer has cavities both in the rotor and barrel housing; the combination of shearing and reorientation appears to give effective distributive mixing. A mixer similar to the CTM mixer was developed earlier by Barmag in Remscheid, Germany [58]. The mixer reportedly performs both dispersive and distributive mixing with the ability to reduce the particle or drop size of additives down to the micrometer (10^{-6} m) range. Reifenhauser in Troisdorf, Germany, also has a similar mixer called the Staromix; it has ellipsoidal cavities in the axial direction rather than hemispherical cavities. Another German extruder manufacturer, Paul Kiefel Extrusionstechnik, offers their CT mixer, which uses ellipsoidal cavities in the helical direction. At this point in time there are several mixers with characteristics very similar to the CTM; since the basic RAPRA patent has expired, companies can freely use the CTM or modifications of it.

One of the drawbacks of the CTM and similar mixers is that the barrel is not completely wiped by the screw (or rotor). As a result, the CTM is difficult to clean and there is a possibility of stagnation. Therefore, the CTM is not attractive for short runs with frequent material changes because the changeover time can be quite long—it can take two to three hours to clean a CTM. In addition, the CTM is quite expensive and has no pressure generating capability. Because of these disadvantages the CTM is not used as widely as one might expect based on its good mixing characteristics.

8.7.2.1 Ring or Sleeve Mixers

An interesting mixing device with features similar to the CTM was developed at Twente University in the Netherlands by Semmekrot and patented in several countries [83]. This mixer is called the Twente Mixing Ring or TMR. The TMR consists of a screw with hemispherical cavities in the screw like the CTM. However, it does not have cavities in the barrel. Instead, the CTM uses an annular ring between the screw and the barrel with circular holes machined through the ring in the radial direction [84, 85]. Figure 8.101 shows a picture of the TMR.

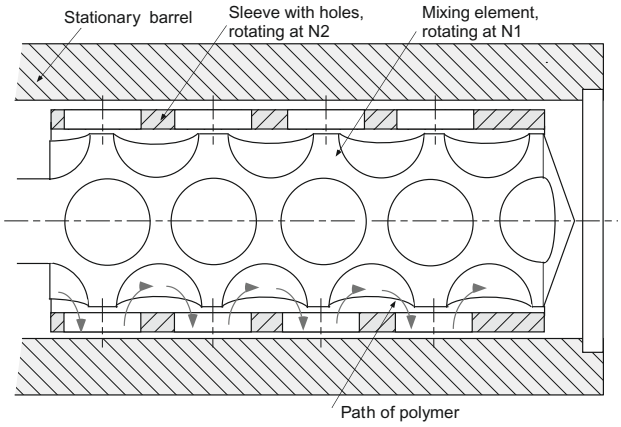


Figure 8.101
The Twente Mixing Ring (TMR)

The ring in the TMR rotates with the screw by the dragging action of the screw but at a lower rotational speed. As a result, there is a relative motion between the cavities in the screw and the holes in the ring, which results in a mixing action similar to the CTM. An important advantage of the TMR over the CTM is that it does not have cavities in a stationary barrel. This improves the self-cleaning action of the mixer and makes installation significantly easier. The CTM requires a special barrel section and an extension of the screw; this is both costly and makes installation difficult. The TMR fits within the normal length of an extruder or injection molding machine. This makes the TMR less expensive and easier to install. The TMR is also used in injection molding as part of the non-return valve. Figure 8.102 shows a picture of a TMR non-return valve.



Figure 8.102
TMR non-return valve for injection molding

The TMR non-return valve combines the mixing action with the valve action, similar to the CRD non-return valve shown in Fig. 8.93. The TMR started a new class of mixers called "ring" mixers, also called "sleeve" mixers. The design of TMR is patented [83]; however, other companies have found ways to get around this patent and even obtain patents on their own ring mixer. An example is the Fluxion mixer by Robert Barr [86]. This mixer differs from the CTM in that the sleeve has circumferential rings on the outside surface. Obviously, this is a potential source of stagnation and, therefore, not attractive from a functional point of view. However, this feature made it possible to get around the TMR patent. The Fluxion mixer has been tested at Dow Chemical [87, 88].

8.7.2.2 Variable Depth Mixers

In variable depth mixers, the channel depth of the mixer is varied to obtain improved mixing. An example of a variable depth mixer is the double wave screw shown in Fig. 8.81 and the energy transfer screw; see Fig. 12.23. Another example is the Pulsar mixing section shown in Fig. 8.103.

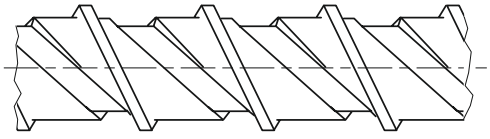


Figure 8.103
The Pulsar mixing section

In the Pulsar mixer a helical groove is machined into the root of the screw; the helix angle of the groove is greater than the helix angle of the flight. As a result, some

cross-channel mixing is induced by the groove. The Strata-blend mixer is another variable depth mixer; the mixer is shown in Fig. 8.104.

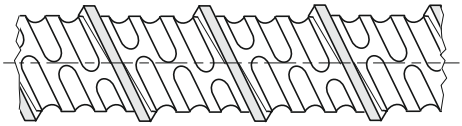


Figure 8.104
The Strata-blend mixer

Three grooves are machined into the root of the screw in the Strata-blend mixer. The grooves have the same helix angle as the flight, and the grooves are not continuous. This forces material to flow from one groove to the next. Most variable depth mixers have little flow splitting and reorientation; therefore, their distributive mixing capability tends to be limited.

8.7.2.3 Summary of Distributive Mixers

Based on the important characteristics of mixers we can compile the various distributive mixers and list how they perform with respect to different criteria; this is shown in Table 8.4.

Table 8.4 Comparison of Various Distributive Mixers

Mixers	Pressure drop	Dead spots	Barrel wiped	Operator friendly	Mixer cost	Disp. mixing	Shear strain	Splitting, reorienting
Pins	High	Yes	Partial	Good	Low	No	Low	Fair
Dulmage	Low	No	Partial	Good	Fair	No	High	Good
Saxton	Low	No	Yes	Good	Fair	No	High	Good
CRD	Low	No	Yes	Good	Fair	Yes	High	Good
CTM	High	Yes	Yes	Bad	High	Some	High	Good
TMR	High	Yes	Yes	Fair	Medium	Some	High	Good
Axon	Low	No	Yes	Good	Low	No	High	Low
Double wave	Low	No	Yes	Good	High	Some	High	Low
Pulsar	Low	No	Yes	Good	Fair	No	Fair	Low
Strata-blend	Low	Yes	Yes	Good	Fair	No	Fair	Low

The last column in Table 8.4 is the most important when it comes to distributive mixing effectiveness. The Dulmage, Saxton, CTM, and TMR all do very well in this category. The Saxton mixer combines good mixing with low cost, good streamlining, ease of use, and low pressure drop. The CRD has characteristics similar to the Saxton mixer with the difference that the CRD is also capable of dispersive mixing.

It should be remembered that static mixing devices can also be quite effective in distributive mixing capacity; see Section 7.7.2. Thus, if distributive mixing is required, one should consider application of a static mixing device.

8.8 Efficient Extrusion of Medical Devices

8.8.1 Introduction

Medical extrusion can present special challenges in terms of product size, dimensional control, physical properties, and others. Automation of the extrusion line is critical to achieve high levels of process stability and reproducibility. Polymer degradation can be a significant concern in medical extrusion. Degradation is affected by the stresses and temperatures that occur in extrusion; both depend strongly on the screw geometry.

Melt temperatures can vary significantly in extrusion. Therefore, screws with mixing elements are required to achieve good melt temperature uniformity. Barrier screws can achieve relatively uniform melt temperatures but can result in large melt pressure variation. Barrier screws also tend to result in significant reduction in molecular weight (MW). This is likely due to the high shear stresses that occur when the polymer melt flows over the barrier flight. The same problem occurs in fluted mixing sections. This explains why screws with fluted mixing sections (e.g., the LeRoy-Maddock mixer) tend to result in significant MW reduction as well.

Mixing screws based in elongational mixing devices and without barrier flights result in minimal MW reduction. These screws have little melt temperature and pressure variation, can disperse gels, and achieve a high quality product with minimal dimensional variation. As a result, such extruder screws are attractive in medical extrusion operations where MW reduction has to be minimized and dimensional control and product quality maximized.

In the extrusion of medical devices, there are special requirements that go beyond those that apply to the extrusion of non-medical products [106–108, 134]. Figure 8.105 illustrates the multiple requirements that apply to the extrusion of medical products.

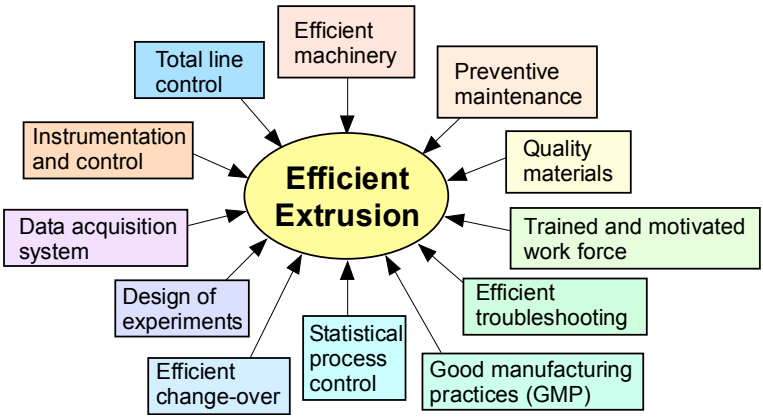


Figure 8.105 There are multiple requirements for efficient medical extrusion

Essentially all of these requirements apply to all extrusion operations. However, too often, a number of these requirements are disregarded; this is unacceptable in medical extrusion.

8.8.2 Good Manufacturing Practices in Medical Extrusion

Good manufacturing practices (GMP) are essential in medical extrusion and involve both a high level of sanitation and process reproducibility. Process reproducibility can be quantified with statistical techniques that have been developed in the field of statistical process control (SPC). Therefore, SPC is a necessary requirement in medical extrusion [107]. GMP also requires full documentation and traceability. With respect to medical extruder machine design, the following aspects are of great importance:

- Polished, detailed design for all components with respect to cleaning
- Stainless steel machine frame and barrel cover
- Ground and polished welding seams
- Complete documentation and calibration of all process parameters
- Quick-release couplings for cooling and heating system
- FDA-approved gear oils and lubricants
- Mercury-free pressure sensors
- Contact surfaces made out of stainless steel or nickel-based alloys
- FDA-approved paints for parts that cannot be made out of stainless steel
- Validated programmable logic control (PLC) and computer-based control

8.8.3 Automation of the Medical Extrusion Process

The extrusion process allows a high degree of automation. In fact, once the extruder has reached steady-state operation, operator intervention is no longer necessary if complete line control is effectively used. These types of operations offer multiple advantages, such as:

- Several extrusion lines can be handled by a single operator (“lights-off operation”)
- Product dimensions, such as diameter and wall thickness, are controlled automatically
- Product variability is minimized with full line control
- Electronic data acquisition systems (DAS) allow real-time monitoring of all process variables and pertinent product dimensions
- Pertinent process and product data can be processed by the DAS to yield process control charts and process capability; SPC information is available real-time

- On-line SPC allows instant detection of out-of-spec conditions or out-of-control conditions; this allows immediate corrective action, minimizing scrap

8.8.4 Minimizing Polymer Degradation

One of the critical aspects of polymer extrusion is degradation of the polymer. Degradation reduces physical properties with or without discoloration of the product; in some cases, gels are produced. There are a number of degradation mechanisms [110], the main ones being thermal, mechanical, biological, and radiation. Degradation in extrusion is affected by temperatures, mechanical stresses, and residence times. The extruder should be designed to minimize all three of these factors.

Degradation most often results in the reduction of the molecular weight (MW) of the polymer and the generation of monomers and oligomers. This leads to lower physical properties; this, in turn, can lead to out-of-spec conditions for the extruded product.

The melt temperatures and stresses to which the polymer is exposed in the extruder are strongly influenced by the geometry of the extruder screw. The functions of the extruder screw are

- Conveying
- Pressure build-up
- Heating and melting
- Mixing, both distributive and dispersive
- Degassing (in vented extruders)

Currently, in most medical extrusion operations, the mixing of screws is used. This is necessary to make high-quality extruded medical products. Simple conveying screws (without mixing elements) are rarely used anymore because they lead to poor homogeneity in the product, as well as dimensional variation.

8.8.5 Melt Temperatures Inside the Extruder

Melt temperatures in the extruder tend to be highly nonuniform because of the low thermal conductivity of polymers. Therefore, it is more efficient to heat the polymer by viscous heat generation than by heat from the barrel heaters. The actual melt temperatures inside the machine can be quite different from the barrel temperature. Also, temperature peaks within the machine are often much higher than the bulk average melt temperature.

Melt temperatures inside the extruder are difficult to measure because one cannot use an immersion melt temperature sensor along the barrel because the probe will be sheared off by the screw flight. Downstream of the screw, the melt temperature is normally measured with an immersion probe; these can be made with adjustable depth of the probe; see Fig. 8.106.



Figure 8.106 Immersion melt temperature probe with adjustable depth

Steady state melt temperatures can be calculated using finite element analysis [111–113]. Figure 8.107 shows the melt temperature distribution in a cross-section of the screw channel in the metering section. Figure 8.107 shows that significant temperature changes can occur across the width and depth of the channel. The greatest temperature gradients occur across the depth of the channel.

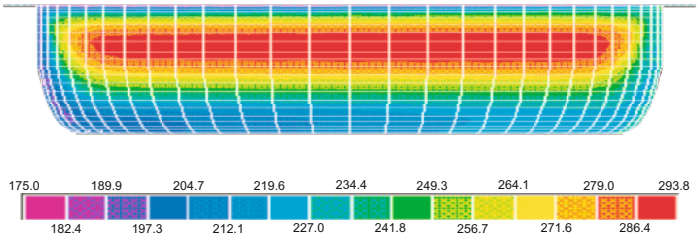


Figure 8.107 Melt temperature distribution in a 63.5-mm single screw extruder

In reality, the temperature distribution is dynamic; in other words, melt temperature changes with time. These changes can be significant, but short-term (0–10 seconds) temperature changes cannot be measured with a conventional melt temperature sensor because the thermal mass of the probe is too large. Infrared melt temperature measurement allows detection of rapid (millisecond range) melt temperature fluctuation [114–118].

8.8.6 Melt Temperatures and Screw Design

Short-term melt temperature changes can be measured with fast-response thermocouples. A number of studies using a fast-response thermocouple mesh were conducted at Polymer IRC, School of Engineering, Design, and Technology at the University of Bradford, England [121–125]. In these studies, dynamic melt temperatures

were observed on a 63.5 mm single screw extruder running a high-density polyethylene at different screw speeds; three screw geometries are shown in Fig. 8.108.

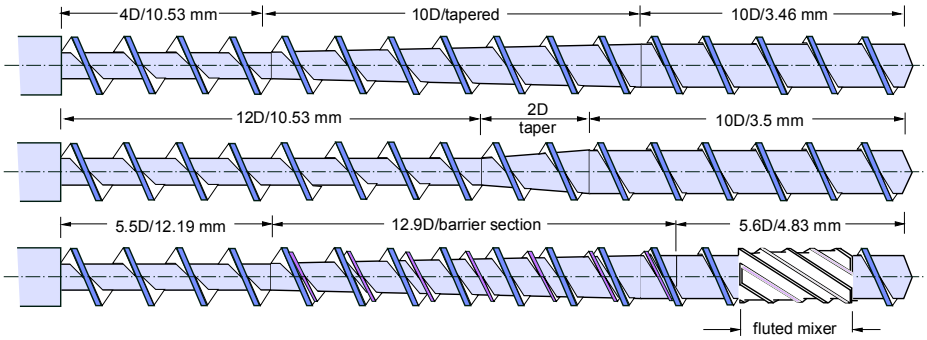


Figure 8.108 Three screw geometries tested

In Fig. 8.108, the first screw (top) is a simple conveying screw with gradual compression (10 D length). The second screw (middle) is a simple conveying screw with rapid compression (2 D length); the third screw (bottom) is a barrier screw with a long barrier section (12.9 D) and a fluted mixing section (3 D) in the metering section of the screw.

In these studies, it was found that significant melt temperature variations occur, as much as 45°C over 5 to 10 seconds. Figure 8.109 shows these melt temperature variations for three screw geometries at three barrel temperature profiles and at two screw speeds.

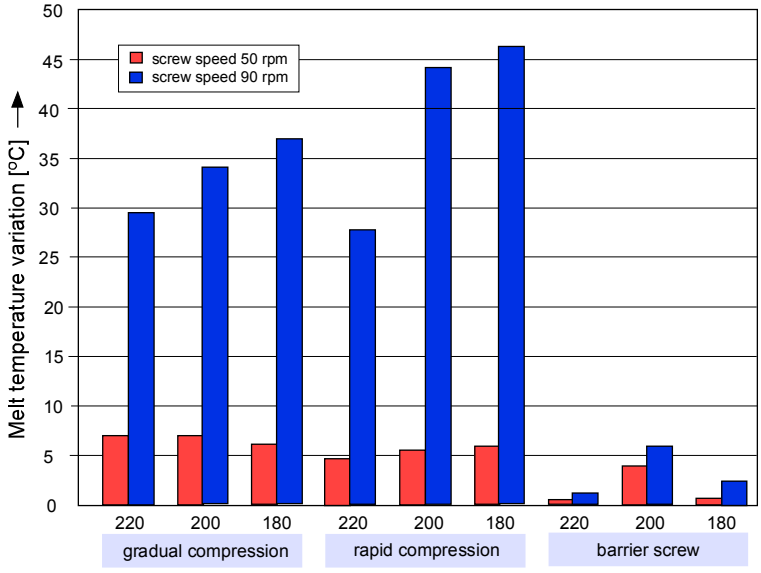


Figure 8.109 Melt temperature variations for three screw geometries

It is interesting to note that the melt temperature variation for the simple conveying screws is quite large. The melt temperature variation at a screw speed of 90 rpm is greater than at 50 rpm—this is true for all three screws. The melt temperature variation at 90 rpm for the simple conveying screws is about an order of magnitude higher than for the barrier screw.

In simple conveying screws, the helical screw channel extends over the entire length of the screw without interruptions, slots, or barriers. As a result, these screws have poor melting and mixing characteristics. These screws are susceptible to unmelt; this is a condition where unmelted particles reach the discharge end of the extruder.

It is well known [126] that simple conveying screws have very limited melting and mixing capability. Therefore, it is not surprising that these screws generate melt temperature variations. However, the magnitude of these changes is surprising. In the extrusion industry it is often assumed that the melt temperature changes are quite small (less than 2 to 3°C). The data in Fig. 8.109 show that the actual melt temperature variations can be higher by at least an order of magnitude.

High melt temperature variations do not necessarily result in large pressure fluctuations. This is evident in Fig. 8.110 where the melt pressure variation is shown for the same three screws at the same screw speeds and barrel temperature profiles.

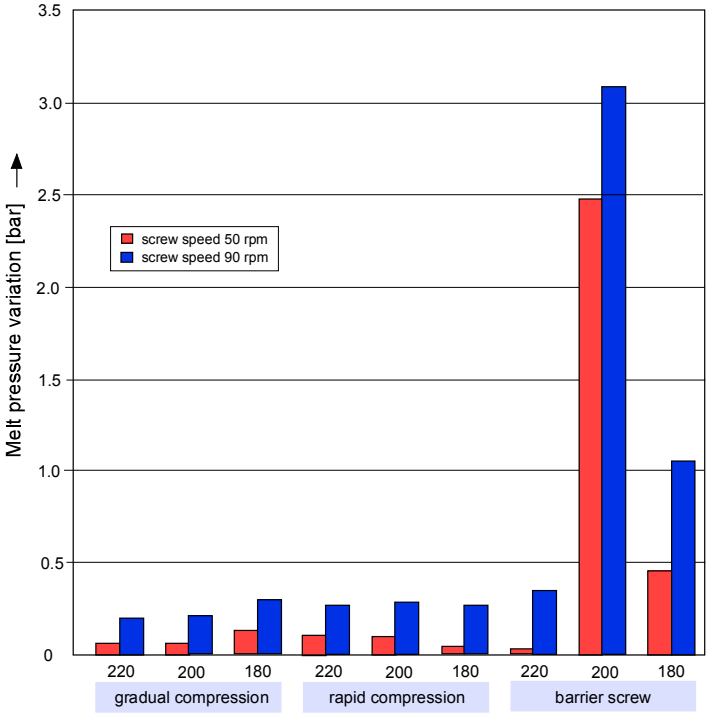


Figure 8.110 Melt pressure variations for three screw geometries

The 220 barrel temperature refers to the temperature of the last barrel temperature zone; the actual profile is 150-185-205-220. For the 200 barrel temperature the actual profile is 140-170-185-200 and for the 180 barrel temperature the actual profile is 130-155-165-180. For the simple conveying screws, the barrel temperature profile (BTP) has little effect on the pressure variation, and the pressure variation is quite small. For the barrier screw, the BTP has a significant effect on the pressure variation and the pressure variation is much higher—as much as an order of magnitude.

The small melt temperature variation with the barrier screw is a distinct advantage; however, the large melt pressure variation with the barrier screw is a distinct disadvantage. This large pressure variation is likely due to plugging; this is a condition where the solid bed does not melt fast enough to accommodate the reduction in the size of the solids channel. Barrier screws with a long barrier section (over 10 D) are particularly susceptible to this problem [110, 133].

8.8.7 Molecular Degradation and Screw Design

In the extrusion of medical devices, molecular degradation is often a critical issue. This degradation of the MW can be strongly influenced by the geometry of the extruder screw. Unfortunately, little information on this problem is available in the open literature. Paakinaho et al. [127] published results of a study on the MW reduction along the length of a single screw extruder for three polylactic acid (PLA) resins; see Fig. 8.111.

PLA22 is a low MW resin, PLA48 a medium MW resin, and PLA63 a high MW resin. Figure 8.111 shows that PLA22 has little or no MW reduction along the length of the extruder, while PLA48 has a moderate MW reduction, about 25%, while PLA63 has significant MW reduction, over 50%. In fact, the final MW of PLA63 at the discharge is actually lower than that of PLA48. This indicates that for this extrusion operation, there is no benefit to using the high MW PLA63 because its MW at the discharge end of the extruder is lower than that of the medium MW PLA48.

Figure 8.112 shows the effects of screw speed and extruder length on the MW at the discharge of a 0.75-inch extruder in the extrusion of PLLA polymer. The results demonstrate that lower screw speed results in lower MW. This is likely caused by longer residence time at lower screw speed. Figure 8.112 also shows that the longer extruder (L/D = 25:1) results in a lower MW than the shorter extruder (L/D = 20:1).

Finally, Fig. 8.112 shows that using a nitrogen blanket at the feed opening results in a slight increase in MW compared to standard air at the feed opening. These data were generated by a medical company in a study to increase their understanding on how to best retain PLLA molecular weight and the physical properties that depend upon the MW.

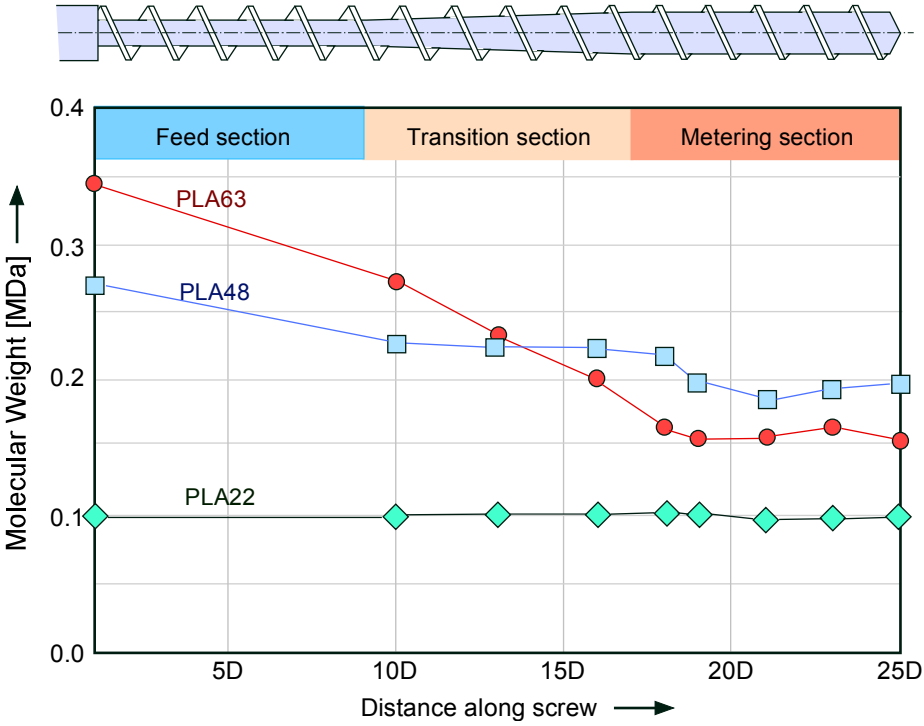


Figure 8.111 MW reduction along extruder screw for three PLA resins

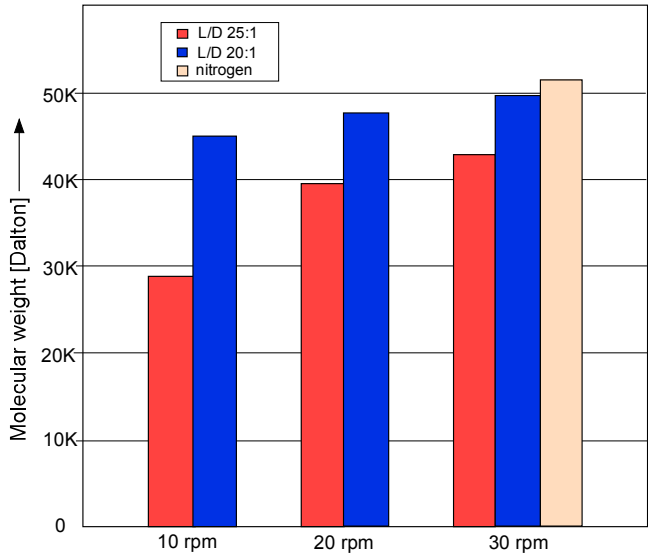


Figure 8.112 Molecular weight changes by screw speed, screw length, and atmosphere

The effect of screw geometry on MW is shown in Fig. 8.113. In this study, a 0.75-inch extruder was used with a thermoplastic elastomer (TPE). Three screw geometries were tested: a barrier screw, a CRD mixing screw, and a Maddock mixing screw.

These studies were conducted by a large medical device company in the development of implantable devices. The MW results are critical because the polymer is used for implantable CRM lead wire insulation, which is susceptible to hydrolytic and metal ion degradation in the body.

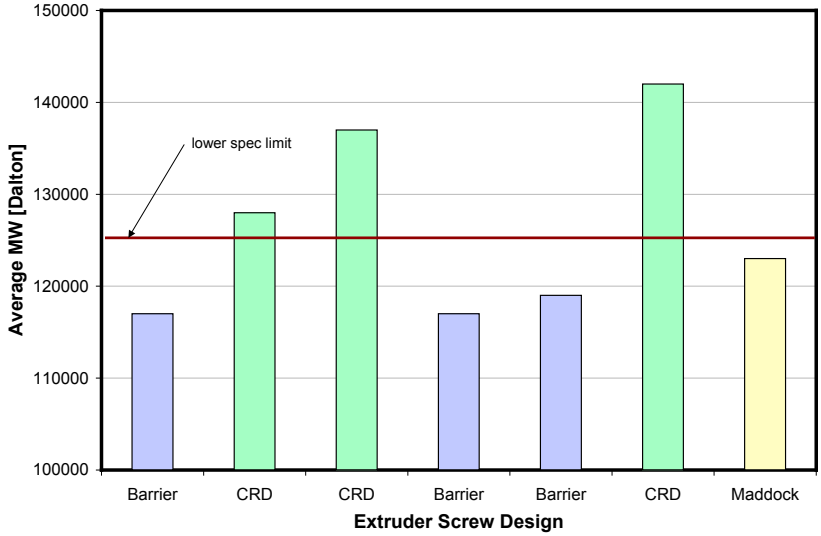


Figure 8.113 Molecular weight for three extruder screws

In this particular application, the molecular weight of the extruded product had to be above a certain minimum level. This turned out to be a significant challenge because the early extrusion trials did not achieve the minimum MW level in the TPE. As a result, a special screw was designed for this application to minimize the stresses that the polymer melt is exposed to in the extrusion process—this is the CRD mixing screw.

The barrier screw geometry is shown in Fig. 8.108. The Maddock screw has a fluted mixing element similar to the one shown in the bottom of Fig. 8.108. The CRD screw is a screw with a distributive mixing element that is based on elongational flow rather than shear flow [128–131].

Figure 8.113 shows that the barrier screw results in the lowest MW. The Maddock mixing screw resulted in a slightly higher MW. The barrier screw and Maddock screw were not able to produce MW values above the specification level. In barrier screws and fluted mixers, the polymer melt is forced over a barrier flight. As a result, all the melt is exposed to the high shear stresses that occur between the crest of the barrier flight and the extruder barrel. These shear stresses can be high enough to result in a significant reduction of the MW.

Figure 8.114 shows more results of the MW for the different extruder screws. Each screw was run at three different temperature profiles. *Low* indicates barrel tempera-

tures of 375, 385, and 395°F. *Medium* indicates barrel temperature of 395, 420, and 415°F. *High* indicates barrel temperatures of 400, 420, and 420°F.

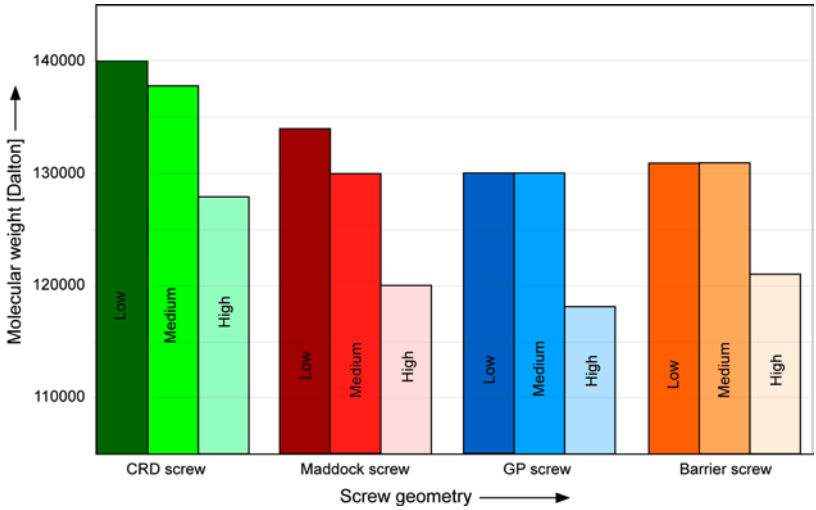


Figure 8.114 Molecular weight for four screw and three barrel temperatures

The MW results for the Maddock screw, general-purpose screw, and barrier screw do not differ markedly; for each barrel temperature profile, the CRD screw achieved the best MW results, resulting in the highest MW values. In all trials with the CRD screw the MW values were above the specification limit. As a result, this screw was selected for the production process. Figure 8.115 shows a photograph of a slotted CRD mixer.



Figure 8.115 Example of CRD mixing element

This CRD mixer uses multiple flights with right-handed orientation. As a result, this mixer has forward pumping capability. The mixing action is achieved by machining slots into the flights. The slots are tapered to generate elongational flow in the slots.

Elongational flow results in less viscous heating than shear flow. Therefore, elongational mixing devices offer the following benefits:

- Lower melt temperatures
- Fewer gels created
- Higher viscosity
- Lower motor load
- Better dispersion
- Gels can be dispersed in elongational flow
- Less degradation

Gels are generally crosslinked droplets that can be created in the polymerization process as well as in the extrusion process [110]. However, gels cause frequent problems in medical tubing extrusion where wall thicknesses tend to be very small. Most gels cannot be dispersed in shear flow because the viscosity of the gel is much greater (one or two orders of magnitude) than the matrix viscosity. Grace [132] studied drop breakup in shear and elongational flow. He found that drop breakup in shear flow is not possible when the viscosity of the drop is four times the matrix viscosity or higher. In elongational flow, drop breakup is possible even at very high viscosity ratios (as high as 1000:1).

8.8.8 Conclusions

Efficient extrusion of medical devices is a multi-faceted problem. Only some of the critical issues are discussed here. Melt temperatures in extrusion can be highly non-uniform, particularly in simple conveying screws. Therefore, screws with mixing devices are required to produce acceptable melt temperature uniformity. Barrier screws can achieve more uniform melt temperatures than simple conveying screws, but they can have greater melt pressure variation. Pressure variation results in dimensional variation of the extruded product. Therefore, pressure variation in extrusion needs to be kept as low as possible.

High stresses and temperatures in the extrusion process result in molecular weight reduction. This reduction is dependent on a number of factors, screw design being one of the most significant issues. Barrier screws tend to result in significant MW reduction. This is likely due to the high shear stresses that occur when the polymer melt flows over the barrier flight. The same problem occurs in fluted mixing sections. This explains why screws with fluted mixing sections (e.g., the LeRoy-Maddock mixer) tend to result in significant MW reduction as well.

Mixing screws based in elongational mixing devices and without barrier flights result in minimal MW reduction. These screws have little melt temperature and pressure variation, can disperse gels, and achieve a high-quality product with minimal dimensional variation. As a result, such extruder screws are attractive in medical extrusion operations when MW reduction must be minimized while dimensional control and product quality are maximized.

■ 8.9 Scale-Up

One of the first articles on scale-up was written by Carley and McKelvey [59]. By analyzing the melt pumping function, they showed that output and power consumption increase by the diameter ratio cubed if channel depth and width are increased in proportion to the diameter ratio and if the screw speed is kept constant. This analysis is only applicable to melt fed extruders where the polymer melt exhibits Newtonian flow characteristics. In plasticating extruders, one has to be concerned with solids conveying, melting, pumping, mixing, and the temperature profiles in the polymer melt. The actual scale-up factors will generally be a compromise between the various functional requirements because different functional requirements often result in conflicting scale-up factors, e.g., mixing and heat transfer.

8.9.1 Common Scale-Up Factors

The most commonly used scale-up method maintains constant shear rate by increasing the channel depth proportional to the square root of the diameter ratio and by reducing the screw speed by the square root of the diameter ratio [60]. The resulting scaling factors for output, residence time, melting capacity, power consumption, and specific energy consumption are shown in Table 8.5.

The pumping capacity can be checked by using Eq. 7.291. The drag flow rate can be written as:

$$\dot{V}_d = \left(\frac{4+n}{10}\right) pW\,H\,\pi D\,N\cos\varphi \tag{8.168}$$

If the helix angle φ is constant, $W \propto D$, $H \propto \sqrt{D}$, and $N \propto 1\sqrt{D}$, the drag flow rate ratio becomes:

$$\frac{\dot{V}_{d2}}{\dot{V}_{d1}} = \left(\frac{D_2}{D_1}\right)^2 \tag{8.169}$$

The pressure flow rate can be written as:

$$\dot{V}_p = \frac{p\,W\,H^3}{4\,\mu(1+2n)}\frac{\Delta P}{\Delta z} \tag{8.170}$$

The pressure flow ratio becomes:

$$\frac{\dot{V}_{p2}}{\dot{V}_{p1}} = \left(\frac{D_2}{D_1}\right)^{2.5}\frac{\Delta z_1}{\Delta z_2} \tag{8.171}$$

In order for the pressure flow rate to increase by the same rate as the drag flow, the helical length for pressure build-up has to be:

$$\frac{\Delta z_2}{\Delta z_1} = \left(\frac{D_2}{D_1}\right)^{0.5} \tag{8.172}$$

This means that the axial length of the metering section can be increased by the square root of the diameter ratio. Thus, the L/D of the metering section can be reduced by the square root of the diameter ratio.

The melting capacity can be evaluated by examining Eq. 7.166. The melting rate $\dot{M}_p$ can be written as:

$$\dot{M}_p = \left(\frac{\rho_m k_m v_b \sin\varphi \Delta T_b\, F_1(K_2)}{\Delta H}\right)^{1/2} \Delta z \sqrt{W_s} \tag{8.173}$$

Thus, the ratio of melting capacity becomes:

$$\frac{\dot{M}_{p2}}{\dot{M}_{p1}} = \left(\frac{v_{b2}}{v_{b1}}\right)^{0.5}\frac{\Delta_{z2}}{\Delta_{z1}}\left(\frac{W_{s2}}{W_{s1}}\right)^{0.5} \tag{8.174}$$

With $v_b \propto \sqrt{D}$, Δz_2 ‰ D, and $W_{s2} \propto D$, the ratio becomes:

$$\frac{\dot{M}_{p2}}{\dot{M}_{p1}} = \left(\frac{D_2}{D_1}\right)^{1.75} \tag{8.175}$$

This indicates that the increase in melting rate does not keep up with the increase in output. This problem can be alleviated by increasing the length of the melting section more than a simple proportional increase. In order to keep the increase in melting rate the same as the increase in total throughput, the length of the melting section should increase by $\Delta z_2 \propto D^{1.25}$. Thus, the L/D of the melting section will increase by $L/D_{melt} \propto D^{0.25}$. In order to match the melting capacity and the pumping capacity, the L/D of the melting section has to be increased and the L/D of the pumping section reduced.

The solids conveying rate can be evaluated by using Eqs. 7.46 and 7.48:

$$\dot{M}_s = \rho H p W v_b \left(\cos\varphi - \frac{\sin\varphi}{\tan(\theta + \varphi)} \right) \tag{8.176}$$

If the solids conveying angle is considered to be relatively constant, the solids conveying ratio can be written as:

$$\frac{\dot{M}_{s2}}{\dot{M}_{s1}} = \frac{H_2}{H_1} \frac{W_2}{W_1} \frac{v_{b2}}{v_{b1}} = \left(\frac{D_2}{D_1} \right)^2 \tag{8.177}$$

Thus, the solids conveying rate increases at the same rate as the pumping capacity.

The screw power consumption can be evaluated by considering that the power consumption is roughly determined by the barrel surface area A, the shear stress acting at the barrel surface area τ, and the barrel velocity v_b:

$$Z \propto A \tau v_b \tag{8.178}$$

Considering that $A = \pi DL$ and that the shear stress will be constant because the shear rate is constant as long as the polymer melt viscosity remains constant, the power consumption becomes:

$$Z \propto D^2 L N \tag{8.179}$$

If $L \propto D$ and $N \propto 1/\sqrt{D}$, the power consumption becomes:

$$Z \propto D^{2.5} \tag{8.180}$$

This is not a good situation because the power consumption increases more rapidly than the output, causing an increase in specific energy consumption and thus melt temperature. If the length L is reduced less than proportional to D, then the increase in power consumption can be reduced. In order to match the increase in power consumption to the increase in output, the total length L should increase as:

$$L \propto \sqrt{D} \tag{8.181}$$

This would mean a reduction in the total L/D by $\sqrt{D}$. For the pumping section this is possible; however, it is not possible for the melting section. The other alternative is to reduce the screw speed by more than the square root of the diameter ratio.

The effect of the common scale-up factors on extruder performance is presented in tabular form in Table 8.5.

The scale-up factors listed in Table 8.5 are the exponents of the diameter ratio. For instance, if the exponent for channel depth is 0.5, then the channel depth of the large extruder H_2 is related to the channel depth of the small extruder H_1 by the fol-

lowing relationship: $H_2 = H_1 (D_2/D_1)^{0.5}$; D_2 is the diameter of the large extruder and D_1 of the small extruder.

Table 8.5 Common Scale-Up Factors

	Common scale-up	Scale-up for heat transfer	Scale-up for mixing
Channel depth	0.5	0.5	1
Screw speed	–0.5	–1.0	0
Output	2.0	1.5	3
Shear rate	0.0	–0.5	0
Tip speed	0.5	0.0	1
Residence time	0.5	1.0	0
Melting rate	1.75	1.5	2
Solids conveying	2.0	1.5	3
Screw power	2.5	1.5	3
Specific energy	0.5	0.0	0

8.9.2 Scale-Up for Heat Transfer

In Section 5.3.3, heat transfer was analyzed in a Newtonian fluid between two plates, one stationary at temperature T_0 and one moving at velocity v and at temperature T_1. When conduction, convection, and dissipation all play a role of importance, the temperature profile is described by Eq. 5.69. Two dimensionless numbers determine the temperature distribution, the Graetz number, and the Brinkman number. If these numbers remain the same in scale-up, the temperature profile in the polymer melt will also remain the same. A constant Graetz number requires that:

$$\frac{v H^2}{\alpha L} = \text{constant} \tag{8.182}$$

It can be assumed that the thermal diffusivity (α) is constant. Considering that $v = \pi DN$ and the L/D ratio is usually constant, Eq. 8.182 can be written as:

$$N H^2 = \text{constant} \tag{8.183}$$

A constant Brinkman number requires that:

$$\frac{\eta v^2}{k \Delta T} = \text{constant} \tag{8.184}$$

If it can be assumed that the viscosity η, the thermal conductivity k, and the imposed temperature difference ΔT are constant, Eq. 8.184 becomes:

$$v = \text{constant} \tag{8.185}$$

This means that the circumferential speed ($v = \pi DN$) has to be constant. With Eqs. 8.183 and 8.184 the channel depth and screw speed can be expressed as a function of diameter:

$$N \propto 1/D \tag{8.185a}$$

$$H \propto \sqrt{D} \tag{8.185b}$$

The effect of these scale-up factors on extruder performance is shown in Table 8.5. It can be seen that there is a good match between pumping rate, melting rate, and solids conveying rate. Further, the specific energy consumption remains constant, thus the melt temperature level should be about the same in scale-up. The main disadvantage of this approach is that the output will be considerably lower than the common scale-up factors; see Table 8.5. For instance, if D_1 = 50 mm and $\dot{M}_1$ = 100 kg/hr, then for D_2 = 150 mm, the common scale-up factor will give $\dot{M}_2$ = 900 kg/hr, whereas the scale-up for heat transfer will give $\dot{M}_2$ = 520 kg/hr. In practice, therefore, the screw speed will be increased until the melt temperature almost reaches the maximum acceptable temperature. The residence time increases faster than with the common scale-up factors.

8.9.3 Scale-Up for Mixing

If it is assumed that the two most important parameters in mixing are shear rate and residence time, then scale-up rules can be derived that will keep these parameters constant. The shear rate is approximately:

$$\dot{\gamma} \cong \frac{\pi D N}{H} \tag{8.186}$$

The residence time is:

$$t = \frac{L}{\pi D N} \tag{8.187}$$

If L/D is constant, then Eq. 8.187 requires that the screw speed be constant. From Eq. 8.186, it can be seen that with constant N the ratio of diameter to channel depth also must be constant. Thus, the scale-up factors for mixing become:

$$N = \text{constant} \tag{8.187a}$$

$$H \propto D \tag{8.187b}$$

The effect of these geometric scale-up factors on extruder performance is shown in Table 8.5. The main problem with this scale-up approach is that the output increases much faster than the melting capacity. This approach, therefore, will not work

unless special design changes are made in the melting section of the screw to substantially enhance the melting capacity; see Section 8.2.2. The advantage of this scale-up approach is that very high outputs are obtained and the specific energy consumption remains constant.

A comparison of the effect on output of the different scale-up strategies is shown in Table 8.6. If the diameter of the small extruder is 50 mm (2 in) and the output 100 kg/hr (220 lbs/hr), the output for a 150-mm (6 in) extruder will be as shown in Table 8.6.

From Table 8.6, it can be seen that scale-up for mixing results in very high output values. Summarizing, it can be stated that scale-up for heat transfer will result in matched solids conveying, melting, and pumping in addition to constant specific energy consumption. Scale-up for heat transfer, therefore, will result in good extruder performance and melt temperature control. However, outputs according to the scale-up for heat transfer are rather low. Outputs can be increased by increasing the screw speed by more than $N \propto 1/D$; however, this will result in an increase in specific energy and insufficient melting capacity. Thus, the melt quality will deteriorate. In practice, one would increase the screw speed to just below where the melt quality becomes unacceptable.

Table 8.6 Output According to Various Scale-Up Rules

Scale-up method	Throughput large extruder (150 mm)
Common scale-up factors	900 kg/hr
Scale-up for heat transfer	520 kg/hr
Scale-up for mixing (geometric)	2700 kg/hr

Geometric scale-up has many attractive features. The main drawback is that the melting capacity does not increase as fast as the solids conveying and melt conveying capacity. This can create melting problems on the larger machine unless special measures are taken to improve melting. One simple way of doing this is to increase the length of the extruder. The melting problem is less likely to be a problem with amorphous polymers than with semi-crystalline polymers because the enthalpy rise with amorphous polymer tends to be significantly lower than with semi-crystalline polymers; see Section 6.3.4.

8.9.4 Comparison of Various Scale-Up Methods

Rauwendaal [91] compared a number of existing scale-up methods and proposed two new methods. The different scale-up methods are compared by how the three primary variables are changed in the scale-up. The primary variables are channel depth, length, and screw speed. The resulting performance of the extruder can be

expressed as a function of the exponents of the primary variables. This is shown in Table 8.7 with the primary variables listed at the top.

Table 8.7 Basic Relationships and Three Scale-Up Methods

	Relations	I	II	III
Channel depth	h	1	0.5	(1+n)/(1+3n)
Axial length	l	1	1	1
Screw speed	v	0	–0.5	–(2+2n)/(1+3n)
Shear rate	1+v–h	0	0	–2/(1+3n)
Pumping rate	h+2+v	3	2	(1+5n)/(1+3n)
Melting[1)]	1+0.5v+lt	2	1.75	(1+5n)/(1+3n)
Melting[2)]	$2+v+0.5nv+l_t$	3	2.5–0.25n	$(-n^2+6n+1)/(1+3n)$
Solids conveying	2+h+v	3	2	(1+5n)/(1+3n)
Residence time	–1–v+l	0	0.5	(2+2n)/(1+3n)
Shear strain	1–h	0	0.5	2n/(1+3n)
Power consumption	2+n+l+nv+v-nh	3	2.5	(1+5n)/(1+3n)
Specific energy	1–h+n+nv–nh	0	0.5	0
Area/throughput	–1–h+l–v	–1	0	(1+n)/(1+3n)

I scale-up proposed by Carley and McKelvey [92]
II scale-up proposed by Maddock [93]
III scale-up proposed by Pearson [94]
1) at low Brinkman number
2) at high Brinkman number

The scale-up proposed by Carley and McKelvey [92] is the same as the scale-up for mixing also called geometrical scale-up, discussed in Section 8.8.3. The scale-up proposed by Maddock [93] is the same as the common scale-up discussed in Section 8.8.1. The scale-up proposed by Pearson is the most comprehensive and consistent. There is good balance between solids conveying, melting, and melt conveying; further, the specific energy consumption is constant. A drawback of the Pearson scale-up is that the output increase is rather low; this makes the scale-up unattractive in practice. More scale-up methods are listed in Table 8.8.

The scale-up by Fenner and Yi [95] suffers from the fact that the specific energy consumption increases a large amount. This is generally detrimental in scale-up. Potente and Fischer [96] developed scale-up rules for both conventional and feed controlled (grooved feed) extruders. The features of this scale-up are not attractive. The solids conveying rate does not match the melting or melt conveying rate, the throughput increase is rather low, the residence time increases considerably, and the specific energy increases for shear thinning polymers ($n < 1$).

Rauwendaal [97] proposed two new scale-up methods that result in constant mechanical specific energy consumption and high throughput rates. The first one keeps the specific surface area constant. This scale-up should work well for high values of

the Brinkman number; at low values of the Brinkman number the melting rate may be insufficient. The second scale-up method keeps the melting rate at a low Brinkman number equal to the pumping rate and, thus, should be useful in cases where the first scale-up method cannot be used.

Table 8.8 Comparison of Several Scale-Up Methods

	IV	V	VI	VII
Channel depth	0.3	0.7	(1+n)/(1+2n)	1/(2n)
Axial length	1	1	1	(1+n)/(2n)
Screw speed	–0.3	–0.6	–(1+n)/(1+2n)	–1
Shear rate	0.4	–0.3	–1/(1+2n)	–1/(2n)
Pumping rate	2	2.1	2	(1+2n)/(2n)
Melting[1)]	1.85	1.7	(3+7n)/(2+4n)	(1+2n)/(2n)
Melting[2)]	2.7–0.15n	2.4–0.3n	$(-n^2+9n+6)/(2+4n)$	$(-n^2+3n+1)/(2n)$
Solids conveying	2	2.1	2	(1+2n)/(2n)
Residence time	0.3	0.6	(1+n)/(1+2n)	(1+n)/(2n)
Shear strain	0.7	0.3	n/(1+2n)	0.5
Power consumption	2.7+0.4n	2.4–0.3n	2	(1+2n)/(2n)
Specific energy	0.7+0.4n	0.3–0.3n	0	0
Area/throughput	0	–0.1	0	0.5

IV scale-up proposed by Fenner and Yi [95]
V scale-up proposed by Fischer and Potente [96]
VI scale-up proposed by Rauwendaal [97]
VII scale-up proposed by Rauwendaal [97]
1) at low Brinkman number
2) at high Brinkman number

■ 8.10 Rebuilding Worn Screws and Barrels

In a correctly designed extruder, the majority of the wear should be concentrated on the screw because the screw can be replaced and rebuilt more easily than the barrel. In fact, the rebuilding of extruder screws has become so common that the rebuilding business has become a major segment of the extrusion industry. There are more than 70 companies in the U.S. involved in the rebuilding of extrusion equipment. For a number of these companies, screw rebuilding constitutes the major part of their business.

One reason for the popularity of screw rebuilding is the fact that rebuilding is usually considerably less expensive than replacement with a new screw. Rebuilding is usually done with hardfacing materials. With the proper choice of hardfacing material, the rebuilt screw can be better than the original screw. It usually makes no

economic sense to rebuild small extruder screws (diameter less than 40 mm) because the cost of rebuilding may be the same (or higher) as the manufacture of a new screw. Also, applying hardfacing to a worn, small-diameter screw is difficult and the results are often less than satisfactory. However, larger diameter screws can be hardfaced without much trouble and generally can be rebuilt numerous times.

Properties of several hardfacing materials are listed in Table 8.9 [104].

Table 8.9 Properties of Hardfacing Materials

Product	Base material	Hardness Rc	Cracking Tendency	% Carbon	% Chromium	% Tungsten	% Boron	Cost/lb [$]
Stellite 1	Cobalt	48–54	High	2.5	30.0	12	–	25–40
Stellite 6	Cobalt	37–42	Medium	1.1	28.0	4	–	25–40
Stellite 12	Cobalt	41–47	Medium	1.4	29.0	8	–	25–40
Colmonoy 5	Nickel	45–50	Medium	0.65	11.5	–	2.5	15–25
Colmonoy 56	Nickel	50–55	High	0.70	12.5	–	2.7	15–25
Colmonoy 6	Nickel	56–61	High	0.75	13.5	–	3.0	15–25
Colmonoy 83	Nickel	50–55	High	2.0	20.0	34	1.0	40–50
N-45	Nickel	30–40	Medium	0.3	11.0	–	2.2	15–25
N-50	Nickel	40–45	Medium	0.4	12.0	–	2.4	15–25
N-56	Nickel	45–50	High	0.6	13.5	–	2.8	15–25

The steps involved in rebuilding a screw are [104]:

1. The screw is set up in a lathe and a center is found. At this time the screw is checked for straightness and concentricity;
2. The screw is polished and prepped for stripping off the existing chrome;
3. The entire screw is submerged in an acid bath to remove the chrome plating;
4. The screw then moves to the grinder where it is ground undersize;
5. The screw flights are welded with a hardfacing material such as Colmonoy 56 or Stellite 12;
6. The screw goes back to the grinder for rough grind after welding. The screw is also checked for straightness;
7. The flight grinder is used to trim the sides of the flight;
8. The screw goes to the polishing booth for a rough polish;
9. The screw is inspected and buffed for chrome plating if needed;
10. Chrome plating is applied to the entire root and bearing surface;
11. The screw is buffed after chrome;
12. The screw is ground to the final O.D. specification;

13. Final polish and buff as needed;
14. Grind front surface, size register and board the O.D.;
15. Final inspection.

8.10.1 Application of Hardfacing Materials

There are four commonly used hardfacing techniques in the industry [105]. They are oxyacetylene, tungsten inert gas (TIG), plasma transfer arc (PTA), and metal inert gas (MIG). Each method has certain advantages and disadvantages that will be discussed next. Sometimes a layer of stainless steel is applied on the flight before applying the hardfacing material. This can be done to control the dilution of the hardfacing material with the screw base material, to improve the bond, and to reduce the cracking of the hardfacing.

8.10.1.1 Oxyacetylene Welding

In this process an intense flame is produced by burning a controlled mixture of oxygen and acetylene gas; see Fig. 8.116.

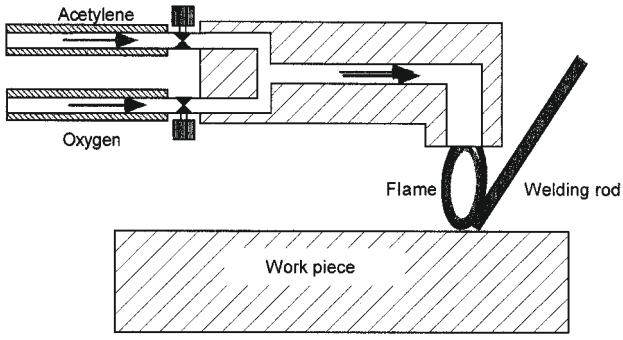


Figure 8.116
Oxyacetylene welding

The gases are drawn from separate sources through pressure regulators and introduced into a torch for mixing. The gases exit the welding nozzle where they are ignited. The flame intensity depends on the flow rate of the gases, the gas mixture ratio, the properties of the fuel gas selected, and the type of nozzle used.

Welds are formed from the weld puddle created through contact of the flame, the work piece, and the welding rod. Oxyacetylene welding requires a high degree of skill to obtain high-quality deposits and the process is slow. The benefit of oxyacetylene welding is that it provides the least base metal dilution of any method. A one-layer deposit is usually sufficient to reach the desired hardness.

8.10.1.2 Tungsten Inert Gas Welding

TIG welding is an arc fusion welding process in which intense heat is produced by an electric arc between a non-consumable, torch-held tungsten electrode and a work piece; see Fig. 8.117.

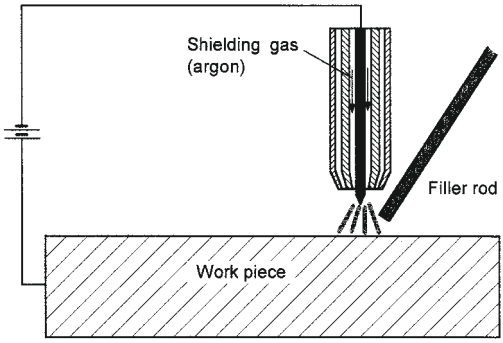


Figure 8.117
Tungsten inert gas welding process

An inert shielding gas, generally argon, is introduced through the torch to protect the weld zone from atmospheric contamination. TIG welding is the method most commonly used in the manufacturing and rebuilding of extruder screws. The localized, intense heat of TIG results in some base metal dilution. As a result, it may be necessary to apply a second layer to achieve full hardness of the hardfacing material.

8.10.1.3 Plasma Transfer Arc Welding

A PTA torch consists of an electrode in the center surrounded by a double-walled tube that carries the powdered metal. Argon gas passes through this annulus while metal powder is metered through the holes in the inside wall of the tube. Both exit onto the work piece through an arc struck between the electrode and the work piece; see Fig. 8.118. Argon gas is circulated around the welding zone to provide a shield around the arc region.

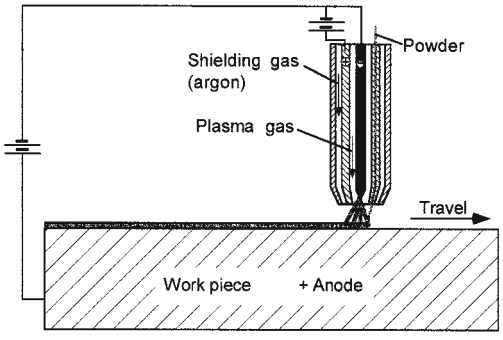


Figure 8.118
Plasma transfer arc welding process

8.10.1.4 Metal Inert Gas Welding

In the MIG welding process, an electric arc is established between the work piece and a wire electrode. The electrode is continuously fed by a wire feeder through a torch. The arc continuously melts to form the weld puddle. An appropriate gas or gas mixture shields the weld area from atmospheric contamination. The MIG process has advantages of high deposition rates, faster speed, and excellent weld quality. A drawback of MIG is that base metal dilution is more than other processes. As a result, a second layer of weld may have to be applied to achieve the desired hardness.

8.10.1.5 Laser Hardfacing

Another method of applying hardfacing is laser hardfacing on the flight lands. The common hardfacing materials listed in Table 8.9 can be applied by laser hardfacing along with tungsten carbide composites. The tungsten carbide particle can be spherical or angular in shape. Important benefits of the laser process are the low heat input, the low dilution of the deposited alloy, the large variety of hardfacing compositions (powder fed), and the overlays are metallurgically bonded and impervious.

These characteristics lead to high quality overlays without cracks, minimal porosity, and high hardness values. For instance, Colmonoy 56 PTA powder can be laser deposited with resulting hardness values in the low 60s Rc. The final thickness that can be achieved for crack sensitive materials ranges from 0.4 to 1.5 mm. The final thickness achievable for less crack sensitive materials like Stellite 6 is not limited because multi-layer deposits can be applied. This method can be used on new screws; the use in rebuilding screws is evaluated on a case-by-case basis. See Table 8.10 for a comparision of different welding methods.

Table 8.10 Comparison of Different Welding Methods

Method	Speed of application	Metal dilution	Integrity of the weld	Ease of automation
Oxyacetylene	Poor	Good	Fair	Poor
TIG	Good	Fair	Good	Fair
PTA	Fair	Fair	Good	Good
MIG	Excellent	Poor	Good	Excellent
Laser	Excellent	Excellent	Excellent	Excellent

8.10.2 Rebuilding of Extruder Barrels

Rebuilding barrels is usually considerably more difficult than rebuilding screws. If the barrel wear does not exceed about 0.5 mm, the whole barrel can be honed to a larger diameter and an oversized screw can be placed in the machine. The obvious

disadvantage of this procedure is that non-standard barrel and screw dimensions result. Thus, screws from other machines can no longer be used in the non-standard extruder. If barrel wear occurs near the end of the barrel, a sleeve can be placed in the barrel. In most cases, however, the barrel wear is such that replacement of the barrel makes more sense than sleeving or increasing I.D. by honing.

References

1. R.T. Fenner and J.G. Williams, Polym. Eng. Sci., 11, 474–483 (1971)
2. C.J. Rauwendaal, SPE ANTEC, Chicago, 186–299 (1983)
3. J. Dekker, Polytechnisch Tijdschrift (Dutch), 31, 742–746 (1976)
4. C.J. Rauwendaal, SPE ANTEC, Chicago, 151–154 (1983)
5. C.J. Rauwendaal, Plastics Technology, August, 61–63 (1983)
6. C.J. Rauwendaal, U.S. Patent 4,129,386, "Extruder Screw to Increase Throughput"
7. C.J. Rauwendaal, SPE ANTEC, New York, 110–113 (1980)
8. B. Miller, Plastics World, March, 34–38 (1982)
9. R.M. Bonner, 89 October, 1069–1073 (1963)
10. W. Backhoff, R. von Hooren, and F. Johannaber, Kunststoffe, 6, 307 (1977)
11. J.L. Duda, J.S. Vrentas, S.T. Ju, and H.T. Liu, AIChE J., 28, 279 (1982)
12. D. Anders, in "Entgasen von Kunststoffen," VDI-Verlag, Duesseldorf (1980)
13. J.F. Carley, SPE J., 24, 36–41 (1968)
14. W.H. Willert, paper given at Newark section of the SPE on February 8 (1961)
15. B.H. Maddock and P.P. Matzuk, SPE J., 18, 405–408 (1962)
16. D. Anders, Kunststoffe, 66, 250–257 (1976)
17. H. Werner and J. Curry, SPE ANTEC, Boston, 623–626 (1981)
18. N.J. Brozenick and G.A. Kruder, SPE ANTEC, San Francisco, 176–181 (1974)
19. R.J. Nichols, G.A. Kruder, and R.E. Ridenour, SPE ANTEC, Atlantic City, 361–363 (1976)
20. D. Bernhardt, SPE J., 12, 40–57 (1956)
21. B. Franzkoch, in "Entgasen von Kunststoffen," VDI-Verlag, Duesseldorf (1980)
22. B.H. Maddock, SPE ANTEC, San Francisco, 247–251 (1974)
23. Ch. Maillefer, Swiss Patent 363,149
24. Ch. Maillefer, German Patent 1,207,074
25. Ch. Maillefer, British Patent 964,428
26. P. Geyer, U.S. Patent 3,375,549
27. J.F. Ingen Housz and H.E.H. Meijer, Polym. Eng. Sci., 21, 352–359 (1981)
28. R. Barr, U.S. Patent 3,698,541
29. C.I. Chung, U.S. Patent 4,000,884

30. W.H. Willert, European Patent Application 34,505, August 26, 1981
31. R.F. Dray and D.L. Lawrence, U.S. Patent 3,650,652
32. J.S. Hsu, U.S. Patent 3,858,856
33. D.T. Kim, U.S. Patent 3,867,079
34. D.T. Kim, U.S. Patent 3,897,938
35. J.F. Ingen Housz, U.S. Patent 4,218,146
36. J.F. Ingen Housz and H.E.H. Meijer, Polym. Eng. Sci., 21, 1156–1161 (1981)
37. G. LeRoy, U.S. Patent 3,486,192
38. B.H. Maddock, SPE J., July, 23–29 (1967)
39. G. Kruder, U.S. Patent 4,173,417
40. G. Kruder, U.S. Patent 3,870,284
41. F.E. Dulmage, U.S. Patent 2,753,595
42. R.L. Saxton, U.S. Patent 3,006,029
43. German Patent 2,026,834
44. G.M. Gale, SPE ANTEC, Chicago, 109–112 (1983)
45. British Patent 930,339
46. F.J. Brinkschroeder and F. Johannaber, Kunststoffe, 71, 138–143 (1981)
47. R.B. Gregory and L.F. Street, U.S. Patent 3,411,179
48. R.B. Gregory, U.S. Patent 3,788,614
49. R.G. Dray, U.S. Patent 3,788,612
50. R.A. Worth, Polym. Eng. Sci., 19, 198–202 (1979)
51. Z. Tadmor and I. Klein, Polym. Eng. Sci., 13, 382 (1973)
52. B. Elbirli, J.T. Lindt, S.R. Gottgetreu, and S.M. Baba, SPE ANTEC, Chicago, 104 (1983)
53. C.J. Rauwendaal, SPE ANTEC, New Orleans, 59–63 (1984)
54. G. Martin, Industrie-Anzeiger, 14, 2651 (1971)
55. I. Manas-Zloczower, A. Nir, and Z. Tadmor, Rubber Chem. Technol., 55, 1250 (1983)
56. P. Heidrich, German Patent 1,145,787 (1959)
57. F.K. Lacher, U.S. Patent 3,271,819
58. M.H. Pahl, "Dispersives Mischen mit Dynamischen Mischern," VDI-Verlag, Duesseldorf, 177–196 (1978)
59. D.F. Carley and J.M. McKelvey, Ind. Eng. Chem., 45, 985 (1953)
60. C.I. Chung, Polym. Eng. Sci., 24, 626–632 (1984)
61. J.C. Miller, Tappi J., 67, 64–67, June (1984)
62. D. Kearney and P. Hold, SPE ANTEC, Washington, DC, 17–22 (1985)
63. C.J. Rauwendaal, Polymer Extrusion III Conference, London, 7/1–7/16, September 11–13 (1985)

64. M. A. Spalding, J. Dooley, and K. S. Hyun, "The Effect of Flight Radius Size on the Performance of Single-Screw Extruders," 57th SPE ANTEC, 190–194 (1999)
65. C. J. Rauwendaal, U. S. Patent 4,798,473, "Extruder Screw to Reduce Energy Use"
66. C. J. Rauwendaal, "Polymer Mixing, A Self-Study Guide," Carl Hanser Verlag, Munich (1998)
67. L. A. Utracki, "Mixing in Extensional Flow," 14th Annual Meeting Polymer Processing Society, Yokohama, Japan, June 8–12 (1998)
68. X. Q. Nguyen and L. A. Utracki, U. S. Patent 5,451,106
69. W. Thiele, Polyblends '95-RETEC, Montreal, October 19–20 (1995)
70. Z. Tadmor and I. Manas-Zloczower, Adv. Polym. Technol., 3, no. 3, 213–221 (1983)
71. T. H. Kwon, J. W. Joo, and S. J. Kim, "Kinematics and Deformation Characteristics as a Mixing Measure in the Screw Extrusion Process," Polym. Eng. Sci., 34, no. 3, 174–189 (1994)
72. C. J. Rauwendaal in "Mixing and Compounding of Polymers, Theory and Practice," I. Manas-Zloczower and Z. Tadmor (Eds.), Carl Hanser Verlag, Munich (1994)
73. F. N. Cogswell, J. Non-Newtonian Fluid Mech., 4, 23 (1978)
74. P. J. Gramann, L. Stradins, and T. A. Osswald, Int. Polym. Proc. 8, 287 (1993)
75. BEM*flow*, Boundary Element Fluid and Heat Transfer Simulation Program, (c)1996, The Madison Group: PPRC
76. J. Cheng and I. Manas-Zloczower, Polym. Eng. Sci., 29, 11 (1989)
77. C. J. Rauwendaal, M. del Pilar Noriega, A. Rios, T. Osswald, P. Gramann, B. Davis, and O. Estrada, "Experimental Study of New Dispersive Mixer," SPE ANTEC, New York (1999)
78. A. Gale, "Compounding in Single-Screw Extruders," Adv. Polym. Technol., 16, no. 4, 251–262 (1997)
79. C. J. Rauwendaal, U. S. Patent 5,932,159, "Screw Extruder with Improved Dispersive Mixing," August 3 (1999)
80. C. Rauwendaal, P. Gramann, B. Davis, and T. Osswald, U. S. Patent 6,136,246, "Screw Extruder with Improved Dispersive Mixing Elements," October 24 (2000)
81. C. J. Rauwendaal, "Non-Return Valve with Distributive and Dispersive Mixing Capability," 58th SPE ANTEC, Orlando, FL, 638–641 (2000)
82. C. J. Rauwendaal, "The ABCs of Extruder Screw Design," Adv. Polym. Technol. 9, no. 4, 301–308 (1989)
83. G. Semmekrot, U. S. Patent 5,013,233 (1991)
84. M. Esseghir et al., Adv. Polym. Techno., 17, 1 (1998)
85. A. J. Ingen Housz and S. A. Norden, Int. Polym. Process., 10, 120 (1995)
86. R. Barr, U. S. Patent 5,988,866 (1998)
87. J. A. Myers, R. A. Barr, M. A. Spalding, and K. R. Hughes, SPE ANTEC Tech. Papers, 45, 157 (1999)

88. B. A. Salamon, M. A. Spalding, J. R. Powers, M. Serrano, W. C. Sumner, S. A. Somers, and R. B. Peters, SPE ANTEC Tech. Papers, 46, 479–483 (2000)
89. C. Bos and C. J. Rauwendaal, internal research report (2001)
90. R. A. Barr, U. S. Patent 4,405,239
91. C. J. Rauwendaal, "Scale-Up of Single Screw Extruders," Polym. Eng. Sci., 27, no. 14, 1059–1068 (1989)
92. J. F. Carley and J. M. McKelvey, Ind. Eng. Chem., 45, 985 (1953)
93. B. H. Maddock, SPE J., 15, 983 (1959)
94. J. R. A. Pearson, Plast. Rubber Process., Sept., 113 (1976)
95. R. T. Fenner and B. Yi, Plast. Rubber Process., Sept., 119 (1976)
96. E. Fischer and H. Potente, Kunststoffe, 67, 242 (1977)
97. C. J. Rauwendaal, Polym. Eng. Sci., 27, no. 14, 1059–1068 (1987)
98. J. Fogarty, C. J. Rauwendaal, D. Fogarty, and A. Rios, "Turbo-Screw, New Screw Design for Foam Extrusion," SPE ANTEC Tech. Papers (2001)
99. A. Rios, P. Gramann, T. Osswald, M. Noriega, "Experimental and Numerical Study of Rhomboidal Mixing Sections," Int. Polym. Process., 9, no. 1, 12–19 (2000)
100. P. Gramann, M. Noriega, A. Rios, T. Osswald, "Understanding a Rhomboid Distributive Mixing Head Using Computer Modeling and Flow Visualization Techniques," SPE ANTEC Tech. Papers (1997)
101. J. Fogarty, U. S. Patent 6,015,227, "Thermoplastic Foam Extrusion Screw with Circulation Channels," (1998)
102. K. Luker, "Laboratory Tools for Compounders," Continuous Compounding Conference, Beachwood, OH, November 14–15 (2000)
103. K. Luker, "Recent Laboratory and R&D Developments in Wood-Plastic Composites," Wood-Plastic Conference, Baltimore, MD, December 5–6 (2000)
104. "Plasticating Components 2000," a publication from Spirex Corporation, Youngstown, Ohio (2000)
105. V. Anand and K. Das, "The Selection of Screw Base and Hard Facing Materials," publication CEC SSB 493.01 from Canterbury Engineering Company, Inc., Champlee, Georgia
106. C. Rauwendaal, "How to Get Peak Performance & Efficiency Out of Your Extrusion Line," Plast. Technol. Mag., June, 33–35 (2010)
107. C. Rauwendaal, "Boosting Extruder Productivity—Optimize Product Changeover and Purging," Plast. Technol. Mag., Sept. (2010)
108. C. Rauwendaal, "Boosting Extruder Productivity—Trim Your Material & Energy Cost," Plast. Technol. Mag., Nov., 26–28 (2010)
109. C. Rauwendaal, "Statistical Process Control in Extrusion and Injection Molding," Carl Hanser Verlag, Munich (2000)
110. M. del Pilar Noriega E., and C. Rauwendaal, "Troubleshooting the Extrusion Process," 2nd ed., Carl Hanser Verlag, Munich (2010)

111. C. Rauwendaal, “Leakage Flow in Screw Extruders,“ Doctoral Thesis, Twente University of Technology, Department of Mechanical Engineering–Polymer Processing, The Netherlands (1988)

112. J. Anderson and C. Rauwendaal, “Finite Element Analysis of Flow in Extruders,” 52nd SPE ANTEC, 298–305, San Francisco, CA (1994)

113. C. Rauwendaal, “Modelling and Simulation of Plasticating Single Screw Extrusion, State of the Art and Remaining Challenges,” softEXTRUSION Workshop, Alvor, Portugal, Oct. 15 (2004)

114. X. Shen, R. Malloy, J. Pacini, “An Experimental Evaluation of Melt Temperature Sensors for Thermoplastic Extrusion,” SPE ANTEC Tech. Papers, 918–926 (1992)

115. K.D. Sabota, D.R. Lawson, and J.S. Huizinga, “Advanced Temperature Measurements in Polymer Extrusion,” SPE ANTEC Tech. Papers, 2832–2842 (1995)

116. W. Obendrauf, G.R. Langecker, and W. Friesenbichler, “Temperature Measuring in Plastics Processing with Infrared Radiation Thermometers,” Int. Polym. Process., 13, no. 1, 71–77 (1998)

117. C. Maier, “Infrared Temperature Measurement of Polymers,” Polym. Eng. Sci., 36, no. 11, 1502–1512 (1996)

118. A. Bendada, M. Lamontagne, “A New Infrared Pyrometer for Polymer Temperature Measurement during Extrusion Molding,” Infrared Phys. Technol., 46, 11–15 (2004)

119. W. Schlaffer and H. Janeschitz-Kriegl, “Measurements of Radial Temperature Profiles in a Single-Screw Extruder,” Plast. & Polym., 193–199 (1971)

120. I. Bruker, C. Miaw, A. Hasson, and G. Balch, “Numerical Analysis of the Temperature Profile in the Melt Conveying Section of a Single Screw Extruder: Comparison with Experimental Data,” Polym. Eng. Sci., 27, no. 7, 504–509 (1987)

121. E.C. Brown, A.L. Kelly, and P.D. Coates, “Melt Temperature Field Measurement in Single Screw Extrusion using Thermocouple Meshes,” Rev. Sci. Instrum., 75, no. 11, 4742–748 (2004)

122. A.L. Kelly, E.C. Brown, and P.D. Coates, The Effect of Screw Geometry on Melt Temperature Profile in Single Screw Extrusion, Polym. Eng. Sci., 46, no. 12, 1706–1714 (2006)

123. A.L. Kelly, E.C. Brown, K. Howell, and P.D. Coates, “Melt Temperature Field Measurement in Extrusion Using Thermocouple Meshes,” Plast. Rubber Comp., 37, 151–157 (2008)

124. E.C. Brown, P. Olley, and P.D. Coates, “In-line Melt Temperature Measurement during Real Time Ultrasound Monitoring of Single Screw Extrusion,” Plast. Rubber Comp., 29, 3–13 (2000)

125. A.L. Kelly et al., “Thermal Optimisation of Polymer Extrusion using In-process Monitoring Techniques,” paper submitted for International Conference on Sustainable Thermal Energy Management, Oct. 25–26, Newcastle upon Tyne, UK (2011)

126. C. Rauwendaal, “Polymer Extrusion,” 4th ed., Carl Hanser Verlag, Munich (2001)

127. K. Paakinaho et al., “Melt Spinning of Poly (L/D) Lactide 96/4: Effects of Molecular Weight and Melt Processing on Hydrolytic Degradation,” Polym. Degrad. Stab., 94, 438–442 (2009)

128. T. Osswald, P. Gramann, B. Davis, and C. Rauwendaal, "A New Dispersive Mixer for Single Screw Extruders," 56th SPE ANTEC, Atlanta, GA, 277–283 (1998)

129. T. Osswald, P. Gramann, B. Davis, M. del Pilar Noriega, O. Estrada, and C. Rauwendaal, "Experimental Study of a New Dispersive Mixer," 57th SPE ANTEC, New York, 167–176 (1999); also the annual meeting of the Polymer Processing Society in Den Bosch, The Netherlands (1999)

130. G. Ponzielli and C. Rauwendaal, "Performance Characteristics of Elongational Mixing Screws," SPE ANTEC, Chicago, IL, (2004)

131. C. Rauwendaal, "New Developments in Extruder Screw Design," Plast. Technol. Asia, July, 14–17 (2006)

132. H.P. Grace, "Dispersion Phenomena in High Viscosity Immiscible Fluid Systems and Application of Static Mixers as Dispersion Devices in Such Systems," Chem. Eng. Commun., 14, 225–277 (1982)

133. C. Rauwendaal, "Recent Advances in Barrier Screw Design," Plast. Addit. Compd., Sept./Oct., 2–5 (2005)

134. C. Rauwendaal, "Efficient Extrusion of Medical Devices," presentation at conference on Plastics in Medical Products, organized by Plastics News, April 11–13, Huron, Ohio (2011)

9 Die Design

Die design is one aspect of extrusion engineering that has remained more of an art than any other aspect. The obvious reason is that it is difficult to determine the optimum flow channel geometry from engineering calculations. Realistic analysis of flow through dies in many cases requires computation of three-dimensional velocity profiles inside the die. This can be a challenge for simple Newtonian fluids. For viscoelastic fluids the computational complexity is greater still. If temperature effects are considered as well, the problem gets even more complicated. Even if the flow inside the die can be modeled accurately, it is equally important to predict what happens to the extruded polymer once it leaves the die. At this point effects like extrudate swell, drawdown, cooling, and relaxation start affecting the actual size and shape of the extrudate. Describing all these events quantitatively with good accuracy and within a reasonable time frame will remain an engineering challenge for some time to come.

Accurate description of flow of the polymer melt through the die requires knowledge of the viscoelastic behavior of the polymer melt. The polymer melt can no longer be considered a purely viscous fluid because elastic effects in the die region can be significant. Unfortunately, there are no simple constitutive equations that adequately describe the flow behavior of polymer melt over a wide range of flow conditions. Thus, a simple die flow analysis is generally very approximate, while more accurate die flow analyses tend to be quite complicated.

Finite element analysis (FEM) has become a popular method for numerical simulation of flow through dies. One of the benefits of FEM is that it can handle non-linear fluids well. A newer numerical technique gaining popularity is boundary element analysis (BEM) Three-dimensional flow analysis with BEM can handle complex flow geometries well; however, BEM at this point is not as good as FEM in handling non-linear fluids. Less detailed analyses often use control volume analysis to reduce the computational effort. The different numerical techniques will be discussed in more detail in Chapter 12.

Michaeli's book on extrusion dies [1] contains some information on the use of FEM in die design. The book by Crochet, Davies, and Walters [30] contains general information on the use of FEM in the analysis of non-Newtonian flow. More recent books on computer simulation in polymer processing are the books by Tucker [38] and O'Brien [39]. The last book deals specifically with modeling for extrusion.

9.1 Basic Considerations

The objective of an extrusion die is to distribute the polymer melt in the flow channel such that the material exits from the die with a uniform velocity. The actual distribution will be determined by the flow properties of the polymer, the flow channel geometry, the flow rate through the die, and the temperature field in the die. If the flow channel geometry is optimized for one polymer under one set of conditions, a simple change in flow rate or in temperature can make the geometry non-optimum. Except for circular dies, it is essentially impossible to obtain a flow channel geometry that can be used, as such, for a wide range of polymers and for a wide range of operating conditions. For this reason, one often incorporates adjustment capabilities into the die by which the distribution can be changed externally while the extruder is running. The flow distribution is generally changed in two ways: i) by changing the flow channel geometry by means of choker bars, restrictor bars, valves, etc., and ii) by changing the local die temperature. Mechanical adjustment capabilities complicate the design of the die but enhance its flexibility and controllability.

Some general rules that are useful in die design are:

- No dead spots in the flow channel
- Steady increase in velocity along the flow channel
- Assembly and disassembly should be easy
- Land length about 10X land clearance
- Avoid abrupt changes in flow channel geometry
- Use small approach angles

In die design, problems often occur because the product designer has little or no appreciation for the implications of the product design details on the ease or difficulty of extrusion. In many cases, small design changes can drastically improve the extrudability of the product. Some basic guidelines in profile design to minimize extrusion problems are:

- Use generous internal and external radii on all corners; the smallest possible radius is about 0.5 mm
- Maintain uniform wall thickness (important!)
- Avoid very thick walls
- Make interior walls thinner than exterior walls for cooling
- Minimize the use of hollow sections

Figure 9.1 illustrates applications of these guidelines to different profiles and flow channel geometries.

9.1.1 Balancing the Die by Adjusting the Land Length

Mechanical adjustment of the die flow channel can be done in two basic ways. The length of the channel can be adjusted to make sure the average flow velocity is uniform. The other method is to adjust the height of the channel. In this section we will discuss how to achieve uniform flow by adjustment of the land length.

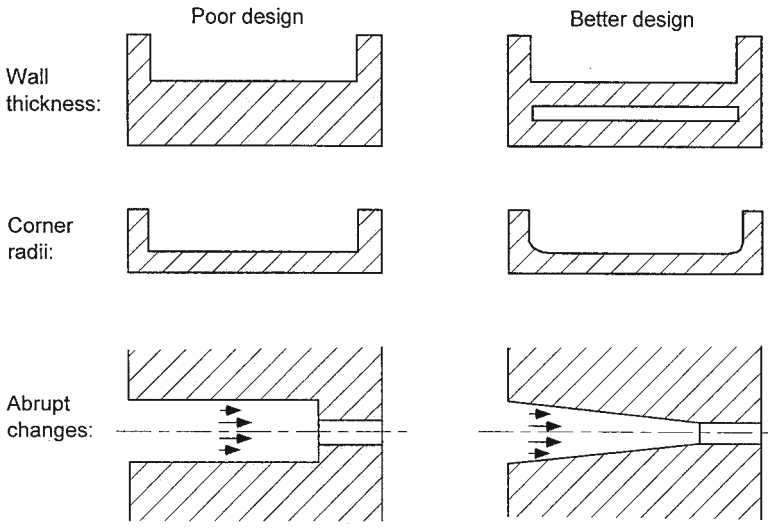


Figure 9.1 Examples of application of die design guidelines

In this analysis we will assume that the width of the flow channel is large relative to the height of the channel. In this case the flow rate for a power law fluid can be expressed as:

$$\dot{V} = \frac{n\,W\,H^2}{2(1+2n)}\left[\frac{H\,\Delta P}{2m\,L}\right]^{\frac{1}{n}} \tag{9.1}$$

The geometrical factors are the channel width W, the channel height H, and the channel length L. The important flow properties are the power law index n and the consistency index m. Equation 9.1 represents the volumetric flow rate through the die flow channel. The average flow velocity can be obtained by dividing the volumetric flow rate by the cross-sectional area of the channel. This results in the following expression for the average velocity:

$$v = \frac{n\,H}{2(1+2n)}\left[\frac{H\,\Delta P}{2m\,L}\right]^{\frac{1}{n}} \tag{9.2}$$

This expression shows that the average velocity is no longer dependent on the width of the channel. This is true as long as the channel width is much greater than the height (W >> H). If the extruded profile has sections with different thickness, the channel height will have to be different in different sections of the die flow channel. If the land length is the same in all sections of the die, differences in channel height will result in large differences in average velocity. This can be quantified by the following expression showing the ratio of average velocities v_1/v_2 as a function of the height ratio H_1/H_2.

$$\frac{v_1}{v_2} = \left(\frac{H_1}{H_2}\right)^{1+1/n} \tag{9.3}$$

Figure 9.2 shows how the velocity ratio changes with the thickness ratio at several values of the power law index.

From Fig. 9.2 it is clear that even small differences in thickness can result in large velocity differences, particularly for small values of the power law index. Even with thickness differences of 50% the velocity difference can be as high as 5:1 up to 10:1 for power law index values between 0.2 and 0.4. Most high-volume polymers have power law index values in this range. Velocity differences of 10:1 will cause severe distortion in the extrudate, which means that balancing the flow will be absolutely necessary.

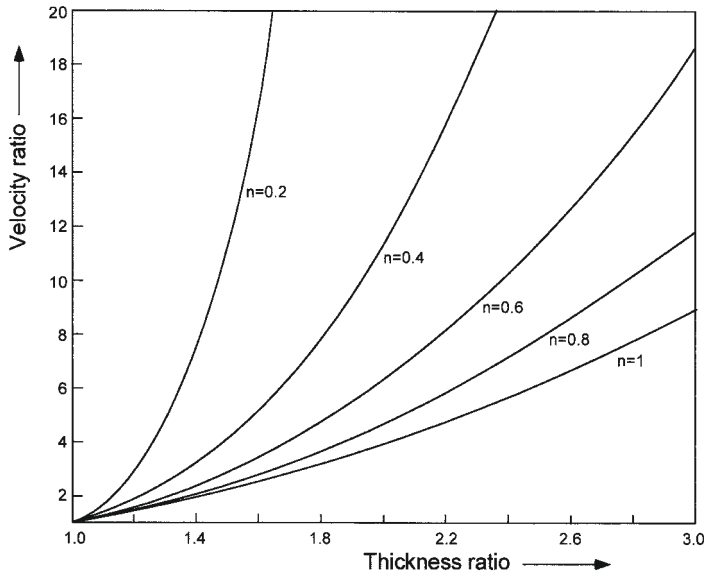


Figure 9.2 Velocity ratio versus thickness ratio for several values of the power law index

Equation 9.2 can be used to determine how the land length can be changed to maintain uniform average velocity. In order for the average velocity in the channel section with height H_1 to be the same as in the section with height H_2, the land length ratio has to be:

$$\frac{L_1}{L_2} = \left(\frac{H_1}{H_2}\right)^{1+n} \tag{9.4}$$

Figure 9.3 shows how the land length ratio changes with height ratio at several values of the power law index.

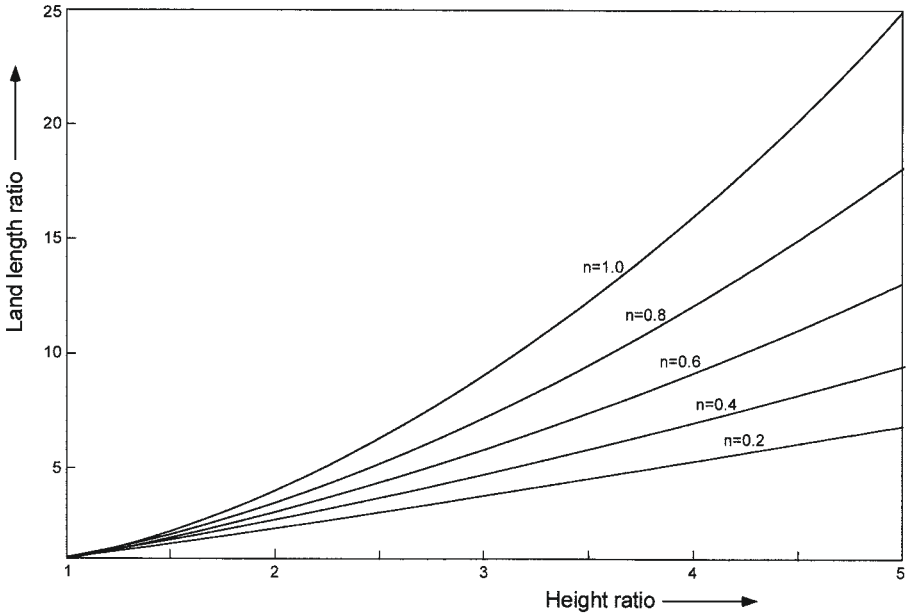


Figure 9.3 Land length ratio versus height ratio at several values of the power law index

When the height ratio is large the land length ratio has to become very large to maintain uniform flow, particularly for large values of the power law index. When the land length ratio has to be greater than about 5:1 it may no longer be practical to adjust by land length. For a polymer with a power law index of n = 0.4, this means that the height ratio should be no greater than about 3:1.

One of the problems with balancing by land length is that it induces transverse pressure differences along the length of the flow channel. Pressure differences across the channel will create cross flow, and this will make the effect of balancing by land length unpredictable unless a three-dimensional flow analysis is used. One way to avoid cross flow is to place partitions between the sections with different thickness of the die so that cross flow between the different sections is not possible. In effect, this creates separate die flow channels; an example is shown in Fig. 9.4.

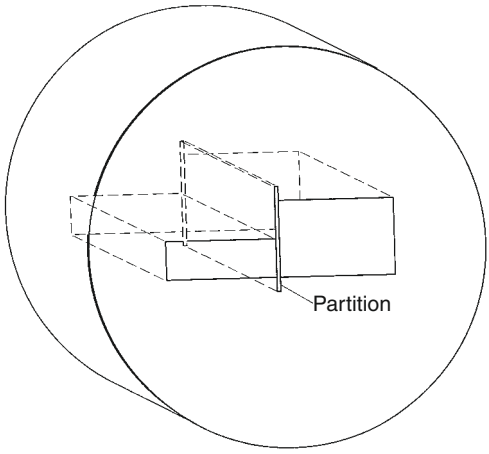


Figure 9.4
Example of partitions in a die flow channel

The partitions can be terminated just before the exit of the die to allow the separate streams to merge. This approach allows greater control of the flow through the die. The drawback with partitions is that they can create knit lines between the various partitions. Knit lines will be discussed more in Section 11.3.7.5.1. Partitions between sections of the die with different thickness can be considered as a way of balancing by channel width.

The land length is usually adjusted by changing the land length at the entry to the land; this is called "back relieving" the land. An example of back relieving is shown in Fig. 9.5(a).

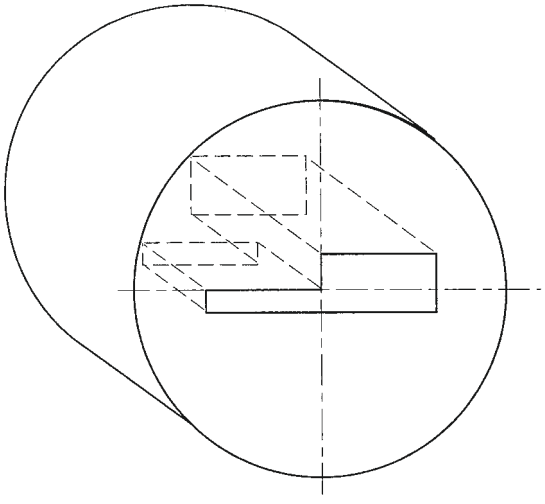


Figure 9.5(a)
Example of back relieving a profile die

It is also possible to change the land length at the end of the land, at the die exit. This is called front relieving of the die; an example of front relieving is shown in Fig. 9.5(b).

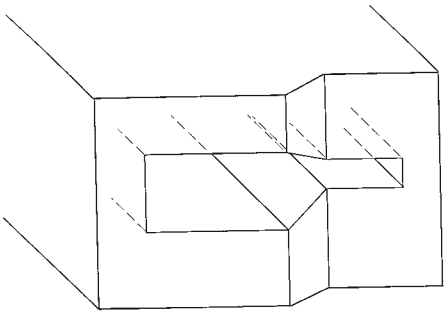


Figure 9.5(b)
Example of front relieving a profile die

Obviously, front relieving results in a die exit surface that is no longer flat. This makes it difficult to clean the die surface; as a result, front relieving of dies is practiced less than back relieving.

9.1.2 Balancing by Channel Height

As discussed in the previous section, balancing by land length does not always lead to satisfactory results. The other method is to balance by channel height. An example is shown in Fig. 9.6.

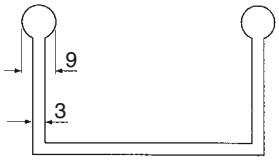


Figure 9.6
U-shaped profile with circular sections

In Fig. 9.6 there is a thin wall connected to larger diameter circular sections. Without balancing, the flow through the circular section will be substantially greater than the slit section. The average velocity in the circular section will be:

$$v = \frac{n\,D}{2(1+3n)}\left[\frac{D\,\Delta P}{4m\,L}\right]^{\frac{1}{n}} \tag{9.5}$$

As a result, the ratio of the average velocity in the circular section and the slit section will be:

$$\frac{v_{circle}}{v_{slit}} = \frac{1+2n}{2^{1/n}(1+3n)}\left(\frac{D}{H}\right)^{1+1/n} \tag{9.6}$$

This relationship is shown in Fig. 9.7.

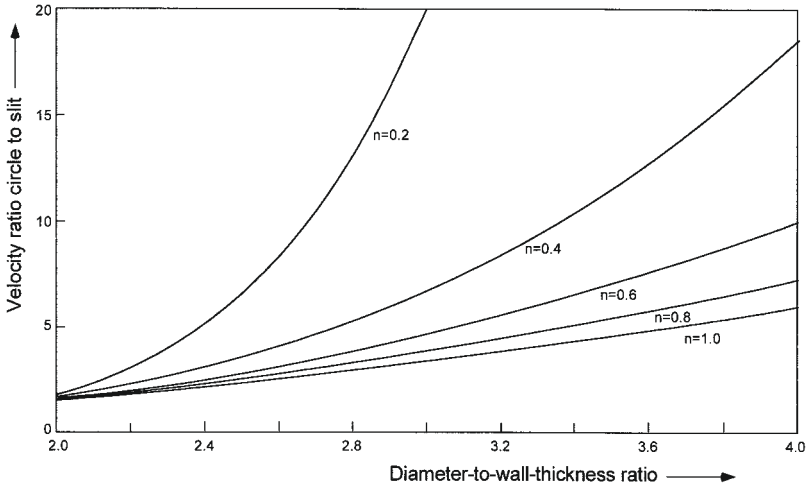


Figure 9.7 Velocity ratio circle-to-slit versus the diameter-to-wall-thickness ratio

The average flow velocity in the thin section is given by Eq. 9.2. With the wall w = 3 mm and the diameter of the circular section D = 9 mm the velocity ratio will be 3.375 when the power law index is 1. When the power law index is 0.4, the velocity ratio will be 6.764. This will clearly cause problems; therefore, balancing will be required. The balancing can be done by land length. This will require the following ratio of land length:

$$\frac{L_{slit}}{L_{circle}} = \left(\frac{1+3n}{1+2n}\right)^{n}\left(\frac{H}{D}\right)^{1+n} \tag{9.7}$$

This relationship is shown in Fig. 9.8.

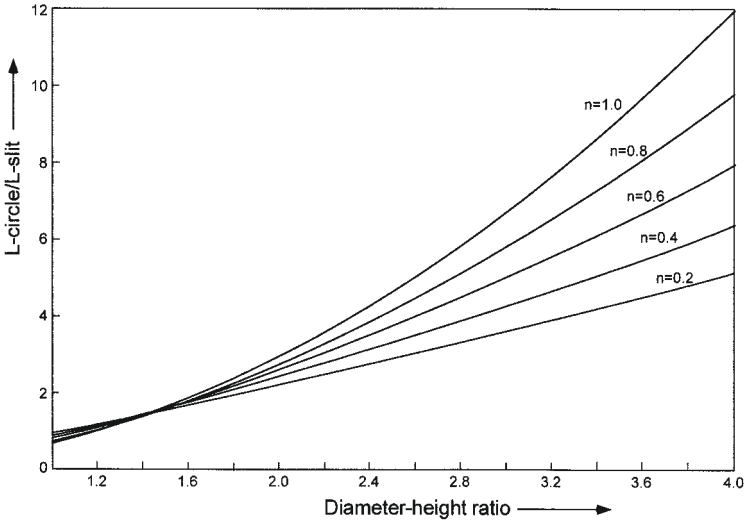


Figure 9.8 Ratio of L_{circle}/L_{slit} versus the ratio D/H at several values of the power law index

When D/H = 3, the land length of the circular section has to be 4.3 times longer than the land of the slit. This is quite a large difference and will likely result in cross flow. In this case, a better method of balancing the flow will be to place cylindrical pins in the circular section of the die as shown in Fig. 9.9.

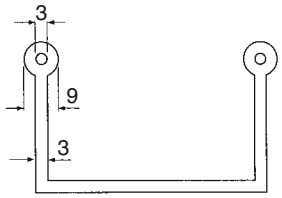


Figure 9.9
Example of balancing by adjusting the channel height

If the circular sections of the profile need to be solid the cylindrical pins can be terminated before the exit of the die so that the polymer melt can fill the entire cylindrical section.

Another example of balancing by channel height is the profile shown in Fig. 9.10.

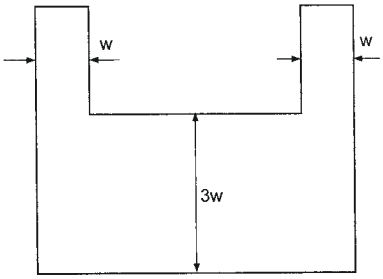


Figure 9.10
Example of profile with large difference in channel height

This profile will be difficult to extrude because the wall thickness differs by a factor of three; this will result in large velocity differences. One way to solve this problem is to make the profile hollow as shown in Fig. 9.1. However, if the profile needs to be solid, a different approach will be required. One possible approach is to place partitions in the thick section of the die so that the thickness of the individual sections will be approximately the same. This is shown in Fig. 9.11.

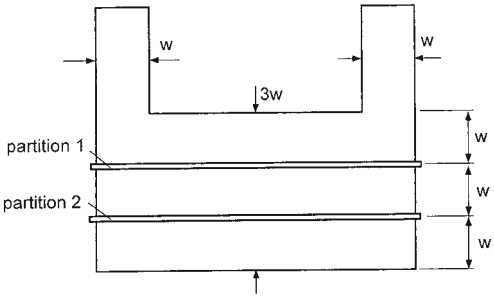


Figure 9.11
Example of adjusting channel height by partitioning the flow channel

Obviously, there are other ways that the die can be partitioned to balance the flow, but the method shown in Fig. 9.11 can work quite well to avoid large velocity differences in profile with thin and thick sections.

9.1.3 Other Methods of Die Balancing

Balancing problems frequently occur when the extruded product has differences in wall thickness. However, even without differences in wall thickness there can be distortion in the extruded product. An example is a simple rectangular or square profile; the velocity distribution on a square channel is shown in Fig. 7.105. Clearly, the velocities in the corner are less than they are along the middle of the wall. As a result, there will be more drawdown at the corners than at the mid-sections of the wall. Obviously, this problem is inherent to shapes with corners, particularly corners with a small radius and corners smaller than right-angle corners.

For this reason, the easiest shapes to extrude are circular and annular shapes. The lower velocities in the corners of a square or rectangular profile can be increased by reducing the land length in the corners. This can be done several ways as shown in Fig. 9.12.

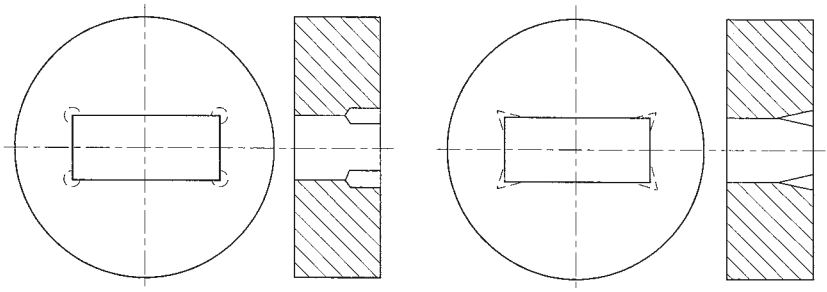


Figure 9.12 Examples of back relieving to increase velocities in corner

The examples shown in Fig. 9.12 are methods for local balancing of the land length. Another method of adjusting the shape of the die is to incorporate moveable elements in the channel such as choker bars, flex lips, and membranes. These elements are frequently used in film and sheet dies. However, they can be used in other types of dies as well.

9.2 Film and Sheet Dies

Dies for flat film are essentially the same as dies for sheet extrusion. The difference between sheet and film is primarily the thickness. Webs with a thickness of less than 0.5 mm are generally referred to as film, while webs with a thickness of more than 0.5 mm are generally referred to as sheet. Three distribution channel geometries used in sheet dies are shown in Fig. 9.13.

Fig. 9.13(a) shows the T-die. This flow channel geometry is simple and easy to machine. However, the distribution of the polymer melt is not very uniform and the flow channel geometry is not well streamlined. Thus, this die is not suitable for high-viscosity polymers with limited thermal stability. The T-die is used in extrusion coating applications. Analyses of the flow in a T-die have been made by Weeks [3, 4], Ito [5], and Pearson [6].

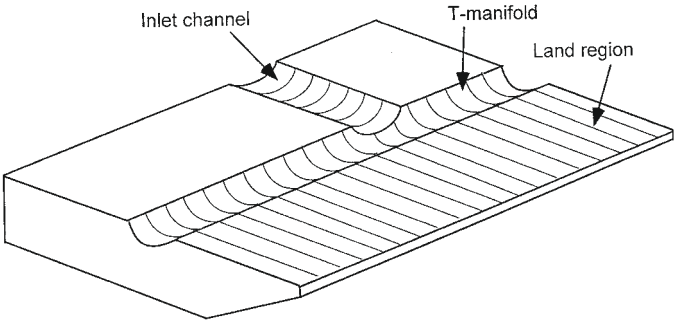


Figure 9.13(a)
The T-die

The fishtail die is shown in Fig. 9.13(b). This die results in a more uniform melt distribution than the T-die; however, a completely uniform distribution is still difficult to obtain with this geometry. Analyses of the flow in fishtail dies have been made by Ito [7] and Chejfec [8].

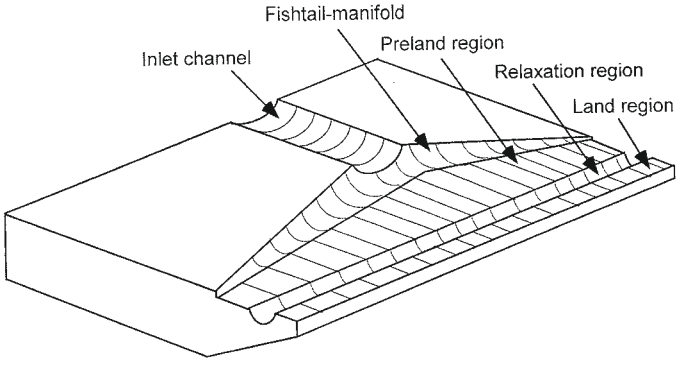


Figure 9.13(b)
The fishtail die

Figure 9.13(c) shows the coat hanger die.This is a die geometry commonly used in sheet extrusion. The geometry of the coat hanger section can be designed to give a very uniform distribution of the polymer melt. Obviously, the coat hanger die is more difficult to machine and, therefore, more expensive than the T-die and fishtail die. Analyses of the flow in coat hanger dies have been made by Ito [9, 10], Wortberg [11], Goermar [12, 13], Chung [14], Klein [15], Schoenewald [16], Vergnes [17], Matsubara [18, 19], and many more. Goermar used the sinh law (see Eq. 6.32) as the constitutive equation for the polymer melt. He obtains a remarkably simple expression for the geometry of the coat hanger section; see Fig. 9.13(c). For the manifold radius as a function of distance, Goermar derived the following expression:

$$R(x) = R_o\left(\frac{x}{b}\right)^{1/3} \tag{9.8a}$$

and for the land length:

$$L(x) = L_o\left(\frac{x}{b}\right)^{2/3} \tag{9.8b}$$

where x is the distance from the edge of the die, b the half width, R_0 the manifold radius in the center, and L_0 the preland length in the center.

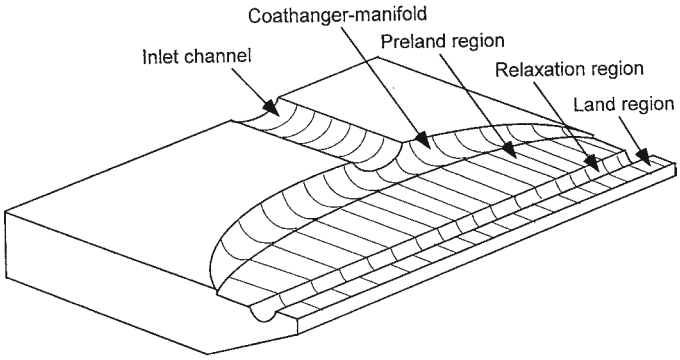


Figure 9.13(c)
The coat hanger die

9.2.1 Flow Adjustment in Sheet and Film Dies

Figure 9.14 shows two commonly used techniques to change the flow channel geometry in sheet dies.

The first is the flex lip adjustment. A number of bolts along the width of the die allow local closing of the final land gap. This allows fine adjustments of the extrudate thickness at discrete points. The gap can be adjusted by as much as 1 mm or more if the flex lip is properly designed. The choker bar is not used as often as the

flex lip. The choker bar adjustment works in a similar fashion as the flex lip adjustment. The choker bar can be locally deformed by a number of bolts located along the width of the die. The deformation of the choker bar causes a change in the height of the flow channel and, thus, allows an adjustment of the flow distribution in the die. A third adjustment possibility, not shown in Fig. 9.14, is the die temperature. Local heating or cooling of certain die sections enhance or restrict flow; this is another means of flow distribution adjustment. Temperature adjustment will be more effective with polymers whose viscosity is quite sensitive to temperature; this includes most amorphous polymers (see also Table 6.1).

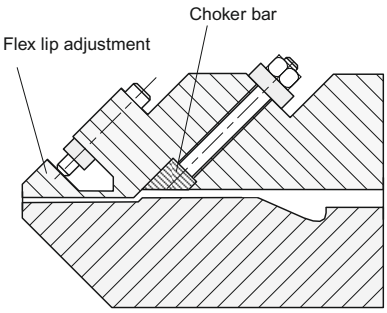


Figure 9.14
Methods to change the flow channel geometry in sheet dies

Figure 9.15 also shows a feature of the sheet die that is useful when a large thickness range is necessary.

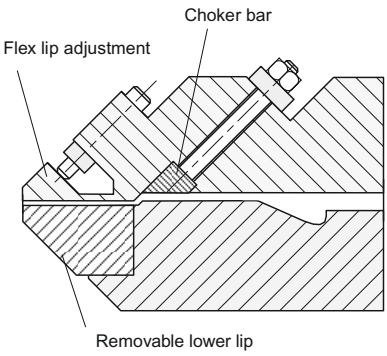


Figure 9.15
Sheet die with removable lower lip

By incorporating a removable lower die lip, the die can be used, for instance, for 1-mm sheet extrusion and for 4-mm sheet extrusion by changing only the lower die lip. Without the removable die lip, another sheet die would have to be used because the flex lip can only adjust over a limited range. In some automated extrusion lines, the gap of the sheet die is adjusted automatically. This is done with heat expandable die lip bolts [20], first developed by Welex in the early 1970s. A similar type of sheet die using thermal bolts is now also offered by Egan Machinery Company and a number of other companies.

Another concept is used by Harrel, Inc. Their sheet die has die temperature adjustment capability at various locations along the width of the die. By raising or lowering the temperature automatically, the sheet thickness can be controlled without changing the die lip gap. An interesting automatically adjustable sheet die was developed by Hexco. This sheet die uses a PC servo positioner to hydraulically control each die bolt. This design is said to reduce response time from minutes, which is typical in thermally adjusted sheet dies, down to a few seconds. Hexco went out of business in 1983; as result, this particular die is no longer available. However, similar systems have been developed by other manufactures. For instance, Japan Steel Works has developed an automatic die gap adjustment system that uses a servo motor that can travel along the width of the die to adjust any die bolt a certain amount as determined by an automatic sheet thickness measurement downstream of the die. The advantage of a mechanical adjustment as opposed to heat expandable bolts is that the thickness adjustment occurs more rapidly.

An elegant approach to thickness adjustment in sheet and film dies was developed by Gross [46]. Gross developed a system with a flexible membrane inside the die to allow rather simple thickness adjustment using low force actuators to create a smoothly curved surface without sharp angles or dead spots. This system is schematically shown in Fig. 9.16. The membrane die has been licensed by several manufacturers of extrusion dies worldwide [46].

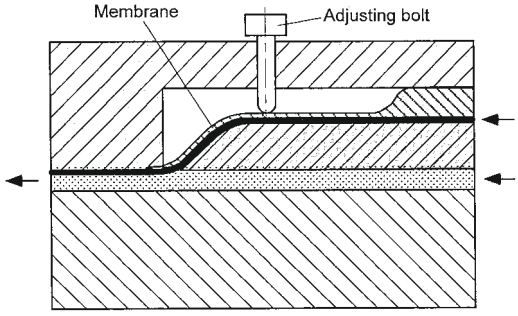


Figure 9.16
Schematic of coextrusion membrane die

A drawback of the conventional coat hanger die with the teardrop-shape distribution channel is the fact that the distribution changes when the power law index of the material changes. Thus, the distribution will change when a change in polymer is made and also when the output is changed because the power law index is generally somewhat dependent on shear rate. Therefore, flex lips and choker bars are generally used to compensate for the imperfect distribution in the die. A modified coat hanger geometry was proposed by Winter and Fritz [31] that eliminates the problem of the power law index dependence of the distribution.

9.2.2 The Horseshoe Die

The main feature of the new coat hanger geometry is a slit-shaped distribution in the shape of a horseshoe channel, see Fig. 9.17.

If the ratio of channel width W to channel depth H is larger than about 10, the shape factor becomes independent of the power law index. For a manifold with constant channel width W, the distribution channel geometry is given by (see Fig. 9.17):

$$H(x) = h\sqrt{(b-x)/W} \tag{9.9a}$$

and:

$$y(x) = 2W\sqrt{(b-x)/W - 1} \tag{9.9b}$$

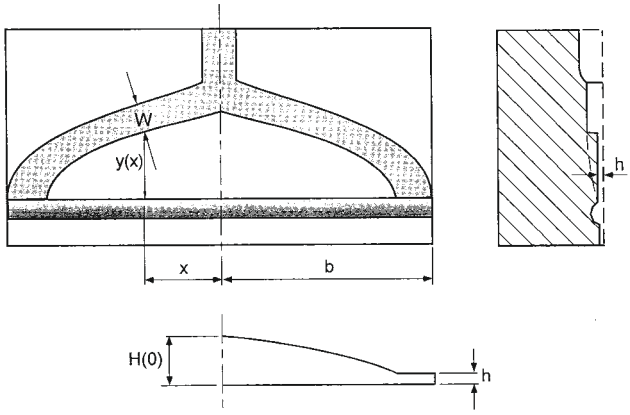


Figure 9.17
Geometry of the horseshoe manifold

For a manifold with constant aspect ratio, W/H = a, the depth profile is given by:

$$H(x) = h\left(\frac{b-x}{ah}\right)^{1/3} \tag{9.9c}$$

The corresponding contour line is given by:

$$y(x) = \frac{3b}{2A}\left[\left(\frac{1+g(x)}{g^2(x)}\right)^{1/2} - 0.5\ln\left(\frac{\sqrt{1+g(x)}-1}{\sqrt{1+g(x)}+1}\right)\right] + C \tag{9.9d}$$

where:

$$g(x) = \frac{h^2}{F^{2n}\,H^2(x) - h^2} \tag{9.9e}$$

The integration constant C is determined by setting H(x) = h at y = 0. The front factor is defined as:

$$A = \frac{F^{3n}\, b}{ah} \tag{9.9f}$$

The shape factor F for a rectangular flow channel is given by Eqs. 7.219 and 7.221. If the shape factor is taken as unity, the contour line becomes:

$$y(x) = \frac{3}{2}ah\left[\frac{\sqrt{1-\alpha^2}}{\alpha^2} - \frac{1}{2}\ln\left(\frac{1-\sqrt{1-\alpha^2}}{1+\sqrt{1-\alpha^2}}\right)\right] + h \tag{9.9g}$$

where:

$$\alpha = \frac{h}{H(x)} = \left(\frac{ah}{b-x}\right)^{1/3} \tag{9.9h}$$

The new coat hanger geometry can be applied to flat sheet dies as well as annular dies. Winter [31] reports on applications with blow molding dies with a circumferential thickness distribution of the parison between 5 and 8%. Very good results were also obtained on a flat sheet die of 0.25 m width and a flat profile die with a width of 2 m. A drawback of the horseshoe manifold is that the pre-land is quite long. This makes the die more susceptible to clamshelling (the separation of the die lips in the center region of the die due to high pressure of the polymer melt inside the die). As a result, this manifold is less suitable for very wide dies when high internal pressures occur inside the die.

■ 9.3 Pipe and Tubing Dies

The difference between pipe and tubing is mainly determined by size. Small diameter products (less than 10 mm) are generally referred to as tubing, while large products are generally referred to as pipe. Annular products can be extruded on in-line dies and crosshead dies. In the crosshead die the polymer melt makes a turn as it flows through the die; an example of a crosshead die Fig. 9.18.

The direction of the inlet flow is perpendicular to the outlet flow. The polymer melt makes a 90° turn and splits at the same time over the core tube. The polymer melt recombines below the core tube; this is where a weld line will form. After the 90° turn, the polymer melt flows through the annular flow channel where it adopts more or less the shape of the final land region.

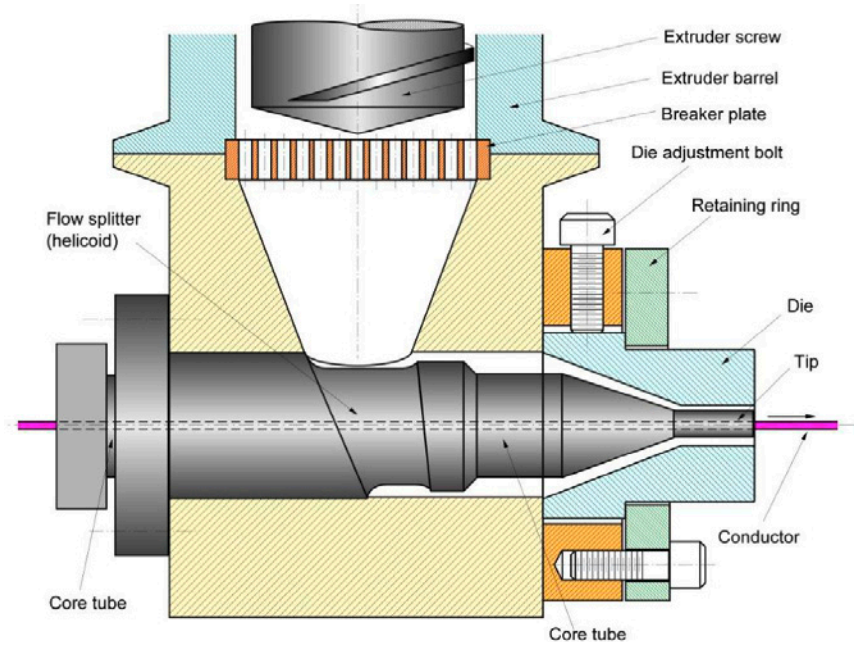


Figure 9.18 Example of a crosshead die

Weld lines are usually unavoidable in hollow extruded products. The polymer has to be given sufficient opportunity to "heal" along the knit lines. This healing process is essentially a reentanglement of the polymer molecules. Important parameters in this process are time, temperature, and pressure. Analyses of the healing process have been made by Prager and Tirrell [21] and Wool et al. [22–24]. The problem of weld lines also occurs in injection molding, as discussed, for instance, by Malguarnera and Manisali [25]. The healing time reduces with temperature but increases with molecular weight. In practical terms, this means that the point of weld line formation has to be a reasonably large distance upstream of the die exit to enable the polymer to heal sufficiently.

The crosshead die is also used for wire coating. In wire coating, a conductor passes through the hollow center of the core tube and becomes coated with polymer melt close to the die exit. The conductor may be a bare conductor or it may already have been coated with one or more layers of polymer. In wire coating, one distinguishes between high-pressure extrusion and low-pressure extrusion; see Fig. 9.19.

In high-pressure extrusion, Fig. 9.19, the polymer melt meets the conductor before the die exit. This allows for good contact between the conductor and the polymer. In low-pressure extrusion, Fig. 9.19, the polymer melt meets the conductor after the die exit. The polymer is tubed down over the conductor. Low-pressure extrusion is used when good contact between the wire and the polymer is not essential, for instance, when a loose jacket needs to be extruded over a coated wire.

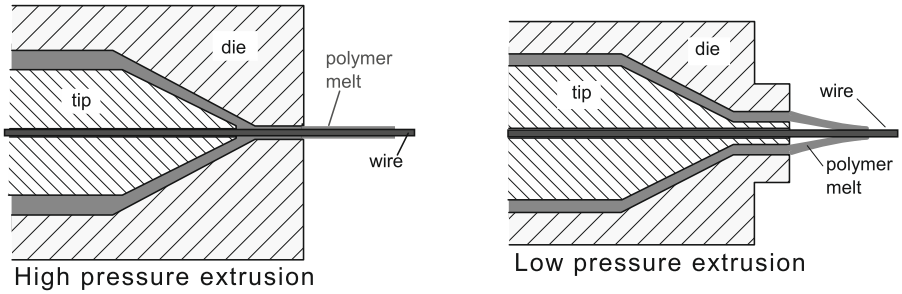


Figure 9.19 High- and low-pressure wire coating

In most crosshead dies, the location of the die relative to the tip can be adjusted by means of centering bolts; see Fig. 9.18. This allows adjustment of the wall thickness distribution and concentricity. In some extrusion lines with in-line wall thickness measurement, an automatic wall thickness control is obtained by using the signal from the wall thickness probe to automatically adjust the position of the die. In some cases, a slight internal air pressure is applied through the center of the core tube in order to maintain the I.D. of the tubing or to prevent collapse of the tubing. This is particularly useful in extrusion of tubing with very small I.D., 0.1 mm or less. In wire coating, sometimes a vacuum is applied to the center of the core tube to prevent air being dragged along with the conductor; this can cause imperfect contact between the polymer and the conductor.

Pipes are often extruded with in-line pipe dies; see Fig. 9.20.

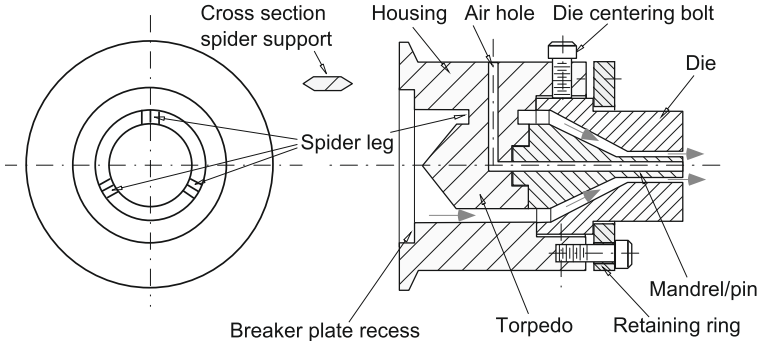


Figure 9.20 In-line pipe die

In these dies, the center line of the die is in line with the center line of the extruder. The central torpedo is supported by a number of spider legs, usually three or more. The spider legs are relatively thin and streamlined to minimize the disruption of the velocity profile. Of course, as the polymer recombines after the spider leg, a weld line will form. Thus, the location of the spider support should be far enough from the die exit to enable the polymer to heal. The location of the die is generally adjustable relative to the pin, just as in the crosshead die.

A manifold geometry that largely eliminates weld lines is the spiral mandrel die. These dies were originally developed for blown film extrusion; see Section 9.4. However, it became clear that spiral mandrel dies are equally (if not more) beneficial in pipe and tubing extrusion. Conventional tubing and pipe dies create a weld line (actually a weld region) that runs along the length of the extruded product and extends from the I.D. to the O.D. of the tube. Such a weld line reduces the hoop strength of a tube because the weld line (weld region) has the least favorable orientation relative to the stresses in the tube caused by internal pressure.

On the other hand, a spiral mandrel manifold creates flow in the helical direction, resulting in some degree in circumferential orientation. This combined with the near absence of weld lines make spiral mandrel dies capable of producing a tube or pipe with better mechanical properties simply by modifying the flow inside the die.

Another method of improving circumferential orientation in tubing and pipe dies is by inducing relative motion between the tip and the die. This can be done by rotating the tip relative to a stationary die or by rotating the die relative to a stationary tip. It is even possible to rotate both the tip and the die separately and in different directions. With rotation of the tip and/or die there is a greater degree of control over the orientation of the extruded tube than with a spiral mandrel section. Obviously, this is at the expense of increased mechanical complexity.

An example of a rotating tubing die is shown in Fig. 9.21.

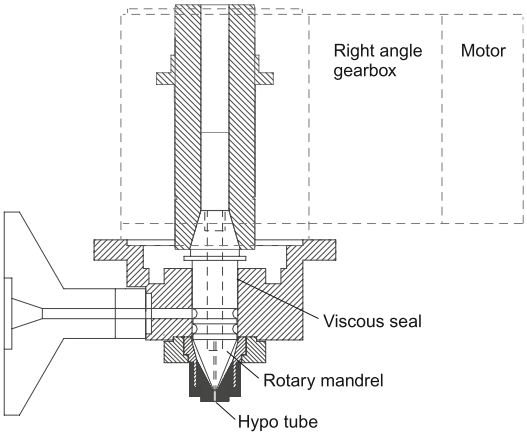


Figure 9.21
Tubing crosshead with capability to rotate the tip

9.3.1 Tooling Design for Tubing

Tubing is used in many industries for the transport of fluids. One of the more interesting applications is heat shrinkable tubing, which is made by extrusion, followed by crosslinking and expansion. Another important use is in the medical industry as catheter tubing. One of the more sophisticated medical devices based on polymeric tubing is the balloon catheter used for percutaneous transluminal coronary angioplasty.

The requirements for medical tubing with respect to dimensional tolerances and overall quality are stricter than almost any other application. This, coupled with the small tubing sizes typically produced, presents major challenges to the producers of medical tubing. The requirements are often so severe that off-the-shelf extrusion equipment may not do the job well enough. As a result, a number of producers of medical tubing have developed some of their own machinery.

9.3.1.1 Definitions of Various Draw Ratios

Tooling design for tubing is a critical issue in tubing extrusion but there is limited useful information available. Important issues in the design of tubing tooling are the various draw ratios that define the tooling and the extrusion process. The dimensions of the tip (mandrel) and die are determined by the drawdown in the extrusion process. There are various draw ratios in tubing extrusion that describe how the tubing is drawn down at the exit of the die. The diameter draw ratio (DDR) is the average diameter of the tip and die divided by the average diameter of the tubing.

$$\mathrm{DDR} = \frac{D_t + D_d}{D_o + D_i} \tag{9.10}$$

where D_t is the tip diameter, D_d is the die diameter, D_o is the tubing outside diameter, and D_i the tubing inside diameter; see Fig. 9.22.

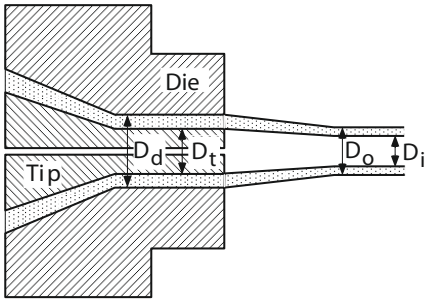


Figure 9.22
Definition of D_d, D_t, D_o, and D_i

Another important parameter is the wall draw ratio (WDR). This is the gap between the tip and die divided by the wall thickness of the tubing.

$$\mathrm{WDR} = \frac{D_d - D_t}{D_o - D_i} \tag{9.11}$$

A third measure is the area draw ratio (ADR). This is the cross-sectional area between the tip and die divided by the tubing cross-sectional area.

$$\mathrm{ADR} = \frac{D_d^2 - D_t^2}{D_o^2 - D_i^2} \tag{9.12}$$

It should be noted that sometimes the area draw ratio is represented by the letters DDR as an acronym for drawdown ratio. Obviously, this can cause confusion with the diameter draw ratio. Often the area draw ratio is called simply the draw ratio. It is important therefore to check what exactly is meant when the term draw ratio is used. The ADR can be calculated from the WDR and the DDR as follows:

$$ADR = DDR * WDR \tag{9.13}$$

Thus, the wall and diameter draw ratios determine the area draw ratio in the extrusion process. A high ADR increases orientation and the chance of pinholes and breakaways. A low ADR reduces orientation and increases the chance of melt fracture.

A fourth measure of drawdown is the draw ratio balance or DRB. This is the diameter ratio of the die and tip divided by the diameter ratio of the tubing.

$$DRB = \frac{D_d / D_t}{D_o / D_i} \tag{9.14}$$

The draw ratio balance should be equal to or larger than one: DRB ≥ 1. Yet another parameter that is used is the sizing ratio or SR. This is the wall draw ratio divided by the diameter draw ratio.

$$SR = \frac{WDR}{DDR} \tag{9.15}$$

A balanced draw occurs when the sizing ratio ranges from 1.0 to 1.3. When the SR is larger than 1.3, there is a danger of getting tear holes in the tubing. Low SR values can cause instabilities in the sizing of the tubing. Rubbers and high molecular weight polymers can be run with low SR values. Low viscosity polymers should be run with high SR values. High SR values will increase orientation and the chance of breakaways. High SR values will require higher internal and/or lower external air pressure to obtain tubing size.

Different polymers can be drawn down by varying amounts. Fluoropolymers, such as FEP, PFA, and ETFE, can be drawn down a great deal with ADR values of 10 to 100 and higher. With special extrusion techniques, PFA can have an ADR of over 250:1. Polyethylenes have a medium ability to be drawn down, polyurethanes and polyvinyls low to medium.

9.3.1.2 Land Length

In addition to the tip and die diameter, the land length and the cone angle are important design parameters. In many situations a long land length is desired because a long land tends to:

- Reduce tip and die drool
- Increase orientation

- Reduce the chance of pinholes
- Reduce the swelling of the extrudate (die swell)
- Improve shape definition

The main drawback of a long land length is increased diehead pressure. Because the land region usually has the highest restriction to flow, a longer land can increase pressure substantially. Another drawback of a long land length is that a long tip is more susceptible to mechanical deformation; the tip can bend more easily. This is a particular concern in small diameter tubing. Typical rules for the land length are:

- Land length divided by gap between tip and die (L/H) from 10:1 to 20:1
- Land length divided by the diameter of the tip (L/D_t) from 10:1 to 25:1

The gap between the tip and the die, H, is half the die diameter minus half the tip diameter, or $H = 0.5D_d - 0.5D_t$. The land length values that follow from these rules often result in excessive pressures with dealing with high viscosity materials. In many cases, therefore, the pressure drop will determine what land length is practical.

A special extrusion technique that is occasionally used is the extended mandrel. This is particularly used for thin wall tubing. In this technique the tip extends beyond the die by a considerable distance. The purpose of the extended mandrel is to obtain better shaper definition. Another use of the extended mandrel is to provide localized heating of the tip using an induction coil at the die exit. This is a variation of the G-Process discussed under special features. It is a suitable method to eliminate internal melt fracture or internal die drool. The mandrel extension should be made of a ferro-magnetic material to obtain an efficient temperature increase under the influence of the alternating magnetic field of the induction coil.

9.3.1.3 Taper Angles

The taper angle of the tip and die depends largely on whether the tooling is self-centering or adjustable; see Fig. 9.23.

The taper angle used in self-centering tooling typically ranges from 30° to 40°, in adjustable tooling from 8° to 15°. The term self-centering tooling is not totally correct because it does not always center itself; a more appropriate term is non-adjustable tooling. Relatively few studies have been published on the influence of die entry angle on the extrudate quality. Han [32] found that the entry angle affects melt fracture in certain polymers such as LDPE. When the entry angle is as large as 120°, melt fracture occurs in LDPE. At smaller entry angles melt fracture does not occur. In other polymers, such as HDPE, the entry angle has no effect on the extrudate distortion.

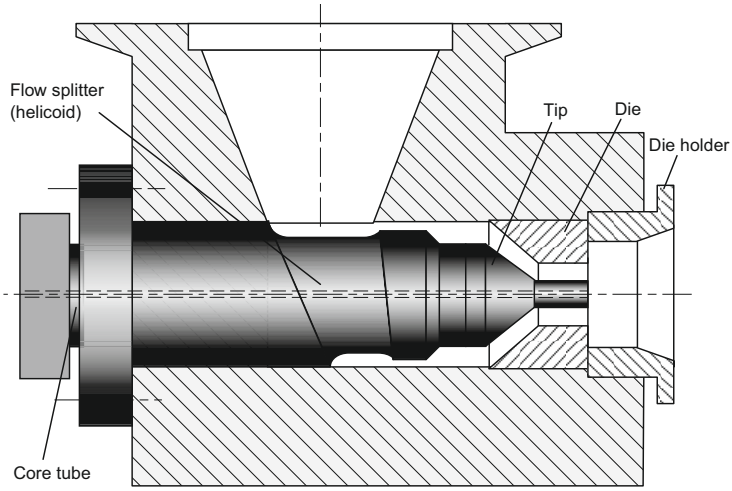


Figure 9.23 Example of self-centered crosshead die

Usually the taper angle of the die is slightly larger than the tip. It is also possible to make the taper angle of the tip equal to the die. It is important to have a gradual reduction in the cross-sectional area of the flow channel. Since the average diameter of the flow channel reduces, the area will reduce even if the taper angles are the same. Powell [33] describes design procedures to determine the length and included angle of converging sections such that the critical tensile deformation rate is not exceeded. In converging flow the tensile stress increases in the flow direction and reaches a maximum value at the narrow end of the taper. The average tensile deformation rate at the narrow end of a tapered wedge with included angle of 2α is given by:

$$\dot{\varepsilon} = \frac{\dot{\gamma}\tan\alpha}{3} \tag{9.16}$$

where $\dot{\gamma}$—is the shear rate in the small end of the wedge.

In a rectangular geometry this shear rate can be calculated from:

$$\dot{\gamma} = \frac{2(1+2n)\dot{V}}{n\,W\,H^2} \tag{9.17}$$

Typical values of the critical tensile deformation rate range from about 1 to 100 s^{-1}, depending on the type of polymer. When a polymer melt flows from a large to a small channel, it forms a natural streamline angle. When the taper angle of the tooling is larger than the natural streamline angle, dead spots will form. This can be avoided by making the half-angle of the entry to the die equal to or smaller than the natural half-angle.

9.3.1.4 Special Features

In some cases a slight taper is used in the land region. Haas and Skewis [34] reported that a slight taper reduces extrudate roughness. For high draw ratios, DuPont recommends [36, 37] to radius the face of the tip with a radius of 0.1 of the tip diameter. In some cases, a small chamfer is used on the I.D. of the die, e.g., 0.8 mm by 45°. In order to obtain higher and/or faster drawdown, a cone heater can be used according to Blair [37]. This is a heater at the exit of the die used to prevent the cone of polymer from cooling too rapidly. The cone heater primarily heats the air surrounding the cone.

With materials that are susceptible to melt fracture, the exit region of the tooling can be heated to temperatures considerably higher than the rest of the extruder. One approach is to use an induction heater at the die exit to heat just the region surrounding the die orifice. This is called the G-Process by DuPont [35, 36]. In this process a high-frequency heater is used. The heat is generated due to the metals resistance to the flow of electrons and to the hysteresis losses occurring during rapid magnetization and demagnetization.

■ 9.4 Blown Film Dies

The most common die used in blown film extrusion is the spiral mandrel die. In this die, the polymer is divided into a number of spiraling channels with the depth of the channels reducing in the direction of flow. The popularity of the spiral mandrel die is due to its relatively low pressure requirement and its excellent melt distribution characteristics. Spiral mandrel dies can be used with a wide range of materials over a wide range of operating conditions.

A simpler die is the conventional crosshead die; see Fig. 9.24. This design is more susceptible to weld lines; however, with the correct design good blown film can be produced.

The distribution characteristics of conventional crosshead dies may not be good enough for application in blown film extrusion, where wall thicknesses are generally quite small (the typical range is 0.005 mm to 0.25 mm). Spiral mandrel dies can achieve good flow distribution and largely eliminate weld lines. As a result, spiral mandrel dies are widely used in blown film extrusion.

A simplified picture of a spiral mandrel die is shown in Fig. 9.25.

The incoming polymer melt stream is divided into separate feed ports. Each feed port feeds the polymer into a spiral groove machined into the mandrel. The cross-sectional area of the groove decreases with distance, while the gap between the mandrel and the die increases towards the die exit. This multiplicity of flow chan-

nels results in a smearing or layering of polymer melt from the various feed ports, yielding a good distribution of the polymer melt exiting from the die. It is obvious that local gap adjustment is not possible as it is with flat sheet dies. As a result, the wall thickness uniformity with spiral mandrel dies is generally not as good as with flat sheet dies. The latter can generally achieve a wall thickness uniformity of about ±5%, while the blown film die achieves a wall thickness uniformity of about ±10%. For this reason, the die is generally made to rotate to evenly distribute the wall thickness non-uniformities. If this were not done, the final roll of product would show very noticeable variations in diameter.

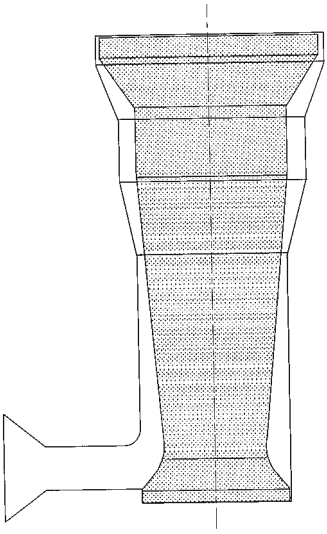


Figure 9.24
Example of simple crosshead die for blown film

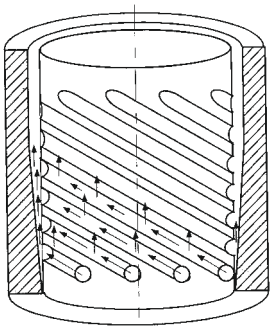


Figure 9.25
Example of a spiral mandrel die

Analyses of flow in spiral mandrel dies have been made by Ast [26], Wortberg and Schmidtz [27], Proctor [28], Predoehl [29], Menges et al. [40], Rauwendaal [41], and others. Proctor showed the effect of the spiral runout angle, the spiral helix angle, and the taper angle of the annular channel; he assumes that the pressure gradient is constant. Rauwendaal removed this simplifying assumption and studied the effect of die design variables on flow distribution.

Rauwendaal [41] used the following assumptions to analyze the flow in the spiral mandrel die:

- The polymer melt behaves as a temperature-independent power law fluid.
- The curvature of the mandrel can be neglected.
- Zero pressure gradient in tangential direction.
- The flow in the spiral channel can be approximated by pressure flow in a rectangular channel of width W and height H by using a shape factor.
- The leakage flow in the flight clearance can be approximated by a pressure flow in a rectangular channel with height δ.
- The leakage flow does not affect the flow in the spiral channel.

The flow will be analyzed by unrolling the spiral mandrel onto a flat plane as shown in Fig. 9.26.

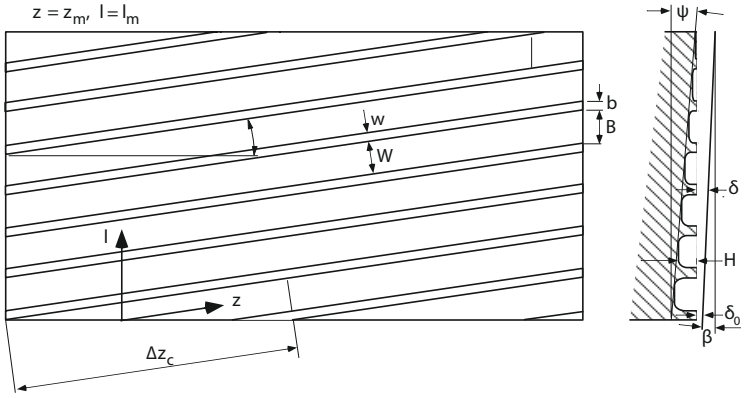


Figure 9.26 Unrolled spiral mandrel geometry

The flow in the spiral mandrel channel can be expressed as:

$$\dot{V} = \frac{F_p W H^2}{2(s+2)} \left[\frac{H g_z}{2m} \right]^s \tag{9.18}$$

where g_z is the helical down-channel pressure gradient, F_p the shape factor for the spiral channel, and s the reciprocal power law index (s = 1/n). For small values of the height-to-width ratio (H/W < 0.5) the shape factor can be taken to be constant, $F_p = 0.45$. The leakage flow per unit tangential distance can be expressed as:

$$\dot{V}'_l = \frac{\delta^2}{2(s+2)} \left[\frac{\delta g_l}{2m} \right]^s \tag{9.19}$$

where g_l is the axial pressure gradient.

The pressure gradient in the down-channel direction can be related to the axial pressure gradient by:

$$g_z = g_1 \sin\varphi \tag{9.20}$$

Within the first Δz_c of helical distance the flow in the spiral mandrel channel is not affected by the leakage flow from a channel below it. For this section of the die the following mass balance is valid, assuming the melt density to be constant:

$$\dot{V}(z+\Delta z) = \dot{V}(z) - \dot{V}_1(z)\,\Delta z \cos\varphi \tag{9.21}$$

Beyond the first Δz_c of helical distance the flow in the spiral channel is affected by the leakage flow from the channel below it. For this section of the die the following mass balance is valid:

$$\dot{V}(z+\Delta z) = \dot{V}(z) + \dot{V}_1(z-\Delta z_c)\Delta z\cos\varphi - \dot{V}_1(z)\Delta z\cos\varphi \tag{9.22}$$

With these equations, the flow distribution can be calculated in a straightforward fashion. This calculation proceeds in a step-wise fashion. The step size has to be small enough to make sure that the ratio of $\dot{V}(z + \Delta z)/\dot{V}(z)$ is close to unity.

9.4.1 The Spiral Mandrel Geometry

The important design parameters are:

N the number of grooves

φ the groove helix angle

ψ the spiral runout angle

β the taper angle of the annular channel

W the perpendicular groove width

w the perpendicular flight width

H_0 the initial groove depth

D the mandrel diameter

δ_0 the initial flight clearance

l_m the axial groove length

The axial groove width B is related to the perpendicular groove width W by the following relationship:

$$B = \frac{W}{\cos\varphi} \tag{9.23}$$

A similar relationship is valid for the axial flight width. The tangential flight and channel width, W/sinφ and w/sinφ, are related to the mandrel diameter D and the number of flights N by the following expression:

$$\frac{N(W+w)}{\sin\varphi} = \pi D \tag{9.24}$$

The groove depth can be expressed as a function of helical distance z by the following relationship:

$$H(z) = H_0 - z \sin\varphi \tan\psi \tag{9.25}$$

The flight clearance can be expressed as a function of z by:

$$\delta(z) = \delta_0 + z \sin\varphi \tan\beta \tag{9.26}$$

With these expressions a complete analysis of the flow process in the spiral mandrel section can be made.

9.4.2 Effect of Die Geometry on Flow Distribution

A standard die geometry was chosen with a diameter of 250 mm with 10 grooves, a helix angle of 20°, and an axial length of 250 mm. Further, the initial channel depth was 19 mm and the taper angle of the annular channel 2°. The total flow rate was taken as 82 cm^3/s. The consistency index of the polymer melt is 0.145 $Pa \cdot s^n$ and the power law index n = 0.5.

The development of the leakage flow along the length of the die is shown in Fig. 9.27.

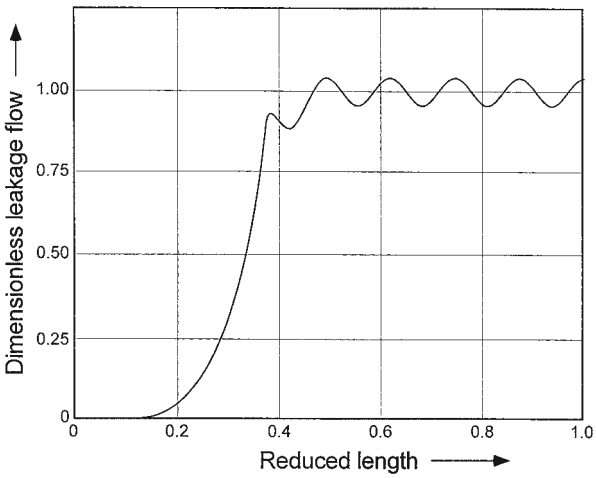


Figure 9.27
Development of leakage flow along the length of the die

Figure 9.27 shows the leakage flow per tangential distance against the dimensionless helical distance along the spiral channel. The leakage flow increases rapidly at about 1/3 the channel length and reaches its final distribution at about 2/3 the channel length. The corresponding flow rate in the helical channel is shown in Fig. 9.28.

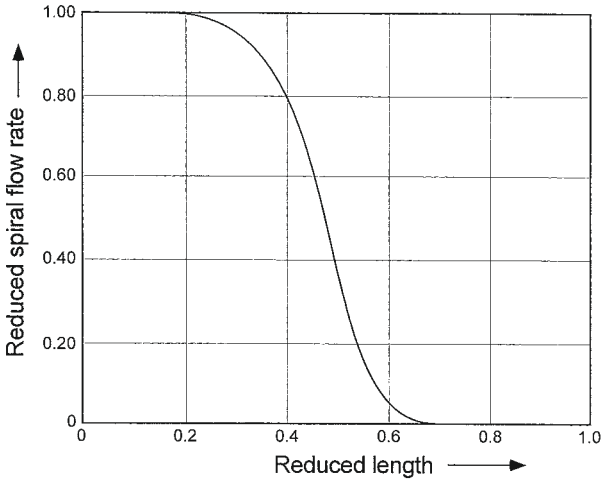


Figure 9.28
Flow rate in the helical channel versus reduced length

In the midsection of the channel the spiral flow drops quickly and reaches almost zero value at about 2/3 the channel length; this is where the leakage flow reaches its final distribution.

The pressure profile along the channel is shown in Fig. 9.29.

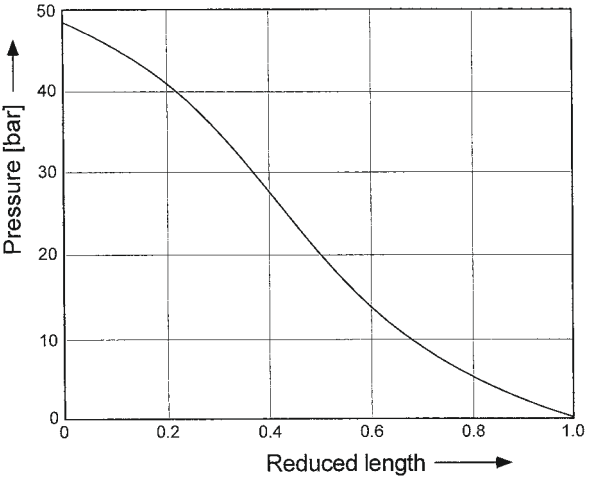


Figure 9.29
Pressure profile along the length of the channel

The pressure gradient reduces at first, reaches a minimum at about the center region, and then increases to a relatively low value. It is clear that the pressure gra-

dient is by no means constant; there is about a 5X difference between the high and low value. Therefore, the pressure gradient should not be assumed to be constant along the channel.

The effect of the number of grooves is shown in Fig. 9.30.

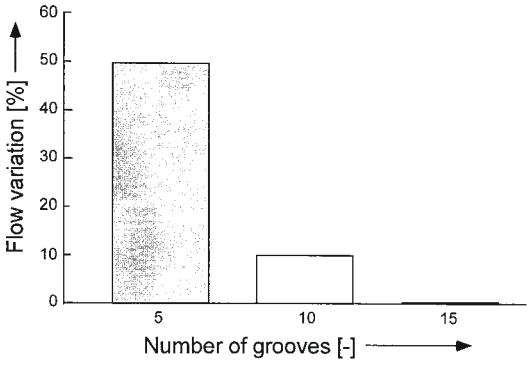


Figure 9.30
Effect of the number of grooves on flow distribution

The effect of the number of grooves on flow distribution is quite strong. With five grooves the distribution is poor, with ten grooves acceptable, and with 15 grooves very good. An additional benefit of more grooves is reduced pressure drop. Therefore, increasing the number of grooves has two important benefits.

Another important design variable is the taper angle of the annular channel. This effect of the taper angle on the distribution is shown in Fig. 9.31.

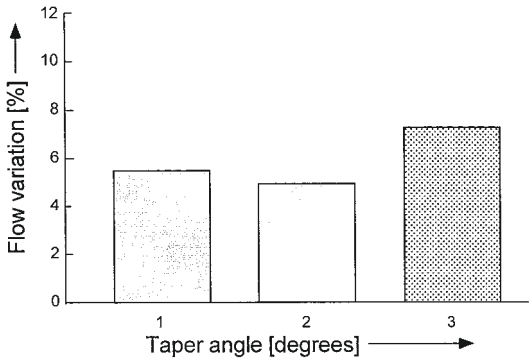


Figure 9.31
Effect of taper angle on flow distribution

The best distribution is obtained when the taper angle is 2°. Taper angles of 1° and 3° result in a less uniform distribution.

A third design variable with an interesting effect is the initial clearance. Figure 9.32 shows how the flow distribution is affected by the initial clearance.

A significant improvement in flow distribution can be obtained by using a non-zero initial clearance. However, if the value is taken too large the distribution becomes more non-uniform again. In this example there is an optimum value between 0 and 5 mm. A further benefit of the increased initial clearance is reduced pressure drop.

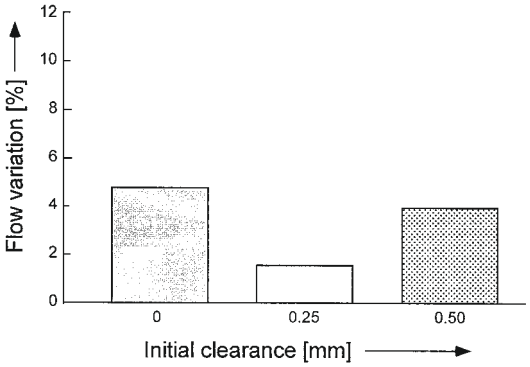


Figure 9.32
Effect of initial clearance on flow distribution

Another important design variable is the groove helix angle. Figure 9.33 shows how the helix angle affects the flow distribution.

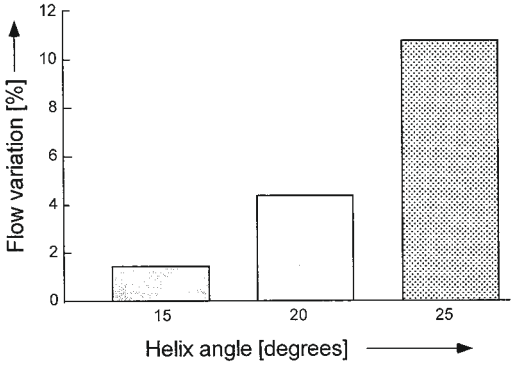


Figure 9.33
Effect of helix angle on flow distribution

The helix angle has a strong effect on the flow distribution. At a helix angle of 15° a very good flow distribution is obtained, while the distribution gets progressively worse when the helix angle is increased. A disadvantage of reduced helix angle is increased pressure drop. However, the increase in pressure drop is rather small.

The initial groove depth is another important design variable. The effect of groove depth is shown in Fig. 9.34.

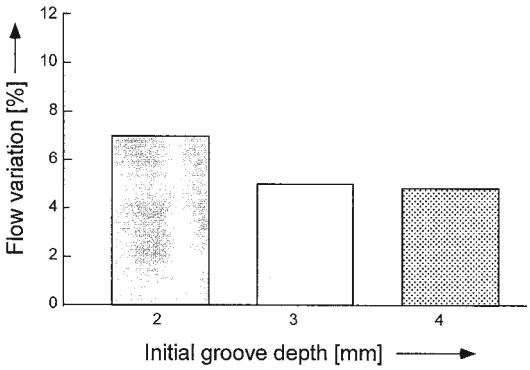


Figure 9.34
Effect of initial groove depth on flow distribution

The flow distribution improves as the initial groove depth is increased. By increasing the groove depth from 12.5 to 25 mm the distribution uniformity improves about 40%. Finally, the effect of reducing groove width was studied from 19 mm initial width to 10 mm final width. Within this range of width values the reduction of groove width did not improve the flow distribution.

9.4.3 Summary of Spiral Mandrel Die Design Variables

Three design variables have a strong effect on the flow distribution in spiral mandrel dies. These are the number of grooves, the initial clearance, and the groove helix angle. Increasing the number of grooves improves distribution and reduces pressure drop. Typical values of the number of grooves range from 1 to 2 per inch (25 mm) of die diameter. A small non-zero clearance improves the flow distribution and reduces pressure drop. There is an optimum initial clearance beyond which the flow distribution exhibits more variation. Small groove helix angles improve the flow distribution; however, this increases pressure drop.

The optimum taper angle was found to be between 1° and 3°. The flow distribution uniformity improves with initial groove depth, while the pressure drop reduces at the same time. A gradually reducing groove width does not result in improved flow distribution.

Obviously, the actual flow variation in spiral mandrel dies can be greater than the values predicted. Other variations in flow distribution can occur because of consistency variations in the polymer melt due to temperature non-uniformities and/or insufficient mixing. Flow variations can also occur due to mechanical variations in the dimensions of the die. Further, elastic effects can affect the flow distribution. As a result, good quality film requires not only a good die design but also an extruder with good melting and mixing capability, consistent resin properties, uniform film cooling, constant tension, etc.

■ 9.5 Profile Extrusion Dies

Apart from rectangular and annular extrudates, there is a tremendous variety of extruded profiles with other shapes. Profile dies usually describe dies used to produce shapes other than rectangular or annular. Profile extrusion is often the most difficult type of extrusion. This is, to a large extent, due to the fact that it is very difficult to accurately predict the required geometry of the flow channel that will yield an extruded product of proper shape and dimensions.

In profile extrusion, there are two extremes in die design. One extreme is the plate die shown in Fig. 9.35.

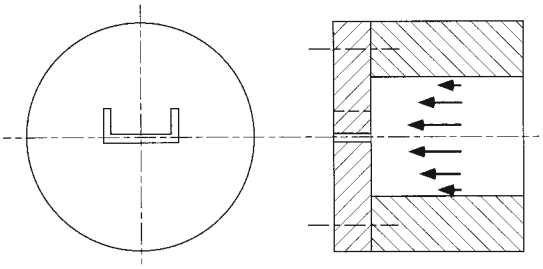


Figure 9.35
Plate die

In this design, a plate with the required opening is placed abruptly at the end of the die flow channel with a minimum amount of streamlining. This type of die is simple, easy to make, and easy to modify. However, there is a large dead flow region, and degradation is a definite concern with polymers with limited thermal stability. This type of die, therefore, should be used with relatively stable polymers and preferably only for short times.

The other extreme is the highly streamlined die shown in Fig. 9.36.

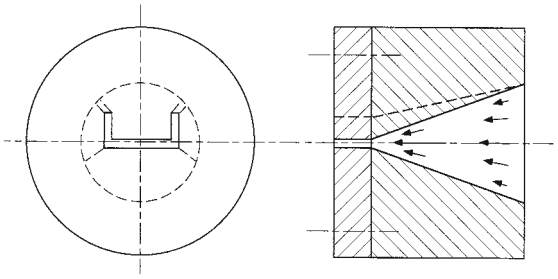


Figure 9.36
Fully streamlined profile die

In this die, there is a gradual transition from the geometry of the die inlet channel to the geometry of the die outlet channel. Obviously, this die is more complex, more difficult to manufacture, and more difficult to modify. Good streamlining is important if the polymer is susceptible to degradation. A well-streamlined profile die is more likely to be used for a long extrusion run because the manufacturing cost can be spread over a larger amount of product and because degradation becomes more of a problem in longer runs. Obviously, there are an infinite number of intermediate die designs between the totally non-streamlined plate die and the fully streamlined profile die.

9.6 Coextrusion

Coextrusion is the simultaneous extrusion of two or more polymers through a single die where the polymers are joined together such that they form distinct, well-bonded layers forming a single extruded product. Coextrusion has been applied in film, sheet, tubing, blown film, wire coating, and profile extrusion.

Advantages of coextrusion are better bonds between layers, reduced materials and processing costs, improved properties, and reduced tendency for pinholes, delamination, and air entrapment between the layers. Another advantage of coextrusion is that it is often possible to reuse scrap material and locate it in an inside layer of the extruded product so that it does not affect the appearance of the product. An obvious disadvantage of coextrusion is that the tooling is more difficult to design and manufacture and, therefore, more expensive. Further, it requires at least two extruders, and it takes more operational skill to run a coextrusion line.

Coextrusion is used in a variety of packaging applications to obtain the required combination of properties, for instance, good moisture resistance, gas barrier properties, reduced costs, tear strength, etc. A combination of polyethylene/nylon/polyethylene is popular in sterile-packaged disposables. A combination of LDPE/HDPE is used for shrink film and shopping bags to obtain a balance of rigidity and low cost. PS/foamed-PS coextrusion is used in production of egg cartons and meat trays. In sheet extrusion, the combination ABS/polystyrene is used for refrigerator door liners and margarine tubs. The ABS is applied for chemical resistance and the polystyrene for economy. Essentially the number of applications is infinite and certainly the number of coextruded products will continue to rise.

There are basically three different techniques for coextrusion. The first employs feed block dies where the various melt streams are combined in a relatively small cross-section before entering the die. The advantage of this system is simplicity and low cost. Existing dies can be used with little or no modification. Disadvantages are that the flow properties of the different polymers have to be quite close to avoid interface distortion. There is no individual thickness control of the various layers, only an overall thickness control. Figure 9.37 shows a schematic of a feed block sheet die.

The second coextrusion technique uses multi-manifold internal combining dies. The different melt streams enter the die separately and join just inside the final die orifice. The advantage of this system is that polymers with large differences in flow properties can be combined with minimum interface distortion. Individual thickness control of the different layers is possible; this enables a higher degree of layer uniformity. Disadvantages are complex die design, higher cost, and limited number of layers that can be combined.

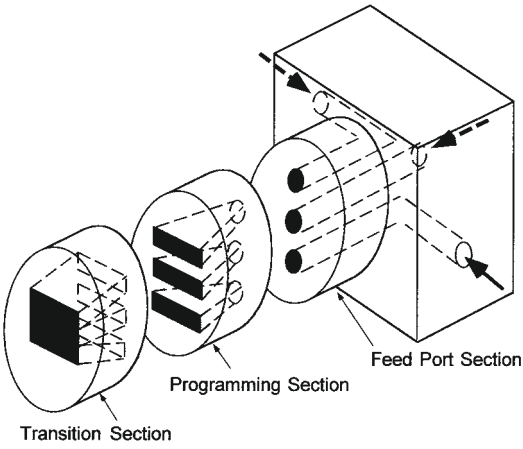


Figure 9.37
Schematic of feed block system

Figure 9.38 shows a multi-manifold blown film coextrusion die enabling extrusion of three different polymers.

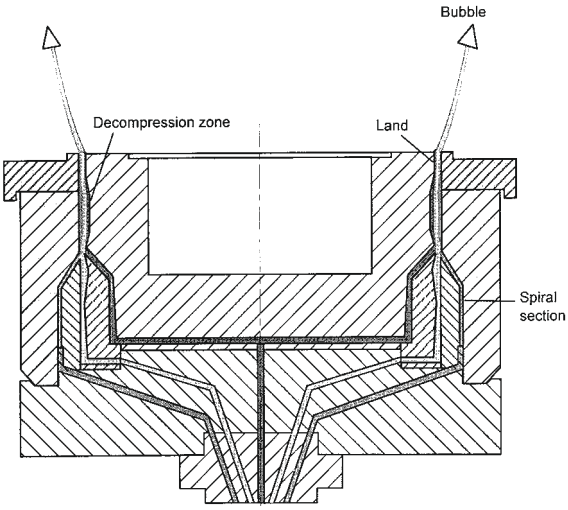


Figure 9.38
Multi-manifold blown film die, three layers

Coextrusion is practiced on a wide scale in blown film. There are many five-layer blown film coextrusion dies used in the industry; five-layer films are now considered a commodity [41]. Even seven-layer dies are not unusual. Some coextrusion dies use as many as 8 to 10 layers. Most of these multi-layer dies are used in high-barrier packaging for food. Conventional blown film coextrusion dies have a concentric arrangement of spiral mandrel manifolds. In some cases conical spiral mandrel sections are used, while in other cases the spiral mandrel section is machined into a flat horizontal surface. The latter arrangement is referred to as a "pancake" coextrusion die, because the different sections of the die are stacked like pancakes. A schematic of a pancake coextrusion system is shown in Fig. 9.39.

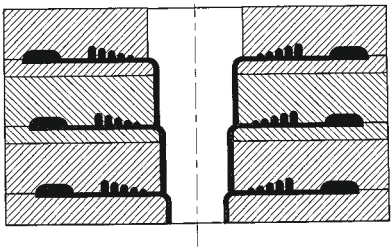


Figure 9.39
Example of a "pancake" coextrusion system

The advantage of the pancake system is that many modules (disks) can be stacked together in a more or less modular fashion, allowing for as many as ten layers to be produced. Another advantage is the relatively compact design that keeps the space requirements to a minimum.

Figure 9.40 shows a multi-manifold sheet die for two-layer coextrusion.

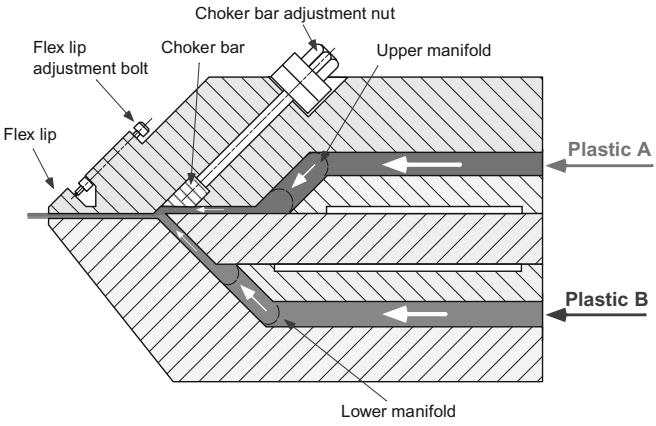


Figure 9.40
Multi-manifold sheet die, two layers

The upper layer can be adjusted with a choker bar, while the final combined layer thickness can be adjusted with the flex lip.

Coextrusion of more than three layers is difficult in a sheet die because the die geometry becomes quite complex. Figure 9.41 shows another design of a triple-layer coextrusion sheet die.

In this design, the layer thickness can be adjusted by die vanes. The internal vane adjustment allows a greater degree of adjustment in overall actual layer thickness; however, it does not enable local thickness adjustment as is possible with the choker bar.

The third coextrusion technique uses multi-manifold external-combining dies, which have completely separate manifolds for the different melt streams as well as distinct orifices through which the streams leave the die separately, joining just beyond the die exit. This technique is also referred to as multiple lip coextrusion. The layers are combined after exiting while still molten and just downstream of the die. For flat film dies, pressure rolls are used to force the layers together. In blown

film extrusion, air pressure inside the expanding bubble provides the necessary pressure for combining the layers. This technique is more expensive than the feed block technique; however, gage control of individual layers is more accurate, pinholes are eliminated, and the system is easier to start up.

One interesting benefit that can be obtained with coextrusion is a more uniform temperature distribution in the material. This can be realized by coextruding a thin, low-viscosity outer layer over a high-viscosity inner layer. The highest shear rate and heat generation normally occurs at the wall. By having a low-viscosity material at the location of maximum shear rate, the heat generation is reduced at this point and a more even temperature profile is obtained. This is a useful technique for thermally unstable polymers. As discussed before in Section 7.5.3, this technique can also avoid the occurrence of shark skin and melt fracture type flow instabilities.

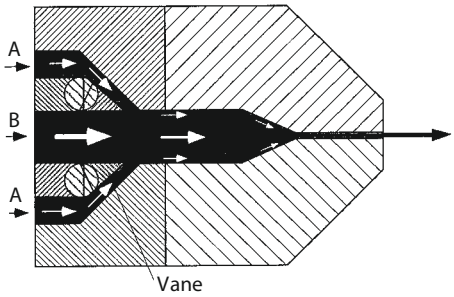


Figure 9.41
Three-layer coextrusion sheet die with vanes

The feed block system and the multi-manifold system are compared in Table 9.1.

Table 9.1 Comparison of Feed Block and Multi-Manifold Systems

Feed block system	Multi-manifold system
Low cost	High cost
Many layers can be combined	Limited number of layers
Simple design	Complex design
Viscosities have to be closely matched	Viscosities can vary considerably
Limited number of polymers can be combined	Many different polymers can be combined
Limited layer uniformity	Good layer uniformity
Different number of layers in same die	Number of layers is fixed by die design
Suitable for sheet and flat film	Suitable for many different shapes

It is possible to combine a feed block with a multi-manifold die to obtain a highly versatile coextrusion system that can handle many layers and polymers with large differences in flow characteristics.

9.6.1 Interface Distortion

One of the challenges in coextrusion is to control the uniformity of the individual layers. It is well known that when two fluids with different viscosity flow side by side the interface will distort because the fluid with the lowest viscosity has a tendency to flow to the high shear rate regions. As a result, the low-viscosity material will tend to encapsulate the high-viscosity material. This situation is illustrated in Fig. 9.42.

The extent of the interface distortion will depend on the length of the flow channel. If the channel is long enough the high-viscosity fluid will be completely encapsulated as shown in Fig. 9.42. If the channel is short the interface distortion will show an intermediate configuration as shown in time t_1 or t_2 in Fig. 9.42. The process of viscous encapsulation was studied by Gifford, as discussed in Section 12.4.2; see Fig. 12.18.

The distortion shown in Fig. 9.42 is driven by viscosity differences. However, even when coextruding polymers with exactly the same viscosity, interfacial distortion has been observed [43].

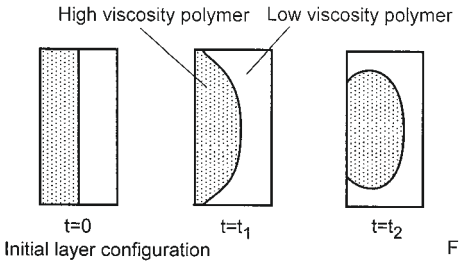


Figure 9.42
Illustration of encapsulation due to viscosity differences

Clearly, there are other mechanisms by which interfacial distortion occurs. Dooley and Hughes [43] performed careful experiments to illustrate the extent of interface distortion in coextrusion of polymers with the same flow characteristics. In their analysis they attribute the interface distortion to normal stress differences within the polymer melt, and they used a finite element program capable of handling viscoelastic fluids to predict the distortion within the fluid. This issue is discussed further in Section 12.4.2; see Figs. 12.19 to 12.21.

Svabik, Samsonkova, and Perdikoulias [45] proposed another explanation for the interface distortion in coextrusion of fluids with equal viscosity. They performed three-dimensional flow analysis of coextrusion flow and found that even in coextrusion with Newtonian fluids with equal viscosity layer distortion takes place. Obviously, this type of distortion cannot be caused by normal stress differences since these do not occur in Newtonian fluids. Also, with the viscosities being equal the distortion cannot be caused by viscosity differences. The predicted layer distortion is schematically illustrated in Fig. 9.43. The authors call the distortion resulting from purely viscous flow geometrical encapsulation.

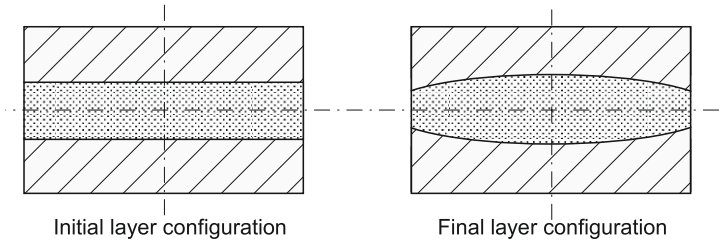


Figure 9.43 Illustration of geometrical encapsulation

Geometric encapsulation is caused by the parabolic velocity profiles in the die flow channel. Because the velocities are highest in the center region of the channel the layer thickness increases in this part of the channel, while the thickness of the outside layers reduces in the center region of the channel. At the side walls the inner layer thickness reduces while the outside layer thickness increases. The distortion caused by geometric encapsulation becomes more severe as the fluid becomes shear thinning.

It appears that there are several mechanisms for interface distortion. One is distortion caused by viscosity differences (viscous encapsulation), another is caused by normal stress differences in the fluid (elastic encapsulation), and a third is caused by normal velocity differences within the fluid (geometrical encapsulation). Obviously, the distortion will increase when viscosity differences are large and when normal stress differences play a significant role.

There are two approaches to minimizing the interface distortion. One is to reduce the length over which the different melt streams flow together. This is done in multimanifold dies where the different melt streams are combined just before the exit of the die. Another approach is to modify the initial configuration of the layers in such a way that the final layer configuration is the one desired. This approach is called profiling, and this is a method frequently used in feed block coextrusion systems to achieve uniform layer distribution at the exit of the die. This principle is illustrated in Fig. 9.44.

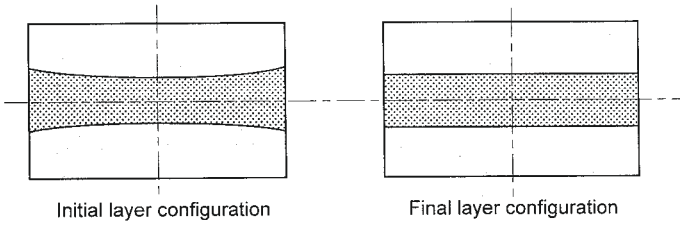


Figure 9.44 Illustration of profiling in coextrusion

Profiling can be used with feed block coextrusion systems and also with vane-type coextrusion dies as shown in Fig. 9.41. With 3-D flow simulation the rearrangement of the layers can be predicted. Particles defining a flat interface can be tracked upstream to the input plane to determine the appropriate initial layer geometry. Examples of this approach are discussed by Perdikoulias et al. [45].

■ 9.7 Calibrators

In pipe extrusion, the extrusion die is often followed by a sizing die, where the actual dimensions of the pipe are primarily determined. Such a device is generally referred to as a calibrator. Calibrators are required if the extrudate emerging from the die has insufficient melt strength to maintain the required shape. The calibrator is in close contact with the polymer melt and cools the extrudate. When the extrudate leaves the calibrator, it has sufficient strength to be pulled through a haul-off device such as a catapuller without significant deformation of the extruded product.

In a vacuum calibrator, a vacuum is applied to ensure good contact between the calibrator and the extrudate and to prevent collapse of the extrudate. The use of a vacuum calibrator is generally easier than the use of positive air pressure within the extrudate because a vacuum is easier to maintain at a constant level. Positive internal air pressure tends to vary with the length of the extrudate and it is difficult to maintain when the extrudate has to be cut into discrete lengths. Calibrators are useful when good, accurate shape control is important. When the requirements for shape control are less stringent, the extrudate shape is often maintained by support brackets placed downstream of the extrusion die. In fact, the extrudate shape can be modified substantially by the support brackets. This can be useful because it allows modification of the shape of the extrudate without changing the die, but only by changing the shape of the support brackets.

As discussed by Michaeli [1], there are five types of calibrators:

1. Slide calibrators
2. External calibrators with internal air pressure
3. External vacuum calibrators
4. Internal calibrators
5. Precision profile pultrusion (Technoform process)

Slide calibrators are used for simple and open profiles. The extrudate is more or less in contact with cooled plates, and the profile is pulled through the calibrator, causing some amount of drawdown.

A schematic of a water-cooled slide calibrator is shown in Fig. 9.45.

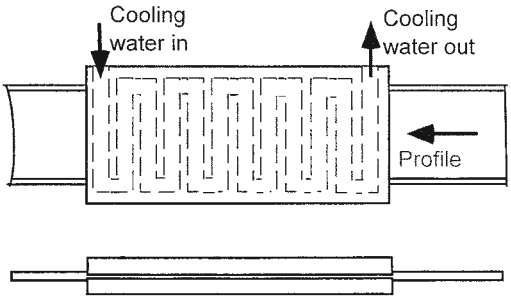


Figure 9.45
Example of profile calibration system

An example of an external calibrator with internal air pressure is shown in Fig. 9.46.

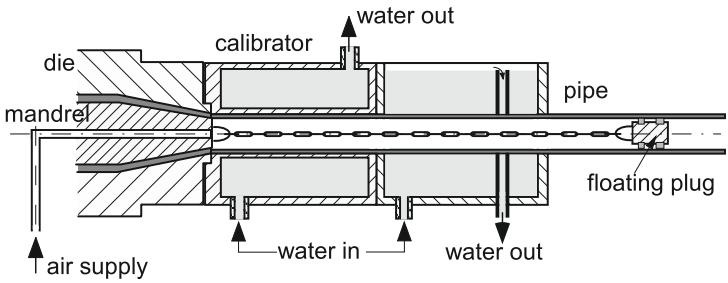


Figure 9.46 External calibrator with internal air pressure

The air pressure is maintained by a sealing mandrel located inside the extrudate downstream of the calibrator. The mandrel is attached to the tip by a cable to fix its position. This type of calibration is used in larger diameter pipe for PVC (D > 350 mm) and PE (D > 100 mm). An example of an external vacuum calibrator is shown in Fig. 9.47.

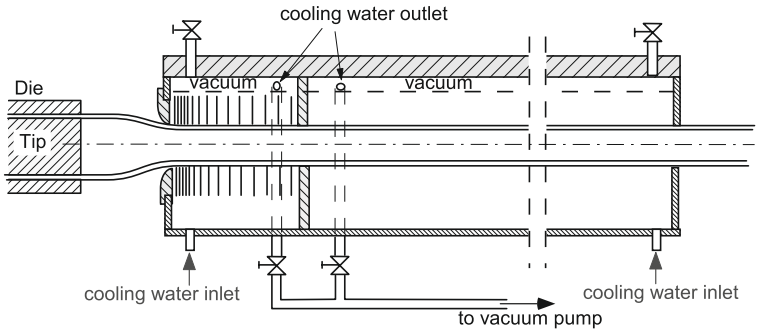


Figure 9.47 Calibrator with external vacuum

This internal calibrator modifies the annular shape of the extrudate emerging from the die into a more or less triangular shape. This allows shape modification just by

the calibrator. However, internal calibration is not used very often. In precision profile pultrusion, a small amount of polymer is allowed to accumulate between the die and the calibrator. The accumulation is controlled by a sensor through adjustment of the haul-off speed. The extrudate is pulled through a short, intensely cooled calibrator followed by a water bath. This type of calibration is referred to as the Technoform process; it was developed by Reifenhäuser KG.

An example of a dry vacuum calibration system is shown in Fig. 9.48

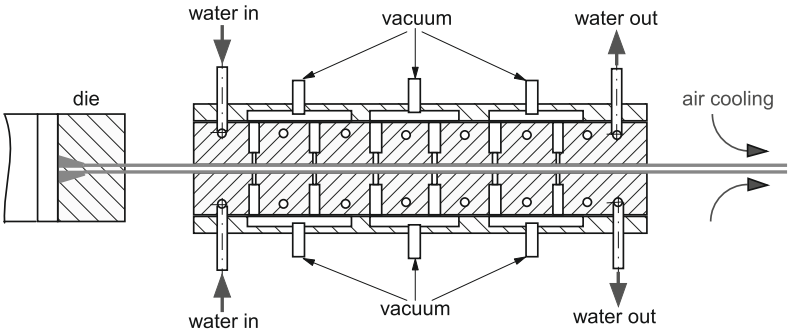


Figure 9.48 Example of dry vacuum calibration system

References

1. W. Michaeli, "Extrusionswerkzeuge fuer Kunststoffe," Carl Hanser Verlag, Munich (1979), in German
2. W. Michaeli, "Extrusion Dies," Hanser Gardner Publications, Cincinnati, OH (1984)
3. D.J. Weeks, Br. Plast., 31, 156–160 (1958)
4. D.J. Weeks, Br. Plast., 31, 201–205 (1958)
5. J.M. McKelvey and K. Ito, Polym. Eng. Sci., 11, 258–263 (1971)
6. J.R.A. Pearson, Trans. Plast. Inst., 32, 239–244 (1964)
7. K. Ito, Jpn. Plast., 4, 27–30 (1970)
8. M.B. Cheijfec, Plast. Massy, 12, 31–33 (1973)
9. K. Ito, Jpn. Plast., 2, 35–37 (1968)
10. K. Ito, Jpn. Plast., 3, 32–34 (1969)
11. J. Wortberg, Ph. D. thesis, RWTH Aachen, Germany (1978). Also in: "Berechnen von Extrudierwerkzeugen," VDI-Verlag GmbH, Duesseldorf, Germany (1978)
12. P. Fischer, E.H. Goermar, M. Herner, and U. Kosel, Kunststoffe, 61, 342–355 (1971)
13. E.H. Goermar, Ph.D. thesis, RWTH Aachen, Germany (1968)
14. C.I. Chung and D.T. Lohkamp, SPE ANTEC, Atlanta, 363–365 (1975)
15. I. Klein and R. Klein, SPE J., 29, 33–37 (1973)
16. H. Schoenewald, Kunststoffe, 68, 238–243 (1978)
17. B. Vergnes, P. Saillard, and B. Plantamura, Kunststoffe, 70, 750–752 (1980)

18. Y. Matsubara, Polym. Eng. Sci., 19, 169–172 (1979)
19. Y. Matsubara, Polym. Eng. Sci., 20, 716–719 (1980)
20. J. Sneller, Mod. Plast., 48–52 (1983)
21. S. Prager and M. Tirrell, J. Chem. Phys., 75, 5194–5198 (1981)
22. Y.H. Kim and R.P. Wool, Macromolecules, 16, 1115 (1983)
23. R.P. Wool and K.M. O'Connor, J. Polym. Sci., Letters Ed., 20 (1982)
24. R.P. Wool and K.M. O'Connor, J. Appl. Phys., 52 (1981)
25. S.C. Malguarnera and A. Manisali, SPE ANTEC, New York, 124–128 (1980)
26. W. Ast, Kunststoffe, 66, 186–192 (1976)
27. J. Wortberg and K.P. Schmidtz, Kunststoffe, 72, 198–205 (1982)
28. B. Proctor, SPE ANTEC, Washington, D.C. , 211–218 (1971)
29. W. Predoehl, "Technologie Extrudierter Kunststoffolien," VDI-Verlag GmbH, Duesseldorf, Germany (1979)
30. M.J. Crochet, A.R. Davies, and K. Walters, "Numerical Simulation of Non-Newtonian Flow," Elsevier, Amsterdam, The Netherlands (1984)
31. H.H. Winter and H.G. Fritz, SPE ANTEC, New Orleans, 49–52 (1984)
32. C.D. Han, "Influence of the Die Entry Angle on the Entrance Pressure Drop, Recoverable Elastic Energy, and the Onset of Flow Instability in Polymer Melt Flow," J. Appl. Polym. Sci., 17, 1403–1413 (1973)
33. P.C. Powell, "Design of Extruder Dies Using Thermoplastics Melt Properties Data," Polym. Eng. Sci., 14, 298–307 (1974)
34. K.U. Haas and F.H. Skewis, "The Wire Coating Process: Die Design and Polymer Flow Characteristics," SPE ANTEC, 8–11 (1974)
35. "Extrusion Guide for Melt Processable Fluoropolymers," DuPont Technical Literature
36. J.A. Blair, "Teflon FEP Fluorocarbon Resin, Techniques for Processing by Melt Extrusion," DuPont Technical Literature, TR 108
37. J.A. Blair, "Methods for Increasing Extrusion Rates of Teflon FEP Fluorocarbon Resins," DuPont Technical literature, TR 108
38. C.L. Tucker III, "Fundamentals of Computer Modeling for Polymer Processing," Hanser Publishers, Munich (1989)
39. K. O'Brien, "Applications of Computer Modeling for Extrusion and Other Continuous Polymer Processes," Carl Hanser Publishers, Munich (1992)
40. G. Menges, A. Mayer, T. Bartilla, and J. Wortberg, "A New Concept for the Design of Spiral Mandrel Dies," Adv. Polym. Technol., 4, no. 2, 177–185 (1984)
41. C.J. Rauwendaal, "Flow Distribution in Spiral Mandrel Dies," Polym. Eng. Sci., 27, 186–191 (1987)
42. P.A. Toensmeier, "High-Value Niche Grows in Multi-Layer Die Design," Mod. Plast., Dec., 52–54 (2000)
43. J. Dooley and K. Hughes, "Analyzing the Flow Through Dies Containing Different Channel Geometries," SPE ANTEC (1996)

44. B.L. Koziey, J. Vlachopoulos, J. Vlcek, and J. Svabik, “Profile Die Design by Pressure Balancing and Cross Flow Minimization,” SPE ANTEC (1996)

45. J. Svabik, P. Samsonkova, and J. Perdikoulias, Proceedings of Vinyltech, Mississauga, Canada, 111 (1999)

46. H. Gross, W. Michaeli, F. Pöhler, and J. Ullrich, “(Membran Statt Staubalken) Membrane instead of Restrictor Bar,” Kunststoffe, Oct., 1352–1358 (1994)

47. J. Callari, “Flow Tuner, Precise Block the Latest in Flat Dies,” Plast. World, Oct., 16 (1996)

10 Twin Screw Extruders

10.1 Introduction

The first twin screw extruders for polymer processing were developed in the late 1930s in Italy. Roberto Colombo developed the co-rotating twin screw extruder, and Carlo Pasquetti developed the counter-rotating twin screw extruder. Early twin screw extruders had a number of mechanical problems. The most important limitation was the thrust bearing design. Because of the limited space, it is difficult to design a thrust bearing with good axial and radial load capability. The early thrust bearings were not strong enough to give the twin screw extruders good mechanical reliability. In the late 1960s, special thrust bearings were developed especially for application in twin screw extruders. Since that time, the mechanical reliability of twin screw extruders has been comparable to that of single screw extruders. However, twin screw extruders generally still do not have as high a thrust bearing rating as single screw extruders.

Twin screw extruders have established a solid position in the polymer processing industry. The two main areas of application for twin screw extruders are profile extrusion of thermally sensitive materials (e.g., RPVC) and specialty polymer processing operations, such as compounding, devolatilization, chemical reactions, etc. Twin screw extruders used in profile extrusion have a closely fitting flight and channel profile and operate at relatively low screw speeds, in the range of about 20 rpm. These machines offer several advantages over single screw extruders. Better feeding and more positive conveying characteristics allow the machine to process hard-to-feed materials (powders, slippery materials, etc.) and yield short residence times and a narrow residence time distribution (RTD). Better mixing and larger heat transfer area allow good control of the stock temperatures. Good control over residence times and stock temperatures obviously are key elements in the profile extrusion of thermally sensitive materials. Most twin screw extruders used in profile extrusion are closely intermeshing and counter-rotating, although a few co-rotating twin screw extruders are used.

Specialty polymer processing operations are performed on a number of twin screw extruders with a variety of designs. An overview of the different types of twin screw extruders is shown in Table 2.2, Chapter 2. High speed intermeshing co-rotating

extruders are used in compounding and devolatilization. Co-rotating twin screw extruders are also used as chemical reactors. Co-rotating twin screw extruders used in compounding often operate at high speeds, with typical screw speeds ranging from 300 to 600 rpm. Very high speed co-rotating twin screw extruders are available that can run at speeds as high as 1200 to 1400 rpm. Obviously, not all compounds can be processed at screw speeds this high.

Non-intermeshing extruders are used for mixing, chemical reactions, and devolatilization. The conveying mechanism in non-intermeshing extruders is considerably different from that in intermeshing extruders; it is closer to the conveying mechanism in a single screw extruder, although there are substantial differences. As a result, non-intermeshing twin screw extruders do not have positive conveying characteristics. However, it should be realized that positive conveying characteristics generally result in poor axial mixing capability. Thus, if axial mixing is required, positive conveying characteristics can be a disadvantage. Table 10.1 compares high speed to low speed twin screw extruders.

Table 10.1 Comparison of High Speed to Low Speed Twin Screw Extruders

High speed TSE	Low speed TSE
Primarily used in compounding	Primarily used in profile extrusion
Screw speeds from 200 to 1400 rpm	Screw speeds from 10–40 rpm
Always operated by starve feeding, flood feeding not possible	Can be operated by starve feeding, in some cases flood feeding is possible
Operates at a low degree of fill, around 20–40% typically	Operates at a high degree of fill
Good mixing characteristics in most cases	Poor mixing capability in most cases
Fair conveying characteristics, limited pressure generating capability	Good conveying characteristics, good pressure generating capability
Fair output stability	Good output stability
Pressures in the extruder are generally low	Pressures can be relatively high
Machines generally have long L/D ratio, typically over 30:1	Machines have short L/D ratio, typically less than 30:1
Sequential feeding commonly used	Sequential feeding not common
Modular screws and barrel commonly used	Most extruders use non-modular screws and barrel
High price, much higher than single screw extruders of same diameter	Low price, closer to the price of single screw extruders
Parallel screws are used in high speed extruders, conical screws are not used	Small diameter extruders can use conical screws, large diameter extruders are all parallel

10.2 Twin versus Single Screw Extruder

The characteristics of twin screw extruders may be better appreciated by considering the fundamental differences between single and twin screw extruders. One major difference is the type of transport that takes place in the extruder. Material transport in a single screw extruder is a drag-induced type of transport: frictional drag in the solids conveying zone and viscous drag in the melt conveying zone. Therefore, the conveying behavior is to a large extent determined by the frictional properties of the solid material and the viscous properties of the molten material. There are many materials with unfavorable frictional properties, which cannot be fed into single screw extruders without experiencing feed problems. On the other hand, the transport in an intermeshing twin screw extruder is to some extent a positive displacement type of transport. The degree of positive displacement depends on how well the flight of one screw closes the opposing channel of the other screw. The most positive displacement is obtained in a closely intermeshing, counter-rotating geometry. For instance, a gear pump can be considered to be a counter-rotating twin screw extruder with the helix angle of the screw flights being 90° or close to it. However, even a gear pump is not a pure positive displacement device because the machine cannot be designed with zero clearances. Thus, leakage flows will reduce the degree of positive conveying that can be achieved in a twin screw extruder.

Another major difference between the single and twin screw extruder is the velocity patterns in the machine. The velocity profiles in single screw extruders are well defined and fairly easy to describe; see Section 7.4. The situation in twin screw extruders in more complicated. The velocity profiles in twin screw extruders are complex and more difficult to describe. A number of workers have analyzed the flow patterns by neglecting the flow in the intermeshing region [1–5]. However, the mixing characteristics and the overall behavior of the machine is primarily determined by the leakage flows occurring in the intermeshing region. Thus, results from analyses that do not consider the flow in the intermeshing region have limited practical applicability. On the other hand, analyses that attempt to accurately describe the flow in the intermeshing region can easily become very complex [6, 7].

The complex flow patterns in twin screw extruders have several advantages, such as good mixing, good heat transfer, large melting capacity, good devolatilization capacity, and good control over stock temperatures. One disadvantage of the complex flow patterns is that they are difficult to describe. The theory of twin screw extruders is not as well developed as the theory of single screw extruders. As a result, it is difficult to predict the performance of a twin screw extruder based on extruder geometry, polymer properties, and processing conditions. Conversely, it is equally difficult to predict the proper screw geometry when a certain performance is required in a particular application. This situation has led to twin screw extruders of modular

design. These machines have removable screw and barrel elements. The screw design can be altered by changing the sequence of the screw elements along the shaft. In this way, an almost infinite number of screw geometries can be put together. The modular design, therefore, creates excellent flexibility and allows careful optimization of screw and barrel geometry to each particular application. Unfortunately, modular screws and barrels also increase the cost of the extruder a great deal. A number of modular screw elements for a co-rotating extruder are shown in Fig. 10.1.

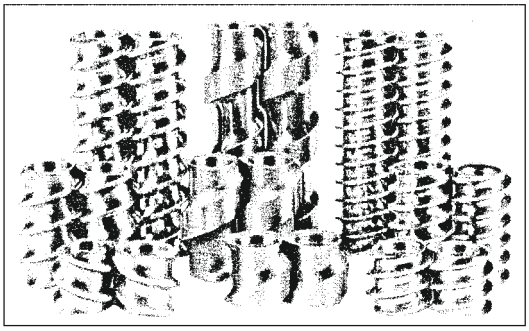


Figure 10.1
Screw elements for co-rotating twin screw extruder

Modular screw elements for a counter-rotating extruder are shown in Fig. 10.2.

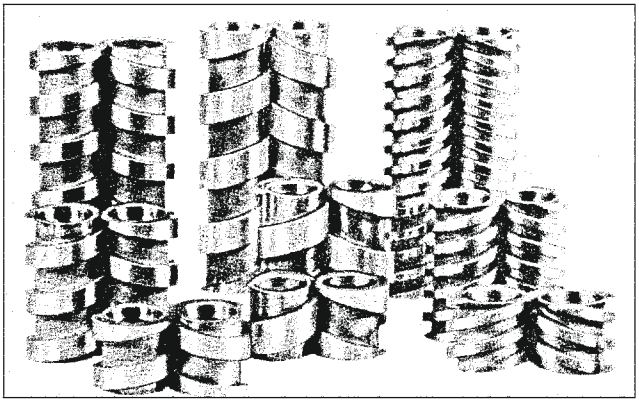


Figure 10.2
Screw elements for counter-rotating twin screw extruder

Table 10.2 presents a comparison of characteristics of twin and single screw extruders. The comparison is based on intermeshing twin screw extruders.

Table 10.2 Comparison of Twin Screw and Single Screw Extruder

Twin Screw Extruder (TSE)	Single Screw Extruder (SSE)
Used in profile, compounding, and reactive extrusion	Used in simple profile extrusion and coextrusion
Often used with modular design of screw and barrel—great flexibility	Modular design of screw and barrel is rarely used—less flexibility
Prediction of extruder performance is often difficult	Prediction of extruder performance less difficult than for twin screw extruder

Twin Screw Extruder (TSE)	Single Screw Extruder (SSE)
Good feeding, can handle pellets, powder, liquids	Fair feeding, slippery additives tend to give problems
Good melting; dispersed solids melting mechanism	Fair melting; contiguous solids melting mechanism
Good distributive mixing with effective mixing elements	Good distributive mixing with effective mixing elements
Good dispersive mixing with effective mixing elements	Good dispersive mixing with effective mixing elements
Good degassing	Fair degassing
Intermeshing TSE can have completely self-wiping characteristics	Not self-wiping: barrel is wiped but screw root and flight flanks are not
Modular TSE is very expensive	SSE is relatively inexpensive
Co-rotating TSE can run at very high screw speed, up to 1400 rpm	SSE usually run between 10–150 rpm; high screw speeds possible but not often used

10.3 Intermeshing Co-Rotating Extruders

There are two types of intermeshing co-rotating extruders: the low speed extruder and the high speed extruder. The two machines are different in design, in operating characteristics, and in areas of application. The low speed co-rotating twin screw extruder is primarily used in profile extrusion, while the high speed extruder is primarily used in compounding.

10.3.1 Closely Intermeshing Extruders

The low speed extruder has closely intermeshing screw geometry where the flight profile fits closely into the channel profile, i. e., a conjugated screw profile. A typical screw geometry of the closely intermeshing co-rotating (CICO) twin screw extruder is shown in Fig. 10.3.

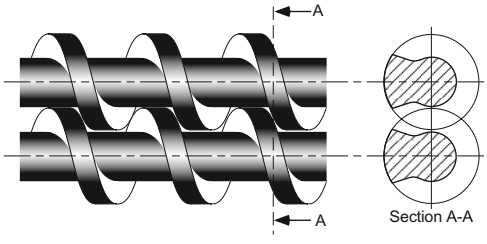


Figure 10.3
Screw geometry of a CICO extruder

The conjugated screw profile shown in Fig. 10.3 appears to form a good seal between the two screws. However, a cross-section through the intermeshing region, shown in Fig. 10.4, reveals the presence of relatively large openings between the channels of the two screws.

Therefore, the conveying characteristics of the CICO extruder are not as positive as those of a closely intermeshing counter-rotating extruder (CICT); see also Figs. 10.27 and 10.28.

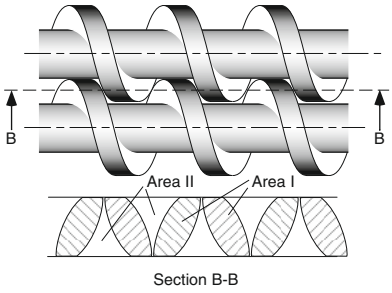


Figure 10.4
Cross-section through the intermeshing region of a CICO extruder

The co-rotating twin screw extruder has a sliding type of intermeshing as shown in Fig. 10.5.

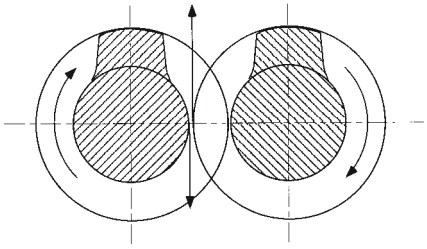


Figure 10.5
Sliding type of intermeshing in co-rotating twin screw extruders

The screw velocities in the intermeshing region are in opposite directions. Therefore, material entering the intermeshing region will have little tendency to move through the entire intermeshing region unless the flight flank clearance is quite large; this situation is shown in Fig. 10.6(a).

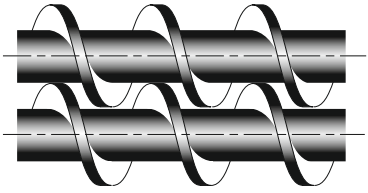


Figure 10.6(a)
Intermeshing region with a large flank clearance

Because of the relatively large open areas between the channels, material entering the intermeshing region will tend to flow into the channel of the adjacent screw. The material will move in an open figure-eight pattern, as shown in Fig. 10.6(b), while at the same time moving in the axial direction.

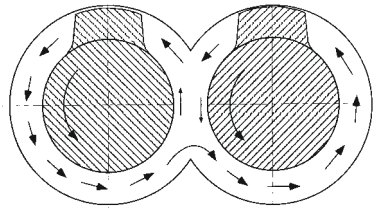


Figure 10.6(b)
Movement of material in open figure-eight pattern

The material close to the passive flight flank cannot flow into the channel of the adjacent screw because it is obstructed by the flight of the adjacent screw. The material, therefore, will undergo a circulatory flow as shown in Fig. 10.7.

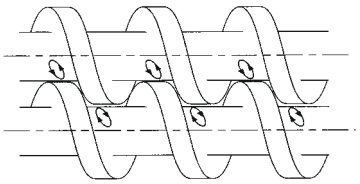


Figure 10.7
Circulatory flow at the passive flight flank

This material fraction will move forward at axial velocity v_a:

$$v_a = \pi DN \tan\varphi \tag{10.1}$$

The obstructed material fraction will contribute to the positive conveying characteristics of the extruder. If the obstructed area (Area I in Fig. 10.4) is large relative to the open area (Area II in Fig. 10.4), then the conveying characteristics will be quite positive. If the open area is large relative to the obstructed area, then the positive conveying characteristics will be considerably reduced, resulting in a wide residence time distribution (RTD) and a more pressure-dependent throughput. CICO extruders have relatively positive conveying characteristics because their screw geometry is such that the open area is small relative to the obstructed area.

The sliding type of intermeshing will result in high pressure regions at the point where the material enters the intermeshing region; this is shown in Fig. 10.8.

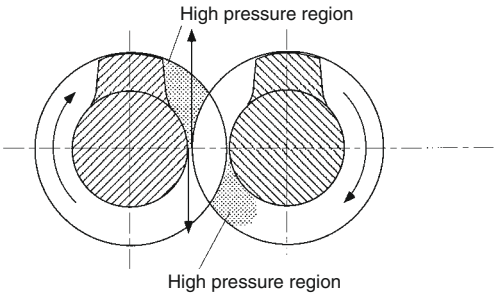


Figure 10.8
High pressure regions at the entrance to the intermeshing region

The pressure build-up occurs primarily because of the reduction in cross-sectional area of the flow channel as the material enters the intermeshing region. Pressure build-up also occurs because of the change in flow direction that occurs as the material enters the intermeshing region. Obviously, the pressure build-up will be most severe when the open area is small compared to the obstructed area, which is the case in CICO twin screw extruders. These high pressure regions will result in lateral forces on the screws trying to push the screws apart. These separating forces will increase with screw speed. Clearly, the separating forces should not be as large as to cause contact between the screws and barrel, since this will result in severe wear. Therefore, CICO extruders have to run at low speed in order to avoid large pressure peaks in the intermeshing region.

10.3.2 Self-Wiping Extruders

High speed co-rotating extruders have a closely matching flight profile, as shown in Fig. 10.9.

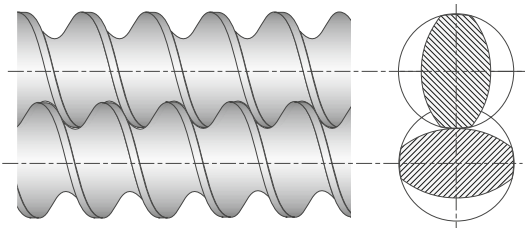


Figure 10.9
Flight geometry in CSCO extruders

There is considerable openness from one channel to the adjacent channel. This is obvious both from the top view of the screws shown in Fig. 10.9 as well as from the cross-section through the intermeshing region, shown in Fig. 10.10.

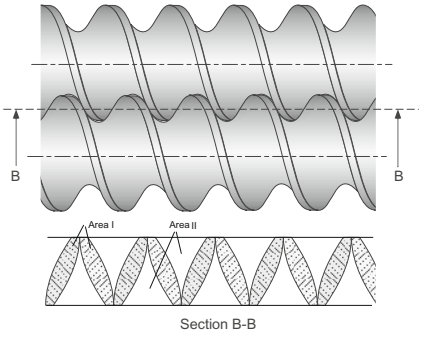


Figure 10.10
Cross-section through the intermeshing region in CSCO extruders

Thus, the open area II is large relative to the obstructed area I. Therefore, there is relatively little tendency for large pressure peaks to form in the intermeshing region. The screws can therefore be designed with relatively small clearances between the

two screws; the screws are then closely self-wiping. Twin screw extruders of this design are generally referred to as closely self-wiping co-rotating extruders (CSCO).

Since the tendency to develop large pressure peaks in the intermeshing region is quite small with CSCO extruders, they can run at high speeds, as high as 1400 rpm. This is made possible by the relatively large open area in the intermeshing region. However, this geometrical characteristic also results in a relatively non-positive conveying characteristic with a corresponding wide RTD and pressure-sensitive throughput. These machines, therefore, are not well suited for direct profile extrusion. A large fraction of the material will follow the figure-eight flow pattern discussed earlier. This fraction in the CSCO extruder will be considerably larger than in the CICO extruder. The progression of the material in one channel is shown in Fig. 10.11 for a double-flighted geometry.

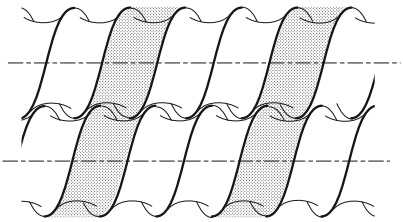


Figure 10.11
Transport in a double-flighted CSCO extruder

Note that the material is displaced by an axial distance of three times the pitch when it reenters the screw. Thus, in a double-flighted geometry, there are three more or less independent down-channel flows. When the number of parallel flights is p, the number of independent down-channel flows n_i is:

$$n_i = 2p - 1 \tag{10.2}$$

10.3.2.1 Geometry of Self-Wiping Extruders

The flight and channel geometry of self-wiping co-rotating twin screw extruders is determined by the screw diameter, centerline distance, helix angle, and the number of parallel flights. When these geometrical parameters are selected, the cross-section geometry is fixed and can be determined from kinematic principles as described in detail by Booy [8]. If α_t is the tip angle, α_i the angle of intermesh, p the number of parallel flights, and D the screw diameter, then the centerline distance L_c can be determined from:

$$L_c = D\cos\left(\frac{\pi}{2p} - \frac{\alpha_t}{2}\right) \tag{10.3}$$

Thus, when the diameter, centerline distance, and number of flights are selected, the tip angle and thus the flight width are fixed by Eq. 10.3. The angles α_t and α_i are angles in the plane perpendicular to the screw axis; see also Fig. 10.12.

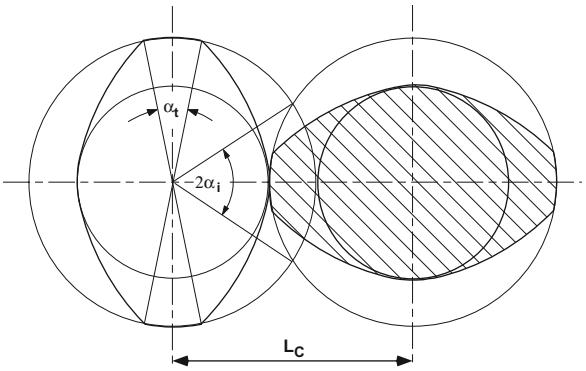


Figure 10.12
Geometry of self-wiping twin screw extruders

The angle of intermesh α_i is related to the tip angle by:

$$\alpha_i = \frac{\pi}{2p} - \frac{\alpha_t}{2} \tag{10.4}$$

Thus, the centerline distance can be expressed simply as:

$$L_c = D\cos\alpha_i \tag{10.5}$$

When the angle of intermesh is zero, the centerline distance simply equals the screw diameter. The maximum channel depth at the root of the screw is given by:

$$H_{max} = D - L_c = D - D\cos\left(\frac{\pi}{2p} - \frac{\alpha_t}{2}\right) \tag{10.6}$$

For non-zero values of the tip and root angle, the centerline distance has to increase with the tip angle (see Fig. 10.13[A]), with a corresponding reduction in the intermesh angle and channel depth. Fig. 10.13(B) shows a graph of the ratio of channel depth to screw diameter plotted against the tip angle for three values of the number of flights.

Once the tip angle and the number of flights are selected, the centerline distance and the root diameter are fixed in a self-wiping co-rotating extruder. This imposes a considerable design constraint on co-rotating twin screw extruders.

One of the implications of this constraint is that the centerline distance for triple-flighted or trilobal screws, p = 3, has to be quite large. The smallest centerline distance for a triple-flighted geometry is $C_L/D = 0.5\sqrt{3}$ (= 0.866); see Eq. 10.3 and the maximum channel depth 0.134 D. As a result, the channel depth of the screw becomes relatively small and so does the channel volume. Consequently, the throughput capability of triple-flighted screws is limited.

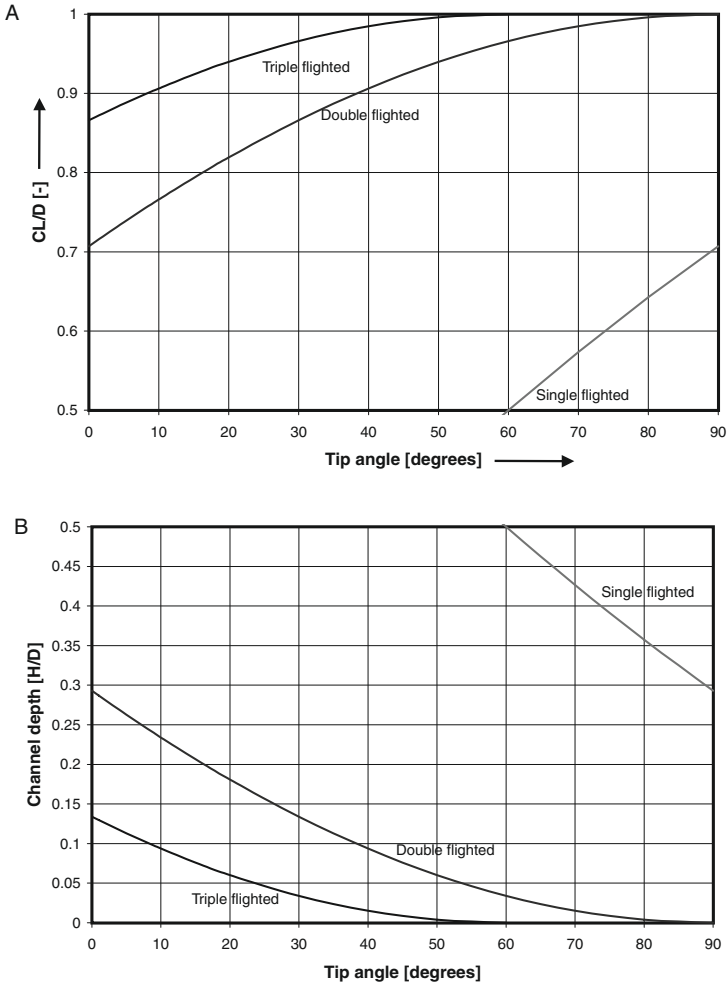


Figure 10.13(A–B) Channel depth versus tip angle for self-wiping co-rotating twin screws

The centerline distance can be made considerably shorter in double-flighted, bilobal screws (p = 2). In this case the smallest centerline distance is $C_L/D = 0.5\sqrt{2}$ (= 0.707) and the maximum channel depth 0.293 D. Thus, the channel depth and channel volume can be made substantially larger, which results in improved throughput capability. These considerations have led several twin screw extruder manufacturers to switch from triple-flighted co-rotating extruders to double-flighted extruders.

The free volume of self-wiping co-rotating extruders can be expressed as $CR^3(L/D)$. For single-flighted screws the constant C = 7.0, for double-flighted screws C = 6.8, and for triple-flighted screws C = 3.8. Clearly, the free volume reduces a great deal when going from a double-flighted to a triple-flighted geometry.

Because the leading flight flank of one screw sweeps both the leading and trailing flight flank of the other screw, the geometry of the leading flight flank has to be the

same as that of the trailing flight flank. This is not the case for counter-rotating twin screw extruders.

The construction of the screw geometry for co-rotating extruders was described in detail by Booy [8]. Figure 10.14 shows the steps involved in constructing the exact geometry of the screws.

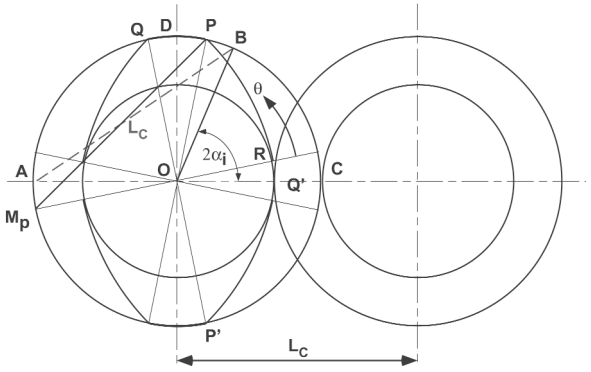


Figure 10.14
Construction of the geometry of self-wiping co-rotating screws

The steps in the construction are as follows:

1. Draw line AB such that AB equals the centerline distance; this defines the intermesh angle $2\alpha_i$
2. Locate point D such that angle COD equals π/n, where n is number of flights
3. Point P is located on the circle midway between points B and D
4. Make PD equal to QD; this defines one screw tip; the other tip is Q'P'
5. Center M_p of flank curve through P lies on a circle at distance L_c from P
6. Construct flank curve PR, then add other flank curves
7. One screw cross-section is now completely defined

The channel depth reduces along the flight flank. If circumferential angle θ starts at the beginning of the flight flank the channel depth as a function of angle θ can be written as:

$$H(\theta) = \frac{D}{2}(1+\cos\theta) - \left(L_c^2 - \frac{1}{4}D^2\sin^2\theta\right)^{1/2} \tag{10.7}$$

Figure 10.15 illustrates how the channel depth varies with circumferential angle θ.

The axial coordinate 1 is related to the circumferential angle θ by:

$$1 = \frac{D}{2}\theta\tan\varphi \tag{10.8}$$

where φ is the helix angle of the screw flight.

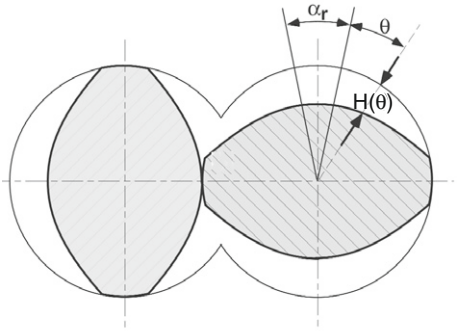


Figure 10.15
Channel depth as a function of angle θ

Thus, the channel depth profile as a function of axial distance 1 is:

$$H(1) = \frac{D}{2}\left[1 + \cos\left(\frac{2l}{D}\cot\varphi\right)\right] - \left[L_c^2 - \frac{1}{4}D^2\sin^2\left(\frac{2l}{D}\cot\varphi\right)\right]^{1/2} \tag{10.9}$$

The cross-channel coordinate x is related to the circumferential angle θ by:

$$x = \frac{D}{2}\theta\sin\varphi \tag{10.10}$$

Thus, the channel depth as a function of cross-channel distance is:

$$H(x) = \frac{D}{2}\left[1 + \cos\left(\frac{2x}{D\sin\varphi}\right)\right] - \left[L_c^2 - \frac{1}{4}D^2\sin^2\left(\frac{2x}{D\sin\varphi}\right)\right]^{1/2} \tag{10.11}$$

When the coordinate x is zero, the channel depth reaches its maximum value; see Eq. 10.6. The maximum channel depth is maintained over a circumferential angular distance of α_t, which corresponds to a cross-channel distance 0.5 $D\alpha_t\sin\varphi$.

In CSCO extruders, a major portion of the material entering the intermeshing region in a channel of one screw will transfer to an adjacent channel of the other screw. This is shown in Fig. 10.16 where the material transport in one channel is shown in a cross-section perpendicular to the screw axes.

Just before the intermeshing region, the flow channel area is determined by the area between the screw and the barrel, i. e., the screw channel area A_1. In the intermeshing region itself, the flow channel area is determined by the area between the two screws and the barrel. Initially, the flow channel area increases to a maximum value and then it reduces back to area A_1 at the end of the intermeshing region. This action causes a relatively effective transfer of material from one screw to the other and vice versa if the flight width is small relative to the width of the channel–this is the case in CSCO extruders. As the flight width increases, the interscrew material transfer becomes more restricted, resulting in increased circulatory flow at the entrance to the intermeshing region and increased pressure build-up at this point.

In fact, when the flight width becomes sufficiently large, the characteristics of the extruder will change to those of a CICO extruder; see Fig. 10.17.

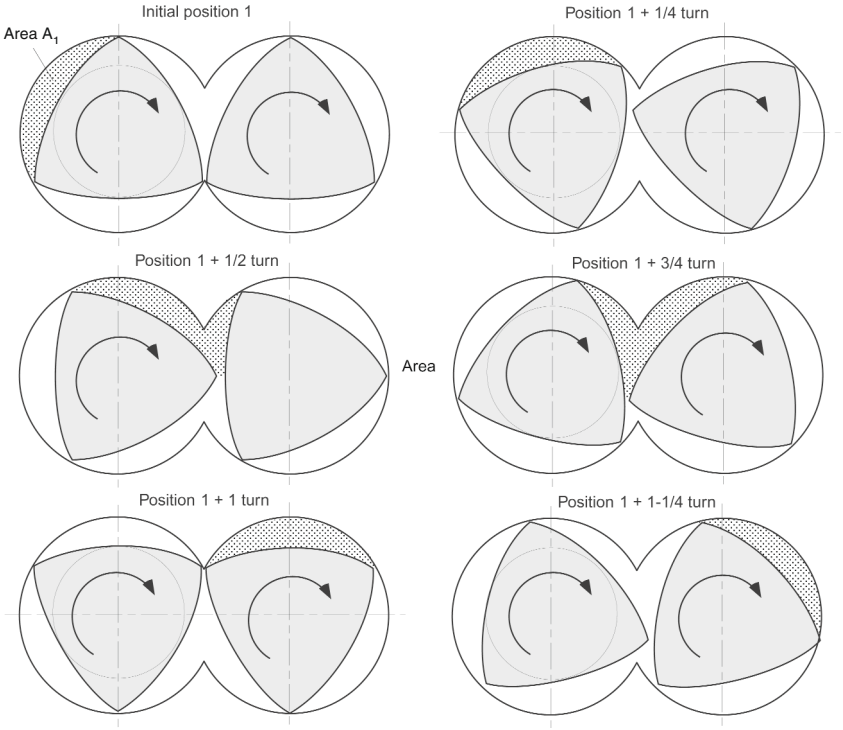


Figure 10.16 Material transfer in a CSCO extruder

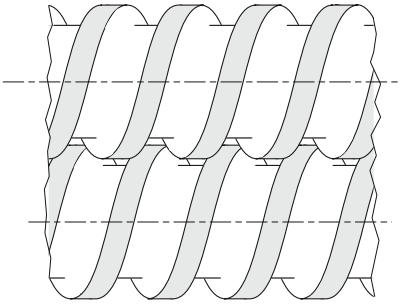


Figure 10.17
Co-rotating extruder with wide flights

The cross-sectional area of the barrel is:

$$A_b = \frac{1}{2}(\pi - \alpha_i)D^2 + \frac{1}{2}L_c D \sin\alpha_i \tag{10.12}$$

The cross-sectional area of one screw is:

$$A_s = p\,\alpha_i L_c^2 - \frac{1}{2} p\, L_c D \sin\alpha_i + \frac{1}{2} p\,\alpha_i \left(L_c^2 + \frac{1}{2} D^2 - L_c D \right) \tag{10.13}$$

The open cross-sectional area between barrel and screw is simply:

$$A_o = A_b - 2A_s \tag{10.14}$$

This can be written as:

$$A_o = D^2 \left[\left(p - \frac{1}{2} \right) \alpha_i + \left(p + \frac{1}{2} \right) \sin\alpha_i \cos\alpha_i - \pi \cos^2 \alpha_i + (\pi - 2p\alpha_i) \cos\alpha_i \right] \tag{10.15}$$

Thus, at a certain diameter, the open area is primarily a function of the number of parallel flights p and the intermeshing angle α_i; see Fig. 10.18.

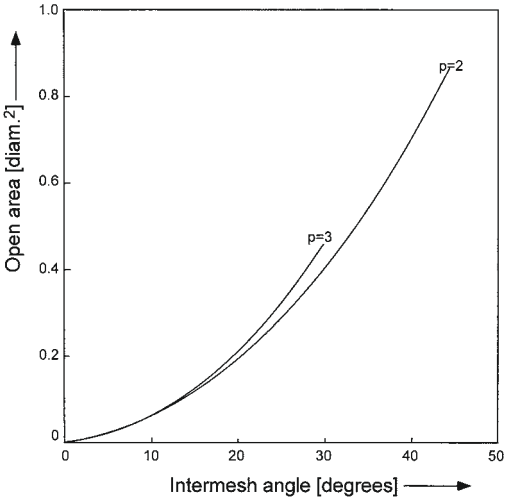


Figure 10.18
Open area versus intermesh angle with double- and triple-flighted screws

The open volume is obtained by simply multiplying the open area with axial screw length L:

$$V_o = A_o L \tag{10.16}$$

The surface area of the screw is obtained by multiplying the periphery of the screw with axial length L:

$$A_S^S = \pi L_c L \tag{10.17}$$

The surface area of the barrel is:

$$A_b^s = 2\,L\,D\,(\pi - \alpha_i) \tag{10.18}$$

The channel area formed between the screw and barrel, screw channel area A_1 (see Fig. 10.16) is:

$$A_1 = \frac{0.25\,\pi\,D^2 - A_s}{p} \tag{10.19}$$

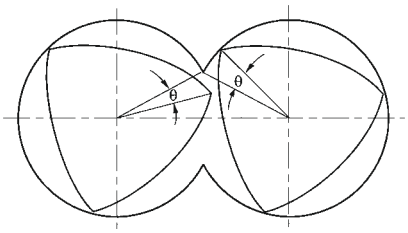


Figure 10.19
Angle θ from leading tip to start of intermeshing region

By using Eq. 10.13 for A_s, Eq. 10.19 can be written as:

$$A_1 = D^2\left[\frac{1}{2}\alpha_i - \left(\alpha_i + \frac{1}{2}\alpha_t\right)\cos^2\alpha_i + \left(\frac{1}{2}\sin\alpha_i + \frac{1}{2}\alpha_t\right)\cos\alpha_i\right] \tag{10.20}$$

When the leading tip of a screw channel enters the intermeshing region, the flow channel area increases because of the contribution of the adjacent screw; see Fig. 10.16. The flow channel area reaches a maximum A_{max}, when the leading tip reaches the end of the intermeshing region. The flow channel area then reduces again and becomes area A_1 when the trailing tip of the screw channel enters the intermeshing region. The open cross-sectional area A_0 is thus formed by 2p –1 channels, two of which are in the intermeshing region, A_{top} and A_{bot}. When A_{top} is increasing, A_{bot} is decreasing and vice versa. The total area of intermesh A_{int} is the sum of A_{top} and A_{bot}; this is a constant. Area A_{int} is obtained from:

$$A_{int} = A_{top} + A_{bot} = A_0 - (2p-3)A_1 \tag{10.21}$$

The maximum value of A_{top} and A_{bot} is simply:

$$A_{max} = A_0 - (2p-2)A_1 \tag{10.22}$$

If angle θ is the angle from the leading tip to the start of the intermeshing region (see Fig. 10.19), then the area A_{top} can be expressed as a function of angle θ.

This relationship is shown graphically in Fig. 10.20 for a geometry with p = 3 and $\alpha_t = 0$.

Area A_{top} increases from $A_1 = 0.0856D^2$ to reach a maximum of $A_{max} = 0.1259D^2$, an increase of 47%. At the same time, area A_{bot} reduces from the maximum A_{max} down to A_1. Thus, when area A_{top} is decompressed, area A_{bot} is compressed and vice versa. This action will promote leakage flow through the nip when the degree of fill is high and will cause an alternating dynamic pressure field in area A_{top} and A_{bot}.

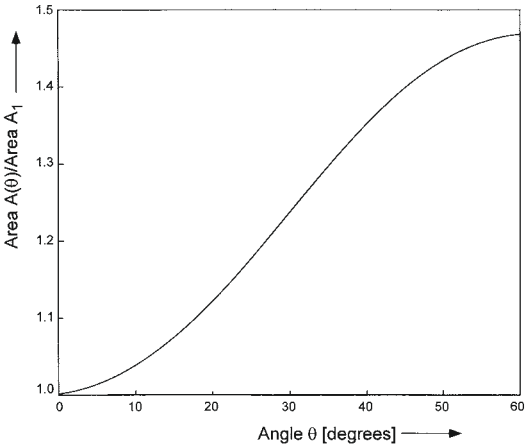


Figure 10.20
A_{top} as a function of angle θ

10.3.2.2 Conveying in Self-Wiping Extruders

The conveying process in single screw extruders is generally analyzed by using the flat plate model; see Chapter 7. A similar analysis can be used in CSCO extruders when both screws are rolled onto a flat plate as shown in Fig. 10.21.

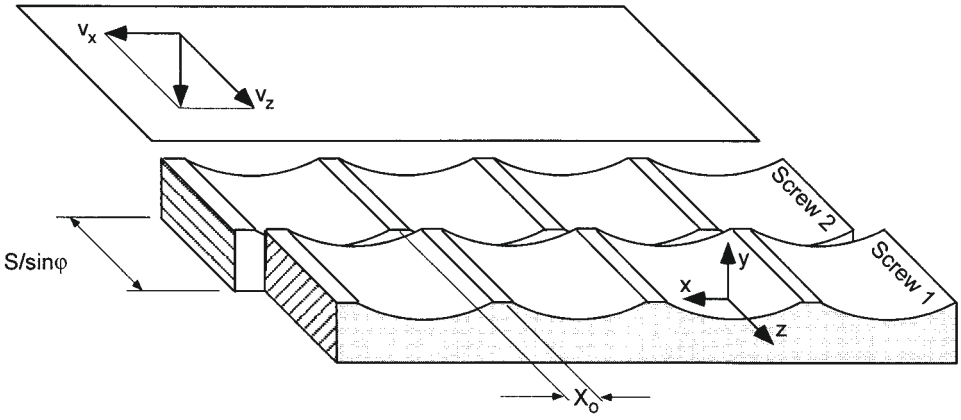


Figure 10.21 Flat plate model in CSCO extruders

The down-channel length of each flat screw segment is S/sinφ, where S is the pitch of the screw flight and φ the helix angle. The screws are offset in the cross-channel direction by a distance X_o, where X_o is often taken to be equal to the cross-channel flight width. Obviously, this model is a severe simplification of the actual conveying process because it cannot accurately represent the interscrew material transfer in the intermeshing region. However, the advantage of the flat plate model is that one can follow a very similar approach to the one used in single screw extruders.

In most cases, the CSCO extruder will be starve fed. Thus, the output from the extruder is determined by the device feeding the extruder and not by the extruder

itself. This means that the screw channels are partially filled with material over a considerable length of the extruder. Only certain sections of the screw will be fully filled. The last section of the screw is generally completely filled because it must generate the required diehead pressure. Other sections of the screw that will be completely filled are screw sections with neutral or reversing screw elements.

The fully filled length of the machine will increase with diehead pressure. The reason that the fully filled length of the machine is determined by the pressure-generating requirement is that pressure can only be generated when the channel is completely filled with material. If the screw channel is only partially filled with material, no pressure can be generated in the down-channel direction. Local sections of the screw can be fully filled if a restrictive screw element is placed along the screw, such as a reversed-flighted screw element or a kneading block.

10.3.2.2.1 Partially Filled Screws

Following Werner [9], the degree of fill ε is defined as the ratio of filled channel area A_ε to total area:

$$\varepsilon = \frac{A_\varepsilon}{A} \tag{10.23}$$

This is shown graphically in Fig. 10.22, where the areas are determined perpendicular to the screw flights.

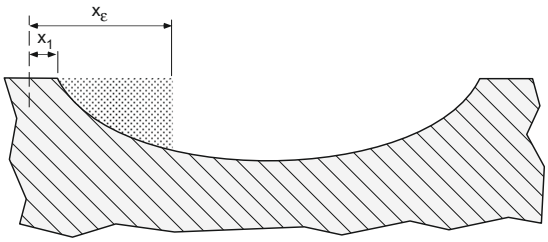


Figure 10.22
Partially filled screw channel

The total cross-channel area A is simply:

$$A = A_1 \sin\varphi \tag{10.24}$$

where A_1 is the channel area in a plane perpendicular to the screw axis given by Eq. 10.20.

Area A_ε is related to the filled cross-channel distance x_ε by:

$$A_\varepsilon = \int_{x_1}^{x_\varepsilon} H(x)dx \tag{10.25}$$

where $x_1 = 0.25\ \alpha_t D \sin\varphi$.

A typical relationship between the degree of fill and a normalized cross-channel distance is shown in Fig. 10.23.

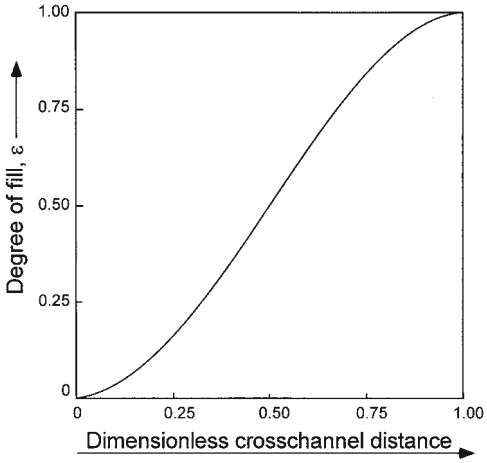


Figure 10.23
Degree of fill versus normalized cross-channel distance

The velocity profiles can be determined if the following assumptions are made:

1. The fluid is Newtonian
2. The flow is steady and fully developed
3. The flow is isothermal
4. No slip at the wall
5. Body and inertia forces are negligible
6. Channel curvature in the down-channel direction is negligible

The equation of motion in the down-channel direction can be written as:

$$\frac{\partial^2 v_z}{\partial x^2} + \frac{\partial^2 v_z}{\partial y^2} = 0 \tag{10.26}$$

The solution to this equation for a rectangular channel is given in Section 7.4. However, the channel of a CSCO extruder does not have a rectangular shape but resembles more the segment of a circle. Since the channel depth is a rather lengthy function of the cross-channel distance (see Eq. 10.11), a simple analytical solution to Eq. 10.26 is not very likely to be found. Thus, one has to resort to numerical techniques to solve Eq. 10.26. If it is assumed that:

$$\frac{\partial^2 v_z}{\partial x^2} << \frac{\partial^2 v_z}{\partial y^2} \tag{10.27}$$

then the down-channel velocity profile becomes simply:

$$v_z = \frac{y v_{bz}}{H} \tag{10.28}$$

The equation of motion in the cross-channel direction can be written as:

$$\frac{\partial^2 v_x}{\partial x^2} + \frac{\partial^2 v_x}{\partial y^2} = \frac{1}{\mu}\frac{\partial P}{\partial x} \tag{10.29}$$

If it is assumed that:

$$\frac{\partial^2 v_x}{\partial x^2} << \frac{\partial^2 v_x}{\partial y^2} \tag{10.30}$$

then the cross-channel velocity profile can be written as:

$$v_x = \frac{y^2 + Hy}{2\mu}\frac{dP}{dx} + \frac{yv_{bx}}{H} + v_{bx} \tag{10.31}$$

where y is measured from the barrel surface in the negative direction.

The cross-channel pressure gradient can be determined from the condition that the net flow in the x-direction is zero, i.e., leakage flow is neglected. Thus, the cross-channel pressure gradient is:

$$\frac{dP}{dx} = \frac{6\mu v_{bx}}{H^2} \tag{10.32}$$

and the resulting cross-channel velocity profile becomes:

$$v_x = \frac{3v_{bx}y^2}{H^2} + \frac{4v_{bx}y}{H} + v_{bx} \tag{10.33}$$

If the leakage flow over the flights is neglected and also the forced positive conveying of the obstructed material fraction (see Eq. 10.1), then the volumetric flow rate can be expressed as:

$$\dot{V} = (2p-1)\int_{-H}^{o}\int_{x_\varepsilon}^{x_1} v_z dx dy \tag{10.34}$$

If it is assumed that the down-channel velocity profile can be approximated with Eq. 10.28, then the volumetric throughput is approximately:

$$\dot{V} = \frac{1}{2}(2p-1)A_\varepsilon v_{bz} \tag{10.35}$$

By using Eq. 10.23, the equation can be written as:

$$\dot{V} = \frac{1}{2}(2p-1)\ \varepsilon A\pi DN\cos\varphi \tag{10.36}$$

Thus, the throughput according to Eq. 10.36 is directly proportional to the degree of fill ε and the screw speed N. The power consumption in the screw channel can be determined from:

$$dZ_{ch} = (2p-1)v_{bz}dz\int_{x_t}^{x_\varepsilon}\tau_{yz}(0)dx + (2p-1)v_{bx}dz\int_{x_t}^{x_\varepsilon}\tau_{yx}(0)dx \tag{10.37}$$

The power consumption in the flight clearance can be written as:

$$dZ_{cl} = \frac{(2p-1)\,v_b^2\mu_{cl}\,D\sin\varphi dz}{2\delta} \tag{10.38}$$

The total power consumption per unit down-channel length is:

$$dZ = dZ_{ch} + dZ_{cl} \tag{10.39}$$

The specific energy consumption (SEC) over axial length L is:

$$SEC = \frac{\int_0^{L/\sin\varphi} dz}{\rho\dot{V}} \tag{10.40}$$

Another approach to the analysis of the conveying process of partially filled screws was proposed by Booy [29]. By assuming that the bank of material at the leading flight edge is approximately symmetrical with respect to the bisectrix (see Fig. 10.24), and that the screw flank contacting the bank of material is reasonably flat, the velocity distribution in the bank can be analyzed as follows. The motion of the bank of material can be considered as a superposition of the motions of Fig. 10.24(b) and (c).

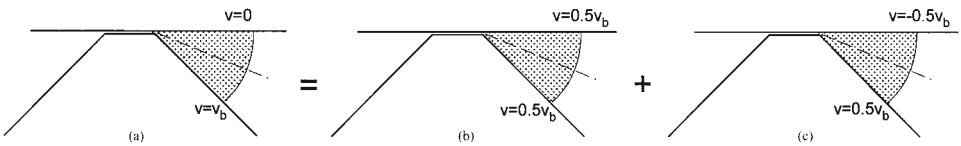


Figure 10.24(a–c) Partially filled screw channel

The velocity distribution in Fig. 10.24(c) will be such that no net flow occurs in the down-channel direction. The velocity distribution in Fig. 10.24(b) will cause a down-channel flow at a uniform velocity of $v_{bz}/2$. The average total velocity of the material in the bank is the resultant of v_{bx} and $v_{bz}/2$, as shown in Figs. 10.24. The axial velocity component is:

$$v_a = \frac{1}{2}v_b\sin\varphi\cos\varphi \tag{10.41}$$

When the flight clearances are neglected, this approach yields the same expression for throughput as the one derived earlier; see Eqs. 10.35 and 10.36. When the flight clearance is not neglected, it can be assumed that the thin layers smeared out on the screw and barrel surfaces are mostly stagnant and about half the thickness of the clearance. With the expressions for the screw surface area A^S_S, barrel surface area A^S_b, and open area A_0, the degree of fill resulting from non-zero clearances can be expressed as:

$$\varepsilon_1 = \frac{\pi L_c \delta_c + 2D(\pi - \alpha_i)\delta}{2A_0} \tag{10.42}$$

where δ_c is the clearance between the screws and δ the clearance between screw and barrel.

Open area A_0 is given by Eq. 10.15. The rest of the material moves at an axial velocity v_a and corresponds to a degree of fill ε_0. The cross-section A_L through the moving material is:

$$A_L = \varepsilon_0 A_0 \tag{10.43}$$

The flow rate is then:

$$\dot{V} = \varepsilon_0 A_0 v_a = \frac{1}{2}\ \varepsilon_0 A_0 v_b \sin\varphi\cos\varphi \tag{10.44}$$

The total degree of fill now becomes:

$$\varepsilon = \varepsilon_0 + \varepsilon_1 \tag{10.45}$$

When the extruder is run empty, the remaining degree of fill will be ε_1 when the effect of gravity is negligible.

10.3.2.2.2 Fully Filled Screws

Booy [29] analyzed the pumping performance of fully filled co-rotating twin screw extruders by distinguishing two flow regimes. One flow regime (I) is bounded by both screw and barrel surface, and one flow regime (II) is bounded primarily by the two screw surfaces in the intermeshing region; see Fig. 10.25.

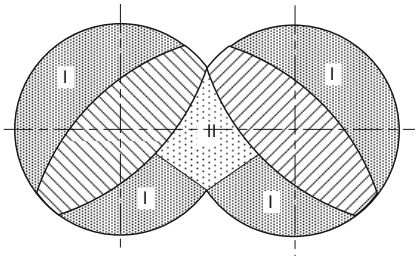


Figure 10.25
Flow regimens in twin screw extruder

The flow in regime I is analyzed by unwrapping screws as shown in Fig. 10.26.

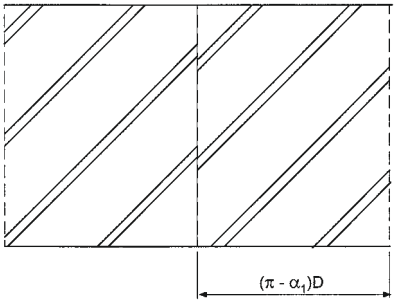


Figure 10.26
Unwrapped twin screw geometry

The drag flow rate is written as:

$$\dot{V}_d = \frac{1}{2}(2p-1)F_d\, H_{max}\, W\, v_{bz} \tag{10.46}$$

The pressure flow rate is written as:

$$\dot{V}_p = \frac{(2p-1)F_p H_{max}^3 W}{12\mu}\frac{\partial P}{\partial z} \tag{10.47}$$

Equations 10.46 and 10.47 can be applied only when the tip angle α_t is small. Regime II is assumed not to contribute to the pressure generation and is further assumed to move forward at a rate of one lead per revolution. If the cross-sectional area of regime II is A_a, then the flow rate through this domain is:

$$\dot{V}_a = v_a A_a = A_a v_b \tan\varphi \tag{10.48}$$

The total flow rate then becomes:

$$\dot{V} = \dot{V}_d + \dot{V}_a - \dot{V}_p \tag{10.49}$$

When the width W of the channel is large relative to the depth H_{max} of the channel, the shape factor for drag can be approximated by [29]:

$$F_d \cong \int_{-W/2}^{+W/2} \frac{H(x)dx}{WH_{max}} \tag{10.50a}$$

Similarly, the shape factor for drag can be approximated by:

$$F_d \cong \int_{-W/2}^{+W/2} \frac{H(x)^3 dx}{WH_{max}^3} \tag{10.50b}$$

Expressions for the limiting shape factors when the width of the channel is small relative to the depth ($W << H_{max}$) are given by Booy [29]. However, this type of channel geometry is generally not encountered in commercial twin screw systems. Numerical simulation of the flow and heat transfer in twin screw extruders is covered in Chapter 12. Section 12.3.2 discusses 2-D analysis of twin screws, and Section 12.4.3.3 deals with 3-D analysis of flow and heat transfer in twin screw extruders. Since 2000, major advances have been made in the numerical methods used to simulate twin screw extruders. The boundary element method now allows full 3-D analysis of flow in TSEs. A significant advance in the finite element method is the mesh superposition technique that allows analysis of complicated geometries with relative ease. This is discussed in more detail in Chapter 12.

10.4 Intermeshing Counter-Rotating Extruders

A typical screw geometry of a closely intermeshing counter-rotating (CICT) twin screw extruder is shown in Fig. 10.27.

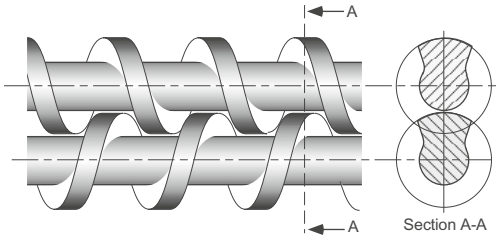


Figure 10.27
Geometry of a CICT extruder

A cross-section through the intermeshing region (see Fig. 10.28) shows that the openings between the channels of the two screws are quite small.

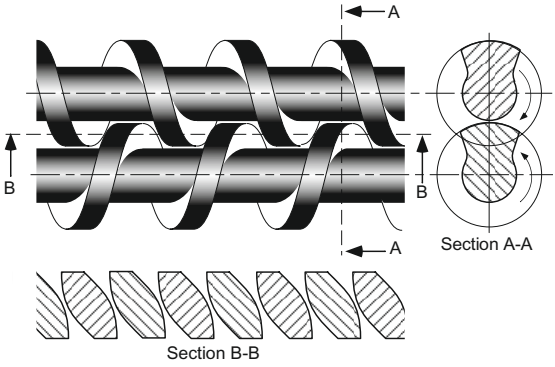


Figure 10.28
Cross-section through the intermeshing region in a CICT extruder

These openings are considerably smaller than in intermeshing co-rotating extruders; see also Figs. 10.3 and 10.4. As a result, CICT extruders can achieve relatively positive conveying characteristics.

The counter-rotating twin screw extruder has a milling type of intermeshing as shown in Fig. 10.29.

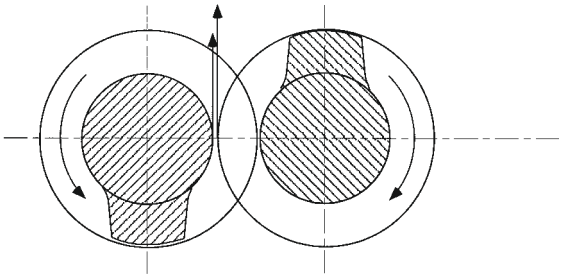


Figure 10.29
Milling type of intermeshing in counter-rotating extruders

The screw velocities in the intermeshing region are in the same direction. Therefore, the material entering the intermeshing region will have a strong tendency to flow through the intermeshing region. If the clearances between the two screws are rather small, the flow through the intermeshing region will be quite small. This will result in a bank of material accumulating at the entry of the intermeshing region. The material drawn into the nip will exert considerable pressure on the two screws. This can cause deflection of the screws. Therefore, CICT extruders generally run at low speed to avoid excessive pressures developing in the intermeshing region. By designing the screws with larger clearances, the allowable screw speeds can be increased; however, this is at the expense of the positive conveying characteristics. Thus, the maximum allowable screw speed on a CICT extruder is often a good indication of the conveying characteristics of the machine. A low maximum screw speed (about 20 to 40 rpm) indicates a machine with positive conveying characteristics with the most likely area of application being profile extrusion. A high maximum screw speed (about 100 to 200 rpm or higher) indicates a machine with less positive conveying characteristics with likely areas of application being compounding, continuous chemical reactions, and other specialty polymer processing operations.

The theoretical maximum output of a CICT extruder is:

$$\dot{V}_{max} = 2\,p\,N\,V \tag{10.51}$$

where p is the number of parallel flights, N the screw speed, and V the volume of the C-shaped chamber.

In Eq. 10.51, it is assumed that the screw channels are fully filled with material and that there is no leakage of material. Equation 10.51 was first proposed by Schenkel [10]. It was found that the actual throughput of CICT extruders is usually considerably below $\dot{V}_{max}$. Doboczky [11, 12] and Klenk [13, 14] introduced correction factors

to bring the predicted throughput values in line with actual throughput values. However, these correction factors were mostly empirical and, thus, of limited usefulness. Janssen [15] performed a detailed analysis of the leakage flows in counter-rotating extruders. He distinguished four kinds of leakage; see Fig. 10.30.

1. Leakage through the clearance between the screw flight and barrel, $\dot{V}_f$
2. Calender leakage, $\dot{V}_c$, between the root of the screw and the tip of the flight
3. Interscrew leakage through the gap between the flight flanks (the tetrahedron gap), $\dot{V}_t$, in the radial direction
4. Leakage through the side gap, $\dot{V}_s$, in the tangential direction

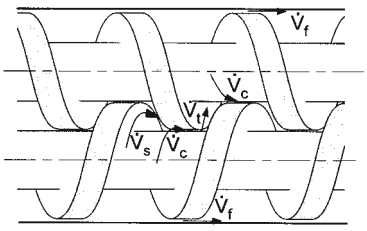


Figure 10.30
Leakage flows in CICT extruder

The volume of the C-shaped chamber is approximately:

$$V = \frac{\pi DHW_m}{\cos\varphi_m} - \frac{w_m D^2 (2\alpha_i - \sin 2\alpha_i)}{4\cos\varphi_m} \tag{10.52}$$

The geometry of a C-shaped chamber is shown in Fig. 10.31.

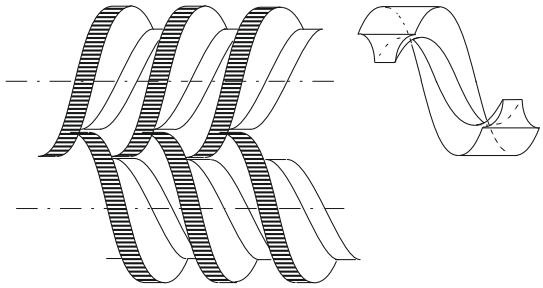


Figure 10.31
Geometry of a C-shaped chamber

For screws with straight flight flanks, the flight width is:

$$w(r) = w + 2(R - r)\tan\psi \tag{10.53}$$

where ψ is the flight flank angle.

Thus, the mean flight width w_m is:

$$w_m = w + (D - H)\tan\psi \tag{10.54}$$

and the mean channel width is:

$$w_m = \frac{\pi(D-H)\sin\varphi_m}{p} - w_m \tag{10.55}$$

The axial pressure gradient in the screw channel, using the same assumptions as in Section 10.3.2.2, becomes:

$$\frac{\partial P}{\partial l} = \frac{6\mu v_a}{H^2} \tag{10.56}$$

The axial velocity v_a is given by Eq. 10.1. The derivation of the axial pressure gradient is essentially the same as the derivation of the cross-channel pressure gradient given in Eq. 10.32.

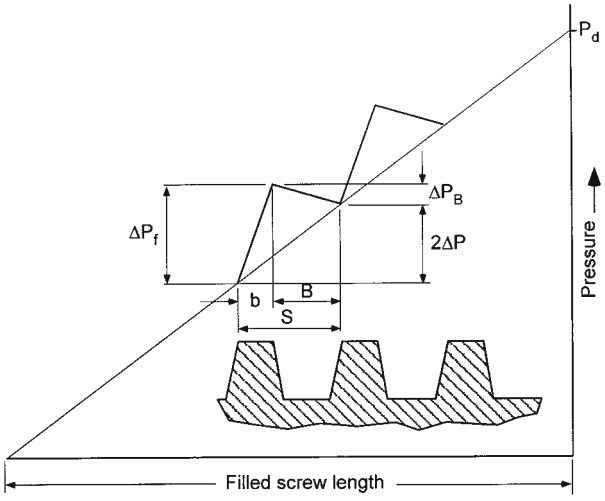


Figure 10.32
Pressure profile in CICT extruder

If it is assumed that the diehead pressure P_d is built up uniformly along the filled length of the extruder L_f, the drag-induced axial channel pressure (Eq. 10.56) can be superimposed on the linear pressure profile, as shown in Fig. 10.32.

The pressure drop ΔP_B over the axial channel width B becomes:

$$\Delta P_B = \frac{6\mu v_a B}{H^2} \tag{10.57}$$

The axial drop over a screw flight ΔP_f is:

$$\Delta P_f = 2\Delta P + \Delta P_B \tag{10.58}$$

where ΔP is the pressure drop per chamber as a result of the diehead pressure.

The leakage flow over the flight of a C-shaped chamber can be written as:

$$\dot{V}_f = (\pi - \alpha_i)D\left[\frac{1}{2}v_a\delta + \frac{\delta^3\Delta P_f}{12\mu b}\right] \tag{10.59}$$

The pressure drop across the calender gap ΔP_c, according to Janssen [15], can be written as:

$$\Delta P_c = \frac{3\pi\mu\sqrt{D\delta_c}}{4\delta_c^3}\left[\frac{3b\dot{V}_c}{4} - 2\pi N\delta_c(D-H)\right] \tag{10.60}$$

where δ_c is the calender gap; see Fig. 10.33.

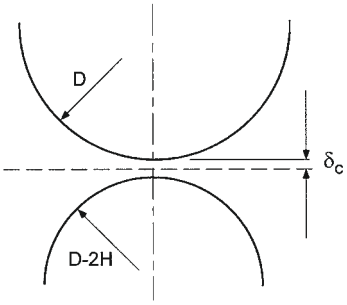


Figure 10.33
Calender gap geometry

Pressure drop ΔP_c must equal the tangential pressure drop over a chamber plus the contribution of the diehead pressure. In order to determine the calender leakage flow $\dot{V}_c$, the tangential pressure drop over a chamber must be known. If $\dot{V}_{tan}$ is the tangential flow in the C-shaped chamber, the tangential pressure gradient $\partial P/\partial\theta$ after Janssen [15] can be determined from the following relationship:

$$\dot{V}_{tan} = \frac{4v_aB^2}{\pi^2}\sum_{n=1,3,5\ldots}^{\infty}\left\{\frac{1}{n^2}\left[A(n)\left[I_0\left(\frac{\pi nR}{B}\right) - I_0\left(\frac{R-H}{B}\pi n\right)\right]\right.\right.$$
$$\left.\left. - B(n)\left[K_0\left(\frac{\pi nR}{B}\right) - K_0\left(\frac{R-H}{B}\pi n\right)\right]\right] - \frac{2B}{n^2\pi^2\mu v_a}\left(\frac{\partial P}{\partial\theta}\right)\ln\left(\frac{R}{R-H}\right)\right\} \tag{10.61}$$

where:

$$A(n) = \frac{C(n)}{F(n)}\left[\left(\frac{R-H}{R} - \frac{2}{n\pi C(n)}\right)K_1\left(\frac{R-H}{B}\pi n\right) - K_1\left(\frac{R\pi n}{B}\right)\right] \tag{10.62}$$

$$B(n) = \frac{C(n)}{F(n)}\left[I_1\left(\frac{R\pi n}{B}\right) - \left(\frac{R-H}{R} - \frac{2}{\pi nC(n)}\right)I_1\left(\frac{R-H}{B}\pi n\right)\right] \tag{10.63}$$

$$C(n) = \frac{B^2}{v_a (R-H) n^3 \pi^3} \left(-\frac{\partial P}{\partial \theta} \right) \tag{10.64}$$

$$F(n) = I_1\left(\frac{R-H}{B}\pi n\right) K_1\left(\frac{R\pi n}{B}\right) - I_1\left(\frac{R\pi n}{B}\right) K_1\left(\frac{R-H}{B}\pi n\right) \tag{10.65}$$

Functions I_0 and I_1 are modified Bessel functions of the first kind and zero and first order; K_0 and K_1 are modified Bessel functions of the second kind and zero and first order. A correction factor is required, which has to be subtracted from the throughput. This correction factor F_c is the channel volume displaced in one revolution multiplied with the rotational speed:

$$F_c = 2\pi N \left[B\left(RH - \frac{1}{2}H^2 \right) + \left(\frac{2}{3}H^3 - H^2 R \right) \tan\Psi \right] \tag{10.66}$$

Equations 10.61 through 10.66 allow the determination of the tangential pressure gradient, which, in turn, allows the determination of the leakage flow through the calender gap.

Leakage through the tetrahedron gap causes interscrew material transfer. In fact, it is the only leakage flow that causes interscrew transfer. The tetrahedron gap increases when the flight flank angle is increased. Janssen, Mulders, and Smith [16] developed an empirical formula for the leakage flow through the tetrahedron gap:

$$\dot{V}_t = \frac{0.0054\,\Delta P_B\, R^3}{\mu} \left(\frac{H}{R} \right)^{1.8} \left[\Psi + 2\left(\frac{\delta_f + \sigma_c \tan\Psi}{H} \right)^2 \right] \tag{10.67}$$

where δ_f is the clearance between the flight flanks:

$$\delta_f = \frac{S}{2p} - b - H \tan\Psi \tag{10.68}$$

The drag component $\dot{V}_{sd}$ of the side leakage is:

$$\dot{V}_{sd} = \pi N (2R - H)(H - \delta_c)(\delta_f + \delta_c \tan\Psi) \tag{10.69}$$

The pressure component $\dot{V}_{sp}$ of the side leakage flow is approximately:

$$\dot{V}_{sp} = \frac{\Delta P_c\, F_\delta^3\, (H-\delta_c)^4}{12\mu L \cos^4\Psi} (1 - 0.630\, F_\delta + 0.052\, F_\delta^5) \tag{10.70}$$

where:

$$F_\delta = \frac{\delta_f + \delta_c \tan\Psi}{H - \delta_c} \cos^2\psi \tag{10.71}$$

and:

$$L = \frac{2R\sin\alpha_i}{\cos\varphi} \tag{10.72}$$

The calender leakage and side leakage can be combined as:

$$\dot{V}_{cs} = K_1 \Delta P_c + \dot{V}_2 \tag{10.73}$$

The pressure generation in the C-shaped chamber can be determined from:

$$\dot{V}_{tan} = K_{tan} \Delta P_{tan} + \dot{V}_{tan2} \tag{10.74}$$

The drag-induced pressure generation in the C-shaped chamber plus the pressure rise due to the diehead pressure should equal the pressure drop through the calender gap:

$$\Delta P_{tan} + 2\Delta P = \Delta P_c \tag{10.75}$$

where ΔP is the pressure drop per chamber as a result of the diehead pressure.

Since the combined calender and side leakage flow equals the tangential flow in the chamber, this flow can be expressed as:

$$\dot{V}_{cs} = \dot{V}_{tan} = \frac{2K_{tan}K_1}{K_{tan} - K_1}\Delta P + \frac{\dot{V}_{tan2}K_1 - K_{tan}\dot{V}_2}{K_{tan} - K_1} \tag{10.76}$$

The total output of the extruder can be determined from:

$$\dot{V} = 2pNV - 2p\dot{V}_{cs} - 2\dot{V}_f - \dot{V}_t \tag{10.77}$$

This relationship allows the determination of the throughput pressure relationship for the filled length of a CICT extruder as a function of viscosity and machine geometry. Experimental verification with Newtonian fluids [15] has shown this relationship to be accurate to about 5 to 10%. Figure 10.34 shows the dimensionless output $\dot{V}^0$ as a function of flight flank angle when the dimensionless pressure drop ΔP^0 = 1E4.

The dimensionless output is:

$$\dot{V}^0 = \frac{\dot{V}_{actual}}{2pNV} \tag{10.78}$$

Figure 10.34 is valid for a CICT extruder with the following dimensions: p = 1, D = 70 mm, S = 20 mm, H = 10 mm, δ = 0.1 mm, δ_c = 0.2 mm, and δ_f = 0. Increasing the flight flank angle causes a significant drop in output. Thus, increased flight flank angle strongly reduces the positive conveying characteristics. Figure 10.35 shows

the dimensionless output as a function of the calender clearance when ΔP^0 = 1E4 and ψ = 6°; all other dimensions are as in Fig. 10.34.

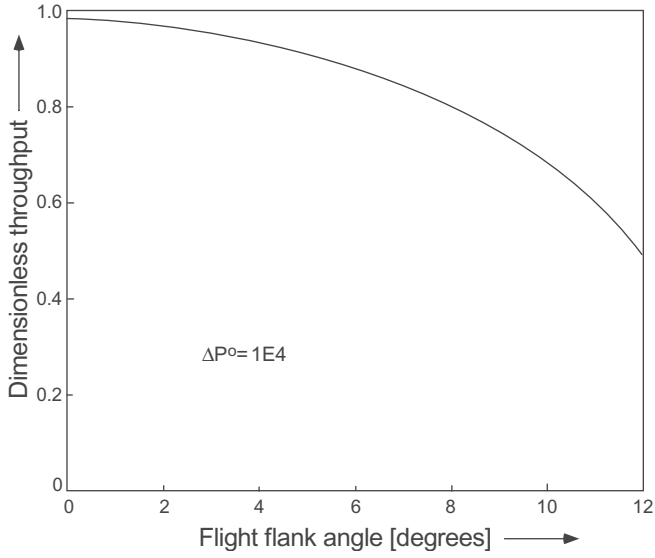


Figure 10.34
Dimensionless output versus the flight flank angle

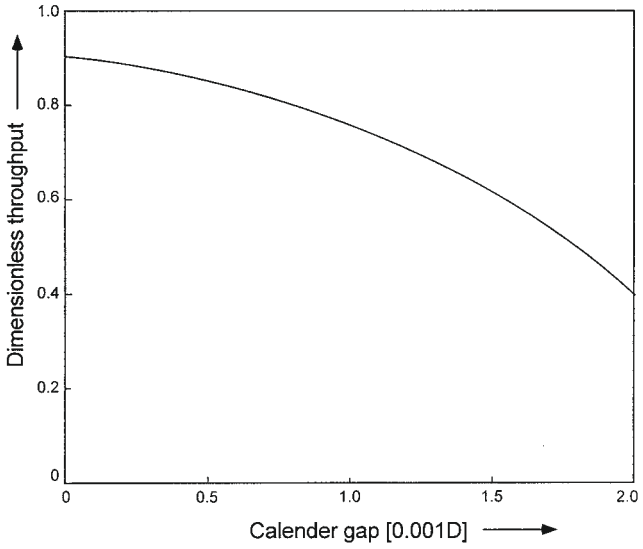


Figure 10.35
Dimensionless output versus the calender gap

Clearly, the effect of calender clearance is similar to the effect of flight flank angle. The effect of the radial flight clearance is shown in Fig. 10.36 when ΔP^0 = 1E4.

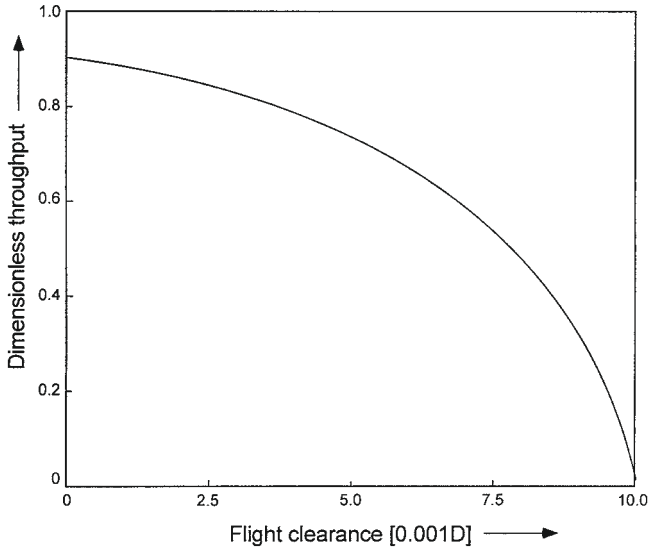


Figure 10.36
Dimensionless output versus radial flight clearance

The output starts to drop off rapidly when the flight clearance becomes larger than 0.005 D. The radial flight clearance normally ranges from 0.001 to 0.002 D. Figure 10.37 shows the effect of side clearance when ΔP^0 = 1E4. Increased side clearance causes a strong reduction in output.

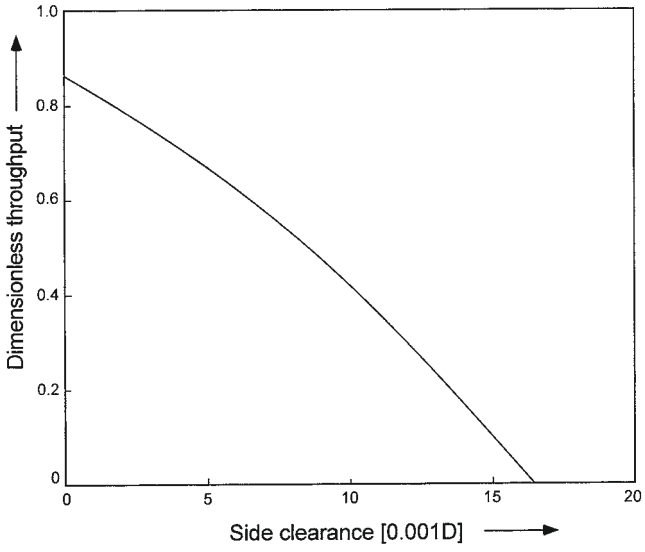


Figure 10.37
Dimensionless output versus side clearance

The effect of flight pitch is shown in Fig. 10.38.

When the pitch is larger than 1/4 D, the dimensionless output is relatively insensitive to the pitch. However, the dimensionless output reduces strongly when the pitch becomes less than 1/4 D.

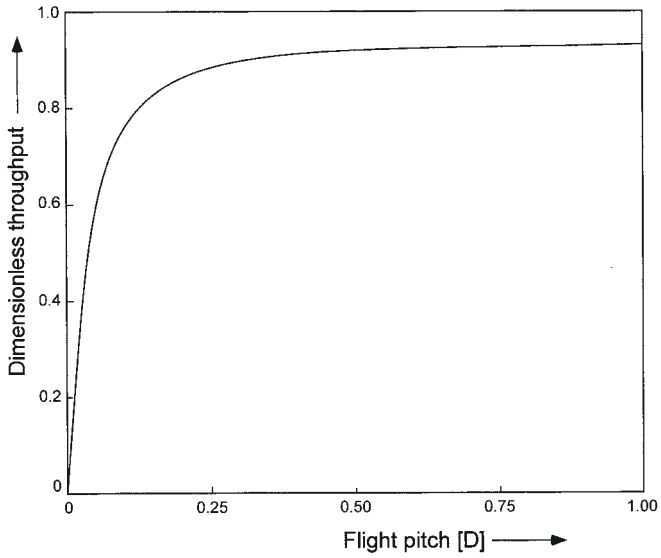


Figure 10.38
Dimensionless output versus flight pitch

The effect of the channel depth is shown in Fig. 10.39 for two values of the pressure differential, ΔP^0 = 2E4 and ΔP^0 = 5E4.

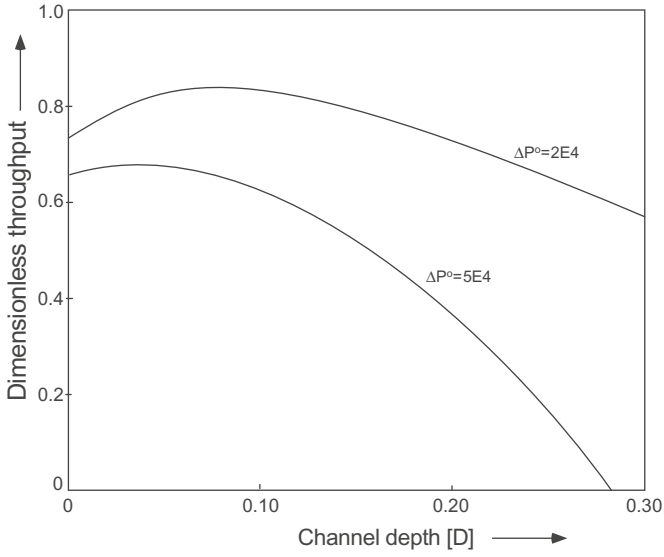


Figure 10.39
Dimensionless output versus channel depth

At each pressure gradient, there is an optimum channel depth for which the output reaches a maximum value. This is similar to the situation in single screw extruders. The optimum channel depth in these examples ranges from about 0.05 to 0.010 D. As the pressure gradient increases, the optimum channel depth decreases.

10.5 Non-Intermeshing Twin Screw Extruders

Non-intermeshing twin screw extruders are double screw machines where the centerline distance between the screws is larger than the sum of the radii of the two screws. Commercial examples of non-intermeshing twin screw extruders are counter-rotating (NOCT extruders). The conveying in NOCT extruders is similar to that in a single screw extruder. The main difference is the fact that there is a possibility of exchange of material from one screw to another. If the apex area (see Fig. 10.40) is zero, the NOCT extruder behaves as two single screw extruders.

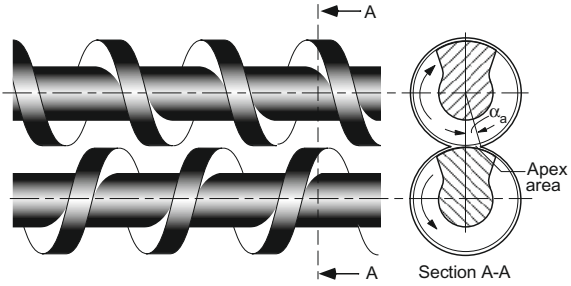


Figure 10.40
NOCT extruder geometry

Because of the non-zero apex area, the output of the NOCT extruder will be less than twice the output of a single screw extruder with the same screw diameter.

The NOCT extruder has less positive conveying characteristics than a single screw extruder. As a result, however, it has better backmixing characteristics than a single screw extruder. Therefore, the NOCT extruder is primarily used in blending operations, devolatilization, chemical reactions, etc. The particular conveying characteristics of the NOCT extruder make it undesirable for profile extrusion. In one commercial example of a NOCT extruder, the screws are of different length such that the last section of the extruder has a single screw discharge. This design is shown in Fig. 10.41.

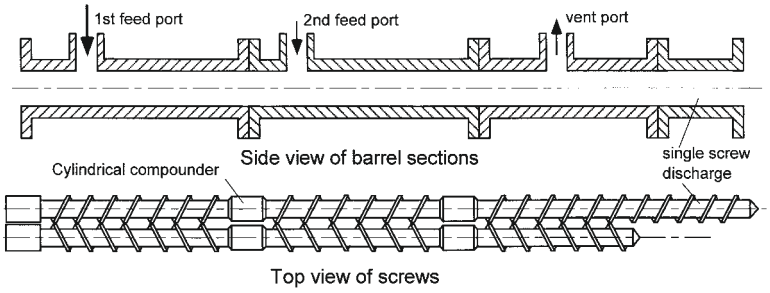


Figure 10.41 NOCT extruder with unequal screw lengths

Two advantages of this configuration are improved pumping characteristics and a thrust load on one screw only. The thrust load on the secondary (short) screw is very small. Thus, the thrust bearing design is greatly facilitated. A disadvantage of this construction is a non-symmetrical conveying process with a chance of hang-up of material in the transition region.

The first theoretical study of the conveying process in non-intermeshing twin screw extruders was made by Kaplan and Tadmor [17]. They simplified the actual geometry (see Fig. 10.42) to a flat plate model.

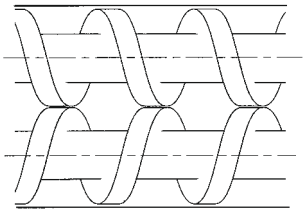


Figure 10.42
Actual geometry of NOCT extruder

The flat plate model involves three plates: the two outside plates representing the screw surface and the middle plate representing the barrel; see Fig. 10.43.

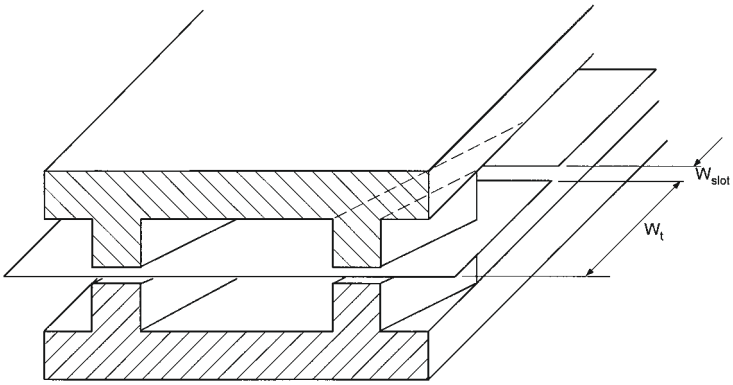


Figure 10.43 Flat plate approximation of NOCT extruder

The center plate has slots that run perpendicular to the circumferential velocity v_b. The tangential slot width is:

$$W_{slot} = D\alpha_a \tag{10.79}$$

where α_a is the apex angle; see Fig. 10.40.

The tangential distance between the slots is:

$$W_t = D(\pi - \alpha_a) \tag{10.80}$$

This model yields the following output-pressure relationship for Newtonian fluids:

$$\dot{V} = \frac{1}{2} WHv_{bz} F_{DTW} - \frac{WH^3}{12\mu}\left(\frac{\Delta P}{\Delta z}\right) F_{PTW} \tag{10.81}$$

where:

$$F_{DTW} = \frac{4f}{1+3f} \tag{10.82}$$

$$F_{PTW} = \frac{4}{1+3f} \tag{10.83}$$

$$f = \frac{\alpha_a}{\pi} \tag{10.84}$$

Equation 10.81 gives the output for one screw. Thus, the total output is twice the value from Eq. 10.81. The factor f is the ratio of uninterrupted barrel circumference to the total barrel circumference. Considering that the drag flow occurs as a result of adherence to the barrel surface, it seems that the drag flow correction factor F_{DTW} overestimates the drag flow considerably. If the barrel circumference is reduced by a factor f, one would expect a proportional reduction in the drag flow rate. Thus, the drag flow correction factor should be approximately:

$$F_{DC} = f \tag{10.85}$$

The difference between the two drag flow correction factors is shown in Fig. 10.44.

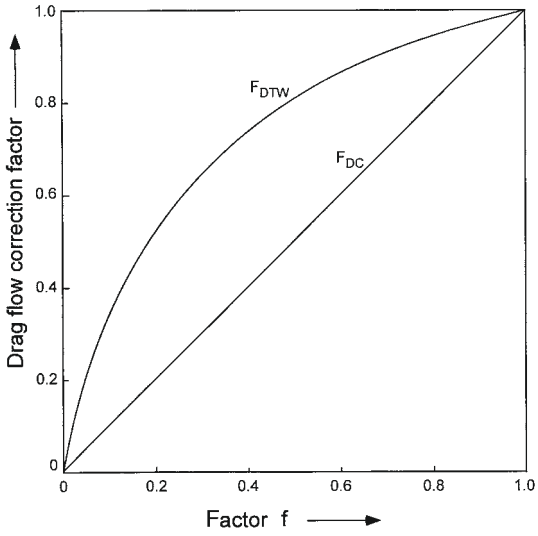


Figure 10.44
Comparison of two drag flow correction factors

In the normal range of f, Eq. 10.83 overestimates the drag flow correction factor by about 10 to 20%. Another drawback of Eq. 10.82 is the fact that the slots in the barrel plate are considered infinitely thin. This corresponds to assuming an essentially zero apex area. Furthermore, the pressure flow correction assumes that pressure leakage because of the open barrel occurs in the crosshatched area shown in Fig. 10.45.

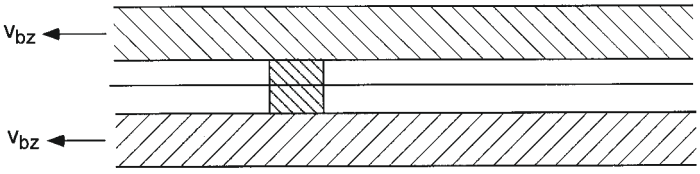


Figure 10.45
Assumed area of pressure-induced leakage

However, a top view (see Fig. 10.46) shows that in a matched screw configuration, the screw flights will prevent such leakage from taking place.

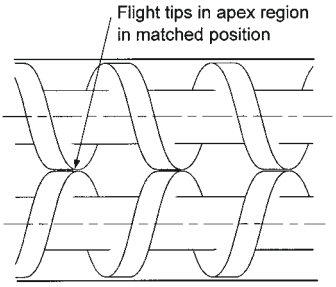


Figure 10.46
Top view of a matched screw geometry

If the slot width is considered infinitely small, pressure leakage can only take place in the down-channel direction. This would indicate that the pressure flow does not require a correction factor when the screw flights are matched. However, if the screw configuration is staggered, as shown in Fig. 10.47, the pressure flow does require a correction term.

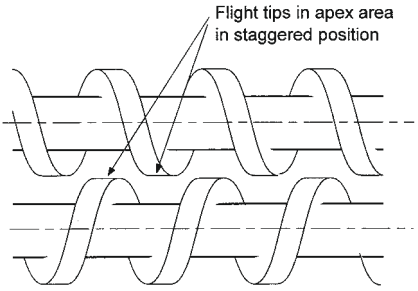


Figure 10.47
Staggered screw configuration

In actual NOCT extruders, the apex area has a non-zero value. The effect of the apex area on the pumping performance is quite important, as discussed by Nichols and Yao [18]. In actual experiments on a two-inch NOCT extruder with dimethylsiloxane,

Nichols [19] found less than satisfactory agreement between actual output values and output predictions based on Eq. 10.82. The actual apex area A_T, shown in Fig. 10.40, is:

$$A_T = \frac{1}{2}D^2\left(2\sin\alpha_a - \sin\alpha_a\cos\alpha_a - \alpha_a + 4\alpha_a\frac{\delta}{D}\right) \tag{10.86}$$

Nichols [24] developed a modified output model in cooperation with Lindt. The model is based on a flat three-plate model with the thickness of the center plate having a finite thickness equal to the apex width W_a; see Fig. 10.48.

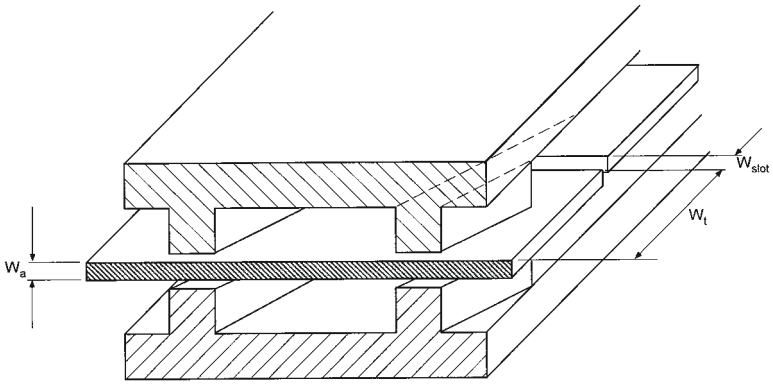


Figure 10.48 Modified flat plate model for NOCT extruder

This model yields the following output relationship for Newtonian fluids:

$$\dot{V} = \frac{1}{2}WHv_{bz}F_{DCRT} - \frac{WH^3}{12\mu}\left(\frac{\Delta P}{\Delta z}\right)F_{PCRTI} \tag{10.87}$$

where:

$$F_{DCRT} = \frac{fF_dF_p(2 + W_a/H)^3}{f(2 + W_a/H)^3 + 2F_p(1-f)} \tag{10.88}$$

and:

$$F_{PCRTI} = \frac{F_p(2 + W_a/H)^3}{f(2 + W_a/H)^3 + 2F_p(1-f)} \tag{10.89}$$

where F_d and F_p are the shape factors for drag flow and pressure flow as given by Eqs. 7.218 and 7.219, respectively.

When W_a = 0, Eqs. 10.88 and 10.89 become the same as Eqs. 10.83 and 10.84, respectively. In addition to the correction factors established from the three-plate model, another correction is introduced to account for leakage in the apex area. The apex area is approximated by a triangle as shown in Fig. 10.49.

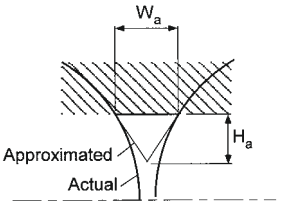


Figure 10.49
Apex approximation

The pressure flow rate through a triangle is expressed as (see reference 32 of Chapter 1):

$$\dot{V} = \frac{W_a H_a^3 M_o}{12\mu}\left(\frac{\Delta P}{\Delta L}\right)_{fl} \tag{10.90}$$

where W_a is the apex width and H_a the height of the triangle shown in Fig. 10.49, and M_o is a shape factor for a triangle.

The pressure gradient over the flight is taken as:

$$\left(\frac{\Delta P}{\Delta L}\right)_{fl} = \left(\frac{\Delta P}{\Delta L}\right)\frac{S}{b} \tag{10.91}$$

where S is the pitch and b the axial flight width.

With Eqs. 10.87 through 10.91, an additional pressure flow correction term F_{PCRT2} can now be formulated:

$$F_{PCRT2} = \frac{M_o W_a H_a^3 \pi D}{WH^3 w} \tag{10.92}$$

where M_o is shown graphically in reference 32 of Chapter 1.

The two pressure flow correction factors are now combined to give:

$$F_{PCRT} = F_{PCRT1} + F_{PCRT2} \tag{10.93}$$

which yields the final result obtained by Nichols [24]:

$$\dot{V} = \frac{1}{2} WHv_{bz} F_{DCRT} - \frac{WH^3}{12\mu}\left(\frac{\Delta P}{\Delta z}\right) F_{PCRT} \tag{10.94}$$

Comparison of predictions from Eq. 10.94 to experimental results [19] yielded considerably improved agreement as compared to predictions from Eq. 10.82. A drawback of Eq. 10.94 is the fact that the derivation of the pressure flow correction term F_{PCRT2} for the apex area is not consistent with the flat three-plate model. Furthermore, the approximated apex area is smaller than the actual apex area as shown in Fig. 10.49. The graphical results of the shape factor for triangles shown in Chapter 1 [32] do not extend beyond a height-to-base ratio of unity. In reality, the H_a/W_a

ratio will usually be larger than unity; thus, the graphical results in reference [32] cannot be used. Finally, the actually pressure gradient over the screw flight also contains a drag-induced component, which is not taken into account in Eqs. 10.92 through 10.94.

Another approach used to predict the output-pressure characteristics of non-intermeshing extruders is to abandon the three-plate model and follow more closely the analysis used for single screw extruders. The circumference of the barrel is interrupted for a fraction 1-f; see Fig. 10.50.

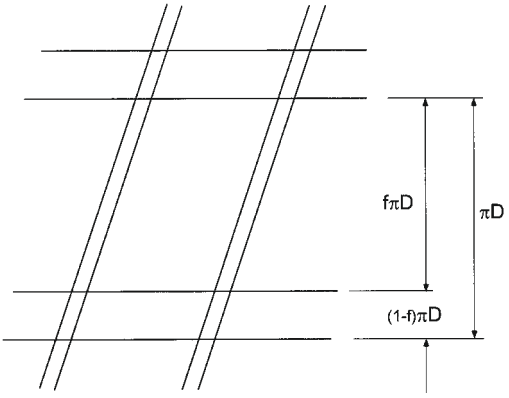


Figure 10.50
Effective barrel circumference

Since drag flow occurs as a result of polymer melt adhering to the barrel surface, the reduced barrel circumference will affect the drag flow rate. The drag flow per revolution is found by moving the barrel with respect to the screw over a distance of πD. With a full barrel circumference, this results in a volume per revolution equal to:

$$V_d = \frac{1}{2} B H \pi D \tag{10.95}$$

This results in the familiar drag flow rate equation:

$$\dot{V}_d = \frac{1}{2} W H v_{bz} \tag{10.96}$$

However, when the barrel circumference is reduced by 1–f, the volume dragged forward per revolution will be reduced correspondingly:

$$V_d = \frac{1}{2} BH\pi D - \frac{1}{2}(1-f)BH\pi D \tag{10.97}$$

The actual drag flow rate becomes:

$$\dot{V}_d = \frac{1}{2} f W H v_{bz} \tag{10.98}$$

The pressure flow in the screw channel outside of the apex area will be the same as it is in a single screw extruder. However, in the apex area there will be an additional pressure-induced leakage flow. If the apex area is approximated by an isosceles triangle of width W_a and height H_a (see Fig. 10.51), an expression can be derived for leakage in this region.

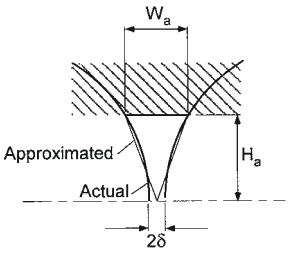


Figure 10.51
Apex area approximation

An expression for the pressure flow through an isosceles triangle was derived by Bird et al. [25] by following the variational principle due to von Helmholtz. Other expressions have been proposed by Kozicki et al. [26, 27], who used a simple geometric parameter method to predict the pressure drop-flow rate relationship in flow channels of arbitrary cross-section. Following Bird's approach, the output-pressure relationship for an isosceles triangle can be written as:

$$\dot{V}(\Delta) = \frac{7m^3 H_a^4 (27m^2 + 5)}{90(55m^4 + 38m^2 + 3)} \left(\frac{\Delta P}{\mu \Delta L} \right) \tag{10.99}$$

where:

$$m = \frac{W_a}{2H_a} \tag{10.99a}$$

For values of W_a less H_a ($m < 0.5$), Eq. 10.99 can be approximated reasonably well by:

$$\dot{V}(\Delta) = 0.017(H_a - 0.61W_a)W_a^3 \left(\frac{\Delta P_f}{\mu b} \right) \tag{10.100}$$

where:

$$W_a = D(1 - \cos\alpha_a) + 2\delta \tag{10.101}$$

$$H_a = \frac{1}{2} D \sin\alpha_a \tag{10.102}$$

The difference between Eq. 10.99 and Eq. 10.100 over most of the range is only about 2 or 3%; see also Fig. 10.52.

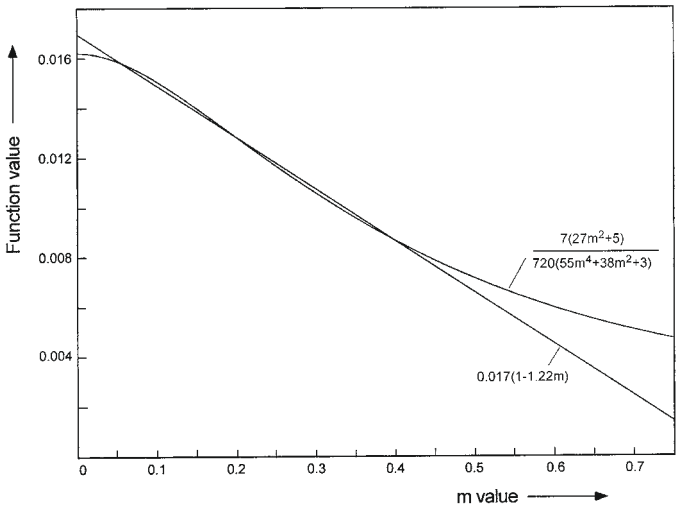


Figure 10.52 Output versus m according to Eqs. 10.99 and 10.100

Thus, the pressure-induced leakage flow through the apex area can be written as:

$$\dot{V}_{12} = 0.017(H_a - 0.61W_a)W_a^3\left(\frac{g_a S}{\mu p b}\right) \tag{10.103}$$

where g_a is the axial pressure gradient.

In addition to the pressure-induced leakage flow through the apex area, there is the usual leakage flow through the flight clearance; refer to Section 7.4.1.

$$\dot{V}_{11} = \frac{\pi D \delta^3 \cos\varphi}{12\mu_{cl} w}\left(\frac{\pi D g_z \cos\varphi}{p} + \frac{6\mu v_{bx} W}{H^2}\right) + \frac{p w \delta^3}{12\mu_{cl}} g_z \tag{10.104}$$

Thus, the output per screw for a non-intermeshing twin screw extruder can be written as:

$$\dot{V} = \frac{1}{2} f W H v_{bz} - \frac{W H^3 g_z}{12\mu} - \dot{V}_{11} - \dot{V}_{12} \tag{10.105}$$

This relationship is valid for a matched screw geometry. The apex leakage term $\dot{V}_{12}$ is determined by the apex width cubed; see Eq. 10.103. Thus, increases in the apex angle α_a will cause very strong increases in the apex leakage flow. Figures 10.53 and 10.54 compare output predictions made with Eq. 10.105 to the experimental results obtained by Nichols with dimethyl-siloxane polymeric fluids [19].

It can be seen that reasonable agreement is obtained between predictions and actual data.

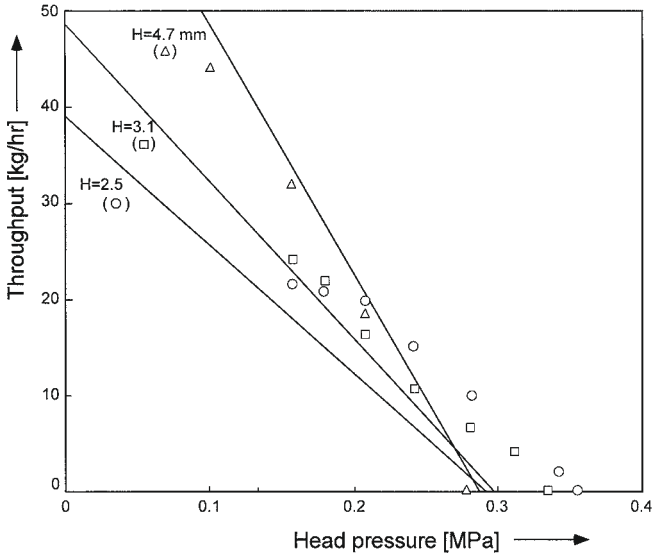


Figure 10.53 Comparison of output predictions using Eq. 10.105 to experimental data by Nichols [19]; viscosity 12 Pa·s

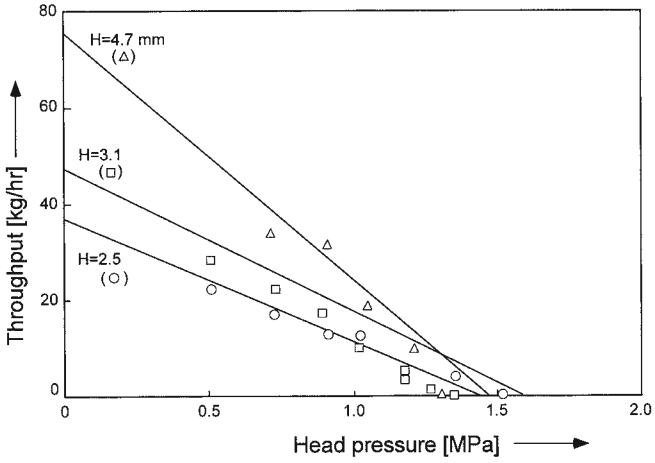


Figure 10.54 Comparison of output predictions using Eq. 10.105 to experimental data by Nichols [19]; viscosity 58 Pa·s

The analysis of the conveying characteristics becomes considerably more complicated when the screws are placed in a staggered configuration. In this case, there will be considerably more leakage in the apex region as illustrated in Fig. 10.55.

With the matched screw configuration, the tangential pressure profiles in the two screws are symmetrical. Thus, there will be little interscrew material transfer. In the staggered screw configuration, however, the tangential pressure profiles are nonsymmetrical because the flights are 180° offset. When the flight of the left screw is

approaching the apex area, the pressure on the left side (P_L) of the apex area will be larger than the pressure on the right side (P_R). As a result, material will flow through the apex area from left to right, as shown in Fig. 10.55.

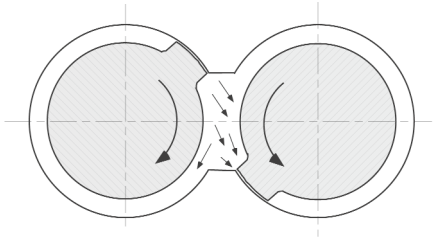


Figure 10.55
Interscrew material transfer with staggered screw configuration

When the flight of the right screw approaches the apex area, P_R will be larger than P_L, causing a flow from right to left. Therefore, in the staggered configuration there will be a significant amount of interscrew material transfer. This material transfer will change direction every half turn of the screw. In the staggered screw geometry, the pressure-induced leakage flow through the apex region will be larger because of the larger area. In the staggered configuration, the drag-induced leakage flow through the apex region also has to be taken into account because of the non-symmetrical tangential pressure profiles. The apex leakage flow can be written as:

$$\dot{V}_{l2} = \dot{V}_{ld} + \dot{V}_{lp} \tag{10.106}$$

where $\dot{V}_{ld}$ is the drag-induced leakage flow and $\dot{V}_{lp}$ is the pressure-induced leakage flow.

The drag-induced leakage flow can be determined from the drag-induced pressure gradient g_{d2}. If the effective channel height is H_{eff} and the effective channel width W_{eff}, then the drag-induced leakage flow can be written as:

$$\dot{V}_{ld} = \frac{W_{eff} H_{eff}^3 g_{d2}}{12\mu} \tag{10.107}$$

In order to determine the drag-induced leakage flow, the drag-induced pressure gradient needs to be known. Consider the simplified situation shown in Fig. 10.56.

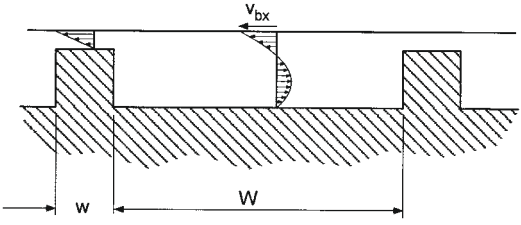


Figure 10.56
Simplified geometry to determine the drag-induced pressure gradient

The drag-induced pressure gradient in the clearance g_{d2} can be related to the drag-induced pressure gradient in the channel g_{d1} by stating that the net cross-channel flow equals the flow through the clearance:

$$\int_0^{\delta} v_{x2}\,dy = \int_0^{H+\delta} v_{x1}\,dy \tag{10.108}$$

where:

$$v_{x1} = \left(\frac{v_{bx}}{H+\delta} - \frac{g_{d1}(H+\delta)}{2\mu}\right)y + \frac{g_{d1}y^2}{2\mu} \tag{10.109}$$

$$v_{x2} = \left(\frac{v_{bx}}{\delta} - \frac{g_{d2}\delta}{2\mu}\right)y + \frac{g_{d2}y^2}{2\mu} \tag{10.110}$$

In the case of pure drag flow, the following relationship must be satisfied:

$$g_{d2}w + g_{d1}W = 0 \tag{10.111}$$

With these equations, the following expression for the drag-induced pressure gradient in the clearance is obtained:

$$g_{d2} = \frac{6\mu H v_{bx} W}{w(H+\delta)^3 + W\delta^3} \tag{10.112}$$

Considering that the actual clearance value ranges from the flight clearance to the channel depth, the pressure gradient over the screw flight can be approximated by:

$$g_{d2} \cong \frac{6\,\mu\, v_{bx}}{(H+0.5W_a)^2} \tag{10.113}$$

The resulting leakage flow can be approximated by:

$$\dot{V}_{ld2} = \frac{\pi D\,(1-f)(H+0.5W_a)^3 g_{d2}}{12\mu} \tag{10.114}$$

The total drag-induced leakage flow in the apex region now becomes:

$$\dot{V}_{ld} = \frac{1}{2}(1-f)\pi D(H+0.5W_a)v_b \sin\varphi \tag{10.115}$$

The pressure-induced leakage flow in the apex region can be approximated by:

$$\dot{V}_{lp} = \frac{0.5\,\pi D\,(1-f)(H+0.5W_a)^3 g_a}{12\mu} \tag{10.116}$$

The output per screw for the staggered screw geometry can be written as:

$$\dot{V} = \frac{1}{2} f W H v_{bz} - \frac{W H^3 g_z}{12\mu} - \dot{V}_{II} - \dot{V}_{Id} - \dot{V}_{Ip} \tag{10.117}$$

Figure 10.57 compares output predictions made with Eq. 10.117 to the experimental results obtained by Nichols [19].

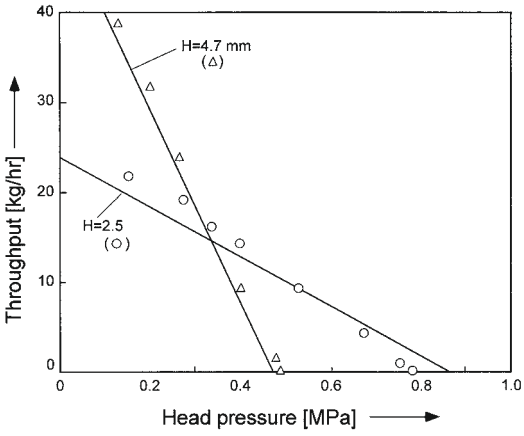


Figure 10.57
Output prediction using Eq. 10.117 to experimental results by Nichols [19], viscosity 58 Pa·s

The agreement between predictions and experimental results is reasonable. Both the drag flow rate and the pressure-generating capacity of the staggered screws are lower than the same screws in a matched configuration. However, the mixing capability of the staggered screws will be significantly better as a result of the interscrew material transfer. The mixing process in non-intermeshing twin screw extruders was studied by Howland and Erwin [28] for screws in a matched configuration. They found that the mixing efficiency of the twin screw extruder was markedly better than the single screw extruder. Howland and Erwin did not report on the mixing efficiency of the twin screw extruder with the staggered screw configuration. However, it can be expected that this will be considerably better than the mixing efficiency of screws in a matched configuration.

A different type of NOCT extruder is the Farrel Continuous Mixer (FCM). It is a short twin screw mixer that runs at high speed, up to 1200 rpm for the smallest unit (2 FCM). A schematic picture of an FCM is shown in Fig. 10.58.

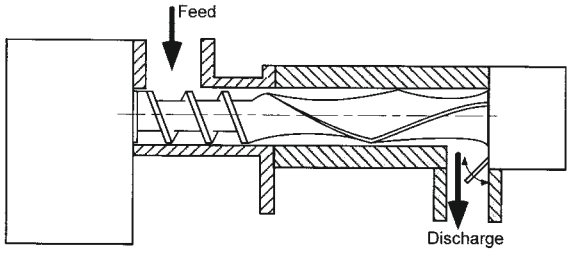


Figure 10.58
Farrel continuous mixer (FCM)

The length of the screws is about 5 D, where the first 2 D is conventional screw geometry and the last 3 D a sigma type geometry, similar to the Banbury mixer. The actual mixing takes place in the sigma screw section. Since the twin screw mixer does not generate much pressure, material is dumped into a discharge extruder or a gear pump for pressure generation. A typical residence time in the FCM is about three to five seconds. The mixing action, therefore, is very intensive because energy is dissipated in the material at a very fast rate. This type of mixing is particularly useful in applications where dispersive mixing is required. The intensive mixing action is attended with high shear stresses, causing effective breakdown of gels and agglomerates in the polymer.

■ 10.6 Coaxial Twin Screw Extruders

An unusual type of twin screw extruder is the coaxial twin screw (CTS) extruder. The CTS extruder is basically a single screw machine where the main screw is hollow towards the end of the screw. In the hollow portion of the main screw an inner screw is placed to aid in the conveying process in the extruder. The inner screw is generally stationary with a cantilever support against a disk at the end of the barrel. Thus, the I.D. of the main screw forms a rotating barrel for the stationary inner screw. If the flights of the inner screw have an opposite pitch to the flights of the main screw, the material transport in the inner screw will be forward. If the flights of the inner screw have the same pitch as the flights of the main screw, the material transport in the inner screw will be backward.

There are two versions of CTS extruders commercially available. In one version, molten material from the outer screw is transferred to the inner screw where it is pumped towards the die. In this case, the inner screw is used for forward pumping; see Fig. 10.59.

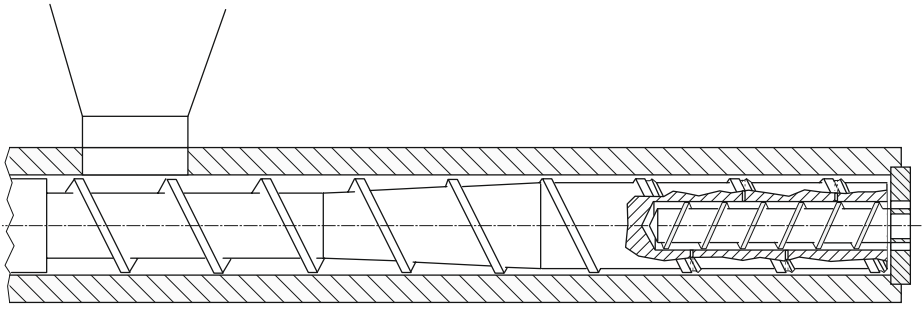


Figure 10.59 Inner screw for forward melt conveying

If the channel depth of the outer screw is reduced to zero, all the polymer melt is pumped toward the die by the inner screw. This inner melt removal (IMR) screw was invented by Kovacs [20] of Midland-Ross Corporation. It is essentially a very complicated version of a barrier screw and does not offer any obvious advantages over conventional barrier screws.

Another version of a CTS extruder is the solids draining screw (SDS) originally developed by Klein and Tadmor [21] of Scientific Process & Research, Inc. In this design, unmolten polymer drains into the inner screw; see Fig. 10.60.

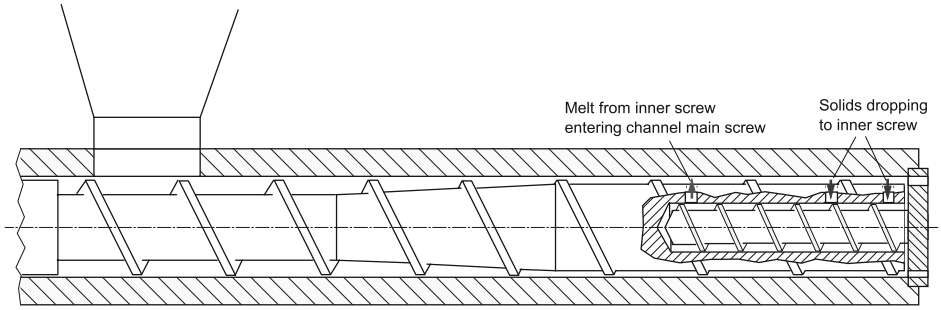


Figure 10.60 Solids draining screw (SDS)

Material is transported upstream in the inner screw and plasticated. At the end of the inner screw, the polymer, which is now molten, is pumped back into the channel of the main screw. A modified version of the SDS screw for use in a molding machine was patented on September 22, 1981 [22]. Another modification of the SDS screw involves using a barrier type main screw to improve the solids draining process. This barrier SDS screw was patented on June 14, 1983 [23]. The SDS screw is claimed to give higher output and lower energy consumption. However, from a functional analysis it is difficult to see why recirculation of a fraction of the polymer flow would increase output or reduce power consumption.

The mechanical design of CTS extruders is considerably more complex than conventional single screw extruders. Since material has to leak through holes in the main screw, there is a chance of plugging and of stagnant areas. Also, maintenance and operating procedures of CTS extruders will be considerably more complex than single screw extruders.

10.7 Devolatilization in Twin Screw Extruders

Twin screw extruders are finding increasing use in specialty operations such as reactive processing of polymers and devolatilization. Twin screw extruders are used as continuous chemical reactors for polymerization and polymer modifications, e.g., grafting of side groups.

Both co-rotating (e.g., [30–32]) and counter-rotating (e.g., [33–35]) twin screw extruders are used for this purpose, intermeshing as well as non-intermeshing [36]. In the extrusion of reacting materials, another degree of difficulty is added to the description of the process because the material properties will change as the reaction progresses along the machine. The theory of extrusion of reacting materials is still in a stage of development. However, one aspect of specialty polymer processing operations, namely continuous devolatilization in twin screw extruders, has reached a point where a reasonably accurate description of the process is possible.

Todd [37] proposed an equation to describe devolatilization in co-rotating twin screw extruders based on the penetration theory discussed in Section 5.4 and Section 7.6. The equation contains the Peclet number (see Eq. 7.371), which represents the effect of longitudinal backmixing. The Peclet number must be measured or estimated to predict the devolatilizing performance of an extruder. Todd selected a Peclet number of 40 to correlate predictions to experimental results. A similar approach was followed by Werner [38]. A visualization study was made by Han and Han [39], particularly to study foam devolatilization. They found substantial entrainment of the bubbles in a circulatory flow region in a partially filled screw devolatilizer. Collins, Denson, and Astarita [40] published an experimental and theoretical study of devolatilization in a co-rotating twin screw extruder. The experimentally determined mass transfer coefficients were about one-third those predicted by the mathematical model. They concluded, therefore, that the effective surface area for mass transfer is substantially less than the sum of the areas of the screws and barrel.

Secor [41] presented an intermeshing model for devolatilization in co-rotating twin screw extruders that incorporates the major characteristics of fluid motion. These characteristics were experimentally observed in a twin screw extruder with a transparent barrel. The observed flow pattern consisted of alternating rotation in the tangential direction with the screw and axial forward motion at the entrance to the intermeshing region; see Fig. 10.61.

These fluid flow patterns are fully consistent with the flow patterns described in Section 10.3. The model is based on the following assumptions:

1. All the fluid is exposed for a series of intervals, each of duration λ, in which devolatilization occurs.
2. Between exposures, perfect mixing occurs during the forward axial motion in a time that is very small compared with λ.

3. The diffusion coefficient is constant.
4. The fluid layers in the screw channel are effectively of infinite depth.
5. The volumetric flow rate of the fluid is constant.
6. No flow of fluid relative to the underlying flight faces takes place during devolatilization.
7. Nucleation and bubble growth are negligible.

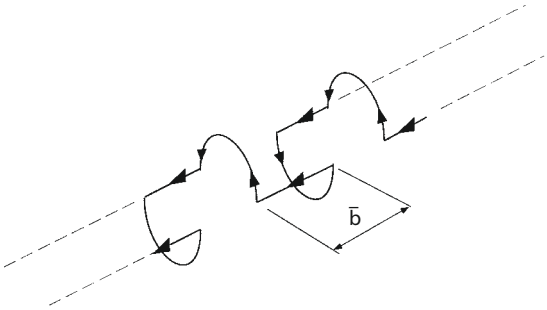


Figure 10.61
Predominant fluid flow pattern

A material balance on the volatile component can be written as:

$$\dot{V}C_0 = \dot{V}C_1 + \dot{E}_1 \tag{10.118}$$

where

C_0 = concentration of the volatile component in the feed to the extruder in gr/cm^3

C_1 = average concentration of the volatile component in the liquid at the end of the first exposure in interval in gr/cm^3

$\dot{V}$ = volumetric liquid flow rate in cm^3/s

$\dot{E}_1$ = average rate of evaporation in the first exposure interval in gr/s

If the surface concentration of the volatile component is maintained at zero, the rate of evaporation is:

$$\dot{E}_1 = A_e C_o \left(\frac{4D'}{\pi\lambda}\right)^{1/2} \tag{10.119}$$

This equation corresponds to Eq. 7.434 for devolatilization in single screw extruders. In Eq. 10.119, the variables are:

A_e = area for evaporation in cm^2/s

D' = diffusion coefficient in cm^2/s

λ = exposure time in s

The effective area for evaporation is given by:

$$A_e = f\,A \tag{10.120}$$

where A is the total leading face area of a 360° section of a single screw and f is the ratio of channel area outside the intermeshing region to the channel area inside the intermeshing region. Thus, the exposure time λ can be written as:

$$\lambda = \frac{f}{N} \tag{10.121}$$

where N is the rotational speed of the screws in rev/s. With Eqs. 10.120 and 10.121, the rate of evaporation becomes:

$$\dot{E}_1 = A\, C_o \left(\frac{4D' f N}{\pi} \right)^{1/2} \tag{10.122}$$

Substituting Eq. 10.122 into Eq. 10.118 gives:

$$\frac{C_1}{C_0} = 1 - \frac{A}{\dot{V}} \left(\frac{4D' f N}{\pi} \right)^{1/2} \tag{10.123}$$

For the n-th exposure, Eq. 10.123 becomes:

$$\frac{C_n}{C_{n-1}} = 1 - \frac{A}{\dot{V}} \left(\frac{4D' f N}{\pi} \right)^{1/2} \tag{10.124}$$

For a sequence of n exposures:

$$\frac{C_n}{C_{n-1}} \frac{C_{n-1}}{C_{n-2}} \cdots\cdots \frac{C_1}{C_0} = \left[1 - \frac{A}{\dot{V}} \left(\frac{4D' f N}{\pi} \right)^{1/2} \right]^n \tag{10.125}$$

Each exposure is followed by a short axial movement, which has been determined to be equal to the mean flight thickness $\bar{b}$. If the total length of the screws is L, the number of exposures is given by:

$$n = \frac{L}{\bar{b}} \tag{10.126}$$

Thus, Eq. 10.125 can be written as:

$$\frac{C_n}{C_0} = \left[1 - \frac{A}{\dot{V}} \left(\frac{4D' f N}{\pi} \right)^{1/2} \right]^{L/\bar{b}} \tag{10.127}$$

Equation 10.127 is graphically represented in Fig. 10.62.

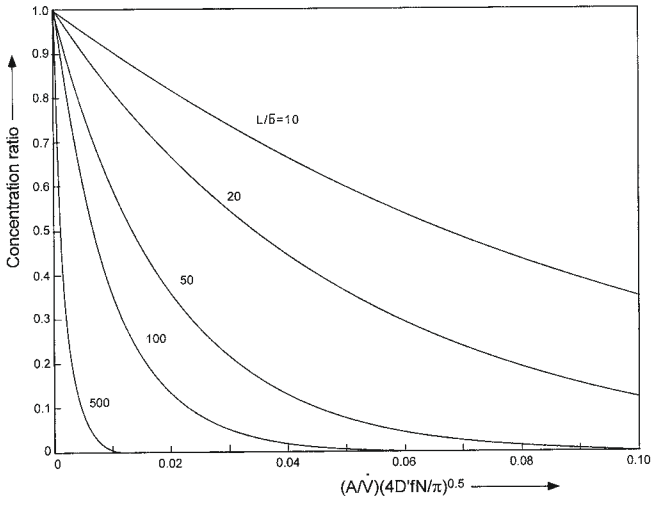


Figure 10.62
Graphical representation of Eq. 10.127

The concentration ratio decreases with increasing diffusivity, screw speed, area, and number of exposures. The concentration ratio increases with increasing flow rate. When the following inequality is fulfilled:

$$\frac{A}{\dot{V}}\left(\frac{4D' f N}{\pi}\right)^{1/2} < 0.02 \tag{10.128}$$

Equation 10.127 reduces to:

$$\frac{C_0}{C_n} = \exp\left[\frac{LA}{\bar{b}\dot{V}}\left(\frac{4D' f N}{\pi}\right)^{1/2}\right] \tag{10.129}$$

with an error of less than 1%.

Experiments were performed on a 20 cm twin screw extruder with a screw length of 27 cm. The liquid was a polybutene and the volatile halocarbon. Figure 10.63 shows the correlation between experimental results and theoretical predictions.

The agreement between theory and experiments is quite good. Even though bubble formation was observed during some of the experiments, the mass transfer rate was not significantly affected. Reasons for this include axial short-circuiting of fluid along the bottom of the figure-eight bore and incomplete mixing at points of transfer between the screws. Another reason is the likelihood of the bubble actually being retained by the liquid phase. This is supported by visual observations by Han and Han [39].

Evaporation from the liquid on the barrel was assumed to be of minor importance compared with evaporation from the liquid in the screw channels. This assumption is supported by experimental work by Biesenberger and Lee [42] who found the

contribution of devolatilization through the barrel film to be essentially negligible. This is an important point because if the contribution through the melt film is negligible in a twin screw extruder, it should also be of minor importance in a single screw extruder. One note of caution is that Secor's experiments were performed on a machine with a rather unusual geometry. The screw channel had a very small width to depth ratio (W/H), the actual value being W/H = 0.384, and the screw length was very short (1.36 D). In this case, the area of the melt pool is much larger than the area of the melt film. Thus, in this geometry, the contribution of the melt film has to be very small from simple geometric arguments. In most commercial extruders, however, the W/H ratio is at least an order of magnitude higher and the screw length is also at least an order of magnitude higher. Thus, the Secor model may not give equally good results with twin screw extruders of more standard geometry.

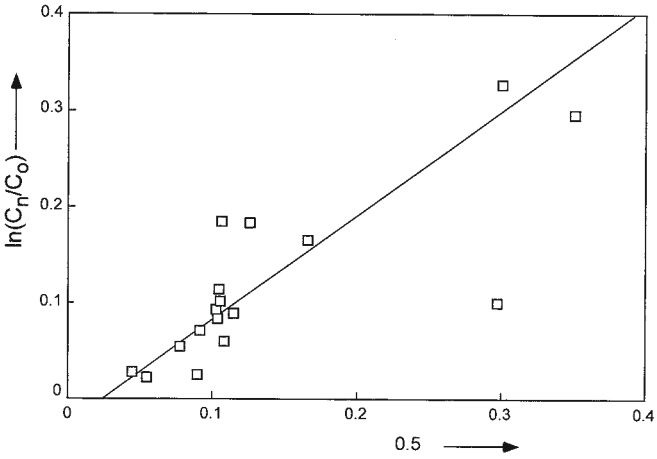


Figure 10.63
Correlation of experimental results [41] and theoretical predictions

10.8 Commercial Twin Screw Extruders

Since twin screw extruders have become an important segment of the field of extrusion it is reasonable to discuss important aspects of commercial twin screw machinery. A good reference on capabilities of twin screw extruders is the book edited by David Todd [43]. In this book, some of the main suppliers of twin screw extruders describe their machinery and capabilities; the companies are Leistritz, Werner & Pfleiderer, Berstorff, APV (Baker Perkins), Japan Steel Works, Welding Engineers, Farrel, and Buss. The book describes both co- and counter-rotating twin screw extruders and internal mixers. Another good reference on twin screw extruders is the book by James White [44]. This book gives an excellent historical over-

view of twin screw extruders with broad coverage of early patents. White's book also covers theoretical analysis in detail; there is less emphasis on practical applications.

Roberto Colombo and Lavorazione Materie Plastiche (LMP) of Turin, Italy, developed and patented the first commercial co-rotating twin screw extruder in 1938. LMP sold their first twin screw extruders to I.G. Farbenindustrie in Germany in 1939. Meskat and Erdmenger were involved in a separate development at I.G. Farbenindustrie in the 1940s. These workers developed and patented the fully intermeshing self-cleaning twin screw extruders. After I.G. Farbenindustrie was broken up after World War II, Meskat and Erdmenger worked for Bayer AG. In 1953 Bayer AG worked with Werner & Pfleiderer to develop a new generation of intermeshing self-wiping twin screw extruders; these machines were manufactured and sold by W&P.

In 1957 W&P introduced the first high speed, co-rotating, twin screw compounding extruder and has been a major player in the twin screw extruder industry ever since. W&P offers a wide range of sizes from as small as 25 mm to as large as 380 mm. Data on the various W&P extruders is shown in Table 10.3.

Table 10.3 Technical Data for ZSK Type Twin Screw Compounders by W&P

Model	Torque per screw [N·m]	Motor power at N_{max} [kW]	Max. screw speed [rpm]	Screw diam. [mm]	Flight depth [mm]	Max. L/D ratio	Screw shaft height [mm]	Machine dimensions, length, width, height L×W×H (mm)	Total weight [kg]
25 WLE	82	21.5	1200	25	4.2	42	1100	1800×780×1400	900
40 MC	425	110	1200	40	7.1	48	1100	3900×720×1400	2400
50 MC	815	215	1200	50	8.9	48	1100	4600×840×1400	2750
58 MC	1250	325	1200	58	10.3	48	1100	5200×1000×1500	5600
70 MC	2275	600	1200	70	12.5	48	1100	5800×1100×1550	8000
92 MC	5000	1100	1000	92	16.3	48	1100	7300×1150×1650	14000
133 MC	15100	3300	1000	133	23.5	48	1100	9900×1700×2000	28500
170 SC	25000	1925	350	170	25.5	48	1100	12500×2200×1600	32000
177 MC	35000	2700	350	177	31.5	42	1100	13000×2300×1600	37000
240 SC	70000	4150	270	236	33	42	1300	16000×3300×1960	60000
250 MC	87500	5200	270	248	44	42	1300	16000×3300×1960	60000
300 SC	130000	7720	270	298	39.8	42	1500	20000×4000×2250	105000
320 MC	170000	10100	270	315	55.8	42	1500	20000×4000×2250	105000
380 MC	356000	17200	220	380	67.4	42	2000	29000×4800×4200	210000

WLE = World-Lab-Extruder
MC = Mega Compounder
SC = Super Compounder

Table 10.4 Historical Development of Extruder Generations

1957	Introduction of first commercial ZSK extruder (1st generation)
1963	Change to variable design (2nd generation)
1975	Change from triple- to double-flighted screw geometry (3rd generation) 60% increase in volume
1978	40% increase in torque (4th generation)
1983	30% volume increase with 15% increase in torque (5th generation, Super Compounder)
1995	30% increase in torque (6th generation, Mega Compounder)

From 1957 to 1995 both the volume and torque capability have more than doubled in ZSK extruders. The original W&P twin screw extruders (ZSK53, 83, 120, 160) used a three-lobe (triple-flighted) screw geometry. As discussed in Section 10.3.2 triple-flighted screws have relatively low open area and thus low conveying capability because of their low O.D./I.D. ratio, around 1.2:1. The first two-lobe machines (ZSK57, 90, 130, 170) had greater free volume but used the same gearbox as the three-lobe extruders. As a result, no additional power transmission could be incorporated.

In the late 1970s, W&P redesigned the gearbox for more power, and the shafts were changed to a six-key design for better torque transmission. The fifth generation (Super Compounder) was designed with a 24-spline shaft to allow greater power transmission and greater free volume. The sixth generation (Mega Compounder) increased torque capability another 30%; this extruder can run at screw speeds up to 1200 rpm. Table 10.5 summarizes the developments of the W&P twin screw extruders.

Table 10.5 Comparison of Six Generations of ZSK Extruders by W&P

Generation number	Number of flights	O.D./I.D. ratio	Torque/centerline distance cubed
1	3		3.7–3.9
2	3	≈1.22	4.7–5.5
3	3	≈1.44	4.7–5.5
4	2 or 3	≈1.22 or ≈1.44	7.2–8.0
5	2	≈1.55	8.7
6	2	≈1.55	11.3

The ratio of torque to centerline distance cubed is expressed in $N{\cdot}m/cm^3$. Older ZSK extruders have O.D./I.D. ratios that vary slightly with machine size. The O.D./I.D. ratio of the Super and Mega Compounders does not vary with machine size. This geometric consistency simplifies scale-up.

Distributive mixing is achieved in kneading disks and slotted mixing sections placed along the screw. W&P has developed a mixing tip [45] that has a protruding helical flight as shown in Fig. 10.64.

The mixing tip shown in Fig. 10.64 was designed to improve thermal homogeneity. In tests, it was found that the mixing tip reduced the melt temperature variation from 60°C with a standard tip to 20°C with a mixing tip. Obviously, the benefits of a mixing tip are not limited to co-rotating twin screw extruders. Mixing tips can be used beneficially in counter-rotating twin screw extruders and single screw extruders.

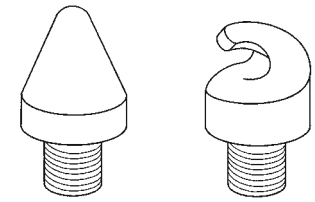


Figure 10.64
Mixing tip (MSSP) by Werner & Pfleiderer

Most suppliers of co-rotating twin screw extruders, such as W&P, supply only one type of extruder. However, there are a few manufacturers that supply both co- and counter-rotating twin screw extruders; examples are Leistritz and Japan Steel Works. In fact, both these companies manufacture machines that can change from a co-rotating mode of operation to a counter-rotating mode. Obviously, the screws have to be changed when a switch is made from co- to counter-rotational operation and vice versa. Co-rotating extruders require screws with equal pitch (both right handed or left handed), while counter-rotating extruders require screws with opposite pitch (one right handed and the other left handed). Such machines offer a great deal of flexibility and versatility.

The main specifications of TEX-α extruders by Japan Steel Works are shown in Table 10.6.

Table 10.6 Main Specifications of TEX-α Extruders by JSW

Model	Diameter [mm]	Torque [kg·m]	Power [kW]	Speed [rpm]
TEX30α	32.0	41	15	358
TEX44α	47.0	129	45	339
TEX54α	58.0	243	75	300
TEX65α	69.0	410	132	314
TEX77α	82.5	700	220	306
TEX90α	96.5	1121	355	309
TEX105α	113.0	1799	560	303
TEX120α	129.5	2708	850	306
TEX140α	152.0	4379	1350	300
TEX160α	174.0	6569	2000	297
TEX180α	196.0	9389	2875	298

The smaller extruders can run at higher screw speeds with correspondingly higher power rating. The TEX extruders are available with shallow and deep-flighted screws. Screws and barrel are completely segmented. Typical L/D values of the TEX extruders range from 30:1 to 60:1. Studies at JSW [43] and elsewhere have shown that counter-rotating extruders are more efficient than co-rotating extruders with respect to feeding, melting, devolatilization, and dispersive mixing. These are important functions in compounding extruders. These results are surprising in light of the fact that the majority of twin screw extruders used in compounding are co-rotating twin screw extruders.

The reason that co-rotating twin screw extruders are so widely used in compounding is probably related to the fact that in the past more developmental work has been directed to co-rotating than counter-rotating TSEs. When a twin screw extruder is considered for a particular compounding task or for reactive extrusion, it should be remembered that a counter-rotating TSE may be more appropriate than a co-rotating TSE. Also, with new developments of mixing devices for single screw extruders the use of single screw extruders in compounding is likely to increase.

There are many manufacturers (over 50) of twin screw compounders. These manufacturers offer a variety of ancillary equipment such as loss-in-weight feeders, twin screw side feeders, vent stuffers, screw segment disassembly units, screen changers, etc. There are many different screw and barrel materials available with special wear and/or corrosion-resistant characteristics. This is important because TSEs are often used with abrasive and corrosive materials.

10.8.1 Screw Design Issues for Co-Rotating Twin Screw Extruders

The main difference in screw design for twin and single screw extruders is that in TSEs the root diameter of the screws is constant in most cases, while in SSEs the root diameter usually varies considerably along the length of the screw. In intermeshing TSEs the root diameter has to be constant if self-cleaning action is to be achieved—this is desired in most cases. Obviously, in non-intermeshing extruders the root diameter can vary (and often does vary) along the length.

Another important difference between SSEs and TSEs is that SSEs are normally flood fed while high speed TSEs are starve fed. In starve fed extruders the regions of partial fill contribute little to melting, mixing, and temperature rise; the partially filled regions are pressureless. Most of the melting, mixing, and temperature increase occurs in fully filled regions of the extruder. Starve-feeding adds an important control element to the process because it allows for a variation of the effective length of the extruder. Generally, the effective length can be increased by raising the feed rate and/or reducing the screw speed. Increasing the effective length usually reduces the specific energy consumption in the extruder; this results in less mixing and lower stock temperatures.

In high speed TSEs, the fully filled length is relatively short, typically 20 to 40% of the length of the extruder. The fully filled regions occur where restrictive elements are placed along the screw and at the end of the screw where the diehead pressure has to be developed. Restrictive elements are often placed just upstream of a vent port to create a melt seal. In a starve fed extruder, a melt seal is necessary to be able to draw a vacuum at the vent port. This is illustrated in Fig. 10.65.

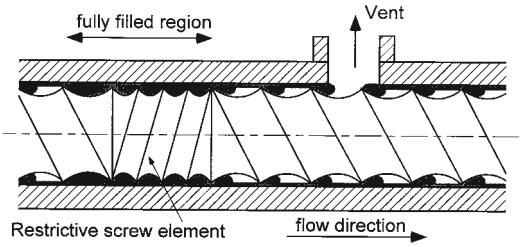


Figure 10.65
A left-handed screw element used before vent port to create a melt seal

The length of the filled section depends on the pressure generating capability of the screw section upstream of the restrictive element and on the level of pressure that is required to override the restrictive element. A small pitch restrictive element will require more pressure than a large pitch element and, therefore, will create a stronger seal. A longer restrictive element will also create a stronger seal. Similarly, a neutral kneading block will not create as strong a seal as a reversing kneading block.

The mixing action of conveying elements is limited; the same is true of single screw extruders. As a result, the mixing action has to be achieved by placing mixing elements along the screw. In the past, the only mixing elements were kneading disks. Kneading elements are basically screw elements with a 90° helix angle. This means the flight runs in the axial direction. The benefit of kneading disks is that they are completely self-wiping just like conveying elements. For distributive mixing, narrow disk kneading blocks are used while for dispersive mixing wide disk kneading blocks are used.

The reason that wide kneading disks achieve good dispersive mixing is that a substantial amount of material is forced into the high-stress region of the kneading disk. When the disk is wide, there is little chance for material to bypass the high-stress region; see Fig. 10.66.

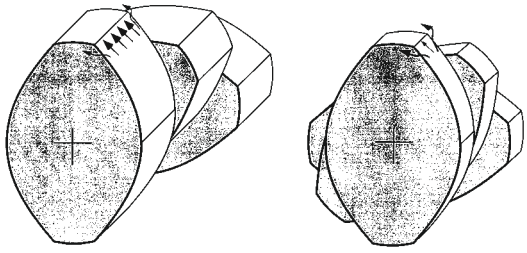


Figure 10.66
Mixing with wide (left) and narrow (right) kneading disks

With wide kneading disks, a large amount of material is drawn into the tip clearance and the material is exposed to strong shear and elongational stresses in the process. With narrow kneading disks, most material will bypass the high stress region of the tip clearance. As a result, the dispersive mixing action is limited; however, the distributive mixing capability is improved because of the frequent splitting of the flow.

The mixing action of kneading blocks depends not only on the width of the kneading disks, but it also depends on the stagger angle. In a bilobal screw geometry, a stagger angle of 90° will create a neutral kneading block. If the stagger angle is between zero and 90° the kneading block becomes a forwarding section. If the stagger angle is between zero and –90° the kneading block becomes reversing; see Fig. 10.67. The mixing action in neutral and reversing kneading blocks is better than in forwarding kneading blocks.

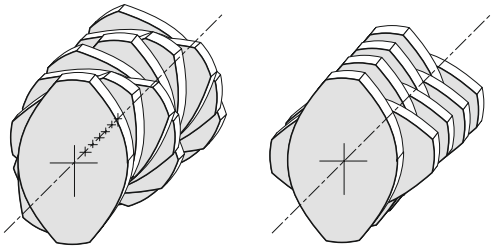


Figure 10.67
Example of forwarding (left) and neutral kneading block (right)

Even though narrow kneading disks provide reasonable distributive mixing, certain applications required better distributive mixing. Therefore, single screw extrusion technology was applied, using a variety of screw elements with slotted flights; see Section 8.7. Some TSE manufacturers resisted this trend, because slotted mixing elements are not completely self-wiping. As a result, slotted mixers compromise the self-cleaning capability of TSEs. In practice, however, the benefits of slotted mixers have been greater than the partial loss of self-cleaning action.

Slotted mixers are usually flighted elements with axial or angled slots machined into the flights. The helix angle of the flights can range from zero to 90°. With a zero degree helix angle the flight becomes a circumferential ring and the mixer looks like a gear type or torpedo mixing element; see Fig. 10.68.

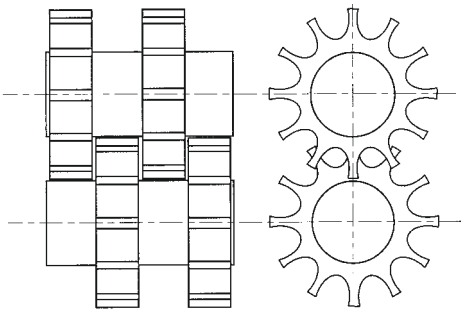


Figure 10.68
Example of gear type mixing element

To improve both the distributive and dispersive mixing, tapered slots can be used according to the CRD mixing technology as discussed in Chapters 7 and 8. Tapered slots create elongational flow as the polymer passes through the slots. This improves dispersive mixing as well as distributive mixing. A set of CRD mixing elements for a twin screw extruder is shown in Fig. 10.69.



Figure 10.69
Example of CRD mixing elements for twin screw extruder

10.8.2 Scale-Up in Co-Rotating Twin Screw Extruders

For scaling extruders similar in design the throughput can be scaled as:

$$\frac{\dot{M}_1}{\dot{M}_2} = \frac{D_1 N_1}{D_2 N_2} \tag{10.130}$$

The power consumption in kilowatts (kW) can be determined from:

$$kW = \frac{N * (\%\ \text{torque}) * (\text{gearbox rating})}{955000} \tag{10.131}$$

where the screw speed N is expressed in revolutions per minute and the gearbox rating in N·m.

The specific mechanical energy consumption (SMEC) is obtained by dividing the power consumption by the mass flow rate (throughput):

$$SMEC = \frac{kW}{\dot{M}} \tag{10.132}$$

When the throughput is expressed in kg/hr, the units of SMEC become kW · hr/kg. In scale-up it is often desirable to keep the specific mechanical energy consumption constant.

If the process is heat transfer limited, the following relationship can be used to determine the throughput of the larger extruder:

$$\frac{\dot{M}_1}{\dot{M}_2} = \frac{D_1^2 N_1}{D_2^2 N_2} \tag{10.133}$$

The average shear rate is proportional to the screw speed; it can be determined from:

$$\dot{\gamma}_{ave} = K_m N = \frac{\pi D N}{H_{ave}} \tag{10.134}$$

The factor K_m is determined by the screw geometry: K_m equals the screw circumference divided by the average channel depth. The K_m value is about 0.4 for third- and fourth-generation ZSK extruders with screw speed N expressed in rev/min. The value of the average channel depth is about 85% of the channel depth of the screw. For a ZSK57 the value K57 = 0.367; for a ZSK130 the value K130 = 0.427. The K values for Super Compounders and Mega Compounders are lower because of the larger channel depth of these machines.

If the shear rates are to be the same in the small and large extruder, then the screw speed of the target extruder can be adjusted to achieve equal shear rates. The screw speed of the large extruder D_1 can be determined from:

$$K_1 N_1 = K_2 N_2 \tag{10.135}$$

The effective volume is the product of the internal volume ratio and the screw speed ratio of the two extruders:

$$\frac{V_{e1}}{V_{e2}} = \frac{V_1 N_1}{V_2 N_2} \tag{10.136}$$

The target TSE must run at the same degree of fill to have the mixing elements perform the same as on the model extruder. The output rate of the target extruder is determined by making the rate ratio the same as the effective volume ratio.

$$\frac{\dot{M}_1}{\dot{M}_2} = \frac{V_{e1}}{V_{e2}} = \frac{V_1 N_1}{V_2 N_2} \tag{10.137}$$

We will take a ZSK57 that runs at 150 kg/hr, 300 rpm, and 90% torque as an example. We will determine what rate and torque can be expected on a ZSK130 at equal shear rate and SMEC. With K57 = 0.367 and K130 = 0.427 the screw speed of the ZSK130 will be 300 * 0.367/0.427 = 258 rpm. The effective volume of the ZSK57 is V_{57} = 1.67 l/m * 0.057 m = 0.0953 l. The effective volume of the ZSK130 is V_{130} = 7.808 l/m * 0.130 m = 1.015 l. Thus, the effective volume ratio becomes: V_{e1}/V_{e2} = (1.015/0.095) * (258/300) = 9.17. The rate on the ZSK130 will be:

$$\dot{M}_{130} = \dot{M}_{57} \frac{V_{e130}}{V_{e57}} = 150 * 9.17 = 1376 \quad [\text{kg/hr}] \tag{10.138}$$

If the gearbox rating of the ZSK57 is 1000 [N·m], the power consumption will be:

$$kW_{57} = \frac{300[rpm]*90\%*1000[Nm]}{955000} = 28.27[kW] \tag{10.139}$$

With a throughput rate of 150 [kg/hr] the specific mechanical energy consumption is SMEC = 28.27/150 = 0.1885 [kWhr/kg]. The power consumption of the ZSK130 at constant SMEC will be kW_{130} = 0.1885 * 1376 = 259 [kW]. If the ZSK130 has a gearbox rating of 13,000 [N·m], the torque on the ZSK130 will be:

$$Torque_{130} = \frac{259[kW]*9550}{258[rpm]*13000[Nm]} = 74\% \tag{10.140}$$

This means that there is enough extra torque to operate the ZSK130 at a screw speed of 258 [rpm] and a throughput of 1376 [kg/hr].

10.9 Overview of Twin Screw Extruders

The following three tables give a brief overview of important aspects of twin screw extruders. Table 10.7 compares intermeshing to non-intermeshing twin screw extruders.

Table 10.7 Comparison of Intermeshing to Non-Intermeshing Twin Screw Extruders

Intermeshing TSE	Non-intermeshing TSE
Self-wiping action possible	No self-wiping action possible
Good melting characteristics	Fair melting capability
Good distributive mixing	Good distributive mixing
Good dispersive mixing	Poor dispersive mixing
Good degassing	Good degassing
L/D up to about 60:1	L/D up to over 100:1
Large market share in polymer industry	Small market share in polymer industry

Table 10.8 compares co- to counter-rotating twin screw extruders.

Table 10.9 gives an overview of some of the most important performance characteristics of twin screw extruders and single screw extruders. The performance characteristics compared are feeding capability, dispersive mixing capability, distributive mixing capability, the ability of the machine to run at high screw speeds, the self-cleaning action of the extruder, the pressure generating capability, and the degassing capability. This table provides a useful overall view of the performance capabilities of the most important commercial extruders.

Table 10.8 Comparison of Co- to Counter-Rotating Twin Screw Extruders

Co-rotating TSE	Counter-rotating TSE
Screws have equal pitch	Screws have opposite pitch
Effective self-wiping action	Less effective self-wiping action
Limited number of screw geometries allow fully self-wiping action	Wider range of screw geometries possible
Sliding action in intermeshing region, most material will bypass intermeshing region	Milling type of intermeshing, material likely to be drawn into intermeshing region
Fair pumping capability, limited pressure development capability	Good pumping capability, good pressure development capability
Good melting characteristics	Excellent melting capability
Good distributive mixing with effective distributive mixing elements	Good distributive mixing with effective distributive mixing element
Good dispersive mixing with effective dispersive mixing elements	Inherently better dispersive mixing capability
Can run at very high screw speeds, up to 1400 rpm	Can run at moderately high screw speeds, up to about 500 rpm
Good degassing	Excellent degassing
Large market share in compounding application, very small market share in profile extrusion	Small market share in compounding, very large market share in profile extrusion (low speed extruders)
Large market share in polymer industry	Large market share in polymer industry

Table 10.9 Comparison of Various Single and Twin Screw Extruders

Extruder	Feeding	Disp. mixing	Distr. mixing	Screw speed	Self-cleaning	Pressure build-up	De-gassing
SSE	0	+	+	+	–	+	0
Pin barrel	0	+	+	+	0	0	0
Kneader	+	+	++	++	++	–	+
PGE	0	++	++	–	++	–	–
KCK	+	++	++	0	0	0	+
CICO	+	–	0	–	+	+	0
CSCO	+	+	++	++	++	0	+
CICT	++	–	0	–	+	++	+
HSCT	++	++	+	+	+	+	++
NOCT	+		+	+	–	–	–
BIM	+	+	+	0	–	–	–
CIM	+	+	+	++	–	–	0

SSE is single screw extruder
PGE is planetary gear extruder
KCK is Kishihiro Continuous Kneader
CICO is closely intermeshing co-rotating twin screw extruder (low speed)
CSCO is closely self-wiping co-rotating twin screw extruder (high speed)
CICT is closely intermeshing counter-rotating twin screw extruder (low speed)
HSCT is high speed counter-rotating twin screw extruder
NOCT is non-intermeshing counter-rotating twin screw extruder
BIM is batch internal mixer
CIM is continuous internal mixer

Table 10.9 compares important characteristics of different types of extruders; the ranking ranges from—(poor or low) to ++ (very good or very high). The comparison in Table 10.9 is a global comparison. Obviously, differences in screw and barrel geometry can change characteristics significantly. For instance, the mixing characteristics of CSCO extruders are poor when simple conveying screws are used; the same is true for single screw extruders. However, CSCO extruders can achieve very good distributive mixing and good dispersive mixing when appropriate mixing elements are used along the length of the screws.

From an overall point of view the CICT and HSCT twin screw extruders have attractive characteristics. They have good feeding, mixing, and degassing capabilities; they can handle a high level of fillers and have good self-cleaning action. From a performance point of view the kneader is quite competitive. However, from a price point of view these machines are substantially more expensive than single screw extruders. As a result, single screw extruders will likely maintain their dominance in the polymer processing industry.

References

1. K. Eise, S. Jakopin, H. Herrmann, U. Burkhardt, and H. Werner, Adv. Plast. Technol., April, 18–39 (1981)
2. K. Burkhardt, H. Herrmann, S. Jakopin, Plast. Compd., Nov./Dec., 73–78 (1978)
3. H. Herrmann and U. Burkhardt, Kunststoffe, 11, 753–758 (1978)
4. C.D. Denson, B.K. Hwang, Jr., Polym. Eng. Sci., 20, 965–971 (1980)
5. C.E. Wyman, Polym. Eng. Sci., 15, 606–611 (1975)
6. J. Maheshri and C.E. Wyman, Ind. Eng. Chem. Fundam., 18, 226–233 (1979)
7. J.C. Maheshri, Ph.D. thesis, Univ. of New Hampshire, Durham, NH (1977)
8. M. L. Booy, Polym. Eng. Sci., 18, 973–984 (1978)
9. H. Werner, Ph.D. thesis, Univ. of Munich, Germany (1976)
10. G. Schenkel, "Kunststoff-Extrudertechnik," Carl Hanser Verlag, Munich (1963)
11. Z. Doboczky, Plastverarbeiter, 16, 57–67 (1965)
12. Z. Dodoczky, Plastverarbeiter, 16, 395–400 (1965)
13. P. Klenk, Plastverarbeiter, 22, 33–38 (1971)
14. P. Klenk, Plastverarbeiter, 22, 105–109 (1971)
15. L.P.B.M. Janssen, "Twin Screw Extrusion," Elsevier, Amsterdam (1978)
16. L.P.B.M. Janssen, L.P.H.R.M. Mulders, and J.M. Smith, Plast. Polym., June, 93–98 (1974)
17. A. Kaplan and Z. Tadmor, Polym. Eng. Sci., 14, 58–66 (1974)
18. R.J. Nichols and J. Yao, SPE ANTEC, San Francisco, 416–422 (1982)
19. R.J. Nichols, SPE ANTEC, Chicago, 130–133 (1983)

20. L. Kovacs, U.S. Patent 3,689,182
21. I. Klein and Z. Tadmor, U.S. Patent 3,924,842
22. R. Klein and I. Klein, U.S. Patent 4,290,702
23. R. Klein, Edison, and I. Klein, U.S. Patent 4,387,997
24. R.J. Nichols, SPE ANTEC, New Orleans (1984)
25. R.B. Bird, R.C. Armstrong, and O. Hassager, "Dynamics of Polymeric Liquids," Volume 1, Fluid Mechanics, Wiley, NY (1977)
26. W. Kozicki, C.H. Chou, and C. Tiu, Chem. Eng. Sci., 21, 665 (1966)
27. W. Kozicki, C.J. Hsu, and C. Tiu, Chem. Eng. Sci., 22, 487 (1967)
28. C. Howland and L. Erwin, SPE ANTEC, Chicago, 113–116 (1983)
29. M.L. Booy, Polym. Eng. Sci., 20, 1220–1228 (1980)
30. W.A. Mack and R. Herber, Chem. Eng. Prog., 72, Jan., 64–70 (1976)
31. L. Wielgolinski and J. Nangeroni, Adv. Polym. Technol., 3, 99–105 (1984)
32. M. Eyrich, 3rd Int. Congress on Reactive Processing of Polymers, Strasbourg, France, Sept., 165–180 (1984)
33. L.P.B.M. Janssen, B.J. Schaart, and J.M. Smith, Polymer Extrusion II Conference, London, England, May, 15.1–15.7 (1982)
34. N.P. Stuber and M. Tirrell, 3rd Int. Congress on Reactive Processing of Polymers, Strasbourg, France, Sept., 193–201 (1983)
35. J.A. Speur and L.P.B.M. Janssen, 3rd Int. Congress on Reactive Processing of Polymers, Strasbourg, France, Sept., 363–372 (1984)
36. R.J. Nichols and R.K. Senn, Paper presented at 53rd Annual Meeting of the Society of Rheology, Louisville, KY, Oct. 15 (1981)
37. D. B. Todd, SPE ANTEC, 472–475 (1974)
38. H.W. Werner, Kunststoffe, 71, 18–26 (1981)
39. H.P. Han and C.D. Han, SPE ANTEC, Washington, DC (1985)
40. G.P. Collins, C.D. Denson, and G. Astarita, AIChE J., Aug., 1288–1296 (1985)
41. R.M. Secor, 3rd Int. Congress on Reactive Processing of Polymers, Strasbourg, France, Sept., 153–164 (1984)
42. J.A. Biesenberger and S.T. Lee, SPE ANTEC, Washington, DC (1985)
43. D.B. Todd (Ed.), "Plastics Compounding, Equipment and Processing," Carl Hanser Verlag, Munich (1998)
44. J.L. White, "Twin Screw Extrusion, Technology and Principles," Carl Hanser Verlag, Munich (1990)
45. A. Grimminger et al., U.S. Patent 4,863,364 (1989)

11 Troubleshooting Extruders

Troubleshooting is often the most critical element of extrusion engineering because of the huge financial impact that extrusion problems can have. As a result, this topic may be the most important in the whole book. For that reason it was decided to devote a separate publication to this subject. The book "Troubleshooting the Extrusion Process" [159] is an expanded text of this chapter, with many detailed case studies. Therefore, for more details on troubleshooting the reader is referred to that book.

11.1 Requirements for Efficient Troubleshooting

Before dealing with specific extrusion problems, there are some issues that should be addressed first. When an extruder develops a problem, it is very important to be able to diagnose the extruder quickly and accurately in order to minimize downtime or off-quality product. Important requirements for efficient troubleshooting are good instrumentation and good understanding of the extrusion process. Instrumentation is very important in process control, but it is absolutely essential in troubleshooting. Without good instrumentation, troubleshooting is a guessing game at best, no matter how well one understands the entire process. Thus, lack of instrumentation can prove to be very costly if it delays solving a certain problem for even a limited length of time.

Important prerequisites to an efficient problem-solving process are:

- Good instrumentation
- Good understanding of the extrusion process
- Collect and analyze historical data
- Team building
- Good information on the condition of the equipment
- Good information on the feedstock

11.1.1 Instrumentation

The extrusion process is largely a black box process. In other words, it is not possible to visually observe what goes on inside the extruder. We can see material going into the extruder and material coming out of the extrusion die. However, what happens between the feed opening and the die exit cannot be seen on normal extruders, because the process is obscured by the extruder barrel. That means that we are largely dependent on instrumentation to determine what happens inside the extruder. We can think of instrumentation as our "*window to the process.*"

It is not sufficient to have ample instrumentation on the extruder; it is also important to make sure that the sensors and readouts are working correctly. For instance, if a temperature zone along the extruder is showing an excessively low or high temperature, it should be verified that the temperature reading is correct. The measuring instruments have to be correctly calibrated, and it should be ascertained that the instrument is capable of measuring the variation in the parameter it is supposed to monitor. In SPC, specific procedures have been developed to determine the capability of the measuring instrument [78].

11.1.2 Understanding of the Extrusion Process

In order to solve extrusion problems efficiently, one has to have a good understanding of the extrusion process. For people new to extrusion, it is recommended to take classes that cover material characteristics of plastics, typical features of extrusion machinery, instrumentation and operating control, the inner workings of the extruders, as well as screw and die design. Classes are available from a variety of sources. Some colleges have classes on extrusion. Many organizations provide continuing education short courses on extrusion. Further, there are a number of training programs available [79] such as video training programs, interactive computer-based training, and web-based training.

In many extrusion operations, the primary mode of training is on-the-job training. However, it should be realized that on-the-job training is often the least effective and most expensive method of training. Extruders are expensive machines that have to be operated correctly to produce good parts. If extruders are not operated correctly, out-of-spec parts may be produced or the extruder may be damaged. It is also important to realize that extruders are potentially dangerous devices. Serious accidents can occur when extruders are not operating properly. Therefore, it is imperative that people operating extrusion equipment receive comprehensive safety training.

11.1.3 Collect and Analyze Historical Data (Timeline)

To understand why a process is not behaving correctly, we have to compare the current process conditions to previous conditions when the problem did not exist; this is also referred to as constructing a timeline. This means collecting not only process information from the extruder, such as temperatures, pressures, motor load, line speeds, barrel dimensions, screw dimensions, etc., but also collecting information on the material and any other variables that can affect the process. Changes in the process can occur not only because of machine parameters, but also because of material changes. For instance, a change in the stabilizer level in the plastic can cause degradation problems without any changes in the machine conditions and settings; see Section 11.1.6.

The importance of a timeline is based on the fact that the process was running well for a certain period of time. In order for the process to become unstable, there has to be an identifiable change or changes that precipitated the process upset. The task is to identify these changes and correct them to get the process back in control. The timeline creation process starts during a period of process stability and ends some time after the process upsets were noticed. All events, even those remotely connected to the process, are listed on the timeline. Once the timeline is finished it becomes a helpful tool in identifying the event(s) that precipitated the problem.

It should be noted that not all changes have an immediate effect on the process. In some cases, there can be a considerable incubation time before the effects of a change become noticeable. This, of course, complicates the troubleshooting process; it is important to keep this in mind and not jump to conclusions. The author experienced a case where a disastrous wear problem was related to an event that took place four months earlier. The wear remained insignificant until about four months after a new feed housing was installed. However, when the rapid wear started, the screw was destroyed within a time period of only 48 hours.

Figure 11.1 shows an example of a timeline leading up to a gel problem.

In constructing the timeline make sure to list all events that can potentially affect the process. Obvious events are things like power outage, new or refurbished extruder screw, resin lot change, etc. Some events are less obvious but may still affect the process such as construction in the area, changes in materials handling, maintenance on plant water system, operator training, power surges, etc.

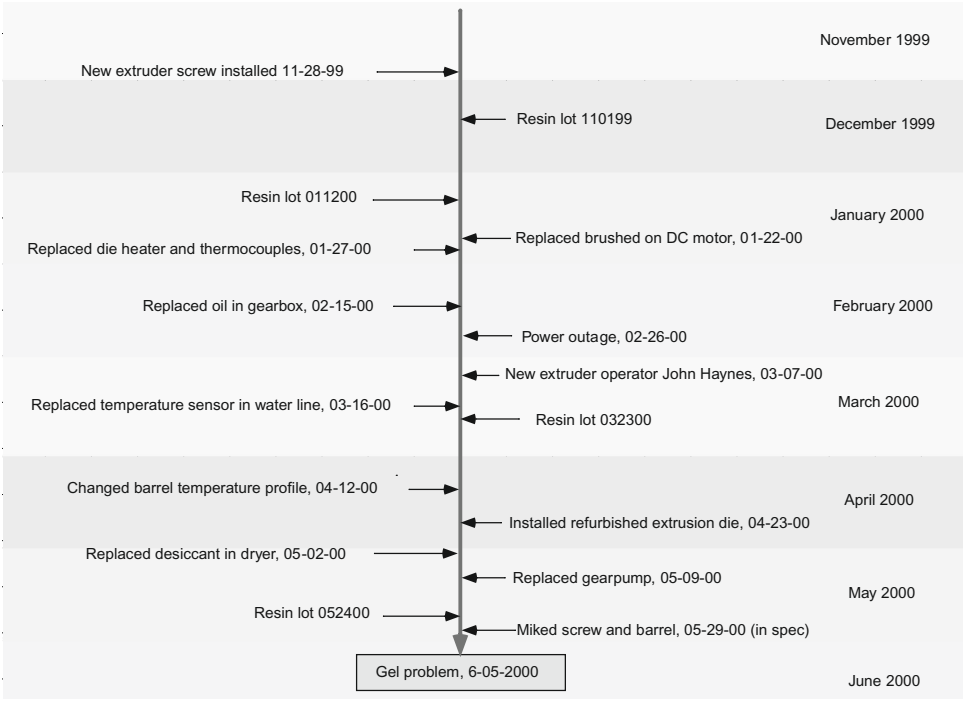


Figure 11.1 Example of timeline leading up to a gel problem

11.1.4 Team Building

If the scope of a problem is small, a single individual can go through the problem solving process and there is no need to organize a team. In many cases, however, problems involve different departments and functions and require a wide range of skills to come to a solution. In such cases, problem solving requires a team effort. Extrusion problems often require input from materials QC, purchasing, maintenance, engineering, and possibly other departments.

11.1.5 Condition of the Equipment

When a problem develops on an extruder, it is important to have good information on the condition of the equipment. Extruders should be well maintained, and good maintenance records should be available so that the condition of the various components of the machine can be assessed. Maintenance recommendations from the extruder manufacturer should be followed to ensure good performance.

Extruder screws and barrels will wear over time. The wear rate depends on many factors. Extruder screws can last for several years or only several weeks. It is impor-

tant to measure the I.D. of the barrel and the O.D. of the screw on a regular basis (at least once a year) so that the life of the screw and barrel can be predicted. This allows screws and barrel to be replaced at predetermined intervals without unpleasant surprises.

11.1.6 Information on the Feedstock

The performance of an extruder is determined as much by the characteristics of the feedstock as it is by the machine. Feedstock properties that affect the extrusion process include bulk properties, melt flow properties, and thermal properties. Important bulk flow properties are the bulk density, compressibility, particle size, particle shape, external and internal coefficient of friction, and agglomeration tendency. Important melt flow properties are the shear and elongational viscosity as a function of strain rate and temperature. The commonly used melt indexer provides only limited information on the melt viscosity. Important thermal properties include the specific heat, the glass transition temperature, the crystalline melting point, the latent heat of fusion, the thermal conductivity, the density, the degradation temperature, and the induction time as a function of temperature.

A change in the material can cause a problem in extrusion when it affects one or more polymer properties that determine the extrusion behavior of the material. If a material problem is suspected, one should first examine the quality control (QC) records on incoming material to see if a change in feedstock properties was determined. Unfortunately, often the only QC test on incoming material is a melt index (MI) test. This test is only able to detect a very limited number of material-related extrusion problems. Thus, in many cases, material testing may have to be more extensive than the regular QC testing.

There are a number of problems associated with making measurements on the critical properties of the feedstock. The total number of properties that need to be measured is about ten, with some of the measurements being rather time-consuming. Thus, it may take considerable time to fully characterize the extrusion properties of a material; this does not help when a quick solution is required. Another problem is the fact that some important properties are difficult to measure and require a high degree of accuracy and reproducibility. The most notable property in this respect is the external coefficient of friction. A further problem can be that instruments to measure all the pertinent properties may not be readily available. Not all companies can afford to maintain a fully instrumented laboratory to completely analyze the extrusion characteristics of a certain compound. Finally, even after a material is fully characterized and no significant changes in properties have been found, there is no guarantee that the extrusion problem is not material related because the material sample used for testing may not have been a representative sample. Since most

tests are done on samples of about 0.01 kg or less and most extruders run at a throughput of several hundred to several thousand kg/hr, there is a considerable chance that the test sample is not representative of the entire feedstock.

A practical test for a material-related extrusion problem is to extrude some material from an old batch to see if the problem will disappear. If this is indeed the case, then this provides a very strong indication that the problem is material related. For this reason, it is helpful to retain some material of older batches, which will also provide a reference for more detailed measurements.

If the problem is material related, there are two possible solutions. The easiest solution from an extrusion point of view is to change the material back to the way it was before the problem developed. However, this may not always be possible for other reasons. Thus, if the change in the material is permanent, then the extrusion process will have to be adjusted to accommodate the material change. At this point, the nature of the problem may change from an upset to a development problem. The chance of solving the problem will depend on the nature and the magnitude of the change in the material.

■ 11.2 Tools for Troubleshooting

There are a number of tools that will help during the troubleshooting process. A discussion of a number of the important tools follows.

11.2.1 Temperature Measurement Devices

A useful tool is a pyrometer with a surface contact probe and a melt probe (needle probe). The contact probe can be used to check for heater burnout, barrel temperatures, die temperatures, and temperature distribution and variation. The melt probe can be used to check melt thermocouple accuracy and to measure the actual melt temperature as it exits the die. The melt temperature at the die exit can be higher than the melt probe temperature at the end of the extruder barrel.

Another useful troubleshooting tool is the infrared thermometer. Figure 11.2 shows an example of a handheld infrared thermometer.

The non-contacting IR thermometer allows temperature measurement in spots that are difficult to reach with a contacting thermometer. Also, the IR thermometer allows measurement of polymer melt temperature without damaging the extruded product. It allows determination of the melt temperature variation across the melt stream coming out of a sheet die. Large melt temperature variations will generally create problems downstream.



Figure 11.2 Example of a handheld infrared thermometer

11.2.2 Data Acquisition Systems (DAS)

Data acquisition systems are extremely useful in extrusion because problems often occur when the operator is not watching the instrument panel of the extruder. Even if the operator is watching the instrument panel, he can only observe a limited number of variables at one time. A DAS that captures and saves important process data is indispensable in troubleshooting. When a problem occurs at 2:30 AM, it is very difficult for a process engineer coming in at 7:00 AM to reconstruct the events at 2:30 AM if important process data was not recorded at that particular time.

A simple DAS is a chart recorder that can track important variables like screw speed, diehead pressure, melt temperature, motor amperage, etc. More useful is a computer-based DAS; these come in two forms: portable data collectors/machine analyzers and fixed-station data acquisition system.

11.2.2.1 Portable Data Collectors/Machine Analyzers

Portable data collectors, PDCs, are similar to check sheets in that they can be easily moved around. In injection molding, these devices are often referred to as portable machine analyzers, PMAs. They have some important advantages:

- They can record data in computer readable form.
- They can take data directly from electronic sensors and gauges. This makes PMAs fast and minimizes errors.

- Data can be analyzed internally to yield information on mean, range, maximum value, minimum value, standard deviation, etc.
- They are available with limit checking; the PMA can give an alarm when data just taken is out of specification.

PMAs can collect variables as well as attributes data. The use of PMAs has increased considerably as the prices have come down to levels that are affordable even for small operations [162]. Several PMAs are presently available for less than $10,000.

Most PMAs offer the user some flexibility in assigning inputs to the data acquisition channels; this even extends to auxiliary equipment, e.g., dryers, and external signals, such as plant ambient temperature and relative humidity. Important inputs are:

- Melt pressure(s)
- Melt temperature(s)
- Screw speed
- Motor load
- Temperature feed housing
- Barrel temperatures
- Die temperatures
- Line speed
- Extrudate dimensions
- Heating power at various temperature zones
- Cooling rate at various temperature zones

Other parameters to be monitored may depend on the specifics of the operation. For instance, in vented extrusion it is often important to monitor the vacuum level at the vent port. For in-depth process analysis a system capable of handling 32 channels or more should be used.

11.2.2.2 Fixed Station Data Acquisition Systems

As the name implies, fixed station data acquisition systems are fixed to one location, either because of size or because the wiring makes it very difficult to move the unit. A fixed station DAS can have a wide range of capabilities. A simple DAS may record data from only one extruder, i.e., a dedicated DAS. A number of machine suppliers now offer extruders with integrated data acquisition and SPC capability.

A more sophisticated DAS may be able to record data from various sources, analyze the data, present control charts, show trend plots for different variables, etc. These systems are often referred to as plant-wide monitoring systems. Central computer-based systems are now available that allow the user to view the operation of plant equipment and change the operating parameters on any selected equipment. A fixed

station DAS can take many different forms depending on the application. A good DAS can be a very valuable tool in improving process control as well as in problem solving. For the application of DAS to extrusion operations, the following capabilities are useful:

- *Monitoring of many variables.* A typical extrusion process requires about 40 to 80 process parameters to be monitored.
- *Data on slowly changing variables* should be taken at least once a second. For rapidly changing variables, such as melt pressure and hydraulic pressure, data should be collected at higher frequency, typically 100 points/s. Some high-end systems sample up to 100,000 points/s.
- *Trending*—the capability to display the variation of one or more process parameters over a particular time period. It is useful if the scales in these displays are adjustable. This capability is extremely helpful in troubleshooting and problem solving.
- *Determination of statistical parameters* on process and product parameters, such as mean, standard deviation, control limits, etc.
- *Alarms for out-of-spec data* and/or indications of assignable causes of variation.
- *Recipes*—the capability to store important process parameters for different products. This allows previous process conditions to be reproduced quickly and reliably.
- *Production summaries*—the capability to follow the amount of material being produced and present summaries per shift, per day, per week, etc. This is a useful management tool for analyzing productivity on different production lines.

The following features have to be considered:

- *User friendliness.* The system should be easy to use, intuitive, and should not require very long training for operators to become accustomed to it.
- *Accessibility.* Is access from a remote computer possible? With remote access, integration into a plant-wide information control system is possible.
- *Connectivity.* Can the DAS software work together with other software packages?
- *Upgradability.* Can new upgraded versions of software and/or hardware be readily implemented?
- *Cost.* An analysis should be made to determine whether the cost savings in terms of improved production efficiency and quality outweigh the cost of a data acquisition system.

The different methods of data collection each have their advantages and disadvantages. Check sheets are slow, prone to human errors and transcription errors; however, they are also inexpensive, flexible, efficient for small amounts of data, and easy to use. Fixed station data acquisition systems are fast, not prone to human errors and transcription errors, can handle large amounts of data; however, they tend to be

expensive and more difficult to use. Thus, check sheets and fixed station data acquisition systems have complementary areas of applications. Portable data collectors fall between check sheets and fixed station data acquisition systems. Table 11.1 shows a comparison of different data recording methods.

For plant-wide monitoring systems, the extrusion process can be integrated with upstream and downstream operations. Bar coding can be used to achieve parts traceability and integrated with automatic product tracking and warehousing. With these systems, accurate data can be collected for job costing, such as cycle times, yields, efficiencies, scrap, labor allocation, and downtime—essential information for efficient plant management. Functions that can be included in plant-wide monitoring systems are preventive maintenance, production scheduling, inventory, production reporting, order entry, job histories, real-time alarms, quality control, SPC, etc.

Some plant-wide monitoring systems allow changes to be made by remote control from a central terminal, in such parameters as screw speed or barrel temperature. Obviously, the results from these changes have to be monitored carefully, because they can make the process not only better, but also worse.

11.2.3 Light Microscopy

This technique allows the observation of a polymeric sample in order to obtain important information about its structure, processing or manufacturing, and failure or damage causes. Therefore, it is a very common technique for quality control, troubleshooting, and failure analysis.

In the case of a high-magnification microscope, the possible magnification ranges are 50, 100, 200, and 500X. The illumination can be transmitted, reflected, or polarized light. In a low-magnification microscope, the magnification ranges vary from 7 to 80X. There is the possibility of a three-dimensional view. Figure 11.3 shows a microscope.

For sample preparation, a microtome with a range from 0 to 340 microns with 0.5 micron resolution and a polishing machine are required.

Table 11.1 Comparison of Data Recording Methods

	Check sheets	Portable data collectors	Fixed station DAS
Speed	slow	fair	fast
Human errors	substantial	small	very small
Transcription errors	substantial	no	no
Efficient for:	small amount of data	large amount of data	huge amount of data
Cost	minor	fair	substantial
Flexibility	very good	fair	good
User skill required	low	medium	high

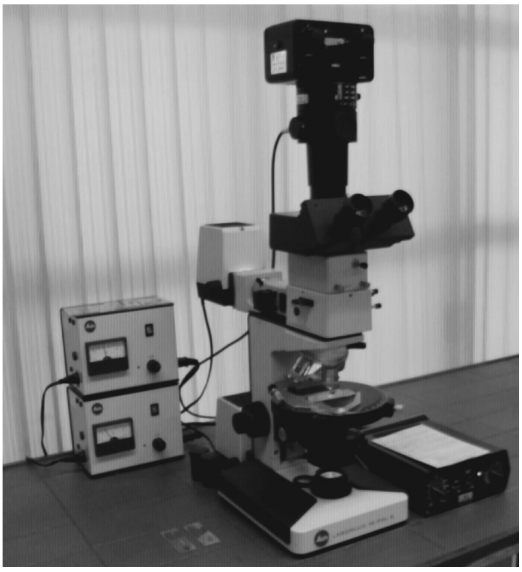


Figure 11.3
Light microscope

The application field of this technique includes:

- Analysis of defects in plastic products
- Dispersion of a filler or a pigment in a polymeric matrix
- Residual stresses under polarized light
- Dimensional studies
- Differences due to orientation
- Crystallization analysis
- Polymer reinforcement analysis
- Coextruded film analysis using colorimetry

Colorimetry involves the treatment of a sample to impart color to selected materials in the sample. For instance, in multi-layer film it can be difficult to distinguish the different layers when natural polymers are used (no colorants added). Certain chemicals color certain polymers but do not color others. For example, iodine will color nylon-6 red, EVOH brown, and typical tie layers gray, but will not change the color of PE or PET.

11.2.4 Thermochromic Materials

Thermochromic substances can be very useful in temperature-related problems. These materials change color irreversibly at a particular temperature, and they are used in a number of applications. For instance, thermochromic paints are used on heat shrinkable sleeves so that the installer who is heating the sleeve with a torch can see whether the product has reached proper installation temperature.

It is difficult to measure the actual polymer melt temperatures inside an extruder. The reason is that an immersion probe cannot be used because the rotating screw will shear it off. Flush-mounted temperature sensors do not give a good indication of the actual stock temperature. Thermochromic materials can be added to the feedstock to determine whether the stock temperatures in the extruder exceed the color transition temperature of the material.

Mennig [160] published a paper quite some time ago on a preliminary investigation into the use of temperature-indicating materials in extrusion. The thermochromic materials that were used in the study were not clearly identified and suffered from the fact that the color transition temperature was time dependent. Obviously, this limits the usefulness of these materials for accurate temperature indication.

Rauwendaal [152] conducted a study using thermochromic powders used commercially in thermochromic paints to study melt temperature in extruders. The study involved a small laboratory twin screw extruder processing a highly filled HDPE. It was found that the material degraded inside the extruder even though the barrel temperatures and exit melt temperature were quite reasonable. The barrel temperatures were set a 200°C and the exit melt temperature was measured at about 215 to 220°C.

These are normal temperatures for HDPE and should not cause degradation under normal circumstances. However, it was suspected that the melt temperatures inside the extruder were much higher than the barrel temperature. Therefore, a thermochromic powder with a color transition temperature of 250°C was added to the feed. With this material, a very clear discoloration was noticed in the material exiting the die. Next, a thermochromic powder was added with a color transition temperature of 300°C. This material unexpectedly resulted in very clear discoloration just as in the first material, indicating that stock temperatures in the extruder exceeded 300°C.

At this point, the cause of degradation was quite clear. However, the location of high stock temperatures needed to be determined as well. Therefore, the screws were pulled and the color change along the screw was visually observed. It was found that the color change took place in a screw section with high-restriction kneading blocks. Clearly, the shearing action in this part of the screw caused excessively high melt temperatures, resulting in degradation of the polymer. Based on these findings, the screw geometry was changed to a less severe mixing geometry and the problem disappeared.

In this study the thermochromic powders were found to be very useful because they provided information very difficult to obtain by any other means. The drawback of this method is that thermochromic powders are not readily available. It would be helpful if a little troubleshooting kit were available with several thermochromic powders with different color transition temperatures.

11.2.5 Thermal Analysis

In thermal characterization, a controlled amount of heat is applied to a sample and its effect measured and recorded. In isothermal operations, the effect is recorded as a function of time at constant temperature. In a programmed temperature operation, the temperature is changed in a predetermined fashion, e. g., at a certain rate, and the effect is recorded as a function of temperature.

The main thermal analysis techniques are differential thermal analysis (DTA), differential scanning calorimetry (DSC), thermo-gravimetric analysis (TGA), thermo-mechanical analysis (TMA), and dynamic mechanical analysis (DMA). These methods are discussed in more detail in Section 6.3.8.

11.2.6 Miscellaneous Tools

A tape measure can be used to measure distances from about 20 cm up to several meters. Dial calipers are useful for closely measuring extruded products, dimensions of the extruder screws, extrusion tooling, etc. A stopwatch is an indispensable tool for measuring screw speed, line speed, blender calibration, etc. A scale can be used to measure the output of an extruder. A small voltmeter is very useful in making sure that voltage and resistance levels of various components are at their required values. A millivolt source can be used for verifying thermocouple inputs and to check controller response and line continuity.

A digital still camera is a valuable tool in troubleshooting to accurately document the configuration of the extrusion line, details of the screw geometry, die geometry, wear regions on the screw, contamination in the product, unusual build-up on the screen pack, etc. A digital camera is an excellent tool in the preparation of clear operating procedures and other process documentation. The digital photos can be easily transferred to a PC, and the photos can be used in reports, manuals, presentations, etc.

A digital video camera is also a very useful troubleshooting tool because of its ability to capture motion. This allows determination of the frequency of pulsing of the extrudate coming out of the die. Another benefit of the video camera is that it can record sound as well as images. The soundtrack can be analyzed separately. For instance, the sound of a high-frequency vibration can be captured on video and downloaded to a PC, and the frequency of the vibration can be determined from the soundtrack. Digital still cameras are better for high-quality capture of a static event. However, a video camera is an excellent tool for capturing dynamic events. In troubleshooting, the dynamic events are often the most important.

11.3 Systematic Troubleshooting

11.3.1 Upsets versus Development Problems

In this chapter, the problems that will be primarily focused on are upsets. These are problems that occur in an existing extrusion line for some unknown reason. If the extrusion line has been running fine for a considerable period of time, then it is clear that there must be a solution to the problem. Thus, the objective of troubleshooting is to find the cause of the upset and to eliminate it. On the other hand, when one deals with a development problem, there may not be a solution. In a development problem, one tries to establish a condition that has not been achieved before. If the desired condition is physically impossible, then clearly there is no solution to the problem. From a functional analysis of the process, one should be able to determine the bounds of the conditions that can be realized in practice.

11.3.2 Machine-Related Problems

In machine-related problems, mechanical changes in the extruder cause a change in extrusion behavior. These changes can affect the drive system, the heating and cooling system, the feed system, the forming system, or the actual geometry of screw and barrel. The main components of the drive are the motor, the reducer, and the thrust bearing assembly. Drive problems manifest themselves either in variations in rotational speed and/or the inability to generate the required torque. Problems in the reducer and thrust bearings are often associated with clear audible signals of mechanical failure. If the problem is suspected to be the drive, make sure that the load conditions do not exceed the drive capability.

11.3.2.1 Drive System

Older motor drive systems generally consist of a DC brush motor, a power conversion unit (PCU), and operator controls. A frequent problem with the motor itself is worn brushes; these should be replaced at regular intervals as recommended by the manufacturer. In troubleshooting an extruder drive, one should follow the procedure recommended by the manufacturer of the drive. A typical troubleshooting guide for a DC motor is shown in Table 11.2.

Table 11.2 Troubleshooting Guide for DC Motor

Problem	Possible cause	Action
Motor will not start	Low armature voltage	Make sure motor is connected to proper voltage
	Weak field	Check for resistance in the shunt field circuit
	Open circuit in armature or field	Check for open circuit
	Short circuit in armature or field	Check for short circuit
Motor runs too slow	Low armature voltage	Check for resistance in armature circuit
	Overload	Reduce load or use larger motor
	Brushes ahead of neutral	Determine proper neutral position for brush location
Motor runs too fast	High armature voltage	Reduce armature voltage
	Weak field	Check for resistance in shunt field circuit
	Brushes behind neutral	Determine proper neutral position for brush location
Brushes sparking	Brushes worn	Replace
	Brushes not seated properly	Reseat brushes
	Incorrect brush pressure	Measure brush pressure and correct
	Brushes stuck in holder	Free brushes, make sure brushes are of proper size
	Commutator dirty	Clear commutator
	Commutator rough or eccentric	Resurface commutator
	Brushes off neutral	Determine proper neutral position for brush location
	Short circuit in commutator	Check for shorted commutator, check for metallic particles between commutator segments
	Overload	Reduce load or use larger motor
	Excessive vibration	Check driven machine for balance
Brush chatter	Incorrect brush pressure	Measure and correct
	High mica	Undercut mica
	Incorrect brush size	Replace with proper size
Bearings hot	Belt too tight	Reduce belt tension
	Misaligned	Check alignment and correct
	Bent shaft	Straighten shaft
	Bearing damage	Inspect and replace

11.3.2.2 The Feed System

The most important component of the feed system in a flood-fed extruder is the feed hopper with possible stirrer and/or discharge screw. A mechanical malfunction of this system can be determined by visual inspection. If the feed hopper is equipped with a discharge screw (crammer feed), constancy of the drive should be checked. For proper functioning of a crammer feeder, the drive of the crammer feeder should have a torque feedback control to ensure constant feeding and to avoid overfeeding.

Many extruders have square feed hoppers with rapid compression in the converging region. Extruder manufacturers often choose this geometry because of the ease of manufacture. However, this hopper geometry does not promote steady flow. When flow instabilities occur in a feed hopper, the extruder operator will often hit the hopper with a heavy object to get the flow going again. As a result, hoppers that cause flow problems often shows signs of abuse such as mars, dents, scrapes, etc. Such mars are a strong indication of poor feed hopper design.

11.3.2.3 Different Feeding Systems

The feeding system of the extruder is of utmost importance in achieving a stable and consistent extrusion process. In flood-feeding, the design of the feed hopper determines to a large extent how stable the bulk material can flow through the hopper. This subject is covered in Section 7.2.1. In starve-fed extruders, the stability of the process is to a large extent determined by the quality of the feeders. Feeders are either volumetric or gravimetric. Feeders are often integrated into an overall control system for the extrusion line or even a complete plant.

Volumetric feeders are basically speed-controlled and deliver a constant mass flow rate as long as the bulk density of the feed material is constant. When variations occur in bulk density, volumetric feeders are less suitable. Gravimetric feeders control the mass flow rate generally by weighing the total weight of the feeder and the material in the feeder. The discharge rate is controlled such that there is a linear reduction in weight with time. When the gravimetric feeder is recharged with material, it generally switches to volumetric mode for a brief time to handle the disturbance in weight during this time. The book by Wilson [161] contains a large amount of detail on feeding systems.

11.3.2.4 Heating and Cooling System

The heating and cooling system is used to achieve a certain degree of control of the polymer melt temperature. However, stock temperature deviations do not necessarily indicate a heating or cooling problem because heat is added directly to (or removed from) the barrel and only indirectly to (from) the polymer. The local barrel temperature as measured with a temperature sensor determines the amount of barrel heating or cooling. The temperature that is controlled is actually a barrel temperature.

The stock temperature is generally controlled by changing the setpoint of the temperature zones along the extruder. However, due to the slow response of the melt temperature to changes in heat input, only very gradual stock temperature changes can be effectively controlled by setpoint changes. Rapid stock temperature fluctuations, a cycle time of less than about five minutes, can usually not be reduced with a melt temperature control system. Such fluctuations are indicative of conveying instabilities in the extrusion process and can only be effectively reduced by eliminating the cause of the conveying instability.

The heating system can be checked by changing the setting to a much higher temperature, for instance 50°C above the regular setting. The heater should turn on a full 100% and the measured barrel temperature should start rising in about one to two minutes. If the heater does not turn full on, the barrel temperature measurement is in error or there is a problem in the electronic circuit of the temperature controller. If the heater turns full on but the temperature does not start to rise within two to four minutes, either the barrel temperature measurement is incorrect or there is poor contact between heater and barrel.

The cooling system can be checked by changing the setting to a much lower temperature, for instance 50°C below the regular setpoint. The cooling should turn full on and the measured barrel temperature should start to drop in about one to two minutes. If the cooling does not turn full on, the barrel temperature measurement is in error or there is a problem in the circuit of the temperature controller. If the cooling turns full on but the temperature does not start to drop within two to four minutes, either the barrel temperature is incorrect or the cooling device is inoperable. This checkout procedure is summarized in Table 11.3.

Table 11.3 Heating and Cooling System Check

Heating system: Increase setpoint of temperature zone by 50°C:	
Heater turns on full blast and the barrel temperature rises in about 2 minutes	Heating system normal
Heater turns on full blast but the barrel temperature does not change	Poor contact of heater to barrel, insufficient heating capacity, temperature sensor failure
Heater output does not change	Heater failure, controller bad
Cooling system: Reduce setpoint of temperature zone by 50°C:	
Cooling on full blast and the barrel temperature drops in about 2 minutes	Cooling system normal
Cooling on full blast but the barrel temperature does not change	Temperature sensor failure, insufficient cooling capacity, cooling system not functioning at all
Cooling output does not change	Cooling system bad, controller bad

If a substantial amount of cooling is required to maintain the desired stock temperature, this is generally a strong indication of excessive internal heat generation by frictional and viscous dissipation. The internal heat generation can be reduced by lowering screw speed or by changing the screw design. The main screw design variable that affects the viscous heating is the channel depth. Increasing the channel depth will reduce the shear rates and viscous heating.

Mechanical changes in the forming system relate to the extrusion die and downstream equipment. These elements can be subjected to simple visual inspection, and mechanical changes can thus be easily determined. Changes to the geometry of screw and barrel are often caused by wear. Since wear is a very important phenomenon in extrusion, it will be discussed in detail in the following section.

11.3.2.5 Wear Problems

Wear occurs in all machinery with moving parts. Unfortunately, extruders are no exception. Wear problems in extrusion can take many shapes and forms. A good general text on wear in polymer processing is the book by Mennig [80].

Wear in extruders generally causes an increase in the clearance between screw flight and barrel. Wear often occurs towards the end of the compression section. This type of wear is more likely to occur when the screw has a high compression ratio. Wear in the compression section of this type of screw reduces the melting capacity and will lead to temperature non-uniformities and pressure fluctuations. Wear in the metering section of the screw will reduce the pumping capacity; however, the reduction in pumping capacity is generally quite small as long as the wear does not exceed two to three times the design clearance. An increased flight clearance will also reduce the effectiveness of the heat transfer from the barrel to the polymer melt and vice versa; this may contribute to temperature non-uniformities in the polymer melt.

Wear can only be detected by disassembling the extruder and by inspection of the screw and barrel. If the wear is serious enough to affect the extruder performance, it will often be noticeable with the naked eye. However, it is recommended to measure the I.D. of the barrel and the O.D. of the screw over the length of the machine. If this is done regularly, then it is easy to determine how fast wear is progressing with time. By extrapolating to the maximum allowable wear, a determination can be made at what point in time the screw and/or barrel should be replaced or rebuilt. If replacement resulting from wear is necessary after several years of operation, the easiest solution is to simply replace the worn parts. However, if replacement resulting from wear becomes necessary within a short period of time, for instance several months, then simple replacement will not provide an acceptable solution. In short-term wear problems, the cost of downtime and replacement parts can easily become unacceptable, and the solution has to be found in reducing the actual wear rate instead of simply replacing the worn parts. To reduce the wear rate, one has to

understand the wear mechanism(s) in order to determine the most effective way to reduce wear.

11.3.2.5.1 Wear Mechanisms

Five mechanisms of wear can be distinguished:

1. Adhesive wear
2. Abrasive wear
3. Laminar wear
4. Surface-fatigue wear
5. Corrosive wear

When wear occurs, often more than one mechanism is at work. Adhesive wear occurs with metal-to-metal contact under high stresses. Since the actual contact area is much smaller than the apparent contact area, local welds can form at points of contact. This phenomenon is often referred to as cold welding. The sliding motion causes a rupture in the weld region, and small fragments of the weld region are carried away with one member of the sliding system. Usually fragments of the softer material transfer to the harder material. Adhesive junctions are only formed between clean surfaces. The attrition rate depends on the shear strength of the adhesive junctions. Adhesive wear is generally more severe with sliding contact of similar metals. Adhesive wear between similar metals is often referred to as galling. In sliding motion between dissimilar metals, the adhesive junction will contain a spectrum of compositions. Adhesive wear can be significantly reduced when the spectrum of compositions in a junction contains brittle intermetallic compounds that fracture easily. Lubricants are often used to reduce the chance of adhesive wear. When oxide layers form at the interface, this will also reduce adhesive wear because oxides will not bond.

Abrasive wear occurs by a micro-cutting process. In two-body adhesive wear, the asperities of the harder member penetrate the softer one and remove material as a result of the sliding motion. In three-body abrasive wear, hard particles are embedded in the material of at least one member of the wear system. The hardness ratio has been found to be the most important material characteristic in abrasive wear, although the influence of fracture toughness seems to play a role [1]. Krushchov [2] found that the wear resistance of pure metals and annealed steels increases proportionally with hardness. Strain hardening or precipitation hardening does not result in improved abrasive wear resistance because the micro-cutting process already yields maximum local strain hardening.

Laminar wear occurs when the shear strength in the heterogeneous interfacial layer is higher than the shear strength of the homogeneous portion of the interfacial layer. Laminar wear takes place only at the thin outer layers of the interface. Laminar wear is sustained only if the outer layer of the heterogeneous interface continu-

ously regenerates as an oxidic or other reactive layer. The formation of wear-reducing reactive layers can be controlled by additives in the lubricant. Laminar wear, to a certain extent, is a mild form of corrosive wear. A mild corrosive or oxidative action affects only a thin layer of the newly generated metallic surface. When the new surface layer is formed, the reaction will stop.

In surface fatigue wear, there is a separation of microscopic and macroscopic material particles from the surface, which is caused by fatigue crazing, cracking, and breakup under specific mechanical, thermal, and chemical loads in rolling contact between two surfaces. Fatigue cracking is initiated by alternating thermal or mechanical loads. This type of wear can occur even with direct metallic contact. Surface fatigue wear is characterized by considerable induction times and relatively large depth of penetration. A familiar example is the pitting of roller bearings and gears.

In corrosive wear, a chemical reaction attacks at least one of the sliding surfaces. Corrosive wear in extrusion occurs usually in combination with one or more of the other wear mechanisms. The combined chemical and mechanical attack of the sliding surface can cause wear rates far in excess of what would be expected based on their individual contribution. In extrusion, the most important wear mechanisms are adhesive, abrasive, and corrosive wear.

11.3.2.5.2 Test Methods for Wear

There are basically two ways to test the wear characteristics in the extrusion process. One method is to run the actual machine under normal operating conditions and to measure the progress of wear at regular intervals. This approach is time consuming and expensive, but it does yield accurate and representative results. However, it does not allow a simple analysis of the parameters that influence the wear process.

An interesting technique to do wear studies relatively fast on actual extruders was developed at the IKT in Stuttgart, Germany, by Fritz and coworkers [31]. A reference surface of the machine is made radioactive by proton and neutron bombardment to a depth of 30 to 80 μm. The impulse rate from the measuring isotope reduces linearly with activation depth. This allows accurate measurement of wear over short time periods. It was found that the wear process could be accurately characterized in about one to three hours. In the particular study mentioned [31], wear was measured in the feed section of a screw; the extruder was equipped with a grooved barrel section. The abrasive filler was titanium dioxide, which was added to the virgin polymer as a masterbatch. When the virgin polymer was in pellet form, considerable wear occurred, while no wear was measured when the virgin polymer was in powder form.

Another method involves testing on model systems. In such a test, a test specimen is subjected to certain load conditions to simulate actual service conditions. Such wear

testers allow the tribological relevant loads to be pre-selected; tribological parameters such as temperature, coefficient of friction, etc., can be measured and recorded continuously. This method allows a relatively quick and inexpensive determination of wear characteristics. However, information obtained from a wear tester can only be transferred to practice if the wear conditions in the model system are essentially the same as those in the real system, i. e., the extruder. Many mistakes have been made in transferring information from a short wear test to actual extruders, simply because of the differences in the tribological conditions of the wear process. It is often not realized that the tribological parameters, friction and wear, are not material properties, but properties of a complex system. Thus, the transfer from a model system to an actual extruder has to be made cautiously. Measurements on the actual extruder are required to ensure that results from the model system are also valid for the real system. A good review and analysis of test methods for wear in the polymer processing industry was given by Mennig and Volz [3]. Considering that there are many different types of wear in polymer processing, there is, unfortunately, no universal wear tester. Mennig and Volz distinguish four types of testing: metal-liquid wear, metal-solid polymer wear, corrosive wear, and metal-to-metal wear.

As early as 1944, a test device was proposed by Mehdorn [4] to measure metal-liquid wear. This test was to simulate wear conditions in a press used for injection of thermosets. The test geometry is shown in Fig. 11.4.

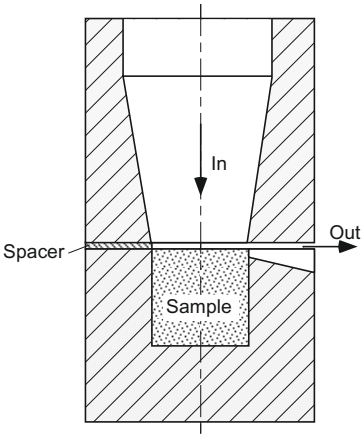


Figure 11.4
Wear test device proposed by Mehdorn

A molten or liquid mass of polymer is forced onto a test specimen, from which it is deflected; the material exits through a small clearance of 0.4 mm. This test device gives relatively quick results. Disadvantages are the complex geometry of the clearance, non-uniform flow conditions at the specimen, and that increased wear changes the resistance to flow and thus the wear conditions. Another method was developed by Bauer, Eichler, and John [5] in 1967. Figure 11.5 shows the geometry of their test apparatus.

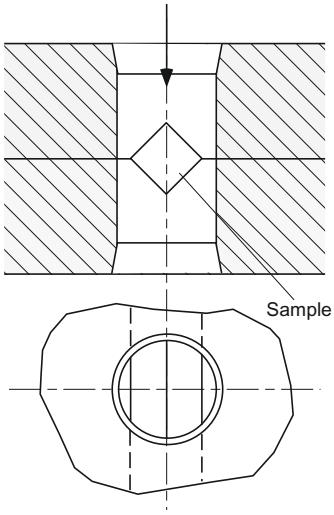


Figure 11.5
Wear test proposed by Bauer et al.

The specimen is a diamond-shaped obstruction in the center of a flow channel. A commercial wear test apparatus based on this geometry is the Tribotest from Brabender OHG in Duisburg, Germany. This test is often referred to as the "Siemens-Method" wear test. Eichler and Frank [6] modified this test to make it more suitable for injection molding. Entirely different test geometry was developed at the DKI (Deutsches Kunststoff Institut, Darmstadt). This test utilized a flat plate geometry as shown in Fig. 11.6.

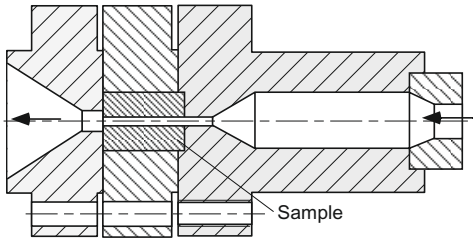


Figure 11.6
DKI flat plate wear test apparatus

The rectangular test gap has a length of 12 mm, a width of 10 mm, and a height that is adjustable from 0.1 to 1.0 mm. This geometry has been used for studies with thermoplastics [7] as well as with thermosets [8]. A modification of the flat plate wear tester is the BASF wear tester. This test simulates the wear process in a molding machine. Another test apparatus developed at the DKI is the ring method, shown in Fig. 11.7.

This test simulates conditions occurring in the annular space between the tip of the screw flight and the extruder barrel [7, 9]. Plumb and Glaeser [10] developed a test method for filled elastomers based on a capillary rheometer. The specimen in this test is a cone-shaped torpedo in the flow channel. The flow conditions change in

axial direction and with it, the local wear rate. A test developed at Georgia Marble Company, a supplier of calcium carbonate, uses an aluminum breaker plate at the end of a screw extruder to evaluate abrasive wear of mineral fillers. The amount of wear is determined by measuring the weight loss of the breaker plate over a certain run time [25].

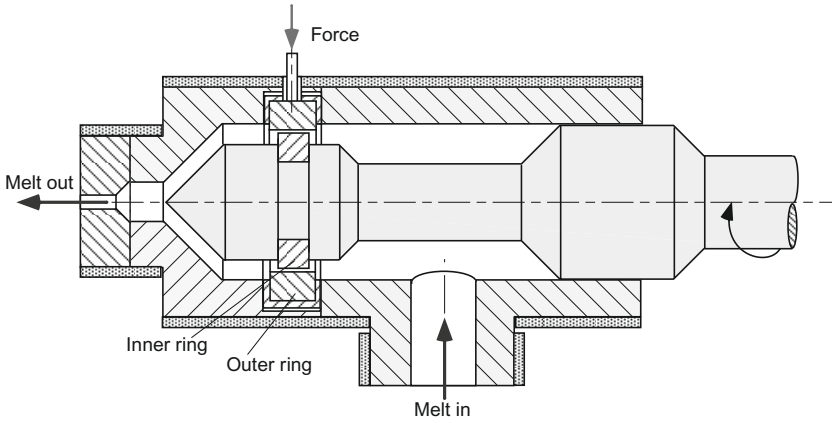


Figure 11.7 DKI ring wear test apparatus

Metal-to-solid polymer wear occurs in the solids conveying zone of the extruder. The introduction of the grooved barrel extruder has significantly increased the interest and concern about wear in this portion of the extruder. Grooved barrel sections substantially increase the shear and normal stresses between the polymer solid bed and the metal surfaces. As a result, grooved barrel sections are much more susceptible to wear than smooth barrels. The first systematic study of wear in the solids conveying section of extruders was made by Fritz [11]. He used a diamond-shaped specimen that protruded into the screw channel.

A model system was developed at the DKI in the form of a disk wear tester. This universal disk-tribometer was discussed by Volz [12]. The concept of the disk-tribometer is partially based on a modified friction tester developed at Enka Glanzstoff [13]. The geometry of the disk-tribometer is schematically shown in Fig. 11.8.

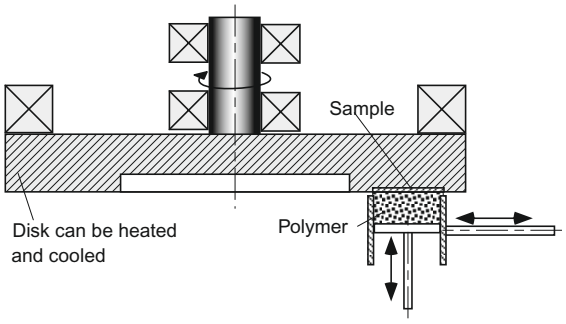


Figure 11.8
Universal disk tribometer

The disk can be heated and cooled. The annular groove at the bottom surface of the disk contains the metal specimen. The disk-tribometer allows measurement of frictional force, normal force, and wear at contact pressures of up to 150 MPa. A test for corrosive wear was first proposed by Calloway, Morrison, and Williams [14]. They used a vacuum pyrolysis at normal process temperature.

A metal specimen is suspended in the extracted volatiles for 24 hours at room temperature. A similar apparatus was used by Mahler [7] and Braun and Maelhammar [15] in order to test for corrosion at elevated temperatures and pressures. A disadvantage of vacuum pyrolysis is the fact that the corrosion conditions are different from those existing in the actual extrusion process. This drawback is reduced in the test procedure used by Knappe and Mahler [9].

Other tests have been described by Moslé et al. [16] and Maelhammar [17]. The latter test is a combination of metal-liquid wear and corrosive wear. The apparatus was modified by Volz [18] for thermosets. The volatiles are extracted from the polymer melt, which has been prepared in an injection molding machine and has been sheared through a test gap. Through electrochemical measurements, Volz could prove that significant differences exist in the corrosive action of volatiles separated from injection molded samples of thermosetting polymers.

Tests for metal-to-metal wear can utilize the standard test methods, provided the proper intermediate material can be introduced between the metallic surfaces. Broszeit utilized the cylinder-disk apparatus to study metal-to-metal wear [19]. Saltzman, et al. [20–22] used the Alpha LFW-1 test apparatus; see Fig. 11.9.

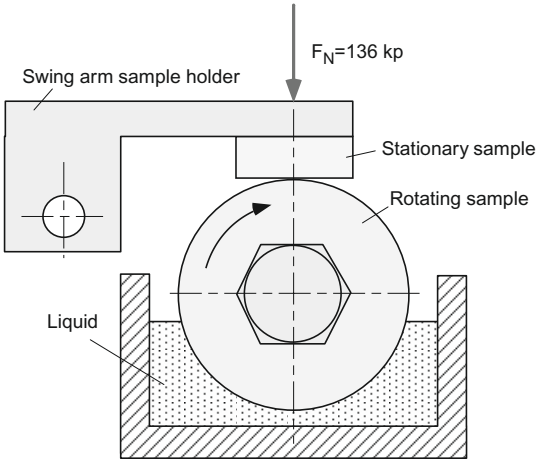


Figure 11.9
Alpha LFW-1 wear test apparatus

A stationary block is forced against a rotating ring by a dead-weight load. The bottom part of the ring is immersed in a water-oil emulsion. The presence of the water-oil emulsion is a drawback in this test because the actual wear behavior in an extruder with a polymer melt as the intermediate material between screw and barrel is bound to be substantially different from the wear behavior in the LFW-1 test appa-

ratus. No data have been published on metal-to-metal wear with a polymer melt as the intermediate material.

11.3.2.5.3 Causes of Wear

In polymer-metal wear, the main causes of wear are abrasive wear and corrosive wear. Abrasive wear is generally due to abrasive components in the polymer matrix. Whether these components are classified as fillers, reinforcements, or additives, they can cause significant wear when the filler is hard and available in significant amounts. Factors affecting the wear are particle hardness, particle size, particle shape, and loading [23]. One indication of the abrasive wear ability of a filler is its ranking on the Mohs scale. This scale ranks a material from 1 to 10 according to its ability to scratch another material or to be scratched by another material. A very soft material, such as talc, is ranked at the bottom of the scale, rank 1, and a very hard material, such as diamond, is ranked at the top of the scale, rank 10. The Mohs scale ranking of several fillers is given in Table 11.4.

Table 11.4 Mohs Scale Ranking of Various Fillers

Calcined Kaolin	7
Silica	6.5
Glass	6
Perlite	5.5
Wollastonite	5.5
Mica	3
Calcium Carbonate	3
Kaolin	2
Alumina trihydrate	1
Talc	1

It should be realized, however, that the filler hardness only partially determines the wear characteristics of a filled compound. The particle size is another important parameter. Generally, the severity of wear reduces with reducing particle size. In glass fiber reinforced compounds, the wear reduces when the fiber length reduces [12]. This is believed to be due to greater mobility and reduced kinetic energy of the smaller glass fibers. The particle shape has a very strong influence on the wear characteristics. Experiments done by Mahler [26] with glass fiber reinforced nylon and glass bead reinforced nylon showed the wearing intensity of the fiber reinforced compound to be 14 times higher than the compound reinforced with glass spheres. The ability to wear is larger when the particle has sharp corners and a large aspect ratio. The particle shape that best minimizes wear is a spherical shape. Unfortunately, the spherical shape is often undesirable with respect to mechanical properties, electrical properties, etc.

In a study on glass-reinforced polymers, Mahler [7] found that with some polymers the wear intensity could be much higher than with others because of corrosive wear in addition to abrasive wear. He found that the wear intensity of glass fiber reinforced nylon-6,6 against 9S20K steel was about 13 times higher than reinforced SAN and PC. A similar finding was made by Olmsted [27] in injection molding of glass fiber reinforced nylon-6, where severe wear occurred on both the screw and the barrel. The wear was found to be primarily corrosive-type wear, caused by a silane wetting agent on the fiber. The decomposition temperature of the wetting agent was lower than the process temperature and, hence, degradation occurred with resulting corrosive attack of screw and barrel. However, similar work by Mahler [7] with nylon-6,6 filled with glass fibers coated with an aminosilane coupling agent did not reveal any corrosive wear resulting from the coupling agent.

Surface treatment of fillers can reduce wear. A comparison between coated and uncoated calcium carbonate showed the wear intensity of a rigid PVC compound with the coated filler to be about 3 to 9 times lower than the same compound with the uncoated filler [25]. The wear intensity was measured by using the aluminum breaker plate test discussed earlier. When incorporating abrasive fillers, such as glass fibers, it is good practice to add the filler at a location where the polymer is already molten. This practice allows the melt to coat the filler and reduce the wear intensity. When abrasive fillers are added with solid polymer particles, the abrasive action is much more severe and rapid wear will occur in the solids conveying section of the extruder. This is why glass fiber is generally added in a downstream barrel opening or in a downstream extruder in the case of a tandem extrusion set-up.

Corrosive wear also occurs in non-filled polymers; well-known examples are fluoropolymers and chlorine containing polymers, such as HPFA and PVC. Fluoropolymers have a tendency to form hydrofluoric acid at high temperatures in combination with air and moisture. PVC tends to generate hydrochloric acids at elevated temperatures. The corrosion problem is generally more severe with rigid PVC than with flexible PVC. With polymers like these, the metal parts in contact with the polymer should be made out of a corrosion-resistant metal, such as Hastelloy, 17–4 PH, 15–5 PH, etc.

Corrosion can also occur with hygroscopic polymers, such as ABS, PA, PET, PMMA, etc., when moisture is released under high temperature and pressure, forming high-pressure steam. Braun and Maelhammer [15] found that PA 6,6 splits into various corrosive components. Calloway et al. [14] found that the corrosive attack of HIPS is dependent on the chlorine and sulfur content of the carbon blacks. Moslé et al. [16] found that degradation products of ABS can cause corrosive attack in extruders.

Sometimes abrasive components in the compound are foreign objects resulting from contamination or human error. Hard foreign objects, such as wrenches, bolts, knives, etc., can cause severe wear in a very short period of time. Magnetic traps are available to catch metallic objects. However, there is not a simple method to successfully remove all foreign objects from the feed stock. Good housekeeping procedures and

conscientious personnel will go a long way in reducing the chance of foreign objects ending up in an extruder. One word of caution is in order for barrier-type screws. If small particles are present in the polymer feedstock that do not melt at operating temperatures, they will get trapped at the end of the barrier section when the particle size is larger than the barrier clearance. This can result in very rapid wear, as the author has been able to verify personally.

Another important cause of wear in extrusion equipment is metal-to-metal wear. Unfortunately, relatively little is known about this type of wear. A number of circumstances can cause metal-to-metal contact between screw and barrel. In addition, metal-to-metal contact will occur at start-up. It can also occur as a result of misalignment, or a warped barrel, or a warped screw. Metal-to-metal contact can occur at the feed opening of an extruder as described by Luelsdorf [28], particularly when the feed opening is offset and when it forms a sharply tapered angle with the circumference of the screw.

The author has also experienced cases where metal-to-metal wear occurred in the feed throat of an extruder as a result of improper feed opening geometry. Radiographic analysis of wear particles indicate [28] that temperatures in the contact zone between screw and barrel may exceed 800°C. This is confirmed by personal observations of a screw subjected to severe metal-to-metal wear with a very noticeable purple discoloration of the metal in the wear region. Discoloration indicates exposure to temperatures over 500°C.

Metal-to-metal wear can also occur in intermeshing twin screw extruders. Counter-rotating twin screw extruders are more susceptible to metal-to-metal wear than co-rotating twin screw extruders. Counter-rotating twin screw extruders, therefore, generally operate at rather low screw speeds. Unfortunately, co-rotating extruders also can experience serious metal-to-metal wear problems.

Lai Fook and Worth [29] proposed modified flight geometries to increase the centering force on the screw in order to reduce metal-to-metal contact. The two flight geometries they proposed based on theoretical calculations are shown in Fig. 11.10.

Actual measurements of the tangential pressure profile differed from predicted values by a factor of about 10. This indicates that the analysis employed was not entirely realistic; in particular, neglecting side leakage results in large errors in the predicted values. No data was presented on the actual centering force acting on the screw. Winter [30] analyzed the non-isothermal flow of a power law fluid in the flight clearance; solutions were obtained by employing a numerical procedure. Very high temperature increases were found to occur in the polymer melt in the clearance; these temperature changes affect the velocity profile. Since the mass flow rate cannot change, Winter adjusted the pressure gradient along the gap to satisfy the continuity equation. This led to a prediction of large negative pressure gradients at the leading edge of the flight and large positive pressure gradients at the trailing edge of the flight, as shown qualitatively in Fig. 11.11.

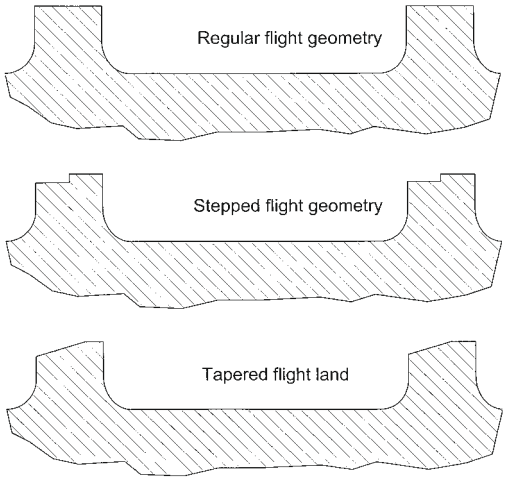


Figure 11.10
Flight geometry to reduce the chance of metal-to-metal wear

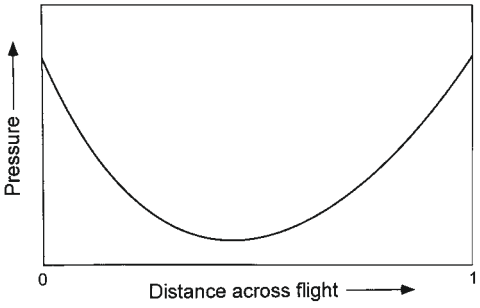


Figure 11.11
Pressure profile in the flight clearance as predicted by Winter [30]

Extreme values of the actual pressure occur at about 1/3 from the leading edge, and the calculated values range from 5 to 20 MPa.

The predicted pressure profile is obviously a direct result of the assumptions made in the calculations. Winter assumed isothermal conditions at the barrel wall and adiabatic conditions at the flight tip. With stock temperature increases in the order of 100°C and more, it is unlikely that the isothermal boundary condition is valid for the barrel. For the same reason, it is unlikely that the adiabatic boundary condition is valid for the flight tip, particularly since the rest of the screw will be at much lower temperature. Unfortunately, it is difficult to measure actual temperature and pressure profiles. Thus, the predicted temperature and pressure profiles have not been compared to experimental results.

Winter postulated that the pressure minimum in the middle of the clearance could cause the screw to be pushed against the barrel by pressure on the other side of the screw. This would only be true if the clearance pressure profile changed along the helical length of the screw flight and if the pressure profiles in the screw channel itself do not play a role of significance. Most likely, the actual situation will be considerably more complex. Following Lai Fook and Worth, Winter recommended be-

veling the flight tip to create a tapered gap between flight and barrel. Another recommendation was to alter the thermal boundary conditions, for instance by heating the barrel above the temperature of the screw flight. It is interesting to note that the chance of metal-to-metal contact is reduced when the flight clearance and helix angle are increased and when the flight width is decreased, according to Winter's analysis. If this is true, then these measures will have a dual benefit because they will also reduce the power consumption. Unfortunately, actual experience contradicts Winter's recommendations.

A disadvantage of the stepped or beveled flight geometry is that when the extruder is running empty or partially empty, the apparent contact area between screw and barrel will be considerably reduced. As a result, the stresses at the actual contact area will be considerably increased and wear, particularly adhesive wear, is more likely to occur. Nonetheless, Volz [12] reports that flight lands with hydrodynamic slide bearing function are used by a number of extruder manufacturers. However, it does not appear that this flight geometry is widely used in the industry.

Metal-to-metal contact between screw and barrel will occur when the extruder is empty because of gravitational sag of the screw. This type of wear will reach a maximum at the very end of the screw and reduce in the upstream direction. In practice, however, the location of maximum wear generally occurs towards the end of the compression section of the screw. This indicates that the screw is supported by the polymer melt at the end of the screw and is subjected to a substantial lateral force in the compression section of the screw. It is unlikely that this lateral force is caused by temperature-induced pressure gradients in the flight clearance because the flow process in the flight clearance will not change significantly from the start of melting to the very end of the screw. Therefore, it seems more likely that the lateral force is caused by the conveying process in the screw channel.

In the melting zone of the extruder, there is a continuous deformation of the solid bed. In the compression section of the screw, the solid bed is compressed between the root of the screw and the barrel. Very large pressure can be built up in this screw section, particularly when the compression ratio is high. These rapid pressure changes along the screw can easily cause an imbalance of the lateral forces acting on the screw. Thus, it seems that rapid pressure changes along the screw channel are the most likely cause of metal-to-metal contact between screw and barrel. Considering the frequent occurrence of this wear problem, it is surprising how little attention this problem has received as judged from the open technical literature.

11.3.2.5.4 Solutions to Wear Problems

The key to find the best solution to a wear problem is to identify the cause of wear and the wear mechanism. For example, if the screw O.D. is worn but not the flight flanks and the root diameter, then the problem is probably caused by contact be-

tween screw and barrel. In this case, one could put hardfacing on the tip of the flight. However, this would not eliminate the cause of the problem, but it may reduce the magnitude of the problem. The actual problem can be eliminated by a change in screw design or by another method that will alter the pressure profile along the screw, e. g., by starve feeding the extruder.

Corrosive wear can usually be identified by a pitted, worn surface. The best solution to corrosive wear is to eliminate the corrosive component from the compound. However, this is often not possible for other reasons. In this case, one has to use corrosion-resistant materials of construction, such as stainless steel, Inconel, Hastelloy, etc. In order to select the best material of construction, one should know the chemical species that are causing the corrosive attack. Various metal handbooks contain information about the chemical resistance of many metals against a number of chemical species. Figure 11.12 shows a flow chart that allows systematic troubleshooting of wear problems.

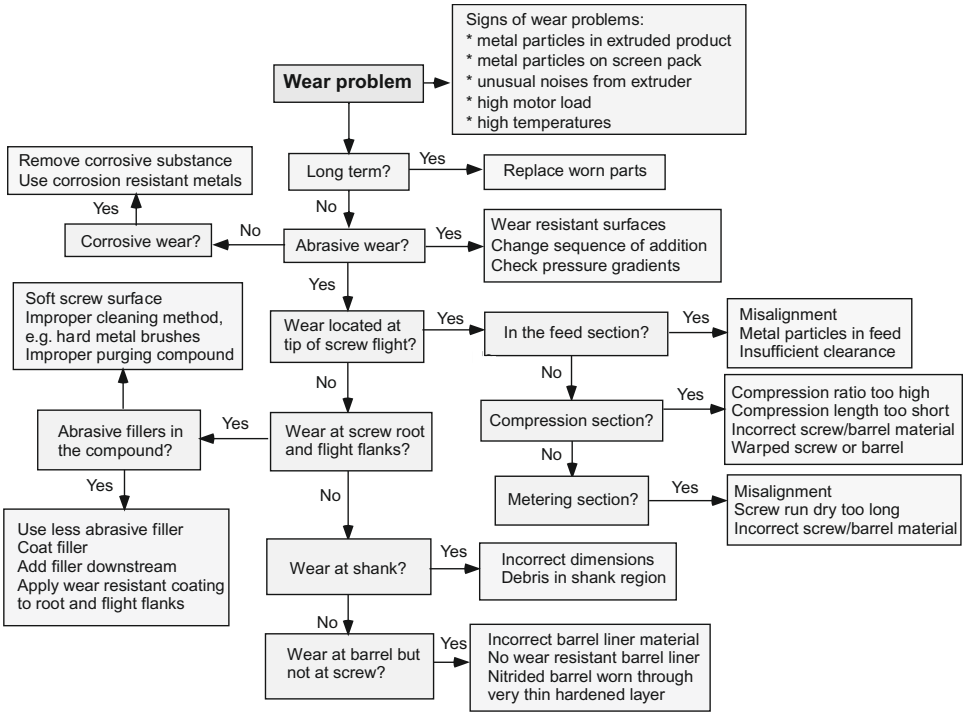


Figure 11.12 Flow chart for troubleshooting wear problems

A large number of materials are available for the screw and barrel. Most extruder barrels in the U. S. have a liner, which is centrifugally cast into the barrel. The barrel liner is made of a wear-resistant material, often boron-stabilized white irons with a Rockwell C hardness of about 65 containing iron chromium boron carbides. Bimetallic barrels provide better wear resistance than nitrided barrels as reported, for

instance, by O'Brien [32] and Thursfield [33]. The liner material can be formulated to give good abrasion resistance, good corrosion resistance, or a combined abrasion and corrosion resistance. It should be kept in mind that the correct choice of screw material depends to some extent on the liner material, particularly if metal-to-metal contact takes place. Recommended screw materials for several commercial barrel liners are shown in Table 11.5. The recommendations are based on metal-to-metal wear tests on the Alpha LFW-1 wear test machine. As discussed earlier, this test does not simulate actual conditions in an extruder too well; however, results from more realistic tests are not available in the open literature.

Table 11.5 Recommended Screw Flight Materials, Courtesy of [22]

Barrel liner material		
Xaloy 101	Xaloy 306	Xaloy 800
Screw material		
Colmonoy 56	Colmonoy 6	Colmonoy 6
Colmonoy 6	Colmonoy 56	Colmonoy 56
Haynes 711	Colmonoy 63	Xaloy 008
Colmonoy 5	Stellite 1	Nye-Carb
Colmonoy 63	Nye-Carb	Xaloy 830
Stellite 1	Stellite 6	Ferro-Tic
Ferro-Tic (Iron)	Stellite 6H (severe wear)	Stellite 6H (severe wear)
HC-250		
Colmonoy 84		
Triballoy T-700		

The most common screw material is 4140 steel. Advantages of 4140 steel are low price, good machinability, and the ability to be used with hardfacing and chrome plating. A disadvantage of the 4140 steel is its relatively poor wear resistance, as discussed, for instance, by Hoffmann [34]. As a result, 4140 screws are often flame-hardened, plated, or hardfaced when used in more demanding applications. Chrome plating is often used on extruder screws. This produces a hard corrosion-resistant layer, up to 70 R_c hardness. The layer is usually quite thin, about 25 to 75 μm, and does not form a hermetic seal to most corrosive substances. Thus, the chrome plating does not substantially improve the corrosion resistance of the screw due to its porosity. Chrome plating is quite resistant to abrasive wear, but because of its limited thickness, it does not provide much protection.

Nickel plating is also used quite frequently on extruder screws. It is applied with a thickness similar to chrome plating. The surface hardness of nickel plating tends to be somewhat lower than chrome plating. However, the thickness of the nickel coating is generally more uniform and the coating is much less porous than chrome plating. Therefore, nickel plating usually offers better protection than chrome plating.

A very large number of proprietary plating materials and plating processes are available today. Without exception, the claims made by the supplier of the proprietary plating are quite impressive. Unfortunately, these claims are rarely based on long-term extrusion tests. Thus, one has to be quite cautious in selecting a proprietary plating.

An interesting proprietary plating is the Poly-Ond plating. It is basically an electroless nickel plating impregnated with a fluoropolymer. This yields a moderately hard, corrosion-resistant layer with a low coefficient of friction. The low coefficient of friction makes it attractive to use in injection molds and on extruder screws. Luker from Killion Extruders reported [35] on tests with Poly-Ond plated extruder screws. He reported output increases from 5 to 36% for a number of different polymers. Another Teflon-impregnated nickel plating is Nedox plating as discussed by Levy [74]. A Teflon-impregnated chrome plating was discussed by Tropler [75].

Metal coatings such as chrome and nickel plating are generally more effective in reducing wear than hardening of the base material. Various methods are used for hardening, such as flame hardening, nitriding, carburizing, and induction hardening. All of these techniques are basically case-hardening processes with limited depth of penetration and limited improvement in wear characteristics. Further, heat-treated steels have reduced hardness and wear resistance at elevated temperatures.

Hardfacing Materials

Another technique used for improving the wear resistance of screws and barrels is hardfacing or hardsurfacing. Hardfacing materials are generally nickel or cobalt based containing various metal carbides, such as chromium carbide, tungsten carbide, etc. The most common alloys are Stellite and Colmonoy, but many other materials are available today. Hardfacing materials are applied by welding, spraying, or casting with a thickness ranging from 1 to 3 mm. There are several steps involved in the hardfacing process as shown in Fig. 11.13. On a worn screw the flights are ground to a uniform undersize, the hardfacing material is welded onto the flights, the hardfacing is ground to the original O.D., and the sides of the flights are machined to provide a smooth transition from the flight flank to the hardfacing material.

A critical step in the application of the hardfacing is the preheating of the screw before application and, more importantly, the gradual cooling of the screw after the hardfacing is applied. If the screw cools too rapidly, thermal stresses will develop in the hardfacing and cracks will form. Considering that hardfacing materials are hard and brittle it is quite easy for small cracks to form. In fact, for many hardfacing materials small hairline cracks cannot be completely avoided. In general, the higher the carbon content of the hardfacing material, the greater its tendency to crack and the better its wear characteristics.

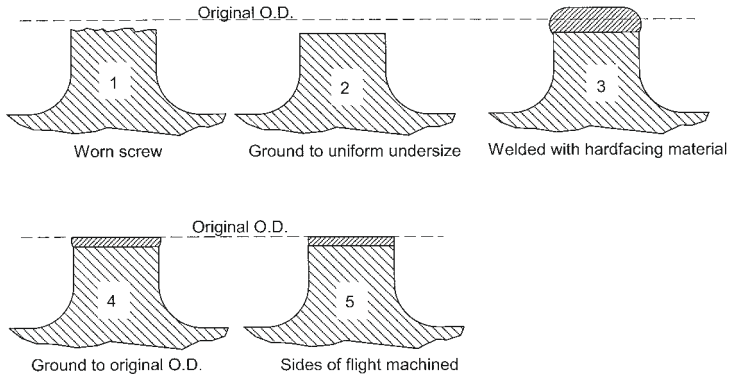


Figure 11.13 Steps involved in applying hardfacing to a worn screw

Screws using the high carbon, highly wear resistant hard facing materials generally will show some degree of small hairline cracks. If such hardfacing does not show any hairline cracks, the hardfacing material may be suspect. It is possible that softer, less wear resistant hard facing is actually used. It is also possible that the hardfacing material has been diluted too much with the base screw material; this will result in a softer hardfacing material that will wear rapidly. For this reason it is a good idea to measure the hardness of the hardfacing after the screw is manufactured. If the hardness is substantially below the normal value, it is likely that the hardfacing is overdiluted or that the wrong hardfacing was applied.

Cracks that are cause for concern are those that traverse completely through the hardfacing material and then turn in a circumferential direction. When such cracks occur, parts of the hardfacing may come loose. This may happen when the hardfacing is not properly applied. It may also occur when the screw is not handled properly before installation or if the screw is exposed to excessive stresses during the extrusion process.

Most hardfacing materials do not plate well, i.e., a wavy line occurs at the intersection of the welded material. This problem can be eliminated by the use of an inlay, as shown in Fig. 11.14. Here, two basic hardfacing geometries are shown: one that has the hardfacing applied to the full width of the flight and the other that has an inlay with hardfacing. Inlays can only be applied to new extruder screws.

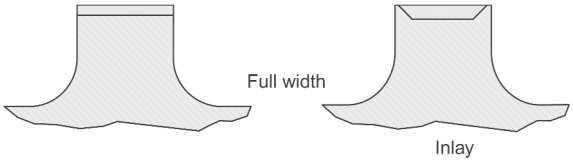


Figure 11.14
Full width and inlay hardfacing

Applying hardfacing to small screws (diameter less than 40 mm) is more difficult than to large screws. For this reason, smaller screws are often manufactured without hardfacing. For small screws, it makes economic sense to make the screw out of a wear-resistant tool steel such as D2 or CPM because the weight of the screw is small and the material cost relatively low. For large screws, the material cost is a more important issue because of the large weight of the screw. As a result, for large screws it is more important to use a low-cost steel.

Hardfacing can offer substantial improvements in wear resistance over heat treated steels. Lucius reports increases in service life by a factor of 2 to 25 by using hardfacing on a screw used in extrusion of glass fiber reinforced nylon-6,6 [36]. Two common hardfacing materials are Stellite (trademark Cabot Corp.) and Colmonoy (trademark Wall Colmonoy Corp.). Colmonoy is a nickel-based alloy containing chromium, iron, boron, and silicon. Stellite is a cobalt-based alloy containing chromium and tungsten. Other hardfacing materials are Haynes 711, HC-250, Triballoy T-700, Ferro-Tic HT6 and M6, Nye-Carb, and Xaloy 008, 830, 101, 306, and 800. Properties of various hardfacing materials were given in Table 3.4. A larger list of hardfacing materials is shown in Table 11.6.

Table 11.6 Properties of Hardfacing Materials

Product	Base material	Hardness Rc	Cracking tendency	%C	%Cr	%W	%B	Cost/lb [$]
Stellite 1	Cobalt	48–54	High	2.5	30.0	12	-	25–40
Stellite 6	Cobalt	37–42	Medium	1.1	28.0	4	-	25–40
Stellite 12	Cobalt	41–47	Medium	1.4	29.0	8	-	25–40
Colmonoy 5	Nickel	45–50	Medium	0.65	11.5	-	2.5	15–25
Colmonoy 56	Nickel	50–55	High	0.70	12.5	-	2.7	15–25
Colmonoy 6	Nickel	56–61	Very high	0.75	13.5	-	3.0	15–25
Colmonoy 83	Nickel	50–55	High	2.0	20.0	34	1.0	40–50
N-45	Nickel	30–40	Medium	0.3	11.0	-	2.2	15–25
N-50	Nickel	40–45	Medium	0.4	12.0	-	2.4	15–25
N-56	Nickel	45–50	High	0.6	13.5	-	2.8	15–25

Metal-to-metal wear tests of these materials were described by McCandles and Maddy [22]. Welding techniques for applying these materials are tungsten inert gas (TIG), transferred arc plasma, and oxyacetylene.

Molybdenum-based hard alloys have also been used on extruder screws. These materials are relatively soft, about 40 Rockwell C, but have good lubricity. In some instances, wear resistance with the molybdenum hardfacing improved about 500% over the more common, but harder, hardfacing compounds. Molybdenum-based hardfacing alloys are used primarily with nitrided barrels, not only in single screw

extruders but also in twin screw extruders. The use of molybdenum hardfacing in bimetallic barrels often results in rapid wear of the screw. Since most extruders in the U.S. have bimetallic barrels, molybdenum-based hardfacing for extruder screws has not found widespread use.

In some cases, improvements in wear resistance can be obtained by diffusion coating hardfacing alloys. Panzera and Saltzman [37] tested treated and untreated hardfacing alloys against carburized SAE 4620 rings using the Alpha Model LFW-1 wear tester. Three case-hardening processes were selected: aluminum diffusion coating, boron diffusion coating, and ion nitriding. It was found that cobalt-based hardfacing alloys exhibited significant improvement in wear resistance against carburized SAE 4620 steel; however, nickel-based hardfacing alloys were unaffected by ion nitriding. Aluminized cobalt-based alloys showed improved wear resistance after a porous outer layer was ground off. Boriding reduces the wear resistance of both nickel and cobalt-based facing alloys. Removing the porous outer layer improved the wear properties of the borided nickel-based alloy.

The effect of work hardening of hardfacing alloys was also studied by Panzera and Saltzman. The work hardening was done by shot peening. The cobalt-based alloy hardened to a depth of about 250 μm; the nickel-based alloy did not work harden. It was found that work hardening the cobalt-based alloy did not improve its wear resistance against carborized SAE4620 steel as measured on the LFW-1 wear tests. Another process that has been used to surface-harden extruder screws is chemical vapor deposition (CVD). The process and some of its applications have been described by Bonetti [73]. This process has been used to apply a thin layer, approximately 4 micron, of a very hard titanium nitride coating to the screw surface. Hardness values of about 110 Rockwell C can be obtained. Obviously, with such extreme hardness of the screw, be very careful that the barrel material is compatible with the screw material. Rebuilding of extruder screws is covered in Section 8.9.

11.3.2.6 Screw Binding

There is a special problem that can occur in extruders where the screw suddenly stops rotating and gets stuck in the extruder barrel and/or feed housing. This problem does not occur very often but when it occurs it wreaks havoc with the machine. The most frequent cause of this problem is differential thermal expansion between the screw and barrel. Corrosion-resistant screws commonly used in the extrusion of fluoropolymers are particularly susceptible to screw binding. There are certain characteristics of the corrosion-resistant materials that make these screws susceptible to locking up in the extruder. This usually results in considerable damage to the machine and substantial downtime. We will analyze the mechanism of screw binding and give recommendations on how to prevent this problem [147].

11.3.2.6.1 Basic Facts

In the extrusion of fluoropolymers, the extruder screw and die generally have to be made out of a highly corrosion-resistant material. Common materials used for this purpose are Hastelloy, Monel, Inconel, and Duranickel. These materials not only have corrosion resistance that is much better than the typical 4140 steel used for most extruder screws, but there are other properties that are quite different from 4140 steel as well. Because of these other properties these corrosion-resistant screws are much more susceptible to getting stuck in an extruder barrel than screws made of 4140 steel. Since screw binding usually results in considerable damage to the extruder with associated downtime and cost, not to mention aggravation, it is important for processors to be aware of the pitfalls of using screws made out of highly corrosion-resistant materials.

11.3.2.6.2 The Mechanics of Screw Binding

When a screw is installed in an extruder, the typical radial clearance between the screw and the barrel is 0.001 D, where D is the diameter of the extruder. This is the clearance at room temperature. When the machine is in operation the actual clearance between the screw and the barrel can be quite different. There are two main reasons for the change in clearance under actual processing conditions. One reason is temperature; the other is compressive load on the screw. When the processing temperature is much greater than room temperature, the clearance can change when a) the coefficient of thermal expansion (CTE) of the screw and barrel is different and b) the temperature of the screw is different from the barrel.

11.3.2.6.3 Changes in Clearance Because of Temperature Differences

When the screw and barrel increase in temperature, both the screw and barrel will increase in diameter due to thermal expansion. If the CTE of the screw is greater than the barrel, the clearance between the screw and barrel will reduce with increasing temperature. Values of the CTE for several materials are shown in Table 11.7 together with data on thermal conductivity and elastic modulus.

For a 25.40 mm barrel running at 333.3°C above room temperature, the increase in I.D. is 9.652E–2 mm when the CTE is 11.34/°C. For a 25.3492 mm Monel screw with a CTE of 13.86E–6/°C running at 333.3°C above room temperature, the increase in screw diameter will be 0.1168 mm. Thus, the difference between the thermal expansion of the screw and barrel diameter is about 0.02 mm or 0.01 mm based on the radius. If the radial clearance is 0.0254 mm, the clearance will reduce to 0.01524 mm due to the differential thermal expansion. Thus, the clearance is reduced but still greater than zero provided both the screw and barrel are at the same temperature.

In an operating extruder, however, it is not very likely that the screw and barrel are at the same temperature. The largest difference between the screw and barrel tem-

perature is likely to occur in the feed throat. The feed throat of most extruders is water-cooled and therefore close to room temperature in many cases. The screw temperature in the feed section, however, can be (and in many cases will be) much higher because the high temperatures in the compression and metering section will raise the feed section temperature due to thermal conduction.

If the feed throat is maintained at room temperature and the screw temperature in the feed section is 166.7°C higher, then the screw diameter will increase from 25.3492 mm to 25.4076 mm if the CTE = 13.86E-6/°C. This corresponds to 0.0023 mm per mm of screw diameter. The screw diameter now is larger than the diameter of the feed throat and the screw will bind! The question can be asked, is this temperature difference not equally likely to occur in a screw made of 4140 steel? The answer is no and the reason has to do with the thermal conductivity of these materials. The thermal conductivity of corrosion-resistant metals tends to be considerably lower than that of steel, by a factor of three to five: see Table 11.7.

Table 11.7 Thermal Properties and Elastic Modulus for Several Screw Materials

Material	Coefficient of Thermal Expansion, [/°C]	Thermal conductivity J/ms[°K]	Elastic modulus [MPa]
Hastelloy C276	11.16E-6	11.25	2.00E5
Inconel 718	12.96E-6	11.42	2.00E5
Inconel 625	12.78E-6	9.86	2.07E5
Monel 400	13.86E-6	21.80	1.79E5
Monel 500	13.68E-6	17.47	1.79E5
4140 steel	11.34E-6	42.56	2.00E5
4340 steel	11.34E-6	42.21	2.00E5
17-4 stainless	10.44E-6	17.82	2.00E5
316 stainless	18.54E-6	16.09	2.00E5
304 stainless	18.72E-6	16.26	2.00E5

The lower thermal conductivity of corrosion-resistant materials will reduce the amount of heat that can be transferred from the screw shank to the reducer. As a result, the shank and feed section of the screw will be at higher temperature as compared to a high-conductivity screw. Figure 11.15 shows the thermal expansion graphed against the temperature difference between the screw and barrel.

The graph shows two typical values of the coefficient of thermal expansion. From Fig. 11.15 it is clear that it takes only a temperature difference of about 167 to 222°C to have the screw lock up in the barrel, considering that the coefficient of thermal expansion is in the range of 10E-6 to 17E-6/°C. It is clear that if a polymer is processed at 371°C, it is quite possible that the screw temperature will be more than 167°C above the barrel temperature.

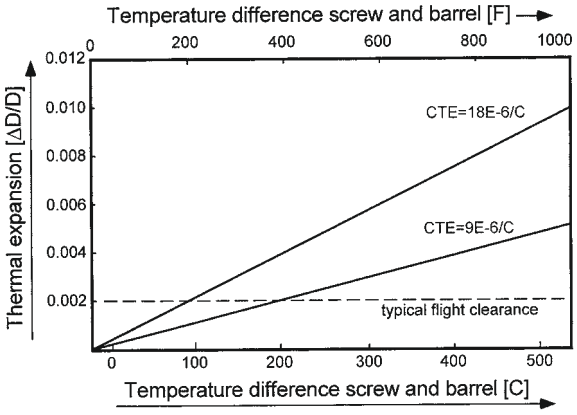


Figure 11.15
Thermal expansion vs. temperature difference

When viscous heating is significant, the screw temperature will tend to be higher than the barrel temperature, at least with a neutral screw. Janssen et al. [148] found that in extruders without screw cooling the screw temperature gives a much better indication of the mean polymer temperature than does the barrel temperature. Finite element analysis of non-isothermal, non-Newtonian flow in extruders [84] also found that screw temperatures tend to be higher than barrel temperatures when viscous heating is significant. As a result, the screw temperature in the metering section of the screw may be significantly higher than the barrel temperature. Therefore, the temperature difference between screw and barrel in the feed section may be greater than what might be assumed based on the measured barrel temperatures.

Few publications are available that provide data on screw and plastic temperatures along an extruder. The publication by Marshall et al. [149] provides some interesting experimental data. They confirm that the screw temperature in the metering section is higher than the barrel temperature. Further, they measured screw temperatures in the feed section and found temperatures in the range of 115 to 127°C (240 to 260°F) with barrel temperatures of 190°C (375°F). When barrel temperatures are around 371°C (700°F), it can be expected that the feed section of the screw will be in the range of 204 to 260°C (400 to 500°F) if not higher.

11.3.2.6.4 Analysis of Temperature Distribution in Extruder Screws

In order to confirm whether the mechanism proposed in the previous section is correct, predictions of the temperature distribution in extruder screw processing of FEP were made using finite element analysis. The program used is FEHT [150], developed at the University of Wisconsin-Madison.

Figure 11.16 shows the thermal boundary conditions that were used in the analysis; 697 nodes were used with 1280 triangular elements.

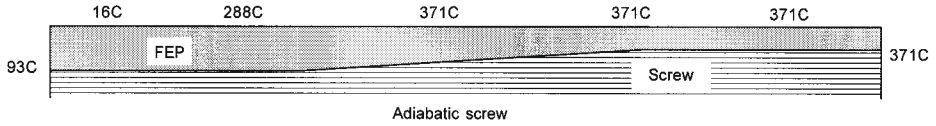


Figure 11.16 Schematic of thermal boundary conditions for FEA

The feed throat temperature is set at 15.6°C, the barrel temperatures are set at 288, 371, 371, and 371°C, the screw shank is set at 93°C, the screw tip is at 371°C, and the heat flux at the screw centerline is zero in the radial direction. The program does not take into account viscous dissipation or convection; the heat transfer is purely by conduction. The thermal conductivity of the FEP is taken as 0.246 J/ms°K.

Figure 11.17 shows the predicted temperature distribution in a screw that is made of 4140 steel. Figure 11.18 shows the temperature distribution in a Monel screw.

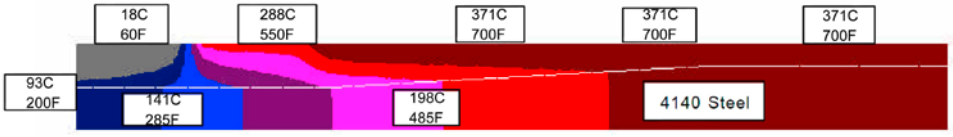


Figure 11.17 Predicted temperature distribution in a 4140 steel screw

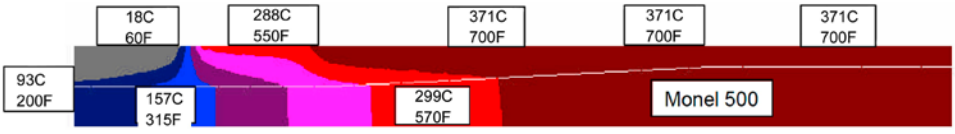


Figure 11.18 Predicted temperature distribution in Monel screw

Comparing Figs. 11.17 and 11.18 it is clear that with the Monel screw higher temperatures occur in the feed section of the screw. This must be due to the thermal conductivity since this is the only difference between the two cases. These predictions confirm that a lower thermal conductivity of the screw material can lead to higher temperatures in the feed section of the screw. In the case of the Monel screw shown in Fig. 11.18, the screw temperatures in the feed section range from about 150 to 260°C (300 to 500°F).

11.3.2.6.5 Change in Clearance Because of Compressive Load

When an extruder screw develops pressure in the plastic melt to force it through a die, the pressure at the end of the screw will cause a compressive thrust load on the screw. As a result, the length of the screw will reduce, while at the same time the diameter of the screw will increase. The relative increase in the screw diameter can be expressed as:

$$\frac{\Delta D}{D} = \frac{\Delta L}{2L} = \frac{P}{2E} \tag{11.1}$$

Values of the elastic modulus for several materials are shown in Table 11.7. If the pressure is 34.5 MPa (5000 psi) and the modulus 2.07E5 MPa (30E6 psi), the $\Delta D/D$ = 8.3E–5. Thus, for a 25.4 mm (1 in) screw, the increase in diameter will be 0.0021 mm (0.000083 in). This means that the increase in diameter due to compressive load is quite small compared to the effect of differential thermal expansion. As a result, the effect of radial expansion due to compressive load is likely to be only a minor factor in the chance of the screw locking up in the barrel.

11.3.2.6.6 Conclusions and Recommendations

The analysis above confirms that corrosion-resistant screws do indeed have a greater chance of locking up in an extruder than screws made of regular 4140 steel. The main culprit appears to be the low thermal conductivity of highly corrosion-resistant metals, causing a large temperature difference between the feed throat and the feed section of the screw. The higher screw temperature will cause the screw to expand much more than the feed throat and the barrel, causing the screw to bind. Finite element analysis results confirm that a lower thermal conductivity of the screw leads to higher temperatures in the feed section of the screw.

The reason that screw binding problems often occur with highly corrosion-resistant materials is that these screws are typically used for fluoropolymers that are processed at high temperatures, around 370°C or 700°F. In this case, there are several factors that make screw binding more likely. One, at the high process temperatures there will be a higher temperature difference between the screw and barrel in the feed section. Two, the highly corrosion-resistant material of the screw has a much lower thermal conductivity than 4140 steel and, therefore, will tend to have an even higher temperature difference between screw and barrel in the feed section. Three, the highly corrosion-resistant material of the screw will have a higher coefficient of thermal expansion than 4140 steel and thus expand more.

There are a number of measures that can be taken to reduce the chance of screw binding. They are:

- Screw cooling of the feed section
- Increased temperatures on the feed throat
- Reduced temperatures in the transition section

- Reduced temperatures in the metering section
- Increased clearance in the feed throat region

In most cases, the best way to avoid binding problems is to reduce the screw diameter in the feed section by at least 0.002 mm per mm (0.002 per in) of screw diameter. Because most plastics are fed in pellet form, increasing the flight clearance in the early part of the feed section is most likely not going to have an effect on the performance of the extruder. On the other hand, an increased flight clearance in the feed section will substantially reduce the chance of the screw locking up in the extruder barrel or feed throat.

11.3.3 Polymer Degradation

Polymer degradation is a frequent problem in extrusion. Degradation usually manifests itself as discoloration, loss of volatile components (smoking), or loss of mechanical properties. According to the mode of initiation, the following types of degradation can be distinguished:

1. Thermal
2. Chemical
3. Mechanical
4. Radiation
5. Biological

Degradation processes are generally quite complex; often more than one type of degradation is operational, e. g., thermo-oxidative degradation, thermo-mechanical degradation, etc. This situation is quite similar to wear in extruders, where usually more than one wear mechanism is operational at any one time.

11.3.3.1 Types of Degradation

In extrusion, the first three types of degradation are the most important: thermal, mechanical, and chemical degradation.

11.3.3.1.1 Thermal Degradation

Thermal degradation occurs when a polymer is exposed to an elevated temperature in an inert atmosphere under exclusion of other compounds. The resistance against such degradation depends on the nature and the inherent thermal stability of the polymer backbone. There are three main types of thermal degradation: depolymerization, random chain scission, and unzipping of substituent groups.

Depolymerization or unzipping is a reduction in length of the main chain by sequential elimination of monomer units. Polymers that degrade by this mechanism are polymethylmethacrylate, polyformaldehyde, polystyrene, etc. Polystyrene unzips to

some extent during degradation, although only about 40% is converted to monomer. Random scission occurs in many polyolefins because of their simple carbon chain backbone. Unzipping of substituent groups is an important thermal degradation mechanism since it is the primary breakdown process for polyvinylchloride.

It is often difficult to distinguish between thermal and thermo-chemical degradation because polymers are rarely chemically pure. Impurities and additives can react with the polymeric matrix at sufficiently high temperatures.

11.3.3.1.2 Mechanical Degradation

Mechanical degradation refers to molecular scission induced by the application of mechanical stresses. The stresses can be shear stresses, elongational stresses, or a combination of the two. Mechanical degradation of polymers can occur in the solid state, in the molten state, and in solution. An extensive review of the field of mechanically induced reactions in polymers was published by Casale and Porter [38]. In an extruder, mechanical stresses are applied mostly to the molten polymer.

Various theoretical approaches have been developed to describe mechanical degradation. One of the earlier studies was made by Frenkel [39] and Kauzmann and Eyring [40]. They proposed that linear macromolecules are extended in a shear field in the direction of motion. The strain of the molecules is primarily concentrated at the middle of the chain. No degradation is expected when the degree of polymerization is below a certain critical value. Bueche [41] predicts that entanglements produce preferential tension in the mid-section of macromolecules. Thus, chain scission is more likely to occur in the center of the chain. He also predicts that main chain rupture increases dramatically with increasing molecular weight.

These theoretical considerations suggest that mechanical degradation in polymer melts or solutions is a non-random process, producing new low molecular weight species with molecular weights of one-half, one-fourth, one-eighth, etc., the original molecular weight. Mechanical degradation in polymer melts is essentially always combined with thermal degradation, and possibly chemical degradation, because of the elevated temperature of the melt. When a polymer melt is exposed to intense mechanical deformation, local temperatures can rise substantially above the bulk temperature if the rate of deformation is non-uniform.

Thus, bulk temperature measurements may not properly reflect actual stock temperatures. This is the case in screw extruders where very high local temperatures can occur. The same holds true for high intensity internal mixers. In such devices, pure mechanical degradation is unlikely to occur. Therefore, degradation processes in polymer melts involving mechanical stresses tend to be rather complex.

Some workers have reported that degradation at processing conditions is almost exclusively thermal [43, 44], while others conclude that degradation is mainly mechanical [45, 46]. Most workers, however, deduce that, though the nature of deg-

radation is basically thermal, there is a distinct reduction in the temperature needed for reaction due to the mechanical energy stored within the polymer chains as a result of the mechanical deformation. This corresponds to a shear-induced change in the potential energy function for thermal bond rupture as proposed by Arisawa and Porter [42]. What this means in practice is that the polymer induction time determined under quiescent conditions will be longer than the actual induction time if the polymer is exposed to a mechanical deformation.

Because of the aforementioned complications in mechanical degradation in polymer melts, mechanical degradation can be more easily studied in polymer solutions. Casale and Porter [38] have reviewed most work in this area up to 1978. Work in this area published between 1978 and 1984 is summarized in a later publication [77]. More recent work by Odell, Keller, and Miles [47] describes an elegant technique to continuously monitor the molecular weight distribution (MWD) of a polymer solution undergoing mechanical deformation. They use a cross-slot device to apply a pure elongational flow field to dilute solutions of narrow MWD atactic polystyrene. By measuring birefringence, information was obtained on the MWD of this polymer. They observed repeated breakage of the stretched molecules at their centers, as shown by the MWD before and after mechanical deformation of the polymer; see Fig. 11.19.

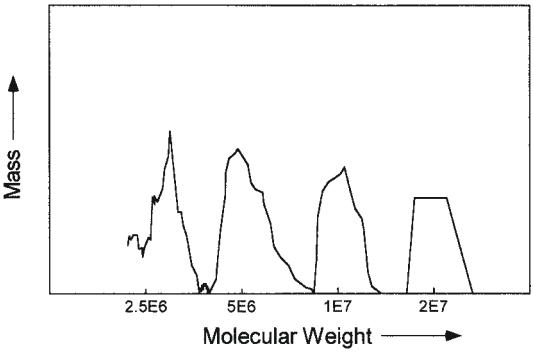
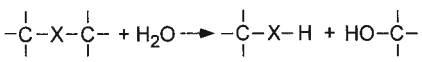


Figure 11.19
MWD after mechanical deformation [47]

11.3.3.1.3 Chemical Degradation

Chemical degradation refers to processes induced under the influence of chemicals in contact with a polymer. These chemicals can be acids, bases, solvents, reactive gases, etc. In many cases, a significant conversion is only observed at elevated temperatures because of high activation energy for these processes.

Two important types of chemical degradation are solvolysis and oxidation. Solvolysis reactions concern the breaking of C–X bonds, where X represents a non-carbon atom. Hydrolysis is an important type of solvolysis; schematically the reaction can be described as follows:



This type of degradation occurs in polyesters, polyethers, polyamides, polyurethanes, and polydialkylsiloxanes. Polymers that tend to absorb water are more likely to undergo hydrolysis. Thus, in the extrusion of polyester and polyamide, it is very important that the polymer be properly dried before extrusion. The stability of polymers against solvolytic agents is important in many applications. Some important polymers that have poor stability against acids and bases at room temperature are PVC, PMMA, PA, PC, PETP, PU, PAN, and POM. Polyolefins and fluoropolymers tend to have good stability against these solvolytic agents.

Oxidative degradation is a very common type of degradation in polymers. In extrusion, oxidation occurs at elevated temperatures; thus, the degradation becomes a thermo-oxidative degradation.

Polymer degradation starts with the initiation of free radicals. Free radicals have a high affinity for reacting with oxygen to form unstable peroxy radicals. The new peroxy radicals will abstract neighboring labile hydrogens, producing unstable hydroperoxides and more free radicals that will start the same process again. This results in an autocatalytic process, i. e., one that self-propagates once the process has started. Under continuous initiation, the reaction rate is accelerated, resulting in an exponential increase conversion with reaction time. The process will stop when a reacting chemical species is depleted or when the propagation is inhibited by reaction products.

The oxidative degradation in polymers is generally combated with the addition of antioxidants. The purpose of the antioxidant is the interception of radicals or prevention of radical initiation during the various phases of a polymer's life: polymerization, processing, storage, and end use. According to their functionality, antioxidants can be classified as primary or secondary antioxidants. Primary antioxidants or chain terminators interrupt chain reactions by tying up free radicals. They are also referred to as free-radical scavengers. Secondary antioxidants, or preventive antioxidants, destroy hydroperoxides. They are also referred to as peroxide decomposers. Primary antioxidants consist primarily of hindered phenols and aromatic amines. These materials tie up polymeric peroxy radicals through hydrogen donation, forming polymeric hydroperoxide groups and relatively stable antioxidant species. Secondary antioxidants consist of various phosphorous or sulfur containing compounds, particularly phosphites and thioesters. These materials reduce hydroperoxides to inert products, thus preventing the proliferation of alkoxy and hydroxy radicals. Selecting an effective antioxidant package is a key factor to the success of a plastic product. Some of the factors that should be considered in the selection of an antioxidant are toxicity, volatility, color, extractability, odor, compatibility, supply, cost, and performance.

11.3.3.2 Degradation in Extrusion

Degradation during the extrusion process will often be a combination of thermal, mechanical, and chemical degradation. Factors that are important in determining the rate of degradation are:

1. Residence time and residence time distribution (RTD)
2. Stock temperature and distribution of stock temperatures
3. Deformation rate and deformation rate distribution
4. Presence of solvolytic agents, oxygen, or other degradation promoting agents
5. Presence of antioxidants and other stabilizers

The first three factors are strongly influenced by the machine geometry and by the operating conditions. The presence of solvolytic agents or oxygen can be influenced by operating conditions, e. g., oxygen can be eliminated from the extruder by putting the feed hopper under a nitrogen blanket. The presence of antioxidants and other stabilizers is part of the material selection process. Proper selection of a stabilizer package is very important; however, the details to determine the right stabilizer package are outside the scope of this book.

11.3.3.2.1 Residence Time Distribution

Knowledge of the residence time distribution (RTD) of an extruder provides valuable information about the details of the conveying process in the machine. The RTD is directly determined by the velocity profiles in the machine. Thus, if the velocity profiles are known, the RTD can be calculated. Various workers have made theoretical calculations of the RTD in single screw extruders [48–50]. Obviously, theoretical calculations of the RTD require knowledge of the velocity profiles in the machine. Thus, the predicted RTD is only as accurate as the velocity profiles that form the basis of the calculations. In single screw extruders, the velocity profiles can be determined reasonably well, although usually a substantial number of simplifying assumptions are made. In other screw extruders, e. g., twin screw extruders, calculation of velocity profiles is rather complex and thus prediction of the RTD more difficult.

Experimental determination of the RTD of an extruder yields information about the conveying process in the extruder. This information is useful in a number of areas, not just to analyze the chance of degradation in the machines. The RTD can be used to analyze the mixing process in an extruder. When an extruder is used as a continuous chemical reactor, the RTD provides important information for process design and process analysis. The RTD also provides a good selection criterion, e. g., an extruder used in profile extrusion should have a narrow RTD and short residence time. Experimental studies of RTD in single screw extruders have been reported by Wolf and White [51], Bigg and Middleman [49], Schott and Saleh [55], Rauwendaal [52], Golba [53], and Kemblowski and Sek [54]. Experimental studies of RTD in twin

screw extruders have been reported by Todd [56], Janssen et al. [57, 58], Rauwendaal [52], Walk [59], and Nichols et al. [60].

The RTD is determined by measuring the output response of a change in input. This is referred to as the stimulus response method as discussed by Levenspiel [61] and Himmelblau and Bischoff [62].

The system is disturbed by a stimulus and the response of the system to the stimulus is measured. Two common stimulus response techniques are the step input response and the pulse input response; see Fig. 11.20.

Other stimuli that can be used are a random input and a sinusoidal input. The response of a step input is an S-shaped curve; see Fig. 11.20 top. The response of a pulse input is a bell-shaped curve; see Fig. 11.20 bottom. The ideal pulse input is of infinitely short duration; such an input is called a delta function or impulse. The normalized response to a delta function is called the C curve. Thus, the total area under the curve equals unity.

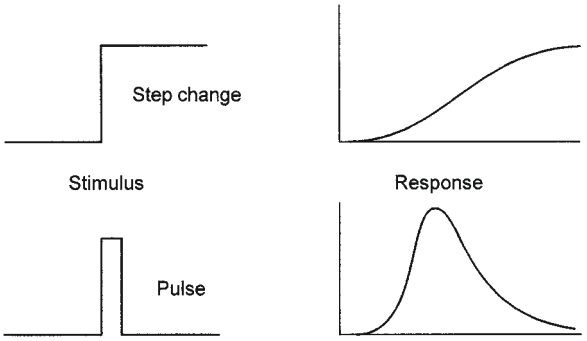


Figure 11.20
Response to step change and pulse input

The definition of RTD functions is due to Danckwerts [63]. The internal RTD function g(t)dt is defined as the fraction of fluid volume in the system with a residence time between t and t + dt.

The external RTD function f(t)dt is defined as the fraction of exiting flow rate with a residence time between t and t + dt. The cumulative internal RTD function G(t) is defined as:

$$G(t) = \int_{o}^{t} g(t)\,dt \tag{11.2}$$

G(t) represents the fraction of fluid volume in the system with a residence time between 0 and t. The cumulative external RTD function is defined as:

$$F(t) = \int_{t_o}^{t} f(t)\,dt \tag{11.3}$$

where t_o is the minimum residence time.

F(t) represents the fraction of exiting flow rate with a residence time equal to or shorter than t. For very long times t, both functions G and F become equal to unity:

$$G(\infty) = F(\infty) = 1 \tag{11.4}$$

The mean residence time $\bar{t}$ is given by the following expression:

$$\bar{t} = \int_0^\infty t\, f(t)\, dt \tag{11.5}$$

The mean residence time is determined by the volume of the machine V, the degree of fill X of the machine, and the volumetric flow rate $\dot{V}$:

$$\bar{t} = \frac{XV}{\dot{V}} \tag{11.6}$$

The relationship between the internal RTD function and the external RTD function is given by:

$$g(t) = \frac{1 - F(t)}{\bar{t}} \tag{11.7}$$

In the flow of a Newtonian fluid through a pipe, the RTD can be calculated rather easily by using the expression for the velocity profile given earlier. The external RTD function is:

$$f(t) = \frac{2t_0^2}{t^3} \qquad \text{for } t \geq t_o \tag{11.8}$$

where the minimum residence time is:

$$t_o = \frac{4\mu L^2}{\Delta P R^2} \tag{11.9}$$

Figure 11.21 shows a typical cumulative RTD curve for a single screw extruder as determined experimentally [52].

The curve is for a 25-mm extruder running at 20 rpm with an output of 2.3 kg/hr. The mean residence time in this example is 5.9 minutes. This type of information is useful because one can easily tell how large a fraction of the material spends how long a time in the machine. For instance, in Fig. 11.21, more than 1% of the material is exposed to a residence time of three times the mean time, i.e., 17.7 minutes! If the induction time of the material at process temperature is less than 17.7 minutes, one can expect more than 1% of the material to be degraded.

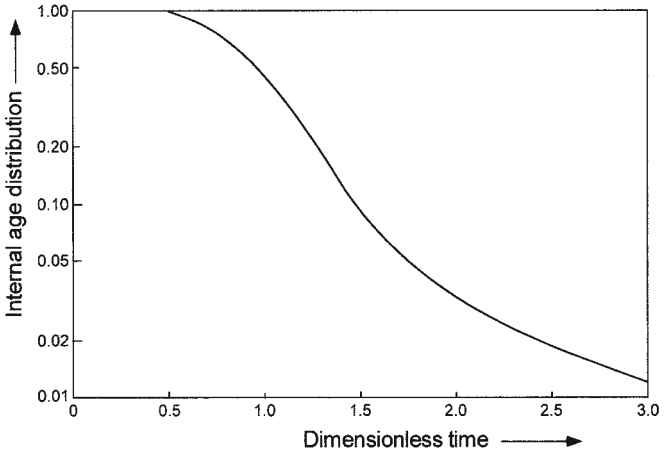


Figure 11.21
RTD for a single screw extruder

Figure 11.22 shows several cumulative RTD curves for an intermeshing counter-rotating twin screw extruder [52].

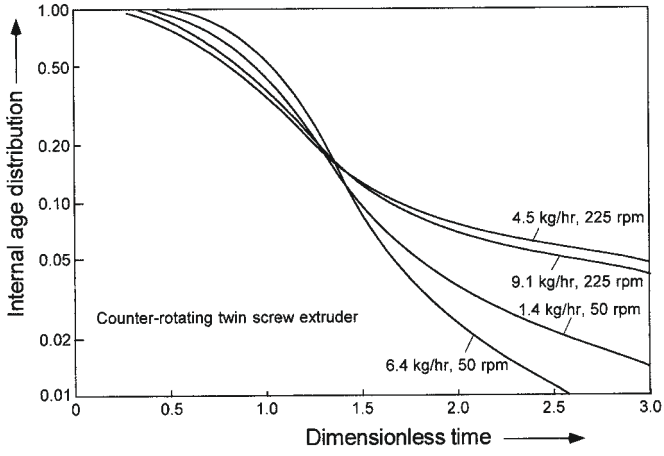


Figure 11.22
RTD for an intermeshing counter-rotating twin screw extruder

It can be seen that the shape of the curve changes substantially when the processing conditions are changed. The narrowest RTD is obtained by running the extruder at low speed and high output. Figure 11.23 shows several cumulative RTD curves for an intermeshing co-rotating twin screw extruder [52].

It is clear that the curves indicate considerable deviations from positive conveying characteristics for the co-rotating twin screw extruder.

A major advantage of these normalized RTD curves is that conveying characteristics of different extruders can be directly compared. From comparison of Figs. 11.21–11.23 it is clear that the conveying characteristics of the single screw extruder are quite positive compared to the two twin screw extruders. This is partially due to the plug flow of the solid bed in the single screw extruder. The solid bed in a twin screw

extruder is not continuous and generally does not extend over a long length of the machine. It should be realized that the RTD is strongly dependent on the screw design and the operating conditions. This point was discussed in some detail by Kemblowski and Sek [54] with regard to single screw extruders and by the author [52] with regard to twin screw extruders.

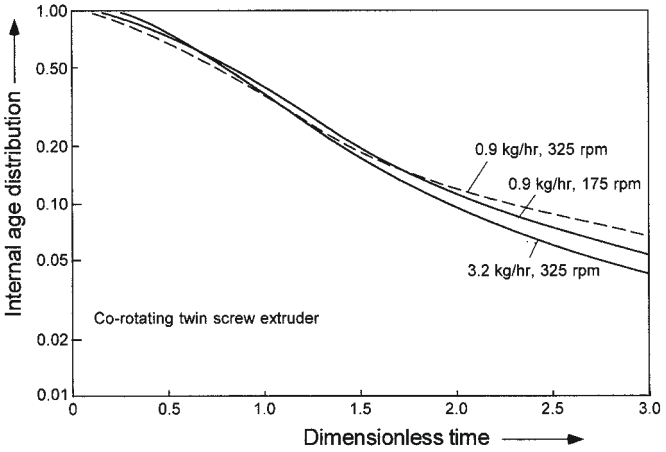


Figure 11.23
RTD for an intermeshing co-rotating twin screw extruder [52]

11.3.3.2.2 Temperature Distribution Simple Calculations

Obviously, the residence time and its distribution only partially determine the chance of degradation in an extruder. The other factors that play an important role are the actual stock temperatures and the strain rates to which the polymer is exposed. The actual stock temperatures and strain rates are closely related. In the extruder, there are two major areas of concern: the screw channel and the flight clearance. Janssen, Noomen, and Smith [65] studied temperature distribution of the polymer melt in the screw channel. Temperature distribution of the polymer right after the end of the screw was measured, for instance, by Anders, Brunner, and Panhaus [66]. The temperature variations in the screw channel at the end of the screw were reported to be less than 5 to 10°C and relatively close to the barrel temperature. More recently, Noriega et al. [145] measured melt temperature distribution with a thermocomb and found temperature variations as high as 20 to 30°C.

The situation in the screw clearance is substantially different from the screw channel. The strain rates in the screw channel are relatively low, but the melt temperature variations can be high [84]. In the screw clearance, however, the strain rates are very high, and the stock temperature increase can also be very high. This can be verified by the following simple analysis. The shear rate in the clearance is approximately the Couette shear rate:

$$\dot{\gamma}_{cl} = \frac{\pi D N}{\delta} \tag{11.10}$$

The corresponding viscous heat generation per unit volume for a power law fluid is:

$$\dot{E}_{cl} = m\left(\frac{\pi DN}{\delta}\right)^{1+n} \tag{11.11}$$

If it is assumed that there is no exchange of heat between the polymer melt and the screw and between the polymer melt and the barrel, the average adiabatic temperature rise can be determined from:

$$\Delta\overline{T}_a = \frac{\dot{E}_{cl}\,\bar{t}_R}{C_p\,\rho} \tag{11.12}$$

where $\bar{t}_R$ is the average residence time of the polymer melt in the flight clearance. The average residence time in the flight clearance is approximately:

$$\bar{t}_R = \frac{2w}{\pi DN \sin\varphi} \tag{11.13}$$

Combining Eqs. 11.11, 11.12, and 11.13, the average adiabatic temperature rise in the clearance can be written as:

$$\Delta\overline{T}_a = \frac{2mw(\pi DN)^n}{\rho \sin\varphi C_p\,\delta^{1+n}} \tag{11.14}$$

The average temperature rise is directly proportional to the consistency index m and the tangential flight width w/sinφ. The temperature rise is strongly dependent on the radial clearance δ, the power law index of the polymer melt n, and the screw speed N. Figure 11.24 shows the effect of flight clearance δ and the power law index n for a 114-mm (4.5-in) extruder running at 100 rpm; the specific heat is 2250 J/kg°C, the melt density is 900 kg/m^3, and the consistency index is 10^4 Pa·s^n.

It is clear that the adiabatic temperature rise in the flight clearance can be very high. However, the actual temperature rise will be less than the adiabatic temperature rise because there will be transfer of heat to the screw and to the barrel. In reality, the thermal boundary conditions at the barrel and the flight land will be somewhere between adiabatic and isothermal.

The temperature rise in the clearance can be substantially reduced by simply reducing the flight width and increasing the flight helix angle. These same measures will also substantially reduce the power consumption of the extruder. Thus, proper design of the screw flight is of great importance when it comes to reducing power consumption and reducing the chance of degradation in the extruder.

Another reason that the flight clearance is so important in degradation processes occurring in the extruder is the fact that, in addition to high stock temperatures, the polymer melt is exposed to very high strain rates, both elongational and shear. As

discussed earlier, this causes a flow-induced change in the potential energy function for thermal bond rupture. Thus, the degradation will be more severe than it would be based on just the effect of temperature. Obviously, another important point is to eliminate dead spots in the screw design and in the die design. Hang-up of material can be very detrimental and should be avoided if at all possible. For instance, fluted mixing sections with a 90° helix angle should not be used with polymers that have a tendency to degrade because such mixing sections have stagnating regions.

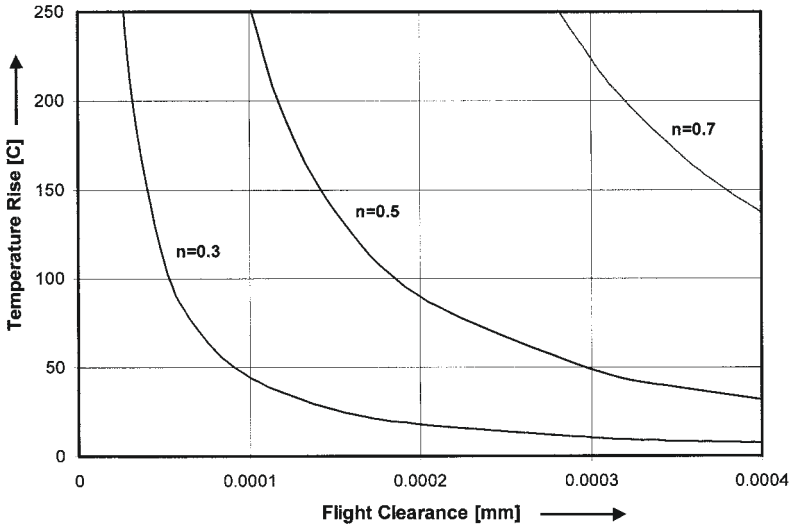


Figure 11.24 Adiabatic temperature rise versus flight clearance

The values of the temperature increase in the flight clearance calculated with Eq. 11.14 are surprisingly high, particularly considering the very short residence time of the polymer in the flight clearance, which is usually in the order of 0.1 s. Obviously, in reality the temperature rise will not be as high as the adiabatic temperature rise because there will be exchange of heat with the screw and with the barrel.

The lowest temperature rise will occur in the extreme case that both screw flight surface and barrel surface can be maintained at constant temperature, i.e., isothermal boundary conditions. This situation was analyzed by Meijer, Ingen Housz, and Gorissen [67] with the primary purpose to determine the thermal development length. They assumed that the clearance flow is dominated by drag flow in the tangential direction. The thermal development length for the Newtonian case was found to be approximately 0.36 N_{pe}, where N_{pe} is the Peclet number. Thus, the length required for thermal development can be written as:

$$L_t = \frac{0.36\, v_b\, \delta^2}{\alpha} \tag{11.15}$$

where α is the thermal diffusivity.

The thermal development length is directly proportional to the barrel velocity v_b (and thus the screw speed) and to the radial clearance squared. With thermal diffusivity values of about 10^{-7} m^2/s, the thermal entrance length will be the same order of magnitude as the tangential flight width when the clearance has the normal design value ($\delta \cong 0.001$ D). Thus, the temperature profile at the exit of the flight clearance will be very close to the fully developed temperature profile. The fully developed temperature profile for the isothermal case can be written as [67]:

$$T_i = \frac{\mu v_b^2}{2k}\left(\frac{y}{\delta} - \frac{y^2}{\delta^2}\right) + \frac{(T_b - T_s)\,y}{\delta} + T_s \tag{11.16}$$

The maximum temperature T_{max} that can develop in the isothermal case is:

$$T_{max} = \frac{\mu v_b^2}{8k} + \frac{1}{2}T_b + \frac{1}{2}T_s \tag{11.17}$$

The first term to the right of the equal sign represents the viscous temperature rise. If the viscosity in the flight clearance is written as a power law fluid the viscous temperature rise can be written as:

$$\Delta T_{viscous} = \frac{m\, v_b^{n+1}}{8\, k\, \delta^{n-1}} \tag{11.18}$$

The viscous temperature rise with isothermal conditions is plotted against the flight clearance in Fig. 11.25. The isothermal viscous temperature rise data were calculated for a 114 mm extruder running at 100 rpm with a polymer melt with a consistency index of $m = 10^4$ $Pa \cdot s^n$ and a thermal conductivity $k = 0.25$ $J/m \cdot s \cdot °C$.

It is interesting to see that the isothermal viscous temperature rise increases with clearance while the adiabatic temperature rise decreases with clearance. For both thermal boundary conditions, the temperature rise increases strongly with the power law index of the polymer melt. This indicates that highly shear thinning polymers (low power law index) will have much lower melt temperature rise in the flight clearance than weakly shear thinning polymers.

In reality, true isothermal conditions may not be achieved because the high heat fluxes at the screw and barrel interface required to maintain isothermal conditions may not be physically possible. Thus, the actual maximum stock temperature in the clearance will be somewhere between the adiabatic and the isothermal case. It should be noted that the expressions for the melt temperature rise are valid only for purely viscous fluids with a temperature independent viscosity in pure drag flow. Obviously, for a temperature dependent fluid the melt temperature rise will be reduced relative to the temperature independent fluid. Also, the pressure gradient in the flight clearance will affect the velocities and temperatures. With pressure

normally reducing from the pushing to the trailing flight flank the pressure gradient in the flight clearance will usually be negative. This will reduce the melt temperature rise in the flight clearance relative to the pure drag flow case.

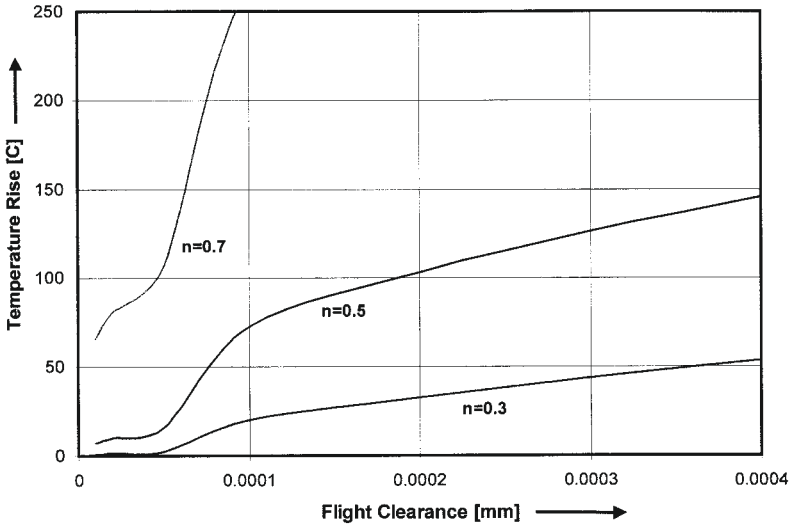


Figure 11.25 Isothermal viscous temperature rise vs. flight clearance

The melt temperature rise values in the flight clearance for both adiabatic and isothermal conditions are shown in Fig. 11.26.

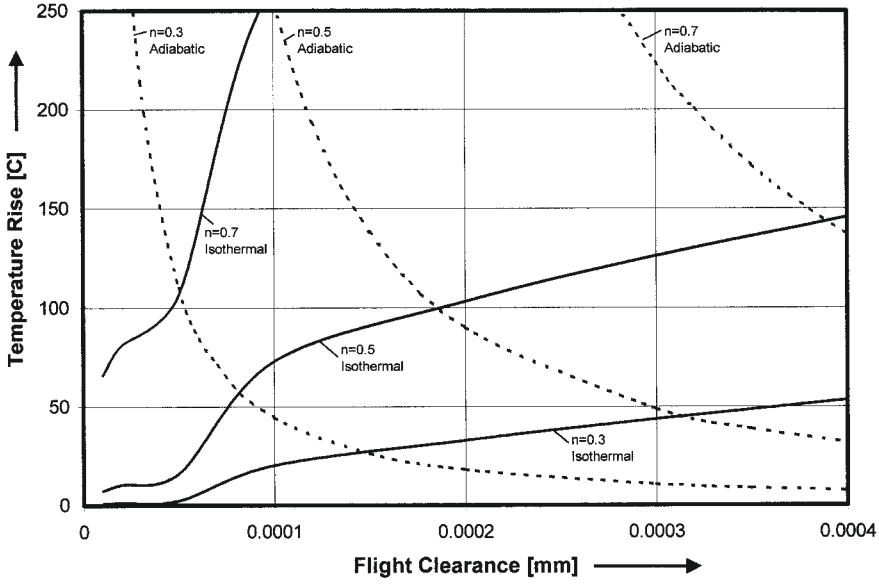


Figure 11.26 Adiabatic and isothermal melt temperature rise vs. flight clearance

At small values of the flight clearance the adiabatic temperature rise is much greater than the isothermal temperature rise. However, at some clearance value the adiabatic and isothermal curves intersect. At clearance values higher than the intersection the isothermal temperature rise is actually greater than the adiabatic temperature rise. For low values of the power law index the crossover clearance (where $\Delta T_{adiabatic} = \Delta T_{isothermal}$) is about 0.001 D, which is a typical flight clearance in single screw extruders. At higher values of the power law index the crossover clearance becomes larger.

The isothermal melt temperature rise values for large values of the flight clearance ($\delta > 0.001$ D) are probably unrealistic due to the fact that the thermal development length will be greater than the width of the flight; see Eq. 11.15. In this case, fully developed temperatures cannot be reached in the flight clearance, and Eqs. 11.17 and 11.18 will not yield accurate values for the melt temperature rise. Figure 11.26 shows that melt temperature rise values from about 25°C to over 100°C can be expected in a typical flight clearance ($\delta = 0.001$ D) of a 114 mm extruder running at 100 rpm.

11.3.3.2.3 Temperature Distribution Numerical Calculations

Winter [30] has performed numerical calculations of the developing temperature profile in the flight clearance for power law fluids. He assumed isothermal conditions at the barrel wall and adiabatic conditions at the screw flight surface. These assumptions are considerably more realistic than the purely adiabatic case or the purely isothermal case, although a better boundary condition would probably be a prescribed maximum heat flux. Winter calculates a typical maximum temperature increase of about 150°C. This value is closer to the maximum temperature rise in the adiabatic case than the maximum temperature rise in the isothermal case. These analyses indicate that the temperature rise in the flight clearance can be quite significant and can play a very important role in degradation in extruders.

Rauwendaal [84] developed a finite element method (FEM) program to determine temperature profiles in the melt conveying zone of extruders. This FEM program allows the calculation of three-dimensional velocities and temperatures at any point in the screw channel. The program is based on a 2½-D analysis, which means that the velocities are assumed to change little in the down-channel direction.

The temperature field is shown in Chapter 12, Fig. 12.7. The barrel surface is set at 175°C and the screw surface is taken as adiabatic (zero heat flux). The melt temperatures at any point in the channel are considerably higher than the barrel temperature. The highest temperatures occur at about two-thirds of the channel height; this is where the cross-channel velocities are the lowest. The highest temperatures are about 31°C above the barrel temperature. This agrees well with experimental results published earlier [83].

The isotherms in the bottom half of the screw channel clearly show the effect of cross-channel circulation on the temperature field. In fact, the lower temperatures at the flight flanks and the bottom of the screw channel are a direct result of the re-circulation in the channel. The re-circulation causes the low-temperature melt close to the barrel surface to move close to the screw surface, keeping the melt temperatures low in this region.

It is interesting to note that the melt temperatures in the flight clearance are lower than in the screw channel. Since the shear rate in the flight clearance is higher than it is anywhere else, one might expect the highest temperatures to occur there as well. The key to the low temperatures in the clearance is the fact that the clearance is quite thin. The high level of viscous heat generated in the clearance is efficiently conducted away to the barrel because of its close proximity. This effect was confirmed by results of numerical analysis by Pittman [86] and an analytical solution of non-isothermal drag flow by Rauwendaal and Ingen Housz [87]. Further confirmation was provided by experimental work on leakage flow [83].

When the flight clearance is increased under the same conditions, the major change occurs in the temperature field as shown in Figure 11.27. The temperatures in the lower portion of the channel increase significantly with increasing clearance. This is due to a thicker, relatively stagnant layer of polymer melt at the barrel surface. This insulating, stagnant layer inhibits heat transfer between the material in the screw channel and the barrel. These results agree well with experimental work [83].

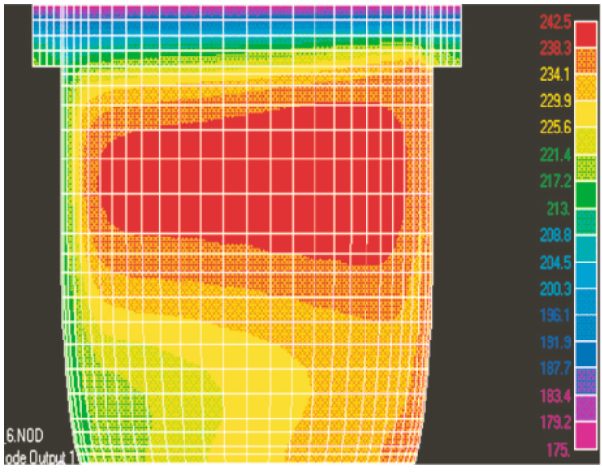


Figure 11.27
Melt temperature distribution with increased flight clearance

A larger flight clearance not only increases the maximum temperature in the channel, but the size of the high-temperature region also expands considerably. This is due to a weaker re-circulating flow with a large clearance. With a large clearance, the flow rate through the clearance is large, causing a corresponding reduction in the re-circulating flow. A large flight clearance reduces melt temperature control.

The high melt temperatures close to the screw surface can lead to degradation. This is because the residence times are longest at the screw surface. The combination of high temperatures and long residence times at the screw surface with large flight clearance make degradation more likely.

11.3.3.2.4 Conclusions from Finite Element Analysis

FEA can be very helpful in analyzing details of flow and heat transfer inside extruders that are very difficult to determine on operating extruders. FEA can predict three-dimensional velocity profiles in screw extruders. In addition, the pressure and temperature fields can be determined.

When the viscous heat generation is important, high melt temperature regions form in the center of the channel. This is due to the thermal convection caused by the recirculating flow pattern in the screw channel. Thus, the melt temperature non-uniformities that form are inherent to the flow in single screw extruders.

When the flight clearance increases, the melt temperatures inside the screw channel can rise considerably. Also, the high-temperature region expands towards the root of the screw. This can have serious consequences, because the residence times at the screw root are quite long and this can easily lead to degradation of the plastic.

The results indicate that it is very important to make sure that the flight clearance between screw and barrel is within reasonable limits. In practice, the radial flight clearance should be no more than 0.003 D, with D being the diameter of the screw. Also, the inherently non-uniform melt temperatures make distributive mixing sections almost indispensable.

The thermal development length increases with the screw diameter as shown in Fig. 11.28. For small diameters ($D \leq 60$ mm), the thermal development time is about 10 to 20 s. For larger diameters ($D > 100$ mm), the thermal development time is greater than 30 s. Considering that a typical residence time in the melt conveying zone of an extruder is about 15 to 20 s, it is clear that in large extruders fully developed temperature conditions will not always be achieved in the extruder. Fully developed conditions may occur at low screw speed; however, at high screw speed it is unlikely that fully developed temperatures can be reached within the length of the extruder.

The increases in melt temperature and the temperature non-uniformities in large extruders are greater than in small extruders. This is due to the fact the surface-to-volume ratio becomes less favorable with increasing screw diameter. As a result, in large extruders it is more difficult to keep the melt temperatures low and uniform. Of course, this is well known in practice, and this is the reason that large extruders generally run at lower screw speed than small extruders. Also, it is more important to incorporate good mixing along the extruder screw when the screw diameter is large and when the extruder is operated at high screw speed.

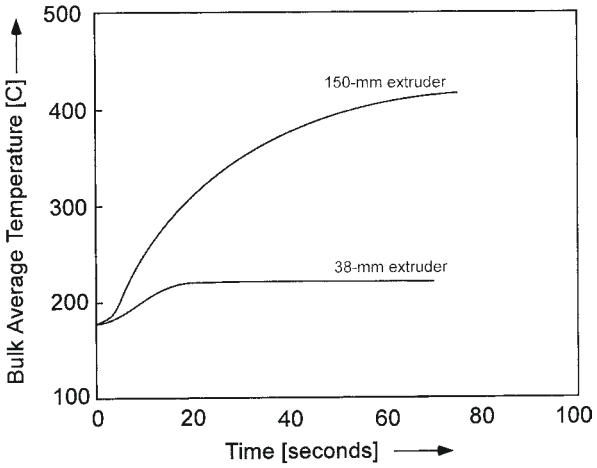


Figure 11.28
Evolution of bulk average temperature over time

11.3.3.2.5 Reducing Degradation

The following changes to the process can reduce the chance of degradation in the extruder:

1. Reduce residence time and achieve a narrow RTD
2. Reduce stock temperature and avoid high peak temperatures
3. Eliminate degradation-promoting substances

The residence time can generally be reduced by designing the screw for maximum throughput. Low stock temperatures and reduced peak temperatures can be obtained by designing the screw for minimum specific energy consumption. Further, stagnating regions should be avoided if at all possible. Thus, the design of both the screw and die has to be made as streamlined as possible.

In some special cases, it may be beneficial to design an extruder screw for low output and small inventory. An example of such a case can be a medical extrusion of a very small catheter where production occurs at a screw speed of 2 rpm. At such a low screw speed, the average residence time in the extruder will range from 30 to 60 minutes, and degradation is likely to occur at such long residence times. In such a case, it is beneficial to design an extruder screw that has low output per revolution and a small total channel volume. This can be achieved by reducing the flight helix angle, reducing the channel depth, increasing the flight width, and increasing the number of flights. With such a low output, the screw speed may increase from 2 to 10 rpm and the average residence reduce from 60 minutes to less than 10 minutes.

High stock temperatures are likely to be a problem in extrusion operations where the extruder is run at high screw speed and where the polymer melt viscosity is high. The main screw design variable that affects viscous heating is the channel depth. Increasing the channel depth will reduce the shear rate and thus the viscous heating. There are limits to how deep the screw can be cut. One limit is the physical

strength of the screw. Another limit is the solids conveying and melting capacity of the screw. It is not possible to increase the depth of the screw channel to the point where the melt conveying rate exceeds the melting rate. This is a case where a barrier type extruder screw can be useful.

One of the most demanding situations for controlling melt temperature is in foam extrusion. In the secondary extruder of a tandem foam extrusion line, the cooling screw is usually made with very deep channels to minimize viscous heating. Also, multiple (usually six) thin flights with a large helix angle are used to increase the heat transfer capability of the screw.

If degradation occurs by a thermo-oxidative mechanism, air should be excluded from the extruder. This can be done by putting a nitrogen blanket on the feed hopper, vent port, or at the die, depending on where the air is introduced. If degradation occurs by hydrolysis, moisture has to be excluded from the process. If degradation occurs by a chemical reaction with the metal surfaces of screw and barrel, a non-reacting material of construction has to be selected for the screw and barrel.

11.3.4 Extrusion Instabilities

Variations in extruder performance is perhaps the most frequent problem encountered in extrusion. One possible reason for the frequent occurrence of instabilities is the fact that they can have a large number of causes, some of which are:

- Bulk flow problems in the feed hopper
- Solids conveying problems in the extruder
- Insufficient melting capacity
- Solid bed breakup
- Melt temperature non-uniformities in the die
- Barrel temperature fluctuations
- Screw temperature fluctuations
- Variations in the take-up device
- Melt fracture/shark skin
- Variations in screw speed
- Barrel wear/screw wear
- Insufficient mixing capacity
- Very low diehead pressure
- Insufficient pressure-generating capacity

Proper instrumentation is vitally important to be able to diagnose a problem quickly and accurately as discussed in Chapter 1. A prerequisite for stable extrusion is a good extruder drive, good temperature control system, good take-up device, and

most importantly, a good screw design. Probably more instabilities result from improper screw design than from any other cause. However, a change in screw design is often only considered as the very last option.

The extruder drive should be able to hold the screw speed constant to about 0.1% or better; the same holds true for the take-up device. However, this is not always the case on actual extrusion lines. The extruder should be equipped with some type of proportioning temperature control, preferably a PID-type control or better. On-off temperature control is inappropriate for most extrusion operations.

11.3.4.1 Frequency of Instability

Various workers [68, 69] have classified extrusion instabilities based on the time frame in which they occur. The frequency of the instability is often an indication of the cause of the problem. Most of the earlier works distinguished only three or four types of instabilities based on the frequency. However, it is probably more appropriate to distinguish at least five types of instabilities:

1. High-frequency instabilities occurring faster than the frequency of screw rotation
2. Screw frequency instabilities occurring at the same rate as the frequency of screw rotation
3. Low-frequency instabilities, about 5 to 10 times slower than the frequency of screw rotation
4. Very slow fluctuations occurring at a frequency of at least several minutes
5. Random fluctuations

11.3.4.1.1 High-Frequency Instabilities

High-frequency instabilities are often associated with die flow instabilities, such as melt fracture, shark skin, or draw resonance. They can also be caused by drive problems, melt temperature non-uniformities, or vibration.

Shark Skin

Shark skin manifests itself as a regular ridged surface distortion, with the ridges running perpendicular to the extrusion direction. A less severe form of shark skin is the occurrence of matness of the surface, where the glossy surface cannot be maintained. Shark skin is generally thought to be formed in the die land or at the exit. It is dependent primarily on the temperature and the linear extrusion speed. Factors such as shear rates, die dimensions, approach angle, surface roughness, L/D ratio, and material of construction seem to have little or no effect on shark skin.

The mechanism of shark skin is postulated to be caused by the rapid acceleration of the surface layers of the extrudate when the polymer leaves the die. If the stretching rate is too high, the surface layer of the polymer can actually fail and form the char-

acteristic ridges of the shark skin surface [96]. High-viscosity polymers with narrow molecular weight distribution (MWD) seem to be most susceptible to shark skin instability [97, 98].

The shark skin problem can generally be reduced by reducing the extrusion velocity and increasing the die temperature, particularly at the land section. There is some evidence that running at very low temperatures can also reduce the problem [99]. Selection of a polymer with a broad MWD will also be beneficial in reducing shark skin. Using an external lubricant can also reduce the problem. This can be done by using an additive to the polymer or by coextruding a thin, low-viscosity outer layer.

Melt Fracture

Melt fracture is a severe distortion of the extrudate, which can take many different forms: spiraling, bambooing, regular ripple, random fracture, etc.; see Chapter 7, Fig. 7.108. It is not a surface defect like shark skin, but is associated with the entire body of the molten extrudate. However, many workers do not distinguish between shark skin and melt fracture, but lump all these flow instabilities together under the term melt fracture. There is a large amount of literature on the subject of melt fracture (e. g., [100–112]); however, there is no clear agreement as to the exact cause and mechanism of melt fracture. It is quite possible that the mechanism is not the same for different polymers and/or different flow channel geometries [113]. Linear polymers tend to develop an instability of the shear flow in the die land, while branched polymers tend to develop instabilities in the converging region of the die flow channel.

However, there is relatively uniform agreement that melt fracture is triggered when a critical wall shear stress is exceeded in the die. This critical stress is in the order of 0.1 to 0.4 MPa (15 to 60 psi). A number of mechanisms have been proposed to explain melt fracture. Some of the more popular ones are:

- Critical elastic deformation in the entry zone
- Critical elastic strain
- Slip-stock flow in the die

The effect of the entry zone has been demonstrated by many workers. In general, the smaller the entry angle, the higher the deformation rate at which instability occurs. Gleissle [114] has proposed a critical elastic strain as measured by recoverable strain. Based on measurements with 11 fluids, he proposed the existence of a critical value of the ratio of first normal stress difference to the shear stress, the average value being 4.63 for 11 widely different fluids with a standard deviation of about 5%. Much larger differences were found in the critical shear stress; the average being 3.7E5 Pa with a standard deviation of about 55%. In 1961, Benbow, Charley, and Lamb [111, 115] introduced the slip-stick mechanism to explain flow instability and extrudate distortion. Above a certain critical stress, the polymer melt is believed to

experience intermittent slipping due to lack of adhesion between the melt and the die wall in order to relieve excessive deformation energy absorbed because of flow through a die. A large number of workers have observed slippage by various techniques.

More recent work by Utracki and Gendron on pressure oscillations in extrusion of polyethylenes [116] led them to conclude that the pressure oscillation does not seem to be related to elasticity or slip. They conclude that the parameter responsible for pressure oscillations is the critical strain (Hencky) value ε_c of the melt. For LLDPE, $\varepsilon_c < 3$, for HDPE, $\varepsilon_c < 2$, while for LDPE, $\varepsilon_c > 3.5$. The instability seems to be based on the inability of the polymer melt to sustain levels of strain larger than the critical strain.

Streamlining the flow channel geometry has been found to reduce the tendency for melt fracture in branched polymers. Increased temperatures, particularly at the wall of the die land, enable higher extrusion rates before melt fracture appears. The critical wall shear stress appears to be relatively independent of the die length, radius, and temperature. The critical stress seems to vary inversely with molecular weight, but seems to be independent of MWD. Certain polymers exhibit a super-extrusion region, above the melt fracture range, where the extrudate is not distorted [117]. This process is particularly advantageous with polymers that melt fracture at relatively low rates, such as FEP. In super-extrusion, the polymer melt is believed to slip relatively uniformly along the die wall. The occurrence of slip in extruder dies has been studied by a number of investigators, e.g., [118, 119]. However, it is still not clear whether the slip is actual loss of contact of polymer melt and metal wall or whether it is failure of a thin polymeric layer very close to the metal surface.

The melt fracture problem can be reduced by streamlining the die, increasing the temperature at the die land, running at lower rates, reducing the MW or the polymer melt viscosity, increasing the cross-sectional area of the exit flow channel, or by using an external lubricant. In some instances, the melt fracture problem can be solved by going to super-extrusion; this process is used particularly often in the wire coating industry where high line speeds are quite important for economic production.

Draw Resonance

Draw resonance occurs in processes where the extrudate is exposed to a free surface stretching flow, such as blown film extrusion, fiber spinning, and blow molding. It manifests itself in a regular cyclic variation of the dimensions of the extrudate. An extensive review [113] and an analysis [120] of draw resonance were done by Petrie and Denn. Draw resonance occurs above a certain critical draw ratio while the polymer is still in the molten state when it is taken up and rapidly quenched after take-up.

Draw resonance will occur when the resistance to extensional deformation decreases as the stress level increases. The total amount of mass between die and take-up may vary with time because the take-up velocity is constant but the extrudate dimensions are not necessarily constant. If the extrudate dimensions reduce just before the take-up, the extrudate dimensions above it have to increase. As the larger extrudate section is taken up, a thin extrudate section can form above it; this can continue for a long time. Thus, a cyclic variation of the extrudate dimensions can occur. Draw resonance does not occur when the extrudate is solidified at the point of take-up, because the extrudate dimensions at the take-up are then fixed [121, 122]. Isothermal draw resonance is found to be independent of the flow rate. The critical draw ratio for almost Newtonian fluids such as nylon, polyester, polysiloxane, etc. is approximately 20. The critical draw ratio for strongly non-Newtonian fluids such as polyethylene, polypropylene, polystyrene, etc. can be as low as 3 [123]. The amplitude of the dimensional variation increases with draw ratio and drawdown length.

Various workers have performed theoretical studies of the draw resonance problem by linear stability analysis. Pearson and Shah [124, 125] studied inelastic fluids and predicted a critical draw ratio of 20.2 for Newtonian fluids. Fisher and Denn [126] confirmed the critical draw ratio for Newtonian fluids. Using a linearized stability analysis for fluids that follows a White-Metzner equation, they found that the critical draw ratio depends on the power law index n and a viscoelastic dimensionless number. The dimensionless number is a function of the die take-up distance, the tensile modulus, and the velocity at the die. Through their analysis, Fisher and Denn were able to determine stable and unstable operating regions. In some instances, draw resonance instability can be eliminated by increasing the draw ratio, although under most operating conditions, draw resonance is eliminated by reducing the draw ratio.

White and Ide [127–130] demonstrated experimentally and theoretically that polymers whose elongational viscosity increases with time or strain do not exhibit draw resonance, but undergo cohesive failure at high draw ratios. A polymer that behaves in such a fashion is LDPE. Polymers whose elongational viscosity decreases with time or strain do exhibit draw resonance at low draw ratios and fail in a ductile fashion at high draw ratios. Examples of polymers that behave in such a fashion are HDPE and PP. Lenk [131] proposed a unified concept of melt flow instability. His main conclusions are that all flow instabilities originate at the die entrance and that melt fracture and draw resonance are not distinct and separate flow phenomena; both are caused by elastic effects that have their origin at the die entrance. Lenk's analysis, however, is purely qualitative and does not offer much help in the engineering design of extrusion equipment or in determining how to optimize process conditions to minimize instabilities.

11.3.4.1.2 Screw Frequency Instabilities

Screw frequency instabilities occur to a small extent in essentially every extrusion operation. This can be caused by variation in the intake of polymer from the feed hopper to the feed housing when the flow is interrupted every time the flight passes by the feed opening. This can cause a cyclic pressure change that can be detected if the extruder has accurate pressure readout. One way to reduce the unsteady intake of polymer from the feed hopper is to use a double-flighted screw geometry in the feed section. Generally, a better solution is to change the shape of the feed opening. According to Wheeler [132], the screw frequency instability is more likely to occur at very low diehead pressures.

Screw frequency variations can also be caused by the pressure difference across the screw flight. This pressure difference is responsible for the re-circulating flow in the cross-channel direction. When pressure is measured along the screw or at the very end of the screw, the pressure pattern will have a sawtooth shape; see Fig. 11.29.

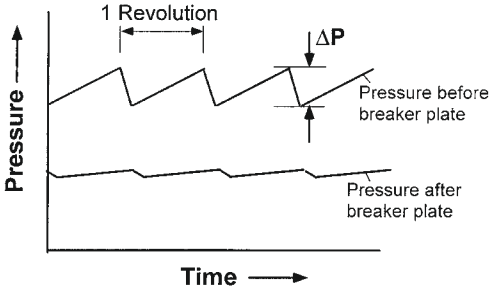


Figure 11.29
Pressure variation over time ("screw beat")

In most cases, the major cause of screw frequency instabilities will be the pressure difference between the leading and trailing edge of the flight in the pump section. This pressure fluctuation is often called "screw beat." This pressure difference is inherent to the conveying process. It occurs even if no pressure is developed in the pump section because this pressure difference is a drag-induced pressure difference. If the flight clearance can be neglected the pressure difference ΔP across the screw flight is:

$$\Delta P = \frac{6\mu v_{bx} W}{p H^2} \cong \frac{6\mu\pi^2 D^2 N \sin^2\varphi}{p H^2} \tag{11.19}$$

where μ is the viscosity, D the screw diameter, N the rotational speed, φ the screw flight helix angle, p the number of parallel flights, and H the channel depth.

This expression is valid for a Newtonian fluid. The pressure difference increases with viscosity, diameter, screw speed, and helix angle; the pressure difference reduces with channel depth. When the helix angle increases from 17.5° to 25.0°, the pressure difference will double. Thus, large helix angle screws will exhibit more screw frequency pressure fluctuations than small helix angle screws. The screw

frequency pressure fluctuation can be reduced by placing a multi-flighted screw section at the end of the screw, such as a Saxton [95] or CRD [88–94] mixing section as shown in Fig. 11.30. A multi-flighted mixing section at the end of the screw will reduce the amplitude of the pressure fluctuation but increase its frequency.

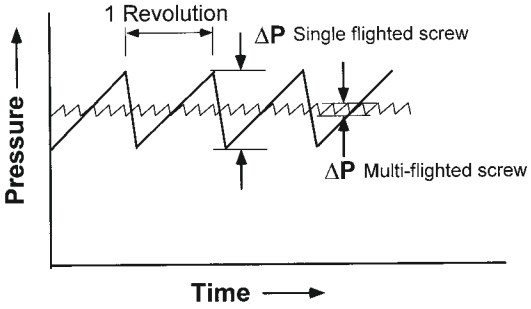


Figure 11.30
Pressure fluctuation with single- and multi-flighted screws

It should be noted that these pressure fluctuations will be most severe at the very end of the screw, but they will reduce with increasing distance from the screw because the polymer melt is slightly compressible. Thus, the actual pressure fluctuation will be very much dependent on the location of the pressure transducer. When a breaker plate is used, the pressure fluctuation will reduce significantly because the breaker plate will largely break up the flight-induced pressure fluctuation as shown in Fig. 11.29.

Obviously, the screw frequency pressure fluctuation will be problematic when the value of ΔP is large relative to the actual diehead pressure. This will occur when the diehead pressure is low, as pointed out by Wheeler [68], when the polymer melt viscosity is high, the screw diameter large, the screw speed high, the helix angle or pitch large, or when the channel depth is shallow.

11.3.4.1.3 Low-Frequency Instabilities

Low-frequency instabilities have been associated with solid bed breakup [69, 70]. Fenner et al. have attempted to theoretically predict solid bed breakup [69]. They proposed that solid bed breakup is due to acceleration of the solid bed in the plasticating zone of the extruder and claimed that no solid bed acceleration occurs in the absence of a melt film between the solid bed and the screw. In practice, formation of a melt film can be avoided by cooling the screw [71]. Earlier, Maddock [72] found that screw cooling helped in reducing surging. The most likely reason that screw cooling reduces surging is that it reduces the throughput rate by a substantial amount, about 20% in the experiments of Fenner and Edmondson [71]. Therefore, the melting process will be completed over a shorter axial distance, reducing the stresses acting on the solid bed. Solid bed breakup is also more likely to occur on screws with a high compression ratio. Fenner et al. [69, 71] found solid bed breakup with high compression ratio screws (3:1 and 4:1), but did not find solid bed breakup

with a low compression ratio screw (2.25:1). A low compression ratio screw would seem a better solution than a high compression ratio screw with screw cooling. Another method by which formation of a melt film on the screw surface can be avoided is by using barrier screw geometry.

Fluctuations occurring over about 10 to 30 s can be caused by temperature fluctuations along the extruder barrel. The temperature fluctuations may not be noticeable from the temperature readouts. This can be due to the slow response of many temperature sensors and because the sensors are often located a considerable distance from the polymer/metal interface. However, if the actual temperature at the interface fluctuates, there will be a corresponding fluctuation in the flow rate. In time-proportioning temperature control systems, power is added or removed at relatively short intervals, typically about 15 to 20 s. These bursts of heating or cooling energy will cause short-term changes in the polymer/metal interface temperature with corresponding variations in throughput rate. The variation in throughput can be as much as 5 to 10%. Therefore, from a stability point of view, the true proportioning temperature control is significantly better than the time-proportioning temperature control.

Throughput variations caused by wall temperature changes have been described by Gitschner and Lutterbeck [76]. They were able to show a very clear correlation between the on-and-off cycling of barrel cooling and the diehead pressure fluctuations. They also found that the pressure fluctuations correlated very closely with the resulting throughput fluctuations. It should be clear that these temperature-induced throughput fluctuations could be considerably more severe in the case of on-off temperature control.

11.3.4.1.4 Very Slow Fluctuations

Very slow fluctuations are often associated with poor temperature control, changes in ambient conditions (room temperature, relative humidity), plant voltage variation, and similar causes. A steady, slow reduction in output is often caused by build-up of contaminants on the screen pack.

11.3.4.1.5 Random Fluctuations

Random fluctuations are often associated with irregular feeding. Maddock [72] discussed a case where the extruder performance was very sensitive to the level of fill in the feed hopper. Random fluctuations can also result from a combination of cyclic fluctuations. Figure 11.31 shows the pattern of a regular sinusoidal variation.

Figure 11.32 shows a combination of three sinusoidal variations with different frequency and amplitude. This variation appears to be random; however, it is made up of three different components with each component being a very regular sinusoidal variation.

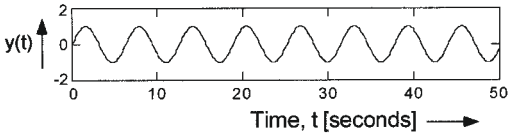


Figure 11.31
Regular sinusoidal variation

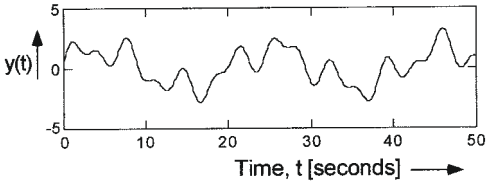


Figure 11.32
Combination of three sinusoidal variations

This situation frequently occurs in extrusion because in many cases the process is affected by variation from different sources. The variation from different sources will typically have different frequencies and amplitudes. Obviously, the more sources of variation act on the process, the more complicated and random the information from the process will tend to be.

The pattern of variation as shown in Fig. 11.32 is often detected by measuring melt pressure. Obviously, the response time of the measurement has to be short enough to capture high-frequency variations occurring in the process. Fast Fourier Transform (FFT) analysis can be used to analyze a complex signal and decompose it into the base frequencies. As a result, FFT is a powerful tool in troubleshooting complex extrusion problems. Becker et al. [133, 134] used FFT of melt pressure signals to analyze extrusion instabilities. Reinhard et al. [144] describe the application of spectral analysis to surging problems in extrusion.

11.3.4.2 Functional Instabilities

Another method of classifying instabilities is by the functional zone in which the instability originates. Thus, the following instabilities can be distinguished:

- Solids conveying instabilities
- Plasticating instabilities
- Melt conveying instabilities
- Devolatilization instabilities
- Mixing instabilities
- Die forming instabilities

We will discuss each of these in detail.

11.3.4.2.1 Solids Conveying Instabilities

Solids conveying instabilities have three major causes: flow problems in the feed hopper, internal deformation of the solid bed in the screw channel, and insufficient friction against the barrel surface. Flow problems in the feed hopper can be detected by observing the flow from the feed hopper when it is disconnected from the extruder. Solids conveying problems in the extruder itself are difficult to diagnose. One method that can be used is to Teflon-coat the screw. Even though the coating may not last very long, it will substantially reduce the retarding force acting on the solid bed and thus improve solids conveying. If the coating eliminates the instability, this is a strong indication of a solids conveying problem. A more permanent solution can be provided by a grooved barrel section or a nickel-plated screw impregnated with a fluorocarbon polymer.

The stability of solids conveying is strongly related to the uniformity of the feedstock. The best stability is achieved with uniform pellet size and pellet shape. Large variations in particle size and shape invariably lead to variations in extruder performance. This is often observed when regrind is added to the virgin feedstock. Since the regrind usually has non-uniform particle size and shape, increasing amounts of regrind will reduce the stability of the extrusion process. In many cases, this reduction in stability will put an upper limit on the amount of regrind that can be added to the extruder.

11.3.4.2.2 Plasticating Instabilities

Plasticating problems are likely to occur on screws with a high compression ratio and a short compression section length. They are also likely to occur when the overall length of the extruder is short. A short extruder will run into melting-related instabilities at lower output than a longer extruder. This is one of the reasons behind the trend in the extrusion industry to go to longer extruders. In the 1950s and 1960s, most single screw extruders were about 20 D long. In the 1970s and 1980s, most extruders were about 25 D long. In the 1990s and 2000s, most single screw extruders are about 30 D long.

Insufficient melting capacity can be diagnosed by preheating the feedstock. If preheating reduces or eliminates the instability, then the problem is most likely insufficient melting capacity. Melting can be improved either by changing the processing conditions or by changing the screw geometry. Processing conditions that can improve melting:

- Preheating of the feedstock
- Increasing the barrel temperature when running at low screw speed
- Reducing the barrel temperature when running at high screw speed
- Reducing the screw speed
- Increasing the barrel pressure

Screw design changes that can improve the melting capability are:

- Increased flight helix angle in transition section
- Reduced flight clearance in transition section
- Increased length of transition section
- Multi-flighted design in transition section
- Use of fluted mixing section at the end of the transition section

11.3.4.2.3 Melt Conveying Instabilities

Most melt conveying or pumping problems are caused by improper design of the metering section. The most common problem is excessive channel depth; the second most common problem is insufficient length of the metering section. If the channel depth is too large, the metering end of the screw can be cooled to reduce the effective depth. Conversely, if the channel depth is too small the metering end of the screw can be cooled to increase the effective depth of the channel and increase the melt conveying capability. However, if the metering depth is incorrect it is better to switch to a screw design with proper dimensions of the metering section.

In some cases, the melt conveying capability cannot be improved sufficiently by a simple change in screw design. An example is a two-stage extruder screw that has to operate at high discharge pressure. If the second stage of the screw is not long enough, it may not be possible for the screw to generate the required pressure. Such a condition will result in vent flow; this is molten polymer flowing out of the vent port. One possible solution to such a problem is to place a gear pump between the extruder and the die. In this set-up the gear pump can generate the required diehead pressure, and the screw only has to generate enough pressure to feed the gear pump. Other possible solutions for vent flow problems are:

- Reduce diehead pressure
- Increase the length of the extruder
- Use internal screw heating in the second stage of the screw
- Reduce the barrel temperature in the second stage

11.3.4.2.4 Devolatilization Instabilities

Devolatilization instabilities can be caused by plugging of the vent port, variation in the vacuum level, or by variations of the volatile level in the feedstock. The efficiency of devolatilization can be improved by:

- Increasing barrel temperatures in the first stage
- Increasing the vacuum level at the vent port
- Preheating the feed stock
- Use of a stripping agent

Screw design can affect the devolatilization efficiency a great deal. A multi-flighted extraction section can improve degassing. Further, it is important that the polymer is fully melted in the first stage of the screw. To ensure complete melting it is beneficial to place a fluted mixing section at the end of the first stage of the screw.

11.3.4.2.5 Mixing-Related Instabilities

Extrusion instabilities are often related to insufficient mixing capacity of the screw. Mixing can be improved a small amount by increasing the diehead pressure. However, this is a relatively ineffective method to improve the mixing capacity of the extruder: it also increases the chance of degradation. The mixing capacity of a screw can be improved significantly by adding one or more mixing sections to the design of the screw.

The polymer melt has to be well mixed when it leaves the extruder screw and enters into the die. For this reason it is beneficial to have an efficient distributive mixing device at the very end of the screw. Mixing was discussed in detail in Section 7.7 and mixing devices and mixing screws in Section 8.7.

Solving Mixing Problems

In addition to have efficient mixing devices along the screw, there are several other issues that are important in achieving good mixing. The method of feeding plays an important role in the mixing action in the extruder.

Flood Feeding versus Starve Feeding

Most single screw extruders are flood fed; however, flood feeding is often detrimental to achieving good mixing in the extruder. With flood feeding, high pressures are generated in the solids conveying and plasticating zones of the extruder. These high pressures tend to agglomerate ingredients that later need to be dispersed and distributed [135–137]. Obviously, this can be highly counter-productive.

In starve feeding the material is metered into the extruder with a feeder. As a result, there is no accumulation of material at the feed opening. The first several turns of the screw are partially filled with material without any pressure development in this part of the extruder. The screw channel does not become completely filled until some distance from the feed opening; at this point, the pressure will start building up in the extruder. In effect, starve feeding reduces the effective length of the extruder.

One of the benefits of starve feeding is that the pressures along the extruder are lower than in flood feeding. Therefore, there is less chance of agglomeration, resulting in improved mixing action in the extruder. Recently, a number of workers have analyzed the effect of starve feeding on the mixing capability of extruders and injection molding machines [138–142]. Without exception, all these investigators found

major improvements in mixing quality in starve feeding compared to flood feeding. Starve feeding has become the standard mode of operation for twin screw extruders used in compounding. However, the benefits of starve feeding are not limited to twin screw extruders. Mixing in single screw extruders can be improved significantly by using starve feeding.

Initial Scale of Segregation

The mixing action that is required in an extruder is determined both by the initial and final scale of segregation. The required final scale of segregation is usually around 1 micron. If the initial scale of segregation is the size of a pellet (about 3000 micron), the mixing action will have to produce a 3000-fold reduction in the scale of segregation. In simple shear mixing, this will require a total strain rate of 3000 units [143]. If the average shear rate is 50 s^{-1} the polymer melt will have to be exposed to this shear rate for 60 s to produce a total shear strain of 3000. Considering that a typical residence time in the melt conveying zone is 15 to 20 s, it is clear that the mixing action will be insufficient to reduce the scale of segregation down to the micron level.

This situation can be improved if we start the mixing process with ingredient in powder form rather than in pellet form. If the size of the powder particles is 100 micron and the powder is well mixed before extrusion, the initial scale of segregation will be 100 micron. In this case, the mixing action will have to produce only a 100-fold reduction in the scale of segregation to achieve a final scale of one micron. At a shear rate of 50 s^{-1} this will take a shear time of 2 s. Clearly, there is a very good chance that a single screw extruder will be able to accomplish this mixing task without much trouble. The difference in the scale of segregation is illustrated in Fig. 11.33.

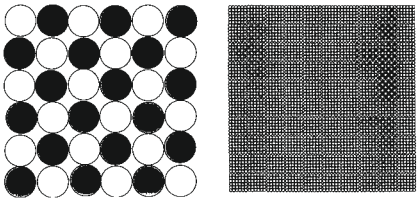


Figure 11.33
A coarse scale of segregation (left) and a fine scale of segregation (right)

One of the most difficult mixing tasks is to mix a low percentage of a pelletized color concentrate (CC) with natural pellets. Assume that the pellet size is 3 mm (3000 micron) and that 1% CC is added to the natural pellets. This means that for every CC pellet there will be 100 natural pellets. The initial scale of segregation in this case will be about 30 mm (30,000 micron). Since not all CC pellets will have the same distance from one another, the actual scale of segregation can be as high as 100 mm (100,000 micron). If we want to achieve a final scale of segregation of 1 micron, the mixing action will have to achieve a 100,000-fold reduction in scale. If the average

shear rate is 50 s^{-1} the polymer melt will have to be exposed to this shear rate for 200 s (more than 3 minutes) to produce a total shear strain of 100,000. It is very unlikely that this can be accomplished in a simple conveying screw in a single screw extruder. As a result, a very efficient mixing screw will have to be used to accomplish this mixing task successfully.

11.3.4.3 Solving Extrusion Instabilities

There are many different causes of extrusion instabilities. Even though the mechanism of the instability is not always clear, the following measures often reduce extrusion instabilities:

- Reduce the screw speed
- Reduce the screw temperature
- Reduce the barrel temperature at the delivery end
- Reduce the channel depth in the metering section
- Increase the length of the compression section
- Increase the rear barrel temperatures
- Increase the diehead pressure

The first approach to the problem is generally adjustment of the temperature profile or other process conditions. If temperature adjustment does not solve the problem, one should check the hardware: thermocouples, controllers, screw, barrel, drive, etc. If the problem is not associated with the hardware, it must be a functional problem and one should determine what functional zone is causing the problem. The troubleshooting flow chart in Fig. 11.34 can help in systematically exploring the possible causes of the instability.

If the problem cannot be solved by changing the processing conditions, which is, of course, the first choice, then one can generally solve the problem either by making a material change or by making a change in screw or barrel design. In most cases, material changes are not possible. In that case, the problem usually has to be solved by a new screw design. Another option is to add a gear pump at the end of the extruder. Figure 11.35 illustrates some of the important interactions that take place during the extrusion process.

Because of the complicated interactions that occur during the extrusion process, it is often difficult to predict the effect of a change in process conditions or in screw design. For instance, increasing the barrel temperature will generally increase the polymer melt temperature at the discharge end of the extruder. However, it is also possible for the melt temperature to reduce with increasing barrel temperatures. This is possible because, when the barrel temperature is increased, the local melt viscosity can reduce, which will reduce the local viscous heating. This effect can result in lower melt temperature at the discharge end of the extruder.

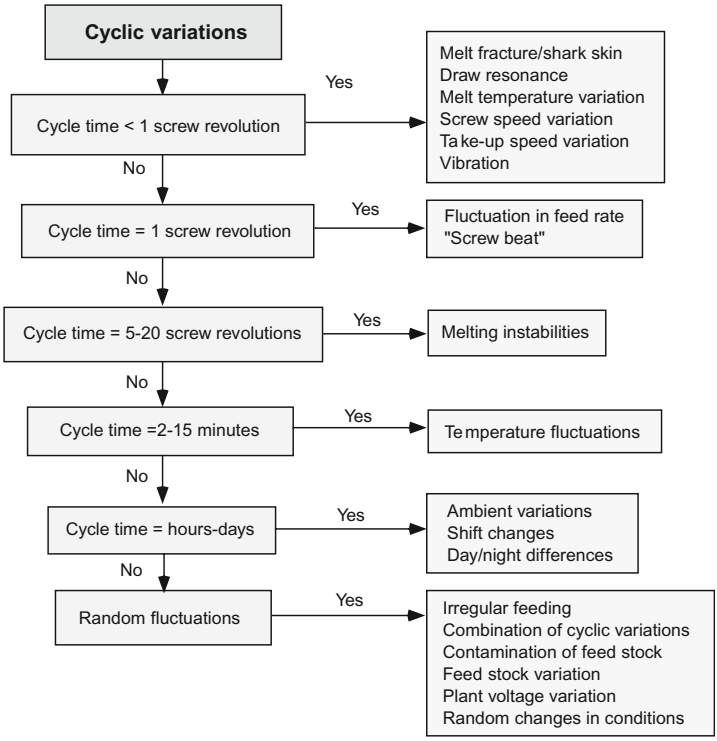


Figure 11.34 Troubleshooting flow chart for fluctuation in extruder performance

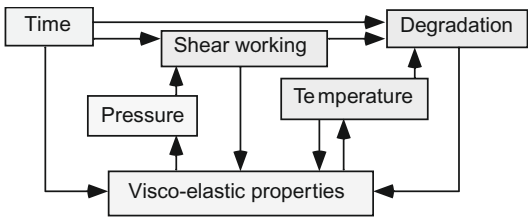


Figure 11.35
Interactions during the extrusion process

11.3.5 Air Entrapment

Air entrapment is a rather common problem in extrusion. It is caused by air being dragged in with particulate material from the feed hopper. Under normal conditions, the compression of the solid particulate material in the feed section will force the air out of the solid bed. However, under some circumstances the air cannot escape back to the feed hopper and travels with the polymer until it exits from the die. As the air pockets exit from the extruder, the sudden exposure to a much lower ambient pressure may cause the compressed air bubbles to burst in an explosive manner. However, even without the bursting of the air bubbles, the extrudate is generally rendered unacceptable because of the air inclusions.

There are a number of possible solutions to air entrapment. The first approach should be to change the temperature in the solids conveying zone to achieve a more positive compacting of the solid bed. Often, a temperature increase of the first barrel section reduces the air entrapment; however, in some cases, a lower temperature causes an improvement. In any case, the temperatures in the solids conveying zone are important parameters in the air entrapment process. It should be realized that both the barrel and screw temperatures are important. Thus, if a screw temperature adjustment capability is available, it should definitely be used to reduce the air entrapment problem.

The next step is an increase in the diehead pressure to alter the pressure profile along the extruder and to achieve a more rapid compacting of the solid bed. The diehead pressure can be increased by simply adding screens in front of the breaker plate. Another possible solution is to starve feed the extruder; however, this may reduce extruder output and requires additional hardware, i.e., an accurate feeding device.

The aforementioned recommended solutions can be implemented rather easily. However, if these measures do not solve the problem, more drastic steps have to be taken. One possibility that needs to be explored is a change in particle size or shape. If this is a reasonable option, it will most likely solve the problem. A rather safe solution is to utilize a vacuum feed hopper system; however, these systems are rather complex and expensive. Another possible solution is to use a grooved barrel section. Pressure development in a grooved barrel section is much more rapid than in a smooth barrel. Thus, a grooved barrel section causes a rapid compacting of the solid bed and, therefore, less chance of air entrapment. Instead of grooving the barrel, one can opt for reducing the friction on the screw, which would have a similar effect. A coating that might be used for this purpose is described by Luker [35]. Air entrapment is also often successfully eliminated by vented extrusion using a multi-stage extruder screw. Increasing the compression ratio of the screw is also likely to reduce air entrapment.

It should be noted that bubbles in the extrudate are not only a sign of air entrapment, but it may also be an indication of moisture, surface agents, volatile species in the polymer itself, or degradation as shown in the fishbone diagram shown in Fig. 11.36.

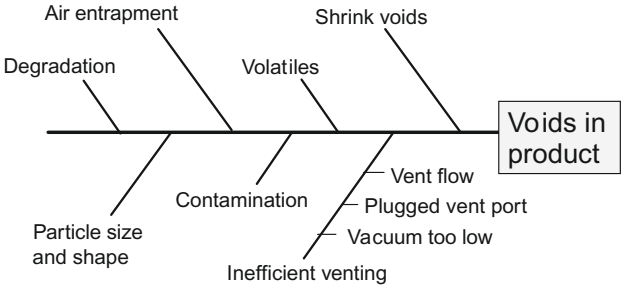


Figure 11.36
Fishbone chart for voids in extruded product

Thus, before concentrating on solving an apparent air entrapment problem, one should make sure that the problem is indeed caused by air entrapment. In some cases, the pellets contain small air bubbles within the pellet itself. In this case, one of the few possible solutions is vented extrusion; most of the other recommended solutions will not work in this situation. The fishbone diagram shown above helps in systematic troubleshooting. The diagram can be used to put together a troubleshooting flow chart for this kind of problem. Figure 11.37 shows an example of a troubleshooting flow chart for voids in the extruded product.

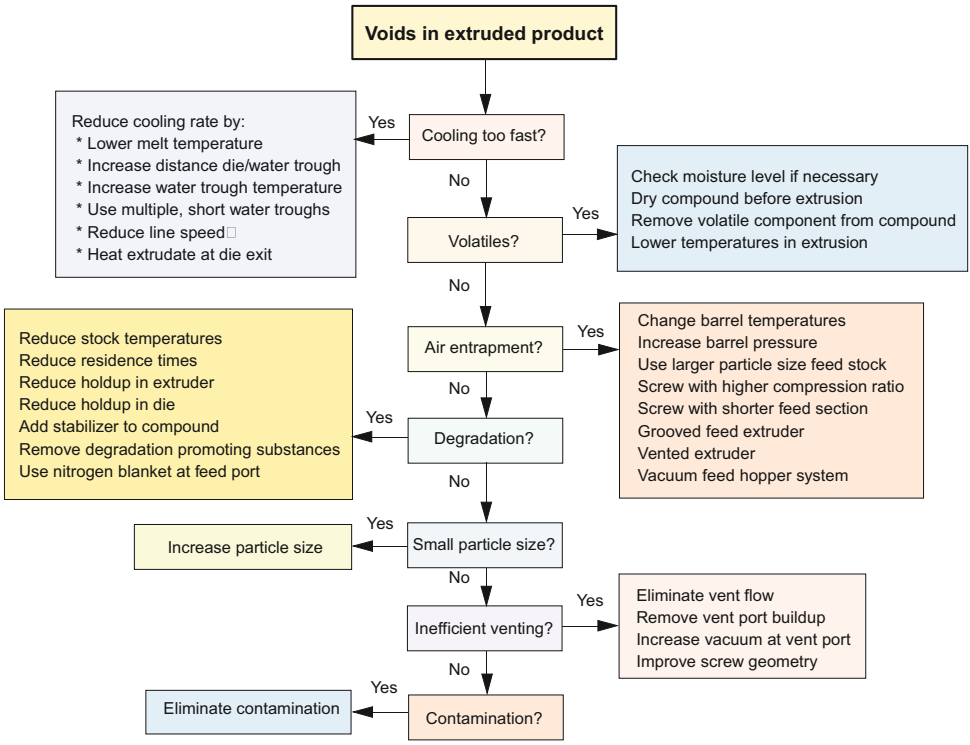


Figure 11.37 Troubleshooting flow chart for voids in the extruded product

11.3.6 Gels, Gel Content, and Gelation

The term "gel" has different meanings in the polymer extrusion industry. The term gel is used as "gel content" in crosslinked polymers. Determination of gel content is described in ASTM D2765, standard test methods for determination of gel content and swell ratio of crosslinked polyethylene plastics [163]. The gel content (insoluble fraction) produced in ethylene plastics by crosslinking is determined by extracting with solvents such as decahydronaphthalene or xylenes.

The term "gelation" is used in extruded products made of rigid polyvinylchloride (PVC). The term gelation is the fusion of the primary particles of the PVC [164]. In

the plastics industry the term gelation is only used for PVC plastics. Insufficient gelation leads to premature failure of PVC products [164, 165]. Two techniques are widely used to determine the level of gelation in PVC. One is the acetone immersion test described in ASTM D2152; the other is the dichloromethane test described in ISO 9852. Gramann and Cruz describe the use of testing by differential scanning calorimetry to determine the extent of gelation in rigid PVC [165].

Low levels of gelation are generally associated with stock temperatures that are too low in the PVC extrusion process. Proper levels of gelation typically require stock temperatures above 190°C. However, at temperatures above 200°C, rigid PVC (RPVC) degrades rapidly. As a result, the process window for RPVC is quite narrow, and close control of stock temperatures is essential in making a high-quality RPVC product. Also, proper melt temperature measurement in RPVC extrusion is critical. If melt temperature is not properly measured, the melt temperature cannot be controlled and improper gelation levels can result in the extruded product.

Gels are generally defined as small, more or less round defects in extruded products, especially film or thin walled tubing. Some people define gels as any particle in an extruder plastic product that has visual properties different from the rest of the product. This includes discolored specks, contamination, crosslinked polymer droplets, etc.

We will define gels as small spherical droplets or specks with a distinct boundary that can be observed by simple visual inspection. The material making up the gel particle is basically the same as the polymer of the surrounding film. Therefore, a gel particle is different from contamination. In many cases the gel particle has no discoloration; see for instance Fig. 11.38. Small droplets with strong discoloration are generally referred to as discolored specks; this topic is discussed in Section 11.3.7.4.

Section 11.3.7.4 also shows expressions that can be used to relate the frequency of discolored specks in the raw material to the frequency of discolored specks in the extruded product. These expressions can also be used to relate the frequency of gels in the raw material to the frequency of gels in the extruded product.

A photograph of a gel defect in blown film is shown in Fig. 11.38.

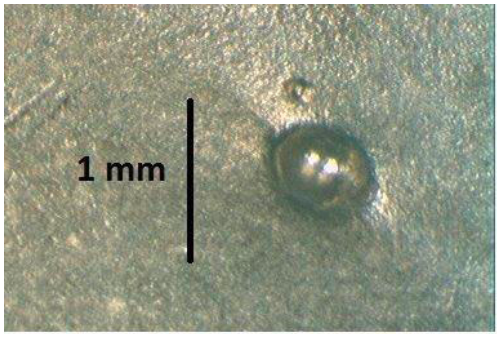


Figure 11.38
Transparent gel particle in HDPE film, courtesy of Dr. Cantor

The gels shown in Figs. 11.38 and 11.39 were created in a blown film extrusion process. The polymer is an HDPE (ExxonMobil Paxon AA45-004) with a melt index of 0.35 gr/10 min. The gel in Fig. 11.38 is about 0.5 mm in diameter; it has no significant discoloration.

Figure 11.39 shows two pictures of gel defects with discoloration.

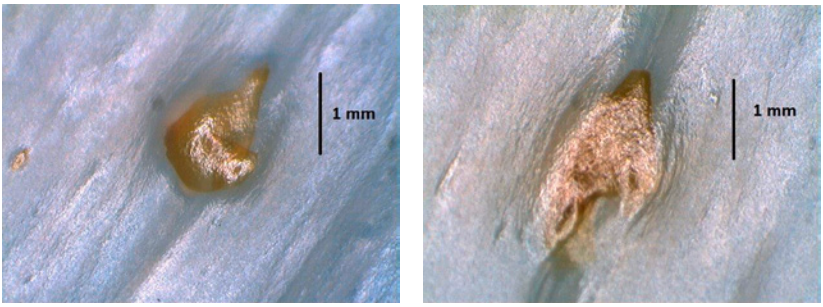


Figure 11.39 Photographs of gel defects in polyethylene film, courtesy of Dr. Cantor

The gel defects are approximately 1 mm in size and show brownish discoloration, indicative of oxidative degradation.

There used to be an ASTM standard for test method for counting gels in film; this was ASTM D3351-93. However, this standard was withdrawn and has not been replaced. Gels can range in size from 100 micron or smaller to as large as 1500 micron or even larger. Sizes smaller than 100 micron are difficult to detect; see Fig. 11.40. The pellets in this figure have a length of 3.5 mm and height of 1.5 mm.

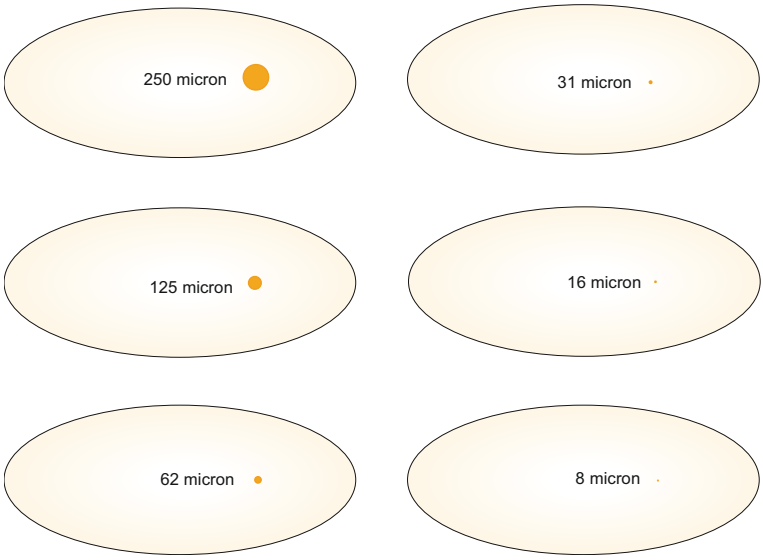


Figure 11.40 Pellets with defects ranging from 250 to 8 micron

Gels are usually crosslinked polymer particles or highly entangled particles that behave as crosslinked particles. Gels can be generated in polymerization, pelletizing, resin transfer, transport to processor, conveying through transfer lines, contamination, extrusion, in regrind, etc. It is important to understand that gels are not only formed inside the extruder at the processor. Gels generated in the extrusion process are referred to as E-gels.

Gels created in polymerization and downstream operations such as pelletizing are referred to as P-gels. Resin producers are well aware of this fact. Specialized equipment is available that allows resin producers to detect defects in the pellets. An example of a company that manufactures high-speed inspection systems is Optical Control Systems GmbH (OCS); see [166]. This equipment allows analysis of millions of pellets. As a result, resin producers can determine how many gels are produced in their resin manufacturing processes.

11.3.6.1 Measuring Gels

When there is a problem with gels in an extruded product, it is important to determine whether the gels are in the incoming raw material or created in the extrusion process. Clearly, this is an issue where the resin supplier may be in disagreement with the processor! To determine whether the incoming material contains gels, the material must be tested for gels. One method to test for P-gels is to press a thin plaque using the polymer pellets as supplied by the resin producer and visually examine the plaque for gels. The plaque has to be prepared in such a way as to minimize the exposure to high temperatures to make sure that gels are not created in the sample preparation process. The number of gels per unit area can be counted using an overhead projector and polarized film to project an image on a screen. The number of gels per unit area is a measure of the amount of gels in the material. Obviously, the conditions used to press the plaque and the thickness of the plaque have to be standardized for the measurements to be meaningful.

For extruded film there is an existing standard for manual gel counting that does not appear to be used much today [155]. There are automatic gel counting methods that are used by a number of companies; these methods are based on laser or CCD camera technology. However, these methods are not standardized and each company tends to use their own procedures. A proposed ASTM procedure has been submitted for these automatic gel detection methods. However, many issues remain to be resolved such as a standardized method to report the results, what size gels to count, how to report the distribution of gel sizes, etc. Various end-use applications have different requirements with regard to gels. As a result, it is difficult to develop one standardized test method that satisfies all requirements.

In fiber extrusion, in particular PP, a screen build-up test is used in some cases. This test reflects not just the gel level in the polymer because other materials can be trapped in the screen as well. Also, not all gel particles may be captured in the

screen. For best gel capture capability a 3-D fiber filter with a specified rating should be used. The build-up can be quantified by monitoring the increase in pressure drop over time. The time to reach a specific pressure drop is a measure of the percentage of gels greater than a certain size removed in the filtration process. A regular wire mesh screen pack is not suitable for this test because wire mesh screens have very limited gel capture capability.

Gels can be characterized using hot-stage microscopy (HSM). This method allows slow heating of a film sample with a gel on a microscope hot stage to a temperature above the melting point of the polymer. Transmitted light is passed through cross-polarized filters. By analyzing the melting point of the film and the gel, different types of gels can be identified. Birefringence effects allow further identification.

Gels caused by contamination will have a different chemical composition from the polymer used to make the product. As a result, chemical analysis can determine whether a gel particle is contamination or if it has the same chemical composition as the polymer. Gels can be analyzed by micro-infrared analysis. The infrared spectrum can determine whether the gel is from a foreign material or if it similar to the polymer.

Crosslinked gels can have crystallinity; therefore, they can be birefringent under polarized light. A hot-stage polarizing microscope is useful for this analysis. To determine whether the gel is crosslinked the gel can be heated above the melting point of the polymer. At this elevated temperature the gel can be stressed by carefully applying a force to the gel. A crosslinked gel will appear birefringent under polarized light. If the size and shape of the gel remains after cooling, the gel is crosslinked. If the gel was not crosslinked but highly entangled, the gel would disappear after the stress was applied and subsequent cooling.

Fines are created when off-spec product is shredded into regrind. If the fines are not removed they will tend to show up as gels in the extruded product. The thermomechanical action of the shredder creates fines that do not melt like regular pellets. For that reason it is important to remove fines from the regrind before it is reintroduced to the extruder. Special equipment is available to remove fines from pellets; these machines are called dedusters.

11.3.6.2 Gels Created in the Extrusion Process

To avoid E-gels, it is important to avoid dead spots in the extruder. This can be accomplished by making sure that both the screw and the die have a streamlined design. Mixing sections with stagnating regions, such as the Maddock mixing section, should be avoided. It is also important that the screw, barrel, and die surfaces are smooth without grooves, scratches, or gouges that might collect melted plastic and cause degradation. Another method of reducing gel formation in the extruder is to start up the extruder with a highly stabilized version of the plastic, or even a

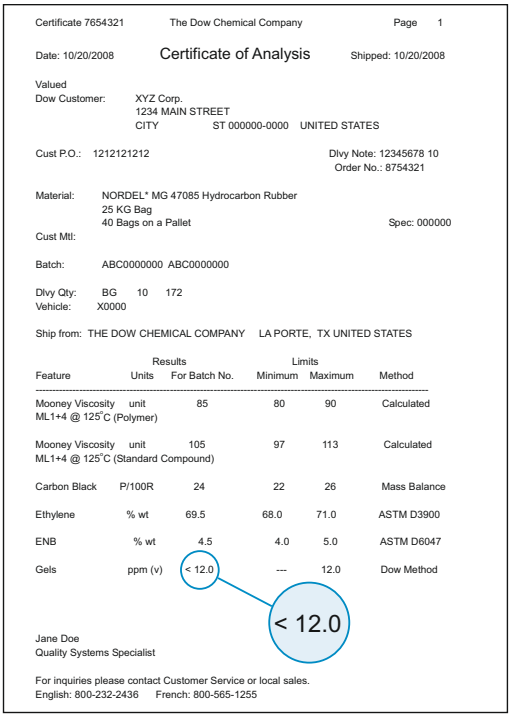
different plastic, to coat the critical surfaces with a degradation-resistant layer of plastic. This can reduce the chance of degradation and gel formation.

It is also important to check the resin feed tubes, blenders, feeders, hoppers, and other bulk handling hardware components for fines, streamers, or contamination from another plastic. To avoid fines, streamers, and contamination, the bulk handling equipment should be completely blown down and cleaned when a material change is made.

11.3.6.3 Removing Gels Produced in Polymerization

Howard [168] discusses gels created in polymerization. He mentions that the most common defect found by resin suppliers is the crosslinked gel. These result from dislodged pieces of reactor or separator "plaque." These crosslinked gels tend to be evenly distributed in the polymer and are carried through processing extruders in a predictable manner.

Some resin producers supply their customers with spec sheets that show the maximum level of gels in the resin. An example is shown in Fig. 11.41 [167].



Certificate 7654321 The Dow Chemical Company Page 1

Date: 10/20/2008 **Certificate of Analysis** Shipped: 10/20/2008

Valued
Dow Customer: XYZ Corp.
1234 MAIN STREET
CITY ST 000000-0000 UNITED STATES

Cust P.O.: 1212121212 Dlvy Note: 12345678 10
Order No.: 8754321

Material: NORDEL* MG 47085 Hydrocarbon Rubber
25 KG Bag
40 Bags on a Pallet Spec: 000000
Cust Mtl:

Batch: ABC0000000 ABC0000000

Dlvy Qty: BG 10 172
Vehicle: X0000

Ship from: THE DOW CHEMICAL COMPANY LA PORTE, TX UNITED STATES

Feature	Units	Results For Batch No.	Limits Minimum	Maximum	Method
Mooney Viscosity ML1+4 @ 125°C (Polymer)	unit	85	80	90	Calculated
Mooney Viscosity ML1+4 @ 125°C (Standard Compound)	unit	105	97	113	Calculated
Carbon Black	P/100R	24	22	26	Mass Balance
Ethylene	% wt	69.5	68.0	71.0	ASTM D3900
ENB	% wt	4.5	4.0	5.0	ASTM D6047
Gels	ppm (v)	< 12.0	---	12.0	Dow Method

< 12.0

Jane Doe
Quality Systems Specialist

For inquiries please contact Customer Service or local sales.
English: 800-232-2436 French: 800-565-1255

Figure 11.41
Certificate of resin producer for maximum gel level

The processor should know the level of gels in the incoming raw material to know the gel level and to determine whether this level is relatively constant or subject to substantial variation.

Unfortunately, it is quite difficult to remove P-gels in a regular extrusion process. Adding dispersive mixing elements to the extruder screw usually does not achieve sufficient mixing to eliminate P-gels. Also, the screen pack typically used before the breaker plate does not have enough gel capture capability to significantly reduce the gel level. New dispersive mixers capable of generating elongational flow such as the CRD mixer (see Section 3.4.2.5) can disperse gels [88–94] and provide a valuable tool in reducing gel problems.

One of the best tools available to remove gels is a depth filtration medium, such as sintered metal or a random 3-D fiber. These depth filters have been in use for decades and have proven themselves in high-quality film and fiber applications where gels have to be kept to the lowest possible level. Several companies sell large area depth filtration devices that are well suited for gel removal. Unfortunately, such filters are expensive, maintenance intensive, and require replacement on a regular basis. However, they are effective in removing gels from the plastic melt. Figure 11.42 shows a flow chart for troubleshooting gel problems.

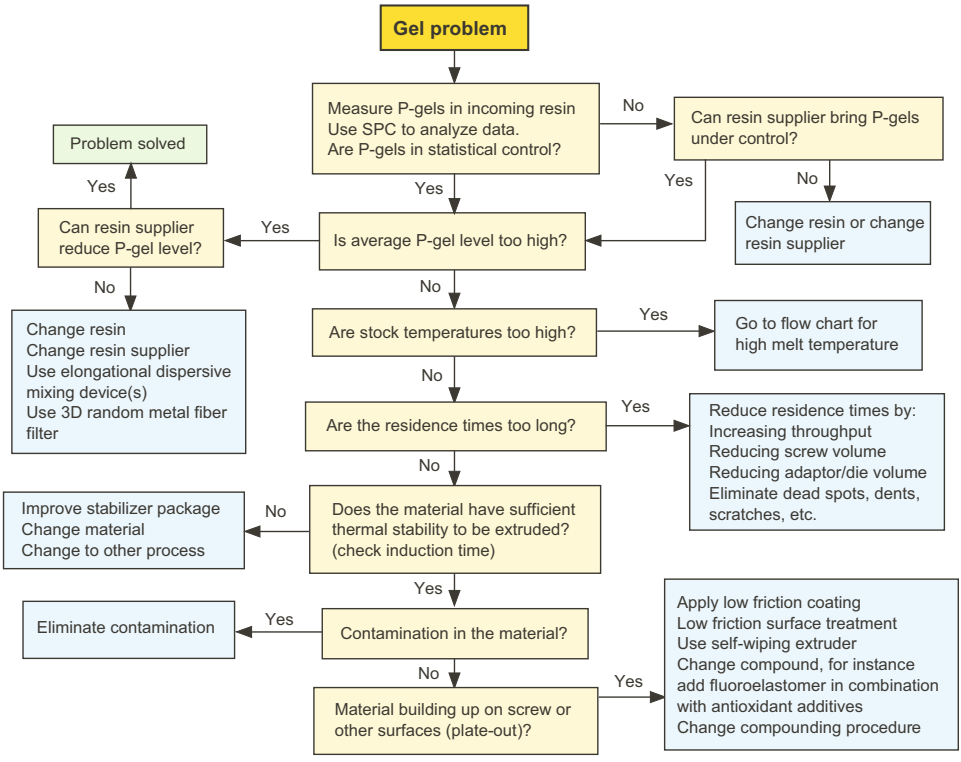


Figure 11.42 Flow chart to troubleshoot gel problems

11.3.7 Die Flow Problems

Die flow problems typically result in appearance problems. These can be related to melt fracture, die lip build-up, gels, v- or w-patterns, specks, color variation, lines, and change in optical properties (e.g., transparency, mattness, gloss, haze).

11.3.7.1 Melt Fracture

Melt fracture was discussed in Section 7.5.3.2. It manifests itself as extrudate surface roughness, shark skin, orange peel, and other distortions. Melt fracture can be reduced or eliminated by:

- Streamlining the die flow channel
- Reducing the shear stress in the land region (operating below the critical shear stress for melt fracture)
- Use a processing aid (e.g., a fluoroelastomer for polyethylene)
- Use "super-extrusion" (operating above the critical shear stress for melt fracture)
- Ultrasonic vibration

Streamlining the die flow channel is always a good idea but it will increase the cost of a die. For a high-volume product, it generally makes sense to design and manufacture a fully streamlined die. For a small-volume product, it may not make economic sense to design and manufacture a fully streamlined die.

Reducing the shear stress in the land region can be done by:

- Increasing the die land temperature
- Opening up the die land region (increase die gap)
- Reduce the extrusion rate
- Use process aid (e.g., external lubricant, viscosity depressant)
- Increase the melt temperature
- Reducing the polymer melt viscosity
- Use a more shear thinning plastic

Several polymer processing aids (PPA) are available to eliminate or reduce melt fracture. An effective method to eliminate melt fracture in high molecular weight polyolefins is to add a small amount of fluoroelastomer [153], about 500 to 1000 ppm (parts per million). When a fluoroelastomer PPA is added to a polyolefin it usually takes a certain amount of time for a critical coating of fluoropolymer to form on the die. This conditioning time can vary from 5 minutes to more than 1 hour [154].

Silicon-based polymers such as polydimethyl siloxanene (PDMS) have been used as polymer processing aids for many years. Dow Corning has developed ultra-high molecular weight PDMS additives that work as process aids in polyethylene and polypropylene. Because these materials solidify with the polymer, they reportedly

do not affect printability or paint adhesion. HMW PDMS has been used to reduce surface roughness of extruded LLDPE tape [158].

Super-extrusion is a technique whereby the shear stress in the die land is above the critical shear rate for melt fracture; see Section 7.5.3.2. This is possible with polymers that exhibit a second stable region above the melt fracture region. Linear polymers such as HDPE, FEP, and PFA exhibit super-extrusion behavior. The melt fracture behavior can be determined on a capillary rheometer by running a polymer melt at different shear rates and observing the corresponding condition of the extrudate. A typical flow curve for a linear polymer is shown in Fig. 11.43.

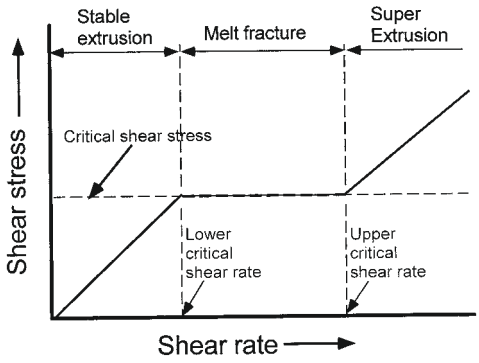


Figure 11.43
Flow curve of a linear polymer showing melt fracture and super-extrusion regions

Melt fracture can be avoided by keeping the shear stress in the die below the critical level for melt fracture. This requires operating at a shear rate below the lower critical shear rate for melt fracture. Melt fracture can also be avoided by running under conditions where the shear stress in the die is above the critical shear stress level for melt fracture. In this case, one has to operate at a shear rate above the upper critical shear rate for melt fracture.

Ultrasonic vibration of the die is done by mounting external transducers on the die, which deliver ultrasonic energy in the kHz range. Little quantitative information is available on this technique; however, it is known that it is successfully practiced in the extrusion industry. The principle behind ultrasonic vibration is related to the shear thinning characteristics of polymers. As discussed in Chapter 6, the melt viscosity of polymers reduces by orders of magnitude when the rate of deformation in increased. This applies not only to steady deformation but also to cyclic deformation. Therefore, when a polymer melt is exposed to a high-frequency vibration, its viscosity will reduce by a large amount depending on the degree of shear thinning.

With ultrasonic die vibration the polymer melt layer at the die wall is most exposed to the high-frequency deformation. This causes a large drop in melt viscosity at the die wall with several beneficial effects, such as:

- Reduced diehead pressure
- Reduced extrudate swell

- Reduced melt fracture
- Reduced die lip build-up (die drool)

11.3.7.2 Die Lip Build-Up (Die Drool)

Die lip build-up is a common problem in the extrusion industry; it is a condition where material accumulates right at the die exit as illustrated in Fig. 11.44.

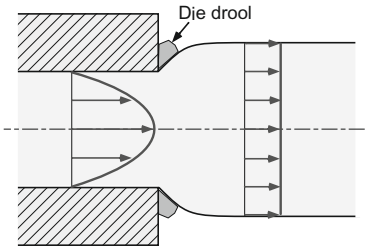


Figure 11.44
Illustration of die lip build-up

Material build-up right at the die exit can cause lines in the extruded product. This problem is often referred to as "die drool." It typically results from incompatible components in the compound, even though it can also happen in non-compounded plastics. Die drool can be caused by gas or moisture in the molten plastic, degradation, or poor dispersion of fillers or additives. Die drool can be reduced either by changing the material, the process, or the die design.

To reduce die drool by changing the material:

- Remove the incompatible component
- Add a fluoroelastomer
- Add a compatibilizer
- Change the compounding procedure

To reduce die drool by changing the process:

- Adjust the die temperature (usually lower)
- Blow air at the die exit
- Use scraper at the die exit
- Use ultrasonic vibration

To reduce die drool by changing the die design:

- Use a low-friction coating in the die
- Use another die material, for instance ceramic
- Use a longer land length
- Use small taper in the land region of the die

It is also important to inspect the condition of the die internal surfaces for scratches, bad plating, a pitted surface, or general poor surface quality. Any of these conditions have to be corrected to minimize die lip build-up. It is interesting to note that several of the measures that reduce die drool also reduce melt fracture. Processing aids that reduce melt fracture often reduce die drool as well [155–157].

11.3.7.3 V- or W-Patterns

These patterns are often related to line tension, more specifically uneven line tension. In advanced cast film lines (BOPP or BOPET), there are tension-control systems that allow tension adjustment in specific regions of the film. In these lines, a gear pump is often necessary to minimize output variation. The diehead pressure in such extrusion operations can be very high (up to 600 bar).

These patterns can also be related to uneven flow out of the die. Check the die design and make sure the melt temperature is uniform in the extrusion direction as well as across the die. In some cases, a static mixer can be used; it can be placed even inside the die just before the manifold region of the die.

11.3.7.4 Specks and Discoloration

Discolored specks are a common problem in extrusion and molding. This problem is similar to another common defect, which is the problem of gels. Like gels, discolored specks are formed not only in extrusion and molding at the processor but also in polymerization at the resin producer. As a result, in order to get a handle on the problem, we need to know how many specks are in the incoming raw material. We will distinguish between a speck formed in polymerization and located inside the pellet (P-speck) and a speck formed in extrusion (E-speck).

11.3.7.4.1 Specks Formed in Polymerization

One of the challenges in testing pellets produced at the resin supplier is that pellets are quite small. A typical plastic pellet may have a diameter and length of about 3 mm with a volume of about 20 mm^3. If we assume a density of 1 gr/cm^3, the mass of a typical pellet will be about 20 milligram. This means 1 kg of resin will have about 50,000 pellets. If we run an extruder at 300 kg/hr, approximately 1,500,000 pellets will pass through the extruder every hour.

Today commercial instruments are available that allow analysis of millions of pellets. Optical Control Systems (OCS) GmbH produces systems for defect detection. OCS makes instruments for defect detection in pellets as well as in extruded sheet and film. Pellet defect detection systems by OCS are used by many resin producers. Therefore, most resin companies know how many defects occur in the pellets they produce. Figure 11.45 shows an example of pellets with discolored specks.



Figure 11.45 Pellet with black and discolored specks (courtesy OCS)

If we have one pellet with a discolored speck for every N pellets, we can determine the average incidence of specks in the extruded product. If the cross-sectional area of the extruded product is A_e and the volume of the pellet or powder particle is V_p, the average length over which a P-speck will occur in the extruded product is:

$$L_{ps} = NV_p/A_e \tag{11.20}$$

As an example, we will consider the extrusion of tubing with an inside diameter of 10.0 mm with a wall thickness of 1.0 mm. The cross-sectional area of this product is:

$$A_e = 0.25\pi(D_o^2 - D_i^2) = 0.25 \bullet 3.14\ (144 - 100) = 34.45\ mm^2 \tag{11.21}$$

The volume of the pellet is 20 mm^3. We will consider a plastic raw material that contains one pellet with a discolored P-speck for every 10,000 pellets; this corresponds to 100 ppm. With this input data, we find the average length over which a P-speck will occur is 5806 mm or 5.8 m. If we generate specks in the extrusion process, the average length over which a speck occurs in the extruded product will be less than 5.8 meter.

If we cannot tolerate one speck every 5.8 meter there is only one option: reducing the number of P-specks in the raw material. Since resin producers can scan millions of pellets for specks, it is also possible to remove pellets with specks from the pellet stream. In other words, the processor can specify the ppm level of pellets with specks that can be tolerated by the processor.

Clearly, sorting the pellets carries a certain cost to the resin producer. The resin producer will pass this cost on to the customer. Alternatively, the customer can do this sorting in-house. In this case, the customer will have to purchase the pellet scanning and sorting (S&S) system. If in-house scanning and sorting is less expensive than the cost of pre-sorted pellets, it makes sense for the processor to perform this task in-house.

Pellets can be scanned and sorted not only for discolored specks but also for irregular pellets, for instance, pellets with tails. Figure 11.46 shows a picture of pellets with tails; such pellets can cause problems in extrusion and are preferably eliminated from the feed stream.

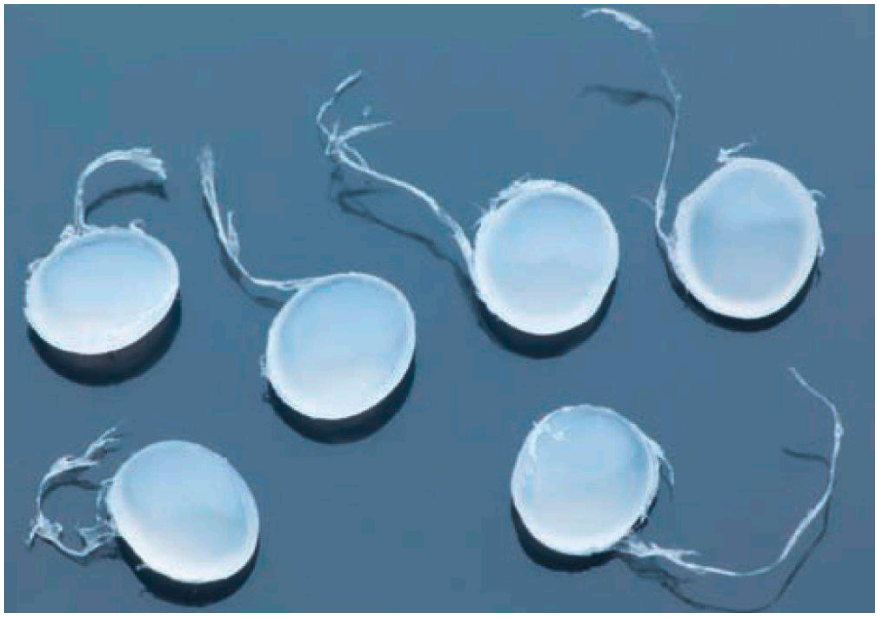


Figure 11.46 Pellets with tails (courtesy OCS)

11.3.7.4.1.1 Specks Formed in Extrusion

Discoloration of the plastic inside the extruder can be caused by degradation, contamination, and several other causes. Figure 11.47 shows a listing of possible causes of specks generated in the extrusion process.

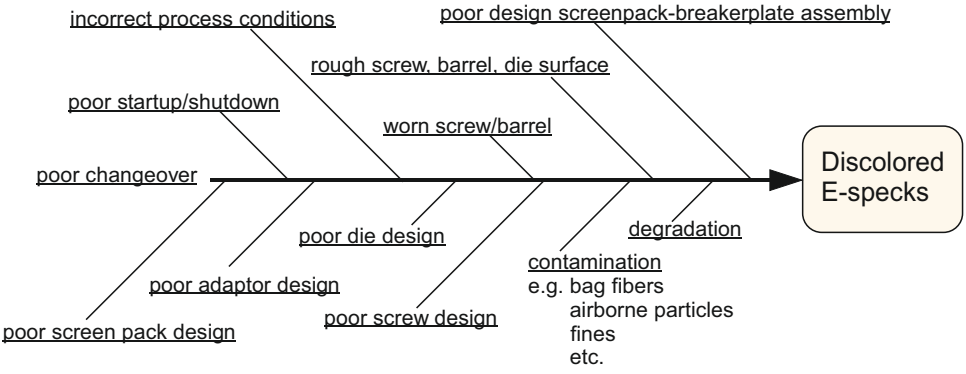


Figure 11.47 Fishbone chart for discolored E-specks

The causes listed in Fig. 11.47 by no means present a complete listing. Figure 11.47 shows some of the more common causes of discolored specks; however, other causes can certainly play a role. A detailed discussion of all the causes listed in Fig. 11.47 is beyond the scope of this book, but we will discuss one cause in detail: screw wear.

11.3.7.4.2 Screw Wear

Screw wear is a fact of life. The question is not whether or not screw wear occurs; while running an extruder, wear takes place at all times. Therefore, the pertinent question is how fast the wear reduces the outside diameter (O.D.) of the screw. More importantly, we need to know when the wear has progressed to the point where it starts causing unacceptable problems. At that point, the worn screw will need to be replaced with a new or refurbished screw.

In order to determine when the screw needs to be replaced, it is necessary to measure the O.D. of the screw over the entire length. This has to be done regularly! Special tools are available to measure the O.D. of an extruder screw; for example, see Fig. 11.48. In a typical extrusion operation, the screw and barrel should be measured at least once a year. Sometimes a company believes that they need not monitor screw and barrel wear. As a result, this company has no idea how badly the wear is affecting their process and product. When product quality starts deteriorating because of wear the appropriate corrective action is not obvious.

A simple problem that could have been solved quickly and less expensively can potentially become very expensive if the corrective action is not obvious. A problem that could have been solved by installing a spare screw may cost $500,000 if the solution to the problem is not taken. The spare screw may cost $15,000; but not being able to solve the problem in a timely fashion will cost 10 to 100 times more!

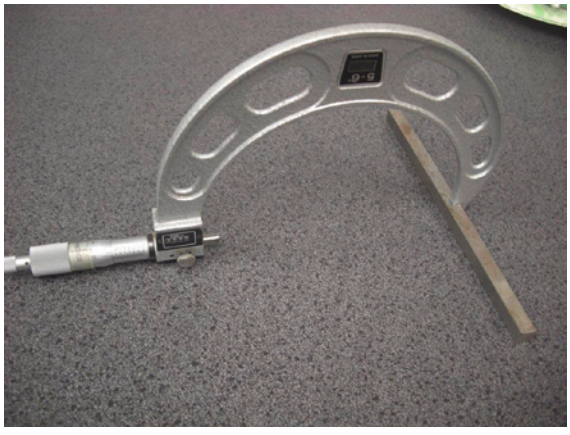


Figure 11.48
Special micrometer to measure the outside diameter

By careful process monitoring we can often detect the effects of wear. The process parameters that are affected by wear are melt temperature, output, and motor load. As wear progresses, the quality of the extruded product tends to deteriorate. This may manifest itself as discoloration, streaks, discolored specks, holes, etc. It is very important to monitor the specific energy consumption (SEC) and specific extruder throughput (SET) because changes in these parameters often correlate with wear. SEC is the ratio of motor power divided by the throughput. It is the mechanical power consumed per unit mass of plastic. The SEC tends to correlate with the melt temperature. The SEC is normally expressed in kWh/kg. A typical value of the SEC is 0.25 kWh/hr for extrusion of polyolefins.

SET is the output divided by screw speed; it is often expressed in kg/h/rpm. For instance, for a 75-mm extruder the SET may be 2.0 kg/h/rpm; this corresponds to 0.033 kg/rev. The SET is the amount of resin extruded per screw revolution.

Both SEC and SET are normalized performance parameters that allow comparison of data achieved at different process conditions, i.e., screw speed. As wear progresses, the SEC values tend to increase and the SET values tend to reduce.

Why should we be concerned about screw and barrel wear? As wear progresses the gap between the screw and barrel increases. This will reduce the pumping capability of the screw. However, the more critical issue may be the fact that the thickness of the stagnant melt layer on the barrel increases. This will increase degradation inside the extruder and reduce extrudate quality.

Screw wear will create a thicker insulating melt layer at the barrel surface. This will inhibit heat transfer between the barrel and the melt in the screw channel. As a result, the control of melt temperature will be diminished and excessively high melt temperatures are more likely. This further increases the chance of degradation.

There are additional adverse effects of screw and barrel wear. Increases in clearance will reduce the ability of the screw flights to wipe the barrel surface. This will increase the average residence and broaden the residence time distribution. As a result, changeover from one resin to another will take longer. Also, purging will take longer, as well as startup and shutdown. This means that more scrap will be produced, and the downtime will increase with a corresponding reduction in uptime. This can have a significant negative effect on the production cost.

Conclusions

Discolored specks are ubiquitous in the plastic extrusion industry. Controlling specks starts with quantifying P-specks in the incoming raw material. Once we can control P-specks to an acceptable level, we can address E-specks. Important factors that affect E-specks have been identified with one factor, screw wear, discussed in detail.

Specks are a common problem in extruded products, particularly in thin or transparent products. The specks can be black, brown, yellow, or almost any other color different from the matrix material. Specks are usually caused by contamination, degradation, or wear. Degradation can manifest itself as discoloration, specks, pinholes, loss of volatiles (smoking), or loss of physical properties in the extruded product.

To find the cause of specks and discoloration:

- Check for contamination
- Check for high temperatures
- Check for stagnation
- Check thermal stability of the plastic (perhaps improve stabilizer package)
- Check for foreign particles (wear)

Degradation can generally be reduced by:

- Reducing stock temperatures in the extruder
- Reducing the residence time in the extruder
- Eliminating the presence of degradation-promoting substances, e.g., oxygen
- Adding a thermal stabilizer or improve the stabilizer package

Poor color uniformity can be caused by mixing problems in the extruder, variation in the color additive or color concentrate, variation in the addition of the color additive or concentrate, and compatibility problems between the virgin and masterbatch. Mixing of a small amount of color concentrate (CC) in a natural polymer is actually quite difficult as discussed in Section 7.7.4. Mixing can be improved by improving the mixing capability of the extruder screw. Another way to improve mixing is to reduce the initial scale of segregation of the mixture. This can be done by:

- Reducing the particle sizes of the CC and virgin material
- Using liquid colorants

Liquid colorants can create problems in extrusion such as solids conveying problems. This can be avoided by using a porous carrier resin. Several resin suppliers (e.g., DSM, Akzo, Montell) now have porous carriers for use with liquid additives; these can be colorants or other additives, such as antioxidants, peroxides, silanes, etc. Mixing can further be improved by starve feeding the extruder as discussed in Section 11.3.4.2.5.

11.3.7.5 Lines in Extruded Product

Lines can be caused by the die, breaker plate, extruder screw, die lip build-up, and downstream equipment such as calibrators, cooling baths, catapullers, etc. If the line is visible right at the die exit, it must be formed at the die exit (e.g., by die drool), in the die (poor internal surface conditions in the die or build-up in the die), or upstream (breaker plate, screen pack, screw). A single line is often formed in a

crosshead die. With in-line dies, the number of lines often will match the number of spider supports in the die. The breaker plate can cause a large number of lines in the product.

In blown film extrusion, the number of lines in the film frequently corresponds to the number of ports in the die. As a result, these lines are often referred to as port lines. These port lines are obviously related to the die design but they are also very dependent on the melt flow characteristics of the polymer. High molecular weight polymers have very long relaxation times and are more likely to exhibit port lines or other types of die lines.

Lines can also originate downstream of the die, for instance in the calibrator. Lines can result from an object touching the extrudate or local cold or hot sections. These problems can generally be diagnosed easily by observing at what point in the production line the surface line originates.

11.3.7.5.1 Weld Lines

Lines in the extruded product can result from weld lines. These form when the polymer melt is split and recombined in the die or even before the die. Weld lines are also called knit lines; they can form in tubing and pipe dies where a mandrel is held in place by spider supports. The polymer melt is split at the start of the spider leg and flows together again behind (downstream) the spider support. Because of the limited mobility of long polymer molecules, it takes a certain amount of time for the molecules to re-entangle. This re-entanglement process is also called a “healing” process. Longer molecules take longer to re-entangle. As a result, high molecular weight (high viscosity) polymers are more susceptible to weld lines than low molecular weight (low viscosity) polymers.

The severity of the weld line problem will be determined by:

1. The length of time from the point where the melt streams recombined to the exit of the die (residence time)
2. The healing time of the polymer melt

If the residence time is longer than the healing time, the weld line will disappear inside the die and not cause a problem in the extruded product. However, if the residence time is shorter than the healing time, the weld line will not disappear inside the die and the weld line will cause a problem in the extruded product. The weld line problem can be reduced or eliminated by increasing the residence time in the die or reducing the healing time of the polymer melt.

The residence time in the die can be increased by reducing the flow rate (extruder throughput) or by changing the die geometry. The flow splitter has to be located as far away from the die exit as possible. Some die geometries reduce weld line problems. For instance, spiral mandrel dies for pipe, tubing, and blown film spread out

the weld line as the melt flows through the spiral mandrel section; this largely eliminates problems with weld lines. Tubing and pipe dies with a rotating mandrel and/or die can also effectively spread out the weld lines and eliminate weld line problems. Some dies incorporate relaxation zones to enhance the healing process. Relaxation zones are basically local regions in the die flow channel where the cross-sectional area of the channel is increased.

The healing time depends on the molecular characteristics of the polymer and the melt temperature. Reducing the molecular weight of the polymer will speed up the re-entanglement process. Also, higher melt temperatures will increase the mobility of the polymer molecules and reduce the healing time. The molecular architecture also plays an important role. The molecules of linear polymers tend to align more readily and, as a result, entangle more slowly when separate flow streams meet. This is a particular problem in liquid crystalline polymers (LCPs), which have rod-like molecules. As a result, LCPs are highly susceptible to weld lines. Another method to promote re-entanglement is to subject the material in the die to a high-frequency vibration. Some processors use ultrasonic vibration of the die by mounting external transducers that deliver ultrasonic energy in the kilohertz range. Because polymers are not only shear thinning but also frequency thinning, the effective viscosity of the polymer melt is reduced by high-frequency vibration. Other benefits of high-frequency vibration are reduced extrudate swell, reduced extrudate distortion at the die exit, reduced melt fracture, and reduced die lip build-up (die drool).

11.3.7.6 Optical Properties

Optical properties such as transparency, matness, gloss, and haze are strongly determined by the cooling conditions of the extruded product. In crystalline polymers, the crystal growth is very much temperature and stress dependent. As a result, the morphology of the extruded product will depend on how rapidly the polymer melt is cooled as it leaves the die. Slow cooling generally promotes crystal growth. Rapid cooling reduces crystallization; in fact, in some semi-crystalline polymers the crystallinity can be suppressed completely with rapid cooling.

In sheet extrusion where the molten sheet of polymer is forced through a set of rolls, the surface conditions are strongly determined by the surface texture of the rolls. If the rolls are polished, they will impart a polished surface onto the polymer sheet—this is why these rolls are often called polishing rolls. Obviously, a variety of different textures can be machined into the rolls and, consequently, a number of different textures can be imparted to the extruded sheet.

References

1. E. Wagner, Ph. D. thesis, Technische Hochschule Darmstadt, Germany (1978)
2. M. M. Kruschchov, Ind. Lab (USSR), 20, 372–376 (1962)
3. G. Mennig and P. Volz, Kunststoffe, 70, 385–390 (1980)
4. W. Mehdorn, Kunststoffe, 34, 133–136 (1944)
5. W. Bauer, K. Eichler, and W. John, Kunststoffe, 57, 53–55 (1967)
6. K. Eichler and W. Frank, Ind. Anzeiger, 95, 2033–2035 (1973)
7. W. D. Mahler, Ph. D. thesis, Technische Hochschule Darmstadt, Germany (1975)
8. P. Volz, W. D. Mahler, and G. Menning, Kunststoffe, 66, 428–434 (1976)
9. W. Knappe and W. D. Mahler, Kunststoff-Rundschau, 19, 45–51 (1972)
10. R. S. Plumb and W. A. Glaeser, Wear, 46, 219–229 (1978)
11. H. G. Fritz, Kunststoffe, 65, 176–182 and 258–274 (1975)
12. P. Volz, Kunststoffe, 69, 758–771 (1979)
13. P. Volz, Kunststoffe, 67, 279–283 (1976)
14. G. P. Calloway, E. D. Morrison, and R. F. Williams, Jr., SPE ANTEC, 354–360 (1972)
15. D. Braun and G. Maelhammer, Angew. Makromol. Chem., 69, 157–167 (1978)
16. H. G. Moslé, H. F. Schmidt, and J. Schroeder, Kunststoffe, 67, 220–223 (1977)
17. G. Maelhammar, Ph. D. thesis, Technische Hochschule Darmstadt, Germany (1978)
18. P. Volz, Kunststoffe, 69, 259–262 (1979)
19. E. Broszeit, Ph. D. thesis, Technische Hochschule Darmstadt, Germany (1972)
20. G. A. Saltzman and J. H. Olson, SPE ANTEC, 173–175 (1974)
21. V. Murer and G. A. Saltzman, Kunststoffe, 66, 219–220 (1976)
22. W. W. McCandles and W. D. Maddy, Plast. Technol., Feb., 89–93 (1981)
23. S. H. Collins, Plast. Compd., May/June, 113–124 (1982)
24. S. H. Collins, Plast. Compd., July/Aug., 16–28 (1982)
25. E. L. Moon and R. A. Hunter, "An Abrasion Study of Surface Treated Calcium Carbonate Fillers in Rigid PVC," Technical Bulletin, Georgia Marble Corp., Atlanta, GA
26. W. D. Mahler, Kunststoffe, 67, 224–226 (1977)
27. B. A. Olmsted, SPE J., 26, 42–43 (1970)
28. P. Luelsdorf, "Grundlagen der Extrudertechnik" VDI-Lehrgang (1975)
29. R. A. Lai Fook and R. A. Worth, SPE ANTEC, Washington, DC, pp. 450–452 (1978)
30. H. H. Winter, SPE ANTEC, New Orleans, 170–175 (1979)
31. H. Schuele and H. G. Fritz, Kunststoffe, 73, 603–605 (1983)
32. K. O'Brien, Plast. Technol., Feb., 73–74 (1982)
33. G. Thursfield, Mod. Plast., Oct., 94–96 (1975)
34. M. Hoffmann, Plast. Technol., April, 67–72 (1982)
35. K. Luker, Paper presented at the TAPPI Paper Synthetics Conference in Lake Buena Vista, Florida (1983)

36. W. Lucius, Kunststoffe, 63, 433–435 (1973)
37. C. Panzera and G. A. Saltzman, Proceedings of the 2nd International Conference on Wear of Materials, 441–448 (1979)
38. A. Casale and R. S. Porter, "Polymer Stress Reactions," Vol. 1 and 2, Academic Press, New York (1978)
39. Y. I. Frenkel, Acta Physicochim. (USSR), 19, 51 (1944)
40. W. J. Kauzmann and H. Eyring, J. Am. Chem. Soc., 62, 3113 (1940)
41. F. Bueche, "Physical Properties of Polymers," Wiley, New York (1962)
42. K. Arisawa and R. S. Porter, J. Appl. Polym. Sci., 14, 879 (1970)
43. A. Holmstrom, A. Andersszon, and E. M. Sorvik, Polym. Eng. Sci., 17, 728–273 (1977)
44. P. W. Springer, R. S. Bradley, and R. E. Lynn, Polym. Eng. Sci., 15, 583–587 (1975)
45. V. L. Folt, Rubber Chem. Technol., 42, 1294 (1969)
46. R. W. Ford, R. A. Scott, and R. J. B. Wilson, J. Appl. Polym. Sci., 12, 547 (1968)
47. J. A. Odell, A. Keller, and M. J. Miles, Polym. Commun., 24, 7–10 (1983)
48. G. Pinto and Z. Tadmor, Polym. Eng. Sci., 10, 279–288 (1970)
49. D. Bigg and S. Middleman, Ind. Eng. Chem. Fundam., 13, 66–71 (1974)
50. G. Lidor and Z. Tadmor, Polym. Eng. Sci., 16, 450–462 (1976)
51. D. Wolf and D. H. White, AIChE J., 22, 122–131 (1976)
52. C. J. Rauwendaal, Polym. Eng. Sci., 21, 1982–1100 (1981)
53. J. C. Golba, SPE ANTEC, New York, 83–87 (1980)
54. Z. Kemblowski and J. Sek, Polym. Eng. Sci., 21, 1194–1202 (1981)
55. N. R. Schott and D. V. Saleh, 36th SPE ANTEC, Washington, DC, 536–539 (1978)
56. D. B. Todd, Polym. Eng. Sci., 15, 437–443 (1975)
57. L. P. B. M. Janssen, "Twin Screw Extrusion," Elsevier, New York (1978)
58. L. P. B. M. Janssen, R. W. Hollander, M. W. Spoor, and J. M. Smith, AIChE J., 25, 345–351 (1979)
59. C. J. Walk, SPE ANTEC, San Francisco, 423–426 (1982)
60. R. J. Nichols, J. C. Golba, and P. K. Shete, paper presented at the AIChE Annual Meeting, Paper No. 59F (1983)
61. O. Levenspiel, "Chemical Reaction Engineering," Wiley, New York (1965)
62. D. M. Himmelblau and K. A. Bischoff, "Chemical Process Analysis," Wiley, New York (1966)
63. P. V. Danckwers, Chem. Eng. Sci., 2, 1 (1953)
64. Z. Tadmor and C. G. Gogos, "Principles of Polymer Processing," Wiley, New York (1979)
65. L. P. B. M. Janssen, G. H. Noomen, and J. M. Smith, Plast. Polym., Aug., 135–140 (1975)
66. S. Anders, D. Brunner, and F. Panhaus, Plaste und Kautschuk, 23, 593–598 (1976)
67. H. E. H. Meijer, J. F. Ingen Housz, and W. C. M. Gorissen, Polym. Eng. Sci., 18, 288–292 (1978)

68. N.C. Wheeler, Annual Conv. Wire Assoc., Baltimore, MD, Oct. 22–25 (1962)
69. R.T. Fenner, A.P.D. Cox, and D.P. Isherwood, Polymer, 20, 733–736 (1979)
70. Z. Tadmor and I. Klein, "Engineering Principles of Plasticating Extrusion," p. 413, Van Nostrand Reinhold, New York (1970)
71. I.R. Edmondson and R.T. Fenner, Polymer, 16, 49–56 (1975)
72. B.H. Maddock, SPE J., 20, 1277 (1964)
73. R. Bonetti, Met. Prog., June (1981)
74. S. Levy, Plast. Mach. Equip., March (1984)
75. S. Trompler, Kunststoffe, 73, 596 (1983)
76. H.W. Gitschner and J. Lutterbeck, Kunststoffe, 74, 12–14 (1984)
77. R.S. Porter and A. Casale, Polym. Eng. Sci., 25, 129–156 (1985)
78. C.J. Rauwendaal, "Statistical Process Control in Injection Molding and Extrusion," Carl Hanser Publishers, Munich (1999)
79. C.J. Rauwendaal and K. Cantor, 56th SPE ANTEC, Atlanta, GA, 340–344 (1998), also published in Plast. Eng., June, 41–43 (1998)
80. G. Mennig, "Wear in Plastics Processing," Carl Hanser Publishers, Munich (1995)
81. "Plasticating Components 2000" a publication from Spirex Corporation, Youngstown, Ohio (2000)
82. V. Anand and K. Das, "The Selection of Screw Base and Hard Facing Materials," publication CEC SSB 493.01 from Canterbury Engineering Company, Inc., Champlee, Georgia
83. C.J. Rauwendaal, "Leakage Flow in Extruders," Doctoral Thesis, Twente University, the Netherlands (1988)
84. C.J. Rauwendaal and J. Anderson, 52nd SPE ANTEC, 298–305 (1994)
85. C.J. Rauwendaal, 47th SPE ANTEC, New York, NY, 108–110 (1989)
86. J.F.T. Pittman, Dev. Plast. Technol., 3, 203–273 (1986)
87. C.J. Rauwendaal and J.F. Ingen Housz, Int. Polym. Proc., 3, 123–133 (1988)
88. P. Gramann, T. Osswald, B. Davis, and C.J. Rauwendaal, 56th SPE ANTEC, Atlanta, GA, 277–283 (1998)
89. C. Rauwendaal, "New Dispersive Mixers for Single and Twin Screw Extruders," Annual Meeting of the Polymer Processing Society, Yokohama, Japan, June 8–12 (1998)
90. C.J. Rauwendaal, "A New Dispersive Mixer," Plast. Addit. Compd., Sept. (1999)
91. C.J. Rauwendaal, "Eliminate Gels and other Mixing Problems," Film Conference 99, Somerset, NJ, 141–148, Dec. 7–9 (1999)
92. C.J. Rauwendaal, "How to Improve Mixing by Generating Elongational Flow," Compounding Conference, Cleveland, OH, 219–228, Nov. 14–15 (2000)
93. U.S. Patent 5,932,159, C.J. Rauwendaal (1999)
94. U.S. Patent 6,136,246, C.J. Rauwendaal, P. Gramann, B. Davis, T. Osswald (2000)
95. U.S. Patent 3,006,029 (1961)
96. F.N. Cogswell, J. Non-Newtonian Fluid Mech., 2, 373–47 (1977)

97. M.T. Dennison, Trans. J. Plast. Inst., 35, 803–808 (1967)
98. I.J. Benbow and E.R. Howells, Trans. J. Plast. Inst., 30, 240–254 (1960)
99. British Patent 32559/72
100. I.P. Tordella, in "Rheology," Vol. 4, Chapter 3, F.R. Eirich (Ed.), Academic Press, New York (1969)
101. J.L. White, Appl. Polym. Symp., No. 20, 155 (1973)
102. J.M. Lupton and J.W. Regester, Polym. Eng. Sci., 5, 235 (1965)
103. I.L. Blyler and A.C. Hart, Polym. Eng. Sci., 10, 193 (1970)
104. S.M. Barnett, Polym. Eng. Sci., 7, 168 (1967)
105. E. Boudreaux and J.A. Cuculo, J. Macromol. Sci.—Rev. Macromol. Chem., C16, 39–77 (1977–1978)
106. C.D. Han and R.R. Lamonte, Polym. Eng. Sci., 11, 385 (1971)
107. J.L. den Otter, Rheol. Acta, 10, 200–207 (1971)
108. T.W. Huseby, Trans. Soc. Rheol., 10, 181–190 (1966)
109. A.P. Metzger and C.W. Hamilton, SPE Trans., 4, 107–112 (1964)
110. G.V. Vinogradov et al., Polym. Eng. Sci., 12, 323–334 (1972)
111. J.J. Benbow and P. Lamb, SPE Trans., 3, 7–17 (1963)
112. W. Phillippoff and F.H. Gaskins, Trans. Soc. Rheol., I, 263–284 (1958)
113. C.J.S. Petrie and M.M. Denn, AIChE J., 22, 109–236 (1976)
114. W. Gleissle, Rheol. Acta, 21, 484 (1982)
115. J.J. Benbow, R.V. Charley, and P. Lamb, Nature, 192, 223 (1961)
116. L.A. Utracki and R. Gendron, J. Rheol., 5, 28, 601–623 (1984)
117. U.S. Patent 2,991,508 by R.T. Fields and C.F.W. Wolf to E.I. DuPont de Nemours and Company, issued July 11 (1961)
118. A.M. Kraynik and W.R. Schowalter, J. Rheol., 25, 95–114 (1981)
119. R.A. Worth, J. Parnaby, and H.A.A. Helmy, Polym. Eng. Sci., 17, 257 (1977)
120. C.J.S. Petrie and M.M. Denn, AIChE J., 22, 236–246 (1976)
121. J.C. Miller, SPE Trans., 3, 134 (1963)
122. S. Kase, J. Appl Polym. Sci., 18, 3279 (1974)
123. G.F. Cruz-Saenz, G.J. Donnelly, and C.B. Weinberger, AIChE J., 22, 441 (1976)
124. J.R.A. Pearson and Y.T. Shah, Trans. Soc. Rheol., 16, 519 (1972)
125. J.R.A. Pearson and Y.T. Shah, Ind. Eng. Chem. Fundam., 13, 134 (1979)
126. R.J. Fischer and M.M. Denn, Chem. Eng. Sci., 30, 1129 (1975)
127. Y. Ide and J. L. White, J. Appl. Polym. Sci., 20, 2511–2531 (1976)
128. Y. Ide and J.L. White, J. Non-Newtonian Fluid Mech., 2, 281–298 (1977)
129. Y. Ide and J.L. White, J. Appl. Polym. Sci., 22, 1061–1079 (1978)
130. J.L. White and Y. Ide, J. Appl. Polym. Sci., 22, 3058–3074 (1978)
131. R.S. Lenk, J. Appl. Polym. Sci., 22, 1781–1785 (1970)

132. N.C. Wheeler, Annual Convention Wire Association, Baltimore, MD, Oct. 22–25 (1962)
133. J. Becker, P. Bengtsson, C. Klason, J. Kubat, and P. Saha, Int. Polym. Process., VI, no. 4, 318–325 (1991)
134. J. Becker, C. Klason, J. Kubat, and P. Saha, Int. Polym. Process., VI, no. 4, 326–331 (1991)
135. G.M. Gale, 49th SPE ANTEC, 95 (1991)
136. G.M. Gale, Adv. Polym. Technol., 16, no. 4, 251 (1997)
137. M.H. Mack, Plast. Eng., 47, no. 12, 39 (1991)
138. I.R. Thompson, G. Donoian, and J.C. Christiano, 57th SPE ANTEC, 145 (1999)
139. P. Elemans and J.M. van Wunnik, 58th SPE ANTEC, 265–267 (2000)
140. P. Elemans, 58th SPE ANTEC, 2582–2586 (2000)
141. K. Luker, paper presented at the Continuous Compounding Conference, Beachwood, Ohio, Nov. 14–15 (2000)
142. K. Luker, paper presented at the Wood Composite Conference, Dec. 5–6 (2000)
143. C.J. Rauwendaal, "Polymer Mixing, A Self-Study Guide," Carl Hanser Publishers, Munich (1998)
144. R.H. Reinhard, A.R. Crixell, C.L. Loney, and P.W. Tidwell, 32nd SPE ANTEC, 40–42 (1974)
145. T. Osswald, P. Gramann, B. Davis, M. del Pilar Noriega, and O.A. Estrada, 57th SPE ANTEC, New York, 167–176 (1999), also the annual meeting of the Polymer Processing Society in Den Bosch, the Netherlands (1999)
146. P. Limbach, in "Extrusion Solutions," publication by the SPE Extrusion Division, p. 6 (1999)
147. C.J. Rauwendaal and P. Gramann, 56th SPE ANTEC, Atlanta, GA, 102–106 (1998)
148. L.B.P.M. Janssen, G.H. Noomen, and J.M. Smith, Plast. Polym., Aug., 135–140 (1975)
149. D.I. Marshall, I. Klein, and R.H. Uhl, SPE J., 20, no. 4, April, 329 (1964)
150. S.A. Klein, W.A. Beckman, and G.E. Myers, FEHT: Finite Element Analysis, Vol. 6.98, University of Wisconsin-Madison (1997)
151. T. Butler, Private communication (2001)
152. C.J. Rauwendaal, Unpublished study (1978)
153. S.E. Amos, G.M. Giacoletto, J.H. Horns, C. Lavallée, and S.S. Woods, in "Plastics Additives Handbook," H. Zweifel (Ed.), 5th ed., Carl Hanser Publishers, Munich (2000)
154. T.J. Blong, K. Focquet, C. Lavallée, SPE ANTEC Tech. Papers, 3011 (1997)
155. C.M. Chan, "Viscosity and the Formation of Die Drool at the Polymer-Metal Interfaces," Int. Polym. Process., 10 (1995)
156. D.E. Priester, G.R. Chapman, "Reducing Die Build Up in Extrusion Applications," Technical Information, DuPont Dow Elastomers
157. S.E. Amos, SPE ANTEC Tech. Papers, pp.133–143 (1997)
158. D.E. Hauenstein, D.J. Cimbalik, and P.G. Pape, SPE ANTEC Tech. Papers, 3002–3010 (1997)

159. M. del Pilar Noriega and C.J. Rauwendaal, "Troubleshooting the Extrusion Process," Carl Hanser Publishers, Munich (2001)

160. G. Mennig, 36th SPE ANTEC, Washington, DC, 529–531 (1978)

161. D.H. Wilson, "Feeding Technology for Plastics Processing," Carl Hanser Publishers, Munich (1998)

162. J. Ogando, Plast. Technol., Feb., 54–63 (1995)

163. ASTM D2765, Standard Test Methods for Determination of Gel Content and Swell Ratio of Crosslinked Polyethylene Plastics

164. H. Overeijnder, "Extrusion of PVC Pipe," Course "Extrusie" at Twente University of Technology, Feb. 4–6 (2013)

165. P. Gramann and J. Cruz, "Determining the Quality of Failed PVC Pipe," SPE Plast. Res. Online, 10.1002/spepro.000056

166. "Pellet, Powder, Quality Control," brochure by Optical Control Systems, GmbH (www.ocsgmbh.com)

167. "Fewer Gels Means More Peace of Mind," publication by Dow Chemical, (http://msdssearch.dow.com/PublishedLiteratureDOWCOM/dh_08cb/0901b803808cbf1e.pdf?filepath=elastomers/pdfs/noreg/265-12101.pdf&fromPage=GetDoc)

168. K.A. Howard, "Gel Defects in LDPE Film—Resolving Polymer and Process Effects," TAPPI 2001 PLACE Conference (2001)

12 Modeling and Simulation of the Extrusion Process

Paul J. Gramann, Bruce A. Davis, and Tim A. Osswald

12.1 Introduction

In most polymer processes, the quality of the final part is greatly dependent on the melting, flow and mixing of the polymer. The optimization of the equipment and manufacturing process, as done today, is time consuming and expensive. It is often necessary to build complex flow visualization equipment, i.e., model extruders with transparent barrels, to qualify the flow during processes. Quantifying flow and heat transfer is an even more intimidating task. Furthermore, reproducing the properties of a particular blend from batch to batch can be extremely difficult. Obviously, these barriers make numerical simulation a viable alternative when optimizing and analyzing the extrusion process.

Traditionally, when simulating polymer processes, the main concern of the engineer has been to accurately represent the material behavior using complex models. Although many problems still exist regarding polymer material models and will continue to be a field of research, today one can easily deal with the shear thinning behavior, temperature dependence and to some degree the viscoelasticity of polymers. In fact, to date a large number of processes have been realistically simulated in polymer processing ranging from mold filling with fiber orientation, shrinkage and warpage, to extrusion with viscoelastic effects. However, only a few fully three-dimensional models of realistic processes have been solved. Simulating a fully three-dimensional process involves intensive labor, trying to accurately represent the geometry of the device and also requires large amounts of computation time and data storage. Obviously, computational demands have been reduced by the enormous increase in computational power available to the engineer at the desktop. However, the labor intensity and requirements of computer performance are multiplied by the added complexity of moving boundaries. Two types of moving boundaries are very common in polymer processing: *moving free boundaries* and *moving solid boundaries*.* Moving free boundary problems are encountered in such areas as mold filling, extrudate swell, coating problems, inside the extruder at the screw, to name a few. Solid moving boundaries are those where the actual cavity that con-

* The name "moving solid boundary problems" for this category of problems was introduced by Prof. C. L. Tucker III in his keynote talk "Mathematical Modeling: ON to Maturity!," PPS 9 Manchester, 1993

tains the polymer changes in shape during the process, i.e., the rotating mixing heads in an internal batch mixer, or the screw and mixing elements in a single screw extruder.* The most complex process involving solid moving boundaries is the intermeshing twin screw extruder. Here, the domain of interest, i.e., the polymer, is constantly changing shape as the screws, mixing heads, and kneading blocks rotate. The self-wiping arrangement of these systems adds to the complexity of the problem, since it involves very small gaps, which introduce numerical complications. One should regard the complete simulation of the single or twin screw extrusion processes including melting, melt conveying, mixing, and die flow to the prediction of final morphology, including coalescence and a partially filled system, as one of the grand challenge problems in polymer processing.

Before attempting to solve such problems, their complex geometry and processing conditions can be simplified to a form in which they can be modeled with two-dimensional simulations. Simplifications may include laying-flat curved surfaces, neglecting thinner dimensions, assuming planar problems, etc., at the cost of possibly losing important features that dominate the flow and heat transfer in the process. The advent of more powerful computers and efficient numerical techniques are now beginning to make it possible to simulate three-dimensional problems of complex geometry with non-linear material behavior.

This chapter gives a general overview of the state-of-the art techniques used for the modeling and simulation of the extrusion process. Recent developments of computational and numerical technologies are presented along with a discussion of the direction this growing field is taking. A brief background on numerical techniques and basic modeling in polymer processing is presented. A discussion on two-dimensional models that are used to simulate three-dimensional flows is followed by recent advancements in full three-dimensional models.

12.2 Background

12.2.1 Analytical Techniques

Before describing numerical methods, the technique of using analytical or pseudo-analytical solutions will be discussed. Strictly speaking, a problem has an analytical solution if a mathematical equation can fully describe the phenomena examined. This is usually reserved for simple geometries, with simple conditions and properties. However, by applying specific assumptions and limiting the scope of the problem to be solved, analytical techniques can be applied to more realistic situations. In

* An assumption that the device is completely filled is taken, which may not always be realistic.

1922, Rowell and Finlayson [1] solved the down channel velocity profile for a screw pump.

The major design variables of the screw, including throughput, pressure, and power consumption are described by Tadmor et al. [2]. The value of being able to predict the output, melt temperature, and pressure development along the screw is fairly obvious, but computer simulation can show even more. One example is the rate of solids melting and the corresponding solid bed width. In the feed section of the extruder, the solid bed occupies 100% of the channel width. As the solids melt, the solid bed will occupy less of the channel so that ideally no solids remain at the end of the extruder. Figure 12.1(a) shows a plot of the solid bed width as predicted by simulation* for a given design and operating condition [3]. The x-axis represents the fraction of the channel occupied by the solid bed and the y-axis the relative position along the screw. The solid bed width begins with a value of 1.0 in the feed section and gradually reduces to 0.0 at around 60% along the screw length, which allows room for mixing sections to be used.

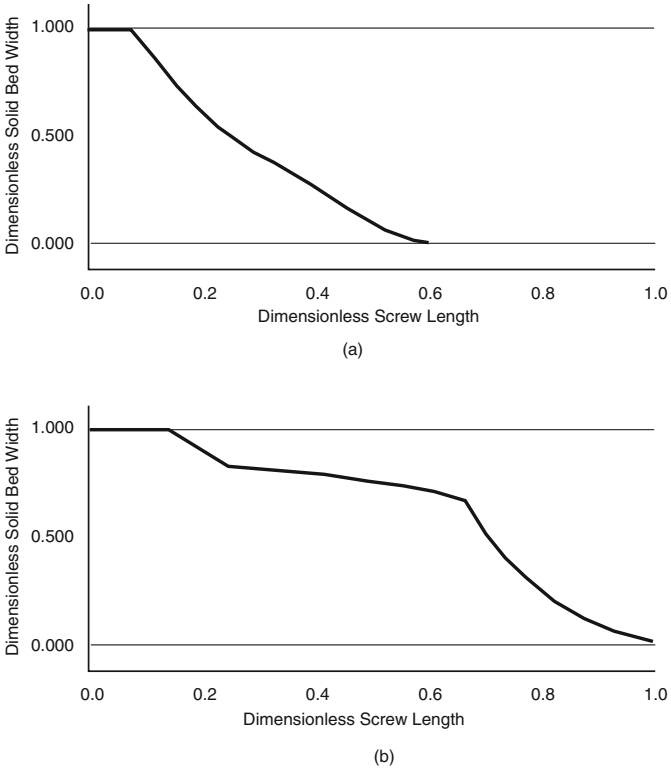


Figure 12.1 Predicted solid bed profile down the channel of a single screw extruder [4] (a) Solid bed melts completely before metering section (b) solid bed is not completely melted when it reaches the metering section

* Flow 2000(TM) Suite of CAE Tools for Extrusion, Compuplast International

Modifying the screw design, material or operating conditions can result in a completely different solid bed profile as shown in Fig. 12.1(b) [4]. In this case, the simulation predicts that the solid bed width reduces much slower and that melting is not completed until the very end of the screw. This is clearly a less desirable condition than the one shown in Fig. 12.1(a) because there is the potential for some material not to melt and mix properly before leaving the extruder. An extreme case of this can result if the reduction in the solid bed is slower than the compression rate of the screw. In this case, the volume of the channel is reducing faster than the volume of the solid bed. This forces the solid bed to expand, accelerate, or break-up. Premature solid bed break-up can lead to extrudate surging and a poorly mixed material.

The method of applying analytical techniques for the simulation of the extrusion process is currently the most common to design an extrusion system.* When the fine details of flow and how it influences the quality of the extrusion process are of interest, more detailed numerical techniques are typically preferred.

12.2.2 Numerical Methods

In order to predict and model complex polymer flows, a basic understanding of the mathematics that govern the flow is necessary. Regardless of the complexity of the flow, it must satisfy certain physical laws. These laws can be expressed in mathematical terms as the conservation of mass, the conservation of momentum, and the conservation of energy. In addition to these three conservation equations, there may also be one or more constitutive equations, which describe material properties, i. e., shear thinning behavior. Since these equations may also be coupled together, i. e., temperature dependent viscosity, the solution becomes even more complex. The goal of the modeler is to take a physical problem, apply these mathematical equations, and solve them to predict the flow phenomena. Although analytical solutions to the conservation equations for some simple two-dimensional shapes are available, when more complex two-dimensional problems need to be solved or a three-dimensional analysis is required, numerical methods are to be used.

Beyond using analytical solutions, there are three basic classes of numerical techniques that are commonly used to solve complex fluid flow problems: the finite difference method (FDM), the finite element method (FEM), and the boundary element method (BEM) [5]. Each of these methods has its advantages and disadvantages and, therefore, one may be preferred for a certain type of process or material. Each technique has been adapted in some form for specific problems encountered in polymer processing. Although it is not the purpose of this chapter to provide a detailed deri-

* Examples of commercial programs of this type are: Flow 2000(TM) from Compuplast Intl., Extrud 2000 from SPR, Inc., REX from the University of Paterborn

vation of the three numerical methods mentioned, it is necessary to provide a general description of each.

12.2.2.1 Finite Difference Method

The finite difference method started gaining prevalence in the 1930s for use in hand calculations and is the simplest to use and understand. Figure 12.2(a) shows the grid constructed to represent the geometry of a two-dimensional domain.

Once the grid is created, the governing differential equations are rewritten in a discretized form and then applied at each nodal point. The resulting system of algebraic equations can then be solved by standard Gaussian elimination or by more elaborate numerical algorithms. Because of the simplicity of the method, it can be implemented in a wide variety of problems. Since the method discretizes the governing equations at the start of the analysis, it relatively easy to model non-linear problems. The finite difference method is straight forward to program and can have quick computation times. While the simple nature of the finite difference method allows for easy programming, this simplicity also yields certain limitations and other disadvantages. The first consideration when implementing the FDM is that it is best suited for cases that have relatively simple geometries. Even though more complex geometries have been modeled with special differential equations or coordinate transformations, limitations still exist, and the other methods presented in this chapter often prove to be more efficient. Because discretization of the actual governing equations occurs at the start of the analysis, more error is introduced early in its derivation, which is then carried through the computation. Therefore, FDM can have problems with obtaining a convergent solution for non-linear problems. Since the FDM is a domain method, it typically takes considerable effort to discretize the geometry of interest, which can severely limit its application to realistic devices. In addition, FDM is not well suited to model problems with moving solid boundaries.

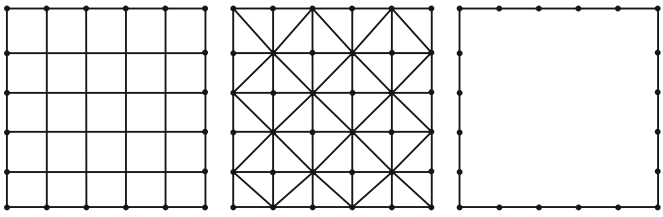


Figure 12.2 Mesh representation for common numerical methods (a) FDM (b) FEM (c) BEM

12.2.2.2 Finite Element Method

In contrast to FDM, the finite element method (FEM) is a relatively new technique used for solving fluid flow problems. Popularized in the 1960s along with the advent of digital computers, FEM has become the basis for most commercial structural dynamic and fluid flow simulation programs. Like FDM, FEM is a domain method in which the entire geometry to be modeled must be discretized into nodes and elements. The mesh shown in Fig. 12.2(b) represents the discretization required for FEM to model a two-dimensional geometry. Although several different methods are available to obtain the final equations, the Galerkin method [5] of weighted residuals is normally preferred in fluid flow problems. Once the mesh has been created, the governing differential equations are then expressed in integral form and numerically integrated to obtain an algebraic system of equations. Because of the nature of the finite element method, it is capable of modeling much more complex geometries than FDM. It can also provide quite accurate solutions to the field variables, such as fluid velocities or pressures, for a wide variety of problems that include non-linear flows. However, higher order derivative solutions, such as velocity gradients, tend to be less accurate. Without complex adaptive meshing techniques, FEM is also difficult to use for problems with moving solid boundaries. Since the governing equations are approximated with the Galerkin method, they have a certain amount of intrinsic error even before numerical errors are accounted for, which is carried throughout the computation. This can cause the FEM to become unstable in highly non-linear situations. Although this can be partially alleviated by special upwinding techniques [6], it nonetheless increases the amount of computation effort. In addition, because the solution is computed only at the nodes and the velocity field must be interpolated, the tracking of particles in the flow field in not easily accomplished with FEM.

To overcome the limitations that exist with FEM when dealing with moving boundaries, Avalosse et al. [7] used a special FEM method referred to as the Mesh Superposition Technique (MST). With this technique, a finite element mesh is created for each part of the system. For example, when analyzing a batch mixer, a fully three-dimensional mesh is generated for the bowl without the mixer. Another three-dimensional mesh of the mixing apparatus alone without the bowl is also created. Both meshes are then combined to create an overlapping of both regions. The overlapping region is accounted for by using a penalty formation that imposes the proper velocity. For example, with extrusion, the nodes from the mesh of the barrel that are within the domain of the screw are given the rotational speed of the screw, everywhere else the nodes are handled in the normal way. With this technique, Avalosse et al. [7] were able to take into account non-isothermal, non-Newtonian effects when simulating solid moving boundaries.

The finite element has proved to be ideal when simulating the mold filling, fiber orientation, shrinkage, and warpage of thin plastic parts. With more difficulty, it has

been used to simulate the fluid flow in batch mixers, dies, and single and twin screw extruders.

12.2.2.3 Boundary Element Method

In contrast to both the finite difference and finite element methods, the boundary element method (BEM) is a technique that only requires the boundary or surfaces of the geometry be discretized. As shown in Fig. 12.2(c), a two-dimensional geometry only requires a discretization of the curve that makes up the boundary of the part. In essence, the order of analysis being made is reduced by one. For example, the two-dimensional geometry shown in Fig. 12.2(c) is meshed (discretized) with one-dimensional elements. Similarly, a three-dimensional geometry is meshed with two-dimensional elements because only the surface of the geometry is defined. It is important to note that a two-dimensional BEM analysis is still two-dimensional and a three-dimensional BEM analysis is three-dimensional because the velocity and velocity gradients and other attributes can be calculated at any place in the domain (where the fluid is) of the geometry.

BEM gained prevalence around the same time as FEM, but because of the relatively complex mathematics involved with BEM, it has been relatively slow to gain the same level of acceptance that FEM did in the engineering community, and has primarily been used by mathematicians. The formulation of the boundary element method begins with a different form of the governing equations, which are expressed in terms of domain integrals. These integrals are manipulated by Green-Gauss transformations until they are reduced to boundary integrals [8–11]. The integrals are then numerically evaluated to yield an algebraic system of equations. Up to the point of evaluating the integrals, no approximations have been made in the governing equations. Thus, the boundary element method, unlike the FDM or FEM, does not introduce any error to the solution until the boundary is discretized—the boundary element solution is *exact* until the geometry is meshed.* Another advantage of BEM is the fact that the accuracy of higher order derivatives is excellent. This becomes extremely important when calculating heat transfer effects or tracking particles. Here, the boundary element method is well suited to track particles in the flow of material since the solution at any location in the fluid can be obtained quite easily and very accurately.

The reduction of the dimensionality is a key advantage to modeling polymer flows in complex geometries with this technique. Because only the boundary or surface of the domain needs to be defined, which is relatively simple with the many commercially available solid modelers, the amount of work for the engineer is dramatically reduced. Moreover, this method can handle moving solid boundaries with relative

* An exact solution with regards to the material model used, which up to this point has been limited to Newtonian flows.

ease because the mesh moves right along with the moving boundary. For example, when simulating the extrusion process, the mesh describes the geometry of the screw and when it rotates the nodes and elements that make up the screw simply rotate with it.

Although BEM is quite an elegant technique for linear problems, it loses many of its advantages when non-linear problems are investigated. The standard BEM is only able to handle non-linearities by using domain meshing, thus eliminating the boundary-only discretization. Recently, Nardini and Brebbia [12] have developed a variation of BEM, known as the Dual Reciprocity Method (DRM), which has the ability to solve non-linearities with a boundary-only formulation. The application of DRM to polymer processing fluid flow applications is still an open problem [9, 13] and will be examined later in this chapter.

12.2.3 Remeshing Techniques in Moving Boundary Problems

The major difficulty, which arises when simulating a mixing process, is the transient free surface or solid moving boundaries, respectively. The material constantly changes shape as it flows, making it necessary to redefine the geometry of the domain of interest after each successive time step. Redefining the finite element mesh or finite difference grid is the most tedious part of simulations when dealing with moving boundary problems and many times makes it unreasonable to simulate.

Wang, Hieber and Wang [14] implemented a mesh editing procedure or dynamic mesh generator into an injection molding simulation.* After carefully choosing a time step and advancing the flow fronts, the user is required to fill the gap between the old and the updated melt fronts with new triangular finite elements. Obviously, this procedure not only requires extensive user interaction but also makes the mesh sizing dependent on the size of the chosen time step.

The compression mold filling simulation of Lee, Folger and Tucker [15] used a finite element mesh to represent the initial charge. The same mesh was used after each time step to fit the shape of the charge. This was accomplished with a finite element calculation, which used the displacements of the nodes on the free flow fronts as boundary conditions. This procedure is analogous to drawing the original mesh on a sheet of rubber and then stretching it to conform to the shape of the charge at any time step. The mesh stretching technique kept elements from becoming so distorted as to cause large numerical errors. This technique required a minimum amount of computation and ran automatically once the problem was set. However, it does not

* A review of simulation processes for injection molding can be found in a chapter by Davis, B. A. and Rios, A. C. in the Injection Molding Handbook edited by Osswald, T. A., Turng, T., and Gramann, P. J., Carl Hanser (2001)

handle problems that have multiple charges, mold inserts, or problems where the initial shape of the charge differs greatly from the mold shape or final shape of the charge. However, the technique applies very well to the blow molding and thermoforming process. Here, the initial finite element mesh that represents the parison or sheet is stretched to fit the shape of the material as it is formed into its final shape. Kouba and Vlachopoulos [16] and deLorenzi and Nied [17] used such a technique to model membrane stretching during blow molding and thermoforming. Although the processes are basically three-dimensional, they can be represented with two-dimensional plate elements oriented in three-dimensional space.

Brown [18] developed another mesh generation scheme that has been extensively used, which begins by covering the entire mold surface with elements. The initial charge is described by specifying the location of its boundary. The technique includes in its finite element calculations only those elements that form part of the charge. The elements are either "full," "empty," or "partially filled." The elements that are partially filled are temporarily distorted in order to make the element boundaries coincide with the flow fronts. Although this method is promising, it requires some user interaction. Problems are encountered when two element sides lie on the free flow front. Due to the nature of the shape functions for each element, the corner node that lies on the flow front will never move as it will always have zero velocity. Crochet et al. [19] developed a similar technique to simulate the injection mold filling process of complex non-planar parts. Their mesh fitting technique was extended to simulate flows with solid moving boundaries such as the ones encountered in internal batch mixing and extrusion processes.

Tadmor, Broyer and Gutfinger [20, 21] used a spatial finite difference formulation to solve two-dimensional flow problems in complex geometrical configurations. Using a Hele-Shaw [22] formulation to simulate the flow, their method is applicable to flows in narrow gaps of variable thickness, such as injection molding of thin parts and flows inside certain extrusion dies. This technique is known as the Flow Analysis Network (FAN), and works well for Newtonian and non-Newtonian fluids. The method uses an Eulerian grid of cells that covers the flow cavity. A fill factor is associated with each cell, a number that varies between zero and one. A fill factor of zero denotes an empty cell, and a fill factor of one denotes a cell that is full of material. The fluid is assumed to be concentrated at the center of each cell. A local mass balance is made around each cell, which results in a set of linear algebraic equations with pressures at the center of the cells as the unknown parameters. The pressure field that results from solving the set of equations is used to calculate the flow distribution between the cells, which in turn is used to advance the flow inside the cavity by updating the cell fill factors. A major disadvantage of this technique is that relatively fine meshes are required, especially if curved boundaries are present in the geometry. This disadvantage can be overcome by using finite difference operators, however, this makes the simulation awkward and difficult to use.

Osswald and Tucker [23] and Wang et al. [24] modified the flow analysis network to model the non-isothermal flow of non-Newtonian fluids inside thin three-dimensional cavities using finite elements. The technique, which is commonly known as the control volume approach (CVA) requires that the three-dimensional molding surface be divided in flat three- or four-noded finite elements. Cells or control volumes are generated by connecting element centroids with element mid-sides. When applying the mass balance to each cell, the resulting equations are the same as those that result from applying the Galerkin method to the governing equation for pressure. This allows the use of standard finite element assembling techniques when generating the set of linear algebraic equations.

12.2.4 Rheology

Most polymer processes are dominated by the shear strain rate.* Consequently, the viscosity used to characterize the fluid is based on shear deformation measurement devices. The rheological models that are used for these types of flows are usually termed *Generalized Newtonian Fluids* (*GNF*). In a GNF model, the stress in a fluid is dependent on the second invariant of the stain rate tensor, which is approximated by the shear rate in most shear dominated flows. The temperature dependence of GNF fluids is generally included in the coefficients of the viscosity model. Various models are currently being used to represent the temperature and strain rate dependence of the viscosity.

The power law model proposed by Ostwald [25] and de Waele [26] is a simple model that accurately represents the shear thinning region in the viscosity curve, but neglects the Newtonian plateau at small and large strain rates. The major disadvantage of this model is that the viscosity approaches infinity at low stain rates and zero at high strain rates. The infinite viscosity leads to erroneous results in problems where there is a region of zero shear rate such as in the center of a tube. However, this problem can be overcome by using a truncated model where a constant viscosity is assumed in the strain rate region of Newtonian behavior. A model that fits the complete range of strain rate was developed by Bird and Carreau [27]. The Bird-Carreau model accurately models the Newtonian plateau observed at low and sometimes high strain rates, and the shear thinning region in-between.

The tendency of polymer molecules to “curl-up” while they are being stretched in shear flows results in normal stresses in the fluid that greatly affect the flow field in certain cases. Additionally, most polymer melts exhibit an elastic as well as a viscous response to strain. This puts them under the category of viscoelastic materials. There are no precise models accurately representing this behavior in polymers.

* A resource for viscosity vs. shear rate and other multipoint and single point data is the CAMPUS® materials databank, which can be found on-line at www.campusplastics.com

However, various combinations of elastic and viscous elements have been used to approximate the material behavior of polymer melts.* Some models are combinations of springs and dashpots to represent the elastic and viscous responses, respectively. The most common ones being the Maxwell model for a polymer melt and the Kelvin or Voight model for a solid. One model that represents shear thinning behavior, normal stresses in shear flow and elastic behavior of certain polymer melts is the K-BKZ model [28–29].

Elongational or "shear-free" flows are the least studied types of flows that occur in polymer processing. A major reason for this is that they are not as common as shear flows that dominate extrusion and injection molding. However, in certain polymer processes, such as fiber spinning, blow molding, thermoforming, foaming, and compression molding, under specific processing conditions, the major mode of deformation is elongational. Moreover, the elongational viscosity that is needed for simulation is difficult to measure and thus requires expensive equipment.

■ 12.3 Simulating 3-D Flows with 2-D Models

The flow and heat transfer in polymer processes is essentially three-dimensional. Historically, complex systems such as flow inside extruders or dies have been simplified from three-dimensions to one-dimensional or two-dimensional channel flow systems. Sometimes, the geometry of a system is simple enough that it can be simplified to a planar type flow problem. Other times, the thickness of the cavity or die is thin enough that the lubrication approximation can be used to model the process. Though there is some degree of loss of accuracy caused by neglecting or approximating one of the dimensions, these types of simulations offer good insight into the process and have been used for many years to help design plastic parts and to analyze and optimize the polymer processing operation. The simplifications taken with this type of simulation will be discussed in more detail in this section.

12.3.1 Simulating Flows in Internal Batch Mixers with 2-D Models

A high intensity mixer commonly used in the plastic and rubber industry is the Banbury type mixer. The figure eight shaped chamber with the spiral lobed rotors creates a complex, transient flow. This flow is ideal for mixing different polymers into a homogenous blend, but makes analysis extremely difficult. In the Banbury

* For a more detailed presentation concerning rheological models the reader is referred to Bird, R. B., Armstrong, R. C., and Hassager, O., Dynamics of Polymeric Liquids, Vol. 1, Wiley, New York (1987)

mixer, flow exists in the axial direction of the two rotors, however, the majority of the mixing occurs when the polymer is exchanged between the two lobes. Thus, it is common to use a 2-dimensional model to analyze the mixing that occurs in these types of processes. Yang et al. [30] found that in spite of neglecting the axial flow, the 2-dimensional model predicts the flow field characteristics of the chamber quite well.

Using a finite element fluid dynamics analysis package, FIDAP [31], Cheng and Manas-Zloczower [32] simulated the isothermal flow patterns in the Banbury type mixer. To represent the dynamic motion that is present with the moving rotors, they selected eighteen different geometries to represent the mixing cycle. To describe the rheological behavior of the fluid, the power law model was used. To characterize the flow and assess the efficiency of dispersive mixing, Cheng and Manas-Zloczower [33] used the flow number λ, defined as

$$\lambda = \frac{\text{Rate of Strain}}{\text{Rate of Strain} + \text{Vorticity}} \tag{12.1}$$

A value of 0.5 for λ signifies simple shear, while values of 0.0 and 1.0 represent pure rotation and pure elongation, respectively. During mixing, Elmendorp [34] experimentally observed that in the dispersion of liquids with high viscosity ratios, elongational flows are more effective than shear flows. Thus, using the simulation, areas of high λ indicate efficient dispersion of agglomerates into the liquid.

During experiments, tracking tracer ink through a process is a common method to use when attempting to understand the occurring mixing phenomena. Using traditional methods of simulation, the finite difference and finite element methods, moving boundaries of mixers make the tracking of "ink" lines very cumbersome. This is due to the difficulty encountered when reorganizing the finite difference grid or finite element mesh to rapidly fit different mixer geometries after every consecutive time step when the computational domain changes shape. Furthermore, when computing the internal velocities an interpolation function must be used, making it difficult to track particles accurately through the process. A method that overcomes these difficulties and is well suited to analyze these types of processes is the boundary element method. As the domain changes shape, i. e., rotors rotate, the boundary elements follow along because they describe the shape of the device, thus eliminating the need for remeshing. Moreover, when capturing the velocity at key points in the domain, interpolation methods are not needed, allowing for more accurate tracking of particles through the process. Several authors, Gramann et al. [8, 11, 36], Stradins [37], and Davis et al. [38] have used this method to analyze the flow, heat transfer, and mixing that occur in internal batch mixers during processing.

As they simulated the flow in a Banbury type mixer, Gramann and Osswald [11] were able to track particles throughout the processes. Figure 12.3 shows the deformation that can take place as the rotors turn.

Here, one half of one chamber has a different color to help visualize the mixing that takes place. As the rotors turn, the mixing effect is easily seen. From Fig.12.3 it can be seen that though there is a lot of deformation, exchange between chambers is quite low. A small portion of material is squeezed from one side to the other. The exchange of fluid between mixer halves is necessary to optimize mixing. Using this type of simulation, the geometry of the rotors and chamber wall can be easily modified allowing the engineer to find the optimum geometry.

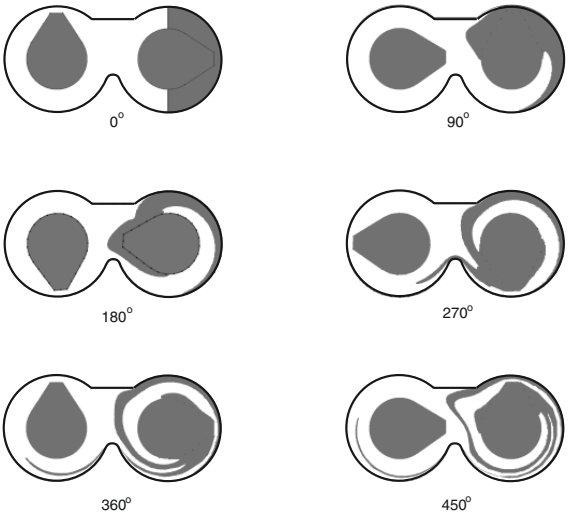


Figure 12.3
Simulated fluid deformation in a Banbury-type mixer

When mixing one or more polymeric materials into a homogeneous blend, the major task of the mixing equipment is to break up the individual agglomerates or droplets and distribute them throughout. In the compounding industry, a great deal of difficulty is encountered when trying to reproduce blends from batch to batch. Using simulation, the stress and velocity fields during blending can be predicted. With this information, an engineer has the ability to characterize the mixing by calculating how much deformation is produced in the mixer. When simulating the blending of multiple fluids, two important properties must be considered: the viscosity of each fluid and the effect of surface tension. Figure 12.4(a) depicts the initial state of a rotor-cylinder mixer with a circular outline of particles within the matrix and a drop or sub-domain of different viscosity, shown in black. Figure 12.4(b) shows the deformation of a drop that has half the viscosity of the surrounding fluid. As the viscosity ratio of the drop to the surrounding fluid increases, Figs. 12.4(c–d), the deformation becomes significantly less.

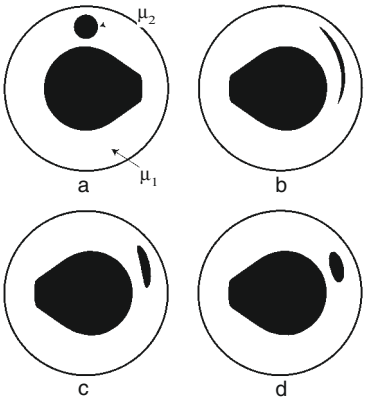


Figure 12.4
Deformation of a droplet with a varying viscosity ratio (continuous phase/droplet = μ_1/μ_2) (a) initial state (b) $\mu_1/\mu_2 = 2$ (c) $\mu_1/\mu_2 = 1/2$ (d) $\mu_1/\mu_2 = 1/5$

When including surface tension effects, forces that tend to keep the drop spherical resist deformation even further. The basic parameter that must be considered when breaking-up droplets with surface tension effects is the Capillary (or Weber) number defined as

$$\mathrm{Ca} = \frac{\text{shear stress}}{\text{interfacial stress}} = \frac{\tau R}{\sigma_s} \tag{12.2}$$

where τ is the magnitude of the deviatoric stress, R the radius of the dispersed phase and σ_s the surface tension. The interfacial stress is the ratio of the surface tension to the radius of curvature of the droplet. In order to break-up droplets the value of Ca must reach the critical Ca number, which is about 1 for shear flow and about 0.4 for elongational flow, when the drop viscosity equals the matrix viscosity. Hence, this critical Capillary number, Ca_{crit}, is more difficult to achieve as the droplet becomes smaller during the mixing process. Using the boundary element method, Biswas and Osswald [39] simulated droplet deformation, and Stone and Leal [40] the break-up of an initially stretched droplet during relaxation in a quiescent matrix.

As mentioned earlier in this chapter, the boundary element technique is not well suited for solving non-linear problems. An extension of this technique that has shown great promise in taking into account non-linearities, while still requiring only a boundary or surface mesh, is the Dual Reciprocity boundary element Method (DRM) [12, 13]. The DRM is essentially a collocation method in which the non-linear terms are collected into an extra term in the governing equation and then mathematically manipulated to a boundary-only formulation. Mätzig et al. [13, 38] used this method to model the convective and viscous dissipation that occurs in a single rotor mixer. Their analysis used a temperature dependent viscosity model and an iterative approach between the BEM flow and DRM heat transfer solutions to converge on the viscosity. The resulting streamlines, found by particle tracking points, are shown in Fig. 12.5.

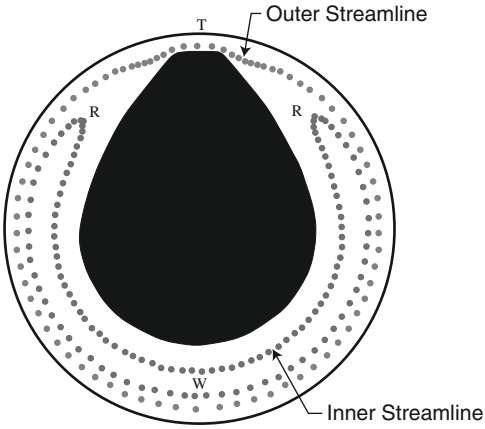


Figure 12.5
Calculated streamlines in a mixer using BEM

The boundary conditions for this mixer were a zero heat flux for the rotor and a constant temperature of 180°C on the barrel. Polyethylene was used for the simulation where the material properties were: thermal conductivity 63000 g cm/s^3°C, thermal diffusivity 0.0021 cm^2/s, density 0.95 g/cm^3, specific heat 0.55 cm^2/s^2°C and a viscosity of 53,000 g/s cm at 185°C and 13,000 g/s cm at 250°C. The temperature, shown in Figs. 12.6(a–b), of the outer streamline was computed for two different rotor speeds, 0.125 rev/s and 1.0 rev/s. In each graph, one curve shows the combined effect of viscous heating and thermal conductivity and the other curve has the additional effect of convection. The high strain rates present during the mixing process generate heat by viscous dissipation, greatly influencing the temperature of the polymer inside the cavity. The importance of the energy generated by viscous dissipation and its transport by convection become more significant as the rotor speed is increased. When the rotor speed is 0.125 rev/s the viscous dissipation causes a 7°C rise in temperature, Fig 12.6(a).

As expected, the temperature profile caused by viscous heating (neglecting convection) is symmetric on both sides of the rotor. In the wide gap region of the mixer, signified as “W,” the temperature of the fluid is approximately that of the barrel wall temperature. This is caused by the low viscous heating in this area and direct heat conduction to the barrel wall. The high temperature areas of the graph correspond to the two recirculation areas of the mixer, “R.” Although, the viscous heating is significant in the area of the rotor tip, “T,” the heat conduction to the barrel wall lowers the temperature of the fluid due to the close proximity of the material to the wall and the narrow gap. When the energy transport by convection is included, the temperature profile is slightly shifted with more variability in temperature in the recirculation area. However, because of the low rotational speed, the energy transported by convection is relatively small.

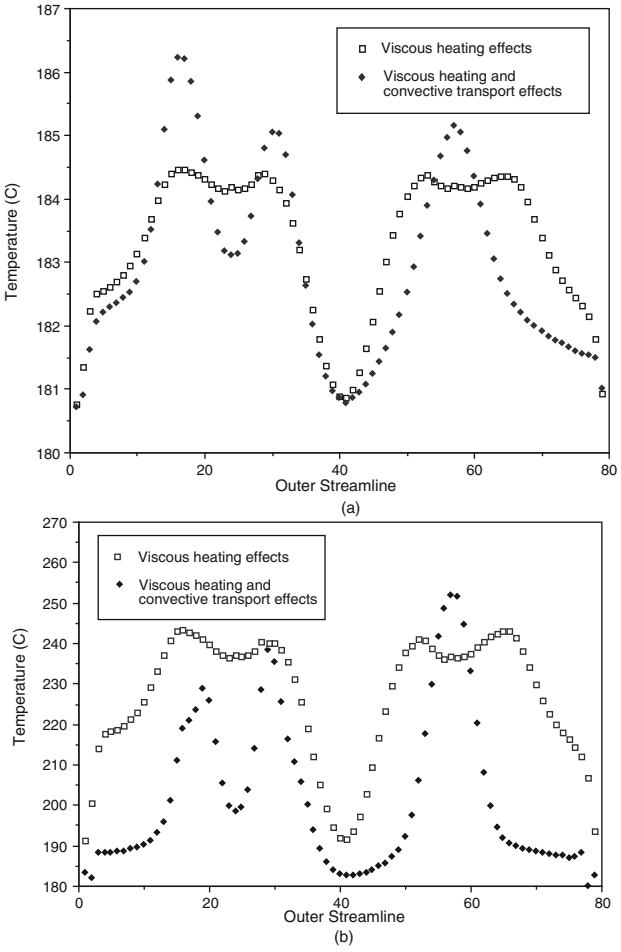


Figure 12.6
Calculated temperature of a particle traveling on the outer streamline (Fig. 12.5) caused by viscous heating with and without convective transport;
(a) rotor speed of 0.125 rev/s
(b) rotor speed of 1.0 rev/s

Increasing the speed of the rotor to 1.0 rev/s the temperature increase caused by viscous dissipation can be quite high. In the analysis, a low Nahme-Griffith number was assumed, hence, a constant viscosity throughout the domain. This assumption does not hold for high temperature variation, however, the results shown here give a good qualitative value when studying the effects of viscous dissipation and convective energy transport. When compared to the 0.125 rev/s rotor speed results, the temperatures increase maintaining a similar profile, Fig 12.6(b). However, when the effects of energy transport by convection are included, the temperature profiles significantly decrease with the highest variation in the recirculation regions. The Graetz number, ratio of convection transport to conduction, for the system analyzed was on the order of 10,000. Most numerical solutions will have great difficulty at this high of a Graetz number and become unstable, and as a result, up-winding techniques are required. However, for the BEM analysis no special upwinding techniques were needed.

12.3.2 Simulating Flows in Extrusion with 2-D Models

At some stage of manufacture, virtually all polymers go through some type of extruder one or more times. This may include the extrusion that occurs during the production of pellets, or the final extrusion to produce the finished product. There is a growing need to be able to accurately model and predict the phenomena occurring within the extruder so that it is possible to optimize both the extruder and the properties of the final product without the use of timely and expensive experiments. Extrusion, the most widely used process in the polymer processing industry—almost all injection molding machines have an extruder (plasticating unit) attached to it, and its flow phenomena have been well studied experimentally [41–49] and due to its geometric complexity to a lesser degree numerically [11, 50–56]. Experimental data is of extreme importance when studying the extruder, however, the time consumption and expense of these experiments creates the need for numerical simulation. Moreover, experimental set-ups are sometimes difficult to control and measure, and many times introduce unexpected variables, such as leakage. Despite controversies* involving the assumptions of the analytical models, referred to as classical theory, these models have been used successfully since Rowell and Finlayson [1] modeled the extruder with a moving barrel and a stationary unwrapped rectangular channel to represent the screw. The barrel is represented as a flat plate moving over the rectangular channel; this system is called the flat plate system (FPS). Obviously, the FPS neglects the curvature of the channel.

It is interesting to note that, in the FPS, moving the screw relative to a stationary barrel introduces a much larger error than moving the barrel relative to a stationary screw. This error is assessed relative to an analysis using cylindrical coordinates (CCS). The CCS analysis shows no difference between a rotating screw and a rotating barrel as discussed in Chapter 7, Section 7.4.3.4.

A simulation program to model the cross flow and down channel flow phenomena in single screw extruders was developed by Rauwendaal, Muller, and Anderson [56]. This model accounts for the non-isothermal, non-Newtonian flow effects in a single screw extruder using a two dimensional finite element formulation. Although this model is, in essence 2-D and represents an idealization to the extruder flow, it does incorporate down-channel flow, leakage, viscous heating, and non-Newtonian effects in the analysis. This is done by assuming that the changes in flow in down channel direction are small relative to the changes in cross channel and normal direction. This is frequently called a 2.5-D analysis because the mesh is 2-D but the calculated

* The authors Campbell, G. A., Sweeney, P. A. and Fenton [49] claimed that significant differences exist between flow and throughput if the barrel is rotated in lieu of the screw. The paper by Rauwendaal, C., Osswald, T. A., Tellez, G., and Gramann, P. J. [50] used analytical, experimental and numerical techniques to show that rotating the barrel is a correct method to analyze the fluid flow in extrusion.

velocities, stresses, and temperatures are 3-D. An example of this simulation program is shown in Fig. 12.7.

Figure 12.7 presents the temperature distribution in a single-flighted 38 mm-diameter screw extruder. For clarity, the graphic display is exaggerated in the channel height direction. Due to cross flow the highest melt temperature occurs in the mid-region of the channel, while the outside region of the channel is at a lower temperature. The dramatic difference in temperature in this relatively small area can be the source of instabilities or other problems. The use of mixing sections can help alleviate this and create a more homogeneous temperature in the extrudate.

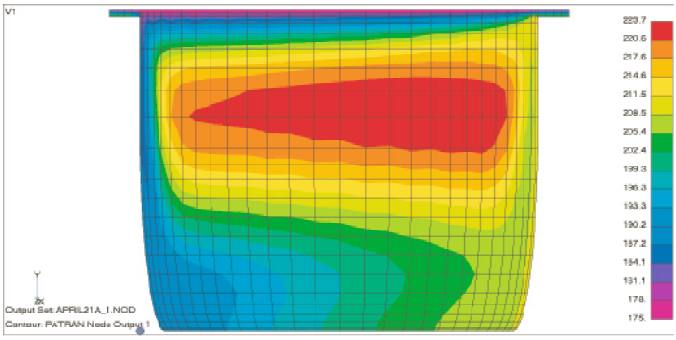


Figure 12.7
Predicted melt temperature in the screw channel using FEM

A screw extruder can have one or more screws. The most common multi-screw extruder is the twin screw extruder, which has two screws. These types of extruders can have the screws rotate in the same direction, called co-rotating, or in an opposite direction, called counter rotating twin screw extruders. The flow that is created in these types of extruders is of great interest since they have the ability to produce very homogeneous blends. However, the complexity of the movement of fluid that is generated by two moving screws that are fully intermeshing is a daunting task, both experimentally and with simulation. Obviously, the method of using a stationary screw with a rotating barrel, as used in the analysis of the single screw, is not applicable. Here, a moving solid boundaries simulation must be utilized if particles are to be tracked.

Rios [57] used a two-dimensional boundary element simulation program to simulate the crosssectional flow in several different co and counter rotating twin screw geometries. To create the geometries needed for the self-cleaning twin screw cross section, equations by Booy [58] were used. All geometries were created using AutoCAD™ or ProEngineer™. To quantify the mixing, numerous mass-less particles were placed throughout the domain of the mixer and the velocity and velocity gradients of each were computed. With this information, particles were tracked throughout the process giving a visual representation on how the material mixes, strain rates were computed to predict a stress level, and the flow number, Eq. 12.1, was calculated to determine the type (rotation, shear or elongation) of flow. Though a

two-dimensional analysis was used to analyze a highly three dimensional flow, a great deal of insight was gained on how these extruders work and comparisons from one system to another was easily made. Figure 12.8 shows the simulated velocity vectors at points throughout the domain of a cross section of a self-cleaning, double-flighted co-rotating twin screw extruder in two different positions.

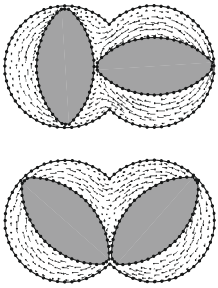


Figure 12.8
Velocity vectors in a double-flighted co-rotating twin screw extruder at different rotor positions

The nodes and elements that were used for the simulation are shown. Because the boundary element method was used, nodes and elements are needed only at the boundaries of the barrel chamber and screws. As the screws rotate, the nodes and elements move as well, essentially eliminating the need for remeshing. The velocity vectors give an indication of stagnant and recirculation zones and are used to advance the particle to the next time step. Figure 12.9 shows the movement of a line, which is made up of many points, through the mixer as the screws turns.

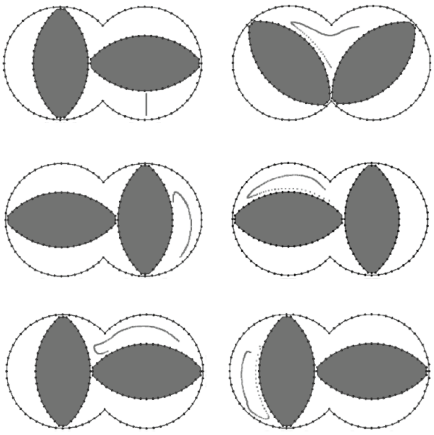


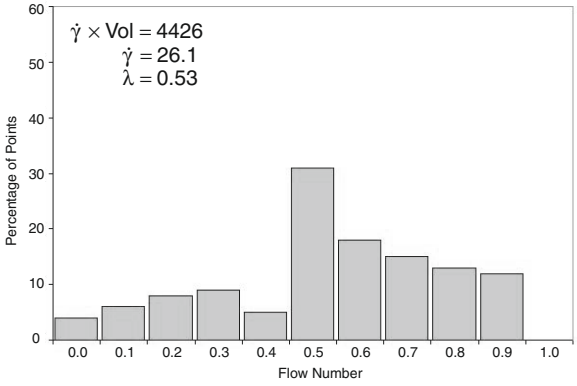
Figure 12.9
Deformation of a tracer line in a double-flighted twin screw

The influence of the intermeshing region can be seen as the deformation of the line increases. Portions of the line that were separated enough so that individual particles can be seen indicate that a great deal of deformation has occurred. More insight on the flow field was obtained by calculating the flow number, Eq. 12.1, of the particles as they flow through the system. Rios [57] found that the double-flighted co-rotating twin screw produces a flow that is primarily shear with some elongation.

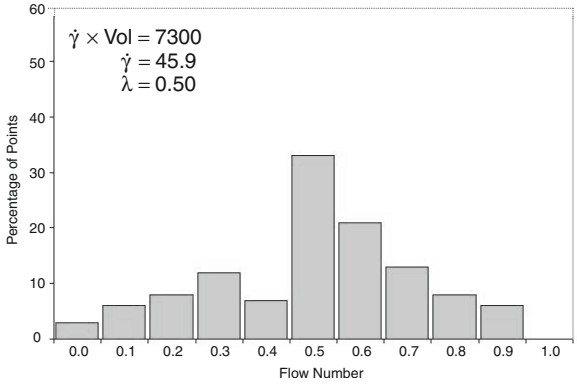
Recall from Section 12.3.1 that a flow number of 0.5 indicates shear flow while a flow number of 1.0 indicates pure elongational flow. For mixing purposes, a flow number near 1.0 is preferred. Figures 12.10(a–c) illustrate that the co-rotating, double-flighted twin screw produces a flow that is mainly shear to elongation.

Rios [57] made a similar analysis on a single- and triple-flighted, co-rotating twin screw extruder. In the analysis, an average strain rate and volumetric strain rate were calculated for each system and compared, Figs. 12.10(a–c).

(a)



(b)



(c)

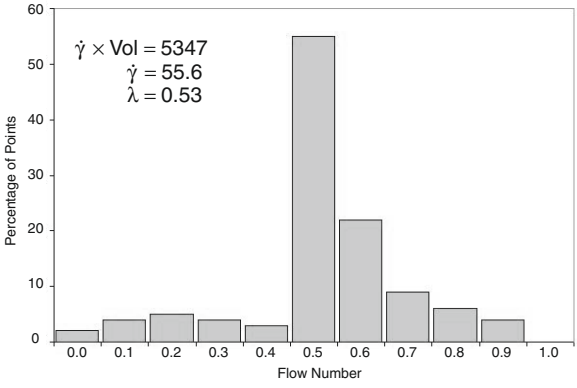


Figure 12.10 Flow number and strain rate for the twin screw extruder. (a) single-flighted (b) double-flighted (c) triple-flighted

Figures 12.10(a–c) shows that the flow number distribution for the single- and double-flighted screws are nearly identical, whereas, the triple-flighted screw produces mainly shear flow due to the small gaps that are present with this geometry. Interestingly, the geometry that created the highest volumetric strain rate was the double-flighted screw, which is the most commonly used screw geometry for twin screw extruders.

12.3.3 Simulating Flows in Extrusion Dies with 2-D Models

Several types of extrusion dies are used in the polymer industry, including: tubing, film-blowing, wire-coating, profile, and sheeting. Die design is a difficult task that is often performed by trial-and-error. Various aspects of the flow through extrusion dies affect the quality of the final product. In addition, flow in dies has several processing variables that contribute to the quality of the final product. The difficulty in achieving acceptable die designs makes simulation and numerical optimization a viable and useful tool, preferably used before ever cutting metal. Through simulation, the engineer can also gain a better understanding and control of the processing parameters that affect product quality. In the past few years, there has been an increase in work done regarding die optimization using computer simulation. Several researchers have used simulation to analyze flow through extrusion dies [59–65].

The process of wire coating is used extensively throughout the wire and cable industry. Wire coating dies are discussed in Chapter 9, Section 9.3 and shown in Fig. 9.19. During this continuous process, one or more layers of polymer are coated onto the wire or cable in a single step. In the coextrusion process, two melt streams are supplied by two different extruders. Hen and Mitsoulis [61] analyzed this process using both the lubrication approximation theory and the finite element method. In their analysis, they modified an initial die design to meet criteria needed for better operation. The criterion was to eliminate all recirculation regions throughout the die, have smooth stresses along the die wall—especially at the converging point of the two polymer melts, and have the interface of the two polymers melts lie parallel to the wire. If recirculation areas appear in the die during the process, the polymer can degrade in these regions. Smooth stresses and a parallel interface are needed for a uniform coating. Using lubrication approximation theory and simulating HDPE and PS as the two polymer streams, they analyzed the effect of the flow rate ratio of these two polymers. To take into account the double layer flow, a double-node technique was used at the interface.

Simulating an isothermal flow and investigating several different combinations of flow rates, Hen and Mitsoulis found that by having PS as the outer layer and HDPE as the inner layer, a recirculation area is formed that cannot be eliminated by changing the flow rate ratio alone. To find the affect that the viscosity ratio (outer layer viscosity/inner layer viscosity) has they used the finite element method to model

flow through a die. Simulating a Newtonian flow, they found that with a viscosity ratio of 0.2, a large recirculation region exists; see Fig. 12.11(a).

Whereas, with a viscosity ratio of 2.0, smooth streamlines appear, see Fig. 12.11(b). They found that the recirculation regions disappear when the viscosity ratio is greater than 1.5, however, when having a viscosity ratio greater than 1.0, interfacial instabilities occur [66]. Thus, to eliminate the recirculation areas and at the same time have no interfacial instabilities (viscosity ratio greater than one), the effect of constraining the flow area in the die was examined. In the analysis, the final thickness ratio (outer layer thickness/inner layer thickness) of the two layers was varied (1/15, 1/3, 1/1) to see which one would give a uniform interface and also have the smoothest streamline pattern. From the simulation, the reduced flow area that gave a 1/3 thickness ratio and reduced the die-taper provided the best results—a level interface, no recirculation areas, and a smooth shear stress transition at the die wall, see Fig 12.11(c). Next, using this die configuration with the favorable viscosity and thickness ratios, they simulated the flow with nonisothermal effects. Because of the high speeds that are present with extrusion, viscous dissipation and energy transport by convection must be considered. To handle the high convective flows, their simulation used a streamline-upwind Petrov-Galerkin technique along with higher order elements. From the analysis, they found that the streamlines for the non-isothermal simulation were, in essence, identical to the isothermal case—an isothermal simulation predicted quite well the phenomena that occur.

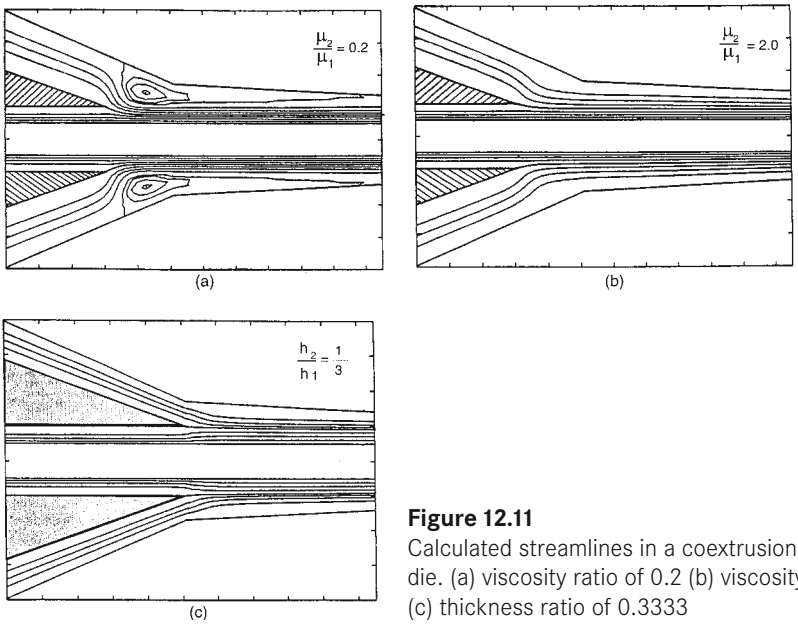


Figure 12.11
Calculated streamlines in a coextrusion wiring-coating die. (a) viscosity ratio of 0.2 (b) viscosity ratio of 2.0 (c) thickness ratio of 0.3333

Utilizing extrusion to make intricate profiles is a major advantage of this process, but one that requires a great deal of die design knowledge. An incorrect die can produce a profile that is dramatically different than expected. Figure 12.12(a) demonstrates an example of such a case [67].

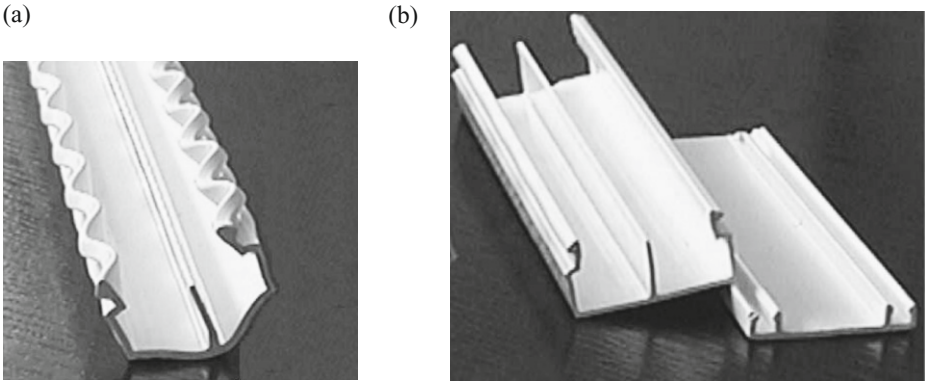


Figure 12.12 Cable tray profile made from PVC. (a) Result of a poorly designed die (b) Result of a properly designed die [67]

Figure 12.12(a) shows two arms of a cable tray designed to be smooth and flat that have taken a wavy shape, making it completely useless. Using a two-dimensional simulation program* one can analyze why this problem occurred. Figure 12.13(a) clearly shows a non-uniform velocity profile indicating a poor distribution of material.

Specifically, a large portion of the material is predicted to flow out of the large triangular sections at well over 200 mm/s while the average velocity (and average line speed) will be closer to 60 mm/s. This discrepancy in the velocity field for the cross section results in the waviness shown. Once the cause of the problem is determined, the software can be used as a tool to analyze design changes before they are implemented in the actual die. The calculated velocity in a modified die that places a restriction in the triangular sections of the die is shown in Fig. 12.13(b). The velocities are uniformly balanced across the die, which produces a part that does not have a wavy shape, Fig. 12.12(b) [67].

While an experienced die designer may intuitively know where flow balancing is required within a profile, it is difficult to quantify this. This is compounded if a requirement comes along for a profile to be produced from a new material with which the designer has little experience. The ability to simulate the flow distribution based on the geometry and the flow characteristics of the polymer allows the designer to more accurately determine the flow channel details for successful extrusion.

* The simulation results for this die were performed with Flow 2000 by Compuplast, Inc.

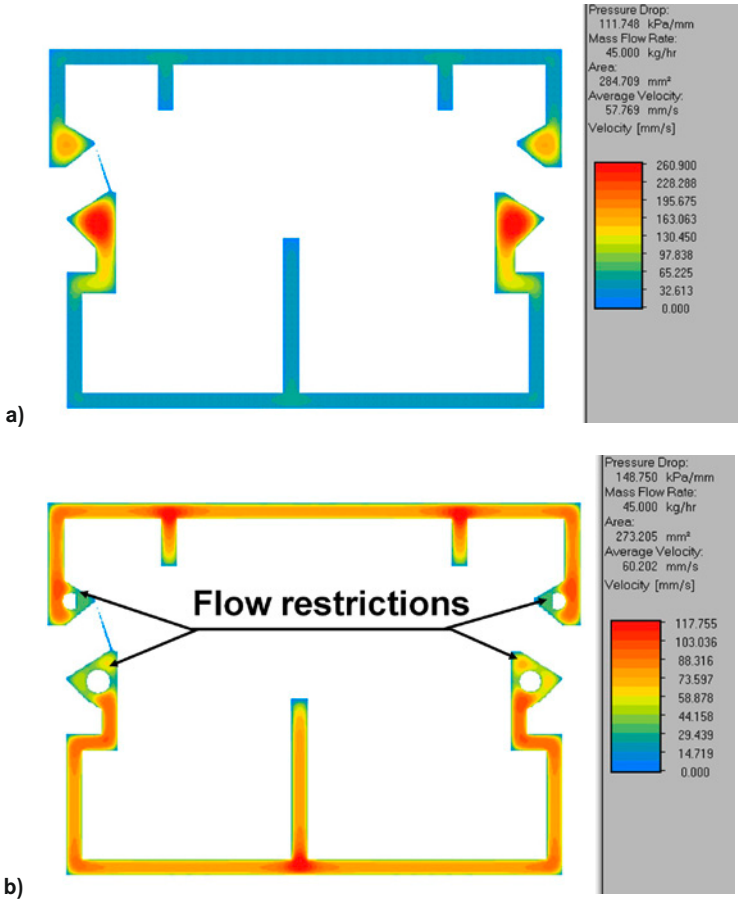


Figure 12.13 Computed velocity in a cable tray profile die. (a) Original die (Fig. 12.12[a]) (b) Corrected die (Fig. 12.12[b])

During the extrusion process, viscoelastic behavior of polymers is readily exhibited as swelling at the end of the die. This behavior is the result of the "memory" phenomena associated with polymeric materials, normal stresses and sudden changes in boundary conditions—as the material separates from the die. For short dies with a large contraction, the material will tend to "remember" its original configuration and swell at the die exit. Whereas in longer dies with small contractions the material will "forget" its original state and swelling is less prominent. The number of rheological models that correctly predict this phenomena is small [68]. A commonly used model is the K-BKZ model proposed independently by Kaye [28] and Bernstein et al. [29]. Kiriakides et al. [64] used special integration procedures to apply the K-BKZ model when simulating flows in common dies. They found good agreement between experimental and numerical results, including small vortexes that form and change in size and intensity at different flow rates.

12.4 Three-Dimensional Simulation

The complex three-dimensional geometries common in polymer processing equipment, molds, and dies make it difficult to analyze their fields using two-dimensional models. Although experiments often give good insight into a problem, they are costly and the results are difficult to analyze for a quantitative evaluation of the process. For example, measuring temperature fields is often impossible.

These shortcomings can be ameliorated using numerical techniques. The advantages offered by numerical simulation open up vast resources, many of which have not been fully explored. As shown earlier in this chapter, many complex flows can be analyzed with two-dimensional models that give the engineer a broad understanding of the occurring phenomena. However, when accurate detail of the flow field is sought during the evaluating processes, which have "strong" three-dimensional flows, a full three-dimensional simulation must be used. Adding one more dimension to the problem dramatically increases the complexity of the model as well as the computational time. However, with the advent of more advanced computers and the development of more efficient numerical techniques, along with the industrial increase in demand for higher quality, three-dimensional simulation is becoming a reality.

This section presents various examples and applications of three-dimensional simulation using finite element and boundary element techniques. These are presented to offer the reader an idea of what is possible with the current state-of-the-art of simulation programs. As examples, the authors have chosen cases that are of great interest to the academic, as well as, the industrial research community. These are internal batch mixers, extrusion dies and extrusion mixing sections.

12.4.1 Simulating Flows in the Banbury Mixer with Three-Dimensional Models

As discussed earlier, a common type of batch mixer used in the rubber and plastics industry is the Banbury mixer. The previous sections included a review of the experimental and two-dimensional studies that have been completed to analyze the flow and mixing behavior in this type of mixer. However, the flow in these mixers is three-dimensional with an important axial flow component that contributes to mixing. Using six sequential geometries to represent the entire mixing process, Yang and Manas-Zloczower [30] used a three-dimensional finite element simulation, FIDAP™ [31], to simulate the flow patterns inside the mixer. The polymer used in their simulation had a power law index, n, of 0.22 and a consistency index, m, of 9.87×104 N $s^{0.22}/m^2$. The calculated velocity contours in the axial, z, direction located at Z = 9 cm are shown in Fig. 12.14(a).

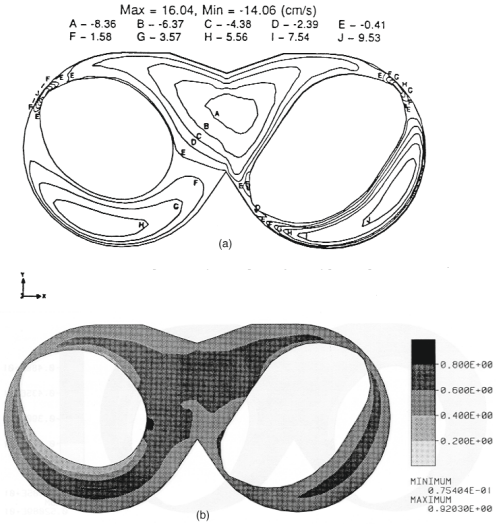


Figure 12.14
Calculated velocity in the axial direction (a) and the flow number (b) in the Banbury mixer using FEM

The fluid in the upper region of the mixer flows backward while the fluid in the lower portion flows forward. From the simulation it was also determined that the minimum pressure regions were located behind the rotor tips while the local maximum pressure regions were located in front of the rotor. Figure 12.14(b) shows the predicted flow number distribution at one position of the rotors. Analyzing the flow number, along with the strain rate, through time one can use this information to help design the mixer for optimal mixing conditions. Figure 12.14 shows that this mixer is shear dominated with isolated areas of elongation flow. Figures 12.15(a–b) show the simulated velocity profiles of both the 2-D and 3-D models, respectively. In the bridge region of the mixer there are differences in velocity vectors for the two models, whereas, away from this region the velocity vectors are quite similar.

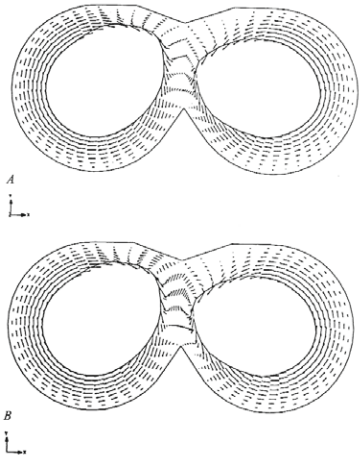


Figure 12.15
Calculated in-plane velocity of the Banbury mixer using FEM (a) 2-dimensional analysis (b) 3-dimensional analysis

The comparison between the two models shows that a two-dimensional model will give the engineer a broad view of the flow patterns that occur, however, when a more precise velocity field is needed to accurately qualify the mixing effect, a three-dimensional model must be used.

12.4.2 Simulating Flows in Extrusion Dies with 3-Dimensional Models

Due to the flexibility and low cost of the overall extrusion process, complex profiles are commonly extruded. Such shapes lead to full three-dimensional flows inside the die, which can be studied in detail* only through simulating with a full three-dimensional simulation program. Various researchers have performed experimental and numerical investigations on flow through extrusion dies [69–78].

The coat-hanger die, used in the fabrication of large polymer sheets, is a commonly used die in the polymer industry. The geometry of the die is designed so that the extruded sheet maintains a constant thickness and uniform temperature. The optimal geometry that transports the polymer from the circular cross section at the exit of the extruder into one that produces a uniform thickness sheet has been extensively researched [2, 79–87] Using a three-dimensional finite element flow program, Dooley [62] optimized the geometry of a sheeting die. To obtain an optimal geometry, one that has a uniform velocity at the exit, the finite element method was used. Numerous rheological models were used to simulate the flow in the die: Newtonian, Power Law, Carreau, Polynomial, and the Cross-model. Figures 12.16(a–c) show the simulated pressure contours in the die.

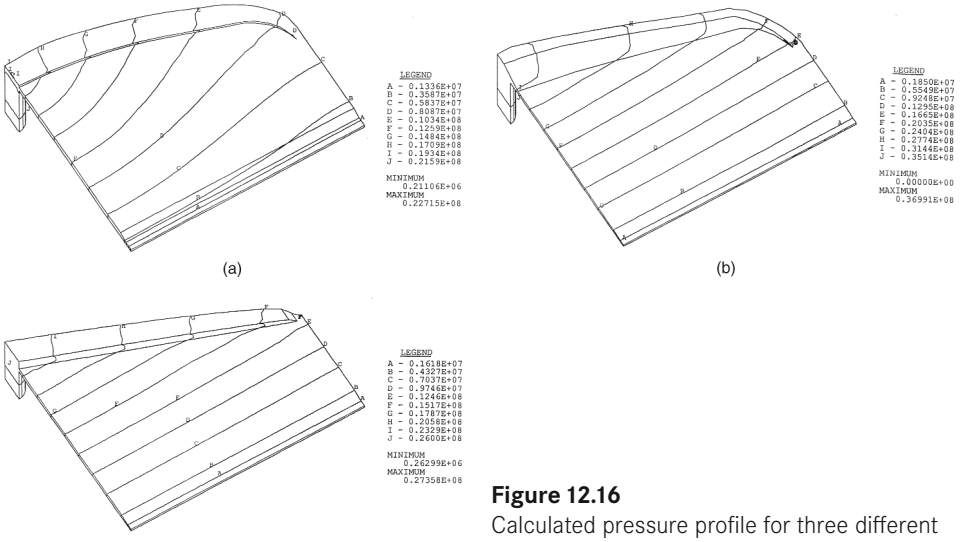


Figure 12.16
Calculated pressure profile for three different coat hanger sheeting dies

* A complex die can often be simplified into simple elements that can be modeled using analytical models. For further reading on this topic, the reader is referred to [83].

The pressure profile throughout sheeting die “A” is not parallel to the die exit, while it is in sheeting die “C.” This creates a more uniform velocity at the exit of the die. To evaluate each die, results were compared to experimental data. Figures 12.17(a–c) show the comparison between experimental and numerical data as the percent deviation from uniform flow versus normalized die width for the three die geometries. From Fig. 12.17 it can be seen that the numerical results correctly predict the trends in experimental data. Geometry “C” creates the most uniform flow and is clearly the best design both experimentally and numerically.

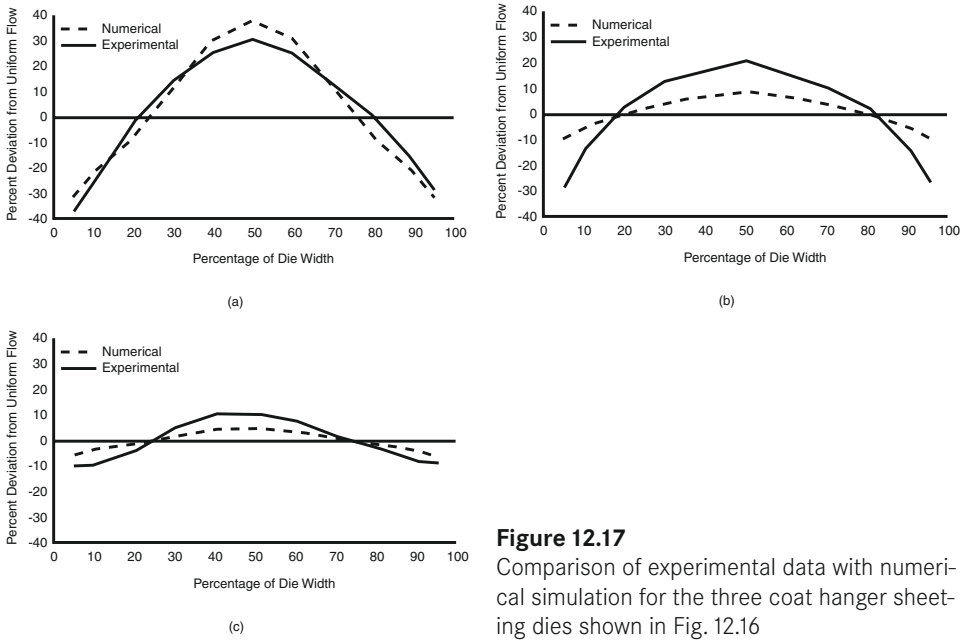


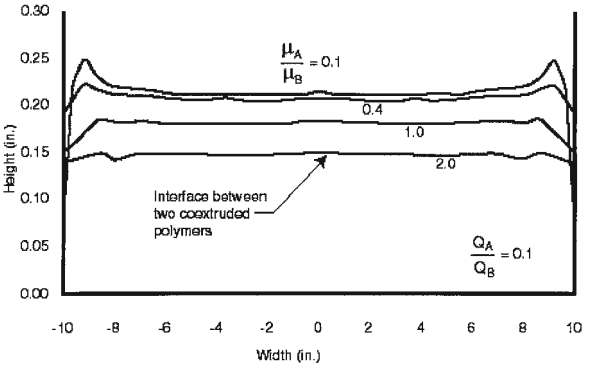
Figure 12.17
Comparison of experimental data with numerical simulation for the three coat hanger sheeting dies shown in Fig. 12.16

Multi-layer polymer sheets or films are produced using a coextrusion process in which two or more polymers are extruded and joined together. This allows the processor to combine desirable properties of multiple polymers into one structure. For example, in packaging it is common to have a layer comprised of recycled polymer sandwiched between virgin and barrier layers. The coextrusion process is typically configured in either of two possible die designs. One option is to use a different manifold for each layer. The layers are then joined together just before the exit of the die. Here, the design of each die is specific for the polymer passing through it. Techniques for die design include non-Newtonian and non-isothermal effects [88], as well as die body deflection [71].

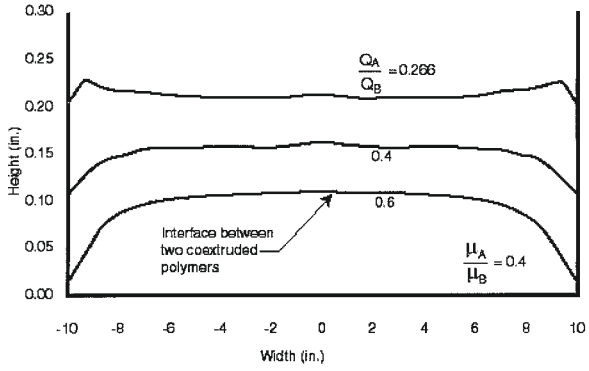
Another configuration used for coextrusion is a single die for all layers with a feedblock that combines and distributes the various layers so that they all maintain a uniform thickness across the exit of the feedblock. The design of the die is made to produce a product with the desired width and thickness while maintaining thick-

ness uniformity in all layers. With this type of die, the existence of an interface between the layers in the feedblock and the die make simulation quite difficult. The objective when designing a single manifold die for coextrusion is similar to designing a single layer—produce a uniform flow rate across the exit of the die. The goal is to create a sheet, film, or coating that is uniform in thickness. However, with the coextrusion process there is the additional requirement that each layer should be uniform in thickness as well.

Gifford [74] used the finite element method to examine the effect of the flow rate ratio (flow rate of one layer/flow rate of the second layer) and viscosity ratio (material viscosity of one layer/material viscosity of the second layer) on the die exit flow distribution. Decreasing the viscosity ratio (μ_A/μ_B) results in the interface between the two materials moving upward toward the less viscous material. Figure 12.18(a) shows the interface of the two polymers at several different viscosity ratios.



(a)



(b)

Figure 12.18
Calculated effect of viscosity ratio (a) and flow rate (b) on the interface of two coextruded polymers using FEM

The smallest viscosity ratio simulated, ($\mu_A/\mu_B = 0.1$), demonstrates that the smaller viscosity material is starting to flow around the higher viscosity material producing a nonuniform layer thickness—a phenomenon called *viscous encapsulation.* The effect of the flow rate ratio (Q_A/Q_B) on the interface between the two polymers is

shown in Fig. 12.18(b). As this ratio decreases, the interface rises upward toward the lower viscosity material. However, the interface between the two becomes smoother and yields a more stable interface.

Layer nonuniformity in coextruded products is also common when the viscosities of the polymers are nearly the same, implying that another factor besides viscous encapsulation is affecting the flow during coextrusion. To study this phenomenon, Dooley et al. [76] investigated the effect of polymer viscoelasticity on layer thickness uniformity of multi-layer coextruded structures. This was done experimentally by coextruding multi-layer structures through die channels of different cross-sectional shapes and observing the location of the interface. Here, the experiments were conducted with identical materials in each layer that were pigmented to allow observation of the layer interface. Setting the experiment like this eliminated any effects of viscous encapsulation and demonstrated the effect of viscoelasticity on coextrusion. The materials studied in the experiment were polystyrene, polyethylene and polycarbonate. Based on the storage moduli, the polystyrene is the most elastic, followed by the polyethylene resin and then the polycarbonate resin.

In the experiment, the shapes (square, teardrop, circular, and rectangular) that were used are commonly found in the design of feed blocks, dies, and transfer lines. Figure 12.19(a) shows the initial cross section of the material as it flows through a square channel, which measures 0.95×0.95 cm.

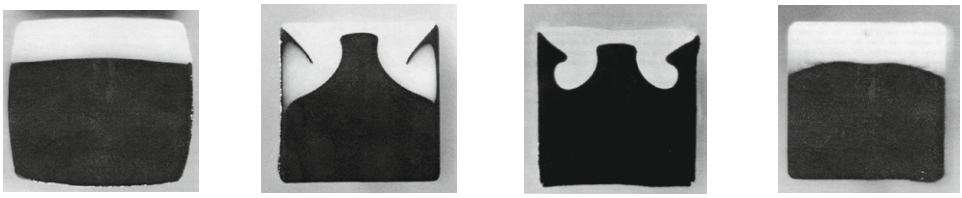


Figure 12.19 Experimental cross section of a two-layer coextruded structure; (a) initial condition; (b) polystyrene; (c) polyethylene; (d) polycarbonate 50 cm downstream [76]

Notice that the white material occupies approximately 20% of the area while the black occupies 80%. It should be reiterated that both materials are identical except for the color pigment—the change in viscosity caused by the color pigment is insignificant.* Figures 12.19(b–d) show a cross section of the square die 50 cm downstream for the polystyrene, polyethylene, and polycarbonate, respectively. In both the polystyrene and polyethylene samples, a thin black substrate layer is shown moving up along the channel walls while the interface in the center is moving up towards the top of the channel. Interestingly, the black substrate material, which flowed along the walls, turned after it reached the corner and flowed back towards

* The black and white pigmented material was switched for each layer to ensure that identical results were observed.

the center at 45°—viscous encapsulation does not explain this layer rearrangement. Dooley et al. [76] explained this movement of layers in the polystyrene and polyethylene samples as the existence of secondary flows produced by differences in normal forces created when flowing through a non-radial symmetric channel. The amount of relative layer movement in the three samples corresponds to their storage modulus. Here, the polystyrene has the greatest layer movement and the highest storage modulus, while the polycarbonate has the smallest layer movement and the lowest storage modulus.

To help understand and quantitatively evaluate the secondary movement shown above, Debbaut et al. [75, 77] augmented this experimental work with a three-dimensional flow simulation* that incorporated viscoelastic effects. The finite element method, using a 4-mode Giesekus model as the viscoelastic constitutive equation,** was used for the simulation. The polymer used for the experiment and simulation was a low-density polyethylene. Figures 12.20 and 12.21 show the experimental observations and the numerical predictions of the deformations of the interface for the rectangular straight channel [78], and for the teardrop channel [75], respectively.

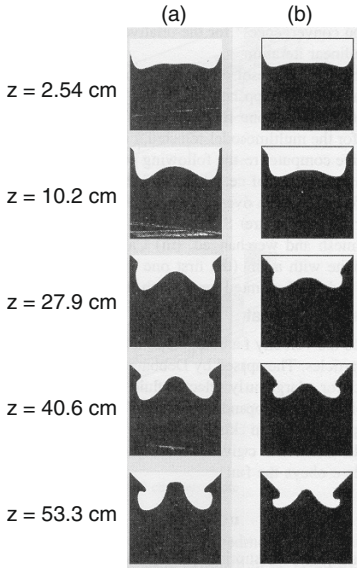


Figure 12.20 Flow of polyethylene trough a square channel for both experimental (a) and numerical (b) [78]

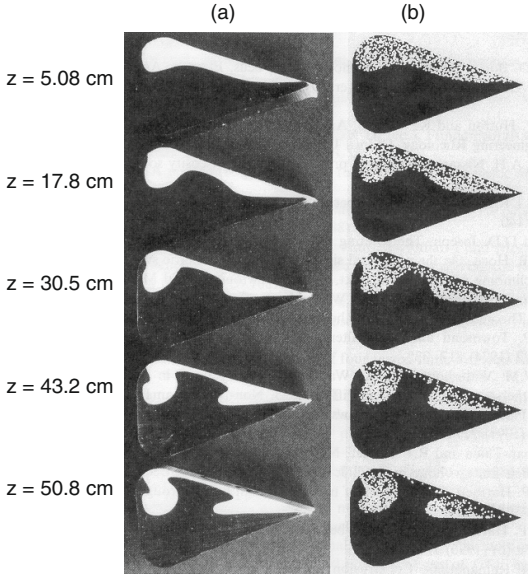


Figure 12.21 Flow of polyethylene trough a teardrop channel for both experimental (a) and numerical (b) [75]

* Polyflow simulation program, 16 Place de l'Université, B-1348 Louvain-la-Neuve, Belgium

** The application of the White-Metzner, Phan-Thien Tanner and Giesekus models was done by Dietsche, L., and Dooley, J., SPE ANTEC, 53, 188 (1995)

Figures 12.20 and 12.21 both show excellent agreement between the experiments and the predictions with some slight differences, which could be attributed to the selection of a particular fluid model used with its material parameters. A simulation analysis of this type is indispensable when investigating abnormalities in die flows and allows for the quantification of the processing conditions and material properties on the development of secondary motions.

12.4.3 Simulating Flows in Extrusion with 3-Dimensional Models

The helical geometry of the screw creates important three-dimensional flow effects that influence the overall performance of the extrusion process. The complexity and three-dimensionality of the screw kept researchers from simulating the flow and heat transfer in the actual geometry, leaving experimental work as the only means to analyze the actual process. To circumvent the time consuming disadvantages of experiments and to take advantage of simulation, recently more research has been performed on the extrusion process using finite element and boundary element techniques. This work is presented in this section.

12.4.3.1 Regular Conveying Screw

To study the flow in the metering section of a single screw extruder, Spalding et al. [51] used the finite element flow simulation program FIDAP [31] and verified the results with experiments. The resin used was a low-density polyethylene with a melt flow index of 2.0, solid density of 0.922 g/cm^3, a melt density of 0.74 g/cm^3, thermal conductivity of 0.182 W/(m °C) and a heat capacity of 1260 J/(kg °C). A single-flighted, square-pitched screw had a flight width of 7.94 mm and a flight clearance of 0.07 mm was simulated. For the numerical calculations, a non-isothermal flow of a non-Newtonian liquid was modeled. The effect of the flight land and the curved flight radii were also included in the geometric representation. Spalding et al. [51] simulated the process with both a rotating barrel and stationary screw and a stationary barrel and rotating screw. The mesh used to represent the extruder channel contained 51,714 elements and 50,197 nodes. The processing conditions used were a flow rate of 41 kg/hr, rotational speed of 60 rpm, a barrel temperature of 205°C, a screw temperature of 200°C and an inlet temperature of 205°C. The average pressure gradient computed was around –1.0 MPa/turn, which is in excellent agreement with the experimentally measured pressure gradient of –0.96 MPa/turn. The computed shear rate and temperature fields at the specified conditions are shown in Fig. 12.22.

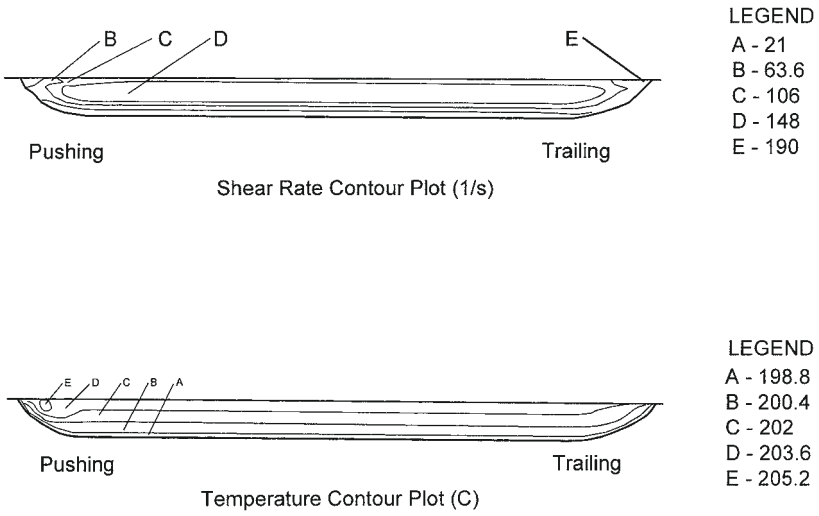


Figure 12.22 Calculated shear rate and temperature contour of a cross-section in the metering section of a single screw extruder using fully 3D FEM [51]

At these processing conditions, with a LDPE resin, the temperature rise due to viscous dissipation is minimal. Figure 12.22 shows a slight temperature rise near the pushing flight due to heat conduction through the hot barrel and convection back to the advancing pushing flight.* When analyzing the results for both a rotating barrel and a stationary screw and a stationary barrel with a rotating screw, Spalding et al. [51] found the pressure and temperature fields to be identical. Results from their research are extremely valuable since they show a viable mean to actually look into the extruder and to gain insight into the temperature, pressure and velocity field development.

12.4.3.2 Energy Transfer Mixer

A mixing section that has been used to improve thermal mixing and to lower the extrudate temperature is the wave-type or Energy Transfer (ET) screws. These mixing sections typically have two or more channels that create cross-channel mixing by having their channel depths vary periodically out of phase with one another. The flights between the channels are strategically undercut to permit flow of material between the channels. Thus, as the depth of one channel decreases it forces the material to the other channel where the depth is increasing. To study the thermal mixing ability of these type of screws, Somers et al. [89] used the 3-dimensional simulation program FIDAP [31] to simulate particle trajectory and heat transfer effects, including conduction, convection, and viscous dissipation.

* Spalding, M. A., personal communication, April, 1994

The non-Newtonian, non-isothermal analysis included the simulation of the ET mixing section as well as a conventional metering section for comparison reasons. The mesh for the ET section consisted of 155,520 8-noded brick elements, while the mesh for the conventional system had 186,192 8-noded brick elements. To analyze the thermal mixing, Somers et al. [89] simulated one channel (A) to be fed a fluid at a temperature of 230°C, while the other channel (B) was fed a fluid at 190°C (Fig. 12.23). Likewise, the inlet fluid for the conventional system was specified as 230°C, and 190°C for the pushing and trailing sides, respectively. Figure 12.23 shows the calculated temperature contours for the ET at cross-sectional planes taken down the screw.

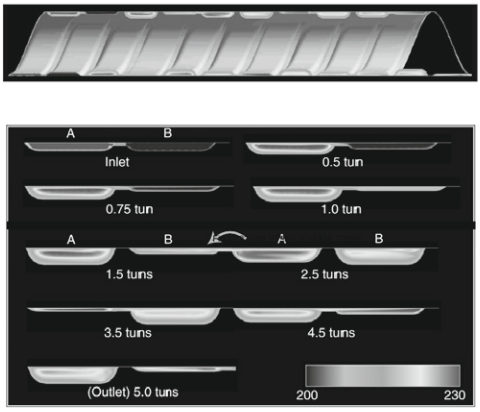


Figure 12.23
Calculated temperature contour in the Energy Transfer section [89]

Recall that Channel A in Fig. 12.23 will become deeper and Channel B shallower and the undercut connecting the channels will permit fluid to transfer between them. As one moves down Channel A, the temperature decreases as cooler material from Channel B transfers in and heat is conducted out through the barrel wall and screw surfaces. Inversely, the fluid in Channel B will increase in temperature due to the combination of viscous dissipation and conduction of heat in through the barrel wall and screw root. At an axial distance of 4.2 diameters, a relatively large thermal gradient is created in Channel A due to viscous dissipation, while the thermal gradients in Channel B are minimal. In the conventional screw, the cross-flow mixes the two fluids of different temperature through convection. After 1 diameter, the temperature difference between the channel halves was significantly reduced. Results for the total bulk temperature for both systems show that the temperature gradients imposed at the inlet were eliminated after about 1.5 diameters for the ET and 1 diameter for the conventional section; see Fig. 12.24. The bulk temperature for the ET after several diameters is predicted to be several degrees higher than the conventional screw. This is due to the high level of viscous dissipation generated as material passes from one channel to the other.

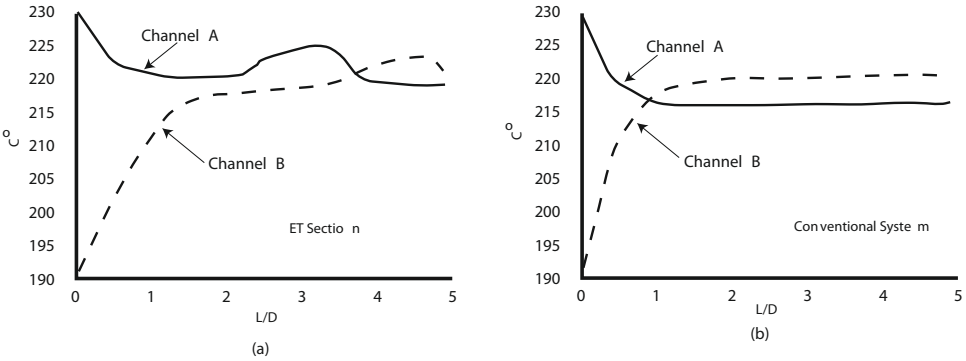


Figure 12.24 Calculated mean temperature of regions in the (a) Energy Transfer section and the (b) conventional system using fully 3-D FEM [89]

Though the temperatures generated are predicted to be higher with the ET mixing section, the distributive mixing intuitively is greater than that found in the conventional screw. To analyze this mixing, Plumely et al. [90] calculated the trajectory of two particles in both systems—one for each channel of the ET, shown in Fig. 12.25. Recall that the particle path in the conventional screw has a repetitive helical motion. In the ET section the particle cross over from one channel to the other and increases the distributive mixing effect.

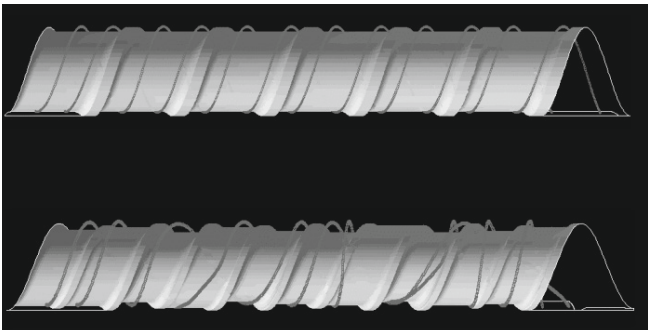


Figure 12.25
Particle tracking using FEM
(a) Energy Transfer section
(b) conventional system [90]

12.4.3.3 Twin Screw Extruder

Twin screw extruders (TSE) have been used for the processing of viscous materials for several decades. The TSE has additional mixing capabilities that are not found in the typical single screw extruder. The flow in this device is quite complex and highly 3-D due to the movement of two screws, thus making simulation a daunting task. However, the increase in mixing ability over the single screw has led many researchers to study this device both numerically and experimentally.

Using the Mesh Superposition Technique (MST), described earlier, Avalosse et al. [91] studied the non-isothermal flow of polypropylene in co-rotating and counter-rotating twin screw extruders. Recall that this technique simplifies the meshing of the geometric entities and avoids remeshing at each time step. To validate the simulation, results were compared to experimental measurements made on a Japan Steel Works TEX30, a 30 mm twin screw extruder, where the screws were made to rotate at 200 rpm with a flow rate of 15 kg/hour. Here, the screw was designed so that it could operate as both co- and counter rotating. The numerical measurements were taken along the line of A–A' and B–B', shown in Fig. 12.26.

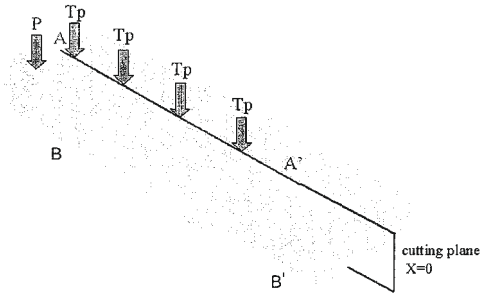


Figure 12.26
Mesh of twin screw with places of measurement shown

Figure 12.27(a) displays the pressure values along A–A. Except for the higher angle values, there is very good agreement with the measured pressure. Avalosse et al. [91] explained that the discrepancy occurs because at higher angle values the gap size decreases, thus reducing the mesh density in this area. The predicted temperatures also compare very well to the measured values, as shown in Fig. 12.27(b).

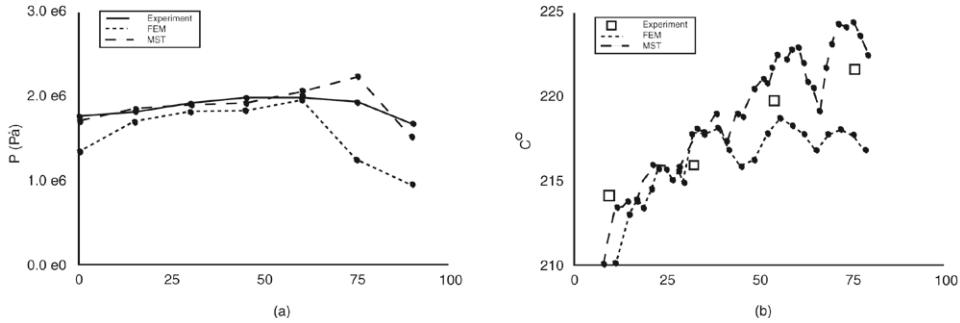


Figure 12.27 Experimental and numerical pressure (a) and temperature (b) profile in a twin screw extruder along plane A-A shown in Fig. 12.26

In the next step of their analysis, Avalosse et al. [91] used simulation to compare the co-rotating and counter-rotating twin screw to one another. Figure 12.28(a) shows the calculated pressure and Fig. 12.28(b) shows the temperature along B–B' (the symmetric of line AA' at the bottom of the X = 0 plane) for both systems. There is an obvious difference between the two systems with the counter-rotating system

producing a smoother pressure profile. The co-rotating system appears to generate significantly more shear heating with a 6°C higher temperature is some regions. Moreover, it was found that the co-rotating system required 20% more torque to run than the counter-rotating system.

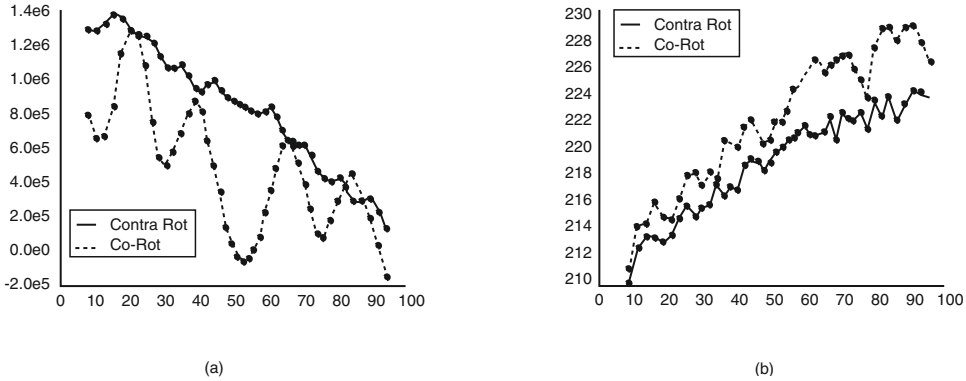


Figure 12.28 Numerically calculated pressure (a) and temperature (b) profile in a twin screw extruder along plane B-B shown in Fig. 12.26

Avalosse et al. [91] used the simulation program to further study the co-rotating twin screw system with and without kneading blocks, Fig. 12.29.

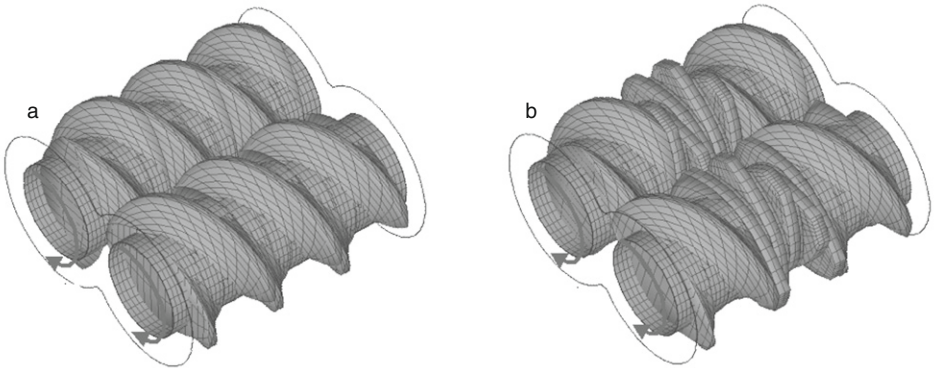


Figure 12.29 Partial finite element mesh used to analyze the twin screw extruder; (a) conventional system (b) kneading block mixing section

The calculated velocity vectors of a conventional co-rotating system with no mixing sections and the kneading block region are shown in Fig. 12.30.

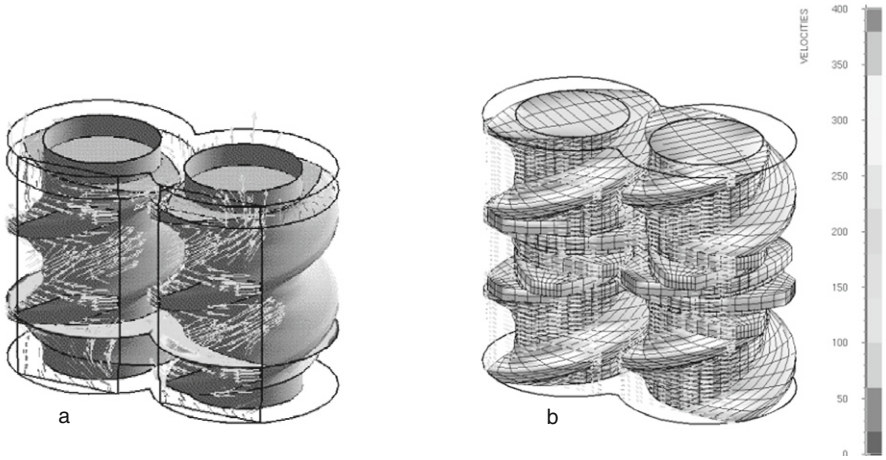


Figure 12.30 Calculated velocity vectors in the twin screw extruder using FEM; (a) conventional system (b) kneading block mixing section

Figures 12.31 to 12.33 show the pressure profile, strain rate and flow number of the kneading block region along a plane in the domain of the mixer at one time step, respectively.

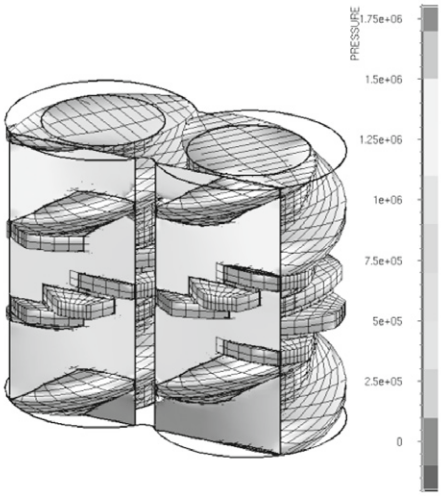


Figure 12.31 Calculated pressure in the kneading block region of a twin screw extruder using MST-FEM

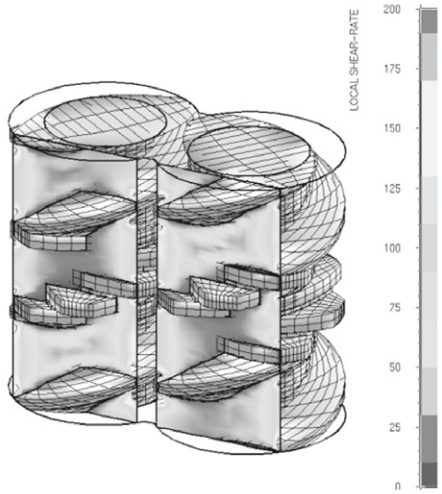


Figure 12.32 Calculated shear rate in the kneading block region of a twin screw extruder using MST-FEM

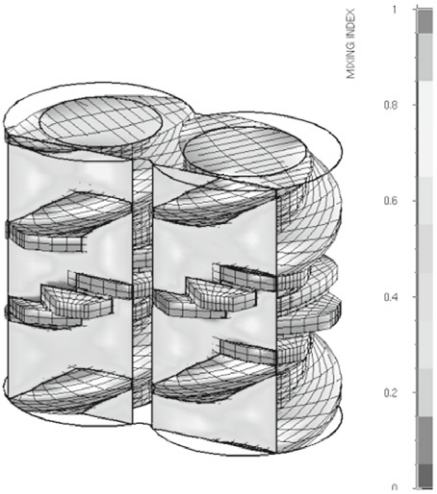


Figure 12.33
Calculated flow number in the kneading block region of a twin screw extruder using MST-FEM

Simulation programs like this create abundant information and one needs to know how to interpret these data to make it useful, i.e., predict mixing. One method is to track particles through a system to determine where they go, if there are any stagnant regions and how long they stay in the system. Figure 12.34 shows the tracking of particles that originated on a plane at the inlet to the mixer. After only a short period, the particles become distributed throughout the twin screw. Using some of the techniques described earlier, the distributive and dispersive mixing capability of this system can be quantitatively analyzed.

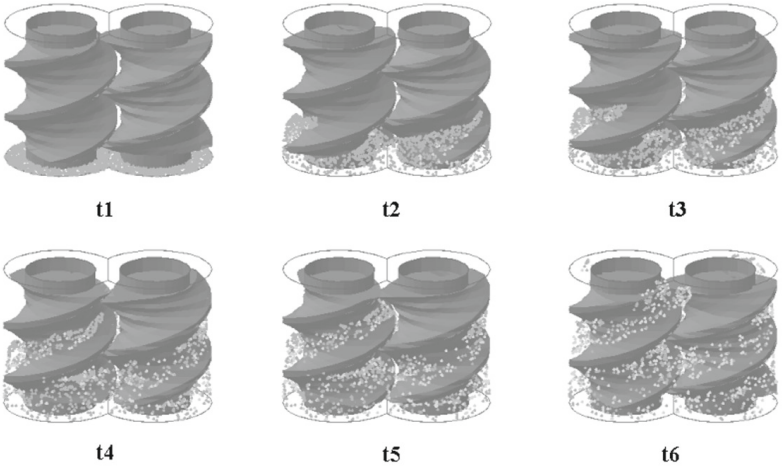


Figure 12.34 Calculated particle tracking in a co-rotating twin screw extruder using MST-FEM

The addition of fibers to a polymer melt in order to increase the mechanical properties of a part is common practice. The most common fiber used for plastics is glass; however, wood fiber is making inroads in many important applications, along with carbon, aramid, and boron for advanced engineered materials. The amount of fiber, how it is oriented in the part, and the length of the fiber influence greatly the effectiveness of increasing, or possibly decreasing, the properties of the part. The extrusion process is commonly used as the device to mix fibers into a resin to create a composite blend. However, during this process, fibers become oriented and fiber length is reduced. This is caused by the flow field and high stresses in the extruder. To investigate the degradation of fiber length, Krawinkel et al. [92] used the boundary element method to calculate the evolution of stresses in the kneading block and double-flighted screw of the twin screw extruder. Figure 12.35 shows the calculated particle tracking in a double-flighted twin screw while Fig. 12.36 shows the velocity and stress gradient at a plane in the kneading block region.

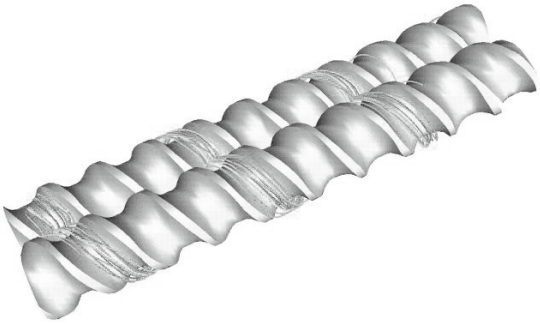
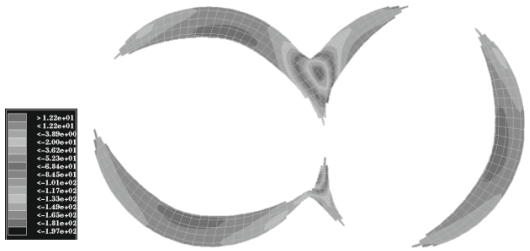


Figure 12.35 Calculated particle trajectories inside a double-flighted co-rotating twin screw extruder



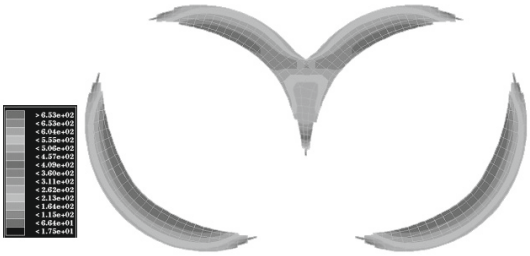


Figure 12.36
Calculated velocity (a) and stress (b) contour at a plane along the kneading block region in a twin screw extruder using BEM [92]

As expected, the highest stresses occur at the nip region of the mixer. Knowing the stress history of the mixer, Krawinkel et al. used the following relationship [93] to solve for the fiber length for a given critical stress.

$$\text{Critical Stress for Fiber Breakage} = E_f \frac{L\,n\,(2L/D) - 1.75}{2\,(L/D)^4} \tag{12.3}$$

Developing or synthesizing new polymeric materials is becoming increasingly expensive and difficult. However, it is possible to develop new engineering materials by mixing two or more polymers or by modifying existing ones by adding various ingredients. These polymer blends can be made to provide a wide range of properties. The morphology of these blends plays a critical role in the development of these properties, and the final morphology is a direct result of how the polymer blend was mixed. The ability to qualitatively and quantitatively predict mixing through simulation has led to a better understanding on how materials are mixed or de-mixed and has led to the development of a new generation of mixers.

12.4.3.4 Rhomboidal Mixers and Fluted Mixers (Leroy/Maddock)

A device that has become a standard in single screw, and to a lesser degree, in twin screw extrusion, is the rhomboidal-pineapple mixing section. This device must be well designed for the number of rhomboids in the axial and circumferential directions, length, pitch, and channel depth to create the optimal mixing environment. Using the boundary element method along with experiments Gramann et al. [94] and Rios et al. [95] studied the rhomboid mixing section. Gramann et al. [94] showed with both simulation and a flow visualization experiment that multiple stagnant regions may occur on the sides of the rhomboid depending on its shape. In the numerical analysis, particles were tracked through the mixer generating the streamlines shown in Fig. 12.37.

Figure 12.37 reveals a large region of stagnant fluid on the top of the rhomboid, which is detrimental to mixing and potentially damaging for polymeric materials that easily degrade. To verify these results, Gramann et al. [94] built an experimental set-up consisting of a 25.5 mm clear acrylic cylinder and five scaled-up rhomboids. A Newtonian fluid, Dow Corning 200, 10,000 centiStokes polydimethylsiloxane, was used as the medium fluid. A vertical ink-line was placed in front of the 5 rhomboids in the visual experiment; see Fig. 12.38(a). Figures 12.38(b–d) show the deformation of the ink-line after rotation and clearly show a stagnant region on the upper surface of the rhomboid.



Figure 12.37 Predicted streamlines in a rhomboid mixing section using BEM

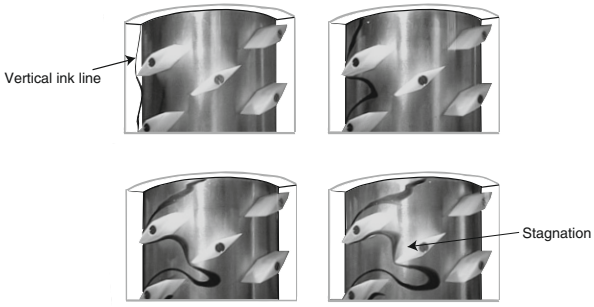


Figure 12.38 Deformation of an ink line in a visual experiment of a rhomboid mixing section

Rios et al. [95] investigated several different configurations of the rhomboid mixing section by changing the two helix angles that define the mixing section. The different sections analyzed are shown in Fig. 12.39, where the notation of each indicates the pitch in both directions.

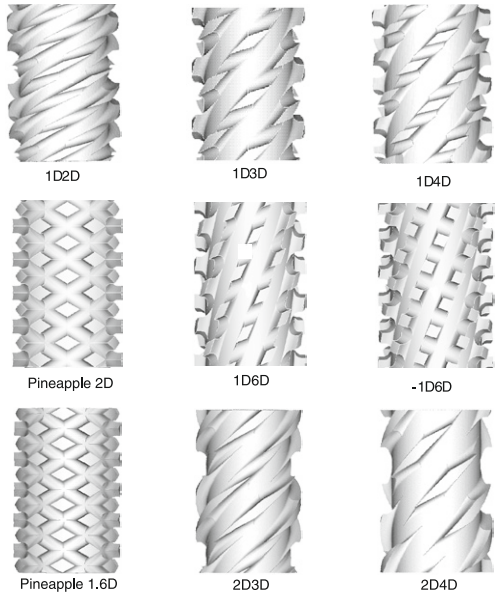


Figure 12.39
Geometries of rhomboidal mixing sections analyzed by [95]

The geometries were compared according to mixing efficiency, pressure, and energy consumption. The experiments for this study were performed on three of the mixing sections shown in Fig. 12.39, using a high density polyethylene on a highly instrumented Extrudex ED-N-45–25D single screw extruder equipped with a 45 mm three-zone screw. The performance of each mixer was evaluated by means of a characteristic curve and a subjective comparison of micrographs taken from the ex-

trudate; see Fig. 12.40, of material that originally contained a yellow master batch pigment.



Figure 12.40 Extrudate micrographs 50X (a) rhomboid 1D3D (b) rhomboid 1D6D and (c) pineapple 1.6D

The numerically calculated characteristic curves of the nine rhomboids are shown in Fig. 12.41. Here, data on the positive side of the chart (right) represent a mixing device that produces pressure and the negative side (left) consumes pressure. Here, it can be seen that the pineapple 1.6D is the highest pressure consumer while the rhomboid 1D4D has the highest pumping capability. The pineapple 1.6D has the most restrictions or rhomboids, through which the material must flow and experiences a bigger pressure loss. The neutral effect (zero flow rate at a zero pressure difference) for the two pineapple mixers is caused by the two counter helixes—one helix pumps material forward while the other pumps backwards.

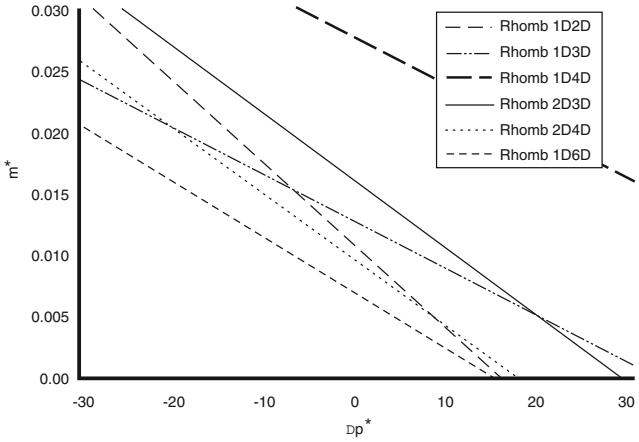


Figure 12.41(a) Numerical calculated characteristic curves of rhomboidal mixing sections

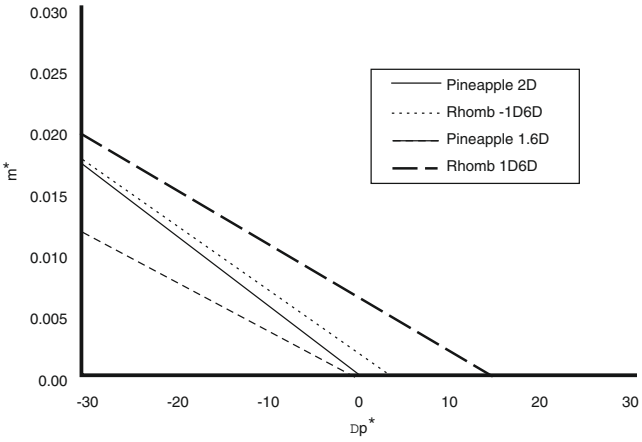


Figure 12.41(b) Numerical calculated characteristic curves of rhomboidal mixing sections

The residence time distribution was calculated numerically by tracking particles (stimulus) and measuring the time that each particle spends in the mixing device. The cumulative residence time distribution (CRTD) is computed by integrating the residence time distribution and is shown in Fig. 12.42 for five of the rhomboids. Recall that the mixer that gives steepest CRTD curve has the worst distributive mixing since all the stimulus exits at nearly the same time. Figure 12.42 shows that the rhomboid 1D3D has the steepest CRTD while the two pineapple mixers give a much better response. Comparing these results to the micrographs shown in Fig. 12.40, and performing a qualitative analysis, the pineapple 1.6D exhibits the thinnest striations and the rhomboid 1D3D developed the thickest, indicating that the pineapple mixer is a better distributive mixer.

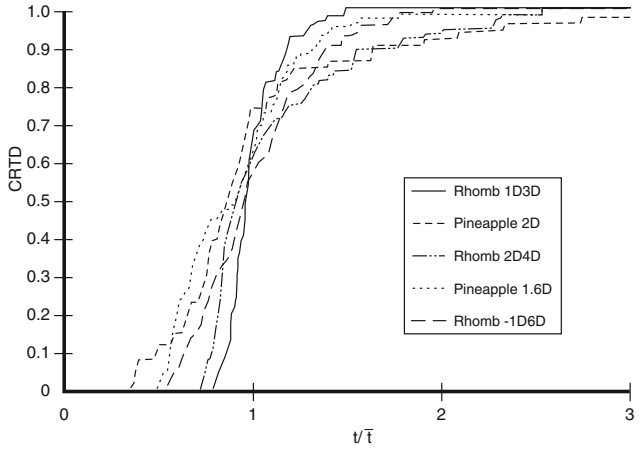


Figure 12.42 Calculated residence time distribution of rhomboidal mixing sections using BEM

The counter part to the distributive rhomboid mixing section is the Maddock or LeRoy dispersive mixing section. This device is commonly used to ensure that any unmelted polymer particles entering are subjected to high shear and are melted before leaving the extruder. This mixer consists of several sets of semicircular grooves that run parallel or helically to the axis of the screw. One groove acts as an inlet while the other acts as an outlet with the two grooves connected by an undercut flight that produces high shear as the material passes through. Fluted mixers were discussed in detail in Section 8.7.1. The LeRoy/Maddock mixer has been analyzed numerical by several investigators using FDM [96], FEM [97], and BEM [8]. Figure 12.43 presents the results of tracking particles through the inlet and outlet of one repeating set of grooves for this mixer.

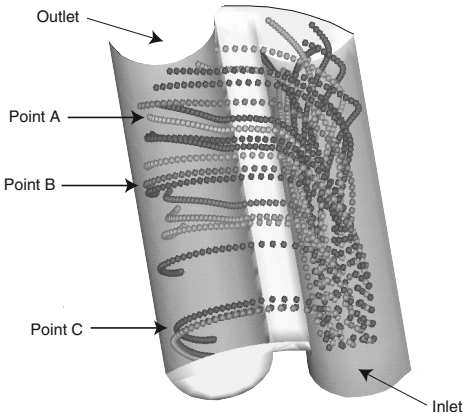


Figure 12.43
Calculated streamlines in one repeating section of a LeRoy-Maddock dispersive mixing section

After the material enters from the bottom, it goes through a cross-flow before going over the undercut flight. Because all material entering at one instant does not pass over the flight at the same time, this mixer does a good job at distributive mixing as well as at dispersive mixing. Looking at the strain rate and flow number of three specific particles, shown in Fig.12.44, as they travel through the mixer one can get a feel for how this mixer creates a dispersive mixing environment. Figure 12.44(a) shows the history of the strain rates for these three particles. From Fig. 12.44 it is obvious when the particle travels over the undercut flight by the rapid increase in strain rate. For example, particle C goes over the flight quickly after entering the mixer while particles A and B go through a cross-flow before going over. The flow number, Fig. 12.44(b), for the particles indicate that the mixer is mainly a shear-type mixer, i.e., flow number averages around 0.5. However, a short elongational flow generated as the particle enters and exits the narrow region, which should be expected due to the funneling effect that occurs.

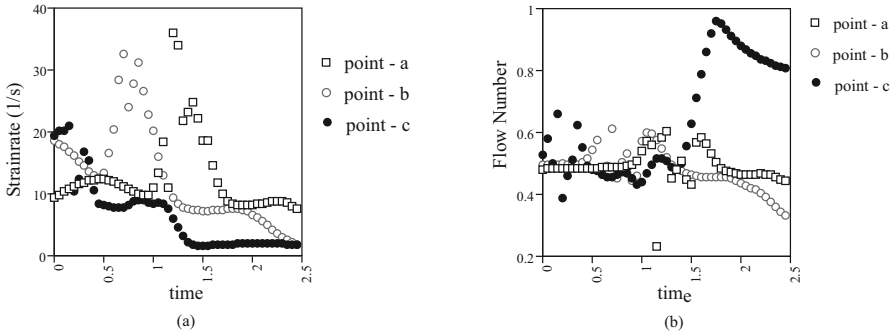


Figure 12.44 Calculated strain rates (a) and flow number (b) of three particles as they travel through a LeRoy-Maddock dispersive mixing section

12.4.3.5 Turbo-Screw

During the production of foamed polymeric products, keeping the amount of heat generation and the thermal gradients to a minimum are extremely important. The quality of the foam product is mainly dictated by cell size and uniformity. If the temperature becomes too high, the cell structure of the foam will break down leaving large cells with random sizes throughout the extrudate. The Turbo-Screw has been used to create efficient mixing and heat transfer for foam extrusion [98]. Figure 12.45 shows a perspective view of this multi-flighted mixing section.

This screw uses deep screw channels to minimize heat generation while utilizing numerous openings through the flight that allow the polymer melt to flow from one channel to the next. This mixing section has been found to increase output from 45% to 70% over conventional foamed extrusion operations. To analyze the effectiveness of this mixing section, Fogarty et al. [99] used the boundary element method to calculate the streamlines in two different screw geometries where Screw B was made to have larger holes in the screw flight than Screw C, see Fig. 12.45. Figures 12.46(a–b) show the particle tracking for Screw B from a side and front view, while Figs. 12.47(a–b) show the results for Screw C.

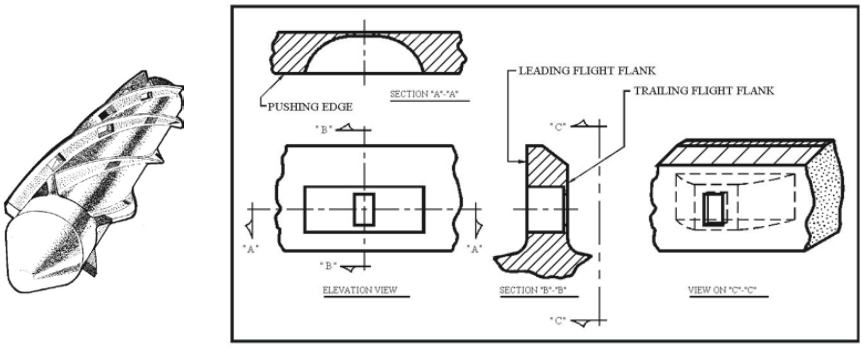
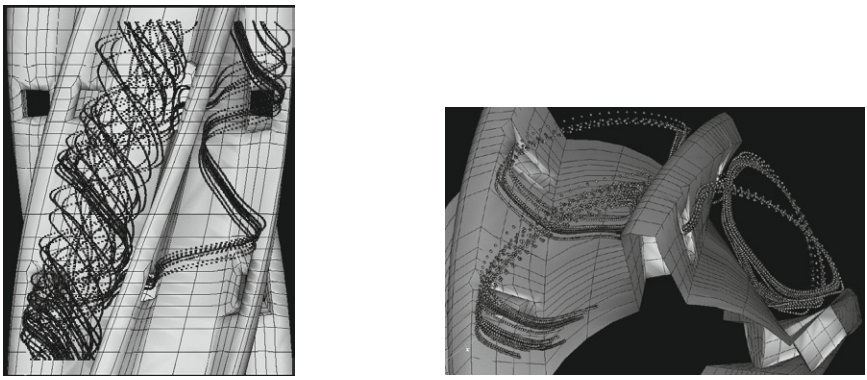
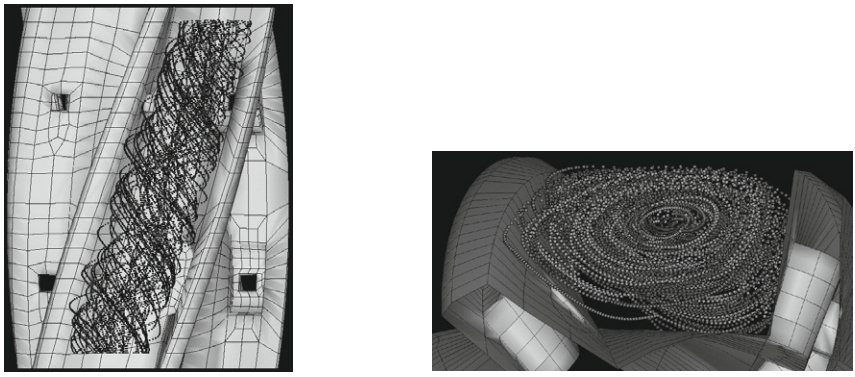


Figure 12.45 A perspective view of the Turbo-cool screw and schematic of two different openings put into flight wall



(a) (b)

Figure 12.46 Particle tracking in Screw B of the Turbo Screw. Note: Screw moves from left to right



(a) (b)

Figure 12.47 Particle tracking in Screw C of the Turbo Screw. Note: Screw moves from left to right

The particles follow a spiral pattern with a significant number of particles flowing through the flight hole in Screw B, while no particles flow through the hole in Screw C, thus making it less of a distributive mixer than Screw B. Here, the material close to the leading flight is at a relatively low temperature. Some of this material will end up flowing through one of the holes where it will combine with the hotter material on the trailing flight and barrel resulting in a cooler, more thermally consistent melt.

12.4.3.6 CRD Mixer

Most extrusion dispersive mixers are ineffective because shear is the main mode of deformation and the plastic melt is exposed to a high stress region only once. A mixer developed to overcome these shortcomings, is the Chris Rauwendaal Dispersive (CRD) mixer [100–104] shown in Fig. 12.48, see also Section 8.7.1.1.

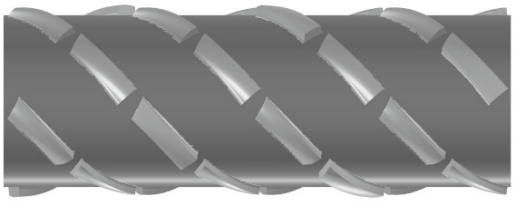


Figure 12.48
CRD dispersive/distributive mixing section

These mixers create elongational flow by incorporating a curved flight flank with a larger than normal flight clearance and tapered slots machined into the flights. The flow in the CRD mixer is a combination of shear and elongational flow with the latter dominating in the wedge shaped regions of the mixer. The slots also serve to increase the distributive as well as dispersive mixing. If the material is not randomized in its passage through a mixer, only the outer shells of fluid will be dispersed leaving the inner shells undispersed [105]. Therefore, it is critical to incorporate both distributive and dispersive mixing within one mixer. The initial design of the CRD mixer was developed using the concept of the passage distribution function [106], while the final geometry was developed using a detailed three-dimensional boundary element flow analysis [107]. Here, simulation was used to give a complete description of the flow so that stresses, the number of passes over the mixing flights, the number of passes through the tapered slots and residence time could be quantified for a large number of particles. The simulated tracking of particles, as they travel over the curved flight flank of the CRD and the tapered slot in the flight, are shown in Fig. 12.49.

In Fig. 12.49, the flow number of the particles is displayed with a color contour and the strain rate is shown for two particles in a separate graph. As expected, as the material goes through the wedge shaped area, it experiences an extensional flow and high strain rate—both required for effective dispersive mixing. The distributive mixing of this device can be seen by simulating particles that are initially grouped in the same area and observing how they spread apart as they travel through the mixer. The amount of pressure that the material must overcome influences the degree of mixing that will occur [107]. This effect, along with the distributive mixing in the CRD, is shown in Fig. 12.50, for a high and a low pressure, respectively.

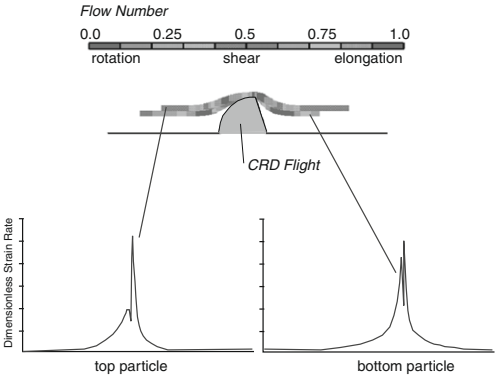


Figure 12.49(a)
Flow of two tracer points over the CRD flight showing the history of the Flow Number and strain rate

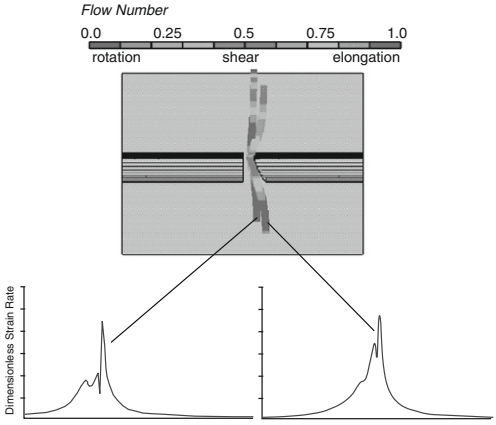


Figure 12.49(b)
Flow of two tracer points through the CRD flight slot showing the history of the Flow Number and strain rate

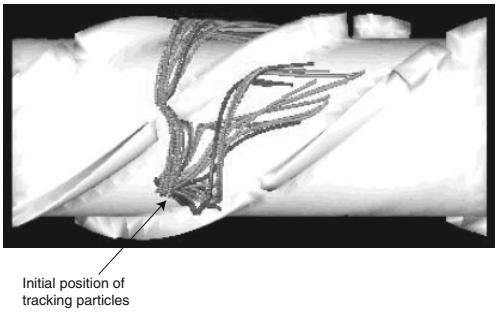


Figure 12.50(a)
Computed particle tracking in the CRD mixer with a high Δp simulated across the mixing section

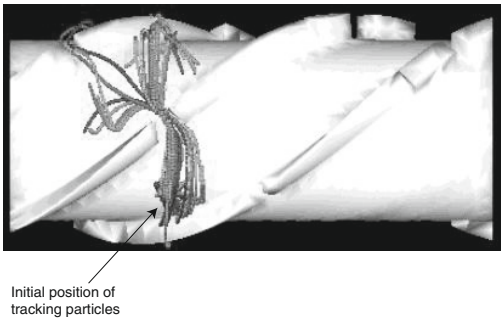


Figure 12.50(b)
Computed particle tracking in the CRD mixer with a low Δp simulated across the mixing section

12.4.4 Static Mixers

When adding compounds to a melt stream to produce a specific color or enhance properties, it is often desirable to produce the required mixing in the absence of moving parts. In these cases, a static mixer is necessary to produce a homogenized uniform melt. Fluids entering a static mixer are typically divided by baffles and mixing occurs by the repeated splitting and recombination of flow streams. The repeated dividing flows improve uniformity in composition, concentration, viscosity, and temperature. Figure 12.51 shows a common static mixer that is configured with crossing fingers, which split and divide that material as it passes through.

This mixer has been studied using both FEM and BEM to evaluate its mixing capability. Figure 12.52 shows simulated particle tracking through one repeating section of the mixer using BEM.

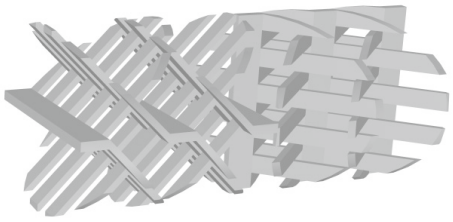


Figure 12.51 SMX static mixer

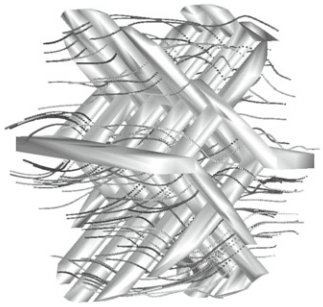


Figure 12.52 Computed particle tracking in one repeating unit of the SMX static mixer using BEM

Figure 12.53 shows the predicted pressure profile from low to high pressure (inlet to exit).



Figure 12.53
Computed pressure distribution of several repeating units of the SMX static mixer using BEM

In this analysis, the history of each particle can be monitored for such quantities as velocity and velocity gradients as it travels through the mixer. With this information, the distributive and dispersive mixing of the device can be evaluated qualitatively and quantitatively. For instance, the distributive mixing can be calculated using the residence time distribution by monitoring the time it takes for the parti-

cles to go through the system. Stagnant areas, which are a common problem with these mixers, can be found by viewing the particle paths or the streamlines of the mixer. The dispersive mixing, or ability to break-up liquid agglomerates or solid particulates, can be calculated by considering the stress and flow number (type of flow) history of the particles as they pass through the system. A more complete analysis can be made by taking into account coalescence [108].

The distributive mixing of a number of the current generation of static mixers are known to be quite good, however, their dispersive mixing is such that they often are unable to sufficiently break-up the dispersed phase. To alleviate some of the shortcomings found in many static mixers Gramann et al. [109] used the boundary element method to design a new type of static mixer that creates elongational flows for highly effective dispersive mixing, while creating distributive mixing by repeatedly splitting and folding the material. The Dispersive/Distributive Static Mixer (DDSM) [110] creates a dispersive environment by utilizing baffles that define a converging pathway for the mixing materials. Distributive mixing is accomplished by providing a series of baffles along the length of the mixing tube with each baffle angled relative to previous baffles. Figure 12.54 shows two units of the mixer that are repeated in series in the direction of flow.

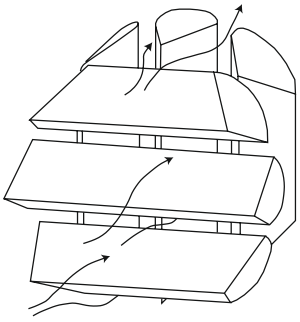


Figure 12.54
Two repeating units of the Dispersive/Distributive Static Mixer

The calculated streamlines are shown in Fig. 12.55 with corresponding values of the flow number Fig. 12.56.

From Fig. 12.56 it is obvious that the mixer is creating a high degree of elongational flow. The arrangement of the baffles is such that the fluid element experiences a continual elongational flow, ensuring enough time for break-up. Further, all material passing through the mixer is assured to encounter this high stress region a number of times corresponding to the number of mixer elements put in series.



Figure 12.55 Computed particle tracking in one module of the Dispersive/Distributive Static Mixer using BEM

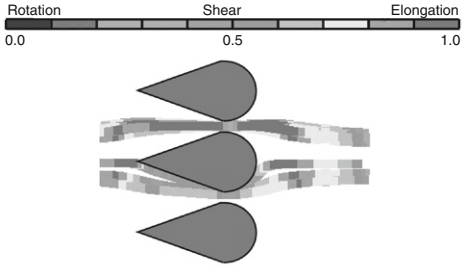


Figure 12.56 Computed flow number history of several particles as they travel through one unit of the Dispersive/Distributive Static Mixer

12.5 Conclusions

While the extrusion process has been utilized for commercial products since the mid-1800s, modeling and computer simulation is merely in its infancy. However, the tremendous advantages offered by simulation make it well suited to further advance the extrusion process through the next century. Simulation and CAE of the extrusion process and equipment permits a systematic design rather than *ad hoc* designs based solely on experience. While traditional experimental design of the extrusion process is focused on producing an acceptable product, oftentimes there is no explicit understanding of how process variables interrelate with one another and affect the final extrudate. Simulation provides insight into how process variables influence the flow field and contribute to the quality of the final product. Additionally, simulation provides feedback on variables that cannot easily be measured, e. g., temperature in the channel, during the actual extrusion process. Furthermore, simulation permits the engineer to quantify the effects of modifying a single variable on the final extrudate quality.

Simulation also offers significant advantages in the design of extruder screws and mixing devices. Computer simulation allows an engineer the possibility to “try out” new designs on the computer rather than expend time and costs associated with developing and testing a prototype. These virtual designs permit numerous trials to fine-tune the design in a cost effective manner prior to production.

With the increasing requirements to decrease costs, improve product quality, and increase productivity, computer aided engineering (CAE) provides an important tool to improve quality and throughput and, thus, profitability. It should be remembered, however, that modeling and computer simulation cannot capture all problems accurately; experimental verification continues to be critically important. Therefore, it is the combination of CAE and experimental work, which will provide the surest avenue to process improvements and innovations.

References

1. Rowell R.S., Finlayson, D. "Screw Viscosity Pumps," *Engineering,* 114, 606 (1922)
2. Tadmor, Z., Gogos, C.G., Principles of Polymer Processing, Wiley & Sons, New York (1979)
3. Vlcek, J., Perdikoulias, J., "Extrusion Seminar Presentations," Compuplast International, Zlin, Czech Republic (2000)
4. Perdikoulis, J., "A Brief Introduction to the Flow 2000(TM) Suite of CAE Tools for Extrusion," Compuplast Intl. (2001)
5. Cook, R.D., Malkus, D.S., Plesha, M.E., Concepts and Applications of Finite Element Analysis, Wiley & Sons, New York (1989)
6. Tucker III, C.L., Computer Modeling for Polymer Processing, Carl Hanser Publishers (1989)
7. Avalosse, T., Rubin, Y., Fondin, L., "Non-isothermal modeling of co-rotating and contra rotating twin screw extruders," SPE ANTEC Proceedings (2000)
8. Gramann, P.J., "Simulating Polymer Flow in Complex Geometries Using the Boundary Element Method," Ph.D. Thesis, University of Wisconsin—Madison (1995)
9. Davis, B.A., "Simulating Non-Linear Effects Using the Boundary Element Method," Ph.D. Thesis, University of Wisconsin—Madison (1995)
10. Rios, A.C., "Simulation of Mixing of Single Screw Extrusion Using the Boundary Element Method," Ph.D. Thesis, University of Wisconsin—Madison (1999)
11. Gramann, P.J., Osswald, T.A., *Int. Polym. Proc.,* 7, Vol. 4, p. 303 (1992)
12. Nardini, D., Brebbia, C.A., in "New Approach for Free Vibration Analysis Using Boundary Elements: Boundary Element Methods in Engineering," Springer Verlag (1982)
13. Mätzig, J.C., M.S. Thesis, University of Wisconsin, Madison (1991)
14. Wang, V.W., Hieber, C.A., Wang, K.K., SPE ANTEC, p. 826–829 (1992)
15. Lee, C.C., Folger, F., Tucker, C.L., *J. Eng. Ind.,* 106, p. 114–125 (1984)
16. Kouba, K., Vlachopoulos, J., SPE ANTEC, p. 114–116, (1992)
17. deLorenzi, H.G., Nied, H.F., in "Modeling of Polymer Processing" Isayev, A.I., (Ed.) Carl Hanser (1991)
18. Brown, P.F., M.S. Thesis, University of Illinois (1983)
19. Crochet, M., Couniot, A., Proc 2nd Int. Conf. on Num. Methods in Ind. Form. Process, Gothenberg (1986)

20. Tadmor, Z., Broyer, E., Gutfinger, C., *Polym. Eng. Sci.,* 14, p. 660–665 (1974)
21. Broyer, E., Gutfinger, C., Tadmor, Z., *Trans. Soc. Rheol.,* 9, p. 423–444 (1975)
22. Hele-Shaw, H. S., Proceed. Royal Inst., 16, p. 49–64 (1899)
23. Osswald, T. A., Tucker III, C. L., *Int. Polym. Proc.,* 5, p. 79–87 (1990)
24. Wang, V. W., Hieber, C. A., Wang, K. K., in "Applications of Computer Aided Engineering in Injection Molding," L. T. Manzione (Ed.), Carl Hanser Publishers (1987)
25. Ostwald, *W., Kolloid-Z,* 36, p. 99–117 (1925)
26. de Waele, A., *Oil and Chem. Assoc. J.,* 6, p. 33–88 (1923)
27. Carreau, P. J., Ph. D. Thesis, University of Wisconsin—Madison (1968)
28. Kaye, A. College of Aeronautics, Cranfield, Note No. 134 (1962)
29. Bernstein, B., Kearsley, E., Zapas, L., *Trans. Soc. Rheol.,* 7, p. 391–410 (1963)
30. Yang, H. H., Manas-Zloczower, I., *Int. Polym. Proc.,* 3, 203 (1992)
31. FIDAP Package, Fluid Dynamics International, Inc., Evanston, IL, USA.
32. Cheng, J. J., Manas-Zloczower, I., *Polym. Eng. Sci,* 29, p. 1059 (1989)
33. Cheng, J. J., Manas-Zloczower, I., *Int. Polym, Proc., 5,* p. 178 (1990)
34. Elmendorp, J. J., *Polym. Eng. Sci,* 26, p. 418 (1986)
35. Yang, H. H., Wong, T. H., Manas-Zloczower, I., in Mixing and Compounding of Polymers: Theory and Practice, I. Manas-Zloczower, Z. Tadmor (Eds.) Carl Hanser Publishers, Munich (1994)
36. Gramann, P. J., Stradins, L., Osswald, T. A., *Int. Polym. Proc.,* 8, p. 287 (1993)
37. Stradins, L., M. S. Thesis, University of Wisconsin—Madison (1993)
38. Davis, B. A., Gramann, P. J., Mätzig, J. C., Osswald, T. A., BETECH Conf. (1993)
39. Biswas, A., Davis, B. A., Gramann, P. J., Stradins, L. U., Osswald, T. A., SPE-ANTEC, p. 336 (1994)
40. Stone, H. A., Leal, L. G., *J. Fluid Mech.* 206, p. 223 (1989)
41. Salamon, B. A., Spalding, M. A., Powers, J. R., Serrano, M., Summer, W. C., Somers, S. A., Peters, R. B., "Color Mixing Performance in Injection Molding: Comparing a Conventional Screw and Non-Return Valve to Those Designed for Improved Mixing," SPEANTEC (2000)
42. Eccher, S., Valentinotti, A., *Industrial and Engineering Chemistry,* 5 (1958)
43. Mohr, W. D., Squires, P. H., Starr, F. C., *Soc. Plastics Eng. J.,* 16, p. 1015 (1960)
44. Mohr, W. D., Clapp, J. B., Starr, F. C., SPE Transactions, 113 (1961)
45. Griffith, R. M., *Ind. Eng. Chem. Fund.,* 1, p. 180–187 (1962)
46. Tadmor, Z., Klein, I., "Engineering Principles of Plasticating Extrusion," Van Nostrand Reinhold, New York (1970)
47. Yabushita, Y., Brzoskowski, R., White, J. L., Najakima, N., *Int. Polym. Proc.,* 5, p. 219 (1989)
48. Tellez, G., M. S. Thesis, University of Wisconsin—Madison (1994)

49. Campbell, G. A., Sweeney, P. A., Fenton, J. N., SPE-ANTEC, p. 219 (1991)
50. Rauwendaal, C. J., Osswald, T. A., Tellez, G., Gramann, P. J., *Int. Polym. Proc.,* Vol. 8, 4, p. 327–333 (1998)
51. Spalding, M. A., Dooley, J., Hyun, K. S., Strand, S. R., SPE-ANTEC p. 1533 (1993)
52. Chen, Z., White, J. L., SPE-ANTEC, p. 3401 (1993)
53. Cheng, H., Manas-Zloczower, I., *Polym. Eng. Sci,* Vol. 37, 6, p. 1082 (1997)
54. Yao, C., Manas-Zloczower, I., *Polym. Eng. Sci,* Vol. 38, 6, p. 1082 (1998)
55. Shearer, C. J., *Chem. Eng. Sci.,* 28, p. 1091–1098 (1973)
56. Rauwendaal, C. J., Doctoral Thesis, Twente University, the Netherlands (1988)
57. Rios, A. C., MS Thesis, University of Wisconsin—Madison (1994)
58. Booy, M. L., *Polym. Eng. Sci,* 18, 12, p.973 (1978)
59. Mitsoulis, E., *Adv. Polym. Technol,* 6, p. 467 (1986)
60. Mitsoulis, E., Wagner, R., Proc. World Congress III Chem. Engr., 4, p 534 (1986)
61. Heng, F. L., Mitsoulis, E., *Int. Polym. Proc.,* 1, p. 44 (1989)
62. Dooley, J., Polymers, Laminations & Coatings Conf., p. 957 (1990)
63. Wang, Y., *Polym. Eng. Sci.,* 3, p. 204 (1991)
64. Kiriakidis, D. G., Mitsoulis, E., *Adv. Polym. Tech.,* 2, p. 107 (1993)
65. Pittman, J. F. T. in Computer Modeling for Polymer Processing, C. L. Tucker III (Ed.) Carl Hanser Publishers, Munich (1989)
66. Kim, Y. J., Han, C. D., *Polym. Engr. Rev.,* 2, p. 385 (1975)
67. Perdikoulis, J., "A Brief Introduction to the Flow 2000(TM) Suite of CAE Tools for Extrusion," Compuplast Intl. (2001)
68. Bird, R. B., Armstrong, R. C., Hassenger, O., Dynamics of Polymeric Liquids, 1, Wiley & Sons, New York (1987)
69. Gupta, M., Jaluria, Y., Sernas, V., Essenghir, M., Kwon, T. H., *Polym. Eng. Sci.,* 7, p. 393 (1993)
70. Lawal, A., Railkar, S., Kalyon, D. M., "Mathematical Modeling of Three-Dimensional Die Flows of Viscoplastic Fluids with Wall Slip," SPE-ANTEC (1999)
71. Gifford, W. A., "A Three-Dimensional Analysis of the Effect of Die Body Deflection in the Design of Extrusion Dies," SPE-ANTEC (1998)
72. Reddy, M.P, Schaub, E. G., Reifschneider, L. G., Thomas, H. L. "Design and Optimization of Three Dimensional Extrusion Dies Using Adaptive Finite Element," SPE-ANTEC (1999)
73. Sun, J., Waucquez, C., Rubin, Y., "Elongational Effects of Die Flows: Pressure Distribution and Shape Predicton," SPE-ANTEC (2000)
74. Gifford, W. A., *Polym. Eng. Sci.,* Vol. 40, 9, p. 2095 (2000)
75. Debbaut, B., Avalosse, T., Dooley, J., Hughes, K., J. *Non-Newt. Fluid Mech.,* 69, 2–3, p. 255 (1997)
76. Dooley, J., Hyun, K. S., Hughes, K. R., *Polym. Eng. Sci.,* 38,7, p. 1060 (1998)

77. Debbaut, B., Dooley, J., *J. Rheology,* 43, 6, p. 1525 (1999)
78. Debbaut, B., Dooley, J., "Flow of a Low Density Polyethylene in Straight and Tapered Channels: Experiments and 3-D Finite Element Simulation," XIII-th International Conference on Rheology, Cambridge, UK, 2, 170 (2000)
79. Goodenberger, D.E., U.S. Patent 1,350,722 (1920)
80. Acrivos, A., Babcock, B.D., Pigford, R.L., *Chem. Eng. Sci.,* 10, 112 (1959)
81. Procter, B., *SPE Journal,* 28, 34 (1972)
82. Klein, I , Klein, R., *SPE Journal,* 29, 33 (1973)
83. Michaeli, W., Extrusion Dies, Carl Hanser Publishers, Munich (1984)
84. Winter, H.H., Fritz, H.G., *Polym. Eng. Sci.,* 26, 543 (1986)
85. Liu, T., Hong, C., Chen, K., *Polym. Eng. Sci.,* 28, 1517 (1988)
86. Vergnes, B., Sailard, P., Agassant, J.F., *Polym. Eng. Sci.,* 24, 980 (1984)
87. Menges, G., Masberg, U., Gesenhues, G., Berry, C., in "Numerical Analysis of Forming Processes", Pittman, J.F., Aienkiewicz, O.C., Wood, R.D., Alexander, J.M. (Eds.), Wiley & Sons, New York (1984)
88. Gifford, W.A., *J. of Reinf. Plast Compos.,* 16, 661 (1997)
89. Somers, S.A., Spalding, M.A., Dooley, J., Hyun, K.S. "Numerical Analysis of the Thermal Mixing Effects of an Energy Transfer (ET) Screw Section," SPE-ANTEC (1995)
90. Plumley, T.A., Spalding, M.A., Dooley, J., Hyun, K.S., SPE-ANTEC, 39 (1993)
91. Avalosse, Y. R., Fondin, L., "Non-isothermal Modeling of Co-Rotating and Contra-Rotating Twin Screw Extruders," SPE-ANTEC (2000)
92. Krawinkel, S., Bastian, M., Osswald, T.A., "Simulation der Strömungsverhältnisse im Gleichdrall-Doppelschneckenextruder," Institut für Kunststofftechnik, Paderborn, Germany (1999)
93. Osswald, T.A., Menges, G., Materials Science of Polymers for Engineers, Carl Hanser Publishers, Munich (1995)
94. Gramann, P.J., Noriega, M.P., Rios, A.C., Osswald, T.A., "Understanding a Rhomboid Distributive Mixing Head Using Computer Modeling and Flow Visualization Techniques," SPE Technical Conference, Toronto (1997)
95. Rios, A.C., Gramann, P.J., Osswald, T.A., Noriega, M.P., Estrada, O.A., *Int. Polym. Proc.* 9,1, pp 12–19 (2000)
96. Wang, Y., Tsay, C.C., *Polym. Eng. Sci.* (1996)
97. Samsonkova, P., Vlcek, J., "Modeling of Fluted Mixing Elements," SPE ANTEC (2001)
98. U.S. Patent 6,015,227, Thermoplastic Foam Extrusion Screw with Circulation Channels, James Fogarty (1998)
99. Fogarty, J., Fogarty, D., Rauwendaal, C.J., Rios, A., "Turbo-Screw, New Screw Design for Foam Extrusion," SPE ANTEC (2001)
100. Rauwendaal, C.J., Osswald, T.A., Gramann, P.J., Davis, B., "A New Dispersive Mixer for Single Screw Extruders," 56th SPE ANTEC (1998)

101. Rauwendaal, C.J., Osswald, T.A., Gramann, P.J., Davis, B., Noriega, M.P., Estrada, O.A., "Experimental Study of a New Dispersive Mixer," 57th SPE ANTEC (1999)

102. Rauwendaal, C.J., Osswald, T.A., Gramann, P.J., Davis, B.A., "Design of Dispersive Mixing Sections," *Int. Polym. Proc.,* Vol.13 (1999)

103. Rauwendaal, C.J., "Screw Extruder with Improved Dispersive Mixing," US Patent 5,932,159 (1999)

104. Rauwendaal, C.J., Gramann, P.J., Davis, B.A., Osswald, T.A., "Screw Extruder with Improved Dispersive Mixing Elements," US Patent 6,136,246 (2000)

105. Kwon, T.H., Joo, J.W., Kim, S.J., *Polym. Eng. Sci.,* Vol. 34, 3 (1994)

106. Tadmor, Z., Manas-Zloczower, I., *Adv. Polym. Tech.,* Vol. 3 (1983)

107. BEMflow: A boundary element fluid dynamics simulation program, The Madison Group: Polymer Processing Research Corporation

108. Janssen, J.M.H., Ph.D. Thesis, Eindhoven University of Technology, The Netherlands (1993)

109. Gramann, P.J., Davis, B.A., Osswald, T.A., Rauwendaal, C.J., "A New Dispersive and Distributive Static Mixer for the Compounding of Highly Viscous Materials," SPEANTEC (1999)

110. Davis, B.A., Gramann, P.J., Osswald, T.A., New Dispersive Static Mixer, US Patent 5,971,603 (1999)

Conversion Constants

Length

1	kilometer	km	= 1E3 m (meter)
1	centimeter	cm	= 1E-2 m
1	millimeter	mm	= 1E-3 m
1	micron	μm	= 1E-6 m
1	nanometer	nm	= 1E-9 m
1	Ångstrom	Å	= 1E-10 m
1	inch	in	= 2.54E-2 m
1	milliinch	mil	= 2.54E-5 m
1	foot	ft	= 0.3048 m
1	mile	mile	= 1609 m

Volume

1	cubic decimeter	dm^3	= 1E-3 m^3 (cubic meter)
1	cubic centimeter	cc	= 1E-6 m^3
1	liter	1	= 1E-3 m^3
1	deciliter	dl	= 1E-4 m^3
1	milliliter	ml	= 1E-6 m^3
1	cubic inch	in^3	= 1.639E-5 m^3
1	cubic foot	ft^3	= 2.832E-2 m^3
1	barrel	barrel	= 0.159 m^3
1	gallon (US)	gal US	= 3.785E-3 m^3
1	gallon (UK)	gal UK	= 4.546E-3 m^3

Mass

1	ton	t	= 1E3 kg (kilogram)
1	gram	gr	= 1E-3 kg
1	ounce	oz	= 2.83E-2 kg
1	pound	lbm	= 0.4536 kg
I	ton (US)	to	= 907 kg
1	ton (UK)	ton	= 1016 kg

Density

1	gram per cc	gr/cc	= 1E3 kg/m^3
1	pound per cu ft	lb/ft^3	= 16.02 kg/m^3
1	pound per cu in	lb/in^3	= 2.77E4 kg/m^3
1	gram per cc	gr/cc	= 3.61E-2 lbs/$inch^3$

Force

1	dyne	dyn	= 1E-5 N (Newton)
1	kilogram-force	kgf	= 9.81 N
1	ton-force	tf	= 9810 N
1	pound-force	lbf	= 4.448 N

Stress

1	megapascal	MPa	= 1E6 Pa (Pascal)
1	dyne per cm^2	dyn/cm^2	= 0.1 Pa
1	Newton per m^2	N/m^2	= 1 Pa
1	Joule per m^3	J/m^3	= 1 Pa
1	atmosphere	atm	= 1.013E5 Pa
1	mm mercury (torr.)	mm Hg	= 133.3 Pa
1	mm water	mm H_2O	= 9.81 Pa
1	bar	bar	= 1E5 Pa
1	pound per $inch^2$	psi	= 6890 Pa
1	kgf per cm^2		= 9.81E4 Pa
1	megapascal	MPa	= 145 psi

Viscosity

1	poise	poise	= 0.1 Pas
1	poise	poise	= 1 $dyns/cm^2$
1	pound-sec per in^2	psi · sec	= 6897 Pas
I	poise	poise	= 14.5E-6 psi·sec

Energy/Work

1	erg	dyn·cm	= 1E-7 J (Joule)
1	Newton-meter	N · m	= 1 J
1	watt-second	W · s	= 1 J
1	kgf-meter	kgf · m	= 9.81 J
1	foot-pound	ft · lbf	= 1.356 J
1	horsepower-hour	hp · h	= 2.685E6 J
1	kilowatt-hour	kW · h	= 3.60E6 J
1	calorie	cal	= 4.19 J
1	Brit. thermal unit	Btu	= 1055 J
1	inch-pound	in · lbf	= 0.113 J

Power

1	kilowatt	kW	= 1000 W (Watt)
1	horsepower	hp	= 745.7 W
1	foot-pound per sec	ft · lbf/s	= 1.356 W

Specific Energy

1	calorie per gram	cal/gr	= 4190 J/kg
1	Btu per pound	Btu/lb	= 2326 J/kg
1	hp·h per pound	hp · h/lb	= 5.92E6 J/kg
1	hp·h per pound	hp · h/lb	= 1.644 kWh/kg
1	kWh per kg	kW · h/kg	= 3.60E6 J/kg
1	kWh per kg	kW · h/kg	= 0.608 hp·h/lb

Thermal Conductivity

1	cal/cm·s·°C	= 419 J/m·s·°K
1	kcal/m·h·°C	= 1.163 J/m·s·°K
1	Btu/ft·h·°F	= 1.73 J/m·s·°K
I	Btu/in/ft^2·h-°F	= 0.144 J/m·s·°K
1	Btu/ft·s·°F	= 6230 J/m·s·°K
1	W/m·°K	= 1 J/m·s·°K

Temperature

Unit	Degrees Kelvin	Degrees Celcius	Degrees Fahrenheit
Symbol	°K	°C	°F
Boiling point water	373.15	100.00	212.00
Melting point ice	273.15	0.00	32.00
Absolute zero	0.00	–273.15	-459.67

1 degree Fahrenheit °F = 1/1.8°C
1 degree Celcius °C = 1.8°F
1 degree Kelvin °K = 1°C

Index

Numeric

4-mode Giesekus model 891

A

abrasive wear 787
absorptivity 170
AC drive systems 49
– adjustable frequency drive 49
– adjustable transmission ratio drive 49
actual energy requirement 34
actual stock temperatures, and degradation 811
adiabatic temperature 401
adjustable frequency drives 49, 51
adjustable groove depth 299
adjustable grooved feed extruder 297
adjustable transmission ratio drive 49
air entrapment
– solutions to 834
analytical solution 862
analytical techniques 862
angle of repose 193
apex area 730
Archimedean solids transport 269
arching 268
arching or bridging in hopper flow 260
area draw ratio (ADR) 672
AutoCAD™ 878
autogenous process 78
automatic gel detection methods 839
automatic reset 123, 124
autoscreen 74
average flow velocity in the thin section 660
Avogadro's number 158
axial mixing (backmixing) 483, 484

B

backmixing (axial mixing) 483, 484
– prevention 488
"back relieving" the land 658
balance by channel height 659
Banbury type mixer 871, 885
– modeling 871
– simulating 873
barrel temperature measurement 100
barrier flight extruder screws 569
– patent history 569
Barr screw 575
basic guidelines in profile design 654
batch extruders 2
BEM simulation 611
Bessel functions 725
best straight line (BSL) 93
bimetallic barrels 67
Bingham model 213
Biot number 167, 424
blister ring 587, 618
blown film extrusion 676
BMK mixer *see* SMV mixer
Boltzmann constant 169
boundary element method (BEM) 610, 653, 872
breakdown force 470
breaker plate 72
Brinkman number 164, 638
Brownian motion 469
brushless DC drives 55
BT mixer 585
buckling 515
bulk density 191, 193
bypass vented extruder 559

C

calibrator 692
– external calibrators 693
– internal calibrator 693
– slide calibrator 692
– Technoform process 694
– vacuum calibrator 692
CAMPUS, Computer Aided Material Preselection 249
cantilever 515
capacitance measurement 112
Capillary (or Weber) number 874
capillary rheometer 223
– melt index tester 223

capillary transducers 89
Carreau model 213
cascade devolatilization 562
Cauchy's equation 150
cavity transfer mixing (CTM) 620
chain drives 50
change-over 23
– time 23
channel depth 537
characterization of the mixture 442
chemical degradation 805
Chris Rauwendaal Dispersive (CRD) 908
Chung 5
classification of polymer extruders 14
classification of twin screw extruders 25
clearance 70, 350
closely intermeshing co-rotating (CICO) twin screw extruder 701
closely intermeshing counter-rotating extruder (CICT) 702, 720
closely self-wiping co-rotating extruders (CSCO) 705
coalescence 479
coat hanger die 664, 666
coaxial twin screw (CTS) extruder 743
coefficient of cohesion 193
coefficient of friction 195, 290
– of the bulk material 194
coefficient of variation (COV) 464
coextrusion 686
color concentrates (CC) 614
color measurement 116
commercial twin screw machinery 749
common screw materials 70
– european equivalents 70
comparison of various temperature sensors 98
comparison, type of thrust bearings 65
compatibilizers 480
compression characteristics of bulk materials 194
compression mold filling simulation 868
compression ratio (X_c) 518, 536
computer aided engineering 3
computer simulation 610
– melting theories 332
conservation of energy 864
conservation of mass 864
conservation of momentum 864
"constant torque" characteristic 60
constructing a timeline 765
contiguous solids melting (CSM) 304, 333
continuous extruders 2, 13, 28
– disk extruders 28
controllers, factory-tuned and non-adjustable parameters 139
controller transfer curve (power input curve) 122
control volume approach (CVA) 870
conventional extruders 23
conventional multi-flighted screw 568
conveying mechanism 33
conveying process, self-wiping extruders 713
co-rotating extruders, screw geometry 708
corrosive wear 788
Couette flow 169 *see* drag flow
Couette shear rate 405, 520, 594
Coulomb friction 260
crammer feeders 68, 258
CRD (Chris Rauwendaal Dispersive mixing) barrier screw 581
CRD fluted mixer 586, 603, 613, 614
critical screw speed 400
critical tensile deformation rate range 675
critical Weber (Capillary) number 475
cross-channel flow 361
crosshead die 669
crosslinking 1
cross-sectional mixing 483
CT mixer 621
cumulative residence time distribution (CRTD) 904
curved plate model 277
cylindrical coordinate system (CCS) 413

D

data acquisition systems (DAS) 769
DC brush motor 776
dead spots 675
degradation 245
– polymer 624, 626
– reducing 819
del Pilar Noriega 5
design parameters for spiral mandrel die 679
determinant, det 211
developing melt temperatures 390
devolatilization 175, 180, 435, 554
– continous 745
– efficiency 830
– particulate polymer 180
– polymer melts 181
devolatilizing extruder screws 553
diameter draw ratio (DDR) 672
diaphragms 92
die 72
die assembly 72
die drool *see* die lip build-up
die flow instabilities 431
die flow problems 843
die forming zone 419
die geometry, effect on flow distribution 680
diehead pressure 87, 419
dielectric heating 171
die lip build-up 845
dies, film and sheet 663
die swell *see* extrudate swell

die temperature adjustment 665
differences in screw design 753
differential thermal analysis (DTA) 247
dilatant fluid 205
dimensional analysis 161
dimensionless numbers 161, 163
dimensionless throughput 364
dimensionless viscosity 423
discharge screw (crammer feed) 778
discolored specks 846
– in the raw material 837
discontinuous extruders 2, 13
disk extruder *see* screwless extruder
– diskpack extruder 31
– spiral disk extruder 31
– stepped disk extruder 28
dispersed solids melting (DSM) 304, 333, 617
Dispersive/Distributive Static Mixer (DDSM) 911
– CRD mixing technology 463
dispersive mixers 604, 618
dispersive mixing 469
– elements 584
– liquid-liquid systems 471
distributive mixers 623
distributive mixing 441, 619
double wave mixing screw 601, 622
down channel velocity 863
drag flow 202
– of power law fluids 374
– rate 635
– term 43
drag induced solids conveying 270
draw ratio balance (DRB) 673
draw resonance 434, 823
Dray and Lawrence screw 578
Dray fluted mixing section 587
drop rupture 467
drum extruder 30
DSM process *see* dispersed solids melting theory
dual output temperature controllers 128
dual reciprocity boundary element method (DRM) 874
dual sensor temperature control 125
Dulmage mixing section 619
dynamic analysis 231
dynamic process model 141
dynamic testing of pressure tranducers 94, 95

E

effective angle of friction, β_e 199
effective yield locus (EYL) 198
Egan mixing section 587
E-gels 839
Ehring model 213
elastic encapsulation 691
elastic melt extruder 35
elastomers 1
electric friction clutch drive 50
electric heating 75
electric resistance heaters 75
electronic data acquisition systems (DAS) 625
electronic integrator 123
Ellis model 213
elongation 203
elongational deformation 203
elongational flows
– shear-free flows 871
elongational viscosity 205
empirical identifications technique 142
– deterministic functions 142
– stochastic (random) identification functions 142
energy balance equation 151, 242
energy consumption 23
energy efficiency for pressure generation 34, 43
Energy Transfer (ET) screws 622, 893
entropy 155, 157
equation of continuity 149
equation of motion *see* momentum balance equation
equilibrium melt temperature *see* fully developed melt temperature
equivalent spherical diameter (esd) 200
Esde 22
E-speck 846
Euler equation 150
extended mandrel 674
extensional flow mixer (EFM) 602
extensive mixing 441
external coefficient of friction 194
extrudate swell *see* die swell
extrudate thickness, measure 110
extruder 1
– barrel 64
– cooling 77
extruder drive 49
– AC motor drive systems 49
– DC motor drive systems 49
– hydraulic drives 49
extruder screw 13, 70
– functions 626
extruder screw for rubber
– EVK screw (Wener & Pfeiderer) 20
– Pirelli rubber extruder screw 19
– Plastiscew 19
– QSM Extruder 20
– Transfermix 20
extruders without gear reducer 23
extrusion instabilities 820
– solutions to 833

F

Farrel continuous mixer (FCM) 742
feedback ratio 436
feed block dies 686
feed-controlled extrusion 7
feed hopper 68
feed port design 65
feedstock properties 767
feed throat 64
F-H relationship *see* Flory-Huggins relationship
fibrillation 482
Fick's law 175
filtration systems 74
finite element analysis (FEM) 653, 800
finite element fluid dynamics analysis package, FIDAP 872, 892
first law of thermodynamics 151, 153
fishtail die 663
five-layer blown film coextrusion dies 687
flash devolatilization 182
flat plate model 275
flat plate system (FPS) 208, 877
flat slanted flight flanks
– trapezoidal flight geometry 279
flat three-plate model 734
flex lip adjustment 664
flight flank 347
flight geometries 514, 539
flood feeding 7, 302, 831
Flory-Huggins (F-H) relationship 177
Flow Analysis Network (FAN) 869
flow behavior of polymer melt 653
flow distribution 682
flow function 270
flow number 610
– distribution 881
flow patterns 699
flow rate 43, 265, 415
fluoropolymers 673
flux vector (FV) 52
form factor 54
Fortran program 363, 493
Fourier number 168, 310
Fourier's law of heat transfer 152, 160, 176
four-motor CMG torque drive 22
four-screw extruder 26
Frequon 173
frictional heat 67
– generation 282, 290
frictional properties, polymer 196
friction, attributions 195
fully developed melt temperature *see* equilibrium melt temperature
functional instabilities 828
funnel flow 260
funneling 268

G

Gaussian elimination 865
gear pump extruder 27
gear reducer 23
gel 836, 837, 839
– content 836
– crosslinked 840
– defects with discoloration 838
gelation 836
general characteristics of the standard extruder 549
Generalized Newtonian Fluids (GNF) 870
geometrical encapsulation 691
geometrical relationships 257
geometry, extruder screw 255 *see* single stage
– feed section of screw 13
– metering section (pump section) 13
– transition section (compression section) 13
Gibbs free energy 159
gloss 853
gloss, quantitative measurement 115
GMP, good manufacturing practices 625
G-process 676
Graetz number 166, 638
gravity flow 261, 266
grooved barrel sections 66, 284, 288
grooved feed extruder 296
grooves, number 682
grooves, wear 286

H

hardfacing or hardsurfacing 794
hardfacing techniques 644
– laser hardfacing 646
– metal inert gas (MIG) welding 646
– oxyacetylene welding 644
– plasma transfer arc (PTA) welding 645
– tungsten inert gas (TIG) welding 645
haze 853
– and luminous transmittance of transparent plastics, measurement 115
HDPE 39
– melt extruded, properties 39
– solid-state extruded, properties 39
heating extruders 75
– electric heating 75
– fluid heating 75
– steam heating 75
heat transfer 160
– conductive heat transfer 160
– convective heat transfer 161
helix angle 532, 538, 578, 594, 683
Henry's law 177
Henry's law constant 177
high-frequency instabilities 821
high-pressure extrusion 669

high speed co-rotating twin screw extruders, compared to low speed twin screw extruders 698
high-speed extrusion 22
high-speed single screw extruders (HS-SSE) 22, 23
high stress region, HSR 602
high-viscosity polymers 23
Hi-mixer 463
history of polymer extrusion 6
homopolymers 245
horseshoe die 667
hot-stage microscopy (HSM), to characterize gels 840
hydraulic drive
– hydrostatic drive 55
hygroscopic resins 564
hysteresis 93, 118
– curve 118

I

improper screw geometry 509
increase in the screw diameter 802
induction time 245
infrared (IR) heating 171
infrared (IR) melt temperature measurement 106
infrared (IR) sensors 98
infrared thermometer 768
Ingen Housz barrier screw 581
initial scale of segregation 832
inner melt removal (IMR) 744
instrumentation 85, 86
insufficient melting capacity 829
insufficient mixing capacity of the screw 831
integrator 123
interface distortion 690
intermeshing co-rotating extruders 701
intermeshing twin screw extruder (TSE) 304, 862
internal coefficient of friction 194
ion-nitriding 67
iron-constantan thermocouple (TC) 98
ISG mixer 461
ITX 5

J

Janssen model 481

K

K-BKZ model 884
Kelvin model 871
Kenics mixer 462
Kennaway 19
Kim screw 579
kinematic viscosity 167
Kirchhoff's law 170

L

laminar mixing (laminar flow) 457
land length 657, 673
leakage 722
leakage flow 350
LeRoy/Maddock mixer 585
light microscope 772
linear low-density polyethylene, LLDPE 546
linear variable differential transformer (LVDT) 110
lines in extruded product 851
liquid crystalline polymers (LCPs) 853
lobal mixing 603
low-frequency instabilities 826

M

machinery, wear 780
Maddock mixing section 585
Maddock or LeRoy dispersive mixing section 905
magneto-strictive ultrasound transducer 112
Maillefer extruder screw 572, 573
mass balance equation 149
mass flow (hopper flow) 260
material consumed in the change-over 24
mathematical modeling 610
maximum melting efficiency 571
maximum normal stress 512
maximum shear stress 513
maximum stress 511
Maxwell model 871
"MC3" and "MC4" screw 576
mechanical adjustable speed (MAS) 50
mechanical adjustment of the die flow channel 655
mechanical degradation 804
mechanical specific energy consumption 23
medical devices, molecular degradation 630
medical extrusion 624
– automation 625
– good manufacturing practices (GMP) 625
– requirements 625
medical tubing 672
melt conveying of isothermal fluids 342
melt conveying or pumping problems 830
melt conveying theory of Newtonian fluids 440
melt fracture 432, 822, 843, 844
melt index (MI) 223
melting mechanism, for diskpack
– dissipative melt mixing (DMM) 34
– drag melt removal (DMR) 34
melting models 326
melting point 245
melting rate for a non-zero clearance 534
melting theory for temperature-dependent fluids 319
melting zone (plasticizing zone) 103

melt pressure 86, 87
melt pressure control systems 141
melt temperature 22
– distribution 627
– parameters 407
– variations 628
membrane stretching model during blow molding and thermoforming 869
mesh editing procedure
– dynamic mesh generator 868
mesh generation scheme 869
mesh superposition technique (MST) 896
metallic filter medium 73
metallocenes 546
metal-to-metal wear 789
mettalic filter medium
– relative performance comparison 73
microwave heating 173
minimum set of instrumentation 85
mixing 441
– element 584
– of immiscible fluids in a twin screw extruder 482
– zone in the extruder 442
modeling, linear control system 130
molecular weight (MW) 624
– reductions 624
momentum 150
– convection of momentum 150
momentum balance equation 150
moving boundaries 861
– moving free boundaries 861
– moving solid boundaries 861
multi-flighted screw geometry 568
multiflux mixer 460
multi-manifold external-combining dies 688
multi-manifold internal combining dies 686
multi-manifold sheet die 688
multi-screw extruder 878
multi-vent devolatilization 561

N

Nahme number 321, 324
– also Griffith number 167
Newtonian flow rate equation 528
Newtonian fluids 205, 210, 343, 367
Newton-Raphson method 542
nitriding 67
– gas nitriding 67
– liquid bath nitriding 67
noise level 23
non-intermeshing twin screw extruders 730
– are counter-rotating (NOCT extruders) 730
non-Newtonian and non-isothermal, polymer melt 316
non-Newtonian fluid 205, 210
non-return valve (NRV) 615
nuclear radiation sensors 113
numerical techniques 864
– boundary element method (BEM) 867
– finite difference method (FDM) 865
– finite element method (FEM) 866
Nusselt number 166

O

objective of an extrusion die 654
offset 121, 124
one-dimensional flow analysis 356
one-dimensional power law analysis 525
on-off controller 133
on-off control of temperature 117, 118
on-off differential 118
optical properties 853
optimize the channel depth and helix angle 521
optimizing output 519
optimum channel depth 519
optimum channel depth H* 542
optimum helix angle ϕ* 541
optimum screw geometry for melt conveying 519
oxidative degradation 806

P

“pancake” coextrusion die 687
parallel flights 532
parallel plate analysis with moving barrel 411
particles
– broken solids 201
– granules 201
– pellets 201
– powders 201
– semi-free-flowing granules 201
particle size 200
Peclet number NP_e 166, 389, 439
PET powder 564
Petrov-Galerkin technique 882
P-gels 839
piezoelectric pressure transducers 90, 93
piezoelectric ultrasonic transducer 112
piezo-resistive pressure transducers 91
piezo-resistive transducer 88
pineapple mixer 620
pin mixing section 619
pipe dies 668
piping 260
Planck constant 169
Planck’s law of radiation 169
planetary roller extruder 25
plasticating 548, 551, 562
plasticating extrusion 2
plasticating instabilities 829
plasticating zone *see* melting zone

plug flow 203
– zone 261
plugging 536
pneumatic pressure transducers 90
Poiseuille equation 187
Poiseuille flow 169
Poisson ratio 244
polymer degradation 803
polymer density ρ 236
polymer processing aids (PPA) 843
polymers 1, 2, 219
– elastomers 1
– thermoplastics 1
– thermosets 1
polypropylene 23
polystyrene 23
polytetrafluoroethylene (PTFE)
– extrusion of 37
portable data collectors (PDCs) 769
portable machine analyzers (PMAs) 769
positive displacement 699
positive displacement devices 27 *see* gear pump extruder
Potente 5
power consumption (z) 43, 353, 391, 540
– in the melting zone 330
– measurement 108
power conversion unit (PCU) 776
power factor 108
power law equation 209, 212, 216
power law fluid 356, 588
power law index 209, 529
power law model 870, 872
power law of Ostwald and de Waele *see* power law equation
Prandtl number 167
pressure differential (ΔP) 512
pressure distribution 262
pressure drop 465, 596, 601
pressure flow 202
pressure flow rate through a triangle 735
pressure flow term 43
pressure transducers 88, 89, 90, 91, 92
– selection 93
problem-solving process 763
process model 137, 138
process monitoring, of wear 850
process reaction curve
– response curve 128
process transfer curve 122
ProEngineer™ 878
profile dies 684
profile extrusion 684
profiling 691
profitability of an extrusion operation 23
properties of the bulk material 191
proportional band 119, 120, 123
proportional control 123
proportional controller 119, 123
proportional plus integral (PI) controllers 124
proportional plus integral plus derivative (PID) control system 124
– PID controller 136
P-speck 846
Pulsar mixer 622
Pulsar mixing section 622
pumping efficiency in diskpack extruder 42
pump ratio (X_p) 555
pushrod transducer 88
pyrometer 768

R

Rabinowitsch and Weissenberg, fluid relationship 213
Rabinowitsch correction 222
Rabinowitsch equation 213
radial clearance 543, 544
radiation, absorption 113
radio frequency heating *see* dielectric heating
ram extruder
– multi-ram extruder 41
random fluctuations in instability 827
rapid flow 260
rate of solids melting 863
Rayleigh disturbances 472
reaction-curve method 138
rear valving 559
rearward devolatilization 560
rebuilding extruder barrels 646
rebuilding extrusion equipment 642
reducer 59
reducing gel formation in the extruder 840
reduction in noise level 23
residence time 23, 24, 449
– distribution functions (RTD) 455, 466, 485, 807
resistance temperature (RT) curve 97
resistive temperature sensors
– conductive-type temperature (RTD) 97
– semiconductor type 97
resonance frequency 516
Reynolds number 163
rheological models 887
rheological properties 191
rheometer 220
– capillary rheometer 220
– cone and plate rheometer 227
– slit die rheometer 228
rheopectic 219
rhomboid mixing section 902
roller die 21
rotating drum devolatilizer (RDD) 564
rotational speed, measure 109

RPVC extrusion 837
rubber elasticity, theory 157
rubber extruders 17
– cold feed 18
– hot feed 18

S

sag at the end of the screw 514
Saxton mixer 619, 620
Saxton mixing section 609
scale-up 635, 641
– factors 639
– method 635
scanning and sorting (S & S) system 847
screen
– autoscreen system 74
screens 72 *see* metallic filter medium
screw beat 825
screw binding 797
– problems 802
screw extruders
– multi screw 13
– single screw 13
screw frequency instabilities 825
screw geometry 540
screwless extruders 28
– drum extruder 30
screw, outside diameter (O. D.) 849
screw shank, rear vacuum seal round 69
screw wear 849
second law of thermodynamics 156
Secor's model for devolatilization in co-rotating twin screw extruders 745
self-tuning temperature controllers 140
self-wiping co-rotating twin screw extruders 705
setpoint 119, 121, 133
shark skin 431, 821
shear 202
– rate 203
– strain 204
– – rate 870
– strength 197
– stress 43
– viscosity 204
sheet extrusion 853
shish-kebab crystal morphology 238
short extruder 829
short residence times 24
simple conveying screws 629
simple proportional controller 123
simulating a mixing process 868
simulating polymer processes 861
simulation 873, 912
single screw extruders (SSE) 22
single screw extrusion 22
single screw residence time distribution (RTD) 487
single stage 13
sinh law 213
six-step variable voltage inverter 52
slenderness ratio 513
slide-plate screen changers 73
slot flank angle 610
slot geometry 609
slotted mixing sections 620
slow fluctuations in instability 827
slow frictional flow 260
SMV mixer *see* BMK mixer
solids conveying 6, 192, 537, 562
– angle θ 272, 277
– instabilities 829
– rate 286, 637
– zone 258
solids draining screw (SDS) 744
solid-state extrusion 38
– direct solid-state 38
– hydrostatic 38
spatial finite difference formulation 869
specifications on pressure transducers 93
specific energy consumption (SEC) 23, 301, 542, 850
specific enthalpy 241
specific extruder throughput (SET) 850
specific heat 239
spherulitic crystal morphology 238
spiral disk extruder 31
spiral mandrel die 671, 676, 678
square feed hoppers 68
square pitch extruder screw 509
standardize evaluation and testing of temperature sensors 105
standard or conventional extruder screw 23, 549
Staromix mixer 621
starve feeding 303, 831
state-of-the art techniques 862
static coefficient of friction 194
static mixers, geometry 460
static mixer, simulation 910
static mixing 459
stationary screw, barrel rotates, assumption 411
statistical process control (SPC) 625
statistical rated life of a thrust bearing, formula 62
Stefan-Boltzmann law 169
stock temperature measurement 102
– flush-mounted temperature sensor 104
– straight immersion temperature sensor 104
Stokes drag force 479
strain distribution functions (SDF) 455
strain gauge transducer 88
strain-induced crystallization 159
strain rates, and degradation 811
Strata-blend mixer 623
super-extrusion 843, 844

T

Tadmor melting model 326
taper angle 674
T-die 663
Technoform process 694
temperature 86
temperature controller 126
– analog 126
– digital 126
temperature control system 116
– closed loop 116
– feedback 116
temperature measurement 96
– radiation pyrometers 97
– resistive temperature sensors 97
– thermocouple temperature sensors 97
temperature profiles 367, 420
test methods for P-gels 839
test methods for wear 782
The Madison Group 610
thermal analysis techniques 775
thermal barrier 65
thermal characteristics of the system 128
thermal characterization 247
thermal conductivity 234, 235
thermal degradation 803
thermal diffusivity 167, 242
thermal homogenization 467
thermal optical analysis (TOA) 248
thermal properties 191, 233
thermal stability 23
– of a polymer 246
thermal time distribution 467
thermistors 97
thermochromic materials 774
– for temperature related problems 773
thermochromic powders 774
thermocouple (TC) temperature sensors 97–99
thermodynamics 153
thermoelectric effect 97
thermoelectric transducers 97
thermogravimetric analyzer (TGA) 247
thermomechanical analysis (TMA) 248
thermoplastics 1
thermosets 1
thixotropic 219
three-dimensional BEM package 610
three-dimensional finite element simulation, FIDAP™ 885
three-dimensional models 861
three-dimensional simulation 885
three-phase full wave rectifier 54
three-stage extruder screw 562
throttle ratio, ratio between pressure flow to drag flow 43, 353
thrust bearing assembly 61
time constant of the closed-loop system 132
timeline, leading up to problem 765
time-proportioning power controller 126
tipstreaming 477
torque 510
torque (T) 207
torsional braid analysis (TBA) 248
total flight width (pw) 544
total process control 140
total strain 453
tracking tracer ink 872
transfer function for a reverse-acting controller 119
transparency 853
troubleshooting 763
– feeding system 778
– heating and cooling system 778
– machine-related problems 776
– tools 768
Troubleshooting the Extrusion Process, book 763
true proportional power controller
– current proportioning controller 126
– phase-angle-fired proportional controller 127
true total extrusion process control 141
tubing 671
– dies 668
Turbo-Screw™ 620, 906
Twente Mixing Ring (TMR) 621
twin ram extruder 41
twin screw devolatilization systems 561
twin screw extruder (TSE) 22, 24, 895
– advantages over single screw extruders 697
– characteristics 699
two-dimensional BEM analysis 610
two-dimensional flow analysis 361
two-dimensional power law analysis 525
two-stage devolatilizing extruder screw 554
types of mixing motion
– convective motion 441
– molecular diffusion 441
– turbulent motion 441

U

ultrahigh molecular weight polyethylene (UHMWPE)
– extrusion of 37
ultrasonic transducers 112
ultrasonic transit time (“Laufzeit”) 113
ultrasonic vibration 843, 844
ultrasound transmission time (UTT) 105
understanding of the extrusion process 764
uniformity 690
Union Carbide (UC) mixing section 585

V

vacuum feed hopper 69
variable decreasing pitch (VDP) 19
variable depth mixers 622
variable pitch extruder screw 550
variable reducing pitch (VRP) screw 551
velocity patterns 699
velocity profiles 379, 420, 715
– for a Newtonian fluid 42
vented extruders 16
– with axial adjustment capability of the screw 559
vernier screw mechanism 50
viscoelastic fluids 653
viscometric flow 210
viscosity, and pressure 214
viscosity, and temperature 214
viscous dissipation 390
viscous encapsulation 691, 889, 891
viscous flow *see* rapid flow
viscous heat generation 168
viscous heating 800
Voight model 871
volumetric melt conveying rate for a Newtonian fluid 519

W

wall draw ratio (WDR) 672
wear
– abrasive 787
– causes of wear 787
– corrosive 788
– five mechanisms of wear 781
– grooves 286
– machinery 780
– metal-to-metal 789
– monitoring 850
– screw 849
– test methods 782
weighted average total strain (WATS) 455
weld lines in product 852
whirling 516
Wien's law 169
Williams-Landel-Ferry (WLF) equation 216
wire coating 881

X

Xanthos 4

Z

zero-meter screw 551
Ziegler-Nichols method 137